

# **PROCEEDINGS**

**Eleventh International Symposium on  
Space Terahertz Technology**

**May 1-3, 2000**

**On the Grounds of  
The University of Michigan  
Ann Arbor, Michigan**



**Organized by: The University of Michigan, Solid-State Electronics Laboratory**

## Preface

The 11<sup>th</sup> International Symposium on Space Terahertz Technology was held on the campus of The University of Michigan on May 1-3, 2000. The Symposium was attended by 120 scientists and engineers from around the world. Nearly 70 papers were presented in 10 regular sessions, a poster session and an opening session with 2 invited papers. The papers covered the wide range of topics included in THz technology. Superconducting technologies such as SIS and HBT mixers, semiconductor based mixers and multipliers, semiconductor sources and several other THz technologies were covered. The two invited papers in the opening session discussed potential future uses of this technology for DARPA and ARO needs.

I would like to thank Ms. Catharine June for handling the infinite number of tasks involved in this conference, including running the Web page, organizing the local arrangements and putting together the Symposium Digest.

The 2001 conference will be held at

Humphrey's Half Moon Inn  
Shelter Island  
San Diego, California  
February 14-16, 2001

The abstract due date is December 1, 2000. This early date will allow an overlap with the FIRST science workshop to be held during the same week in San Diego. Additional conference information is available from

Dr. Imran Mehdi  
Mail Stop 168-314  
Jet Propulsion Laboratory  
Pasadena, CA. 91109-8001  
Phone 818-354-2001  
Fax 818-393-4683  
Email: [imran@merlin.jpl.nasa.gov](mailto:imran@merlin.jpl.nasa.gov)

I am looking forward to seeing all of you in San Diego.

Jack East  
Chair, 11th Symposium on Space Terahertz Technology

# 11TH INTERNATIONAL SYMPOSIUM ON SPACE TERAHERTZ TECHNOLOGY



**Monday - Wednesday, May 1-3, 2000**  
**University of Michigan**  
**Ann Arbor, Michigan**

---

## DAY 1 - MONDAY, MAY 1

---

### Opening Session

**Chair: Jack East**

Introduction and Welcome	Fawwaz Ulaby	U. Michigan	
Next Generation of Terahertz Sources and Detectors	Edgar J. Martinez	DARPA	1
Terahertz Electronics Research for Defense: Novel Technology and Science	Dwight Woolard	ARO	22

---

### Session 1: HEB 1

**Chair: Eyal Gerecht**

Frequency Dependence Noise Temperature of the Lattice Cooled Hot-Electron Terahertz Mixer	A. D. Semenov, H.-W. Huebers, J. Schubert, G.N. Gol'tsman, A.I. Elantiev, B. M. Voronov, E. M. Gershenzon	State Ped. U., Moscow DLR, Germany	39
Successful Operation of a 1 THz NbN Hot-Electron Bolometer Receiver	C.-Y. E. Tong, J. Kawamura, T. R. Hunter, D. C. Papa, R. Blundell, M. Smith, F. Patt, G. Gol'tsman, E. Gershenzon	Harvard Caltech Submillimeter Telescope Obs. Moscow State Ped. U.	49
Microstripline-Coupled Quasi-Optical Niobium Hot Electron Bolometer Mixers around 2.5 THz	W. F. M. Ganzevles, J. R. Gao, P. Yagoubov, T. M. Klapwijk, P. A. J. de Korte	DIMES SRON	60
Direct and Heterodyne Response of Quasi Optical Nb Hot-Electron Bolometer Mixers Designed for 2.5 THz Radiation Detection	W. F. M. Ganzevles, J.R. Gao, W.M. Laauwen, G. de Lange, T. M. Klapwijk, P. A. J. de Korte	DIMES SRON	69
Aluminum Sub-Micron Superconducting Hot-Electron Bolometer Mixer	I. Siddiqi, A. Verevkin, D. E. Prober, A. Skalare, B.S. Karasik, W.R. McGrath, P. Echternach, H.G. LeDuc	Yale JPL	82

---

**Session 2: SIS 1****Chair: Vladimir Mitin**

Broadband Array SIS Mixers for 780-880 GHz with Aluminum Tuning Circuits	S. Haas, S. Wulff, D. Hottgenroth, N. Honingh, K. Jacobs	KOSMA, Germany	95
A 350 GHz SIS Imaging Module for the JCMT Heterodyne Array Receiver Programme (HARP)	J. Leech, S. Withington, G. Yassin, H. Smith, B.D. Jackson, J.R. Gao, T.M. Klapwijk	U. Cambridge SRON DIMES	105
A Low Noise NbTiN-based 850 GHz SIS Receiver for the Caltech Submillimeter Observatory	J. W. Kooi, J. Kawamura, J. Chen, G. Chattopadhyay, J.R. Pardo, J. Zmuidzinas, T.G. Phillips, B. Bumble, J. Stern, H.G. LeDuc	Caltech JPL Tohoku University	116
Quasi-Optical Terahertz SIS Mixer	A. M. Baryshev, B. D. Jackson, G. de Lange, S. V. Shitov, N. Iosad, J. R. Gao, T. Klapwijk	SRON IREE RAS, Russia DIMES	129

**Session 3: SEMI 1****Chair: George Haddad**

State of the Art of Two Terminal Devices as Millimeter- and Submillimeter-Wave Sources	H. Eisele, G. Haddad	U. Michigan	139
The Oxide Barrier Varactor	T. W. Crowe, Y. Duan	UVa	153
Power Generation with Fundamental and Second-Harmonic Mode InP Gunn Oscillators - Performance Above 200 GHz and Upper Frequency Limits	R. Kamoua, H. Eisele	SUNY, Stony Brook U. Michigan	155
GaN-based NDR Devices for THz Generation	E. Alekseev, A. Eisenbach, D. Pavlidis, S.M. Hubbard, W. Sutton	U. Michigan	162
Broadband Fixed-Tuned Subharmonic Receivers to 640 GHz	J. Hesler	UVa	172
Stabilized, Integrated, Far-Infrared Laser System for NASA/Goddard Space Flight Center	E. R. Mueller, J. Fontanella, R. Henschke	DeMaria ElectroOptics Systems, Inc., CT	179

**DAY 2 - TUESDAY, MAY 2****Session 4: HEB 2****Chair: Sigrid Yngvesson**

Superconducting Transition Edge Sensor Bolometer Arrays for Submillimeter Astronomy	D.J. Benford, C. A. Allen, A. S. Kutyrev, S.H. Moseley, R.A. Shafer, J. A. Chervenak, E. N. Grossman, K. D. Irwin, J. M. Martinis, C. D. Reintsema	NASA NIST	187
---	--	--------------	-----

Comparison of Two Types of Andreev Reflection Hot-Electron Microbolometer for Submillimeter Radio Astronomy	A. N. Vystavkin	IREE RAS, Russia	197
Development of Focal Plane Arrays Utilizing NbN Hot Electron Bolometric Mixers for the THz Regime	E. Gerecht, C. F. Musante, Y. Zhuang, M. Ji, K. S. Yngvesson, T. Goyette, J. Waldman	U. Mass.	209
IF Bandwidth of Phonon Cooled HEB Mixers Made from NbN films on MgO Substrates	S. Cherednichenko, M. Kroug, P. Yagoubov, H. Merkel, E. Kollberg, K.S. Yngvesson, B. Voronov, G. Gol'tsman	Chalmers U. U. Mass. Moscow State Ped. U.	219
<b>Session 5: SIS 2</b>		<b>Chair: Robb McGrath</b>	
Anomalous Pumped and Unpumped I-V Characteristics of Nb SIS Terahertz Mixers with NbTiN Striplines	B. Leone, B. D. Jackson, J. R. Gao, T. M. Klapwijk, W. M. Laauwen, G. de Lange	U. of Groningen, DIMES SRON	228
NbTiN/SiO <sub>2</sub> /NbTiN and NbTiN/SiO <sub>2</sub> /Al Tuning Circuits for 1 THz Waveguide SIS Mixers	B. D. Jackson, G. de Lange, W.M. Laauwen, J. R. Gao, N.N. Iosad, T.M. Klapwijk	SRON DIMES	238
A Single-Chip Balanced SIS Mixer for 200-300 GHz	A. R. Kerr, S.-K. Pan, A.W. Lichtenberger, N. Horner, J. E. Effland, K. Crady	NRAO UVa	251
Performance of Sub-Harmonic Mixing With an SIS Junction	S.-C. Shi, W.-L. Shan, T. Noguchi, K.-C. Xiao	Purple Mountain Observatory, China NRO, Nagoya U.	260
<b>Session 6: MICROMACHINING</b>		<b>Chair: John Papapolymerou</b>	
Micromachined Waveguide Components for Submillimeter-Wave Applications	K. Hui, W. L. Bishop, J. L. Hesler, D. S. Kurtz, T. W. Crowe	UVa	269
A New Laser Micromachining System for the Fabrication of THz Waveguide and Quasi-Optical Components	C. Walker, C. D. D'Aubigny, C. Groppi, J. Papapolymerou, G. Chin, A. Lichtenberger	U. Arizona NASA UVa	275
Development of W-Band Low-Loss MEMS Switches	J. Rizk, J. Muldavin, G.-L. Tan, G. M. Rebeiz	U. Michigan	276
The Frameless Membrane: A Novel Technology for THz Circuits	J. Bruston, S. Martin, A. Maestrini, E. Schelcht, P. Smith, I. Mehdi	JPL	277
200 and 400 GHz Schottky Diode Multipliers Fabricated with Integrated Air-Dielectric "Substrateless" Circuitry	E. Schlecht, J. Bruston, A. Maestrini, S. Martin, D. Pukala, R. Tsang, A. Fung, R. P. Smith, I Mehdi	JPL Cree, Inc., NC	287

Development of Efficient Backward Wave Oscillators for Submillimeter Applications	J. Nielson, L. Ives, M. Caplan	Calabazas Creek Research, Inc., CA	296
---	--------------------------------	------------------------------------	-----

---

**Session 7: POSTER SESSION**

**Chair: Tom Crowe**

Two-Stream Ballistic Instability and Terahertz Oscillation Generation in $n^+nn^+$ -Ballistic Diodes and Field-Effect Transistors	Z. S. Gribnikov, N. Z. Vagidov, V. V. Mitin	Wayne State U.	304
Sb-Heterostructure High Frequency Zero-Bias Direct Detection Diodes	J. N. Schulman, D. H. Chow, C. W. Pobanz, H. L. Dunlap, C. D. Haeussler	HRL	311
Phase Gratings as LO-Distributors in Submm Heterodyne Arrays	T. Klein, G.A. Ediss, R. Güsten, C. Kasemann	MPIfR-Bonn	313
Narrow-Band Terahertz Waveform Generation in Periodically-Poled Lithium Niobate	T. Meade, Y.-S. Lee, V. Perlin, H. Winful, T. B. Norris, A. Galvanauskas	U. Michigan IMRA America, MI	326
Resonant Tunneling THz Oscillator at Fixed Bias Voltages	P. Zhao, H. L. Cui, D. Woolard	Stevens Inst. Tech., NJ ARO	336
SuperMix Now Available	F. Rice, J. Ward, J. Zmuidzinias, G. Chattopadhyay	Caltech	341
Simulated Performance of Multi-Junction Parallel Array SIS Mixers for Ultra Broadband Submillimeter-Wave Applications	M. Salez, Y. Delorme, M.-H. Chung, F. Dauplay	DEMIRM, Paris	343
Integrated Superconducting Receiver as a Tester for Sub-millimeter Devices at 400-600 GHz	S. V. Shitov, A. M. Shtanyuk, V. P. Koshelets, G. V. Prokopenko, L. V. Filippenko, A. B. Ermakov, M. Levitchev, A. V. Veretennikov, H. Kohlstedt, A. V. Ustinov	IREE RAS, Russia IAP RAS, Russia ISI Res. Ctr. Inst. of Solid State Physics, Russia U. Erlangen-Nuernberg	359
Modelling Few-Moded Horns for Far-IR Space Applications	R. Colgan, J. A. Murphy, B. Maffei, C. O'Sullivan, R. Wylde, P. Ade	National U., Ireland Queen Mary and Westfield College, UK	368
Submillimeter-Wave Spectral Response of Twin-Slot Antennas Coupled to Hot Electron Bolometers	R.A. Wyss, A. Neto, W.R. McGrath, B. Bumble, H. LeDuc	JPL	379
Tunable Antenna-Coupled Intersubband Terahertz (TACIT) Detectors for Operation Above 4K	C. L. Cates, J. B. Williams, M. S. Sherwin, K. D. Maranowski, A. C. Gossard	UC - Santa Barbara	389
SIS Receivers for the 1.2 THz Frequencies Using NbTiN/AlN/Nb Junctions	A. Karpov, J. Zmuidzinias, F. Rice, D. Miller, J.A. Stern, H.G. LeDuc	Caltech JPL	397
Study of Parylene as Anti-reflection Coating for Silicon Optics at THz Frequencies	M. Ji, C. Musante, S. Yngveson, A. J. Gatesman, J. Waldman	UMass	407

Optimization of Superconducting Hot-Electron Sensors: Controlling of Electron-Phonon Relaxation	A. Sergeev, V. Mitin	Wayne State U.	416
A Compact Fiber-Pigtailed, Terahertz Time Domain Spectroscopy System	D. Zimdars, J.V. Rudd, M. Warmuth	Picometrix, Inc.	423
An Efficient Technique for the Optimization of Submillimeter-wave Schottky-diode Harmonic Multipliers	C.-C. Lee, B. Gelmont, D. Woolard	UVa ARO	433
Developments of the 810-GHz SIS Receiver with Nb-based Junctions	H. Maezawa, T. Noguchi, S.-C. Shi, Y. Sekimoto, S. Yamamoto	U. Tokyo Nobeyama Radio Obs. Purple Mountain Obs.	444
Bias Dependence of the Thermal Time Constant in Nb Superconducting Diffusion-Cooled HEB Mixers	D. Wilms Floet, J. R. Gao, T. M. Klapwijk, P. A. J. de Korte	DIMES SRON	455
A Cryosystem for Optical Evaluation of the Normal Metal Hot-electron Bolometer	D. Chouvaev, L. Kuzmin	Chalmers U.	465

---

### DAY 3 - WEDNESDAY, MAY 3

---

#### Session 8: HEB 3

Chair: Eric Kollberg

A Distributed Device Model for Phonon-Cooled HEB Mixers Predicting IV Characteristics, Gain, Noise and IF Bandwidth	P. Khosropanah, H. Merkel, S. Yngvesson, A. Adam, S. Cherednichenko, E. Kollberg	Chalmers U. U. Mass. Supélec	474
Properties of Nb Thin Films and their Application for Diffusion-Cooled Hot-Electron Bolometer	M. Frommberger, F. Mattiocco, P. Sabon, M. Schicke, K. F. Schuster, O. Laborde	IRAM, France CRTBT, France	489
Diffusion-Cooled Aluminum Hot-Electron Bolometer Mixers at Submillimeter Wavelengths	A. Skalare, W. R. McGrath, P. M. Echternach, H. G. LeDuc, I. Siddiqi, A. Verevkin, D.E. Prober	JPL Yale U.	501
Noise and Mixing in Aluminum Based Sub-Micron Hot-Electron Bolometers	A. Verevkin, I. Siddiqi, D. E. Prober, A. Skalare, B.S. Karasik, W.R. McGrath, P.M. Echternach, H.G. LeDuc	Yale U. JPL	513
Hot-Electron Detectors: Toward Record Sensitivity Via Disorder-Suppressed Electron-Phonon Coupling	M. E. Gershenson, D. Gong, T. Sato, B. S. Karasik, W. R. McGrath, A. V. Sergeev	Rutgers U. JPL Wayne State U.	514

#### Session 9: HIGH TC

Chair: Jeffrey Hesler

Quasi-optical High-Tc Superconductor Josephson Mixer at Terahertz Frequencies	M. Darula, A. D. Semenov, H.-W. Hübers, J. Schubert	ISI Research Center, Germany State Ped. U., Moscow DLR, Germany	524
---	---	--	-----

Systematic Study of IF Bandwidth in HTS Hot-Electron Bolometer Mixers	O. Harnack, K. Ilin, M. Siegel, B. S. Karasik, W. R. McGrath, G. de Lange	IfSI, Germany JPL SRON	525
YBa <sub>2</sub> Cu <sub>3</sub> O <sub>7-δ</sub> Hot-Electron Bolometer Mixer at 0.6 THz	S. Cherednichenko, F. Rönning, G. Gol'tsman, E. Kollberg, D. Winkler	Chalmers U. Moscow State Pedagogical U., Russia	526
Externally Phase Locked Submm-Wave Flux Flow Oscillator for Integrated Receiver	V. P. Koshelets, A. B. Ermakov, S. V. Shitov, P. N. Dmitriev, L. V. Filippenko, A. M. Baryshev, W. Luinge, J. Mygind, V. L. Vaks, D. G. Pavel'ev	IREE, Russia SRON Tech. U., Denmark IPM, RAS, Russia Nizhny Novgorod State U. Russia	532
Evaluation of High-Tc Elements in Submm-Mixers	D. Diehl, R. Zimmerman, J. Scherbel, M. Darula, O. Harnack, M. Siegel	RPG Radiometer-physics, Germany IfSIF, Germany	542

---

## Session 10: SEMICONDUCTOR 2

Chair: Imran Medhi

Planar Frequency Doublers and Triplers for FIRST	N. R. Erickson, G. Narayanan, R. P. Smith, S. C. Martin, I. Mehdi, T. W. Crowe, W. L. Bishop	UMass JPL UVa	543
High Q InP-based Varactor Diodes	T. David, S. Arscott, P. Mounaix, X. Mélique, F. Mollot, O. Vanbésien, M. Chaubet, D. Lippens	U. of Science and Technology, U. de Lille Centre Nat. d'Etudes Spatiales, France	552
Heterostructure Barrier Mixers for Terahertz Applications	F. Podevin, P. Mounaix, O. Vanbésien, M. Chaubet, D. Lippens	U. of Science and Technology, U. de Lille Centre Nat. d'Etudes Spatiales, France	561
A 4-8 GHz Quasi-MMIC IF Amplifier for a 690 GHz SIS Receiver	J. Ward, D. Miller, J. Zmuidzinas, P. O'Brien, H. G. LeDuc, R. Bicknell-Tassius	Caltech JPL	570
Nonlinear Transport in Ballistic Semiconductor Diodes with Negative Effective Mass Carriers	B.R. Perkins, J. Liu, A. Zaslavsky, Z.S. Gribnikov, V.V. Mitin, E.P. De Poortere, M. Shayegan	Brown U. Wayne State U. Princeton	582

---

## Session 11: ANTENNAS AND QUASI OPTICAL STRUCTURES

Chair: Linda Katehi

Instrumentation and Testing of Submillimeter Wave Compact Antenna Test Ranges	J. Säily, J. Ala-Laurinaho, J. Häkli, J. Tuovinen, A. Lehto, A. V. Räisänen	Helsinki U. MilliLab, Finland	590
A Pickett-Potter Horn-Reflector Antenna for Submillimetre-Wave Applications	P. Kittara, G. Yassin, S. Withington, H. Smith	U. Cambridge	598
A Novel Type of Phase Grating for THz Beam Multiplexing	U. U. Graf, S. Heyminck	KOSMA	608

Quasi-Optical Multiplexing Using Reflection Phase Gratings	W. Lanigan, N. Trappe, J. A. Murphy, R. Colgan, C. O'Sullivan, S. Withington	National U., Ireland U. Cambridge	616
Design and Analysis of a Hybrid Feed Antenna for a Flux-Flow Oscillator Integrated 460 GHz SIS Receiver	M.-H. Chung, M. Salez	DEMIRM, Paris	626



# *Next Generation of Terahertz Sources and Detectors*

*Dr. Edgar J. Martinez  
Program Manager  
Microsystems Technology Office*

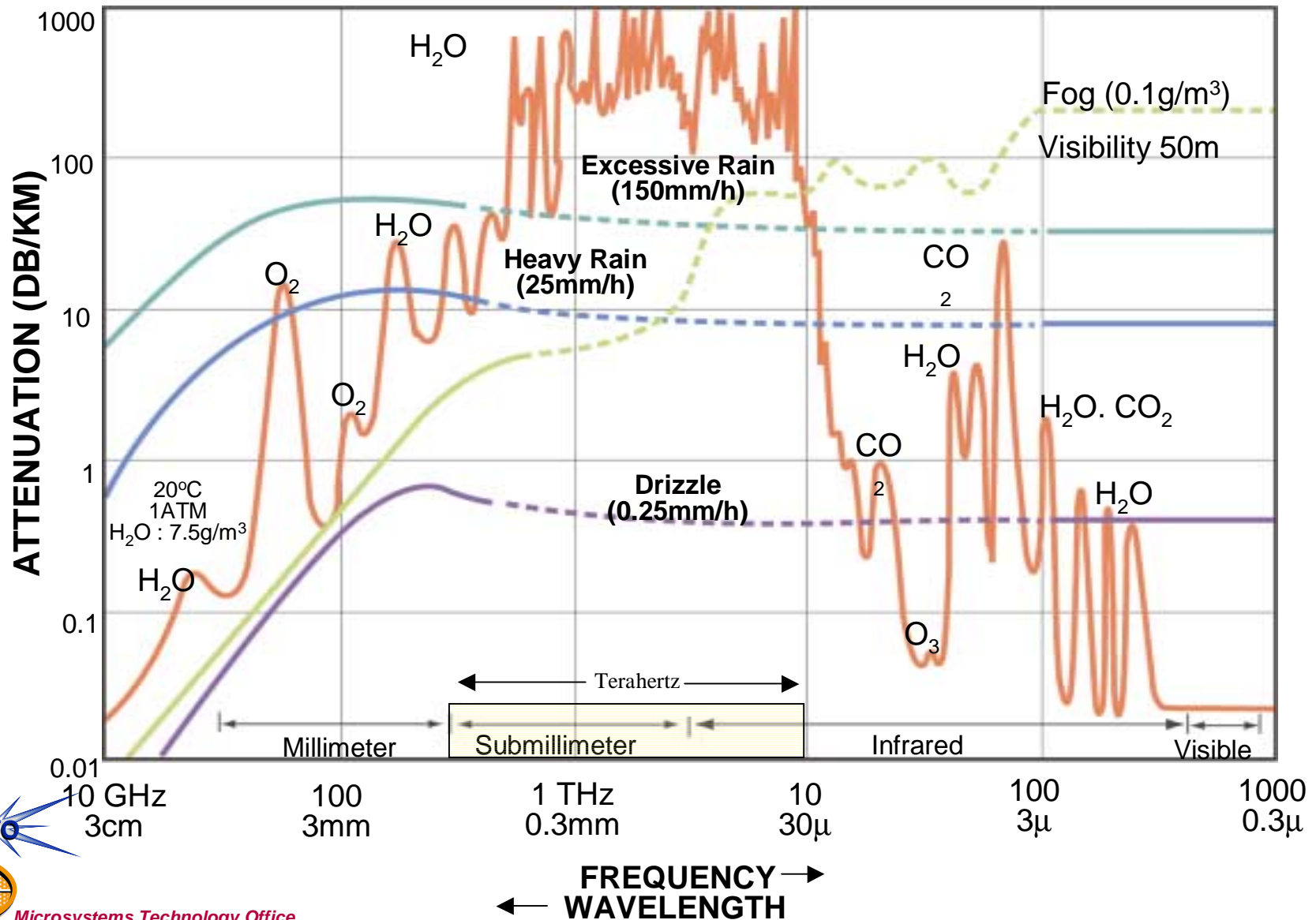
3701 N. Fairfax Drive  
Arlington, VA 22203  
Tel. (703) 696-7436  
emartinez@darpa.mil



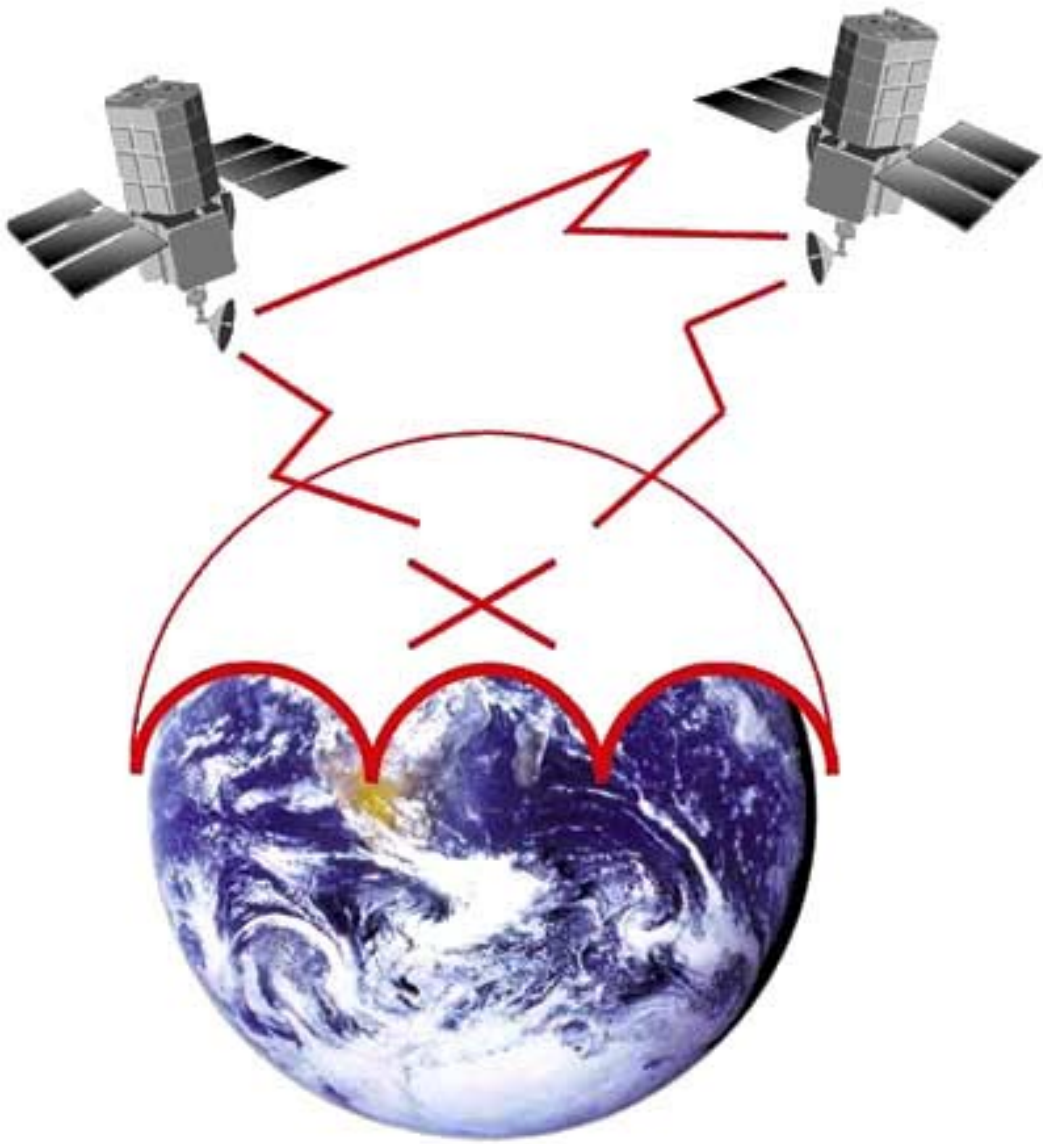
*Microsystems Technology Office*

# *E/M Attenuation vs Frequency*

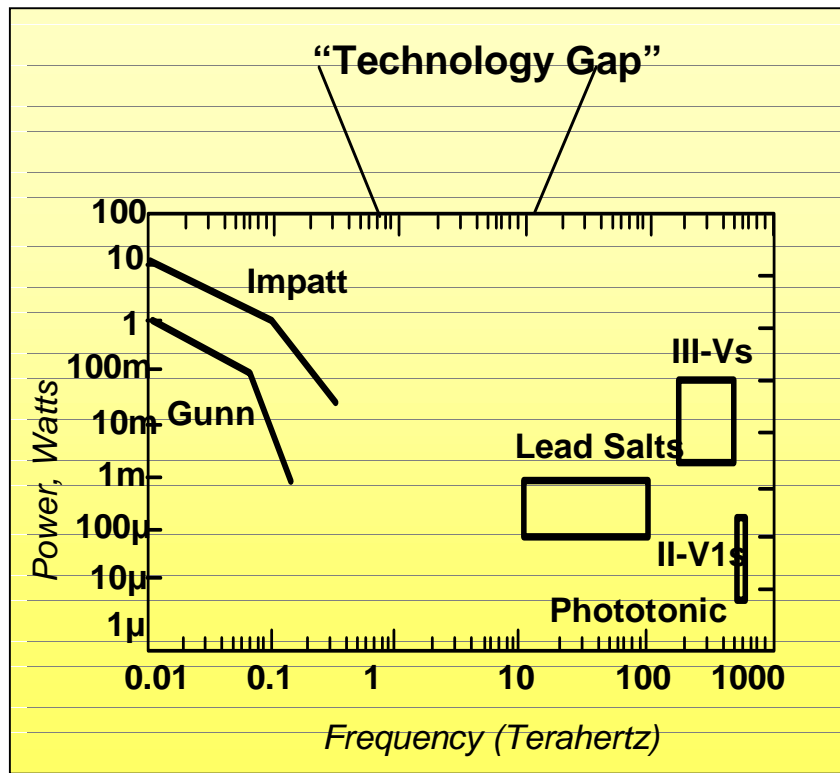
## *Limitations of Current Technology*



*Using a limitation to our advantage!!!*



# Program Objectives



Explore innovative semiconductor device and circuit concepts for the demonstration of high power sources and high sensitivity detectors for the region of the electromagnetic spectrum between 0.3-10 THz (1 - 0.03 mm)



# *Technical Challenges*

## *THz Sources*

- Achievement of high output power (at least mWs)
- Efficiency
- Compactness
- Tunability for certain applications

## *THz Detectors*

- High Sensitivity and Detectivity
- Quantum Efficiency
- Compactness





# Technical Approaches

## THz Sources

### Electrical

- InP- and Sb-based HEMTs
- GaN-based Gunn diodes
- Sb-based Stark Ladders and Quasi-optic Combiners
- Passives and Waveguides

### Optical

- Optical Photomixing
- SiGe VCSELs

## THz Detectors

- RTD-based
- Electro-acoustic Detectors (HEMTs)
- Photon assisted tunneling in QWs



Department of Physics  
Microwave Laboratory



# Quantum Device Technologies for THz Communications and Imaging

## OBJECTIVE:

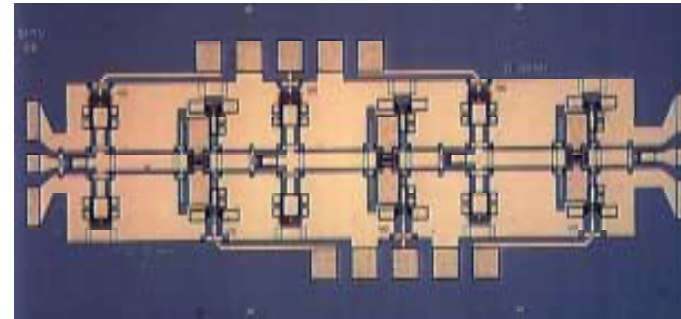
Develop monolithic integrated circuits capable to generate power at 0.33 THz, 0.66 THz, 1 THz and 3 THz.

## APPLICATIONS:

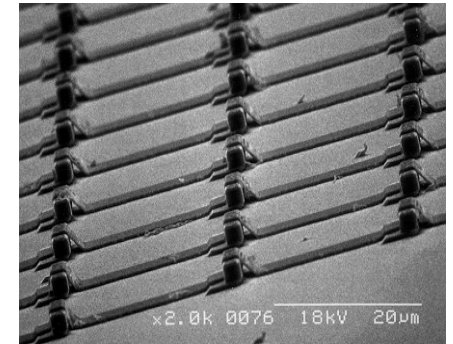
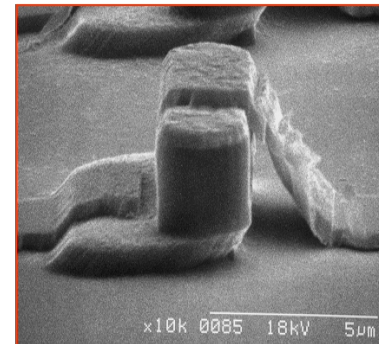
- Remote sensing
- High resolution imaging
- High data-rate space communication

## APPROACH:

- Develop high performance HEMT MMIC sources with integrated antennas for 0.3 THz to 1 THz frequency range
- Develop novel superlattice oscillators and multipliers for 1 THz to 10 THz frequency range

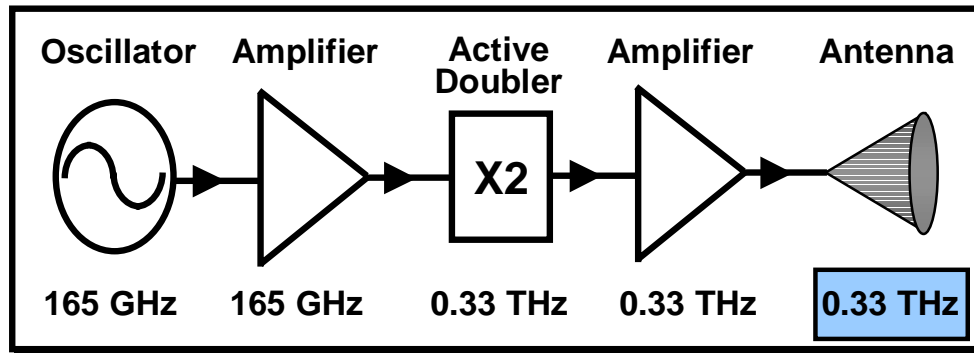


State of the art HEMT MMIC



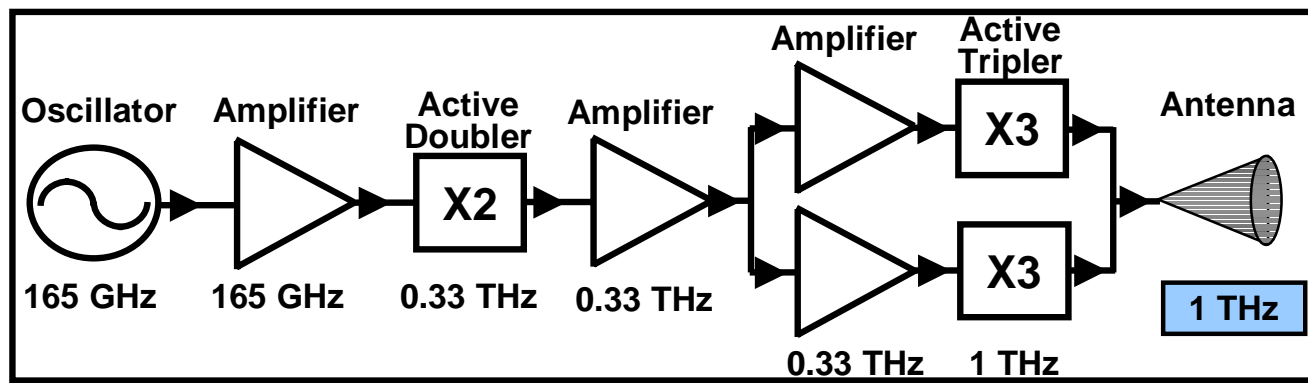
Quasi-optical superlattice array for harmonic generation

# 0.3 THz to 1 THz SOURCES



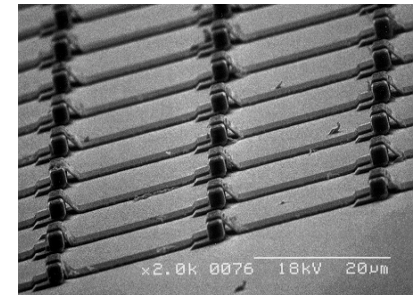
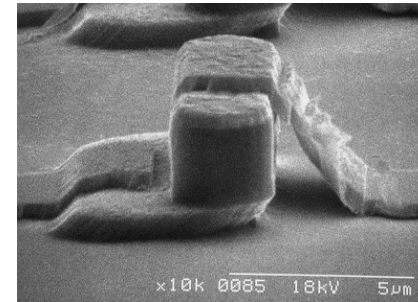
## CHALLENGES

- MMIC design
- Low-loss passive components
  - Antennas
  - Transmission lines
  - Power combiners
- Spatial power combining
- Packaging
- Testing

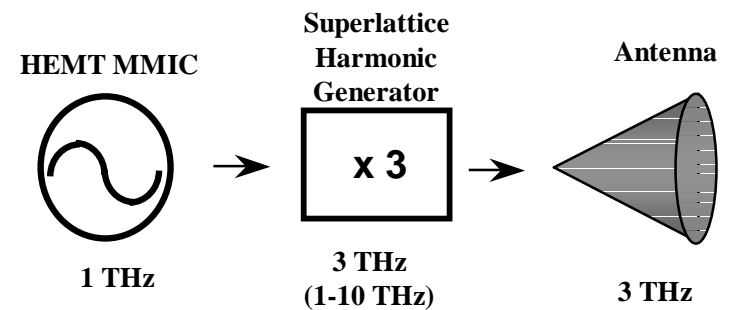


# *InAs/AlSb/GaSb Materials Effort*

- 1-10 THz source development
  - collaboration with UCSB (Allen)
  - InAs/AlSb superlattice devices
  - emphasis on harmonic generation
- Materials support for Raytheon (Frazier)
  - RTD structures
  - High  $J_p$
  - IMSC MBE Capability



**Quasi-optical superlattice array  
for harmonic generation**



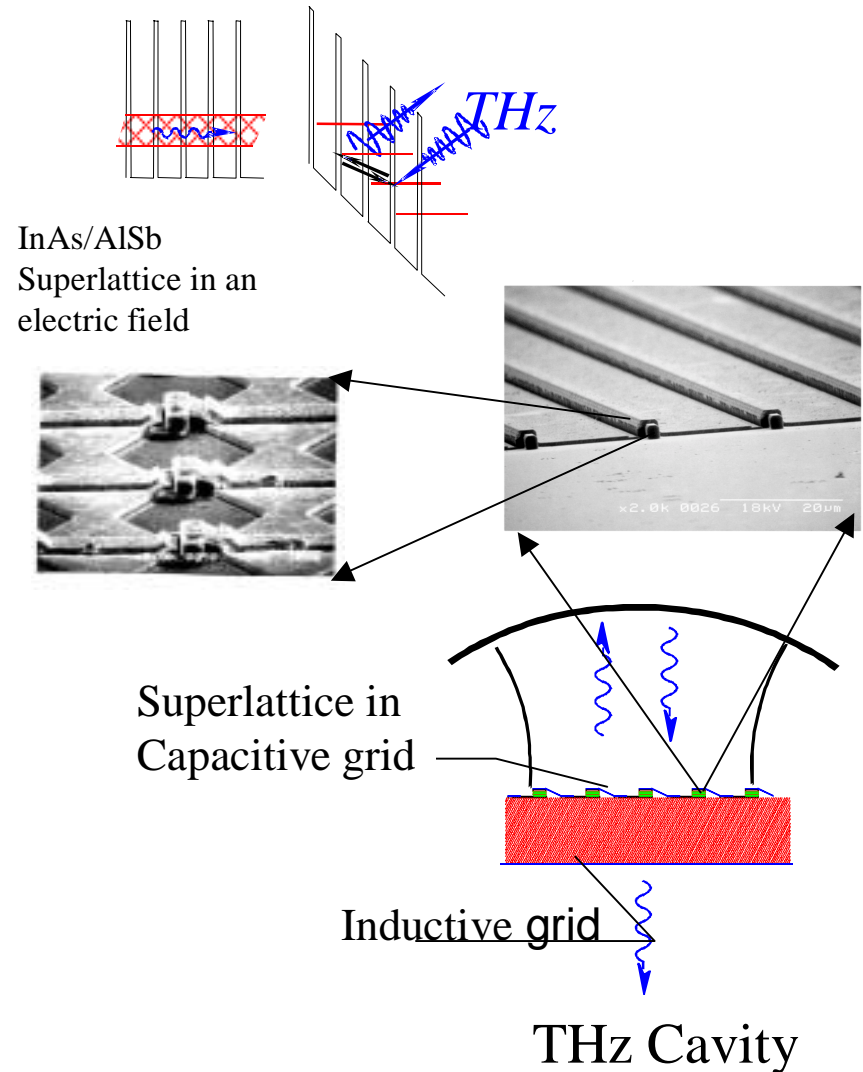
# Solid State Terahertz Sources for Sensing and Satellite Communications

## OBJECTIVE:

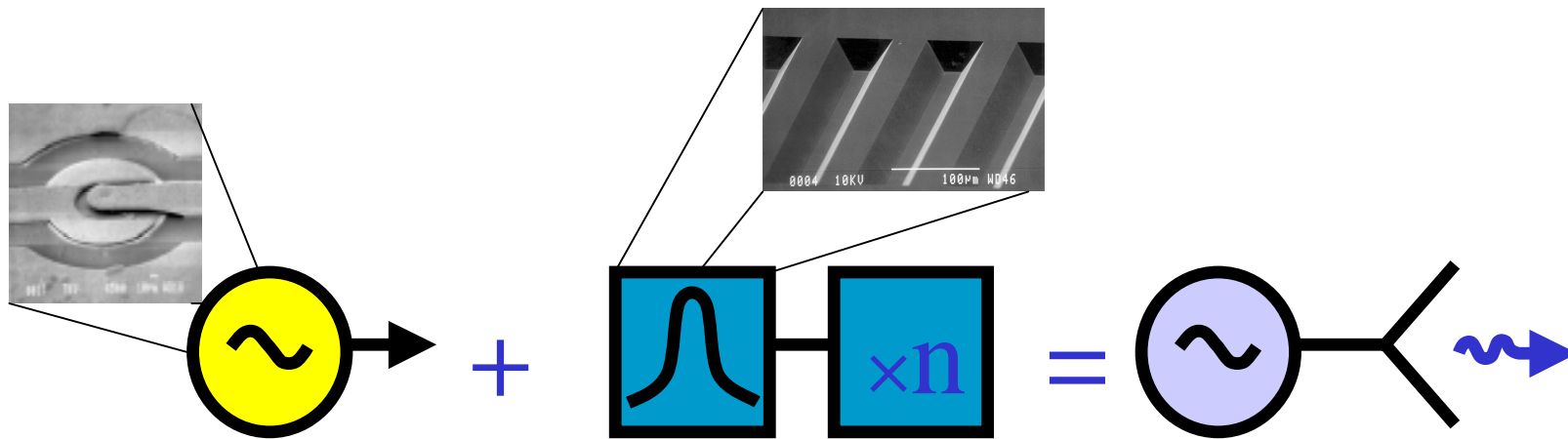
Develop and demonstrate an electrically excited solid-state Terahertz sources, capable of delivering  $>1$  mW of power in the range above 1 THz

## APPROACH:

- Implementation of InAs/AlSb superlattice, Stark ladders for THz generation
- Implementation of Quasi-optic arrays for power combining
- Demonstration of THz harmonic generation



# Solid-State Terahertz Sources



GaN NDR Diodes  
for THz signal  
Generation

Micromachined  
Resonator;  
Filter/Multiplier

Solid-State  
Terahertz Source

## TECHNICAL APPROACH:

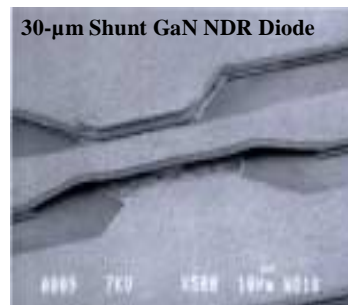
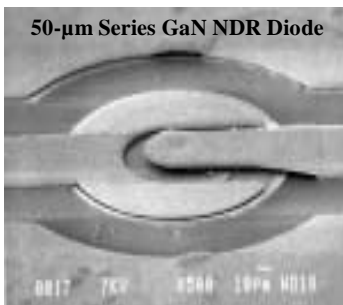
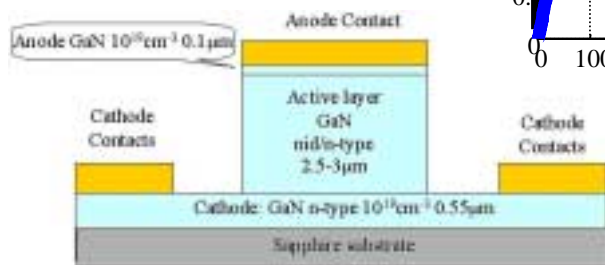
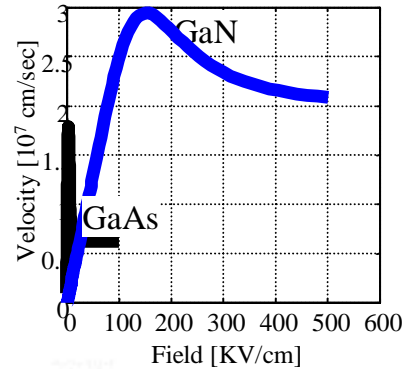
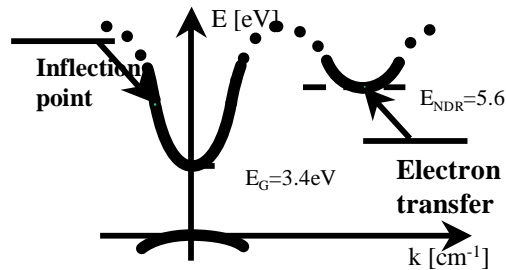
- Unique approach combining new semiconductor and micromachined concepts
- Semiconductor device potential for high-power fundamental or harmonic sources
- Possibility to apply micromachined concept to other sources developed under this program



Microsystems Technology Office



# III-N Terahertz Gunn Diodes



## OBJECTIVE:

Take advantage of the electron transport and material properties of III-N semiconductors for the demonstration of Gunn diode THz sources

## CHALLENGES:

- Achieve good quality GaN materials
- Demonstrate NDR performance in WBG semiconductors
- Demonstrate generation of THz radiations

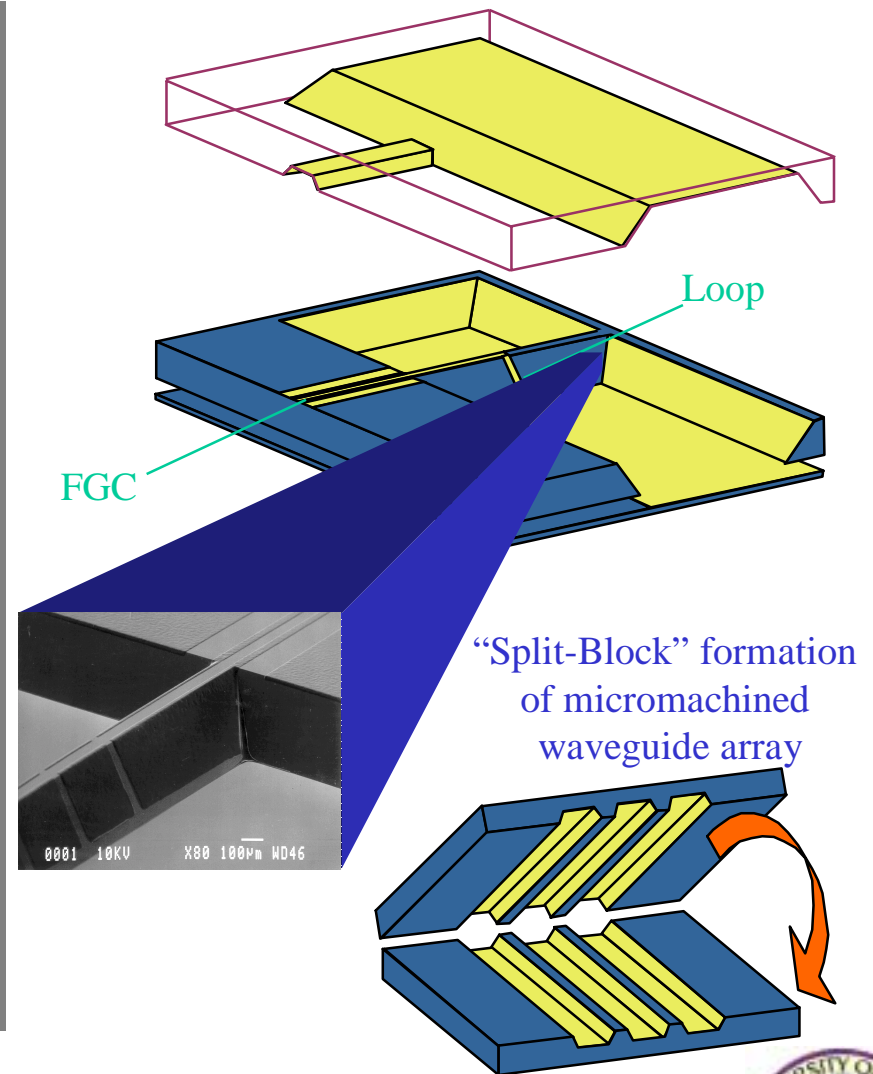
# Passive Silicon Micromachined Structures for THz Applications



## APPROACH:

*Use Silicon Micro-machining Technology for the Development of:*

- THz waveguides for high-performance low-loss circuits
- Electric and magnetic transitions from planar transmission lines to micromachined waveguides
- Transitions between waveguides and planar micromachined antennas
- Compact resonators for GaN Gunn sources



# All-Solid-State Photomixing Transmitter



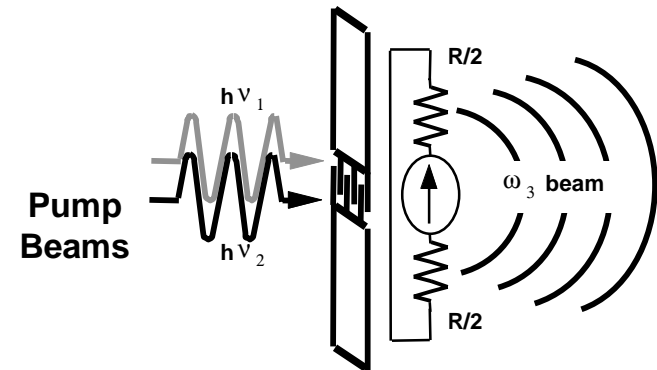
## OBJECTIVES:

Develop a solid-state source for the THz region having up to 1 mW output power and:

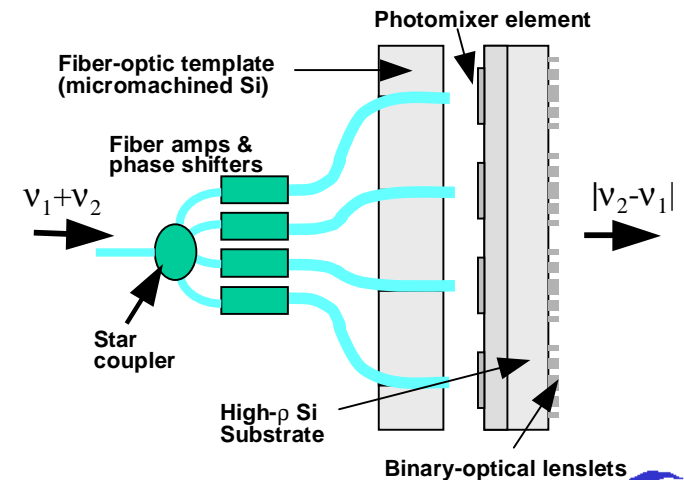
- Stable continuous-wave performance
- Room-temperature operation
- Tunability up to ~1 octave
- Instantaneous frequency stability  $> 1:10^6$
- Phase lockability (required for comms)
- Good beam characteristics (TEM<sub>000</sub> Gaussian desirable)

## TECHNICAL APPROACH:

- Optical mixing in an ultrafast photoconductor (LT-GaAs)
- Couple internal THz photocurrents to a THz load (antenna)
- Implementation of power combining techniques



$$P_3 = \frac{R}{2} \eta_1 \lambda_1 \eta_2 \lambda_2 \left( \frac{e g}{h c} \right)^2 \frac{P_1 P_2}{\left[ 1 + (\omega_3 \tau)^2 \right] \left[ 1 + (\omega_3 R C)^2 \right]}$$



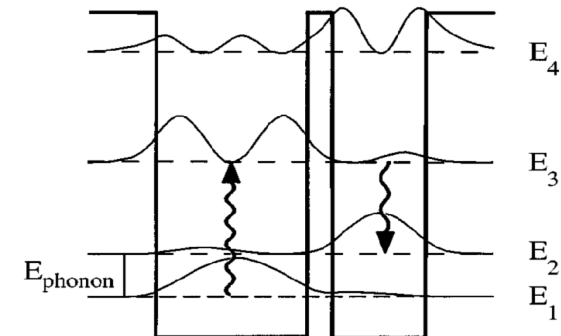
# THz Sources Based on Intersubband Transitions in SiGe Quantum Wells

## OBJECTIVE:

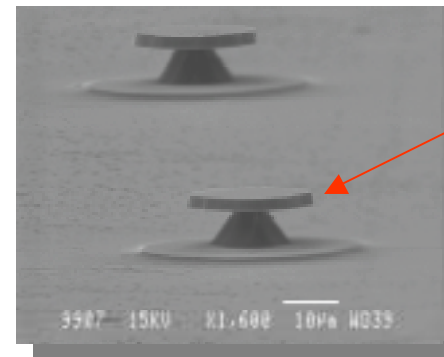
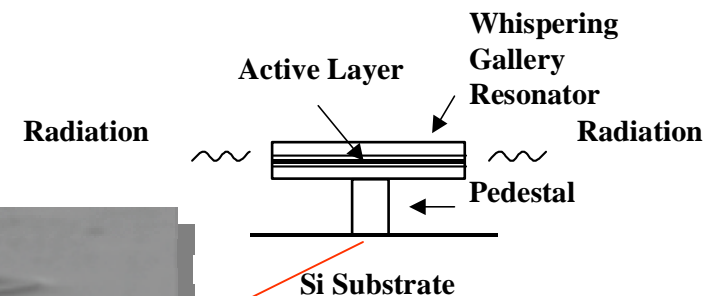
To demonstrate a SiGe, micro-disk cavity, intersubband laser suitable for communication systems

## APPROACH:

- Silicon micromachining for novel resonator design
- SiGe unipolar architecture
- E/M simulation for device optimization
- 1-10 THz operation

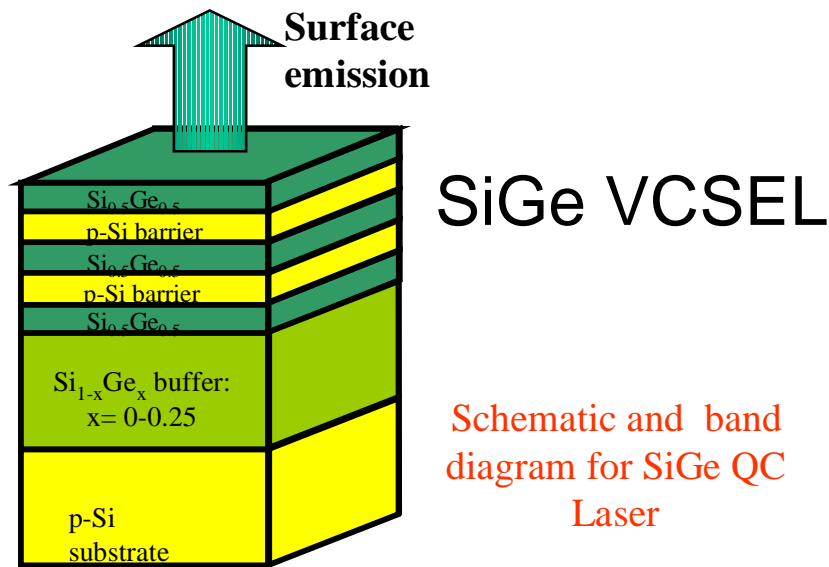


Quantum well transitions between  $E_3$  and  $E_2$ . Proposed device will use SiGe quantum wells and hole intersubband transitions.



Micro-disk lasers

# Vertical Cavity Silicon-Germanium Quantum Cascade Lasers for Terahertz Emission



## OBJECTIVE:

Develop and demonstrate a vertical cavity SiGe quantum cascade laser capable to operate in the THz region of the electromagnetic spectrum

## APPROACH:

- Characterization of ISB lifetimes in p-SiGe QWs
- Demonstrate FIR emission in p-SiGe tunnel barrier structures
- Demonstrate surface emission in p-SiGe quantum cascade structures
- Demonstrate vertical cavity SiGe quantum cascade device

# Solid-State Terahertz Detector Technology

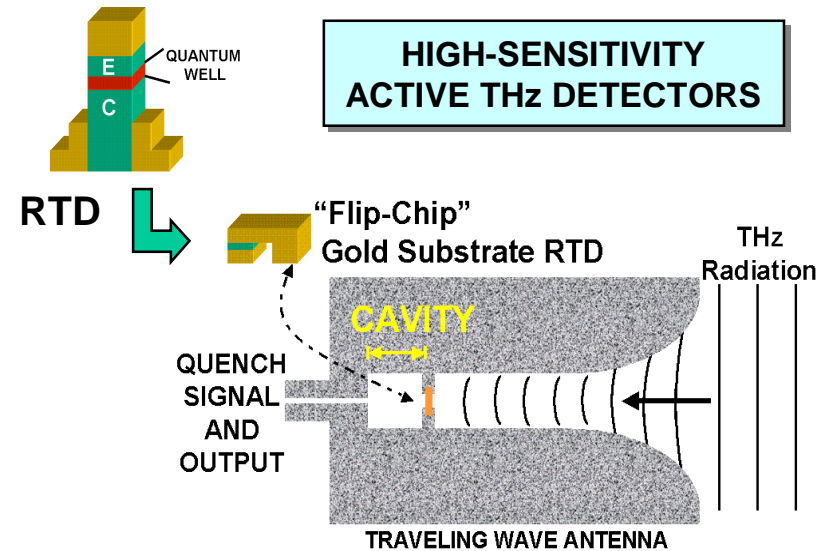


## OBJECTIVE:

- Develop high-sensitivity, solid-state RF detector MMICs for the 0.3 - 3 THz frequency band.

## APPROACH:

- Design and develop low-parasitic InP & GaSb resonant tunneling diodes (RTDs)
- Use epitaxial transfer to integrate RTDs with low-loss THz antenna structures.
- Demonstrate passive and super-regenerative RTD detector-antenna MMICs
- Demonstrate simplex THz communication link. (with HRL & UCSB)

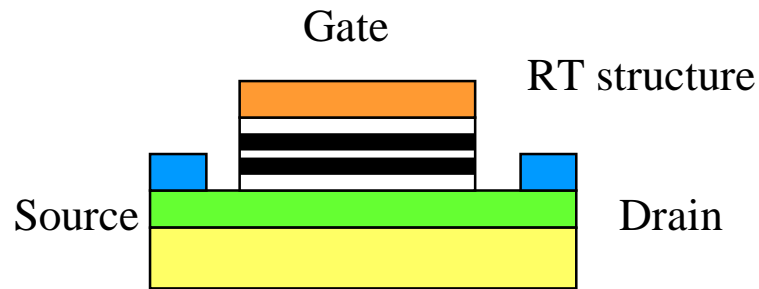


## DOD FUTURE USES:

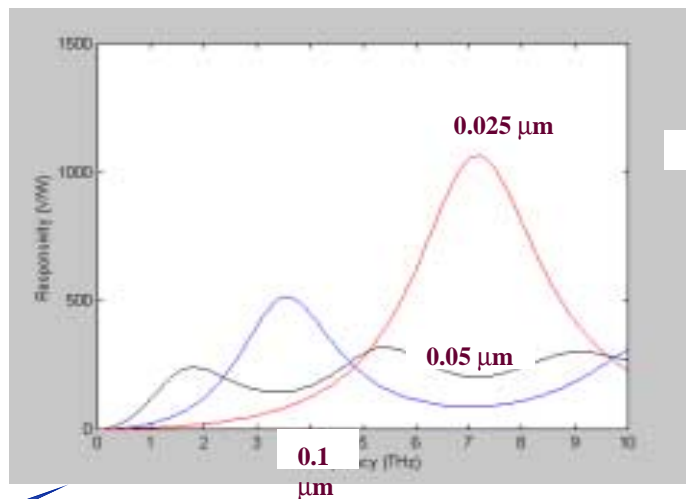
- Man-portable, ultra-secure THz communication links
- Space-based imaging of upper atmosphere
- Phased array missile seekers/munitions



# Plasma Wave Terahertz Electronics



Enhanced detectivity in sub-micron HEMT structures



## OBJECTIVES:

- Demonstrate resonant terahertz detector with high sensitivity
- Observe terahertz radiation from a field effect transistor
- Explore applications of plasma wave electronics to silicon

## APPROACH:

- Implement detectors using GaN based HEMTs
- Increase the growth of plasma waves using resonant tunneling structure
- Use “light” electrons in deep submicron silicon



Microsystems Technology Office



# THz Molecular Interactions

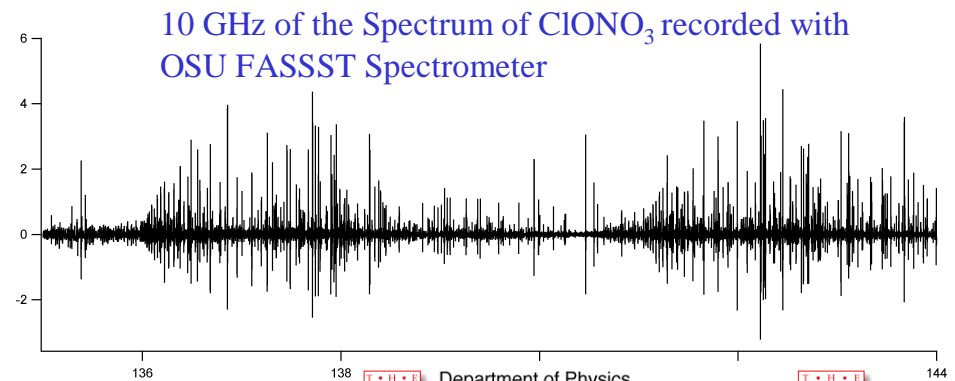
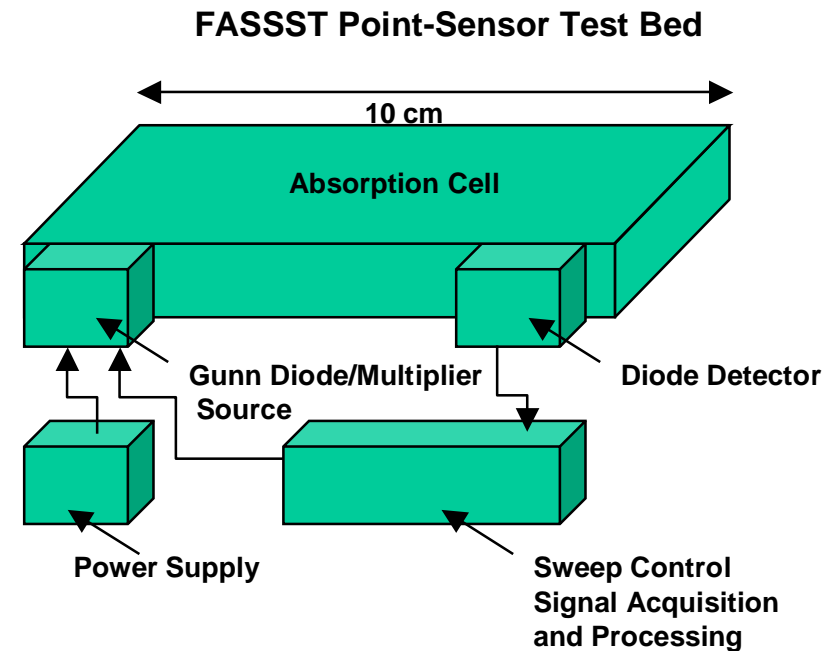
## OBJECTIVE:

Build test bed for compact THz sources and detectors.

Experimentally determine rotational energy level spectrum of various gas phase molecules

## TECHNICAL CHALLENGES:

- Specific identification of chemical species
- Quick response (< 1 second)
- Small (<< 1 ft<sup>3</sup>)
- Low Power
- Simple-Based on FASSST Concept
- Potentially Inexpensive in Quantity



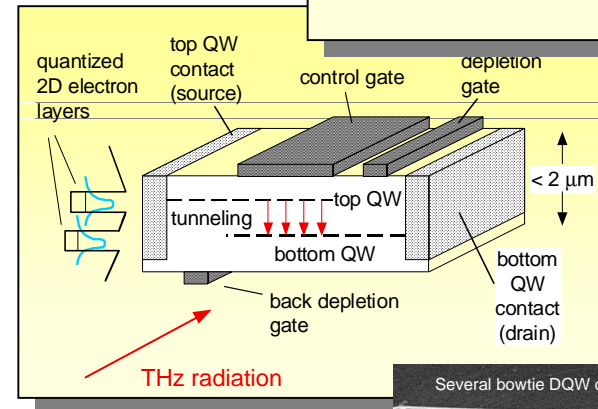
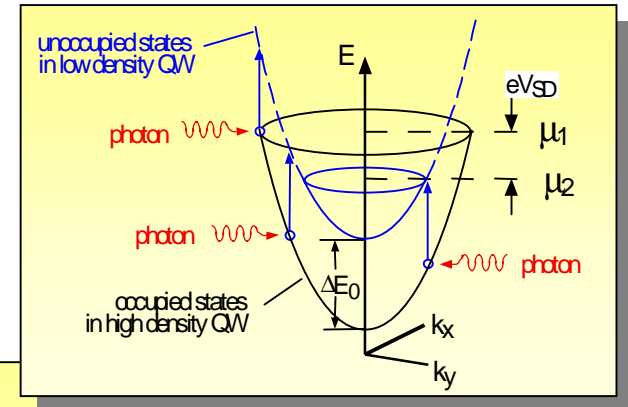
# THz Detection Based on Photon-assisted Tunneling on Double Quantum Wells

## OBJECTIVE:

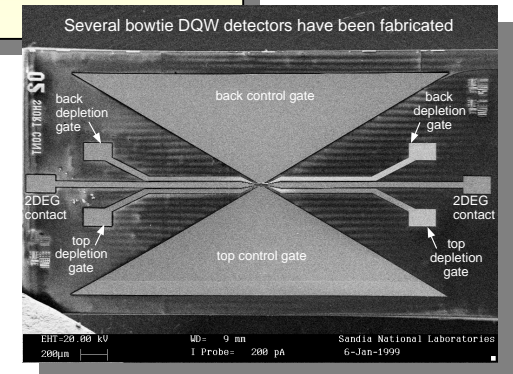
Demonstrate tunable, narrowband photon-assisted tunneling in double quantum well (DQW) heterostructures.

## TECHNICAL APPROACH:

- Use bandgap engineering to optimize photodetector performance.
- Develop antenna structure compatible with THz detectors
- Bench-demonstration of THz detector system

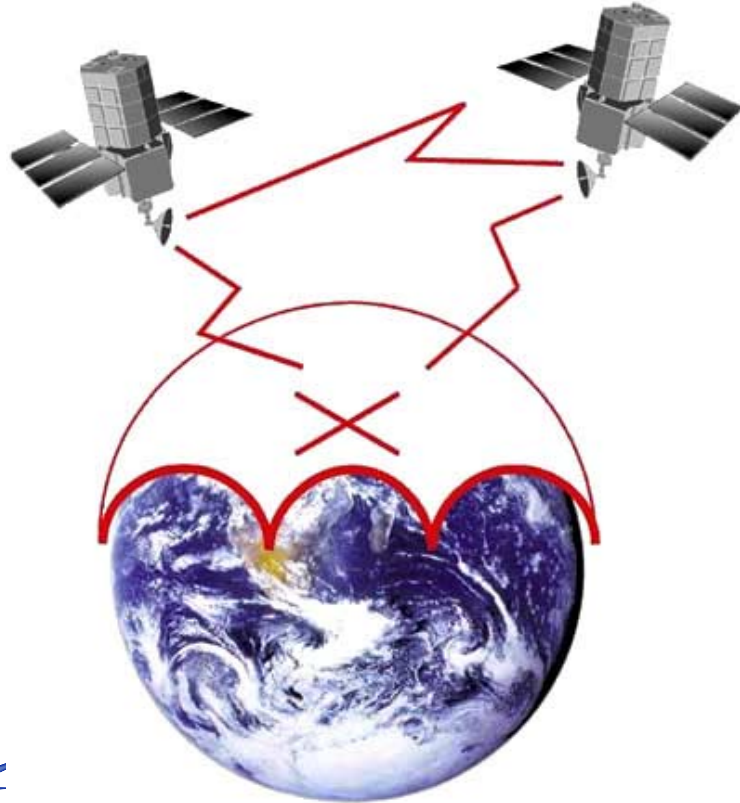


Double quantum well THz detector concept



# Summary

*DARPA is Creating Future Opportunities for THz Technology in:*



- **Environmental sensing**
- **Upper-atmosphere imagery**
- **Covert satellite communications**
- **Chem/Bio Detection (Near Distance)**

# **TERAHERTZ ELECTRONICS RESEARCH FOR DEFENSE: NOVEL TECHNOLOGY AND SCIENCE**

Dwight Woolard

U.S. Army Research Laboratory  
Army Research Office  
RTP, NC 27709

## **ABSTRACT**

The general objectives and motivations for a terahertz-frequency (THz) electronics research program are overviewed and discussed from the U.S. Army and national defense perspective. The potential impact of THz electronics research is defined in the context of the Army's future strategic vision. As illustrated, THz electronics has the potential for augmenting and enhancing the Army's concept of a Future Combat System within a microsensor network scenario. Hence, this paper demonstrates that present Army investments in THz electronics research are future enablers for a full spectrum (electromagnetic) capability in battlefield sensing and communications.

## **I. INTRODUCTION: A GENERAL PERSPECTIVE ON THE PROGRAM.**

The direction and evolution of the Terahertz (frequency-regime) Electronics Research Program at the U.S. Army Research Office (ARO) is strongly tied to national defense issues and therefore follows general ARO objectives. The principle objective of the Electronics Division, within the ARO, is to generate a new and fundamental base of knowledge within the field of electronics. Here, the overwhelming focus is towards novel scientific and engineering investigations that possess the potential for revolutionary solutions to the U.S. Army's most critical research problems, both now and in the future [1]. Collectively, research programs in Electronics are relevant to nearly all Army systems; therefore, high quality research from this area has applicability to a wide variety of developmental efforts and has the potential to impact many technological areas. Indeed the efforts toward expanding the science and technology base by the ARO Electronics Division is classified into two major areas, namely, (1) Physical Electronics Research and (2) Communications, Signal Processing and Target Acquisition, and these components strongly contribute to the concept of "Digitization of the Battlefield." The purpose of this paper is to address the general science and technology goals of the "Quantum and High Frequency Electronics" thrust within the Electronics Division. Here, the specific emphasis is upon science and engineering research related to the terahertz (THz) frequency regime. The research challenges and the technological advantages, associated with achieving and utilizing, a robust THz-frequency electronics capability has some relevance to all the major ARO thrust areas in electronics (i.e., Solid State Device

Research, High Frequency Electronics, Quantum and Optoelectronics, Information Processing and Circuits, Communications and Networks, and Electromagnetics). In addition, THz-frequency electronics introduces scientific features that have foreseeable impact to many multidisciplinary areas (e.g., chemistry, biology, molecular physics and medical science) and also has the potential to introduce new and revolutionary capabilities.

Today, ARO exists as an important component of the U.S. Army Research Laboratory (<http://www.arl.mil>) and assumes the primary role of identifying and supporting fundamental research and development that is external to the Army Laboratory system. Specifically, ARO seeks innovative research proposals from educational institutions, nonprofit organizations and private industry that possess current and future value to the Army Material Command (AMC). The overall strategic vision of ARO's research programs [2] are formulated in concert with ARL's directorates, AMC's Research, Development and Engineering Centers (RDECs), the Army Medical Research and Material Command (AMRMC), the Army Corps of Engineers and the Army Research Institute for Behavioral and Social Science. The mission of ARO is to seed scientific and far reaching technological discoveries that will enhance Army capabilities. Therefore, the majority of the programs are direct-funded from Army Program Elements "Defense Research Sciences" and "University/Industrial Research Centers" and the Office of the Secretary of Defense (OSD) Program Element "University Research Initiatives" (URI). Here it is important to note that the OSD programs fall under the executive oversight of the Defense Committee on Research chaired by the Director of Research, Office of the Deputy Under Secretary of Defense (Science and Technology). Research is also supported utilizing customer funds from other Department of Defense (DoD) agencies (e.g. Department of Defense Research Projects Agency (DARPA) with closely aligned goals to those of the Army. In addition, ARO participates in joint research programs with the Office of Naval Research (ONR) and the Air Force Office of Scientific Research (AFOSR) through Defense Reliance under the executive direction of the Defense Basic Research Panel. Hence, the investment strategy in the Quantum and High Frequency Electronics program is strongly influenced by the strategic vision and by the peer review participation of the Army and DOD (for specifics see Army Investment Strategy in [2]). However, the new ideas, the discoveries and the ongoing scientific/technological advancements that occur within academic and other non-DoD institutions also naturally influence practical program formulation.

In this paper, ARO's program in Terahertz Electronics Research for defense will first be reviewed in the context of the current needs and future directions of the Army and the DoD. In addition, the Terahertz Electronics program formulation will be presented in relation to the advancement of science and technology occurring at universities and other external research institutions. In Section II of this paper, the potential impact of THz electronics research will be demonstrated from the perspective of the Army's future strategic vision. Here, the insight will be developed via surveying the Army's critical needs, the long-range goals, and from the focus and current direction of some of its major research and laboratory programs. In Section III of this paper the current investment and anticipated future direction of the ARO program in THz electronics is overviewed and

discussed. As will be shown, a robust and integrated THz electronics has the potential for significantly enhancing and extending the Army's capability in sensing and communications. Specifically, THz sensing and communications is compatible with the Future Combat System concept of a battlefield force integrated via a microsensor network.

## **II. THE U.S. ARMY: AN OVERVIEW OF THE STRATEGIC VISION.**

The future value of any science-based research program to the U.S. Army is best defined through a consideration of the Army's overall strategic vision. Indeed, valuable insight into the potential impact of a THz electronics capability to the Army can be determined from the critical needs, the long-range goals, and from the focus and current direction of its present research and laboratory programs. This section will assess the value of THz electronics in relation to the U.S. Army's strategic vision and place the many virtues of THz electronics into a national defense perspective.

The strategic vision of the U.S. Army has been clearly defined by its leadership. For example, the Honorable Louis Caldera, Secretary of the Army, envisions an Army that possesses "*strategic dominance across the entire spectrum of operations.*" Here, an Army is required that is responsive and dominant for all perceivable land force missions and against all existing military obstacles (e.g., weapons of mass destruction [3]). Specifically, this means an Army that is "*deployable, agile, versatile, lethal, survivable, and sustainable.*" In addition, these forces must be "*affordable and capable of reversing the conditions of human suffering rapidly and resolving conflicts decisively.*" This same future vision was also echoed in the words of General Eric Shinseki, Army Chief of Staff, in his speech at the Army Chief of Staff Arrival Ceremony on June 22, 1999. In this speech [4], General Shinseki indicated a commitment to maintaining an Army that is "*preeminent in land warfare*" through improvements that allow for "*responding to a wider range of missions.*" Specifically, General Shinseki seeks "*early entry forces that can operate jointly without access to fixed forward bases,*" and recognizes that today "*our heavy forces are too heavy and our light forces lack the staying power.*" To correct these mismatches, General Shinseki seeks to change the paradigms where "*heavy forces must be more strategically deployable and more agile with a smaller logistical footprint, and light forces must be more lethal, survivable, and tactically mobile.*" How this strategic vision influences programs in the Army and what specific opportunities it offers for THz electronics is best revealed by a review of some individual research and development efforts. As will be shown, this strategic vision is pervasive across many Army research and development programs and defines many insertion points for THz – frequency science and technology.

Perhaps the best starting point for observing how the Army's strategic vision shapes its research and development efforts is the Office of the Assistant Secretary of the Army (Acquisition, Logistics and Technology) (ASA(ALT)) [5]. ASA(ALT) serves, when delegated, as the senior research and development office for the Department of the Army. Within ASA(ALT), the Office of the Deputy Assistant Secretary for Research and Technology established the *Army Science and Technology Master Plan* (ASTMP). The

ASTMP [6] is the Army's key Science and Technology (S&T) planning document and provides guidance to the entire Army S&T program. Here, the goal is to insure a strong and stable S&T program that can achieve "the timely development and transition of technologies into weapons systems and system upgrades and to explore alternative concepts to provide future warfighting capabilities for Force XXI, Army Vision 2010 and Army After Next (AAN)." It should be noted that these three previously cited blueprints for the Army's future vision were conceptual models to provide guidance for the S&T programs. Furthermore, while the Army's vision is continuously evolving (i.e., recently to just Army Vision 2010 and AAN) its historical and even most recent concept, namely "Objective Force," contains elements for achieving dominance across a full spectrum of military operations. The ASTMP addresses all of the individual DoD S&T program areas namely, The Basic Research (6.1) Program, The Applied Research (6.2) Program and The Advanced Technology Development (6.3) Program. Needless to say, the ASTMP provides guidance across a vast array of S&T efforts and is in a constant state of transformation in efforts to identify the patterns of operations needed for the Army to fulfill its role of full spectrum dominance in the future. As will be now shown, the ASTMP and some of the recent evolutions in Army S&T programs are in direct agreement with the Army's overall strategic vision. Most important, this collective vision and the S&T efforts to realize the final objective define specific areas where a THz Electronics Research Program can make important contributions.

The primary goal under the Army's Strategic Vision is a concept that has been referred to as "full spectrum dominance" and to address this the Army S&T Program is currently undergoing a major realignment and acceleration in one specific area related to ground combat. In particular, the new Future Combat Systems (FCS) program seeks to focus science and technology towards meeting future Objective-Force capability requirements [7]. The FCS is envisioned to be an ensemble of manned and potentially unmanned combat systems and represents the future centerpiece of the Army's ground combat force. Specifically, this future system is to be a highly mobile, deployable, lethal and survivable platform, and the combat effectiveness will be enhanced via the incorporation of advanced technology. The Army S&T program is now working in partnership with the Defense Advanced Research Projects Agency (DARPA) to develop and refine systems concepts and to conduct technology demonstrations. Here, a system-of-systems is targeted that will be multi-functional, multi-mission and re-configurable and that will be able to accomplish an array of strategic missions including direct and indirect fire, air defense, reconnaissance, troop transport, counter mobility, non-lethal, and command & control (C2) on the move.

Major General Lon Magget, then commanding general of the U.S. Army Armor Center at Fort Knox, Kentucky, has been attributed with first introducing this FCS vision, in 1996 [8]. This original FCS concept of a futuristic "tank" that sought greatly increased levels of lethality, survivability, deployability, mobility (agility) and sustainability also recognized the serious need for revolutionary technology insertion. One of the key specifications of the concept from the very inception was significantly reduced weight (i.e., from the present 68 tons of the Abrams M1A2). Indeed, the original targets for the manned-tank components were in the 40-45 tons range to enhance mobility and enable

force-projection transport and deployment (e.g., via C17's). More recent projections emerging from Army Science and Technology Working Groups (ASTWG) organized by ASA(ALT) and from DARPA [9] indicate that weight requirements are evolving to even lower levels (e.g. ~ 20 tons). While issues of weight and size (i.e., target silhouette) are only one of many strategic elements, they are certainly valuable assets for rapid deployment (via air transport), mobility and survivability (via reduction in target signature). On the other hand, reductions in size and weight introduce new difficulties when one considers the requirements for defense against agents of mass destruction (e.g., chemical and biological (CB) agents). Indeed, a contrast between FCS limitations on size and weight and state-of-the-art CB detection systems is very valuable for revealing areas where THz electronics has the potential to make important contributions in the future.

The issue of establishing an automatic detection, alert, avoidance and protection system for areas contaminated by weapons of mass destruction has always been a component of the FCS concept. Furthermore, the threat of CB agents against manned vehicles, troop carriers and the foot soldier is one of increasing concern. For example, in the past decade there has been a proliferation of CB agents as instruments of warfare and terrorism. An adequate military defense against CB warfare agents will require rapid detection and identification of both known and unknown threat-agents. Clearly, the most serious threat of CB agents is the potential harm they present to the short and long-term health of the victim(s). However, the actual or perceived threat of CB warfare agents can impact the operational capability of a military force in the field even when conventional counter-measures (i.e., protective equipment and clothing) are successfully employed. This is true because protective equipment can interfere with vision, speech intelligibility, personal recognition and dexterity. For these reasons, the development of reliable approaches for the detection and identification of CB agents in the field of operation has been a high imperative.

In fact, the Department of Defense maintains an entire effort (i.e., Office of the Deputy Assistant to the Secretary of Defense for Counterproliferation and Chemical and Biological Defense Programs DATSD (CP/CBD)) dedicated to addressing the problem of defense against weapons of mass destruction [10]. Indeed, there are a long list of CB detector and monitor systems supported under this program that exist both in the fielded and development states. While some systems are quite compact, these are usually somewhat limited in either the number of agents that they detect (e.g., limited to certain nerve agents) or in the level of agent specificity (e.g., only assay size and number of particles). The Army's state-of-the-art for CB agent detection actually exists at this time as two large platform systems, namely, one primarily for chemical and one for biological [11]. The FOX System (M93A1 Block I), and planned upgrades to it, represents the Army's most general approach to Nuclear, Chemical and Biological (NCB) Defense. The FOX, which is actually identified as a reconnaissance vehicle, incorporates an M21 Remote Sensing Chemical Agent Alarm (RSCAAL), which is an 8-12 micron FTIR (Fourier Transform Infrared) spectrometer for passive standoff detection of nerve and mustard agents. The system also incorporates an M22 Automatic Chemical Agent Detector/Alarm (ACADA), which is an ion mobility spectrometer (IMS) for detecting nerve and blister agent vapors. It also has a Mobile Mass Spectrometer (MM1) for

chemical liquid detection using a pair of silicone wheels that roll on the ground behind the vehicle and in an alternating fashion are lifted up to the inlet gas port of the MM1. It is also equipped with an AN/VDR2 radiacmeter (an ion gauge/Geiger counter) for radiological monitoring. The biological capability of the FOX is presently limited to glove-port sampling whereby a suspect biomaterial is collected and contained for transport back to a laboratory where it can be cultured and assayed to determine if it is a biological agent. The currently fielded version of the FOX now weighs 20-tons combat-loaded and the upgraded version, dubbed Joint Services Lightweight NBC Recon System, targets either a High-Mobility Multipurpose Wheeled Vehicle - HMMWV (11,500 lbs.) or a light armored vehicle (28,200 lbs.) platform. The currently fielded Biological Integrated Detection System (BIDS) is the Army's state-of-the-art ground based biological aerosol point detector. The BIDS is an aerosol collection system (i.e., via high impedance airflow stacks) combines an ultraviolet particle sizer, a liquid sampler, an adenosine triphosphate (ATP) luminometer, a mini-flow cytometer, an immunosensor, and a mass spectrometer [11]. The BIDS has a reported [10] capability of "detecting and presumptively identifying four BW agents simultaneously in less than 45 minutes," and is acclaimed as the DoD's "first credible and rapidly deployable biological detection capability." The entire BIDS system consists of a shelter unit mounted upon a dedicated vehicle (M1097 Heavy HMMWV) plus a trailer-mounted 15-kw generator (PU-801) to provide the necessary electrical power. Hence, the BIDS system approaches at least several tons in total weight. The previous descriptions make it evident that the state-of-the-art systems for both chemical and biological agents are grossly incompatible with the size and weight requirements of the FCS vision.

As noted earlier, weapons of mass destruction are broadly recognized as a very serious threat to the war fighter and the general public. Hence it is not surprising that there exists a great and concerted effort within the DoD for applying S&T toward anticipating CB threats and for developing innovative countermeasures. While much work remains to improve the overall capability of chemical sensing in the field (e.g., sensitivity, size, weight, etc.), methods for point-detection are available for all *known* chemical agents. On the other hand, the present capability for point-detection of biological (bio) agents is limited to the identification of only four species. This limitation in point-detection and the absence of any standoff (i.e., remote) capability has recently drawn considerable attention. In fact, the development of a bio early-warning capability is of the *highest priority* to the Joint Future Operation Capability [12], as well as to the Joint Service Leader for Contamination Avoidance [13] and most importantly to the Department of Defense [14]. When these general problems are combined with the need to realize a compact (i.e., very small size and weight) total CB systems package for the FCS concept, it is obvious that new approaches will be necessary. Recent scientific work in both chemical and biological spectroscopy at very high frequencies has suggested a novel avenue for a THz electronic approach to warfare agent detection and identification [15]. Specifically, a portion of the submillimeter-wave spectra (i.e., ~ 0.1 – 1.0 THz) obtained from DNA and complete cellular biological samples has revealed unique numerical structures possibly due to vibrational lattice and local phonon modes and other physical mechanisms of interactions between radiation and the biological material. Hence, there is significant evidence of a new THz spectroscopic-based approach for both the point and

standoff detection of biological aerosols. In addition, fundamental physical phenomenon leads to a peaking of the intensity profile for chemical molecules in the submillimeter-wave regime and this suggests certain advantages for THz-based detection techniques. A more detailed discussion of new scientific research in the area of THz-frequency spectroscopy will be given in the next section of this paper. However, it is most important to note here that a fully-integrated electronic-based THz-frequency technology has very important ramifications to the Army vision of a effective FCS that is survivable against CB warfare agents.

The goals under the Army's new *Objective Force* vision and its highest priority S&T initiative, namely the FCS, introduce a great number of technological challenges. Leadership within the Army also recognizes the need for the S&T community to provide imaginable possibilities for making projections on what transformations in the Army are required to meet these specified future goals [16]. The latest vision of FCS is a fighting ensemble of capabilities that meets the weight constraints for C-130 transport (i.e., 20 ton class) and one that can provide land combat platforms with the levels of force and mobility emphasized by General Shinseki (see earlier comments). Concept development for the FCS is underway through a joint effort between DARPA (LTC M. Van Fosson [17]) and the Army, and initial studies indicate that a network-centric distributed combat capability has the potential to deliver the more lethal, survivable, mobile and supportable fighting force that is envisioned. This system-of-systems concept will achieve lighter and more mobile future-combat-vehicle (FCV) based force, and one that possesses the desired levels of lethality and survivability, by integration of innovative operational concepts. This system-of-systems concept will integrate such elements as direct and indirect fire, nonlethal technologies, active and passive protection, tactical internet for enhanced situational awareness, and a common-chassis multifunctional tactical force [16]. Here, the U.S. Army is envisioned to reach a condition of combat-overmatch against foreseeable enemies through a combination of manned and unmanned (robotic) vehicles that are equipped with modern fire support, novel protective technology, and through an advanced electronic-based tactical capability. But what does all this mean in more simple terms. Clearly one interpretation of the goal is a transformation from the existing heavy ground forces to a lighter and more mobile force while at the same time maintaining and increasing lethality and survivability [17]. What does this really mean? Well one might characterize it as a lighter force with less traditional firepower and armaments, however, one that relies on completely new warfare concepts. Here, new concepts for increasing survivability such as smaller vehicle signatures, active armor (e.g., missile defense systems), greater situational awareness (e.g., advanced sensors and wireless internet) and improved battlefield tactics (e.g., integrated units). In addition, increased lethality is sought through such assets as advanced weapons (e.g., electromagnetic gun), weapon systems (e.g., robotic platforms) and more rapid identification of, and response to, the enemy (e.g., advanced sensors and sensor fusion). In the simplest of terms the goals are to be extremely mobility, to be difficult to detect, to see the enemy first and to deliver an integrated and lethal attack.

While the early phases of Army's transformation to the FCS concept will certainly be carried by S&T efforts at the 6.2 and 6.3 levels, many of the far term goals must be

augmented by fundamental research contributions (i.e., 6.1). For example, many of the technological elements required for achieving the FCS are being developed in the U.S. Army Research Laboratory's (ARL) Federated Laboratory (FedLab) Program. The ARL FedLab Program is one of the Army's largest research and development efforts and also reflects many aspects of the FCS future strategic vision. Indeed, the theme of the ARL FedLab 2000 Symposium [3] was "transforming the Army through science and technology" and clearly demonstrated support to the Army in creating a lighter and more lethal force through the application of science and technology. Furthermore, FedLab provides an excellent platform for anticipating the needs of the future warfighter and military system. Hence the FedLab program is an excellent guide for envisioning where and in what capacity THz electronics might play an important role in the future.

The ARL FedLab Program represents a partnership between ARL's research teams and those from the academic and industrial communities. The FedLab program was first launched in 1996 and established three consortiums to focus on military-specific objectives in the areas of Advanced Sensors, Advanced Displays & Interactive Displays, and Advanced Telecommunication & Information Distribution [19]. The Advanced Sensors Consortium (ASC) focuses on enabling technologies for the next generation of more affordable and more capable Army sensor systems. The work under the ASC is divided into five technical areas, namely, Multi-Domain Smart Sensors (MDSS), Multi-Sensor Fusion Automation Target Recognition (MSFATR), Radar (Millimeter-Wave and Ultra-Wideband), Signal Processing, and Microsensors. This array of research and development work on advanced sensing and imaging is directly in line with the FCS needs for expanded battlefield situational awareness. The Advanced Telecommunications & Information Distribution Consortium (ATIDC) focuses on research in the area of mobile wireless communications with the goal of providing support to the Army's digitization efforts. The work under the ATIDC seeks to provide fundamental advances that will enable the rapid and secure transmission of large quantities of multimedia information (speech, data, graphics and video). Hence, this work is also strategically important to future FCS needs. The Advanced Displays & Interactive Displays Consortium (ADIDC) focuses on developing new technologies for facilitating human-computer interaction in areas related to battlefield information. Hence, the ADIDC is concerned with the efficient and effective processing (i.e., filtering, analyzing and displaying) of information for the warfighters and commanders and it is an excellent compliment to the ASC and the ATIDC.

The ARL FedLab Program has collective efforts in sensors, telecommunications and information displays and is certainly a good road map for looking forward to how the FCS concept of a system-of-systems might function in the future. More to the point of this paper, the FedLab program can be used as a guide for envisioning future uses of a THz electronics capability. Specifically, some of the new concepts and the bottleneck problems that exist within the FedLab program are valuable in finding future advantages of an integrated electronics technology with an operating capability at THz frequencies. Historically, the THz portion of the frequency spectrum has not been an issue for either remote sensing or communications, within lower portions of the atmosphere, due to the extremely high propagation attenuation that exists between about 300 GHz and a few

THz [20]. Indeed, there is a large preference for large and small molecules to absorb electromagnetic energy within the THz band. Hence, it is not too surprising that THz spectroscopy is a good tool for the interrogation of chemical and biological agents as was noted earlier. While the THz regime offers a number of general advantages (e.g., wider bandwidth, improved spatial resolution, and compactness) it is certainly a good question, in light of the high attenuation, to ask why this frequency region would have any value to remote sensing or communications in a battlefield environment. However, the FCS concept where the military force will be heavily dependent on a tactical internet does allow for new paradigms where THz frequency sensing and communications is feasible and may offer dramatic advantages.

To illustrate specific technological areas where THz electronics may make contributions, it is valuable to consider some of the recent evolutions within the ARL FedLab Program. For example, remotely deployable self-configurable micro-sensor networks are an area of interest within the FedLab Program to enable continued unmanned surveillance at very-low energy requirements [21]. In one particular concept, called Sensing Position Integrated Network (SPIN), full situational awareness (i.e., where am I, where are my friends, and where is everyone/everything else) is proposed for the dismounted soldier through an integration of microsensor networks (wireless) and GPS technology. In the SPIN [22] approach low-bandwidth information (i.e., achieved by embedded processing capabilities) and routing through multiple short intermediary links are combined to realize low-power transmitter (i.e., and battery) requirements. Certainly this type of tactical internet has tremendous potential value to the warfighter. Specifically, when emerging microsensor technologies (i.e., unattended ground sensors such as acoustic, seismic, magnetic, visual, and IR) are efficiently and effectively wireless-linked one can expect new levels of battlefield C4I (command, control, communications computers and intelligence) such as vehicle identification, area surveillance, perimeter defense, troop movement and communications infrastructure support. Furthermore, while such integrated sensor concepts need more demonstrations and advancements to prove their full utility in tactical situations [23], there is certainly reason to believe that they will directly support the FCS vision.

So what if anything does THz electronics have to offer sensing and communications on the battlefield? To begin, it should be noted that THz frequency sensing and communications does not exist in any fieldable capacity (i.e., military or commercial) at the present time. Clearly, the absence of an application of a THz based technology is due to the large atmospheric attenuation (i.e. 100's of dBs per kilometer) over the band. Of course, the solid-state electronics capability within the THz frequency regime remains extremely limited from a basic signal source and systems perspective but this lack of development may be largely due to the lack of applications. However, it is also true that traditional remote sensing and communications is considered in a venue of at least many kilometers. However, if we consider sensing and communications from a shorter-range perspective (i.e., as in the tactical network picture discussed about) then the requirements, as well as the conclusions, are seen to change dramatically. Consider for a moment the plot of transmission function, given in Fig. 1, for a series of short-range distances at sea level and standard pressure and humidity. The simulated results indicate that a number of

feasible windows exist for a number of large bands in the region 300 GHz to 2 THz as well as in the region 6 THz to 10 THz. Indeed, below 1 THz there are two large windows with transmission reaching over 50 % at 100 meters (i.e., ~ 600-700 GHz and 800-900 GHz). These results clearly demonstrate that THz-frequency sensing and communications is viable, or at least possible, in situations where the link extends up to, and possibly exceeds, hundreds of meters.

### HITRAN-PC ATMOSPHERE TRANSMISSION RESULTS

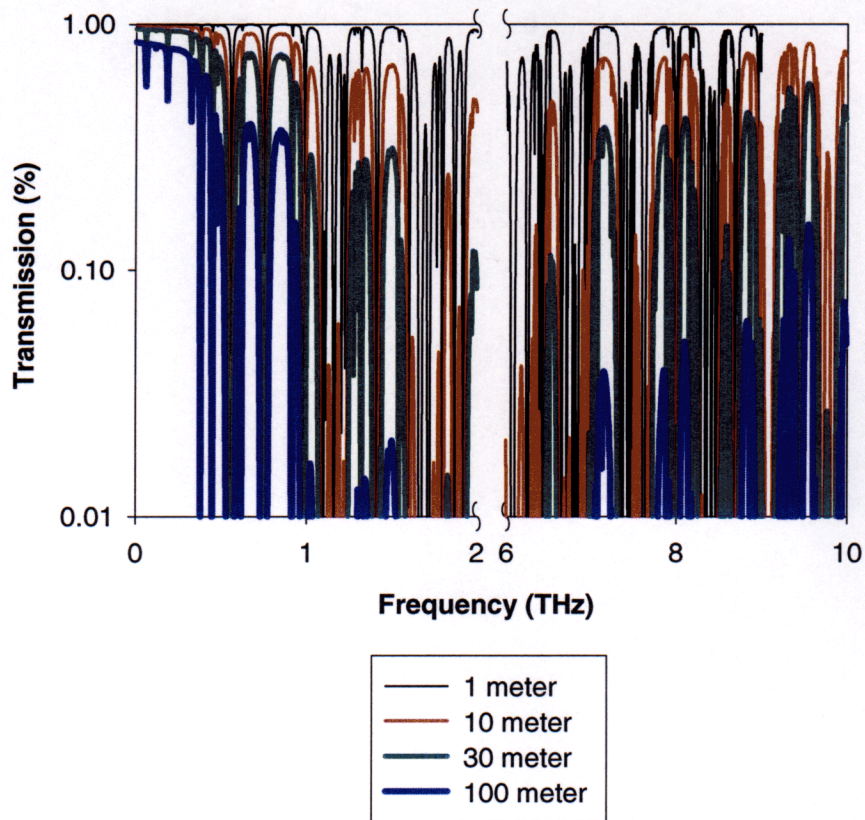


**Figure 1.** Percent transmission, as a function of THz frequency, calculated from the program HITRAN-PC. A special thanks to Professor SJ Allen, of UCSB, for providing these results.

The results of Fig. 1 show that a tactical system for sensing and communications could be successfully employed on the battlefield if a wireless-network with short-range links were utilized. However, one aspect of going to THz frequencies is in direct contradiction with the existing conceptualizations (i.e. as in SPIN discussed above). Specifically, it is true that utilizing high frequencies, where the transmitting attenuation is greater, will increase power requirements for the ground sensors and ground links. On the other hand, there are significant efforts within the area of signal processing (i.e., on the remote nodes [24]) aimed at accommodating the large data payloads to the limited bandwidths

available on existing communication channels. As the requirements for more sensing and imaging data grows in the future, as can be expected from the FCS vision, the tradeoffs requirements on power consumption between bandwidth-use and signal processing may not be so clear. Also, it is all together possible that the existing communications channels that are now in use may not be able to handle the data demands for the FCS of the distant future. Finally on this point, the development of an integrated electronics capability at requirements on power consumption between bandwidth-use and signal processing may not be so clear. Also, it is all together possible that the existing communications channels that are now in use may not be able to handle the data demands for the FCS of the distant future. Finally on this point, the development of an integrated electronics capability at THz frequency would also support and augment the realization of very high-speed digital hardware that could be used for enhanced signal processing. Hence, THz electronics has the potential to impact both sides of this general argument.

The implementation of an integrated sensor-network at THz frequency also affords other advantages in communications. For example, the increased bandwidth-space at THz would further enhance traditional spread spectrum techniques, therefore reducing the communicator's detectability and further combating the problem of enemy-introduced interference (i.e., jamming) [25]. The proposal of introducing a THz frequency communications system also represents a conceptual extension of a newly emerging theme in modern communications, namely what is being refereed to as Ultra-WideBand (UWB) [26]. The UWB technological concept is seen as a new wave in wireless technology and is being lauded as a revolution in wireless communications, radar and positioning. For example, UWB Code Division Multiple Access (CDMA) communication schemes such as *Impulse Radio* [27] utilize a train of sub-nanosecond pulses and a resultant low power spectral density (e.g., spread over ~ 2 GHz). Hence, the Impulse Radio approach possesses advantages such as a high immunity to fading (i.e., less multi-path interference), a large processing gain (i.e., integrates over a WB), a low probability of interception/detection (i.e., individual spectral components are below the noise), and is more energy efficient (i.e., pulsed or nonlinear operation). Finally, moving to a higher-frequency technology offers a potential reduction in the size of sensor elements due natural reduction in the integrated-circuit elements and antennas at the shorter wavelengths.

The application of THz sensing and imaging also has possible feasibility within an integrated wireless-network. The pursuit of multi-sensor fusion schemes [28] that utilize imaging and non-imaging sensors both above and below the THz domain are presently an active and important part of the Army's research and development effort. For example, the MSFATR project under the ARL FedLab program combines infrared (IR), multi/hyperspectral (MS/HS), synthetic aperture radar (SAR) and laser radar (LADAR) to improve the detection of camouflaged targets. In addition, combinations of ground penetrating radar (GPR) and forward looking IR (FLIR) have been used for improvements to buried mine detection. Of course, airborne platforms have already demonstrated the remarkable success of UWB radar in detecting tactical targets concealed by foliage and of surface and subsurface landmines. Furthermore, millimeter wave (MMW) is useful for high-resolution target acquisition and has demonstrated

marked advantages (i.e., over IR and optical) in imaging through common obscurants. When implemented in a sensor-network type scheme, THz technology offers the possibility of further extending the Army's electronic capability to the "full electromagnetic (EM) spectrum." Hence, in addition to the use of THz sensing for CB detection as discussed earlier, this shorter wavelength region possess enhanced target resolution. Indeed, a long-standing and analogous use of THz technology can be found in work being performed, and supported by, the U.S. Army's National Ground Intelligence Center (NGIC) [29]. Here, NGIC combines unique high frequency (0.16 – 1.5 THz) compact radar ranges, computational EM codes and down-scaled, precision-engineered models of military vehicles to rapidly and efficiently derive radar signatures for lower frequency systems. This higher resolution capacity of THz systems may also offer advantages to actual battlefield imaging (e.g., enhanced identification and end-game missile guidance). Finally, extending the operating range of sensors and imaging into the THz domain may afford for completely new tactical strategies. For example, in one futuristic scenario, designer obscurants might be used in combination with shorter-wave imaging sensors to increase both the lethality and survivability of Army forces in close combat engagements.

Hence, a robust and integratable THz technology has much relevance on the future battlefield when viewed from an electronic-based sensing and communications perspective. In particular, THz electronics has the potential for augmenting and enhancing the Army's concept of a Future Combat System within a microsensor network scenario. In the next section, ARO support of THz electronics research will be outlined.

### **III. A BRIEF OVERVIEW OF THE ARO PROGRAM IN THZ ELECTRONICS.**

The U.S. Army Research Office (ARO) maintains active support for THz electronics under its Quantum and High Frequency Electronics research program within the Electronics Division. It should also be noted that general support from this part of the ARO electronics program is used to address many diverse areas (e.g., low-power electronics, ultrafast switching transistors, fundamental quantum device concepts, nanolithography, etc) that have technological relevance to the future Army. However, the goal of establishing a solid foundation of scientific and engineering knowledge for THz electronics has extremely high merit and is one that has particularly significant relevance to some of the Army most critical needs. Furthermore, this goal of establishing a knowledge base and electronics capability within the THz regime may be viewed as the ultimate high frequency electronics challenge. Indeed, the last research frontier in high-frequency electronics now lies in the THz (or submillimeter-wave) regime between microwaves and the infrared (i.e., 0.3 – 10.0 THz). While the THz frequency regime offers many technical advantages (e.g., wider bandwidth, improved spatial resolution, compactness), the solid-state electronics capability within the THz frequency regime remains extremely limited from a basic signal source and systems perspective (i.e., <  $\mu$ watts). Historically, this limited development results from the confluence of two fundamental factors. First, extremely challenging engineering problems exist in this region where wavelength is on the order of component size. Second, the practical and

scientific applications of this shorter-wavelength microwave region have been restricted in the past to a few specialized fields (e.g., molecular spectroscopy).

However as we enter the new millennium, important applications of THz technology are rapidly emerging that are extremely relevant to national defense. As discussed earlier in this paper, THz electronics has relevance to the problem of defense against weapons of mass destruction (i.e., chemical and biological) and to battlefield sensing and communications. Of course, THz electronics and related ultra-fast processes can be expected play future roles in such areas as space communication, high speed information processing & computing, material characterization, molecular science, biology, and in medical applications. Hence, ARO is proud of the role it plays in encouraging the pursuit of fundamental investigations within this specialized field of electronics.

At the present time, the ARO provides support for THz electronics research within three main thrust areas. Specifically, ARO is coordinating with other Army components and DoD agencies (e.g., ARL-SEDD, SBCCOM and DARPA) to support research and development in sensing science at THz frequency, novel quantum and nanotechnology based solutions for THz sources and detectors, and robust and integrated (i.e., semiconductor based) THz devices and components.

For example, ARO, ARL-SEDD and SBCCOM has previously established a base for the use of both millimeter-wave and submillimeter-wave spectroscopy as a tool for the identification and interrogation of biological agents [30]. More recent university research [31] supported by this collective Army group has demonstrated that phonon modes within the DNA provide a unique and repeatable signature for the biological agent under test. More recently this Army group has joined with DARPA to engage in a seed program that will assess the utility and feasibility of a "GHz and THz Spectroscopic-based Perimeter Defense System." Under this support, both the experimental science and the theoretical interpretation of molecular resonance phenomenon is being pursued. Furthermore, this general area of sensing science is currently being emphasized and is being supported broadly (e.g., DURIP) out of the ARO electronics division. Another noteworthy effort of mention is the near-THz (200 GHz) research on spectroscopy of biological aerosols which is attempting to put sensitivity boundaries on signature detection in lieu of extended future studies. Finally, ARO assists DARPA with the support of research on the development of a compact, cost-effective and robust Terahertz (THz) spectroscopic instrument for application toward the detection and identification of large molecules within the THz regime.

ARO is also a leader in seeding research that seeks to identify novel device concepts for the generation and detection of THz radiation. One very noteworthy example is the work on "Gain and Loss in Semiconductor Quantum Structures," carried out by Professor Allen from UCSB (see [www.qi.ucsb.edu](http://www.qi.ucsb.edu)), which has subsequently become a part of the new DARPA program for "THz Sources for Sensing and Satellite Communications." ARO contributes core support for research in the areas of interband resonant tunneling structures (RTD), intrinsic oscillations in convention RTD's and in coupled quantum dot-laser structures as potential new approaches for THz sources. ARO also supports work in

plasma wave technology and in Fermi electronics (noise-correlated) research both of which target novel approaches for very high sensitivity receivers. The goal of these high-risk efforts is to assess, and possibly identify, new forms of electronic technology for the future.

ARO certainly recognizes the difficult challenge of realizing an electronic capability at THz frequency. Hence, ARO is also presently challenging the high frequency device and circuits community to extend existing solid-state technology (e.g., multipliers) to bridge the THz technology gap. Recognizing that a militarily useful terahertz technology must be compact and cost effective, ARO funds research into maturation of planar semiconductor-based approaches. At present, support is being provided for establishing a robust diode-based monolithic millimeter (& submillimeter) -wave integrated circuits (MMIC's) technology. A recently announced Small Business Innovative Research (SBIR) will provide funding starting in Fiscal Year 2002 (FY02) to facilitate the development of semiconductor-based, fully-integrated, terahertz-frequency, transmit/receive modules. Here, the most successful terahertz device technologies (e.g., Schottky and Heterostructure Barrier Varactors and Schottky mixers) will be targeted to realize frequency agile and reliable components in a cost effective manner. This research and development will provide valuable test beds for facilitating additional innovations in sensing and for conceptualizing new uses of THz technology (e.g., communication networks).

The significant potential impact of THz technology towards battlefield sensing and communications (i.e., in a microsensor network scenario) and the extreme challenges of realizing robust sources imply that that ARO will continue to support innovation in very high frequency electronic-based technology. New areas of potential contribution include the further leveraging of nanoscale device concepts, molecular electronics and dynamical phenomenon at THz frequency. The investigation of THz-frequency capability towards new communication techniques (e.g., possibly even THz/Optical hybrids), its implementation for very high-speed data processing and its application to medical uses are also anticipated areas of emphasis. Indeed, the potential impact of THz electronics in future Army applications suggests its continued support and emphasis.

#### **IV. CONCLUSIONS.**

This paper has addressed THz electronics research from the U.S. Army and national defense perspective. In particular, the potential role of THz electronics is evaluated from a consideration of the Army's overall strategic vision. This paper has shown that a THz electronics capability would address critical needs and long range goals of the U.S. Army. Specifically, the development of a robust and integrated THz electronics capability would have significant value when placed into the context of the Army's Future Combat System (FCS) concept. Furthermore, fundamental research in the field of THz electronics will enhance and extend electronic capabilities that presently exist in Army science and technology programs (e.g., ARL FedLab). The U.S. ARO is presently investing in novel science and technology within the THz frequency regime to enable a full electromagnetic-spectrum capability for sensing and communications. There is

certainly significant evidence to suggest that the ARO program in THz electronics will contribute to the Army's future ability to achieve the "full spectrum of dominance" articulated by its leadership.

### ACKNOWLEDGEMENTS

The author would like to extend his sincere gratitude to Dr. William Sander of ARO, and Drs. Alan Samuels and Jim Jensen, of SBCCOM, for supplying valuable information that was used in the preparation of this manuscript.

### REFERENCES

- [1] "U.S. Army Research Office Electronics Division: 1999 Selected Significant Accomplishments", see the Proceedings to the 1999 Electronics Program Review, April 20-21, 1999.
- [2] "U.S. Army Research Office in Review – 1999", see Army Research Office Publications, internet site (<http://www.aro.mil>).
- [3] "The Army Vision: Soldiers On Point for the Nation ... Persuasive in Peace, Invincible in War", see The Secretary of the Army internet site (<http://www.hqda.army.mil/secarmy>).
- [4] "Army Chief of Staff Arrival Ceremony Remarks", June 22, 1999, see Army Chief of Staff on internet site (<http://www.army.mil>).
- [5] The Office of the Assistant Secretary of the Army (Acquisition, Logistics, and Technology) see internet site (<http://www.sarda.mil>).
- [6] "1998 Army Science and Technology Master Plan," see internet site (<http://www.sarda.mil/AboutUs/about/sardzt.htm>).
- [7] "Future Combat System," see Federation of American Scientists web site (<http://www.fas.org/man/dod-101/sys/land/fcs.htm>).
- [8] A.H. Sharoni and L.D. Bacon, "The Future Combat System (FCS)," *ARMOR*, pp. 7-11, July-August, 1997.
- [9] M. H. Van Fossen "Future Combat System," presented at the FY01 Sensors & Electron Devices Directorate (SEDD) Program Formulation Workshop, 28 Feb. – 01 March, 2000.
- [10] The Office of the Under Secretary of Defense for Acquisition, Technology and Logistics internet site (<http://www.acq.osd.mil>).
- [11] Information derived from conversations with Dr. A. Samuels and Dr. J. Jensen of The Soldier Biological and Chemical Command (SBCCOM), Edgewood, MD.
- [12] LTC M. Lamphere, "DoD Needs for CB Detection," presented at the Army Research Office Workshop on Nanostructures for DoD Applications, Ga. Tech, Atlanta, GA, Oct 14-16, 1998.
- [13] K. Phelps, "DoD Chem/Bio Detection Program," presented at the Army Research Office Workshop on Nanostructures for DoD Applications, Ga. Tech, Atlanta, GA, Oct 14-16, 1998.

- [14] The 1996 edition of "Defense and Technology Strategy" published by DDR&E lists the capability for standoff detection of biological agents and as "our most pressing single need". The May 1996 issue of the "Joint Warfighting Science and Technology Plan" states that early warning of biological attack is the "highest CINC counter proliferation priority".
- [15] D. Woolard, R. Kaul, R. Suenram, A. Height Walker, T. Globus and A. Samuels, "Terahertz Electronics for Chemical and Biological Warfare Agent Detection," Keynote paper presented at focus session on Submillimeter-wave and Terahertz Technology, 1999 International Microwave Symposium, June 13-19, Anaheim, CA.
- [16] Dr. A. M. Andrews II and Dr. T. Killion, "Accelerating the Pace of Transformation," *Army & ALT*, pp. 13-16, March-April, 2000.
- [17] Future Combat Systems Program description under DARPA - Tactical Technology Office (TTO), see internet site ([www.darpa.mil/tto](http://www.darpa.mil/tto)).
- [18] MG J. M. Cosumano Jr., "Transforming the Army to a Full-Spectrum Force," *Army & ALT*, pp. 13-16, March-April, 2000.
- [19] 2000 Annual Report(s) on the ARL Federated Laboratory (Consortiums on Advanced Sensors, Advanced Displays & Interactive Displays, and Advanced Telecommunications & Information Distribution) available via website (<http://atirp.isr.umd.edu>).
- [20] RF and Microwave Circuit Design for Wireless Communications, edited by L. E. Larson (Artech House, Boston, 1997).
- [21] D. G. Mills, "Low-Energy Communications and Routing for Microsensor Networks," Proceeding of the ARL Federated Laboratory 4<sup>th</sup> Annual Symposium on Advanced Telecommunications & Information Distribution, College Park, MD, March 21-23, 2000.
- [22] J. Agre, L. Clare, N. Romanov, V. Panov, J. Kelly and R. Klingeman, "Sensing Positioning Integrated Network (SPIN): Providing Situational Awareness to the Warfighter," Proceeding of the ARL Federated Laboratory 4<sup>th</sup> Annual Symposium on Advanced Sensors, College Park, MD, March 21-23, 2000.
- [23] S. R. Blatt, D. M Hull and A. M. Filpov, "Microsensors in a Changing World: Extended Sensing," Proceeding of the ARL Federated Laboratory 4<sup>th</sup> Annual Symposium on Advanced Sensors, College Park, MD, March 21-23, 2000.
- [24] S. Natkunanathan, A. Sipos, S. Avery, G. J. Pottie and W. J. Kaiser, "A Signal Search Engine for Wireless Integrated Network Sensors," Proceeding of the ARL Federated Laboratory 4<sup>th</sup> Annual Symposium on Advanced Sensors, College Park, MD, March 21-23, 2000.
- [25] L. B. Milstein and M. K. Simon, "Spread Spectrum Communications," Chapter 11 in *The Mobile Communications Handbook*, Edited by J. D. Gibson (CRC Press, 1996)
- [26] see Proceedings to The 1999 International Ultra-Wideband Conference, Washington, DC, September 28-30 (1999).
- [27] S. S. Kolenchery, J. K. Townsend and J. A. Freebersyer, "A Novel Impulse Radio Network for Tactical Military Wireless Communications," Proceedings of MILCOM 98, pp. 1-7 (1998).

- [28] see 1999 the ARL FedLab Annual Report of the Advance Sensors Consortium.
- [29] M. J. Coulombe, T. Ferdinand, T. Horgan, R. H. Giles and J. Waldman, "A 585 GHz Compact Range for Scale Model RCS Measurements," in the Antenna Measurements and Techniques Association Proceedings, Dallas, TX, Oct. 1993.
- [30] D. L. Woolard, et. al., "Millimeter Wave Induced Vibrational Modes in DNA as a Possible Alternative to Ainal Tests to Probe for Carcinogenic Mutations," The Journal of Applied Toxicology, 17, pp. 243-246, May (1997).
- [31] T. R. Globus, D. L. Woolard, M. Bykhovskaia, B. Gelmont, J. L. Hesler, and T. W. Crowe, "FTIR-Spectroscopic Characterization of DNA Macromolecules," in the Proceedings to the International Semiconductor Device Research Symposium, December 1-3, Charlottesville, VA, 1999.

# Frequency Dependent Noise Temperature of the Lattice Cooled Hot-Electron Terahertz Mixer

A.D.Semenov<sup>a)</sup>, H.-W. Hübers<sup>b)</sup>, J.Schubert<sup>b)</sup>, G.N. Gol'tsman<sup>a)</sup>, A.I. Elantiev<sup>a)</sup>,  
B.M. Voronov<sup>b)</sup>, and E.M. Gershenzon<sup>a)</sup>

<sup>a)</sup> Physical Department, State Pedagogical University of Moscow, 119891 Moscow, Russia

<sup>b)</sup> DLR Institute of Space Sensor Technology and Planetary Exploration, 12489 Berlin, Germany

## ABSTRACT

We present the measurements and the theoretical model on the frequency dependent noise temperature of a lattice cooled hot electron bolometer (HEB) mixer in the terahertz frequency range. The experimentally observed increase of the noise temperature with frequency is a cumulative effect of the non-uniform distribution of the high frequency current in the bolometer and the charge imbalance, which occurs near the edges of the normal domain and contacts with normal metal. In addition, we present experimental results which show that the noise temperature of a HEB mixer can be reduced by about 30% due to a Parylene antireflection coating on the Silicon hyperhemispheric lens.

## I. INTRODUCTION

Heterodyne spectroscopy in the frequency range from 1 THz to 6 THz yields important information on astronomical objects as well as on the chemical composition of the earth's atmosphere. Some prominent examples are the CII fine structure line at 1.6 THz and the OI fine structure line at 4.75 THz, which are major coolant lines of the interstellar medium. The OH rotational transitions at 2.5 THz and 3.5 THz allow determination of the OH volume mixing ratio in the stratosphere and provide important information on the catalytic cycles, which are responsible for the destruction of stratospheric ozone [1,2]. Superconducting hot-electron bolometer (HEB) mixers are presently the most promising candidates for quantum limited terahertz heterodyne mixers at frequencies above 1.2 THz. In a sufficiently small device only electrons are heated by the incoming radiation providing the response time of the order of the electron-phonon interaction time. This results in a small noise temperature as well as in intermediate frequencies of several GHz. Another consequence of electron heating only is the small power of the local oscillator, which is required for optimal operation of the HEB mixer.

In this article we report noise temperature measurements performed with the same phonon-cooled NbN HEB mixer in the frequency range from 0.7 THz to 5.2 THz and develop a model that describes the frequency dependence of the mixer performance.

In addition we present results of an experimental investigation of Parylene as an antireflection coating for Si at THz frequencies.

## II. MIXER DESIGN AND EXPERIMENTAL DETAILS

The lattice-cooled HEB mixer was manufactured from a thin superconducting NbN film. The film with the nominal thickness 3.5 nm was deposited by dc reactive magnetron sputtering on a 350  $\mu\text{m}$  thick high resistivity ( $>10\text{ k}\Omega\text{ cm}$ ) Si substrate. The details of the process are described elsewhere [3,4]. After deposition films usually had a room temperature square resistance of  $\approx 500\ \Omega$  that increased to  $\approx 660\ \Omega$  at 20 K and dropped abruptly to almost zero (residual resistance less than  $1\ \Omega$ ) at the transition temperature close to 10 K. The processing during the device fabrication leads to degradation of superconductivity and the square resistance at room temperature increases up to  $\approx 700\ \Omega$  ( $\approx 940\ \Omega$  at 20 K) while the transition temperature decreases to a value slightly above 9 K and the transition width increases to  $\approx 0.5\text{ K}$ . The bolometer was defined by means of electron beam lithography and represented a  $1.7\ \mu\text{m}$  wide and  $0.2\ \mu\text{m}$  long bridge connecting the inner terminals of a planar feed antenna. The complementary logarithmic-spiral planar antenna was lithographed from a thermally evaporated gold film (for details see Ref. 4). According to an estimate [5], the complementary spiral antenna should have an impedance of about  $75\ \Omega$  when suspended in free space. We expect  $\varepsilon^{1/2}$  times smaller value for our antenna since it is supported by the dielectric substrate with the dielectric constant  $\varepsilon$  and the thickness much larger than the wavelength. The substrate with the HEB was glued onto the flat side of an extended hemispherical lens from pure silicon.

The mixer performance was investigated at seven different frequencies ranging from 0.7 THz up to 5.2 THz. Experimental setup, which we used for noise temperature measurements, has been described elsewhere [6]. Briefly, an optically pumped far-infrared gas laser served as local oscillator (LO). Signal radiation from the Eccosorb black body was superimposed on the LO radiation by a mylar  $6\text{-}\mu\text{m}$  thick beam splitter. The approximately half-meter long optical path from the black body to the cryostat window was not evacuated. The intermediate frequency (IF) circuit inside the cryostat comprised an isolator associated with a bias tee and a low noise (6 K noise temperature) amplifier. The IF signal was recorded after additional amplification in the 75 MHz bandwidth centered at 1.5 GHz.

## III. NOISE TEMPERATURE

Noise temperatures reported in this paper are typical for our devices. The frequency dependence was usually measured with the same device once mounted in the holder. Here we report data obtained with the 6-mm lens without antireflection coating. In Fig. 1 the DSB receiver noise temperature is shown as a function of the LO frequency

between 0.7 THz and 5.2 THz. Also shown is the DSB receiver noise temperature corrected for optical losses. In this case the increase of the noise temperature with frequency follows closely the  $10 h\nu/k_B$  level. For the estimation of the lower cut-off frequency of our log-spiral antenna we use the criterion [5]  $\lambda^*/2 \leq C$  where  $C$  is the maximal diameter of the spiral structure and  $\lambda^*$  is the wavelength in the substrate. For our design with  $C = 130 \mu\text{m}$  this yields a wavelength in free space of  $884 \mu\text{m}$  (0.34 THz). The wavelength corresponding to the upper cut-off frequency of the antenna is about 10 times the inner radius at which the actual shape deviates from the ideal spiral [7]. In our case this is  $1.3 \mu\text{m}$  yielding the lower limit  $44 \mu\text{m}$  (6.8 THz) for the wavelength in free space. We, therefore, believe that besides conductivity losses in the gold itself the antenna does not contribute any frequency dependence to the noise temperature. For an analysis of the optical losses and the antenna pattern see Ref. [6,8].

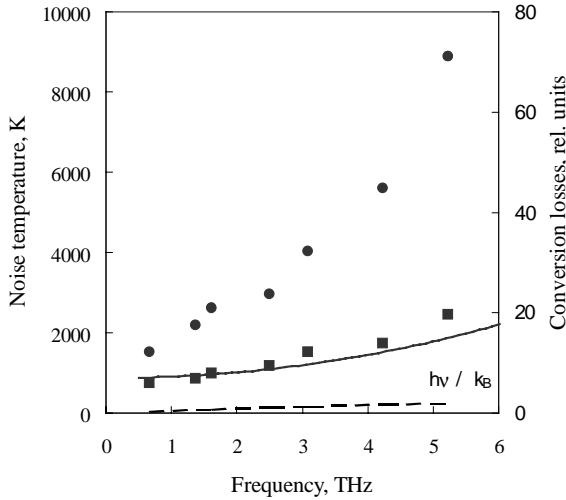


**Fig. 1:** DSB system noise temperature measured (circles) and corrected (squares) for losses in the optical elements. The dashed line represents the quantum limited noise temperature  $h\nu/k_B$ . The solid line shows the calculated conversion losses. The scale of the right axis was adjusted in order to match calculated conversion losses and corrected noise temperature.

#### IV. ANTIREFLECTION COATING

The main contribution to the optical losses originates from the Silicon lens. The uncoated lens has a reflection loss of about 1.5 dB. Therefore an antireflection coating can significantly reduce the receiver noise temperature. Parylene is a good candidate as an antireflection coating. It is a polymer with a refractive index of about 1.62 and therefore matches closely the required value for a single antireflection layer on silicon, which is  $n_{\text{Si}}^{1/2} \approx 1.84$ . Beside this it has a high thermal stability and is chemically inert with low water absorption. Parylene is deposited from the gas phase. This results in films of uniform thickness and high conformity. Parylene exists in different forms. In this study Parylene C was investigated.

Two plane-parallel samples from high resistivity Silicon ( $> 5 \text{ k}\Omega \text{ cm}$ ) with a thickness of 5 mm were prepared. One of the samples was coated on one side with a Parylene layer of  $18.5 \mu\text{m}$  thickness while the other remained uncoated. The transmittance of both samples was measured in a Fourier-transform spectrometer in the wavelength range between  $100 \mu\text{m}$  and  $320 \mu\text{m}$ . The results are shown in Fig. 2. The lowest curve displays the transmittance of the uncoated Silicon sample and the curve in the middle displays the transmittance of the coated sample. While the uncoated sample has a transmission between 50% and 53% the coated sample has a peak transmittance of 64% at  $130 \mu\text{m}$  which decreases to 59% and 55% at  $100 \mu\text{m}$  and  $320 \mu\text{m}$ , respectively. From these data the transmittance of the coated Silicon surface which is relevant for the quasioptical HEB mixer was calculated assuming multiple reflections inside the Silicon and an absorption coefficient of  $0.05 \text{ cm}^{-1}$  [9]. The result is presented in the uppermost curve of Fig. 2. A transmittance of 93% at  $130 \mu\text{m}$  is achieved. It stays above 90% between  $115 \mu\text{m}$  and  $165 \mu\text{m}$ . This is sufficient for most practical receiver applications. The solid line in Fig. 2 represents the calculated transmission of a single layer of Parylene on a Silicon substrate.

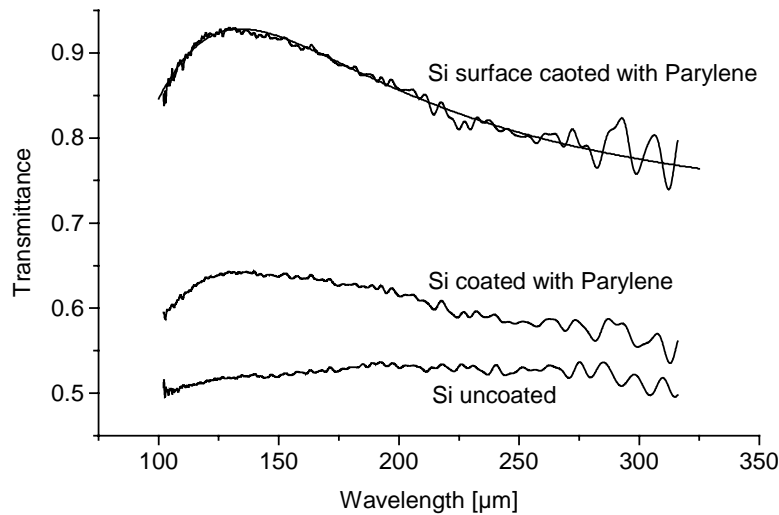


**Fig. 2:** Transmittance of Silicon with and without a coating of Parylene C.

The thickness of the Parylene layer and its absorption coefficient were chosen to give the best match between the measured and the calculated curve. From this we derive a layer thickness of  $20 \mu\text{m}$  and an absorption coefficient of  $25 \text{ cm}^{-1}$  for Parylene C. Both are independent of the frequency in the considered range. The thickness as derived from the optical data is slightly higher than measured with a profiler which yielded  $18.5 \mu\text{m}$ . This difference is well in the error limit of both methods. The absorption coefficient is significantly lower than the previously reported one of  $75 \text{ cm}^{-1}$  [10]. However, all measurements are indirect, i.e. the absorption coefficient is derived from transmittance measurements of a sample coated by Parylene and not by a direct transmission measurement of Parylene itself. In addition the quality of the film may differ and contribute to different absorption coefficients.

The improvement of the noise temperature due to a lens coated with Parylene C was investigated for two HEB mixers. Two lenses each with a diameter of 6 mm were made from the same silicon crystal. One of the lenses was coated with an  $18.5 \mu\text{m}$  thick Parylene C layer.

For both HEB mixers the noise temperature was measured at four different frequencies between 0.7 THz and 2.5 THz by using the coated lens as well as the uncoated lens. In Table 1 the results are shown. A significant improvement of about 30% was achieved at 2.5 THz. This improvement decreases towards the smaller frequencies as it is expected because the thickness of the Parylene layer corresponds to about a quarter wavelength at 2.5 THz. Fig. 3 illustrates the relative improvement, i.e. the difference in noise temperature divided by the noise temperature measured with the uncoated lens. Also shown is the relative improvement as it is expected from the transmittance measurements described above. In this case, the relative improvement is the difference in transmittance between the coated and the uncoated flat Silicon sample divided by the transmittance of the uncoated sample

Freq. [THz]	Device A, $T_{rec}$ [K]		Device B, $T_{rec}$ [K]	
	no AR coating	Parylene coating	no AR coating	Parylene coating
0.693	2200	2100	5300	5300
1.397	2700	2300	7600	5500
1.627	2800	2200	7500	6200
2.523	3900	2500	9400	6500

**Table 1:** DSB receiver noise temperature for two HEB mixers. Both were measured with a Silicon lens with and without a Parylene antireflection coating.

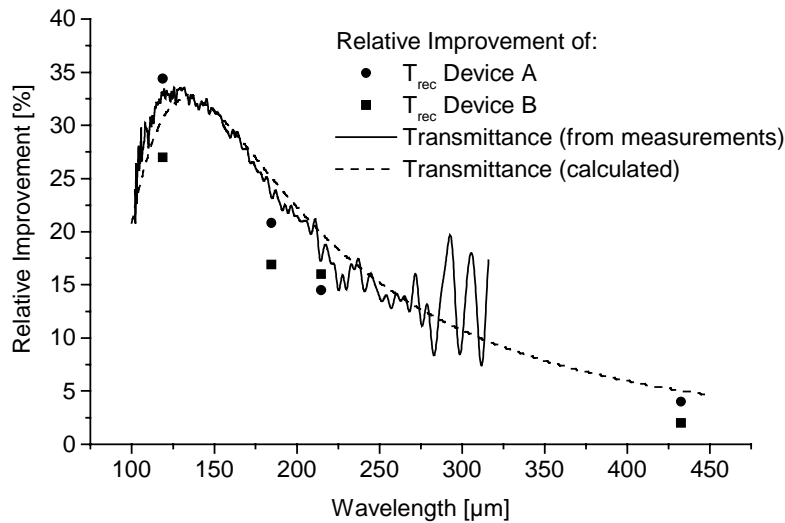


**Fig. 3:** Relative improvement of noise temperature and transmittance due to coating with Parylene C.

## V. FREQUENCY DEPENDENCE OF THE MIXER PERFORMANCE

We discuss now features, which can not be understood in terms of the traditional hot-electron model. This model suggests that the mixers under optimal operation may be driven into either quasi-homogeneous [11] or non-uniform resistive state [12,13]. In both cases, though, the energy of the quantum corresponding to the LO frequency is supposed to be large

compared to the actual magnitude of the energy gap. Consequently, it is further supposed that absorption of radiation in the mixer is spatially uniform while the Joule heating due to bias occurs only in those parts, which are driven in the normal state. With an appropriate set of fitting parameters, both approaches fairly well describe current-voltage characteristics of the hot-electron mixer and predict reasonable values of the noise temperature and conversion efficiency. These models suggest that the noise temperature of the mixer, when corrected for optical losses, should not depend on the LO frequency unless it approaches the quantum limited value  $h\nu/k_B$ . On the contrary, analysis of the experimental data in the LO frequency range from 0.7 THz to 5.2 THz shows [6,8] that the DSB system noise temperature of the lattice-cooled hot-electron NbN mixer increases with frequency and that this increase can-not fully account for the optical losses. In this section we compare the performance of the same mixer optimally operated at LO frequencies 2.5 THz and 0.7 THz (118.8  $\mu\text{m}$  and 432.6  $\mu\text{m}$ ) using the setup described earlier in this paper. Thorough analysis of the experimental data shows that there are more features in contradiction with the traditional model.

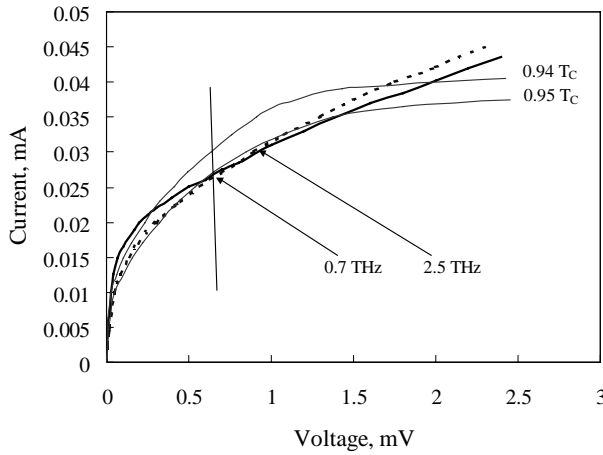


**Fig. 4:** CVC of the mixer with optimal LO power at 2.5 THz (dotted line) and 0.7 THz (thick solid line) recorded at the bath temperature 4.5 K and CVC without LO power (thin solid lines) recorded at 8.0 K (0.94  $T_C$ ) and at 8.1 K (0.95  $T_C$ ). Arrows point optimal bias regimes. The tilted straight line represents the trajectory of the operation point when the LO power changes.

Current-voltage characteristics (CVC) of the mixer are presented in Fig. 4. One can clearly see that optimal operation regimes for 2.5 THz and 0.7 THz are different and so are the CVC recorded with optimal LO power. It is worth noting that the ac resistance does not change much, thus providing in both regimes approximately the same matching of the device to the IF network. Characteristics recorded at an elevated temperature without local oscillator differ in shape from characteristics recorded at optimal LO power, although the temperature in the former case was adjusted in order to provide the best possible match between the two types of characteristic. Moreover, the noise power under optimal operation is noticeably larger when the mixer is pumped by the LO with smaller frequency. The corrected system noise temperature at 2.5 THz amounts 1140 K that is 1.6 times the corrected noise temperature at 0.7 THz, whereas the noise of the HEB drops almost twice within the same frequency interval. This observation implies that the mixer conversion efficiency decreases from -10 dB at 0.7 THz to -14.5 dB at 2.5 THz. The frequency dependence of the conversion efficiency may arise from the intrinsic mixing mechanism as well as from the frequency dependent coupling of radiation. We first consider the mixing mechanism.

## A) Intrinsic Mixing Mechanism

Since the thermal approach relying on an elevated effective temperature of electrons and phonons does not suggest any frequency dependence we take into account effects inherent to the superconducting state. Indeed, it has been shown that suppression of superconductivity due to irradiation occurs differently depending on the energy of the radiation quantum  $h\nu$ , i.e. whether  $h\nu - 2\Delta$  ( $\Delta$  is the energy gap) is small or large compared to the energy gap. Qualitatively, the high frequency limit corresponds to the steady-state nonequilibrium distribution function of quasiparticles, which are spread over the energy interval from  $\Delta$  to  $h\nu$ . In the limiting case,  $h\nu \gg 2\Delta$ , the temperature dependence of the energy gap under irradiation flattens compared to the equilibrium situation [14].

In the opposite limiting case,  $h\nu - 2\Delta \ll 2\Delta$ , quasiparticles are produced in the narrow energy interval above the gap. Detailed calculations of the nonequilibrium distribution function [15] show that, indeed, excess quasiparticles are located mostly around the energy  $h\nu/2$  above the gap edge. The localized nonequilibrium distribution suppresses the energy gap in a manner similar to that suggested by the  $\mu^*$ -model [16]. In particular, this model predicts that under external pair breaking the gap initially decreases down to the value  $0.62 \Delta$  at which the first-order transition to the normal state occur. At small disturbances the first order transition is also expected for the energy gap versus temperature whereas under strong disturbance the slope of the transition becomes smoother and reaches the value typical for the transition in equilibrium. Thus, the rate of the gap decrease under external pair breaking should be larger at smaller radiation frequencies. In the mixing experiment, the difference between two limiting cases can be detected only if the resistance of the mixer in the operation point depends directly on the energy gap. We consider the superconducting strip with a normal domain. The bias current passing the interface between the domain and the remaining superconducting portion of the strip generates charge imbalance in the superconducting side. This is accompanied by penetration of the electric field into superconductor over the distance  $\Lambda_E$ . Each side of the domain contributes additional resistance  $\rho \Lambda_E / S$  ( $\rho$  is the normal resistivity and  $S$  is the cross-section of the strip). The same additional resistance appears at each contact of the bolometer with normal metal. This simple picture strictly holds only if the penetration depth of the electric field is comparable or larger than the thermal healing length  $\Lambda_T = (D\tau_\theta)^{1/2}$ , which controls thermal smearing of the domain walls and, on the other hand, represents the smallest length of the normal domain. Here  $\tau_\theta$  and  $D$  are the electron cooling time and electron diffusivity, respectively. We estimate that for our NbN films in equilibrium at  $T = 0.9 T_C$  both thermal healing length and penetration length equal approximately 25 nm. Under optimal operation, the local oscillator suppresses the energy gap in the superconducting part of the bolometer. Though the exact value of the gap is hard to calculate, an estimate can be made comparing CVC (see Fig. 4) recorded with and without LO power. In our case the energy gap at optimal operation approximately equals the equilibrium energy gap at  $T = 0.9 T_C$ . At optimal bias the dc resistance of the HEB ranges typically from 1/3 to 1/2 of the normal resistance that corresponds, for a 200-nm long device, to the normal portion of about 80-nm length. Thus, the charge imbalance may be responsible for the part of the resistance under optimal operation conditions. Both  $dr/dW$  and  $dr/dT$ , which mainly determine the conversion efficiency and the electric noise due to thermal fluctuations, bear contribution from the normal domain and from the charge imbalance regions. The contribution due to charge imbalance is determined by the actual value of the energy gap in the superconducting part of

the strip and, therefore, depends on the radiation frequency. The present qualitative model appears capable to explain why pumping of the mixer by the LO with larger frequency results in the decrease of the output noise. The model also suggests smaller conversion efficiency at higher LO frequencies due to the decrease of  $dr/dW$ . The mechanism described above does not necessarily result in variations of the system noise temperature with frequency since changes of the output noise power and conversion efficiency may compensate each other.

## B) Coupling Efficiency

Dependence of the mixer performance on the LO frequency may arise due to the change of the coupling efficiency. We consider here coupling of the high frequency current flowing in the arms of the planar spiral antenna with the superconducting bolometer. The simplified, although, relevant prototype is an infinitely long slot line on a dielectric substrate and a metal strip which bridges opposite sides of the line to mimic the bolometer. Since the resistivity of the bolometer for the LO frequency is large compared to the resistivity of the contacts and its width is much smaller than the wavelength, one can use the quasi-static approximation to find the distribution of the current in the strip. Inside the strip, the electric field  $E$  of the frequency  $\omega$  satisfies the equation [17].

$$\nabla^2 \vec{E} = i \frac{\omega \mu_0}{\rho} \vec{E} \quad (1)$$

The thickness of the bolometer is small compared to the skin depth  $\delta = (2\rho/\mu_0\omega)^{1/2}$ , which in turn is much larger than the electron mean free path in NbN. We, therefore, deal with the normal skin effect and uniform distribution of the high frequency current through the film thickness. If the high frequency voltage  $U$  is fixed at the antenna terminals, the solution of Eq. 1 for the current distribution across the strip  $j(x) = E(x)/\rho_n$  is given by

$$j(x) = j_0 \left( csh^2(x/\delta) \cos^2(x/\delta) + i sh^2(x/\delta) \sin^2(x/\delta) \right) \quad (2)$$

$$j_0 = \frac{U}{\rho_n L} \left[ csh(a/2\delta) \cos(a/2\delta) + i sh(a/2\delta) \sin(a/2\delta) \right]^{-1}$$

where  $x$  varies from  $-a/2$  to  $a/2$  and  $L$  is the bolometer length. Fig. 5 shows the distribution of the dissipated power  $U(j(x)j^*(x))^{1/2}$  according to Equation 2 for frequencies 2.5 THz and 0.7 THz in a 1.7  $\mu\text{m}$  wide strip having the normal resistivity 3.5  $\mu\Omega\cdot\text{m}$  that is typical for our devices. One can see that at 2.5 THz power is absorbed mostly near the bridge edges. The central part of the strip remains in a regime, which is not optimal and effectively shunts the peripheral area of the device. The non-uniformity should result in the conversion efficiency smaller than it could be in the case of the uniform distribution of the high frequency current. Thus, hampering of the conversion efficiency due to non-uniformity should strengthen for our devices with frequency in the relevant frequency interval. Knowing the distribution of the current, it is straightforward to calculate the effective impedance of the strip and the coupling between the antenna and the mixer. For the equivalent circuit comprising the bolometer with the normal square resistance  $R_s$  and the antenna with the real impedance  $R_a$ , the radiation coupling efficiency is given by

$$K = \frac{4 \frac{R_a}{R_s} \frac{2\delta}{L} \frac{sh(a/2\delta) + \sin(a/2\delta)}{csh(a/2\delta) - \cos(a/2\delta)}}{\left( \frac{sh(a/2\delta) - \sin(a/2\delta)}{csh(a/2\delta) - \cos(a/2\delta)} \right)^2 + \left( \frac{sh(a/2\delta) + \sin(a/2\delta)}{csh(a/2\delta) - \cos(a/2\delta)} + \frac{R_a}{R_s} \frac{2\delta}{L} \right)^2} \quad (3)$$

Due to the non-uniform distribution of the high frequency current, the conversion efficiency of the mixer should have approximately the same frequency dependence. We, therefore, compare the frequency dependence of the noise temperature with  $K^2$  that accounts for both frequency dependent contributions. For calculations we used the antenna impedance  $25 \Omega$ , the normal square resistance  $900 \Omega$  and actual parameters of our device. Results of simulation are presented in Fig. 1. There is reasonable agreement between model results and experimental data at frequencies up to 4 THz. In this frequency range, decrease of the conversion efficiency with LO frequency explains almost uniquely the degradation of the mixer noise temperature. At higher frequency, displacement currents, which we did not take into account, may cause additional decrease of the coupling efficiency. Contribution to the frequency conversion that arises from the charge imbalance area may also modify the frequency dependence of the noise temperature. We believe that the frequency dependent non-uniform distribution of the high frequency current and the frequency dependent excess noise due to charge imbalance are both responsible for the increasing noise temperature of the HEB mixer at terahertz frequencies.

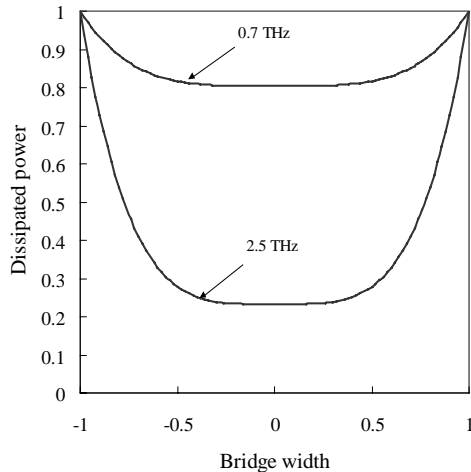


**Fig. 5:** Distribution of the dissipated high frequency power in the HEB. Position across the bolometer is plotted in units of its half width. The absorbed power is normalized to unity at the bolometer edges.

## VI. CONCLUSION

We have shown that the noise temperature of the lattice-cooled hot-electron bolometer mixer increases with frequency and that this increase can not be explained neither by the frequency dependent parameters of the coupling optics nor by the conventional models of the hot-electron bolometer. We have developed a new model, which takes into account the non-uniform distribution of the high frequency current in the bolometer and the frequency dependent contribution to the electric noise and conversion efficiency stemming from charge imbalance phenomenon. We have demonstrated that the former effect explains almost by itself

the frequency dependence of the corrected noise temperature and the magnitude of the conversion losses in the frequency range from 0.7 THz to 4 THz. Further improvement of the performance of the HEB mixer may be achieved making use of narrower bolometers. This should result in more uniform current distribution and, consequently, in better coupling. To maintain the resistance of the bolometer and, thus, the maximal coupling efficiency unchanged, the length of the bolometer should be proportionally decreased. In addition, we have shown that Parylene works as an antireflection coating for Silicon at terahertz frequencies. An improvement of the noise temperature of about 30% at 2.5 THz was achieved by using a Silicon lens with a Parylene coating.

The work was supported by the German Ministry of Science and Education (WTZ RUS-149-97) and NATO Division of Scientific Affairs.

## REFERENCES

- [1] H. P. Röser, H.-W. Hübers, T. W. Crowe, W. C. B. Peatman, *Infrared Phys. Technol.* **35**, 451 (1994).
- [2] A. L. Betz, R. T. Boreiko, *Proc. of the 7<sup>th</sup> Int. Symp. on Space Terahertz Technology*, 503 (1996).
- [3] S. Cherednichenko, P. Yagoubov, K. Il'in, G. Gol'tsman, E. Gershenson, *Proc. of the 8<sup>th</sup> Int. Symp. on Space Terahertz Technology*, 245 (1997).
- [4] S. Svechnikov, A. Verevkin, B. Voronov, E. Menschikov, E. Gershenson, G. Gol'tsman, *Proc. of the 9<sup>th</sup> Int. Symp. on Space Terahertz Technology*, 45 (1998).
- [5] J. D. Kraus, *Antennas*, McGraw-Hill, Inc., (1988).
- [6] J. Schubert, A. Semenov, G. Gol'tsman, H.-W. Hübers, G. Schwaab, B. Voronov, E. Gershenson, *Supercond. Sci. Technology* **12**, 748 (1999).
- [7] H. Büttgenbach, R. E. Miller, M. J. Wengler, D. M. Watson, T. G. Phillips, *IEEE Trans. on Microwave Theory Tech.* **36**, 1720 (1988).
- [8] H.-W. Hübers, J. Schubert, A. Semenov, G. Gol'tsman, B. Voronov, G. Gershenson, A. Krabbe, H. P. Röser, to appear in: *Proc. of SPIE Conf. on Airborne Astronomy Systems*, Munich, March 2000.
- [9] D. Grischkowsky, S. Keiding, M. van Exter, Ch. Fattinger, *J. Opt. Soc. Am. B* **7**, 2006 (1990).
- [10] P. G. J. Irwin, P. A. R. Ade, S. B. Calcutt, F. W. Taylor, J. S. Seeley, R. Hunnemann, L. Walton, *Infrared Phys.* **34**, 549 (1993).
- [11] S. Nebosis, A.D. Semenov, Yu.P. Gousev, and K.F. Renk, *Proc. of the 7<sup>th</sup> Int. Symp. on Space Terahertz Technology*, 601 (1996).
- [12] D. Wilms Floet, E. Miedema, J.J.A. Baselmans, T.M. Klapwijk, J.R. Gao, *IEEE Transactions on Applied Superconductivity* **9**, 3749 (1999).
- [13] H. Merkel, P. Khosropanah, P. Yagoubov, E. Kollberg, *IEEE Transactions on Applied Superconductivity* **9**, 4201 (1999).
- [14] V.F. Elesin, *Sov. Phys. JETP* **44**, 780 (1976).
- [15] V.F. Elesin, Yu.V. Kopaev, *Sov. Phys. Uspekhi (USA)* **24**, 116 (1981).
- [16] C.S. Owen and D.J. Scalapino, *Phys. Rev. Lett.* **28**, 1559 (1972).
- [20] Landau and E.M. Lifshitz, *Course of Theoretical Physics*, vol. 8 (Electrodynamics of Continuous Media), Reed Educational and Professional Publishing Ltd, 1984, ISBN 0-750-62634-8.

# SUCCESSFUL OPERATION OF A 1 THz NbN HOT-ELECTRON BOLOMETER RECEIVER

C.-Y. Edward Tong<sup>a</sup>, Jonathan Kawamura<sup>b</sup>, Todd R. Hunter<sup>a</sup>,  
D. Cosmo Papa<sup>a</sup>, Raymond Blundell<sup>a</sup>, Michael Smith<sup>a</sup>  
Ferdinand Patt<sup>c</sup>, Gregory Gol'tsman<sup>d</sup>, and Eugene Gershenzon<sup>d</sup>

## Abstract

A phonon-cooled NbN superconductive hot-electron bolometer receiver covering the frequency range 0.8 - 1.04 THz has successfully been used for astronomical observation at the Sub-Millimeter Telescope Observatory on Mount Graham, Arizona. This waveguide heterodyne receiver is a modified version of our fixed-tuned 800 GHz HEB receiver to allow for operation beyond 1 THz. The measured noise temperature of this receiver is about 1250 K at 0.81 THz, 560 K at 0.84 THz, and 1600 K at 1.035 THz. It has a 1 GHz wide IF bandwidth, centered at 1.8 GHz. This receiver has recently been used to detect the CO (9 → 8) molecular line emission at 1.037 THz in the Orion nebula. This is the first time a ground-based heterodyne receiver has been used to detect a celestial source above 1 THz.

<sup>a</sup> Harvard-Smithsonian Center for Astrophysics, 60 Garden St., Cambridge, MA 02138.

<sup>b</sup> California Institute of Technology, 320-47, Pasadena, CA 91125.

<sup>c</sup> Submillimeter Telescope Observatory, 933 N. Cherry Av., Tuscon, AZ 85721.

<sup>d</sup> Moscow State Pedagogical University, Moscow, 119435, Russia.

## I. INTRODUCTION

As superconducting receiver technology has matured in recent years, low-noise heterodyne receivers have been developed for the THz frequency band. The first laboratory superconducting heterodyne mixer operating above 1 THz was reported in 1996 [1]. This receiver used an SIS mixer, which can offer nearly quantum-limited noise performance up to 1 THz, but which becomes very noisy above 1 THz. Since then, several groups have reported low noise performance at THz frequencies using receivers that employ superconductive hot-electron bolometer (HEB) mixers [2-4].

The Submillimeter Receiver Laboratory at the Harvard-Smithsonian Center for Astrophysics has been collaborating with the Moscow State Pedagogical University since 1994 to develop phonon-cooled HEB waveguide mixers. This effort has been very fruitful, and we have been able to routinely produce submillimeter and terahertz receivers having noise temperatures in the range of  $10 - 20h\nu/k$ , at operating frequencies up to 1.26 THz in our laboratory [5,6]. In the winters of 97/98 and 98/99, we installed our 800 GHz HEB receiver on the 10-m Heinrich Hertz Telescope on Mt. Graham, Arizona. This receiver was the first superconductive HEB receiver deployed outside a laboratory environment [7]. It was used successfully to detect molecular emission lines from a number of astronomical sources at 690 and 810 GHz [8].

In this paper, we report on improvements to this receiver that extend its frequency of operation to beyond 1 THz. Earlier this year, this receiver was successfully used to detect the molecular emission of CO(9  $\rightarrow$  8) at 1.037 THz in the Orion Nebula (M42). This marks the first time a ground-based heterodyne instrument has ever detected a celestial source above 1 THz.

## II. INSTRUMENT DESIGN

### A. Hot Electron Bolometer Elements

The mixer elements are made from high-purity NbN film deposited on a heated 0.1-mm-thick  $z$ -cut crystalline quartz substrate. The film is about 4 nm thick. The critical temperature,  $T_c$ , of the film is about 9 K, and it has a transition width of about 0.5 K. The active area of the bolometer, lying between two normal-conducting TiAu electrodes, is about  $2 \mu\text{m}$  wide by  $0.2 \mu\text{m}$  long. The normal-state resistance ( $R_N$ ) of the bolometers is fairly uniform over a single wafer.

The quartz wafer is first diced into small blocks of about 5 mm square before being lapped and polished to a thickness of  $23\ \mu\text{m}$ . After lapping, the individual mixer chips measuring  $90\ \mu\text{m}$  wide and 1.4 mm long are diced from these square blocks. Even with these small dimensions the mixer chips are quite robust and are rather easy to handle. The particular device used in the astronomical receiver has a room temperature resistance of about  $350\ \Omega$  and a critical current of  $85\ \mu\text{A}$ . The useful upper limit to the IF bandwidth of these devices is about 2.5 GHz.

## **B. Mixer Assembly Design**

The mixer assembly is adapted from the design of the highly successful fixed-tuned SIS mixer we developed for the Submillimeter Array [9]. It is made in two sections. The front section carries the corrugated feed horn, which is electroformed and shrunk-fit into a copper mounting block. The horn terminates in a section of half-height rectangular waveguide, measuring  $254 \times 64\ \mu\text{m}$ . The back section of the mixer assembly houses a shorted section of waveguide, measuring  $200 \times 50 \times 60\ \mu\text{m}$ . The quartz chip is suspended across the waveguide and is clamped between the two halves of the mixer assembly. It is electrically contacted by two  $75\ \mu\text{m}$  diameter wires, one to the IF connector, the other is grounded in the mixer block.

## **C. Receiver Layout**

The layout of the receiver is shown in Fig. 1. The mixer assembly is mounted to the cold plate of a liquid helium-cooled cryostat that has a liquid nitrogen cooled radiation shield. The corrugated feed horn illuminates a  $30^\circ$  off-axis parabolic mirror ( $f = 55\ \text{mm}$ ) positioned near the center of the dewar cold plate. The beam reflected off the paraboloid passes through two layers of porous Teflon sheet thermally anchored to the cold plate. These are followed by a 5 mm thick crystalline quartz infrared blocking filter mounted on the 77 K radiation shield.  $55\ \mu\text{m}$  deep grooves are machined into both sides of the quartz for the purposes of eliminating surface reflections. A 0.5 mm-thick Teflon sheet is used as the vacuum window.

Radiation from the LO assembly is collimated by a  $90^\circ$  off-axis parabolic mirror before it is combined with the signal beam from the signal port in a Martin-Puplett interferometer (MPI), which is placed in front of the cryostat vacuum window. In the laboratory, the interferometer employs free-standing wire grid polarizers with  $10\ \mu\text{m}$  diameter wire. On the telescope, wire grid polarizers with  $20\ \mu\text{m}$

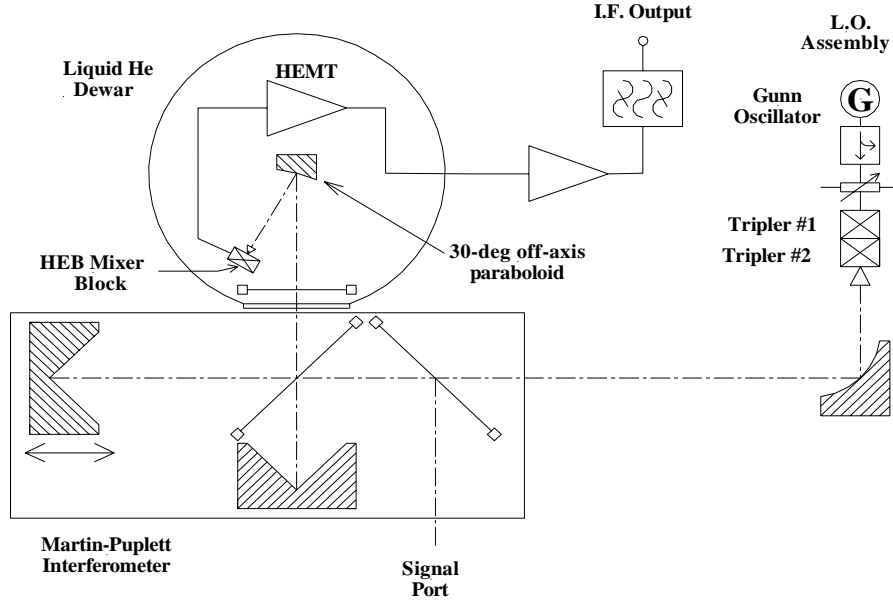


Fig. 1 Layout of the Receiver. The mixer assembly, parabolic mirror and the HEMT amplifier are mounted on the 4.2 K cold plate. The MPI is placed in front of the cryostat vacuum window. The optical path from the vacuum window to the signal port is approximately 0.5 m.

diameter wire are used. The insertion loss of the MPI is estimated to be  $\sim 1$  dB.

The output of the mixer is connected to a 1.4–2.2 GHz high-electron mobility transistor (HEMT) amplifier, mounted on the same 4.2 K cold plate, through a bias tee. No isolator is used between the mixer block and the amplifier. After second-stage room temperature amplification, the IF signal is fed through an equalizer to flatten the receiver output across the entire IF band. During actual telescope operations, the usable IF bandwidth is 1 GHz wide: 1.3–2.3 GHz. In our laboratory, a 100 MHz wide IF filter, centered at 1.5 GHz, was employed for hot/cold load receiver noise measurement.

#### D. Local Oscillator Sources

We estimate that the incident LO power at the LO port of the MPI is less than  $1 \mu\text{W}$ , when the mixer is biased at its optimal operating point. With some care in the optics design, we were able to provide sufficient LO power using all solid-state LO units, each comprised of a Gunn oscillator followed by 2 stages of varactor multiplication [10].

Two LO units were available for operation at the telescope. The first one

covers 780–840 GHz. This unit uses a 130 - 140 GHz Gunn oscillator and a cascaded frequency doubler and tripler. The second LO unit covers 1.017–1.035 THz, with a 112 - 115 GHz Gunn oscillator and a cascade of two triplers. In addition, a third unit covering 800 - 936 GHz was available in the laboratory. This unit incorporates a Gunn oscillator operating between 100 and 117 GHz, linked to a first-stage doubler and a second-stage quadrupler.

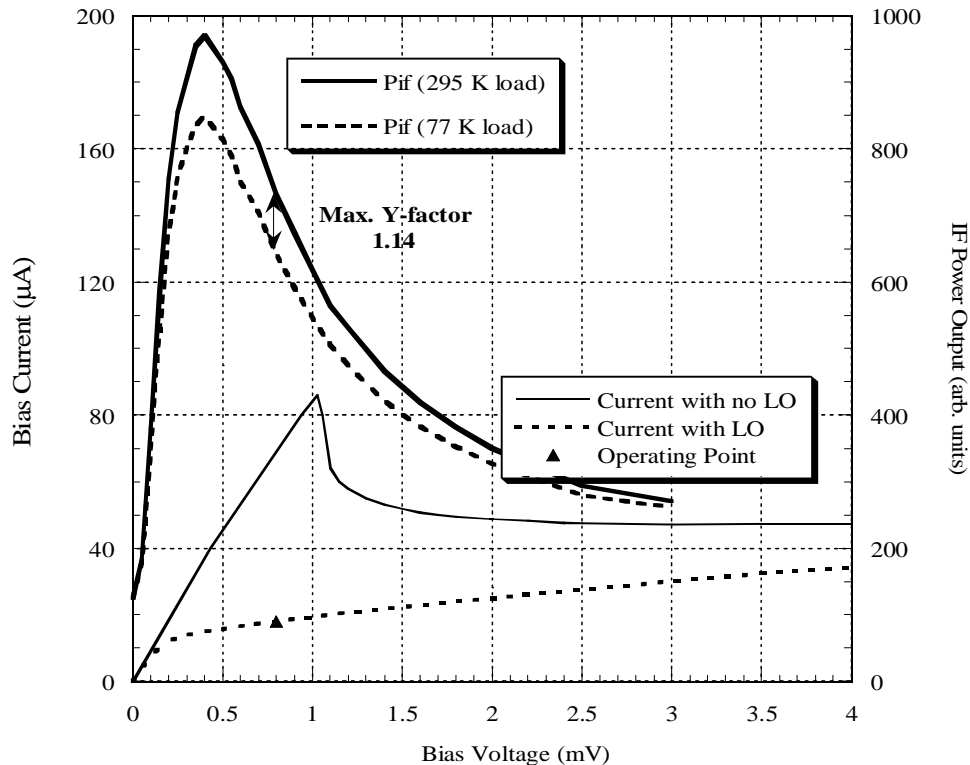


Fig. 2 Current-voltage characteristics of the HEB mixer, with and without LO drive at 1.035 THz. Also shown is the receiver IF power as a function of bias voltage in response to the hot (295 K) and cold (77 K) loads. A maximum Y-factor is recorded at a bias voltage of 0.8 mV and a bias current of 18  $\mu\text{A}$ .

### III. MEASURED PERFORMANCE

The current-voltage ( $I - V$ ) characteristics of the mixer are plotted in Fig. 2. Shown in the same figure are the curves of receiver IF output power in response to hot and cold loads placed at the signal port, the LO frequency was 1.035 THz. The graph shows that a Y-factor of 1.14 was obtained at a bias voltage of 0.8 mV and a bias current of 18  $\mu\text{A}$ . The double-side-band (DSB) conversion loss at this

operating point is estimated to be about 17 dB. The choice of this operating point is also dictated in part by stability consideration. At slightly lower bias voltage, the conversion efficiency of the mixer is higher and the Y-factor is comparable but the stability is not as good. At our optimal operating point, the receiver IF output power fluctuates by less than 0.5% over about 1 minute.

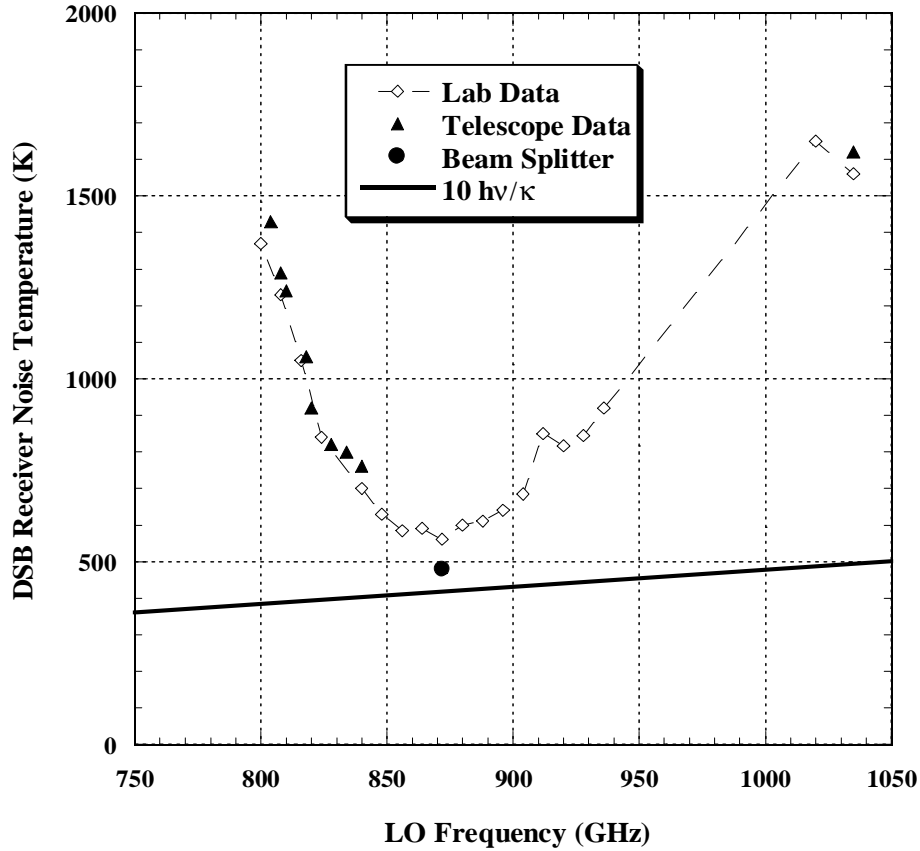


Fig. 3 Double-side-band receiver noise temperature calculated from the Y-factor for both hot/cold load measurements in the laboratory and on the telescope. Also shown is the data for the case when the MPI was replaced by a beam splitter in the laboratory.

In Fig. 3, we have plotted the receiver noise temperature calculated from the measured Y-factor as a function of LO frequency. The receiver is most sensitive at around 872 GHz where a DSB noise temperature of 560 K was measured in our laboratory. When the MPI was replaced by a wire grid diplexer with 10% coupling, the Y-factor improved to 1.39, corresponding to a receiver noise temperature of 480 K, or  $11.5 h\nu/k$ . The receiver noise temperatures measured on the telescope were found to be comparable to those measured in the laboratory, demonstrating that low noise performance is repeatable in drastically different environments, and

with different operators.

The radio beam emerging from the cryostat was measured and aligned in our laboratory using a near-field vector measurement set-up [11,12]. In this procedure, the MPI was first replaced by a mylar beam splitter. A Gunn oscillator pumping a harmonic generator was mounted on a near-field measurement X-Y stage. Measurements were carried out at 807.5 GHz. A WR-1.5 probe was employed to give a spatial resolution of 0.4 mm. On the measurement plane, the diameter of the beam at the  $-10$  dB points is about 12 mm. Therefore, the ratio between the beam size to the cross-sectional area of the waveguide probe is about 3000. Even so, a signal-to-noise ratio in excess of 30 dB was obtained at the center of the beam. We believe that this is the highest frequency near-field vector scan that has ever been performed.

Successive scans were performed. The resultant vectorial beam maps were used to determine the optical axis of the receiver. Using these data, the various optical elements of the receiver setup were adjusted. As a result of defects of the dewar, the  $30^\circ$  off-axis paraboloid inside the cryostat had to be shimmed substantially to obtain a straight beam. Finally, the MPI was inserted, and the output beam of the receiver was mapped again. Both the amplitude and phase maps of the beam are plotted in Fig. 4. Note there are no side lobes above  $-25$  dB. The final beam size is larger than the design value. This is probably caused by the shimming of the parabolic mirror, which results in a change of the effective focal length of the mirror. Our calculation suggests that this slower beam would produce an edge taper of about 17.5 dB on the telescope's secondary instead of the 12 dB designed taper.

The receiver is not affected by saturation and direct detection effects. From the total power - voltage curve in Fig. 2 and our estimate for the conversion loss, we estimate that the mixer would require about 10 nW at its input to be driven into output saturation. This value is significantly higher than the power due to incident thermal radiation from an ambient load with an IF bandwidth of about 2 GHz. From the noise temperature plot of Fig. 3, we estimate that the RF bandwidth of the receiver is about 200 GHz. The incident radiation from an ambient load with 200 GHz bandwidth is more than an order of magnitude smaller than the LO power used to operate the receiver. Thus, direct detection effects are also expected to be minimal. At the optimal operating point given in Fig. 2, the bias current changes by 60 nA, or about 0.3%, when switching between hot and cold loads,

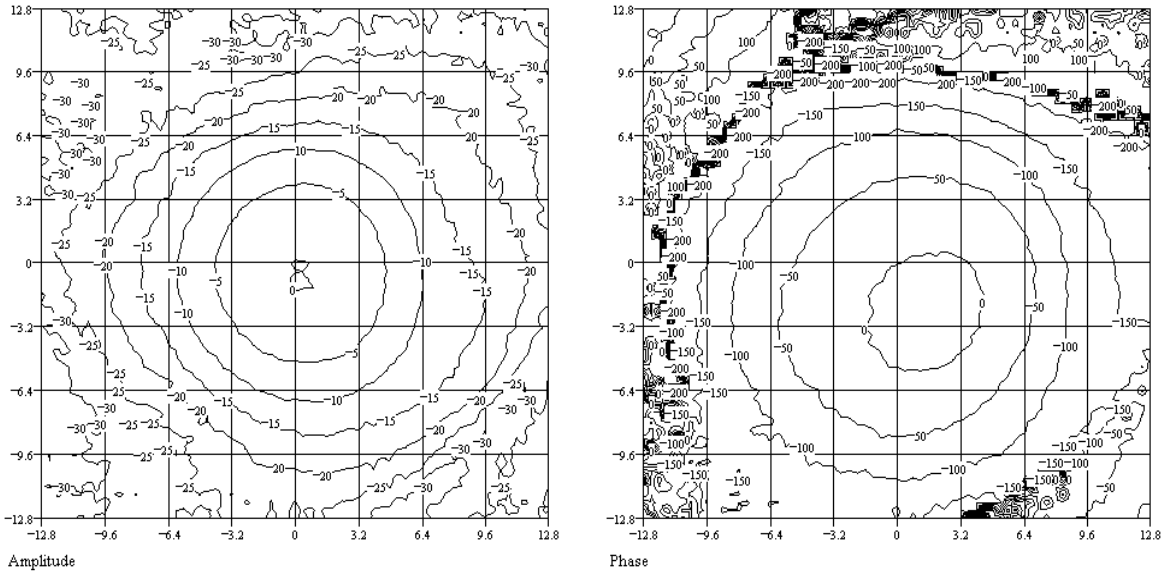


Fig. 4 Amplitude (dB) and phase (deg) maps of the receiver beam at the signal port of the MPI at 807.5 GHz. 65 x 65 data points are taken at a step size of 0.4 mm. At the center of the beam, a signal-to-noise ratio of more than 30 dB was obtained. The phase map shows that there is a residual beam tilt of 0.3 degrees off boresight. This residual misalignment was taken out during installation on the telescope.

under constant voltage bias. When the MPI is replaced by a beam-splitter, the change in bias current is approximately doubled because the MPI admits only half of the bandwidth of the incident thermal radiation from the hot and cold loads. In all our measurements, bias current changes due to direct detection are less than 1%. Therefore, the effects of direct detection on the actual heterodyne sensitivity are very small. This is confirmed by the fact that the calibration of astronomical spectral lines recorded by this receiver matches that of the same spectral lines recorded by other telescopes.

#### IV. TERAHERTZ DETECTION

In January this year, we took advantage of a period of excellent weather conditions on Mount Graham to operate the receiver above 1 THz. The zenith opacity of the sky at 225 GHz dropped to below 0.03, as indicated by a tipping radiometer near the telescope. Near 1.037 THz, the receiver noise temperature was 1600 K, and the total system single-sideband noise temperature was about  $4 \times 10^5$  K. The zenith atmospheric transmission was approximately 3%, and towards the source

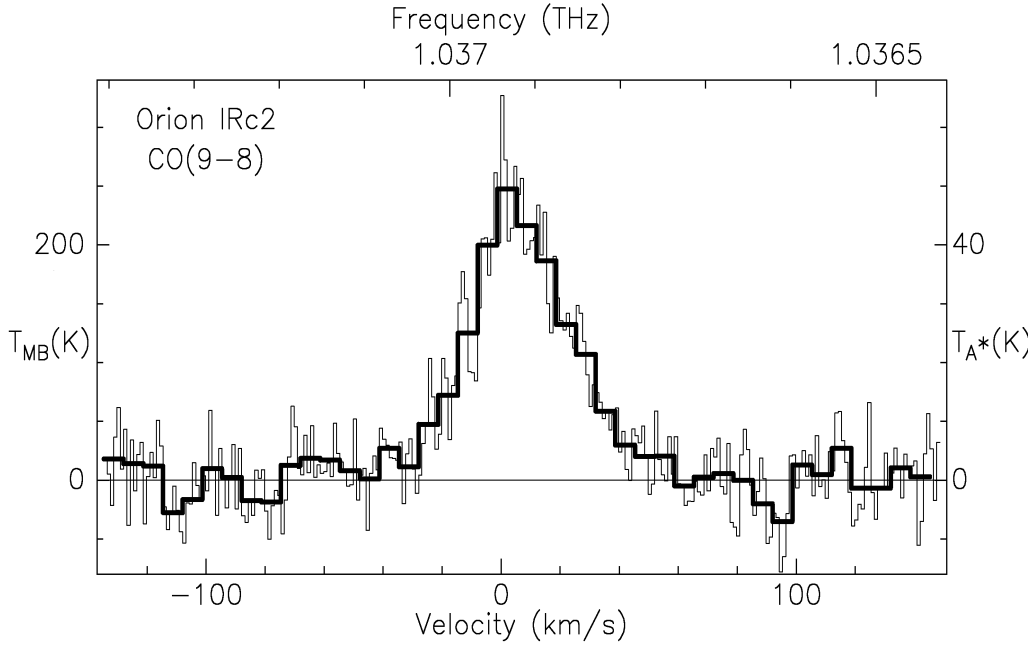


Fig. 5 Spectrum recorded by the HEB receiver at an LO frequency of 1.0352 THz from the Orion nebula. The resolution of the IF spectrometer was 4 MHz. The solid line shows a smoothed spectrum at a resolution of 25 MHz. The temperature scale of the spectrum is calibrated by taking into account the receiver noise temperature, estimated atmospheric opacity and estimated efficiency of telescope.

we observed, which is at an elevation angle of  $50^\circ$ , the transmission was about 1%. However, with just 8 minutes of integration time and a spectral resolution of 4 MHz, we recorded a fully resolved, clear spectrum of the CO( $9 \rightarrow 8$ ) molecular line emission at 1.037 THz in the Orion Nebula. Fig. 5 shows the spectrum recorded by the acousto-optical spectrometer of the telescope. The peak antenna temperature,  $T_A^*$ , which is corrected for atmospheric absorption, is about 50 K and the baseline rms noise level is about 5 K, at a resolution of 4 MHz.

Since no observations of planets were possible, we have no reliable measurement for neither the telescope aperture efficiency nor the main-beam efficiency. However, by extrapolating the data that we obtained near 800 GHz with the same receiver, we estimate the efficiency of the telescope to be about 20%. We therefore infer that the brightness temperature,  $T_{MB}$ , of the emission line is  $\sim 250$  K within the  $8''$  diameter beam of the telescope. Note that the signal-to-noise ratio is in excess of 10 for a spectral resolution of 25 MHz.

## **V. CONCLUSION**

A waveguide-mounted phonon-cooled NbN hot-electron bolometer receiver has successfully been installed for operation at the Submillimeter Telescope Observatory on Mount Graham, Arizona. The receiver covers the frequency range 0.8 - 1.04 THz, and it has been used in the first ground-based heterodyne detection of a spectral emission from a celestial source above 1 THz. We have demonstrated the feasibility of making THz observations even from ground-based instruments. Recent FTS measurements at other, higher altitude sites confirm that there are atmospheric windows with sufficiently high transmission above 1 THz [13] to justify a ground-based facility for THz radio-astronomy.

## **Acknowledgements**

We would like to thank Peter Strittmatter and Tom Wilson of Submillimeter Telescope Observatory (SMTTO) for their support, as well as Bill Peters and Bob Stupak of SMTTO, for their valuable help in the observation of Orion nebula at 1.037 THz. We are also grateful to Christian Henkel from MPIfR, Germany, for agreeing to give up his allocated observing time for the THz opportunity.

## **References**

- [1] M. Bin, M.C. Gaidis, J. Zmuidzinas, T.G. Phillips and H.G. LeDuc, "Low-noise 1 THz niobium superconducting tunnel junction mixers with a normal metal tuning circuit," *Appl. Phys. Lett.*, vol. 68, pp. 1714-1717, 1996.
- [2] B.S. Karasik, M.C. Gaidis, W.R. McGrath, B. Bumble, and H.G. LeDuc, "Low noise in a diffusion-cooled hot-electron mixer at 2.5 THz," *Appl. Phys. Lett.*, vol. 71, pp. 1567-1569, 1997.
- [3] P. Yagoubov, M. Kroug, H. Merkel, E. Kollberg, J. Schubert, H.W. Hubers, G. Schwaab, G. Gol'tsman, and E. Gershenson, "NbN hot electron bolometric mixers at frequencies between 0.7 and 3.1 THz," in *Proc. 10th Intl. Symp. Space THz Tech.*, Charlottesville, VA pp. 237-245, Mar. 99.
- [4] E. Gerecht, C.F. Musante, Y. Zhuang, K.S. Yngevesson, T. Goyetter, J.C. Dickinson, J. Waldman, P.A. Yagoubov, G. Gol'tsman, B.M. Voronov, and E.M. Gershenson, "NbN hot electron bolometric mixers — a new technology for low-noise THz receivers," *IEEE Trans. Microwave Theory Tech.*, vol. 47, pp. 2519-2527, 99.
- [5] J. Kawamura, C.E. Tong, R. Blundell, D.C. Papa, T.R. Hunter, G. Gol'tsman, S. Chered-

- nickenko, B. Voronov, and E. Gershenzon, "An 800 GHz NbN phonon-cooled hot-electron bolometer mixer receiver," *IEEE Trans. Appl. Superconductivity*, vol. 9(2), pp. 3753-3756, June 99.
- [6] C.E. Tong, J. Kawamura, R. Blundell, G. Gol'tsman, and E. Gershenzon, "Low-noise Terahertz Waveguide Hot-Electron Bolometer Heterodyne Receiver," in *1999 IEEE 7th Intl. Conf. on THz Electronics Proc., Nara, Japan*, 44-47, Nov. 99.
- [7] J. Kawamura, R. Blundell, C.E. Tong, D.C. Papa, T.R. Hunter, S.N. Paine, F. Patt, G. Gol'tsman, S. Cherendichenko, B. Voronov and E. Gershenzon, "Superconductive hot-electron bolometer mixer receiver for 800 GHz operation," *IEEE Trans. Microwave Theory Tech.*, vol. 48, pp. 683-689, 2000.
- [8] J.H. Kawamura, T.R. Hunter, C.E. Tong, R. Blundell, Q. Zhang, C. Katz, D.C. Papa, and T.K. Sridharan, "First image with the CfA superconductive HEB receiver: the protostellar outflow from IRAS 20126+4104 in CO (J=7-6)," *Pub. of the Astronomical Soc. of the Pacific*, vol. 111, pp. 1088 - 1094, Sept. 99.
- [9] R. Blundell, C.E. Tong, D.C. Papa, R.L. Leombruno, X. Zhang, S. Paine, J.A. Stern, H.G. LeDuc, and B. Bumble, "A wideband fixed-tuned SIS receiver for 200-GHz operation," *IEEE Trans. Microwave Theory Tech.*, vol. 43, pp. 933-937, Apr. 95.
- [10] C.E. Tong, R. Blundell, D.C. Papa D.C., M. Smith, J. Kawamura, G. Gol'tsman, E. Gershenzon, and B. Voronov, "An all solid-state superconducting heterodyne receiver at Terahertz frequencies," *IEEE Microwave & Guided Wave Lett.*, vol. 9(9), pp. 366-368, Sept. 99.
- [11] C.E. Tong, S. Paine, and R. Blundell, "Near-field characterization of 2-D beam patterns of submillimeter superconducting receivers," in *Proc. 5th Int. Symp. Space THz Tech., Ann Arbor, MI* pp. 660-673, May. 94.
- [12] C.E. Tong, M.T. Chen, D.C. Papa, and R. Blundell, "A novel radio-wave alignment technique for millimeter and sub-millimeter receivers," in *Proc. 9th Intl. Symp. Space THz Tech., Pasadena, CA* pp. 397-404, Mar. 98.
- [13] S. Paine, R. Blundell, D.C. Papa, J.W. Barrett, and S.J.E. Radford, "A Fourier transform spectrometer for measurement of atmospheric transmission at submillimeter wavelengths," *Pub. of the Astronomical Soc. of the Pacific*, vol. 112, pp. 108 - 118, Jan. 2000.

# MICROSTRIPLINE-COUPLED QUASI-OPTICAL NIOBIUM HOT ELECTRON BOLOMETER MIXERS AROUND 2.5 THZ

W.F.M. Ganzevles<sup>†</sup>, J.R. Gao<sup>§</sup>, P. Yagoubov<sup>§</sup>, T.M. Klapwijk<sup>†</sup>  
and P.A.J. de Korte<sup>§</sup>

Department of Applied Physics and Delft Institute for Microelectronics  
and Submicron Technology (DIMES),

<sup>†</sup>Delft University of Technology,

Lorentzweg 1, 2628 CJ Delft, The Netherlands

<sup>§</sup>Space Research Organization of the Netherlands,

Postbus 800, 9700 AV Groningen, The Netherlands

## Abstract

For the first time, the measured direct and heterodyne response of a hot electron bolometer mixer (HEBM) at 2.5 THz applying a microstripline coupling circuit is reported. A new fabrication process for quasi-optically coupled HEBMs essentially consisting of a twin slot antenna, microstripline transformer and Nb microbridge has been developed. In a Fourier transform spectrometer, the frequency response of the device is measured. We find a peak response at a frequency of 2.0 THz and the bandwidth equals 1.5 THz. The peak frequency is about 20% lower than predicted by a model based on coupling the impedance of the constituting elements. By applying 2.5 THz RF radiation from a FIR laser, the mixer can be fully pumped as is suggested by the current-voltage curves. Using a chopped Y-factor technique, an uncorrected noise temperature  $T_{N,rec}$  of 4200 K has been measured.

## 1 INTRODUCTION

Superconducting HEBMs are very promising candidates to fulfill the need for low-noise, high frequency detectors in astronomical missions like FIRST.

Practical application of these devices requires a suitable antenna like a twin-slot antenna. To match the antenna-impedance to the bridge impedance, a transmission line is needed. In the literature, the use of Co-Planar Waveguide (CPW) transmission lines at 2.5 THz is reported (Ref. 1, 2). An alternative is the use of microstripline transmission lines. So far, this coupling structure has only been used in SIS mixers and has never been introduced in HEBMs.

There are various reasons to change from CPW-transmission lines to microstriplines in high-frequency receivers. First, in a CPW-design, there is a disturbance of the antenna properties due to the fact that all other structures also are situated in the ground plane. This might have an impact on the antenna beam

pattern. This disadvantage does not take place in a design based on the microstrip-line. Second, it allows for a much larger variation in characteristic impedance of the transmission line, making it easier to match a diffusion cooled HEB, which usually has a low impedance. Besides, filter characteristics and matching can be improved significantly due to the large impedance ratios achievable. Third, the microstrip transmission line has proven to work very well in an SIS-mixer up to about 1 THz (Refs. 3, 4). Then, with respect to the fabrication, the microstripline design could be easier than that of the CPW transmission line because the structures can be defined by conventional optical lithography without the need of a high-resolution lithography such as e-beam lithography as is required for CPW-based devices. Lastly, microstriplines are widely used and the simulation models are well developed, where CPW calculations have proven to be difficult for structures having very small slots.

First, we will sketch the sample production, followed by the dc characteristics of the device. Then, we describe the simulation procedure used to predict the direct response and the measured response obtained in an Fourier transform spectrometer. We report the characteristics of the device using it as a mixer. Finally, we discuss and conclude the results obtained.

## 2 MICROSTRIPLINE-COUPLED HEBM LAY-OUT AND FABRICATION

The lay-out of the coupling structure (Fig. 1) is described as follows. A twin slot antenna is used to receive the signal. For symmetry reasons, this design intrinsically implies that no direct antenna-bridge contact can be made. To guide the signal from the antenna to the microbridge, we have made a new design in HEBM technology. A microstrip line transformer is introduced to match the antenna impedance to the microbridge impedance. The microstrip line consists of an Au ground plane, in which the antenna is defined, an Al/Nb top wiring, and a SiO<sub>2</sub> dielectric separating the top wiring from the ground plane. A microstrip line RF filter avoids leakage of the RF signal into this IF chain.

A fabrication process for Nb HEBMs has been developed using two-step electron beam lithography (EBL) to define both bridge length and width. Near UV lithography is used to define the rest of the device.

We use a high-resistivity, double-sided polished Si substrate. In the first step, a ground plane of 250 nm thick Au is evaporated on a layer of 5 nm sputtered Al, which serves as an adhesion layer. The ground plane contains the twin slot antenna and the IF CPW as well as alignment markers for consequent steps. In order for the SiO<sub>2</sub> dielectric to stick, 1.5 nm Ti is evaporated and subsequently oxidized, so that no RF currents will run in the lossy Ti (Ref. 5). In a lift-off process, a dielectric of 250 nm SiO<sub>2</sub> is sputtered on the areas where the microstripline will be located. Then we deposit 16 nm Nb using dc sputtering. Using a lift-off mask, patches of 12  $\mu\text{m}$   $\times$  12  $\mu\text{m}$  on top of the SiO<sub>2</sub> are covered. Au cooling pads are then

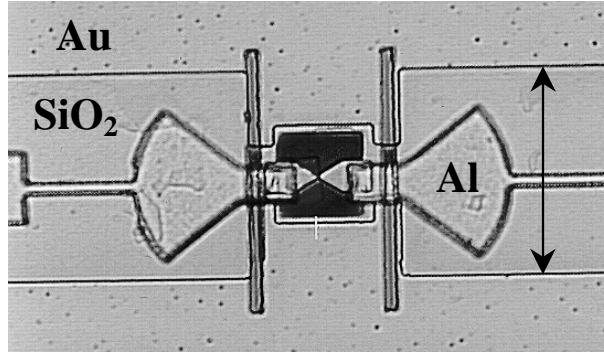


Figure 1: *Optical micrograph of a microstripline-coupled HEBM. The arrow represents 31  $\mu\text{m}$ . Left and right of the dark (Nb) square, the antenna slots in the ground plane are visible. On top of the big  $\text{SiO}_2$  rectangles, the Al/Nb top wiring is visible. Radial stubs serve as rf shorts to the ground plane, picking up radiation from the antenna. They also form the first section of the rf filter. The triangles form the cooling pads, defining the bridge length. Since this picture has been taken before defining the width of the microbridge, the Nb square is still visible.*

defined using EBL in a double layer PMMA system. RF cleaning of the Nb in an Ar-plasma is performed to remove the native Nb oxide, in order to achieve a high interface transparency. In situ,  $\sim 10$  nm Au is sputtered. Then, in a separated system, 80 nm Au is e-beam evaporated at a pressure of  $2 \times 10^{-6}$  mbar.

The top wiring layer of the microstripline is a layer of 550 nm Al, on top of which 75 nm Nb is sputtered to reduce DC- and IF series resistance. This top wiring is defined in an optical lift-off process. The deposition of this layer is the bottleneck of our process. In contrast to the typical SIS process, the superconducting bridge is in series with the top wiring. This means that contact between top- and bottom layer is established via a step coverage on the vertical wall of the  $\text{SiO}_2$ , which turns out to be rather difficult. As a last optical step, we deposit 90 nm Nb on the IF CPW-transmission line, again to avoid loss at IF. In the last production step, we define the bridge width. Using EBL, we define a PMMA bridge in the double layer resist system as before. Only the Nb parts that have to be etched are opened up. In a mixture of  $\text{CF}_4+3\%\text{O}_2$ , the Nb is reactive ion etched. We monitor the process by measuring the optical reflectivity of the Nb on the  $\text{SiO}_2$  by using a laser interferometer as an endpoint detection system. Using this process we are able to produce Nb bridges as small as  $60 \text{ nm} \times 80 \text{ nm}$  (Ref. 6).

After wire bonding, dc measurements are performed in a metal vacuum box. dc measurements are used as a quality assessment of the devices. A typical unpumped IV-curve, taken at 3 K, is shown in Fig. 3. The normal resistance is about  $15 \Omega$ , the critical current about  $70 \mu\text{A}$  and the critical temperature  $T_c = 4.6$  K. These values are similar to the ones measured in the CPW-coupled devices we measured (Ref. 2).

The RT- and IV curves found in this batch show some degradation compared to previous batches. We speculate this is related to interference of multiple processes executed in our sputtering chamber.

### 3 DIRECT RESPONSE

The geometry we use has been designed using a method that splits the structure in four separate parts. First, the microbridge itself is considered. We assume its impedance can be expressed as  $Z_{\text{HEB}} = R_N$  (Ref. 2) where  $Z_S$  is the surface impedance of the superconducting bridge and  $R_N$  equals the normal state resistance.

Second, the impedance of the antenna as a function of frequency is calculated using a moment method in the Fourier transform domain, developed by Kominami et al. (Ref. 7). For details, see Refs. 2 and 8. Throughout this paper, it is assumed that the peak response of the antenna is in practice 12% lower than predicted (Refs. 2, 8).

Third, the impedance of the microstripline is calculated based on models generally used for microstripline calculation (see e.g. Refs. 9 and 10). The characteristic impedance of the line is calculated as a function of frequency, line width and thickness of metal and dielectric layers including an effective  $\varepsilon_{r, \text{SiO}_2}$  and fringing field effects. By varying these parameters, the impedance can be tuned from about 5  $\Omega$  to 35  $\Omega$  without introducing orthogonal modes, i.e. without making the line wider than about  $\lambda/4$ . The ratio of obtainable characteristic impedance values in the microstripline is much larger than that reported for CPW lines, offering more freedom in transformer- and filter design.

Since we did not measure dc properties of the films used in the HEBMs, we use a dc conductivity  $\sigma = 1 \times 10^8 \Omega^{-1} m^{-1}$  for both top and bottom wiring layer. These values have been measured for Al previously in our group (Refs. 11 and 12). From this, the surface impedance of the top- and bottom plane are calculated in the extreme anomalous according to:

$$Z_S = 1.5 \cdot \frac{1}{3^{\frac{1}{2}} \pi^{\frac{1}{3}}} (1 + \sqrt{3}i) \left( \frac{9\omega^2 \mu_0^2 l_e}{16\sigma} \right)^{\frac{1}{3}}, \quad (1)$$

in which  $\omega$ ,  $\mu_0$ ,  $l_e$  and  $\sigma$  are frequency, magnetic permittivity, electron mean free path (assumed to be  $l_e = 125 \text{ nm}$ ) and dc conductivity, respectively. The additional factor 1.5 in Eq. 1 is an empirical multiplication factor added because the film is strictly speaking not in the extreme anomalous limit.

The RF filter we use is designed such that it reflects the RF signal back to the microbridge. This avoids signal being lost into the IF chain. It is important to note that the filter has low impedance. If not, the impedance match would be strongly influenced, since an infinite metal ground plane is assumed around the

slots, acting as a short. The filters are designed to have a small number of  $\lambda/4$ -sections to keep the series resistance due to the Al top wiring as low as possible. Although a low number of filter sections decreases the steepness at the cutoff frequencies, the impedance around the center frequency  $f_{\text{center}}$  is not affected. The filter is made of microstrip transmission line. The impedance of the separate sections is calculated using microstripline formulae (Ref. 9). The impedance of a microstripline filter with characteristic impedance  $Z_0$ , length  $l$  and terminated with a load  $Z_{\text{load}}$ , then, is given by repeated application of

$$Z_{\text{filter}} = Z_0 \frac{Z_{\text{load}} + iZ_0 \tan(\gamma \cdot l)}{Z_0 + iZ_{\text{load}} \tan(\gamma \cdot l)} \quad (2)$$

where  $\gamma$  is the propagation constant.

The last part of the geometry consists of the microstripline transformer, which transforms the added antenna- and filter impedance into the impedance  $Z_{\text{embed}}$  seen by the bridge according to an equation similar to Eq. 2 with  $Z_{\text{embed}}$  instead of  $Z_{\text{filter}}$ , the characteristic impedance of the transformer instead of  $Z_0$  and for  $Z_{\text{load}}$  we take  $Z_{\text{ant}} + Z_{\text{filter}}$ . In the calculations, the tapered structure of the cooling pads is approximated by a series of rectangles.

The intrinsic response  $\eta_{\text{int}}$  of the microstripline coupled HEBM can be calculated using

$$\eta_{\text{int}} = 1 - \left| \frac{Z_{\text{HEB}} - Z_{\text{embed}}}{Z_{\text{HEB}} + Z_{\text{embed}}} \right|^2. \quad (3)$$

The direct response in current  $\Delta I(f)$  of an HEBM measured in an FTS can be described by (Refs. 2,8)

$$\Delta I(f) \propto \eta_{\text{int}} \cdot \eta_{\text{opt}} \cdot \eta_{\text{FTS}}, \quad (4)$$

with  $\eta_{\text{opt}}$  the combined transmission of the window and heat filter and  $\eta_{\text{FTS}}$  the power transfer function of the FTS.

Fig. 2 shows the response  $\Delta I(f)$  of the device measured in an FTS at a bath temperature  $T_{\text{bath}} = 3$  K and the direct response predicted by the model above. The setup is described elsewhere (Ref. 8).

The measured 3 dB-bandwidth  $B_m$  equals 1.6 THz and  $f_{\text{center},m}$  is found to be 1.9 THz. The plot also shows the predicted response  $\eta_{\text{int},\text{sim}} \cdot \eta_{\text{opt}} \cdot \eta_{\text{FTS}}$  with  $B_{\text{sim}} = 1.4$  THz and  $f_{\text{center},\text{sim}} = 1.95$  THz. The peak frequencies of both curves are comparable, assuming the dip not to be due to the HEB (Ref. 13).  $B_m$  is slightly larger than  $B_{\text{sim}}$ . Similar data has been obtained from several devices. If we assume the downshift in peak response is at least partly caused by the antenna, as is the case in the CPW coupling scheme (as mentioned, this is done throughout this paper) (Ref. 2), the data are well described by the model.

An even better agreement between measurement and model is obtained if we assume a reduction in the dc conductivity by a factor of 3 to 5. Intuitively, this

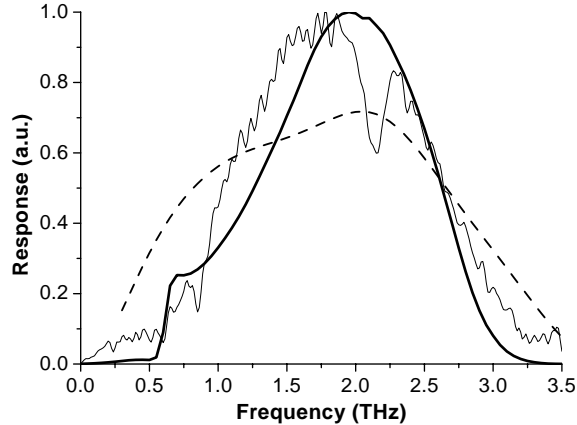


Figure 2: *Direct response as a function of frequency of a typical microstripline coupled HEB together with the transmission of the Fourier transform spectrometer and optics. Shown are the normalized measured data (solid thin), transmission of the optics and FTS  $\eta_{\text{opt}} \cdot \eta_{\text{FTS}}$  (dashed thin) and normalized intrinsic response  $\eta_{\text{int,sim}}$  (solid thick).*

can be explained as follows: most of the RF current will run in the bottom layer of the top wiring. This part of the film will have a lower-than-average quality due to the sputter process and surface roughness of the  $\text{SiO}_2$ . Therefore, it does not see the average value of the dc-conductivity  $\sigma$  as measured in a dc experiment. The transmission line will then have a higher loss than expected based on the dc value of  $\sigma$ .

We suggest that the thickness of the metal layer has to be taken into account in the model, since the thickness becomes of the order of the antenna slot width, possibly changing the effective  $\epsilon_r$  in the antenna slots (see Ref. 2).

The model for describing the microstrip line behavior around 2.5 THz seems to work reasonably well. However, because of the uncertainty in  $\sigma$  we cannot draw quantitative conclusions.

As expected, the influence of the metal conductivity is seen in the simulations in both center frequency and bandwidth.

We have also measured several devices with a slightly different design regarding the top wiring layer. Devices having a rectangular coupler instead of a radial stub (Fig. 1) do not show significant deviations from the observed direct response. A device having a filter with 6  $\lambda/4$  sections (instead of 2 sections as in the data shown) on either side shows a larger bandwidth (1.9 THz) and a lower  $f_{\text{center}}$  (1.5 THz).

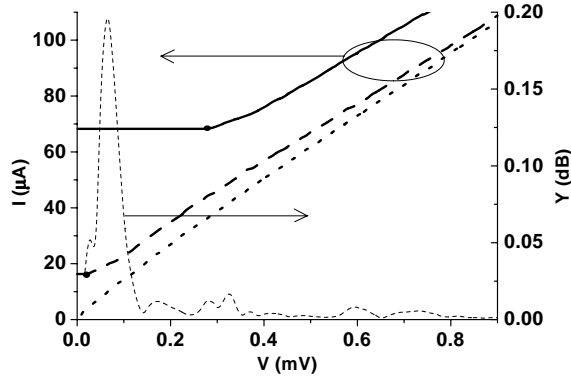


Figure 3: *IV-curves of the HEBM pumped with 2.5 THz-radiation: unpumped (solid) IV curve, optimally pumped (dashed) and overpumped (dotted) measured at 3 K, IF=1.25 GHz. The thin dashed line shows the chopped Y-factor in the optimally pumped situation.*

#### 4 HETERODYNE MEASUREMENTS

Heterodyne measurements are performed at 2.5 THz using a FIR laser. Using this laser it is possible to pump the IV curves of the devices fully flat using a 6  $\mu\text{m}$  Mylar beam splitter. The laser stability is on the order of 0.1%/min, measured using a pyro-detector. To average out possible instabilities in the system, we use a chopped hot/cold load at 300K/77K. At the IF, both the ac- and dc part of the power are recorded. From the Y-factor,  $Y = \frac{(P_{dc} + \alpha \cdot P_{ac})}{(P_{dc} - \alpha \cdot P_{ac})}$ , the noise temperature is determined. For the noise measurements reported here we use  $\alpha=1$ , although this  $\alpha$  in practice is larger than 1. The IF-chain (Ref. 14) consists of a standard bias Tee, isolator and HEMT amplifier and has 79 dB gain and a noise temperature of 7 K.

Fig. 3 shows the unpumped, optimally pumped and overpumped current-voltage curves of the mixer. The thin dashed line represents the Y-factor as a function of bias voltage. An optimal, chopped Y-factor of 0.20 dB has been measured. This corresponds to an uncorrected Callen and Welton-noise temperature  $T_{N,uncorr}$  of  $4200 \pm 1000$  K. A receiver gain of -23 dB has been measured. This is a few times the best noise temperature measured using CPW transmission lines (Ref. 15).

An optimization of the antenna size may improve the coupling efficiency by as much as 2 dB, decreasing the noise temperature considerably. Increasing the critical temperature  $T_c$  allows us to measure in the regime where  $T_c - T_{bath}$  is larger. This may lead to a lower  $T_N$  (Ref. 16).

## 5 DISCUSSION

Initially, it was believed that the fabrication of microstripline coupled samples would be easier than the CPW coupled devices since –except for the microbridge– no sub-micron structures are needed. However, the step coverage of the top wiring to the ground plane turns out to be difficult, even if the top metal is sputtered and of the same thickness as the dielectric. We believe that high ridges of SiO<sub>2</sub> remain at the edges of the areas where the SiO<sub>2</sub> layer is deposited. These are due to incomplete lift off and have been observed using an atomic force microscope. These ridges inhibit good contact to the ground plane. In the end, increasing the metal layer thickness to about twice the dielectric layer thickness and carefully brushing the wafer during SiO<sub>2</sub> lift off yields good step coverage.

The direct response of the microstripline coupled HEBM can be described well assuming a down shift in peak response of 10-12%. We believe that this can be solved by reducing the antenna size.

## 6 CONCLUSIONS

We have designed and produced a novel type of HEBM using microstripline coupling structures. The direct response of the device is well understood and can be described based on the current model if a downshift of about 12% is assumed. A heterodyne experiment using a FIR laser as an local oscillator shows a noise temperature of 4200 K.

## 7 ACKNOWLEDGMENTS

The authors thank Maarten Stokhof and Anja van Langen for their invaluable help in sample production, Willem-Jan Vreeling and Fabian Wahle for technical support in setting up the laser and Pierre Echternach for interesting discussion. This work is financially supported by the Stichting voor Technische Wetenschappen, which is part of the Nederlandse Organisatie voor Wetenschappelijk Onderzoek and, by ESA under contract no. 11738/95/NL/PB.

## REFERENCES

- [1] B.S. Karasik, M.C. Gaidis, W.R. McGrath, B. Bumble, and H.G. LeDuc. IEEE Trans. on Appl. Supercond., **7**:3580, 1997.
- [2] W.F.M. Ganzevles, L.R. Swart, J.R. Gao, T.M. Klapwijk, and P.A.J. de Korte. To appear in Appl. Phys. Lett., May 2000.
- [3] J. Zmuidzinas and H.G. LeDuc. IEEE Trans. on Microwave Theory Tech., **40**:1797, 1992.

- [4] M. Bin, M.C. Gaidis, J. Zmuidzinas, T.G. Phillips, and H.G. LeDuc. *Appl. Phys. Lett.*, **68**:1714, 1996.
- [5] P. Echternach, Private communication.
- [6] W.F.M. Ganzevles, J.R. Gao, D. Wilms Floet, G. de Lange, A.K. van Langen, L.R. Swart, T.M. Klapwijk, and P.A.J. de Korte. Proceedings of the 10<sup>th</sup> International Symposium on Space Terahertz Technology, Charlottesville, VA, March 16-18, 1999, pages 247–260, 1999.
- [7] M. Kominami, D.M. Pozar, and D.H. Schaubert. *IEEE Transactions on Antennas and Propagat.*, **33**:600, 1985. We used a computer code of this method supplied by Zmuidzinas and Chattopadhyay.
- [8] To appear in: Proceedings of the 11<sup>th</sup> International Symposium on Space Terahertz Technology, Ann Arbor, MI, May 2000, 2000.
- [9] D.M. Pozar. *Microwave Engineering*. Addison-Wesley, 1990.
- [10] G. Yassin and S. Withington. Electromagnetic models for superconducting millimetre-wave and submillimeter wave microstrip transmission lines. *ESA Technical Report RDG 4*, 1995.
- [11] P. Dieleman. *Fundamental Limitations of THz Niobium and Niobiumnitride SIS Mixers*. PhD thesis, University of Groningen, 1998.
- [12] B.D Jackson. Private communication.
- [13] We do not attribute the dip to the device since devices with very different parameters and even different transmission lines show the dip at the same frequency.
- [14] The IF chain consists of an isolator, Berkshire cryo-amplifier (44dB), Radiall bias Tee, room temperature amplifier (44dB), band pass filter (80 MHz at 1.25 GHz) and a Hewlett Packard power meter.
- [15] R.A. Wyss, B.S. Karasik, W.R. McGrath, B. Bumble, and H. LeDuc. Proceedings of the 10<sup>th</sup> International Symposium on Space Terahertz Technology, Charlottesville, VA, March 16-18, 1999, pages 215–228, 1999.
- [16] D. Wilms Floet, J.R. Gao, W.F.M. Ganzevles, T.M. Klapwijk, G. de Lange, and P.A.J. de Korte. Proceedings of the 10<sup>th</sup> International Symposium on Space Terahertz Technology, Charlottesville, VA, March 16-18, 1999, page 228, 1999.

# DIRECT AND HETERODYNE RESPONSE OF QUASI OPTICAL NB HOT-ELECTRON BOLOMETER MIXERS DESIGNED FOR 2.5 THZ RADIATION DETECTION

W.F.M. Ganzevles<sup>†</sup>, J.R. Gao<sup>§</sup>, W.M. Laauwen<sup>§</sup>, G. de Lange<sup>§</sup>  
T.M. Klapwijk<sup>†</sup> and P.A.J. de Korte<sup>§</sup>

Department of Applied Physics and Delft Institute for Microelectronics  
and Submicron Technology (DIMES),

<sup>†</sup>Delft University of Technology,

Lorentzweg 1, 2628 CJ Delft, The Netherlands

<sup>§</sup>Space Research Organization of the Netherlands,

Postbus 800, 9700 AV Groningen, The Netherlands

## Abstract

We measure the direct response of a Nb diffusion-cooled hot electron bolometer mixer in a frequency range between 0.5 THz and 3.5 THz. The mixer consists essentially of a twin slot antenna, a co-planar waveguide transmission line and a Nb superconducting bridge. It is designed for use in receivers with astronomical and atmospheric applications around 2.5 THz. We calculate the impedance of the antenna, the transmission line and the bridge separately using models which are developed for frequencies below 1 THz and predict the direct response of the mixer. We demonstrate that these models can be applied to much higher frequencies. However, the measured central frequency is 10-15% lower than predicted. Using a far infrared (FIR) laser, the device can be fully pumped at 2.5 THz. A preliminary Y-factor measurement shows a corrected noise temperature of 4700 K.

## 1 INTRODUCTION

Astronomic and atmospheric observations in the THz frequency range require highly sensitive radiation detectors. Until recently, Schottky-diodes were the only heterodyne detectors available. Although well understood and not dependent on cryogenic equipment, they show fairly high noise levels. Superconductor-Insulator-Superconductor (SIS) mixers have shown very high sensitivity up to the superconducting gap frequency of Nb, about 700 GHz. At higher frequencies, the losses in both the junction itself and the coupling structures between the antenna and junction increases considerably. Although a lot of effort is dedicated to improvement of the coupling structures by using superconductors with a higher gap, like NbTiN, the upper limit of SIS mixers is considered to be about 1.3 THz. Above that, superconducting hot-electron bolometer mixers (HEBMs) are the heterodyne

detector of choice. The mixing element in these devices is a short superconducting strip, contacted by normal metal cooling pads.

Since there is an interesting spectral line of the hydroxyl-group around 2.5 THz, much attention has been paid to heterodyne detection at this frequency. Several groups have reported heterodyne response at that frequency, some with very good sensitivity (Refs. 1, 2, 3).

The sensitivity of a receiver is determined by its coupling efficiency from free space to the microbridge, its intrinsic noise and its conversion gain. In this work, we focus on the coupling efficiency: is it possible to describe the frequency response of an HEB in terms of a relatively straightforward model and if so, how can we use this model to improve the coupling and ultimately reduce the receiver noise? In this work, we also describe the first heterodyne measurement at 2.5 THz performed using the far infra-red (FIR) laser at SRON.

This paper describes the direct and heterodyne response of quasi optical (QO) HEBMs around 2.5 THz. Part of this work has been described in a separate paper (Ref. 4). It is organized as follows: we will first describe the device layout and secondly, we outline the model we use to predict the direct response of the HEB as a function of frequency. Thirdly, we address the device fabrication and DC characteristics. After a description of the radiofrequency (RF) setup, we compare the direct response as measured in a Fourier Transform Spectrometer (FTS) with the predictions of our model. Then we describe the results of a heterodyne experiment. Lastly, we discuss the results obtained, after which conclusions are drawn.

## 2 DEVICE LAYOUT

Fig. 1 shows a scanning electron microscopy (SEM) micrograph of a mixer designed for 2.5 THz. It consists of a twin slot antenna, a co-planar waveguide (CPW) transmission line and a Nb microbridge. The twin slot antenna is formed by two gaps in the Au ground plane. The CPW transmission line is used to match the impedance of the antenna to that of the bridge, thus feeding the signal from the antenna to the microbridge.

On one end, the CPW is terminated by the low (practically zero) impedance of the antenna ground plane. On the other end, the CPW transmission line is connected to the intermediate frequency (IF)- and direct current (DC) bias contact via a quarter wavelength ( $\frac{1}{4}\lambda$ ) RF reflection filter, preventing RF radiation from leaking into the IF chain. The  $\frac{1}{4}\lambda$  sections are also made of CPW lines. A similar structure was used at 2.5 THz by Karasik et al. (Ref. 1). The fixed polarization, narrow bandwidth, reasonably high gaussicity and efficiency make the twin slot a suitable antenna for application in receivers for use on a telescope.

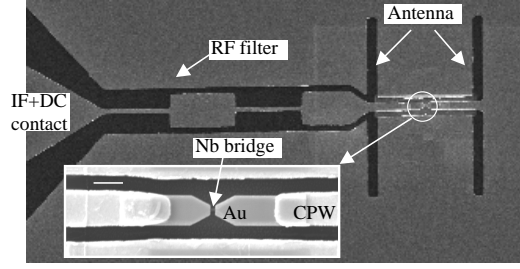


Figure 1: SEM micrograph of a twin slot antenna coupled Nb HEBM. The nominal slot length  $L$ , width  $w$  and separation  $s$  are  $36.0 \mu\text{m}$ ,  $1.8 \mu\text{m}$ ,  $19.2 \mu\text{m}$ , respectively. The Nb microbridge and part of the CPW transmission line are shown in the inset, where the bar represents  $2 \mu\text{m}$ .

### 3 DEVICE MODELING

A coupling structure similar to the one we use has been applied in a Schottky-mixer at 250 GHz (Ref. 5). A twin slot antenna combined with a microstripline has been used for a SIS mixer around 1 THz (Refs. 6, 7). These studies show that twin slot antennas can be used and modeled up to 1 THz. However, the results of Karasik et al. and Ganzevles et al. (Refs. 1, 8) suggest that the high-frequency behavior is not well understood. Both authors see a considerable downshift of  $f_{\text{center}}$ . Therefore, in this paper we compare the direct response of the detector as measured in an FTS with the response predicted by a model based on the coupling of successive impedances.

The direct response in current  $\Delta I(f)$  of an HEBM measured in an FTS can be described by

$$\Delta I(f) = S\eta_{\text{int}}\eta_{\text{opt}}\eta_{\text{FTS}}P_l, \quad (1)$$

where  $S$  is the current responsivity of the microbridge,

$\eta_{\text{int}}$  the intrinsic coupling efficiency of the mixer,  $\eta_{\text{opt}}$  the combined transmission of the window and heat filter,  $\eta_{\text{FTS}}$  the power transfer function of the FTS.  $P_l$  is the power spectrum of the lamp. The current responsivity  $S$  is considered to be frequency independent as long as the frequency is higher than the superconducting gap frequency, which is justified for our devices. However, the value of  $S$  is expected to depend on the mode of operation. If the operating temperature is close to  $T_c$ , the detector is operated in the 'transition edge'-regime (Ref. 9). Otherwise, the detector is in the electronic hot-spot regime (Ref. 10).  $P_l$  is assumed to be a slowly varying function of frequency and can be considered constant throughout the frequency range of interest. The transmission of the lens is not included in equation 1 since it is assumed frequency independent (Ref. 11). Thus, the measured relative response reflects the product of  $\eta_{\text{int}}$ ,  $\eta_{\text{opt}}$  and  $\eta_{\text{FTS}}$ .

The direct response is measured at a constant bias voltage. The signal from the lamp is chopped with a frequency of 16 Hz and  $\Delta I(f)$  is measured using a lock-in

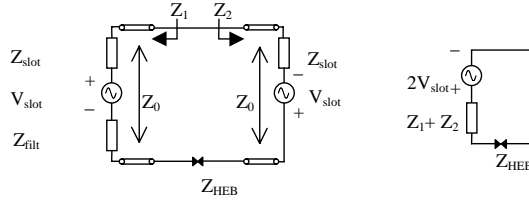


Figure 2: *Equivalent circuit of the antenna-filter-CPW-HEB combination. The antenna is modeled as a voltage source in series with its impedance.*

amplifier. The FTS is operated in a step-and-integrate mode with an integration time of 2 sec. The spectrum is obtained by Fourier transforming the interferogram, which is apodized using a sinusoidal apodization function. The measurements are performed at a temperature close to the superconducting critical temperature  $T_c$ .

We start by describing the model to calculate the intrinsic coupling efficiency  $\eta_{\text{int}}$  of the mixer, namely the power transmitted from the antenna to the bridge. To calculate  $\eta_{\text{int}}$ , we consider each single slot antenna as a voltage generator in series with the antenna impedance. The RF choke filter is assumed in series with one voltage generator/antenna impedance.

As can be seen in Fig. 2, on one side, the microbridge sees an impedance  $Z_1$  equal to the added filter- and antenna slot impedance transformed by the CPW transmission line. On the other side, only the transformed antenna slot impedance  $Z_2$  is present. A similar approach is used for a Schottky-mixer by Gearhart and Rebeiz (Ref. 5). The intrinsic frequency-dependent coupling between the embedding impedance,  $Z_{\text{embed}} = Z_1 + Z_2$ , seen at the bridge terminals and the bolometer impedance  $Z_{\text{HEB}}$  can now be calculated using

$$\eta_{\text{int}} = 1 - \left| \frac{Z_{\text{HEB}} - Z_{\text{embed}}}{Z_{\text{HEB}} + Z_{\text{embed}}} \right|^2. \quad (2)$$

The impedance of the antenna as a function of frequency is calculated using a moment method in the Fourier transform domain, developed by Kominami et al. (Ref. 12). In the simulation of  $\eta_{\text{int}}$  we take into account the decrease of the antenna beam efficiency when the frequency is much higher than the design frequency. This effect suppresses the appearance of the second antenna resonance (Ref. 13). The characteristic impedance  $Z_0$  of the CPW transmission line is calculated for several widths of the center conductor and the gap using a software package (MOMENTUM, Ref. 14). It is important to note that the impedances of both the antenna and the CPW are calculated for *printed slots* at the interface between two semi-infinite regions, air and substrate. Basically, the thickness of the metal layer is fully neglected. Because of this, the effective relative dielectric constant  $\epsilon_{\text{eff}}$  is  $(\epsilon_{r,\text{Si}} + \epsilon_{\text{air}})/2$ , where  $\epsilon_{r,\text{Si}}$  and  $\epsilon_{\text{air}}$  are the relative dielectric constant of the Si substrate and air, respectively.

The bolometer impedance  $Z_{\text{HEB}}$  can be expressed as (Ref. 15)

$$Z_{\text{HEB}} = Z_S \frac{l}{d} + Z_l, \quad (3)$$

where  $Z_S$  is the surface impedance of the superconducting bridge,  $l$  and  $d$  are its length and width and  $Z_l$  the impedance due to the geometrical inductance of the bridge.  $Z_S$  reduces to the square resistance  $R_{\square}$  when the frequency is higher than the superconducting gap frequency of the bridge and the film thickness is much smaller than the skin depth (Ref. 16). Furthermore,  $Z_l$  is small, on the order of  $1\text{ i } \Omega$  for our device. Therefore,  $Z_{\text{HEB}}$  in practice equals the normal state resistance  $R_N$ . The effective impedance of the 4-section RF filter is calculated by loading each  $\frac{1}{4}\lambda$ -CPW section with the effective impedance of its predecessor.

Based on this model we find the maximum coupling efficiency at 2.5 THz for the following mixer geometry: for the antenna we choose length  $L$ , separation  $s$  and slot width  $w$  equal to  $0.30 \cdot \lambda_0$ ,  $0.16 \cdot \lambda_0$  and  $0.05 \cdot L$ , respectively. Here  $\lambda_0$  is the free-space wavelength ( $120 \mu\text{m}$  at 2.5 THz). For the CPW transmission line we choose the center conductor width to be  $2 \mu\text{m}$  and the width of both gaps  $0.5 \mu\text{m}$ , giving  $Z_0$  equal to  $39 \Omega$ . For optimal coupling,  $R_N$  of the bridge is assumed to be  $75 \Omega$ . Using these parameters, we predict a maximum value for  $\eta_{\text{model,int}}$  of 90%.

#### 4 DEVICE FABRICATION

A fabrication process for Nb HEBMs has been developed using two-step electron beam lithography (EBL) to define both bridge length and width. Deep UV lithography is used to define the layer containing the antenna, CPW, filter etc. In this section, we shortly sketch the fabrication process of the device and present DC measurements.

We use a double-sided polished Si substrate ( $300 \mu\text{m}$  thick) with a high resistivity ( $\rho = 3 - 5 k\Omega\text{cm}$ ). In the first step,  $75 \text{ nm}$  thick Au squares are DC sputtered. These are used as alignment markers in subsequent optical and e-beam lithography steps. Then we deposit  $12 \text{ nm}$  Nb using magnetron sputtering. Using a lift-off mask, only patches with a size of  $12 \mu\text{m} \times 12 \mu\text{m}$  are covered. In this way, only a small fraction of RF current has to run in lossy Nb. Furthermore, it decreases the amount of Nb to be opened up for etching, thus reducing the writing time of the EBL machine.

Au cooling pads are patterned using EBL in a double layer of PMMA as a lift-off mask. To achieve a high interface transparency, RF sputter cleaning of the Nb in an Ar-plasma is used to remove its native oxide. In situ,  $\sim 10 \text{ nm}$  Au is sputtered. Then,  $90 \text{ nm}$  Au is deposited in an e-beam evaporator at a pressure of  $2 \times 10^{-6} \text{ mbar}$ . The antenna, CPW and filter are defined using a lift-off mask in Shipley DUV III-resist. This step requires the use of DUV lithography because of the  $0.5 \mu\text{m}$  slots in the CPW structure.  $5 \text{ nm}$  Al plus  $10 \text{ nm}$  Au is sputtered, after

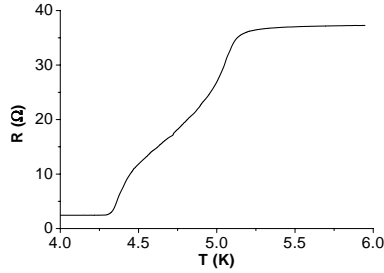


Figure 3: *RT-curve of a typical HEBM.*

which 160 nm Au is evaporated under similar conditions as the cooling pads. As a last optical step, we sputter deposit 100 nm Nb on the IF CPW-transmission line.

For the definition of the bridge width we follow the approach of Wilms Floet et al. (Ref. 17): a PMMA bridge is defined using EBL. Only the Nb parts that have to be etched are opened up, see Fig. 1. In a mixture of  $\text{CF}_4+3\%\text{O}_2$ , the Nb is reactive ion etched. We monitor the process by measuring the optical reflectivity of the Nb on the Si substrate by using a laser endpoint detection system. Using this process we are able to produce Nb bridges as narrow as 60 nm.

During processing, all devices are electrically shorted. While dicing in tap water (to avoid electric discharge), these shorts are opened. Therefore, all further handling must be done with extreme care to prevent damage due to electrostatic discharge. After wire bonding, DC measurements are performed in a metal vacuum can immersed in liquid He. Devices suitable for RF measurements are selected based on IV- and RT curves.

The Nb layer in which the bridge is defined has a residual resistance ratio (RRR) equal to 1.5 and  $R_{\square,\text{Nb},10\text{K}} = 33 \Omega$ , measured on a large structure. The ground plane (Au, 175 nm) is found to have an RRR of 3.5 and a square resistance  $R_{\square, \text{Au}}$  of  $0.1 \Omega$  at 4 K.

As can be seen in Fig. 3, the critical temperature of the Nb bridge  $T_{c,\text{bridge}}$  is 4.8 K. For Nb under the cooling pads  $T_{c,\text{pads}}$  is found to be 4.4 K. Both values are considerably lower than those found in literature (Refs. 1,18,19). We suspect that this is caused by the interference of processing different materials in the same sputtering chamber.

We observe a critical current density  $j_c$  of  $2 \times 10^{10} \text{ Am}^{-2}$  at a temperature of about 3.5 K. An unpumped IV-curve of an HEBM (nominally 250 nm long, 250 nm wide, 12 nm thick) is shown together with pumped curves in Fig. 6 (dashed line).

A QO mixer block has been designed and built as described in Ref. 20 to feed signal from free space to the mixer chip. The chip containing the mixer is glued in the second focus of a hyperhemispherical, high-resistivity Si lens. Before applying glue, we align the antenna to the optical axis (accuracy better than  $5\ \mu\text{m}$ ) by moving the chip to the center of the lens using micrometers .

The lens itself is held in a copper block. To obtain good thermal contact, 4 springs press the lens softly into the In foil or vacuum grease between the flange of the lens and the Cu block. We find the temperature of the lens to be 4.8 K, without pumping the He-bath.

The block is bolted to the cold plate of a standard 8" dewar, applying a small amount of vacuum grease for thermal contact. Connection to a standard IF-chain (Ref. 21), centered at 1.4 GHz, is made by wire bonding to a microstrip line on an epoxy printed circuit board, 0.5 mm thick,  $\varepsilon_{\text{r, PCB}} = 4.7$ ), having  $< -15$  dB reflection over a bandwidth of over 4 GHz. A standard SMA-connector is soldered to its end to connect to the IF chain.

The window of the dewar is made of  $40\ \mu\text{m}$  Mylar. We use Zitex (Ref. 22) as an IR filter at 77 K. The transmissivity of these materials as a function of frequency is measured in an FTS. Using a description in terms of a Fabry-Perot etalon, a fit to these measured data is generated. From the period of the transmission oscillations (see Fig. 4), we determine  $\varepsilon_r$  of the sheet once the thickness is accurately known. The loss factor is determined from the damping in the oscillation maxima. Curves showing the calculated transmissivity as a function of frequency obtained from these measurements are shown in Fig. 4. Although strictly speaking the Zitex does not act as an FP, the data are accurately described by the fit. Table 1 shows the data we obtain for several optical materials of interest in this frequency range.

In order to verify the predictions of the model described above, we measure the frequency dependent response of the mixer using the HEB as a direct detector in

Table 1: *Optical properties of window- and filter materials. The table gives empirical values for  $\beta$  and  $\gamma$  in the description for the absorption coefficient  $\alpha(f) = \beta \cdot (f(\text{THz}))^\gamma [\text{m}^{-1}]$ . The absorption factor is then given by  $a = e^{-\alpha \cdot \delta/2}$ , with  $\delta$  the effective material thickness (i.e. taking into account the angle of incidence).*

	n	$\beta$	$\gamma$
Mylar	1.72	600	1.2
Zitex G104	1.20	40	2.4
Kapton	1.76	480	1.2
Black Polyethylene	1.50	450	1.7

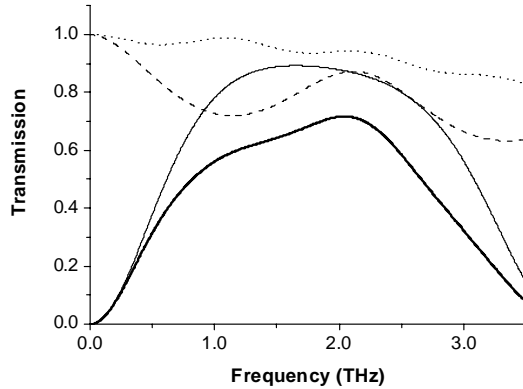


Figure 4: Calculated transmission of the beam splitter in an interferometer (thick solid curve), transmission of the  $40\ \mu\text{m}$  Mylar vacuum window (thin dotted curve) and Zitex G104 (thin dashed curve) as a function of frequency. The thick solid line represents the product of the three. The frequency-dependence of the lamp and thin lens in the FTS are not taken into account. The calculations are based on the measured values quoted in Table 1.

an FTS. The FTS measurement setup consists of a Michelson interferometer with a chopped Hg arc lamp providing broadband THz radiation. One of the mirrors is fixed, while the other can be moved over a range of 32 mm with an accuracy of  $5\ \mu\text{m}$ . These parameters give a maximum spectral resolution and frequency range of 5 GHz and 16 THz, respectively. To remove effects of absorption due to water, the whole optical path is in vacuum. For the beam splitter in the FTS (a Mylar sheet,  $25\ \mu\text{m}$  thick) the transmissivity vs. frequency is calculated. To do this, we consider it as a beam splitter *in an interferometer* with finite thickness and loss, i.e. taking into account the interference from the waves in both arms (see, e.g. Refs. 23 and 24). For this, we again use the data obtained from the transmission measurements. The thin solid line in Fig. 4 shows the transmission of the beam splitter (Mylar,  $25\ \mu\text{m}$  thick) in the FTS.

Heterodyne measurements are done using a FIR laser as a local oscillator (LO) source. The first trap of this system is a  $\text{CO}_2$  laser. This laser pumps a FIR ring laser, containing methanol.

A standard hot/cold setup is used as a calibrated source for Y-factor measurements. Systematic measurements require a fairly stable LO signal for longer periods of time (typically a few minutes). Since the LO power was only stable for several tens of seconds, manual Y-factors have been obtained only.

## 6 DIRECT RESPONSE MEASUREMENTS

Two similar mixers designed for 2.5 THz are measured. Fig. 5 shows a typical measured relative direct response. To obtain the measured  $\eta_{\text{int}}$ , we divide the

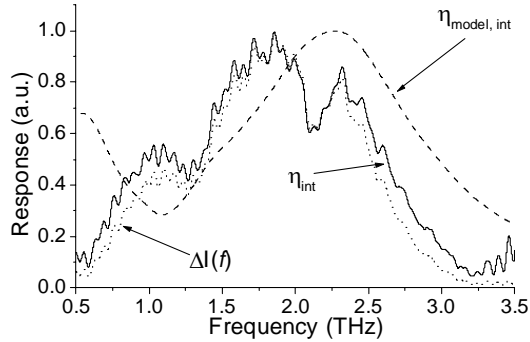


Figure 5: *Direct response of the HEBM designed for 2.5 THz as a function of frequency. The dotted line gives the measured direct response  $\Delta I(f)$ , reflecting the product of intrinsic coupling efficiency  $\eta_{\text{int}}$ , the combined transmission of the window and heat filter  $\eta_{\text{opt}}$  and the power transfer function of the FTS  $\eta_{\text{FTS}}$ . The solid line represents the experimental  $\eta_{\text{int}}$ , while the dashed line represents the theoretical prediction  $\eta_{\text{model,int}}$ . All curves are normalized to their maximum value.*

direct response by the product of  $\eta_{\text{opt}}$  and  $\eta_{\text{FTS}}$ , as shown in Fig. 4. The frequency dependence of the thin lens in the FTS is not considered. The intrinsic response  $\eta_{\text{int}}$  is also shown in Fig. 5. We find a peak response frequency (the average of the 3 dB values) of  $1.9 \pm 0.1$  THz from the intrinsic mixer response. The 3 dB bandwidth is about 1.3 THz. The unexpected dip around 2.1 THz is not understood but may be due to the FTS lamp (Ref. 25).

To understand this result we calculate the theoretical response  $\eta_{\text{int,model}}$  using the model described above. Since the actual device parameters differ from those in the initial design, the calculation of the  $\eta_{\text{int,model}}$  shown in Fig. 5 is done using the actual values, namely  $R_{\text{N}} = 41 \Omega$  and  $Z_0 = 46 \Omega$  for the CPW transmission line (Ref. 14) because of a larger gap ( $0.8 \mu\text{m}$ ).

The model predicts a peak response frequency of 2.3 THz and a 3 dB bandwidth of 1.3 THz. The overall response predicted coincides well with the measured curve if a frequency down shift of about 300 GHz is introduced. By doing this, we infer a peak frequency of 2.0 THz from the measured  $\eta_{\text{int}}$ , consistent with the value determined from the 3 dB points.

We also calculate the relative direct response of the same mixer in an alternative way using Momentum. The result is in general consistent with the simulation shown in Fig. 5. The peak response however is 2.1 THz, also higher than what we measured.

## 7 HETERODYNE MEASUREMENTS

Heterodyne measurements are performed at a bath temperature of about 3 K. As an LO, the FIR laser is set at a spectral line of methanol at 2.5 THz. The signal

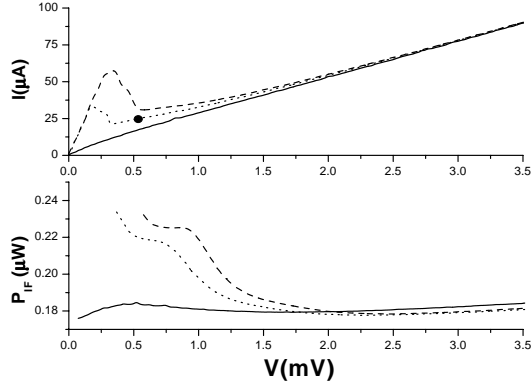


Figure 6: <sup>a)</sup> Current vs voltage curve for a typical HEBM. The dashed line represents the unpumped curve, the dotted line is optimally pumped and the solid line is overpumped. The dot gives the point where the best Y-factor (0.12 dB) has been measured. Note the series resistance of 5  $\Omega$  indicated by the slope in the IV curve near zero bias. This is due to the filter and IF contact. For this device,  $R_N$  equals 41  $\Omega$ . <sup>b)</sup> The IF output power  $P_{IF}$  vs voltage for the same device. The curves correspond to the ones in Fig. 6<sup>a</sup>

is coupled into the dewar via a 15  $\mu\text{m}$  Mylar beam splitter. The transmission of a Mylar splitter at 45° is about 56%. For this particular measurement, the output power of the laser did not allow us to use a thinner splitter. Therefore, we correct the measured noise temperature  $T_N$  for the splitter.

At an IF of 1.4 GHz, the best Y-factor obtained is  $0.12 \pm 0.04$  dB. This corresponds to a corrected  $T_N$  of 4700 K, about 3 times state of the art for heterodyne receivers at this frequency (Refs. 2, 3). Careful examination of the IV-bias point on an oscilloscope confirms that the bias point is not influenced by the hot/cold load directly, i.e. there is no direct detection. Since the LO is only stable over several tens of seconds, no systematic measurements have been performed to find the optimal bias point, operating temperature or LO power.

## 8 DISCUSSIONS

Systematic research to the direct response of QO HEBMs has been performed. The measured direct response is compared to the predictions by a simple model based on the coupling of impedances. The influence of the optics in the setup is described based on experimental data of the materials used. The quantitative difference between the measured peak frequencies and those predicted in our calculations occurs only around 2.5 THz but not at low frequencies. We have measured and analyzed similar mixers designed for 1 THz, showing good agreement between measured and predicted response. Although our experimental study does not reveal the origin of this discrepancy, we suggest that the difference is caused by neglecting the finite thickness of the metal layer. For our devices, the thickness

of the metal layer has become comparable to the gap width of the CPW. For the antenna slots at 2.5 THz, this is also the case. Reasoning qualitatively, this causes a considerable fraction of the field to run in the gap between the slot walls, giving rise to an  $\epsilon_{\text{eff}}$  lower than assumed for a CPW slot in a metal film with zero thickness. This, in its turn, causes a rise of the characteristic impedance of the CPW lines. Calculations show that a change in characteristic impedance has more influence at 2.5 THz than at 1 THz. Furthermore, the ratio of metal layer thickness over slot width in the antenna slots is larger in the 2.5 THz device. We suppose this changes the antenna impedance more than in the 1 THz device. Both these effects give rise to a more pronounced shift in peak frequency at 2.5 THz than at 1 THz. In order to improve the accuracy of the present model, it would be worthwhile investigating the influence of the thickness of the metal layer.

It becomes clear now that the mixer designed using the present model will not lead to a peak response at 2.5 THz. To achieve ultimate sensitivity at 2.5 THz one can design a mixer in an engineering way by reducing the antenna size by 15% and the CPW gap size to  $0.3 \mu\text{m}$ . The impedance of the HEB device is kept at a practical value of  $\sim 40 \Omega$ . Our calculations show that this does not change the peak coupling efficiency, but the size reduction may affect other properties of the antenna. A similar experimental approach has been made by Wyss et al. (Ref. 2).

The Y-factor obtained in heterodyne mode is expected to increase if the coupling scheme can be optimized as described above. Another improvement in Y-factor may come from improving the stability of the LO. Long chopped or even manual scans of the IF output power or Y-factor are expected to be possible, allowing systematic research on the optimal operating conditions of these HEBMs.

## 9 CONCLUSIONS

In conclusion, we have measured the direct response of Nb HEBMs with a twin slot antenna/CPW transmission line combination around 2.5 THz and compared the results to the present model. The influence of the receiver optics is calculated based on empirical data from FTS measurements. This allows us to take into account the frequency dependence of the transmission due to the optics. We convincingly show that the measured direct response is 10-15% lower in frequency than predicted by the model, although the overall shape of the spectrum agrees with the prediction. Preliminary Y-factor measurements show a noise temperature of 4700 K.

## 10 ACKNOWLEDGEMENTS

We thank J. Zmuidzinas for useful discussions and making the computer code to calculate the antenna impedance available. M.J.M.E. de Nivelles is acknowledged

for his efforts to make the laser LO ready for heterodyne measurements. Helpful discussions with W. Jellema, N.D. Whyborn, D. Wilms Floet and A. Baryshev are acknowledged. This work is financially supported by the Stichting voor Technische Wetenschappen, which is part of the Nederlandse Organisatie voor Wetenschappelijk Onderzoek, and by ESA under contract no. 11738/95/NL/PB.

#### REFERENCES

- [1] B.S. Karasik, M.C. Gaidis, W.R. McGrath, B. Bumble, and H.G. LeDuc. IEEE Trans. on Appl. Supercond., **7**:3580, 1997.
- [2] R.A. Wyss, B.S. Karasik, W.R. McGrath, B. Bumble, and H. LeDuc. Proceedings of the 10<sup>th</sup> International Symposium on Space Terahertz Technology, Charlottesville, VA, March 16-18, 1999, pages 215–228, 1999.
- [3] P. Yagoubov, M. Kroug, H. Merkel, and E. Kollberg. Proceedings of the 10<sup>th</sup> International Symposium on Space Terahertz Technology, Charlottesville, VA, March 16-18, 1999, pages 238–246, 1999.
- [4] W.F.M. Ganzevles, L.R. Swart, J.R. Gao, T.M. Klapwijk, and P.A.J. de Korte. To appear in Appl. Phys. Lett., May 2000.
- [5] S.S. Gearhart and G.M. Rebeiz. IEEE Trans. on Microwave Theory Tech., **42**:2504, 1994.
- [6] J. Zmuidzinas and H.G. LeDuc. IEEE Trans. on Microwave Theory Tech., **40**:1797, 1992.
- [7] M. Bin, M.C. Gaidis, J. Zmuidzinas, T.G. Phillips, and H.G. LeDuc. Appl. Phys. Lett., **68**:1714, 1996.
- [8] W.F.M. Ganzevles, J.R. Gao, D. Wilms Floet, G. de Lange, A.K. van Langen, L.R. Swart, T.M. Klapwijk, and P.A.J. de Korte. Proceedings of the 10<sup>th</sup> International Symposium on Space Terahertz Technology, Charlottesville, VA, March 16-18, 1999, pages 247–260, 1999.
- [9] D. Wilms Floet, J.J.A. Baselmans, T.M. Klapwijk, and J.R. Gao. Appl. Phys. Lett., **73**:2826, 1998.
- [10] D. Wilms Floet, E. Miedema, T.M. Klapwijk, and J.R. Gao. Appl. Phys. Lett., **74**:433, 1999.
- [11] D.F. Filipovic, S.S. Gearhart, and G.M. Rebeiz. IEEE Trans. on Microwave Theory Tech., **41**:1738, 1993.

- [12] M. Kominami, D.M. Pozar, and D.H. Schaubert. IEEE Transactions on Antennas and Propagat., **33**:600, 1985. We used a computer code of this method supplied by Zmuidzinis and Chattopadhyay.
- [13] J. Zmuidzinis. Private communication.
- [14] Hewlett Packard Advanced Design Software, Momentum Planar Solver.
- [15] J. Mees, M. Nahum, and P.L. Richards. Appl. Phys. Lett., **5**:2329, 1991.
- [16] S. Sridhar. J. Appl. Phys., **63**:159, 1988.
- [17] D. Wilms Floet, J.R. Gao, W. Hulshoff, H. van de Stadt, T.M. Klapwijk, and A.K. Suurling. *IOP Conf. Series 158, edited by H. Rogalla and D.H.A. Blank*, page 401, 1997.
- [18] D. Wilms Floet, J.J.A. Baselmans, J.R. Gao, and T.M. Klapwijk. Proceedings of the 9<sup>th</sup> International Symposium on Space Terahertz Technology, Pasadena, CA, March 17-19, 1998, 1998.
- [19] P.J. Burke, R.J. Schoelkopf, D.E. Prober, A. Skalare, B.S. Karasik, M.C. Gaidis, W.R. McGrath, B. Bumble, and H.G. LeDuc. J. Appl. Phys., **85**:1644, 1999.
- [20] Technical Note I: Hot Electron Bolometer Mixer for 2.5THz, Contract no. 11738/95/NL/PB. Technical report, ESA, 1998.
- [21] The IF chain consists of a Berkshire cryo-amplifier (44dB), an isolator, room temperature amplifier (44dB), band pass filter (80 MHz at 1.4 GHz) and a Hewlett Packard power meter. The total gain is 79dB.
- [22] Zitex G104: Norton Performance Plastics, Wayne, New Jersey, (201)696-4700.
- [23] R.J. Bell. Introductory Fourier Transform Spectroscopy. Academic Press, 1972.
- [24] L.R. Swart. Analysis of the direct response of twin slot antenna coupled Nb HEB mixers designed for 2.5 THz detection. MSc. thesis, University of Groningen, 1999.
- [25] We do not attribute the dip to the device since devices having different types of antenna and transmission lines show the dip at the same frequency.

# ALUMINUM SUB-MICRON SUPERCONDUCTING HOT-ELECTRON BOLOMETER MIXERS

**I.Siddiqi, A. Verevkin, and D.E. Prober**

*Department of Applied Physics, Yale University, 15 Prospect Street, New Haven, Connecticut 06520-8284*

**A. Skalare, B.S. Karasik, W.R. McGrath, P. Echternach, and H.G. LeDuc**

*Center for Space Microelectronics Technology, Jet Propulsion Laboratory,  
California Institute of Technology, Pasadena, California 91109*

We report on microwave measurements of superconducting aluminum hot-electron bolometers (Al HEBs). Diffusion-cooled Al HEB mixers are ideal candidates for space-borne and terrestrial remote-sensing applications in the Terahertz frequency range since they are predicted to have small local oscillator (LO) power requirements, intermediate frequency (IF) bandwidths  $\geq 10$  GHz, and a noise temperature lower than that of Nb and NbN HEBs.<sup>1</sup> Mixer measurements were made at an LO frequency  $\sim 30$  GHz LO, with an IF in the range 0.1-7.3 GHz. For  $T < 0.8$  K, a magnetic field  $H=0.1-0.3$ T was applied to suppress the superconductivity in the contact pads, and partly in the bridge. For a  $0.6 \mu\text{m}$  long Al HEB, we measure an IF bandwidth of 4 GHz, a conversion efficiency  $\eta = -8$ dB, and a mixer noise temperature  $T_m \geq 4$ K, DSB ( $T_{\text{mixer}}=T_{\text{output noise}}/2\eta$ ). These results are shown to be in quantitative agreement with simple theoretical predictions.

## I. Introduction

Recent studies on Nb and NbN hot-electron bolometer (HEB) mixers have demonstrated that they are excellent candidates for Terahertz spectroscopy applications.<sup>2-4</sup> For Nb HEB mixers, the largest intermediate frequency (IF) bandwidths are obtained for devices much shorter than the inelastic electron-phonon length. These rely on the out-diffusion of hot electrons from the microbridge into cold reservoirs as the dominant mode of energy relaxation.<sup>5</sup> Diffusion-cooled Nb mixers have demonstrated IF bandwidths up to 10 GHz, with the local oscillator (LO) power needed for optimal operation typically  $\sim$  tens of nW at Terahertz frequencies. The noise performance of diffusion-cooled Nb devices is excellent, with an achieved receiver noise temperature  $T_R=1800$ K, DSB at 2.5THz.<sup>3</sup>

Recently, HEBs employing superconductors with a lower transition tem-

perature than Nb ( $T_c \sim 6$ K) have been proposed.<sup>1</sup> The devices studied here are diffusion-cooled HEBs based on Al, with  $T_c \sim 1.5$  to 2.4K. Improvements in mixer performance are predicted because clean Al films have a lower transition temperature and a higher diffusivity  $D$  than Nb films.

We present measurements for Al HEB mixers at microwave frequencies. The frequency of the LO source used is  $\sim 30$  GHz. The primary motivation for studying mixing at microwave frequencies is that much of the device physics relevant to THz mixing can be explored with the simpler microwave measurements. Previous microwave studies of Nb HEBs has been useful in this respect.<sup>2</sup>

We present here predictions for mixer performance of Al HEB<sup>1,2</sup> devices. The IF bandwidth of the HEB mixer can be estimated from the thermal time constant  $\tau_{\text{th}}$  of the device. The thermal relaxation rate has a term due to inelastic electron-phonon scattering, and one due to the

“out” diffusion rate --  $\tau_{th}^{-1} = \tau_{e-ph}^{-1} + \tau_{diff}^{-1}$ . In our devices, electron-phonon scattering is negligible, and the thermal time constant is given by the diffusion time<sup>2</sup>

$$\tau_{th} \approx \tau_{diff} = L^2/\pi^2 D, \quad (1a)$$

and the -3dB intermediate frequency rolloff is given by:

$$f_{-3dB} = 1/(2\pi\tau_{eff}) = 1/(2\pi\tau_{th}). \quad (1b)$$

L is the length of the bolometer. Eq. (1b) applies when electro-thermal feedback is small, so that  $\tau_{eff} = \tau_{th}$ . Otherwise  $\tau_{eff}$  is given by Eq. 5. The conversion efficiency thus drops by a factor of two at  $IF = f_{-3dB}$ .

The diffusivity can be expressed as a function of the resistivity by using free electron relations.<sup>12</sup> The mean free path  $l$  is given by  $mv_f/ne^2\rho$ , where  $m$  is the electron mass,  $v_f$  is the Fermi velocity,  $n$  is electron concentration,  $e$  is the electron charge, and  $\rho$  is the resistivity. The diffusion constant is related to the mean free path by  $D=lv_f/3$ . Combining these equations gives

$$D = \frac{mv_f^2}{3ne^2\rho}. \quad (2)$$

For Al, using  $1.3 \times 10^8$  cm/s for the Fermi velocity and  $18.1 \times 10^{22}$  cm<sup>-3</sup> for the electron concentration, Eq. (2) reduces to  $D[\text{cm}^2/\text{s}] = 114/\rho[\mu\Omega\text{-cm}]$ . In Fig. 1, diffusivity data for thin Al films<sup>6-11</sup>, including measurements on the films discussed in this work, are presented along with the prediction from Eq. (2). Al HEBs can offer large IF bandwidth.

To maximize the IF bandwidth, or equivalently to minimize the thermal time

$\tau_{th}$ , the device length is first minimized. Calculations for the order parameter in an N-S-N structure<sup>13,14</sup> indicate that  $L_c \sim 2\xi$  is the minimum length for the existence of superconductivity at  $T/T_c=0.3$ .  $\xi$  is the coherence length in the Al microbridge. The order parameter will approach the bulk Ginzburg-Landau value in the middle of the microbridge for devices twice this critical length.<sup>15</sup> Since the coherence length in Al is relatively large, it is possible with current lithographic techniques to make devices a few coherence lengths long. Substituting  $L=4\xi$  into Eq. (1a) for the thermal time gives  $\sim 4.5$  ps. The maximum IF bandwidth is thus  $\sim 35$  GHz.

Al HEBs are also promising since the LO power required for operation is predicted to be lower than that of Nb and NbN mixers. The LO power for a diffusion-cooled device is given by<sup>2,16</sup>

$$P_{LO} = 4\mathcal{E}(T_c^2 - T^2)/R. \quad (3)$$

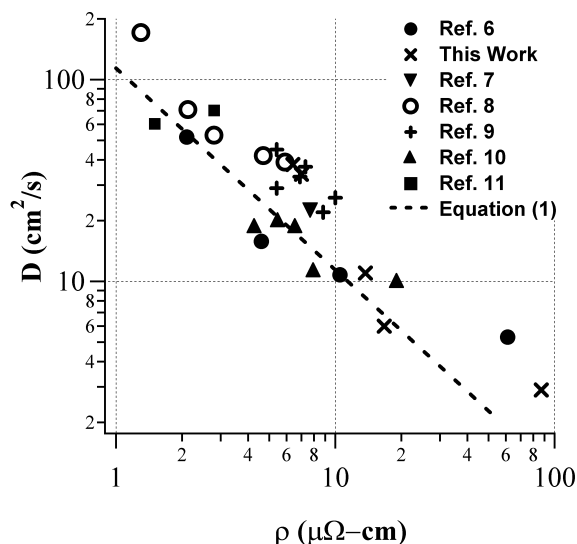


Fig. 1: Diffusivity vs. resistivity for thin Al films with thickness 7-25 nm.

Device	$R_n$ ( $\Omega$ )	$L$ ( $\mu\text{m}$ )	$\rho$ ( $\mu\Omega\text{-cm}$ )	$D$ ( $\text{cm}^2/\text{s}$ )
A	52	0.6	15	6.0
B	145	0.3	65	2.5
C	260	1.0	36	4.4
D	387	0.6	85	2.9

Table I: Device parameters. Diffusion constant value of devices A and D are measured, while those for B and C are inferred from the resistivity. The device width is  $0.1\mu\text{m}$ . For mixer tests,  $T_c=1.0\text{K}$  for device A in a magnetic field to  $2.4\text{K}$  for device B in zero field.

where  $\mathcal{E} = 2.45 \times 10^{-8} \text{ Watt-Ohm/K}^2$  is the Lorenz constant and  $R$  the device resistance. At  $2.5 \text{ THz}$ , for Nb HEBs,  $P_{\text{LO}} \sim 20 \text{ nW}^3$  and  $P_{\text{LO}} \sim 100 \text{ nW}^{17}$  for NbN phonon-cooled HEBs. In the Al mixer, the critical temperature is approximately 4x smaller than in Nb devices, and thus the LO power should decrease by 16x if the device is operated at a bath temperature well below the critical temperature. The LO power dissipated in the mixer in Al should be  $\sim 0.2 \text{ nW}$  based on scaling of the data obtained for Nb at  $20 \text{ GHz}^2$ , and  $\sim 2 \text{ nW}$  for THz operation.<sup>18,26</sup>

Though HEB mixer theories for noise are currently under discussion, we discuss here two main thermal noise sources: thermal fluctuation noise and Johnson noise. The contribution of thermal fluctuation noise to the total device noise is proportional to the critical temperature<sup>19</sup>, and should thus be smaller in Al devices than in Nb ones. Lowering the  $T_c$  of the HEB will similarly result in a decrease of the Johnson noise. Quantum noise, however, must also be considered. A lower bound on the contribution to the mixer noise is  $T_M^Q \approx h\nu/k^{19a}$ . At the microwave frequencies we used, the quantum noise is almost negligible,  $\sim 1\text{K}$ . At Tera-

hertz frequencies, the quantum noise limit is not negligible.  $T_M^Q = 120\text{K}$  at  $2.5 \text{ THz}$ . Since the measured mixer noise of Nb HEBs is much greater than  $T_M^Q$ , we believe that reducing the two thermal contributions, by use of Al HEBs, will reduce  $T_M$ . This should hold true even for more advanced noise theories. The mixer noise temperature at  $30 \text{ GHz}$  due to thermal sources is predicted to be  $\sim 8 \text{ K}$  by scaling the best results obtained with Nb at  $20 \text{ GHz}$  by  $T_c$ .

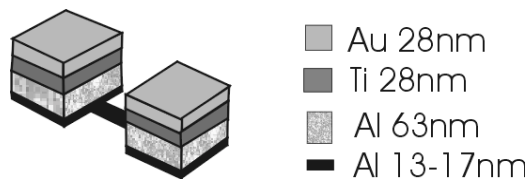


Fig. 2: Device geometry

## II. Devices

The devices consist of a thin, narrow Al microbridge with dimensions  $d=13\text{-}17\text{nm}$ ,  $W=0.1\mu\text{m}$ , and  $L=0.2\text{-}1\mu\text{m}$ , where  $d$ ,  $W$ , and  $L$  are the thickness, width, and length, respectively. Thick contacts consist of a tri-layer of Al, Ti, and Au with thickness  $\sim 68\text{nm}$ ,  $28\text{nm}$ ,  $28\text{nm}$  respectively on top of the thin Al film. To avoid the formation of an oxide interface layer between the thin Al in the microbridge and the contact pads, both structures are metalized in the same deposition cycle using a double angle evaporation process. The fabrication details can be found in Ref. 20. Fig. 2 gives an illustration of the device geometry, and the device parameters are summarized in Table I.

The superconducting transition temperature of the Al microbridges in zero field ranged from  $\sim 1.5\text{-}2.4 \text{ K}$  depending on length and resistivity. The contact pads are a combination of normal and super-

conducting metals, and have a transition temperature which is lower than that of the microbridge, with  $T_{c,\text{contact pads}} \approx 0.6\text{-}1.0\text{K}$ . For tests below  $T_{c,\text{contact pads}}$  a perpendicular magnetic field is applied to suppress the superconductivity in the contact pads. The resistivity of the microbridge is significantly higher than that of the contact pads. The upper critical field of the microbridge is thus several kOe higher than that of the contact pads.<sup>21</sup>

The smallest magnetic field in which no signs of Josephson effects are observed is chosen as the operating field. Typically, this operating magnetic field is less than half of the upper critical field of the microbridge.

### III. Experimental Setup

The devices are mounted on the cold stage of a variable temperature  $^3\text{He}$  cryostat. The bath temperature was varied from 0.25-1.6K for the mixing experiments, and up to 40K for Johnson noise calibrations and other measurements. A schematic of the measurement setup is shown in Fig. 3.

Microwave signals are applied using the internal synthesized generator of a HP8722D vector network analyzer (0.05-40 GHz) and an AvanteK YIG Oscillator (26.5-40 GHz).<sup>22</sup> A waveguide high-pass filter is used to remove noise from the HP8722D in the  $\leq 1$  GHz range. The RF and LO signals are combined at room temperature via a coaxial direction coupler. A cold (4K) directional coupler is used to feed the RF/LO signals into the mixer block, and to couple out the IF signal. The mixer block uses a coaxial-microstrip transition to couple to the device. The mixer block uses a coaxial-microstrip transition to couple to the device.

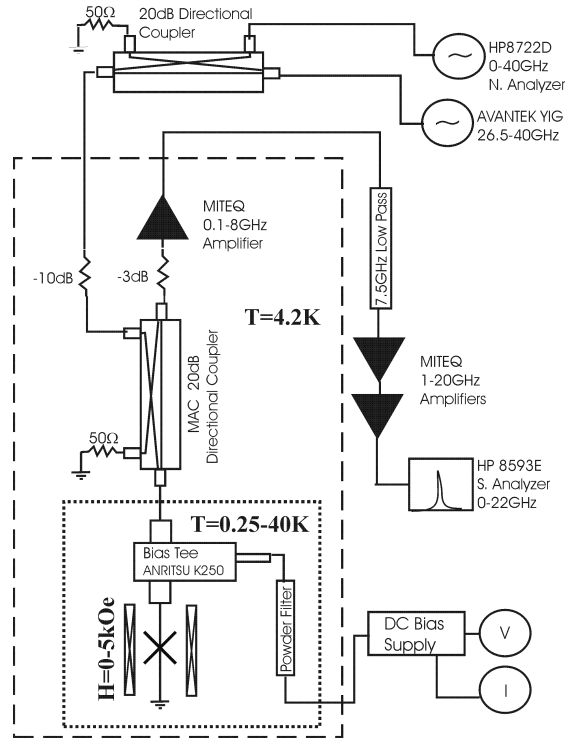


Fig. 3: Schematic of Measurement Setup

The IF amplifier chain consists of three broadband Miteq HEMT amplifiers. The first IF amplifier is immersed in liquid  $^4\text{He}$  close to the device. By measuring the Johnson noise output of the HEB in the normal state as a function of bath temperature, the gain and noise temperature of the IF chain is obtained.

The output noise at IF = 1.20-1.25 GHz from the device is measured using a room temperature Schottky diode detector. The conversion efficiency at the same IF is used to calculate the mixer noise.

### IV. Results

#### A. I-V Curves and R vs. T

I-V curves of device C in the absence of an external magnetic field are shown in Fig. 4. At temperatures  $\sim 0.6\text{K}$  and below, the small series resistance pre-

sent is that of the cables and microstrip line used in a two point measurement of the resistance.

When the contact pads are in the normal state, a significant resistance ( $\sim 0.25 R_n - 0.5R_n$  depending on microbridge resistivity and length) exists even at temperatures well below  $T_c$  of the microbridge. For example, in device D, the transition temperature of the Al microbridge is  $\sim 2.4\text{K}$  and that of the contact pads is  $\sim 0.6\text{K}$  (see Fig. 5). At temperatures just below  $2.4\text{K}$  where the superconducting energy gap is small, the observation of resistance can be explained due to charge imbalance effects.<sup>23,24</sup> However, at  $0.6\text{K}$  ( $t=T/T_c=0.25$ ) and at small voltages, nearly all of the single electrons incident on the N-S boundary should be converted to Cooper pairs via Andreev reflection.<sup>23</sup> Yet we observe a large finite resistance (Fig. 6). Dividing this observed resistance by the normal state resistance and multiplying by the length of the microbridge gives us the effective length of the resistive area in the microbridge.

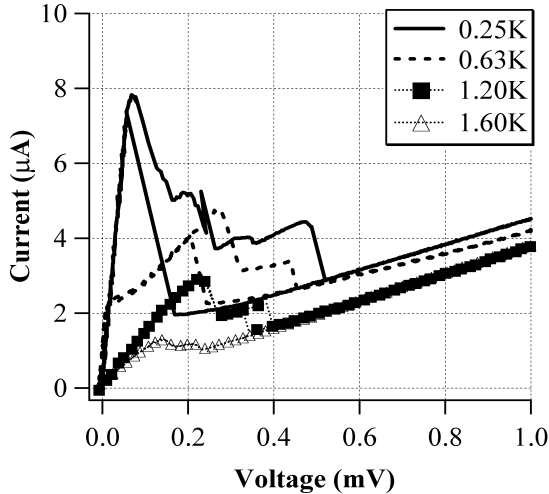


Fig. 4: I-V Curves for device C for bath temperature 0.25-1.6K,  $H=0$ .

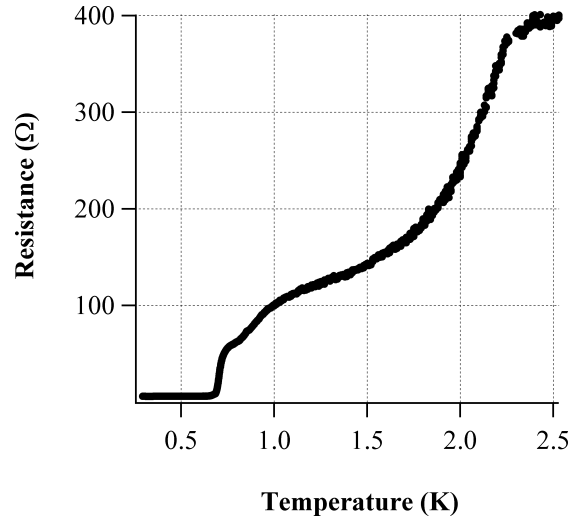


Fig 5:  $R$  vs.  $T$  of device D,  $H=0$ . The IV curves of thus device are like those of device C, Fig. 4.

Comparing this length to the superconducting coherence length, determined by upper critical field measurements, we see that the length of the resistive region is several coherence lengths in size.

One batch of devices has been manufactured without thick Al in the contact pads. The contact pads in this case are always in the normal state in the temperature regime used. Measurements on these devices also indicate that a large resistance remains down to the lowest temperature measured.<sup>25</sup> Measurements of  $R$  vs.  $T$  for device A are shown in Fig. 6 in an external magnetic field. The  $R$  vs.  $T$  for the devices with normal contact pads look very similar to Fig. 6, in which the superconductivity of the contact pads is suppressed in a magnetic field. The resistance depends only weakly on the bath temperature below  $0.5\text{K}$  and appears to remain finite even as  $T \rightarrow 0$ . In the limit of zero temperature, when measuring resistance with a small excitation current, there should not be any resistance. We do not understand this low temperature resistance.

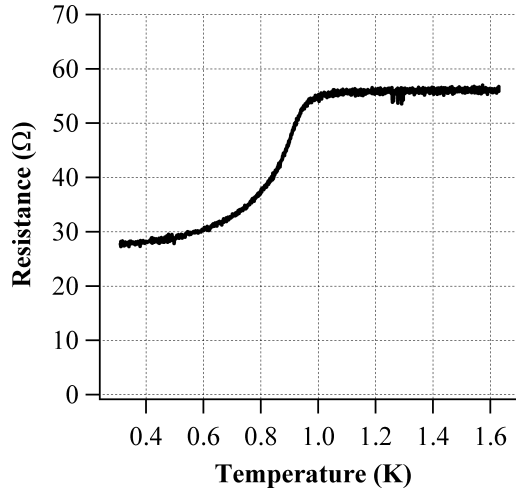


Fig 6: R vs. T of device A.  $H=1.2\text{kOe}$ .

Extrapolating the R vs. T dependence given in Fig. 6 to  $T=0$ , for example gives us a finite resistance, of larger value  $R_n$  ( $6\xi/L$ ). For example,  $\xi(0.25\text{K})=50\text{nm}$  for device A. The measured resistance at low bias voltages is  $0.5 R_n$ , corresponding to a length of  $6 \xi(T)$ .

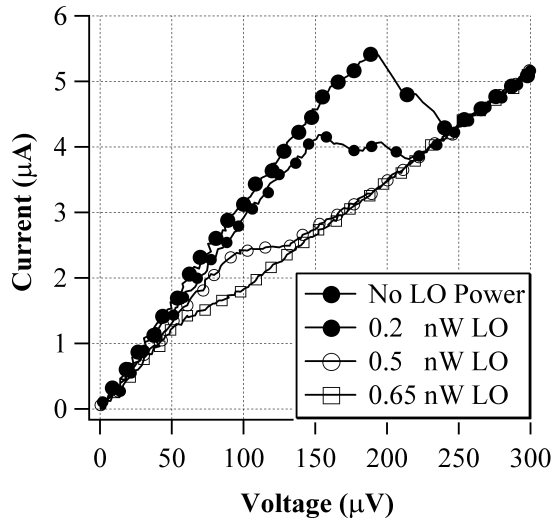


Fig. 7: I-V curves as a function of LO power.  $H=1.2\text{kOe}$  for Device A.  $T=0.25\text{K}$

Additional features which may be due to phase-slip centers are also present in the I-V characteristics. It is not clear what will be the nature of these phase-slip structures at low temperatures in our device geometry. Further investigation is needed. Mixing is observed when biasing the device at low voltages, where the device is partly resistive at  $0.25$  to  $0.5 R_n$  as discussed above, and when biasing the device at higher voltages, above the “kink” in the I-V curve (see Fig. 8). This “kink” is likely associated with the critical current of the microbridge. For  $P_{LO}=0.5\text{nW}$ , shown in Fig. 7, this kink occurs between  $100$  and  $140\mu\text{V}$ , and the “high voltage” region is for larger voltages. The response observed at these higher bias voltages is hereafter termed the “resistive state” response. Though mixing at low bias voltage also may be promising, only the resistive state response is discussed in this work, as the conversion efficiency is better.

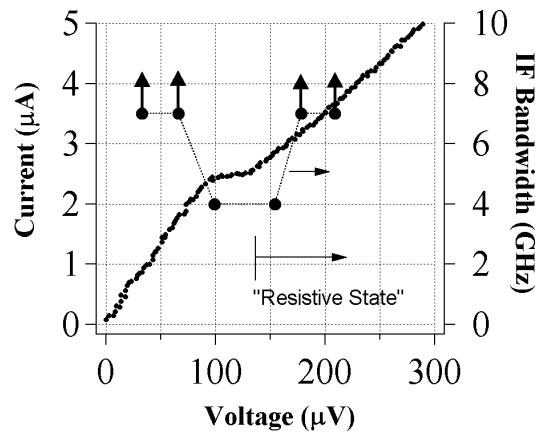


Fig. 8: IF bandwidth vs. bias voltage. The solid black line is the pumped I-V curve. The arrows indicate a bandwidth greater than measurement limit of this setup. Device A.  $T=0.25\text{K}$ .

## B. IF Bandwidth

IF bandwidth depends on the bias point. For higher bias voltages in the resistive branch of the I-V curve (above 160  $\mu\text{V}$  in Fig 8.), the IF bandwidth increases. Accompanying the increase in bandwidth is a sharp decrease in conversion efficiency. The best conversion in the resistive state is seen when biasing on the section of the resistive branch of the I-V curve just above the kink where it connects to the lower voltage branch, 140 $\mu\text{V}$  in Fig. 8. The IF signal was examined carefully to ensure that no sideband generation was observed for the data reported here. Sideband generation is seen for unstable bias points, where the dc differential resistance is negative.

The application of a magnetic field seems not to affect the bandwidth in the resistive state. For example, the IF bandwidth was measured at the lowest bath temperature with an applied magnetic field, and at temperatures above the transition temperature of the contact pads without a magnetic field. The two bandwidths coincide. The conversion efficiency measured at the lower bath temperature is slightly better.

In Fig. 9, a comparison is made between the measured IF bandwidth and the value predicted from a calculation of the diffusion time using Eq. 5, with  $f_{-3\text{dB}} = 1/(2\pi\tau_{\text{eff}})$ . The bias points considered in determining the IF bandwidth were the ones which gave the maximum conversion efficiency in the resistive state. We can see good agreement with the prediction for a diffusion-cooled mixer.

## C. Optimum LO Power

The LO power used in the mixing experiments is in the range of  $\leq 1.0$  nW delivered to the mixer block. Values of the conversion efficiency and mixer noise are presented as a function of LO power in Fig. 10. The mixer noise temperature is calculated from the output noise of the device and the conversion efficiency:  $T_{\text{m(DSB)}} = T_{\text{output}}/2\eta$ . The LO power needed for optimum conversion efficiency is approximately the same value that gives the best noise performance. Experimentally this is the case since the output noise is slowly varying with bias voltage and thus the dominant factor in determining the voltage dependence of the mixer noise is the conversion efficiency.

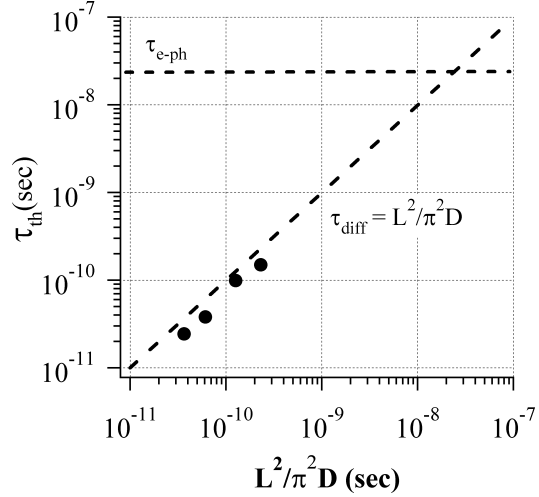


Fig. 9: IF Bandwidth: Measured & Predicted. The electron-phonon inelastic time is calculated from Ref. 8 for  $T=1.6\text{K}$ . The vertical axis is the measured relaxation time, where  $\tau_{\text{th}}$  is determined experimentally using  $\tau_{\text{eff}}=(2\pi f_{-3\text{dB}})^{-1}$  and Eq. 5. Data points are for devices B,A,D,C starting with the smallest time.

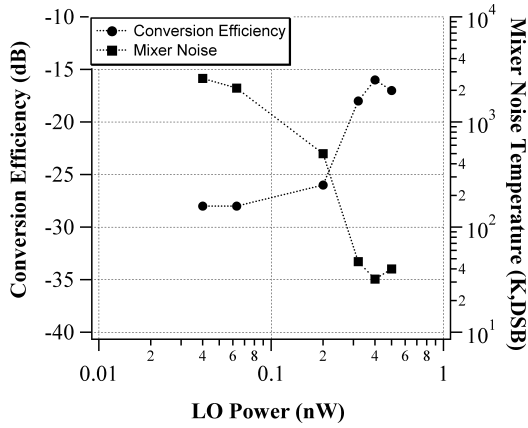


Fig. 10: Conversion Efficiency & Mixer Noise Temperature vs. LO Power. Device D.  $T=0.25\text{K}$ .

The term “optimum” will therefore be used to describe the situation when the device is nearly optimized for both mixer noise and conversion efficiency. The magnitude of the LO power is in quantitative agreement with the prediction in section I (Fig. 10).

Measurements of the temperature dependence of the optimum LO power were also made (Fig. 11). The temperature dependence is in agreement with the relation presented in Eq. (3).

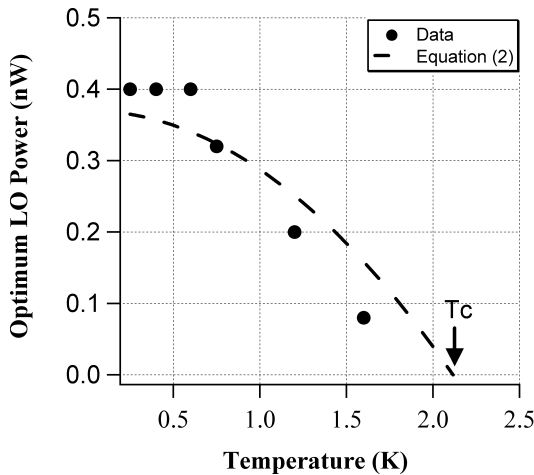


Fig. 11: LO Power vs. Temperature. Device D.

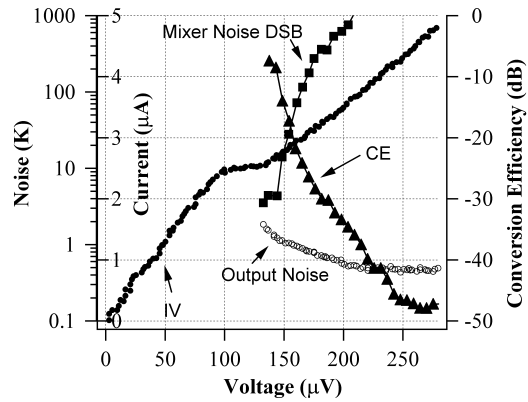


Figure 12: Conversion Efficiency, Output Noise, and Mixer Noise vs. Bias Voltage for Device A.  $T=0.25\text{K}$ .  $H=1.2\text{kOe}$ .

#### D. Mixer Noise

In Fig. 12, the dependence of mixer noise and of conversion efficiency on bias voltage is shown for device A, using  $T_m=T_{\text{out}}/2\eta$ . The minimum of the mixer noise temperature is  $\sim 4\text{K}$  for device A. At the LO frequency used, this is  $\sim 3\text{hv/k}$ . This mixer noise temperature is somewhat lower than predicted by simply scaling Nb data at 20 GHz according to  $T_c$ . The mixer noise temperature with a 20 GHz LO in Nb HEBs was  $\sim 120\text{hv/k}$  in the case with a finite critical current, but  $33\text{hv/k}$  when the critical current was fully suppressed by  $P_{\text{LO}}$ .<sup>16</sup>

By looking at the dependence of the output noise on IF, Burke et al in Ref. 2 were able to separate the thermal fluctuation noise and Johnson noise components of the output noise. At zero intermediate frequency the output noise should be a combination of the thermal fluctuation noise and Johnson noise. Well above the rolloff frequency of the thermal fluctuation noise, the dominant noise should be Johnson noise. The values obtained for the “Johnson noise” contribution to the output noise were

output noise were several times larger than calculated for Johnson noise at the transition temperature of the Nb HEB,  $\sim 5.5\text{K}$ . The origin of this excess noise for Nb was not explained. For the Al HEBs, the total output noise is consistent with thermal fluctuation and Johnson noise contributions with Johnson noise of the magnitude expected for  $T \sim T_c$ .

The noise we reported above used an applied magnetic field. The output noise is less than the  $H=0$  case. IV curves in a magnetic field, at bias voltages  $>1\text{mV}$ , do not exhibit excess current. At the same voltages, in zero field, the differential resistance is equal to  $R_n$ , but there is excess current:  $I > V/R_n$ . This implies that the contacts are still superconducting even though the bridge is in the normal state. The experimental correlation suggests that the additional output noise observed in zero field is correlated with the existence of superconductivity in the contact pads.

When pumped at microwave frequencies, the excess current still remains. Pumped IV curves where the superconductivity in the edges of the microbridge is suppressed by radiation at  $618\text{GHz}$ <sup>26</sup> do not show excess current. Measurements of the output noise in a magnetic field with LO power at  $30\text{GHz}$  agree with those at  $618\text{GHz}$  in zero field.<sup>26</sup>

The IV curves for the Nb devices show similar behavior in terms of excess current. Devices pumped at  $20\text{GHz}$  show excess current. It is possible that the additional output noise observed at  $20\text{GHz}$  is due to the existence of superconductivity in the Nb areas underneath the thick Au contacts, like the case of Al microbridges.

## V. Mixer Performance: Experiment and Theory

In this section we compare measured mixer performance with that predicted by theory. The conversion efficiency, output noise, and IF bandwidth can be calculated from thermodynamic considerations based on the device operating parameters – the dynamic resistance, bias current, temperature, thermal conductance, LO power, and the derivative of resistance with temperature.<sup>19,27-29</sup> A summary of these formulas is presented in Ref. 29, and are repeated here.

The conversion efficiency is defined as the ratio of the output power at the IF divided by the input power at the RF. The frequency dependent single-sideband (SSB) conversion efficiency is given by

$$\eta(\omega) = \frac{2R_L}{(R + R_L)^2} P_{LO} \left( \frac{I_{DC} \left( \frac{dR}{dT} \right)}{G_{eff}} \right)^2 \quad (4)$$

$$\times \frac{1}{1 + (\omega\tau_{eff})^2}$$

where  $P_{LO}$  is the LO power,  $R$  is the device resistance,  $G_{eff}$  is the effective thermal conductance,  $I_{DC}$  is the device bias current, and  $\omega$  is the IF. The resistance  $R$  is defined as the dc voltage divided by the dc current.  $R_L$  is the load resistance – which in this case is the  $50\Omega$  input impedance of the first stage IF amplifier. Electro-thermal feedback effects which tend to modify the thermal conductance and time constant are included using the factor  $\alpha$ .

$$\tau_{eff} = \tau_{th} / (1 - \alpha), \quad (5)$$

$$G_{eff} = G(1 - \alpha), \quad (6)$$

Table II: Mixer parameters: Experimental results and theoretical predictions.

Device	Experiment						Theory			
	Rn (Ohm)	T <sub>b</sub> (K)	IF BW (GHz)	η (dB)	T <sub>out</sub> (K)	T <sub>mix</sub> =T <sub>out</sub> /2η (K,DSB)	IF BW (GHz)	η (dB)	T <sub>out</sub> (K)	T <sub>mix</sub> =T <sub>out</sub> /2η (K,DSB)
A	52	0.25	4	-8	1.3	4	2.5	-9	1.3	5
B	145	1.2	6	-27	...	...	5	-22	...	...
C	260	1.2	1.2	-33	...	...	0.8	-31	...	...
D	387	0.25	2	-16	1.6	32	1.7	-15	1.6	27

$$\alpha = \frac{I_{DC}^2}{G} \frac{dR/dT}{\left( \frac{R_L - R}{R_L + R} \right)} \quad (7)$$

The parameter  $\alpha$  can be determined from the pumped I-V characteristics using the following relation from Ref. 28:

$$\alpha_0 = \frac{I_{DC}^2}{G} \frac{dR}{dT} = \frac{\frac{dV}{dI} - \frac{V}{I}}{\frac{dV}{dI} + \frac{V}{I}}. \quad (8)$$

The thermal conductance  $G$  can be estimated from the device resistance and the Wiedemann-Franz relation.<sup>5</sup>

The output noise is modeled as consisting of thermal fluctuation noise and Johnson noise. The Johnson noise component of the output noise temperature is taken to be equal to the average electron temperature  $\theta$ , which can be estimated from the  $R$  vs.  $T$  characteristic and the device resistance at the operating point;  $\theta = T_c$ . The frequency dependent output noise due to fluctuations in the electron temperature is given by

$$T_{TF}(\omega) = \left( I_{DC} \theta \frac{dR}{dT} \right)^2 \frac{1}{RG_{eff}(1-\alpha)} \quad (9)$$

$$\times \frac{1}{1 + (\omega\tau_{eff})^2} \frac{4RR_L}{(R + R_L)^2}$$

In Table II we present the experimental and predicted values for mixer parameters for near optimum operating conditions. The conversion efficiency and output noise are calculated from the relations given above. The IF bandwidth is estimated from Eq. (1) and Eq. (5). We see good agreement between theoretical predictions and experimental results.

We can calculate the conversion efficiency and output noise using the formulas above for different bias voltages and different LO powers. These calculations are in also good agreement with experimental data. As an example, in Fig. 13, we show how the measured conversion efficiency for device A compares with theoretical prediction.

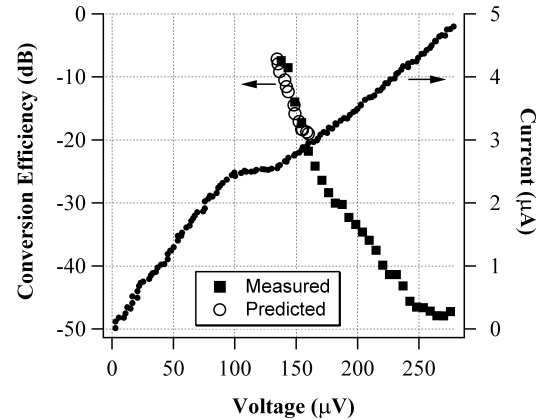


Fig. 13: Measured and predicted conversion efficiency. Device A. T=0.25K.

For operation at Terahertz frequencies, we can empirically estimate the mixer noise from the 30 GHz data by scaling the microwave data linearly with frequency. At 30 GHz we measure  $T_m \sim 3$  hv/k. If the same sensitivity is present at 2.5 THz, the mixer noise is then predicted to be  $T_m \sim 360$ K. As a check, we can compare with measurements at 618 GHz. The output noise of Al HEBs measured at 618 GHz ranges from 1-2K. The conversion efficiency under the same conditions is estimated to be  $\sim -21$  dB.<sup>26</sup> The calculated mixer noise temperature is thus  $T_m \sim 125$  K, DSB. From the 30 GHz data, one would predict  $T_m \sim 90$ K for 618 GHz. So our estimates seem to be consistent with the existing data. These estimates do not include rf submillimeter coupling losses which are present in any receiver. At 30GHz, coupling losses are negligible

## VI. Conclusions

Results for mixing with Al HEBs at microwave frequencies are very good. The IF signal bandwidth scales with device length and diffusivity as predicted in the diffusion cooling model, Eq. (1a). The LO power needed for mixing scales approximately linearly with  $T_c$ . The measured mixer noise is somewhat lower than that predicted by scaling Nb HEB results. The measured IF bandwidth and optimum LO power are in good agreement with lumped element predictions.

The diffusion time in the these devices is comparable to or larger than the inelastic electron-electron time<sup>8</sup>  $\tau_{ee}$ . Recently, predictions were made for HEBs which are very short  $L \ll (D \tau_{ee})^{1/2} = L_{ee}$  in which thermalization via electron-electron interaction would be absent in the micro-

bridge. Such a short device would have large LO power requirements in the  $\mu$ W range.<sup>30</sup> These predictions were made for an operating frequency of 2.5 THz. For device A ( $L=600$ nm),  $L_{ee} = 600$ nm for  $T=T_c$ . The other devices have a larger sheet resistance and are longer than the inelastic electron-electron length. Thus, our devices are not in the regime treated by Ref. 30. In any case, measurements at 30 GHz cannot address this issue, since 30 GHz is below the gap frequency;  $v_{gap} \sim 110$  GHz at  $T=0$  and  $H=0$  for device A. However, measurements at 618 GHz could speak to this issue. Results at JPL<sup>26</sup> on a device comparable to our device A show that  $P_{LO} \leq 10$ nW. We emphasize that the device studied at JPL also had  $L > L_{ee}$ , as proposed in the original theory paper on diffusion cooling.<sup>5</sup> If we scale the predictions in Ref. 30 as the frequency squared, the expected LO power for this bridge with  $L \geq L_{ee}$ , is still substantially less than that predicted for  $L \ll L_{ee}$ .

Currently, a major design issue for space-borne application of HEB mixer receivers is the availability of an appropriate LO source. Molecular lasers are heavy and need high-power sources. A CW solid state generator was demonstrated recently<sup>31</sup> using a p-Ge laser biased at relatively low bias voltages compared with pulse mode voltages. However, it is unclear if it is possible to get a narrow enough spectral line ( $\sim 1$ MHz) with the p-Ge laser. The other real possibilities at present are photomixer sources and multipliers. A successful traveling-wave THz photomixer has been shown to have an output power of at least  $\sim 10$ nW above 1 THz.<sup>32</sup> This is not enough for mixing with Nb HEBs. But our results for the optimum LO power for Al HEB mixers indicate that there is real possibility for integrating a

THz Al HEB mixer with such a photomixer.

## Acknowledgements

The authors thank Prof. R.J. Schoelkopf for use of equipment in his lab, and Rich Lathrop for help in the early experiments. This research was supported by the NSF and NASA Office of Space Science. Funding for I.S. was provided by a NASA Graduate Student Fellowship.

## References

- <sup>1</sup> B.S. Karasik and W.R. McGrath, in *P Proceedings of the 9<sup>th</sup> International Symposium on Space Terahertz Technology*, edited by W.R. McGrath (Pasadena, CA, 1998), pp. 73-80; D.E. Prober (unpublished).
- <sup>2</sup> P.J. Burke, R.J. Schoelkopf, D.E. Prober, A. Skalare, B.S. Karasik, M.C. Gaidis, W.R. McGrath, B. Bumble, and H.G. LeDuc, *J. Appl. Phys.* **85**, 1644 (1999).
- <sup>3</sup> R. A. Wyss, B.S. Karasik, W.R. McGrath, B. Bumble, H. LeDuc, in *Proceedings of the 10<sup>th</sup> International Symposium on Space Terahertz Technology*, edited by T. Crowe and R.M. Weikle (University of Virginia, Charlottesville, VA, 1999), pp. 215-228; B.S. Karasik, M.C. Gaidis, W.R. McGrath, B. Bumble, H.G. LeDuc, *Appl. Phys. Lett* **71**, 1567 (1997).
- <sup>4</sup> E. Gerecht, C.F. Musante, H. Jian, Y. Zhuang, K.S. Yngvesson, J. Dickson, T. Goyette, J. Waldman, P.A. Yagoubov, G.N. Gol'tsman, B.M. Voronov, and E. M. Gershenzon, in *Proceedings of the 10<sup>th</sup> International Symposium on Space Terahertz Technology*, edited by T. Crowe and R.M. Weikle (University of Virginia, Charlottesville, VA, 1999), pp. 200-207.
- <sup>5</sup> D.E. Prober, *Appl. Phys. Lett.* **62**, 2119 (1993).
- <sup>6</sup> J.M. Gordon and A.M. Goldman, *Phys. Rev. B.* **34**, 1500 (1986).
- <sup>7</sup> Y. Bruynserade, M. Gijs, C. Van Haesendonck, and G. Deutscher, *Phys. Rev. Lett.* **50**, 277 (1983).
- <sup>8</sup> P. Santhanam and D.E. Prober, *Phys. Rev. B* **29**, 3733 (1984).
- <sup>9</sup> B. Shinozaki, T. Kawaguti, and Y. Fujimori, *J. Phys. Society Japan* **61**, 3678 (1992).
- <sup>10</sup> E.M. Gershenzon, G.N. Gol'tsman, V.D. Potapov, and A.V. Sergeev, *Solid State Commun.* **75**, 639 (1990).
- <sup>11</sup> M. Park, K.R. Lane, J.M. Parpia, M.S. Isaacson, *J. Vac. Sci. Technol. A* **13**, 127 (1995).
- <sup>12</sup> C. Kittel, *Introduction to Solid State Physics, Seventh Edition* (John Wiley & Sons, Inc., New York, 1996), pp. 158-159.
- <sup>13</sup> W. Liniger, *J. Low Temp. Phys.* **93**, 1 (1993).
- <sup>14</sup> C.C. Chi, P. Santhanam, S.J. Wind, M.J. Brady, and J.J. Bicchigano, *Phys. Rev. B* **50**, 3487 (1994).
- <sup>15</sup> This calculation assumes that the microbridge is connected with contact pads made of the same material as the microbridge, but in the normal state.
- <sup>16</sup> P.J. Burke, Ph.D. thesis, Yale University, 1997, available from authors.
- <sup>17</sup> J. Schubert, A. Semenov, G. Gol'tsman, H.W. Hubers, G. Schwab, B. Voronov, E. Gershenzon, in *Proceedings of the 10<sup>th</sup> International Symposium on Space Terahertz Technology*, edited by T. Crowe and R.M. Weikle (University of Virginia, Charlottesville, VA, 1999), pp. 190-199.
- <sup>18</sup> A magnetic field was not used in measurements made at 618 GHz. Superconductivity in the edges of the microbridge was suppressed using LO power. This might account in part for the higher LO power used.
- <sup>19</sup> B.S. Karasik and A.I. Elantiev, *Appl. Phys. Lett* **68**, 853 (1996).
- <sup>19a</sup> C.M. Caves, *Phys. Rev. D*, **26**, 1817 (1982).
- <sup>20</sup> P.M. Echternach, H.G. LeDuc, A. Skalare, W.R. McGrath, in *Proceedings of the 10<sup>th</sup> International Symposium on Space Terahertz Technology*, edited by T. Crowe and R.M. Weikle (University of Virginia, Charlottesville, VA, 1999), pp. 261-268.
- <sup>21</sup> Applying a magnetic field suppresses the thick contact pads. The thin Al layer underneath is proximitized normal.
- <sup>22</sup> To calibrate out any resonances in the RF input line, the RF power needed to suppress the IV curve to the same state was measured for the frequencies used. The relative difference was then used in the mixing experiments to adjust the input power so that the RF power remained constant.
- <sup>23</sup> G.E. Blonder, M. Tinkham, and T.M. Klapwijk, *Phys Rev B* **25**, 4515 (1982).
- <sup>24</sup> D. Wilms Floet, J.J.A. Baselmans, and T.M. Klapwijk, *Appl. Phys. Lett.* **73**, 2826 (1998).

- <sup>25</sup> P.M. Echternach (unpublished).
- <sup>26</sup> A.Skalare et al, in *Proceedings of the 11<sup>th</sup> International Symposium on Space Terahertz Technology*, edited by J. West (U. Michigan, Ann Arbor, MI, 2000); A. Skalare private communication).
- <sup>27</sup> F. Arams, C. Allen, B. Peyton, and E. Sard, Proc. IEEE 54, 612 (1966).
- <sup>28</sup> H. Ekstrom, B. Karsik, E. Kollberg, and K. Yngvesson, IEEE Trans. Microwave Theory-Tech 43, 938 (1995).
- <sup>29</sup> B. Karasik and A. Elantiev, in *Proceedings of the 6<sup>th</sup> International Symposium on Space Terahertz Technology*, edited by J. Zmuidzinas and G. Rebiez (Caltech, Pasadena, CA, 1995), pp. 229-246.
- <sup>30</sup> A.D. Semenov and G.N. Gol'tsman, J. Appl. Phys 87, 502 (2000).
- <sup>31</sup> Yu. P. Gousev, I.V. Altukhov, K.A. Korolev, V.P. Sinis, M.S. Kagan, E.E. Haller, M.A. Odnoblyudov, I.N. Yassievich, and K.A. Chao, Appl. Phys. Lett. 75, 757 (1999).
- <sup>32</sup> S.Matsuura, G.A.Blake, R.A.Wyss, J.C.Pearson, C.Kadow, A.W.Jackson, and A.C.Gossard, Appl. Phys. Lett. 74, 2872 (1999).

# BROADBAND ARRAY SIS MIXERS FOR 780–880 GHz WITH ALUMINUM TUNING CIRCUITS

Sybille Haas, Stephan Wulff, Dirk Hottgenroth, Netty Honingh, Karl Jacobs

KOSMA, I. Physikalisches Institut, Universität zu Köln,  
Zùlpicher Str. 77, D–50937 Köln, Germany

*Abstract*—As a building block for an 8-pixel 800 GHz array receiver at KOSMA we developed a low noise SIS mixer. The mixerblock is tunerless and similar to the "stamped waveguide cavity" mixers we have used from 345 GHz to 800 GHz before [1]. We embedded the SIS junction into a standard broadband tuning circuit, commonly used at lower frequencies. The circuit consists of a short end-loaded stub in series with two impedance transforming sections.

For the 780–880 GHz band, we fabricated the electrodes of the tuning circuit as a combination of niobium and aluminum layers in different sequences. First heterodyne tests were performed on devices with a tuning microstrip circuit ground plane consisting of 40nm Nb with 200nm of Al on top and a top conductor consisting of a 70 nm thick Nb layer with a 280 nm thick Al layer on top.

The Nb-Al<sub>2</sub>O<sub>3</sub>-Nb junction has an area of about 0.5  $\mu\text{m}^2$  and is fabricated with optical lithography. For anisotropic Nb etching, we use a RIE gas mixture of CCl<sub>2</sub>F<sub>2</sub> and NF<sub>3</sub>. The Al<sub>2</sub>O<sub>3</sub> barrier is removed with Ar sputter etching. Fabrication yield improved considerably when we introduced a light CMP-step after self-aligned SiO dielectric liftoff. For a SIS junction with  $R_n A$  equal to 14  $\Omega\mu\text{m}^2$ , the  $R_{Subgap}/R_n$  value of 15.4 is remarkably good.

We measured uncorrected receiver noise temperatures around 400 K over the whole band from 780 to 880 GHz, with a best noise temperature of 370 K at 804 GHz.

## 1 Introduction

Our aim was to build an 800 GHz prototype mixer for a 2x8-pixel dual frequency array receiver [2] for the atmospheric windows around 800 GHz and 490 GHz to be installed at the KOSMA telescope on Gornergrat (Switzerland) for the next winter observation period (2000/2001).

To take full advantage of a multibeam receiver, array mixers should be just as sensitive as the best available single pixel mixer. For optimum sensitivity around 800 GHz

the best noise temperatures are reported for mixers using superconducting NbTiN integrated tuning circuits [3]. Although we are developing mixers with NbTiN integrated tuning circuits for our contribution to HIFI (Band 2: 640 – 800 GHz) on the FIRST satellite, this development is not yet advanced enough to implement it for a practical array receiver under observatory conditions.

We have, however, long time experience in fabricating devices and mixers with Nb-Al<sub>2</sub>O<sub>3</sub>-Nb junctions embedded in Nb tuning structures [1], [4], [5]. For the mixer described here we designed a type of tuning circuit that was successfully used in Nb at frequencies below its gap frequency, with aluminum electrodes for the 780-880 GHz band. We integrated this device in a fixed tuned waveguide mount.

## 2 Mixer Block Design and Assembly

Our fixed tuned waveguide mixerblock design [1] meets the requirements concerning stacking of individual blocks close together to form an array (size: 20x20x10 mm<sup>3</sup>, all connectors for DC and IF at the backside of the mixer). The magnetic field to suppress the Josephson current is concentrated close to the junction by two iron pole pieces integrated into the mixerblock. The magnet coil itself, with superconducting NbTi wire, connects the two pole pieces at the backside of the mixer. The minimum distance between the junction and the tip of the pole pieces is 0.8 mm. Figure 1 shows a photograph of the mixer without the horn antenna. The waveguide of dimensions 330x90 μm<sup>2</sup> is stamped into a copper block with an appropriate steel tool. The bottom of the stamped guide yields a perfect short circuit at a fixed position behind the junction (50 μm). The mixerblocks are made in house with a mechanical precision of ±5 μm on a CNC lathe. A Potter horn is flanged to the mixerblock for coupling to the receiver optics.

The fused quartz substrate with the junction and tuning circuit is mounted in a substrate channel across the waveguide. Ground and IF-connections are ultrasonically bonded with 25 μm diameter aluminum wires.

Mounting these thin substrates (2740x80x30 μm<sup>3</sup>) usually is a tedious job with the risk of breaking them in this final step of assembly. We applied an innovative method for mounting the substrates with the help of a Nanomotor<sup>TM</sup>-driven [7] micro-gripper station as shown in Figure 2. The waveguide mixer and the Fluoroware<sup>TM</sup> junction storage box are both mounted on a Nanomotor<sup>TM</sup>-driven x-y stage and can be positioned with a smallest step size of only 1 nm under computer control. The storage box is moved under the gripper which is lowered with the z-axis Nanomotor and then opened and carefully closed under computer control to grab the selected substrate. A sliding clutch in the Nanomotor prevents the gripper and the substrate from breaking. The gripper can also be rotated to catch the selected substrate at any given angle. The substrate can then be positioned in the substrate channel under microscope control. A small hypodermic needle attached to the side of the gripper holder is used to distribute

tiny amounts of glue in the  $100\ \mu\text{m}$  wide substrate channel of the mixer block. We use a thermoplastic glue which softens at  $90\ ^\circ\text{C}$ . This microassembly station provides a reliable and reproducible device mounting procedure which is essential for fabricating a larger number of mixers and for space qualification of the waveguide mixer assembly.

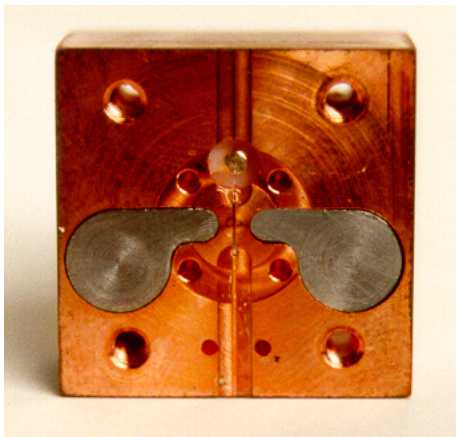


*Fig. 1: Photo of the KOSMA fixed tuned mixerblock (without horn antenna) showing the magnetic pole pieces.*



*Fig. 2: Photo of the KOSMA microassembly station.*

### 3 Junction RF Design

We use the standard materials Nb and Al for the integrated tuning. Even when we use NbTiN tuning circuits in the future, we can probably only replace one of the tuning electrodes by NbTiN as long as we are using Nb-Al<sub>2</sub>O<sub>3</sub>-Nb junctions. Heat trapping in Nb junction electrodes fully embedded in a higher gap superconductor may severely degrade the mixer performance [8]. In order to find an alternative to an NbTiN tuning top conductor, we took the opportunity to investigate which material (Nb or Al) or a combination of both materials could be useful. The crossover point in performance between Nb and Al tuning is somewhere in the frequency range between 760 and 820 GHz, depending on the exact quality of the different layers.

We use Nb-Al<sub>2</sub>O<sub>3</sub>-Nb tunnel junctions embedded in an Nb/Al tuning circuit with a junction area of about  $0.5\ \mu\text{m}^2$  and  $R_nA$  of about  $14\ \Omega\mu\text{m}^2$ . This rather small area junction with high current density facilitates a broadband coupling to the impedance of the waveguide mount. The impedance of this waveguide mount has been determined by reflection measurements on a scaled model of the mixer to be  $40\text{--}50\ \Omega$ . Optimum coupling is accomplished by an end-loaded stub tuning structure with two quarter wavelength transformer sections as was successfully used at lower frequencies [1]. Figure 3 shows a sketch of the junction with its tuning structure on the photolithography mask. The actual layer sequence is given schematically in Figure 4.

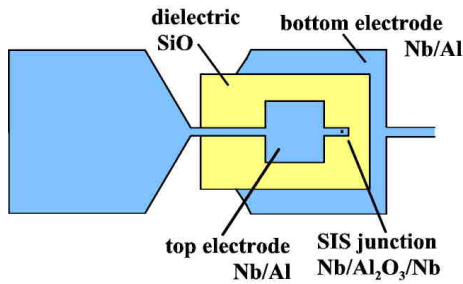


Fig. 3: Sketch of junction and integrated tuning circuit.

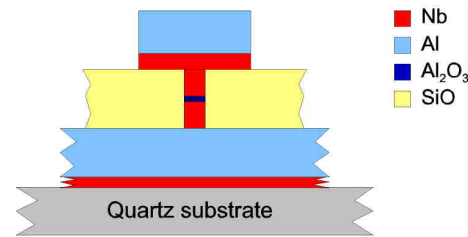


Fig. 4: Sketch of the layer sequence of junction and tuning.

## 4 Device Fabrication

The initial stack of five layers for this type of SIS detectors consists of a 40 nm niobium layer, 200 nm aluminum as the ground plane, 100 nm niobium tunnel junction base layer, 8 nm aluminum for the tunneling barrier followed by 100 nm niobium for the junction top layer. All five layers are sputter-deposited in-situ onto INFRASIL fused quartz substrates into UV lithographically patterned bilayer AZ 7212 (Clariant) photoresist windows. The bilayer technique [9] with its large undercut profile is well suited for a liftoff process with more than 400 nm layer thickness. The base pressure of the sputter chamber is in the  $5 \cdot 10^{-9}$  mbar range. Before depositing the aluminum layer for the barrier, the wafer is cooled to  $-10$  °C. The barrier oxidation is performed in the load lock chamber in a static pure oxygen atmosphere at a pressure of 1.7 Pa for 5.5 minutes, which results in an  $R_nA$  product of about  $14 \Omega\mu\text{m}^2$ . Even with this rather high current density for an  $\text{Al}_2\text{O}_3$  barrier, the subgap to normal resistance ratio is still about 15.

After standard UV-lithography with AZ 7212 to define the  $(0.8 \mu\text{m})^2$  -  $(0.7 \mu\text{m})^2$  junction top electrodes, a mixture of 6 sccm  $\text{CCl}_2\text{F}_2$  and 1.2 sccm  $\text{NF}_3$  is used for reactive ion etching of the niobium top electrodes. This is a variation of the recipe introduced in [10] which replaces the usual  $\text{CF}_4+\text{O}_2$  with nitrogen trifluoride. Pure  $\text{NF}_3$  has high etch rates in Nb ( $>280$  nm/min at 4 Pa,  $0.13 \text{ W/cm}^2$  RF power, self-bias voltage of  $-55$  V) and does not need an oxygen component, as the lack of carbon apparently prevents polymer formation. The disadvantage is that  $\text{NF}_3$  etches almost isotropic. The  $\text{CCl}_2\text{F}_2/\text{NF}_3$  mixture is used at 4 Pa,  $0.17 \text{ W/cm}^2$  and  $-105$  V self-bias with an etch rate of 80 nm/min and results in an aspect ratio of at least 4:1. The etch times are influenced by a latency time of approximately 13 seconds which is probably caused by a thin niobium oxide layer which has a low etch rate. Also, the etch rate is very dependent on the heat sinking (i.e. temperature) of the wafer. To achieve the given etch rate, a 2 mm thick Teflon disk essentially decouples the wafer from the water-cooled stainless steel RIE cathode.

After etching the top niobium layer, the  $\text{Al}_2\text{O}_3$ -Al barrier is etched with Argon at 1 Pa,  $1.1 \text{ W/cm}^2$  RF power, -605 V self-bias for 9 minutes. To avoid excessive heating of the photoresist, this etch is performed in 1 min intervals with 1 min cooling time between the etching steps. The base niobium layer is again etched in  $\text{CCl}_2\text{F}_2/\text{NF}_3$  with the bottom aluminum layer acting as an etch stop. The  $\text{CCl}_2\text{F}_2/\text{NF}_3$  etch leaves a residue on the aluminum layer which is removed with a 2 minute etch with 10 Pa  $\text{O}_2$  at  $0.45 \text{ W/cm}^2$ .

The dielectric layer for junction insulation and for the tuning microstrip consists of 250 nm silicon monoxide, defined in the usual self-aligned liftoff procedure. After liftoff, a 1 minute CMP (Chemical Mechanical Polishing) step [11] was introduced to clean the top niobium electrodes from residues of the photoresist, which is hard baked by the long RIE times and hard to remove. The introduction of this step increased the yield to more than 90 %. After lithography for the wiring layer including the tuning circuit, the wiring electrode layers are sputtered with a subsequent liftoff. After DC-testing of the junctions, the wafer is diced and thinned to  $30 \mu\text{m}$  thickness.

## 5 Measurement and Analysis

In the course of the experiments with different top layer metallisations, one batch was fabricated with 70 nm Nb followed by 280 nm Al. These devices showed good quality I/V-curves and self induced current steps at bias voltages corresponding to a Josephson oscillation frequency in resonance with the tuning circuit within the designed RF band.

We investigated the RF-coupling of one of these devices with a resonance at 830 GHz in a direct detection Fourier transform spectroscopy measurement as well as its heterodyne response in the frequency range from 780 to 880 GHz.

The direct detection measurement was performed with a commercial Fourier Transform Spectrometer [12] with a maximum resolution of 3.5 GHz. The SIS receiver is used as an external detector of the FTS monitoring the DC current at a proper bias voltage as a function of the displacement of the moving mirror of the interferometer. A broadband Hg arc serves as radiation source.

Figure 5 shows the the measured spectral response. The prominent dips around 753 GHz and 990 GHz are due to absorption of water vapor in the non-evacuated spectrometer. The maximum response occurs at the same frequency as the DC resonances in the I-V curves. The response is very broadband: at least 180 GHz. For a more accurate determination of the bandwidth we will have to repeat the measurement with an evacuated spectrometer.

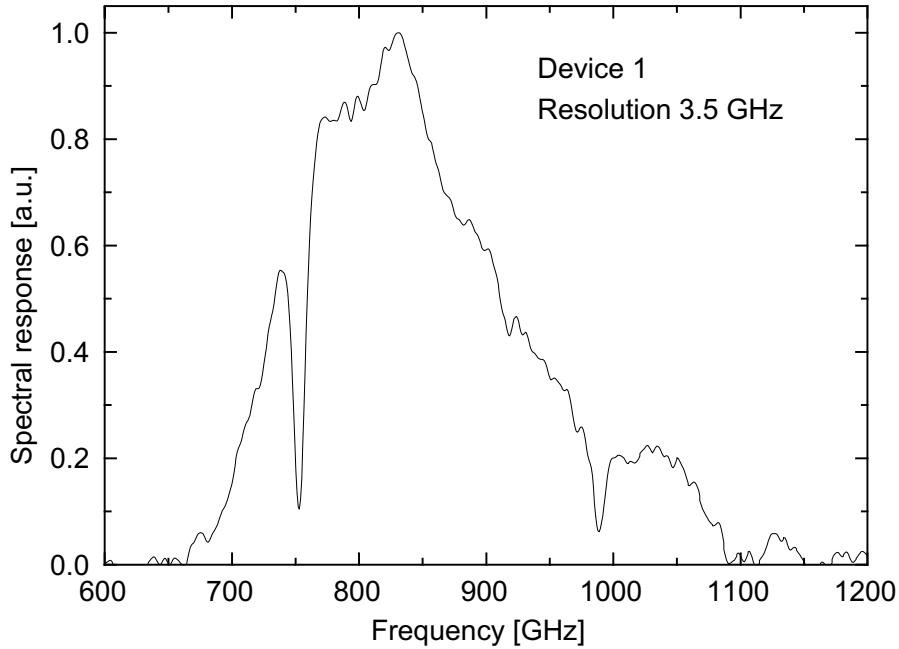


Fig. 5: Spectral response of the device measured with FTS in direct detection.

We used our usual receiver test setup as described in [1] with two solid state local oscillators [6] ranging from 780 to 820 GHz and from 800 to 880 GHz, respectively. The LO power was combined with the hot/cold signal via a  $36 \mu\text{m}$  Mylar beamsplitter. Table 1 gives the measured transmission of the optical components in front of the mixer, measured with a Fourier transform spectrometer together with the calculated noise contribution  $T_{noise}$  referred to its input.

component	material	$T_{phys}$ [K]	d [ $\mu\text{m}$ ]	gain [dB]	$T_{noise}$ [K]
beamsplitter	mylar	295	36	-0.22	14.5
dewar window	teflon	295	500	-0.46	30.6
IR filter	teflon	77	300	-0.36	5.1

Table 1: Loss of optical components at 830 GHz measured with FT spectrometer and deduced noise contributions.

The IF output of the mixer is fed via a  $50 \Omega$  coaxial cable to a HEMT amplifier (1-2 GHz) located on the 4 K-plate. An amplifier chain outside the cryostat amplifies the signal by about 70 dB. A bandpass filter restricts the IF bandwidth to 100 MHz around 1.4 GHz.

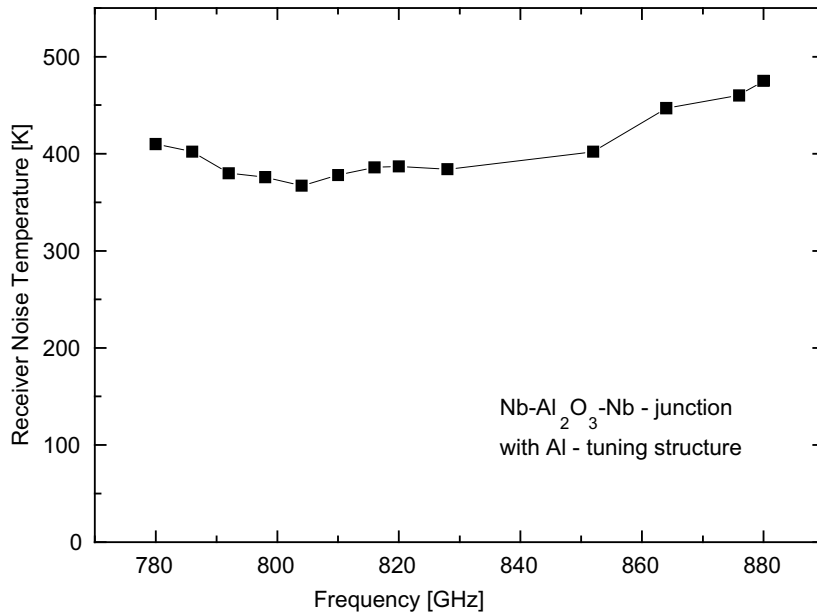


Fig. 6: Measured DSB receiver noise temperatures from 780 to 880 GHz at 4.2K operating temperature.

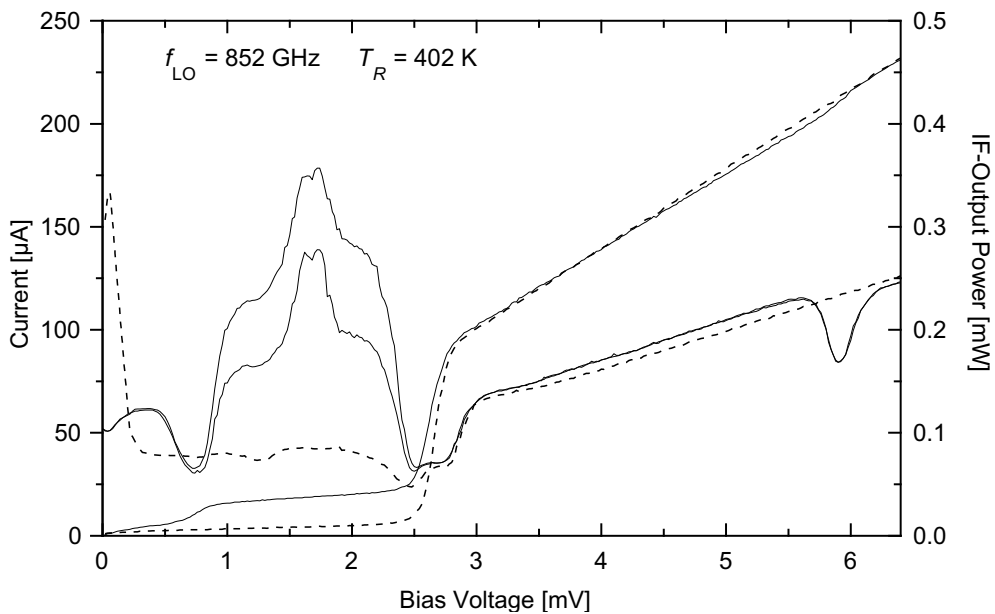


Fig. 7: IF output power as function of bias voltage for a hot (295 K) and a cold (77 K) load input at an LO frequency of 852 GHz.

Figure 6 shows the measured DSB receiver noise temperatures at 4.2 K operating temperature determined from a standard Y-factor measurement calculated with the

Callen-Welton formula. These values are not corrected for any loss. The noise temperature is almost constant over the whole frequency range with a lowest value of 370 K at 804 GHz and increases to only 480 K at 880 GHz. To our knowledge these are the best receiver noise temperatures achieved with Nb-Al<sub>2</sub>O<sub>3</sub>-Nb junctions and Al tuning circuits from 780 to 880 GHz. It is remarkable that there is only a very slow increase in noise temperature at higher frequencies, despite of the rather thick Nb layer under the Al top layer.

Figure 7 gives the IF output power as a function of bias voltage for a hot (295 K) and a cold (77 K) load input at an LO frequency of 852 GHz.

A noise breakdown was calculated at an LO frequency of 828 GHz. The noise contributions of the optics in front of the mixer add up to  $T_{opt} = 55$  K with a (measured) total gain of  $G_{opt} = -1.1$  dB. The shot noise technique [13] was used to determine the noise of the IF system. The noise temperature  $T_{if}$  of the HEMT amplifier has been determined to be 3 K, while the total IF gain is 97.1 dB. The effect of the reflection loss at the mixer output due to mismatch between HEMT amplifier and mixer is described by a term  $T_{mis}|\Gamma_{mis}|^2$ , with  $|\Gamma_{mis}|^2$  being the reflection coefficient between the load impedance (taken as 50Ω) and the differential resistance of the unpumped IV-curve.  $T_{mis}$  is fitted to be 8 K.

From the measured heterodyne response to a hot and a cold load the following parameters  $T_{mix}$  and  $G_{mix}$  – noise temperature and gain of the mixer (including the contribution from the tuning stripline) – can be determined:

$$T_{rec} = T_{opt} + \frac{T_{mix}}{G_{opt}} + \frac{T_{IF}}{G_{opt}G_{mix}} + \frac{T_{mis}|\Gamma_{mis}|^2}{G_{opt}G_{mix}} \quad (1)$$

Values at 828 GHz are  $T_{mix} = 200$  K and  $G_{mix} = -10.2$  dB.

The mixer proved to be very stable during testing. Measurements could be carried out for several hours without readjusting magnet current and bias voltage despite the electrically noisy lab environment.

In conclusion, we achieved a very good noise performance at 780-880 GHz with Nb-Al<sub>2</sub>O<sub>3</sub>-Nb junctions using a Nb-Al tuning circuit. These noise temperatures are only a factor of 2 worse than the best results reported up to now with NbTiN tuning circuits [3]. The excellent stability together with low noise temperatures over a large bandwidth make these mixers very suitable for the planned array application.

## Acknowledgment

We thank Michael Schultz for dicing, thinning and mounting the devices, Marc Sahr for his contribution to the mask design and Michael Brandt for arranging the contact to Klocke Nanotechnik and for the electronic adaptation of the microassembly station. This work was supported by the Verbundforschung Astronomie through grant 05 AH9PK1, by the Ministerium für Wissenschaft und Forschung, Land Nordrhein-Westfalen, by DLR (Deutsches Zentrum für Luft- und Raumfahrt), Förderkennzeichen 50 OF 0001 2 and 50 OF 9902 4 and by DFG (Deutsche Forschungsgemeinschaft), Sonderforschungsbereich 494.

## References

- [1] S. Haas, C. E. Honingh, D. Hottgenroth, K. Jacobs, J. Stutzki, "Low noise broadband tunerless waveguide SIS receivers for 440–500 GHz and 630–690 GHz", *Int. J. of Infrared and Millimeter Waves*, vol. 17, no. 3, pp. 493–506, March 1996.
- [2] U. Graf, S. Haas, C. E. Honingh, K. Jacobs, R. Schieder, J. Stutzki, "Array receiver development at KOSMA for the sub-mm and THz spectral range", *Proc. SPIE*, Kona, Hawaii, 1998.
- [3] J. Kawamura, J. Chen, D. Miller, J. Kooi, J. Zmuidzinas, B. Bumble, H. LeDuc, J. Stern, "Low-noise submillimeter-wave NbTiN superconducting tunnel junction mixers", *Appl. Phys. Lett.*, vol. 75, no. 25, pp. 4013-4015, 1999.
- [4] D. Hottgenroth, C. E. Honingh, S. Haas, K. Jacobs, J. Stutzki, "Design and analysis of a waveguide SIS mixer above the gap frequency of niobium", *Int. J. of IR and MM waves*, vol. 18, no. 3, March 1997.
- [5] C. E. Honingh, S. Haas, D. Hottgenroth, K. Jacobs, J. Stutzki, "Low noise broadband fixed tuned SIS waveguide mixers at 660 and 800 GHz", *IEEE Transactions on Applied Superconductivity*, vol. 7, no. 2, pp. 2582–2586, 1997.
- [6] Radiometer Physics GmbH, Meckenheim, Germany.
- [7] Dr. Volker Klocke Nanotechnik, Aachen, Germany. For details including an animated sequence of the junction gripping see [www.nanomotor.de/het](http://www.nanomotor.de/het)
- [8] B. Leone, B. D. Jackson, J. R. Gao, T. M. Klapwijk, "Geometric heat trapping in superconductor-insulator-superconductor mixers due to niobium titanium nitride leads", *Phys. Rev. Lett.*, vol. 76, pp. 780-782, 2000.
- [9] G. J. Dolan, "Offset masks for lift-off photoprocessing", *Appl. Phys. Lett.*, vol. 31, no. 5, pp. 337-339, 1977.

- [10] H. G. LeDuc, B. Bumble, S. R. Cypher, A. J. Judas, J. Stern, "Submicron Area Nb/AlOx/Nb Tunnel Junctions", *Proc. of the Third Int. Symp. on Space Terahertz Technology*, pp. 408–418, Ann Arbor, University of Michigan, March 1992.
- [11] P. Puetz, K. Jacobs, "E-Beam SIS Junction Fabrication Using CMP and E-Beam Defined Wiring Layer", *Proc. of the Tenth Int. Symp. on Space Terahertz Technology*, pp. 118-129, Charlottesville, University of Virginia, March 1999.
- [12] Bruker Optik GmbH, Rheinstetten, Germany.
- [13] D. P. Woody, R. E. Miller, M. J. Wengler, "85-115 GHz Receivers for Radio Astronomy", *IEEE Trans. Microwave Theory Tech.*, vol. 33, pp. 90-95, 1985.

# A 350 GHz SIS Imaging Module for the JCMT Heterodyne Array Receiver Programme (HARP)

J. Leech<sup>1</sup>, S. Withington<sup>1</sup>, G. Yassin<sup>1</sup>,  
H. Smith<sup>1</sup>, B.D. Jackson<sup>2</sup>, J.R. Gao<sup>2</sup>,  
T.M. Klapwijk<sup>3</sup>.

<sup>1</sup> Cavendish Laboratory, University of Cambridge, Madingley Road, Cambridge, UK.

<sup>2</sup>Space Research Organization of the Netherlands, Postbus 800, 9700 AV Groningen, The Netherlands.

<sup>3</sup>Department of Applied Physics (DIMES), The Delft University of Technology, Lorentzweg 1, 2628 CJ Delft, The Netherlands.

## Abstract

The HARP (Heterodyne Array Receiver Programme) B-band camera will incorporate a focal-plane array of 16, 850 micron (325-375 GHz), SIS heterodyne detectors. This receiver has been commissioned for use on the James Clerk Maxwell Telescope in Hawaii. The complete instrument will offer greatly improved spectroscopic mapping speeds ( $> \times 10$ ) of extended objects complementing existing continuum bolometer detectors and planned millimetre-wave aperture synthesis telescopes. We describe key features of the imaging module, and present some early modelling and experimental work. In particular, we describe the LO injection meander line, the constant slot-depth corrugated horns (including 15 GHz scale models), the radial-probe mixers, and various items of work relating to tolerance assessment and uniformity.

## 1 Introduction

As SIS detector technology matures, the performance of submillimetre-wave telescopes equipped with single element detectors is beginning to approach

fundamental limits that are beyond the control of designers. Consequently, there has been much interest in increasing telescope productivity through the use of multi-feed focal-plane arrays [1]. The HARP (Heterodyne Array Receiver Programme) B-band camera, commissioned for operation on the James Clerk Maxwell Telescope, will incorporate a 16 element array of SIS detectors operating in the  $850\ \mu\text{m}$  (325-375GHz) band. The complete instrument will offer at least an order of magnitude improvement in the speed of spectroscopic mapping of astronomical objects.

The imaging module for HARP incorporates easy to machine split-block corrugated horns, fixed tuned radial-probe mixers and a novel local oscillator injection scheme. We present here an overview of the imaging module including the design of the radial-probe mixers, the design of the constant slot-depth corrugated horns, and the design of the LO injection scheme. Some early modelling and experimental work is also described.

## 2 The Imaging Module and LO Injection

The arrangement of the 16 mixers making up the HARP imaging module is shown in Fig. 1. In an array receiver, the aperture phase errors of the horns have to be corrected individually, and in our design each pixel consists of a corrugated horn with an offset parabolic reflector at its aperture [4]. The horn-reflector antenna has the advantage that the losses, and standing waves, associated with polyethylene lenses are avoided, but it has the disadvantage that it is awkward to pack into arrays. Our solution is the two level design illustrated; the depth of focus of the optical system being sufficiently large for the mixers to effectively share the same focal plane. Inevitably the upper deck will truncate the beams of the lower deck to some extent, but our calculations show that, because the beams are highly collimated, this truncation is at low level.

Injecting local oscillator power into each mixer is a significant design problem. Various schemes exist, including waveguide couplers, and a Dammann grating with an interferometer. We studied the Dammann grating extensively in the context of the project, but abandoned this approach due to the bandwidth limitation associated with the multiple images “breathing” with frequency [5]. The LO injection scheme favoured for HARP is a square array

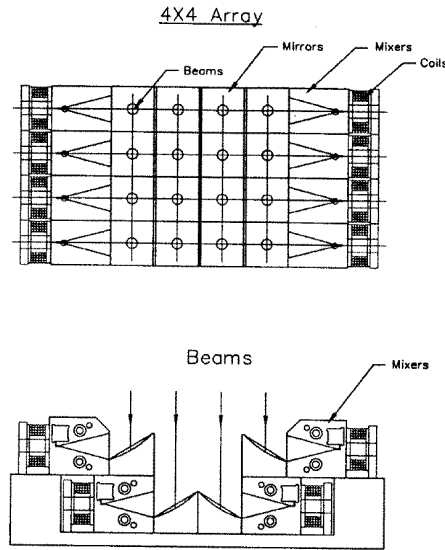


Figure 1: The HARP imaging module.

of Mylar beam splitters. We have called this scheme the “meander line” (Fig. 2). LO power is injected horizontally at a single point and is reflected by a pair of back-to-back parabolic mirrors at the end of each row in such a way that it propagates along the next row. The back-to-back mirrors avoid distortions on folding. The basic operation, which has been verified through the use of multimode Gaussian optics, is quite subtle and involves forming the lowest-order eigenmode of the folded beam guide. Clearly, the power available for each subsequent mixer will be smaller than its previous mixer. The use of -25 dB beam splitters leads to only a 5% power difference between the first and last mixers, which is within the required tolerance. The power coupled to each mixer could be equalised by varying the thickness of each Mylar beam splitter in the array; we may increase the coupling on say the last row.

Work is in progress to model the propagation of the beam through the meander line in more detail. A prototype mount for a single (1x3) row of Mylar beamsplitters has been constructed for experimental investigation (Fig. 3).

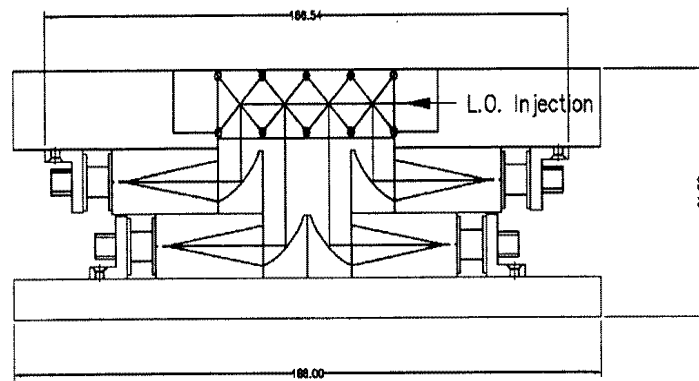


Figure 2: The meander line LO injection above the imaging module.

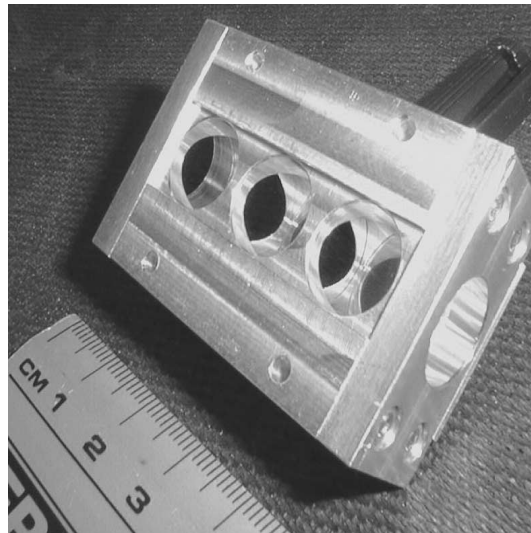


Figure 3: The prototype 1x3 LO injection beamsplitter mount.

### 3 Mixer Block Design

Each corrugated horn is machined directly into two halves of a split aluminium block, which is then coated by a film of sputtered gold. The blocks are easy to machine (electroforming is not required) and very low mass. To aid machining, we have designed a horn that has constant depth slots along the whole of its length, and we have kept the number of slots per wavelength to an absolute minimum (just over one slot and one ridge per half wavelength). The design of this type of horn is a delicate balance between the need for low return loss, low cross polar levels, good beam circularity across the band (325-375 GHz) and ease of reproducibility.

	Scale Model (15 GHz)	Actual (345 GHz)
semi flare angle	15°	15°
no. of grooves	42	42
slot depth	5.97 mm	260 $\mu\text{m}$
slot width*	4.7 mm	204 $\mu\text{m}$
tooth width*	3.3 mm	143 $\mu\text{m}$
start radius of throat	8.15 mm	345 $\mu\text{m}$
length of start taper*	14.6 mm	635 $\mu\text{m}$

Table 1: Details of HARP horn and scale model horn at 15 GHz. Dimensions with an asterisk denote lengths parallel to the symmetry axis of the horn.

We were keen to assess the performance of our constant slot depth horns, and to develop a mode-matching model for tolerance analysis. To this end, we manufactured and tested a 15 GHz scale model on an outside test range (Fig. 4). The horn shows good beam circularity, low cross polarisation (<-27 dB) and low return loss (<-18 dB) over the appropriately scaled HARP bandwidth.

An assessment of the sensitivity to machining tolerances is an important aspect of imaging array production. It is clearly futile to attempt to manufacture 16 horns if the electrical properties of the design are not sufficiently tolerant to the magnitude of the machining errors we expect. Our main concern is detrimental effects of the uncertainties in the depth of slots. As well as a basic machining tolerance of  $\pm 5 \mu\text{m}$ , the depth of the slots is effected by a cyclical error arising in the gear box of the boring head. Fortunately

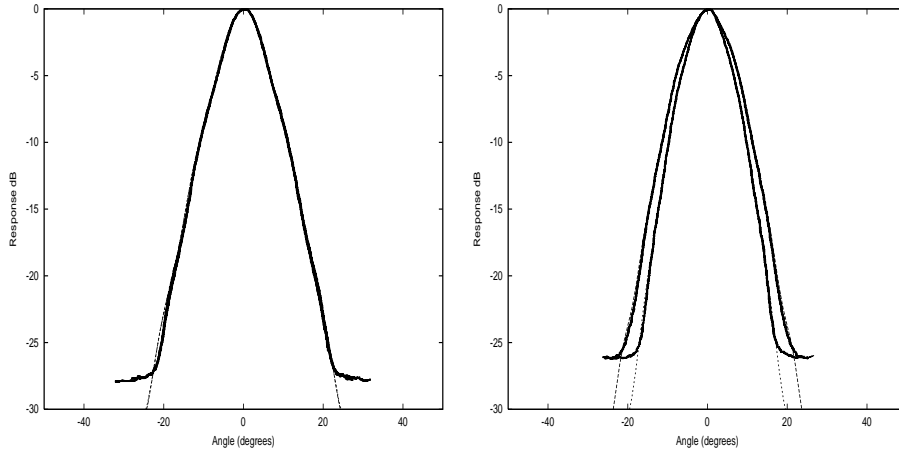


Figure 4: Experimental scale model (solid) and simulated beam patterns (dotted) (E and H plane) for the corrugated horn without parabolic mirror at 13 GHz (left) and 16.5 GHz (right).

this cyclical error is such that the depths of the most electrically important slots near the throat are set to be correct; the depths of the remaining slots are found to vary approximately sinusoidally with an amplitude of  $\pm 12 \mu\text{m}$  and a period which gives around 4 cycles along the entire length of the horn.

Having verified that the mode-matching software confirms the experimental behaviour of the scale model in detail, we were in a position to use the mode-matching software for tolerance analysis. The software model was used to assess the effect of both random and cyclical slot depth machining errors. The design was shown to be robust with respect to the magnitudes of machining tolerances that we have experienced on previous directly machined corrugated horns. The expected return loss and peak cross polar levels for a sample of 5 horns with  $\pm 12 \mu\text{m}$  cyclical slot depth error and a  $\pm 5 \mu\text{m}$  random machining is shown in Figure 5. The horn design is insensitive to the machining errors, indicating our ability to confidently manufacture 16 horns of similar performance.

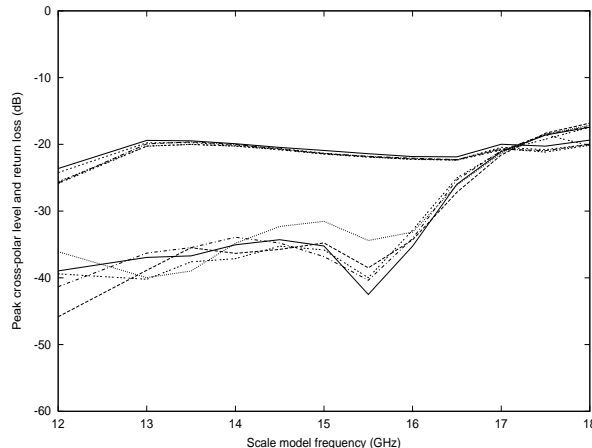


Figure 5: Return loss (upper curves) and peak cross-polar levels (lower curves) simulated for 5 scale model horns (x23 actual size) with cyclical and random slot depth variations as described in the text. HARP bandwidth thus corresponds to 13.8 to 16.2 GHz.

## 4 Mixer Chip Design

Single-sided probe-type SIS mixers [2] have been chosen for use as the individual elements of the HARP array. These give large fixed-tuned bandwidths in full-height waveguide. A schematic diagram of one of the mixer chips shown in Figure 6. The SIS junction is fabricated at the base of a 90 degree radial-probe structure, which has been shown through 5 GHz scale model experiments [3], and previous mixer results, to give a good impedance match to typical SIS junctions. These broadband probes enable mechanical backshort tuners to be avoided greatly reducing the required control complexity in a 16 element array receiver.

The mixer chip is fabricated on a quartz substrate. During manufacture, the RF and IF transmission lines are deposited first, and the earth plane last. This “inverted” geometry is needed to allow the IF earth to be established. The RF tuning is achieved by a stripline end loaded with a radial stub. The chip lies in a  $170 \mu\text{m}$  wide channel and is earthed with a small amount of silver dag applied to a pad, which terminates the earth filter. The earth filter structure consists of 4 quarter wave sections of boxed microstrip with

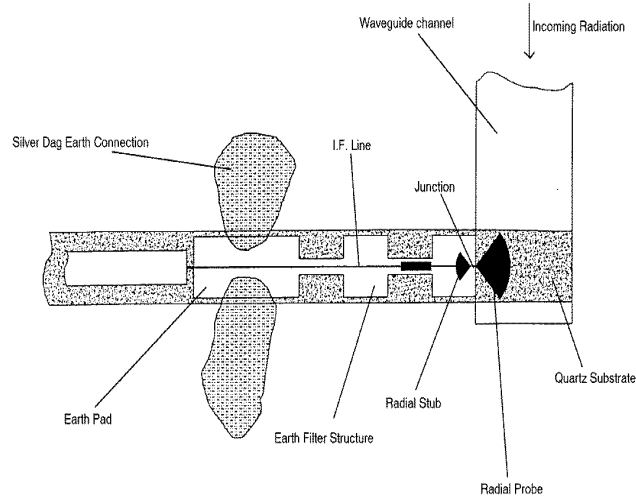
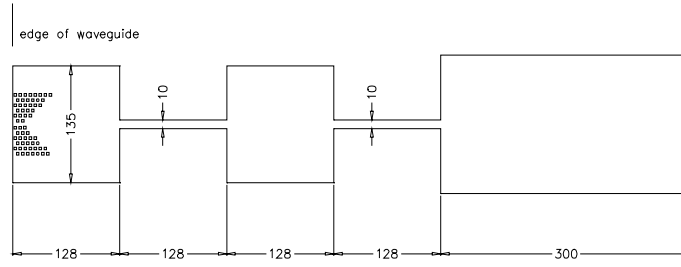


Figure 6: The probe mixer chip in the waveguide channel.

alternating low and high impedance sections. Note that this is not the IF line, it is the earth plane, but nevertheless a filter structure is required to ensure that a good RF earth is established at the edge of the waveguide.

A range of mixer chip designs have been produced for the HARP project. Inspired by broadband radial stubs, a new earth filter design with half elliptical low impedance sections has been produced. Simulations using the full electromagnetic simulation package Sonnet show that the new design is expected to have a 20% larger bandwidth and a better return loss symmetry than previous designs.

Trapped flux can be the cause of many reliability problems when mixers are used on telescopes. When the array consists of 16 separate mixers, the problem has the potential to be acute. To address this issue a new chip design with a matrix of rectangular holes in the superconducting metallisation near the junction has been produced (Fig. 7). This array of holes[6] is expected to prevent the movement of quantised flux vortices in the film, thus preventing any sudden changes in the magnetic environment of the junction



Earth Style; Square, holes, 2nd 10

Figure 7: The metallisation pattern for the anti flux trap earth filter. Note the array of holes in the metallisation near the junction position. The final rectangle is the earth pad which is attached to the mixer block by a small quantity of silver dag.

during operation.

The results of preliminary noise temperature measurements across the band for a mixer featuring an anti flux trapping earth plane filter are presented in Figure 8. The mixer is well tuned with the band centre appearing around 340 - 350 GHz. While further tests on other anti flux trap devices are necessary to evaluate the efficacy of the design, these early results are very promising. The prototype mixer did seem particularly stable and the tests confirm the expectation that the array of holes does not effect the RF performance.

## 5 Conclusion

In this paper we have provided an outline of how the design of the HARP imaging module tackles the principle challenges presented in building state of the art heterodyne array detector for the 850  $\mu\text{m}$  band. Early results indicate the integrity of our design.

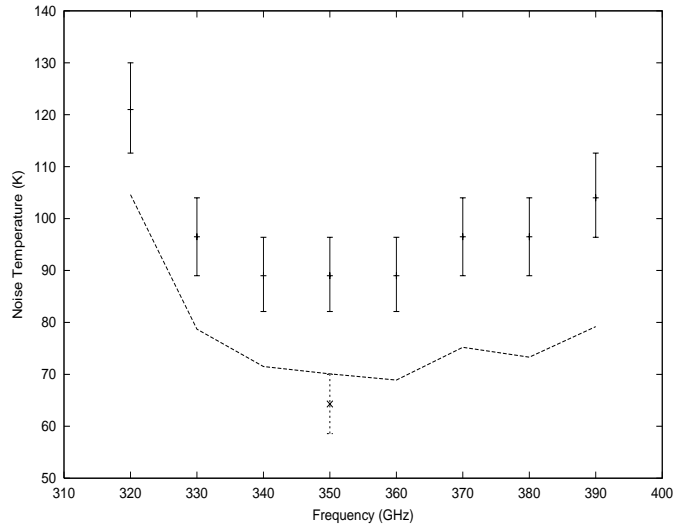


Figure 8: Noise temperatures across the band for a prototype anti flux trap mixer. Upper error bars indicate measured noise temperatures using  $19 \mu\text{m}$  Mylar beamsplitter. Lower curve is expected noise temperatures corrected for the beamsplitter. Lowest error bar ( $\approx 64 \text{ K}$ ) indicates best noise temperature obtained with  $8.5 \mu\text{m}$  ( $\approx 1\%$  loss) beamsplitter (to be used in the final LO injection design) and careful adjustment of LO power. This confirms the form of the corrected curve.

## References

- [1] Astronomical Society of the Pacific Conference Series, Volume 75, "Multi-feed systems for Radio Telescopes," Ed. D.T. Emerson and J.M. Payne.
- [2] S. Withington, G. Yassin, M. Buffey, "Submillimetre-wave Technology for High-Redshift Extragalactic Spectral-Line Astronomy," Proceedings of the Fifth International Workshop on Terahertz Electronics.
- [3] S. Withington, G. Yassin, J. Leech, K. Isaak, "An Accurate Expression for the Input Impedances of One-sided Microstrip Probes in Waveguide," Proceedings of the Tenth International Symposium on Space TeraHertz Technology.
- [4] S. Withington, G. Yassin, M. Buffey, C. Norden, "A Horn-reflector antenna for High Performance Submillimetre-Wave Applications," Proceedings of the Seventh International Symposium on Space TeraHertz Technology.
- [5] J.A. Murphy, C. O'Sullivan, N. Trappe, W. Lanigan, R. Colgan, S. Withington, "Modal analysis of the quasi-optical performance of phase gratings" ,International Journal of Infrared and Millimeter Waves, 1999, Vol.20, No.8, pp.1469-1486.
- [6] E. Dantsker, S.Tanaka and John Clarke " High Tc super conducting quantum interference devices with slots or holes: Low 1/f noise in ambient magnetic fields.", Appl. Phys. Lett. Vol. 70, No. 15, pp2037-2039.

# A Low Noise NbTiN-based 850 GHz SIS Receiver for the Caltech Submillimeter Observatory

J. W. Kooi<sup>1</sup>, J. Kawamura<sup>1</sup>, J. Chen<sup>3</sup>, G. Chattopadhyay<sup>1</sup>, J. R. Pardo<sup>1</sup>, J. Zmuidzinas<sup>1</sup>, T.G. Phillips<sup>1</sup>, B. Bumble<sup>2</sup>, J. Stern<sup>2</sup>, and H.G. LeDuc<sup>2</sup>

<sup>1</sup>California Institute of Technology, MS 320-47, Pasadena, CA 91125

<sup>2</sup>Center for Space Microelectronics Technology/JPL, Pasadena, CA 91108

<sup>3</sup>On leave from the Research Institute of Electrical Communication, Tohoku University, Sendai 980-8577, Japan.

## Abstract

We have developed a niobium titanium nitride (NbTiN) based superconductor-insulator-superconductor (SIS) receiver to cover the 350 micron atmospheric window. This frequency band lies entirely above the energy gap of niobium (700 GHz), a commonly used SIS superconductor. The instrument uses an open structure twin-slot SIS mixer that consists of two Nb/AlN/NbTiN tunnel junctions, NbTiN thin-film microstrip tuning elements, and a NbTiN ground plane. The optical configuration is very similar to the 850 GHz waveguide receiver that was installed at the Caltech Submillimeter Observatory (CSO) in 1997. To minimize front-end loss, we employed reflecting optics and a cooled beamsplitter at 4 K. The instrument has an uncorrected receiver noise temperature of 205K DSB at 800 GHz and 410K DSB at 900 GHz. The degradation in receiver sensitivity with frequency is primarily due to an increase in the mixer conversion loss, which is attributed to the mismatch between the SIS junction and the twin-slot antenna impedance. The overall system performance has been confirmed through its use at the telescope to detect a wealth of new spectroscopic lines.

## 1. Introduction

In 1997 a waveguide receiver<sup>1</sup> covering the 350-micron atmospheric window was deployed at the CSO. It used a novel 1  $\mu\text{m}$  thick Silicon Nitride membrane supporting an all niobium based Superconductor-Insulator-Superconductor (SIS) junction. With an uncorrected receiver sensitivity of  $\sim 500$  K DSB at 810 GHz, it was state of the art at that time. The performance of this receiver was limited however by a large absorption loss in the niobium superconductor films. This loss arises because the mixer is operated above the energy gap of niobium ( $2\Delta = 700$  GHz). In this regime, photons have enough energy to break Cooper pairs in the superconductor films resulting in a large RF loss and poor mixer conversion gain. An alternative to the use of niobium superconducting transmission lines is the use of normal metals such as gold (Au) or Aluminum (Al)<sup>2,3</sup>. However, it is required that any metals employed will have to be compatible with the SIS fabrication process. Even though pure Au and Al conductivity improves by a factor of 5-10 when cooled to 4 K, these metals exhibit a high loss when compared to an ideal

superconductor, such as niobium<sup>7</sup>. Above 800 GHz the loss of Au/Al transmission lines becomes less than that of niobium (~40 % loss per wavelength), but even so the use of a higher bandgap energy superconductor is much preferred.

To minimize loss in front of the waveguide mixer, we designed the optics with mirrors and beamsplitter cooled to 4K where possible. This scheme gave us a total front-end loss of ~1.1 dB, and an overall mixer conversion gain of -12.3 dB at 822 GHz. Of the 12.3 dB conversion loss, about 4dB was due to the actual mixing process, 0.4 dB due to the RF mismatch, and the remaining 6.8 dB due to the niobium film loss! Clearly much was to be gained if the niobium loss could be reduced or even eliminated. And so, even as the 850 GHz waveguide receiver was commissioned at the telescope in 1997, it had become very clear that improved mixer sensitivity would result if a higher bandgap ( $2\Delta$ ) superconductor could be found. Fortunately such a development was underway at JPL in order to facilitate SIS receivers up to 1200 GHz for both ESA/NASA FIRST<sup>4</sup> satellite mission and NASA/SOFIA airborne observatory<sup>5</sup>. At that time we reported<sup>6, 7</sup> on the first RF test results of NbTiN films used in combination with Nb and NbTiN tunnel junctions. Three combinations had been tested up to 650 GHz, namely:

- NbTiN ground plane with Nb wiring and a Nb/Al-O<sub>x</sub>/Nb tunnel junction
- NbTiN ground plane with Nb wiring and a NbTiN/MgO/NbTiN tunnel junction
- NbTiN ground plane with Nb wiring and a Nb/Al-N<sub>x</sub>/NbTiN tunnel junction

The first such combination rendered a receiver noise temperature of 110K at 639 GHz, the second combination resulted in a receiver noise temperature of 250K at 638 GHz, and finally the Nb/Al-N<sub>x</sub>/NbTiN devices yielded a receiver noise temperature of 195K at 588 GHz. These heterodyne measurements, as well as extensive direct detection measurements with a Fourier Transform Spectrometer (FTS), indicated the NbTiN surface loss to be less than 0.1  $\Omega$ /square at 600 GHz. Even the NbTiN/MgO/NbTiN SIS junction results were the best ever recorded and gave credence to the low loss properties of NbTiN.

Though no heterodyne response had been measured above the niobium superconducting gap (700 GHz) at that time, resonances in the dc IV-curves were observed up to 1 THz on certain devices. These as well as many unreported FTS measurements during the course of 1997 yielded valuable information about NbTiN superconducting films and AlN barrier properties. Finally by April 1998 we were ready for another mask design.

## 2. Twin-Slot Mixer Mask Design

Comparative studies of computer simulations and FTS direct detection laboratory measurements provided us with the necessary device properties needed for a new mask design. These properties are summarized in Table I. The layout was designed to maximize the number of possible combinations of Nb, NbTiN, Au, and Al wire & ground planes with AlO<sub>x</sub> and AlN<sub>x</sub> tunnel barriers. AlN<sub>x</sub> being the more compatible barrier for

the NbTiN deposition process<sup>8,9</sup>. The design was done for 550 GHz, 650GHz, 850GHz, and 1050 GHz.

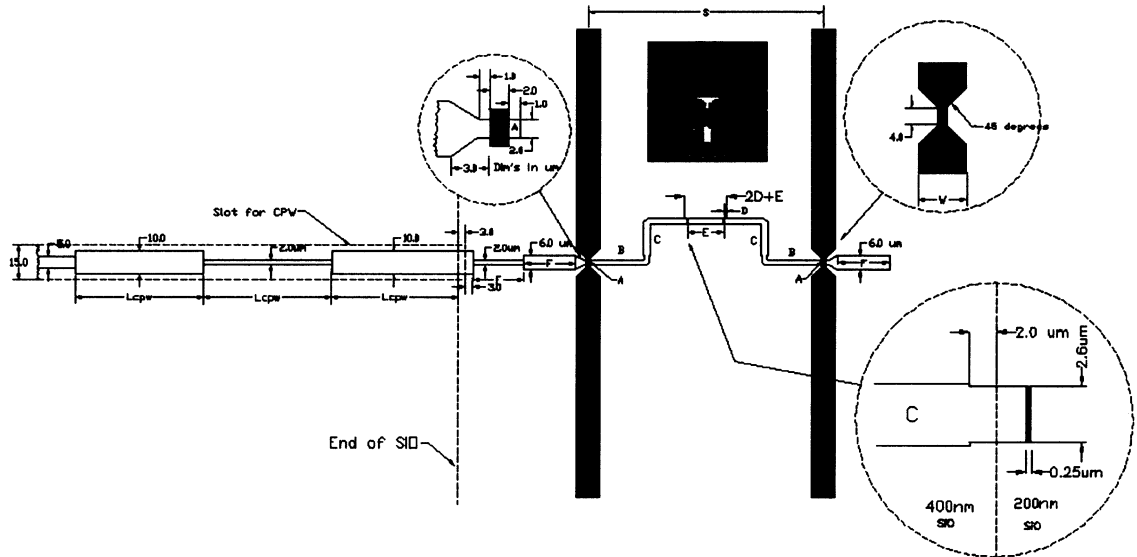


Fig. 1. NbTiN mask design, April 1998.

The three features of the design that are worth noting are the open-ended microstrip line termination of the slot antenna, the CPW IF output and dc bias line, and the introduction of “long” sub-micron e-beam junctions. First, the traditional radial stub termination<sup>11</sup> was replaced by a much lower capacitance  $\lambda/4$  open-ended microstrip line for the purpose of reducing the capacitive load seen at the IF port of the mixer. Second, the IF line was implemented in CPW rather than microstrip for the same reason. The driving motivation for these changes is the eventual need to increase the intermediate (IF) frequency of the mixer from the present 1-2 GHz to 4-8 GHz. This is done in order to better facilitate future extragalactic astronomical observations<sup>4,5</sup>.

RnA/Junction	$20 \Omega\text{-}\mu\text{m}^2$
Junction Area	$0.25 \mu\text{m} \times 2.6 \mu\text{m}$
Wiring Thickness	250 nm
Ground Plane Thickness	300 nm
NbTiN	$\rho = 80 \mu\Omega\text{-cm}$ $\lambda = 230 \text{ nm}$ $T_c = 15.2 \text{ K}$
Nb	$\rho = 5 \mu\Omega\text{-cm}$ $\lambda = 80 \text{ nm}$ $T_c = 9.2 \text{ K}$
Specific Capacitance AlN <sub>x</sub>	$85 \text{ fF}/\mu\text{m}^2$
Specific Capacitance AlO <sub>x</sub>	$85 \text{ fF}/\mu\text{m}^2$

Table I. Device parameters used in the April 1998 mask design.

The results presented in this paper are with a 1-2 GHz IF, however developments are underway to upgrade to a 4-8 GHz bandwidth within the next few years. Thirdly, FTS data seems to indicate the possible effect of kinetic inductance, which is caused by RF currents crowding into the SIS junction<sup>10</sup>. The effect of kinetic inductance can be better understood by considering how the twin-slot mixer<sup>12, 13</sup> tuning circuit works. The twin-slot antennas generate a voltage that is 180 degrees out of phase due to symmetry. Because of this there is a virtual ground in the center of the tuning structure (Fig. 1), and the junction capacitance is cleverly tuned out by the shunt inductance of the microstrip line connecting the two junctions ( $E/2$ ). At the very high frequencies, the tuning inductor ( $E/2$ ) becomes smaller and smaller and any kinetic inductance presented by the SIS junctions becomes proportionally more significant. To circumvent this problem, we introduced “long” e-beam sub-micron junctions in our design. Much effort has gone in making these devices, and as a consequence the fabrication process at JPL has matured considerably in the last few years. The results presented in this paper are produced by “long” sub-micron Nb/ $\text{AlN}_x$ /NbTiN hybrid tunnel junctions with a NbTiN ground plane and wire layer.

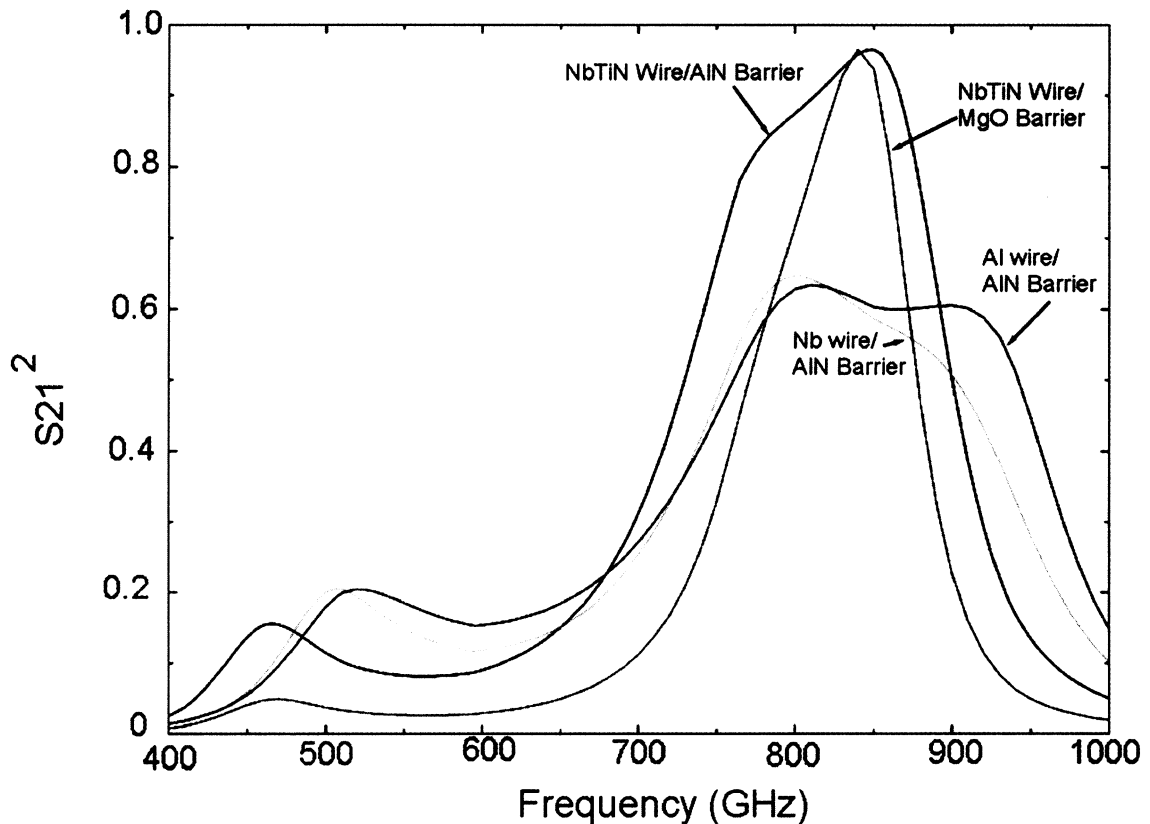


Fig. 2. Circuit Simulations of 4 different style SIS junction and tuning structure configurations. In all cases the ground plane is NbTiN. Design was optimized for 850 GHz.

The details of the fabrication process, the FTS measurement results, and actual device parameters are described in detail in a recent publication by Kawamura <sup>14</sup> *et. al.* The junctions we used for this work have a critical current density of 10 kA/cm<sup>2</sup> and are of reasonably high quality with a sub-gap to R<sub>n</sub> ratio of ~15 (measured at 2 mV). Being a hybrid junction, the gap was expected to be at 4 mV ( $\Delta_{\text{Nb}} + \Delta_{\text{NbTiN}}$ ), however the actual measured gap voltage was about 3.2 mV. The most plausible explanation is that the NbTiN counter electrode in the vicinity of the barrier is of poor quality.

The April 1998 mask incorporates a NbTiN ground-plane and works with 4 different SIS junction configurations (Fig. 2); a NbTiN/AlN<sub>x</sub>/NbTiN tunnel junction with a NbTiN wire layer, which is the mixer under discussion in this paper; a NbTiN/MgO/NbTiN junction with NbTiN wiring; a NbTiN/AlN<sub>x</sub>/NbTiN junction with an Al wire layer, and a NbTiN/AlN<sub>x</sub>/NbTiN junction with an Au wire layer. The specific capacitance of AlO<sub>x</sub> and AlN<sub>x</sub> are very similar, ~ 85 fF/μm<sup>2</sup> for a 10kA/cm<sup>2</sup> current density junction. The specific capacitance of MgO on the other hand is much larger, ~ 145 fF/μm<sup>2</sup> for a 10kA/cm<sup>2</sup> current density device. The latter junction capacitance is much more difficult to tune out, which is evident from Fig. 2. The RF bandwidth of the NbTiN/AlN<sub>x</sub>/NbTiN tunnel junction with NbTiN wire layer & ground plane is about 130 GHz, which agrees well with the measured heterodyne response presented in Fig. 8.

### 3. Cooled Optics

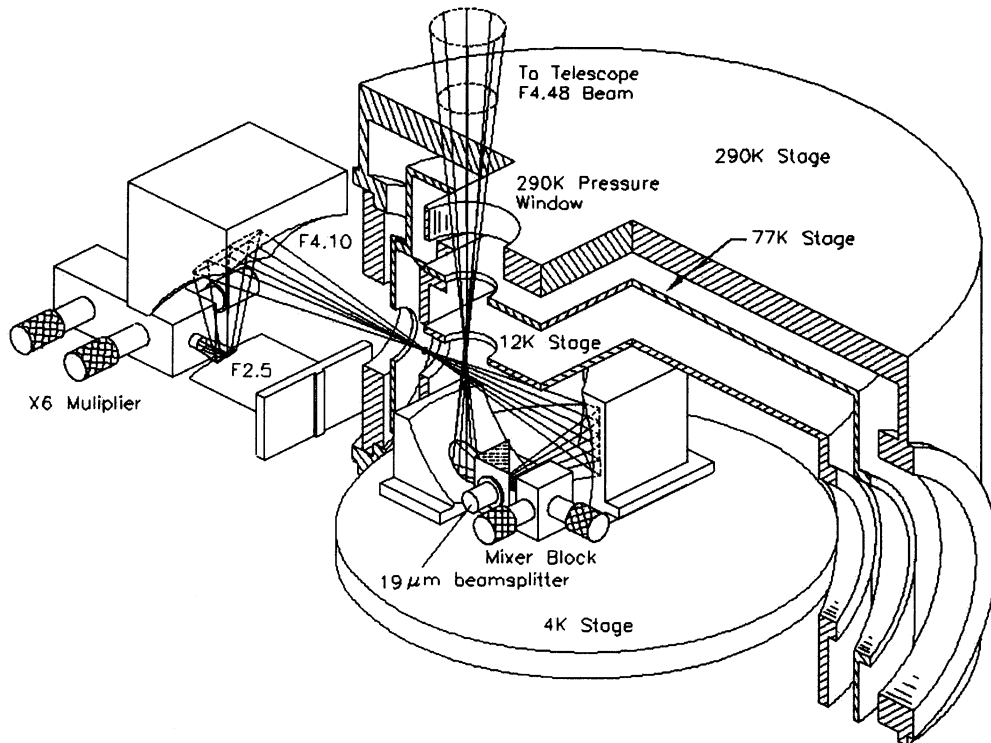


Fig. 3. Isometric view of the cooled optics configuration used in the 850 GHz waveguide receiver. The cryostat is mounted upside down in the Cassegrain focus of the Caltech Submillimeter Observatory.

The noise temperature of a receiver is not only dependent on the conversion gain of the mixer, but also on loss in the front-end optics. In the case of the 850 GHz waveguide receiver<sup>1</sup> we tried to maximize the optics throughput by carefully selecting the IR blocking filters, 300K pressure window, and by eliminating the use of plastic lenses. Furthermore, to minimize the absorption loss contribution from the 19  $\mu\text{m}$  reflective mylar beam splitter, we decided to combine the RF and local oscillator (LO) power on the LHe stage. Fig. 3 shows an isometric view of the optics configuration. The waveguide mixer shown has been replaced with the twin-slot NbTiN SIS mixer under discussion. The infrared and atmospheric pressure windows of the cryostat consist of anti-reflection coated quartz disks.

The twin-slot mixer described by Zmuidzinas<sup>11, 12</sup> *et. al.* is depicted below in Fig. 4. The mixer consists of a twin-slot planar feed antenna connected to a pair of SIS junctions via a microstrip transmission line (Fig. 1). A hyperhemispherical silicon lens and plano-convex teflon lens are used to focus the incident radiation onto the antenna. The silicon lens has a diameter of 12.7 mm (0.500 inches) and has a virtual focus  $\sim 30$  mm behind the planar twin-slot antenna.

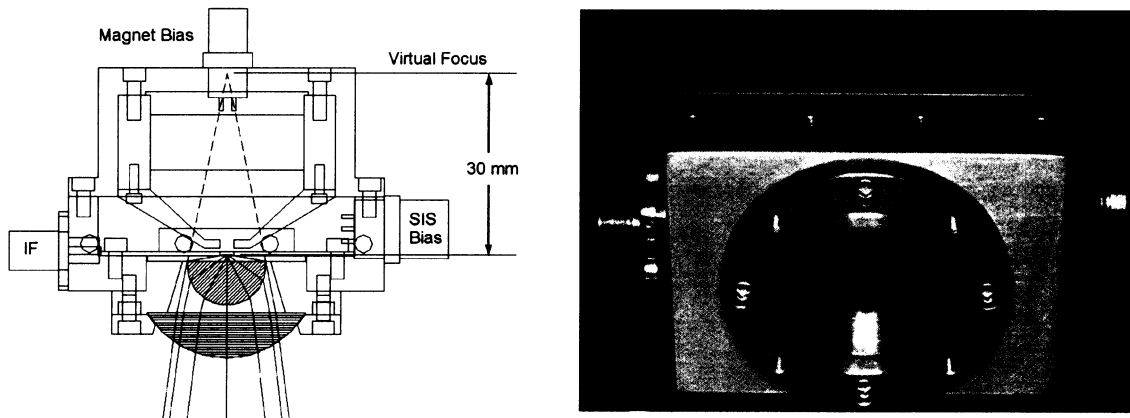


Fig. 4. Optical Configuration of the twin-slot mixer as described by Zmuidzinas *et. al.*

In order to upgrade the niobium based waveguide receiver (Fig. 3) with a NbTiN based twin-slot mixer, and at the same time utilize as much of the existing hardware as possible, two significant changes had to happen. First, the plano-convex teflon lens needed to be removed. And secondly, once this lens was removed, the virtual focus had to be moved much closer to the backside of the hyperhemispherical silicon lens because of the now fast (F/2.5) mixer beam. These changes in effect called for a complete re-design of the twin-slot mixer optics. The reasons for the removal of the plano-convex lens in Fig. 4. can be summarized as follows.

The mixer beam, using reciprocity, has to come to a focus at the F/4.48 Cassegrain focus of the telescope which is located near the 77 K dewar window (Fig. 3). Though this is possible by means of a thick lens, it would introduce unnecessary absorption and reflection loss over the required frequency bandwidth of operation. To complicate matters, the LO injection scheme would have to be changed due to physical constraints

imposed upon by the existing cooled waveguide and telescope optics. Both are critical for proper illumination of the telescope, but are in practice difficult to achieve with a cooled plastic lens.

In 1993 Filipovic *et. al.* published a comprehensive paper<sup>15</sup> on the far-field patterns and Gaussian coupling efficiencies for twin-slot antenna placed on hemispherical lenses with different radii ( $R$ ) and extension length ( $L$ ). In the twin-slot mixer<sup>11-13</sup> the  $L/R$  ratio was 0.291, which is the hyperhemispherical position. This  $L/R$  ratio produces a fast  $F/2.5$  beam at the  $e^{-2}$  power contour, and hence the need for a plano-convex lens to transform the beam to give a smaller divergence angle.

Given the cooled optics<sup>16</sup> and CSO telescope constraints, the optimal beam divergence of the NbTiN mixer turns out to be  $F/4.2$ . This equates to a  $L/R$  ratio of 0.335 and it is this value that has been chosen for the final twin-slot NbTiN mixer optics configuration.

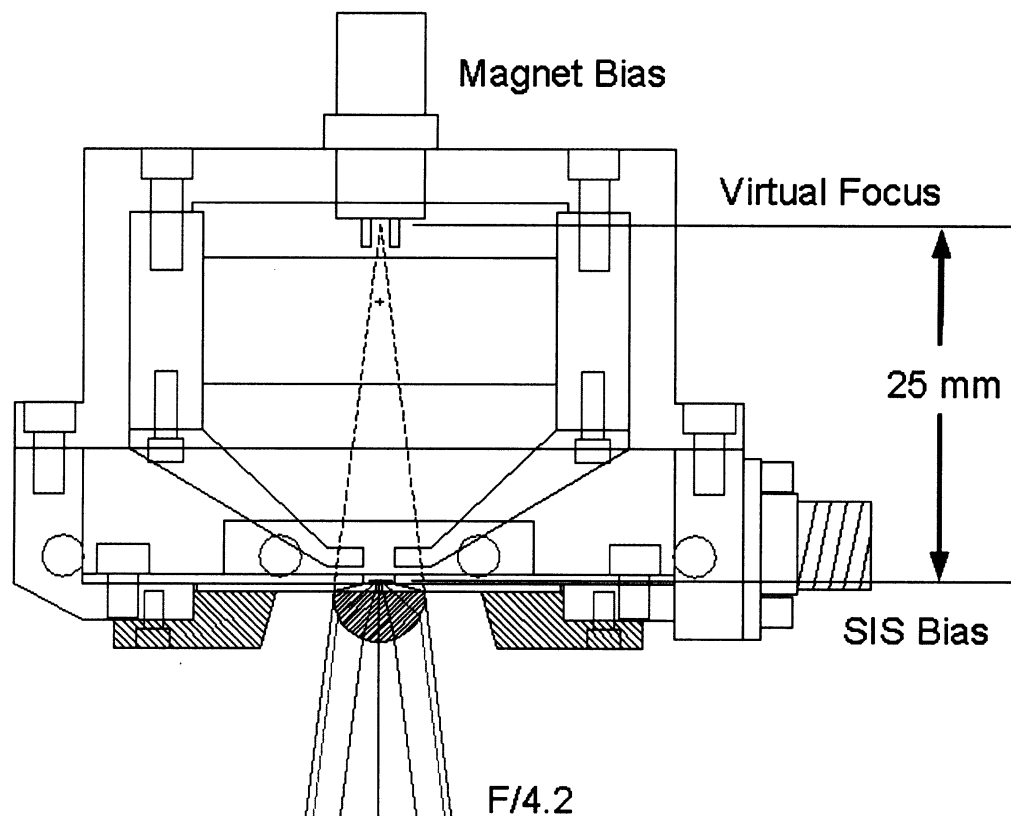


Fig. 5. Modified mixer block with a  $L/R$  ratio of 0.335 and 6.35 mm diameter lens.

In order to satisfy the need for a reduced virtual focus distance, we chose the hemispherical radius to be 3.2 mm (0.125 inches). This value of  $R$  was deemed to be the smallest practical size possible, especially when the criticality of the SIS chip alignment to the extended hemispherical lens is considered. The maximum theoretical gaussian coupling efficiency in the case of  $L/R = 0.335$  turns out to be slightly worse (5%) than with the original  $L/R = 0.291$ .

This tradeoff was considered acceptable in light of the fact that the successful cooled optics scheme of the 850 GHz waveguide mixer could now be re-implemented for the twin-slot NbTiN mixer.



Fig. 6. Photograph of final optical configuration.

### 3. Receiver Performance

The heterodyne response at 800 and 900 GHz as measured at the Caltech Submillimeter Observatory (CSO) is shown in Fig. 7. To fully cover the 780-920 GHz atmospheric window two multipliers/LO chains are in use, both from RPG Physics<sup>17</sup>. The 780 – 845 GHz band is covered with a more traditional X2 –X3 multiplier, while the 845 to 920 GHz band uses an X2 - X2 - X3 multiplication scheme. The first stage is a high efficiency tunerless doubler, while the remaining doubler and tripler stages employ two tuners each.

The Y-factor response in Fig. 7 has been included for reference sake. Notice how with increasing frequency the width of the photon step decreases. This is indeed expected for

frequencies above 800 GHz ( $v_{\text{gap}} = 800$  GHz) because the photon step from the negative bias side partially cancels the photon step from the positive bias side. The optimal bias condition across the entire frequency band appears to be at  $\sim 2.1$  mV with a LO pump current of  $I_c/3$  ( $40 \mu\text{A}$ ).  $I_c$  is defined as the critical current of the junction. The measured leakage current in the junction<sup>22</sup> at 2 mV is  $7.4 \mu\text{A}$ , which corresponds to an  $R_{\text{subgap}}$  to  $R_n$  ratio of 15.

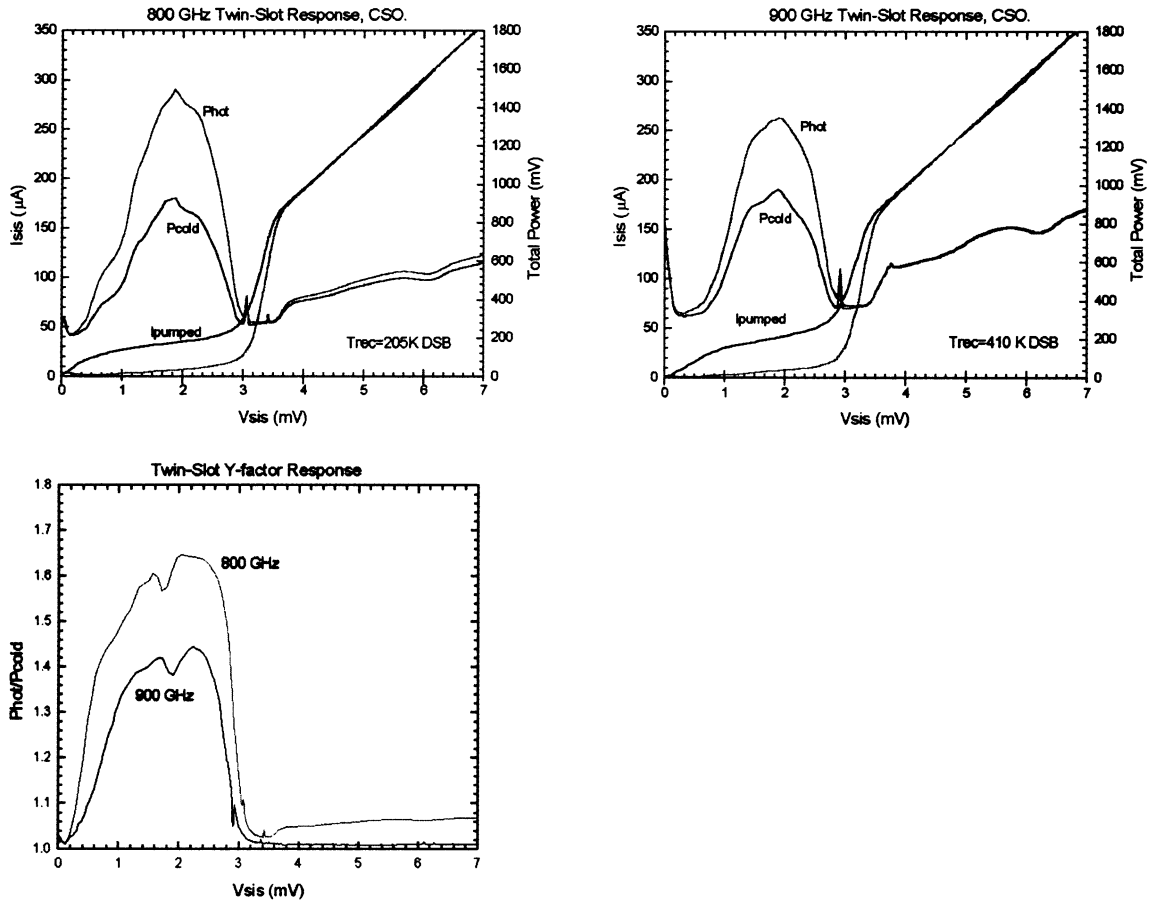


Fig. 7 Receiver and Y-factor response at 800 and 900 GHz.

The frequency response of the newly installed NbTiN twin-slot open structure receiver is shown in Fig. 8. The improvement over the in 1997 installed all-niobium waveguide receiver is primarily due to a decrease in the NbTiN wire layer and ground plane transmission line loss (5 dB). Note that the front-end optics and IF configurations are identical between the two systems. In the text all noise temperatures have been calculated using the Callan-Welton formula<sup>18, 19</sup>. The receiver and mixer properties are summarized in Table II. The optics loss is derived from the intersecting line technique, described by Blundell<sup>20</sup>, Ke, and Feldman<sup>21</sup> *et al.*  $t_{\text{RF}} * G_{\text{mix}}$  is the total mixer conversion gain which includes the loss in the optics in front of the mixer. This quantity should be

compared against the 850 GHz waveguide results<sup>1</sup>, which equated to  $-12.3$  dB at 822 GHz.

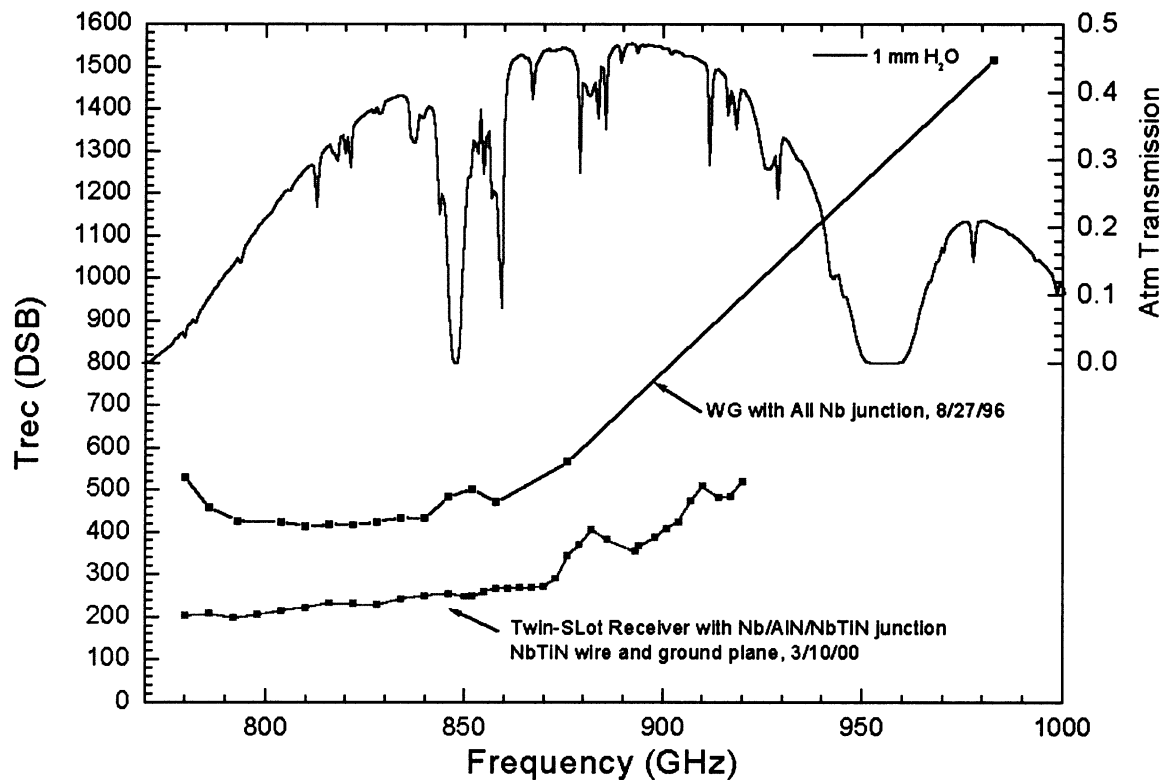


Fig. 8 Receiver sensitivity of the all niobium waveguide, and recently upgraded twin-slot NbTiN open structure mixers.

	800 GHz	900 GHz
$T_{rec}$ (K) DSB	205	410
$T_{optics}$ (K)	70	100
$T_{IF}$ (K)	22	41
$t_{RF} * G_{mix}$ (dB)	-7.2	-9.9
$T_{mix}$ (K) SSB	43	53
$h\nu/k$ (K)	38	43
$T_{LNA}$ (K)	$4.2 + 0.3K$ (measured)	$4.2 + 0.3K$ (measured)
$\Gamma_{Beam Splitter}$ (%)	14	18
$Z_{pumped}$ ( $\Omega$ )	129	80.5
$R_n$ ( $\Omega$ )	17.8	17.8
$Z_{if}$ ( $\Omega$ )	90	90

Table II. Measured and calculated receiver parameters.

$T_{\text{Mix}}$  in Table II is the single sideband mixer noise temperature (referred to the input):  $(T_{\text{rec}} - T_{\text{optics}} - T_{\text{IF}}) * (t_{\text{RF}} * G_{\text{mix}})$ .  $T_{\text{IF}}$  is the total IF noise contribution, while  $T_{\text{LNA}}$  is the actual measured noise temperature of the balanced low noise amplifier directly preceding the mixer.  $Z_{\text{pumped}}$  is obtained from the LO pumped IV curve in Fig. 7, and is needed to take reflection loss in the shot noise calculations into account. The IF matching network presents a  $90 \Omega$  impedance to output of the mixer.

## 5. Astronomical Observations

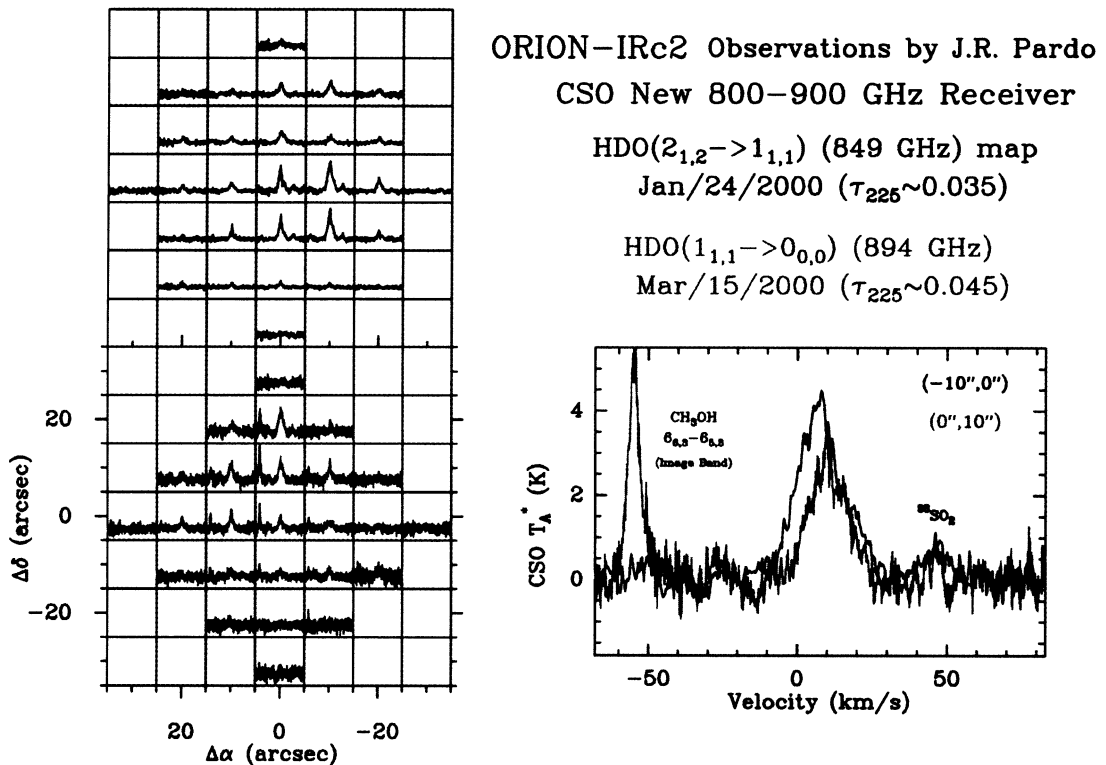


Fig. 9. First Detection of HDO( $2_{1,2} \rightarrow 1_{1,1}$ ) and HDO( $1_{1,1} \rightarrow 0_{0,0}$ ) in Orion-Irc2.

Among the first observations carried out with the new receiver we performed  $10''$  resolution maps of two contiguous HDO transitions  $J_{K_a, K_b} = 2_{1,2} \rightarrow 1_{1,1}$  at 848.9619 GHz and  $J_{K_a, K_b} = 1_{1,1} \rightarrow 0_{0,0}$  at 893.6387 GHz (shown in Fig. 9), and HCN  $J=10 \rightarrow 9$  at 885.9708 GHz (not shown here) towards Orion IRc2. The weather conditions during the observing runs (January and March 2000) were excellent and provided average zenith transmissions above Mauna Kea as high as  $\sim 38.5\%$  (849 GHz) and  $\sim 42\%$  (886 GHz). This resulted on system temperatures at 849 GHz as low as 1700 K at the elevation of the source (70 deg) at the beginning of the observations on Jan/24/2000. Integration time for each point was 3 minutes. The observations show a quite compact source for both HDO lines  $\sim 45''$ . The data are currently being modeled using the same LVG model previously used by Cernicharo<sup>23</sup> et al. (1999) for their analysis of the emission of H<sub>2</sub>O at 183.31 and

325.15 GHz (this last line observed also at the CSO) towards the same source. These two H<sub>2</sub>O lines have a partial maser nature in Orion IRc2, so the newly observed (thermal) HDO lines will probably put better constraints on the density, temperature and H<sub>2</sub>O abundance estimates of the emitting regions. The results of this analysis will be published later.

## 6. Conclusion

A 850 GHz niobium titanium nitride (NbTiN) based twin-slot SIS mixer has been developed and installed at the Caltech Submillimeter Observatory (CSO) on Mauna Kea, Hawaii. The open structure mixer replaces the all niobium based waveguide mixer that was installed as part of a larger receiver system at the observatory in 1997. The 5 dB conversion gain improvement of the new NbTiN mixer is attributed to the use of a higher energy gap superconducting material. The local oscillator (LO) injecting is done at the 4K stage using a set of elliptical mirrors and a beam splitter cooled to 4K. The optics of the twin-slot mixer has been modified to fit with the cooled optics. The upgraded receiver has an uncorrected receiver noise temperature of 205K DSB at 800 GHz and 410K DSB at 900 GHz.

## 7. Acknowledgments

We wish to thank Martin Saur and Clency Lee-Yow at Custom Microwave for their suggestions and tremendous efforts in fabricating the mirrors on a very short notice, and Marti Gould for his incredible overnight machining skills. This work was supported in part by NASA/JPL and its Center for Space Microelectronics Technology, by NASA Grant Nos. NAG5-4890, NAGW-107, and NAG2-1068, by the NASA/USRA SOFIA instrument development program, and by the Caltech Submillimeter Observatory (NSF Grant No. AST-9615025). J. Chen likes to acknowledge the support from the Japanese Ministry of Education, Science, Sports, and Culture.

## References

1. J.W. Kooi, J. Pety, B. Bumble, C.K. Walker, H.G. LeDuc, P.L. Schaffer, and T.G. Phillips, "A 850 GHz Waveguide Receiver employing a Niobium SIS junction fabricated on a 1- $\mu$ m Si<sub>3</sub>N<sub>4</sub> Membrane", *IEEE transactions on Microwave Theory and Techniques*, Vol. 46, No. 2, pp. 151-161, February 1998.
2. M. Bin, M. C. Gaidis, J. Zmuidzinas, T. G. Phillips and H. G. Leduc, "Quasi-Optical SIS mixers with Normal-Metal Tuning Structures", *IEEE Transactions on Applied Superconductivity*, Vol. 7 (2), Part 3, pp 3584-3588, Jun. 1997.
3. P. Dieleman, T.M. Klapwijk, J.R. Gao, and H. van de Stadt, "Analysis of Nb superconductor-insulator-superconductor tunnel junctions with Al striplines for THz radiation detection", *IEEE Trans. Applied Superconductivity* 7, pp 2566-2569, 1997.
4. T.G. Phillips, J. Zmuidzinas, W.D. Langer, C. Lawrence, and J. Pearson, "The FIRST mission", "#41.21, *Bull. American Astronomy Society*" 191, Dec 1997.

5. J. Zmuidzinas, G. Blake, J. Keene, T.G. Phillips, N. Erickson, P. Goldsmith, A. Harris, M. Morris, W. Langer, H. Leduc, and W. McGrath, "A Submillimeter/far-IR heterodyne receiver for SOFIA, "#09.06, *Bull. American Astronomy Society*", 191, Dec 1997.
6. J.W. Kooi, J.A. Stern, G. Chattopadhyah, H.G. LeDuc, B.Bumble, and J. Zmuidzinas, "Low-Loss NbTiN Films for THz SIS Mixer Tuning Circuits", *Int. J. IR and MM Waves*, Vol 19, No. 3, 1998
7. J. Zmuidzinas, J. Kooi, J. Kawamura, G. Chattopadhyah, B.Bumble, H.G. LeDuc, and J.A. Stern, "Development of SIS Mixers for 1 THz", *SPIE; International Society for Optical Engineering Proceedings*, Kona, Hawaii, 1998.
8. B. Bumble, H.G. LeDuc, and J. Stern, "Fabrication of Nb/AlN<sub>x</sub>/NbTiN for SIS mixer applications above 1 THz", *Ninth International Symposium on Space Terahertz Technology*, Pasadena, California, March 1998.
9. J. Stern, B. Bumble, H.G. LeDuc, J.W. Kooi, and J. Zmuidzinas, "Fabrication and DC-characterization of NbTiN based SIS mixers for the use between 600 and 1200 GHz", *Ninth International Symposium on Space Terahertz Technology*, Pasadena, California, March 1998.
10. J. Zmuidzinas, private communication
11. J. Zmuidzinas and H.G LeDuc, "Quasi-optical slot antenna SIS mixers, *IEEE Trans. Microwaves Theory and Techniques*, vol. 40, No. 9, pp. 1797-1804, Sept. 1992.
12. J. Zmuidzinas, H.G. Leduc, J.A. Stern, and S.R. Cypher, "Two-junction tuning circuits for submillimeter SIS mixers," *IEEE Transactions on Microwave Theory and Techniques*, Vol. MTT-42, No. 4, pp 698-706, Apr 1994.
13. M. Gaidis, H. G. LeDuc, M. Bin, D. Miller, J. A. Stern and J. Zmuidzinas, "Characterization of low noise quasi-optical SIS mixers for the Submillimeter Band", *IEEE transactions on Microwave Theory and Techniques*, Vol. 44, No. 7, pp. 1130-1139, July 1996.
14. J. Kawamura, J. Chen, D. Miller, J. Kooi, J. Zmuidzinas, B.Bumble, H.G. LeDuc, and J.A. Stern, "Low-Noise Submillimeter-wave NbTiN superconducting tunnel junction mixers", *Applied Physics Letters*, Vol 75, Number 25, December 1999.
15. D.F. Filipovic, S.S. Gearhart, and G. M. Rebeiz, "Double-Slot Antennas on Extended Hemispherical and Elliptical Silicon Dielectric Lenses", *IEEE Transactions on Microwave Theory and Techniques*, Oct. 1993.
16. Custom Microwave Inc., 940 Boston Avenue, Lonmont, Co 80501.
17. RPG Physics, Birkenmaarstrasse 10, 53340 Meckenheim, Germany.
18. H.B Callen and T.A. Welton, "Irreversibility and generalized noise," *Phys. Rev.*, vol 83, no. 1, pp 34-40, July 1951.
19. A.R. Kerr, M.J. Feldman, and S.K. Pan, "Receiver noise temperature, the quantum noise limit, and the role of zero-point fluctuations," "NRAO, Charlottesville, VA, Electron. Div., Internal Rep. 304, Sept. 1996.
20. R. Blundell, R.E. Miller, and K.H. Gundlach, "Understanding noise in SIS receivers," *Int. J. Infrared and Millimeter Waves*, vol. 13, no. 1, pp 3-26, 1992.
21. Q. Ke, and M.J. Feldman, "A technique for noise measurements of SIS receivers," *IEEE transactions on Microwave Theory and Techniques*, Vol. 42, pp. 752-755, April 1994.
22. P. Dieleman, H.G. Bukkems, T.M. Klapwijk, M. Schicke, and K.H. Gundlach, "Observation of Andreev reflection enhanced shot noise," *Phys. Rev Letters* 79, pp. 3486-3489, 1997.
23. J. Cernicharo, J. R. Pardo, E. Gonzalez-Alfonso, E. Serabyn, T. G. Phillips, D. Benford and D. Mehringer, "Physical conditions in shocked regions of Orion from ground-based observations of H<sub>2</sub>O" *Astrophysical Journal*, 520, L131-L134, 1999.

# QUASI-OPTICAL TERAHERTZ SIS MIXER

**A.M. Baryshev<sup>1,2</sup>, B.D. Jackson<sup>1</sup>, G. de Lange<sup>1</sup>, S.V. Shitov<sup>2</sup>, N. Iosad<sup>3</sup>, J.R. Gao<sup>1</sup>,  
T.M. Klapwijk<sup>3</sup>**

<sup>1</sup>SRON-Groningen, Groningen, The Netherlands

<sup>2</sup>Institute of Radio Engineering and Electronics RAS, Moscow, Russia

<sup>3</sup>DIMES, Delft University of Technology, Delft, The Netherlands

## ABSTRACT

The performance of quasi-optical (QO) SIS mixers designed for operation around 1 THz is evaluated. Mixers incorporating Si elliptical lens with either double slot-line or double dipole antennas with back reflectors have been fabricated and measured. Nb/Al-AlO<sub>x</sub>/Nb superconductor-insulator-superconductor (SIS) tunnel junctions are integrated with a NbTiN-SiO<sub>2</sub>-Al microstrip circuit to tune out the junction's geometrical capacitance and to match the antenna impedance to the junction over a wide frequency range.

The direct response, of the mixer measured by means of a Michelson Fourier transform spectrometer (FTS), is presented showing the mixer's ~30% instantaneous bandwidth. This bandwidth appears to be limited by the material properties of the NbTiN ground plane. Noise temperatures of 245 K @ 850 GHz, 310 K @ 980 GHz and 400 K @ 1020 GHz are presented. This is a two-fold improvement over best previously reported results for frequencies around 1 THz.

A far-field antenna beam pattern of the antenna-lens combination is measured at 900 GHz. The 1-st order side lobe level is -(16-18) dB and total power in the cross-polar beam is 0.3 % of the power in the co-polar beam.

## INTRODUCTION

Heterodyne receivers incorporating Nb/Al-AlO<sub>x</sub>/Nb SIS junctions are known to be extremely sensitive in the sub-mm wave band. Noise temperatures of receivers operating below 680 GHz and using fully superconducting Nb tuning structures are only a few times greater than the quantum limit [1,2]. Above 680 GHz (so-called gap frequency), the microstrip lines based on Nb exhibit increased rf losses.

Alternative, non-superconducting metals microstrip have been used to push the operating frequency of SIS receivers above the gap frequency of Nb. In particular, a mixer based on Al microstrip lines has shown high sensitivity up to 1.1 THz [3,4]. The rf loss in

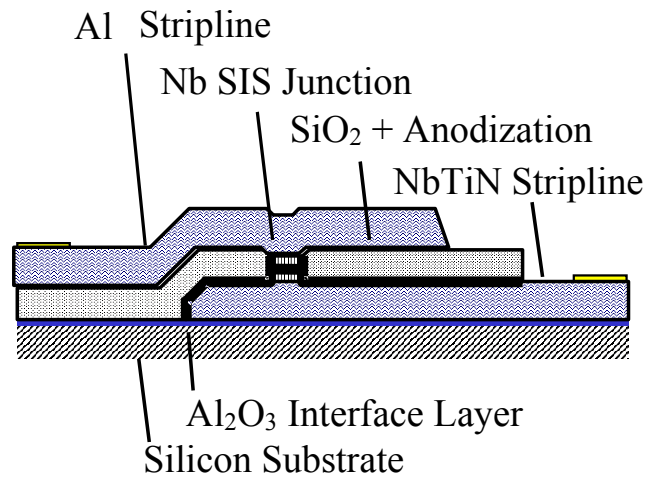


Fig. 1 Cross-section of a Nb SIS mixers with NbTiN/SiO<sub>2</sub>/Al stripline on a Si wafer.

such a microstrip line does not strongly depend on frequency, however, it is higher than in a superconductor below its gap frequency.

Other superconducting materials with higher critical temperature  $T_c$  (and therefore higher gap frequencies) have also been used as a microstrip wiring material. The most promising results have been obtained with NbTiN ( $T_c \approx 15$  K) at frequencies as high as 800 GHz [5]. The gap frequency for bulk NbTiN material is around 1.15 THz and good mixer performance is expected to extend up to this limit. In this paper we present SIS mixers based on a combination of a NbTiN ground plane, Al top wiring layer, and Nb/Al-AIO<sub>x</sub>/Nb SIS junctions.

Waveguide (WG) mixers are commonly used in the mm-wave band. However, as frequency increases, the size of the waveguide decreases and production becomes more difficult. The planar antenna lens combination has been introduced as an alternative technological solution for high frequencies [6]. The main problem for this quasi-optical (QO) configuration is a concern about the receiver beam quality. Thus, this property of the QO mixer will also be addressed in this paper — the measured beam patterns for the double slot line antenna (DSA) on a silicon elliptical lens are presented.

## RECEIVER LAYOUT

The receiver chip cross-section is shown in fig. 1. The substrate material is high resistivity silicon. The NbTiN ground plane is deposited at room temperature on a thin Al<sub>2</sub>O<sub>3</sub> buffer layer. The Nb/Al-AIO<sub>x</sub>/Nb SIS junctions and the SiO<sub>2</sub> insulator layer are fabricated using standard technology [7]. The junction area is 1  $\mu\text{m}^2$  and the current density is about 8 kA/cm<sup>2</sup>. The normal state resistance  $R_n$  and the quality factor ( $R_j/R_n$ ) of the junction is about 30  $\Omega$  and more than 20 respectively. The top wiring is a sputtered Al film. Aluminum has been chosen as the top electrode material instead of NbTiN for

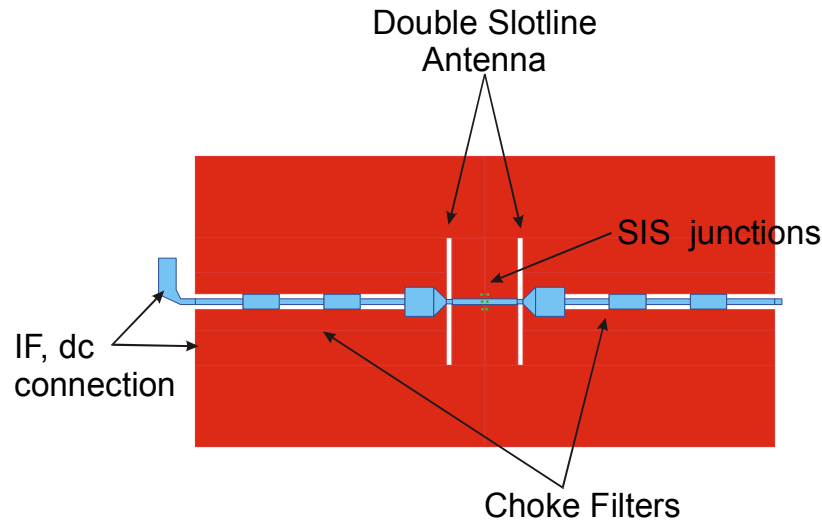


Fig. 2 Receiver chip layout: (slot-line antenna). Ground plane is red.

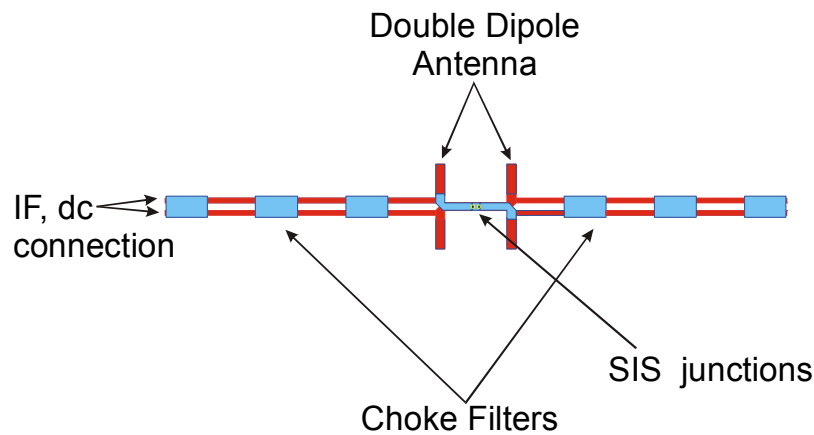


Fig. 3 Receiver chip layout: (double dipole antenna). Ground plane is red.

several reasons. The first reason is to avoid the heating of the Nb SIS junction which is observed in a full NbTiN/Nb-SIS/NbTiN combination due to Andreev reflection at the Nb/NbTiN interface [8]. The second reason is to improve on the stability of the magnetic field across the junction by removing the SQUID loop. Finally, this allows the frequency dependence of the rf properties of the NbTiN ground plane to be studied, due to relatively frequency independent rf properties of the Al top wiring.

The layout of the center part of the chip is shown in fig. 2 for the DSA and in fig. 3 for the double dipole antenna (DDA). Two SIS junctions are used in both designs. The rf signal couples in anti-phase to the junctions, forming a virtual ground in the interconnecting tuner made from microstrip line. This twin-junction tuning circuit was proposed in [9,10]. The antenna impedance is matched to the junction+tuner impedance by means of a quarter-wave microstrip line transformer.



Fig. 4 Antenna-lens combination.

In the DSA design, the combined choke filters are used to reflect the rf power coupled in the direction of the dc/IF leads. The low impedance sections are made of microstrip line and the high impedance sections are made of coplanar waveguide lines. This produces a large impedance ratio, which is also independent of material losses. A series dc resistance of  $\sim 0.2 \Omega$  is expected in the Al top wiring. The calculated central frequency and bandwidth for this design is 950 GHz and 250 GHz respectively. Three tuner lengths and three junction sizes were included in the mask design. This compensates for the potential spread in device parameters due to fabrication tolerances.

In the DDA design, additional measures were taken to ensure that rf currents flow through the NbTiN ground plane. The DDA is formed entirely in ground plane to make it electrically symmetrical. Only the quarter-wave transformer and the junction tuner are made using the Al top wiring. Furthermore, different antenna and tuner sizes were used to cover the 800-950 GHz and 950-1100 GHz ranges.

The antenna lens combination of the quasi-optical receiver is schematically shown in fig. 4. The receiver chip is  $2 \times 2 \times 0.3 \text{ mm}^3$ . Two antennas of the same design are placed on each chip, with a  $250 \mu\text{m}$  offset from the chip center, to increase the device yield. The receiver chip is mounted on the back surface of an elliptical Si lens. The diameter of the lens is 10 mm. A Stycast<sup>TM</sup> antireflection coating with a central frequency of 1 THz is applied to the front surface of the lens and the antenna is placed at the focal point of elliptical surface. A back reflector is used for the DDA -  $20 \mu\text{m}$  thick Si covered on one side by a Nb film. This back reflector is fixed to the mixer chip surface by means of vacuum oil. The DSA is used without a back reflector.

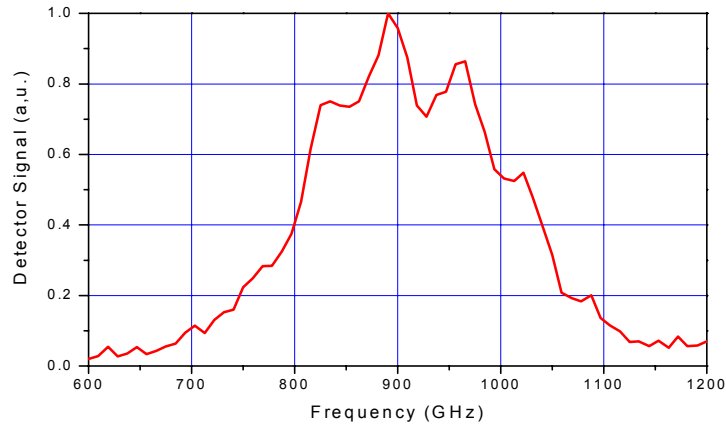


Fig. 5 Typical FTS response of double slot line antenna mixer.

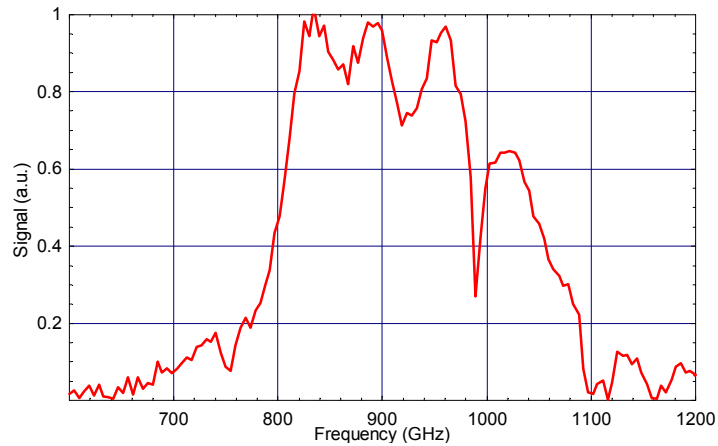


Fig. 6 Typical FTS response of double dipole antenna mixer.

## DIRECT RESPONSE MEASUREMENT RESULTS AND DISCUSSION

The direct response spectra for DSA and DDA samples measured with an evacuated Michelson FTS are shown in fig. 5 and fig. 6, respectively. This data is measured with the critical current suppressed by an external magnetic field to avoid Josephson direct detection that can change the response significantly in this frequency band. The 3 dB bandwidth for both the DSA and the DDA designs is about 250 GHz. The measurements in both figures are shown in the same relative scale. The 50 GHz ripple seen in all measurements is due to the transmission of the Michelson interferometer, and is not seen in heterodyne measurements.

All measurements show a decrease in detected power at frequency above 1 THz. This decrease is independent of the tuner length, and may be attributed to increased surface losses in the NbTiN ground plane. The rf quality of NbTiN film sputtered on the Si

substrate appears to be worse than expected from measured critical temperature,  $T_c = 14.3$  K. A significant improvement may be expected if a MgO substrate is used for NbTiN film deposition.

## NOISE TEMPERATURE MEASUREMENT RESULTS AND DISCUSSION

Noise temperature measurements are performed using a standard Y-factor method. Blackbody radiators at 80 K and 300 K temperatures and the Raleigh-Jeans relation were used to express the equivalent noise power of the source. No vacuum setup was used during heterodyne measurements.

The copper mixer block was mounted on the cold plate of a vacuum LHe cryostat. No additional lenses or mirrors are used to direct the receiver beam out of the cryostat. A thin  $15\ \mu\text{m}$  Kapton<sup>TM</sup> vacuum window is used. Two far-infrared radiation filters (at 80 K and 4.5 K) are made from 1 mm Zitex<sup>TM</sup> G104. The local oscillator power was injected using a Mylar<sup>TM</sup> beam splitter of 15 or  $6\ \mu\text{m}$  thickness. A L-band (1.2-1.7 GHz) amplifier with a circulator, followed by room temperature amplifiers, is used in the receiver IF chain. A narrow pass-band ( $\Delta f = 85$  MHz) filter followed by a power meter is used to analyze the receiver performance. A lower He bath temperature of 2 K is realized by decreasing the bath pressure to  $\sim 15$  mBar. Two backward wave oscillators are used as local oscillators.

The measured IF response vs. SIS junction bias voltage is presented in fig. 7 for the DSA receiver. Traces of Josephson noise are present in the response because of either a small difference in the junction areas, or slightly asymmetric biasing of the junctions. The two junctions do not form a SQUID-like loop because one layer of the tuning structure is not superconducting. This results in improved mixer stability with respect to magnetic field variations. The mixer can be operated over 1 mV bias voltage span.

The receiver noise temperatures of the DSA mixer measured at different LO frequencies are presented in fig. 8. Data is presented for a 2 K bath temperature. The rise in the receiver noise temperature at higher frequencies can be explained by additional rf loss in NbTiN layer of junction tuning structures. The same tendency is observed in the mixer direct response. The noise temperatures of about 340 K (uncorrected for losses in  $15\ \mu\text{m}$  thick beam splitter) have been measured for the same receiver in the 840-920 GHz range at 4.2 K He bath temperatures.

Only preliminary sensitivity results are available for the DDA mixer. A receiver noise temperature of 600 K is measured with a  $15\ \mu\text{m}$  Mylar<sup>TM</sup> beam splitter at a 4.5 K bath temperature, which can be corrected for LO insertion loss to 400 K.

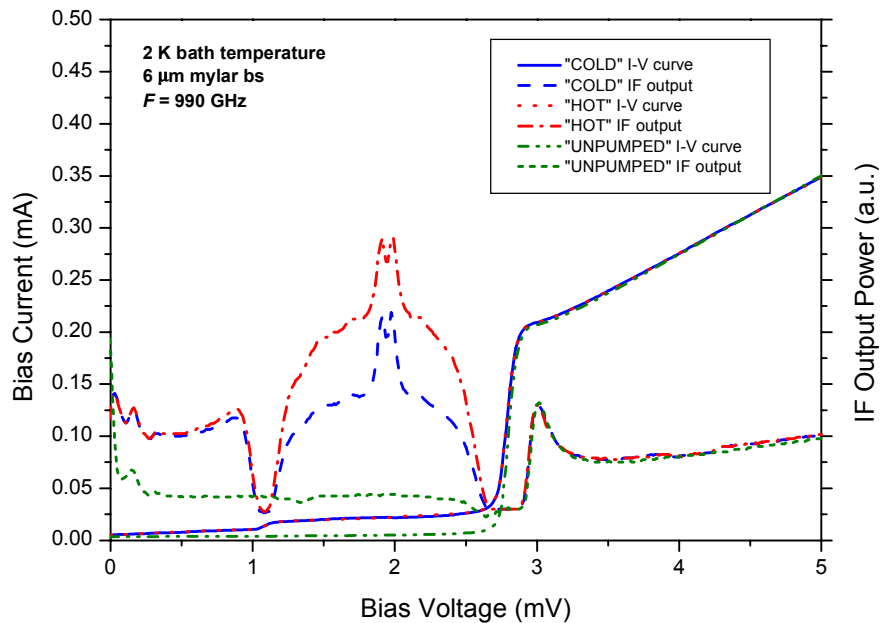


Fig. 7 Receiver Noise temperature for the double slot line antenna mixer at 2 K bath temperature. The noise temperature is 300 K @ 990 GHz, not corrected for beam splitter losses.

#### ANTENNA BEAM PATTERN MEASUREMENT RESULTS AND DISCUSSION

A 2-axis rotational setup is used for the antenna beam pattern measurements. In this setup, the dewar is rotated about two perpendicular axes with the lens-antenna combination placed at the center of rotation. The measured beam pattern is thus independent of the antenna beam pattern of the test source.

Both the cross- and co-polar far-field antenna beam patterns are measured for the DSA receiver at 900 GHz. Results are shown in fig. 9 and 10. The change in pumping level of the SIS mixer is used as a measure of the received power. The co-polar radiation pattern has a good main-lobe symmetry and the first order side-lobe level of  $-16$ - $18$  dB, which is expected theoretically. The  $F/\# \cong 15$  is estimated from the  $-11$  dB taper. The fraction of the power contained in the main-lobe is 83% of total power. The cross-polar radiation pattern has peak power of  $-26$  dB relative to the co-polar pattern. The total power in the cross-polar pattern is only 0.3% of the power in the main-lobe of the co-polar beam.

#### CONCLUSIONS

Quasi-optical mixers, employing a novel microstrip line material combination of NbTiN and Al, were developed and tested around 1 THz. The DSA receiver demonstrates a two-fold improvement of the sensitivity over previously reported mixer results at these frequencies. Noise temperatures of 245 K @ 850 GHz, 310 K @ 980 GHz and

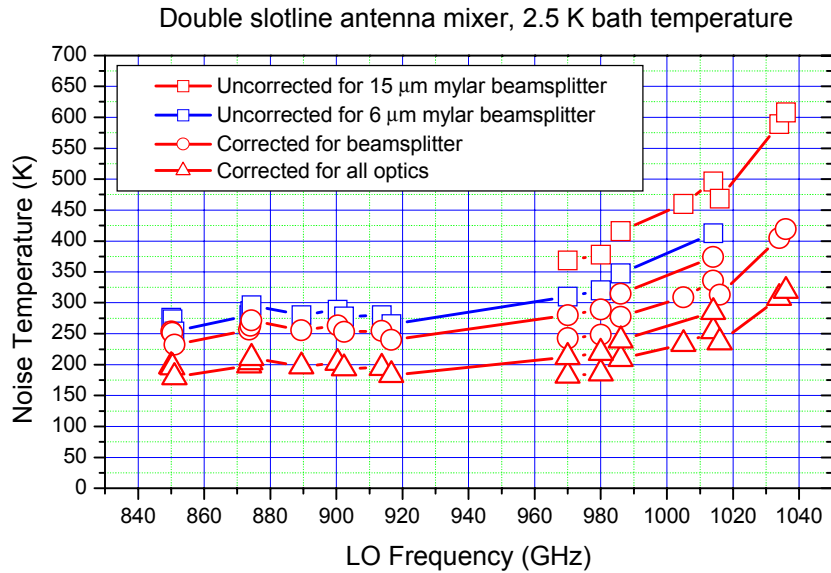


Fig. 8 Receiver Noise temperature for double slot line antenna mixer at 2.5 K bath temperature.

400 K @ 1020 GHz are obtained and a 30% relative bandwidth is demonstrated. Good main antenna beam pattern quality and low level cross-polar response is experimentally demonstrated. This demonstrates that THz quasi-optical mixers are well suited for use in astronomical receivers.

#### ACKNOWLEDGEMENTS

The authors would like to thank M. Eggens, L. de Jong, W. Laauwen, D. Nguyen, and C. Peters for their technical assistance and H. van de Stadt, N. Whyborn, and J. Zmuidzinas for helpful discussions. This work is supported in part by the Nederlandse Organisatie voor Wetenschappelijk Onderzoek (NWO) through the Stichting voor Technische Wetenschappen (STW), by the RFBR project 00-02-16270, the INTAS project 97-1712 and the ISTC project 1199.

## REFERENCES

- [1] J.W. Kooi, M.Chan, B. Bumble, H.G. LeDuc, P. Schaffer, and T.G. Phillips, *Int. J. IR and MM Waves* **16**, 2049 (1995).
- [2] A.Karpov, J. Blondel, P. Pasturel, and K.H. Gundlach, *IEEE Trans. Appl. Supercon.* **7**, 1073 (1997)
- [3] H. van de Stadt, A. Baryshev, P. Dieleman, Th. De Graauw, T.M. Klapwijk, S. Kovtonyuk, G. de Lange, I. Lapitskaya, J. Mees, R.A. Panhuyzen, G. Procopenko, and H. Schaeffer, in *Proc of the 6<sup>th</sup> Int. Symp. On Space THz Technol., CIT, PC*, 66 (1995)
- [4] M. Bin, M.C. Gaidis, J. Zmuidzinas, T.G. Phillips, and H.G. LeDuc, *Appl. Phys. Lett.* **68**, 1714 (1996).
- [5] J. Kawamura, D. Miller, J. Chen, J. Zmuidzinas, B. Bumble, H.G. LeDuc, and J.A. Stern, *App. Phys. Lett.* **76**, 2119 (2000).
- [6] A. Scalare, *Int. J. IR and MM Waves* **10**, 1339 (1989).
- [7] J.R. Gao, S. Kovtonyuk, J.B.M. Jegers, P. Dieleman, T.M. Klapwijk, and H. van de Stadt, in *Prac. Of the 7<sup>th</sup> Int. Symp on Space THz Technol., CIT, PC*, 538 (1996).
- [8] B. Leone, B.D. Jackson, J.R. Gao, and T.M. Klapwijk, *Appl. Phys. Lett.* **76**, 780 (2000).
- [9] V.Yu. Belitsky, S.W. Jacobsson, L.V. Filippenko, S.A. Kovtonjuk, V.P. Koshelets, E.L. Kollberg, *Proc. 4th Space Terahertz Technology Conference*, p.538, March 30 - April 1, Los Angeles, USA.,(1993)
- [10] M.C. Gaidis, H.G. Leduc, Mei Bin, D. Miller, J.A. Stern, and J. Zmuidzinas, *IEEE Transactions of Microwave Theory and Techniques*, p. 1130-1139, (1996)

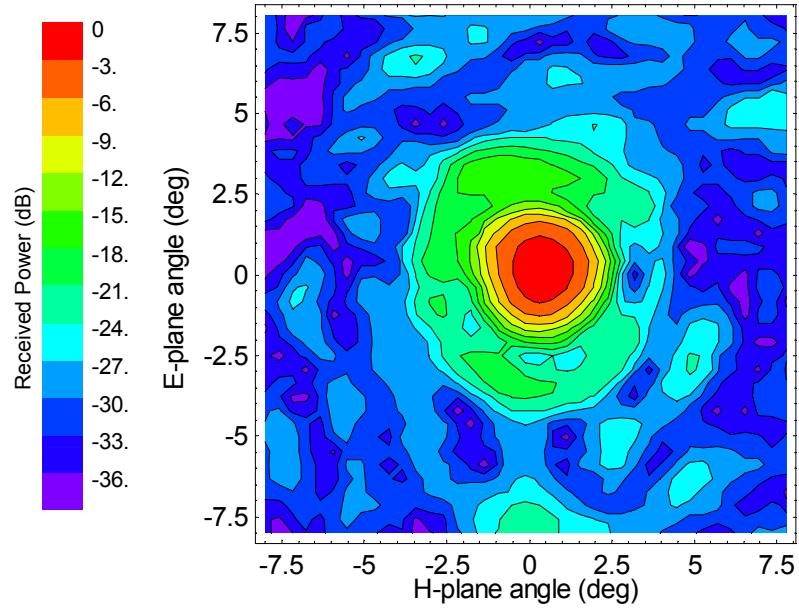


Fig. 9 Main-polarization antenna beam pattern of the double slot line antenna at 900 GHz.

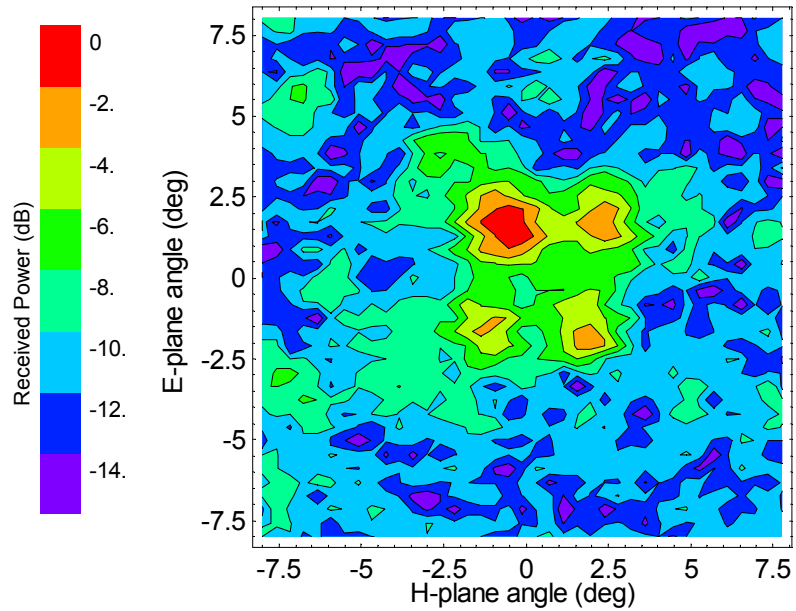


Fig. 10 Cross-polarization antenna beam pattern of the double slot line antenna at 900 GHz. 0-dB power level corresponds to  $-26$  dB power in fig. 9.

# State of the Art of Two-Terminal Devices as Millimeter- and Submillimeter-Wave Sources

Heribert Eisele and George I. Haddad

Solid-State Electronics Laboratory  
Department of Electrical Engineering & Computer Science  
The University of Michigan  
Ann Arbor, Michigan 48109-2122

## ABSTRACT

Devices from three major groups of two-terminal devices, *i.e.*, transit-time diodes, transferred-electron devices, and quantum-well devices, have been employed successfully to generate RF power at frequencies above 200 GHz. At frequencies up to 300 GHz, Si IMPATT diodes yielded the highest RF power levels from any fundamental solid-state source, *e.g.*, 50 mW at 245 GHz. However, the RF power of more than 1 mW from InP Gunn devices around 315 GHz is the highest from any such fundamental source above 300 GHz. GaAs TUNNETT diodes operating as efficient self-oscillating frequency multipliers generated RF power levels of more than 10 mW at 202 GHz. GaAs IMPATT diodes, *e.g.*, yielded 2 mW at 232 GHz. The highest oscillation frequency of 714 GHz was reported from an InAs/AlSb RTD with an RF output power of 0.3  $\mu$ W, whereas GaAs/AlAs superlattice electronic devices yielded 0.2  $\mu$ W at 224 GHz. This paper reviews the power generation capabilities and basic properties of these two-terminal devices as fundamental RF sources. It compares them directly at the RF power level, but also in terms of RF power per unit area as a figure of merit.

## 1. INTRODUCTION

Systems for rapidly emerging applications at submillimeter-wave frequencies such as upper atmospheric imagery, remote sensing, array receivers in radio astronomy, high-resolution near-object analysis, and ultra wide bandwidth intersatellite communications require reliable and compact RF sources with low dc power consumption as one of their key components. RF power generation at high millimeter-wave frequencies was already demonstrated with various types of solid-state devices [1] thus making them good candidates for sources at submillimeter-wave frequencies. The practical application of “classical,” but also more recent principles in device physics [2]–[4] resulted in major advances in device performance, which have also been enabled by epitaxial materials of superior properties or quality as well as much improved processing technologies. Amplifiers with three-terminal devices reach higher and higher frequencies [5]–[9], and improvements in their RF output power [10] as well as their increasing use in systems applications are being reported up to millimeter-wave frequencies. Nonetheless, there have been a few practical demonstrations of fundamental oscillators with three-terminal devices above 100 GHz, and, in addition, only low RF power levels of much less than 1 mW were

reported [11], [12]. This paper gives an overview of the basic properties of different two-terminal devices for continuous-wave (CW) RF power generation at submillimeter-wave frequencies and mainly focuses on devices that in the laboratory already yielded RF power at frequencies above 200 GHz.

## 2. RTDS AND OTHER QUANTUM-WELL DEVICES

Resonant tunneling through discrete energy levels of a so-called quantum well was first demonstrated in 1974 [4]. However, only after major advances in growth techniques, such as molecular beam epitaxy (MBE) and metalorganic chemical vapor deposition (MOCVD), in the 1980s were device structures suitable for oscillators grown and evaluated. As can be seen from Fig. 1, the highest oscillation frequency of any fundamental solid-state RF source were reported from InAs/AlSb resonant tunneling diodes (RTDs) [13], [14]. The dc-to-RF conversion efficiencies, however, are below 1% at millimeter-wave frequencies and the RF power levels of, *e.g.*, 3  $\mu$ W at 360 GHz and 0.3  $\mu$ W at 712 GHz [14] are low, which severely limits the use of RTDs in systems applications.

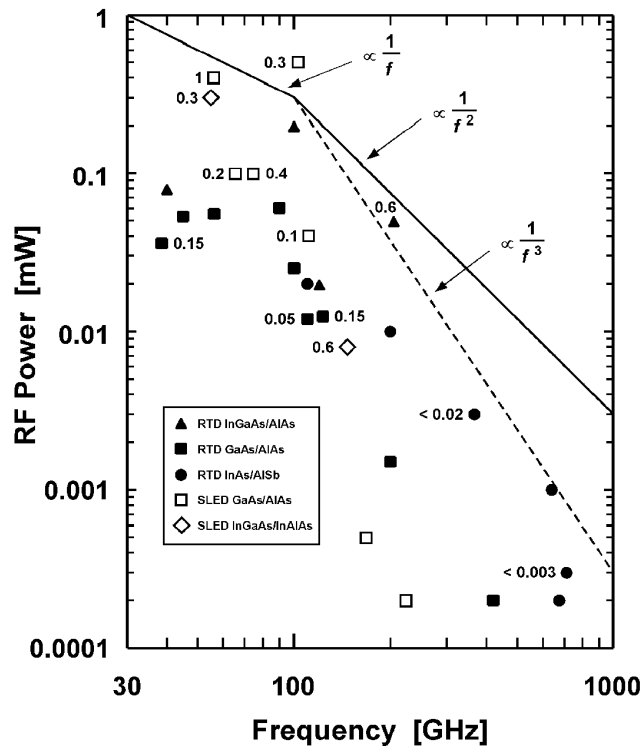


**Fig. 1.** Published state-of-the art results from RTDs and SLEDs in the 30–1000 GHz frequency range. Numbers next to the symbols denote dc-to-RF conversion efficiencies in percent, where applicable.

More recently, superlattice electronic devices (SLEDs) were demonstrated as millimeter-wave oscillators [15]–[18], and the results are included in Fig. 1. The devices were typically not mounted in a resonant cavity, but they were in quasi-planar structures and were contacted with different ground-signal or ground-signal-ground (GSG) probes for *V*-band (50–75 GHz) or *W*-band (75–110 GHz) [16]–[17]. Exceptions are the quasi-planar circuits in a WR-15/WR-6 waveguide combination [15] and in a WR-6 waveguide as shown in Fig. 2 [18]. As an example, Fig. 2 also illustrates the setup with a GSG probe for *W*-band [17]. RF power levels (and corresponding dc-to-RF conversion efficiencies) of 0.4 mW (1%) were reported at the fundamental frequency of 56 GHz and 40  $\mu$ W (0.1%), at the second-harmonic frequency of 112 GHz from the quasi-planar circuit configuration in a waveguide [15]. With the GSG probe and a spectrum analyzer, an RF power of 0.5 mW (0.3%) was determined at 103 GHz [17]. The length of the active region ranges approximately from 0.44  $\mu$ m to 0.64  $\mu$ m in these GaAs/AlAs SLEDs. Therefore, the higher oscillation frequency of 103 GHz is attributed to much narrower barriers of the quantum wells, which are only two monolayers of AlAs thick and cause a larger miniband width of 120 meV [17]. At a similar length of the active region, an InGaAs/InAlAs SLED generated 80  $\mu$ W (0.6%) at the higher oscillation frequency of 147 GHz [18]. Recorded spectra of these SLEDs in free-running oscillators, however, are not as clean as, *e.g.*, those of Gunn devices in free-running oscillators, but are quite narrow-band for a nonresonant circuit or for low quality factors  $Q$ .

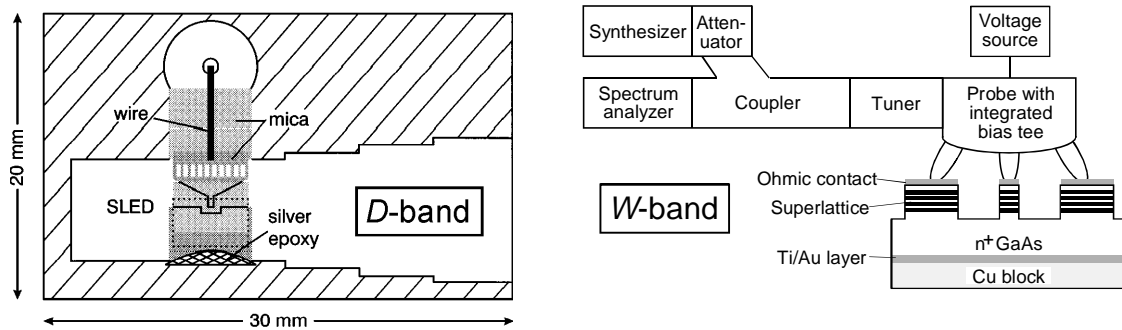


**Fig. 2.** Experimental setup for evaluation of SLEDs at *W*-band and *D*-band frequencies, respectively. After E. Schomburg *et al.* [17], [18].

Up to *D*-band (110–170 GHz) frequencies, RF power levels from SLEDs are higher than those from RTDs of the same material system, whereas dc-to-RF conversion efficiencies are comparable. They are still much lower than the RF power levels from impact avalanche transit-time (IMPATT) and tunnel injection transit-time (TUNNETT) diodes as well as Gunn devices at the same frequencies. These RF power levels  $P_{RF}$  were measured with two-terminal devices of quite different device areas  $A$ . Therefore, the RF power density  $\Phi_{RF} (= P_{RF}/A)$  provides a better comparison of the power generating capabilities of various two-terminal devices and should be considered analogous to the performance

comparisons quoted as RF power per gate length for three-terminal devices, such as field-effect transistors (FETs) or high electron mobility transistors (HEMTs). Fig. 3 shows  $\Phi_{\text{RF}}$  as derived from published state-of-the-art results and device areas in the 30–1000 GHz frequency range for device types that, so far, have yielded measurable RF power levels above 200 GHz. As a result of high bias current densities and high dc-to-RF conversion efficiencies,  $\Phi_{\text{RF}}$  is by far the highest in Si and GaAs IMPATT diodes and exceeds that of RTDs, but also SLEDs, up to *D*-band (110–170 GHz) frequencies by typically more than two orders of magnitude. In addition,  $\Phi_{\text{RF}}$  of GaAs TUNNETT diodes and Gunn devices exceeds that of RTDs and SLEDs up to the highest oscillation frequencies as well.  $\Phi_{\text{RF}}$  of SLEDs from the GaAs/AlAs material system is only higher than that of RTDs from the same material system, but, quite importantly, SLEDs are not associated with the same severe restrictions [1], [19] that bias instabilities impose on the device areas and, consequently, the RF power generation capabilities of RTDs. Therefore, higher RF power levels can be expected from SLEDs with larger areas in appropriate millimeter-wave circuits that match the resulting lower device impedance levels to the RF load. Furthermore, the experimental result at 103 GHz [17] indicates the potential of reaching higher oscillation frequencies with GaAs/AlAs SLEDs than with GaAs Gunn devices.

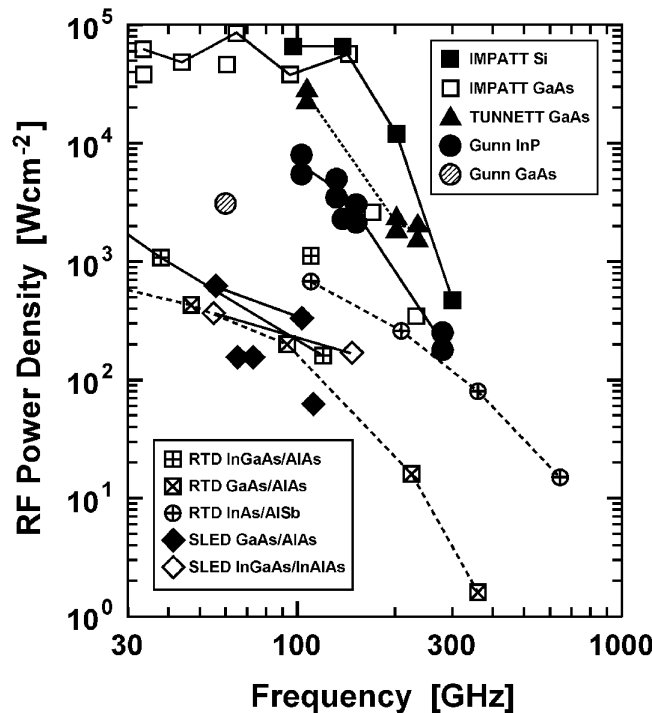


**Fig. 3.** RF power densities  $\Phi_{\text{RF}}$  in two-terminal devices as derived from published state-of-the-art results. Due to uncertainties in device areas, ranges are given for  $\Phi_{\text{RF}}$  of InP Gunn devices and GaAs TUNNETT diodes at particular frequencies. Lines between data points at different frequencies are only as a guide to the eye.

### 3. TRANSIT-TIME DIODES

Si IMPATT diodes were the first semiconductor devices to generate RF power above 300 GHz. As shown in Fig. 4 (and in conjunction with Fig. 1 and Fig. 5), they yielded the highest RF power levels from any solid-state fundamental RF source up to 300 GHz. Exemplary RF power levels (and corresponding dc-to-RF conversion efficiencies) of 50 mW (1.3%) at 202 GHz [20]; 44 mW (1.2%) at 214 GHz [20]; 50 mW (<2%) at 217 GHz [21]; [22], 50 mW (<1%) at 245 GHz [22]; 12 mW (<0.5%) at 255 GHz [22]; 7.5 mW (0.35%) at 285 GHz [23]; 1.2 mW (<0.05%) at 301 GHz [20]; and 0.2 mW at 361 GHz [23] were measured at very high operating junction temperatures of typically more than 300 °C with waveguide circuits at room temperature [21]. Higher RF power levels of, *e.g.*, 4.5 mW (0.13%) at 295 GHz and 2.2 mW (0.047%) at 412 GHz, but also higher oscillation frequencies of up to 430 GHz were attained by cooling the heat sink of the diode and the waveguide circuit to 77 K (liquid nitrogen) [24].

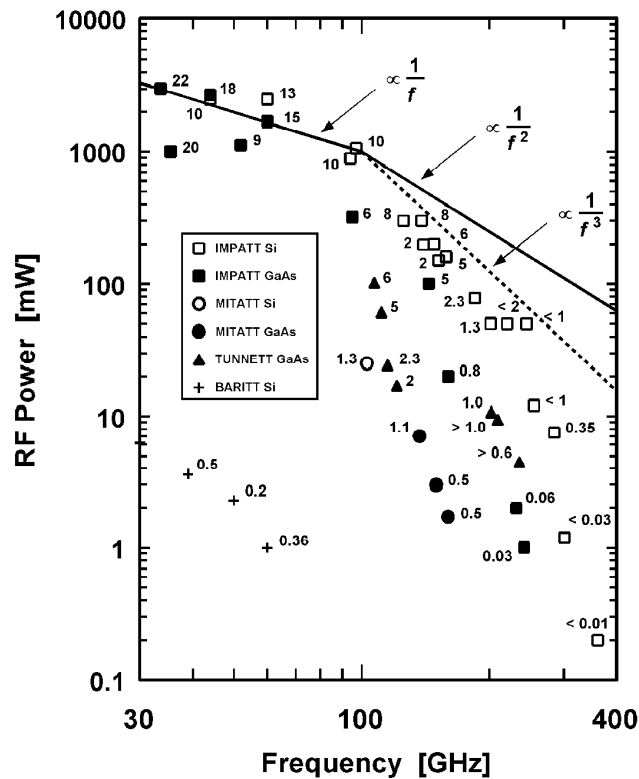


**Fig. 4.** Published state-of-the-art results from Si and GaAs transit-time diodes under CW operation in the frequency range of 30–400 GHz. Numbers next to the symbols denote dc-to-RF conversion efficiencies in percent.

Impact ionization as the carrier generation mechanism in IMPATT diodes is a major contributor to the noise of free-running oscillators compared to, *e.g.*, the smaller contri-

bution from mainly thermal noise in the domain formation process of Gunn devices [1], [2]. Therefore, IMPATT diodes are generally considered quite noisy, although techniques are known on how to reduce noise contributions from impact ionization at the price of typically lower dc-to-RF conversion efficiencies [1], [2]. The noise properties of IMPATT diodes restrict their use as local oscillator (LO) sources to either receiver applications where the highest sensitivity is not of primary concern or sensitive low-noise receivers in which well-balanced Schottky diodes as subharmonically pumped mixers cancel out the noise from the LO [25].

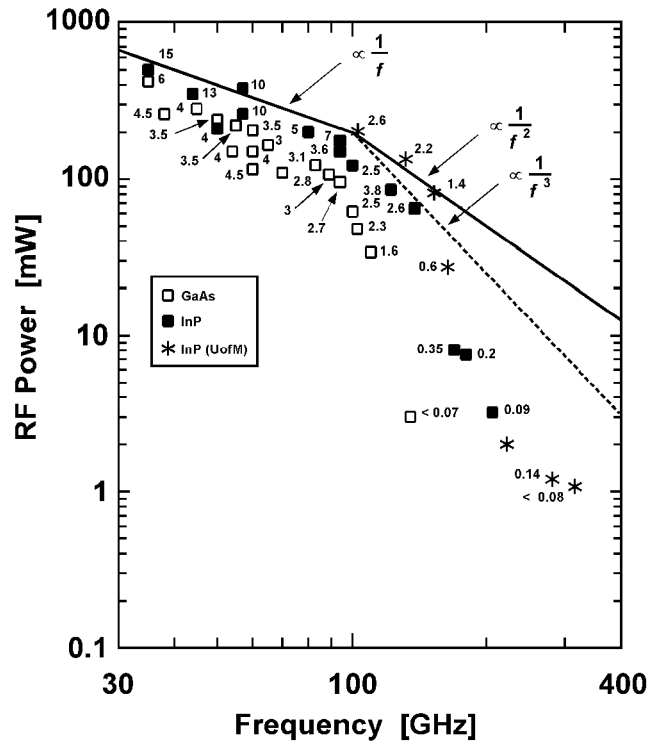


**Fig. 5.** Published state-of-the-art results from GaAs and InP Gunn devices under CW operation in the frequency range of 30–400 GHz. Numbers next to the symbols denote dc-to-RF conversion efficiencies in percent.

TUNNETT diodes, on the other hand, are based on a fast and quiet primary carrier injection mechanism [1], [2], which makes them another prime candidate for RF generation at high millimeter-wave and submillimeter-wave frequencies. RF power levels of  $100 \pm 5$  mW (and corresponding dc-to-RF conversion efficiencies of around 6%) were measured with GaAs TUNNETT diodes on diamond heat sinks in the fundamental mode at oscillation frequencies of 100–107 GHz [19].

Power extraction at higher harmonic frequencies was investigated with Si [20], [26] and GaAs [27], [28] IMPATT diodes as well as GaAs TUNNETT diodes [19] [29]. Diode

structures and properties suggest operation in second- or even third-harmonic mode for some of the aforementioned state-of-the-art results from Si IMPATT diodes above 200 GHz. As an example, the RF power of 1.2 mW at 301 GHz was thought to be generated at the third-harmonic frequency [20], but for many other results at these high millimeter-wave frequencies, no attempts to determine the exact mode of operation were reported.

The aforementioned GaAs TUNNETT diodes were also operated in a second-harmonic mode up to 237 GHz and yielded RF power levels exceeding 10 mW at 202 GHz, 9 mW around 210 GHz, and 4 mW around 235 GHz [29], [30]. These power levels correspond to dc-to-RF conversion efficiencies around 1% at 202 GHz and 210 GHz as well as above 0.6% around 235 GHz [29], [30]. The diodes operate as self-oscillating multipliers with a large modulation of the depletion region, which is akin to that of high-performance varactor diodes and is responsible for the high up-conversion efficiencies of more than 20% [29]. This mode of operation also reaches its performance peak below the maximum permissible bias current density [29]. Therefore, higher RF power levels and higher operating frequencies are expected from TUNNETT diodes that are designed for this mode of operation and have shorter active regions as well as doping concentrations appropriate for higher current densities. Simulations also indicated that RF power levels of the order of 10 mW can be generated in the 240–280 GHz frequency range with GaAs single-drift TUNNETT diodes in the fundamental mode [31].

The measured RF power levels and, particularly, conversion efficiencies of these TUNNETT diodes in a second-harmonic mode are comparable to those obtained from frequency multipliers where, *e.g.*, Schottky-barrier varactor diodes are driven by Gunn devices [32], [33]. Fig. 6 compares these results from various frequency multipliers in the 100–1000 GHz frequency range with select results from GaAs TUNNETT diodes, InP Gunn devices, and RTDs. In addition, very clean spectra were recorded from these GaAs TUNNETT diodes in the fundamental as well as in a second-harmonic mode [19], [29], [30]. TUNNETT diodes also yielded the lowest small-signal frequency-modulation (FM) noise measure reported from any oscillator with a two-terminal device [1], [19].

Contrary to preliminary results from GaAs TUNNETT diodes [19], a very preliminary study of the properties of single-drift GaAs IMPATT diodes in a second-harmonic mode found that the measured spectra of free-running oscillators with these diodes [28] were clearly not as clean as those of free-running oscillators with TUNNETT diodes (or Gunn devices). This result was indeed expected from approximately 7–8 dB higher values of the small-signal FM noise measure and at least 6 dB higher values of the large-signal FM noise measure of GaAs single-drift IMPATT diodes in the fundamental mode at *W*-band frequencies [1], [19]. Furthermore, dc-to-RF conversion efficiencies of, *e.g.*, 0.04% at 194 GHz [28] or 0.06% at 232 GHz [27] were inferior to those of the TUNNETT diodes in a similar circuit configuration [19], [29].

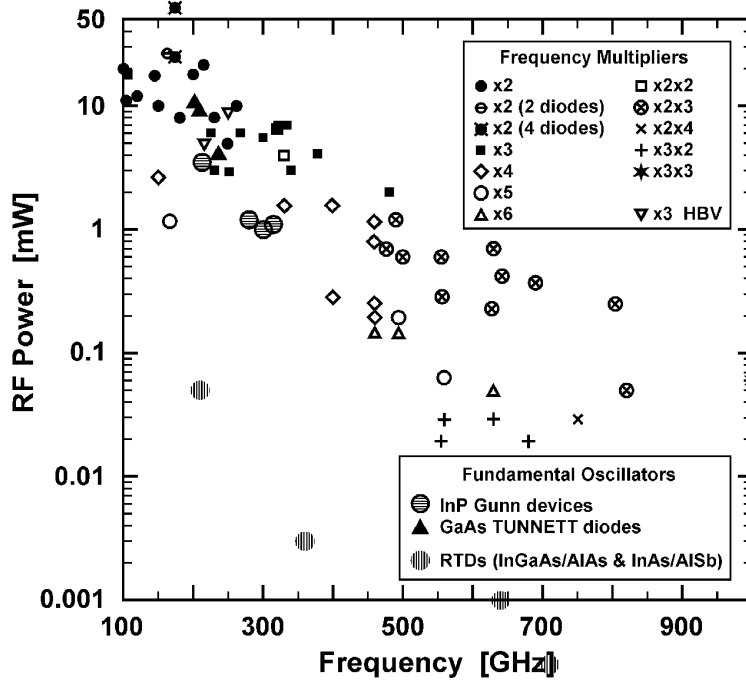


**Fig. 6.** Published state-of-the-art results from frequency multipliers with GaAs Schottky-barrier or InP-based heterojunction-barrier varactor diodes in the 100–1000 GHz frequency range in comparison with published state-of-the-art results from GaAs TUNNETT diodes, InP Gunn devices, and RTDs above 200 GHz.

#### 4. TRANSFERRED-ELECTRON DEVICES

GaAs or InP transferred-electron (or Gunn) devices are quite frequently employed in all-solid-state LO sources for submillimeter-wave frequencies, where they generate RF power at medium millimeter-wave frequencies of 60–150 GHz and then drive one or more stages of frequency multipliers with Schottky-barrier varactor diodes [25], [32], [33] or, more recently, heterojunction-barrier varactor diodes [34]. More than ten semiconductor materials in the III-V and II-VI groups are known to exhibit the transferred-electron effect, [2], [35], however, so far, only GaAs and InP have been exploited commercially. GaAs Gunn devices are not a topic of this paper since only InP Gunn devices yield RF power above 200 GHz.

The highest dc-to-RF conversion efficiencies at low to medium millimeter-wave frequencies and excellent performance up to *D*-band frequencies were reported from InP TEDs with  $n\bar{n}^+$  layer structures and current-limiting contacts at the cathode side of the active region. Examples of RF power levels (and corresponding conversion efficiencies) are 380 mW at 57 GHz (10.6%) in the fundamental mode [36] as well as 175 mW (7%) at 94 GHz, 85 mW (3.8%) at 125 GHz, and 65 mW (2.6%) at 138 GHz in a second-

harmonic mode [37], [38]. As shown in Fig. 5, the highest RF power levels from any Gunn device above 100 GHz were achieved with devices that had an  $n^+n^-n^+$  layer structure as well as a graded doping profile in the active region and were mounted on diamond heat sinks [19], [35], [39]. Operation in the fundamental mode was observed up to 165 GHz. As examples, RF power levels (and corresponding dc-to-RF conversion efficiencies) exceeded 200 mW (2.6%) at 103 GHz [35]; 130 mW (2.2%) at 132 GHz; 80 mW (1.4%) at 152 GHz; and 30 mW at 162 GHz [19], [35]. High RF power levels and excellent noise performance [1], [19], [30], [35], [39] make these InP Gunn devices ideally suited for driving high-performance Schottky-diode frequency multipliers in sensitive terahertz receivers.

Operation in a second-harmonic mode helps overcome the inherent fundamental frequency limit in Gunn devices. RF power levels of more than 3.5 mW at 214 GHz, more than 2 mW around 220 GHz, as well as more than 1 mW up to 315 GHz were measured in this mode of operation [30], [40]. The RF power levels above 300 GHz are the highest reported to date from any solid-state fundamental RF source and, as can be seen from Fig. 6, they approach those from frequency multipliers [32]. These RF power levels even exceed early performance predictions [41]–[44], but the results of more recent simulations indicate that significant increases in RF power levels can be expected from more optimized device structures and circuits up to at least 320 GHz [45], [46]. Fig. 7 compares the experimental results in the fundamental mode, as well as those in a second-harmonic mode with these recent predictions from detailed simulations [46] that employed a Monte Carlo-based harmonic balance technique [45]. Monte-Carlo simulations were originally used in the design of the *D*-band structures [47] and showed good agreement between performance predictions and measured results [45], [48]. Various device structures, which were designed for operation in a second-harmonic mode in the 200–310 GHz frequency range and had a doping gradient in the active region as shown schematically in the inset of Fig. 7, were investigated [46], [49].

The measured RF power levels in the fundamental mode at *D*-band frequencies and the predicted RF power levels for operation in a second-harmonic mode at *J*-band (220–325 GHz) frequencies follow a clear  $1/f^3$  roll-off up to about 300 GHz. This trend evidently shows that substantial performance improvements can be expected from optimized device structures and waveguide circuits at *J*-band frequencies. The trend above 300 GHz may also indicate that the transferred-electron effect in InP could be utilized even above 320 GHz and possibly up to 500 GHz [49] with devices operating in a second- or third-harmonic mode. In addition, the experimental results from InP Gunn devices above 220 GHz imply that the derivations of fundamental physical frequency limits for the transferred-electron effect in InP should be revisited and re-investigated in greater detail.

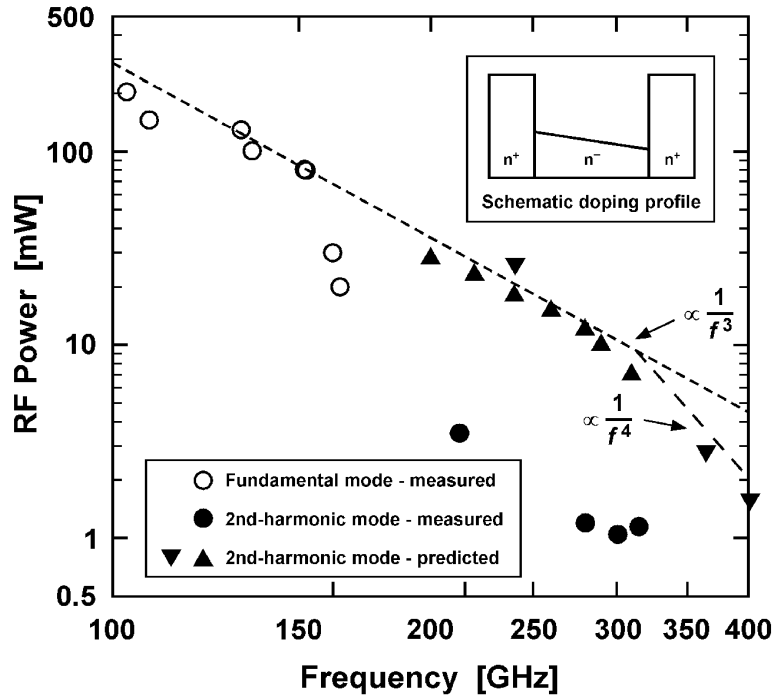


**Fig. 7.** Comparison of predicted [45], [46], [49] and measured [19], [40] CW RF power levels from InP Gunn devices with an  $n^+n^-n^+$  structure and a doping gradient in the active region as shown in the inset for the 100–320 GHz frequency range.

## 5. CONCLUSIONS

RF power generating capabilities of several two-terminal devices were reviewed and compared. Compared to GaAs, InP is the better semiconductor material system to reach submillimeter-wave frequencies with Gunn devices. Experimental results from both GaAs and InP Gunn devices indicate that the fundamental frequency limit of the transferred-electron effect may be higher than previously thought. More detailed studies are necessary to determine the ultimate fundamental frequency limit, *i.e.*, if InP Gunn devices are capable of generating significant RF power levels in the 320–400 GHz frequency range. Nonetheless, simulations predict that substantial performance improvements are feasible at *J*-band frequencies, which may help eliminate one or two stages in a multiplier chain to reach terahertz frequencies.

As can be seen from the published results in Figs. 1, 4, and 6, the RF power levels from InP Gunn devices on diamond heat sinks are the highest reported to date from any solid-state fundamental RF source operated at room temperature and for frequencies above 300 GHz. Likewise, GaAs TUNNETT diodes are considered the second-most powerful solid-state fundamental RF source operated at room temperature and for frequencies above 200 GHz.

Reliable long-term operation requires the heat dissipation in the device to be minimized. Both Gunn devices and TUNNETT diodes on diamond heat sinks meet these requirements since the above-mentioned state-of-the-art-results were obtained at “cool” operating active-layer temperatures estimated to be generally below 200 °C, but most often well below 150 °C [1], [29], [30],[35], [39], [40], [48].

Other semiconductor material systems, such as GaN or InN, are known to exhibit a transferred-electron effect [35] which could be utilized for millimeter-wave Gunn devices. However, various Monte Carlo simulations predict its onset to occur in these semiconductor materials at five to more than ten times higher threshold electric fields than in InP [50]–[53]. Furthermore, much smaller values for the negative differential mobility at electric fields above twice the threshold field, as well as lower values for the low-field electron mobility, require much higher doping  $\times$  length products for rapid domain formation than in GaAs or InP. Higher electric fields and, as a result, bias voltages, will enhance the RF power generating capabilities, but, together with higher doping  $\times$  length products, may cause dc input power densities that are at least one order of magnitude higher than in InP and, even on diamond heat sinks, result in extreme overheating in the device. As a consequence, major advances in material growth, material characterization, and experimental verification of material properties and parameters, as well as appropriate device fabrication technologies, are required before the potential and capabilities of any of these material systems can be assessed fully and eventually utilized.

## ACKNOWLEDGMENTS

Funding from JPL under contracts 961299 and 961527 as well as from NSF under grant ECS 98-03781 is kindly acknowledged.

## REFERENCES

- [1] H. Eisele and G. I. Haddad, “Active Microwave Diodes,” in *Modern Semiconductor Devices*, S. M. Sze, Ed., Ch. 6, John Wiley & Sons, New York, 1997, pp. 343–407.
- [2] S. M. Sze, *Physics of Semiconductor Devices*, 2nd Ed., John Wiley & Sons, New York, 1981.
- [3] L. Esaki and R. Tsu, “Superlattice and negative differential conductivity in semiconductors,” *IBM J. Res. Develop.*, **14**(1), 1970, pp. 61–65.
- [4] L. L. Chang, L. Esaki, and R. Tsu, “Resonant tunneling in semiconductor double-barriers,” *Appl. Phys. Lett.*, **24**(12), 1974, pp. 593–595.
- [5] B. Agarwal, A. E. Schmitz, J. J. Brown, M. Matloubian, M. G. Case, M. Le, M. Lui, and M. J. W. Rodwell, “112-GHz, 157-GHz, and 180-GHz InP HEMT traveling-wave amplifiers,” *IEEE Trans. Microwave Theory Tech.*, **46**(12), 1998, pp. 2553–2559.

- [6] S. Weinreb, T. Gaier, R. Lai, M. Barsky, Y. C. Leong, and L. Samoska, "High-gain 150–215-GHz MMIC amplifier with integral waveguide transitions," *IEEE Microwave Guided Wave Lett.*, **9**(7), 1999, pp. 282–284.
- [7] R. Lai, M. Barsky, T. Huang, M. Sholley, H. Wang, Y. L. Kok, D. C. Streit, T. Block, P. H. Liu, T. Gaier, and L. Samoska, "An InP HEMT MMIC LNA with 7.2-dB gain at 190 GHz," *IEEE Microwave Guided Wave Lett.*, **8**(11), 1998, pp. 393–395.
- [8] Q. Lee, B. Agarwal, D. Mensa, R. Pallela, J. Guthrie, L. Samoska, and M. J. W. Rodwell, "A > 400 GHz  $f_{\max}$  transferred-substrate heterojunction bipolar transistor IC technology," *IEEE Electron Device Lett.*, **19**(3), 1998, pp. 77–79.
- [9] D. Mensa, Q. Lee, J. Guthrie, S. Jaganathan, and M. J. W. Rodwell, "Transferred-substrate HBTs with 254 GHz  $f_t$ ," *Electron. Lett.*, **35**(7), 1999, pp. 288–290.
- [10] Y. C. Chen, D. L. Ingram, R. Lai, M. Barsky, R. Grunbacher, T. Block, H. C. Yen, and D. C. Streit, "A 95-GHz InP HEMT MMIC amplifier with 427-mW power output," *IEEE Microwave Guided Wave Lett.*, **8**(11), 1998, pp. 399–401.
- [11] Y. Kwon, D. Pavlidis, T. L. Brock, and D.C. Streit, "A D-band monolithic fundamental oscillator using InP-based HEMT's," *IEEE Trans. Microwave Theory Tech.*, **41**(12), 1993, pp. 2336–2344.
- [12] S. E. Rosenbaum, B. K. Kormanyos, L. M. Jelloian, M. Matloubian, A. S. Brown, L. E. Larson, L. D. Nguyen, M. A. Thompson, L. P. B. Katehi, and G. M. Rebeiz, "155- and 213-GHz All-nAs/GaInAs/InP HEMT MMIC oscillators," *IEEE Trans. Microwave Theory Tech.*, **43**(4), 1995, pp. 927–933.
- [13] E. R. Brown, C. D. Parker, A. R. Calawa, M. J. Manfra, C. L. Chen, L. J. Mahoney, and W. D. Goodhue, "High-frequency resonant-tunneling oscillators," *Microwave Optical Technol. Lett.*, **4**(1), 1991, pp. 19–23.
- [14] E. R. Brown, J. R. Söderström, C. D. Parker, L. J. Mahoney, K. M. Molvar, and T. C. McGill, "Oscillations up to 712 GHz in InAs/AlSb resonant tunneling diodes," *Appl. Phys. Lett.*, **58**(20), 1991, pp. 2291–2293.
- [15] E. Schomburg, J. Grenzer, K. Hofbeck, T. Blomeier, S. Winnerl, S. Brandl, A. A. Ignatov, K. F. Renk, D. G. Pavel'ev, Yu. Koschurinov, V. Ustinov, A. Zhukov, A. Kovsch, S. Ivanov, and P. S. Kop'ev, "Millimeter wave generation with a quasi planar superlattice electronic device," *Solid-State Electron.*, **42**(7–8), 1998, pp. 1495–1498.
- [16] S. Brandl, E. Schomburg, R. Scheuerer, K. Hofbeck, J. Grenzer, K. F. Renk, D. G. Pavel'ev, Yu. Koschurinov, A. Zhukov, A. Kovsch, V. Ustinov, S. Ivanov, and P. S. Kop'ev, "Millimeter wave generation by a self-sustained current oscillation in an InGaAs/InAlAs superlattice," *Appl. Phys. Lett.*, **73**(21), 1998, pp. 3177–3119.
- [17] E. Schomburg, M. Henini, J. M. Chamberlain, D. P. Steenson, S. Brandl, K. Hofbeck, K. F. Renk, and W. Wegscheider, "Self-sustained current oscillation above 100 GHz in a GaAs/AlAs superlattice," *Appl. Phys. Lett.*, **74**(15), 1999, pp. 2179–2181.
- [18] E. Schomburg, R. Scheuerer, S. Brandl, K. F. Renk, D. G. Pavel'ev, Yu. Koschurinov, V. Ustinov, A. Zhukov, A. Kovsch, and P. S. Kop'ev, "InGaAs/InAlAs superlattice oscillator at 147 GHz," *Electron. Lett.*, **35**(17), 1999, pp. 1491–1492.
- [19] H. Eisele and G. I. Haddad, "Two-terminal millimeter-wave sources," *IEEE Trans. Microwave Theory Tech.*, **46**(6), 1998, pp. 739–746.
- [20] T. Ishibashi and M. Ohmori, "200-GHz 50-mW CW oscillation with silicon SDR IMPATT diodes," *IEEE Trans. Microwave Theory Tech.*, **24**(11), 1976, pp. 858–859.

- [21] N. B. Kramer and R.A. Johnson, "Generating power at mm-wave frequencies," *Microwaves & RF*, **23**(5), 1984, pp. 243–249.
- [22] K. Chang, W. F. Thrower, and G. M. Hayashibara, "Millimeter-wave silicon IMPATT sources and combiners for the 110-260-GHz range," *IEEE Trans. Microwave Theory Tech.*, **29**(12), 1981, pp. 1278–1284.
- [23] M. Ino, T. Ishibashi, and M. Ohmori, "C.W. oscillation with p<sup>+</sup>-p-n<sup>+</sup> silicon IMPATT diodes in 200 GHz and 300 GHz bands," *Electron. Lett.*, **12**(6), 1976, pp. 148–149.
- [24] T. Ishibashi, M. Ino, T. Makimura, and M. Ohmori, "Liquid-nitrogen-cooled submillimeter-wave silicon IMPATT diodes," *Electron. Lett.*, **13**(10), 1977, pp. 299–300.
- [25] I. Mehdi, P. H. Siegel, D. A. Humphrey, T. H. Lee, R. J. Dengler, J. E. Oswald, A. Pease, R. Lin, H. Eisele, R. Zimmermann, and N. Erickson, "An all solid-state 640 GHz subharmonic mixer," *IEEE MTT-S Int. Microwave Symp. Dig.*, Baltimore, MD, June 7–12, 1998, pp. 403–406.
- [26] M. Ohmori, T. Ishibashi, and S. Ono, "Dependency of the highest harmonic oscillation frequency on junction diameter of IMPATT diodes," *IEEE Trans. Electron Devices*, **24**(12), 1977, pp. 1323–1329.
- [27] H. Böhm, J. Freyer, and M. Claassen, "CW harmonic power generation of GaAs IMPATT diodes above 200 GHz," *Proc. Terahertz Spectroscopy Applications II*, Munich, Germany, SPIE **3828**, 1999, pp. 81–88.
- [28] H. Eisele, unpublished results.
- [29] H. Eisele, "Efficient second-harmonic power extraction from GaAs TUNNETT diodes above 200 GHz," *Electron. Lett.*, **34**(13), 1998, pp. 1324–1326 **and** *Electron. Lett.*, **34**(15), 1998, pp. 1531.
- [30] H. Eisele, A. Rydberg, and G. I. Haddad: "Recent Advances in the Performance of InP Gunn Devices and GaAs TUNNETT Diodes for the 100–300-GHz Frequency Range and Above," *Special Issue on Terahertz Electronics, IEEE Transactions on Microwave Theory and Techniques*, vol. 48, no. 4, pp. 626–631, April 2000.
- [31] C-C. Chen, R. K. Mains, G. I. Haddad, and H. Eisele, "Numerical simulation of TUNNETT and MITATT devices in the millimeter and submillimeter range," *Proc. 4th Int. Symp. Space Terahertz Technol.*, Los Angeles, CA, March 30–April 1, 1993, pp. 362–376.
- [32] A. V. Räisänen, "Frequency multipliers for millimeter and submillimeter wavelengths," *Proc. IEEE*, **80**(11), 1992, pp. 1842–1852.
- [33] T. W. Crowe, T. C. Grein, R. Zimmermann, and P. Zimmermann, "Progress toward solid-state local oscillators at 1 THz," *IEEE Microwave Guided Wave Lett.*, **6**(5), 1996, pp. 207–208.
- [34] X. Mélique, A. Maestrini, P. Mounaix, M. Favreau, O. Vanbésien, J.M. Goutoule, G. Beaudin, T. Nähri and D. Lippens, "Record performance of a 250 GHz InP-based heterostructure barrier varactor tripler," *Electron. Lett.*, **35**(11), 1999, pp. 938–939.
- [35] H. Eisele, "Gunn or transferred-electron devices," in *Encyclopedia of Electrical and Electronics Engineering*, J. G. Webster, Ed., vol. 8, John Wiley & Sons, New York, 1999, pp. 523–537.
- [36] B. Fank, J. Crowley, and C. Hang, "InP Gunn diode sources," *Millimeter Wave Technology III*, SPIE **544**, 1985, pp. 22–28.
- [37] J. D. Crowley, C. Hang, R. E. Dalrymple, D. R. Tringali, F. B. Fank, and L. Wandinger, "140 GHz indium phosphide Gunn diode," *Electron. Lett.*, **30**(6), 1994, pp. 499–500.

- [38] J. D. Crowley, R. E. Dalrymple, C. Hang, D. R. Tringali, F. B. Fank, and L. Wandinger, "InP Gunn diodes serve millimeter-wave applications," *Microwaves & RF*, **33**(3), 1994, pp. 143–146.
- [39] H. Eisele and G. I. Haddad, "High-performance InP Gunn devices for fundamental-mode operation in D-band (110–170 GHz)," *IEEE Microwave Guided Wave Lett.*, **5**(11), 1995, pp. 385–387.
- [40] H. Eisele, "Second-harmonic power extraction from InP Gunn devices with more than 1 mW in the 260–320 GHz frequency range," *Electron. Lett.*, **34**(25), 1998, pp. 2412–2413.
- [41] L. Wandinger, "mm-wave InP Gunn devices: status and trends," *Microwave J.*, **24**(3), 1981, pp. 71–78.
- [42] I. G. Eddison, "Indium phosphide and gallium arsenide transferred-electron devices," in *Infrared and Millimeter Waves*, Vol. 11, *Millimeter Components and Techniques, Part III*, Academic Press, Orlando, 1984, pp. 1–59.
- [43] P. A. Rolland, G. Salmer, E. Constant, and R. Fauquembergue, "Comparative frequency behavior of GaAs, InP, and GaInAs transferred-electron devices—derivation of a simple comparative criterion," *IEEE Trans. Electron Devices*, **28**(3), 1981, pp. 341–343.
- [44] M. R. Friscourt and P.A. Rolland, "Optimum design of  $n^+n-n^+$  InP devices in the millimeter-range frequency limitation—RF performances," *IEEE Electron Device Lett.*, **4**(5), 1983, pp. 135–137.
- [45] R. Kamoua, "Monte Carlo-based harmonic balance technique for the simulation of high-frequency TED oscillators," *IEEE Trans. Microwave Theory Tech.*, **46**(10), 1998, pp. 1376–1381.
- [46] R. Kamoua, "Potential of second-harmonic power generation in InP Gunn oscillators above 200 GHz," *Proc. 4th Int. Conf. Millimeter Submillimeter Waves Applications*, San Diego, California, July 20–24, 1998, pp. 32–37.
- [47] R. Kamoua, H. Eisele, and G. I. Haddad, "D-band (110–170 GHz) InP Gunn devices," *Solid-State Electron.*, **36**, 1993, pp. 1547–1555.
- [48] H. Eisele and G. I. Haddad, "Recent advances in the performance of GaAs- and InP-based two-terminal devices as high-power millimeter-wave sources," *Proc. 4th Int. Conf. Millimeter Wave Far Infrared Science Technol.*, Beijing, China, August 12–15, 1996, pp. 2–5.
- [49] R. Kamoua and H. Eisele, "Power generation with fundamental and second-harmonic mode InP Gunn oscillators—performance above 200 GHz and upper frequency limits," these proceedings.
- [50] J. Kolnik, I. H. Oğuzman, K. F. Brennan, R. Wang, P. P. Ruden, and Y. Wang, "Electronic transport studies of bulk zincblende and wurtzite phases of GaN based on an ensemble Monte Carlo calculation including a full zone band structure," *J. Appl. Phys.*, **78**(2), 1995, pp. 1033–1038.
- [51] U. V. Bhapkar and M. S. Shur, "Monte Carlo calculation of velocity-field characteristics of wurtzite GaN," *J. Appl. Phys.*, **82**(4), 1997, pp. 1649–1655.
- [52] S. Krishnamurthy, M. van Schilfgaarde, A. Sher, and A.-B. Chen, "Bandstructure effect on high-field transport in GaN and GaAlN," *Appl. Phys. Lett.*, **71**(14), 1997, pp. 1999–2001.
- [53] E. Bellotti, B. K. Doshi, K. F. Brennan, J. D. Albrecht, and P. P. Ruden, "Ensemble Monte Carlo study of electron transport in wurtzite InN," *J. Appl. Phys.*, **85**(2), 1999, pp. 916–923.

## THE OXIDE BARRIER VARACTOR

**Thomas W. Crowe and Yiwei Duan**

Applied Electrophysics Laboratories  
Department of Electrical Engineering  
351 McCormick Road  
PO Box 400743  
Charlottesville, VA 22904-4743

The heterostructure barrier varactor [1] consists of a layer-cake of alternating low and high band-gap semiconductor materials, for example GaAs and AlGaAs. As bias is applied in either direction across the layers, the electrons in the moderately doped low band-gap layers form a two-dimensional electron gas against the conduction band discontinuity at the heterojunction. Thus, most of each low band-gap layer becomes depleted, forming capacitance modulation layers while the high band-gap materials are barrier layers to prevent conduction current. Since these devices have a symmetric capacitance-voltage characteristic centered at zero-bias, they cannot generate even order harmonics and don't require a bias circuit or even harmonic idler circuits. Thus, they are ideal frequency triplers and quintuplers. Also, since any number of barriers can be epitaxially stacked, the power handling of the device can be made quite large.

The primary problem with HBVs is that the conduction band discontinuity between most suitable semiconductor materials is not large enough to prevent a significant thermionic emission leakage current. This current can greatly reduce the useful capacitance modulation of the HBV. In terms of circuit design, the devices have a very high-Q, which makes it difficult to achieve broadband performance without several mechanical tuners. Although it has recently been shown that the InGaAs/InAlAs system yields much improved characteristics, and excellent results to 250 GHz have been achieved [2], the very limited fixed-tuned bandwidth of HBV multipliers remains a serious drawback that will prevent this technology from being useful in most applications.

Our new device is identical to the HBV except that an oxide replaces the semiconductor barrier layers [3]. The expected result is a much higher barrier height that greatly reduces leakage current. This allows the properties of the modulation layers to be optimized to achieve maximum capacitance modulation without regard to the barrier materials. Also, we can implement this process with GaAs rather than InGaAs, so that avalanche breakdown is not as prevalent. A review of the literature shows that many groups have attempted to find a suitable oxide material on GaAs. In particular, one group has succeeded in laterally oxidizing AlGaAs layers in a mesa structure to form  $\text{Al}_2\text{O}_3$  layers that serve as waveguiding regions for optical devices [4]. Their work was the original basis for our proposed Oxide Barrier Varactor.

To date, we have fabricated several test batches of whisker contacted OBV devices. Since oxidation of the AlGaAs is the last process step, we are able to measure the parameters of the HBV diode before the layers are oxidized to form the OBV device structure. Initial tests have shown that the turn-on voltage (defined here as 1  $\mu\text{A}$ ) was

increased by an order of magnitude after oxidation. However, the resulting OBV device showed no capacitance modulation.

It is now understood that the oxidation process leaves a significant amount of metallic arsenic at the GaAs-oxide interface. This creates a large concentration of interface states that pins the Fermi level near mid-gap and causes the modulation layers to be depleted regardless of applied bias.

There are several possible ways to solve this problem. First, the oxidation process can be varied. Perhaps a different heating cycle or ambient atmosphere will allow more of the arsenic to be removed. Similarly, a new device geometry that has a greater periphery to area ratio may allow more of the Arsenic to escape. Also, other materials might eliminate the problem altogether. For example, perhaps a GaN layer can be substituted for the AlGaAs layer. However, to date no suitable solution has been demonstrated.

### **Summary:**

The oxide barrier varactor is proposed as an adaptation to the more common heterostructure barrier varactor. Its structure is essentially the same except an oxide replaces the high-barrier semiconductor material that forms the heterostructure barrier. The result should be a drastic reduction in conduction current thereby allowing the fabrication of HBV-like devices with greatly improved performance. Although the OBV structure can be formed by lateral oxidation of AlGaAs layers, the resulting interface state density is too high. This causes the modulation layers to be depleted and destroys the capacitance modulation. Although there are many possible solutions to this problem, it remains a major challenge.

**ACKNOWLEDGEMENT:** This work was sponsored by the NASA Office for Space Science (NAG5-8663).

### References:

- [1] S.M. Nilsen, H. Gronqvist, H. Hjelmgren, A. Rydberg, and E.L. Kollberg, "Single Barrier Varactors for Submillimeter Wave Power Generation," IEEE Trans. Microwave Theory Tech., Vol. 41, No. 4, pp. 572-580, April 1993.
- [2] X. Melique, A. Maestrini, P. Mounaix, M. Favreau, O. Vanbesien, J.M. Goutoule, G. Beaudin, T. Nahri, D. Lippens, 12% Efficiency and 9.5 dBm Output Power from InP-Based Heterostructure Barrier Varactor Triplers at 250 GHz, 1999 IEEE MTT-S Intl. Microwave Symp., Anaheim, CA, June 1999.
- [3] T.W.Crowe, Y.Duan, The Oxide Barrier Varactor, Patent Disclosure, Univ. of Virginia, Charlottesville, Nov. 16, 1999.
- [4] K.D. Choquette, K.M. Geib, C.I.H. Ashby, R.D. Twesten, O. Blum, H.Q. Hou, D.M. Follstaedt, B.E. Hammons, D. Mathes, R. Hull, Advances in Selective Wet Oxidation of AlGaAs Alloys, IEEE Journal of Selected Topics in Quantum Electronics, Vol.3 No. 3, pp. 916-925, June 1997.

# Power Generation with Fundamental and Second-Harmonic Mode InP Gunn Oscillators - Performance Above 200 GHz and Upper Frequency Limits

Ridha Kamoua<sup>1</sup> and Heribert Eisele<sup>2</sup>

<sup>1</sup>Department of Electrical and Computer Engineering,  
SUNY at Stony Brook, Stony Brook, NY 11794-2350

<sup>2</sup>Solid-State Electronics Laboratory  
Department of Electrical and Computer Science  
University of Michigan, Ann Arbor, MI 48109-2122

## Abstract

This paper investigates the performance of InP Gunn devices at high millimeter- and submillimeter-wave frequencies through computer simulations. The objective is to estimate the highest frequency at which InP Gunn devices can realistically be used as oscillators. The simulation tool uses the ensemble Monte Carlo method to model the Gunn device while the harmonic balance technique is employed to describe the device-circuit interaction. Thermal effects are taken into account by coupling a heat flow equation to the Monte Carlo algorithm. Results based on this model showed good agreement with available experimental data both for fundamental and second harmonic InP Gunn oscillators. This agreement establishes an acceptable confidence level on the applicability and accuracy at high frequencies. Therefore, the model is used to predict the device performance when the length of the active region in the device is scaled down to less than 1  $\mu\text{m}$ . Results indicate that oscillations up to at least 500 GHz are possible in a second-harmonic mode. These simulations take into consideration realistic load and series resistances as well as safe operating temperatures.

## 1 Introduction

Oscillators based on InP Gunn devices were demonstrated experimentally up to 315 GHz when operated in the second harmonic mode [1]. RF Power levels of 3.5 mW

at 213 GHz and 1.1 mW at 315 GHz were obtained. Efficient fundamental-mode operation of InP Gunn devices was originally thought to be limited to frequencies well below 140 GHz [2]. These results clearly indicate that InP Gunn devices could generate power at much higher frequencies than previously thought. Such sources of RF power reduce the number of multiplier stages required to reach higher terahertz frequencies. The main objectives of this paper are (1) estimates of the power levels that could be obtained from optimized structures with graded doping profiles between 200 GHz and 300 GHz, and (2) the prospects of RF power generation with InP Gunn devices at even higher frequencies.

Results reported in this paper are based on a computer model which incorporates the physical phenomena relevant to the transferred-electron (or Gunn) effect. The model employs an ensemble Monte Carlo technique coupled to Poisson's equation. It can analyze Gunn device structures with arbitrary doping profiles in the active region and various heterostructure injectors at the cathode [3]. At frequencies above 100 GHz, the Monte Carlo method is more appropriate than other techniques that solve for the different moments in the Boltzmann transport equation. In particular, the Monte Carlo method considers the various scattering mechanisms individually rather than through some average relaxation time parameters. This is important in the case of a Gunn device where the operation is based on the intervalley transfer of electrons. Thermal effects are accounted for by coupling a heat flow equation to the basic Monte Carlo method. This allows the device temperature and the various scattering rates to evolve with time until a stable solution is reached. The harmonic balance technique describes the interaction of the device with the circuit and in conjunction with the Monte Carlo method determines a solution that satisfies the oscillation condition. Simulation results obtained with this model were compared with experimental data. Very good agreement was achieved for InP Gunn devices operating in the fundamental and second harmonic modes [3].

## 2 Simulation Results above 200 GHz

The good agreement between predictions and experimental data establishes the validity of the Monte Carlo/harmonic balance model for describing Gunn oscillator operation. Therefore, performance estimates at frequencies above 200 GHz are presumed to be quite accurate as well. The typical Gunn device structure considered in the simulations has a moderately n-doped active region sandwiched between two  $n^+$  layers forming the cathode and anode terminals. The doping in the active region plays a major role in determining the performance of the device. Two types of doping profiles in the active region were considered: uniform and linearly graded. Various Gunn device structures were simulated with the simulation tool as described in the previous section. To identify a structure that yields the optimum performance at a given frequency, the following device parameters were varied: doping at the cath-

$N_{cathode}$ ( $\text{cm}^{-3}$ )	$N_{anode}$ ( $\text{cm}^{-3}$ )	$P_{RF}$ (mW)	$\eta$ (%)	$T$ (K)
1.0	1.0	11.2	0.43	400
1.5	1.5	21.0	0.65	424
1.8	1.8	26.5	0.47	440
2.0	2.0	15.8	0.4	450
0.75	1.5	15.5	0.6	400
0.9	2.25	24.5	0.8	420
1.2	2.25	25.0	0.6	415
1.5	2.2	29.0	0.5	428

Table 1: Simulation results for different 1.0- $\mu\text{m}$ -long InP Gunn device structures on diamond heat sinks at 240 GHz and a bias voltage of 4.5 V.

ode side of the active region ( $N_{cathode}$ ), doping at the anode side of the active region ( $N_{anode}$ ), bias voltage ( $V_{DC}$ ), and device diameter ( $D$ ). Table 1 summarizes the results for 1- $\mu\text{m}$ -long InP Gunn device structures with different doping profiles at 240 GHz and a bias voltage of 4.5 V.

These results indicate that Gunn devices with graded doping profiles yield higher power and efficiency compared to uniformly doped devices. More importantly, a graded doping profile results in a lower operating temperature. This is an important consideration as excessive heating represents a major problem and limiting factor in Gunn devices at these frequencies.

### 3 Upper Frequency Limits

The fundamental oscillation frequency of a Gunn device is determined mainly by the thickness of the active region. Therefore, submicron devices need to be considered if RF power generation at frequencies above 300 GHz is to be investigated. The results presented in this section correspond to InP Gunn devices with graded doping profiles and power extraction at the second-harmonic frequency. Table 2 summarizes the best results obtained as the active region thickness  $L$  is reduced.

The first submicron device considered has a 0.8  $\mu\text{m}$  active region and a linearly graded doping increasing from  $0.9 \times 10^{16} \text{ cm}^{-3}$  at the cathode to  $3.0 \times 10^{16} \text{ cm}^{-3}$  at the anode. Oscillations were obtained at 360 GHz and 400 GHz with output power levels of 2.9 mW and 1.5 mW, respectively. At 0.7  $\mu\text{m}$ , the optimum oscillation frequency is about 450 GHz with a corresponding power level of 1.3 mW. A further reduction

$L$ ( $\mu\text{m}$ )	$f$ (GHz)	$N_{cathode}$ ( $\text{cm}^{-3}$ )	$N_{anode}$ ( $\text{cm}^{-3}$ )	$D$ ( $\mu\text{m}$ )	$V_{DC}$ (V)	$P_{RF}$ (mW)	$\eta$ (%)	$T$ (K)
0.8	360	$0.9 \times 10^{16}$	$3.0 \times 10^{16}$	26	4.25	2.9	0.24	397
0.8	400	$0.9 \times 10^{16}$	$3.0 \times 10^{16}$	24	3.8	1.5	0.16	381
0.7	450	$0.9 \times 10^{16}$	$4.7 \times 10^{16}$	20	3.3	1.3	0.18	380
0.6	500	$0.9 \times 10^{16}$	$5.0 \times 10^{16}$	15	2.9	0.4	0.11	367

Table 2: Simulation results for submicron InP Gunn devices.

of the active region yields optimum performance at 500 GHz with an output power level close to 0.5 mW. These RF power levels are still sufficient to drive a diode mixer at these frequencies in heterodyne receiver applications. The operating temperatures are below 400 K for all investigated devices. The operating temperature is only 367 K for the 0.6  $\mu\text{m}$  device. This clearly indicates that power generation at frequencies above 300 GHz is not necessarily limited by heat dissipation but rather by the ability to match the device to the external circuit. As the frequencies become higher, the negative resistance provided by the Gunn device decreases which renders matching to the load and overcoming any circuit losses more challenging. As illustrated in Table 2, matching to load resistance of  $1 \Omega$  requires the device diameter to be decreased from 26  $\mu\text{m}$  at 360 GHz to 15  $\mu\text{m}$  at 500 GHz.

A simple estimation of the fundamental mode oscillation frequency based on the thickness of the active region and the saturation velocity indicates that a 0.6  $\mu\text{m}$  InP Gunn device should have a fundamental frequency close to 166 GHz. However, the Monte Carlo simulations described earlier provide a much higher frequency of 250 GHz. The simple estimation would even result in a lower frequency if the effect of temperature on the saturation velocity is taken into account. The higher oscillation frequency is attributed to two electron velocity overshoot effects. Figure 1 shows the time evolution of the average electron velocity along the device at eight intervals in one RF period while Figure 2 shows the corresponding electric field profiles. Velocity overshoot is observed in two different parts of the device. As “cold” electrons enter the active region from the  $n^+$  cathode contact, they experience a large increase in the electric field over a short distance. This results in much higher velocities (close to  $4.0 \times 10^7 \text{ cm s}^{-1}$ ) compared to the saturation velocity over a region that extends about 0.25  $\mu\text{m}$  into the active region. In addition to velocity overshoot near the cathode, higher velocities are also observed when the space charge layer is collected at the anode and the electric field rises rapidly in time. This is illustrated by the velocity

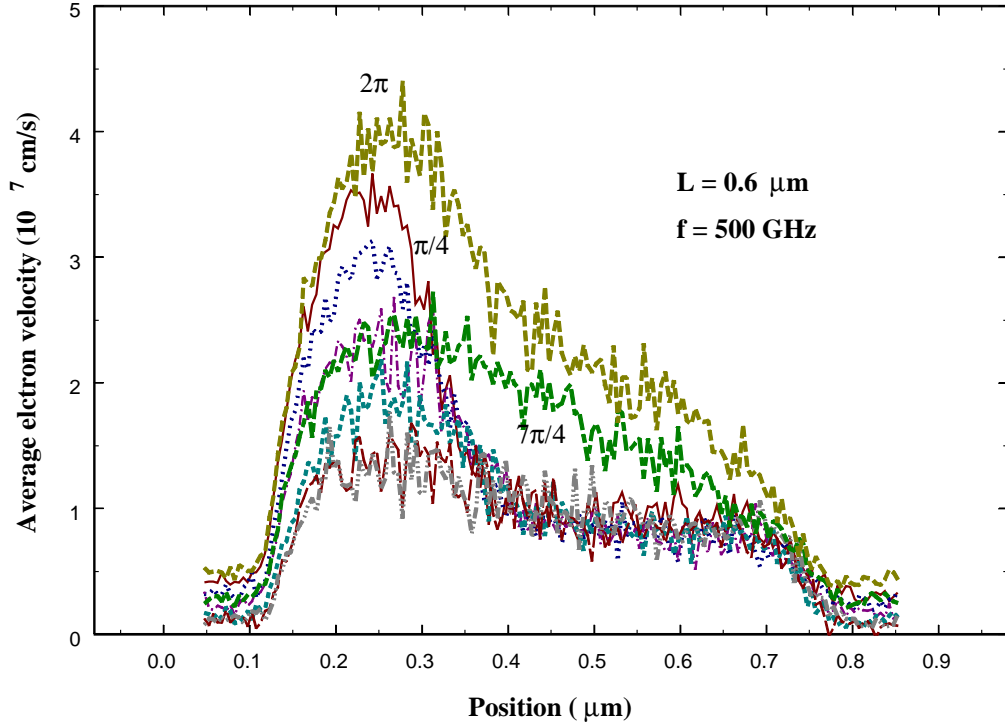


Figure 1: Time evolution of the average electron velocity for a submicron Gunn device structure with a length of the active region of  $0.6 \mu\text{m}$ .

profile at phases  $\frac{7\pi}{4}$  and  $2\pi$ . In particular, at  $2\pi$  the average velocity is higher than  $2.0 \times 10^7 \text{ cm s}^{-1}$  over most of the active region. These two overshoot effects contribute to a higher effective electron velocity in submicron devices and therefore a higher oscillation frequency.

Figure 3 summarizes the simulation results described in this paper and provides a comparison with the current state-of-the-art performance of InP Gunn devices [1]. The data represented by solid circles denote experimental results, which were obtained at the University of Michigan from devices with a graded doping profile. These results already represent the highest measured power levels at frequencies between 100 GHz and 320 GHz. Simulation results (open circles) indicate that significant improvement in the frequency range from 200 GHz to 320 GHz could be obtained with proper device and circuit design. In addition, the highest frequency of InP Gunn devices is estimated to reach at least 500 GHz. The predicted output power is proportional to  $f^{-3}$  at frequencies up to 320 GHz and  $f^{-4}$  up to at least 450 GHz. The  $f^{-4}$  dependence probably underestimates the performance that can be expected from

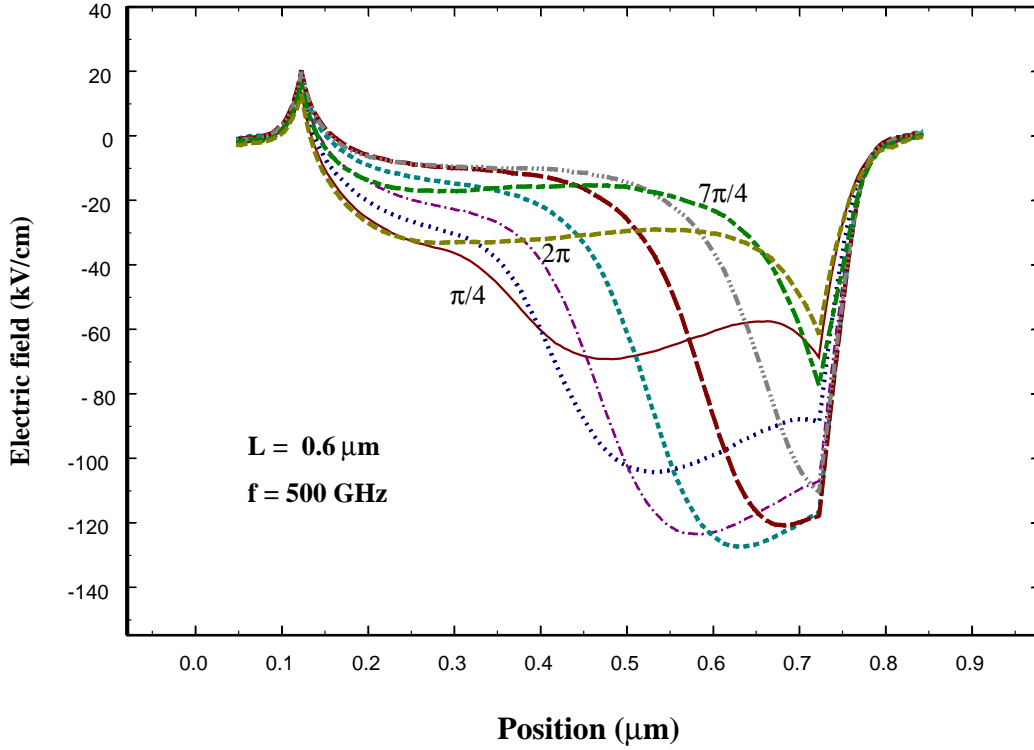


Figure 2: Time evolution of the electric field for a submicron Gunn device structure with a length of the active region of  $0.6 \mu\text{m}$ .

InP Gunn devices in this frequency range as the results in this paper are preliminary. More optimized device structures will result in further improvement of the device performance.

## 4 Conclusion

Realistic simulations of InP Gunn devices for operation above 200 GHz were carried out to identify an optimum design at 240 GHz and to estimate the upper frequency limits of InP Gunn devices operated in the second harmonic mode. At 240 GHz, RF power levels close to 30 mW are predicted for devices with a  $1.0\text{-}\mu\text{m}$ -long active region and a graded doping profile. Operating temperatures remain below 430 K. Decreasing the length of the active region results in oscillations up to 500 GHz, with RF output power levels of 2.9 mW at 360 GHz; 1.5 mW at 400 GHz; 1.3 mW at 450 GHz; and 0.4 mW at 500 GHz. Below 300 GHz, the power generation capabilities of InP Gunn devices are regarded as mainly thermally limited, whereas above 300 GHz, matching to the load becomes more restricting and challenging.

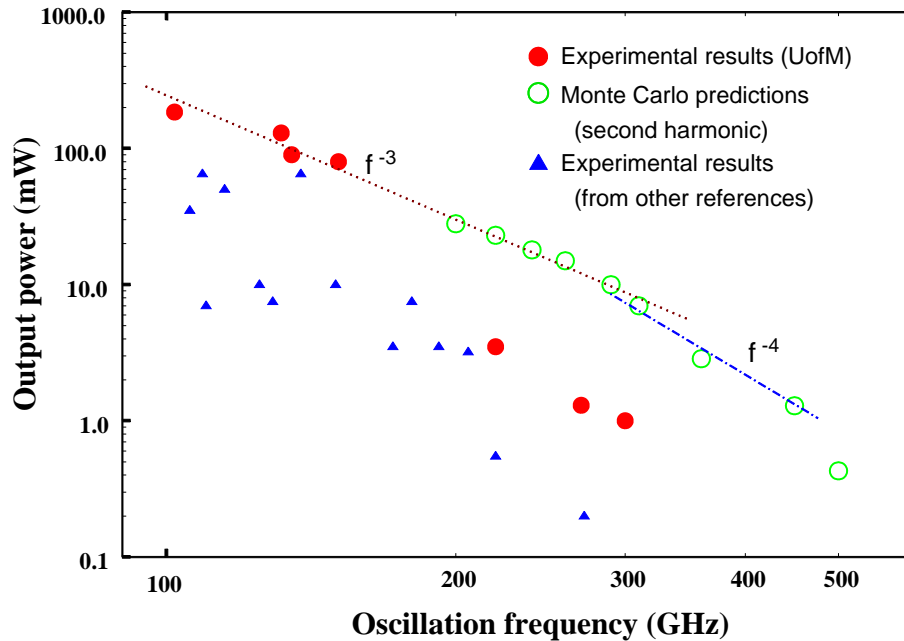


Figure 3: State-of-the-art RF output power from InP Gunn devices and predicted RF performance based on Monte Carlo simulations.

## Acknowledgements

This work was supported in part by NSF Grant ECS-9803781.

## References

- [1] H. Eisele, A. Rydberg, and G. I. Haddad, "Recent Advances in the Performance of InP Gunn Devices and GaAs TUNNETT Diodes for 100-300 GHz Frequency Range and Above", *IEEE Trans. Microwave Theory and Techn.*, vol. 48, pp. 626-631, April 2000.
- [2] I.G. Eddison and D.M. Brookbanks, "Operating Modes of Millimeter Wave Transferred Electron Oscillators", *Electron. Lett.*, vol. 17, pp. 112-113, 1981.
- [3] R. Kamoua, H. Eisele, and G. I. Haddad, "D-Band (110- 170 GHz) InP Gunn Devices", *Solid-State Electron.*, vol. 36, pp. 1547-1555, 1993.
- [4] R. Kamoua, "Monte-Carlo-Based Harmonic-Balance Technique for the Simulation of High-Frequency TED Oscillators", *IEEE Trans. Microwave Theory and Techn.*, vol. 46, pp. 1376-1381, 1988.

# GaN-based NDR Devices for THz Generation

Egor Alekseev, Andreas Eisenbach, Dimitris Pavlidis,  
Seth M. Hubbard and William Sutton

Solid-State Electronics Laboratory  
Department of Electrical Engineering and Computer Science  
The University of Michigan, Ann Arbor, MI 48109-2122, USA

## Abstract

GaN-based Negative Differential Resistance (NDR) diode oscillators have been studied by employing Gunn design criteria applicable to this material system. Numerical simulations were used to carry out large-signal analysis of the GaN NDR diode oscillators in order to evaluate their potential for THz signal generation. It was found that, due to the higher electron velocity and reduced time constants involved in the diode operation, GaN NDR diodes offer significantly higher frequency and power capability than conventional GaAs Gunn diodes. Based on the performed analysis, THz signal generation using GaN-based NDR diodes was predicted. GaN NDR layer structures were grown by MOCVD. The fabrication technology and characterization techniques used for GaN NDR diode oscillators are presented.

## I. Introduction

Active microwave diodes with negative differential resistance (NDR), such as GaAs or InP Gunn diodes, are the preferred devices for generation of microwave signals with high frequency and power. The frequency capabilities of Gunn diodes are limited by the rate of electron intervalley transfer. Thus, the amount of output power available from GaAs Gunn diodes decreases sharply when the oscillation frequency exceeds  $100\text{GHz}$ , which corresponds to the energy-relaxation time in this material of  $\sim 10\text{ps}$  [1]. Due to larger threshold field in InP ( $10.4\text{KV/cm}$  vs.  $3.5\text{KV/cm}$  in GaAs), the energy-relaxation time in InP is shorter, and InP-based Gunn diodes with fundamental operation up to D-band frequencies have been demonstrated [2].

Studies of fundamental properties in III-V nitrides indicate that these wide-bandgap materials also exhibit bulk NDR effect with threshold fields in excess of  $80\text{KV/cm}$  [3,4,5]. Moreover, Monte Carlo studies of electron transport indicate that the energy-relaxation time in GaN is much shorter than in conventional III-V semiconductors [6,7]. Thus, use of GaN with increased electrical strength and reduced electron-transfer time constants offers the possibility to increase the frequency as well as the power-capability of NDR diode oscillators and extend the range covered by more traditional III-V semiconductor-based generators to THz frequencies.

In this work, large-signal numerical simulations are employed to investigate the suitability of GaN-based NDR diodes for millimeter and sub-millimeter (THz) signal generation. Based on the results of the large-signal simulations, several promising GaN NDR layer structures were selected and grown by MOCVD at the University of Michigan. Special device patterns and integrated circuits for experimental validation were developed. The fabrication technology and characterization techniques explored for realization and demonstration of GaN NDR diode oscillators are also discussed.

## II. Theoretical Basis for THz Signal Generation using GaN NDR Diodes

Studies of GaN-based NDR diodes were conducted by employing a commercial semiconductor-device simulator *Medici*. Since this program does not contain material parameters for GaN, these had to be obtained from literature and were evaluated, verified, and properly introduced into the simulator. Comparisons of simulated performance with experimental characteristics of GaN-based MESFETs and PIN diodes were made to enable validation of the selected parameters. Further details on the adopted approach are presented elsewhere [8].

A low-field electron mobility of  $\mu_n=280\text{cm}^2/\text{Vsec}$  and  $60\text{cm}^2/\text{Vsec}$  were assumed for wurtzite ( $W_z$ ) GaN doped at  $N=5\times 10^{16}\text{cm}^{-3}$  and  $1\times 10^{19}\text{cm}^{-3}$ , respectively [9]. The value of electron lifetime  $\tau_n=7\text{ns}$  and hole lifetime  $\tau_p=0.1\text{ns}$  used in the simulations was based on the experimental data measured by an electron-beam-induced current method [10]. Coefficients for calculating impact-ionization rates in GaN were obtained by fitting to the theoretical predictions presented in [11] and verified by comparing simulation results with experimental breakdown voltages reported for GaN PIN diodes [12].

Models for field dependence of electron mobility in GaN were based on the  $v$ - $F$  characteristics calculated by Monte-Carlo simulations [13]. Velocity-field characteristics, evaluated in these studies, demonstrated a bulk NDR effect in the high-field region due to the intervalley transfer. However, the threshold field for intervalley transfer and consequent appearance of NDR in GaN was much larger than in conventional semiconductors such as GaAs. An increase of the threshold field is caused by a larger separation between the satellite and central valleys in  $W_z$  GaN where  $\Delta E$  is  $\approx 2.1\text{eV}$  compared to  $\Delta E\approx 0.3\text{eV}$  for GaAs. The GaN  $v$ - $F$  characteristic, used in the simulations, had a peak velocity  $v_{PEAK}$  of  $3\times 10^7$ , a saturation velocity  $v_{SAT}$  of  $2\times 10^7$ , and a threshold field  $F_{TH}$  of  $150\text{KV/cm}$ .

According to recent studies of GaN bandstructure, the  $\Gamma$ -valley inflection point, at which the group electron velocity is maximal, was found to be located below the lowest satellite valley in both  $Zb$  (zinc-blende) [4] and  $W_z$  GaN [14]. Although further studies are necessary for experimental confirmation, the inflection point mechanism is also expected to cause bulk NDR in GaN. This contrasts other semiconductors, where intervalley transfer or impact ionization are initiated at a lower field than the inflection-point NDR [1].

The reported  $v$ - $F$  characteristics of  $Zb$  GaN calculated using Monte Carlo simulations were based on a band structure containing the  $\Gamma$ -valley inflection point, and the results indicated that NDR was indeed caused primarily by the dispersion of the electron drift velocity in the  $\Gamma$  valley [4]. The inflection-based NDR manifested a threshold field  $F_{TH}$  of  $80\text{KV/cm}$  and peak velocity  $v_{PEAK}$  of  $3.8\times 10^7\text{cm/sec}$  compared with  $F_{TH}=110\text{KV/cm}$  and  $v_{PEAK}=2.7\times 10^7\text{cm/sec}$  calculated in [3] for intervalley-transfer-based NDR. However, by far a more important consequence of the inflection-based NDR is the elimination of the intervalley-transfer relaxation time from the time required for NDR formation and, thus, a possibility of significantly increased frequency capability for GaN inflection-based NDR diodes.

Frequency-independent  $v$ - $F$  characteristics can be used to describe electron transport in the presence of a time-varying electric field as long as the frequency of operation  $f$  is much lower than the NDR relaxation frequency  $f_{NDR}$  defined by  $\tau_{ER}$  (the energy-relaxation time) and  $\tau_{ET}$  (the intervalley relaxation time). The energy-relaxation time of  $0.15\text{ps}$  calculated for  $W_z$  GaN was ten times smaller than the GaAs value of  $1.5\text{ps}$ . The intervalley-transfer relaxation time  $\tau_{ET}$  was

evaluated from the results of Monte Carlo studies of ballistic transport [15]. By extrapolating reconstructed  $\tau_{ET}(F)$  curves to the point of threshold field  $F=F_{TH}$ , electron intervalley transfer times  $\tau_{ET}$  of  $7.7ps$  and  $1.2ps$  were found for GaAs and GaN, respectively.

Based on the results of this estimation, the NDR relaxation frequency  $f_{NDR}$  of GaAs was found to be  $\sim 100GHz$  in excellent agreement with experimental and theoretical results [1]. The frequency capability of GaN-based NDR devices was found superior to that of GaAs Gunn diodes as indicated by the GaN NDR relaxation frequency  $f_{NDR}$  of  $\sim 1THz$  for the case of intervalley-transfer-based NDR and  $\sim 4THz$  for case of inflection-based NDR (with  $\tau_{ET}=0ps$ ). Since the equation and the frequency-response of  $v$ - $F$  characteristics in GaN is not yet well-determined, both intervalley-transfer-based NDR of  $W_z$  GaN and inflection-based NDR of  $Zb$  GaN were considered in order to account for uncertainty in published  $v$ - $F$  characteristics.

Overall, GaN offers higher peak and saturation velocities than GaAs, which leads to reduced transit time and increased frequency of operation. The threshold and breakdown fields are also larger in GaN, which allows operation at a higher bias and leads to increased output power. The increased frequency response of high-energy electrons in GaN is attributed directly to the higher electrical strength of this material compared with GaAs. The THz capability, predicted for GaN devices operating on the inflection-based NDR, is possible due to the exceptionally high frequency response of electrons to the variations of the bandstructure as suggested in [4].

### III. Design of GaN-based NDR Diodes for THz Sources

When a high electric field  $F > F_{TH}$  is applied to bulk GaN, electrons experience a negative differential mobility  $\mu_{NDR}$ . Under these conditions, a non-uniformity of electron concentration would grow at a rate  $1/\tau_{DD}$ , where  $\tau_{DDR}$  is the differential dielectric relaxation time and depends on the electron concentration  $N$ , the dielectric constant  $\epsilon$ , and the peak negative differential mobility  $\mu_{NDR}$ . It is recognized that domain growth lasts for at least  $3 \times \tau_{DDR}$  [16] and, thus, the operation frequency of NDR devices can be limited by the active layer doping. The dependence of frequency capabilities on  $N$  for GaN and GaAs was calculated using their respective material parameters and the results are presented in Figure 1.

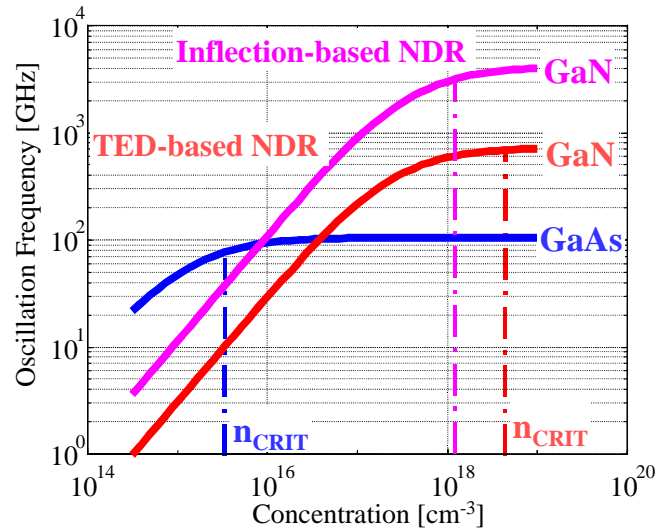


Figure 1. Concentration-frequency diagram of Gunn diodes made of GaAs and GaN

The negative differential mobility in GaAs is larger than in GaN and, therefore, for low doped devices, growth of electron domains occurs faster in GaAs than in GaN. However, as  $N$  is increased,  $\tau_{DDR}$  is reduced, and the frequency capability improves until it reaches the NDR relaxation frequency  $f_{NDR}$  discussed in the previous section. Since  $f_{NDR}^{GaAs} < f_{NDR}^{GaN}$  the frequency capability of GaN-based devices improves for higher  $N$  without being limited by  $f_{NDR}$  as in case of GaAs. This leads to GaN NDR operation that exceeds the GaAs limit of  $105GHz$  for GaN doping levels above  $5 \times 10^{16} cm^{-3}$ .

$(N \times L)$  criteria for the possibility of Gunn domain instability are based on the fact that the domain growth rate  $1/\tau_{DDR}$  should be higher than the transit frequency  $f_T = v_{PEAK}/L_A$ :

$$(N_A \times L_A) > (N \times L)_0 \equiv \frac{3 \times \epsilon \times v_{PEAK}}{q \times \mu_{NDR}} \quad (1)$$

where  $N_A$  is the doping,  $L_A$  is the thickness of the active layer,  $(N \times L)_0$  is the critical value of the  $(N \times L)$  product, and the factor 3 accounts for the domain growth time, as explained earlier. The critical values of  $(N \times L)$  product for GaN and GaAs were calculated using (1), and the results showed that, due to a higher peak velocity and a smaller negative mobility,  $(N \times L)_0$  for GaN is  $\sim 10^{13} cm^{-2}$  which is an order of magnitude larger than for GaAs ( $10^{11} - 10^{12} cm^{-2}$ ).

However, if the active layer doping ( $N_A$ ) exceeds the critical doping concentration  $N_{CRIT}$ , static domains can be formed inside the active layer [16]. Formation of parasitic static domains results in a decrease of output power and may lead to an early breakdown. Due to the large difference in threshold electric fields ( $F_{TH}$ ),  $N_{CRIT}$  in GaN calculated according to (2) [16]

$$N_{CRIT} = \frac{\epsilon \times F_{TH}^2}{q} \quad (2)$$

is much higher than in GaAs and, thus, the active region in GaN diodes can be doped significantly higher ( $\sim 10^{17} cm^{-3}$ ) than in GaAs designs ( $\sim 10^{15} cm^{-3}$ ). The latter is a very important since the availability of low-doped GaN material ( $N_A < 5 \times 10^{16} cm^{-3}$ ) is limited. Higher doping of active layers in GaN NDR diodes also leads to reduction of  $\tau_{DDR}$  in this material, helping to increase its frequency capability. Due to the higher doping of the active layer in GaN NDR diodes, the devices are operated at a higher current level which leads to an increased level of output power.

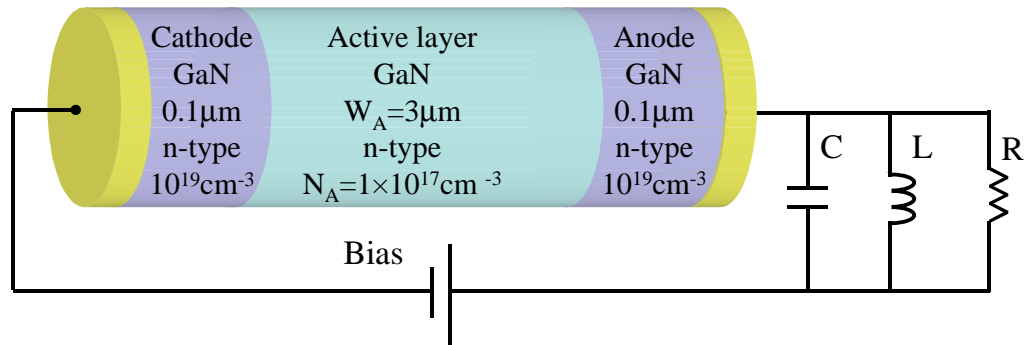


Figure 2. Schematic of GaN NDR diode oscillator.

A typical GaN NDR diode designed to operate at  $\sim 100\text{GHz}$  had an n-type active layer with thickness  $L_A$  of  $3\mu\text{m}$  and doping  $N_A$  of  $1 \times 10^{17}\text{cm}^{-3}$ . The active layer was sandwiched between anode and cathode layers and their corresponding ohmic contacts. Both contact layers were  $0.1\mu\text{m}$ -thick and doped at  $1 \times 10^{19}\text{cm}^{-3}$ . The diameter of the diode  $D$  was selected to be  $50\mu\text{m}$ . A final three-dimensional model of GaN NDR diode oscillator is shown in Figure 2 together with the bias supply and a parallel  $LCR$  circuit used to represent the resonant cavity.

#### IV. Operation of GaN-based NDR Diode Oscillators

Custom *hydrodynamic* simulators have previously been used for studies of Gunn diodes [17,18]. The commercial simulator employed in our work also offers hydrodynamic capabilities, and has been used for large-signal power characterization of GaN NDR diode oscillators and, for comparison purposes, with GaAs Gunn diode oscillators. The equations used in the hydrodynamic simulations of GaN NDR diodes included Poisson's equation, carrier-continuity equations, and electron energy-balance equations. By including the NDR relaxation time  $\tau_{NDR}$  in the energy relaxation time used in the energy-balance equations, NDR in  $v$ - $F$  characteristics was constrained to frequencies lower than the NDR relaxation frequency  $f_{NDR}$ .

When a bias  $V_D$  exceeding the critical value  $V_{CR}=F_{TH} \times L_A$  is applied to the anode contact it results in an electric field  $F > F_{TH}$ . Under such conditions, the GaN NDR diode may become unstable and produce sustained oscillations. The power and frequency of the oscillations depend on the device design, biasing conditions, and termination impedance of the resonant cavity  $Z_L$ . The effect of the latter was modeled by adding a parallel  $LCR$  circuit as shown in Figure 2.

Thus, a  $W_z$  GaN NDR diode designed for W-band operation was biased using  $V_D=2 \times V_{CR}=90\text{V}$  and connected to the  $LCR$  circuit with  $L=17.5\text{pH}$ ,  $C=0.1\text{pF}$ , and  $R=50\Omega$ . Starting at time zero,  $V_D$  was increased from 0 to 90V with a large rise time of  $>1\text{ns}$  in order to minimize voltage overshoot. The growth of oscillations takes place over  $0.5\text{ns}$ , and is followed by a region of sustained oscillations. The dynamic  $I$ - $V$  trace corresponding to sustained oscillations is shown in Figure 3 together with a stable DC  $I$ - $V$  curve simulated for case when the GaN diode was connected directly to a voltage source.

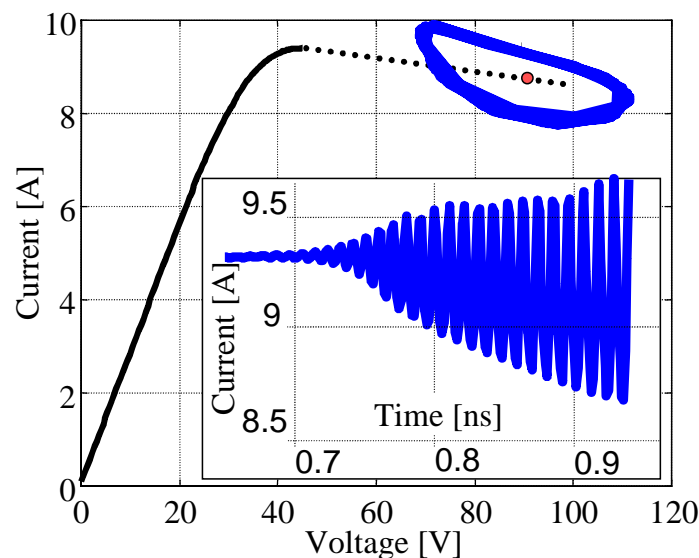


Figure 3.  $I$ - $V$  trace of observed oscillations (build-up of oscillations is shown on the inset).

The figure also shows gradual build-up of the amplitude of current oscillations. Finally, voltage and current waveforms in the region of sustained oscillations were subjected to harmonic power analysis based on Fourier transformed and the obtained spectrum was used to determine the output power and the oscillation frequency.

The power and frequency capability of GaN NDR diodes were compared with that of GaAs Gunn diodes by simulating the performance of the corresponding oscillators. The nominal GaAs Gunn diode had the same dimensions as the nominal GaN NDR diode:  $L_A=3\mu\text{m}$  and  $D=50\mu\text{m}$ , but the doping was reduced to  $3\times 10^{15}\text{cm}^{-3}$  in order to satisfy the design condition  $N_A < N_{CRIT}$  (see previous section). This design of GaAs Gunn diode was analogous to published descriptions of Ka-band Gunn diodes in reference [19]. The bias  $V_D$  for both GaN- and GaAs-based devices was selected to be twice the critical bias  $V_{CR}$  and, for nominal designs, was  $90\text{V}$  and  $2.1\text{V}$ , respectively. Designs of  $LCR$  circuits were optimized to provide maximum output power when used with devices of nominal designs. The results obtained for GaAs and GaN diodes with varying thickness of the active layer are shown in Figure 4.

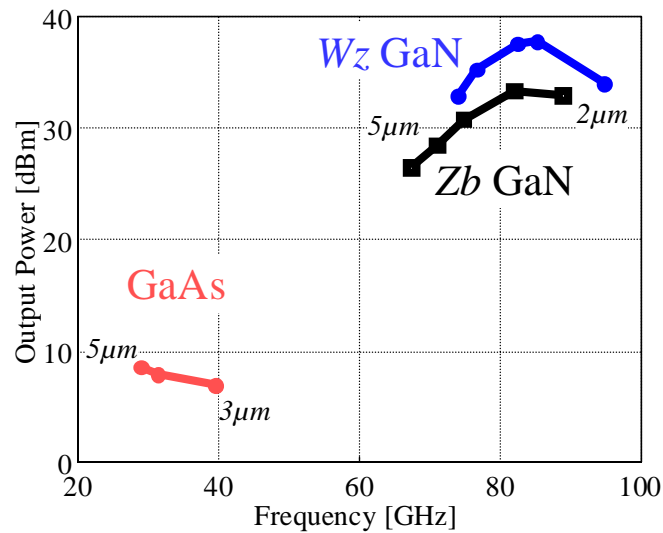


Figure 4. Frequency-power diagram comparing GaAs and GaN NDR diodes

The simulations were conducted for the NDR diodes made of both  $W_z$  and  $Z_b$  phases of GaN in order to account for uncertainty in published  $v$ - $F$  characteristics. The simulations showed that the overall characteristics of GaN-based NDR diodes outperform those of GaAs Gunn diodes in terms of output power and frequency of oscillations independent of the specific  $v$ - $F$  characteristics used to model material properties of GaN. Thus, given the same thickness of the active layer, the operation frequency of GaN NDR diodes ( $65$ - $95\text{GHz}$ ) was approximately twice that of GaAs Gunn diodes ( $27$ - $40\text{GHz}$ ), while given the same device area, the maximum output power of GaN NDR diodes was  $\sim 35\text{dBm}$  compared with  $\sim 10\text{dBm}$  for GaAs Gunn diodes.

The possibility of fundamental THz signal generation using GaN-based sources was investigated by optimizing the design of GaN NDR diodes for operation at higher frequency. Thus, following the results of Figure 1, the thickness of the active layer was reduced from  $3$  to  $0.3\mu\text{m}$  in order to reduce transit time while the doping of the active layer was increased from  $10^{17}\text{cm}^{-3}$  to  $10^{18}\text{cm}^{-3}$  in order to reduce the dielectric relaxation time. At the same time, the size of the diode was decreased from  $50$  to  $10\mu\text{m}$ , which allowed minimization of parasitic shunt capacitance as required for operation at submillimeter-wave frequencies. Large-signal

hydrodynamic simulations of the THz GaN NDR diode with  $0.3\mu\text{m}$ -thick  $10^{18}\text{cm}^{-3}$ -doped active layer revealed appearance of sustained oscillations with fundamental frequency exceeding  $700\text{GHz}$  as illustrated by the output power spectra in Figure 5.

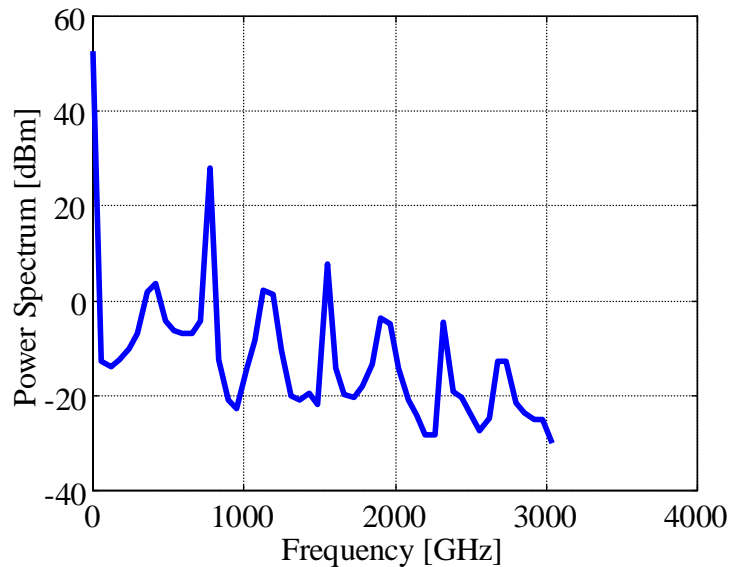


Figure 5. Simulated output power spectrum of THz GaN-based NDR oscillator.

## V. MOVPE Growth of GaN NDR Diode Layers

Layers have been grown by metalorganic vapor-phase epitaxy (MOVPE) in a home-built horizontal quartz reactor. Substrates were placed on a graphite susceptor, which is heated by  $10\text{KW}$  RF generator. Growth was performed at low pressure ( $60 - 110\text{torr}$ ) on c-plane sapphire substrates using  $\text{TMGa}$ ,  $\text{TMAI}$ , and  $\text{NH}_3$  as precursors. First, a thin,  $\sim 20\text{nm}$  thick GaN buffer layer was grown at  $515^\circ\text{C}$ , followed by the high-temperature growth of the bulk GaN layers at  $1120^\circ\text{C}$ . Growth rates for GaN were  $\sim 1.4\mu\text{m/h}$  using a V/III ratio of  $\sim 1600$ .

Using the low-temperature GaN-buffer approach, high-temperature grown undoped bulk GaN layers were smooth, transparent, and uniform. GaN layers with low background carrier concentration are required for successful development of NDR diodes. In addition, NDR diodes use contact layers, which should be highly n-doped to allow for low contact and access resistances. GaN growth conditions for the bulk and especially for the buffer layer have been carefully optimized to satisfy those requirements. After optimization of the buffer thickness, increasing the reactor pressure from  $60$  to  $110\text{torr}$  during both buffer and bulk GaN growth led to a decrease of the background carrier concentration by  $50\%$  to less than  $2 \times 10^{17}\text{cm}^{-3}$  in thin ( $\sim 0.7\mu\text{m}$ ) GaN test layers. Further increase of the reactor pressure led, however, to a deterioration of the electrical characteristics. Increasing the layer thickness to only  $1.4\mu\text{m}$  further decreased the background carrier concentration by another  $50\%$  to  $1.2 \times 10^{17}\text{cm}^{-3}$ , while at the same time increasing the mobility by  $20\%$ , thus providing good material quality for NDR device applications.

Si-doped GaN layers have been grown and investigated to provide low-resistance contact layers for the NDR diodes. Carrier concentration has been found to depend linearly on the  $\text{Si}_2\text{H}_6$  source flow. While Hall mobility decreases with increasing carrier concentration, high-doped contact layers ( $n = 1 \times 10^{19}\text{cm}^{-3}$ ) still have  $\mu > 100\text{cm}^2/\text{Vsec}$ .

After completing the test layers and growth parameter optimization, NDR diode device structures have been grown. The cross-section of the GaN NDR diodes consisted (starting from the top) of the anode layer ( $n^+=1\times 10^{19} \text{cm}^{-3}$ ,  $t=0.15\mu\text{m}$ ), the active layer ( $n^-=1-2\times 10^{17} \text{cm}^{-3}$ ,  $t=2.5\mu\text{m}$ ), and the cathode layer ( $n^+=1\times 10^{19} \text{cm}^{-3}$ ,  $t=0.5\mu\text{m}$ ).

## VI. Fabrication and Characterization of GaN NDR diodes

The NDR diodes were realized on circular mesas formed by dry etching. First, isolation mesas were formed by removing all GaN layers outside the active device area down to the sapphire substrate. Secondly, anode mesas were formed by etching through the anode and active layers down to the second  $n^+$  (cathode) layer. For the experimental layers investigated here, this required  $4.6\mu\text{m}$ -deep isolation etch and  $3.1\mu\text{m}$ -deep anode mesa etch. The dry etching was performed in a low-pressure RIE ( $15\text{mT}$ ) in  $\text{CCl}_2\text{F}_2:\text{Ar}_2$  ( $1:1$ ) atmosphere. The RF power for plasma generation was set to  $150\text{W}$ . This technology employs Ti/Ni masks and produces mesas with near-vertical walls with a GaN etch rate of  $50\text{nm}/\text{min}$ . GaN-based NDR diodes employ two ohmic contacts: anode and cathode. The anode contact was deposited on the top  $n^+$  layer and the cathode was deposited on the bottom  $n^+$  layer. *Ti/Al/Ti/Au/Pt* metals were used for cathode ohmic contacts. *Ti/Ni* metals used for etching mask were used to realize the anode contact on the top  $n^+$  layer. Ohmic metallization was followed by plating of Au interconnects, airbridges, and probing pads combined with integrated on-wafer heatsinks. A fabricated GaN NDR diode suitable for high-frequency on-wafer testing is shown in the SEM photograph of Figure 6.

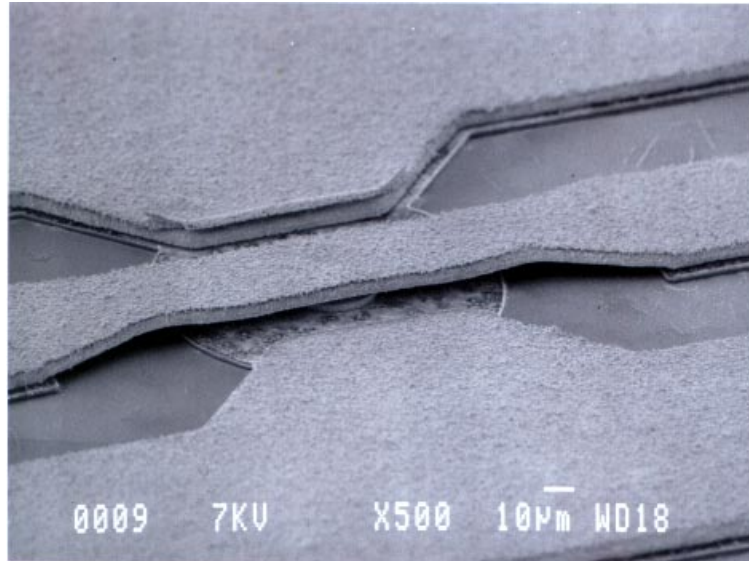


Figure 6. SEM photograph of fabricated GaN NDR diode

Electrical characterization of the fabricated devices revealed increased voltage and current capabilities of the GaN-based NDR diodes. Thus, pulsed I-V characteristics for biasing voltage  $V_D$  and current  $I_D$  up to  $40\text{V}$  and  $1\text{A}$ , respectively, were recorded. However, the low thermal conductivity of sapphire substrates ( $0.3\text{W}/\text{Kcm}$ ) led to self-heating of the integrated devices and prohibited application of DC or pulsed biases required for further testing. Use of GaN NDR diode layers grown on SiC substrates with high thermal conductivity ( $5\text{W}/\text{Kcm}$ ) or removal of sapphire substrates by laser-ablation is planned to be employed in future fabrication runs to improve the efficiency of heat removal.

## VII. Conclusions

The microwave characteristics of GaN NDR diode and GaAs Gunn diode oscillators were evaluated by performing large-signal harmonic power analysis of current and voltage waveforms corresponding to sustained oscillations. The analysis showed that GaN-based NDR diodes outperform GaAs Gunn diodes independent of the specific  $v$ - $F$  characteristics used to model material properties of GaN. GaN NDR diodes optimized for THz operation demonstrated a possibility of fundamental operation with frequency exceeding  $700\text{GHz}$ . The increased frequency capability offered by GaN NDR sources is due to a significantly higher electrical strength of this wide-bandgap material which allows operation with thinner and higher-doped active layers, compared to that of Gunn diodes made of conventional III-V compounds. GaN NDR layers designed for W-band operation were grown on sapphire substrates and integrated GaN NDR diodes were fabricated using dry etching techniques. Electrical characterization of the fabricated devices revealed their high voltage and current capabilities. Laser ablation techniques are expected to allow fabrication of devices with low thermal resistance as required for device optimization.

## References

- [1] P. J. Bulman, G. S. Hobson, B. C. Taylor, "Transferred Electron Devices", Academic Press, London and New York, 1972
- [2] H. Eisele and G. I. Haddad, "Efficient power combining with D-band (110-170GHz) InP Gunn devices in fundamental-mode operation", *IEEE Microwave and Guided Wave Letter*, vol.8, no.1; Jan. 1998; p.24-6
- [3] J. Kolnik et al., "Electronic Transport Studies of bulk zinc-blende and wurtzite phases of GaN based on an ensemble Monte Carlo calculation including a full zone bandstructure", *J. Appl Phys*, 78 (2), July 1995, p 1033-1038
- [4] S. Krishnamurthy et al, "Bandstructure effect on high-field transport in GaN and GaAlN", *Applied Physics Letters*, 71 (14), 6 October 1997, p 1999-2000
- [5] E. Alekseev and D. Pavlidis, "Microwave Potential of GaN-based Gunn Devices", *Electronics Letters*, vol. 36, no. 2, 20 January 2000, p. 176-178
- [6] B. E. Foutz et al., "Comparison of high field electron transport in GaN and GaAs", *Appl Phys Lett*. 70 (21), 1997, p 2849-2852
- [7] S. Wu, A. F. M. Anwar, "Monte-Carlo Simulation in Submicron GaN  $n^+nn^+$  Diodes", *1999 International Semiconductor Device Research Symposium*, Charlottesville, VA, Dec. 1-3, 1999
- [8] E. Alekseev and D. Pavlidis, "DC and High-Frequency Performance of AlGaIn/GaN Heterojunction Bipolar Transistors", *Solid-State Electronics*, , v. 44, n. 4, p 245-252, April 2000
- [9] S. N. Mohammad and H. Morçoç, "Progress and Prospects of Group-III Nitride Semiconductors", *Prog. Quant. Electr.*, vol.20 no 5/6, pp. 361-525, 1996

- [10] Z. Z. Bandic et al., "Nitride Based High Power Devices: Transport Properties, Linear Defects, and Goals", *1998 MRS Symposium Proceedings*, Vol. 512, p 27-32, 1998
- [11] J. Kolnik et al., "Monte Carlo calculation of electron initiated impact ionization in bulk zinc blende and wurtzite GaN", *J. of Appl. Phys.*, vol. 81 (12), p 727-733, 1997
- [12] V. A. Dmitriev et al., "Electric Breakdown in Nitride PN Junctions", *MRS Symposium Proceedings*, vol. 395, p 909-912, 1996
- [13] U. D. Bhapkar and M. S. Shur, "Monte Carlo calculation of velocity-field characteristics of wurtzite GaN", *J. Applied Physics*, 82(4), p 1649-1655, 1997
- [14] A. B. Chen (see also [4]): private communications
- [15] B. E. Foutz et al., "Comparison of high field electron transport in GaN and GaAs", *Appl. Phys. Lett.* 70 (21), p 2849-2852, 1997
- [16] M. Shur, "GaAs Devices and Circuits", Plenum Press, New York and London, 1987
- [17] M. F. Zybura et al., "100-300 GHz Gunn oscillator simulation through harmonic balance circuit analysis linked to a hydrodynamic device simulator", *IEEE Microwave and Guided Wave Letters*, V. 4, N. 8, p 282-284, 1994
- [18] V. A. Posse and B. Jalili, "Gunn effect in heterojunction bipolar transistors", *Electronics Letters*, Vol. 30, No. 14, p. 1183-1184, 1994
- [19] T. G. Ruttan, "High-Frequency Gunn Oscillators", *IEEE Transactions on Microwave Theory and Techniques*, p 142-144, February 1974

# Broadband Fixed-Tuned Subharmonic Receivers to 640 GHz

Jeffrey Hesler

University of Virginia Department of Electrical Engineering  
Charlottesville, VA 22903  
phone 804-924-6106  
fax 804-924-8818  
(hesler@virginia.edu)

## Abstract

This paper will describe the design and testing of solid-state subharmonically-pumped mixers from 380 GHz to 640 GHz. The main goal has been to develop robust, compact, solid-state room-temperature receivers with state-of-the-art sensitivity and broad IF bandwidths for applications such as airborne and space-based microwave sounding. Testing of a 380 GHz integrated mixer has yielded state-of-the-art performance, with a double-sideband (DSB) mixer noise temperature of 850 K and a mixer conversion loss of 8.5 dB (DSB) using 7 mW of local oscillator power. The success of this receiver is due to a combination of integrated diode technology and inherently broadband circuit designs achieved with modern high frequency design tools. The recently developed MASTER integrated diode technology allows for precise control of the circuit geometry and for the reduction of parasitic elements, thus allowing greater accuracy of computer simulations and therefore better high frequency performance and bandwidth. The split block geometry used for these mixers is relatively simple to machine, and yet allows for broad fixed-tuned RF and IF bandwidths, and is also compatible with molded and micromachined blocks. Finally, design techniques have been developed for these mixers that give excellent agreement with measurements, thus allowing for rapid prototyping. The major impact of this research is to demonstrate that excellent harmonically pumped mixers using integrated diodes and modern design tools are now a commercial possibility to at least 640 GHz.

## Mixer Layout

The mixer block, similar to that described in [1], is split in the E-plane of the RF and LO waveguides, thus simplifying mixer assembly and reducing the losses in the waveguides. The planar diode and mixer circuitry are fabricated on a 35  $\mu\text{m}$  thick fused-quartz substrate. The circuits are then placed in a shielded microstrip channel which runs perpendicular to the RF and LO waveguides. A schematic of the mixer block circuit configuration is shown in Fig. 1. The diodes are located in the microstrip channel. Waveguide-to-microstrip transitions are used to couple both the RF and LO into the channel. The microstrip metallization bridges across each guide, necessitating the use of reduced height waveguide to achieve reasonable fixed-tuned bandwidths [2]. For this mixer, half height waveguide was used for the RF, and third height waveguide was used for the LO. A low-pass microstrip filter is used to prevent the RF signal from coupling to the LO guide, and a short-circuited half-wave stub is used to provide the LO termination.

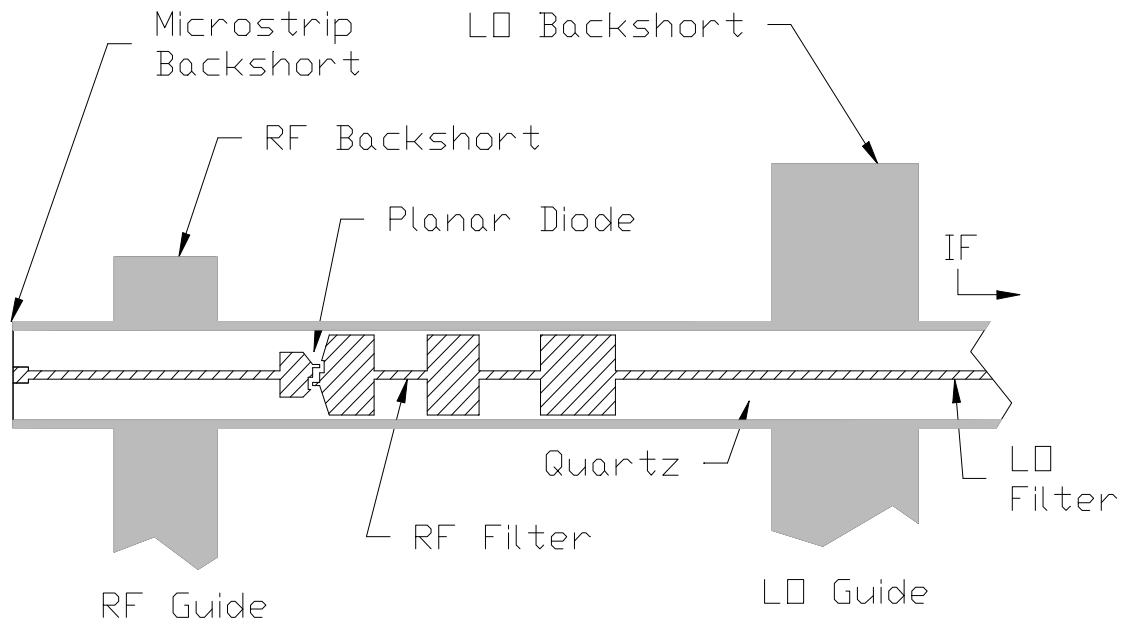


Fig. 1. Schematic of subharmonic mixer configuration.

### Integrated Diode Fabrication

Diode integration has many benefits. First the circuit geometry near the Schottky anodes is nearly planar and defined photolithographically. This simplifies the analysis of the circuit and allows more precise control of the embedding impedances. Second, the elimination of the high dielectric GaAs substrate reduces capacitance. This improves coupling to the Schottky diodes and increases receiver bandwidth. Finally, the assembly of the mixer is much simpler and a higher level of repeatability is achieved. The fabrication process for the integrated diodes is described in [3], and a view of one of the circuits is shown in Fig. 2.

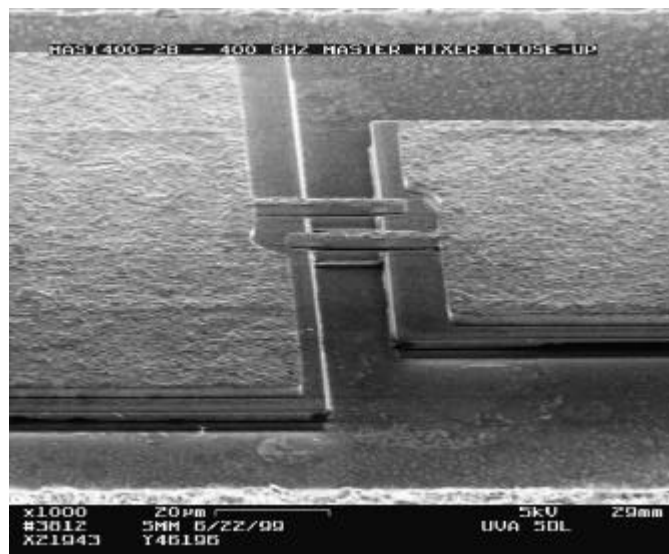


Fig. 2. SEM of an integrated anti-parallel mixer circuit.

## 400 GHz Mixer Design and Testing

The mixer was designed using Ansoft's High Frequency Structure Simulator [4] to model the waveguide transitions, integrated-planar-diode and the quartz circuit. Coaxial probes were artificially introduced at the two diode junctions during the finite element modeling to allow the direct prediction of the diode embedding impedance [5,6]. The loop parasitics predicted for a planar diode with 20  $\mu\text{m}$  fingers was a finger-to-pad capacitance ( $C_{FP}$ ) of 2.5 fF and a finger inductance ( $L_F$ ) of 10 pH. Harmonic balance simulations were performed for the Scottky diode, which had an epitaxial layer doping of  $4 \times 10^{17} \text{ cm}^{-3}$  and an anode diameter of 0.8  $\mu\text{m}$ . The measured DC parameters for this diode were an ideality factor  $\eta=1.32$ , a saturation current  $I_{SAT}=3 \times 10^{-13} \text{ A}$ , and a series resistance  $R_s=10 \Omega$ . The zero bias junction capacitance was calculated to be 1.5 fF per anode based on the anode diameter and the epitaxial layer doping. The simulations predict a mixer conversion loss of 4.0 dB (DSB) and noise temperature of 300 K (DSB) using 1.5 mW of LO power. The total conductor and dielectric loss for the horn, waveguide, microstrip, and diode was estimated to be about 2 dB. Using this estimate the predicted performance is a mixer conversion loss of 6 dB (DSB) and mixer noise temperature of 650 K (DSB). The simulations predict a usable RF bandwidth of better than 20% fixed tuned. The LO bandwidth is difficult to estimate since it is closely linked to the amount of power available from the LO source.

The local oscillator power for this mixer was provided by a Gunn oscillator near 100 GHz with 75 mW output power driving a planar balanced doubler with output power greater than 15 mW at 200 GHz [7]. The sensitivity of the mixer was measured at room temperature using broadband IF amplifiers covering the range from 2-12 GHz. An attenuator was used to vary the IF noise temperature, thus allowing the measurement of the mixer parameters.

Fig. 3 shows a fixed-tuned frequency sweep of a 425 GHz mixer. The upper limit of the

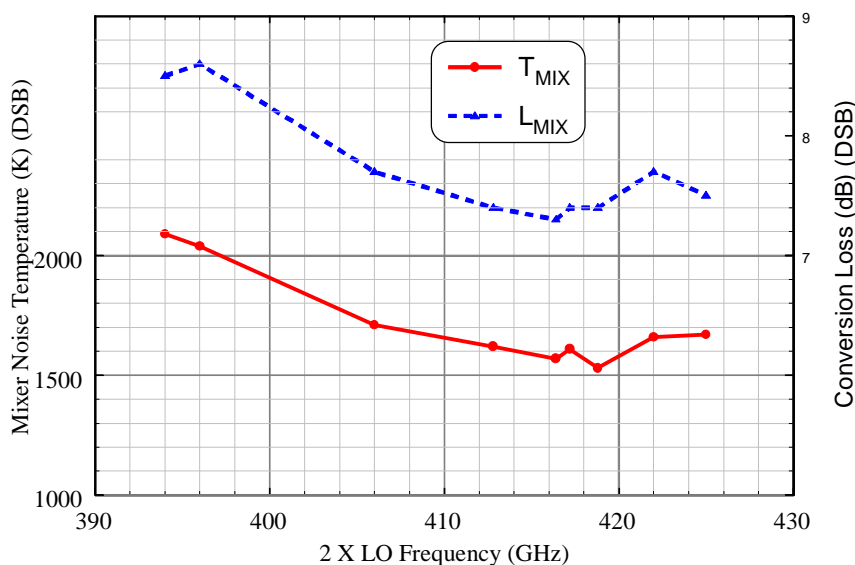


Fig. 3. LO Frequency sweep with fixed backshorts for 425 GHz subharmonic mixer.

frequency range was set by the Gunn oscillator and not the mixer. Fig. 4 shows a typical IF sweep for the same mixer, indicating the broad IF bandwidth of this design. The diode's IF impedance was constant at about  $100\ \Omega$  up to at least 12 GHz, and a mismatch to the  $50\ \Omega$  amplifier impedance was accepted. The slight increase in the mixer noise temperature at the highest frequencies is caused by losses in the Duroid IF circuit, which was designed for operation up to 6 GHz, and could be shortened to improve IF bandwidth. An IF sweep for a 380 GHz mixer is shown in Fig. 5. For this case the RF backshort was several wavelengths away from the circuit, thus causing the increase in noise temperature seen at the higher IF frequencies.

The LO power coupling for these mixers was optimized for operation at 425 GHz, and the 425 GHz mixer required less than 2 mW of LO power. The LO coupling for the 380 GHz mixer used the 425 GHz LO coupling circuit, and the LO power required increased to 7 mW. This LO power requirement could be reduced by re-optimization and re-fabrication of the LO and integrated diode circuit. Fig. 6 shows a fixed-tuned sweep of the LO frequency for the 380 GHz mixer.

### 500 and 640 GHz Mixer Designs

Simulations were performed to evaluate the performance of subharmonic mixers at 500 GHz and 640 GHz. For the first iteration of the design it was assumed that the dimensions of the finger/anode region of the diode were constant, while the rest of the circuit was scaled up to higher frequencies. This compromise would allow the use of previously developed diode fabrication techniques. However, as shown in Fig. 7, the simulations predicted that while the 500 GHz circuit still behaved reasonably well, the mixer's performance was severely degraded at 640 GHz. Further examination revealed that the loop resonance between the finger inductance and the junction and parasitic capacitance was causing this degradation [8]. To overcome this

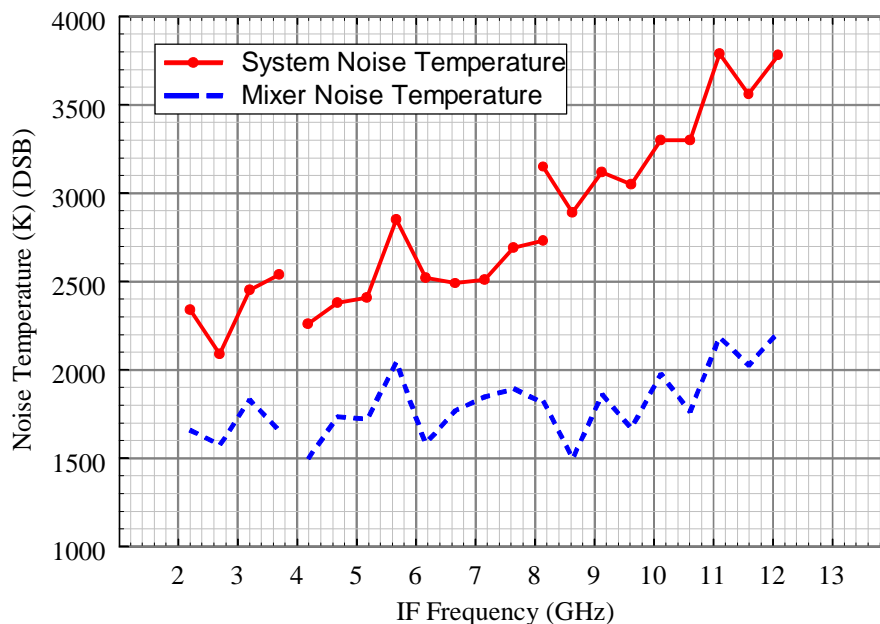


Fig. 4. IF sweep for 425 GHz Receiver.

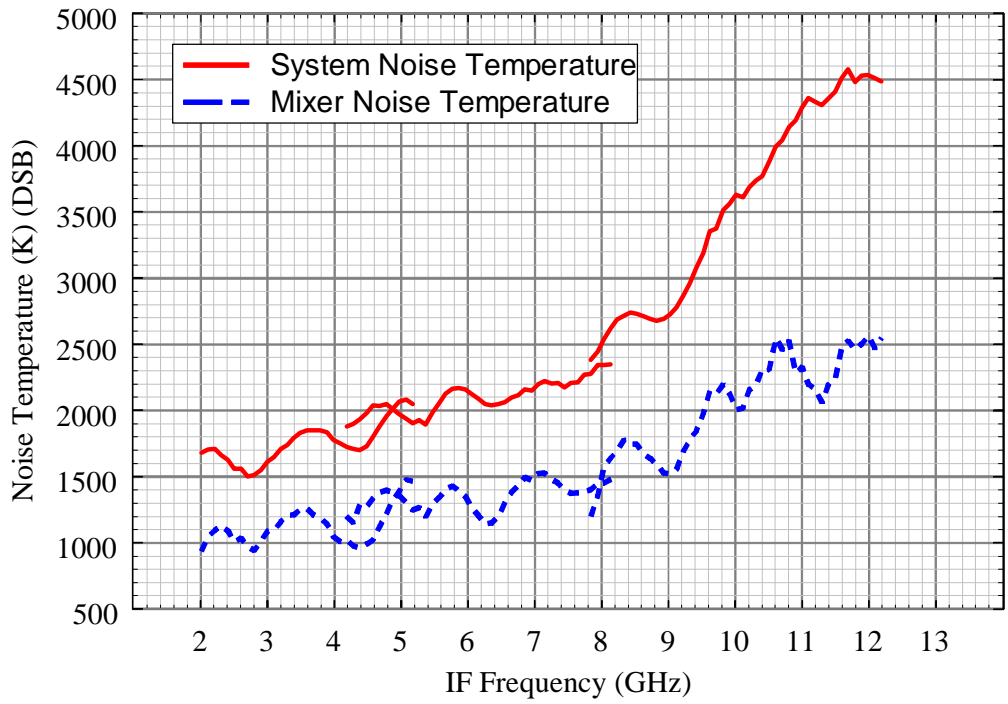


Fig. 5. IF sweep for 380 GHz Receiver. The RF backshort was several wavelengths away from the circuit, thus causing the increase in noise temperature at the high IF frequencies.

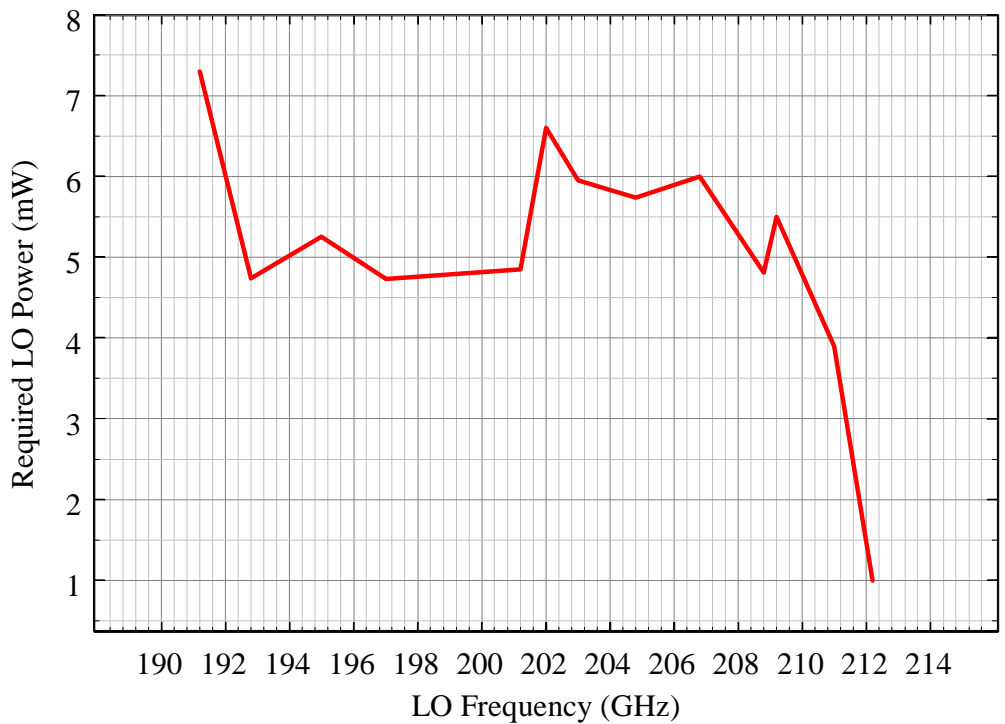


Fig. 6. Required LO power for 380 GHz Receiver.

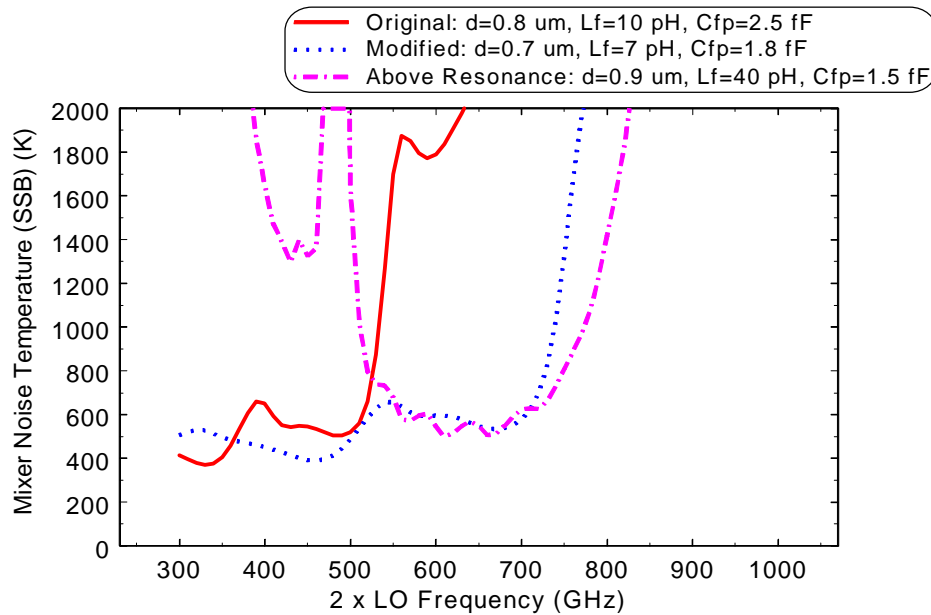


Fig. 7. Predicted performance for various 600 GHz diode configurations.

problem, it was necessary to reduce the finger length and the spacing between the fingers, thus pushing the loop resonance to higher frequencies. The predicted performance for the modified design is shown in Fig. 7.

Another design possibility for the 640 GHz mixer is to operate above loop resonance [8]. For this configuration, the finger length and the spacing between the fingers is increased, thus pushing the loop resonance down in frequency. The predicted performance for a 640 GHz design with  $L_F=40$  pH and  $C_{FP}=1.5$  fF is also shown in Fig. 7. The bandwidth for the mixer above resonance is predicted to be determined by external circuit consideration, and not by the loop characteristics. The above-resonance mixer was also predicted to require a similar amount of LO power and to have a similar sensitivity to fabrication and assembly variations as a below-resonance mixer. Using this configuration, the diode fabrication can be simplified, and the basic circuit configuration used at much higher frequencies with little sacrifice in performance.

## Conclusions

We have demonstrated a subharmonically pumped 380 GHz integrated-diode mixer with broad fixed-tuned LO, RF and IF bandwidths and excellent sensitivity. The mixer was pumped by an all-solid-state LO source. The mixer block was fabricated by standard split-block machining techniques, but was specifically designed to be compatible with micromachining [9] and molding technologies that have recently been demonstrated. The mixer design is also readily scalable to higher frequencies.

This research has enabled us to efficiently design and build submillimeter wavelength mixers that are not only highly sensitive, but also have enhanced mechanical robustness and large fixed tuned bandwidth. The coupling of these new analysis techniques and the new integrated diode technology can be easily extended to other circuit designs such as balanced and subharmonic mixers and frequency multipliers, and will allow the development of a new

generation of SubMillimeter-wave Integrated Circuits (SMICs) for a wide range of scientific, military and commercial applications.

### **Acknowledgments**

The author would like to thank Steve Marazita, Bill Bishop and Thomas Crowe for fabricating the integrated Schottky diode circuits used for this research. This work was supported by NASA-GSFC Grant No. NAG5-6507 and by the U.S. Army National Ground Intelligence Center under contract DAHC90-96-C-0010.

### **Bibliography**

1. A.V. Raisanen, D. Choudhury, R.J. Dengler, J.E. Oswald, and P. Siegel, "A novel split-waveguide mount design for millimeter- and submillimeter-wave frequency multipliers and harmonic mixers," *IEEE Microwave and Guided Wave Letters* Vol. 3, No. 10, Oct. 1993, pp. 369-371.
2. J.L. Hesler, K. Hui, R.M. Weikle, T.W. Crowe, "Design, Analysis and Scale Model Testing of Fixed-Tuned Broadband Waveguide to Microstrip Transitions," *Proc. of Eighth Int. Symp. on Space THz Tech.*, Cambridge, MA, pp. 319-325, March 25-27 1997.
3. S.M. Marazita, W.L. Bishop, J.L. Hesler, K. Hui, W.E. Bowen, and T.W. Crowe, "Integrated GaAs Schottky Mixers by Spin-On-Dielectric Wafer Bonding," *IEEE Trans. on Electron Devices*, Vol. 47, No. 6, pp. 1152-1157, June 2000.
4. Ansoft High Frequency Structure Simulator Version 5.0, Ansoft Corp., Four Station Square, Suite 200, Pittsburgh, PA 15219-1119, 1998.
5. J.L. Hesler, W.R. Hall, T.W. Crowe, R.M. Weikle, II, B.S. Deaver, Jr., R.F. Bradley, and S.-K. Pan, "Fixed-Tuned Submillimeter Wavelength Waveguide Mixers Using Planar Schottky Barrier Diodes," *IEEE Trans. Microwave Theory Tech.*, Vol. 45, pp. 653-658, May 1997.
6. J. Tuovinen, N.R. Erickson, "Analysis of a 170-GHz frequency doubler with an array of planar diodes," *IEEE-Trans. Microwave Theory and Techniques*, vol.43, no.4, pp. 962-968, April 1995.
7. D.W. Porterfield, "A 200 GHz Broadband, Fixed-Tuned, Planar Doubler," *Proc. of Tenth Int. Symp. On Space THz Tech.*, Charlottesville, VA, pp. 463-471, March 16-18 1999.
8. A.R. Kerr, "Noise and loss in balanced and subharmonically pumped mixers, Part II, Application," *IEEE Transactions on Microwave Theory & Techniques*, vol.MTT-27, no.12, Dec. 1979, pp.944-50.
9. K. Hui, J.L. Hesler, D.S. Kurtz, W.L. Bishop, and T.W. Crowe, "A Micromachined 585 GHz Schottky Mixer," submitted to *IEEE Microwave Guided Waves Lett.*, March 2000.

# Stabilized, Integrated, Far-Infrared Laser System for NASA/Goddard Space Flight Center

Eric R. Mueller, Joel Fontanella, and  
Robert Henschke  
DeMaria ElectroOptics Systems, Inc.  
1280 Blue Hills Ave.  
Bloomfield, CT 06002  
(806) 243-9557

## Abstract

DeMaria ElectroOptics Systems (DEOS) has delivered a highly-integrated, turn-key, Far-Infrared laser system to NASA/Goddard Space Flight Center, as a precursor for a system for SOFIA. This system has a number of unique features including: a permanently sealed-off 100W-class pump laser, an absolute heterodyne frequency lock for the pump laser, a folded extended-service sealed-off FIR laser, all electro-optics integrated within a compact easily transported housing, and a GUI controller. The absolute frequency lock not only simplifies the automated tune-up algorithms, but also improves the day-to-day absolute frequency reproducibility of the FIR output. This laser system is designed to be an instrument that can be successfully operated without extensive knowledge on the part of the user. The specifications, design, and performance results will be presented here.

This work was supported by NASA/Goddard Space Flight Center under contract number NAS5-97007.

## Introduction

The Stabilized Integrated Far-Infrared laser system (SIFIR, pronounced sī-fire) for NASA/Goddard represents a significant advancement in the state-of-the-art for FIR laser systems.

The initial design goals for the system were concentrated on ease of use, portability, and frequency & amplitude stability, and are presented in Table 1. As will be described later, the majority of these goals were met either by direct demonstration or by design analysis.

Table 1: SIFIR initial design goals.

Characteristic	Priority	Goal
Reliability	1	Operate without service for > 5000 hours
Amplitude Stability	1	<5 % long term <1 % short term
Ease Of Use	1	Autonomous starting and lockup, GUI interface displays multiple statuses, sealed-off FIR operation (see next characteristic)
FIR Operate Sealed-Off	1	Operate for 12 hrs with <10% degradation in output power
Range of Operation	1	1-3 THz
Prime Power	1	208-240 VAC, <3500 W
Long-Term Absolute Frequency Stability	2	300 kHz @ 2 THz over 8 hours after thermalization
Integrated Linewidth	2	< 50 kHz @ 2 THz
Package Size	2	<12x12x40" – head Rack mount – controller
Durability	2	Handling consistent with periodic transport
Parameter Recording	3	Software write file of system parameters vs time
Mass	3	50 kg for the laser head
Internal FIR Power Monitor	3	An internal FIR power detector

The SIFIR system uses the same permanently-sealed-off CO<sub>2</sub> laser technology DEOS employs in its commercial CO<sub>2</sub> lasers and in the space-based FIR system presently under construction at DEOS.<sup>1</sup> The FIR laser

technology used in the SIFIR is a combination of: development for the space-based FIR system, previous development for radar applications, and design efforts focussed on this program's needs.

### SIFIR Configuration

The configuration for the SIFIR system is illustrated in the photographs presented in Figure 1 and Figure 2, the drawing shown in Figure 3, and in the block diagram displayed in Figure 4. The form of the controller module was dictated by Goddard's requirements. The controller could just as easily be a 24x24x22" box and a separate lap-top computer for the GUI interface.

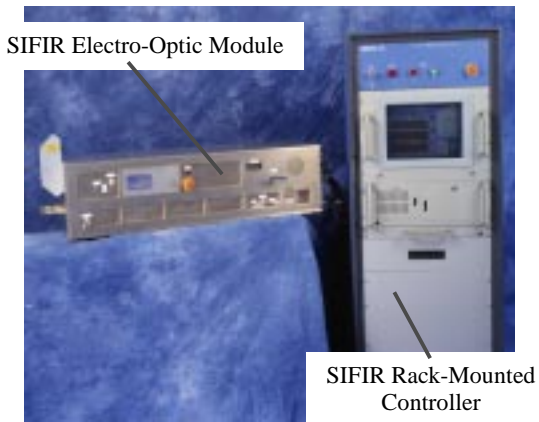


Figure 1: Photograph of the SIFIR system with the rack-mounted controller.

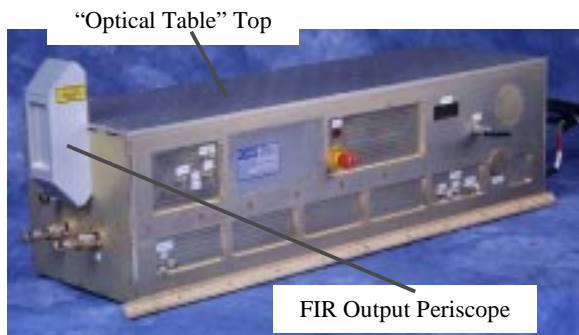


Figure 2: Photograph of the SIFIR Electro-Optic Module (laser head).

The control module contains: the laser RF power supplies, the main power

interface, the system DC power supplies, and the GUI control computer.

The Electro-Optic Module (EOM) contains: the pump laser, the local oscillator (LO) laser, the FIR laser, the IF offset-lock electronics, the LO hill-climber loop electronics, and the local loop supervisory micro processor ( $\mu\text{P}$ ).

The EOM is arranged in a "two-deck" H-structure where the pump laser and LO laser are located on the "bottom deck" and the FIR laser is located on the "top deck". The FIR gas handling system is integrated within the housing and offers access to four gas sources via "flip" valves located on one end of the EOM housing.

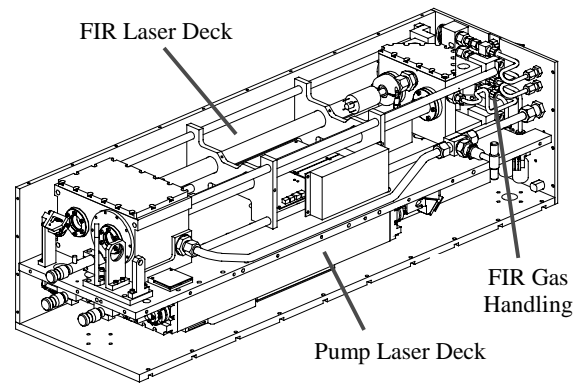


Figure 3: Drawing of the SIFIR EOM with the sides removed.

Both of the  $\text{CO}_2$  lasers are RF-excited and permanently sealed-off; the FIR laser operates sealed-off with an output degradation of less than 10 % in 12 hours, and can be operated without re-pumping for days at a time. The limitations on sealed-off operation of the FIR laser are caused by the use of elastomeric o-rings in several locations. These o-rings were used to provide for easy change of output couplers.

While the system runs reliably it has some behavior which will be improved prior to use on SOFIA. This behavior manifests itself as a requirement for the user to make slight adjustments to the pump laser differential micrometer grating control after

the first 20 minutes of operation and then potentially every 4-5 hours if the environmental temperature changes by  $\sim 5$  C over that time. There are primarily two causes for this undesired behavior. First, with the objective of obtaining larger pump powers at the weaker pump lines a non-standard waveguide geometry was selected. While this did have the effect of increasing the output power it did so at the expense of a significant increase in alignment sensitivity. Before the system was delivered, the alignment was eventually optimized for sensitivity instead of output power, effectively removing a large percentage of the output power gains achieved with the non-standard guide geometry. The second issue relates to the pump laser mounting option. In order to minimize package size, the pump laser was mounted directly to the housing center plate. While this mounting arrangement was also used for the LO laser and functioned very well in that case, in the pump laser it increased the alignment sensitivity of the pump laser, owing to the pump laser's lower stiffness ratio. This was further exacerbated by the waveguide geometry issue. In the future the pump laser will be mounted via a 3-point mount to the EOM housing. This will slightly increase the package height but Goddard has indicated that this will be acceptable.

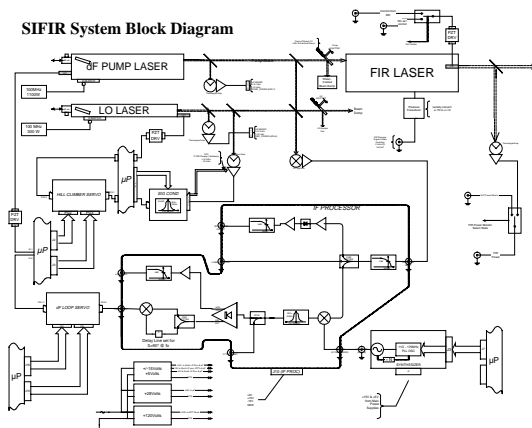


Figure 4: Block diagram of the SIFIR system.

The block diagram presented in Figure 4 illustrates the system interconnectivity and shows where functions are controlled by the  $\mu$ P vs by the system GUI controller. This block diagram will be further explained in the next section where the details of the pump frequency locking method are presented.

### Pump Laser Frequency Control

The pump frequency control approach is illustrated in Figure 5. In operation the pump and LO laser's gratings are set to the same rotational line. The LO laser is dither-stabilized to its line-center to form a frequency reference at the CO<sub>2</sub> frequency. A small sample of the pump laser is then mixed with this LO laser in a

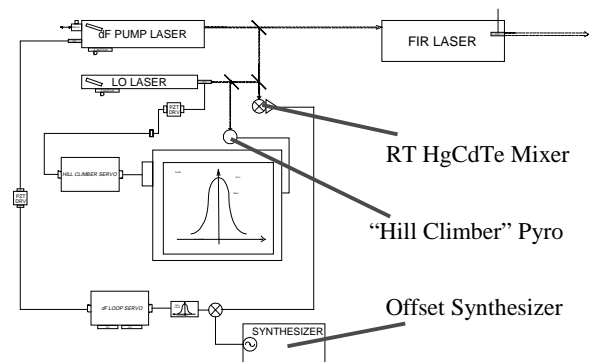


Figure 5: Block diagram of the pump-frequency locking technique.

room temperature HgCdTe mixer. This IF is then mixed with an offset synthesizer. The resulting IF is processed through a delay discriminator to generate an error signal for the pump laser piezoelectric transducer (PZT) control. The sign of the offset (ie. below or above CO<sub>2</sub> line center) is set with a simple sign flip in the error loop circuitry.

The minimum offset obtainable with this topology is determined by the narrowness and steepness of the last IF filter in the discriminator. In the present system a surface-acoustic-wave filter was employed and the minimum offset magnitude settable

for stable performance was 3 MHz. This minimum offset is sufficient to pump almost any FIR line optimally and any FIR line slightly off optimal.

The approach used in this work for absolute pump frequency control is very similar to an earlier technique applied for investigation of Autler-Townes splitting<sup>2</sup> and is a marked improvement in utility over the 4.3  $\mu\text{m}$  fluorescence Lamb dip locked LO used in the past<sup>3</sup> (as that technique requires a cooled detector and a cumbersome setup). However the fluorescence technique offers better absolute pump frequency accuracy (on the order of 3 kHz vs on the order of 100 kHz for the present technique) but this additional accuracy is not relevant for most FIR pumping applications.

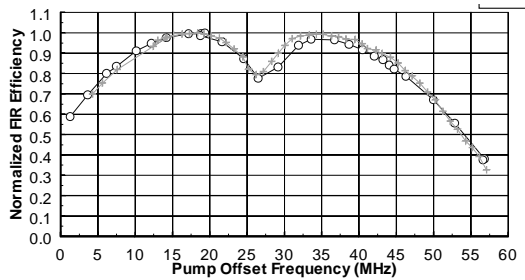


Figure 6: FIR laser efficiency vs pump frequency for a standing-wave resonator operating the 118.83  $\mu\text{m}$  line in  $\text{CH}_3\text{OH}$ .

In considering the implications of absolute pump frequency control one can look at the FIR efficiency vs pump frequency curve for a standing-wave FIR laser operating on the 118.83  $\mu\text{m}$  line in  $\text{CH}_3\text{OH}$  (see Figure 6). The behavior observed there is due to bi-directional pumping creating a “transferred” Lamb dip in the FIR gain.<sup>4</sup> Thus to tune-up such a FIR laser system the user must find both the optimal pump frequency and the optimal FIR cavity length. Owing to the broadness of the efficiency curve this process will tend to have a reproducibility error on the order of 5-10 MHz, depending on line. This error

will then be transferred to the FIR via Doppler pulling and absorption frequency pulling, and manifest itself as a FIR frequency reproducibility error. A lower limit estimate of this error can be calculated from the Doppler-only portion with

$$\Delta\nu = \nu_{epump} \left[ \frac{\nu_{FIR}}{\nu_{pump}} \right], \quad (1)$$

where  $\Delta\nu$  is the FIR frequency error,  $\nu_{epump}$  is the pump frequency error,  $\nu_{FIR}$  is the nominal FIR frequency, and  $\nu_{pump}$  is the nominal pump frequency. This effect is enhanced by absorption frequency pulling and was recognized in the past and its effect measured.<sup>5</sup> Depending on the FIR line this error can be on the order of 0.1 – 1 MHz. In many applications this magnitude of error is not significant but in sub-Doppler spectroscopy this effect can be quite significant.

While this certainly does not exhaust the sources of frequency error it is a significant contributor even in a stabilized FIR system. Another contributor, the pressure dependence of FIR frequency, is mitigated in this system by the fact that the FIR laser operates sealed-off – improving both the knowledge of pressure in the cell and the control & stability of that pressure.

The pump frequency control approach used here is one of the major features of this system. With this configuration the pump laser’s offset can be directly set via the offset-synthesizer. This offers dramatic advantages not only in FIR frequency reproducibility, but also in easy tune-up.

The tune-up advantages stem from the fact that the pump laser’s frequency can be directly set to the optimal point. Thus there is no need to separately optimize this control at start-up. The user simply sets the offset for optimal and then adjusts the FIR cavity length for optimal output.

Additionally the SIFIR system becomes a tool for determining the absolute optimal offset for any FIR line. In the SIFIR system the  $\mu\text{P}$  handles the locking and monitoring of the LO and pump loops, providing for a simple GUI to allow the user to select the pump frequency.

It should also be noted that the pump laser is a true waveguide laser and has NO mode adjustments required or available to the user.

### Integration Optics

The optical system which integrates this system consists of several parts: the pump – to – FIR laser optics, the heterodyne-offset optics, and the FIR power sampling optics.

A photograph of the pump deck of the SIFIR is presented in Figure 7. In that

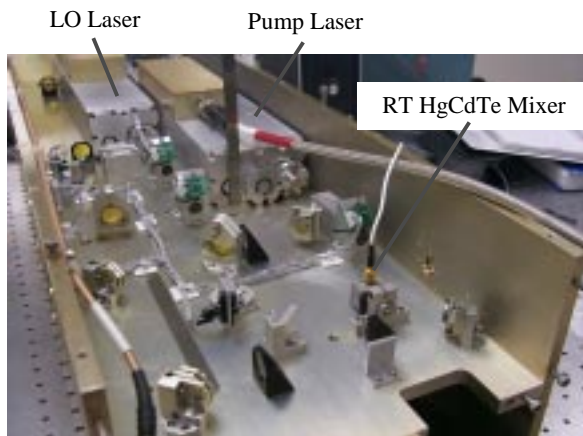


Figure 7: Photograph of the pump deck of the SIFIR EOM. Note 6" rulers for scale.

figure both  $\text{CO}_2$  lasers and all of the  $\text{CO}_2$  optics (except for the two mirrors which direct the pump beam into the FIR laser) are visible.

A plan view of the heterodyne optical area of the pump deck is shown in Figure 8. The solid red line represents the pump beam path, and the dashed blue line represents the LO beam path. Also visible are two shutters and two beam dumps.

These serve to: allow the user to operate the system without exciting the FIR laser, via the pump beam shutter and its water-cooled beam dump, and to send the majority of the LO beam out of the EOM to check the grating calibration or allow it to be “dumped” into the chill-plate-mounted LO beam dump. Both of these shutters are controlled and monitored via the GUI and  $\mu\text{P}$ .

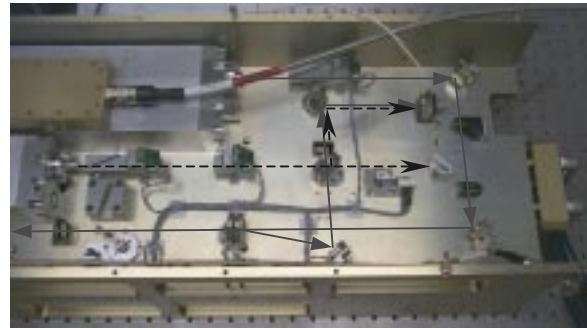


Figure 8: Plan view photograph of the heterodyne-offset optics area of the SIFIR. The solid (red) line represents the pump beam path. The dashed (blue) line represents the LO beam path.

The FIR power sampling optics consist of a  $8\ \mu\text{m}$  Mylar beamsplitter, a 50 mm focal length polyethylene lens, and a FIR thermopile detector. While this technique has significant wavelength and polarization dependence, the GUI software provides for independent individual calibration for each FIR line or use of an external power monitor also read by the SIFIR’s controller.

### FIR Laser

The FIR laser is a thermally-compensated design where the cavity length is set via a differential micrometer and/or PZT, and this length is maintained through thermal compensation. DEOS staff have extensive experience with this design approach and have obtained frequency stability results of 35 kHz over many hours after thermalization. Additionally, through

careful attention to thermalization alignment issues, this laser needs NO alignment adjustments; only the cavity length ever needs user adjustment.

The finite element analysis (FEA) results used in the thermal compensation design of the FIR laser are presented in Figure 9. Those results are only valid after warm-up and indicate a compensation frequency performance of 26 kHz/C at 200  $\mu\text{m}$ . From cold-start to thermalization the uncompensated FIR cavity length change was found to be

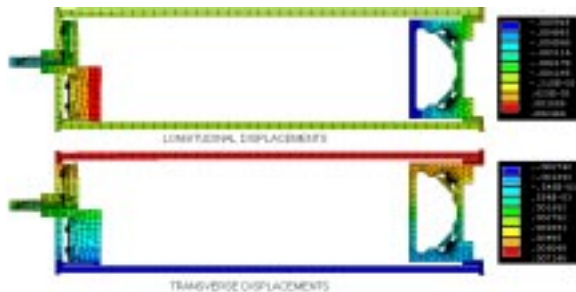


Figure 9: FEA results for the thermal compensation of the FIR laser. (These results are only valid after thermalization.)

15 - 18  $\mu\text{m}$ . This is a convenient result as the FIR PZT has a range of 20  $\mu\text{m}$  and the GUI program includes an FIR auto-tuning algorithm which can periodically correct for this change during warm-up. The 3  $\mu\text{m}$  range of this measurement is due primarily to submicron-scale slip-stick thermalization shifts from one day to the next.

A photograph of the FIR laser is presented in Figure 10. The FIR laser is a folded standing-wave cavity with quartz

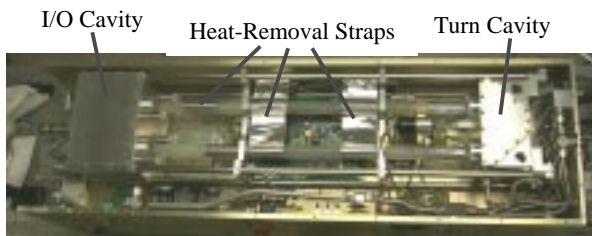


Figure 10: Photograph of the FIR laser.

waveguide sections and ferro-fluid alignment feedthroughs. Heat is removed from the guide sections via metal straps secured from the guides to the water-cooled housing. This basic laser design could also be embodied in a ring configuration by changing the I/O cavity. FIR pressure is measured with a Pirani gauge. While this gauge has a gas composition dependence, it is perfectly applicable as a reference-for-optimal gauge.

The FIR laser performed well in spatial mode, stability, and output power. While the folded design decreases the size of the laser it also decreases its efficiency by roughly a factor of 1.7. At 118.83  $\mu\text{m}$  in  $\text{CH}_3\text{OH}$  we obtained 125 mW in a clean spatial mode (see Figure 11). The stability

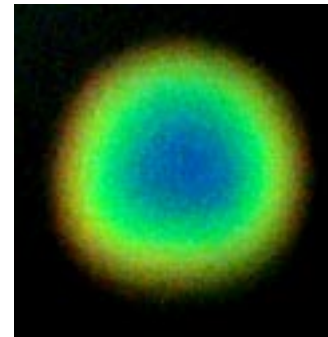


Figure 11: Spatial mode of the FIR laser at 118.83 $\mu\text{m}$ . (This is a digital picture of a liquid crystal sheet image.)

of the output is viewed in two different timescales: hours, and minutes. The long-term (over hours) stability was 5 %. This was dominated by thermal effects in the FIR-to-pump laser feedback. The short-term stability (over minutes) was <0.2 %.

In typical operation the user simply pumps the FIR laser out, fills the laser to the desired pressure, closes off the pump, and shuts the pump down. The user can then expect the system to operate satisfactorily all day (or even longer) without any additional service.

## Graphical User Interface (GUI) Controller

The GUI controller is another major feature of this SIFIR system. It provides for the easy operation and monitoring of the system by a user with little specific laser knowledge. The system can be operated in a “manual” start-up mode or in an auto start-up mode.

In manual mode (or after auto start-up completes) the CO<sub>2</sub> lasers and their frequency locks are controlled with virtual buttons on the screen. Also displayed on the screen are other system parameters including: the status of all of the lasers, their respective PZT voltages, the FIR pressure, and the FIR power. The user has the option of changing FIR lines (either choosing from the catalog or manually optimizing a “new” line) or writing parameters for a “new” line into the catalog.

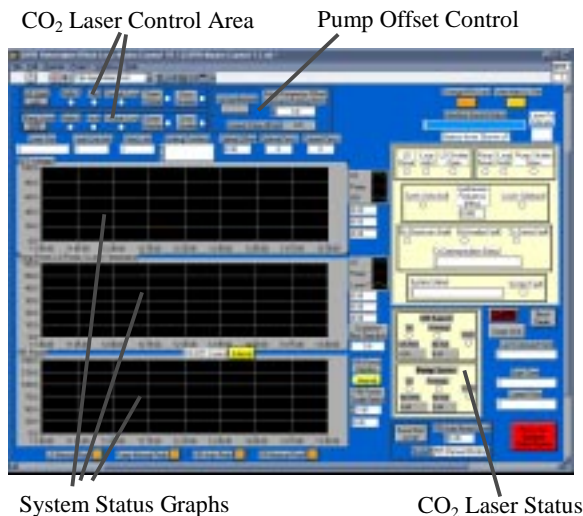


Figure 12: Screen “shot” of the GUI controller user interface.

In auto start-up, the user selects the desired line from the catalog and the system locks the lasers and prompts the user when FIR pumping can begin. At this point the user checks the pressure in the FIR laser against the optimal pressure recorded in the on-line catalog and presses the “Open Pump Shutter” button to begin exciting the FIR

laser. In any mode the user has the option of having the system write a telemetry file which records user and system actions/status every ~3 seconds.

The automatic locking of the pump laser is at the heart of the autonomous operation of the SIFIR. A temporal view of the auto pump lock algorithm is presented in Figure 13. The algorithm ramps the pump PZT and looks at the IF log video to determine if the pump laser is near the correct frequency offset magnitude, and then looks at the order in which the Freq Hi and Freq Lo bits toggle to determine if the sign is correct. Once the correct offset has been found the  $\mu$ P sets the pump PZT to this position and closes the pump frequency control loop via a MDAC. When the system is first turned on (for the first 15-20 minutes) this algorithm will not work reliably as the cavity length is drifting too rapidly for the PZT reset portion to leave the pump laser at the correct frequency for lock capture.

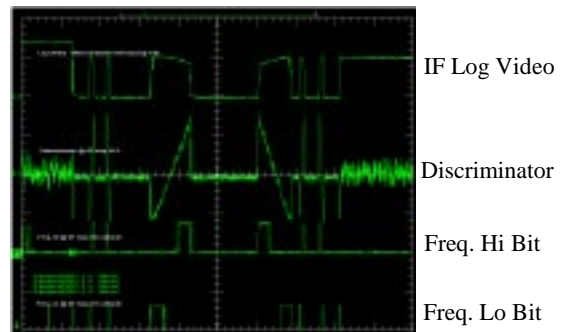


Figure 13: Temporal view of the autonomous acquisition algorithm for the pump-laser offset frequency.

To automatically determine if the LO loop or the pump loop need resetting, the  $\mu$ P monitors the PZT voltages and initiates a reset if these PZT voltages get within 10 % of max or min voltage.

## System Performance

The system performance can be compared against the goals laid out in Table

1. This comparison is presented in Table 2. All the goals but one were met. The laser head mass goal (which was lower priority) was 50 kg and in the delivered system the head mass was 54 kg. The issue of occasional pump grating differential micrometer adjustments while not desirable, did not significantly degrade the usability of the system. Effectively this system is operated with occasional (every 4-5 hours) user adjustment of two controls: the FIR cavity length, and the differential control on the pump laser grating mount. In the future this

Table 2: System performance against initial goals.

Characteristic	Met	Measured How
Reliability	Yes	Life data from similar pump and FIR lasers
Amplitude Stability	Yes	Tested <5 % over many hours <0.2 % over minutes
Ease Of Use	Yes	GUI-driven control of all major functions
FIR Operate Sealed-Off	Yes	Tested
Range of Operation	Yes	Tested from 1.2 – 3.1 THz
Prime Power	Yes	208-240 VAC, 3000 W
Long-Term Absolute Frequency Stability	Yes	Analysis & pump locking reproducibility measurements (Lamb dip)
Integrated Linewidth	Yes	Measurements of pump width and comparison of measurements with similar systems
Package Size	Yes	Measured 12x12x38"
Durability	Yes	Measured performance before and after repeated moves.
Parameter Recording	Yes	Software write file of system parameters vs time
Mass	No	Goal was 50 kg, actual is 54 kg
Internal FIR Power Monitor	Yes	Internal detector present and used by controller.

system will operate with only one user adjustment, the FIR cavity length control. And even that control does not require adjustment after thermalization.

## Conclusions

The SIFIR system delivered to Goddard Space Flight Center is a FIR laser appliance. While the user has access-to and control-of the system parameters in great detail, these parameters are normally set and maintained by the autonomous computer controller. This approach yields a “user system,” where the user can concentrate on the measurement at hand instead of making the laser work.

## Acknowledgements

The authors would like to acknowledge the contributions to this project of a number of talented scientists and technologists including: Adrian Papanide, Shef Robotham, Gordon Chin, Lanny Laughman, Leon Newman, John Kennedy, and Dick Hart.

## References & End Notes

- <sup>1</sup> E. R. Mueller, W. E. Robotham, Jr., R. P. Meisner, R. A. Hart, J. Kennedy, and L. A. Newman, “2.5 THz Laser Local Oscillator for the EOS CHEM 1 Satellite,” Proc. Ninth Int. Symp. Space THz Techno., 563 (1998)
- <sup>2</sup> C. R. Pidgeon, W. J. Firth, R. A. Wood, A. Vass, and B. W. Davis, “Two-Photon Light Shift and Autler-Townes Splitting in Optically-Pumped FIR Lasers,” Int. J. IR MMW, **2**(2), 207 (1981)
- <sup>3</sup> B. Dahmani & A. Claron, “Frequency Stability Limitations of Optically Pumped Lasers Due to Pump Laser Instability Through Dispersion Effect,” Int. J. IR MMW, **5**(7), 1053 (1984)
- <sup>4</sup> The situation is different in ring FIR lasers which switch direction near the FIR absorption center. But this technique would be applicable and potentially even more important for ring laser pumping.
- <sup>5</sup> R. L. Crownover, H. O. Everitt, F. C. DeLucia, and D. D. Skatrud, “Frequency stability and reproducibility of optically pumped far-infrared lasers,” Appl. Phys. Lett, **57**(27), 2882 (1990)

# **Superconducting Transition Edge Sensor Bolometer Arrays for Submillimeter Astronomy**

**Dominic J. Benford, Christine A. Allen, Alexander S. Kutyrav,  
S. Harvey Moseley, Richard A. Shafer**

NASA - Goddard Space Flight Center, Code 685, Greenbelt, MD 20771

**James A. Chervenak, Erich N. Grossman, Kent D. Irwin,  
John M. Martinis, Carl D. Reintsema**

NIST - Boulder, MS 814.09, Boulder, CO 80303

## **Abstract**

Studies of astrophysical emission in the far-infrared and submillimeter will increasingly require large arrays of detectors containing hundreds to thousands of elements. The last few years have seen the increasing from one to a few tens of bolometers on ground-based telescopes. A further jump of this magnitude, to a thousand bolometers, requires a fundamental redesign of the technology of making bolometer arrays. One method of achieving this increase is to design bolometers which can be packed into a rectangular array of near-unity filling factor while Nyquist-sampling the focal plane of the telescope at the operating wavelengths. In this case, the array becomes more nearly analogous to the arrays used in the near-infrared which underwent a substantial growth during the last decade. A multiplexed readout is necessary for this many detectors, and can be developed using SQUIDs such that a  $32 \times 32$  array of bolometers could be read out using 100 wires rather than the  $>2000$  needed with a brute force expansion of existing arrays. Superconducting transition edge sensors are used as the detectors for these bolometer arrays. We describe a collaborative effort currently underway at NASA/Goddard and NIST to bring about the first astronomically useful arrays of this design, containing tens of bolometers. This technology is well-suited to low-background instruments such as SPIRE on FIRST and SAFIRE on SOFIA, and can also be used in broadband, high-background instruments such as HAWC on SOFIA.

Keywords: bolometer, far-infrared, submillimeter, superconducting, SQUID, detector array, multiplexer, transition edge sensor

## **Introduction**

Advances in bolometer fabrication have made possible the construction of submillimeter-wavelength cameras with several tens of detectors (e.g., CSO - SHARC (Wang *et al.* 1996), JCMT - SCUBA (Holland *et al.* 1996), IRAM 30m (Kreysa *et al.* 1998)).

Currently, the sensitivity of these instruments is background-limited, so deep- and wide-field surveys are limited by the number of detectors and the amount of observing time available. In order to achieve a leap to a thousand detectors (of order the largest size usable on current and foreseen telescopes), a scalable detector architecture must be demonstrated. Such an architecture should deal with both the fabrication of an array and the electronics used to read it out. Conventional technologies use semiconducting thermistors as the detection element, with the alternative being superconducting transition edge sensors. Another common feature of most bolometer arrays is the use of feedhorn-coupled (typically spaced by  $2f\lambda$ ) arrays, with the alternative being a filled array ( $f\lambda/2$ ) of close-packed square bolometers. In this paper, we present a suggestion for an architecture which can be readily scaled to kilopixel arrays using superconducting sensors and a multiplexed amplifier technique (Chervenak *et al.* 1999) to reduce the wiring overhead. In our implementation, we choose to use the close-packed geometry, which yields an improvement in mapping speed per focal plane area (Bock *et al.* 1998). However, the superconducting detectors can be used regardless of array geometry, and are equally feasible for arbitrary array implementations.

Detector arrays of this type are currently being developed for use in the SAFIRE instrument for SOFIA (Shafer *et al.* 2000) and for a ground-based spectrometer (Maffei *et al.* 1994). A common figure of merit for bolometers is the Noise Equivalent Power (NEP). This is the power that yield a signal-to-noise ratio of unity in a 1Hz bandwidth, and is expressed in units of  $W/\sqrt{Hz}$ . For SAFIRE, observations of the CII line at 1900GHz (158 $\mu$ m) with a spectral resolving power of 1000, the maximum NEP for the detectors must be  $10^{-17} W/\sqrt{Hz}$ . NEP can be converted into an equivalent noise temperature  $T_N = NEP/(2k\sqrt{\Delta\nu})$  (Phillips 1988). In the above case, this yields a noise temperature of around 8K. While not achievable with heterodyne spectrometers due to the quantum limit, direct detection has no such restriction.

## Superconducting Transition Edge Sensors

The transition between a superconducting and a normal state can be used as an extremely sensitive thermometer. A thin film, held at its transition temperature, requires only a tiny amount of power to warm it above its transition, increasing the resistance by a large fraction. In fact, the superconducting transition can be very sharp, yielding a dimensionless sensitivity  $d \log R / d \log T \approx 1000$  at best. Recently, we have fabricated thin film superconducting bilayers of Molybdenum and Gold with transition temperatures of around 0.5K. One such transition is shown in Figure 1; it features a bilayer with 400Å of molybdenum and 750Å of gold, yielding a normal resistance of 220m $\Omega$ . Near its transition temperature of 440mK, the sensitivity approaches 200.

Because the transition region is narrow ( $\sim 1$ mK) compared to the temperature above the heat sink (140mK above a  $^3$ He refrigerator at 300mK), the TES is nearly isothermal across the transition. In use as a detector, the power applied to raise the TES into its

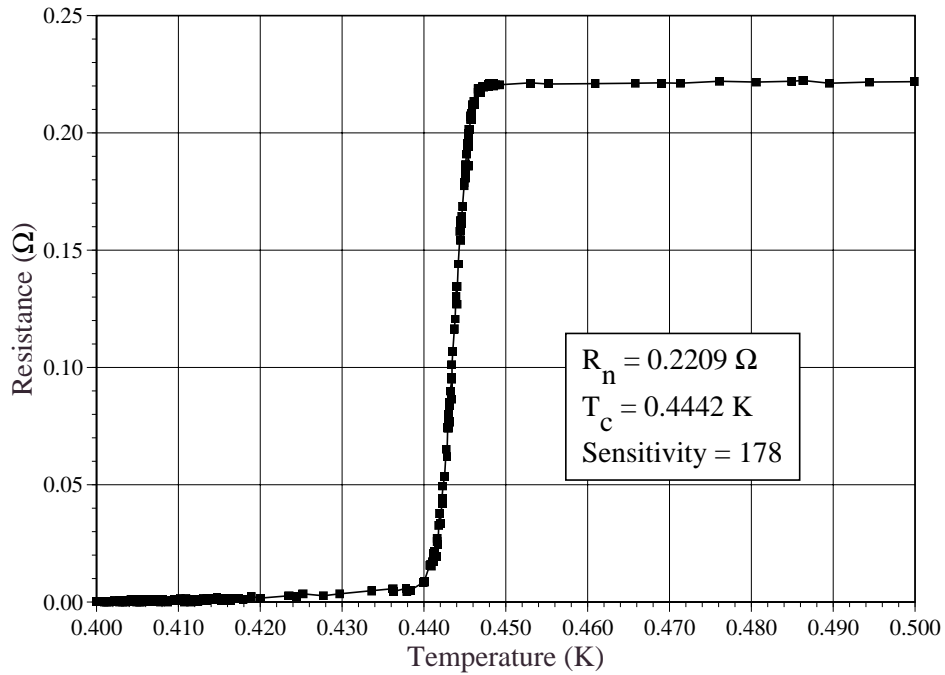


Figure 1. Superconducting transition at 444mK for a Mo/Au bilayer.

transition region is nearly constant. This has the effect that the response becomes linear to better than 1%, substantially better than the typical linearity achieved with semiconducting thermistors.

To date, the best transition we have achieved with Molybdenum and Gold has yielded a sensitivity of  $\approx 1100$ . Many such devices have been made, with transition temperatures reproducible to 2%. Additionally, the normal state resistances are very repeatable and stray resistances are less than  $3\text{m}\Omega$ . This bilayer process allows the transition temperature to be tuned by varying the relative thicknesses of the normal metal (Gold) and superconducting metal (Molybdenum) layers. In this manner, detectors optimized for performance in a variety of different optical loads (e.g. broadband imaging, narrowband spectroscopy) can be produced.

In order to bias the TES, a voltage source of output impedance less than the TES impedance – typically  $100\text{m}\Omega$  – must be provided. In a cryogenic environment this is challenging, but can be solved simply by providing a current bias to a very small shunt resistor in parallel with the TES. Our bias circuit is shown in Figure 2, in which a constant voltage source across a  $1\text{k}\Omega$  resistor produces a constant current through the  $1\text{m}\Omega$  shunt resistor. The inductors shown are for coupling to the SQUID amplifiers described below.

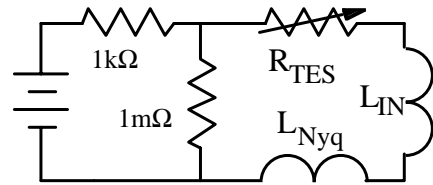


Figure 2. Bias circuit for a TES.

Because the sensitivity of a TES is so large ( $\approx 200$  for the film in Figure 1 vs.  $\approx 5$  for a semiconducting thermistor), a voltage-biased TES is stabilized by strong electrothermal feedback (Irwin 1995). In this mechanism, an increase in temperature yields a sharp increase in resistance, which reduces the current flowing through the TES, lowering the bias power and decreasing the temperature. This enables the devices to be very fast (time constants of  $\approx 1\text{ms}$ ) and has the added benefit of reducing Johnson noise so that phonon noise dominates at low frequencies.

### *TES Bolometers*

In order to make a detector of the appropriate sensitivity, we have fabricated monolithic linear silicon bolometers using micromachining techniques (Figure 3). These bolometers have slim silicon legs which provide thermal isolation and a  $1\text{mm}^2$  absorber to couple to the far-infrared light. The thermal conductance at the operating temperature determines the optical power that the device is optimized for; current arrays are being fabricated for operation with  $\approx 1\text{pW}$  of optical loading. These linear bolometer arrays can be folded such that the legs (and, therefore, electrical connections) are hidden completely behind the absorber, allowing close-packing perpendicular to the array. In this way, a two-dimensional array of large size can be made with near unity filling factor.

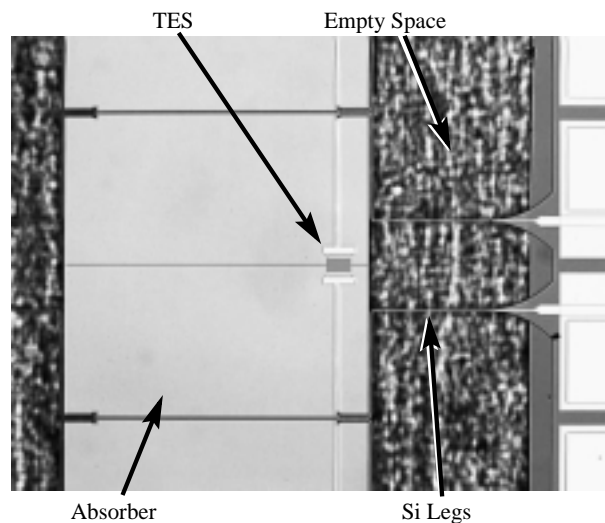


Figure 3. A single element from the middle of a linear array of TES bolometers. The absorber is  $1\text{mm}$  on a side.

A single linear array of bolometers is shown in Figure 4. Each pixel measures  $1\text{mm}$  on a side and is  $1\mu\text{m}$  thick. The silicon legs are barely visible as two thin lines leading to each pixel. An enlargement of the area around a single TES bilayer is shown in an inset. The active area is approximately  $50\mu\text{m}$  square. Once several of these linear arrays are folded, they can be stacked closely, as shown in Figure 5. This mechanical assembly test yielded a  $5 \times 32$  array, as a proof-of-concept prototype for future  $32 \times 32$  arrays.

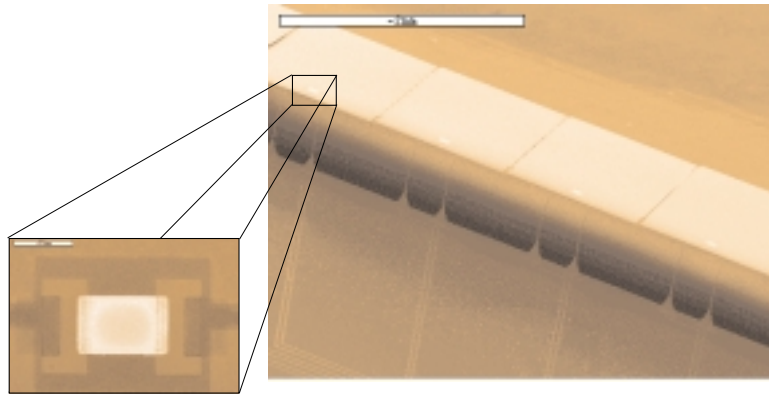


Figure 4. SEM photograph of a single row of bolometers. The enlargement shows the TES bilayer present on each detector.

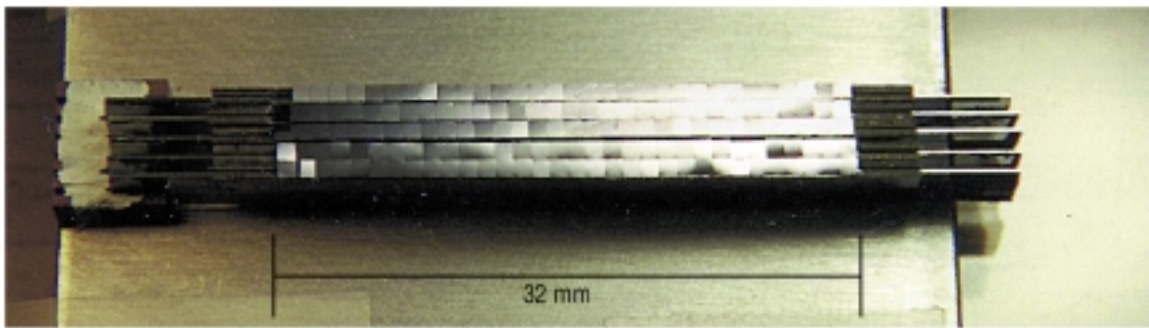


Figure 5. Mechanical assembly of a 5x32 array of bolometers.

### *Bolometer Performance*

Optical performance was measured in a test setup designed to calibrate low-background detectors for SPIRE (Hargrave *et al.* 1999). This setup used a helium-cooled blackbody consisting of a textured, black, carbon-loaded epoxy (Epotek 920) wall in a gold-coated cavity. Selectable apertures allow the throughput to the blackbody to be chosen. The blackbody can be heated to cover temperatures between 2K and 40K. A metal-mesh bandpass filter at 350 $\mu$ m wavelength (850GHz) with a fractional bandpass of  $\sim 1/10$  reduced the total transmitted power to be within the range of our bolometers, which were designed to saturate (i.e., be driven normal) at 5pW. The result of the blackbody calibration is shown in Figure 6, where the measured power has been corrected for a bolometer absorptivity of 90%. The measured response follows the theoretical power very well up to a saturation power of 2.1pW, about half the designed value. The excellent linearity of TES bolometers is one of their best features.

In addition to calibration with the blackbody, the test setup permits an external source to be used. In order to reduce the optical load to an acceptable level, a 1% transmissive neutral density filter is placed in the beam. The time constant was measured by using a

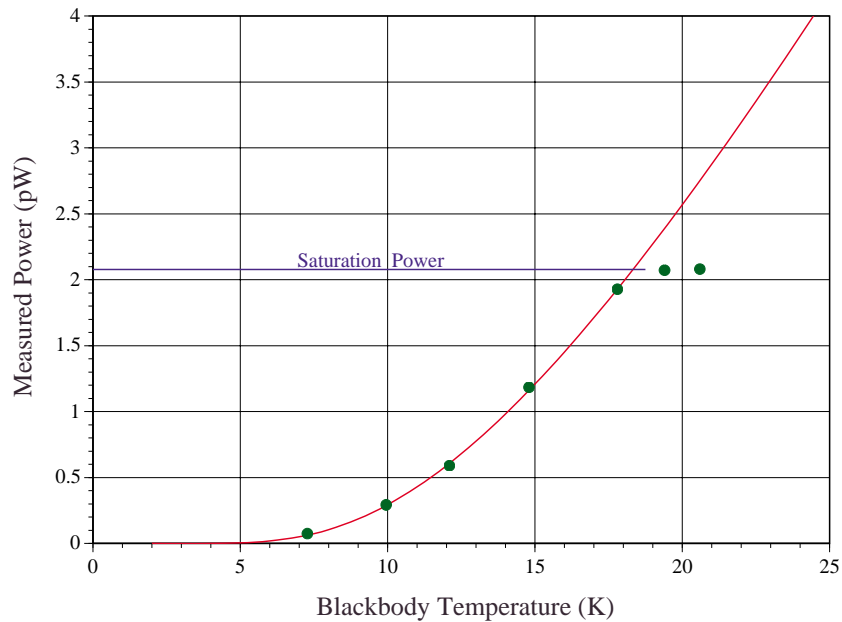


Figure 6. Measured power versus blackbody temperature for a helium-cooled calibration source, assuming a detector absorptivity of 90%.

rapidly chopping blade with a hot/warm load. An upper limit of  $\tau \leq 2\text{ms}$  was found, limited by the speed of the chopper. A Fourier transform spectrometer was used to measure the frequency response, which was limited by the bandpass filter. No bandwidth degradation due to inefficiencies in the absorbing coating were seen. Also, a beam map was made, and excellent rejection of out-of-beam power was found.

In Figure 7, we show the Noise Equivalent Power (NEP) of a TES bolometer using an Aluminum/Silver bilayer operating at a transition temperature of 568mK. The NEP over the desired 10-100Hz bandwidth is  $2.8 \times 10^{-17} \text{W}/\sqrt{\text{Hz}}$ . The phonon noise calculation is shown as a blue curve, demonstrating that phonon-limited performance has been obtained. Over a 100GHz bandwidth at 850GHz, this noise level corresponds to a detector noise temperature of 3.2K. The measured noise levels of lower-transition (440mK) devices have been about 20% above the phonon noise level, indicating excess noise which is believed to arise from edge effects where the bilayer thicknesses are not well defined. Recent results using Molybdenum/Copper bilayers appear not to have this excess noise.

## SQUID Amplifier

A low-impedance detector such as a superconducting TES is well-matched by a superconducting SQUID amplifier. From a fundamental standpoint, a SQUID amplifier functions as a magnetic flux to voltage converter, with extremely low output voltage noise). A voltage-biased TES in series with a “pickup” inductor placed near a SQUID

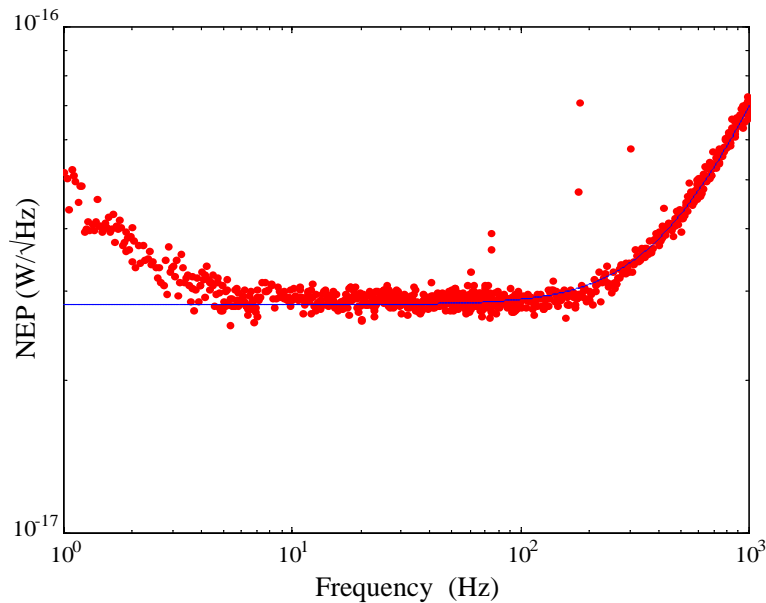


Figure 7. NEP of a detector operating at 568mK. The phonon noise calculation is shown as a blue curve, demonstrating that phonon-limited performance has been obtained over the 10-100Hz signal band.

will induce a changing flux through the SQUID when the TES resistance changes. As in Welty & Martinis (1993), we use the first stage SQUID to drive a series array of SQUIDs which yield a voltage gain of 100. This Series Array Amplifier can produce an output voltage of the order of a millivolt, readily amplified by room-temperature electronics. As shown in Figure 8, a single detector can be read out using eight wires.

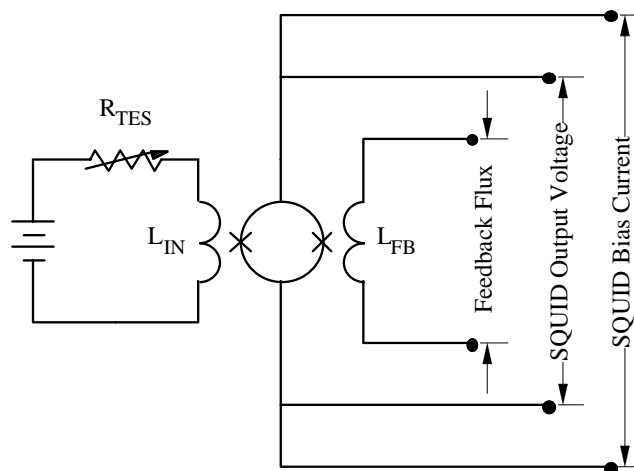


Figure 8. A single SQUID amplifier circuit. Eight wires are needed to read out one detector, assuming separate returns.

### Multiplexed SQUID Amplifier

A SQUID amplifier can be switched rapidly between an operational state and an inoperational, superconducting state by biasing the SQUID with roughly  $100\mu\text{A}$  of current. If we stack  $n$  SQUIDs in series with  $n+1$  electrical “address” leads as shown in Figure 9, driving current between an adjacent pair of leads will result in only one SQUID being operational. With the other SQUIDs in the superconducting state, the output voltage across the entire array is exactly the voltage across the one active SQUID. In this manner, only one amplifier is necessary for  $n$  detectors, although at a data rate  $n$  times faster. Adding in connections for a common TES bias and feedback signal, and a total of  $n+7$  wires are needed.

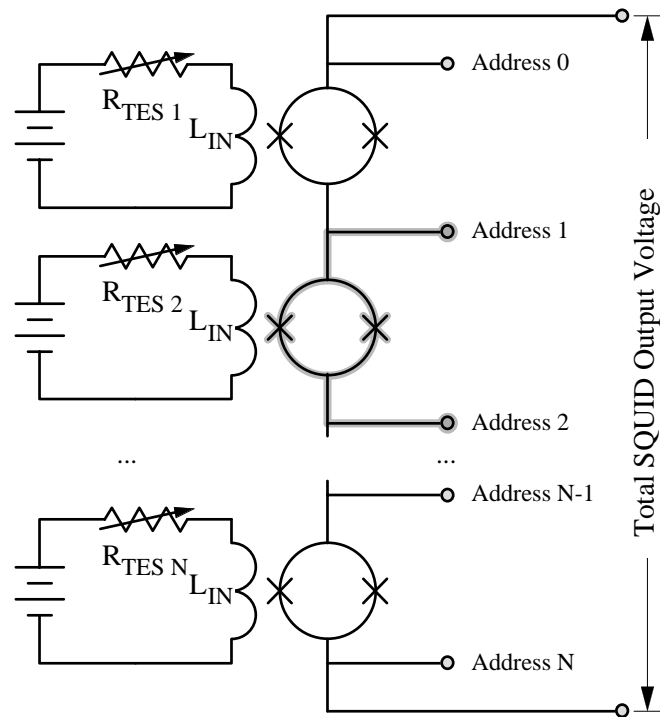


Figure 9. A multiplexed SQUID amplifier reading out  $n$  detectors. A total of  $n+7$  wires are needed (assuming ganged biases).

A  $1\times 8$  SQUID multiplexer has been built and tested using the circuit described in Chervenak *et al.* (1999). Two sine wave inputs were fed into a cold electronics setup so as to mimic the modulation of a signal from infrared light. The multiplexed amplifier was switched between these inputs, amplified, digitized. A sample time series of data at this point is shown in Figure 5 of Chervenak *et al.* (1999). This data can be demultiplexed to recover the original input sine waves, which demonstrates the excellent fidelity of the amplifier. It should be pointed out that the TES is biased at all times, and is low-pass filtered using an inductor with time constant  $L/R\approx 2\mu\text{s}$  to a response time slower than the multiplex switching time. Effectively, the TES self-integrates so that the

multiplexer *samples* an integrated signal; no loss of signal-to-noise is introduced even though the signal from each TES is read out for a shorter time. This is true provided that the noise of the SQUID is substantially less (by a factor of more than  $\sqrt{n}$ ) than that of the TES. Furthermore, in order to remain stable, the devices must be sampled faster than  $f_{L/R}=(3+2\sqrt{2})f_{\text{TES}} \approx 100$  kHz.

### *Two-Dimensional Multiplexed SQUID Readout*

When multiplexing a two-dimensional array consisting of  $m$  rows and  $n$  columns, an advantage can be gained in that the columns share common address lines and only one amplifier is needed. In the most straightforward wiring scheme,  $4n+m+3$  wires are needed, as opposed to  $8mn$  for a fully-wired array of discrete bolometers. Table 1 highlights the wiring advantage for multiplexed arrays, and describes the development status of these arrays at GSFC/NIST. Future advances using cold semiconducting shift registers (wherein a clock pulse will change the multiplex addressing, as opposed to the present direct addressing) may be possible, further reducing the multiplexer wiring requirements.

Table 1. Wiring advantage of multiplexed detectors versus directly-wired detectors and the current state of development.

Columns	Rows	Detectors	Wires (non-muxed)	Wires (muxed)	Status
1	1	1	8	8	Exists
2	4	8	64	15	Exists
2	8	16	128	19	Exists
4	8	32	256	27	In fabrication
1	32	32	256	39	In design
32	32	1024	8192	163	In design
64	64	4096	32,768	323	In design

### **Conclusion**

We have demonstrated a superconducting transition in Molybdenum/Gold bilayers which looks promising for use as TES films on sensitive bolometers. Noise Equivalent Powers consistent with phonon noise have been measured, and optical efficiency of 90% has been achieved. A multiplexed SQUID amplifier has been fabricated and is shown to provide low-noise, high-fidelity readout of several TES detectors with a single signal output. This architecture can be extended to two-dimensional arrays with relatively little increase in the total number of wires. A large-format (thousands of detectors) bolometer array can be made with this technology, having application in future far-infrared instruments such as SPIRE on the FIRST telescope and SAFIRE on the SOFIA observatory.

## References

- Benford, D.J., Hunter, T.R. & Phillips, T.G. 1998, *Int J. IR MM Waves*, **19**, **7**, 931.
- Bock, J.J., Glenn, J., Grannan, S.M., Irwin, K.D., Lange, A.E., LeDuc, H.G. & Turner, A.D. 1998, *Proc. SPIE #3357*, T.G. Phillips, ed., p.297
- Chervenak, J.A., Irwin, K.D., Grossman, E.N., Martinis, J.M., Reintsema, C.D. & Huber, M.E. 1999, *Appl. Phys. Lett.*, **74**, p.4043
- Hargrave, P.C. *et al.* 1999, *Proc. Low Temperature Detectors #8*, in press
- Holland, W.S. *et al.* 1996, *Int J IR MM Waves*, **17**, p.669
- Irwin, K.D. 1995, *Appl. Phys. Lett.* **66**, p.1998
- Kreysa, E. *et al.* 1998, *Proc. SPIE #3357*, “Advanced Technology MMW, Radio, and Terehertz Telescopes”, T.G. Phillips, ed., p.319
- Maffei, B. *et al.* 1994, *Infrared Phys. Technol.*, **35**, **2**, 321.
- Phillips, T.G. 1988, in “Millimetre and Submillimeter Astronomy”, Wolstencroft & Burton, eds., p.1
- Shafer, R.A. *et al.* 2000, in *SPIE Proceedings*, “Astronomical Telescopes and Instrumentation 2000”, Munich, Germany
- Wang, N.W. *et al.* 1996, *Applied Optics*, **35**, p.6639
- Welty, R.P. & Martinis, J.M. 1993, *IEEE Trans. App. Superconductivity*, **3**, p.2605

# COMPARISON OF TWO TYPES OF ANDREEV REFLECTION HOT-ELECTRON MICROBOLOMETER FOR SUBMILLIMETER RADIO ASTRONOMY

A.N. Vystavkin

Institute of Radioengineering and Electronics of RAS, 11 Mokhovaya Str., Moscow 103907, Russia

Review and analysis of results of theoretical estimations and measurements of characteristics of an Andreev reflection hot-electron direct detection microbolometer for submillimeter radio astronomy made by different researchers are given. The consideration is limited to the case when minimized in dimensions absorber of the microbolometer is antenna-coupled and together with antenna are deposited directly onto substrate without a membrane or spider-web and cooled to approximately 100 mK what provides the best noise equivalent power. A comparison of peculiarities and characteristics of the microbolometers using two types of sensors - the SIN-junction sensor and the transition-edge sensor (TES) with electrothermal feedback - for the read-out of a signal arising from the electron temperature increment under the influence of submillimeter radiation is presented. Advantages of the microbolometer with the second type of the sensor when the TES is used simultaneously as the absorber of radiation are shown. Methods of achievement of the best noise equivalent power of the microbolometer in such version as well as methods of the matching of the microbolometer with the incident radiation flow and with the channel of the output signal read-out are considered.

## 1. Introduction.

One of the fundamental problems of the contemporary radio astronomy [1-3] is the problem of the investigation of a celestial sphere electromagnetic radiation in the frequency region 0.3 - 3.0 THz as a result of what they are expecting an abundant information which will bring us forward to the significant broadening of our ideas about the Universe. To attack this problem besides highsensitive narrowband superheterodyne receivers [4] the broadband receivers of direct detection type, most sensitive among which are the receivers based on hot-electron microbolometers [5-8], are necessary. The choice of two types of receivers for frequency region 0.3 - 1.5 THz [3], superheterodyne and direct detection types, is led mainly to the reason that when they are observing weak but broadband radiation sources it may occur that the sensitivity of narrowband superheterodyne receivers could be not enough and at the same time the microbolometers as direct detectors due to their very wide frequency band will detect this radiation. Besides as direct detection microbolometers do not need heterodyne pumping it is much easier to construct multi-element receiving structures on their basis for an observation spatially inhomogeneous distributed radiation sources though having not too high frequency resolution. For many tasks of the submillimeter radio astronomy the noise equivalent power (*NEP*) of direct detection microbolometers of order of  $10^{-17} - 10^{-18} \text{ W} \cdot \text{Hz}^{-1/2}$  is necessary [1-3, 9] and for some tasks in future the *NEP* down to  $10^{-20} - 10^{-21} \text{ W} \cdot \text{Hz}^{-1/2}$  will be required [10].

## 2. Andreev reflection hot-electron microbolometer with a SIN-junction as the output signal read-out sensor.

Amongst mentioned above hot-electron microbolometers Andreev reflection [11] one operating at sub-Kelvin temperatures is recognized as the most promising [7, 8] because of its comparatively high sensitivity and lowest time constant. The first concept of this microbolometer was proposed in [7]. In the first experiments on the realization of this concept

[8] the microbolometer design was comparatively simple structure (the inset of Fig. 1) comprising a normal metal film (Cu) with dimensions: 6-  $\mu\text{m}$ - long, 0.3-  $\mu\text{m}$ -wide, and 75-nm-thick and lead electrodes of Al (the superconductor at temperatures  $< 1.2$  K) deposited on the silicon substrate using the electron-beam lithography and triple-angle evaporation process. A submillimeter radiation has to be absorbed by electrons in the normal metal film and heat them. However due to difficulties of the leading a radiation into the cryostat at sub-Kelvin

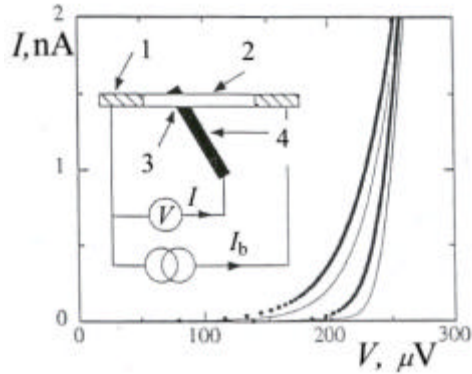


Fig. 1.  $I$ - $V$  characteristics of the SIN-junction. Solid thin curves correspond to temperatures 40 mK (right) and 300 mK (left) at zero bias current through the absorber. Dotted thick curves correspond to a base temperature of 40 mK with 20 fW (right) and 2 pW (left) power dissipated in the normal metal absorber. The scheme of measurements is given at the inset. The power dissipated in the resistor  $R$  of the absorber is  $I_b^2 \cdot R$ : 1 - superconducting lead electrodes bringing bias current into the absorber, 2 - copper absorber, 3 - SIN-junction, 4 - superconducting electrode of SIN-junction [8].

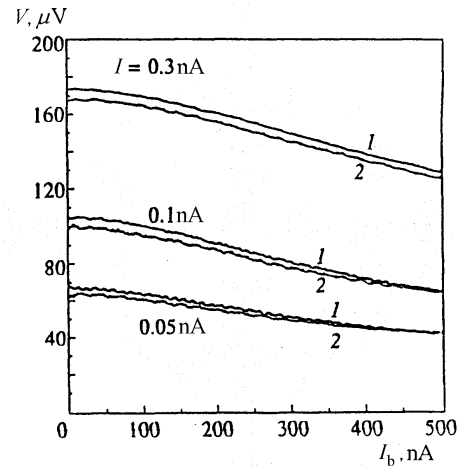


Fig. 2. Dependence  $V=f(I_b)$  at three fixed values of SIN-junction current  $I$  and temperature  $T = 30$  mK for two absorber samples of 6-  $\mu\text{m}$ -length (curves 1) and 12-  $\mu\text{m}$ -length (curves 2) [12-14].

temperatures the measurements with the radiation were not made in first experiments and the heating of electrons was realized by means of the d.c. biasing. Two circumstances lead to the effective heating of electrons: (a) the superlow temperature ( $\leq 0.1$ - $0.3$  K) owing to what the interaction between electrons and metal film through electron-phonon collisions and therefore the energy transfer from electrons to the absorber lattice is extremely low, and (b) the phenomenon of Andreev reflection of electrons at the normal metal - superconductor boundaries which takes place without the energy transfer of electrons to the superconducting electrodes [11]. At temperatures  $< 1$  K the electrical resistance of the normal metal film does not depend on temperature. By this reason unlike to classic bolometers when an increment of voltage drop caused by the absorber resistance increase owing to the temperature increase due to the absorber heating is measured - in case of the described microbolometer the voltage increment at the SIN (superconductor-insulator-normal metal) junction (see Fig. 1) caused by the increment of temperature of electrons in the normal metal film is measured. This junction was made by the following way: before the deposition of the normal metal film (Cu) onto the silicon substrate the 50-nm-thick and 0.2-  $\mu\text{m}$ -wide strip of superconductor (Al) simultaneously with lead electrodes (also Al) were deposited under the central part of the normal metal film (to be deposited) and after that first one was oxidized [8].  $I$ - $V$  curves of the SIN-junction (examples of what are shown at Fig. 1) at different absorber film temperatures  $T = T_{ph}$  and the bias currents  $I_b$  through the absorber where measured [8]. The experimental dependence of the electron

temperature  $T_e$  on the d.c. power  $P = I_b^2 \cdot R$  dissipated in the absorber film was calculated from the  $I$ - $V$  curves and plotted. The obtained dependence is fitted well with the theoretical dependence:

$$P_{e \rightarrow ph} = \Sigma \nu (T_e^5 - T_{ph}^5), \quad (1)$$

where  $\Sigma = 3.7 \text{ nW} \cdot \text{K}^{-5} \cdot \text{mm}^{-3}$  is fitting characteristic material parameter, and  $\nu$  is copper absorber film volume. It follows from good coincidence of the form of the theoretical dependence (1) and the experimental curve that a predominating mechanism of electron energy flow out is the electron energy transfer to the copper film lattice through electron-phonon interaction and other possible mechanisms of electron energy flow out do not give noticeable contribution to this process. In the same time this means that the Andreev reflection of electrons at the normal metal-superconductor boundaries takes place. A voltage responsivity calculated from the  $I$ - $V$  curves is  $S_V \cong 10^9 \text{ V/W}$  at temperature 100 mK, what is in good agreement with preliminary estimations of authors of [8]. The noise voltage measured at the input of the amplifier of SIN-junction output signal is  $\sqrt{u_n^2} \cong 3 \text{ nV} \cdot \text{Hz}^{-1/2}$  what at said above voltage responsivity corresponds to the electrical (i.e. calculated from measurements at d.c.)  $NEP$  of the microbolometer  $NEP = \sqrt{u_n^2} : S_V \cong 3 \cdot 10^{-18} \text{ W} \cdot \text{Hz}^{-1/2}$ .

The results similar to described above ones are obtained in [12-14]. The difference is that an absorber was fabricated not of copper but of 3-nm-thick chrome sublayer for a better adhesion with the substrate and 35-nm-thick silver layer with other dimensions of 6 -  $\mu\text{m}$ -length and 0.25-  $\mu\text{m}$ -width. Besides in said works measurements of the dependence of voltage over SIN-junction on the current  $I_b$  through the absorber at two its lengths: 6 and 12  $\mu\text{m}$  and three fixed SIN-junction currents  $I$  were made (Fig. 2). Practically the dependences at two different lengths coincide. This means that the increase of the power  $I_b^2 \cdot R$  dissipated in the longer absorber due to its higher resistance  $R$  has been exactly compensated by the increase of the heat conductance due to the larger volume  $\nu$ . This is one more confirmation that there is no substantial electron energy transport through normal metal-superconductor contacts, i.e. this is one more confirmation of the Andreev reflection at these contacts.

Initially the Andreev reflection hot-electron microbolometers with the SIN-junction sensors were used as X-ray detectors [15, 16].

### **3. Andreev reflection hot-electron microbolometer based on superconducting transition-edge sensor (TES) for the output signal read-out.**

The application of a sensor based on superconducting transition (transition-edge sensor - TES) with strong electrothermal feedback as output signal read-out sensor for the microbolometer of described type using for detection of X-rays, neutrino and other atomic particles was proposed in [17]. In such sensor a superconductor or a bilayer of superconductor and normal metal with proximity effect is in good thermal contact with an absorber of X-rays [18], neutrino or other atomic particles. A typical electrical circuit into which the TES as the microbolometer output signal read-out sensor is connected is shown at Fig. 3 [19]. A practical circuit of the microbolometer with TES for the detection of X-rays radiation is shown at Fig. 4. Lead electrodes bringing current into the TES are made of a superconductor with significantly higher critical temperature i.e. larger energy gap in comparison with the same value of the TES

structure to provide the functioning of Andreev reflection at the boundaries of the TES and current lead electrodes. The microbolometer realized in accordance with the Fig. 4 was tested and has shown a significantly higher sensitivity to X-ray radiation [20] in comparison with the microbolometer based on SIN-junction as output signal read-out sensor of the same authors [15, 16].

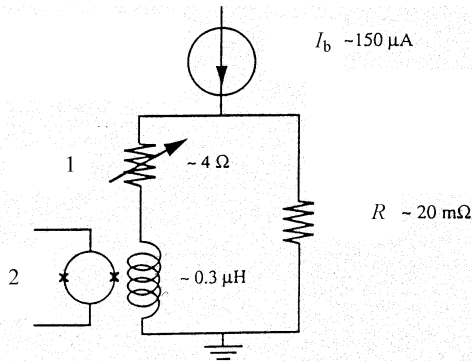


Fig. 3. Schematic of the electrical circuit used to bias the TES: 1 - TES, 2 - SQUID read-out circuit with input coil  $\sim 0.3 \mu\text{H}$  [19]. Fixed bias voltage is applied from shunt resistance  $R \cong 20 \text{ m}\Omega$  to the series connection of the TES and SQUID input coil.

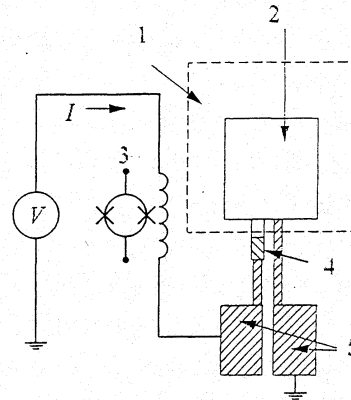


Fig. 4. Schematic of the hot-electron microbolometer for X-rays radiation measurements based on the TES with electrothermal feedback and the SQUID: 1 -  $\text{Si}_3\text{N}_4$  membrane, 2 - silver absorber, 3 - SQUID, 4 - TES, 5 - aluminum contacts [18]. The  $\text{Si}_3\text{N}_4$  membrane is used for the efficiency enhancement of the X-ray photon energy conversion into the electron thermal energy [15].

It is proposed in the work [20] to use the TES combined with the absorber for the detection of the submillimeter and infrared radiation. An electrical circuit into which the absorber-TES connected is the same as at Fig. 3 where 1 is now the combined absorber-TES which as in case of the normal metal absorber of the microbolometer described in the previous paragraph is deposited together with the bringing current lead electrodes onto a substrate, for instance, of silicon. Issues of the leading-in submillimeter radiation into the absorber-TES are considered below. In such version of the microbolometer the substrate with absorber-TES is cooled down to a temperature lower than the temperature of the superconducting transition. The absorber-TES is connected in series with the input coil of SQUID-picoammeter and the d.c. bias voltage  $V$  from the shunt resistance  $\cong 20 \text{ m}\Omega$  is applied across this series connection (Fig. 3). At the mode of fixed bias voltage the equilibrium amount of electron energy and consequently of electron temperature in the absorber-TES is automatically maintained at all area of the superconducting transition due to an electrothermal feedback functioning in the following way [17, 18]. During the process of absorption of the submillimeter radiation by the absorber-TES the electrons in it are heated. The TES resistance  $R$  starts to increase with the heating of the electrons and this leads to the decreasing of the dissipated Joule heat  $V^2/R$  and of course to the decreasing of the current  $V/R$  flowing through the TES. In the same moment the electron temperature returns practically to the initial value and the resistance  $R$  becomes somewhat higher. The return of electron temperature to the equilibrium value is taking place in accordance with the relation [17]:

$$C \frac{d\Delta T_e}{dt} = -\frac{P_0 \mathbf{a}}{T_e} \Delta T_e - G \Delta T_e. \quad (2)$$

In the considered case when the heat coupling of electrons with the absorber-TES lattice is significantly weaker than the heat coupling of the absorber-TES lattice with the substrate lattice [17]  $C$  is electronic heat capacity,  $\Delta T_e$  - electron temperature increment,  $P_0 = \Sigma v T_e^5 = G T_e / 5$  - equilibrium value of electron power dissipated in the absorber-TES,  $G = dP / dT_e = 5 \Sigma v T_e^4$  - heat conductivity from electrons to the absorber-TES lattice,  $\mathbf{a} = d \log R / d \log T$  - the dimensionless measure of the sharpness of the superconducting transition.

In conclusion one may say that the increasing of power dissipated in the absorber-TES on account of the additional power due to the absorption of the submillimeter radiation is compensated by the decreasing of d.c. power corresponding to the Joule heat. At this time the SQUID-picoammeter measures the decreasing of current -  $\Delta I$  what is the output signal of the microbolometer. In the described process the replacement of the d.c. energy by the energy of absorbed radiation takes place in the electron system and consequently this does not lead to the change of energy flow from the electrons to the absorber-TES lattice under the radiation influence. By this reason the effective time constant  $\mathbf{t}_{eff}$  of this process is lower of the intrinsic time constant  $\mathbf{t}_{e \rightarrow ph}$  caused by the energy transfer from electrons to phonons in  $1 + \mathbf{a} / 5$  times [17].

The bilayer of aluminum and silver was used as the absorber-TES in the work [18]: 30-nm-thick Ag layer was deposited first and 17-nm-thick Al layer - second. The sharp superconducting transition at temperature  $\sim 72$  mK and  $< 1$  mK width between 10% and 90% of the normal resistance was obtained (Fig. 5). The parameter  $\mathbf{a} \cong 1,200$  was obtained in the cited work and consequently  $\mathbf{t}_{eff} / \mathbf{t}_{e \rightarrow ph} \cong 1:240$  what corresponds to the strong feedback. The  $I$ - $V$  characteristic and the dependence of dissipated in the absorber-TES power on the bias voltage  $V$  are shown at Fig. 6. The portion of  $I$ - $V$  curve with the negative differential resistance and the plateau at the dependence of dissipated power on the bias voltage due to the functioning of the electrothermal feedback correspond to the superconducting transition area.

In the work [20] the estimation of the noise equivalent power of the microbolometer with TES combined with the absorber made on the basis of measurement results at the d.c. is given. The  $70 \times 100 \text{ } \mu\text{m}^2$  width-to-length and 50 nm-thick Ag/Al bilayer as the absorber-TES having temperature and electrical characteristics close to that shown at Fig. 5 and Fig. 6 was used. Since the replacement of part of d.c. power with the absorbed radiation power takes place in the microbolometer of described type it is easy to derive an expression for the current responsivity:  $P_{rad} = -\Delta I \cdot V$  and the current responsivity  $S_I = \Delta I / P_{rad} = -1/V$  [17]. The beginning of the superconducting transition in the cited work [20] takes place at  $V \cong 0.5 \text{ mV}$  and consequently  $S_I \cong -2 \cdot 10^6 \text{ A/W}$ . The measured root-mean-square noise current of the device was  $\sqrt{i_n^2} \cong 6 \text{ pA} \cdot \text{Hz}^{-1/2}$  what corresponds approximately to the measurement result obtained in [21] as well. One may obtain the NEP of microbolometer from current responsivity and root-mean-square noise current. The result is:  $NEP = \sqrt{i_n^2} / |S_I| \cong 3 \cdot 10^{-18} \text{ W} \cdot \text{Hz}^{-1/2}$ .

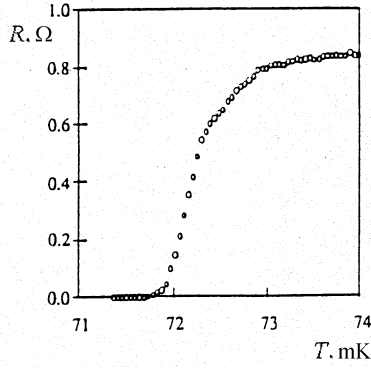


Fig. 5. Characteristic of the superconducting transition of superconductor-normal metal bilayer with proximity effect: 17-nm-thick aluminum layer deposited onto 30-nm-thick silver layer [18].

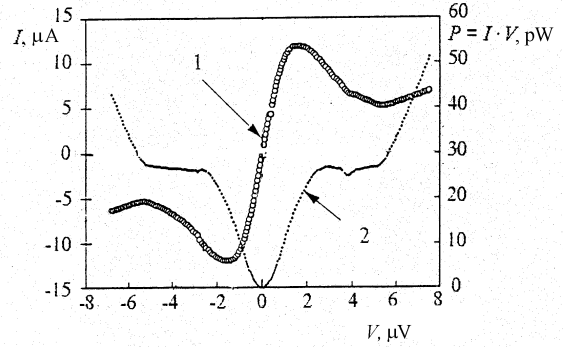


Fig. 6.  $I$ - $V$  characteristic of the absorber combined with the TES with electrothermal feedback and corresponding dependence of power dissipated in absorber-TES on bias voltage; one may see a plateau at the power of 27 pW on the second dependence: 1 - SQUID current  $I$ , 2 - power  $P = I \cdot V$  [18].

#### 4. Estimation of a maximum possible sensitivity of the microbolometer based on the absorber-TES.

The  $NEP$  of the radiation detector which utilizes a bulk detection mechanism, for example the heating of electrons or the intrinsic photoeffect (photoconductivity), and has a noise generated in the whole volume of the detector and depending on its resistance, for example the Johnson noise, is proportional to the square root of its volume  $v$  [22]:

$$NEP \propto \sqrt{v}. \quad (3)$$

The microbolometer under consideration based on the TES combined with absorber utilizes the heating of electrons, i.e. the bulk (volume) effect, and its noise current spectral density is determined by two components [17]:

$$\overline{i_n^2} = \frac{4kT}{R} \cdot \frac{n^2 / \mathbf{a}^2 + \mathbf{w}^2 \mathbf{t}_{eff}^2}{1 + \mathbf{w}^2 \mathbf{t}_{eff}^2} + \frac{4kT}{R} \cdot \frac{n/2}{1 + \mathbf{w}^2 \mathbf{t}_{eff}^2}, \quad (4)$$

where the first component is the Johnson noise and the second one is the phonon noise, i.e. the noise caused by thermal fluctuations during the energy exchange between electrons and phonons. Not going into details we may indicate that both components have similar dependence on the microbolometer resistance  $R$ . This means that the expression (3) is valid at two said noise components as well. In [10] the same dependence of the  $NEP$  on  $v$  is presented taking into account just the phonon noise what corresponds to the said above.

Using results of measurements of the current sensitivity and the noise current as well as the estimation of the  $NEP$  of the microbolometer with the TES on the basis of the said

measurements in [20] and expression (3) one may estimate the  $NEP$  of the microbolometer when its dimensions are decreased. On account of the fixed thickness of the microbolometer ( $\cong 50$  nm [20]) which is the thickness sum of both layers of the bilayer determined experimentally under condition of the obtaining the best parameters of the superconducting transition one may modify (3) into

$$NEP \propto \sqrt{l \times w}, \quad (3')$$

where  $l$  is the length and  $w$  is the width of the absorber-TES. The results of conversion of the  $NEP$  of the TES-microbolometer to new dimensions using (3') are given in the Table 1.

The first row of part I (for dimensions  $100 \times 70$   $\text{mm}^2$ ) is the result of measurements and estimations made in [20]. The second row of part I is the result of the conversion of the  $NEP$  in accordance with (3') to the dimensions  $l \times w \cong 6 \times 0.3$   $\text{mm}^2$  which has the microbolometer with SIN-junction sensor [8] (see above). We remind that its electrical noise equivalent power is  $NEP \cong 3.10^{-18}$   $\text{W} \cdot \text{Hz}^{-1/2}$  (the same value as in case of the TES-microbolometer with  $l \times w = 100 \times 70$   $\text{mm}^2$ !).

Table 1

$l \times w, \text{mm}^2$	$NEP, \text{W} \cdot \text{Hz}^{-1/2}$
I	
100×70	$\cong 3 \cdot 10^{-18}$ [20]
6×0.3	$\cong 4.8 \cdot 10^{-20}$
0.5×0.2	$\cong 1.4 \cdot 10^{-20}$
II	
1800×900	$\cong 3.3 \cdot 10^{-17}$ [23]
6×0.3	$\cong 3.5 \cdot 10^{-20}$

Result of the conversion of the  $NEP$  to new dimensions by means of (3') using as a basis the TES-microbolometer described in [23] is given in part II of the Table 1. It has the combined absorber-TES made of tungsten ( $T_c \sim 95$  mK of W thin film [23]) with  $l \times w = 1.8 \times 0.9$   $\text{mm}^2$  and thickness equal to 40 nm connected into the scheme similar to Fig. 3. Its  $NEP$  is  $\cong 3.3 \cdot 10^{-17}$   $\text{W} \cdot \text{Hz}^{-1/2}$  and the conversion to the dimensions  $l \times w = 6 \times 0.3$   $\text{mm}^2$  gives  $NEP \cong 3.5 \cdot 10^{-20}$   $\text{W} \cdot \text{Hz}^{-1/2}$  what is close to the value in the second row of part I.

It is necessary to notice that the noise in [8] was caused not by the microbolometer itself but by the amplifier of the microbolometer output signal and the authors of [8] have estimated that after the reducing the noise of the amplifier by an order the noise will be caused by the intrinsic noise of the SIN-junction sensor what corresponds to an order better (lower)  $NEP \cong 3 \cdot 10^{-19}$

$\text{W} \cdot \text{Hz}^{-1/2}$ . And even in this case at the same absorber dimensions like in case of the microbolometer with SIN-junction sensor the  $NEP$  of the microbolometer with absorber-TES will be an order better. This is caused by the fact that whole volume of the absorber-TES is working to generate the output signal of the microbolometer but not just a part of the absorber overlapping with SIN-junction as in case of the microbolometer with SIN-junction sensor. The experimental confirmation of the latter fact is the independence of the output signal of the microbolometer with SIN-junction sensor on the power dissipated in the absorber at two its lengths (Fig. 2): at doubled absorber length  $l$  the resistance  $R$  is also twice larger and at the same bias current  $I_b$  the dissipated power  $I_b^2 \cdot R$  in the absorber is also doubled but the microbolometer output signal remains practically unchanged. All said means that the significant portion of hot electrons in the absorber in case of the microbolometer with SIN-junction sensor does not give contribution into the output signal, i.e. the corresponding power is lost (unused) what decreases the effectiveness of this microbolometer in comparison with the microbolometer with TES. It is possible to show this clear with the following judgement. One may assume that instead of one SIN-junction the multiple SIN-junctions are arranged along the whole length of the absorber and all output signal components of the microbolometer are summed by means of a transformer with  $n$  primary coils and one secondary coil where  $n$  is the amount of SIN-junctions. At 6-  $\mu\text{m}$ -long absorber and 0.2-  $\mu\text{m}$ -wide SIN-junction (see above)  $n \cong 30$ . In this case power losses of hot electrons are  $\cong 29:30$  for the single SIN-junction in comparison with thirty SIN-junctions from the viewpoint of the generating of the microbolometer output signal. When the noise of  $n$  SIN-junctions is predominating their noise is summed in the transformer as  $\sqrt{nu_{SIN}^2} = \sqrt{n} \times \sqrt{u_{SIN}^2}$ , i.e. the noise increases in  $\sqrt{n}$  times and the  $NEP$  becomes better (decreases) proportionally to  $\sqrt{n} : n$ . When the noise of the amplifier of output signal of the microbolometer is predominating the  $NEP$  is improved (decreased) proportionally to  $1:n$ . In the case of predominating intrinsic noise of  $n$  SIN-sensors with equal noise the  $NEP$  of SIN-microbolometer with  $l \times w = 6 \times 0.3 \mu\text{m}^2$  will be  $NEP \cong 3 \cdot 10^{-19} : \sqrt{n} \text{ W} \cdot \text{Hz}^{-1/2} = 3 \cdot 10^{-19} : \sqrt{30} \text{ W} \cdot \text{Hz}^{-1/2} \cong 5.5 \cdot 10^{-20} \text{ W} \cdot \text{Hz}^{-1/2}$  what is close to the  $NEP$  of the TES-microbolometer with the same absorber dimensions. This means that whole electron temperature increment of SIN-microbolometer absorber is used now for the generating of the output signal. However the creating of a design of the microbolometer with multiple SIN-junctions appears problematic.

The third row in the Table 1 (part I) corresponds to the dimensions  $l \times w$  accepted for estimations in the work [10]. In this work the thickness of microbolometer is accepted equal to 10 nm unlike to the case of 50 nm what corresponds to estimation results given in the part I of the Table 1. Besides it was proposed in the cited work to increase an electron energy relaxation time in the absorber-TES up to  $t_{e \rightarrow ph} \sim 10^{-3} \text{ s}$  due to the significant decreasing of its thickness or/and by the irradiating it with high-energy ions. As the  $NEP$  depends on the electron energy relaxation time as  $(t_{e \rightarrow ph})^{-1/2}$  [10] it has to be lower in  $\sim 70$  times in comparison with the value in the third row of the Table 1 on account of said two factors: the decrease of the film thickness in 5 times and the increase of  $t_{e \rightarrow ph}$  approximately from  $10^{-6}$  to  $10^{-3} \text{ s}$ , i.e. in  $10^3$  times. This corresponds to  $NEP \cong 2 \cdot 10^{-22} \text{ W} \cdot \text{Hz}^{-1/2}$  and agrees approximately with estimations in [10]. This impressive value requires a fabrication technology on the height of contemporary technological equipment and moves the Andreev reflection hot-electron microbolometer nearer

to the absolute receiver which  $NEP$  is determined by the quantum fluctuations of incident radiation [22, 10].

### 5. The matching of the TES-microbolometer with the incident radiation flow and the output signal read-out channel.

It follows from the analysis made in the previous paragraph that for the achieving the best  $NEP$  of the Andreev reflection hot-electron microbolometer with the combined absorber-TES one should strive for a minimum possible volume of its working part, i.e. the absorber-TES. It means that dimensions of the absorber-TES have to be chosen much less than the wavelength of the incident radiation. To match so small absorber-TES with the incident radiation flow the optical, to be precise - the quasioptical, focusing of the radiation onto the absorber-TES with said dimensions is impossible because of the radiation diffraction phenomenon on it. By this reason the absorber-TES has to be connected into the center of a planar antenna or into a waveguide. The combination of the quasioptical focusing first, for instance by means of a lens or a horn, and then the matching by means of the planar antenna or the waveguide is possible.

Before a further consideration of the problem of the microbolometer matching with the incident radiation flow and the output signal read-out channel it is necessary to make more detailed estimation of parameters of the microbolometer with the TES as the read-out sensor for instance with dimensions  $l \times w = 6 \times 0.3 \text{ mm}^2$  using the conversion method already applied above (see Table 1). We accept again the described in paragraph 3 TES-microbolometer with the dimensions  $l \times w = 100 \times 70 \text{ mm}^2$  as the basis for the conversion. This microbolometer has the d.c. and low frequency resistance  $R \cong 0.2 \text{ } \Omega$  (approximately like as at Fig. 5). The bilayer is working as a normal metal at frequencies of the incident radiation at  $\hbar \omega > \Delta$  where in given case  $\Delta$  is the energy gap of the superconducting bilayer structure. Besides the absorber-TES thickness is significantly less than skin depth. Owing to these circumstances the bilayer resistance  $R_w$  at the incident radiation frequency  $\omega$  corresponds to its normal resistance [7], or

$R_w = R_n \cong 1 \text{ } \Omega$ . Parameters  $V$ ,  $\sqrt{i_n^2}$ ,  $S_I$  and  $NEP$  of this microbolometer are given above and included into the Table 2 as well,  $I = V/R \cong 2.5 \cdot 10^{-6} \text{ A}$ . We will carry out the conversion of part of these values to the microbolometer with dimensions  $l \times w = 6 \times 0.3 \text{ mm}^2$  under condition of the constant bilayer thickness as well as the constant current density through it using the following formulas:  $R$  and  $R_w \propto \frac{l}{w}$ ,  $I \propto w$ ,  $\sqrt{i_n^2} \propto \sqrt{\frac{w}{l}}$  (see (4)). By the way the

expression (3') can be derived from these three ones. The rest parameters:  $V$ ,  $S_I$  and  $NEP$  are calculated from first ones. The initial parameters for  $l \times w = 100 \times 70 \text{ mm}^2$  and results of conversion for  $l \times w = 6 \times 0.3 \text{ mm}^2$  are given in the Table 2. The value of the  $NEP$  for  $l \times w = 6 \times 0.3 \text{ mm}^2$  coincides with corresponding value in the Table 1 what has to be. The values  $R$ ,  $R_w$ ,  $V$  and  $\sqrt{i_n^2}$  are primary parameters for the designing of the TES-microbolometer including issues of connection the absorber-TES into the electrical scheme (Fig. 3) and of the matching it with the antenna and the output signal read-out amplifier. The results of the carried out estimation conversion of course have to be approved experimentally.

The experience of the development of submillimeter waveband receivers on the basis of SIS-mixers (see for example [24]) shows that planar antennas are more convenient than waveguides for the purposes of the matching of receiving elements of small dimensions with the incident radiation flow because they may be deposited onto the substrate together with a receiving element, in our case with the microbolometer. Planar antennas can be

Table 2

$l \times w, \text{ mm}^2$	$100 \times 70$	$6 \times 0.3$
$R, \Omega$	0.2	2.8
$R_w, \Omega$	1.0	14
$I, \text{ A}$	$2.5 \cdot 10^{-6}$	$1.1 \cdot 10^{-8}$
$V, \text{ V}$	$0,5 \cdot 10^{-6}$	$3 \cdot 10^{-8}$
$\sqrt{i_n^2}, \text{ A} \cdot \text{ Hz}^{-1/2}$	$6 \cdot 10^{-12}$	$1.6 \cdot 10^{-12}$
$S_I, \text{ A/W}$	$-2 \cdot 10^6$	$-1/(3 \cdot 10^{-8})$
$NEP, \text{ W} \cdot \text{ Hz}^{-1/2}$	$\cong 3 \cdot 10^{-18}$	$\cong 4.8 \cdot 10^{-20}$

spiral, log-periodic, double-slot [24, 12-14, 25] or of other types. They as it was said are fabricated by microfilm technology methods and the receiving elements are integrated into them. Of course it is necessary to take care of antenna to be made of material with a minimum, better zero, absorption of radiation. It is best of all to fabricate the antenna of a superconductor with the energy gap  $\Delta$  more than  $\hbar\omega$  of the incident radiation so as the antenna material to be superconducting at all incident radiation frequencies. In case when the antenna is made of superconductor its two parts may function as two electrodes as well bringing the bias current into the absorber-TES what will provide the Andreev reflection at the boundaries between the absorber-TES and the antenna. The efficiency of said above antennas is of order of 50% what means that ~50% of the incident radiation flow is absorbed by the matched load in the antenna center [25]. The matching problem of a microbolometer impedance of order of 10-15  $\Omega$  or less with the output impedance of the antenna ~120  $\Omega$  deposited onto substrate, for instance silicon or quartz, may be solved, for example, by means of the connection between the absorber-TES and the antenna output the microstrip transformer of approximately  $\lambda/4$  length, where  $\lambda$  is the wavelength of the incident radiation, fabricated by microfilm technology methods like it was made, for instance, in [24] for the case of SIS-mixer.

The SQUID-picoammeter with the subsequent amplifying stages is the best solution for the measurement of the output signal of the Andreev reflection hot-electron TES-microbolometer because the noise current of the best SQUID-picoammeters is  $\sqrt{i_n^2} \cong 0.5 \text{ pA} \cdot \text{ Hz}^{-1/2}$  [21] what is approximately three times less in comparison with the estimated above intrinsic noise current of the microbolometer at the resistance of units Ohm.

## 6. Conclusion.

The important results of the first works on investigation of the normal metal hot-electron microbolometer with SIN-junction sensor for the signal read-out are the experimental confirmation of the Andreev reflection of electrons at the boundaries of the normal metal absorber and the superconducting lead electrodes when hot electron energy does not flow out from the absorber to the electrodes as well as the estimation of the noise equivalent power of such microbolometer. As the consequence of review and comparison of research results of different authors on two types of the Andreev reflection hot-electron microbolometer made in the present work the advantage of the superconducting transition-edge sensor (TES) with electrothermal feedback used as the sensor for the read-out the signal of such microbolometer compared with the single SIN-junction sensor for the same purpose is shown. The origin of this advantage is that whole volume of the absorber participates in the generation of the microbolometer output signal in case of the combined absorber-TES when only part of the absorber does this in case of the single SIN-junction sensor. On account of this fact the microbolometer with the TES combined with the absorber has at least one order better (lower) noise equivalent power (*NEP*) in comparison with the microbolometer with the single SIN-junction sensor having the same absorber dimensions. In the same time a design of the microbolometer with multiple SIN-junction sensor looks too complicated and problematic. In the first case the absorber-TES has to be made of a superconductor or as an bilayer of superconductor and normal metal with the proximity effect under condition that its superconducting transition temperature has to be somewhat higher than the microbolometer temperature as well as the bias d.c. current and radiation lead electrodes into the absorber-TES have to be fabricated of a superconductor with the energy gap much higher in comparison with this value of the absorber-TES. The main way to achieve the best *NEP* of said microbolometer is the reducing of absorber-TES dimensions limited by technology possibilities and the application of the planar antennas for the matching of the microbolometer with the incident radiation flow as well as the extralow-noise SQUID-picoammeter with SQUID input coil connected in series with the absorber-TES and fixed bias voltage applied over this series connection for the microbolometer output signal read-out and amplification. The *NEP* of the microbolometer in such version of order of  $10^{-20} \text{ W} \cdot \text{Hz}^{-1/2}$  and lower is expected at the existing technological possibilities. At present time experiments for the realization of the proposed solutions are in progress.

The author thanks A.F. Andreev and N.S. Kardashev for the stimulation of this work and J.M. Martinis, K.D. Irvin, P.L. Richards, K.O. Keshishev, G.D. Bogomolov and M.A. Tarasov for useful discussions and suggestions. This work is supported by the International Science and Technology Center (Project N 1239).

## References.

1. V.D. Gromov, N.S. Kardashev, V.D. Kurt et al., The Project “Submillimetron”, *Scientific Session of the Astro Space Center of the P.N. Lebedev Physics Institute of RAS, Pushchino* (in Russian), (January 1998).
2. L.S. Kuzmin, N.S. Kardashev, V.G. Kurt et al., *Proc. of ESTEC Workshop, Noordwijk*, 127 (November 1998).
3. A.N. Vystavkin, D.V. Chuvaev, T. Claeson et al., *Proc. of 10-th Intern. Symposium on Space Terahertz Technology, Charlottesville, USA*, 372 (March 1999).
4. N.D. Whyborn, *Proc. of ESA Symposium devoted to the Far InfraRed and Submillimeter Telescope (FIRST) mission, Grenoble, France, Institut de Radio Astronomie Millimetrique*, 19 (April 1997).
5. M.J. Griffin, *ibid.*, 31.
6. J.J. Bock, H.G. LeDuc, A.E. Lange, J. Zmuidzinas, *ibid.*, 349.
7. M. Nahum, P.L. Richards, C.A. Mears, *IEEE Trans. Appl. Supercond.* **3**, 2124 (1993).
8. M. Nahum, J.M. Martinis, *Appl. Phys. Lett.* **63**, 3075 (1993).
9. European Space Agency Tender AO3370 “Hot-electron Microbolometer Technology for IR and Sub-mmW Application”. Open Date: Oct. 2 (1997).
10. B.S. Karasik, W.R. McGrath, H.G. LeDuc, M.E. Gershenson, *Supercond. Sci. Technol.* **12**, 745 (1999).
11. A.F. Andreev, *Sov. Phys. JETP* **19**, 1228 (1964).
12. A.N. Vystavkin, D.V. Chouvaev, L.S. Kuzmin et al., *Proc. of the 4-th Intern. Conf. on Millimeter and Submillimeter Waves and Applications, San Diego, USA*, 441 (July 1998).
13. D.V. Chuvaev, L.S. Kuzmin, M.A. Tarasov et al., *Proc. of 9-th Intern. Symposium on Space Terahertz Technology, Pasadena, USA*, 331 (March 1998).
14. A.N. Vystavkin, D.V. Chouvaev, L.S. Kuzmin et al., *Russian Phys. JETP* **115**, 1085 (1999).
15. M. Nahum, J.M. Martinis, *Appl. Phys. Lett.* **66**, 3203 (1995).
16. J.M. Martinis, *NIM A370*, 171 (1996).
17. K.D. Irwin, *Appl. Phys. Lett.* **66**, 1998 (1995).
18. K.D. Irwin, G.C. Hilton, J.M. Martinis, B. Cabrera, *NIM A370*, 177 (1996).
19. S.W. Nam, B. Cabrera, B. Chugg et al., *NIM A370*, 187 (1996).
20. K.D. Irwin, G.C. Hilton, D.A. Wolman, J.M. Martinis, *Appl. Phys. Lett.* **69**, 1945 (1996).
21. A.T. Lee, S.-F. Lee, J.M. Gildemeister, P.L. Richards, *Proc. of 7-th Symp. on Low Temp. Detectors, Munich*, 123 (27 July - 2 August 1997).
22. A.N. Vystavkin, V.V. Migulin, *Radiotekhnika i Elektronika* **12**, 1989 (in Russian) (1967).
23. A.T. Lee, P.L. Richards, S.W. Nam et al. *Appl. Phys. Lett.* **69**, 1801 (1996).
24. Yu.V. Belitsky, S.V. Yacobson, L.V. Filippenko et al., *Journal of Communications Technology and Electronics, Russia* **41**, 113 (1996).
25. G.M. Rebeiz, *Proc. of the IEEE* **80**, 1748 (1992).

# Development of Focal Plane Arrays Utilizing NbN Hot Electron Bolometric Mixers for the THz Regime

E. Gerecht<sup>1</sup>, C. F. Musante<sup>2</sup>, Y. Zhuang<sup>2</sup>, M. Ji<sup>2</sup>, and K. S. Yngvesson<sup>2</sup>

<sup>1</sup>Department of Physics and Astronomy,

<sup>2</sup>Department of Electrical and Computer Engineering,  
University of Massachusetts, Amherst, MA 01003

**T. Goyette and J. Waldman**

Submillimeter Technology Laboratory, University of Massachusetts at Lowell Research Foundation,  
Lowell, MA 01854

**ABSTRACT** - Improvements in device development and quasi-optical coupling techniques utilizing planar antennas have led to a significant achievement in low noise submillimeter wave receivers at progressively higher frequencies. Hot Electron Bolometric (HEB) receivers made of thin film superconducting films such as NbN have produced a viable option for instruments designed to measure the molecular spectra for astronomical applications as well as in remote sensing of the atmosphere. Total system DSB receiver temperatures of 500 K at 1.56 THz and 1,100 K at 2.24 THz were measured since the last STTSymposium. These results are 13 and 20 times the quantum noise limit at the respective frequency (the DSB quantum noise limit ( $hf/2k$ ) is about 24 K at 1 THz). Typical best performance for Schottky barrier mixers is about 100 to 200 times the quantum noise limit. The technology of NbN Hot Electron Bolometric (HEB) mixers is progressing from the one pixel platform into a multi pixel system and special considerations of the new requirements for such devices is emphasized. One important characteristic is the LO power consumption which is in the hundreds of nanowatts range and, therefore, makes NbN HEB mixers excellent devices to integrate with a number of promising power sources under development as well as available technologies. Furthermore, new developments are under way which will decrease the optical and microwave coupling loss further; in particular, improvement of the RF match of the device to the antenna, optimization of the input impedance of the IF amplifier, and further improvement of the NbN film active medium quality. Preliminary study of MgO substrates shows an improved IF bandwidth. IF noise bandwidths in excess of 10 GHz are expected in the near future.

The recent results reported here make the development of focal plane arrays with tens of HEB mixer elements on a single substrate for real time imaging systems in the THz region an achievable goal.

## I. INTRODUCTION

The development of low-noise receivers in the THz frequency region is primarily motivated by the need for low noise and low power consumption receivers for the next generation of space-based and air-borne astronomical observatories (FIRST, SOFIA, etc.), as well as space-based remote sensing of the Earth's atmosphere (EOS-MLS). Until a few years ago, the only heterodyne receivers available for the THz

region utilized nonlinear frequency-conversion devices which were either GaAs Schottky Barrier Diodes (SBD) or InSb Hot Electron Bolometers (HEB). THz SBD mixer technology has recently made a transition from cumbersome whiskered diodes in corner-cube mounts to planar versions in waveguide. The Double SideBand (DSB) receiver noise temperature of SBD mixer receivers has remained essentially stationary at about  $(100-200) \times hf/2k$  [1] ( $hf/2k$  is the quantum limit for DSB receiver noise temperature and is about 24 K at 1 THz). Fabrication technology and material parameters limit the size of the monolithic junction and therefore limit the noise temperature performance. In addition, SBD receivers require a few mW of LO power. InSb mixers have always been too restricted in bandwidth (only about 1 MHz) for most applications. Below 1 THz, SIS (Superconductor/Insulator/Superconductor) mixer receivers have excellent noise temperature (only a few times the quantum noise limit). The noise performance is limited to frequencies below or about equal to the superconducting bandgap frequency.

Hot Electron Bolometric (HEB) mixers, which use nonlinear heating effects in superconductors near their transition temperature, have become an excellent alternative for applications requiring low noise temperatures at frequencies from 1 THz up to the Near IR. There are two types of superconducting HEB devices, the Phonon-Cooled (PC) version [2], and the Diffusion-Cooled (DC) version [3][4]. At present, most of the lowest recorded receiver noise temperatures have been obtained with the PC type HEB [5][6], although the difference is not very large. This paper only describes the development of the PC HEB. Superconducting HEB mixers also require much less LO power than SBD receivers (100 nW to 1  $\mu$ W for PC HEBs). The only practical LO source, presently available, is an FIR gas laser although solid state LO sources with sufficient amount of power are under development and will be available in the future. The present state-of-the-art of different THz receivers is compared in FIG. 1.

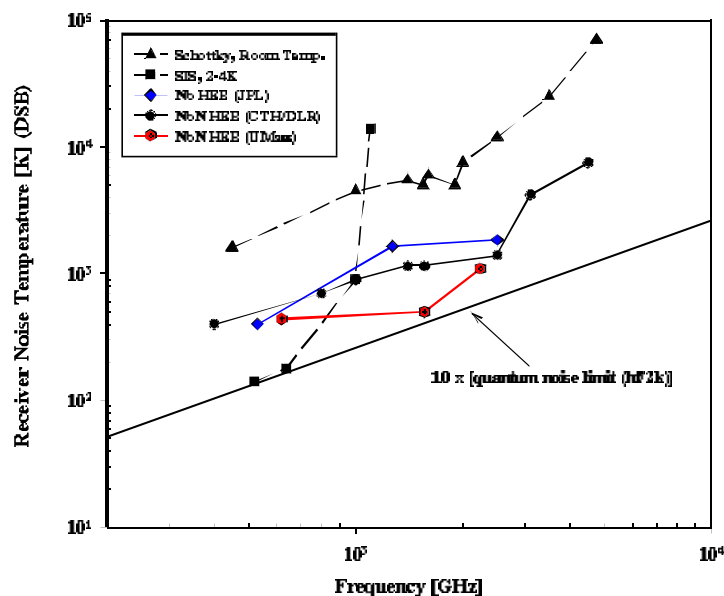


**FIG. 1. Noise temperatures as a function of frequency for receivers in the terahertz regime.**

The conversion gain and output noise of an HEB mixer can be calculated using what has become the “standard” model for HEB devices [7][8]. It is found that there is an optimum amount of LO power which yields the minimum noise temperature. In practice the optimum receiver noise temperature occurs for a bias current which is about 30 - 40 % of the current in the resistive region of the I-V curve without LO power. The standard model, which assumes a uniform electron temperature, is useful for a first order description of the PC HEB, but can not give a complete description of the device. New models for the mixer operation for frequencies in the terahertz regime assuming non-uniform electron temperature are under investigation [9].

The IF bandwidth for the conversion gain is determined by the thermal time-constant ( $\tau_m$ ) of the HEB device. The HEB dissipates the power it absorbs through a two-stage process: the heated electrons first emit phonons, which will then be transmitted through the film/substrate interface into the substrate. An interface resistance due to phonon mismatch has to be taken into account, and this resistance varies with the substrate upon which the thin film is deposited. To maximize the IF bandwidth, the film should be as thin as possible while still having good superconducting properties (high  $T_c$  and low  $\Delta T_c$ ). The mixer time-constant ( $\tau_m$ ) also includes a factor which depends on the self-heating of the bolometer [7]. The receiver noise temperature bandwidth ( $B_{NT}$ ) is wider than the conversion gain bandwidth ( $B_G$ ). The fact that the receiver noise temperature bandwidth is two to three times wider than the conversion gain bandwidth is a well-known feature of HEB mixers. This characteristic can be understood if one realizes that the main noise process in the device (temperature fluctuation noise) yields a noise output which falls at the same rate as the conversion gain, flattening the net receiver noise dependence on the IF frequency.

## II. DEVICE DESIGN AND FABRICATION

A typical HEB device is made from a thin (3 to 4 nm) film of NbN deposited on a substrate of silicon, quartz, sapphire or MgO by DC magnetron sputtering. Thinner films are desirable in order to achieve wider IF bandwidth. The critical temperature of the NbN film is about 10 K, depending on film quality and thickness, and efficient mixing occurs at about half that temperature. Much effort has been spent on improving the quality of the NbN films, which is especially critical for the thinnest films. Above the superconducting bandgap frequency (roughly 1 THz for these films), terahertz radiation sees a resistance roughly equal to the normal resistance, which is 300  $\Omega$ /square to 600  $\Omega$ /square. A device with an aspect ratio (length to width) of from 1:5 to 1:10 will therefore match a typical antenna impedance of 75  $\Omega$ . The critical current of a device is a few hundred  $\mu$ A, while a typical DC bias voltage is 1 mV. Since the device acts as a bolometer, the absorbed LO power, which is a function of the device area, is measured by the device itself and is computed from its I-V curve. Our devices have a length of 0.6 to 1  $\mu$ m and LO power from 0.5 to 1  $\mu$ W.

Quasi-optical coupling is very convenient at the very high THz frequencies where waveguides become increasingly difficult to manufacture. We couple our devices through a 4 mm diameter elliptical lens made from high-purity silicon. In order to facilitate testing over a wide range of frequencies, we have initially used a log-periodic self-complementary toothed antenna. This design is scaled from the millimeter wave design in [10] and is illustrated in FIG. 2. Other antennas under investigation in a number of laboratories are spiral antennas, twin dipole/slot antennas, and slot ring antennas. We have used a log-periodic antenna with a maximum frequency of 3.4 THz most recently (designated as Antenna C). Our log-periodic antennas have a 4:1 bandwidth. The antenna is fabricated from a gold film using lift-off lithography. At the moment, we use no reflection matching for the silicon lens ( $\epsilon_r = 11.8$ ). Optical losses should decrease by about 2 dB once a suitable material for such coatings in the THz range. One such material, which is under investigation, is parylene [11][12].

The HEB receiver is cooled in an IRLAB liquid helium dewar, and THz radiation enters the dewar through a 0.75 mm thick polyethylene window, as shown in FIG. 3. The mixer is connected through a bias tee and a semi-rigid coaxial cable to a cooled HEMT IF amplifier. In the most recent experiments, the IF chain noise temperature was estimated to be 7 K with a bandwidth from 1250 MHz to 1750 MHz.

The LO source was a difluoromethane gas laser, which could be made to lase either at 191  $\mu\text{m}$  wavelength (1.56 THz) or at 134  $\mu\text{m}$  (2.24 THz) by choosing one of two orthogonal polarizations. It has an invar-supported structure which was designed with thermal compensation to maintain constant cavity length. In order to obtain high power single mode output, uniform couplers consisting of wire grids deposited on a silicon substrate (also coated for high reflectivity from 9-11  $\mu\text{m}$ ) were used. The laser beam was measured to have a Gaussian spatial output profile with the first sidelobes 20 dB down. The FIR laser was pumped by an extremely stable two meter long grating-tuned  $\text{CO}_2$ -laser. The available power from the  $\text{CO}_2$ -laser was

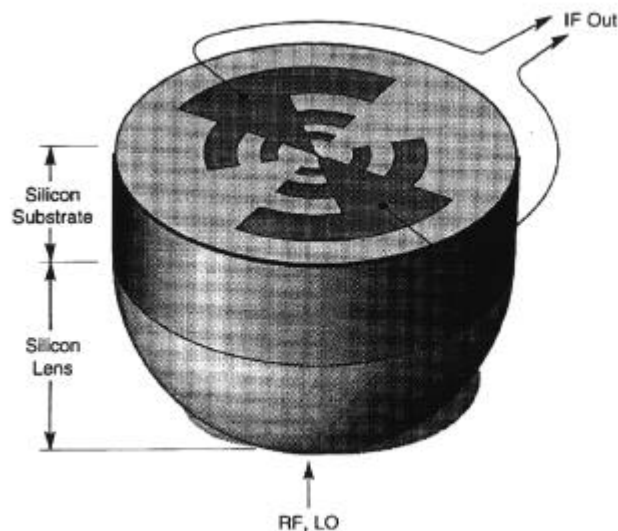


**FIG. 2. Log-periodic toothed antenna fabricated on a silicon substrate and attached to a silicon lens.**

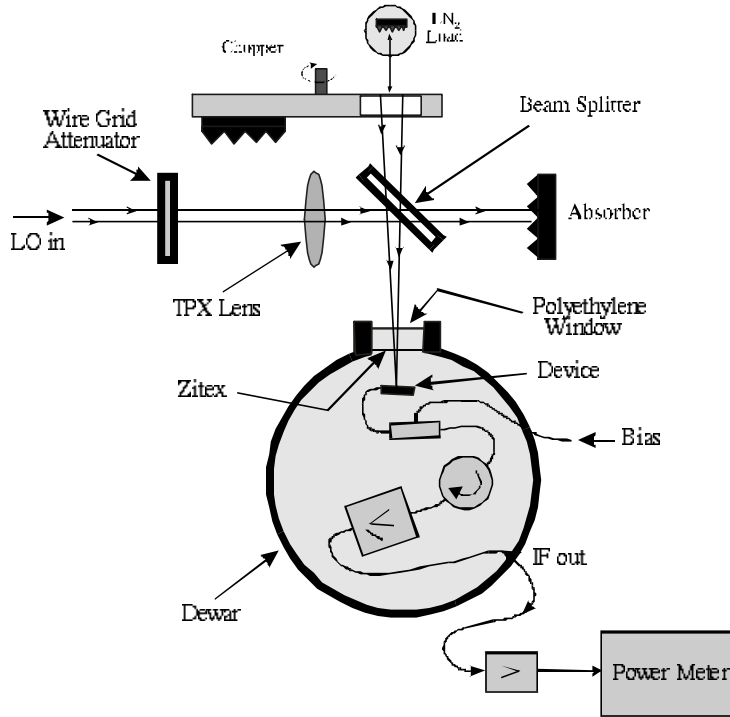


**FIG. 3. Measurement setup for noise temperature.**

about 200 W [13]. A 6  $\mu\text{m}$  thick mylar window was used as beam splitter. A dielectric lens was used to focus the laser LO. The 50-100 mW output power of the laser was attenuated by crossed wire grid polarizers in order to set the optimum LO level. Although mechanical chopping of the hot/cold source is possible and sometimes used, a typical measurement was performed by inserting a room temperature absorber in front of the LN<sub>2</sub> load by hand. The IF output power was detected on a power meter and recorded in a computer with the help of a *Labview* program. The fact that it is possible to perform the Y-factor measurement without the use of a rotating chopper is a tribute to the excellent amplitude stability of the UMass/Lowell laser used for this experiment. The amplitude stability of the 1.56 THz laser source, measured over a period of minutes, with a relatively fast (0.1 s) integration time, was 0.3%. The stability was also evident in the I-V curves recorded by our fast (about 50 ms) computerized recording system.

### III. EXPERIMENTAL RESULTS FOR SINGLE-ELEMENT RECEIVERS

TABLE I gives a summary of data measured for devices which reached DSB noise temperatures at 1.56 THz of 500 K and at 2.24 THz as low as 1,100 K. The output noise temperature was measured by comparing the total output noise power in the optimum operating point (with LO applied) with that of the device in the superconducting state (the bias voltage was decreased to zero). Since the IF noise temperature was

**TABLE I. SUMMARY OF NOISE DATA**

$f$ [THz]	Dev. # / Ant.	$T_{\text{out}}$ [K]	$T_{\text{DSB}}$ [K]	$T_{\text{DSB},i}$ [K]	$L_{c,\text{tot}}$ [dB]	$L_{\text{opt}}$ [dB]	$L_{c,i}$ [dB]
1.56	6/C	110	500	180	9.5	4.5	5.0
2.24	6/C	110	1,100	180	12.9	7.9	5.0

known, we could find the out put noise tem per a ture ( $T_{\text{out}}$ ) from this mea sure ment. The opti cal cou pling loss was es ti mated from known losses in win dows, lens re flection loss, etc. The re main ing con ver sion loss is the in trinsic con ver sion loss,  $L_{c,i}$ , which can be cal cu lated from the ory ac cord ing to the stan dard model. A set of con sistent val ues of  $L_{c,i}$ ,  $T_{\text{out}}$ , and  $T_{\text{R,DSB}}$  can then be ob tained [8]. We have iden ti fied part of the in crease (0.5 dB) in opti cal losses from 1.56 THz to 2.24 THz as be ing due to a res o nance in the poly ethylene win dow ma te rial. Also, the at mo spheric at ten u a tion is higher at 2.24 THz than at 1.56 THz. The thermal noise power from the cold source had a path length of about 0.6 m be fore it reached the dewar win dow and the es ti mated at ten u a tion over this path at 2.24 THz is 0.5 - 1 dB. There is still an un ex plained in crease of about 2 dB. Some of the in creases in opti cal losses are in evi ta ble but care ful opti cal de sign should be able to elimi nate a part of this in crease with fre quency.

#### IV. FOCAL PLANE ARRAYS WITH INTEGRATED HEB RECEIVERS

In order to fully utilize the future space-borne and airborne facilities, it will be advantageous to develop Focal Plane Arrays (FPAs) which incorporate the new low-noise HEB receivers. In astronomical THz observations, for example, one often wants to map an area such as an interstellar cloud or a galaxy. The speed with which this map ping can be done will in crease in pro por tion to the num ber of ele ments in the array. Such systems ex ist at mil li me ter waves in ground-based tele scopes [14][15]. There are well-known limitations for the smallest beam spacings which can be ob tained [16]. These can be dis cussed in terms of the geo metric spacing ( $\Delta x$ ) of ad ja cent ele ments in the ar ray. If each ele ment in the ar ray il lu mi nates a tele scope at an  $f$ -num ber of  $f/D$ , then ideal sam pling of the fo cal plane im age at the Nyquist rate re quires that  $\Delta x = 0.5 \times (f\lambda/D)$  [15][17]. There is no type of feed ele ment which is ca pa ble of be ing spaced this close while still il lu mi nating the tele scope ef fi ciently [15][18]. About the best which has been achieved in prac tice is  $\Delta x = 1 \times (f\lambda/D)$ , and cor rugated horns, for ex am ple, which are very ef fi cient feed an ten nas, must be spaced at about  $2 \times (f\lambda/D)$  [15]. The dis placement ( $N$ ) of the tele scope beam on the sky, mea sured in Full Width Half Maximum Power (FWHM) beam widths is also re lated to  $\Delta x$  by  $N \approx \Delta x / 1.2 \lambda (f/D)$  [16]. An array element spacing of about  $1.2 \times (f\lambda/D)$  thus cor responds to a spacing of ad ja cent beams on the sky of one FWHM beam width.

There are two different methods for coupling dielectric lenses to an antenna array:

- (i) a single-lens configuration; and
- (ii) a multi-lens configuration.

If we first consider the single-lens case, the individual elements placed near the focus of the lens will radiate a beam which has an f-number of roughly 1.0, i.e. a 56 degree FWHM beam width. Filipovic et al. [19] analyzed this case and derived the minimum spacing possible. To obtain a rough estimate, we assume a spacing corresponding to one beam width, and find  $\Delta x \approx \lambda_0 / \sqrt{\epsilon_r}$ , or  $35 \mu\text{m}$  for  $\lambda_0 = 119 \mu\text{m}$ . This leads to very tight constraints on any wiring which has to be connected to the devices and antennas, and it is obviously impossible to place the IF amplifiers close to the antennas.

The multi-lens configuration, on the other hand, is much more flexible. The relatively small (radius  $R \approx 10 \lambda_0$ ) elliptical lens which we have developed, lends itself well for use in this “fly’s eye” type of array, see FIG. 4. Both the LO and the incoming signal are injected through a quasi-optical diplexer. The optics thus are unchanged from our single-element approach. The beam width from each lens is approximately given by  $1.2 \times \lambda / (2R)$ , and the lenses can be placed at a spacing equal to their diameter ( $2R$ ), i.e.  $\Delta x = 2R$ . The f-number of the array elements will be approximately  $2R/\lambda (\approx 20)$ , which may be about right for a typical Cassegrain telescope, without recourse to further focusing. The beam-scan ( $N$ ) will be about one FWHM beam width. The angular resolution (angular spacing between adjacent pixels) will thus be about equal to the diffraction-limited beam width of the telescope, which is typical of the best resolution obtainable for FPA receivers as discussed above.

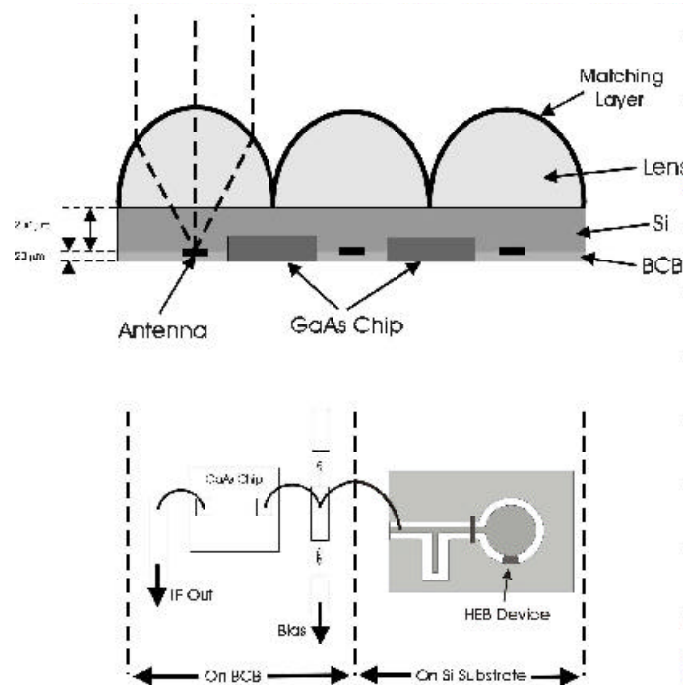


**FIG 4. A portion of an HEB THz focal plane array.**

The FPA can not use the log-periodic toothed antennas which we have employed so far since these are unnecessarily large. The focal plane array system is also not likely to require the very wide bandwidth of these antennas. We instead propose a slot-ring antenna as shown in FIG. 5 (a double-slot antenna would also be possible). The slot-ring antenna has been demonstrated in a four-element array for a 35 GHz monopulse radar [20] and also, for example, in 94 GHz MMIC receivers [21]. This antenna is linearly polarized and can receive radiation in either of two perpendicular polarizations. There are several possible configurations to explore. FIG. 5 shows one such configuration in which the LO and RF are injected in the same polarization as in our present single lens receiver. The IF is extracted through a coplanar waveguide (CPW) from the point on the ring at which the THz fields have a null. It is important to use air bridges in order to cancel the even mode on the CPW. In the above-mentioned monopulse radar project, the LO and signal were injected in opposite polarizations through a simple wire grid and two (reversed) Schottky barrier mixer diodes were placed at the 45 degree positions across the ring thus forming a balanced mixer. HEB devices can not be reversed, as can Schottky diodes, but one or two devices could be placed at the 45 degree positions and this would allow very efficient LO injection (ideally without any loss) through a wire grid. The signal would also be injected without loss, ideally. The RF impedance of the HEB device(s) would be adjusted in the usual way by varying its (their) aspect ratio for optimum coupling to the ring. Different types of filters can be tried on the IF line in order to prevent leakage of the RF and LO through the CPW. FIG. 5 and FIG. 6 show different versions of this.

The entire silicon chip with antennas and NBN mixer devices would be fabricated in one process. MMIC HEMT amplifier chips (size about  $1 \text{ mm}^2$ ) would be integrated with the mixers by inserting them in etched wells in the silicon substrate, and transmission lines could be routed on a thin layer of spun-on dielectric. FIG. 7 shows a wide band MMIC amplifier under development in collaboration with Chalmers University of Technology [courtesy of Herbert Zirath]. The amplifier will include (on chip) the appropriate impedance transformation as well as bias circuitry for the HEB devices. A nominal bandwidth of 4-8 GHz will be suitable for

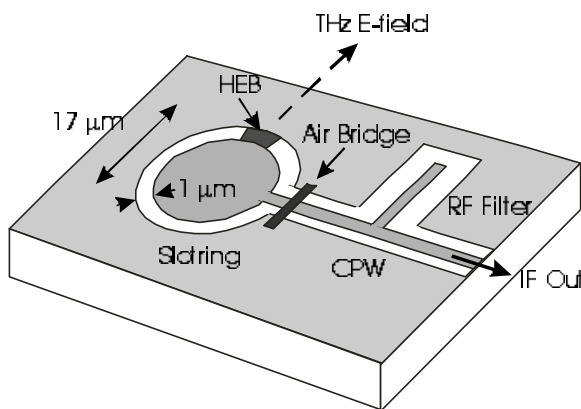


**FIG 5. HEB device coupled to a slot ring antenna with coplanar waveguide output for the IF.**

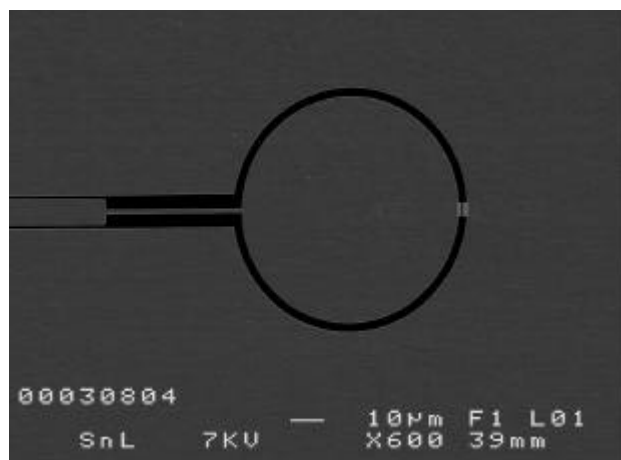


**FIG 6. A different version of the slot ring antenna/HEB device.**

many anticipated system applications. Another important consideration is to minimize the DC power consumption of the MMIC amplifier.

### ACKNOWLEDGEMENTS

This work was supported by the National Science Foundation (ECS-9313920) and NASA (NASA NAG5-7651). We would like to acknowledge Matthias Kroug of Chalmers University of Technology for fabricating one of the devices used for this research, and the slot ring coupled HEB device shown in FIG. 6. We would also like to acknowledge Herbert Zirath and the group of Professor Erik Kollberg at Chalmers University for collaboration on designing IF amplifiers suitable for HEB focal plane arrays.

### REFERENCES

1. P.H. Siegel, R.P. Smith, M. Gaidis, S. Martin, J. Podosek, and U. Zimmermann, "2.5 THz GaAs monolithic membrane-diode mixer," *Proc. Ninth Intern. Space THz Technol. Symp.*, JPL, March 1998, p. 147.
2. E. M. Gershenzon, G. N. Gol'tsman, I. G. Gogidze, Y. P. Gousev, A. I. Elant'ev, B. S. Karasik, and A.D. Semenov, "Millimeter and Submillimeter Range Mixer Based on Electronic Heating of Superconducting Films in the Resistive State", *Soviet Physics: Superconductivity*, **3**, 1582, 1990.
3. D.E. Prober, "Superconducting terahertz mixer using a transition-edge microbolometer," *Appl. Phys. Lett.*, **62**, 2119, 1993.
4. R. Wyss, B. Karasik, W.R. McGrath, B. Bumble, and H. LeDuc, "Noise and bandwidth measurements of diffusion-cooled Nb HEB mixers at frequencies above the superconductive energy gap," *Proc. Tenth Intern. Space THz Technol. Symp.*, U. Virginia, March 1999, p. 214.
5. P. Yagoubov, M. Kroug, H. Merkel, E. Kollberg, J. Schurbert, H.-W. Huebers, S. Svechnikov, B. Voronov, G. Gol'tsman, and Z. Wang, "Hot Electron Bolometric Mixers Based on NbN Films Deposited on MgO Sub-

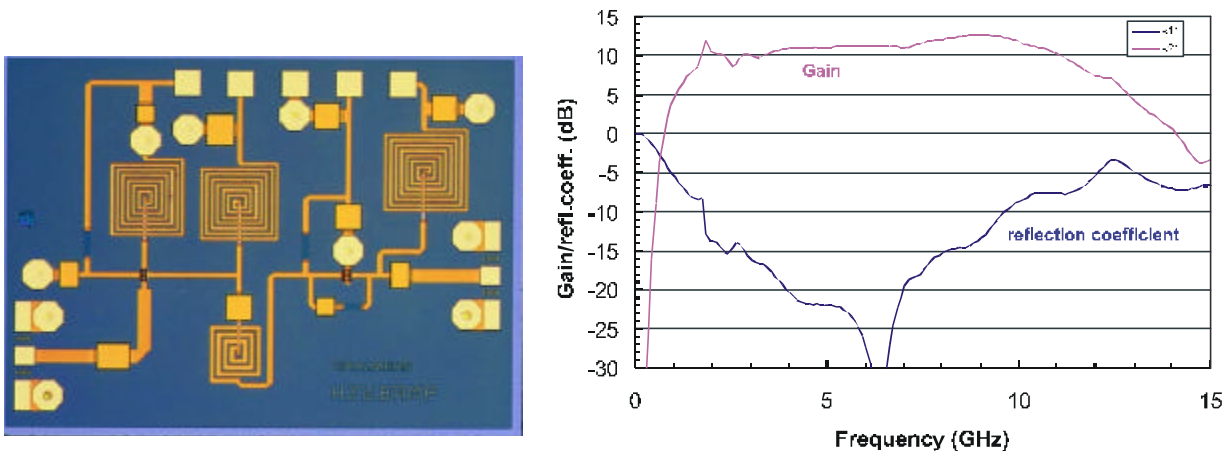


**FIG 7. Wideband (2-12 GHz) MMIC PHEMT amplifier designed at Chalmers University. Measured data for gain and reflection coefficient are also shown.**

- strates," *Fourth European Conference on Applied Superconductivity (EUCAS 99)*, Sitges, Barcelona, Spain, September 1999.
6. E. Gerecht, C.F. Musante, Y. Zhuang, M. Ji, K.S. Yngvesson, T. Goyette, J. Waldman, P.A. Yagoubov, M. Kroug, H. Merkel, E.L. Kollberg, J. Schubert, H.-W. Huebers, G.N. Gol'tsman, B.M. Voronov, and E.M. Gershenzon, "Improved Noise Temperature and Bandwidth of Phonon-Cooled NbN Hot Electron Bolometric Mixers," *Proc. Intern. Semicond. Device Research Symp.*, Charlottesville, VA., Dec. 1999.
  7. H. Ekstroem, E.L. Kollberg, B. Karasik, and K.S. Yngvesson, "Conversion gain and noise of niobium hot-electron mixers," *IEEE Trans. Microw. Theory Techniques*, MTT-43, 938, 1995.
  8. K.S. Yngvesson, and E.L. Kollberg, "Optimum receiver noise temperature for NbN HEB mixers according to the standard model," *Proc. Tenth Intern. Space THz Technol. Symp.*, U. Virginia, March 1999, p. 566.
  9. P. Khosropanah, H. Merkel, S. Yngvesson, A. Adam, S. Cherednichenko, and E. Kollberg., "A Distributed Model for Phonon-Cooled HEB Mixers, Predicting IV Characteristics, Gain, Noise and IF bandwidth," this conference.
  10. B.K. et al., "A planar wideband 80-200 GHz receiver," *IEEE Trans. Microw. Theory Techniques*, MTT-41, 1730, 1993.
  11. M. Ji, C. Musante, S. Yngvesson, A. J. Gatesman, J. Waldman, "Study of Parylene as Anti-reflection coating for Silicon Optics at THz Frequencies", *submitted to IEEE Micro and Guid. Lett.*
  12. H.-W. Huebers, priv. comm.
  13. Manufactured by Pacific Research, 12252 Gorham Ave., Los Angeles, CA.
  14. N.R. Erickson, P.F. Goldsmith, G. Novak, R.M. Grosslein, P.J. Viscuso, R.B. Erickson, and C.R. Predmore, "A 15 Element Focal Plane Array for 100GHz," *IEEE Trans. Microw. Theory Techniques*, MTT-40, 1 (1992).
  15. P.F. Goldsmith, C.-T. Hsieh, G.R. Huguenin, J. Kapitzky, and E.L. Moore, "Focal Plane Imaging Systems for Millimeter Wavelengths," *IEEE Trans. Microw. Theory Techniques*, MTT-41 (1993).
  16. K.S. Yngvesson, "Near-Millimeter Imaging with Integrated Planar Receptors: General Requirements and Constraints," in *Infrared and Millimeter Waves* (K. J. Button, Ed.), Academic Press, Orlando, FL., Vol. 10, Chap. 2, p.91 (1983).
  17. D.B. Rutledge, D.P. Neikirk, and D.P. Kasilingam, "Integrated-Circuit Antennas," in *Infrared and Millimeter Waves* (K. J. Button, Ed.), Academic Press, Orlando, FL., Vol. 10, Chap. 2, p.1 (1983).
  18. K.S. Yngvesson, J.F. Johansson, Y. Rahmat-Samii, and Y.S. Kim, "Realizable Feed-Element Patterns and Optimum Aperture Efficiency in Multi-Beam Antenna Systems," *IEEE Trans. Antennas and Propagat.*, AP-36, 1637 (1988).
  19. D.F. Filipovic and G.M. Rebeiz, "Off-axis Imaging Properties of Substrate Lens Antennas," *Proc. 5<sup>th</sup> Intern. Symp. Space THz Technology*, May 1994.
  20. S. K. Masarweh, T.N. Sherer, K. S. Yngvesson, R. L. Gingras, C. Drubin, A.G. Cardiasmenos, and J. Wolverton, "Modeling of a Monolithic Slot Ring Quasi-Optical Mixer," *IEEE Trans. Microw. Theory Techniques*, MTT-42, 1602 (1994).
  21. S. Raman and G.M. Rebeiz, "Single- and Dual-Polarized Millimeter-Wave Slot-Ring Antennas," *IEEE Trans. Antennas and Propagat.*, AP-44, 1438 (1996).

# **IF Bandwidth of Phonon Cooled HEB Mixers Made from NbN Films on MgO Substrates**

**S. Cherednichenko\***, M. Kroug, P. Yagoubov, H. Merkel, E. Kollberg  
Chalmers University of Technology, S-412 96 Gothenburg, Sweden

**K.S. Yngvesson**  
University of Massachusetts, Amherst, USA

**B. Voronov, G. Gol'tsman**  
Moscow State Pedagogical University, Moscow, Russia

\*serguei@ep.chalmers.se

## ***Abstract***

An investigation of gain and noise bandwidth of phonon-cooled hot-electron bolometric (HEB) mixers is presented. The radiation coupling to the mixers is quasi-optical through either a spiral or twin-slot antenna. A maximum gain bandwidth of 4.8 GHz is obtained for mixers based on a 3.5 nm thin NbN film with  $T_c=10$  K. The noise bandwidth is 5.6 GHz, at the moment limited by parasitic elements in the device mount fixture. At 0.65 THz the DSB receiver noise temperature is 700-800 K in the IF band 1-2 GHz, and 1150-2700 K in the band 3.5-7 GHz.

## ***Introduction***

The ongoing development of superconducting hot electron bolometric (HEB) mixers at THz frequencies is mainly driven by the need in radio astronomy for low noise and wide band heterodyne receivers.

Quasi optically coupled HEB mixers have been tested at frequencies up to several THz. Both the diffusion-cooled type, based on Nb, and the phonon-cooled type, based on NbN, have shown excellent results in terms of sensitivity. In the band between 1 THz and 2.5 THz the DSB receiver noise temperature is roughly 20 times the quantum limit which is much better than competing technologies such as Schottky diodes or SIS mixers [1- 5]. In addition, HEB mixers require much less local oscillator (LO) power than Schottky-mixers, typical is 50-300 nW depending on the bolometer size and critical current [6]. The gain bandwidth ( $f_0$ ) of diffusion-cooled mixers based on very short ( $L \leq 0.1$   $\mu\text{m}$ ) Nb bridges has been measured to be 9 GHz [7]. The best result for phonon-cooled mixers was so far 3.5-4 GHz, obtained with devices made from ultrathin ( $d=3$  nm) NbN films on sapphire substrates [8].

The maximum gain bandwidth of HEB mixers is set by the electron temperature relaxation time  $f_0=(2\pi\tau_\theta)^{-1}$ . A detailed study of electron dynamics in superconducting films under modulated electromagnetic radiation was done in [9]. For the phonon cooled type,  $\tau_\theta$  is a complicated function of several parameters: the electron-phonon interaction time  $\tau_{e-ph}$ , the ratio of the specific heats  $c_e/c_{ph}$  and the escape time  $\tau_{esc}$  of phonons from the film to the substrate.

As was shown earlier, for NbN  $\tau_{e-ph} \propto \Theta^{-1.6}$  and at 10 K  $\tau_{e-ph}$  equals 12 ps [10]. The escape time depends on film thickness ( $d$ ) and acoustic transparency ( $\alpha$ ) of the film-substrate interface,  $\tau_{esc} \propto d/\alpha$ . In the limit of ultrathin NbN films,  $d=3-5$  nm,  $\tau_{e-ph}$  and  $\tau_{esc}$  are of the same order of magnitude, and both time constants must be minimized in order to achieve a short electron relaxation time  $\tau_\theta$ . Therefore, NbN films with a high critical temperature  $T_c$  and good thermal coupling to the substrate are needed for large gain bandwidth.

Recent experiments showed that crystalline MgO as a substrate provides high quality NbN films with a phonon escape time which is two times shorter compared to films on Si or sapphire substrates [1]. An estimate based on [9] shows that 3 nm thin films on MgO with  $T_c=10$  K would allow for 5-6 GHz gain bandwidth.

Following this suggestion, HEB devices with film thickness 3.5 nm and 5 nm have been fabricated and characterized. The results for the mixer gain bandwidth are close to the predicted values. Ongoing work is now aimed at optimization of film technology in the limit of 3 nm thin films.

For practical application of HEB mixers one wishes to maximize the receiver noise bandwidth,  $f_{0N}$ , defined as the frequency band over which the receiver noise temperature stays within 2 times of its minimum value. A special feature of HEB mixers is the fact that  $f_{0N}$  may be 2-3 times larger than the gain bandwidth. This is because the dominating noise source in HEB mixers is thermal fluctuation noise, which has the same IF frequency dependence as the conversion gain [14]. This makes its contribution to the input noise temperature of the mixer independent of the IF frequency. The final goal of the project is to optimize  $f_{0N}$ . Here we present the first results from receiver noise temperature measurements in the 4-8 GHz band. We also show that a noise bandwidth of up to 10 GHz can be realized.

### ***Devices and Experimental Set-up***

NbN films are deposited by dc magnetron sputtering on MgO substrates heated up to 850 °C. Standard lithography techniques are used to pattern a NbN micro bridge integrated with a planar Au antenna. Details of the fabrication process can be found in [11]. HEB devices from three batches, labeled M2, M7 and M8, have been investigated; the device parameters are summarized in Table 1. Both a self complementary spiral and twin-slot antennas are used (see Fig. 1).

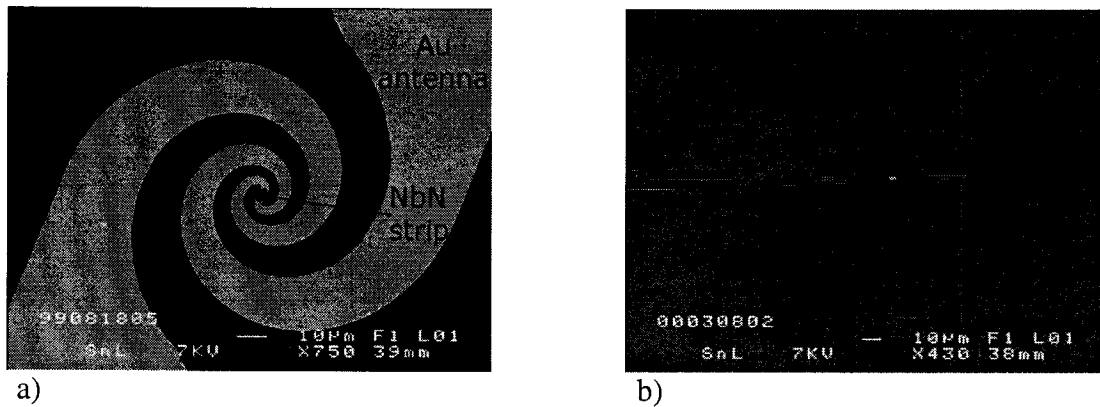


**Figure 1.** SEM micrograph of the antenna integrated mixers: (a) Selfcomplementary spiral (b) Twin-slot.

The measurement set-up is presented in Fig.2. For gain bandwidth measurements two backward wave oscillators (BWO) serve as LO and signal sources. The beams are focused by two Teflon lenses and combined by a 12  $\mu\text{m}$  thick Mylar beamsplitter. The cryostat is equipped with a Teflon window and a cooled 350  $\mu\text{m}$  Zitex G115 IR filter. The mixer is mounted onto a 12 mm diameter Si elliptical lens. The IF chain consists of a broadband bias-T followed by a two stage Miteq amplifier (0.1-20 GHz). With a second mixer the IF signal is down-converted to the 0-50 MHz band and measured by a power meter.

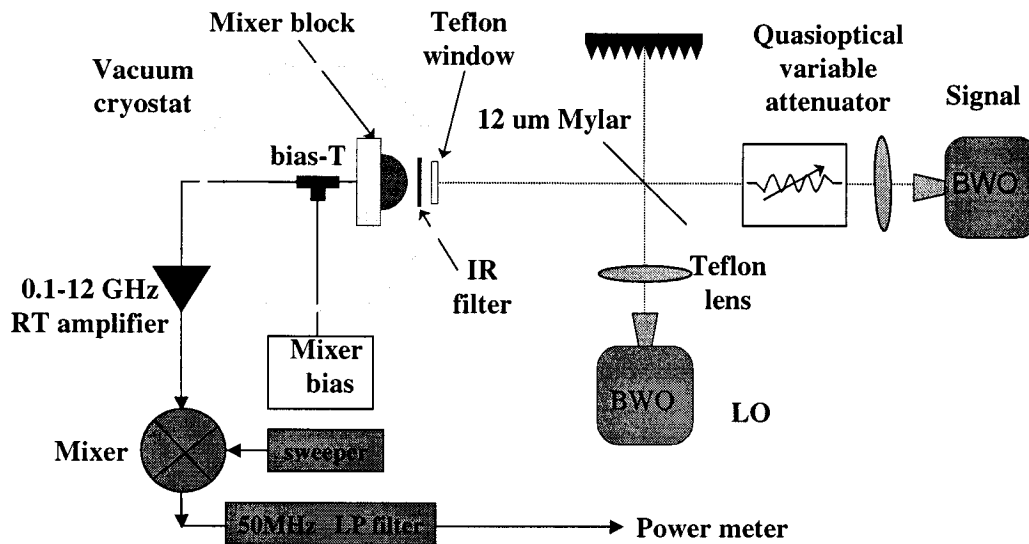


**Figure 2.** Measurement set-up for gain bandwidth measurements.

The DSB receiver noise temperature  $T_r$  is measured using the Y-factor technique with blackbody loads at 300 K and 77 K in the signal path. Two different cooled IF amplifiers with equivalent noise temperatures  $T_{IF}=5$  K (1-2 GHz) and  $T_{IF}=5-10$  K (4-8 GHz) are used in this case. Further amplification and signal registration is done in the same way as described above.

The mixer output noise temperature  $T_{out}$  is obtained by measuring the ratio of the receiver output noise power with the mixer in the operating point and in the superconducting state [12].

### *Gain bandwidth measurements*

The mixer gain bandwidth was measured for devices from three batches (M2, M7 and M8) with film thicknesses 5 nm and 3.5 nm. The mixer operating conditions in terms of dc bias and LO power are the same that yield the lowest receiver noise temperature.

The values obtained for the mixer gain bandwidth are: 4.5-4.8 GHz for the mixers based on a 3.5 nm NbN film with  $T_c = 10$  K (batch M7); 2.8 GHz for the mixers based on a 3.5 nm NbN film with  $T_c = 8.5$  K (batch M8); 3 GHz for the mixers based on a 5 nm NbN film with  $T_c = 8.5$  K (batch M2).

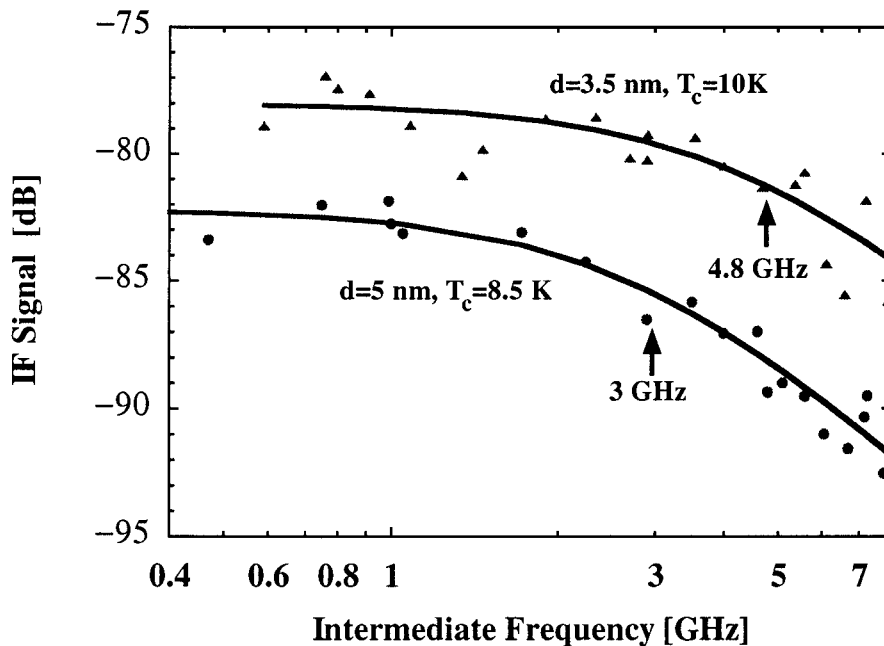


**Figure 3.** IF signal vs frequency for the mixers M2-1 and M7-7.

The detected signal vs. intermediate frequency for the mixers M2-1 and M7-7 is plotted in Fig. 3.

As was shown in [8] the two-temperature model, which was introduced in [9], can be successfully used for estimation of the HEB mixer IF bandwidth. Within this model the major tendencies of the gain bandwidth can be derived. Using the data of  $\tau_{e-ph}=0.4\cdot\Theta^{-1.6}$  (ns) [13] and  $\tau_{esc}=6\cdot d$  (ps), where  $d$  is in nm, [1], we calculated the gain bandwidth of NbN HEB mixers on MgO versus the electron temperature for different film thickness (Fig. 4). It can be seen from the picture that a gain bandwidth up to 6 GHz can be realized for 3 nm thick NbN films with  $T_c \geq 12$  K. The temperature dependence of the gain bandwidth at low electron temperature values and the weak dependence on the film thickness means that the electron-phonon interaction is the bottleneck of the electron cooling process. With an increase of the electron temperature the electron-phonon interaction becomes fast enough to provide rapid heat transfer from electrons to phonons. Under such conditions the phonon escape time becomes the bottleneck and the gain bandwidth is a function of the film thickness only. For each film thickness there is a maximum value of  $f_0$ , which can be reached when  $\Theta$  exceeds a certain value. A decrease of the film thickness can even result in a decrease of  $f_0$  if  $\Theta$  drops much.

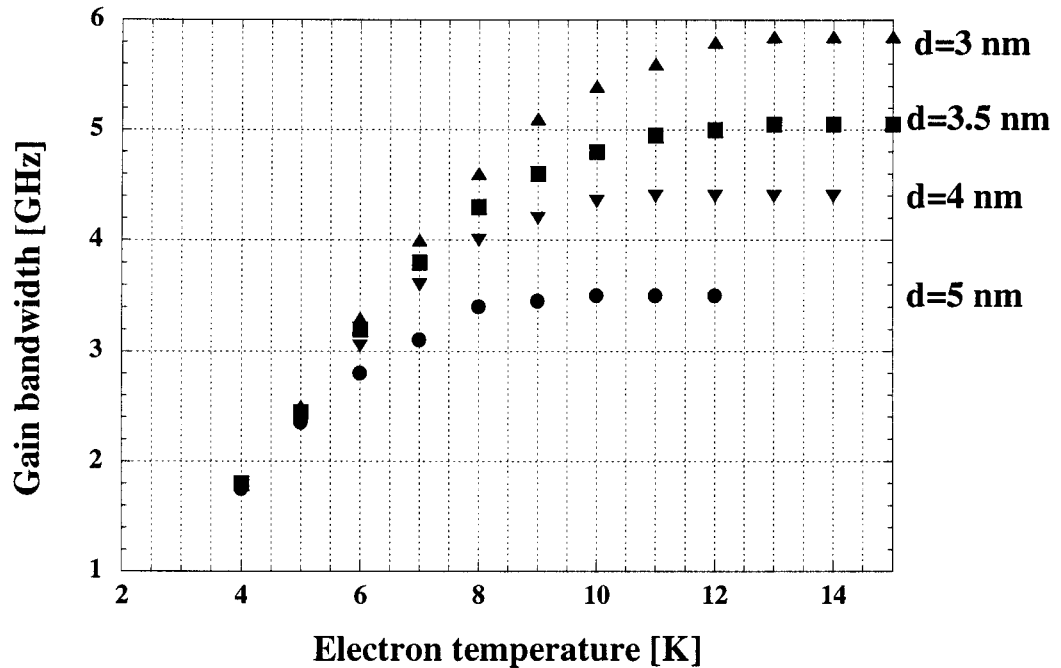


**Figure 4.** IF bandwidth of NbN phonon-cooled mixers according to the two temperature model.

**Table 1.** Device parameters and measurement results: Film thickness  $d$ , critical temperature  $T_c$  bolometer length  $L$  and width  $W$ , critical current  $I_c$  and, DSB receiver noise temperature  $T_r$ , mixer output noise temperature  $T_{out}$ , intrinsic mixer loss  $L_m$ , and mixer gain bandwidth  $f_0$ .

Device number	$d$ , nm and $T_c$ , K	$W \times L$ , $\mu\text{m}^2$	$I_c$ , $\mu\text{A}$	$T_r$ , K 1.5 GHz	$T_r$ , K 4 GHz	$L_m$ , dB 1.5 GHz	$T_{out}$ , K 1.5 GHz	$f_0$ , GHz
M2-1	5, 8.5	4x0.4	435	530	1150			3
M7-5	3.5, 10	2x0.1	290	750				4.5
M7-7	3.5, 10	2x0.1	210					4.8
M7-9	3.5, 10	2x0.3	300	850	1150	10.4	57	4.5
M7-10	3.5, 10	2x0.3	290	850*	1100	10.4*	57*	
M7-13	3.5, 10	2x0.3	260	850	1370	9.2	75	
M8-1	3.5, 8.5	4x0.4	107					2.8
M8-9	3.5, 8.5	2x0.3	120	980				2.5

\* values are extrapolated from mixer M7-9

### **Receiver Noise Temperature**

The receiver noise temperature was measured in the 1-2 GHz and 3.5-8 GHz bands. The best values of the DSB receiver noise temperature at 1.5 GHz are 530 K, 750 K and 980 K for batches M2, M7 and M8 respectively. According to our estimates the optical losses of the receiver are 4 dB.

Most of the mixers are integrated with a self-complementary spiral antenna which has been shown to work well from 0.5 THz up to 3 THz. We also used a twin-slot antenna designed for 600 GHz (sample M7-13). Mixers with both antenna types showed the same performance.

By measuring the receiver output noise power with the mixer in the superconducting state and in the operating point ( $U=P_{sc}/P_{op}$ ) one can calculate the mixer conversion loss  $L_m$  and the mixer output noise temperature  $T_{out}$ . Typical values for  $L_m$  are 9-10 dB, and for  $T_{out}$  50 K to 80 K. The knowledge of  $T_{out}$  allows one to estimate the receiver noise bandwidth  $f_{oN}$  which is given by  $f_{oN} \approx f_0 \cdot \sqrt{\frac{T_{out} + T_{IF}}{T_J + T_{IF}}}$ , where

$T_{out} = T_{fl} + T_J$ .  $T_{fl}$  and  $T_J$  are the electron temperature fluctuation noise and Johnson noise contributions to the mixer output noise [14], and  $T_{IF}$  is the noise temperature of the IF chain. Using the Nyquist theorem one can show that  $T_J$  approximately equals the

electron temperature, which is close to  $T_c$  [14]. From the measured data for  $T_{out}$  one ends up with the ratio  $f_{on}/f_0=2+2.5$  for these HEB mixers.

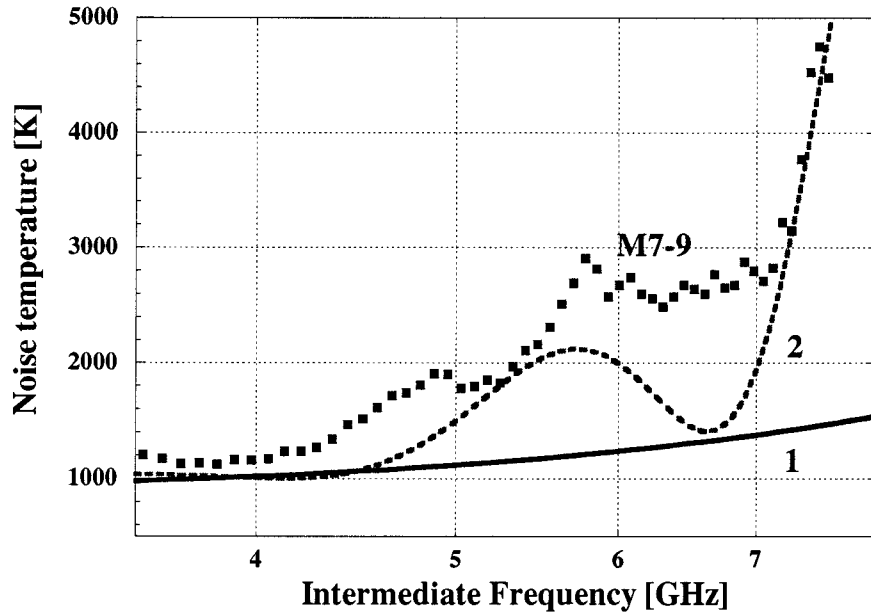


**Figure 6.** Receiver noise temperature in the 4-8 GHz band for device M7-9. Measured data (squares), calculations for ideal mixer mount (1) and coaxial mixer mount (2).

Using the data of  $L_m$ ,  $T_{out}$  (obtained at  $f_{IF}=1.5$  GHz) and  $f_0$  for the mixer M7-9,  $T_r$  as a function of  $f_{IF}$  is calculated for the band 4-8 GHz (see Fig. 6, solid line 1). For this calculation the IF noise is  $T_{IF}=6$  K, independent of frequency.

Measured data of  $T_r(f_{IF})$  are represented by the squares. With  $T_r = 850$  K at 1.5 GHz this yields a noise bandwidth of 4.6 GHz.

Since this value is quite different from the estimate, we used a vector network analyzer to characterize the mixer mount (the part of the IF chain between the mixer and the bias-T). The measurements were done at room temperature with an HEB device in place. At room temperature the device by itself behaves as a resistor with a value equal to the dc resistance. We found that at frequencies above 2 GHz the impedance of the mount develops a reactance and the real part of the impedance drops. As a result, the mixer becomes mismatched to the load, which leads to additional losses increasing with frequency  $L_{mm}(f)$ . Taking into account this function we calculated  $T_r$  vs  $f_{IF}$  again (Fig. 6 curve 2). Curve 2 is close to the measured data.

In order to improve the situation we replaced the semirigid coaxial cable in the mixer mount with a microstrip on a Duroid substrate. The measured receiver noise temperature for the mixer M7-10, which is very similar to M7-9, is shown in Fig 7 (triangles). The receiver noise bandwidth now equals 5.6 GHz but is still limited by the parasitics of the mixer mount. The dotted line represents the calculated  $T_r$  vs IF

where the measured losses of the new mixer mount are inserted. From this figure follows that further improvements of the mixer mount are needed.

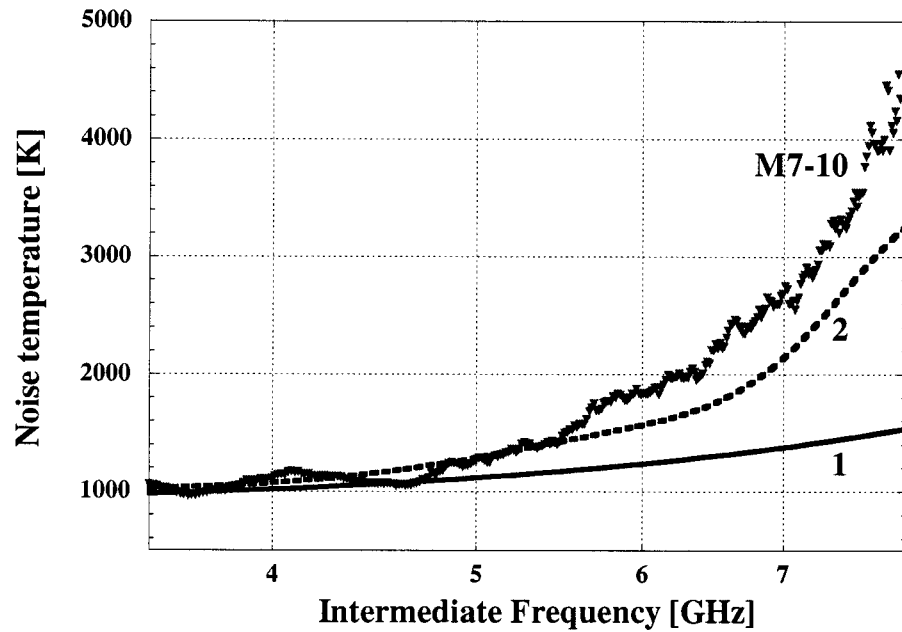


**Figure 7.** Receiver noise temperature in the 4-8 GHz band for device M7-10. Measured data (triangles), calculations for an ideal mixer mount (1) and the microstrip mixer mount (2).

### **Conclusion**

We have fabricated and investigated phonon-cooled HEB mixers based on NbN films on MgO substrate. The maximum gain bandwidth 4.8 GHz was obtained for a 3.5 nm NbN film with  $T_c=10$  K. The best DSB receiver noise temperature for these mixers was 750 K at 0.6 GHz. The first measurements of the receiver noise temperature for a NbN HEB mixer in the IF band 4-8 GHz were done. The receiver noise bandwidth is 5.6 GHz which is now limited by parasitics of the mixer mount. We expect that further improvement of the mixer mount may result in 9-10 GHz receiver noise bandwidth.

## Acknowledgment

This work has been supported by Swedish Research Council for Engineering Sciences, Swedish National Space Board, ESA (ESTEC/No.11738/95/NL/MV) and INTAS project # 96-0268

## References

- 1 P. Yagoubov, M. Kroug, H. Merkel, E. Kollberg, J. Schubert, H.-W. Huebers, S. Svechnikov, B. Voronov, G. Gol'tsman, and Z. Wang, "Hot Electron Bolometric Mixers Based on NbN Films Deposited on MgO substrates", *Proc. Europ. Conf. on Appl. Superconductivity (EUCAS'99)*, Barcelona, 14-17 September, 1999.
- 2 P. Yagoubov, M. Kroug, H. Merkel, E. Kollberg, J. Schubert, H.-W. Huebers, G. Schwaab, G. Gol'tsman, and E. Gershenzon, "NbN Hot Electron Bolometric Mixers at Frequencies Between 0.7 and 3.1 THz", *Proc. 10th Int. Symp. on Space Terahertz Technology*, Charlottesville, VA, 214, 1999.
- 3 J. Kawamura, C.-Y. E. Tong, R. Blundell, D. C. Papa, T. R. Hunter, G. Gol'tsman, S. Cherednichenko, B. Voronov, and E. Gershenzon, "An 800 GHz NbN Phonon-cooled Hot-electron Bolometer Mixer Receiver", *IEEE Trans. on Appl. Superconductivity*, vol. 9, No 2, 3753, 1999.
- 4 A. Skalare, W.R. McGrath, B. Bumble and H. G. LeDuc, "Noise and RF bandwidth measurements of a 1.2 THz HEB heterodyne receiver", *Proc. 8th Int. Symp. on Space Terahertz Technology*, Cambridge, MA, 47, 1997.
- 5 R. Wyss, B. Karasik, W. McGrath, B. Bumble, H. LeDuc, "Noise and Bandwidth Measurements Of Diffusion-Cooled Nb Hot-Electron Bolometer Mixers at Frequencies Above the Superconductive Energy Gap", *Proc. 10th Int. Symp. on Space Terahertz Technology*, Charlottesville, VA, 214, 1999.
- 6 P. Yagoubov, M. Kroug, H. Merkel, E. Kollberg, G. Gol'tsman, S. Svechnikov and E. Gershenzon, "Noise temperature and local oscillator power requirement of NbN phonon-cooled hot electron bolometric mixers at Terahertz frequencies", *Appl. Phys. Lett.*, 73, 2814, 1998.
- 7 R. Wyss, B. Karasik, W. McGrath, B. Bumble, H. LeDuc, "Noise and Bandwidth Measurements Of Diffusion-Cooled Nb Hot-Electron Bolometer Mixers at Frequencies Above the Superconductive Energy Gap", *Proc. 10th Int. Symp. on Space Terahertz Technology*, Charlottesville, VA, 214, 1999.
- 8 S. Cherednichenko, P. Yagoubov, K. Il'in, G. Gol'tsman and E. Gershenzon, "Large bandwidth of NbN phonon cooled hot-electron bolometer mixers on sapphire substrates", *Proc. 8th Int. Symp. on Space Terahertz Technology*, Cambridge, MA, 245, 1997.
- 9 N. Perrin and C. Vanneste, *Phys. Rev. B*, **28**, 5150, 1983.
- 10 Yu. P. Gousev, G. N. Gol'tsman, A. D. Semenov, E. M. Gershenzon, R. S. Nebosis, M. A. Heusinger, and K. F. Renk, "Broadband Ultrafast Superconducting NbN Detector for Electromagnetic Radiation", *J. Appl. Phys.*, vol.75, No 7, 3695, 1994.
- 11 M. Kroug, P. Yagoubov, G. Gol'tsman and E. Kollberg, "NbN quasioptical phonon cooled hot electron bolometric mixers at THz frequencies", *Proc. the 3rd. European Conference on Applied Superconductivity*, Veldhoven, Netherlands, (Inst. Phys. Conf. Ser. No 158, p.405), 1997.
- 12 H. Ekström, E. Kollberg, P. Yagoubov, G. Gol'tsman, E. Gershenzon and S. Yngvesson, "Gain and noise bandwidth of NbN hot-electron bolometric mixers", *Appl. Phys. Lett.* 70, 3296, 1997.
- 13 K.S. Il'in, G.N. Gol'tsman, B.M. Voronov, R. Sobolewski, "Characterization of the electron energy relaxation process in NbN hot-electron devices", *Proc. 10th Int. Symp. on Space Terahertz Technology*, Charlottesville, VA, 390, 1999.
- 14 B.S. Karasik and A.I. Elant'ev, "Noise Temperature limit of a Superconducting Hot Electron Bolometer Mixer," *App. Phys. Lett.*, vol. 68, pp. 853-855, 1996.

# ANOMALOUS PUMPED AND UNPUMPED I-V CHARACTERISTICS OF Nb SIS TERAHERTZ MIXERS WITH NbTiN STRIPLINES

B. Leone<sup>†</sup>, B.D. Jackson<sup>‡</sup>, J.R. Gao<sup>§</sup>, T.M. Klapwijk<sup>§</sup>,  
W.M. Laauwen<sup>‡</sup> and G. de Lange<sup>‡</sup>

<sup>†</sup>University of Groningen,

Department of Applied Physics and Material Science Center,  
Nijenborgh 4.13, 9747 AG Groningen, The Netherlands

<sup>§</sup>Delft University of Technology,

Department of Applied Physics and Delft Institute for Microelectronics  
and Submicron Technology (DIMES)

Lorentzweg 1, 2628 CJ Delft, The Netherlands

<sup>‡</sup>Space Research Organization of the Netherlands,

Postbus 800, 9700 AV Groningen, The Netherlands

## Abstract

To achieve nearly quantum limited noise temperatures around 1 THz in Nb SIS mixers NbTiN is used as stripline material because its high DC conductivity and gap frequency above 1 THz should minimize RF losses. However, one expects problems at the Nb/NbTiN interface due to an energy gap discontinuity. Indeed, the measured I-V curves show features that are absent in all Nb SIS mixers or Nb junctions with normal metal striplines. These include the gap voltage backbending and a severe gap voltage reduction in the pumped case. In an analysis of the unpumped case, it was previously shown that the backbending feature is caused by the DC heat trapped at the Nb/NbTiN interface and that the heat flow is limited by the electron-phonon interaction time. In the present paper, the analysis is extended to the pumped case by introducing an additional power contribution to explain the severe gap depression. This additional power results from the energy spectrum of the photon assisted tunneling electrons as given in the Tien-Gordon theory. Theoretical fits are obtained that faithfully reproduce the main features of the anomalous pumped I-V characteristics.

## 1 INTRODUCTION

Until recent experimental results obtained at the Space Research Organization of the Netherlands (SRON) and Delft University of Technology, [1, 2] the lowest noise temperature around 1 THz was obtained using a Nb SIS mixer with Al tuning circuits. [3] However, a major limiting factor in the mixer performance is the loss in the aluminum striplines. [4] Therefore, one strategy to improve on these results is to use a superconducting stripline material with an energy gap

above the signal photon energy. NbTiN has been shown to be a good candidate both because of its frequency gap larger than 1 THz and its low RF loss. [5–12] However, because of the energy gap discontinuity at the Nb/NbTiN interface one expects problems with this structure. Understanding these is essential to evaluate the mixer performance.

## 2 ANOMALOUS I-V CHARACTERISTICS

The device structure of the Nb SIS mixers with NbTiN striplines investigated here is shown in Fig.1(a). The Nb junction is sandwiched between two NbTiN leads, which, in combination with an insulator SiO<sub>2</sub> layer, form a stripline that functions as an integrated tuning circuit for the mixer. The SIS device is a standard Nb/Al–AlO<sub>x</sub>/Nb junction with an area of typically 0.6 μm<sup>2</sup>. Junctions with two critical current densities, 6.5 and 12 kA/cm<sup>2</sup>, were used. The thickness of both Nb electrodes is 90 nm. The top and bottom NbTiN leads are 400 nm and 280 nm thick, respectively. The critical temperatures of Nb and NbTiN in the device were measured to be 9.1 K and 14.3 K. Device fabrication is described elsewhere. [11] The first I-V measurements on these devices were presented earlier [11] and are reproduced in Fig.2. These showed two striking features believed to be caused by the presence of the gap discontinuity. Firstly, a severe gap depression which worsens with increasing pumping level. Secondly, the gap depression can be seen within the same curve as a backbending of the gap voltage.

## 3 UNPUMPED CASE

The energy diagram of Fig.1(b) corresponds to the device structure for the two electrodes biased at the Nb gap voltage and shows the different energy gaps of Nb and NbTiN. The tunneling electrons see a potential barrier at the Nb/NbTiN interface. In a previous paper [13] we showed that in such a situation there is no quasiparticle trapping. Instead, the charges are Andreev reflected at the interface. As a result, charge is transported across the interface but the quasiparticle equilibrium temperature is raised in both electrodes. Here the assumption is made that the electron-electron interaction time is short enough to obtain a Fermi-like electron energy distribution in the junction. The BCS theory is used to determine the electron temperature from the backbending data, which yields the energy gap, Δ, through the following expression, [14]

$$\frac{1}{N(0)\beta} = \int_0^{\hbar\omega_c} \frac{\tanh \left[ (2kT)^{-1} \sqrt{\epsilon^2 + \Delta^2} \right]}{\sqrt{\epsilon^2 + \Delta^2}} d\epsilon, \quad (1)$$

where  $N(0)$  is the density of states at the Fermi level,  $\beta$  is the BCS interaction constant and  $\hbar\omega_c$  is the Debye frequency and is much greater than  $kT_c$ , where  $T_c$  is

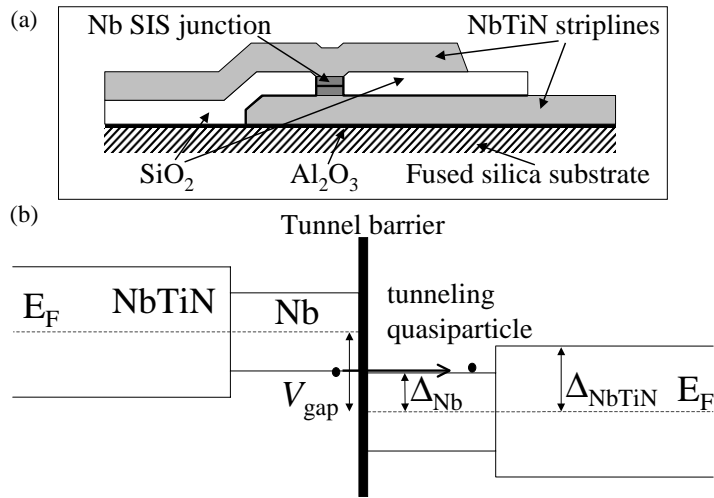


Figure 1: (a) Sketch of the cross-section of a Nb SIS junction with NbTiN striplines. (b) Energy diagram showing the relative energy gaps of Nb and NbTiN under the application of a bias voltage  $V_{gap}$  equal to the gap voltage of Nb.

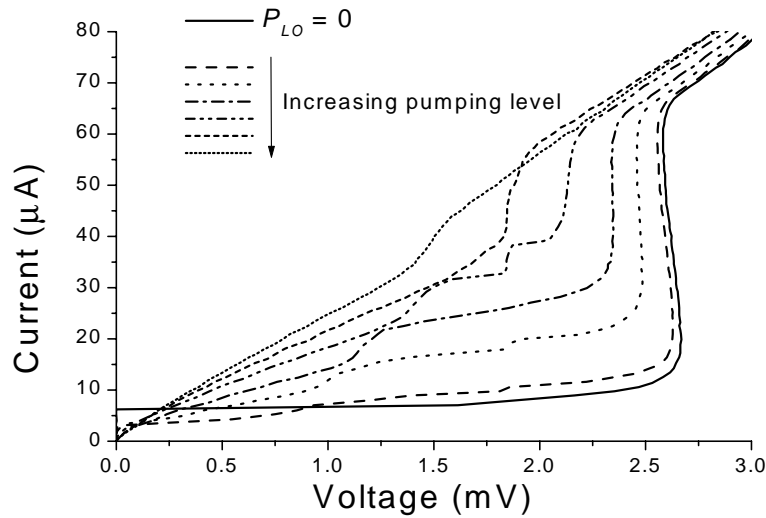


Figure 2: Anomalous pumped and unpumped I-V characteristics of a Nb/Al-AIO<sub>x</sub>/Nb junction with NbTiN striplines at a local oscillator frequency of 895 GHz and a bath temperature of 4.7 K.

the critical temperature of Nb. It was further shown that the heat flow is governed by the electron-phonon interaction time which acts as the heat flow bottleneck of the system and the heat balance equation is given by

$$P_{DC} = \alpha_{heat}(T - T_b), \quad (2)$$

where  $P_{DC}$  is the DC power in the junction;  $T$  and  $T_b$  are the electron and bath temperatures, respectively. The heat transfer coefficient,  $\alpha_{heat}$ , is given by

$$\alpha_{heat} = \frac{vC_e}{\tau_{eph}}, \quad (3)$$

where  $C_e$  is the electron heat capacity,  $\tau_{eph}$  the electron-phonon interaction time and  $v$  the junction volume. Using the above, agreement with the DC I-V characteristics was demonstrated. In particular, quantitative agreement with the backbending data was achieved.

#### 4 PHOTON ASSISTED TUNNELING CONTRIBUTION

However, when the RF signal is coupled into the mixer the severe gap reduction shown in Fig.2 cannot be explained by Eq.2. Indeed,  $P_{DC}$  is only of the order of 100 nW, whereas the heating power required to produce the gap depression of, say, the dash-dotted pumped curve in Fig.2, ranges from 200 to 300 nW, depending on the accuracy of the heat transfer coefficient as obtained from the backbending data. Essentially, there are only two other power sources in our system that could possibly account for this additional required contribution. Firstly, the photon assisted tunneling (PAT) mechanism is responsible for the energy spectrum of the photon assisted tunneled electrons according to the Tien-Gordon picture. [15] In standard junctions, this added energy, delivered in multiples of the photon energy to the electron bath, escapes by heat diffusion. However, in the presence of heat trapping it will have to be dissipated within the electron bath, thus contributing to the overall junction heating. Secondly, because the mixer operates above the gap frequency of Nb, some RF dissipation in the junction is also expected. Let us first turn to the photon assisted tunneling mechanism. Tucker and Feldman [16] give an expression for the dissipative component of the local oscillator (LO) current,  $I'_{LO}$ , across the mixer

$$\begin{aligned} I'_{LO} &= \sum_{n=-\infty}^{\infty} J_n(\alpha)[J_{n-1}(\alpha) + J_{n+1}(\alpha)]I_{dc}(V + n\hbar\omega/e) \\ &= \sum_{n=-\infty}^{\infty} 2n \frac{J_n^2(\alpha)}{\alpha} I_{dc}(V + n\hbar\omega/e) \end{aligned} \quad (4)$$

where  $J_n(\alpha)$  is the  $n^{th}$  order Bessel function and its argument,  $\alpha = eV_{LO}/\hbar\omega$ , is the ratio of the energy associated with the LO voltage across the junction to the

photon energy;  $I_{dc}$  is the measured unpumped I-V characteristic and  $V$  is the bias voltage. We assume here that  $V_{LO}$  is a constant. Therefore, the photon assisted power,  $P_{PAT}$ , is the AC power associated with the dissipative current and is given by

$$\begin{aligned} P_{PAT} &= \frac{I'_{LO} V_{LO}}{2} \\ &= \sum_{n=-\infty}^{\infty} \frac{n\hbar\omega}{e} J_n^2(\alpha) I_{dc}(V + n\hbar\omega/e). \end{aligned} \quad (5)$$

Intuitively, one can understand Eq.5 in the light of the Tien-Gordon theory [15] which pictures the pumped I-V characteristic as resulting from the sum from minus to plus infinity of the unpumped characteristic shifted by multiples of the photon energy and weighted by the corresponding Bessel function, i.e.

$$I_{pumped} = \sum_{n=-\infty}^{\infty} J_n^2(\alpha) I_{dc}(V + n\hbar\omega/e). \quad (6)$$

One sees that Eq.5 multiplies the number of photon assisted tunneled quasiparticles by their corresponding energy, namely  $n\hbar\omega$ , for each value of  $n$ .

## 5 THEORETICAL FITS TO THE ANOMALOUS PUMPED I-V CURVES

In order to produce theoretical fits of the pumped I-V characteristics, dedicated voltage-biased measurements were obtained, taking care to suppress the supercurrent and associated Shapiro steps, which are present in Fig.2. The pumped and unpumped experimental curves used for the theoretical calculations in this section are shown in Fig.4. The pumped measured data is used to calculate the DC power,  $P_{DC}$ , and is simply the product of the current by the voltage at each bias point. The photon assisted power,  $P_{PAT}$ , is calculated using Eq.5, where  $I_{dc}(V)$  is the unpumped measured data. An appropriate value for the Bessel function argument,  $\alpha$ , or, equivalently,  $V_{LO}$ , must also be chosen. However, since the actual LO power seen by the junction cannot be measured,  $V_{LO}$  must be treated as a fitting parameter. Its choice will be discussed later in this section. Fig.3 shows a plot of  $P_{DC}$ ,  $P_{PAT}$  and their sum,  $P_{Total} = P_{DC} + P_{PAT}$ , as a function of bias voltage.

Using  $P_{Total}$  instead of  $P_{DC}$  in Eq.2 one can calculate a temperature profile as a function of bias voltage,  $T(V)$ , also shown in Fig.3.  $T(V)$  is chosen to be constant upon reaching the critical temperature of Nb, which corresponds to the junction transition to the normal state. One can then calculate a unpumped theoretical I-V characteristic using the usual expression

$$I_{dc} = \frac{-1}{eR_n} \int_{n=-\infty}^{\infty} N(E)N(E - eV)[f(E) - f(E - eV)]dE, \quad (7)$$

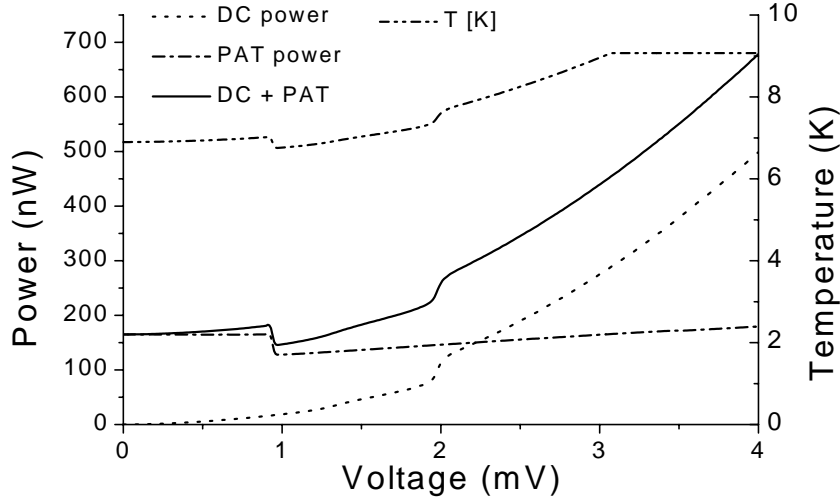


Figure 3: DC, PAT and total=DC+PAT heating powers (nW), and junction temperature (K) corresponding to the DC+PAT case, versus bias voltage (mV).

where  $R_n$  is the normal state resistance, and taking care to assign to the density of states,  $N(E) = N(E, T)$ , and the Fermi-Dirac distribution function,  $f(E) = f(E, T)$  the temperature profile  $T(V)$ . Fig.4 shows the I-V characteristic so obtained and labeled  $I(V, T(V))$ .

It should be appreciated that the calculated unpumped curve,  $I(V, T(V))$ , has the same gap voltage as the pumped data, unlike the measured unpumped curve. Furthermore, by inserting this theoretical curve into Eq.6 one obtains the curve labeled "Tien-Gordon" in Fig.4. This latter procedure is used to fit the LO voltage across the junction,  $V_{LO}$ . The fact that both the reduced gap and the photon step level are reproduced in the fit using only  $V_{LO}$  as fitting parameter, points to the self-consistency of our physical picture of the gap depression mechanism. However, as it stands, the calculated I-V characteristic fails to reproduce the correct photon step onset. This is due to the fact that, according to Eq.6, the photon onset reflects the gap voltage value shifted by a multiple of the photon energy. In fact, in our anomalous case, one should be careful that the value of the gap changes with the bias voltage according to the temperature profile. Hence, Eq.6 should be adjusted as follows,

$$I_{pumped} = \sum_{n=-\infty}^{\infty} J_n^2(\alpha) I_{dc}(V + n\hbar\omega/e, T(V)), \quad (8)$$

where  $I_{dc}(V + n\hbar\omega/e, T(V))$  is now calculated and given by Eq.7, the density of states and the Fermi-Dirac distribution functions shifted by multiples of the

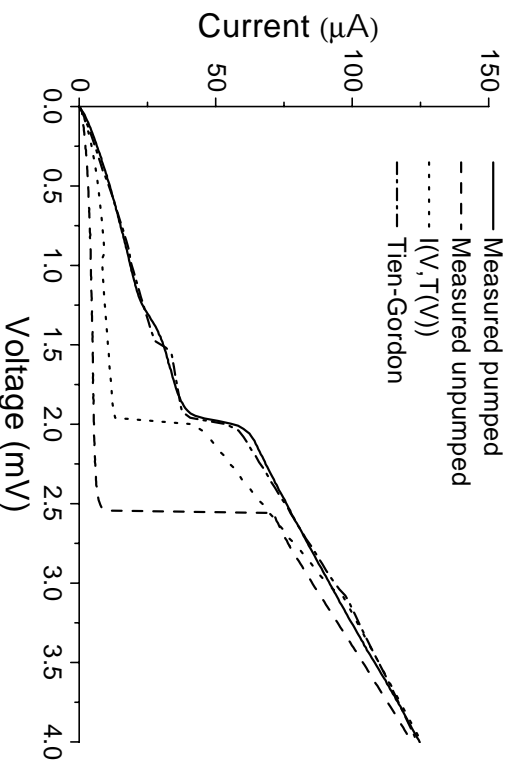


Figure 4: Pumped and unpumped data for a Nb/Al-AlO<sub>x</sub>/Nb junction with NbTiN stripelines at a local oscillator frequency of 845 GHz and a bath temperature of 5.7 K; the calculated unpumped I-V curves using the temperature profiles due to the total power, the DC power only and the PAT power only. The calculated pumped I-V curve using the total power temperature profile plugged into Eq.6 is also plotted.

photon energy are also a function of the temperature profile  $T(V)$ , for all values of  $n$ , and are given by  $N(E + e(V + n\hbar\omega))$ ,  $T(V)$  and  $f(E + e(V + n\hbar\omega))$ ,  $T(V)$ ), respectively.

Fig.5 shows the resulting fits to pumped data for two different pumping levels. Again,  $V_{LO}$  is the only fitting parameter and it can be seen that several anomalous pumped data features are reproduced. These are the gap depression, the photon step level, the photon step onset and the subgap current below the photon step onset. Deviations from the data are also present. Firstly, there is the smoothing of the measured photon step, which is usually ascribed to quasiparticle lifetime effects. Hence, if no smoothing functions are applied, the theoretical counterparts are generally characterized by much sharper gap and photon step onsets. [17] Secondly, the excess current in the measured data just above the gap could be explained by the fact that actual junctions are not, strictly speaking, SIS structures, on which the calculations are based, but more closely resemble SNIS structures, where N stands for the thin Al layer. Hence, the corresponding density of states will be modified accordingly. Thirdly, the calculated curves show an abrupt transition to the normal state around 3.1 mV, not present in the data. Here, the assumption of a constant heat transfer coefficient used for the fits, via Eq.2, breaks down. In fact, Eq.3 clearly indicates that  $\alpha_{heat}$  should

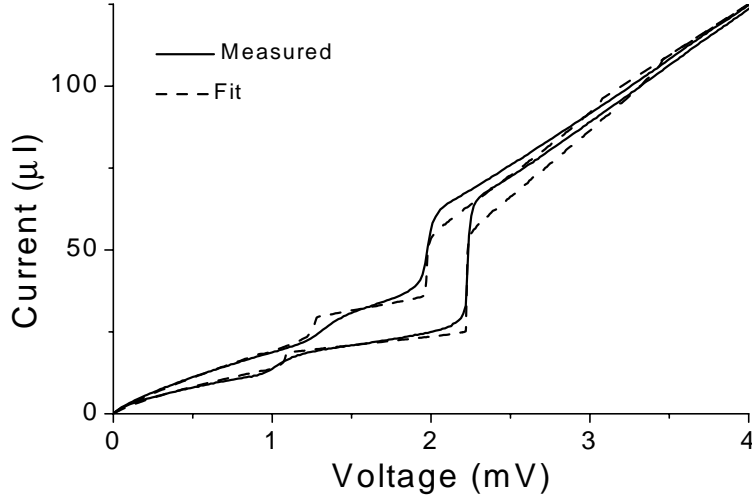


Figure 5: Pumped data of a Nb/Al-AlO<sub>x</sub>/Nb junction with NbTiN striplines at a local oscillator frequency of 845 GHz and a bath temperature of 5.7 K for two different pumping levels fitted using Eq.8.

be temperature-dependent, however, since the temperature-dependent behavior of the electron-phonon interaction is rather complex and strongly dependent on material parameters, [18] it has been left out of this analysis. Suffice it to say that  $\alpha_{heat}$  seems to vary very slowly with temperature across the bias voltage range of interest only to deviate significantly near the critical temperature. There are, nevertheless, indications that an abrupt transition to the normal state has been observed albeit at a higher bias voltage. [19]

Through the above exercise, it has been shown that the DC and PAT heating power contributions can reasonably explain the experimental data. This suggests that the possible contribution from RF absorption is negligible. Taking into account the fit resolution as well as the measurement error in the heat transfer coefficient, it can be estimated that the RF absorption in the junction, if present, should be less than 10% of the photon assisted tunneling contribution.

## 6 CONCLUSION

In conclusion, the heat trapping mechanism and the electron-phonon interaction-limited heat flow process responsible for the gap voltage backbending in the unpumped case are shown to be also responsible for the severe gap depression in the pumped case, provided one takes account of the additional heating power introduced by the photon assisted tunneling process. As a consequence, the proposed

solution [13] to reduce heating by increasing the Nb volume, while keeping the junction area unchanged, is also applicable in the RF case. Furthermore, in addition to explaining the backbending and gap depression anomalies quantitatively, the anomalous pumped I-V curves are also satisfactorily described theoretically.

#### REFERENCES

- [1] B.D. Jackson, G. de Lange, W.M. Laauwen, J.R. Gao, N.N. Iosad, and T.M. Klapwijk. NbTiN and NbTiN/Al tuning circuits for thz SIS mixer. Published in these proceedings.
- [2] A. M. Baryshev, B. D. Jackson, G. de Lange W. Laauwen, S. V. Shitov, J. R. Gao, and T. M. Klapwijk. Quasi-optical terahertz SIS mixer. Published in these proceedings.
- [3] M. Bin, M.C. Gaidis, J. Zmuidzinas, T.G. Phillips, and H.G. LeDuc. Low-noise 1 THz niobium superconducting tunnel junction mixer with a normal metal tuning circuit. *Appl. Phys. Lett.*, 68:1714–1716, 1996.
- [4] P. Dieleman, T.M. Klapwijk, J.R. Gao, and H. van de Stadt. Analysis of Nb superconductor–insulator–superconductor tunnel junctions with Al striplines for thz radiation detection. *IEEE Trans. on Appl. Supercond.*, 7:2566–2569, 1997.
- [5] R. di Leo, A. Nigro, G. Nobile, and R. Vaglio. Niobium-titanium nitride thin films for superconducting rf accelerator cavities. *J. Low Temp. Phys.*, 78:41, 1990.
- [6] J. W. Kooi, J. A. Stern, G. Chattopadhyay, H. G. LeDuc, B. Bumble, and J. Zmuidzinas. Low-loss NbTiN films for THz SIS mixer tuning circuits. In R. Blundell and E. Tong, editors, *The Eighth International Symposium on Space Terahertz Technology: Symposium Proceedings*, pages 310–318, Harvard–Smithsonian Center for Astrophysics, Cambridge, MA, 1997.
- [7] J. A. Stern, B. Bumble, H. G. LeDuc, J. W. Kooi, and J. Zmuidzinas. Fabrication and DC characterization of NbTiN based SIS mixers for use between 600 and 1200 GHz. In *Ninth International Symposium on Space Terahertz Technology: Symposium Proceedings*, pages 305–313, Jet Propulsion Laboratory, Pasadena, CA, March 1998.
- [8] J. W. Kooi, J. A. Stern, G. Chattopadhyay, H. G. LeDuc, B. Bumble, and J. Zmuidzinas. Low-loss NbTiN films for THz SIS mixer tuning circuits. *Intl. J. Infrared and MM Waves*, 19:373–383, 1998.

- [9] J. Zmuidzinas, J. W. Kooi, J. Kawamura, G. Chattodpadhyay, J. A. Stern, B. Bumble, and H. G. LeDuc. Development of SIS mixers for 1 THz. *Proc. SPIE*, 3357:53–61, May 1998.
- [10] J. Kawamura, D. Miller, J. Chen, J. Kooi, J. Zmuidzinas, B. Bumble, H.G. LeDuc, and J.A. Stern. Fabrication and DC characterization of NbTiN based SIS mixers for use between 600 and 1200 GHz. In *Proceedings of the Tenth International Symposium on Space Terahertz Technology*, page 398, University of Virginia, March 1999.
- [11] B.D. Jackson, N.N. Iosad, B. Leone, J.R. Gao, T.M. Klapwijk, W.M. Laauwen, G. de Lange, and H. van de Stadt. Dc and terahertz response in nb sis mixers with nbtin striplines. In *Proceedings of the Tenth International Symposium on Space Terahertz Technology*, pages 144–156, University of Virginia, March 1999.
- [12] N.N. Iosad, B.D. Jackson, T.M. Klapwijk, S.N. Polyakov, P.N. Dmitriev, and J.R. Gao. Optimization of rf- and dc-sputtered nbtin films for integration with nb-based sis junctions. *IEEE Trans. on Appl. Supercond.*, 9:1716–1719, 1999.
- [13] B. Leone, B.D. Jackson, J.R. Gao, and T.M. Klapwijk. Geometric heat trapping in niobium superconductor–insulator–superconductor mixers due to niobium titanium nitride leads. *Appl. Phys. Lett.*, 76:780–782, 2000.
- [14] M. Tinkham. *Introduction to Superconductivity*. McGraw-Hill, New York, 2nd edition, 1996. p. 63.
- [15] P.K. Tien and J.P. Gordon. Multiphoton process observed in the interaction of microwave fields with the tunneling between superconductor films. *Phys. Rev.*, 129:647–651, 1963.
- [16] J.R. Tucker and M.J. Feldman. Quantum detection at millimeter wavelengths. *Rev. of Mod. Phys.*, 57:1055–1113, 1985.
- [17] L. Solymar. *Superconductive Tunnelling and Applications*. Chapman and Hall, London, 1972. p. 43.
- [18] E.M. Gershenzon, M.E. Gershenzon, G.N. Gol'tsman, A.M. Lyul'kin, A.D. Semenov, and A.V. Sergeev. Electron-phonon interaction in ultrathin nb films. *Sov. Phys. JETP*, 70:505–511, 1990.
- [19] Unpublished results.

# **NbTiN/SiO<sub>2</sub>/NbTiN and NbTiN/SiO<sub>2</sub>/Al tuning circuits for 1 THz waveguide SIS mixers**

**B.D. Jackson, G. de Lange, W.M. Laauwen, and J.R. Gao**  
Space Research Organization of the Netherlands  
Postbus 800, 9700 AV Groningen, The Netherlands

**N.N. Iosad and T.M. Klapwijk**  
Department of Applied Physics (DIMES), Delft University of Technology  
Lorentzweg 1, 2628 CJ Delft, The Netherland

## **ABSTRACT**

Waveguide SIS mixers are presented in which Nb/Al-AlO<sub>x</sub>/Nb tunnel junctions are integrated with both NbTiN/SiO<sub>2</sub>/NbTiN and NbTiN/SiO<sub>2</sub>/Al tuning circuits. The mixers with a NbTiN/SiO<sub>2</sub>/NbTiN tuning circuit yield relatively low receiver noise temperatures between 700 and 830 GHz, but their sensitivity drops significantly above ~ 850 GHz. In contrast, low-noise heterodyne mixing near 1 THz is observed in mixers incorporating a NbTiN/SiO<sub>2</sub>/Al tuning circuit. In particular, an uncorrected receiver noise temperature of 585 K is measured at 970 GHz. From an analysis of the receiver sensitivity and gain, it is determined that the loss in the NbTiN ground plane is low ( $\leq 0.6$  dB) below 970 GHz. A decrease in receiver sensitivity above 1 THz is attributed to an onset of rf loss in the NbTiN.

## **1. INTRODUCTION**

The specifications of the HIFI instrument for the Far-Infrared Space Telescope (FIRST) require the development of THz SIS mixers with receiver noise temperatures of  $3.5h\nu/k$  (i.e. 160 K at 960 GHz). Although mixers incorporating Nb/Al-AlO<sub>x</sub>/Nb tunnel junctions and Nb wiring layers have been shown to yield receiver noise temperatures as low as  $2h\nu/k$  below the 680 GHz superconducting gap frequency of Nb [1], Nb tuning circuits become very lossy at higher frequencies [2]. Indeed, above 800 GHz, wiring of a high-conductivity normal metal, such as aluminum, has been shown to yield significant improvements in receiver sensitivity [3], with a best-reported receiver sensitivity of 840 K at 1042 GHz [4]. However, it has also been shown that losses in the Al wiring layers and excess shot-noise in high- $J_c$  Nb/Al-AlO<sub>x</sub>/Nb SIS junctions ( $J_c > 10$  kA/cm<sup>2</sup>) combine to limit the sensitivity of these receivers to ~ 500 K at 1 THz [5-6].

A significant improvement in 1 THz receiver sensitivity will require a corresponding reduction in tuning circuit losses. This may be achieved in two ways. Certainly, an improvement in the quality of high- $J_c$  SIS junctions will yield a reduction in the noise of mixers with normal-metal tuning circuits. However, the ultimate goal of producing

quantum-limited THz receivers will require the development of low-loss superconducting wiring layers with a gap frequency of  $\sim 1.2$  THz or higher. NbTiN, a compound superconductor previously used for thin-film coatings in rf cavities [7], is one promising candidate to fill this need.

Previous work has shown that NbTiN layers with  $T_c = 14.3\text{-}15.5$  K can be integrated with Nb-based SIS tunnel junctions to produce both quasi-optical [8-9] and waveguide [10-11] mixers. Based on the BCS relationship between  $T_c$  and the superconducting energy gap ( $F_{\text{gap}} \sim 3.52 \cdot k_B T_c / h$ ), it is expected that these NbTiN-based tuning circuits will be low-loss up to 1.05-1.14 THz. Indeed, the observation of AC Josephson resonances in I-V characteristics at voltages up to 2.2 mV provides evidence of low-loss performance around 1 THz in these tuning circuits [8-9,11]. Furthermore, the recent demonstration of a receiver noise temperature of 205 K at 798 GHz for a mixer incorporating a NbTiN tuning circuit [12] confirms that NbTiN wiring layers are very low-loss up to at least 800 GHz. However, despite these promising results, it remains to be shown that NbTiN tuning circuits can be used to produce low-noise receivers for frequencies up to  $\sim 1.2$  THz.

In this paper, we demonstrate waveguide SIS mixers in which standard Nb/Al-AIO<sub>x</sub>/Nb tunnel junctions are integrated with NbTiN/SiO<sub>2</sub>/NbTiN and NbTiN/SiO<sub>2</sub>/Al tuning circuits. The direct-detection and heterodyne sensitivities of these devices are presented for frequencies between 0.7 and 1.05 THz. Additionally, the receiver noise and conversion gain of a mixer with a NbTiN/SiO<sub>2</sub>/Al tuning circuit are analyzed to evaluate the RF performance of the NbTiN ground plane at 970 GHz. The parallel development of a quasi-optical THz mixer with a NbTiN/SiO<sub>2</sub>/Al tuning circuit is discussed elsewhere in these proceedings [13].

All of the receiver noise temperatures presented here are calculated using Planck-corrected effective temperatures for the blackbody signal loads and the receiver optics. Corrected noise temperatures, calculated from the measured receiver noise using estimates of the frequency-dependent loss in the receiver optics (beam splitter, vacuum window, heat-filter, and lens) are also presented. This allows the intrinsic mixer performance to be more easily evaluated. Furthermore, the corrected noise temperatures can be directly compared with the HIFI mixer specifications, which are defined for the ideal case of zero optical loss in front of the mixer.

## 2. MIXER DESIGN AND FABRICATION

THz mixers are fabricated by integrating standard 1- $\mu\text{m}$  Nb SIS junctions ( $J_c \sim 7.5$  kA/cm<sup>2</sup>) with a 300-nm NbTiN ground plane and either a 400-nm NbTiN or a 400-nm Al + 100-nm Nb wiring layer, as seen in Fig. 1a. The twin-junction tuning circuit shown in Fig. 1b is used to efficiently couple radiation from the waveguide probes to the SIS junctions over a relatively broad rf bandwidth. A 10- $\mu\text{m}$  wide microstrip transmission line connects the two junctions, which are separated by 4-7  $\mu\text{m}$ . The

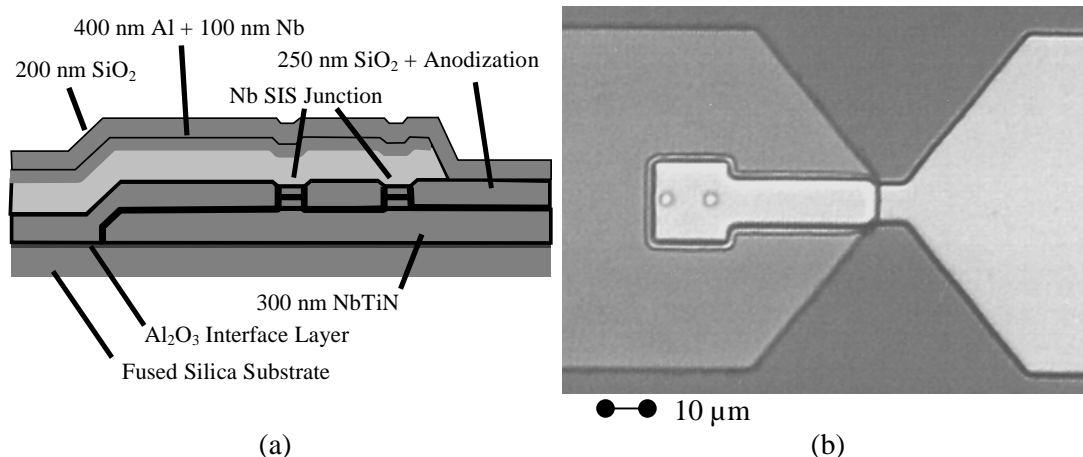


**Figure 1.** a) Cross-section of the NbTiN/SiO<sub>2</sub>/Al tuning circuit (in the NbTiN/SiO<sub>2</sub>/NbTiN tuning circuit, the Al + Nb wiring is replaced with 400-nm of NbTiN and the 200 nm SiO<sub>2</sub> passivation layer is not present). b) Optical microscope image of the twin-junction tuning circuit. The optically defined SIS junctions are nominally 1 μm<sup>2</sup>. The transformer length and junction separation are varied to tune the circuit resonance.

junctions are connected to the waveguide probes by a microstrip impedance transformer 6-μm wide and 18-26 μm long. The waveguide probes and the rf choke structures (not shown) are designed for a 1 THz waveguide mixer block with waveguide and substrate channel dimensions of 120×240 μm<sup>2</sup> and 90×90 μm<sup>2</sup>, respectively. Table 1 summarizes the tuning circuit geometries of the six devices for which results are presented in this paper.

The mixers are fabricated on 200-μm thick fused quartz substrates using processes similar to those described previously for the fabrication of devices with NbTiN and Al striplines [10,11,14]. The primary differences with respect to the previously described

**Table 1.** Tuning circuit parameters for the six devices discussed here.

Device #	NbTiN / SiO <sub>2</sub> / NbTiN		NbTiN / SiO <sub>2</sub> / Al			
	c14	c72	c07	c13	c37	c71
Tuning Section	7x10	4x10	5.5x11	7x11	5.5x11	4x11
Transformer	26x6	20x6	20x7	23x7	20x7	18x7
Junction Area	1.0	1.0	0.58	0.58	0.67	0.64
Wiring Layer	400 nm NbTiN, 14.3 K		400 nm Al + 100 nm Nb			
Dielectric	~ 250 nm SiO <sub>2</sub>		~ 250 nm SiO <sub>2</sub>			
Junction	Nb/Al-AIO <sub>x</sub> /Nb, 28 Ω·μm <sup>2</sup>		Nb/Al-AIO <sub>x</sub> /Nb, 28 Ω·μm <sup>2</sup>			
Ground Plane	300 nm NbTiN, 14.3 K		300 nm NbTiN, 14.3 K			

(all lengths and widths are given in μm, junction areas are in μm<sup>2</sup>)

processes are: (1) the Al + Nb wiring layer is defined using a lift-off process (instead of the etch process used for a NbTiN wiring layer), and (2) in the devices with the Al + Nb wiring, a 200-nm SiO<sub>2</sub> passivation layer is added to protect the Al from chemical attack. The NbTiN ground plane and wiring layer are deposited using a process that was previously shown [10,15] to reproducibly produce films with  $T_c = 14.3\text{-}14.4$  K and  $\sigma_{16K} \approx 0.9 \times 10^6 \Omega^{-1}\text{m}^{-1}$ . Based on previous measurements, the sputtered Al layer is expected to be in the anomalous limit, with  $\sigma_{4K} \approx 2 \times 10^8 \Omega^{-1}\text{m}^{-1}$ . Note that Nb is added to the top of the Al wiring layer to reduce the dc and IF series resistance of the upper wiring layer portion of the rf choke structure.

### 3. DC I-V CHARACTERISTICS

Representative dc current-voltage characteristics are shown in Fig. 2 for one mixer with a NbTiN/SiO<sub>2</sub>/NbTiN tuning circuit (c14) and one mixer with a NbTiN/SiO<sub>2</sub>/Al tuning circuit (c37). For the devices with a NbTiN/SiO<sub>2</sub>/NbTiN tuning circuit, measurements at 4.6 K yield  $V_{\text{gap}} = 2.6\text{-}2.63$  mV,  $R_n \cdot A \approx 28 \Omega \cdot \mu\text{m}^2$ ,  $R_n \approx 14 \Omega$  (thus,  $A \approx 1.0 \mu\text{m}^2$  per junction), and  $R_{2,0}/R_n = 14\text{-}17$ . In comparison, measurements at 4.6 K of the devices with a NbTiN/SiO<sub>2</sub>/Al tuning circuit yield  $V_{\text{gap}} = 2.7\text{-}2.82$  mV,  $R_n \cdot A \approx 28 \Omega \cdot \mu\text{m}^2$ ,  $R_n = 20\text{-}24 \Omega$  (thus,  $A = 0.58\text{-}0.7 \mu\text{m}^2$  per junction), and  $R_{2,0}/R_n = 10\text{-}17$ . Measurements of these same devices at  $\sim 2.8$  K yield an improvement in junction quality –  $V_{\text{gap}} = 2.84\text{-}2.90$  K and  $R_{2,0}/R_n = 13\text{-}40$ .

One point of note is that dc heating of the junction electrodes is minimal in the devices with a NbTiN/SiO<sub>2</sub>/Al tuning circuit, as seen from the large gap voltage and the absence of back-bending in the current-voltage characteristic of device c37 in Fig. 3. This is in contrast to both present and previously reported [11] results from devices with a NbTiN/SiO<sub>2</sub>/NbTiN tuning circuit. This previously observed dc heating has since been shown to be caused by the presence of a heat-flow barrier at the Nb/NbTiN interfaces due

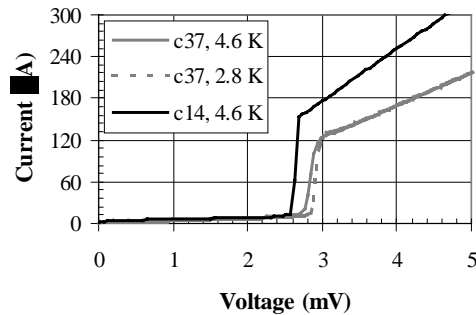


**Figure 2.** Current-voltage characteristics of a device with a NbTiN/SiO<sub>2</sub>/NbTiN tuning circuit (c14) measured at 4.6 K and a device with a NbTiN/SiO<sub>2</sub>/Al tuning circuit (c37) measured at 4.6 K and 2.8 K. The gap suppression in c14 is attributed to heat trapping in the junction electrodes due to the large superconducting energy gap in NbTiN relative to that in Nb [16].

to the larger superconducting energy gap of NbTiN relative to that of Nb [16]. Replacing one NbTiN layer with Al removes this barrier, allowing heat to escape from the junction into the Al wiring.

#### 4. RF MEASUREMENT SETUP

RF measurements are performed in both tuneable and fixed-tuned 1-THz waveguide mixer blocks. The tuneable mixer block, previously used in the study of Al-stripline SIS mixers [3], is a split-block design incorporating a sliding backshort tuner, while the fixed-tuned mixer block has a stamped backshort cavity extending  $60\ \mu\text{m}$  from the bottom of the substrate channel. Both mixer blocks have a  $120 \times 240\ \mu\text{m}^2$  waveguide, a  $90 \times 90\ \mu\text{m}^2$  substrate channel, and a diagonal horn with an  $11^\circ$  cone angle. Radiation is coupled into the mixer block through a  $100\text{-}\mu\text{m}$  Mylar vacuum window at 295 K, a Zitex G104 heat-filter at 77 K, and a high-density polyethylene lens at 4 K.

The direct-detection spectral response of the mixer is measured using a Michelson interferometer in which the optical path can be evacuated to eliminate water vapour absorption lines. Heterodyne sensitivity is measured using a 295-K / 77-K hot-cold measurement, a carcinotron plus doubler operating between 700 and 740 GHz, BWOs operating between 830 and 1100 GHz, and Mylar beamsplitters of 6, 14, and  $49\ \mu\text{m}$  thickness. IF output power from the device is coupled to the cryo-amplifier through a bias-T and an isolator. Following amplification at 4 K, the signal is further amplified and bandpass filtered at room temperature. Using an unpumped mixer as a calibrated noise source, the noise and gain of the IF system are determined to be 3-5 K and  $\sim 68\ \text{dB}$  at 1.46 GHz, over an 85 MHz band-width.

Fig. 3 presents the estimated rf transmission spectra of each of the optical elements in the signal path. The transmissions of the 14 and  $49\ \mu\text{m}$  beamsplitters have been calibrated using the Michelson interferometer and a SIS mixer as a direct detector in the 800-1000 GHz range, while the transmission of the  $6\ \mu\text{m}$  beamsplitter and  $100\ \mu\text{m}$  vacuum window are calculated from previously measured optical properties of Mylar. The transmission of the lens is approximated as a sum of an absorption loss in 3 mm of

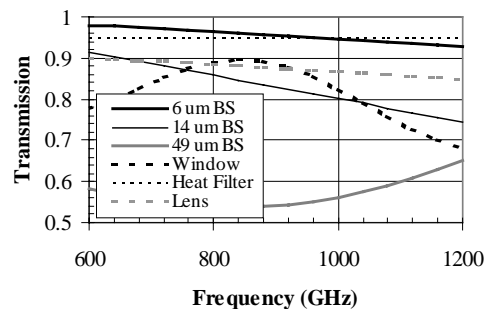


**Figure 3.** Estimated transmissions of the optical components in the signal path.

HDP (an approximate average thickness for the lens) plus incoherent reflection losses at each surface. The rf loss in the Zitex heat-filter is low enough to be hard to accurately measure. As a rough estimate, a loss of 5% is assumed.

## 5. NbTiN/SiO<sub>2</sub>/NbTiN TUNING CIRCUIT DEVICE RESPONSE

The direct-detection and heterodyne response of the two devices with a NbTiN/SiO<sub>2</sub>/NbTiN tuning circuit are shown in Fig. 4. Both devices are measured using the tuneable mixer. Each direct-detection response curve is for a fixed backshort position – curves c14 and c72a are for a 60 μm backshort depth, while curve c72b is for a backshort depth of 180 μm. For the heterodyne measurements, the backshort position is optimized at each frequency. The mixer block temperature is ~ 4.6 K for all of these measurements.

Considering the direct-detection results in Fig. 4a, it is noted that the spectral response of these devices agrees with qualitative predictions of the tuning circuit performance – for the two devices presented here, decreasing the separation from 7 μm (c14) to 4 μm (c72) shifts the resonance to a higher frequency. Unfortunately, a quantified comparison of the measured and predicted device responses is difficult due to a lack of 3-D electromagnetic simulations and/or scale-model measurements of the waveguide, waveguide probe, and rf choke designs used in this work. Thus, it is difficult to use the measured direct-detection response to verify the rf properties of the NbTiN ground plane and wiring layers.

From the heterodyne results in Fig. 4b, it is seen that these devices are relatively

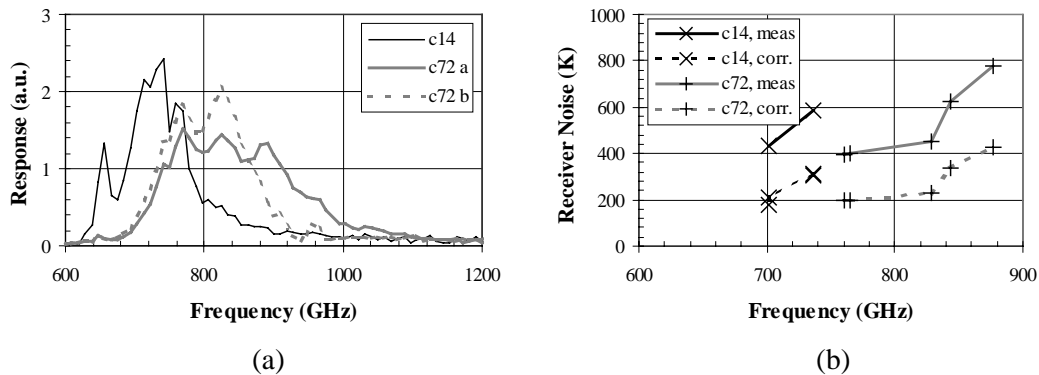


**Figure 4.** (a) Fixed-tuned direct-detection response of the two devices with a NbTiN/SiO<sub>2</sub>/NbTiN tuning circuit. Both devices are measured in the tuneable mixer (c14 and c72a – depth = 60 μm, c72b – depth = 180 μm). (b) Measured and corrected receiver noise temperatures for the same two devices. The corrected noise temperatures are calculated from the uncorrected data and the estimated optical losses in the beamsplitter, dewar window, heat-filter, and lens (see Fig. 3 for the loss estimates).

sensitive in the 700-830 GHz range – device c14 produces a receiver noise temperature of 435 K at 700 GHz, while c72 produces noise temperatures of 395 and 455 K at 760 and 830 GHz, respectively. Correcting for the previously estimated losses (see Fig. 3) in the 14  $\mu\text{m}$  beamsplitter, vacuum window, heat-filter, and lens, the effective noise at the mouth of the horn is estimated to be  $\sim 190\text{-}235$  K over the same frequency range.

The relatively low-noise performance of these devices demonstrates that the NbTiN/SiO<sub>2</sub>/NbTiN tuning circuits are relatively low-loss up to at least 830 GHz. However, one point of concern is the general absence of high sensitivity above 850 GHz in these, and other, devices with a NbTiN/SiO<sub>2</sub>/NbTiN tuning circuit. This may be partially attributed to spreading inductances introduced by the embedding of the 1- $\mu\text{m}$  junctions in a 10- $\mu\text{m}$  wide microstrip (these will effectively lengthen the tuning section, pushing the circuit resonances to lower frequencies). However, the concern is that, due to poor nucleation of NbTiN on SiO<sub>2</sub>, a poor-quality interface layer may be present at the bottom of the NbTiN wiring layer. This interface layer, which could be of non-negligible thickness, may introduce excess tuning circuit loss at frequencies well below the predicted NbTiN gap frequency.

Independent of the rf properties of the NbTiN ground plane and wiring layer, the direct-detection response of device c72 does demonstrate that a moderate improvement in rf coupling can, for some devices, be obtained by tuning the backshort cavity depth. Thus, it is hoped that further improvements in receiver sensitivity may be obtained by a careful optimization of the integrated design of the waveguide, rf choke structure, waveguide probes, and on-chip tuning structure. However, increasing the cavity depth to improve the peak sensitivity also introduces a high-frequency cut-off, reducing the fixed-tuned bandwidth of the device. Thus, the potential for improved sensitivity may be limited by rf bandwidth specifications (i.e. 800-960 GHz and 960-1120 GHz for HIFI Bands 3 and 4).

As a final note on the results presented in Fig. 4, the 70 GHz ripple seen in the direct-detection response of device c72 is observed in the direct-detection responses of a range of waveguide and quasi-optical devices, in multiple measurement cryostats. Thus, it is believed to be an intrinsic property of the measurement instrument.

## 6. NbTiN/SiO<sub>2</sub>/Al TUNING CIRCUIT DEVICE RESPONSE

The fixed-tuned direct-detection responses of the four devices with a NbTiN/SiO<sub>2</sub>/Al tuning circuit are shown in Fig. 5. Devices c07, c13, and c71 are measured in the tuneable mixer block – the response of c13 and c71 are shown for a backshort depth of 60  $\mu\text{m}$ , while the two curves shown for c07 correspond to backshort depths of 60  $\mu\text{m}$  and 120  $\mu\text{m}$ . Device c37 is measured in a fixed-tuned mixer block with a 60- $\mu\text{m}$  deep stamped backshort cavity. Note that the Michelson interferometer is evacuated to eliminate water vapour absorption lines in all of these measurements.

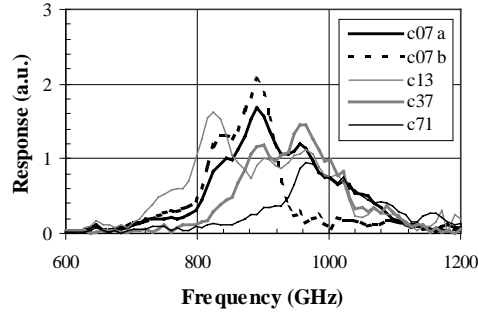


**Figure 5.** Fixed-tuned direct-detection response of the four devices with a NbTiN/SiO<sub>2</sub>/Al tuning circuit. Devices c07, c13 and c71 are measured in the tuneable mixer (c07a, c13, c71 – depth = 60  $\mu\text{m}$ , c07b – depth = 120  $\mu\text{m}$ ). Device c37 is measured in a fixed-tuned mixer (depth = 60  $\mu\text{m}$ ). All measurements are performed in vacuum.

As was the case for the devices with a NbTiN/SiO<sub>2</sub>/NbTiN tuning circuit, the direct-detection response of these mixers agrees qualitatively with predictions of the tuning circuit performance – decreasing the junction separation from 7  $\mu\text{m}$  (c13) to 5.5  $\mu\text{m}$  (c07 and c37) and 4  $\mu\text{m}$  (c71) causes the resonance to shift to higher frequency, as is expected. Unfortunately, the lack of a detailed model for the embedding impedance of the mixer make it difficult to use these results to quantify the rf properties of the NbTiN ground plane. However, it is noted that all four devices share a similar high-frequency roll-off at  $\sim 1$  THz, despite having significantly different low-frequency roll-offs. This high frequency cut-off is believed to be evidence of increasing rf loss in the NbTiN ground plane above 1 THz.

The measured receiver noise temperatures for the same four devices are shown in Fig. 6a for measurements at 4.6 K and  $\sim 2.8$  K. Uncorrected receiver noise temperatures as low as 445 K at 895 GHz (at 4.6 K, with a 6  $\mu\text{m}$  beamsplitter) and 585 K at 970 GHz (at  $\sim 2.8$  K, with a 14  $\mu\text{m}$  beamsplitter) are obtained. Furthermore, 3 combinations of junction separation, transformer length, and junction area (c13, c37, and c71) produce similar responses near 1 THz, with receiver noise temperatures and conversion losses of 585-620 K and 12-13 dB at 950-970 GHz. Note that the  $\sim 20$  % improvement in the response of device c13 upon cooling from 4.6 to 2.8 K is typical of the improvement observed in these devices.

Combining the estimated optical losses in front of the mixer (see Fig. 3) with the Planck-corrected temperatures of each element, the measured receiver noise temperatures in Fig. 6a are corrected and replotted in Fig. 6b. The resulting corrected noise temperatures at 4.6 K are 275 K at 895 GHz for device c07 and 320-350 K at 950-970 GHz for devices c13, c37, and c71. The corrected receiver sensitivities at 2.8 K for devices c13, c37, and c71 are 260-285 K at 950-970 GHz.

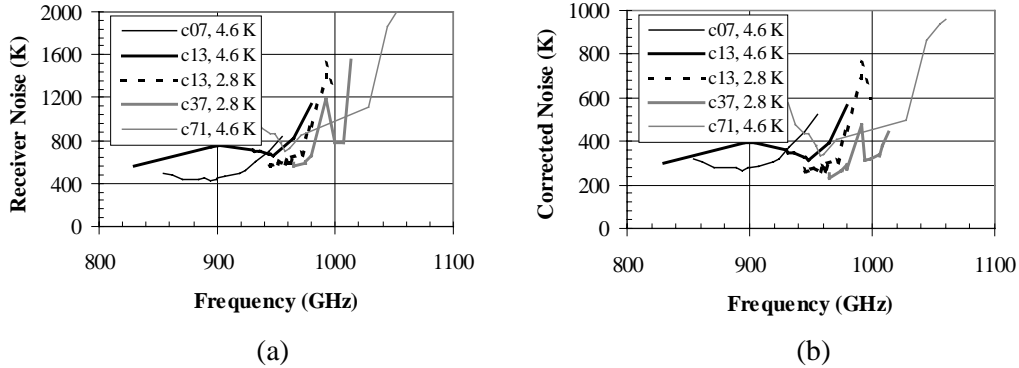


**Figure 6.** (a) Measured receiver noise temperatures for the four devices with a NbTiN/SiO<sub>2</sub>/Al tuning circuit. c07 and c71 are tuned measurements, while c13 and c37 are fixed-tuned measurements. The observed improvement in sensitivity upon cooling for c13 is representative of the effect also seen in c37 and c71 (~ 20 % from 4.6 to 2.8 K). (b) Corrected noise temperatures calculated from the uncorrected data in (a) and the optical loss estimates in Fig. 3 for the beamsplitter, vacuum window, heat-filter, and lens.

The dip in receiver sensitivity at 980-990 GHz seen in Fig. 6 for both c13 and c37 is due to an atmospheric water vapour absorption line. Independent of this absorption line, the noise temperatures of devices c13, c37, and c71 all rise significantly above 1 THz. This agrees with the previously noted drop in direct-detection sensitivity in this frequency range, giving further evidence of an onset of rf loss in the NbTiN ground plane above 1 THz.

## 7. NbTiN GROUND PLANE LOSS ANALYSIS

Focussing on the device that produces the highest receiver sensitivity near 1 THz (c37 at 2.8 K), the receiver noise and gain at 970 GHz are analyzed to identify the factors limiting sensitivity. To simplify the analysis, the twin-junction tuning circuit is approximated by a single SIS junction with an area equal to the total area of the two junctions ( $A = 1.34 \mu\text{m}^2$ ,  $R_n = 21 \Omega$ ). Using the rf voltage match method [17] and measured pumped and unpumped I-V characteristics, the embedding admittance for the model junction is estimated to be  $0.12 + 0.037i \Omega^{-1}$  at 970 GHz. Using this embedding

**Table 2** – Receiver noise and gain breakdown for c37 at 970 GHz and 2.8 K

	T <sub>N</sub> (K)	G (dB)
Optics	126	-2.4
Tuning Circuit	0	-3.2
Mixer (DSB)	$77 + h\nu/2k_B$	-7.2
IF chain	5	0
Total Receiver	586	-12.9

admittance, the DSB mixer gain and noise are calculated using the 3-port Tucker theory [18]. Note that the mixer noise calculation also includes a bias-dependent charge quantization ( $q/e = 1 + 0.45 \cdot V_{\text{gap}}/V_{\text{bias}}$ ) to account for the enhancement of shot-noise by multiple Andreev reflection [19].

From this analysis (summarized in Table 2), it is determined that there is  $\sim 3.2$  dB of excess loss at the input to the mixer, after correcting for the estimated losses in the receiver optics. As a first-order approximation, this loss is attributed to the NbTiN/SiO<sub>2</sub>/Al tuning circuit. A separate calculation of the coupling of radiation from the waveguide probes to the SIS junctions predicts a loss in the Al wiring layer of 2.6 dB (assuming the Al to be in the anomalous limit, with  $\sigma_{4K} = 2 \times 10^8 \Omega^{-1} \text{m}^{-1}$ , and NbTiN to be a loss-less superconductor). The remaining 0.6 dB is thus an estimate of the loss in the NbTiN ground plane.

Unfortunately, the accuracy of this estimate is limited by uncertainties in the optical losses, the embedding admittance, and the surface resistance of the Al wiring layer. However, it is also assumed that the waveguide, the Al/Nb portion of the rf choke, the SiO<sub>2</sub> dielectric layer, and the Nb junction electrodes each contribute zero rf loss. Thus, it seems safe to say that the NbTiN ground plane used in these devices is, indeed, relatively low-loss at frequencies up to 970 GHz.

## 8. DISCUSSION

Reviewing the receiver noise analysis summarized in Table 2, it is noted that there is room for further improvement. In particular, the estimated tuning circuit loss and DSB mixer noise are both relatively high (3.2 dB and 77 K, respectively). Thus, it may be possible to produce a somewhat more sensitive device if a similar tuning circuit loss can be combined with junctions with lower leakage currents. Furthermore, it is expected that the incorporation of recent improvements in the fabrication of very-high current-density junctions ( $J_c \sim 30 \text{ kA/cm}^2$ ) [20-21] should make it possible to significantly reduce the tuning circuit loss while maintaining, or even reducing, the mixer shot-noise.

Although the mixers with a NbTiN/SiO<sub>2</sub>/Al tuning circuit yield promising results at frequencies up to 970 GHz, the observed sensitivity cut-off at  $\sim 1$  THz remains a concern. In particular, this is  $\sim 50$  GHz lower than the gap frequency estimated from the BCS relationship between  $T_c$  and the superconducting energy gap ( $F_{\text{gap}} \sim 3.52 \cdot k_B T_c / h$  and  $T_c = 14.3 \text{ K}$  predict  $F_{\text{gap}} \sim 1050 \text{ GHz}$ ). There are several possible explanations for this discrepancy between the predicted and measured cut-off frequencies. Of these, two are:

1. The  $T_c$  of the NbTiN film used here is lower than has been demonstrated for films deposited on an MgO substrate or at an elevated substrate temperature ( $T_c \sim 16\text{-}17 \text{ K}$ ) [8]. Thus, it is possible that the physical mechanisms that reduce  $T_c$  in these films may also affect the relationship between the energy gap and  $T_c$ .

2. Because the estimated penetration depth in the NbTiN ground plane is approximately equal to the layer thickness (290 nm vs. 300 nm), radiation in the tuning circuit will penetrate to the bottom of the NbTiN layer. Thus, if the initial stages of NbTiN film growth produce a poor-quality interface layer, that layer could induce loss in the tuning circuit below the predicted NbTiN gap frequency.

Additional measurements and analysis are needed to fully explain the upper cut-off frequency of these tuning circuits. However, one means of improvement is clear – the use of higher- $T_c$  NbTiN layers deposited on MgO and/or elevated-temperature substrates. This should increase the cut-off frequency at least proportionally to the increase in  $T_c$  (i.e. to at least 1120 GHz for  $T_c = 16$  K). Note that the high dielectric constant of MgO makes it less desirable than fused quartz as a substrate material for waveguide mixers. However, an MgO substrate would be compatible with a quasi-optical mixer design, such as that presented elsewhere in these proceedings [13].

## 9. CONCLUSIONS

SIS mixers in which standard Nb SIS junctions are integrated with NbTiN/SiO<sub>2</sub>/NbTiN and NbTiN/SiO<sub>2</sub>/Al tuning circuits have been fabricated and tested as both direct and heterodyne detectors.

Mixers with a NbTiN/SiO<sub>2</sub>/NbTiN tuning circuit produce receiver noise temperatures as low as 395-455 K between 700 and 830 GHz. Correcting for optical losses, the corresponding effective noise at the mouth of the horn is estimated to be 195-235 K. From this relatively low-noise performance, it is clear that the NbTiN/SiO<sub>2</sub>/NbTiN tuning circuits are relatively low-loss up to at least 830 GHz. However, the poor sensitivities of these devices above 850 GHz raise concerns that a poor-quality interface layer at the bottom of the NbTiN wiring layer may introduce tuning circuit losses below the NbTiN gap frequency.

Using mixers with a NbTiN/SiO<sub>2</sub>/Al tuning circuit, receiver noise temperatures as low as 445 and 585 K are obtained at 900 and 970 GHz, respectively. Correcting for the optical losses in front of the horn of the mixer yields corrected noise temperatures as low as 260 K at 970 GHz. These results represent the first demonstration of relatively low-noise performance in a 1 THz SIS mixer incorporating a NbTiN-based tuning circuit. Furthermore, this represents a significant improvement over the best previously reported 1 THz receiver sensitivity (840 K at 1042 GHz for an Al stripline device [4]).

Analyzing the device with the highest sensitivity at 970 GHz, it is determined that the most significant contributions to the corrected receiver noise are a DSB mixer noise of 77 K and 3.2 dB of rf loss in front of the mixing element. Of this 3.2 dB, the Al wiring layer is estimated to contribute 2.6 dB of loss. The remaining 0.6 dB is thus an estimate of the loss in the NbTiN ground plane at 970 GHz.

Unfortunately, these results also indicate that the NbTiN ground plane may have a cut-off frequency of  $\sim 1$  THz. However, it is argued that it should be possible to extend the range of low-noise mixer operation to at least 1.12 THz by incorporating NbTiN deposition processes previously shown to produce films with  $T_c \geq 16$  K [7-8]. Furthermore, it is hoped that further optimization of the device parameters will push the range of operation to at least 1.2 THz, while also improving receiver sensitivities below 1 THz.

## 10. ACKNOWLEDGEMENTS

The authors would like to thank S. Bakker, M. Eggens, L. de Jong, D. Nguyen, C. Pieters, H. Schaeffer, and B. Wolfs for their technical assistance and A. Baryshev, H. van de Stadt, N. Whyborn, B. Bumble, R. LeDuc, J. Stern, and J. Zmuidzinas for helpful discussions. This work is supported in part by the Nederlandse Organisatie voor Wetenschappelijk Onderzoek (NWO) through the Stichting voor Technische Wetenschappen (STW), and the European Space Agency under ESTEC Contract No. 1653/95.

## 11. REFERENCES

1. A. Baryshev et al., unpublished result, 1999.
2. G. de Lange, J. J. Kuipers, T. M. Klapwijk, R. A. Panhuyzen, H. van de Stadt, and M. W. M. de Graauw, Superconducting resonator circuits at frequencies above the gap frequency, *J. Appl. Phys.* **77**, 1795-1804, 1995.
3. H. van de Stadt, A. Baryshev, P. Dieleman, Th. de Graauw, T. M. Klapwijk, S. Kovtonyuk, G. de Lange, I. Lapitskaya, J. Mees, R. A. Panhuyzen, G. Prokopenko, and H. Schaeffer, A 1 THz Nb SIS heterodyne mixer with normal metal tuning structure, *Proc. of the 6<sup>th</sup> Int. Symp. on Space THz Technology*, CIT, PC, 66-77, 1995.
4. M. Bin, M. C. Gaidis, J. Zmuidzinas, T. G. Phillips, and H. G. LeDuc, Low-noise 1 THz niobium superconducting tunnel junction mixer with a normal metal tuning circuit, *Appl. Phys. Lett.* **68**, 1714-1716, 1996.
5. P. Dieleman, T. M. Klapwijk, J. R. Gao, and H. van de Stadt, Analysis of Nb superconducting-insulator-superconducting tunnel junctions with Al striplines for THz radiation detection, *IEEE Trans. on Appl. Supercond.* **7**, 2566-2569, 1997.
6. P. Dieleman and T. M. Klapwijk, Shot noise beyond the Tucker theory in niobium tunnel junction mixers, *Appl. Phys. Lett.* **72**, 1653-5, 1998.
7. R. di Leo, A. Nigro, G. Nobile, and R. Vaglio, Niobium-titanium nitride thin films for superconducting rf accelerator cavities, *J. Low Temp. Phys.* **78**, 41, 1990.
8. J. A. Stern, B. Bumble, H. G. LeDuc, J. W. Kooi, and J. Zmuidzinas, Fabrication and dc-characterization of NbTiN based SIS mixers for use between 600 and 1200 GHz, *Proc. of the 9<sup>th</sup> Int. Symp. on Space THz Technology*, CIT, PC, 305-313, 1998.
9. J. W. Kooi, J. A. Stern, G. Chattopadhyay, H. G. LeDuc, B. Bumble, and J. Zmuidzinas, Low-loss NbTiN films for THz SIS mixer tuning circuits, *Int. J. of IR and MM Waves* **19**, 373-383, 1998.

10. N. N. Iosad, B. D. Jackson, T. M. Klapwijk, S. N. Polyakov, P. N. Dmitriev, and J. R. Gao, Optimization of rf- and dc-sputtered NbTiN films for integration with Nb-based SIS junctions, *IEEE Trans. on Appl. Supercond.* **9**, 1716-1719, 1999.
11. B. D. Jackson, N. N. Iosad, B. Leone, J. R. Gao, T. M. Klapwijk, W. M. Laauwen, G. de Lange, and H. van de Stadt, DC and terahertz response in Nb SIS mixers with NbTiN striplines, *Proc. of the 10<sup>th</sup> Int. Symp. on Space THz Technology*, U. of Virginia, Charlottesville, Virginia, 144-156, 1999.
12. J. Kawamura, J. Chen, D. Miller, J. Kooi, J. Zmuidzinas, B. Bumble, H. G. LeDuc, and J. A. Stern, Low-noise submillimeter-wave NbTiN superconducting tunnel junction mixers, *Appl. Phys. Lett.* **75**, 4013-4015, 1999.
13. A. Baryshev, B. D. Jackson, G. de Lange, S. V. Shitov, J. R. Gao, N. N. Iosad, and T. M. Klapwijk, Quasi-optical terahertz SIS mixers, *these proceedings*.
14. J. R. Gao, S. Kovtonyuk, J. B. M. Jegers, P. Dieleman, T. M. Klapwijk, and H. van de Stadt, Fabrication of Nb-SIS mixers with UHV evaporated Al striplines, *Proc. of the 7<sup>th</sup> Int. Symp. on Space THz Technology*, CIT, PC, 538-548, 1996.
15. N. N. Iosad, B. D. Jackson, F. Ferro, J. R. Gao, S. N. Polyakov, P. N. Dmitriev, and T. M. Klapwijk, Source optimization for magnetron sputter-deposition of NbTiN tuning elements for SIS THz detectors, *Supercond. Sci. and Technol.* **12**, 736-740, 1999.
16. B. Leone, B. D. Jackson, J. R. Gao, and T. M. Klapwijk, Geometric heat trapping in niobium superconductor-insulator-superconductor mixers due to niobium titanium nitride leads, *Appl. Phys. Lett.* **76**, 780-782, 2000.
17. A. Skalare, *Internat. J. of Infrared and Millimeter Waves* **10**, 1339, 1989.
18. J. R. Tucker and M. J. Feldman, Quantum detection at millimeter wavelengths, *Rev. of Mod. Phys.* **57**, 1055, 1985.
19. P. Dieleman, H. G. Bukkems, T. M. Klapwijk, M. Schike, and K. H. Gundlach, Observation of Andreev reflection enhanced shot noise, *Phys. Rev. Lett.* **79**, 3486-3489, 1997.
20. B. Bumble, H. G. LeDuc, and J. A. Stern, Fabrication of Nb/Al-Nx/NbTiN junctions for SIS mixer applications above 1 THz, *Proc. of the 9<sup>th</sup> Int. Symp. on Space THz Technology*, CIT, PC, 295-304, 1998.
21. J. Kawamura, D. Miller, J. Chen, J. Zmuidzinas, B. Bumble, H. G. LeDuc, and J. A. Stern, Very high-current-density Nb/AlN/Nb tunnel junctions for low-noise submillimeter mixers, *App. Phys. Lett.* **76**, 2119, 2000.

# A SINGLE-CHIP BALANCED SIS MIXER FOR 200-300 GHz

A. R. Kerr<sup>1</sup>, S.-K. Pan<sup>1</sup>, A. W. Lichtenberger<sup>2</sup>,  
N. Horner<sup>1</sup>, J. E. Effland<sup>1</sup>, and K. Crady<sup>1</sup>

<sup>1</sup>National Radio Astronomy Observatory\*  
Charlottesville, VA 22903

<sup>2</sup>University of Virginia  
Charlottesville, VA 22904

## ABSTRACT

The balanced mixer is fabricated on a 2 x 1 mm quartz substrate which contains an RF quadrature hybrid and two SIS mixers. These components are realized in capacitively-loaded coplanar waveguide, which minimizes stray coupling between adjacent components and coupling to undesired modes in the thick quartz substrate. Signal and LO waveguides are coupled to separate ports of the main substrate via suspended striplines. The mixers were fabricated using the UVA Nb/Al-oxide/Nb process. Over the 225-300 GHz band, the mixer noise temperature was 37-48 K and the overall receiver noise temperature was 46-78 K DSB, both referred to outside the cryostat. The LO-to-RF isolation was >12 dB, which we hope to improve by reducing leakage of power under the substrate between the LO and signal ports.

## INTRODUCTION

At the 1996 THz Symposium we proposed designs for single-chip balanced and sideband separating SIS mixers [1]. Results for a 200-300 GHz sideband separating mixer were reported at the 1998 THz Symposium [2], and the present paper gives results for a balanced SIS mixer in the same band.

Balanced mixers have been used in commercial and military equipment since before WWII. They have three advantages over single ended mixers: (i) a LO coupler or diplexer is not required ahead of the mixer, (ii) the required LO power is substantially less than that of a single-ended mixer with an LO coupler, and (iii) sideband noise from the LO is

---

\*The National Radio Astronomy Observatory is a facility of the National Science Foundation operated under cooperative agreement by Associated Universities, Inc.

suppressed. LO power is usually coupled into a single ended mixer using a directional coupler or beam splitter. If the signal loss through the LO coupler is to be kept small, the LO loss must be substantial, typically 15-20 dB and most of the LO power is wasted. The balanced mixer has a separate LO port with efficient coupling so the required LO power is reduced by 12-17 dB relative to the simple single-ended mixer with LO coupler. In a single ended mixer, noise from the LO source in the signal and image bands is coupled into the mixer and converted to the IF. Depending on the nature of the LO source, its (sideband) noise temperature may be room temperature or higher. If the LO source has an effective noise temperature of 300 K at the sideband frequencies, then with a 15-20 dB beam splitter it will contribute 10-3 K in each sideband at the input of the mixer, which may be comparable with the intrinsic noise temperature of the receiver itself. With some LO sources we have observed a considerably higher excess sideband noise — as much as 50 K of sideband noise at the input of the mixer with some frequency multipliers in the 200-300 GHz range. In a balanced mixer, sideband noise is suppressed by an amount depending on the phase and amplitude balance through the mixer.

Balanced mixers require the relative phasing of the signal and LO at the two component mixers to differ by  $180^\circ$ . This can be achieved either using a  $180^\circ$  hybrid (transformer or magic-T) or a  $90^\circ$  hybrid (3-dB directional coupler). In the present work we use the latter, as shown in Fig. 1, because the quadrature hybrid is more easily realized as a planar circuit. One output of the IF ( $180^\circ$ ) hybrid contains the down-converted signal (upper and lower sidebands), and the other contains the down-converted LO sideband noise.

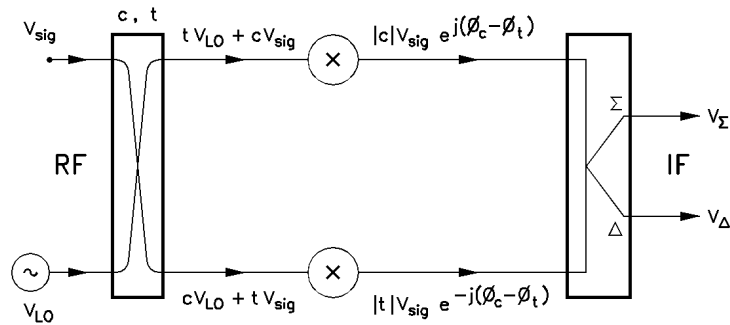


**Fig. 1. Schematic diagram of a balanced mixer of the type used in this work.**

The LO noise rejection of a balanced mixer depends on accuracy of the amplitude and phase matching of the signal and LO through the two branches of the circuit. Fig. 2 shows the effects of amplitude and phase imbalance in a balanced mixer. It is seen that the rejection is quite insensitive to asymmetries in the mixer — even with 2 dB amplitude imbalance *and*  $15^\circ$  phase imbalance, the LO noise rejection is over 15 dB.

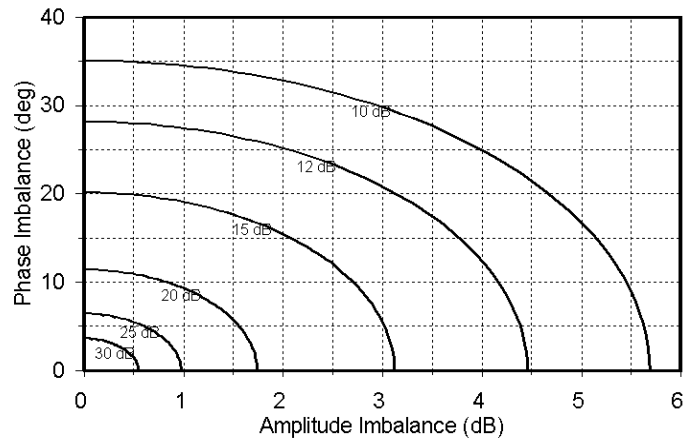


**Fig. 2. LO noise rejection of a balanced mixer as a function of amplitude and phase imbalance.**

## DESIGN

The layout of the balanced mixer is shown in Fig. 3. It is based on that described in [1] and uses the same capacitively loaded coplanar waveguide (CLCPW) and quadrature hybrid, as shown in Figs. 4 and 5. The component single-ended mixers are as described in [3]. They have four SIS junctions in series and are designed with low IF parasitic capacitance and inductance to allow operation with an IF as high as 12 GHz.

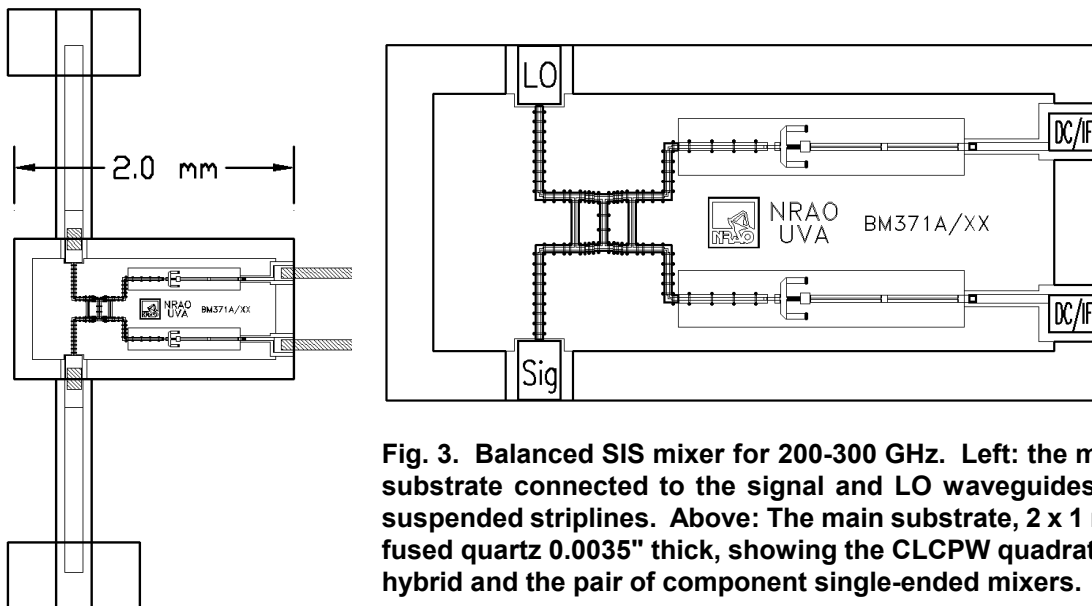


**Fig. 3. Balanced SIS mixer for 200-300 GHz. Left: the main substrate connected to the signal and LO waveguides by suspended striplines. Above: The main substrate, 2 x 1 mm fused quartz 0.0035" thick, showing the CLCPW quadrature hybrid and the pair of component single-ended mixers.**

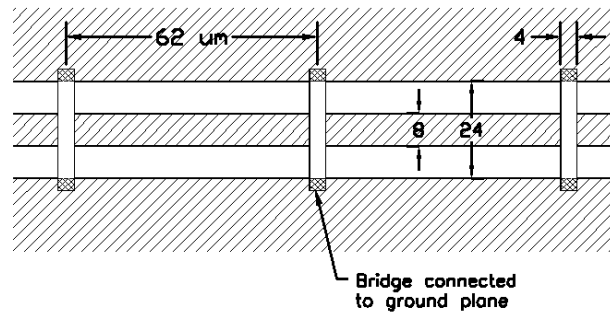


Fig. 4. A length of capacitively loaded coplanar waveguide (CLCPW) on a thick fused quartz substrate [1].  $Z_0 = 50 \Omega$ . Dimensions in microns.

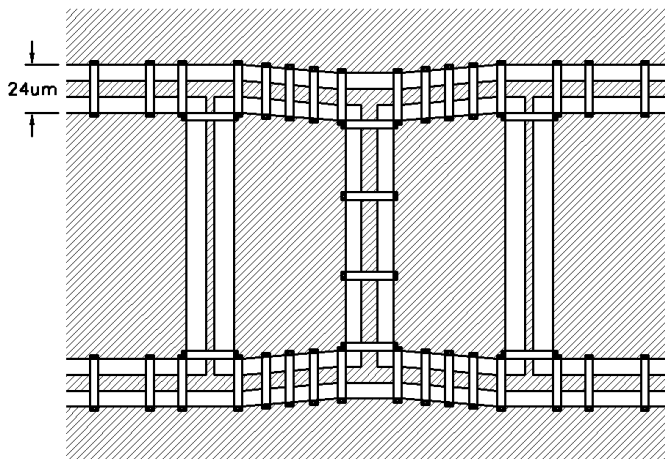


Fig. 5. Quadrature hybrid for 200-300 GHz [1].

## FABRICATION & ASSEMBLY

The mixers were fabricated on chemically polished fused quartz wafers 30 mm diameter and 0.25 mm thick. The SIS junctions are formed on small islands of Nb/Al-oxide/Nb trilayer. An SiO layer 200 nm thick is deposited around the junctions, and an additional 370 nm in the CLCPW sections. Vias connect the ends of the tuning stubs and the bridges in the CLCPW section to the base electrode. JPL's gold overlayer technique [4] was adapted to our process; since gold does not naturally oxidize, an in-situ physical cleaning of the surface of the junction counter electrode is avoided prior to depositing the Nb interconnection layer. Omitting the physical cleaning step has two advantageous: any native Nb and Al oxides which have grown after deposition of the junction SiO insulation will remain, and the SiO insulation layer will not be disturbed. Both these factors tend to prevent micro-shorts between the wiring and base electrodes, and we have been able to fabricate junctions with 200 nm insulation layers without resorting to anodization techniques.

In the gold overlayer process we used a separate DC magnetron sputtering system to deposit layers of Au(1-2 nm)/[Cr(4% wt.)-Au](28 nm) on top of the trilayer wafer after an ion gun clean. The Cr-Au mixture was used to increase the physical durability of the over-layer. Prior to the trilayer etch, the Cr-Au layer is etched in a solution of 10 g I, 40 g  $\text{INH}_4$ , 400 ml DI water, and 600 ml ethanol, which we have found etches Cr-Au films containing as little as 0.4% (wt.) Cr more repeatably and uniformly than pure Au films.

A new quadlevel resist, composed of NFR 200nm/polyimide 200nm/Nb 40nm/NFR (imaging resist) [5] was used as the etch mask in the junction step. The Au/Cr-Au layer is wet etched and the Nb junction defined with an  $\text{SF}_6+\text{CHF}_3+\text{N}_2$  RIE. It was found that the presence of Au in the plasma and in contact with the Nb layer reduces the anisotropy of the Nb etch. The bottom NFR layer was included as it was found to enhance the anisotropy of this Nb etch. The polyimide is included in the quadlevel structure because a trilevel resist of NFR/Nb/NFR will not liftoff satisfactorily due to the lack of a suitable chemical stripper for the NFR. After the junction etch and  $\text{SiO}_2$  deposition, a liftoff of the self-aligned quadlevel resist is performed with NMP [6]. Since the NFR is not fully removed with this stripper, the liftoff is followed by an oxygen plasma etch.

The vias, which connect the ends of the tuning stubs and the bridges in the CLCPW section to the base electrode, can be accomplished in two ways. The first is to use large area junctions, and the second uses a direct contact from wiring layer to base electrode. We have chosen the second approach to avoid possible internal resonances in large-area junctions used as vias. Since an in-situ cleaning step is not used in our Nb wiring process, a second Au overlayer was defined on top of the base electrode after removing the Au/Cr-Au and Nb counter electrode from the via sites.

After dicing, the individual mixers were thinned to 0.0035" using a dicing saw as a surface grinder. (More recently, we have been using a lapping machine to thin the whole wafer with an accuracy of  $\pm 0.0002$ " [7].) The mixer chip was connected to its suspended striplines with 0.0001" gold ribbons using Indalloy #2 solder [8] and Supersafe #334 flux [9]. Soldering to the mixer chip is done using a parallel gap welder [10] with a 0.005" x 0.010" soldering tip and a 900 ms heating pulse. Gold ribbon connections were also soldered to the IF/DC pads. The assembly was placed, circuit side down, in the lower half of the mixer block and the IF/DC connections made. Gold crush wires, 0.0007" diameter, between the edges of the main substrate and the block ensure a good ground contact when the upper half of the block is bolted in place.

## MEASUREMENTS

The mixer was tested in a vacuum cryostat cooled to  $\sim 4$  K by a Joule-Thompson refrigerator. The incoming RF signal enters the cryostat through a plastic film vacuum window [11] supported by a 0.125" sheet of expanded PTFE [12]. It passes through a 50-K infrared filter, also made of 0.125" expanded PTFE, a PTFE lens at 4 K, and into a scalar

feed horn. The LO is connected to the mixer through an (overmoded) stainless steel waveguide. A 4 K IF plate containing a coaxial switch and 50-ohm IF calibration components, similar to that described in [13], enables the noise temperature at either port of the balanced mixer to be measured. The IF noise temperature, including the coaxial switch, two isolators, and a directional coupler, was 3.6 K at 1.4 GHz.

The balanced mixer has separate SMA DC/IF connectors for each component mixer. These were connected through cables of equal length to the 4 K 180° IF hybrid [14]. Bias-T's [15] on the other side of the hybrid were connected through isolators to the IF switch. No IF impedance transformer was used between the junctions and the 50-ohm IF plate. A DC magnetic field was applied to the mixer to suppress the Josephson currents in the junctions.

Fig. 6 shows the I-V characteristics of the two component mixers with and without LO power applied. The critical current,  $I_C = 118 \mu\text{A}$ , was determined from the measured quasiparticle current rise,  $\Delta I_{\text{gap}}$ , at the gap voltage using the relation  $I_C = (\pi/4) \cdot \Delta I_{\text{gap}}$ . An SEM was used to measure the junction diameter,  $1.5 \mu\text{m}$ , from which the critical current density  $J_C = 6700 \text{ A/cm}^2$  is deduced.

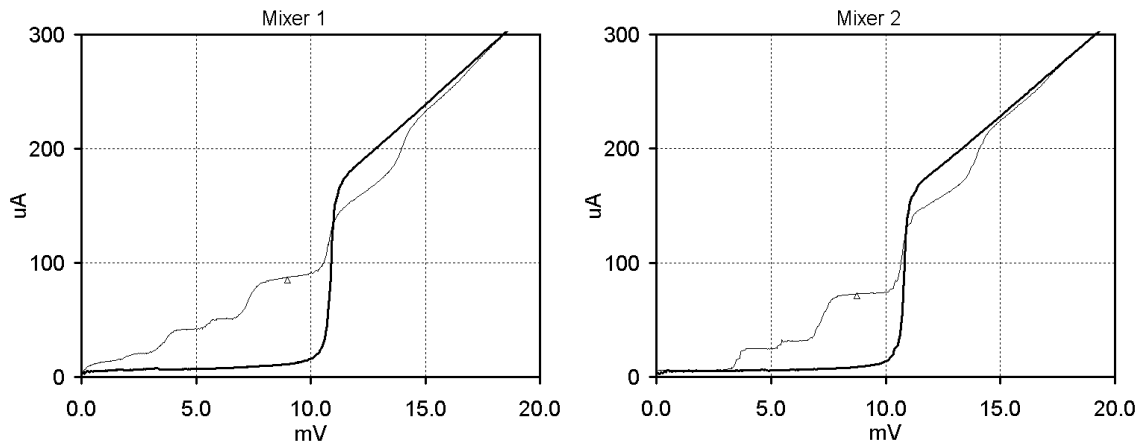


**Fig. 6. I-V characteristic of the two component mixers with LO power applied (light curve) and without LO power (heavy curve). Each mixer has four junctions in series. The bias point is indicated by the marker.  $F_{\text{LO}} = 225 \text{ GHz}$ .**

Measurements were made using RF hot and cold loads (room temperature and liquid nitrogen) in front of the receiver with the IF switch connected in turn to each output of the IF hybrid. The calibrated IF plate enables the mixer noise temperature and conversion loss in each channel to be deduced, and also the overall receiver noise temperature. The LO sideband rejection is simply the quotient of the conversion losses measured at the two IF ports. Fig. 7 shows the DSB mixer and receiver noise temperatures as functions of LO

frequency; note that both noise temperatures include the contributions from all the input components (vacuum window, IR filter, lens, horn). Fig. 8 shows the LO sideband rejection.

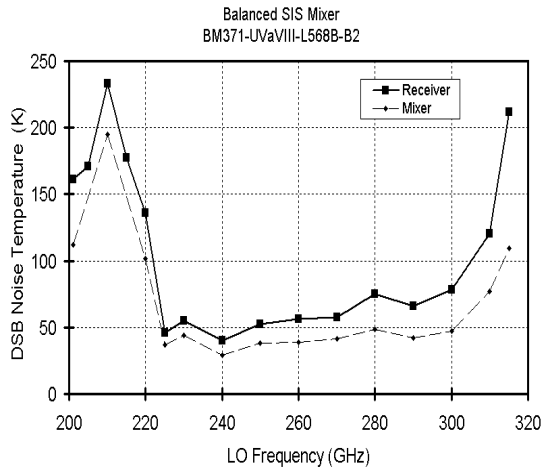


**Fig. 7. Mixer and receiver noise temperature (DSB).**

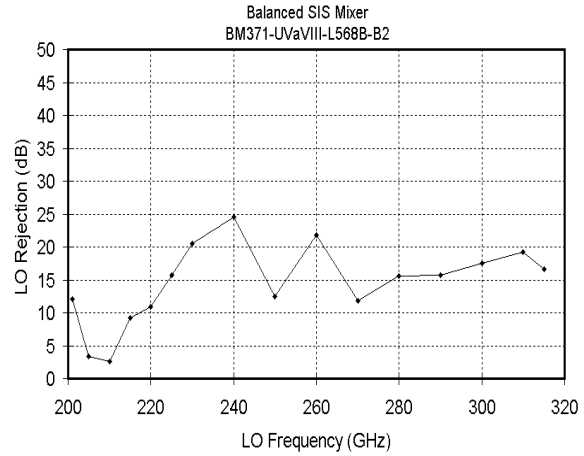


**Fig. 8. LO rejection.**

## DISCUSSION

The performance of the balanced mixer was very close to that of the single-ended mixer [3] on which it was based. It is clear that the loss of the CLCPW quadrature hybrid and transmission lines is not significant in this frequency band.

The variation of the LO rejection with frequency in Fig. 8 results from a small amount of leakage between the signal and LO ports of the balanced mixer chip, whereby some LO power enters the component mixers through the signal port and spoils the amplitude balance and phasing of the LO at the two mixers. Likewise, some signal power enters the LO port, with a similar effect. This leakage does not originate in the CLCPW circuit of the balanced mixer but at the transitions from the suspended striplines to the mixer chip. We suppressed this leakage to the present level using pieces of MF-112 absorber [16] above and below the mixer substrate. (The absorber does not affect propagation on the CLCPW lines as their fields are contained within a small region close to the line.) Further improvement should result from a wider substrate on which the RF and LO ports are further apart so the signal and LO leakage components will be more completely absorbed.

The down-converted signal appears at the  $\Delta$  port of the IF hybrid while the down-converted LO sideband noise appears at the  $\Sigma$  port. By reversing the bias polarity on one of the component mixers, the outputs are reversed, with the signal appearing at the  $\Sigma$  port [17]. In practice, one normally requires only the down-converted signal and not the LO noise, in

which case it is possible to replace the IF  $180^\circ$  hybrid in Fig. 1 with a simple T-connection and operate with opposite bias polarity on the two component mixers. It is important to note that replacing the  $180^\circ$  hybrid with a simple T-junction results in a change in the IF load impedance seen by the component mixers. The (desired) in-phase IF signals from the two mixers each see, at the T, an IF load impedance twice that of the actual load, while the out-of-phase IF signals from the two mixers see a virtual short circuit at the T.

An alternative way to obtain efficient LO coupling and rejection of LO sideband noise is to use a single-ended mixer preceded by a tuned diplexer — often a quasi-optical Martin-Puplett interferometer is used at millimeter and submillimeter wavelengths. This has the advantage of using a simpler mixer but requires a mechanically tunable diplexer if the receiver is to operate at different frequencies. Furthermore, with the Martin-Puplett type of diplexer, the bandwidth over which good LO noise rejection ( $> 10$  dB) and low signal loss ( $< 0.4$  dB) are obtained is restricted to  $\sim 40\%$  of the IF center frequency. By comparison, a balanced mixer based on a broadband RF quadrature hybrid requires no tuning and should be useable with a multi-octave IF, such as the 4-12 GHz IF currently planned for the ALMA radio telescope.

## ACKNOWLEDGMENTS

The authors thank J. Zhang, F. Johnson and A. Marshall for their work fabricating and assembling the mixers and R. Groves for his help in testing them. This work was supported by grants from NASA and the National Science Foundation.

## REFERENCES

- [1] A. R. Kerr and S.-K. Pan, "Design of planar image-separating and balanced SIS mixers," Proceedings of the Seventh International Symposium on Space Terahertz Technology, pp. 207-219, 12-14 March 1996. Available in pdf format at <http://www.mma.nrao.edu/memos/html-memos/alma151/memo151.pdf>.
- [2] A. R. Kerr, S.-K. Pan, and H. G. LeDuc, "An integrated sideband separating SIS mixer for 200-280 GHz," Proceedings of the Ninth International Symposium on Space Terahertz Technology, pp. 215-221, 17-19 March 1998. Available in pdf format at <http://www.mma.nrao.edu/memos/html-memos/alma206/memo206.pdf>.
- [3] A. R. Kerr, S.-K. Pan, A. W. Lichtenberger and H. H. Huang, "A Tunerless SIS mixer for 200–280 GHz with low output capacitance and inductance," Proceedings of the Ninth International Symposium on Space Terahertz Technology, pp. 195-203, 17-19 March 1998. Available at <http://www.mma.nrao.edu/memos/html-memos/alma205/memo205.pdf>

- [4] H. G. LeDuc, B. Bumble, S. R. Cypher, A. J. Judas, and J. A. Stern, "Sub Micron Area Nb/AlO<sub>x</sub>/Nb Tunnel Junctions for Submm Mixer Applications," Third International Symposium on Space Terahertz Technology, 1992.
- [5] NFR is a high resolution negative resist from JSR Microelectronics Inc, Sunnyvale, CA 94086.
- [6] NMP: 1-Methyl-2-Pyrrolidinone.
- [7] A. W. Lichtenberger, in preparation.
- [8] Indium Corporation of America, Utica, NY 13502.
- [9] Superior Flux & Mfg. Co., Cleveland, OH 44143.
- [10] Hughes model VTA-90 parallel gap welder with power supply model MCW-550.
- [11] Hercules HR500-2S film is 0.00075" thick. It consists of 0.0005" biaxially oriented polypropylene coated both sides with polyvinylidene chloride. The plastic film division of Hercules is now operated by Applied Extrusion Technology Inc., Covington, VA. HR500-2S is now obsolete and has been superceded by a similar material called UBS-2.
- [12] Gore RA-7957 expanded PTFE has a submicroscopic open-cell structure. It has a density 25% of that of solid PTFE.
- [13] S.-K. Pan, A. R. Kerr, M. J. Feldman, A. Kleinsasser, J. Stasiak, R. L. Sandstrom and W. J. Gallagher, "A 85-116 GHz SIS receiver using inductively shunted edge-junctions," IEEE Trans. Microwave Theory Tech., vol. MTT-37, no. 3, pp. 580-592, March 1989.
- [14] M/A-Com model 2031-6331-00 1-2 GHz 180° hybrid.
- [15] A. R. Kerr, "The NRAO Type-2B 1-2 GHz SIS Bias-T, " Electronics Division Technical Note No. 173, National Radio Astronomy Observatory, Charlottesville, VA, 15 Feb. 1996.
- [16] Emerson & Cuming, Inc., Canton, MA. Type MF-112 absorber. See G.A. Ediss A.R. Kerr H. Moseley K.P. Stewart, "FTS Measurements of Eccosorb MF112 at Room Temperature and 5 K from 300 GHz to 2.4 THz," ALMA Memo #273, 8 Sep. 1999. Available at: <http://www.mma.nrao.edu/memos/html-memos/alma273/memo273.pdf>.
- [17] The corresponding reversal of output ports in the case of a balanced mixer using conventional diodes also requires the orientation of one diode to be reversed. This is not necessary in the case of a balanced SIS mixer because of the antisymmetry of the I-V characteristics.

# PERFORMANCE OF SUB-HARMONIC MIXING WITH AN SIS JUNCTION

S.-C. Shi<sup>1</sup>, W.-L. Shan<sup>1</sup>, T. Noguchi<sup>2</sup>, K.-C. Xiao<sup>3</sup>

<sup>1</sup>*Purple Mountain Observatory, Nanjing, 210008, P. R. China*

<sup>2</sup>*Nobeyama Radio Observatory, Nobeyama, Minamisaku, Nagano, 384-13, Japan*

<sup>3</sup>*Nagoya University, Japan*

## Abstract

The performance of superconductor-insulator-superconductor (SIS) sub-harmonic mixers is thoroughly investigated in this paper. On account of the importance of the harmonic effect, a full five-port model combined with an enhanced Newton solution is applied to calculate the local oscillator (LO) waveform. The mixer performance is studied as functions of principal parameters including the embedding admittances, LO power and bias voltage. The results are compared with those from the quasi five-port model.

## I. Introduction

It is well known that the local oscillator (LO) power for SIS mixers is proportional to the square of the LO frequency<sup>1</sup>, and that it is still difficult to develop broadband LO sources in the terahertz regime. Hence sub-harmonic SIS mixers, which are pumped by a LO signal of a frequency about one half the RF frequency, are of particular interest in the terahertz regime as far as the LO frequency and power are concerned. Conventional sub-harmonic mixers (e.g., Schottky ones) usually utilize anti-parallel diodes to suppress the fundamental mixing<sup>2</sup>, thereby achieving good sub-harmonic mixing performance. Sub-harmonic mixers with SIS junctions, however, cannot adopt such a scheme because of their symmetric I-V characteristic. The main goal of this research is to investigate the sub-harmonic mixing behavior of SIS mixers with a single junction device. Shen et al<sup>3</sup> and Edward Tong et al<sup>4</sup> have previously studied this theme merely focusing on the investigation of the mixer gain.

The three-port model, the simplest model for SIS junction, cannot be adopted to simulate the mixing behavior of sub-harmonic SIS mixers since all frequencies beyond the fundamental frequency are assumed to be short-circuited by the junction capacitance. The quasi five-port model can be applied for such simulations<sup>5</sup>, by assuming a sinusoidal LO voltage across the junction. For more precise analyses, here we use the full five-port model with a spectral domain approach calculating the waveform of the LO voltage<sup>4</sup>. By simulating a sub-harmonic mixer pumped at 250 GHz, we have thoroughly studied the performance of sub-harmonic SIS mixers, including the mixer's conversion efficiency, noise temperature, input coupling and output coupling.

## II. Theory of Simulation

## II.a Large-Signal Analysis

In the full five-port approximation, the junction's LO wave form is expressed as a finite Fourier series:

$$V_J(t) = V_0 + \text{Re}(V_1 e^{j\omega_p t}) + \text{Re}(V_2 e^{j2\omega_p t}) \quad (1)$$

by neglecting those harmonic terms beyond  $n=2$ . Here  $\omega_p$  is the LO angular frequency. For a given value of the LO source current ( $I_{LO}$ ), Voltages  $V_1$  and  $V_2$  should satisfy the constraints imposed by the embedding network at frequencies  $\omega_p$  and  $2\omega_p$ <sup>4</sup>. A globally convergent multi-dimensional Newton's method<sup>6</sup> is applied to solve  $V_1$  and  $V_2$ . This algorithm optimizes the revising vector of each iteration so as to avoid the oscillating effect that often occurs in conventional Newton's iterations. This method allows any reasonable initial trial solution and the convergence is always achieved in our calculation.

In our simulation, we calculate the mixer's performance as the parameter of interest varies step by step. At each step, the solving process of the nonlinear equation can be accelerated by choosing the previous  $V_1$  and  $V_2$  as the trial solution of the next one, thereby reducing the iteration to only 2~3 loops.

## II.b Small-Signal Analysis

The small-signal analysis has been well discussed in many papers<sup>1,7</sup>. Here we only list those results and performance parameters discussed in the following parts. By using the Fourier series of the phase factor, we easily get the mixer's impedance matrices [ $Z_{mn}$ ] and shot-noise correlation matrix [ $H_{mn}$ ]. The subscript of the matrices  $m=-2,-1,0,1,2$  denotes the sideband whose frequency is  $m f_m + f_n$ . The associated conversion efficiency from the sub-harmonic sideband ( $n = 2,-2$ ) is

$$G_n = 4 \text{Re}(Y_{emb}(n\omega_p + \omega_0)) \text{Re}(Y_{emb}(\omega_0)) |Z_{on}|^2, n = 2,-2. \quad (2)$$

The mixer noise includes the thermal noise and the shot noise. The Josephson noise is not discussed here as we can apply a DC magnetic field to suppress the Josephson effect, and choose the bias point away from the region where the Josephson noise is considerable. The noise temperature of SIS mixers is

$$T_m = \frac{P_0^n}{4k\Delta f \text{Re}(Y_{emb}(2\omega_p)) |Z_{o2}|^2}, \quad (3)$$

where  $\Delta f$  is the bandwidth of the intermediate frequency (IF) and  $P_0^n$  is the IF noise power, which can be expressed by the noise correlation matrix and the impedance matrix.

It is also necessary to concern the mixer's input and output coupling efficiencies in practical receiver systems. In our simulation, the input and output coupling efficiencies are written as:

$$C_{in} = \frac{4 \operatorname{Re}(Y_{emb}(2\omega_p)) \operatorname{Re}(Y_{in})}{|Y_{emb}(2\omega_p) + Y_{in}|^2}, \quad (4)$$

$$C_{out} = \frac{4 \operatorname{Re}(Y_{emb}(\omega_0)) \operatorname{Re}(Y_{out})}{|Y_{emb}(\omega_0) + Y_{out}|^2}. \quad (5)$$

The input admittance at the signal sideband  $Y_{in}$  and the output impedance of the IF port  $Y_{out}$  can be expressed as :

$$Y_{in} = \frac{1}{Z_{22}} - Y_{emb}(2\omega_p), \quad (6)$$

$$Y_{out} = \frac{1}{Z_{00}} - Y_{emb}(\omega_0). \quad (7)$$

It should be mentioned that as we assume  $\omega_0 \ll \omega_p$ , the embedding impedances at the upper and lower sideband are approximately the same. In the following parts, the embedding impedance at the IF port and each sideband are normalized by the junction's normal state resistance ( $R_N$ ) and separated into resistance and reactance as:

$$\tilde{Y}_{emb}(\omega_0) = \frac{1}{R_{if}} + jB_{if}, \quad (8)$$

$$\tilde{Y}_{emb}(\omega_p \pm \omega_0) = \tilde{Y}_{emb}(\omega_p) = \frac{1}{R_{rf}} + jB_{rf}, \quad (9)$$

$$\tilde{Y}_{emb}(2\omega_p \pm \omega_0) = \tilde{Y}_{emb}(2\omega_p) = \frac{1}{R_{hm}} + jB_{hm}. \quad (10)$$

### III. Results and Discuss

The performance of sub-harmonic SIS mixers is affected by a variety of parameters including the embedding admittances at the five frequency ports, the bias voltage and the LO current. To illustrate how these parameters affect the mixer performance, we examined the performance variation under the condition that only one or two parameters changed while others were fixed.

In our simulation, the  $I$ - $V$  curve of a physical Nb/AlO<sub>x</sub>/Nb SIS junction was used. Its gap voltage  $V_{gap}$  is  $2.76\text{mV}$  and normal-state resistance  $R_N$  is  $17.6\Omega$ . Because the performance is directly influenced by the effective embedding admittance  $\tilde{Y}'_{emb}$ :

$$\tilde{Y}'_{emb}(\omega) = \tilde{Y}_{emb}(\omega) + j\omega R_N C_J, \quad (11)$$

the  $\omega R_N C_J$  product was not regarded as an independent variable here.

#### III.a Optimum Bias Voltage and LO Source Current

Firstly, a preliminary optimization was carried out to obtain a set of parameters enabling reasonably good mixer performance on the first photon step. Based on this optimization, we obtained the embedding admittance at each sideband and the IF port such as:  $\tilde{Y}'_{emb}(\omega_p) = 1/2.3 + j0.2$ ,  $\tilde{Y}'_{emb}(2\omega_p) = 1.0$  and  $\tilde{Y}(\omega_0) = 1/2.0$ .

With different LO pumping currents  $\gamma=(I_{LO}R_N/V_{gap})$  from 0.4~1.2, a series of responding conversion efficiencies and noise temperatures were calculated (see Fig. 1(a) and (b)). Obviously,  $G_2$  increases with  $\gamma$  while  $\gamma<1.0$  and tends to fall while  $\gamma>1.0$ . If a proper LO current is applied, positive conversion efficiency is observed just below the gap voltage. Accompanying with the positive conversion efficiency, the differential resistance of the pumped  $I$ - $V$  curve is nearly zero or merely negative, which is actually not desirable for practical SIS receivers. In Fig. 1(b), the noise temperature on the first photon step is 23K, which is about 1~2 times as large as the quantum limit ( $\hbar\omega_s/2k_b$ ). The noise temperature on the second photon step is not optimum because the embedding admittances were optimized for the first photon step.

In order to study the effect of the LO current, we plot  $\alpha_1, \alpha_2, G_2$  and  $T_m$  as a function of  $\gamma$  at a fixed bias point of  $V_{bias}=2.2mV$ . As shown in Fig. 2(a),  $\alpha_1$  varies almost linearly with  $\gamma$  and  $\alpha_2$  increases till  $\gamma=1.8$ , but begins to decrease while  $\gamma>1.8$  possibly due to the junction non-linearity fading out under a large LO power. In Fig. 2(b),  $G_2$  and  $T_m$  have their best values when  $\gamma$  is about 1.0~1.2, and start to deteriorate beyond this range.

The full five-port model gives different result from that by the quasi five-port model does when the harmonic effect is not negligible. The harmonic effect can be evaluated by the ratio of  $\alpha_2/\alpha_1$ . We plot the ratio as a function of  $V_{bias}$  in Fig. 3(a). It is interesting that the harmonic effect is most obvious in the intersectional region of the first photon step and the second one. In this region the noise temperature calculated by the quasi five-port model is lower than that by the full five-port model due to omitting the noise contribution of the harmonic part (shown in Fig. 3(b)). The conversion efficiency calculated by the quasi five-port model is larger on the first photon step but smaller in the second photon step. In the region where  $\alpha_2/\alpha_1<0.1$ , there is almost no difference between the two models.

### III.b Effect of the RF Termination

Just like the fundamental mixing, the sub-harmonic mixer has a good performance when the junction capacitance is nearly tuned out (by an external inductance, for example.) The contours of the performance as a function of  $\tilde{Y}'_{emb}(\omega_p)$  are demonstrated in Fig. 4 with the supposition of  $V_{bias}=2.2mV$ ,  $\gamma=1.2$ ,  $\tilde{Y}'_{emb}(2\omega_p)=1.0$ ,  $\tilde{Y}_{emb}(\omega_0)=0.5$ . Positive conversion efficiency is observed in the region of  $R_{rf}>2$  and  $(B_{rf}-\omega_p R_N C_J)=-1\sim-2$ . Beyond this region, either a smaller  $R_{rf}$  or a larger  $|B_{rf}-\omega_p R_N C_J|$  will cause a poor coupling between the junction and the LO source, and bring about low conversion efficiency and large noise temperature.

Being sensitive with the value of  $(B_{rf}-\omega R_N C_J)$ , the lowest noise temperature is achieved when the junction capacitance is exactly tuned out and  $R_{rf}$  lies in the region of 2~3. The noise temperature oscillates while  $R_{rf}>3$  and the value of  $(B_{rf}-\omega R_N C_J)=0$ .

Directly influenced by  $\tilde{Y}_{emb}(2\omega_p)$  instead of  $\tilde{Y}_{emb}(\omega_p)$  as expressed in Eq. (4) and (6), the input coupling efficiency  $C_{in}$  appears insensitive to  $\tilde{Y}_{emb}(\omega_p)$ . Only in the region where positive conversion efficiency occurs,  $C_{in}$  have small values. The  $C_{out}$  behaves more irregularly. As indicated in Fig. 4(d), while the effective embedding admittance is inductive, there appears a large area that corresponds to a negative  $C_{out}$ . It should be noted that this area covers the region of positive conversion efficiency and also its peripheral area with small negative conversion efficiency.

### III.c Effect of the Harmonic Termination

Being different from the performance of the fundamental mixing, which is insensitive to the embedding admittance at the harmonic sidebands,  $\tilde{Y}_{emb}(2\omega_p)$  plays a more important role in the sub-harmonic mixing. As shown in Fig. 5, the highest conversion efficiency resides in the region of  $R_{hm}=0.4\sim 4$  and  $(B_{hm} - 2\omega_p R_N C_J) = 0 \sim 1$ . It is indeed indicated that besides the necessity of tuning out the capacitance at the fundamental sidebands, good performance requires the capacitance tuned out at the harmonic sidebands as well.

The mixer noise temperature and input coupling efficiency behave very similarly as the conversion efficiency. Their behaviors are nearly symmetrical along the line of  $(B_{hm} - 2\omega_p R_N C_J) = 0$ . The region relating to the highest  $G_2$  is also that with the lowest  $T_m$  and the best  $C_{in}$ , however  $C_{out}$  has a large gradient there and varies very sensitively with  $(B_{hm} - 2\omega_p R_N C_J)$ .

### III.d Effect of the IF Termination

According to our result, the IF load impedance affects the output coupling efficiency and the conversion efficiency, but does not influence the noise temperature  $T_m$  and the input coupling efficiency. The dependences of  $G_2$  and  $C_{out}$  on  $\tilde{Y}_{emb}(\omega_0)$  are plotted in Fig. 6 with the parameters listed in the figure caption. Either capacitive or inductive  $\tilde{Y}_{emb}(\omega_0)$  will deteriorate the performance while a wider range of resistance ( $R_{if}=2\sim 5$ ) is suitable. It is expectable that a reasonably large  $R_{if}$  is advantageous to the output matching, because the output resistance (approximately equal to the differential resistance of the pumped  $I-V$ ) is quite large at the practical bias point. The result also indicates that larger  $R_{if}>5$  is harmful to good output efficiency.

## IV Summary

We have used a full five-port model to simulate a sub-harmonic SIS mixer pumped at 250GHz. It is indicated that to obtain good sub-harmonic mixing performance, the junction capacitance should be tuned out at both the fundamental and harmonic frequency. The best termination resistant at  $\omega_p$  is 2~3 and a wider

range from 0.4 to 4 at  $2\omega_p$ . The IF termination only influences the conversion efficiency and the IF output coupling efficiency. A pure resistive IF load in the range of 2~5 will gain good conversion efficiency and the best output coupling. The optimum  $\gamma$  in our simulation is 1.2, and the corresponding  $\alpha_1$  is 1.7. It is necessary to emphasize that the lowest noise temperature of the sub-harmonic mixer is close to the quantum noise limit. It provides strong evidence that sub-harmonic mixers should be useful at sub-millimeter wavelengths.

### References

- [1] John R. Tucker and M. J. Feldman, "Quantum detection at millimeter wavelengths," Rev. of Mod. Phy. Vol. 57, 1055-1113, 1985.
- [2] S. A. Maas, "Microwave Mixers, 2nd Edition," Boston, MA: Artech House, 1993.
- [3] T. M. Shen and P. L. Richards, "Computer Simulations of the Performance of Quasiparticle Heterodyne Mixer," IEEE Tran. Magn., Vol. MAG-17, No. 1, 677-683, 1981.
- [4] Cheuk-Yu Edward Tong and Raymond Blundell, "Simulation of the superconducting Quasiparticle Mixer Using a Five-Port Model", IEEE Trans. Microwave Theory Tech, Vol. 38, No. 10, October 1990.
- [5] S. C. Shi and T. Noguchi, "SIS mixers with distributed junction arrays," in XXVI<sup>th</sup> General Assembly of Int. Union of Radio Science (JDC.6, Oral Session), Canada, Aug, 13-21, 1999.
- [6] W.H.Press, S. A. Teukolsky, W. T. Vetterling, B. P. Flannery, "Numerical Recipes in C, The Art of Scientific Computing, Second Edition," Cambridge University Press, 324-328, 1992
- [7] John R. Tucker, "Quantum Limited Detection in Tunnel Junction," IEEE J. Quantum electronics, Vol. QE-15, No. 11, November 1979.

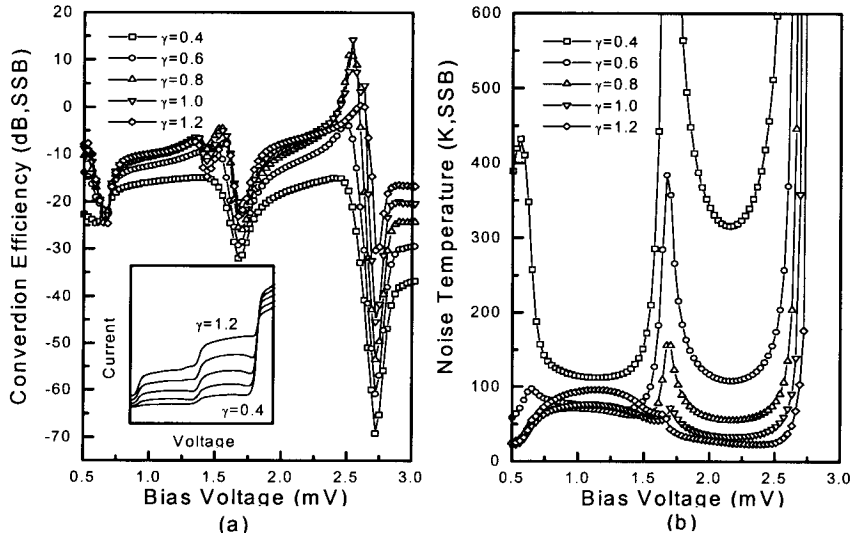


**Fig. 1** The simulated performance shown as functions of bias voltage for normalized LO Source Current  $\gamma = 0.4 \sim 1.2$ . Embedding admittances included are:  $Y'_{emb}(\omega_p) = 1/2.3 + j1.2$ ,  $Y'_{emb}(2\omega_p) = 1.0$  and  $\tilde{Y}(\omega_0) = 1/2.0$ . The inset depicts the pumped  $i-v$  curves.

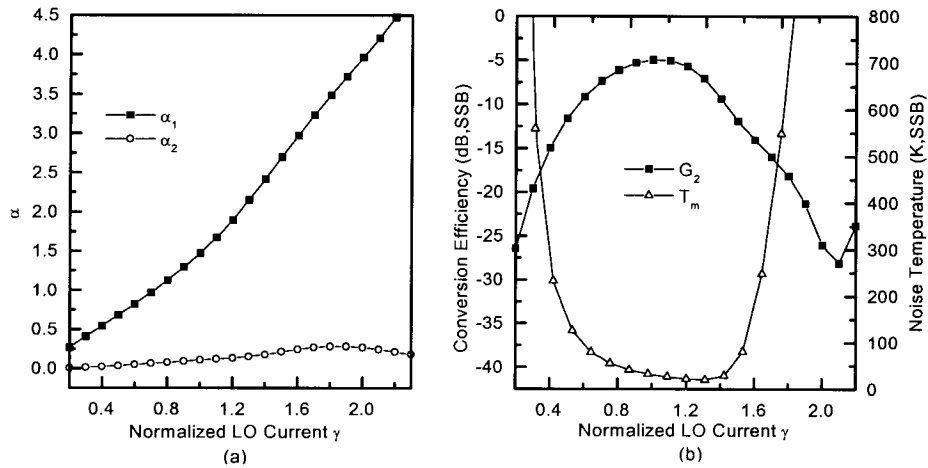


**Fig. 2** Performance of the same mixer of Fig. 1 with fixed bias voltage 2.2mV as function of normalized LO source  $\gamma$ . (a)  $\alpha_1$  and  $\alpha_2$ , (b) mixer gain and noise temperature.

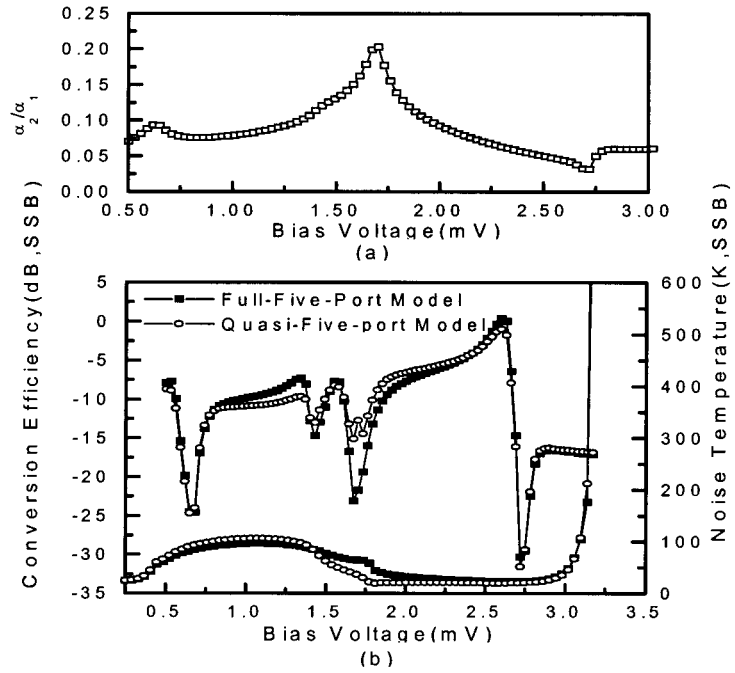


**Fig. 3** Comparison between the results from the full five-port Model and that of the quasi five-port Model.(a)  $\alpha_2/\alpha_1$ , the in indicator of harmonic effect, as function of bias voltage, (b)conversion efficiency and noise temperature calculated from the two models.

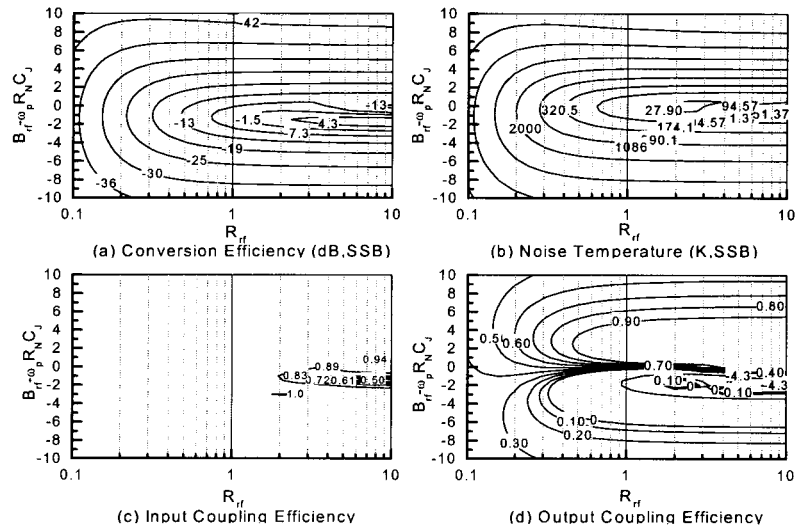


**Fig. 4** Contours of all performances of SIS harmonic mixer as a function of  $\tilde{Y}'_{emb}(\omega_p)$ . The parameters involved are:  $V_{bias} = 2.2mV$ ,  $\gamma = 1.2$ ,  $\tilde{Y}'_{emb}(2\omega_p) = 1.0$ ,  $\tilde{Y}(\omega_0) = 1/2.0$ . (a) Conversion efficiency of the upper harmonic sideband, (b) noise temperature of the mixer, (c) input efficiency and (d) output efficiency.

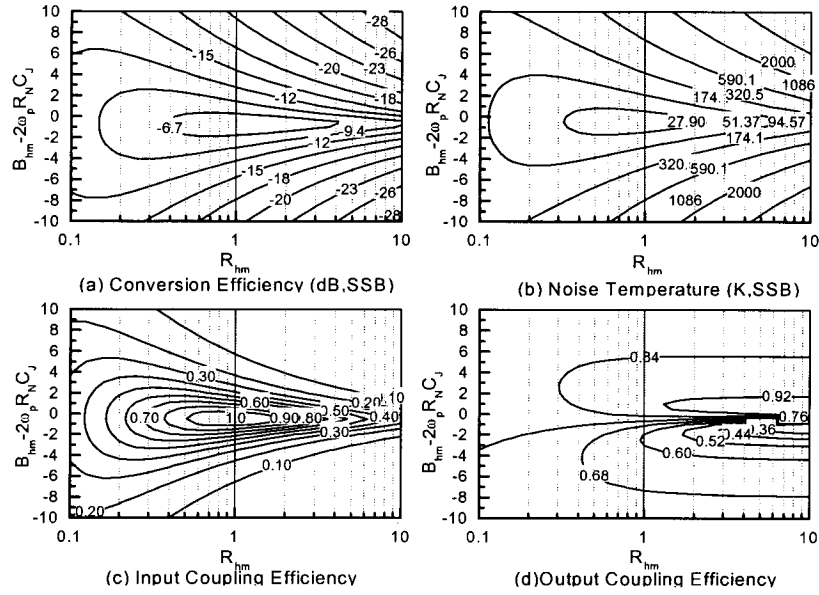


**Fig. 5** Contours of all performances of SIS harmonic mixer as a function of  $\tilde{Y}'_{emb}(2\omega_p)$ . The parameters involved are:  $V_{bias}=2.2mV$ ,  $\gamma=1.2$ ,  $\tilde{Y}'_{emb}(\omega_p)=1/2.3+j0.2$ ,  $\tilde{Y}_{emb}(\omega_0)=1/2.0$ . (a) Conversion efficiency, (b) noise temperature of the mixer, (c) input efficiency and (d) output efficiency.

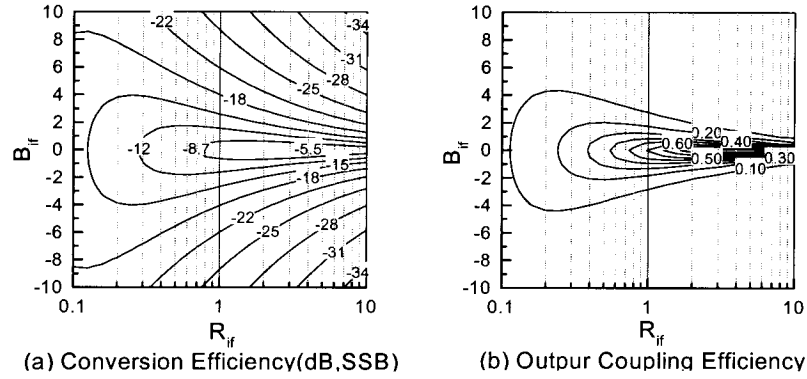


**Fig. 6** Contours of (a) conversion efficiency and (b) output efficiency plotted as a function of the  $\tilde{Y}_{emb}(\omega_0)$ . The parameters involved are:  $V_{bias}=2.2mV$ ,  $\gamma=1.2$ ,  $\tilde{Y}'_{emb}(\omega_p)=1/2.3+j0.2$ ,  $\tilde{Y}_{emb}(\omega_0)=0.5$ ,  $\tilde{Y}'_{emb}(2\omega_p)=1.0$ .

# MICROMACHINED WAVEGUIDE COMPONENTS FOR SUBMILLIMETER-WAVE APPLICATIONS

**K. Hui, W.L. Bishop, J.L. Hesler, D.S. Kurtz and T.W. Crowe**

Department of Electrical Engineering  
University of Virginia  
351 McCormick Road  
PO Box 400743  
Charlottesville, VA 22904-4743

*Abstract* - The high cost of fabricating waveguide components is one of the primary factors limiting the development of terahertz technology. This paper reviews the development of an inexpensive micromachining technology that is suitable for the frequency range from 500 GHz through 5 THz. Our first effort was a 585 GHz direct detector that allowed us to measure the beam patterns of our new micromachined horn antenna. The results were quite good and matched both theoretical predictions and the patterns of a low frequency scaled model of the horn. More recently, a high quality 585 GHz mixer was assembled and tested. The performance was equivalent to that obtained from a traditionally machined block,  $T_{\text{mix,dsb}} = 1,200\text{K}$ . We are now extending this technology to 1.6 THz. A sideband generator and a mixer circuit are being fabricated and the first circuits demonstrate excellent control of the critical features. This paper overviews the new micromachined block fabrication process, summarizes our measurements at 585 GHz and shows the first fabrication results at 1.6 THz.

## I. THE FABRICATION PROCESS

The block fabrication process presented here is a modified version of the process reported in several previous conference publications [1,2,3]. As in the previous work, our new process begins with the formation of a modified diagonal horn by selective crystal etching of a silicon wafer through a silicon dioxide masking layer. This etch creates a very suitable horn structure with easily controlled flare angle and aperture and very good (>90%) Gaussian coupling efficiency [4]. Next, a thin layer of photoresist is spun onto the wafer and exposed to mark the precise position of the waveguide. An automatic dicing saw is then used to slit-cut the waveguide for each half of the block. The photoresist and oxide layers are then removed.

The next step is to form the microstrip circuit channel that runs perpendicular to the waveguide. This is achieved with an ultra thick photoresist known as SU-8 [5]. This resist can be exposed by standard UV lithography to depths of up to 1 mm. The SU-8 layer is intentionally made thicker than our desired channel depth. This resist is then exposed through a mask that protects the horn, waveguide and channel areas. The wafer is then developed to clear the unexposed resist and the wafer is hard-baked. This cures the SU-8 into a plastic layer that remains as a permanent part of our mixer. This plastic is then lapped to the desired thickness on a commercial wafer lapping system. Lapping allows control of the depth of the channel to within a few microns and eliminates any problem with the planarity of the original SU-8 surface.

Alignment grooves are then diced into the wafer, the sample is coated with metal by a combination of sputtering and electroplating and the individual components are diced. Both the

dicing and alignment grooves are patterned in the SU-8 layer to facilitate proper alignment on the wafer. A three-inch process wafer yielded twelve complete waveguide pairs. The result is shown in Fig 1. Note that the features are much sharper than is possible with traditional machining and the fixed backshort is defined with lithographic precision.

## II. MIXER ASSEMBLY AND TESTING

To assemble the mixer, a quartz microstrip circuit with an IF filter, a waveguide probe and an integrated GaAs diode is placed in the microstrip channel [6]. Bond wires attached to the circuit are then attached to the block for the IF return and to the center pin of the coaxial IF connection. Metal shims are placed in the alignment grooves and these shims guide the two halves precisely into place. This yields excellent alignment and the flat SU-8 surface formed by lapping yields no visible gap between the halves.

A molecular gas laser provides an LO source at 585 GHz and a hot/cold load source is used as a calibrated signal. The LO and signal are spatially combined in a diplexer and coupled to the horn through an off-axis parabolic mirror. The lowest system noise temperature measured was 1,700K and a graph of the system noise temperature versus the input noise temperature of the IF amplifier indicated a mixer noise temperature of 1,200K and conversion loss of 8dB (all DSB). The system noise temperature is plotted versus LO power in Fig. 2. The mixer requires about 1 mW of power for optimum performance and the performance is still quite good down to 0.2 mW. These are essentially the same values obtained when a similar integrated mixer circuit was tested in a traditionally machined metal block [6]. The antenna pattern of the micromachined horn is shown in Fig. 3. There is a slight asymmetry in the beam but this can be corrected by adjusting the depth of the horn etch.

## III. FIRST TRIALS AT 1.6 THZ

The success achieved at 585 GHz has encouraged us to use this fabrication process at higher frequencies. Both a 1.6 THz mixer with an integrated GaAs-on-quartz diode circuit and a whisker-contacted sideband generator are planned. The sideband generator uses a novel varactor diode architecture that has been shown to generate unprecedented power and efficiency at this frequency,  $> 50$  W and  $-14$  dB respectively [7]. The result of the first fabrication trial is shown in Fig. 4. The features are again very crisp and the control of all critical dimensions is better than we have obtained from the best commercial suppliers of traditional metal blocks. Our next goal is to test the performance of these circuits.

## IV. DISCUSSION

We have fabricated split block mixer housings for 585 GHz and 1.6 THz with standard semiconductor processing techniques including crystallographic silicon etching, ultra-thick photoresist, automatic dicing and wafer lapping. The results indicate better dimensional control and sharper features than have been demonstrated with traditional machining. The 585 GHz mixers have been RF tested and yield essentially the same performance as the traditional blocks with a diagonal horn antenna. The 1.6 THz designs have not yet been tested, but the dimensional quality is exceptional. This process is readily scaled to even higher frequencies and these blocks have survived rapid immersion in liquid nitrogen with no degradation. Thus, we believe this technology can potentially be used for SIS, HEB and Schottky, mixers

throughout the terahertz band. Thus, micromachining has been demonstrated as a viable solution to greatly reduce the costs of submillimeter-wave receiver components.

#### ACKNOWLEDGEMENTS

This work has been supported by the U.S. Army National Ground Intelligence Center (DAHC90-96-C-0010), The Army Research Laboratory (ARL/UMD-Z847301) and The National Science Foundation (ECS-9623893). Patents are pending on the micromachined fabrication process.

#### REFERENCES

- 
- [1] C.M. Mann, D.N. Matheson, M.L. Oldfield, P.J. Koh, T.W. Crowe, W.L. Bishop, R.M. Weikle, J.L. Hesler, A Simple Micromachining Technique for Millimeter, Submillimeter and Terahertz Waveguide Cavities, Proc. 2nd ESA Workshop on Millimeter Wave Technology and Applications, Helsinki, Finland, pp. 144-149, May 1998.
  - [2] C.M. Mann, J.L. Hesler, P.J. Koh, T.W. Crowe, W.L. Bishop, R.M. Weikle, D.N. Matheson, A Versatile Micromachined Horn Antenna, 20th ESTEC Antenna Workshop on Millimetre Wave Antenna Techn. And Antenna Measurements, Noordwijk, NL, June 1997.
  - [3] T.W. Crowe, P.J. Koh, W.L. Bishop, C.M. Mann, J.L. Hesler, R.M. Weikle, P.A.D. Wood, D. Matheson, Inexpensive Receiver Components for Millimeter and Submillimeter Wavelengths, Proc. Eighth Int. Symp. on Space THz Tech., Cambridge, MA, March 25-27, 1997.
  - [4] J.L. Hesler, K. Hui, R.K. Dahlstrom, R.M. Weikle, T.W. Crowe, C.M. Mann, H.B. Wallace, Analysis of an Octagonal Micromachined Horn Antenna for Submillimeter-Wave Applications, submitted to IEEE Trans. Antennas and Propagation, Jan. 2000.
  - [5] K.Y. Lee, N. LaBianca, S.A. Rishton, S. Zolgharnain, J.D. Gelorme, J. Shaw, T.H.-P. Chang, "Micromachining Applications of a High Resolution Ultrathick Photoresist," J. Vac. Sci. Technol. B 13(6), pp. 3012-3016, Nov/Dec 1995.
  - [6] S.M. Marazita, W.L. Bishop, J.L. Hesler, K. Hui T.W. Crowe, Integrated GaAs Schottky Mixers by Spin-On-Dielectric Wafer Bonding, to appear, IEEE Trans. Electron Devices, June 2000.
  - [7] D.S. Kurtz, Sideband Generation for Submillimeter-Wave Applications, Ph.D. Dissertation, Dept. of Electrical Engineering, University of Virginia, Charlottesville, VA, May 2000.

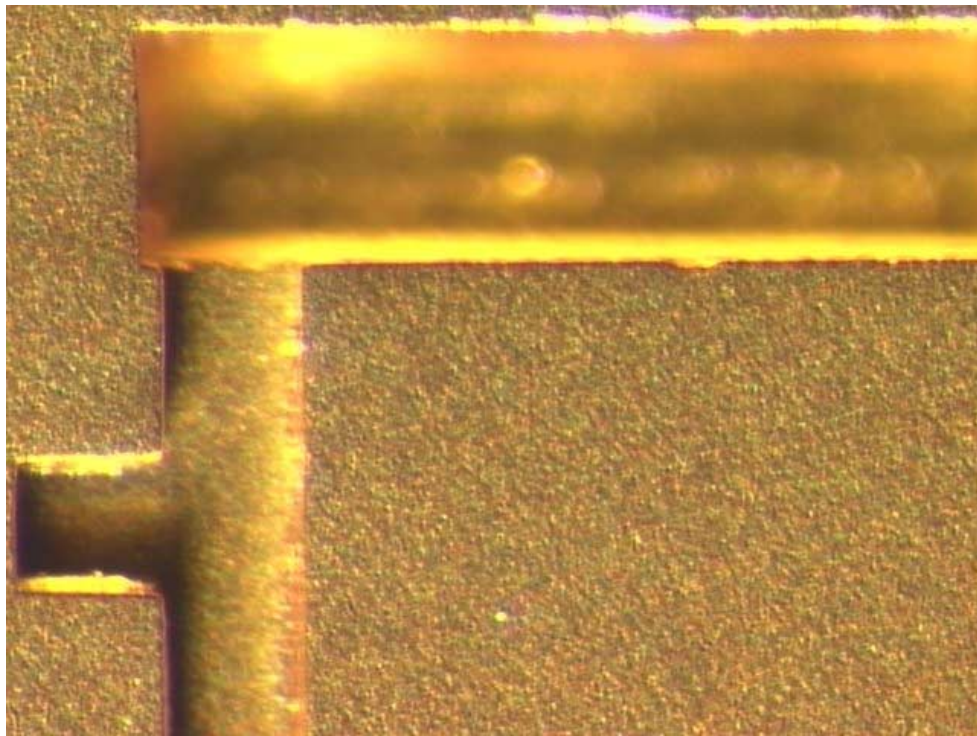
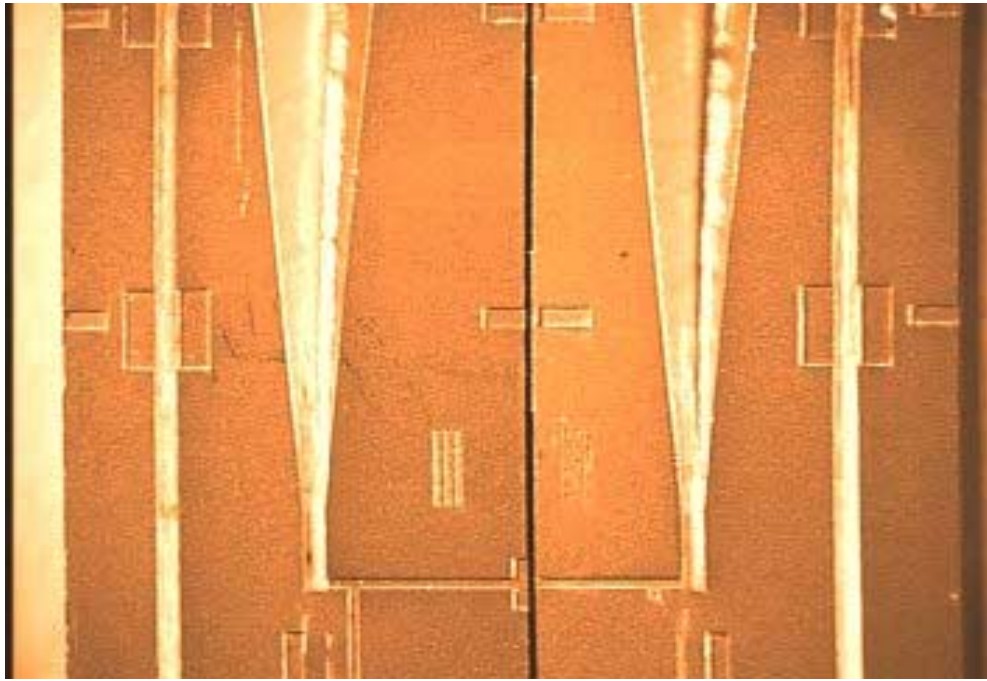


*Fig. 1: Two views of the 585 GHz split-block mixer, top: the flared horn, waveguide and microstrip channel, and bottom: a view of the waveguide, backshort and part of the channel. Note the extremely sharp features. Also, the bottom of the channel is the metallized silicon surface. The microstrip channel width is 120  $\mu\text{m}$ .*

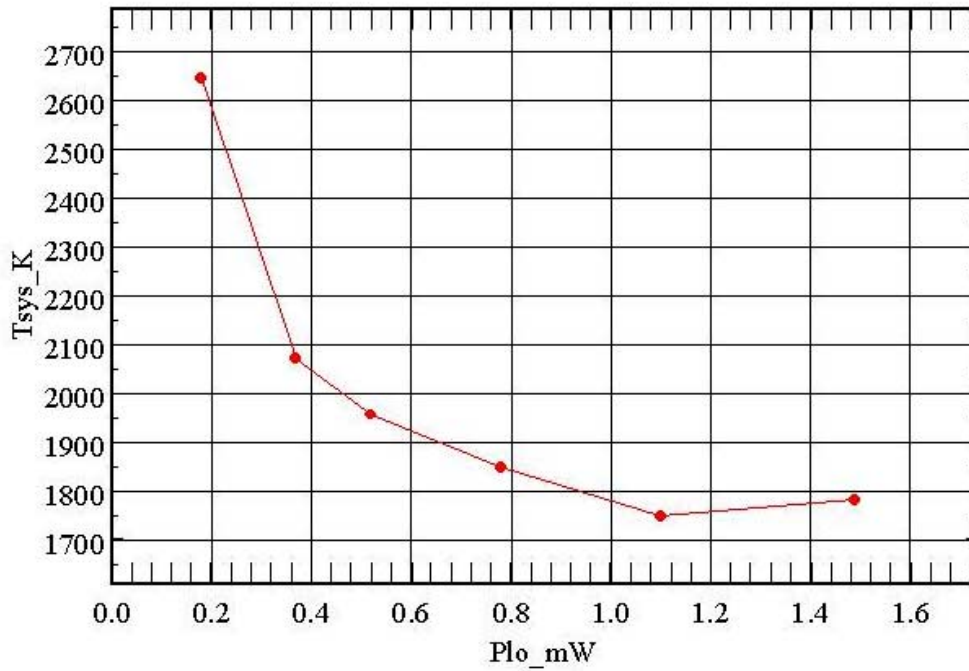


Fig. 2: A graph of system noise temperature versus LO power. The best measured result was 1,700K (DSB).

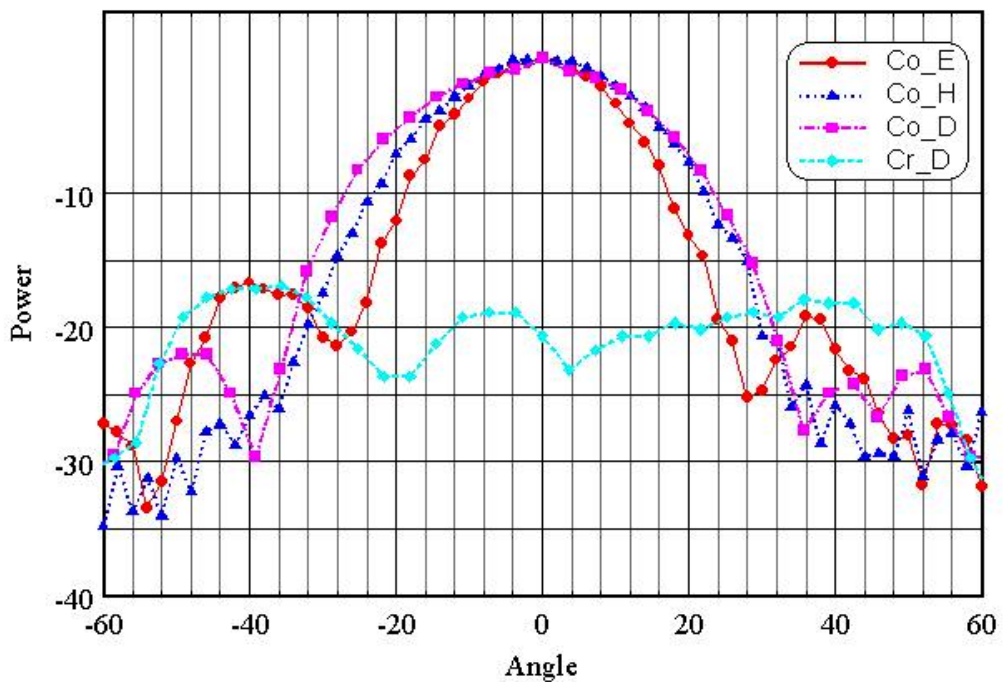
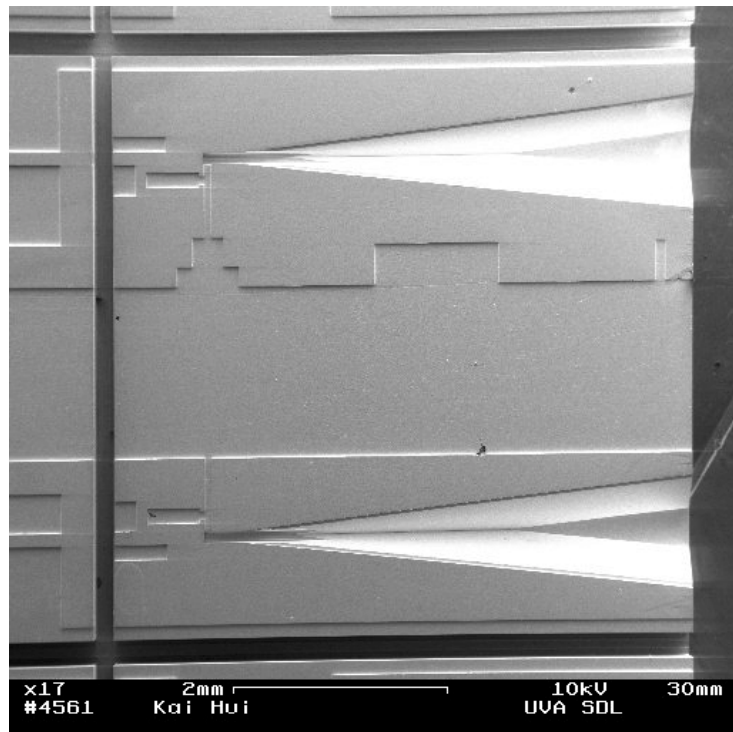
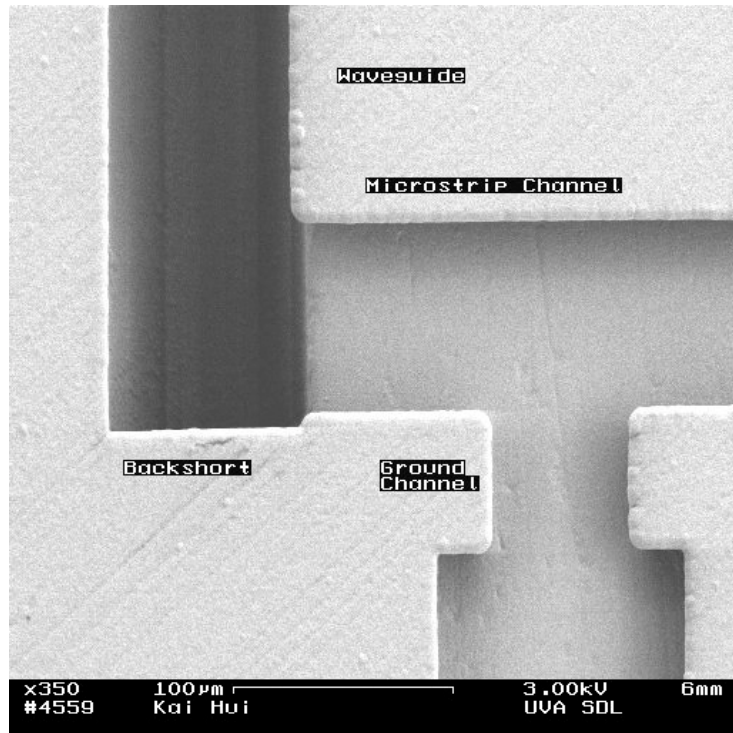


Fig. 3: The measured antenna pattern of the 585 GHz mixer. The slight asymmetry can be removed with a better selection of the silicon etch depth.



*Fig. 4: The first 1.6 THz micromachined waveguide components. The microstrip channel is 60  $\mu$ m wide and 25 micron deep.*

# **A New Laser Micromachining System for the Fabrication of THz Waveguide and Quasi-Optical Components**

**C. Walker, C. Drouet D'Aubigny and C. Groppi**  
Steward Observatory, The University of Arizona

**J. Papapolymerou**  
Dept. of Electrical and Computer Engineering, The University of Arizona

**G. Chin**  
NASA Goddard Space Flight Center

**A. Lichtenberger**  
Dept. of Electrical and Computer Engineering, The University of Virginia

## **Abstract**

Laser micromachining techniques can be used to fabricate high-quality waveguide and quasi-optical components to micrometer accuracies. Successful waveguide designs can be directly scaled to THz frequencies. This technology holds much promise and may permit the construction of the first fully-integrated THz heterodyne imaging arrays. At the University of Arizona, we will soon complete the construction of a laser micromachining system specifically designed for fabricating THz waveguide and quasi-optical structures. Once operational, we plan to use the system to construct prototype THz 1x4 focal plane mixer arrays, AR coated silicon lenses, THz LO sources, and phase gratings. The system can be used to micromachine structures up to 6 inches across. In the paper we will discuss the design and performance of the laser micromachining system, how it compares to other micromachining technologies, and illustrate the type and range of components this exciting new technology will make accessible to the THz community.

# Development of W-Band Low-Loss MEMS Switches

Jad Rizk, Jeremy Muldavin, Guang-Leng Tan and Gabriel M. Rebeiz

The University of Michigan

EECS Department

Ann Arbor, MI 48109-2122

## Abstract

We have developed low-loss MEMS switches for 70-120 GHz applications. The MEMS switches are integrated on a high-resistivity silicon substrate, and are built in a coplanar-waveguide configuration. The MEMS switches are fabricated using a thin gold bridge, suspended 1.5-2.5  $\mu\text{m}$  above the center conductor of the cpw line. The MEMS bridge is 250  $\mu\text{m}$  long with a width of 25-40  $\mu\text{m}$ , depending in the height of the bridge. The inductance of the bridge is around 10 pH, and the MEMS switch is designed to resonate in the down-state position at 70-80 GHz by choosing the down-state capacitance to be only 500 fF. This results in a high isolation at W-band frequencies since, at resonance, the isolation is given by the series resistance of the switch and not by the down-state capacitance. Typical performance, to be shown at the conference, is an isolation better than 20 dB with an insertion loss of less than 0.1 dB at 80-100 GHz.

We have also developed two MEMS switches configured in a Pi-match circuit. In this case, the up-state reflection coefficient is less than  $-20$  dB over the entire W-band frequency range, and the down-state isolation is better than  $-30$  dB over 80-100 GHz. The Pi-match circuit is quite small (less than 100  $\mu\text{m}$ ) and therefore, the insertion loss in the up-state position is only 0.2 dB. This represents state-of-the-art performance at W-band frequencies for MEMS switches, and is much better than PIN diode or FET switches.

The application areas of MEMS switches is in low-loss phase shifters, low-loss tunable matching networks at the input and output of multipliers, and low loss tunable filters for receiver applications.

# **THE FRAMELESS MEMBRANE: A NOVEL TECHNOLOGY FOR THz CIRCUITS**

**Jean Bruston, Suzanne Martin, Alain Maestrini, Erich Schlecht, Peter Smith and Imran Mehdi**

California Institute of Technology, Jet Propulsion Laboratory, Pasadena, CA  
Now at Cree Inc., Durham, NC

## **ABSTRACT**

A novel GaAs based Schottky diode fabrication process has been developed that enables increased design flexibility and robust implementation of monolithic circuits well into the THz frequency range. The fabrication technique builds on the already demonstrated membrane technology for 2.5 THz mixers [1, 2]. Realizing that the small size of the active devices at these frequencies might not require extensive mechanical support, the thick GaAs frame around the device/circuit has been eliminated. Additionally, increased use of metal beam leads is made to provide not only DC connections, but also RF tuning elements, and handling/support structures. This technology allows designers to rethink their approach to high frequency circuits, by permitting many different types of circuit implementations, which were previously not possible with existing technology. We illustrate the flexibility and potential of this technology by presenting two multiplier circuit designs, a 1.2 THz tripler and a 2.4 THz doubler. Both circuits are based on balanced configuration and utilize split waveguide blocks. These circuits are currently under fabrication and once done will be used for the High Frequency (HIFI) instrument on the Far Infrared and Submillimeter-wave Telescope (FIRST).

## **1 INTRODUCTION**

Millimeter and submillimeter heterodyne observations will improve our understanding of physical phenomena present in the universe, the solar system and Earth's atmosphere. To help these studies, several space missions will soon fly instruments with heterodyne receivers working at frequencies up to 2.7 THz (FIRST, EOS-MLS, ROSETTA). High frequency non-cryogenic mixers and local oscillators (LO) are critical to the successful implementation of these missions. The goal of the technology development presented here is to enable design, fabrication, and robust implementation of solid-state components into the THz range.

For years, Schottky mixers developed for the THz range have employed point contact single diodes with corner cube structures. These whisker contacted diodes have worked

well for frequencies even above 2.4 THz [3] but the implementation of this technology, especially for space based missions, suffers from a number of disadvantages as pointed out in [1]. Similarly, current development of high frequency multiplier sources also relies on whisker contacted Schottky diodes. Though these whisker based circuits have worked at frequencies as high as 1395 GHz (about 17  $\mu$ W of power with an input power of 7 mW from a carcinotron source [4]) they tend to suffer similar disadvantages, in that assembly tolerances are extremely tight and can substantially affect RF performance. Moreover, multiple diode configurations are extremely difficult to implement and reliability and bandwidth limitations continue to be a source of concern. To overcome these drawbacks, the monolithic membrane-diode (MOMED) process was developed, integrating Schottky diode mixers with RF filter circuitry on a 3-micron thick GaAs membrane suspended across a frame [1]. Mixer circuits based on this technology have shown excellent performance at terahertz frequencies [2]. The MOMED technology can be utilized for making multiplier circuits into the THz range but it was soon realized that the relatively thick GaAs frame limits the design flexibility especially when it comes to utilizing split-block housings. In order to adequately address this concern and further solidify planar technology for supra THz circuits it was clear that the MOMED technology must be further developed.

## 2 THE FRAMELESS MEMBRANE

In the MOMED approach, a thin (2-3  $\mu$ m) insulating GaAs membrane bridge is left under the diode and RF filter regions, and a thicker support frame falls outside the active area. The membrane bridge can then be coupled to single-mode coaxial and waveguide circuits fabricated by more traditional machining techniques. A picture of a completed MOMED chip is shown in Figure 1. These circuits have proven to be robust and easy to handle with state-of-the-art performance [2]. However, one important draw back found during the design of high frequency multipliers using this architecture, is the necessity of having ports normal to the membrane. In other words, the RF waveguides have to be normal to the membrane, thus reducing the possible implementations. Furthermore, the huge frame (about 1x1mm<sup>2</sup>) takes up a large amount of real estate on the GaAs wafer, thus reducing the number of circuits that can be fabricated at one time.

To adequately address these limitations, the MOMED technology is being extended by:

- *Eliminating the thick GaAs support frame to increase design flexibility.*
- *Developing new beam lead structures to provide RF probes, tuning elements, mechanical support and DC bias contacts.*
- *Implementing multi-diode schemes to expand circuit possibilities.*
- *Shrinking overall circuit dimensions to increase devices per wafer.*
- *Maintaining or developing structures that can assist in circuit handling.*

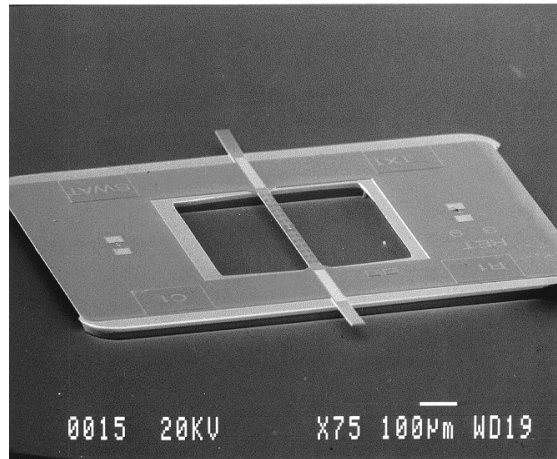


**Figure 1** A 2.5 THz mixer [1,2] on a 3  $\mu\text{m}$  thick GaAs membrane. The central strip is 30  $\mu\text{m}$  wide and is supported by a large 50  $\mu\text{m}$  thick frame, which lies outside the active region. Beam leads extend from the membrane and frame for DC contact and IF removal.

The resulting structures from this technology development will be based on GaAs membranes but will be frameless. This approach results in several significant advantages:

- First, it provides increased design flexibility: The elimination of the frame means that thick GaAs no longer lies in the plane of the membrane. It allows for the waveguides to launch in the same plane as the membrane, as in a split waveguide implementation.
- Second, because the membrane is not supported by a frame, the membrane size and shape can be dictated by the circuit needs rather than constrained by the surrounding frame.
- Third, the drastically reduced total size of the chips (one order of magnitude) means that more designs and variations can be laid out on a given wafer.

One important consideration is the handling, made difficult by the reduced size and the absence of a protective large structure. However, the use of a small sacrificial frame, described below, may eliminate this concern. Moreover, at supra-THz frequencies, the very small dimensions of the chip implies a reasonable thickness to length aspect ratio providing for adequate strength. Preliminary tests of circuits that lack support frames (Figure 2) indicate that the 3 $\mu\text{m}$  thick GaAs membrane is strong enough to support diodes and some circuit elements and does survive mounting into a waveguide block [5].

A further improvement in the implementation scheme for these structures is achieved by the extensive use of beam leads. The advantages are a simplified assembly (no soldering, as chips are dropped in and support beam leads bonded to block), a simplified bias scheme requiring no wire bonds, the possible implementation of low loss, high bandwidth antennas/circuits using air as the dielectric. Again, one possible drawback is handling, as the beam leads may turn out to be rather sensitive to bending.

To protect the beam leads during handling and assembly, we are implementing a metalized membrane frame around the chip, connected by means of small metal tabs (Fig.3). This sacrificial frame provides a handle during positioning of the chip in the waveguide block. Once the support and bias beam leads are tacked to the block, the frame is released by severing the small connecting tabs.

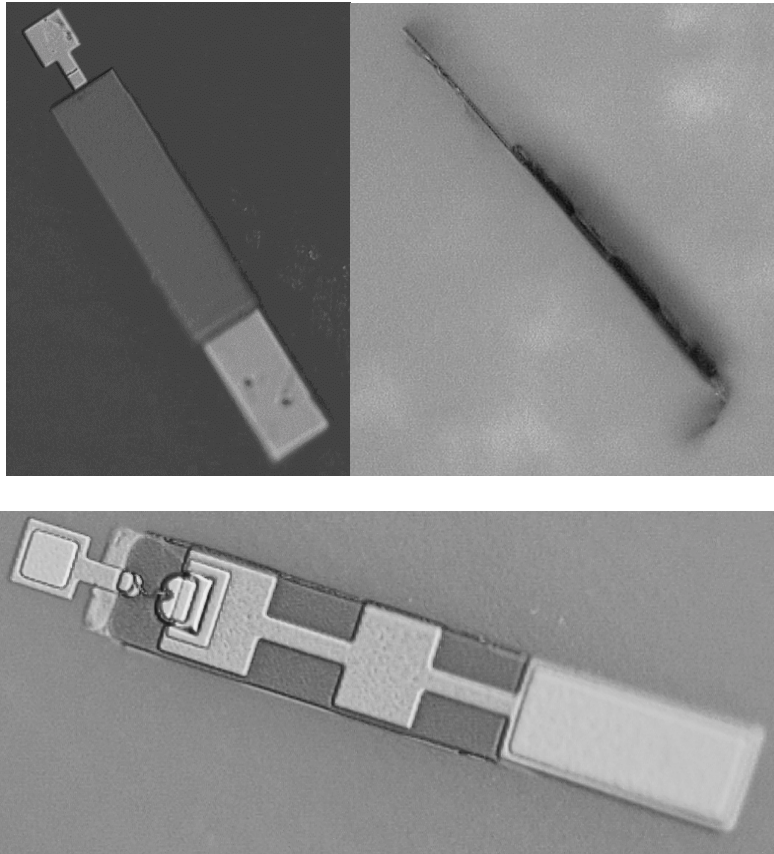


**Figure 2** Three views (bottom, side and top) of a 2.5 THz mixer on a 3  $\mu\text{m}$  thick GaAs frameless membrane (designed by RAL[5]). The membrane is 30  $\mu\text{m}$  wide. Beam leads extend from the membrane for support and assembly, DC contact and IF removal.

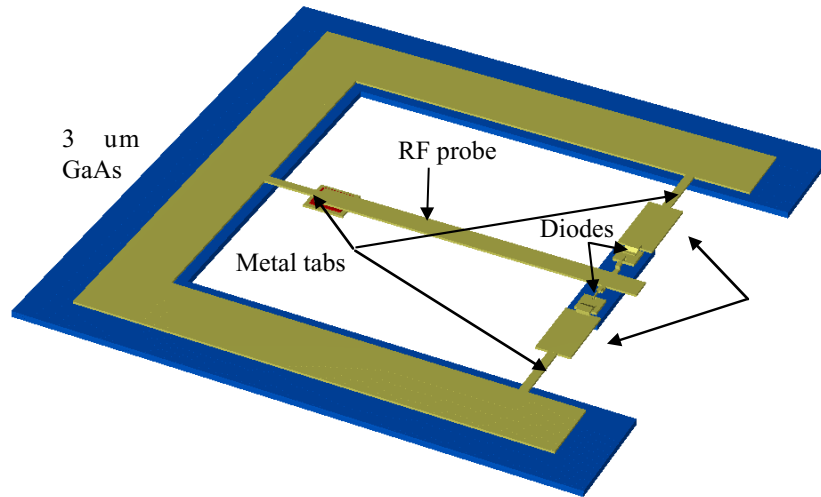


**Figure 3** Example of a sacrificial frame supporting a 2.4 THz doubler chip (details of the design will be presented later). The frame is used for handling, and the metal tabs are cut after bonding of the beam leads to the block.

### 3 FABRICATION TECHNOLOGY

The fabrication of the membrane devices essentially follows the process outlined for the 2.5-THz GaAs monolithic membrane-diode mixers reported earlier [1]. The epitaxial layers are MBE or MOCVD grown on semi-insulating GaAs. The diode structure consists of a 150nm of  $5 \times 10^{17} / \text{cm}^3$  n-type Schottky layer, a heavily doped ( $5 \times 10^{18} / \text{cm}^3$ ), one micron thick n+ layer for low-resistance ohmic contacts on a 50nm  $\text{Al}_{0.5}\text{Ga}_{0.5}\text{As}$  etch-stop layer. Supporting these layers is a  $3\mu\text{m}$  thick undoped GaAs membrane layer and a lower 400nm thick  $\text{AlGaAs}$  etch-stop layer. The ohmic contacts are an alloyed Au/Ge/Ni/Ag/Au metalization, recessed into the n+ GaAs layer. Device mesas are defined using a selective etch containing  $\text{BCl}_3$ ,  $\text{SF}_6$ , and Ar in an electron cyclotron resonance (ECR) reactive ion-etch system (RIE), making use of the upper  $\text{AlGaAs}$  etch stop layer. Interconnect metal is then deposited to the height of the mesas. This is important for the anode definition, where the sample is covered with over  $3\mu\text{m}$  of PMMA, which is subsequently thinned using acetone spray, until the tops of the mesas and interconnect metal are just visible. This lower layer of PMMA forms a support for the PMMA/copolymer/PMMA tri-layer that is used for the electron-beam defined anodes. This resist structure allows the Ti/Pt/Au anode metal to bridge the gap between the interconnect metal and the actual Schottky contact area on the active mesa. Figure (4) shows the anode bridge of a 2.4 THz doubler circuit. At these frequencies Schottky contact dimensions are sub-micron, necessitating the use of e-beam lithography in their definition.

Following anode metalization and lift-off, silicon nitride is deposited using plasma enhanced chemical vapor deposition (PECVD). This acts as the dielectric for any required MIM capacitors in addition to passivating the diodes. A subsequent air-bridged

metal step forms the top contact to the capacitors in addition to providing connections to the on-mesa ohmic metal areas.

The first membrane-related processing step lithographically defines the membrane areas of the circuits from the topside of the wafer. An RIE of  $\text{CF}_4/\text{O}_2$  is used to remove the silicon nitride layer, followed by an ECR RIE of the  $3\mu\text{m}$  GaAs membrane layer, again using  $\text{BCl}_3/\text{SF}_6/\text{Ar}$ , in order to stop on the lower AlGaAs etch stop layer. By defining the membrane during front-side processing of the sample rather than backside lithography, critical spacing between the circuit elements and the membrane edge can be maintained. However, the wafer topography following the membrane etch requires that the final front-side metalization, to define the circuit beam leads, be air-bridged from the top of the vertical-walled membrane layer to the field area,  $3\mu\text{m}$  below. This  $1\text{-}2\mu\text{m}$  thick metal layer will provide bias connections, mechanical support and RF tuning elements for the circuits.

The wafer is next mounted topside-down, using wax, onto a suitable carrier wafer, e.g. silicon, glass or sapphire. The GaAs substrate is thinned then removed by lapping, polishing and, finally, wet etching. A selective wet etch of  $\text{H}_2\text{O}_2$  and  $\text{NH}_4\text{OH}$  is used that will stop on the AlGaAs layer below the membrane. A brief non-selective etch (phosphoric acid/hydrogen peroxide/water) is then used to remove the AlGaAs etch stop. At this point the circuits are separated and can be removed from the carrier wafer by dissolving the mounting wax in an appropriate solvent and collecting the chips on filter paper.

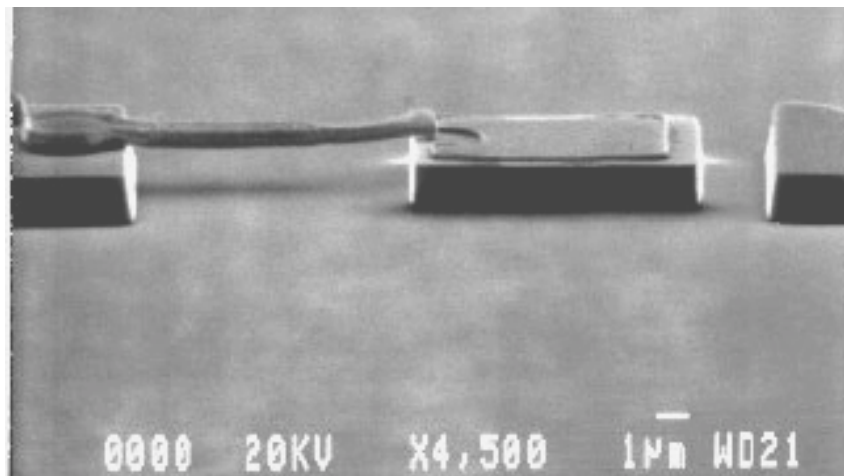


**Figure 4.** SEM image of one diode in the 2.4 THz doubler circuit. At the center is the device mesa mostly covered by the ohmic contact metalization. The anode finger bridges from the interconnect metal, at left, to the  $0.14\mu\text{m}$  by  $0.6\mu\text{m}$  Schottky contact on the GaAs mesa.

## 4 MULTIPLIER DESIGNS AND PERFORMANCE

The multiplier designs currently being developed at JPL are focused towards meeting the LO requirements for the High Frequency (HIFI) instrument on FIRST. Two of the multiplier designs that are made possible due to the development of this technology are discussed in this section.

### 4.1 Tripler to 1.2 THz

The tripler design to 1.2 THz uses a balanced configuration, where two diodes appear as anti-parallel for the odd harmonics (including the fundamental), and parallel for the even harmonics (Fig. 5). This configuration has the advantage of confining the second harmonic idler to the diode loop, reducing the design complexity. The input and output matching circuit need to consider only first and third harmonics, and the required idler tuning can be performed in the diode loop. Such a configuration had been tried previously [6] with limited success. However, the difficult idler tuning optimization is now greatly facilitated by the availability of 3-D electromagnetic simulators.

The circuit is implemented in coplanar waveguide which facilitates the biasing of the diodes, as they appear in series at DC. The idler tuning is accomplished by optimizing the length of the diode air-bridges. This approach has the advantage of making the circuit very simple, but has the drawback of reduced bandwidth. The extra inductance needed for tuning the second harmonic affects the third harmonic match, providing a highly inductive embedding impedance. The resulting matching circuit becomes fairly high Q, hence reducing the realizable bandwidth. However, in this specific case, we were able to compromise the efficiency slightly to achieve the desired bandwidth for FIRST( the predicted 3dB bandwidth is around 15 %). The input and output signals are coupled to the waveguides by means of E-field probes. The diodes are matched to the probes using a very simple high-low impedance matching circuit. On the output side, this is reduced to only one step. This is desirable to reduce loss, and increase the membrane mechanical stability. The membrane is held in the inter-waveguide channel with the help of beam leads, clamped between the two halves of the split waveguide block. The bias is provided via a pad and a line running on one of the beam leads, while the other beam lead is shorted, providing the DC ground.

Using a full simulation of the waveguide and circuit structures together with an harmonic balance simulation of the diodes [7], we find an efficiency better than 1% over the required bandwidth for FIRST, and up to 2% in the lower part of the band. This result is for 10 mW input power, yielding an approximate output power of 100  $\mu$ W over 1104 to 1272 GHz. A very strong roll-off is found at the upper end of the band. It is due to the appearance of higher order evanescent modes in the output waveguide, coming from the interaction with the circuit channel. The next iteration will resolve this problem and a relatively flat response across the design range is expected.

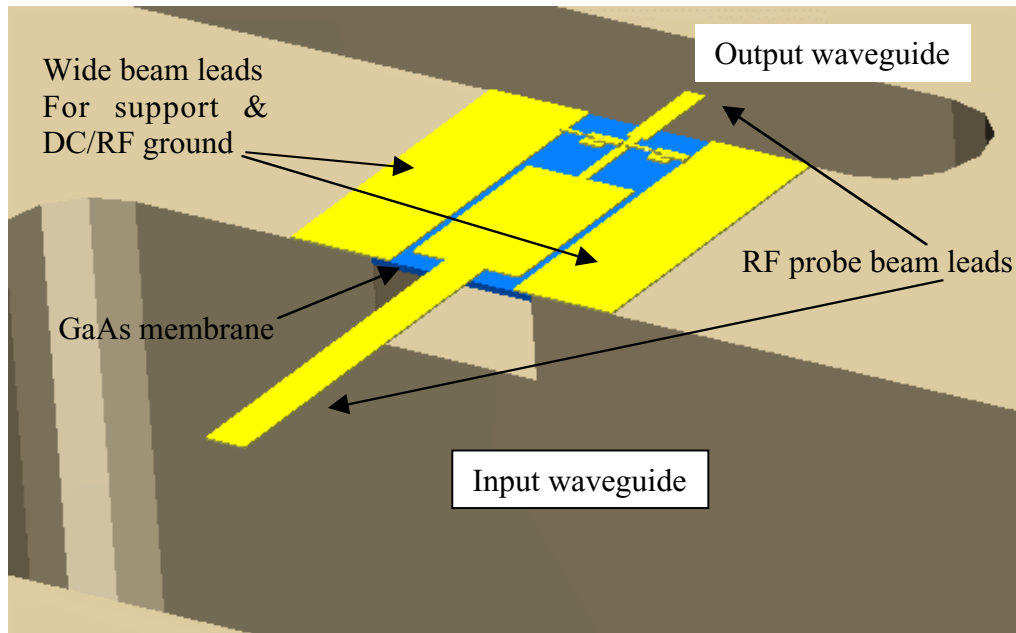


**Figure 5** Sketch of the 1.2 THz tripler layout showing the E-plane probes in the input and output waveguides.

#### 4.2 Doubler to 2.4 THz

The doubler from 1.2 THz to 2.4 THz is designed in a balanced doubler configuration, which provides isolation between the input and the output of the circuit. The general operating principle is the same as for lower frequency doublers, and is described in [8]. In this design, the input signal is coupled directly to the diodes, whereas the output is coupled to the output waveguide by means of an E-field probe. The input matching is done entirely using the waveguide structure. The output matching is realized using different slot dimensions for the inter-waveguide channel, which changes the impedance of the coaxial line. A small open stub is used on the input side of the diodes to tune out some of the varactor capacitance. As with the tripler, the membrane is held in the block by two metal beam leads formed monolithically with the circuit and diodes. Figure 6 shows the final design. Both the 1.2 THz tripler and the 2.4 THz doubler are currently in fabrication.

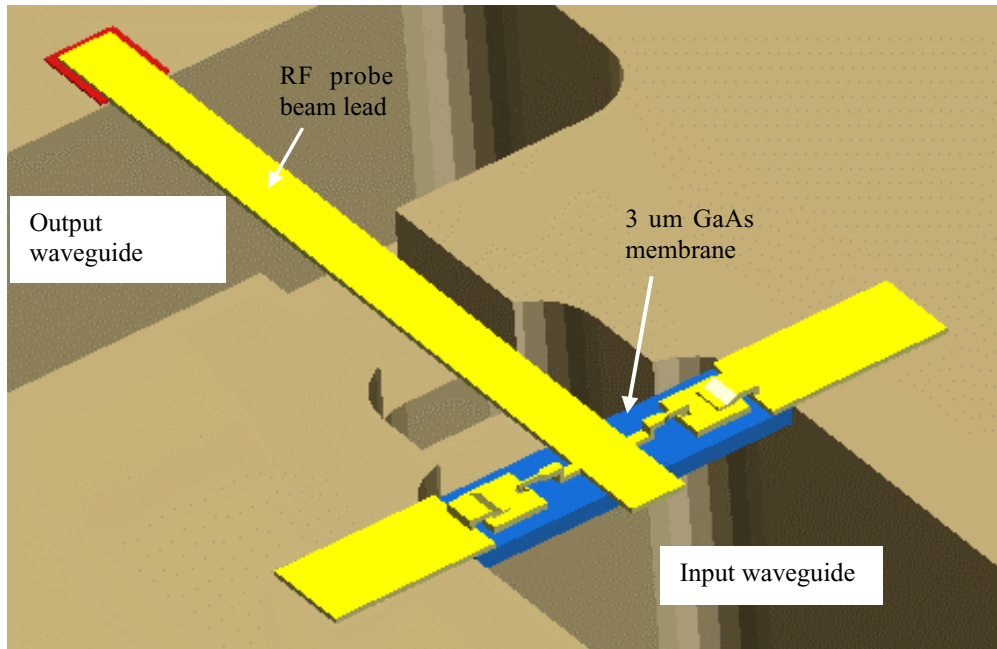


**Figure 6** Sketch of the 2.4 THz doubler. The shorter beamleads provide a ground contact and mechanical support for the chip

## 5 CONCLUSIONS

An innovative and practical scheme of building Schottky diode based circuits for very high frequencies has been proposed which relies on the recent advances made in the fabrication of membrane based structures. The frameless membrane technology allows for the design of monolithic circuits with increased flexibility and lower loss. The enabling power of this technology is demonstrated by the two designs presented that are under fabrication and would be extremely difficult if not impossible to implement with presently available technologies.

## ACKNOWLEDGEMENTS

We are highly appreciative of the numerous technical discussions that we have had with Neal Erickson (UMass), Peter Zimmermann (RPG), Chris Mann (RAL) and Tom Crowe (UVA). We also wish to acknowledge the technical help provided by Barbara Nakamura, Andy Fung, and Ray Tsang (all of JPL) for device fabrication and characterization. The research described in this publication was carried out at the Jet Propulsion Laboratory, California Institute of Technology, under a contract with the National Aeronautics and Space Administration

## REFERENCES

1. P.H. Siegel, R.P. Smith, S. Martin and M. Gaidis, 2.5 THz GaAs Monolithic Membrane-Diode Mixer , *IEEE Trans. Microwave Theory and Tech.*, v. 47, no. 5, May 1999, pp. 596-604.
2. Michael C. Gaidis, Herbert M. Pickett, C. D. Smith, Suzanne C. Martin, R. Peter Smith, and Peter H. Siegel, A 2.5 THz Receiver Front End for Spaceborne Applications, *IEEE Trans. Microwave Theory and Tech.*, v. 48, no. 4, April 2000, pp. 733-739.
3. H. W. Hubers, T. W. Crowe, G. Lundershausen, W. C. B. Peatman and H. P. Roser, Noise temperature and conversion losses of submicron GaAs Schottky-barrier diodes, *Fourth International Conference on Space THz Technology, March 30-April 1, 1993*, pp. 522-527.
4. P. Zimmermann, *private communication*.
5. Chris Mann, *private communication*.
6. R. Bradley, The Application of Planar Monolithic Technology to Schottky Varactor Millimeter-wave Frequency Multipliers, *Ph-D thesis*, Department of Electrical Engineering, University of Virginia, 1992.
7. J. Bruston, R.P. Smith, S.C. Martin, A. Pease and P.H. Siegel, Progress Toward the Realization of MMIC Technology at Submillimeter Wavelengths: A Frequency Multiplier to 320 GHz, *Proc. IEEE Intl. Microwave Symp. Dig.*, Baltimore, MD, June 1998, pp. 399-402.
8. N. Erickson, High Efficiency Submillimeter Frequency Multipliers, *Proc. IEEE Intl. Microwave Symp. Dig.*, Dallas, TX, June 1990, pp.1301-1304.

# 200 AND 400 GHZ SCHOTTKY DIODE MULTIPLIERS FABRICATED WITH INTEGRATED AIR-DIELECTRIC "SUBSTRATELESS" CIRCUITRY

E. Schlecht, J. Bruston, A. Maestrini, S. Martin, D. Pukala, R. Tsang, A. Fung, R. P. Smith, I. Mehdi  
California Institute of Technology Jet Propulsion Laboratory, Pasadena, CA  
Cree, Inc., Durham, NC  
MS 168-314  
4800 Oak Grove dr.  
Pasadena, CA 91109  
310-354-4887 - [erichs@merlin.jpl.nasa.gov](mailto:erichs@merlin.jpl.nasa.gov)

## Abstract

A novel semiconductor fabrication process has been developed at the Jet Propulsion Laboratory for millimeter and submillimeter-wave monolithic integrated circuits. The process integrates the active devices, Schottky diodes, with planar metallic transmission lines. To reduce the RF losses in the passive circuitry, the semiconductor substrate under the transmission lines is etched away, leaving the metal suspended in air and held only by its edges on a semiconductor frame. The frame also allows the circuit to be handled and mounted easily, and makes the whole structure more robust. Moreover, this technology allows for the diodes to be positioned precisely with respect to the circuitry and can be scaled for higher frequency applications. Metallic beam-leads are used extensively on the structure to provide mechanical handles as well as current paths for DC grounding and diode biasing. To demonstrate the utility of this technology, broadband balanced planar doublers based on the concepts in [1] have been designed in the 200 and 400 GHz range. Extensive simulations were performed to optimize the diodes and design the circuits around our existing device fabrication process. The 368-424 GHz circuits were measured and achieve 15% peak efficiency at 369 GHz. The 3-dB bandwidth of the fixed-tuned doubler is around 9%. The maximum output power measured is around 6 mW and drops down to 1 mW at 424 GHz. This represents the highest frequency waveguide based planar doubler to date known to the authors.

## 1 Introduction.

High-resolution spectroscopy missions for astrophysical, Earth and planetary observations are increasingly in demand [2]. The objective of the Far-Infrared and Submillimeter Space Telescope (FIRST) mission is to study the formation and evolution of galaxies in the early universe, stellar formation, and the interstellar medium [3,4]. The heterodyne instrument for FIRST (HIFI) is intended for high resolution observations of molecular lines in bands stretching from 500 to 2700 GHz, many of which can only be made from space because of atmospheric absorption. For maximum sensitivity these heterodyne instruments use either superconducting insulating superconducting (SIS) or hot electron bolometer (HEB) mixers.

The mixers require local oscillator (LO) power in the range of tens of microwatts for the SIS mixers and hundreds of nanowatts for the HEBs. The goal of the technology development program at JPL is to enable construction of solid-state LO sources into the THz range which achieve the required output power over bandwidths of ten percent or more. Using current technology this requires a cascade of doublers and triplers. For example, Figure 1 depicts the FIRST band 5 receiver LO system along with the bandwidth and power requirements [5]. Complex missions such as FIRST require up to 100 or more multiplier units. Due to the large number of required multiplier components, a modular design which reduces cost and simplifies assembly is essential. Additionally, the multipliers must be rugged enough to withstand the temperature, shock and vibration extremes associated with space missions, and must go through a rigorous space qualification process to demonstrate compliance with mission demands.

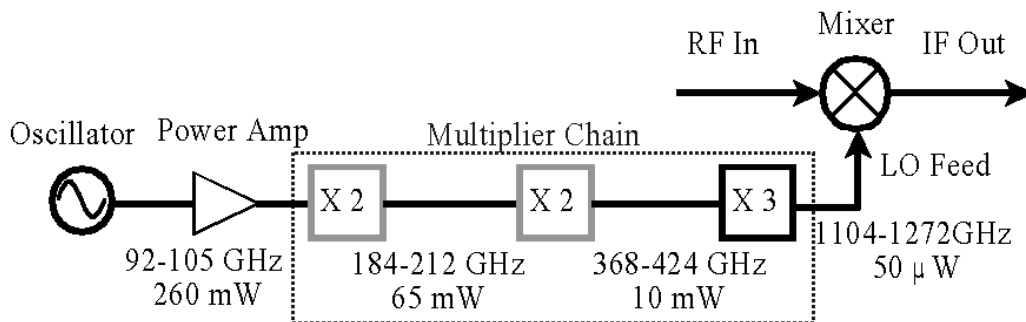


**Figure 1. FIRST LO band 5 receiver. Bandwidth is 14 %.**

There has been considerable development and improvement of planar Schottky diode multipliers in the last few years. However, the required power and bandwidth performance specifications for the FIRST LO sources remain challenging. The highest frequency multiplier circuit reported to date is a tripler to 1395 GHz, which produces about 17 mW of power with a input power of 7 mW from a carcinotron source [6]. The diode used in this multiplier is a whisker contacted Schottky and the circuit is a traditional crossed waveguide block. The highest frequency all solid state multiplier chains reported to date are around 1000 GHz. These used InP Gunn diode oscillators at 111.2 GHz followed by two whisker-contacted triplers in series and obtained output powers of 60-120 μW [7].

At lower frequencies, balanced planar Schottky diode multipliers have been reported in the 350 GHz range with about 5 mW of output power [8]. Balanced doublers incorporate symmetrical pairs of diodes to simplify the circuit design. It is now possible to design and build very high power multipliers in the 150-320 GHz range that can be used to drive follow on stages. A number of variations of the balanced doubler concept [9] have yielded very impressive results [8-11]; 80 mW at 140 GHz, 76 mW at 180 GHz, and 15 mW at 270 GHz have already been demonstrated. In order to implement multiplier chains to 2500 GHz it is essential that the lower frequency stages be capable of handling large input powers around 250 mW.

Referring to Figure 1, the work described in this paper is on the two lower frequency doublers shown in gray. The final tripler is currently being processed using a somewhat different technology, and is described in a companion paper [12].

## **2 Substrateless technology.**

The multipliers each consist of two components — the nonlinear solid state device (the Schottky diode) and the surrounding input, output and impedance matching circuitry. To meet the challenges of space missions successfully it is important to refine and advance both of these critical elements further. As the frequency increases and all relevant dimensions shrink, it becomes difficult to separate the device from the circuit. This makes it important to optimize processing in combination with circuit topology, assembly, and testing procedures.

Submillimeter-wave multiplier technology is undergoing a revolution in implementation and realizable performance, for two main reasons. First, the incorporation of planar GaAs diode MMIC topologies into high frequency circuits has progressed tremendously. This progress stems from improvements in the accuracy and reproducibility of the most dimensionally critical elements due to the use of e-beam lithography and the blending of traditional metal machining with semiconductor micromachining. Second, the availability of high performance CAD tools and models now permits much greater accuracy in the analysis and optimization of circuit performance.

The implementation of GaAs discrete diode chips is limited at very high frequencies for several reasons. In the most successful lower frequency balanced doubler designs [8–11], a small planar diode chip is mounted into a metallic waveguide block by means of solder or silver epoxy. DC bias and RF output coupling is implemented by means of a bond wire, a precision-machined coax structure, or a quartz circuit between the block and the chip [8,9]. A different approach has the diode chip soldered directly to a quartz-based filter which is placed into the waveguide block. Wire bonds are then used to connect the quartz circuit to the block [10,11,13]. In spite of the success of these designs, as the operating frequency increases, these assembly techniques become excessively difficult. For instance, the constraints of reduced waveguide size, increasing substrate loss and higher order mode suppression dictate the use of very thin substrates at these frequencies, and the circuits must be very precisely aligned with the waveguide structure.

In order to circumvent these limitations we have demonstrated a new technology that can work well into the THz range. This technology relies on standard processing techniques such as stepper lithography and reactive ion etching to fabricate the diode structures on the front side of the wafer. After front side processing is completed a backside procedure is used to remove all of the GaAs under the matching circuit. Only a GaAs frame is left where necessary to support the matching structure. The Schottky diodes are formed on

one edge of this frame. The resulting substrateless structure thus has an all metallic matching circuit with no underlying dielectric and the active devices incorporated monolithically. The structure is physically much larger than previous diode chips thus allowing easier handling and mounting. Moreover, beam leads placed on the structure improve heat transfer and simplify the assembly procedure when mounting in the waveguide block.

### **3 Design methodology.**

The multipliers are designed using a three-step process. The first uses a non-linear circuit simulator and a diode model implementation developed at JPL. This model is used with the harmonic balance simulator to optimize the dimensions, doping profile, and number of diodes to be used in the circuit. This process yields the diode junction characteristics and embedding impedances which give the best performance.

Secondly, the multiplier input and output matching circuits are then designed using an electromagnetic (EM) finite-element simulator. The numerical output of the EM simulator comprises scattering parameter matrices referenced to the diode and waveguide ports. The diode ports are attached to probes on each anode so that the individual embedding impedances for each diode can be calculated directly. The parasitics associated with the diode (mesa, air bridges) are thus included as part of the passive circuit. To simplify and speed up the process, the passive circuitry is divided into small elements at electromagnetically appropriate points, giving several S-parameter matrices. These are entered into a linear simulator along with the embedding impedances found using the non-linear simulator. The linear simulator is then used to analyze and optimize the impedance matching input and output circuitry. Finally, the diode non-linear models and the EM simulator S-parameter matrices of the complete passive circuits are combined in the non-linear simulator to determine the total efficiency and power performance of the multiplier.

More details on the simulation methods used for calculating embedding impedances for the diodes and the passive structure were presented in References [9,14,15]. This method has shown to produce good results, and is the basis for much of the recent breakthrough in multiplier performance below 1 THz [8—11]. Very good agreement between the results of this analysis approach and measurements has been found at least up to 350 GHz.

The 200 and 400 GHz doublers are designed to operate with input powers of 200 mW and 40 mW respectively. In order to handle these power levels without compromising efficiency more than one pair of diodes must be utilized. The 200 GHz design uses an array of six diodes and the 400 GHz design uses four.

The designs shown here have been based on the assumption that it is desirable to position the diodes in the input waveguide with most of the output matching circuitry close to the devices; hence, the complicated structure between the waveguide probe and the diodes

shown in Figure 2. The input impedance matching is accomplished in the input waveguide using the full to reduced height waveguide step, the backshort position and the diode geometry. The line extending across the output waveguide is an E-field probe, terminated on the right with a lowpass filter for DC bias. The diodes are grounded to the waveguide block with the two beam leads shown on the left. The beam leads on the right extending from the top and bottom of the GaAs frame are included only to make handling and positioning of the circuit in the waveguide block easier. The filter is a lowpass type which, while large, is effective, straightforward to design and does not require any special processing or additional assembly steps. The beam leads at the right (coming off the bias filter metal) are bonded to a single-layer chip capacitor as a DC standoff. From there a bond ribbon is connected to the input DC bias connector.

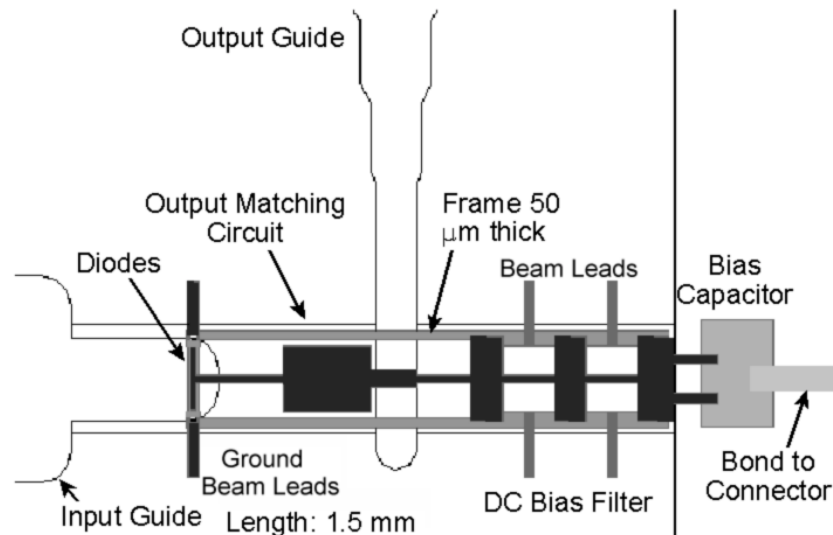


**Figure 2. Schematic of 400 GHz doubler in block. 200 GHz version looks similar.**

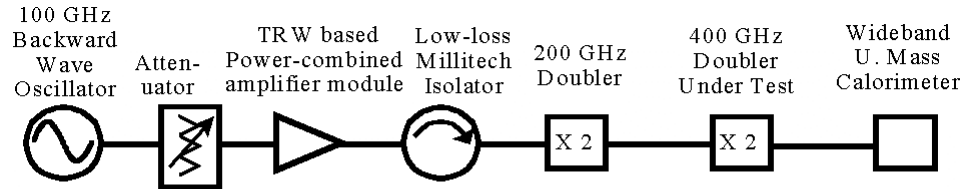
In the future the single layer capacitor used on the DC bias side of the output waveguide will be used without the low-pass filter, reducing the chip size by half. It is also possible to integrate a bypass capacitor directly on the monolithic chip. This makes the assembly alignment less dimensionally critical since a substantial fraction of the DC bypassing is achieved on chip. To further simplify the structure some of the output matching can be performed using stubs near the diode. A single short line will replace the matching structures between the diodes and output guide. The remainder of the output impedance matching is accomplished in the output waveguide.

## 4 Testing and results.

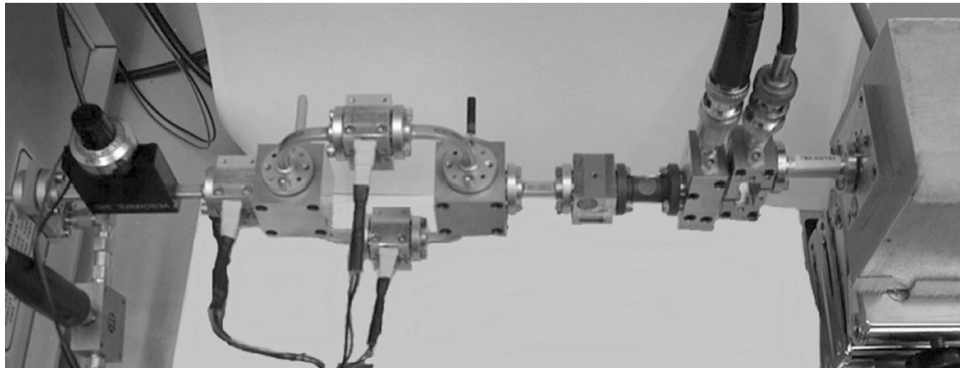
### 4.1 Test Set.

The test set is depicted in Figure 3. It consists of a W-band oscillator followed by a variable attenuator to compensate for oscillator output power variations. In the setup

shown the oscillator is a BWO, although a YIG oscillator followed by a sextupler has also been used. Following the attenuator is a W-band solid-state power amplifier (PA) module. This includes a driver connected to a magic-T splitter feeding two PA modules. Their outputs are combined in another magic-T followed by a low-loss isolator before the 200 GHz doubler.

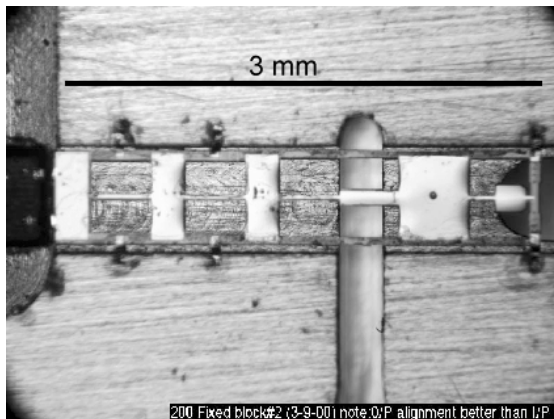


(a)

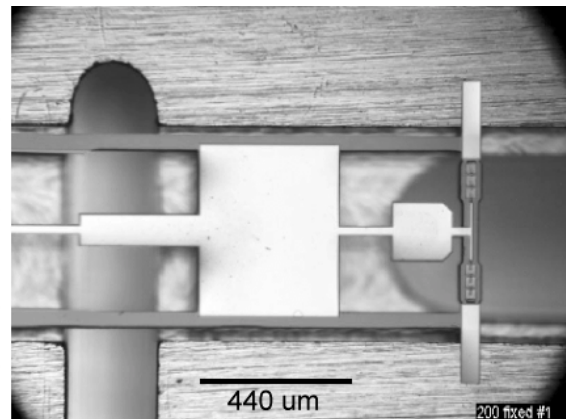


(b)

**Figure 3. 400 GHz test set. (a) Block diagram. (b) Photo.**



(a)



(b)

**Figure 4. 200 GHz doubler in block. (a) Complete chip. (b) Closeup of diode region.**

If this doubler is the device-under-test (DUT), a directional coupler is inserted between the isolator and the DUT with a W-band power meter in the coupled arm for monitoring

input power to the device. For testing the 400 GHz doubler the coupler is not used to maximize input power into the first doubler, which is directly connected to the second doubler as shown in the photo. In this case, a power sweep is made using the University of Massachusetts wideband calorimeter to determine the 200 GHz input power profile. In either case, during the DUT measurement the calorimeter is used to measure the output power. For the 400 GHz measurement a pass-through harmonic multiplier is inserted between the BWO and the attenuator to precisely measure the input frequency.

#### 4.2 Assembly.

After completion of fabrication several 200 and 400 GHz doublers were assembled into waveguide blocks. For assembly the single-layer DC bias chip capacitor is first mounted into the empty block with epoxy. The SMA bias connector is then assembled into the block and a bond ribbon is added to between the connector and the bias capacitor. At this point the devices are simply placed into the channel of the block as shown in Figures 4 and 5. The grounding beam leads are bonded to the block surface with a bonding wedge, and the bias beam leads are similarly bonded to the capacitor top surface. Finally the block halves are assembled together.

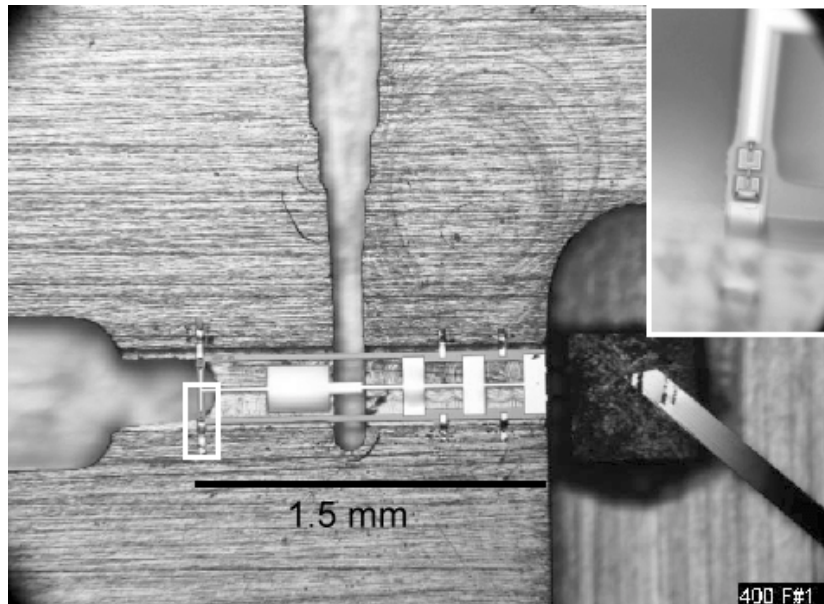


**Figure 5. 400 GHz doubler in block. Inset shows closeup of diodes on frame.**

#### 4.3 Results.

The first doublers to be mounted and measured were the 200 GHz type. They showed an efficiency of 8 % over a narrow bandwidth, much less performance than designed. After further analysis it was found that there were several problems with the design. First, due to a machining error, the blocks that were delivered did not conform to the specified tolerances. Also, a design error made the circuit very susceptible to the positioning of the

circuit in the block, as well as to variations in the machining of the block. These difficulties have been fixed in the next design iteration.

The performance of one of the 400 GHz doubler measured is portrayed in Figure 6. The efficiency varies between 8 and 15 % over the lower half of the band, with output power of 4 to 6 mW. This is the highest power and efficiency we know of reported to date over a comparable bandwidth for a varactor doubler.

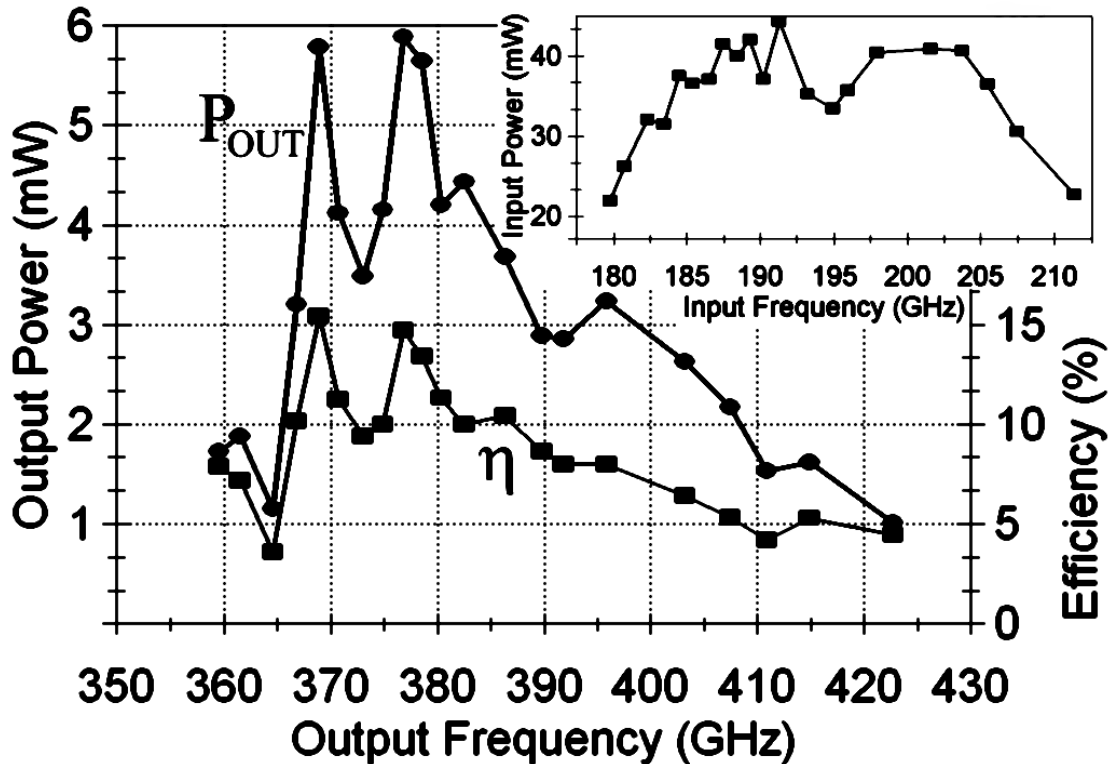


Figure 6. Measured efficiency, output power and input power of 400 GHz doubler.

## 5 Conclusions.

State-of-the-art multiplier performance using a new technology has been demonstrated. This technology is based on suspension of the passive circuitry across an etched semiconductor frame on which the active diodes are fabricated. This substrateless technique represents a new stage enabling the fabrication and performance of planar multipliers in the sub-millimeter and terahertz frequency range. A maximum power of 6 mW with a 3db bandwidth of 34 GHz has been demonstrated at 378 GHz. Work is continuing to improve the performance of the current designs along with an effort towards scaling this technology toward the 700 to 1000 GHz range.

## Acknowledgments.

The authors gratefully acknowledge back-side processing performed by Barbara Nakamura, as well as the technical assistance of Dr. Neal Erickson. Thanks also to Dr. Peter Siegel for supporting the planar diode work at JPL.

The research described in this publication was carried out at the Jet Propulsion Laboratory, California Institute of Technology, under a contract with the National Aeronautics and Space Administration

## REFERENCES

1. Rizzi, B.J., Crowe, T.W., Erickson, N.R., A High-Power Millimeter-Wave Frequency Doubler Using a Planar Diode Array, *IEEE Microwave Guided Wave Lett.*, vol.3, pp. 188-190, June 1993.
2. E. F. van Dishoek and F. P. Helmich, Scientific drivers for future high-resolution far-infrared spectroscopy in space, *Proc. 30th ESLAB Symp., Submillimetre and Far-Infrared Space Instrumentation 1996*, ed. E. J. Rolfe, ESA SP-388, pp. 3-12.
3. G. Pilbratt, The FIRST mission, *Proc. ESA Symp., The Far Infrared and Submillimetre Universe 1997*, ESA SP-401.
4. N. D. Whyborn, The HIFI Heterodyne Instrument for FIRST: Capabilities and Performance, *Proc. ESA Symp, The Far Infrared and Submillimetre Universe 1997*, ESA SP-401.
5. Herman van de Stadt, FIRST Mixer working group, *personal communication*.
6. R. Zimmermann and P. Zimmermann, RPGmbH, *personal communication*.
7. R. Zimmermann, T. Rose, T. Crowe, and T. Grein, An all-solid-state-1-THz-radiometer for space applications, *Proc. Sixth Inter. Symp. on Space Terahertz Technology*, Pasadena, CA, March 1995, pp 13-27.
8. N.R. Erickson, Diode Frequency Multipliers for Terahertz Local Oscillator Applications, *Proc. SPIE*, vol. 3357, pp. 75-84, *Advanced Technology MMW, Radio, and Terahertz Telescopes*, T.G. Phillips, Ed., July 1998.
9. N.R. Erickson, T. W. Crowe, W. L. Bishop, R. P. Smith and S.C. Martin, Progress in planar diode balanced doublers, *Proc. Tenth International Symposium on Space THz Technology*, Charlottesville, VA, March 1999, pp. 472-484.
10. D. Porterfield, T. Crowe, R. Bradley, N. Erickson, An 80/160 GHz Broadband, Fixed-Tuned Balanced Frequency Doubler, *IEEE Intl. Microwave Symp. Dig.*, Baltimore, MD, June 1998, pp. 391-394.
11. D. Porterfield, A 200 GHz Broadband Fixed-Tuned, Planar Doubler, *Proc. Tenth International Symposium on Space THz Technology*, Charlottesville, VA, March 1999, pp. 466-474.
12. S. Martin, J. Bruston, A. Maestrini, E. Schlecht, R.P. Smith, I. Mehdi, The Frame-less Membrane: A Novel Technology for THz Circuits, *Proc. Eleventh International Symposium on Space THz Technology*, Ann Arbor, May 2000, this volume.
13. I. Mehdi, E. Schlecht, A. Arzumanyan, J. Bruston, P. Siegel, R. Peter Smith, J. Pearson, S. Martin and D. Porterfield, Development of millimeter and submillimeter-wave local oscillator circuits for a space telescope, *Proc. SPIE*, vol. 3795, pp. 329-337, *Terahertz and Gigahertz Photonics*, R.J. Hwu, K. Wu, Eds., October 1999.
14. J. Bruston, R.P. Smith, S.C. Martin, A. Pease and P.H. Siegel, Progress Toward the Realization of MMIC Technology at Submillimeter Wavelengths: A Frequency Multiplier to 320 GHz, *Proc. IEEE Intl. Microwave Symp. Dig.*, Baltimore, MD, June 1998, pp. 399-402.
15. N. Erickson, *private communication*.

# Development of Efficient Backward Wave Oscillators for Submillimeter Applications

Jeff Neilson, Lawrence Ives, and Malcom Caplan

Calabazas Creek Research, Inc.  
20937 Comer Drive, Saratoga, CA 95070  
Phone: (408) 741-8680, Fax: (408) 741-8831  
Email: jeff@CalCreek.com

## I. Introduction

Calabazas Creek Research, Inc. is funded by the National Aeronautics and Space Administration to develop efficient, light-weight, backward wave oscillators (BWOs) for applications from 300 GHz to 1 THz. These devices are needed as local oscillator (LO) sources in heterodyne receivers. Very low noise heterodyne receivers are needed at submillimeter wavelengths for low-background radioastronomy observations and remote sensing of comets, Earth and other planetary atmospheres. Above 100 GHz, only BWOs have broad tunability (over 100 GHz) and high output power ( $\sim 1$  mW); however, they are heavy (over 20 kg), consume a lot of power (270 W), required water cooling, and have poor output mode purity. Figure 1 shows a BWO of this design inside its magnet at the Jet Propulsion Laboratory in Pasadena, CA.

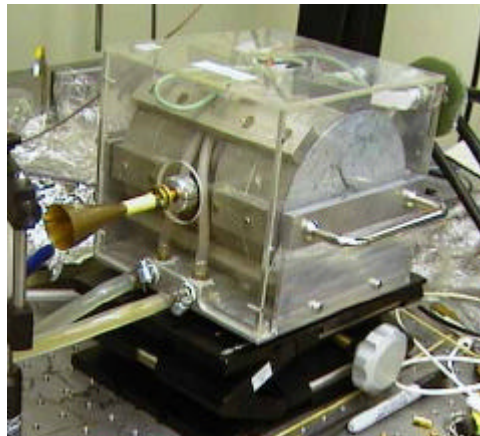


Figure 1. Current state of the art BWO in operation at JPL. The BWO is located inside the cylindrical permanent magnet structure.

Many important molecules play a key role in the energy balance, chemistry, and dynamics of interstellar molecular clouds, planetary atmospheres, and cometary coma. High resolution observations of these species are needed to understand the structure and evolution of the galactic and nearby extragalactic interstellar medium. Heterodyne instruments are required for these observations at ground-based observatories such as the Caltech Submillimeter Observatory, airborne observatories such as the upcoming NASA SOFIA (a 747 aircraft with a 2.5 m telescope), and the ESA Far Infrared and Submillimeter Telescope mission. Currently there are no compact, low-power, broadband LO sources, even above a few hundred GHz. Such a source would enable new science missions and enhance the science return of a given mission as well as expedite the laboratory development of the receiver system.

The technical objectives of the current program are as follows:

- Incorporate a depressed collector to improve the efficiency and eliminate water cooling,
- Improve the electron gun and configuration of the slow wave structure to increase interaction efficiency and reduce body current,
- Improve the output coupling to increase mode purity,
- Reduce the magnet system size and weight,
- incorporate in improved mounting system to facilitate BWO installation and alignment.

In this paper, the various design improvements for the BWO will be covered. Efficiency improvements to the electron gun, slow wave structure and collector will be covered in Section II. In Section III, the design of the output mode coupler will be addressed. Conclusions are given in Section V.

## **II. Efficiency Improvements**

The purpose of the depressed collector is to recover energy from the spent electron beam emerging from the slow wave circuit. Because the electronic efficiency of the BWO is very low, on the order of 1%, a significant amount of the original beam energy is available for recovery. A schematic diagram of the BWO is shown in Figure 1.

A rectangular electron beam is emitted from the cathode in the presence of a high magnetic field. The beam interacting with the slow wave structure is ‘carved out’ by the beam scraper section. This is an innovative approach to beam generation for a series of parallel slow wave structures. The beam scraper is manufactured as part of the slow wave structure which assures precise alignment between the fins of the scraper and the pintles of the slow wave structures. The beam is precisely shaped for optimum interaction and is relatively insensitive to misalignment of the cathode with respect to the circuit. The slow wave structures are currently separated by only 34 microns, yet the positioning of the cathode has only a minor effect on optimum performance.

Unfortunately, it is precisely this characteristic that limits the amount of beam energy that can be recovered by a depressed collector alone. Electron beam energy intercepted by the beam scraper becomes body current and is unavailable for energy recovery. To reduce the amount of energy lost to the body, the circuit can be modified to use four parallel slow wave structures rather than the existing five. In addition, the electron beam can be reduced in size and the separation between slow wave structures increased to 50 microns. To reduce the beam voltage, the periodicity of the slow wave structures can be shortened such that the maximum voltage requirement will be 4000 volts instead of 6000 volts.

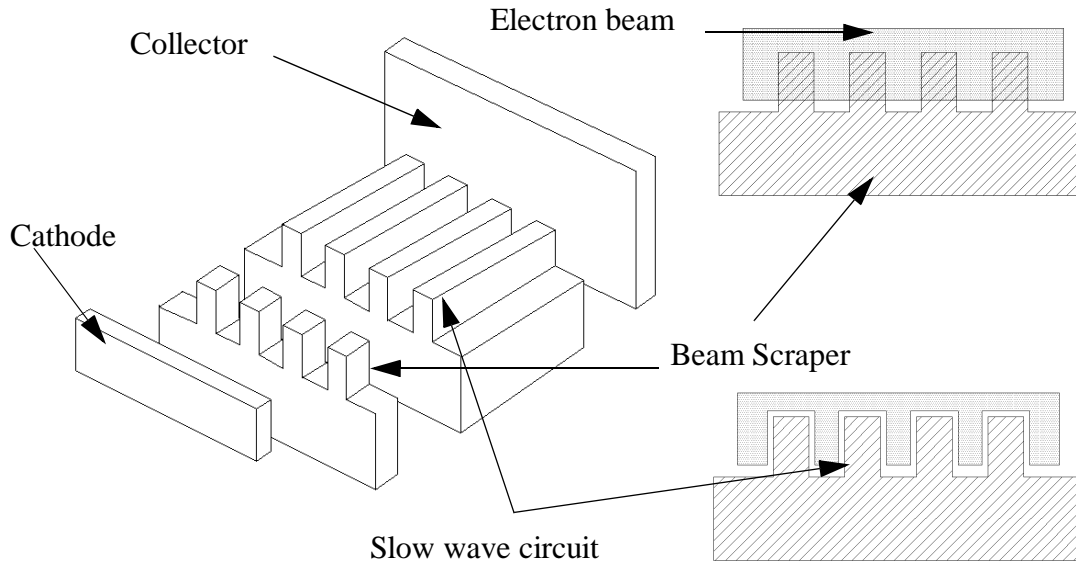


**Figure 1. Basic configuration of the existing BWO design**

Three-dimensional beam simulations were performed to generate a precise energy balance for the existing tube. The final disposition of the original beam power is provided in the following energy balance:

- Beam scraper 17%
- Conversion to RF 1%
- Interception by slow wave structure 5%
- Collector 77%

Simulation results indicate that approximately 3% of the power deposited on the collector cannot be recovered because of velocity spread in the beam.

The next major power loss, however, is the energy intercepted by the beam scraper. Reducing the beam size and modifications to the slow wave structure can reduce the power lost to the beam scraper by approximately 30%. Additional power savings is achieved by the reduction in beam voltage, because the beam current should not change significantly. The estimated input power requirements with a depressed collector for 600

GHz operation would be 15 W and for 700 GHz operation would be 36 W.

Several alternative depressed collector implementations have been explored. The configuration shown in Figure 2 consists of a flat ceramic insulator brazed between two tungsten or molybdenum plates. Issues related to this configuration are the thermal conduction through the ceramic, the possible increase in secondary emission of tungsten or moly over copper, and the stresses generated in the ceramic by steep temperature gradients. The heat is incident on the collector over a very small region (70 x 300 microns).

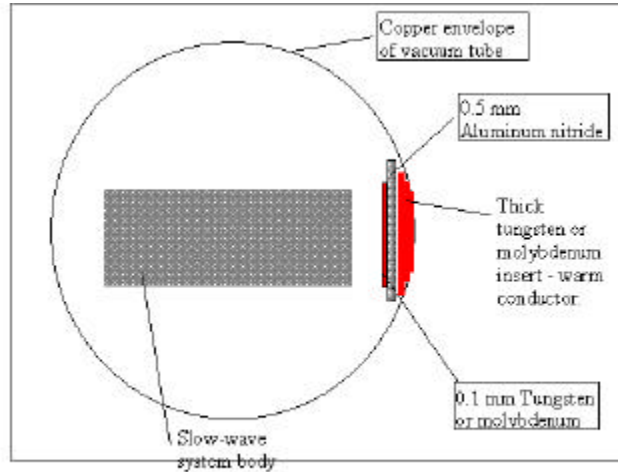


**Figure 2. Alternative implementation of depressed collector**

Combining all the improvements collector and circuit improvements would reduce the input power from the present 270 watts down to approximately 15 watts. The estimated input power versus incremental improvements to the BWO is shown in Table 1. The improvements are listed in order of increasing technical difficulty in implementation.

**Table 1: Estimated Input Power versus Incremental Improvements**

Modification	Input Power (W)
Current Design	270
Depressed Collector	80
Reduced Beam Voltage	50
Circuit Modifications	40
Cathode Grid	15

### III. Output Coupler

Experience at the Jet Propulsion Laboratory indicates that the output mode purity from the current BWO is relatively low. These observations were confirmed by analysis. This means that a significant proportion of the output power is unusable, effectively reducing the output efficiency of the device. The RF power is coupled from the slow wave struc-

tures through a 30 micron gap in the circuit. The rectangular waveguide at the slow wave structure is 30 microns high and 2.4 mm wide in the existing BWOs. The waveguide transitions to a final height of 1.2 mm in a distance of 8 mm. The principle source of the poor mode purity appears to be the coupling from the slow wave circuit to the 30 micron by 2.4 mm waveguide. The waveguide at the slow wave structure is extremely overmoded and excited by an electric field that extends over approximately one eighth of the waveguide width. More than 30 waveguide modes can propagate; however, only 5 or 6 will couple to the excitation field in the slow wave structure. Decomposition of the electric field within the waveguide indicates that only 25% of the power will be coupled into the fundamental waveguide mode.

An obvious way to improve this situation is to reduce the width of the waveguide at the slow wave structure. This will result in power being excited in only the fundamental mode, which will quadruple the usable output power over that of the current design. The new slow wave circuit design has a total width of 230 microns, while the wavelength at 600 GHz is approximately 500 microns. This implies that the waveguide width can be reduced to approximately 260 microns, which will support only the fundamental rectangular waveguide mode at the low frequency end of BWO operation.

It is desirable to have a Gaussian output from the tube due to the low loss and relatively large dimensions of quasi-optical components used to guide and transform the Gaussian beam mode. Several options were considered for generation of the Gaussian mode. Corrugate horns are very efficient generators (98%) of the Gaussian mode but are difficult to manufacture. Rectangular horns are easier to construct but have lower efficiency (84-88%). Potter horns have higher efficiency (96%) but over a narrow bandwidth.

In Potter dual-mode horn designs, the hybrid mode mix ( $TE_{11}/TM_{11}$ ) necessary for efficient coupling to the Gaussian mode is generated by a sudden transition in the circular guide. While this is an effective way to generate the required mode mix it suffers from several deficiencies. First, this transition introduces a mismatch which requires compensation. Second, the transition must occur in a region that is cutoff to all modes higher than the  $TM_{11}$  mode. This means that if a large wavelength aperture is desired, the transition must be followed by a taper which can introduce unwanted mode conversion in addition to adding excess electrical length. The combination of the transition and separate taper result in a design with limited bandwidth.

We have developed a new approach to generate the hybrid mode by use of a computer optimized, non-linear smooth variation in the wall radius (Figure 3). This shape combines the necessary mode conversion as part of the taper to the desired output aperture. Since there is no abrupt transitions in the wall radius, the frequency sensitivity is reduced. A comparison of the efficiency and return loss of this new design (normalized to nominal frequency) was done against designs published by Potter[1] and Pickett[2]. As can be seen in Figure 4, the non-linear design approach has the advantage of higher peak coupling efficiency (>99%), larger bandwidth and improved return loss than the other horn designs while also having a larger aperture area. The polarization coupling factor is also higher than the comparison designs which are shown in Table 2. The waveguide modal amplitudes at the aper-

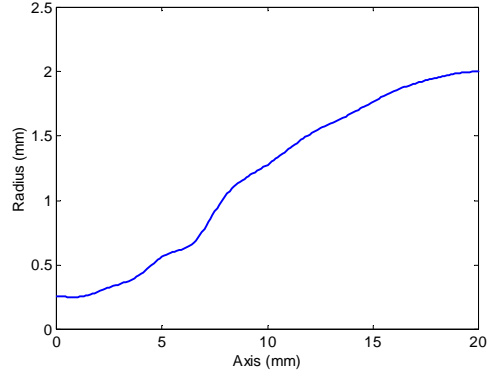


**Figure 3. Non-linear wall variation used to generate hybrid mode.**

**Table 2: Polarization Coupling Factor**

Design Type	$\epsilon_{\text{pol}}$
Non-Linear	0.999
Potter	0.986
Pickett	0.933

ture were calculated by a multi-mode analysis code (*Cascade*[3]) and the coupling of the waveguide modes to the fundamental Gaussian mode by means of the Gauss-Laguerre beam-mode analysis technique[4].

Coupling from the rectangular waveguide circuit output to the circular, Gaussian mode horn is done through a sudden rectangular to circular transition with matching transformer sections. The return loss of this component is greater than -30 dB across the output band.

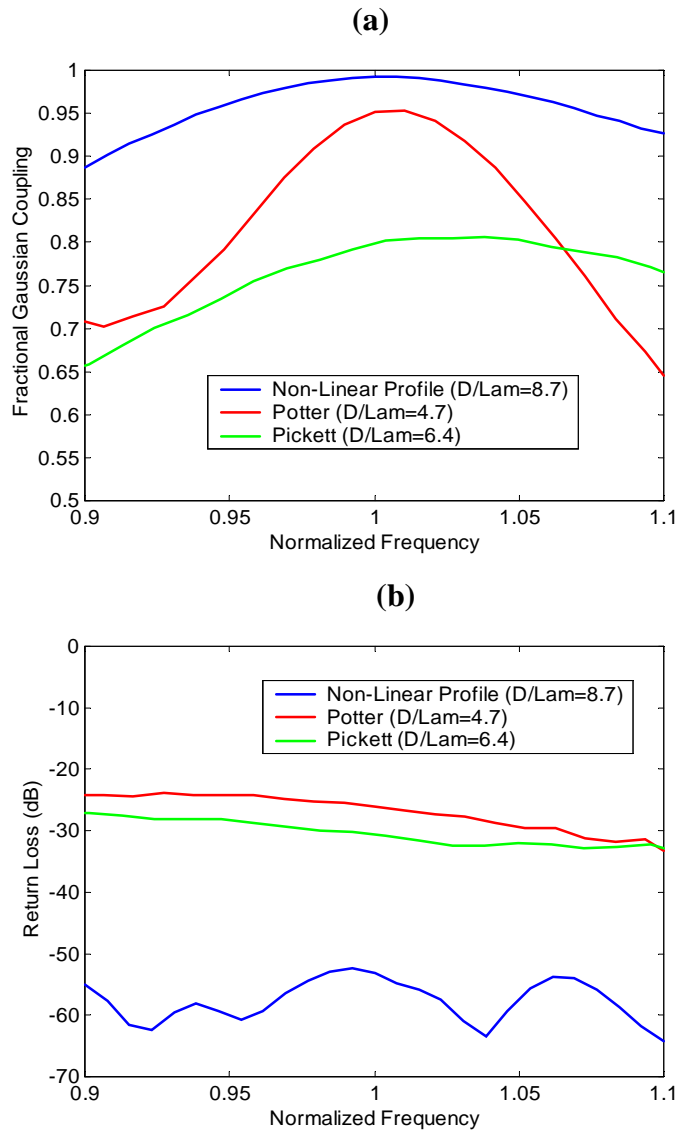


**Figure 4. Comparison of Gaussian coupling and return loss for non-linear taper profile and other published designs. (a) Fractional Gaussian coupling versus normalized frequency. (b) Return loss versus normalized frequency.**

## IV. Conclusions

This proposed effort will address each the drawbacks of existing BWOs using modern innovations in tube and magnet technology which have already been demonstrated. Successful development will result in devices that require significantly less input power (as low as 15W), have reduced weight (8 Kg or less), require much less cooling, and provide significantly improved mode purity. In addition, the power supply for the BWO tube will be smaller and less complicated. Such an LO source would have a significant impact for researchers developing low-noise mixers for heterodyne instruments. It would greatly facilitate the laboratory development of these sensors. This would reduce development costs and time for heterodyne receivers for NASA observational programs. In addition, the potential reduction in required input power to 10 W would allow these sources to be used directly in instruments for aircraft platforms (such as SOFIA), long-duration balloon platforms, and even space missions

1. P.D. Potter, "A New Horn Antenna with Suppressed Sidelobes and Equal Beamwidths," *Microwave J.*, pp 71-78, June 1963.
2. H. Pickett, J. Hardy, and J. Farhoomand, "Characterization of a Dual-Mode Horn for Submillimeter Wavelengths," *IEEE Trans. MTT*, Vol MTT-32, No. 8, pp 936-937, August 1984.
3. W. Vogler, J. Neilson, and L.Ives, "CASCADE - An Advanced Computational Tool for Rapid Waveguide and Circuit Design," 1998 Microwave Vacuum Electron Devices Conference, Monterey, CA May 1998, page 3E.4
4. P. Goldsmith, *Quasioptical Systems*, IEEE press, pp. 158-160.

# Two-stream ballistic instability and terahertz oscillation generation in $n^+nn^+$ - ballistic diodes and field-effect transistors

Z. S. Gribnikov , N. Z. Vagidov, and V. V. Mitin

Department of Electrical and Computer Engineering, Wayne State University,  
Detroit, Michigan 48202, USA

## I. Introduction

Two groups of current carriers naturally coexist in the quasineutral regions (QRs) of the base of ballistic diodes and field-effect transistors (FETs). They are (Fig.1): 1.

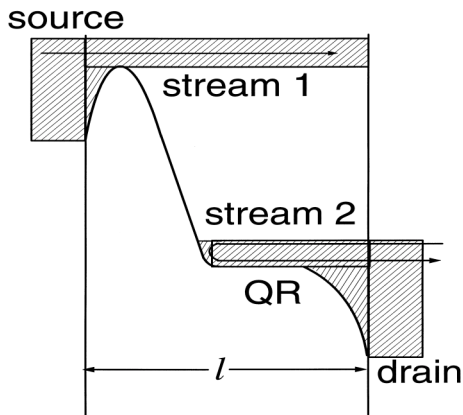


Fig.1. Two streams in a ballistic diode: 1 — traversing ballistic carriers, 2 — nontraversing carriers being in the equilibrium with the drain reservoir.

2. traversing ballistic current carriers emitted by a source and absorbed by a drain, and 2. nontraversing (nonparticipating in a current flow) carriers, which are in the equilibrium with the drain current reservoir. As a result of interactions between these carrier streams a two-stream instability appears and develops in such diodes and FETs if they have appropriate material and geometrical parameters.

The 2-stream instability (2-SI) goes back to the pioneer works of J.R. Pierce [1]. It appears both in gas discharge plasmas and solid state plasmas if these plasmas contain two (or more) mobile components with different directional drift velocities. In the 60-s the 2-SI in electron-hole plasma of bulk InSb was adjusted for description of K-band coherent microwave radiation [2,3]. V.I. Ryzhii and his co-authors [4,5] first paid attention to the 2-SI manifestations in ballistic and quasiballistic electron transport for short-base  $n^+nn^+$ -diodes.

The 2-SI is a result of collective plasma oscillations of both above-mentioned carrier groups. In this work we study analytically dispersion relations for the 2-SI in the QRs of the ballistic diodes and FETs and consider numerically development of this instability in the short-base diodes and FETs.

## II. Two-stream instability

The dispersion equation for plasma oscillations in the QR of the bulk base diode has conventional form for the model cold stream in cold plasma [6]:

$$\frac{\omega_1^2}{(\omega(k) - kv)^2} + \frac{\omega_2^2}{\omega^2(k)} = 1 \quad (1)$$

where  $\omega_{1,2}$  are the plasma frequencies of electrons in the streams 1 and 2 (Fig.1):

$$\omega_{1,2}^2 = e^2 n_{1,2} / \kappa_D m_{1,2}, \quad (2)$$

$v$  is an electron velocity in the stream 1. For the parabolic dispersion relations we have in the QR not only  $m_1 = m_2 = m$ , but also  $n_1 = n_2 = n_0/2$ . Therefore:  $\omega_1^2 = \omega_2^2 = \omega_0^2/2$  and we obtain from Eq. (1):

$$\omega_{(1,2,3,4)}(k) = (1/2) \left\{ kv \pm \left[ k^2 v^2 + 2\omega_0^2 \pm 2(\omega_0^4 + 2k^2 v^2 \omega_0^2)^{1/2} \right] \right\}. \quad (3)$$

The instability occurs if

$$|kv| < 2 \omega_0. \quad (4)$$

In accordance with [6] this instability is always convective. Current oscillations appear as a result of globalization of this instability in the globalization of the finite (short-base!) diodes with shorted (or terminated in a sufficiently small resistance) drain and source.

The condition of Eq. (4) means that the considered instability can occur only for sufficiently low voltages across the diode. Since  $k_{\min} \sim 2\pi/l'$  ( $l'$  is a length of the QR) we can obtain

$$v_{\max} = \sqrt{\frac{2eV_{\max}}{m}} \cong \frac{\omega_0}{\pi} l' \quad (5)$$

and  $V_{\max} \cong en_0 l'^2 / 2\pi^2 \kappa_D$ , where  $n_0$  is a donor concentration. The maximal frequency is of order  $\omega_0$  and does not depend on the length  $l'$ . We are interested in high electron concentrations and in small masses to raise  $\omega_0$ .

For the top- and bottom-gated  $n$ -channel base (Fig.2), that is for the FET (with 2 gates) the dispersion equation, which is analogous to Eq. (1), has a form:

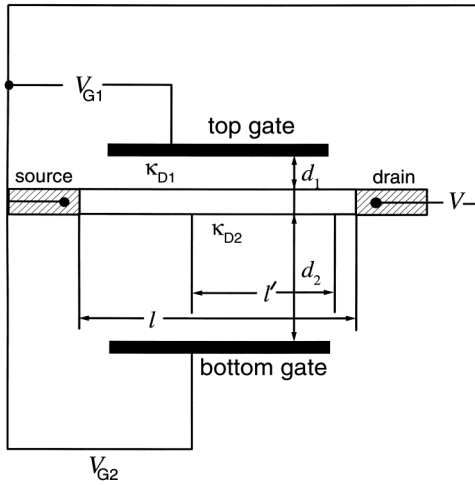


Fig.2. Gated ballistic diode (ballistic FET). Symmetric version:  $d_1 = d_2 = d$ ;  $\kappa_{D1} = \kappa_{D2}$ . Asymmetric version:  $\kappa_{D1} = \kappa_{D2}$ ;  $d_1 = d$ ;  $d_2 -$

$$\frac{g_1 k}{(\omega(k) - kv)^2} + \frac{g_2 k}{\omega^2(k)} = \frac{\kappa_{D1}}{\tanh kd_1} + \frac{\kappa_{D2}}{\tanh kd_2}, \quad (6)$$

where  $g_{1,2} = e^2 N_{1,2} / m_{1,2}$ , and  $N_{1,2}$  are sheet electron concentrations of the 1 and 2 groups (streams) in the channel;  $m_{1,2}$  are their effective masses. For the parabolic electron dispersion,  $m_1 = m_2$ , but now  $N_1 \neq N_2$  (unlike the bulk base case). This is because the gate potentials  $V_{G1,2}$  ( see Fig. 2 ) govern the full channel concentration  $N = N_1 + N_2$  mainly by taking from the concentration  $N_2$  of only immobile electrons. The mobile ( traversing! ) electrons carry the current, and this current determines their concentration  $N_1$ . The concentration  $N_2$  depends on  $V_{G1,2} - V$ , where  $V$  is the potential of the QR and for a certain value of  $V = V_S$  we have  $N_2 = 0$ , and the current saturates. Of course we have no 2-SI in the saturated regime because of absence of the second stream. But for  $V < V_S$  we have both streams with  $N_2 < N_1$ , and the 2-SI is possible. This instability for the ballistic FETs was discovered by Sukhanov with coauthors [7,8].

In a symmetrical case, when  $d_1 = d_2 = d$ ,  $\kappa_{D1} = \kappa_{D2} = \kappa_D$ , Eq. (6) transforms to:

$$\frac{G_1}{(\omega(k) - kv)^2} + \frac{G_2}{\omega^2(k)} = \frac{1}{k \tanh kd}, \quad (7)$$

where  $G_{1,2} = e^2 N_{1,2} / 2 \kappa_D m$ . In an asymmetrical case, when  $d_1 = d$ ,  $\kappa_{D1} = \kappa_{D2} = \kappa_D$ ,  $d_2 \rightarrow \infty$ , and we obtain

$$\frac{G_1}{(\omega(k) - kv)^2} + \frac{G_2}{\omega^2(k)} = \frac{1}{2k \tanh kd} + \frac{1}{2|k|}. \quad (8)$$

In a case of the ungated channel (  $d_1, d_2 \rightarrow \infty$  ) we have the asymptotic formula with  $1/|k|$  on the right-hand side of Eq. (8). Due to existence of  $\tanh kd$  on the right-hand sides of Eqs. (7) and (8) the instability changes its type: it becomes absolute (instead of convective).

The numerical calculations (see below) show that the result of this absolute instability is stratification of the sheet concentration in the conducting channel of the FET. This stratification depends on the concentration ( $N$ ) and the gate-channel distance ( $d$ ). If an amplitude of the stratification and its spatial period are small, this stratification does not impede development of oscillatory regime. It seems that there appears convective instability of the anew formed stratified stationary state. As a result of this secondary convective instability, we obtain the same current oscillations and terahertz radiation. But if the amplitude and spatial period of electron concentration strata are large, the anew formed state is stable and we can not obtain oscillatory regime.

The main problem which must be solved to implement 2-SI terahertz generators is blocking pair electron-electron interactions between electrons from different streams (groups). We have to protect their collective plasma interaction and to avoid their pair (fluctuative) interaction (scattering). This scattering leads to energy and momentum exchange and transforms two streams into a single united stream ( see, for example, [9] ). As a result we lose the 2-SI. To avoid this undesirable fact we suggest to reconstruct a

design of ballistic FET: to replace metallic gates by semiconductor gates with electron concentration which is approximately equal to the concentration  $N_I = N$  of mobile (traversing) carriers in the main channel at saturation regime. This design allows obtaining a certain FET structure with mobile (traversing) electrons only in the main channel ( the 1-st stream ) and with immobile electrons in the additional channel ( that is, in the semiconductor gate ). These nontraversing electrons form the 2-nd stream. Plasma interaction between streams occurs across the barrier layer of width  $d$ , and it is effective for  $kd < 1$ . If  $l' \gg d$  this interaction is sufficiently effective for all actual  $k$ . The range of pair scattering is short and can be suppressed (similarly to the well-known suppression of electron-ion scattering by the modulation doping ). The dependence of the interlayer electron-electron scattering on the distance  $d$  was considered in great detail (see [10] and references therein). The inverse characteristic time  $\tau_D^{-1}$  of this scattering decreases with  $d$  at least as  $d^{-4}$ .

The simplest dispersion equation describing the studied two-stream interaction for the considered two-channel structure ( Fig.3) has the form ( for the saturated regime ):

$$\frac{G_I}{(\omega(k) - kv)^2} + \frac{G_{II}}{\omega^2(k)} = \frac{\tanh kd}{k} \left( 1 + \frac{k^2 G_I G_{II}}{(\omega(k) - kv)^2 \omega^2(k)} \right), \quad (10)$$

where  $G_{I,II} = e^2 N_{I,II} / 2\kappa_D m_{I,II}$ , and indexes I and II relate to the main and the additional channels, respectively. Voltages  $V_D$  and  $V_G$  ( see Fig.3) redistribute concentration  $N_I$  and  $N_{II}$ . Only their sum  $N = N_I + N_{II}$  is constant and is determined by the summary doping. For  $kd \ll 1$  the complex conjugate roots of Eq. (10) have the approximate form:

$$\omega_{(1,2)}(k) \cong k\sqrt{\bar{G}d} \sqrt{1 - \left(\frac{\delta G}{\bar{G}}\right)^2} \left( \sqrt{1 - \left(\frac{\delta G}{\bar{G}}\right)^2} \pm i\sqrt{3/2 + \left(\frac{\delta G}{\bar{G}}\right)^2} \right), \quad (11)$$

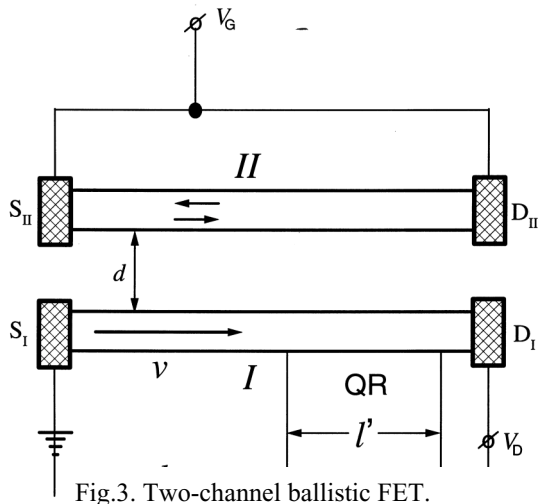


Fig.3. Two-channel ballistic FET.

where  $\bar{G} = \frac{1}{2}(G_I + G_{II})$ ,  $\delta G = \frac{1}{2}(G_I - G_{II})$ , and the instability disappears only if  $G_I = 0$  or  $G_{II} = 0$ . For presaturated regimes in such structures three different streams (groups) of electrons participate in plasma oscillations: mobile electrons in channel I and immobile electrons from both channel II and channel I, and we deal with three-stream oscillations.

### III. Numerical results

IV-characteristics for 5 different samples

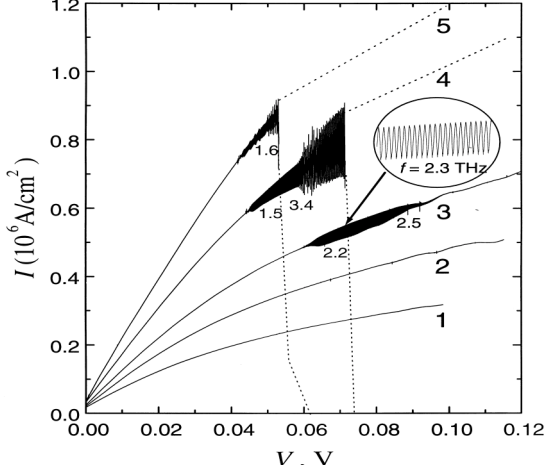


Fig.4. IV-characteristics of  $n^+nn^+$ -ballistic diodes. Parameters:  $T = 30$  K,  $l = 0.15$   $\mu\text{m}$ ,  $m = 0.067m_0$ ,  $\mu_F = 0.025$  eV,  $n_0 = 5 \cdot 10^{16}$   $\text{cm}^{-3}$  (1),  $7.5 \cdot 10^{16}$   $\text{cm}^{-3}$  (2),  $10^{17}$   $\text{cm}^{-3}$  (3),  $1.5 \cdot 10^{17}$   $\text{cm}^{-3}$  (4),  $2 \cdot 10^{17}$   $\text{cm}^{-3}$  (5).

of current oscillation amplitudes. The frequencies of oscillations (in THz) are indicated alongside the characteristics. Distributions of the oscillating electron concentration in the  $n^+nn^+$ -ballistic diode base (with  $n_0 = 10^{17}$   $\text{cm}^{-3}$ ) are shown in Fig. 5. Time interval between each neighboring curves is 0.75 ps. We see a certain travelling wave in the QR and an almost standing oscillation in the depletion layer.

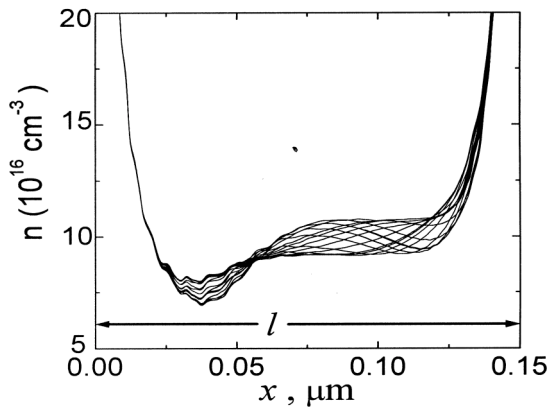


Fig.5. Snapshots of concentration distribution  $n$  in sample 3 from Fig.4. Applied voltage is 0.075 V.

in wide ranges.

of  $n^+nn^+$ -ballistic diodes with quasibulk material bases are shown in Fig.4. The quasibulk material is formed of 2D-electrons (with a parabolic dispersion in plane) tightly stacked to each other without any clearance. Such a material differs from a real 3D-bulk material only in the density of states. All of these bases are of the length  $l = 0.15$   $\mu\text{m}$ , which allows us to consider electron transport for voltages up to 0.12 V as quasiballistic. The samples with  $n_0 < 10^{17}$   $\text{cm}^{-3}$  do not display any current oscillations. The samples with  $n_0 \gtrsim 10^{17}$   $\text{cm}^{-3}$  demonstrate oscillations initiated by the 2-SI. For the samples with  $n_0 \gtrsim 1.5 \cdot 10^{17}$   $\text{cm}^{-3}$  Fermi energy  $\mu_F = 0.025$  eV selected for source and drain contacts is insufficient to keep the effective cathode regime. Therefore N-shaped IV-characteristics appear. It leads to explosion

The same as in Fig. 4 oscillation portraits but for three FETs with a single gate ( $d_2 = \dots$ ) and with quantized electrons in the channels are shown in Fig. 6. The presented samples are of the same parameters (doping, gate potential, Fermi-energies of electrons in the drain and source, etc.) but they differ from each other in the gated base length. We see that oscillations are more intensive in the longer samples but the maximal frequency is in the shortest of them. Dependences of oscillation amplitudes and frequencies on gate potentials  $V_G$  are shown in Figs. 7 and 8. We see both smooth frequency tuning and sharp variations. In both cases gate potential  $V_G$  changes oscillation frequency

Figure 9 demonstrates development of absolute instability in asymmetric gated ballistic FET with extended distance channel-gate ( $d = 0.048 \mu\text{m}$ ). As a result of this extension, the amplitude of concentration stratification is very high and a period of strata is also large. This stratification impedes oscillation regime, but it is not displayed here.

This work is supported by NSF.

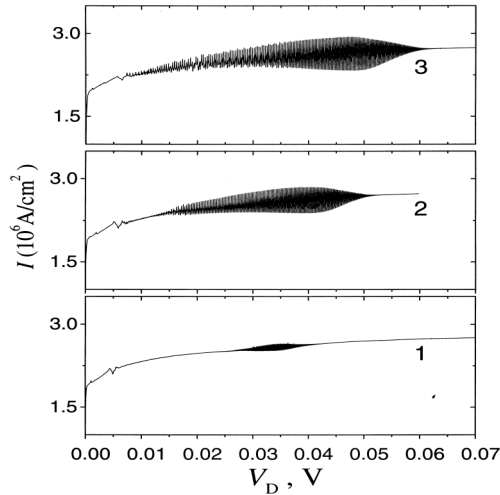


Fig.6. IV-characteristics of asymmetric ballistic FETs of different base lengths  $l$ : 0.125  $\mu\text{m}$  (1), 0.15  $\mu\text{m}$  (2), 0.175  $\mu\text{m}$  (3). Fermi-energies of source-contact  $\epsilon_F^{(S)} = 0.06 \text{ eV}$  and drain-contact  $\epsilon_F^{(D)} = 0.015 \text{ eV}$ ;  $V_G = -0.03 \text{ V}$ ,  $N_0 = 4 \cdot 10^{11} \text{ cm}^{-2}$ ,  $d = 0.016 \mu\text{m}$ . Other parameters are the same as in Fig.4.

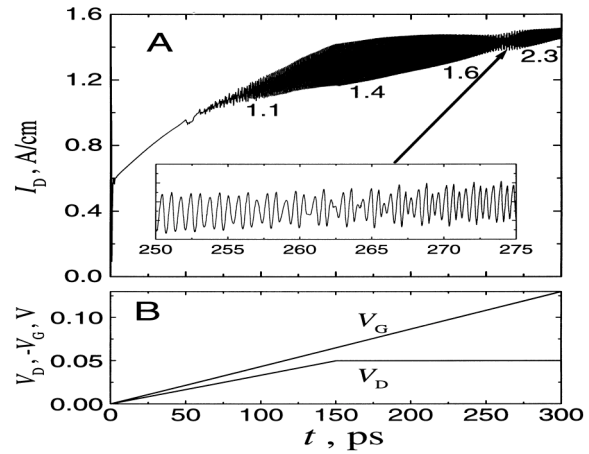


Fig.7. Dependence of FET drain current  $I_D$  on gate potential  $V_G$  (A). Dependences of gate potential  $V_G$  and drain potential  $V_D$  on time  $t$  (B). Parameters:  $l = 0.35 \mu\text{m}$ , length of the gate  $l_G = 0.28 \mu\text{m}$ ,  $N_0 = 2 \cdot 10^{11} \text{ cm}^{-2}$ ,  $\epsilon_F^{(S)} = 0.035 \text{ eV}$ ,  $\epsilon_F^{(D)} = 0.0175 \text{ eV}$ . Other parameters are the same as in Fig.6.

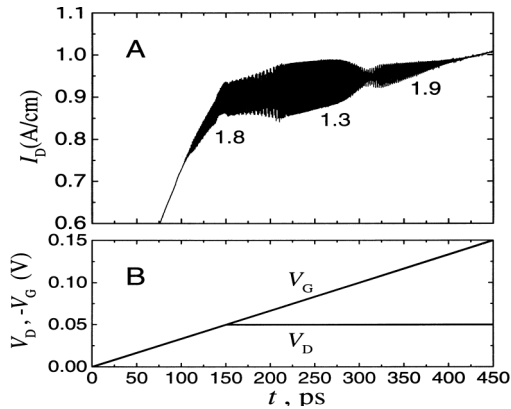


Fig.8. Dependence of FET drain current  $I_D$  on gate potential  $V_G$  (A). Dependences of gate potential  $V_G$  and drain potential  $V_D$  on time  $t$  (B). Up to  $t = 150 \text{ ps}$  both  $V_D$  and  $V_G$  increase simultaneously. After  $t = 150 \text{ ps}$   $V_D$  is constant, and  $V_G$  continues to increase. Parameters:  $l = 0.4 \mu\text{m}$ ,  $l_G = 0.32 \mu\text{m}$ ,  $N_0 = 2 \cdot 10^{11} \text{ cm}^{-2}$ ,  $\epsilon_F^{(S)} = 0.025 \text{ eV}$ ,  $\epsilon_F^{(D)} = 0.025 \text{ eV}$ . Other parameters are the same as in Fig.6.

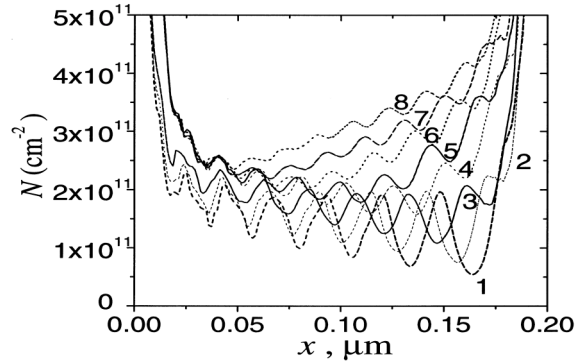


Fig.9. Distribution of electron concentration  $N$  in asymmetric ballistic FET for different applied voltages  $V_D$ : 0.7 V (1), 0.63 V (2), 0.53 V (3), 0.42 V (4), 0.35 V (5), 0.3 V (6), 0.27 V (7), 0.25 V (8). Parameters:  $l = 0.2 \mu\text{m}$ ,  $d = 0.048 \mu\text{m}$ ,  $N_0 = 5 \cdot 10^{11} \text{ cm}^{-2}$ ,  $V_G = -0.03 \text{ V}$ . Other parameters are the same as in Fig.6.

### References:

1. J. R. Pierce, J. Appl. Phys., **19**, 231 (1948).
2. B. B. Robinson and G. A. Swartz, J. Appl. Phys., **38**, 2461 (1967).
3. G. A. Swartz and B. B. Robinson, J. Appl. Phys., **40**, 4598 (1969).
4. N. A. Bannov, V. I. Ryzhii, and V. A. Fedirko, Sov. Phys. Semicond., **17**, 36 (1983).
5. V. I. Ryzhii, N. A. Bannov, and V. A. Fedirko, Sov. Phys. Semicond., **18**, 481 (1984).
6. E. M. Lifshitz and L. P. Pitaevskii, Physical Kinetics, Oxford, New York, Pergamon Press, 1980.
7. A. A. Sukhanov, V. B. Sandomirskii, and Yu. Yu. Tkach, , Sov. Phys. Semicond., **17**, 1378 (1983).
8. V. V. Mantrov and A. A. Sukhanov, Sov. Phys. Semicond., **19**, 882 (1985).
9. V. E. Gantmakher and Y. B. Levinson, Carrier Scattering in Metals and Semiconductors, North Holland, Amsterdam, 1987.
10. J. R. Eisenstein, Superlatt. & Microstruct., **12**, 107 (1992).

# Sb-Heterostructure High Frequency Zero-Bias Direct Detection Diodes

J. N. Schulman, D. H. Chow, C. W. Pobanz, H. L. Dunlap, and C. D. Haeussler  
HRL Laboratories, LLC, Malibu, CA

Contact: J. N. Schulman  
MS RL62  
HRL Laboratories, LLC  
3011 Malibu Canyon Road, Malibu, CA 90265  
Email: schulman@hrl.com  
Phone: 310-317-5085; Fax: 310-317-5840

Backward diodes are a version of Esaki tunnel diodes that are useful for mixing and detection. Ge backward diodes in particular have been used as temperature insensitive, zero bias square law detectors, capable of translating low level RF power into DC voltage or current with extreme linearity and low noise. However, Ge diodes are difficult to reproducibly manufacture, are physically fragile, and are limited to the tens of gigahertz range. Planar doped barrier (PDB) diodes can also operate as zero bias detectors, to over 100 GHz, but are difficult to produce in large numbers due to the challenging doping tolerances required. Here we demonstrate specially designed Sb-heterostructure-based backward diodes grown by molecular beam epitaxy. These diodes have superior figures of merit compared to Ge diodes, especially the current density and junction resistance, and are reliably reproducible and physically rugged. Estimates indicate frequency operation comparable or superior to PDB diodes should be achievable. Millimeter wave detector arrays containing thousands of diodes are now feasible for the first time at 94 GHz and above.

The material system of interest here is the InAs/AlSb/GaAlSb nearly lattice matched combination. For small positive bias the electrons tunnel from the InAs through the AlSb barrier into the p-type GaAlSb. At high enough bias the InAs conduction band edge becomes higher than the GaAlSb valence band maximum at the interface and the current is blocked. Negative bias induces the electrons from the GaAlSb valence band to tunnel into the InAs conduction band in a monotonically increasing manner. This asymmetry in the current flow produces the large nonlinearity near zero bias desired for backward diodes.

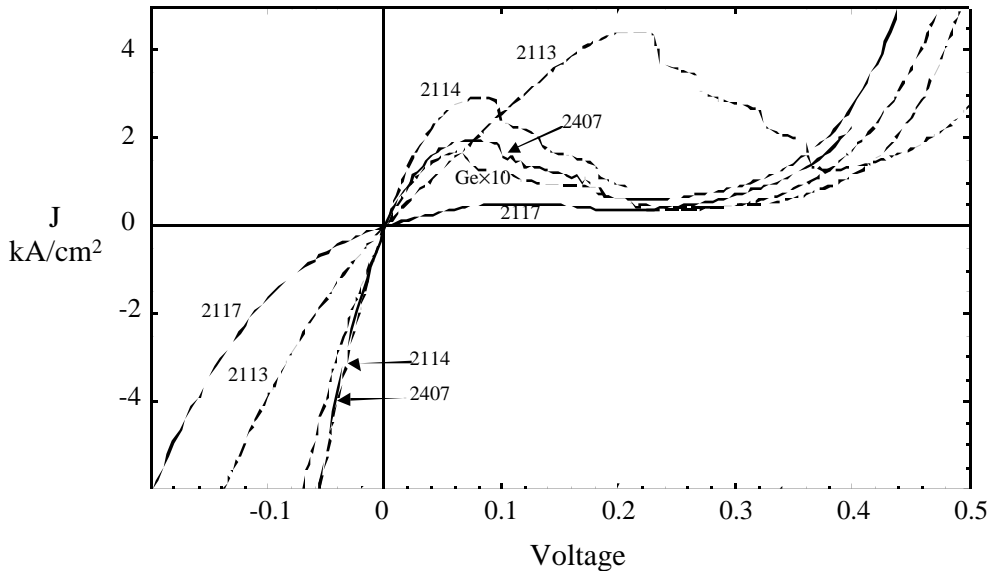
We deposited the InAs/AlSb/GaSb tunnel diode layer structures by molecular beam epitaxy on semi-insulating GaAs substrates. The Table lists the series of samples grown and the Figure shows the I(V)'s of several. Also included for comparison is a similar commercial Ge diode which had been chosen for a square law radiometry application, remote atmospheric temperature measurement.

A large overall current density, consistent with a large backward to forward current ratio, is necessary for maximizing the frequency response of the diode. The substitution of tunneling through the thin AlSb barrier instead of Zener tunneling through the band gap is the critical enabling difference as compared with the conventional Esaki diode. The quantities of most direct relevance in the Table are  $r_j$ , the junction resistance, and  $\gamma$ , the curvature coefficient:  $r_j = dV/dI$  and  $\gamma = d^2I/dV^2 / (dI/dV)$ , at  $V=0$ .  $r_j$  is specified for a 100  $\mu\text{m}^2$  area in the Table, whereas  $\gamma$  is not directly proportional to area.  $R_j \equiv r_j \times (100 \mu\text{m}^2 / \text{Area})$  has several roles in the design of the circuit, and is very important for determining the voltage sensitivity and the frequency response. Its optimum value depends on the particular circuit implementation.  $\gamma$  should be as large as possible. It contributes directly to the small signal rectifying action of the diode, and thus its current and voltage sensitivity .

Samples 2114 and 2407 have values of  $\gamma$  comparable to the Ge diode, but  $r_j$  is an order of magnitude less. Thus for a given desired  $R_j$ , determined by circuit considerations, the area can be decreased by this factor relative to the Ge diode, as can the intrinsic diode capacitance (assuming the capacitance per area is similar). Since the parallel current path created by this capacitance is one of the major limitations on frequency response, this decreased value should allow much higher frequency operation, perhaps several hundred gigahertz.

Sample	$N_D$ (cm <sup>-3</sup> )	x (%Al)	$V_p$ (volt)	$V_v$ (volt)	$J_p$ (A/cm <sup>2</sup> )	$r_j$ ( $\Omega$ )	$\gamma$ (1/volt)
2114	$7 \times 10^{17}$	0	0.085	0.260	2930	13.0	14.4
2112	$2 \times 10^{18}$	0	0.125	0.315	3010	20.3	8.56
2113	$5 \times 10^{18}$	0	0.21	0.380	4460	34.5	4.30
2116	$2 \times 10^{18}$	20	0.125	0.230	308	261	4.11
2117	$2 \times 10^{18}$	20, 0	0.115	0.205	505	113	10.9
2407	$7 \times 10^{17}$	10, 0	0.070	0.230	1980	15.7	19.1
Ge	-	-	0.065	0.245	172	182	15.9

Sample parameters and measurements.  $V_p$  and  $V_v$  are the peak and valley voltages.  $J_p$  is the peak current.  $r_j$  is the junction resistance for a 100  $\mu\text{m}^2$  area.  $\gamma$  is the curvature coefficient.



I(V) characteristics of Sb-based backward diodes and a Ge diode.

# PHASE GRATINGS AS LO-DISTRIBUTORS IN SUBMM HETERODYNE ARRAYS

T.KLEIN, G.A.EDISS, R.GÜSTEN, C.KASEMANN  
*MPIfR-Bonn, Auf dem Hügel 69, 53121 Bonn, Germany*  
*email: tklein@mpifr-bonn.mpg.de*

## ABSTRACT

Phase gratings have found an important application in the submm wavelength range with the development of heterodyne arrays in the past few years. These devices can be used as efficient beam splitters to match the signal beam of a single local oscillator source to an array of detector devices such as SIS-mixers or HEBs. Here we report on a phase grating developed for CHAMP - the Carbon-Heterodyne-Array of MPIfR - which is currently operating at the Caltech Submillimeter Telescope on Mauna Kea [1]. For further applications, such as heterodyne arrays for higher frequencies, we continued our work on designing phase gratings to enhance their efficiencies and to provide solutions for future array projects. Here we report on an algorithm we have developed as a design tool for phase gratings providing solutions for any desired array, nearly independent on the desired beam configuration.

## Introduction

The periodic modulation of the amplitude and (or) the phase of an electromagnetic wave generates a set of waves, called diffraction orders, propagating in discrete directions. Devices stimulating these effects are well known as diffraction gratings for the visible region of the electromagnetic spectrum. A scalar formulation of diffraction at a periodic structure modulating an incident wave can be expressed in Fourier optics [2] by the complex Fourier transform

$$A(x, y) = \int_{-\infty}^{\infty} \int_{-\infty}^{\infty} b(x', y') \cdot t(x', y') \cdot e^{\frac{-2\pi i(x x' + y y')}{\lambda f}} dx' dy' \quad (1)$$

in which the complex field  $b(x', y')$  of the incident wave is modulated by the periodic structure as expressed by the transmission function  $t(x', y')$ . The distribution of the diffracted field  $A(x, y)$  appears in the focal plane of the transforming lens with focal length  $f$ . The wavelength  $\lambda$  and  $f$ , which is the distance between the structure and the lens appear as scaling factors in the equation.  $(x, y)$  and  $(x', y')$  are the coordinates in the object and frequency domain related by the transform.

With this equation the determination of the grating structure is reduced to the calculation of  $t(x', y')$ , which is the result of the inverse Fourier transform. In case

of

$$|t(x', y')|^2 = \frac{|a(x', y')|}{|b(x', y')|} = 1 \quad (2)$$

a phase only modulation is achieved. If the complex field of the incident wave and the desired intensity distribution in the far field is determined by the specific application, the transmission function has to be found which fulfills the condition (2). The result of this consideration is that in case of a phase only modulation there is no direct analytic solution of the problem but an iterative way of calculating equation (1) can be found.

In the following two methods are considered leading to a solution of the problem. Both are based on the equations mentioned above. The method considered first was given by *Dammann and Klotz* [4]. Here the set of possible transmission functions is reduced by a quantisation of the phase levels and a limitation in the number of transition points where the function changes from one phase level to another. An additional reduction can be achieved by taking into account given symmetries of the specific application. How this method can be realised numerically is reported in several publications [4] [5] [6] [7]. Here we focus on a solution of such a grating implemented in the **CHAMP** LO-optics.

A second method is based on a so called *Phase-Retrieval Algorithm*, which uses the known functions in eq.(1),  $\|A(x, y)\|$  and  $b(x', y')$ , as well as an initial estimate for the far field distribution of the phase of  $A(x, y)$ , to calculate the inverse FFT to obtain  $t(x', y')$ , belonging to  $b(x', y')$ . This Fourier pair then leads, after the calculation of the FFT, to a new and better estimate for the far field phase of  $A(x, y)$ , giving the initial function for the next iteration.

The idea of this algorithm was given by *Gerchberg and Saxton* [8] and has been applied in areas where phase information has to be found out of single intensity measurements. The method has been adapted to find the transmission function for a given grating problem.

## THE DAMMANN METHOD

The main simplification in Dammann's method is the separation of the two-dimensional transmission function into a set of two one-dimensional functions. The combination of such one-dimensional solutions can only lead to a regular grid array of  $K \times N$  beams. Table I lists the obtained efficiencies for chosen values  $K$  and  $N$ , which are binary or with 4 allowed phase levels  $\Phi$  between the transition points. With the higher level gratings the efficiency can be increased significantly as shown in the table. Although with the chosen even symmetry for the grating period it is impossible to generate the array configuration of a **CHAMP**-subarray, we used the found solutions for  $K=3$  and  $K=4$  with four phase levels to couple 8 of the 12 generated beams to the subarray. The FFT according to eq. (1) is shown in fig.I for the given problem. The grating structure (blue curve) is illuminated by a gaussian beam (left figure). For simplicity, the grating should be positioned at the waist of the illuminating beam so that the phase of the incident wave can be assumed to be flat. The beamwaist,  $\omega_0$ , should have the same size as the period of the grating as mentioned in [3]. However changing the size of the beamwaist within  $\omega_0 \geq d/2$  does

TABLE I Efficiencies of two-dimensional gratings, binary and four-level type in comparison

	$2 \times 2$	$3 \times 3$	$4 \times 4$	$5 \times 5$	$3 \times 4$	$3 \times 5$	$4 \times 5$
binary	65.8%	44.1%	50.0%	59.4%	46.9%	51.2%	54.5%
4-level		80.3%	68.9%	74.0%	74.4%	77.1%	71.4%

not affect the results significantly because the information remains in the real and imaginary parts (fig.I). If the beamwaist becomes smaller than  $d/2$  more and more information gets lost. In the worst case the complete wave is delayed by the same value which couples the energy only into the zero diffraction order.

The result of the transformation is shown in the real and imaginary part in fig.I, as well as the calculated amplitude and phase of the diffracted field. As the transmission function and the illuminating beam are of even symmetry, amplitude and phase of the image are also even functions. However it is also possible to generate even symmetric images with an odd symmetric transmission function (translation symmetry). In this case the zero diffraction order is rejected because the symmetry implies a transition point at the center of the period [9].

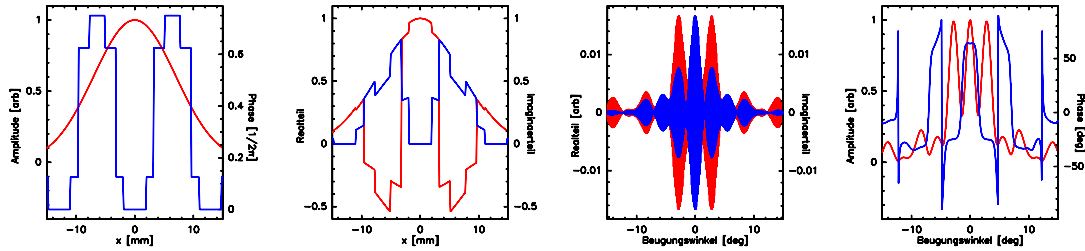


FIGURE I A gaussian beam illuminating a grating surface (4-level type) is shown in the left picture. The next graph shows the modulated amplitude (real and imaginary part) as it is transformed. The resulting real and imaginary part of the diffracted field is shown in the following graph. Finally the intensity and phase of the generated image shows an array of 3 beams.

## Realisation

The fabrication of the surface structure on the material PTFE has been made with a nc-machine in the workshop of our institute. PTFE has been chosen because its refraction index at submm wavelengths minimizes the reflections at the surfaces. The machining of this material however is difficult due of the smoothness of this material. Instead of combining the one-dimensional solutions by adding the phase structures and realizing the complicated structure on the PTFE surface we fabricated a grating layer of each one-dimensional solution and combined the physical

layers to a two-dimensional device. This method has the advantage that only grooves have to be machined on the material. In addition each layer can be characterized in the experiments and can be combined with various other layers.

Fig.II shows photographs of the two types of fabricated layers, each of them as a one-dimensional grating. For an accurate combination of the layers there is a reference edge on each layer to achieve the desired two-dimensional phase delay. Fig.III

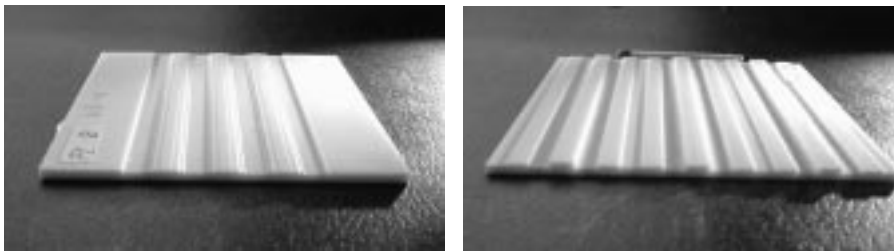


FIGURE II Photographs of both PTFE-layers fabricated on a nc-machine. The left photo shows the grating generating a linear 3-beam array, the photo on the right shows the equivalent grating for a 4-beam array. The square PTFE-plates have a length of 80mm. Each of them carries 3 periods of the specific structure.

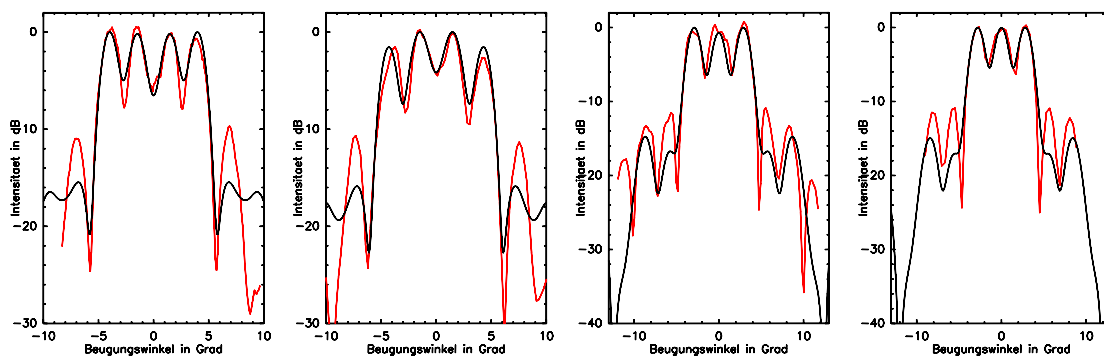


FIGURE III Results of the antenna measurements (red) in comparison with the theoretical expected intensity distributions. (black) at 460.2GHz (left) and 492GHz (right) for each of the grating layers. The results are in good agreement with the theory. Only for the higher orders differences of about 10% occur.

shows the experimental results compared to what is expected from theory. The generated linear arrays with 3 and 4 beams completely agree with the theory in order of the accuracy of measurement. Only differences are that the higher orders are seen at the 10% level. This shows that any effects to the assumption of a real gaussian illumination without any variation in phase of the incident beam are negligible in case of the potter horn antenna used in the experiment.

With measurements at various frequencies, 460.2GHz ( $\Delta\nu_{center} = 15GHz$ ) and

492GHz ( $\Delta\nu_{center} = 17GHz$ ) the frequency dependence of the gratings could be verified. The expected change of the diffraction angles, as well as of the relative intensities are shown by the experiment. Fig.IV shows the intensity measurements for several combinations of the two solutions,  $3 \times 3$ ,  $4 \times 4$  and  $3 \times 4$  arrays. Because the experiments are based on the heterodyne detection of the signals, an accurate experimental value for the achieved efficiency cannot be given here, as the measurement of the detected power with and without the devices is required which implies different beam coupling between the signal source and heterodyne receiver. However the accurate scaling of the parameters for the phase delay is indicated by the rejection of the zero order by more than 20dB in case of the  $4 \times 4$  array. After the

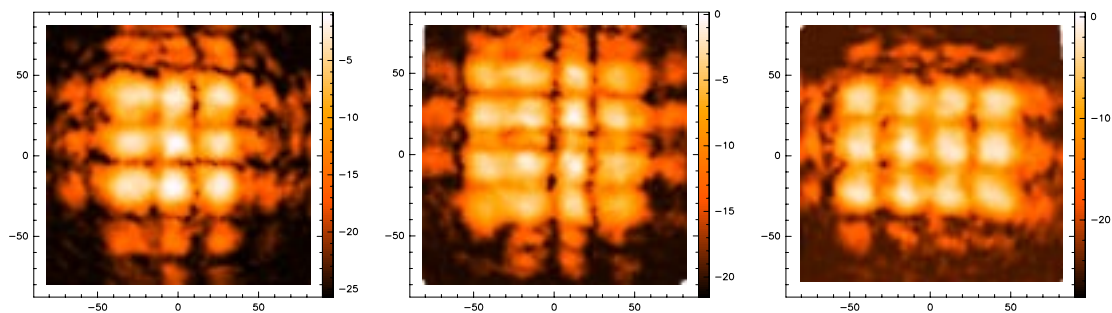


FIGURE IV Two-dimensional diffraction spectra for combined grating layers for  $K=3$  and  $K=4$ . Coordinates are given in mm. The measured intensities are shown in a dB scale.

measurements of the generated intensity distributions it also has to be verified that the device is able to couple a suitable amount of power to an array of SIS-mixers. For this test the components of the CHAMP L.O. system have been set up on an optical frame as shown in fig. VI.

The output power of the frequency stabilized gunn oscillator is adjustable by a mechanical attenuator to vary the power injected into the mixer. A potter horn antenna couples the rf-output of the multipliers to free space generating a beamwaist of 1.1mm. A HDPE lens transforms this waist (7mm) to one at the input of the gaussian telescope lens pair. The intermediate waist (16mm) of the gaussian telescope,  $2f=900mm$ , illuminates the phase grating mounted at the waist position. The generated signal array was then coupled into a SIS mixer device via a Martin-Puplett-Interferometer which could be moved together with the mixer to each array matrix position. The IV-curves then monitored the detected L.O. signal. Starting with one position the L.O. signal power was adjusted to obtain a minimum noise temperature for the mixer. It was seen that the injected L.O. power gave a huge margin because the mixer showed a typical normal resistance feature indicating a sufficient coupling efficiency. After attenuating the power for maximum mixer performance on one position, the noise temperatures for each array position was measured and compared.

The measured iv-curves as well as the total power responses for the noise measurements at a frequency of 492GHz are shown in fig. V, according to the position in

the subarray. The differences in injected L.O. power was indicated by the noise performance variation to be less than 10%.

The described technique of testing the device operating as a L.O. injection system has the advantage of being independent of the mixer's characteristics by using the same mixer for all measurements. Otherwise the results would include the individual behaviour of each mixer, such as its sensitivity to the L.O. signal caused by the individual backshort adjustment or like the individual noise performance itself. Therefore the measured noise temperature variation here characterizes only the functionality of L.O. injection.

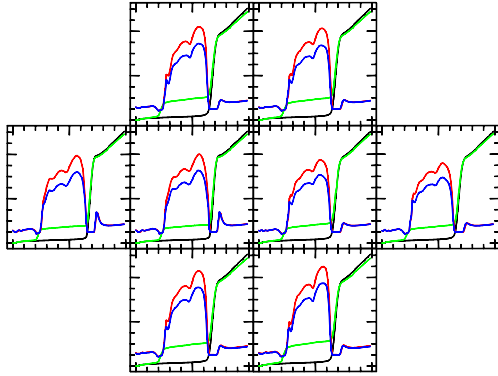


FIGURE V Current/voltage and power/voltage curves of the mixer at various subarray positions. To be independent of the variable characteristics of several mixers the curves are obtained by a single mixer moved to the various positions of the subarray detectors.



FIGURE VI CHAMP L.O. optics. With folding both optical paths the system could be integrated on a mounting plate of 1m in diameter. In the foreground one of the two L.O. sources is visible. The grating is mounted under the gold plated flat mirror injecting the signals into the cold optics of CHAMP.

## THE PHASE-RETRIEVAL ALGORITHM

As mentioned in the previous section the Dammann method can only provide solutions for regular matrix arrays because of the required separableness of the transmission function. In case of non regular arrays a full two-dimensional consideration of eq. 1 is necessary. Hence we apply a phase retrieval algorithm, recovering the phase of an object out of the information given by the intensity distributions of the desired image and the illuminating beam. This method is based on the idea of *Gerchberg and Saxton* [8] and therefore often called *Gerchberg-Saxton-Algorithm*. The principle of the algorithm is to Fourier transform between the two domains back and forth changing the functions in a way that they fulfill the constraints given by the required beams. The adaptation of this principle to the foregoing grating problem is formulated in fig.VII. The algorithm is starting with the desired intensity distribution and a first guess for the phase distribution  $\Phi_0$  of the complex field. Transforming

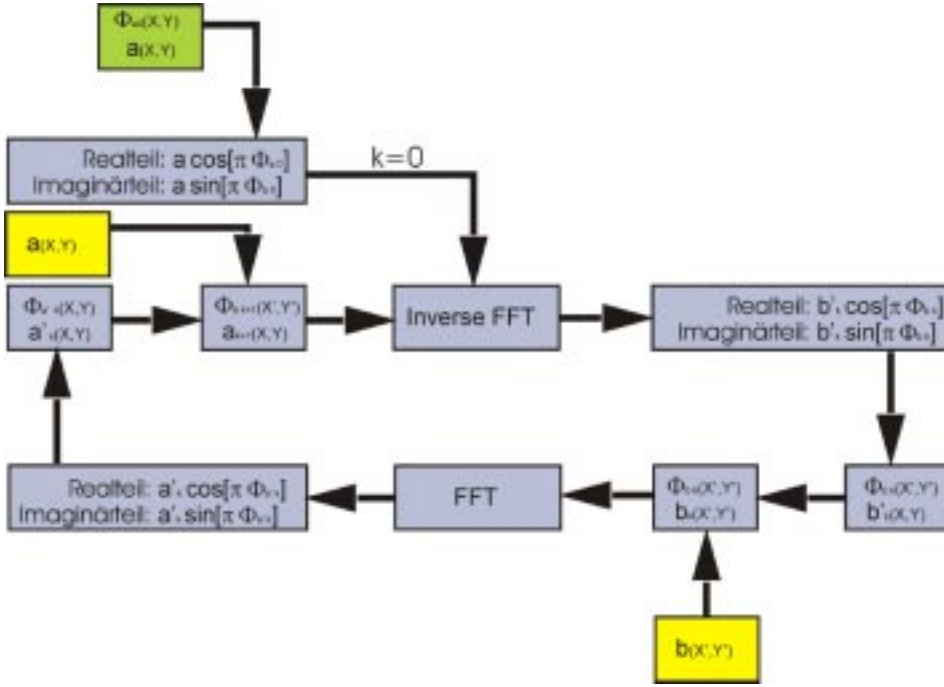


FIGURE VII Flow chart of the algorithm for the grating problem. After initialization of the image with  $a(x, y)$  and  $\Phi_{a0}(x, y)$  (green) the algorithm starts with an inverse FFT. In the object domain  $b_k(x', y')$  is replaced by the illumination function  $b(x', y')$  (yellow), after the FFT  $a'_k(x, y)$  is replaced by the desired image  $a(x, y)$  (yellow). With a monotone decrease of the error function  $a'_k(x, y)$  approximates a solution.

this function via an inverse complex two-dimensional FFT yields phase and amplitude distributions in the object domain where the grating is located. The amplitude however does not fulfill the requirement for a gaussian illumination due to the fact that the phase only modulation is a special case of solution. Therefore the amplitude  $b'_k(x', y')$  has to be replaced by the the desired illumination of gaussian shape  $b(x', y')$  before transforming back. After the FFT a result for the diffraction image is obtained. The efficiency and the differences are calculated to monitor the current status of the results. Before starting the next iteration the amplitude of the diffraction image is replaced by the desired intensity distribution. The phase remains as a new estimate for the next iteration.

The FFT treats the functions in discrete form as

$$A(x, y), B(x', y') \rightarrow A(m, n), B(p, q), \text{ described by} \quad (3)$$

$$A_{mn} = \frac{1}{MN} \sum_{p=0}^{M-1} \sum_{q=0}^{N-1} B_{pq} e^{-2\pi i \frac{qm}{M}} e^{-2\pi i \frac{pn}{N}} \quad (4)$$

is the discrete formulation of eq. (1) as considered in [10].

To characterize the transmission function, merit functions are calculated by

$$\eta_k = \frac{\sum_p \sum_q a'_{pq}}{\sum_m \sum_n a_{mn}}, \quad (5)$$

giving the efficiency achieved at the  $k^{\text{th}}$  iteration the grating efficiency, and an error function  $\epsilon_k$

$$\epsilon_k = \frac{1}{M \cdot N} \frac{\sum_{m=0}^M \sum_{n=0}^N [a'_{mnk} - a_{mn}]}{\sum_{m=0}^M \sum_{n=0}^N a_{mn}^2}, \quad (6)$$

indicating how the intensity in the desired orders is equalized.

## Realization

The algorithm has been realized on a HP-UNIX workstation which operates two fast processors and provides sufficient memory for the huge amount of data. The main part of the program is a routine for the two-dimensional FFT which has been derived from *Numerical Recipes in C* [10]. However the routine was slightly modified to a higher accuracy because rounding errors with the original routine led to significant effects during many iterations.

The data, two-dimensional arrays, have sizes  $2^N \times 2^M$ . The FFT itself has then to treat  $2^{N+M+1}$  array values. The time the computer needs for a single iteration is minimized by careful choice of values for  $N$  and  $M$  which includes a consideration of a useful sampling of data [11] to avoid aliasing. The results presented in the following were calculated with  $M, N=9$  which was related to a computing time of 10 seconds per iteration and a memory allocation of 31MB. The program follows in principle the steps of the flow chart given in fig. VII. In addition the values for the efficiency and error are calculated. An integrated module gives the option to determine an order of quantisation of the transmission function and to change this order during the algorithm iterations to implement practical constraints given by the mechanical fabrication procedures.

## Results

The first problem solved by the algorithm is the 2-4-2 configuration of a CHAMP subarray. As mentioned the data arrays were dimensioned as  $512 \times 512$  pixel arrays. The offsets for the desired diffraction orders  $a_{mn}$  are  $\pm 16$  and  $\pm 48$  pixel in the main axis and  $\pm 32$  pixel in the second axis of the array. The widths of the gaussians are 12 pixels. Fig.VIII shows the results for several phases during iteration. The left column lists the grating structures  $\Phi_{bpq}$ , the column in the middle lists the generated intensity distribution  $a'_{mn}$  and the far field phase is listed in the right column of the figure. The top row shows the result after the 1<sup>st</sup>, the 5<sup>th</sup> and the 30<sup>th</sup> iteration. As indicated by this sequence the intensities in the undesired higher orders are more and more reduced by further iterations. The monotone decrease of

the error becomes visible considering the intensity distributions of fig.VIII, after 30 iterations the intensity is distributed equally over the desired orders of the array. Up to 5 iterations, there are diffraction orders visible between the desired orders indicating that all even orders are rejected as stimulated by the even symmetry of the transmission function. Indeed the initial estimate for the phase distribution in the far field has been chosen to be even which makes the complex initial function for the first FFT symmetric. This has been done to force the algorithm to find a solution on a short time scale. Using another estimate, such as a random distribution for the initial phase, yields similar results but increases the number of iterations needed by a factor of 10. It is obvious that the values for the error function have a strong dependence on the chosen initial phase distribution.

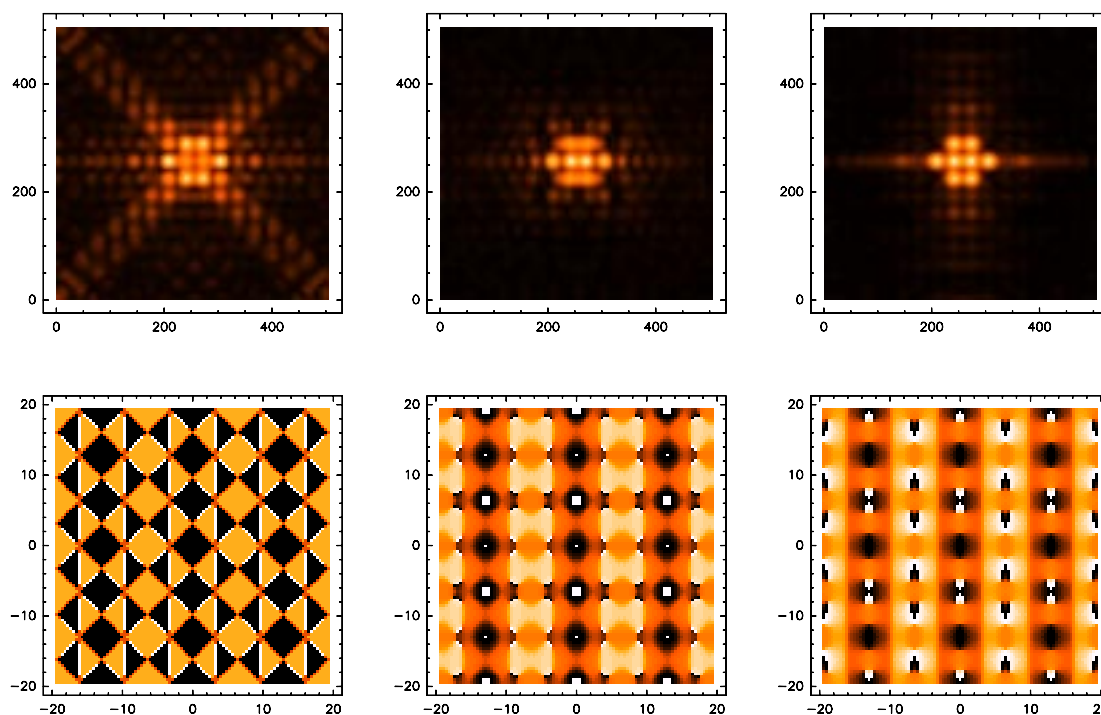


FIGURE VIII Intensity (top) and phase modulation (bottom) after 1,5 and 30 iterations (left to right) of the algorithm. Colours are scaled from zero (black) to  $2\pi$  (white) and zero to unit for intensity.

#### *Quantisation of phase levels*

Simplifying the phase structure can be advantageous for a physical realization of the application of such solutions. Therefore the program is able to implement an order of quantisation of the phase levels ( $l=2,4,8,16,\dots$ ). After each iteration the resulting phase distribution is digitized as:

$$\Phi_{kmn} \rightarrow \frac{2\pi}{l} \cdot s, \quad (7)$$

with  $s$  as an integer in the range 0 to  $l$  chosen that

$$\Phi_{kmn} - \frac{2\pi}{l} \cdot s = \min. \quad (8)$$

Fig. IX shows the results obtained for several quantisation levels. Although the algorithm is limited by the strong quantisation, reasonable results can be obtained. As expected, the more the phase structure is simplified by the chosen order of quantisation the less the efficiency and the higher the value of the error function (see fig. X) is obtained. A digitization to 8 phase levels seems to be possible without significant changes in the devices performance. Going to 4 allowed phase levels there is a significant increase on the error function and the efficiency is limited to 68%. Better results were obtained when the digitization started later after 15 iterations as it is indicated by the dashed lines in fig. X. With this method the results for a four level structure is similar to a 32 level type. In conclusion it is shown that it is possible to simplify the phase structure without significantly changing the performance. This makes the described method interesting for application in practice. Other array

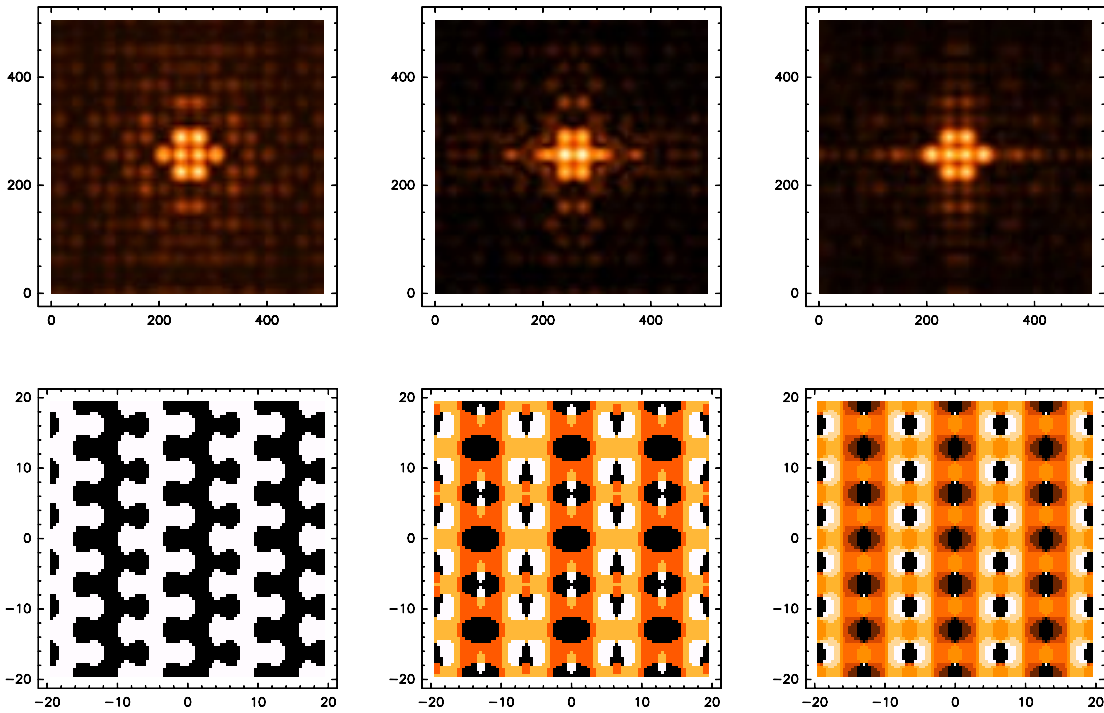


FIGURE IX Generated intensity distributions for 2,4 and 8 discrete phase levels and the resulting grating surfaces (below) are shown. For the binary case the algorithm leads to a translation symmetric transmission function which achieves a significantly better result than for the 4-level type. The 8-level type has nearly the same performance as a non digitized solution (less than 10% decrease of efficiency).

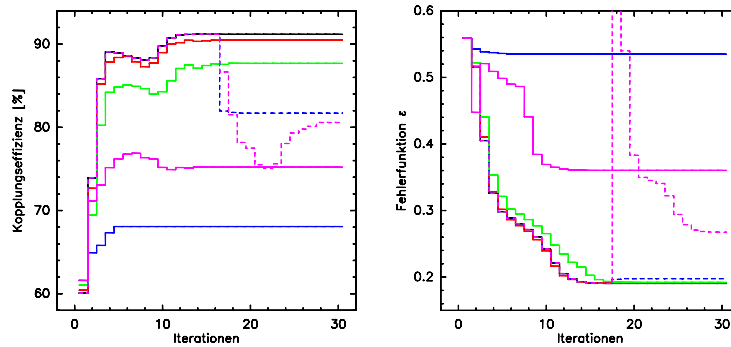


FIGURE X Convergence of the algorithm for 2 (pink), 4 (blue), 8 (green), 16 (black) and 32 (red) allowed phase levels. The left graph shows the grating efficiency, the right graph shows the error function. Digitization was performed at the start of the algorithm except for the dashed lines digitization started after 15 iterations yielding better results.

configurations can be easily calculated because the algorithm only requires for the initial function given by the desired array. Some examples are shown in fig.XI. During testing the algorithm a variety of configurations have been calculated without discovering any limits of this method.

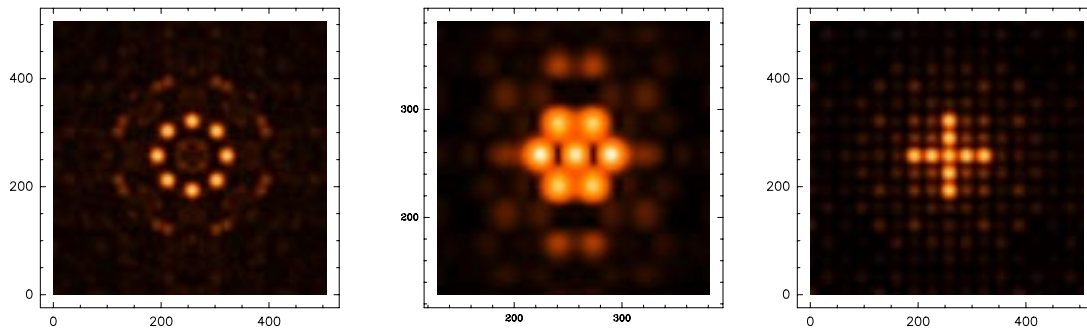


FIGURE XI Some examples of grating solutions for array generation. Between the more exotic configurations, as a circle or a cross, the hexagonal configuration of beams is often used for array receivers. The extension for more beams is possible. In case of the circle the  $0^{th}$  diffraction order has been very well rejected.

### *Distributions without symmetries*

In the following we consider an intensity distribution which has no kind of symmetry. The interesting difference here to the previous calculations is that a desired intensity which can be considered as a frequency in the image domain according to its offset does not have an identical intensity at the same negative frequency.

A photograph <sup>1</sup>, has been digitized as the desired image to be generated by an illuminated phase grating. Fig.XII shows the result for the generated image after 1500 iterations on the left which can be compared to the original image on the right side of the figure. The result is a surprisingly accurate reproduction of the desired image. Only 2% of the intensity is coupled to the outer region not belonging to the image. The size of the original  $164 \times 180$  pixels is according to 29520 diffraction orders in the image domain. The data field for the calculations had a size of  $1024 \times 1024$  (allocating 123MB of workspace) to avoid aliasing. This huge number of diffraction orders is mirrored in the phase structure of the grating shown in the center of fig.XII as a fine structured distribution. The variation of the phase seems not to have any order of direction as it is to be expected from the original image. But it becomes visible in the graph that there are two structures overlaid, a fast changing structure (dark blue and white) and a second with a smooth variation in phase.

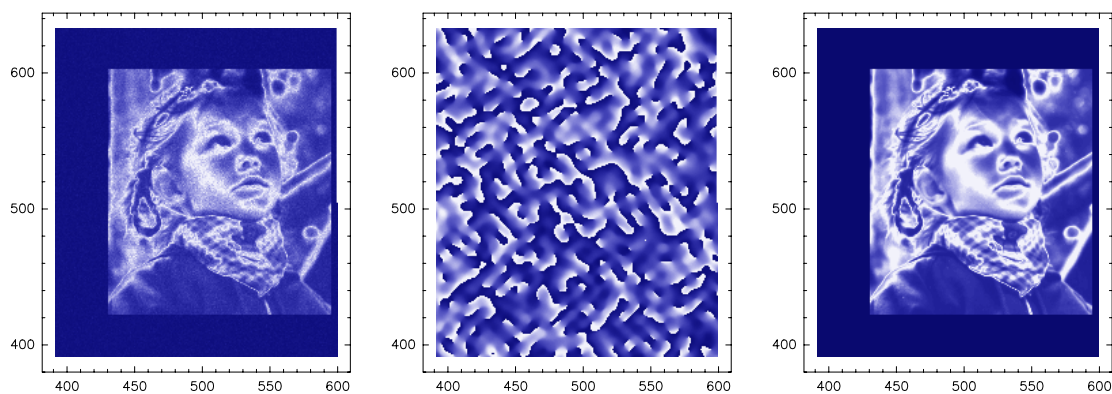


FIGURE XII The picture on the right shows the original picture a photo with a resolution of  $164 \times 180$  pixels to be generated by a holographic phase structure. This structure is shown at the center of the figure as a result after 1500 iterations of the algorithm. On the left the generated image is presented, a surprisingly accurate reproduction of the original.

## Outlook

We reported on the successful application of phase gratings as quasi-optical local oscillator beam splitter as used for our heterodyne array receiver CHAMP. The transmission gratings fabricated of PTFE were calculated by use of the Dammann Method. The experiments and, finally, their implementation in a working system, demonstrate that this type of device provides solutions for a variety of array receiver systems in the submm- and terahertz region for the future. With the phase

---

<sup>1</sup>The photo shows the author's three year old daughter

algorithm, as reported here, gratings can be calculated for every type of beam configuration, especially for non regular arrays. A first prototype for this kind of grating is planned for the near future as it is foreseen for the CHAMP-D project [12], a copy of the existing system covering the  $450\mu\text{m}$  window of the atmosphere.

## REFERENCES

- [1] R.Güsten, G.A.Ediss, F.Gueth, K.H.Gundlach, H.Hauschildt, C.Kasemann, T.Klein, J.W.Kooi, A.Korn, I. Krämer, H.G.LeDuc, H.Mattes, K.Meyer, E.Perchtold, M.Pilz: "CHAMP: the Carbon Heterodyne Array of the MPIfR", Proc. SPIE Vol.3357, pp.167-177, Advanced MMW, Radio, and Terahertz Telescopes, 1998
- [2] J.W. Goodman: "Introduction to Fourier Optics", McGraw-Hill, New York,1968
- [3] J.A. Murphy, S.Withington, M. Heanue: "Local Oscillator Splitting Using Dammann Phase Gratings" Proceedings of the 3rd Interational Workshop on Terahertz Electronics, Zermatt, 1995
- [4] H.Dammann, E.Klotz: "Coherent optical generation and inspection of two dimensional periodic structures", Optical Acta, Vol 24, No.4, pp.505-515, 1977
- [5] S.J. Walker, J. Jahns: "Array generation with multilevel phase gratings", J. Opt. Soc. Am., Vol 7, No.8,1990
- [6] T. Klein, G.A. Ediss, R. Güsten, H. Hauschildt, C. Kasemann: "Local Oszillator Beam Array Generation at 480GHz by Use of Phase Gratings", 8th International Symposium on Space Terahertz Technology, Harvard-Smithsonian Center for Astrophysics, Cambridge MA,1997
- [7] T. Klein: "Entwicklung diffraktiver Beamsplitter und Integration der Systemoptik fuer ein Submillimeter Heterodyn Array", PhD thesis, MPIfR Bonn, 1999
- [8] R.W. Gerchberg and W.O. Saxton, Optik 35, 237, 1972
- [9] R.L. Morrison: "Symmetries that simplify the design of spot array phase gratings", J. Opt. Soc. Am. A, Vol. 9, No. 3, 1992
- [10] W.H. Press, S.A. Teukolsky, W.H. Vetterling, B.P. Flannery: "Numerical Recipes in C", chapter 12, pp.521-525, Cambridge University Press, 1992
- [11] W.H. Press, S.A. Teukolsky, W.H. Vetterling, B.P. Flannery: "Numerical Recipes in C", chapter 12.1, pp.500-502, Cambridge University Press, 1992
- [12] Space Research Organisation Netherlands: "A SRON-MPIfR 16-element Heterodyne array receiver for the 625-720 GHz (D-band) atmospheric window", <http://www.strw.leidenuniv.nl/jcmt/champ.html>

# Narrow-Band Terahertz Waveform Generation in Periodically-Poled Lithium Niobate

T. Meade, Y.-S. Lee, V. Perlin, H. Winful, T.B. Norris

Center for Ultrafast Optical Science, University of Michigan, Ann Arbor, MI 48109-2099

A. Galvanauskas

IMRA America, 1044 Woodridge Ave., Ann Arbor, MI 48105

**Abstract:** We demonstrate a method for generation of narrow bandwidth THz fields by optical rectification, a nonlinear interaction between a 150-femtosecond optical pulse and a periodically-poled lithium niobate crystal. We present time-domain measurements of both amplitude and phase of the THz electric field, along with power spectra. At low temperature (13 K), the signal from a 1.2 mm long crystal is peaked at 1.80 THz with a bandwidth (FWHM) of 0.07 THz; the THz power is approximately 1.5  $\mu$ W. Optical rectification in PPLN could provide a useful source field for characterization of THz sensors.

## 1. Nonlinear optics

The field of nonlinear optics is considered to have begun with the experiment by Franken *et al.* in 1961, in which the optical harmonic (second harmonic generation — SHG) of a ruby laser was produced by nonlinear interaction with a quartz crystal [1]. By nonlinear optics we mean that the interaction between the optical field and the medium, typically a crystal, depends on the field strength in a nonlinear manner. One generally creates nonlinear fields by inducing a nonlinear polarization in the crystal with a strong optical field and measuring the radiation emitted by the decay of the polarization.

In traditional, linear optics, the polarization induced in a medium is proportional to the electric field incident on the medium. This is expressed in the equation  $P = \epsilon_0 \chi E$ . However, with the advent of lasers, and in particular, short-pulsed lasers, electric fields sufficiently large so that linear polarization approximation fails are easily attained. In general, therefore, one must expand the polarization as a power series in the applied field:

$$P = \chi^{(1)} E + \chi^{(2)} E^2 + \chi^{(3)} E^3 + \dots = P^{(1)} + P^{(2)} + P^{(3)} + \dots \quad (1)$$

The term proportional to  $E$  gives the familiar linear polarization. In this paper, we are primarily interested in the second-order term,  $P^{(2)}$ . This term is responsible for such effects as second-harmonic generation, sum- and difference-frequency generation, parametric amplification and oscillation, and optical rectification.

As a concrete example of a second-order nonlinear effect, we will briefly examine difference frequency generation. We represent two fields as  $E_1 = A_1 \exp[i\omega_1 t]$  and  $E_2 = A_2 \exp[i\omega_2 t]$ . Consider the polarization arising from the mixing of  $E_1$  with  $E_2^*$ :

$$P^{(2)} = \chi^{(2)} A_1 \exp[+i\omega_1 t] A_2^* \exp[-i\omega_2 t] = \chi^{(2)} (A_1 A_2^*) \exp[i(\omega_1 - \omega_2)t] \quad (2)$$

It is immediately evident that the polarization oscillates with the difference frequency  $\omega = \omega_1 - \omega_2$ . This polarization acts as a source term in the wave equation:

$$\left( \nabla^2 - \frac{1}{c^2} \frac{\partial^2}{\partial t^2} \right) E(z, t) = -\mu_0 \frac{\partial^2 P(z, t)}{\partial t^2}, \quad (3)$$

and we see that, because of the induced nonlinear polarization, there exists a radiated field at the difference frequency between the two applied fields [2,3]. Other second-order nonlinear interactions are, of course, possible. In the laboratory, a specific orientation of a nonlinear crystal will usually favor only one type of interaction.

The nonlinearity of specific interest to us is optical rectification, which one may think of simply as the degenerate case of difference frequency generation [4]. In optical rectification, the two fields come from the same laser. For a continuous-wave laser, the effect of the polarization is to induce a static DC voltage inside the crystal. Since the second derivative of such a polarization is zero, this term gives no radiation in the far-field. The case is very different for short-pulsed lasers. If the two fields in equation (2) come from the same pulse, then our expression for the polarization simplifies to:

$$P^{(2)}(t) = \chi^{(2)} [A(t)A^*(t)] = \chi^{(2)} I(t), \quad (4)$$

where  $I(t)$  is the optical pulse's intensity profile. The net effect is to strip away the rapidly varying ( $\sim 10^{15}$  Hz) optical carrier frequency, and leave only the relatively slowly varying ( $\sim 10^{12}$  Hz) pulse envelope.

For pulses on the order of 100 femtoseconds, this corresponds to a polarization changing on sub-picosecond time-scales. If we prefer to visualize this process in the frequency domain, we may consider that a 100-femtosecond optical pulse has a spectrum on the order of a few terahertz (THz), and therefore terahertz frequencies may be generated if the optical pulse spectrum is sufficiently broad to support difference frequency generation between different spectral components of the same pulse.

For generating short bursts of coherent THz frequency light, a widely applied method is optical rectification in a velocity-matched medium. To maximize conversion efficiency, the optical pulse should travel with the same speed through the crystal as the THz wave, i.e. the group velocity of the optical pulse should be equal to the phase velocity of the THz wave. Under this condition, the forward-propagating THz wavefronts from different parts of the crystal interfere constructively, and at the output of the crystal, a substantial THz field is emitted. The radiated THz field has a peak frequency on the order of 1 THz, is extremely broad-band ( $\omega \sim 1$ -2 THz), and consists of a single- or few-cycle pulse. The most common means of achieving this are with a pulsed laser operating around 800 nm and a  $\langle 110 \rangle$  ZnTe crystal [5].

In lithium niobate, the optical group velocity is larger than the THz phase velocity, and so the two beams walk-off each other as they propagate through the crystal. The optical beam leads the THz beam by one optical pulse-length after a walk-off length

$$l_w = \frac{c\tau_p}{n_{THz} - n_{opt}} \quad (5)$$

In equation (5),  $\tau_p$  is the optical pulse duration,  $n_{THz}$  and  $n_{opt}$  are the phase and group indices of the THz and optical fields, respectively, and  $c$  is the vacuum speed of light. For crystals significantly longer than  $l_w$ , only the front and back surfaces produce polarizations which contribute to the far-field THz field; everywhere else in the crystal, the polarization is constant and therefore nonradiative [6].

In a velocity-matched medium, it is clear that a long crystal corresponds to a large interaction length, which enables the generation of strong THz fields. In a medium with a velocity mismatch, the effective interaction length is the walk-off length. A crystal longer than the walk-off length is inefficient, since most of the polarization induced will be nonradiative. To generate a strong THz field, we use quasi-phase matching in a velocity-mismatched medium to circumvent this defect. We discuss these ideas in the following section.

## 2. Periodically-poled lithium niobate

Ferroelectric molecules such as lithium niobate (LN) possess a non-zero electric dipole moment even in the absence of an applied field. An edge perpendicular to the domain of a unipolar LN crystal is patterned with a photoresist grating of the desired domain structure. This edge is then covered with a thin metal film. A large ( $\sim 20$  kV/mm) field is applied, which is sufficient to reverse the polarity of the domains where the metal makes contact with the LN crystal, but is not strong enough to affect the domains below the photoresist layer [7].

Because the direction of a domain is a manifestation of the orientation of the molecules within a domain, for optical purposes, it is convenient to think of poling as directing the orientation of the crystal's optic axis. Domains that are anti-parallel have opposite sign nonlinear susceptibilities,  $\chi^{(2)}$ . In bulk PPLN, one domain in the crystal generates a THz pulse with the opposite polarity as the previous domain. This is shown schematically in figure 1. If the domain lengths are approximately equal to the walk-off length, the radiated THz fields from neighboring domains will connect smoothly and have a narrow spectrum centered about

$$f_f = \frac{c}{2l_d(n_{THz} - n_{opt})}. \quad (6)$$

Our effective interaction length therefore increases from the walk-off length to the entire length of the crystal. In our experiments, this increase is approximately a factor of 40 (see section 3). By generating a polarization through many domains of the crystal, we are able to generate a multi-cycle THz waveform, whose structure is determined mainly by the domain structure of the crystal. If the domains of a periodically-poled crystal reverse polarity on a scale  $l_d \cong l_w$ , then radiated field due to optical rectification is essentially a convolution of the crystal's domain structure with the pulse intensity envelope [8].

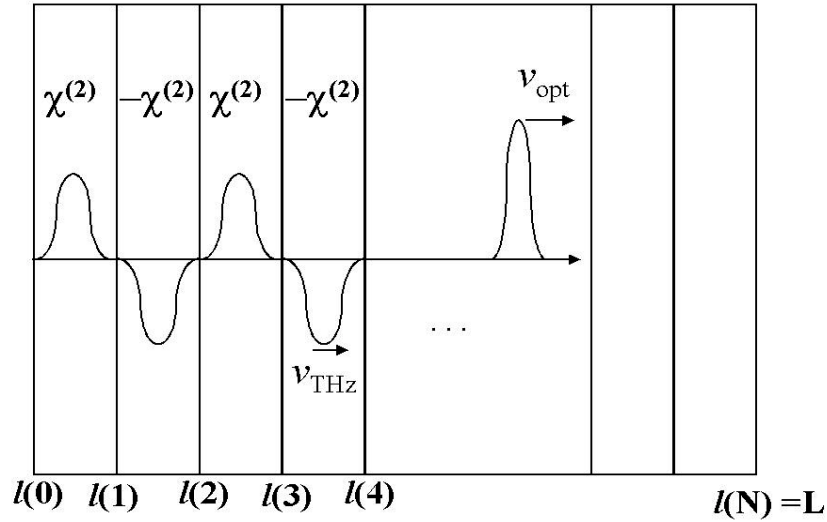


Fig. 1: Schematic diagram of the nonlinear polarization induced in the PPLN crystal.

### 3. Experimental procedure and results

A schematic of our experiment is shown in figure 2. In the figure, THz beams are shown as dotted lines, and optical beams are solid lines. The laser source for the experiments is a Ti:Sapphire regenerative amplifier, which produces 150-fs pulses at 800 nm with a repetition rate of 250 kHz [9]. The index of refraction over a broad range of THz frequencies has been measured to be approximately 5.2 [10]; we measured the optical group index to be 2.3 at room temperature. Using these values and our laser pulse duration in equation (5), we calculated a walk-off distance of approximately 24 microns in the crystal. We therefore chose a z-cut PPLN crystal, 1.2 mm long with a domain length of 30 microns for this work. The pulse energy incident on the sample is 400 nJ, focused to a spot size of roughly 100 microns. This signal beam was modulated at 50 kHz for lock-in amplifier detection. An off-axis parabolic mirror collimated the THz radiation from the PPLN. We measured the THz signal by electro-optic sampling. An optical probe pulse with a known polarization state co-propagated with the THz pulse. A second off-axis parabolic mirror focused both the probe and THz pulses onto a 1-mm thick, <110> ZnTe sensor crystal.

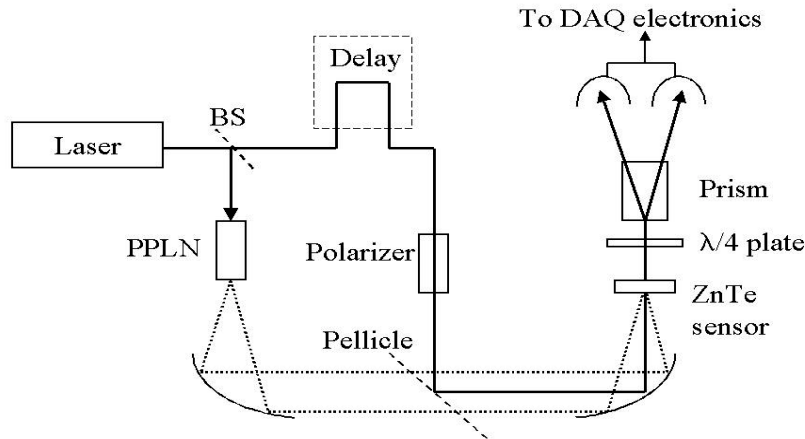


Fig. 2: Experimental set-up.

Free-space electro-optic sampling (FS-EOS) is an extension of conventional electro-optic sampling techniques used for characterizing local electric fields [11-13]. This method provides a means to measure the amplitude and phase of the THz field over a broad detection bandwidth. The main idea of FS-EOS is that the THz field modulates the optical properties of a crystal, and that modulation is probed with an optical beam. The THz electric field induces a birefringence in the sensor crystal, which in turn causes a phase retardation in the optical pulse. The phase retardation is proportional to the THz field strength, and gives a change in the polarization state of the optical beam. We measured the THz field strength by measuring the amount of polarization rotation in the optical probe beam with a pair of balanced photodiodes. Because of the excellent velocity matching between the THz and optical pulses in ZnTe, we can achieve  $\sim 200$  femtosecond resolution of the THz pulse [14].

In figure 3(a), we show the THz waveform at room temperature, and in figure 3(b), its power spectrum. The main features of the signal are oscillations under an exponentially decaying envelope. At room temperature, we measure a peak frequency of 1.67 THz, with a bandwidth (FWHM) of 0.13 THz. Because the THz wave propagates through the crystal more slowly than the optical beam, smaller time delays correspond to signal emitted from near the back surface of the crystal, while larger time delays correspond to the part of the signal from closer to the front surface of the crystal. The emitted field from the back end of the crystal is significantly larger than that from the front end. We see that our main limitation at room temperature is absorption of the THz wave as it propagates through the PPLN crystal. The absorption loss due to phonons is expected to reduce at lower temperatures [15].

To reduce the absorption loss, we performed the same experiment with the PPLN crystal at 13 K. As shown in our time trace of the waveform, figure 3(c), absorption essentially vanishes at low temperatures. Figure 3(d) is the power spectrum at low temperatures, from which we measure a peak frequency of 1.80 THz and a bandwidth of 0.07 THz. We can attribute the discrepancy between the peak frequencies at low and room temperatures to several factors. At low temperatures, the crystal shrinks and so our domain lengths shorten, which increases our peak frequency. Also, the real parts of the indices of refraction may have some temperature dependence.

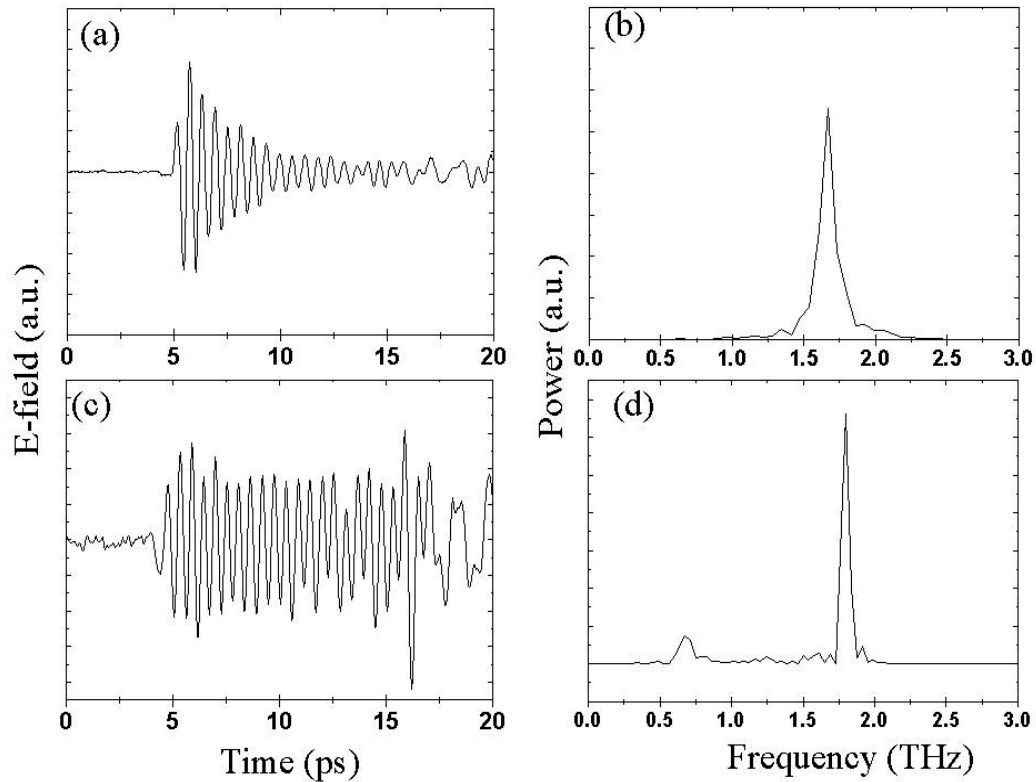


Figure 3: Time traces and power spectra of the THz field at room temperatures (a, b), and 13 K, (c, d).

To generate even narrower bandwidth fields, we tested a 7.2 mm PPLN crystal, with 30 micron domain lengths. At 18 K, this crystal generated 1.81 THz radiation with a bandwidth of 18 GHz (data not shown).

It is interesting to examine one of our room temperature scans over a large time window, as in figure 4(a). What we find is that the oscillations do not finish in a simple manner. After the exponential envelope has decayed, a beat pattern arises. This is a result of a counter-propagating THz polarization in the crystal. When the optical beam reflects off the back surface of the crystal, it induces a polarization which propagates in the opposite direction as the optical beam. This signal has a peak frequency of

$$f_b = \frac{c}{2l_d(n_{THz} + n_{opt})} \quad (7)$$

and lags the co-propagating signal in time. To see this effect more clearly, we can produce a time-frequency spectrogram of figure 4(b). Figure 4(b) is a wavelet decomposition of our signal with a Morlet basis [16,17]. At early times, we see the co-propagating signal, followed by both the counter-propagating signal, and a reflection of the co-propagating signal. The low frequency wave is peaked at 0.67 THz, with a bandwidth of 0.03 THz. Detailed measurements of this low-frequency wave await further study.

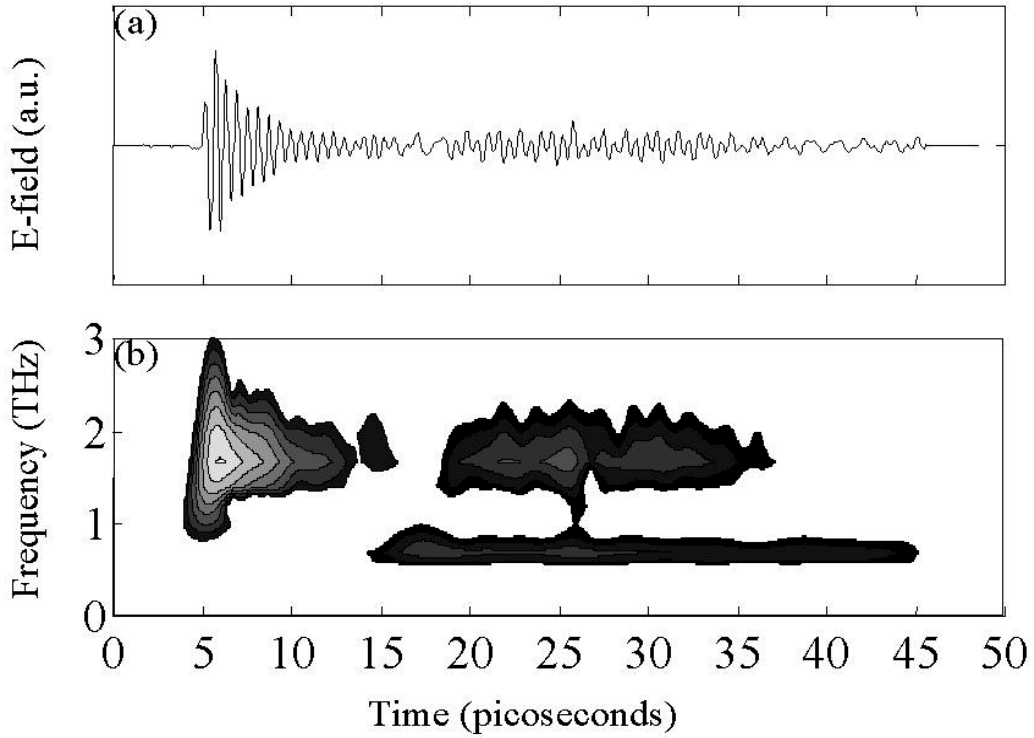


Figure 4: (a) Trace of the THz wave over a long time window; (b) Time-frequency wavelet spectrogram. Brighter areas correspond to higher powers.

To determine the power and spectral brightness of the THz field, we measured the radiated field with a bolometer. For a 400 nJ pulse, we measure approximately  $1.5 \mu\text{W}$  of THz power at low temperature from the 1.2 mm PPLN. This corresponds to a spectral brightness of approximately  $20 \mu\text{W/THz}$  in the 1.75-1.85 THz frequency range, as compared to approximately  $0.5 \mu\text{W/THz}$  for the same frequency range in ZnTe. When focused to a spot size of 300 microns, the peak electric field for our THz pulse is on the order of  $8 \times 10^4 \text{ V/m}$ .

#### 4. Modeling the THz field

To solve for the radiated field, we must first calculate the polarization as a function of position and time in the crystal. For a tractable result, we assume a gaussian plane-wave pulse propagating in the  $z$  direction of a dispersionless medium:

$$E(z,t) = E_0 \exp[i(\omega_0 t - k_0 z) \exp[-((t - z/v_g)/\tau_p)^2 / 2]] \quad (8)$$

where  $v_g$  is the group velocity of the optical pulse,  $c/n_{opt, \omega_0}$  is the center frequency of the optical carrier,  $k_0$  is its propagation constant, and  $E_0$  is the peak field. In principle, we use this pulse shape as the source of our polarization in equation (4), and then solve equation (3) for the THz frequency field. In practice, however, direct time-domain solutions are difficult to calculate; the problem become much more manageable under Fourier transformation to the frequency domain. The wave equation in the frequency domain becomes an inhomogeneous Helmholtz equation:

$$\left( \frac{\partial^2}{\partial z^2} + n^2(\omega) \frac{\omega^2}{c^2} \right) E(z, \omega) = -\mu_0 \omega^2 P(z, \omega) \quad (9)$$

In equation (9),  $n(\omega)$  is the complex refractive index, and we have already accounted for the linear part of the polarization, so that here,  $P(z, \omega)$  is only the nonlinear polarization. A convenient way to solve this equation is by the method of Green's functions. Because Green's functions for the Helmholtz equation are well-known [18], and the case of an optical rectification inhomogeneity has also been studied in detail [19,20], we will simply give the results of the calculation. At the back surface of the crystal ( $z' = L$ ), the radiated field from each position,  $z'$ , is:

$$E(z', \omega) \propto \chi^{(2)}(z', \omega) \omega^2 \exp[-(\omega \tau_p / 2)^2 - i\omega \{ (n_{opt} - n_{THz}) z' / c + L n_{THz} / c \}] \quad (10)$$

This equation may then be Fourier transformed back to the time domain, and integrated over the crystal to yield the measured THz signal as a function solely of time.

Simulations of the THz field are shown in figure 5. Figures 5(a) and (b) are the time domain and power spectrum simulations, respectively, and include a THz absorption term. When the absorption term is included in the THz index, we attain very good agreement between our calculated field and our measured field at room temperature. The spectrum shown in 5(b) is peaked at 1.72 THz and has a bandwidth of 0.10 THz. For the low temperature data, no such absorption term is needed to model the data accurately, as in figures 5(c) and (d). The spectrum in figure 5(d) is also peaked at 1.72 THz (we did not account for index changes and crystal contraction at low temperatures in the simulation), and has a bandwidth of 0.08 THz.

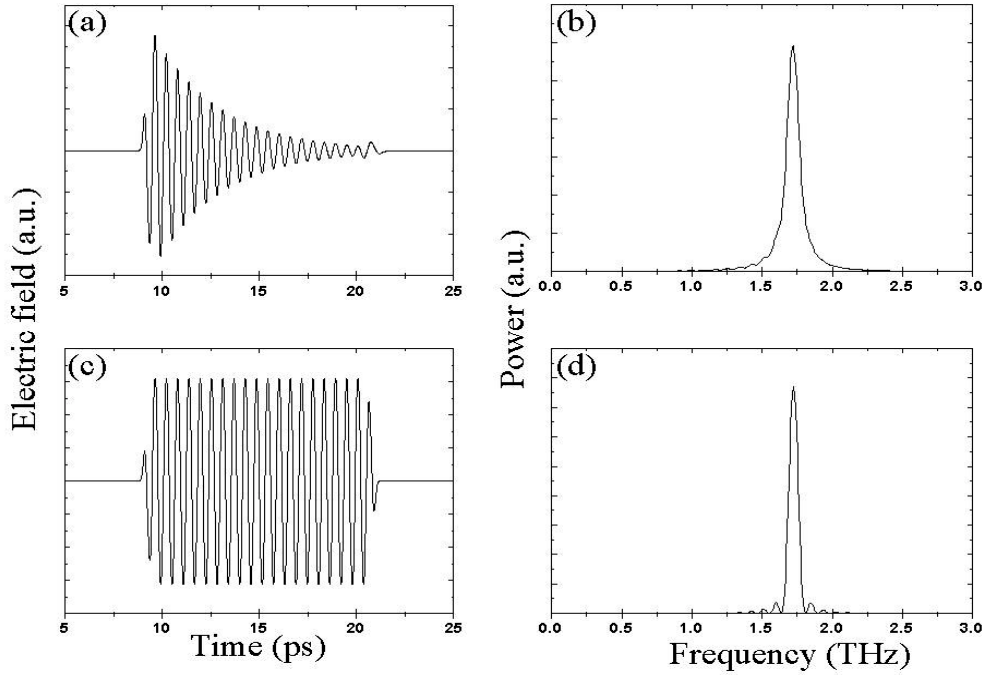


Figure 5: Numerical simulations of the THz field, with absorption (a, b), and without absorption (c, d).

## 5. Summary & future prospects

Research into generation of narrow-bandwidth THz sources has been vigorous recently. Photomixing on THz antennas offers a usable source of continuous wave THz, but antenna response severely limits the power available from such devices on the high-frequency end [21]. Other research has focused on pulse-shaping techniques. To limit the radiated bandwidth, pulse-shapers for the optical beam [22,23] and also for the THz signal itself [24] have been demonstrated. Pulse-shaping, however, is intrinsically inefficient. In contrast to these methods, we demonstrate a method for generating narrow-bandwidth THz by engineering the nonlinear crystal itself to produce the desired waveform.

Ultimately, we anticipate that other poled materials will surpass PPLN as a medium for THz waveform generation. Poled polymers have large nonlinear coefficients [25], and could provide a strong THz system if they are able to be periodically-poled. For spectroscopic and sensing applications, chirped poled media (i.e. poled so that the domain size increases as one moves laterally across the crystal) could be an extremely useful source of tunable THz radiation.

In summary, we have shown that optical rectification of a femtosecond pulse in a periodically-poled lithium niobate crystal gives rise to a THz waveform which largely

depends on the domain structure of the poled crystal. In particular, narrow bandwidth waveforms may be achieved by a proper choice of domain length in a periodic crystal.

## 6. References

1. P.A. Franken, A.E. Hill, C.W. Peters, and G. Weinreich, *Phys. Rev. Lett.*, **7**, 118 (1961).
2. R.W. Boyd, *Nonlinear Optics*, Academic Press, San Diego, 1992.
3. A. Yariv, and P. Yeh, *Optical Waves in Crystals*, Wiley, New York, 1984.
4. A. Bonvalet, M. Joffre, J.L. Martin, and A. Migus, *Appl. Phys. Lett.*, **67**, 2907 (1995).
5. A. Nahata, A.S. Weling, and T.F. Heinz, *Appl. Phys. Lett.*, **69**, 2321 (1996).
6. U. Peschel, K. Bubke, D.C. Hitchings, J.S. Aitchison, and J.M. Arnold, *Phys. Rev. A*, **60**, 4918 (1999).
7. L.E. Myers, R.C. Eckardt, M.M. Fejer, R.L. Byer, W.R. Bosenberg, and J.W. Pierce, *J. Opt. Soc. Am. B*, **12**, 2102 (1995).
8. Y.-S. Lee, T. Meade, V. Perlin, H. Winful, T.B. Norris, and A. Galvanauskas, *Appl. Phys. Lett.*, **76**, 2505 (2000).
9. T.B. Norris, *Opt. Lett.*, **17**, 1009 (1992).
10. H.J. Bakker, S. Hunsche, and H. Kurz, *Phys. Rev. B*, **50**, 914 (1994).
11. B.H. Kolner and D.M. Bloom, *IEEE J. Quantum Electron.*, **22**, 69 (1986).
12. J.A. Valdmanis and G.A. Mourou, *IEEE J. Quantum Electron.*, **22**, 79 (1986).
13. Q. Wu and X.-C. Zhang, *Appl. Phys. Lett.*, **67**, 3523 (1995).
14. Q. Wu and X.-C. Zhang, *Appl. Phys. Lett.*, **68**, 1604 (1996).
15. H. Ito, K. Kawase, and J. Shikata, *IEICE Trans. Electron.*, **E81-C**, 264 (1998).
16. C. Torrence and G.P. Compo, *Bull. Am. Meteorol. Soc.*, **79**, 61 (1998).
17. Wavelet software provided by C. Torrence and G.P. Compo, and is available at <http://paos.colorado.edu/research/wavelets>
18. J.D. Jackson, *Classical Electrodynamics*, Wiley, New York, 1975.
19. D.H. Auston and M.C. Nuss, *IEEE J. Quantum Electron.*, **QE-24**, 184 (1988).
20. C. Kelleck, *J. Opt. Soc. Am. B*, **16**, 1250 (1999).
21. E.R. Brown, K.A. McIntosh, K.B. Nichols, and C.L. Dennis, *Appl. Phys. Lett.*, **66**, 285 (1995).
22. Y.Q. Liu, S.G. Park, and A.M. Weiner, *IEEE J. Sel. Top. Quantum Electron.*, **2**, 709 (1996).
23. C. Messner, M. Sailer, H. Kostner, and R.A. H pffel, *Appl. Phys. B*, **64**, 619 (1997).
24. J. Bromage, S. Radic, G.P. Agrawal, C.R. Stroud, P.M. Fauchet, and R. Sobolewski, *Opt. Lett.*, **22**, 627 (1997).
25. A. Nahata, D.H. Auston, C. Wu, and J.T. Yardley, *Appl. Phys. Lett.*, **67**, 1358 (1995).

# Resonant Tunneling THz Oscillator at Fixed Bias Voltages

Peiji Zhao and H. L.Cui\*

Department of Physics and Engineering Physics  
Stevens Institute of Technology, Hoboken, NJ 07030, USA.

\*Email: hcui@stevens-tech.edu

D. Woolard

Army Research Office, RTP, NC 27709, USA

Resonant tunneling diodes (RTD) have been studied as high frequency oscillators for many years.[1]~[5] Traditionally, RTD's are implemented purely as a negative differential resistance element with one energy storage element, the device capacitance. In terms of this design approach, oscillations must be generated by limit-cycles which exchange energy with resonating elements residing in the external bias circuit. This approach of extrinsically inducing oscillations will always encounter output power restrictions by external losses and low frequency design constraints. At the begin of the 90's, Jensen and Buot, in their numerical simulation of a double barrier quantum well system, found that there are intrinsic high frequency current oscillations in RTD. [4] The current oscillations are independent of external circuit. Their results provide evidence for a possible intrinsic approach to high frequency power generation. However, the causes of the intrinsic current oscillations are not clear for about ten years. It is very important to understand the causes of the oscillations since they are important to the intrinsic approach of design of the THz RTD oscillators. In this paper, we will explain the operational principle of the intrinsic THz RTD oscillators, the origin of the intrinsic high frequency current oscillations.

Our explanation of the origin of intrinsic high frequency oscillations is based on our numerical simulation of a resonant tunneling diode. The device model of our RTD is composed of the coupled Wigner–Poisson equations,

$$\frac{\partial f}{\partial t} + \frac{\hbar k}{2\pi m^*} \frac{\partial f}{\partial x} + \frac{2}{\pi} \int_{-\infty}^{\infty} dk' \int_0^{\infty} dy \sin(2y(k-k')) \{V(x-y) - V(x+y)\} \cdot f(x, k', t) + \left[ \frac{\partial f}{\partial t} \right]_{coll} \quad (1)$$

and

$$\frac{d^2 u}{dx^2} = \frac{q^2}{\epsilon} (N_d(x) - n(x)) \quad (2)$$

The parameters used in our simulation are the following. Momentum and position space is broken into 72 and 86 points, respectively. The donor density is  $2 \times 10^{18}$  particles/ $cm^3$ ; the compensation ration for scattering calculations is 0.3; the barrier and well widths are 30 and 50 angstrom, respectively; the simulation box is 550 angstrom; the barrier potential is 0.3eV, corresponding to  $Al_{0.3}Ga_{0.7}As$ ; the device temperature is 77K; the effective mass of electron is assumed to be a constant and equals to  $0.0667 m_0$ ; the

doping extend to 30 angstrom before the emitter barrier and after the collector barrier; the quantum-well region is undoped. Bulk GaAs parameters are used to calculate the relaxation time and the chemical potential. The chemical potential is determined by  $\int_0^{\infty} d\varepsilon \sqrt{\varepsilon} f(\varepsilon) = \frac{2}{3} \mu(T=0)^{3/2}$ , where  $f(\varepsilon)$  is the Fermi distribution function. The relation time used in this paper is 525fs at 77K.

Fig.1 shows the calculated I-V characteristics of the structure used in this paper. This

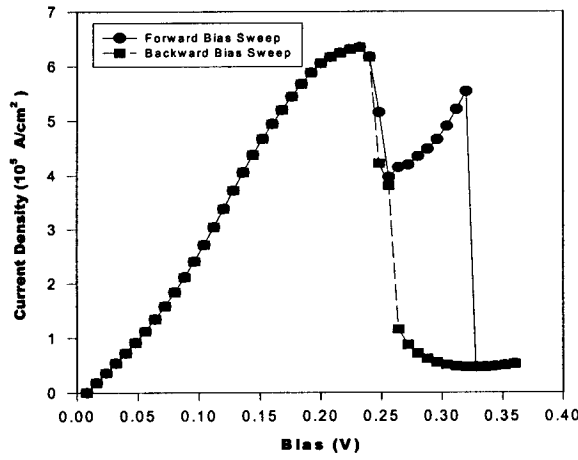


Fig.1 I-V characteristics of RTD. The data are taken from the steady states of the simulation. The values of the current in the BVW are calculated from time-average of the current oscillation.

figure shows all main features of the experimental results: a plateau-like structure and two hysteresis regions. This figure convinces us the correctness of our numerical calculation. Fig.2 shows the relationship between current density and simulation time. From this graph we know that there is a bias voltage window (BVW) in which the current density is oscillatory. The center bias voltage (CBV) of the bias window for the resonant tunneling structure (RTS) employed in this paper is 0.248V. At this bias voltage, the current oscillation is harmonic. Simulation results show if bias voltage is lower than the CBV, the current experiences a damping process at first and then develops into oscillated state. If the bias voltage is greater than the CBV in the BVW, the current densities do not show the initial damping and then harmonic oscillation process that can be observed when bias voltage is less than the CBV. The current gets into a damping process directly with a big initial amplitude. These are the basic features of the current oscillations in the RTS.

Fig.3 shows time-dependent self-consistent potential and electron density at 0.248V . We can see that the current oscillation is concurrent with those of potential and electron density in the whole region of the device. Except the oscillations of potential and density of electron in the whole region of the device, there is emitter quantum well (EQW) in front of the emitter barrier. Of course, the bottom of the EQW oscillates with the increase of the simulation time. Obviously, the current oscillation is related to the creation of an EQW. In our recent paper, we have presented large amount of figures showing the potential and density distribution of electrons in the device. These figures

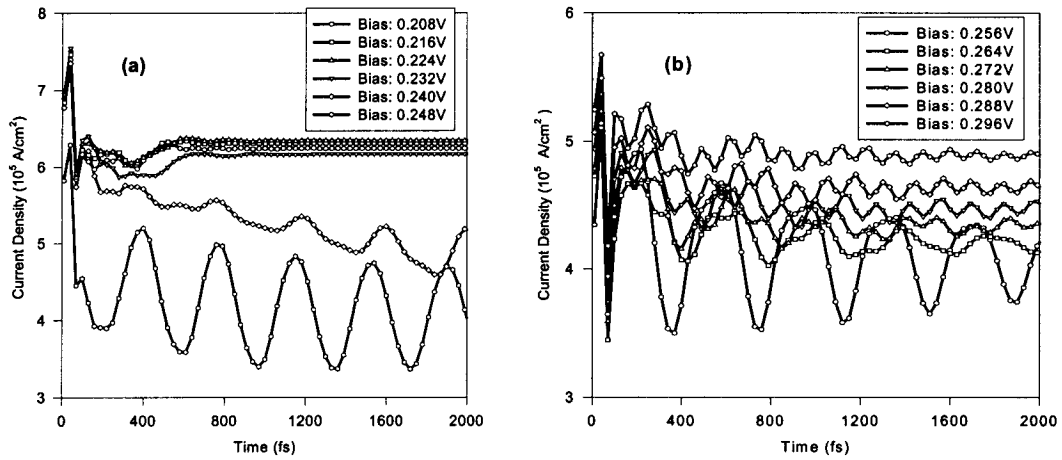


Fig.2 Current-time characteristics of the RTD with bias voltages as parameters in the case of forward bias sweep

and Fig.3 show that the oscillations have the following features. Before the bias get into the BVW, the potential and electron density just irregularly oscillate a short time and then get into stationary state. When the bias just enters the BVW, the potential vibrates a short time before getting into stable oscillation state. The oscillations are

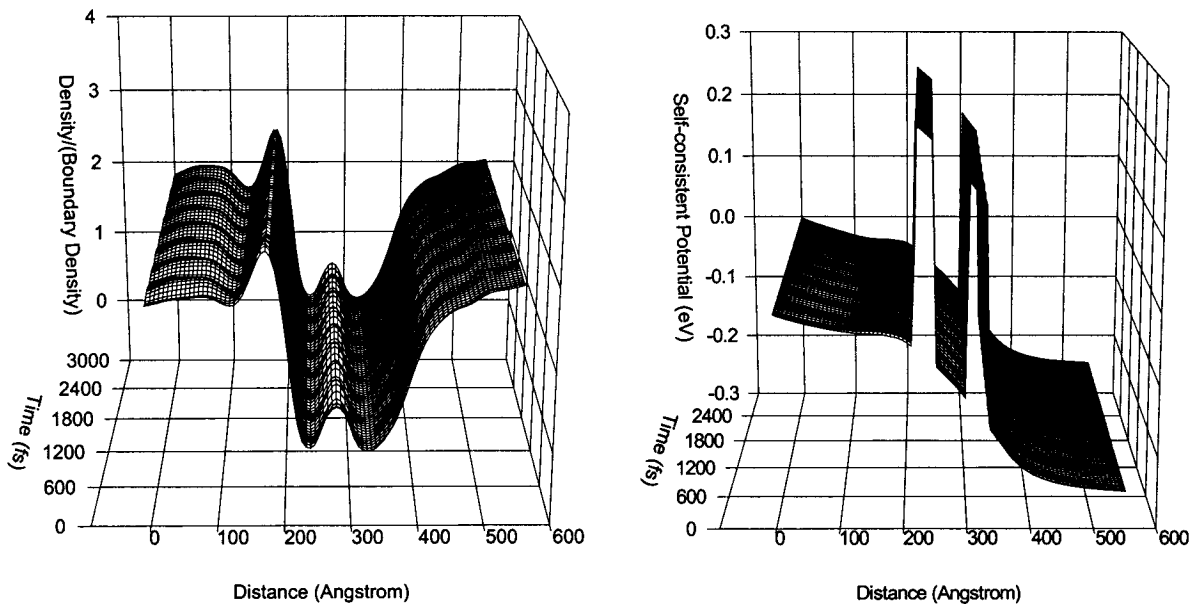


Fig.3 Time-dependent electron density distribution and self-consistent potential at bias voltage 0.248V. The figures show the oscillation of potential and density distribution in stable states. It should be noted that the depth of the EQW is increasing.

periodical rather than irregular. In the BVW, the irregular oscillations of the potential and electron density last a very short time. The potential and electron density get into stable oscillation quickly. After the bias voltage get out of the BVW in the higher bias voltage direction, the current oscillation become a decay oscillation, so do the potential and electron density. These situations last until the bias voltage reaches a special point where the plateau-like structure in the I-V characteristics ended. The oscillation features of potential and density are the same as that of current density stated above.

As we have stated, the oscillation of current is closely related to the creation of an EQW, so do those of potential and density distributions. It is very important to note that the EQW is created just after the current passes the maximum value of the current. Once the current passes the maximum value of the current, the reflection coefficient of the injected electron-wave increases dramatically. Thus, the interference between the injected electron-wave and the reflected electron-wave leads to depletion of electrons in front of the emitter barrier. The depletion of electrons in front of the emitter barrier further leads to a relatively positive charge background thereby an EQW. Once the EQW is created and the energy level in the EQW is separated from the three dimensional states in the emitter, the coupling between the energy level in the EQW and that in the main quantum well will causes the oscillation of current through the double barrier system. Suppose that the wavefunctions for the energy levels in the EQW and the main quantum well (MQW) are expressed respectively as

$$\psi_{EQW}(z, t) = A(z)e^{i2\pi E_{EQW}t/h} \quad (3)$$

and

$$\psi_{MQW}(z, t) = B(z)e^{i2\pi E_{MQW}t/h - \gamma t} \quad (4)$$

The  $\gamma$  factor in Eq.(4) stands for damping caused by electron-phonon interaction. We introduce this factor to the wave-function to reflect the following facts: the energy level in the MQW is next to the three dimensional states of electrons in the emitter and the width of the level is wider than that of the level in the EQW. The value of  $\gamma$  increases with the increase of the applied bias voltage. The total wave function can be expressed as

$$\Psi = c_1\psi_{EQW} + c_2\psi_{MQW} \quad (5)$$

Thus, the current density and electron density can be written, respectively, as

$$\langle \psi | j | \psi \rangle = |c_1|^2 \langle A | j | A \rangle + |c_2 e^{-\gamma t}|^2 \langle B | j | B \rangle + 2 \text{Im}(c_1^* c_2 \langle A | j | B \rangle) e^{i2\pi(E_{MQW} - E_{EQW})t/h - \gamma t} \quad (6)$$

and

$$\langle \psi | \psi \rangle = |c_1|^2 \langle A | A \rangle + |c_2 e^{-\gamma t}|^2 \langle B | B \rangle + 2 \text{Im}(c_1^* c_2 \langle A | B \rangle) e^{i2\pi(E_{MQW} - E_{EQW})t/h - \gamma t} \quad (7)$$

These two equations fully reflect all main features of the simulation results. In Eq.(6), the first term sets the current value at which the oscillation is surrounded at steady states. The second term stands for the damping of the irregularly initial oscillation. The third term represents the oscillation of the current. Separated calculation shows

$\Delta E = E_{MQW} - E_{EQW} \sim 10 \text{meV}$  in BVW. Thus, the current oscillation frequency is in the order of 1THz that coincides with the simulation results shown by Fig.2. In fact, the strength of the oscillations depends on the strength of the coupling between the energy levels and that of the electron-phonon interaction. When bias voltage is small,  $e^{-2\gamma t}$  factor destroys contributions from the second term in Eq.(6) smoothly. However, with the

increase of the depth of the EQW, the strength of the coupling between the two levels increases. The increase of the coupling leads to the increase of the amplitude of the oscillated currents. If this fact balances the effect of electron-phonon interaction, we get a harmonic current oscillation, such as shown by the current oscillation at 0.248V in Fig.2. If the strength of electron-phonon interaction is strong enough, the contribution from the second in Eq.(6) is quickly damped and the influence from  $e^{-\eta}$  in the third term in Eq.(6) gets into effects. This effect is greater at higher bias voltages. Fig.2 confirms our analysis. At bias voltage 0.248V, the self-consistent potential and electron density distribution all exhibit oscillation behaviors. The oscillation of electron density can be qualitatively explained by Eq.(7).

Our simulation results show that there is only one bias voltage region for the device structure employed in this paper in which the current oscillated. With the increase of bias voltage, electron-phonon interaction destroys the current oscillations. Since the structure used in this paper dose not allow another energy level to be created in the EQW, the EQW will collapse once the energy levels exchange their position. The exchange of the position of energy levels leads to the collapse of the EQW and the dramatic decrease of charge density in the main quantum well. The interaction between electron-phonon which dissipates electrons into the EQW, the interaction between the energy levels in the EQW and that in the main quantum, and the applied electric field which drives electrons into the EQW also contribute to the collapse of the EQW and the decrease of the charge density in the MQW. In fact, if the device structure is suitable for the creation of another energy level in the EQW, there will be another bias voltage region in which the current oscillates. [6]

In summary, we have pointed out the operational principle of a THz oscillator in an intrinsic approach. The operation of this kind of oscillators is not relied on external circuit but the intrinsic behavior of micro-particles, the wave behavior. The origin of the current oscillation is traced to the development of a dynamic emitter quantum well and the coupling of its energy level with the level of the main quantum well.

#### **Reference:**

- [1]. R. K. Mains and G. I. Haddad, J. Appl. Phys. **64**, 3564(1988).
- [2]. G. Frazier, A. Taddiken, A. Seabaugh, and J. Randall, IEEE Academic International Solid State Circuits Conference, TP 11.4 (1993).
- [3]. E. R. Brown, in Hot Carriers in Semiconductor Nanostructures (edited by J. Shah), pp469, Academic Press, Boston, 1992; T. C. L. G. Sollner, E. R. Brown, W. D. Goodhue, and H. Q. Le, Appl. Phys. Lett. **50**, 332(1984).
- [4]. K. L. Jensen and F. A. Buot, Phys. Rev. Lett. **66**,1078(1991).
- [5]. Peiji Zhao, H. L. Cui, and D. Woolard, submitted to Phys. Rev. B.
- [6]. Peiji Zhao, H. L. Cui, and D. Woolard, submitted to IEEE/Cornell Conference on AdvConcepts in High Speed Semiconductor Devices & Circuits,2000.

# SuperMix Now Available

F. Rice, J. Ward, J. Zmuidzinas, and G. Chattopadhyay

*California Institute of Technology, 320-47, Pasadena, CA 91125, USA.*

SuperMix, an extensive C++ software library written to aid in the design and optimization of high-frequency circuits, is now available for free download at [www.submm.caltech.edu/supermix](http://www.submm.caltech.edu/supermix). Over the past year SuperMix has been used to develop a terahertz quasioptical SIS receiver design and to optimize the design of a low noise 4-8 GHz HEMT IF amplifier. SuperMix is briefly described in [1].

Containing over 30,000 lines of extensively-documented source code, the SuperMix class library is flexible and complete, allowing users to quickly write, compile, and run sophisticated circuit simulations of arbitrary complexity. By representing circuit components as C++ class objects, the library provides for natural, nearly self-documenting code which reads more like a circuit description than a program. Although primarily intended for superconducting submillimeter circuit design, SuperMix provides a complete set of circuit elements suitable for frequency-domain simulations from DC to the terahertz range. Its lumped elements include detailed HEMT transistor models as well as passive components. Its high frequency distributed elements include standard components such as transmission lines, hybrids, attenuators, etc. What sets SuperMix apart, however, is its inclusion of SIS quasiparticle tunnel junctions and physical transmission line components such as microstrip and CPW lines. The physical transmission line objects can be built up from layers of normal metal and superconducting films and real dielectrics. These components are specified by their material characteristics and dimensions which SuperMix uses to determine electrical behavior.

SuperMix can perform full harmonic balance calculations of SIS quasiparticle receiver designs of arbitrary complexity as well as mixer gain and noise analyses using any number of harmonics and including any number of superconducting tunnel junctions. Its algorithms and capabilities in this regard are described in [2].

SuperMix performs circuit calculations using a wave matrix representation and automatically includes full noise calculations. It can freely convert results between wave and impedance or admittance representations. Supermix includes a sophisticated multiparameter optimizer. Users can quickly tailor the optimizer's error function to their exact needs; the optimizer can then control any set of device parameters in order to refine a circuit design. To achieve this level of flexibility, SuperMix contains a rather complete numerical math library for manipulation of complex-valued matrix, vector, and scalar functions and objects. It includes robust linear algebra, interpolation, integration, root finding, and minimization routines.

SuperMix includes a large set of formatted input and output routines for complex-valued matrix and vector data. SuperMix can construct interpolated circuit elements from Touchstone formatted data. If the provided routines are inadequate for a specific application, the user can easily add to the input/output capabilities using an extensive set of primitives. Of course, since the user creates simulations by writing a C++ program, the full capabilities of the standard C++ class libraries are available as well.

SuperMix is designed to run under Unix or Linux. It currently requires the free g++ (or gcc) compiler, available on most systems. It has been thoroughly tested on Solaris and Intel Linux platforms. Information regarding the system requirements and how to install and use the library are provided in the README files accompanying the library distribution file.

## REFERENCES

- [1] J. Ward, F. Rice, G. Chattopadhyay, and J. Zmuidzinas, "SuperMix: a flexible software library for high-frequency circuit simulation, including SIS mixers and superconducting elements," *Proc. Tenth International Symposium on Space Terahertz Tech.*, pp. 269–281, 1999.
- [2] F. Rice, J. Ward, J. Zmuidzinas, and G. Chattopadhyay, "Fast harmonic balance of SIS mixers with multiple junctions and superconducting circuits," *Proc. Tenth International Symposium on Space Terahertz Tech.*, pp. 282–297, 1999.

# Simulated performance of multi-junction parallel array SIS mixers for ultra broadband submillimeter-wave applications

M. Salez<sup>1</sup>, Y. Delorme, M.-H. Chung, and F. Dauplay

DEMIRM, Observatoire de Paris  
77 avenue Denfert-Rochereau, 75014 Paris, France

## 1. INTRODUCTION

Heterodyne receivers using Superconductor-Insulator-Superconductor (SIS) tunnel junction mixers are the most sensitive at millimeter and submillimeter wavelengths [1]. They are widely employed at ground-based radiotelescopes worldwide, and increasingly in air-borne and space-borne receivers, notably in projects now under development (SOFIA, FIRST, ISS). Today, an important part of the research in this field aims at developing receivers combining ultra wide bandwidths (around 30% relative or more) with ultra low-noise capabilities (a few times the quantum limit), with no mechanical tuning. This goal has been an incentive to explore either new tunnel barrier materials or new types of circuits.

Most mixers use end-loaded single-junction [2,3] or twin-parallel junction [4] designs, where an inductive circuit tunes out the capacitance of the tunnel barrier for the right frequency. In such circuits, the SIS junction's quality factor  $Q=\omega RC$ —where  $R$  and  $C$  are respectively the junction normal resistance and capacitance—sets the maximum achievable relative bandwidth over which the SIS junction can be tuned and impedance-matched to a given source impedance [5]. This matching/tuning bandwidth limitation inevitably translates into conversion gain and mixer noise temperature bandwidth upper limits.

In practice, tuning circuits are integrated with the SIS junctions in thin film technology. They often consist of strongly coupled microstrip structures using either superconductor or normal metal films depending on frequency [6]. A classical circuit with one junction is illustrated in Fig. 1.

Recently, a new kind of SIS mixer based on a distributed array of  $N$  ( $N>2$ ) junctions parallel-connected by microstrip lines was proposed by the Nobeyama Radio Observatory (NRO) group [7] to free the RF coupling bandwidth—and hence the mixer bandwidth—from the junction's  $RC$  product. It can also be viewed as the discrete version of the distributed non-linear quasiparticle SIS mixer proposed by Tong et al [8], also offering high sensitivity over wide bandwidths. The very encouraging experimental results reported by the NRO group [9,10] suggest that this type of circuits might be ideal

---

<sup>1</sup> email : morvan.salez@obspm.fr

to provide tunerless mixers with quantum-limited sensitivities and arbitrarily large bandwidths.

These results have triggered our interest in these circuits as potential solutions for wideband tunerless DSB mixers, such as those needed for FIRST/HIFI. We also believed some optimization could still be done in order to improve the response of the arrays over a particular bandwidth.

## 2. PECULARITIES OF SIS PARALLEL ARRAY MIXERS

The SIS parallel array proposed by the NRO group [7, 9, 10] consists of a microstripline periodically loaded with identical SIS junctions or, put differently, of a number of cells composed each of a junction and a section of microstrip which will resonate at some frequency. In its principle, such a distributed array strongly resembles the long distributed SIS junction mixer investigated by Tong et al [8,11] which yielded excellent measured heterodyne performance (conversion loss above -3dB and DSB mixer noise temperature around 20 K from 400 GHz to 500 GHz). They have over their cousin one advantage, though, in that they do not require electron beam lithography to fabricate the long junction, and therefore are a much more accessible technology.

In their simulations, Shi et al have changed the length of microstrip line between two adjacent junctions, and the number of junctions. They could show that a parallel array allows—unlike single-junction tuning circuits—mixer bandwidths much larger than  $\sim 1/\omega RC$  and that, the larger the number of junctions, the better the mixer and the wider the bandwidth [7]. In their experiments [8], they could clearly confirm the improvement on noise and bandwidth gained by going from a five- to a ten-junction array. They measured  $T_{rec}$  (DSB) around 200 K and at some frequencies as low as 100 K from 320 to 530 GHz, using a 10-junction array with  $j_c=3.5$  kA/cm<sup>2</sup>. According to these authors, the bandwidth of arrays with large numbers of junctions ( $N>5$ ) should be independent on the value of  $Q$ , and the length of microstrip between two junctions should not be too critical a tuning factor.

One big advantage of parallel arrays is to alleviate the need for high current density junctions—that one usually confronts with single-junction mixers in an attempt to reduce  $RC$ —which not only complicates the SIS device fabrication, reduces the yield, but also degrades the  $I-V$  quality. At submillimeter wavelengths one often shoots for 10-20 kA/cm<sup>2</sup> SIS tunnel barriers. At lower current densities, with single-junction tuning, the junction's impedance transformed by the microstrip,  $Z_t = R_n/(1+Q^2)$ , would become exceedingly small and hard to match to the source. On the other hand we know that at high current densities SIS mixers are doubly penalized: first, their conversion efficiency drops due to the smoother  $I-V$  bend and larger subgap leakage current; second, the excess shot noise caused by multiple-Andreev reflections increases, and can up to double the mixer noise [12]. In comparison, parallel arrays then only need a few kA/cm<sup>2</sup>. Indeed, if  $j_{c0}$  was the current density required for a single-junction tuning circuit mixer, one could use arrays with a current density of only  $j_{cN} \approx j_{c0}/N$ .

There is a limit to the number of junctions that can be packed in a parallel array mixer, however, since it will be a technological challenge to produce high-quality wafers with  $N$  identical junctions on every chip when  $N$  is too high.

Both in simulations and experiments, Shi et al. have noticed ripples across the band, both on the DSB mixer noise (fluctuations of several 100 K) and on the gain (up to 5 dB). We have found similar noise and gain curves (Fig. 2) when we simulated the same arrays with  $N=5$  and  $N=10$  that were described in [7, 9]. Actually, our mixer noise and gain simulations of parallel arrays—although using a different algorithm—have qualitatively confirmed all features of the mixer performances reported by Shi et al. These authors hinted at a few avenues which could be explored to minimize these ripples, one of them being to play with the array parameters at our disposal: junctions size, spacings between junctions, width of microstrips.

Grossly, a parallel array mixer with  $N$  SIS junctions functions as a non-linear filter with  $N$  poles. To take full advantage of this property—and to minimize the ripples—we have made the spacings between two adjacent junctions non-uniform along the array.

### 3. DESIGN OPTIMIZATION

Obviously, many non-uniform array configurations would be solutions to the problem and would be hard to guess, so we needed a software to efficiently optimize the electrical lengths and characteristic impedances of the striplines connecting the junctions. We did that using HP Libra's optimizer. We fixed the technological parameters (e.g., microstrip dielectric layer, junction's capacitance and normal resistance) and set as free parameters the spacings (electrical lengths) between junctions and the microstrip width (impedance) to run the circuit design optimization. The criteria of convergence were to reach a certain coupling bandwidth and to stay below a certain level of ripple. With similar initial and limit conditions fed into the optimizer, several different array configurations came out.

In previous works, the source impedance was simply assumed to be the characteristic impedance of the microstrip line leading to the array. This is not so in the case of a practical mixer, and the whole embedding impedance, including waveguide cutoff and RF coupling response must be considered. The source impedance assumed for our circuit optimization was derived from independent 3D EM simulations of our tunerless waveguide mixer mount, well suited to broadband applications in the 480 GHz-650 GHz range and available for heterodyne tests [13]. This mixer mount provides the input of the integrated circuits with a nearly constant and real impedance of  $\sim 70 \Omega$  over the whole bandwidth, as shown in Fig. 3.

Then, we took these sets of optimized electrical lengths and characteristic impedances of the microstriplines to a Mathcad program, to translate these into physical dimensions. The software computes the  $S$  parameters of any superconductive 1-D microstrip circuit [6], and takes into account the fringing field via Wheeler's formulas.

The Mattis-Bardeen formalism which describes the RF losses in the superconductor in the vicinity of the gap frequency was not used here. Table 1 provides the geometries of three parallel arrays A, B and C, optimized for slightly different frequencies; as an example, the mask of one is shown in Fig.4. Their expected  $S_{11}$  response is shown in Fig5. All have  $N=5$  junctions. We chose this number as a reasonable compromise between fabrication complexity and yield constraints, and parallel array efficiency. In the calculations, we assumed the use of Nb/SiO/Nb microstriplines and of Nb/AlO<sub>x</sub>/Nb junctions characterized by a current density  $j_c=10$  kA/cm<sup>2</sup> and a specific capacitance  $C_J=80$  fF/ $\mu\text{m}^2$  (the empirical law  $C_J(\text{fF}/\mu\text{m}^2)=40+4 \cdot j_c$  (kA/cm<sup>2</sup>) [1] was used).

Before simulating—or measuring—the heterodyne performance of these array mixers, we needed to apply the same optimization treatment to the design of more conventional single-junction and twin-parallel junction mixers, to make meaningful comparisons. In the single-junction design, the SIS junction impedance is matched to the desired source impedance by one short inductive section of microstrip followed by two cascading ‘quarter-wave’ sections. All the impedances and electrical lengths of this ‘maximally flat’ Tchebychev transformer were optimized for our bandwidth using HP Libra, prior to being converted into actual superconductive microstrips dimensions.

A non-periodically SIS loaded transmission line is a strongly non-linear device, however, and our circuit optimization has entirely skipped that fact, oversimplifying the true nature of SIS junctions. On one hand we have neglected the non-linear Josephson tunneling currents. On the other hand we have traded the non-linear, bias- and LO-dependent quasiparticle conductance for the plain normal conductance. Therefore, the array was optimized for energy transfer only, on the basis of its similarity with a passive  $N$ -pole filter, and not as a mixing device. But our noise and gain simulations based on quantum theory of mixing will later tell us whether optimizing the junction array this way also optimizes its mixing properties. Let us add that we have used HP Libra not only to optimize the circuits for a given  $R$  and  $C$ , but also to select these two parameters after a statistical analysis in the case of single-junction circuits. The typical dispersion range on fabrication parameters was plugged in, and the current density and junction area were chosen, not on the basis of the *best results* but instead of the *best yield* to expect for any given run.

Assumed fabrication parameters:	Cell number ( $N=5$ )	Optimized cell geometry : $L(\mu\text{m}) \times w(\mu\text{m})$		
		Circuit ‘A’	Circuit ‘B’	Circuit ‘C’
Junction current density $J_c$ : 10 kA/cm <sup>2</sup>	1	49.5 / 4.5	44 / 5	58 / 4
Junction capacitance $C_J$ : 80 fF ( $1\mu\text{m}^2$ area)	2	6 / 5	7 / 7	14 / 5
Penetration depth $\lambda$ (Nb): 85nm	3	12 / 5	11 / 7	12 / 5
Dielectric constant $\epsilon_r(\text{SiO})$ : 5.7	4	42 / 5	44 / 7	58 / 5
Dielectric thickness $h$ :200 nm	5	20 / 5	18 / 7	32 / 5

Table 1. Technological parameters assumed for the design and optimized geometries (i.e. length and width of the microstrip cells) of 5-junction arrays A, B and C.

#### 4. ARRAY MIXER PERFORMANCE ANALYSIS

We have merged the theory of superconductive microstrip lines with the quantum mixing formalism developed by Tucker [1], in the three-port approximation, within a specially developed software allowing us to simulate the heterodyne performances of the SIS mixer circuits, regardless of the number of junctions. The algorithm for the mixer noise temperature and conversion gain calculation is based on the work by Tong et al [11], which was applied to the theory of mixing in superconducting quasiparticle non-linear transmission lines. Figure 6 shows the equivalent circuit corresponding to the calculation. The source admittance  $Y_s$  directly relates to the embedding impedance  $Z_{emb}(\omega)$  seen by the array at its feeding point. The array is terminated by some admittance  $Y_t$ —in our case  $Y_t=0$  for an open circuit. Each cell  $i$  corresponds to a small section of microstrip line loaded with the  $i^{th}$  junction of admittance  $Y_{c,i}+jC_i\omega$ , and can be fully modelled by its ABCD matrix, defined in the small signal analysis by:

$$\begin{pmatrix} v_i \\ i_i \end{pmatrix} = \begin{pmatrix} A_i & B_i \\ C_i & D_i \end{pmatrix} \begin{pmatrix} v_{i+1} \\ i_{i+1} \end{pmatrix}$$

In the three-port approximation model, small currents  $i_i$  and voltages  $v_i$  are 3x1 column vectors projected upon the upper and lower sidebands ( $\omega_{+l,-l}$ ) and the intermediate frequency ( $\omega$ ); and every admittance is therefore represented by a 3 x 3 conversion matrix: these matrices are diagonal for linear admittances ( $Y_s$  and  $Y_t$ ), and non-diagonal for all the non-linear quasiparticle admittances  $Y_{c,i}$  responsible for frequency conversion. Since the array's dimensions are comparable to the wavelength in the microstrip, all conversion matrices  $Y_{c,i}$  must include the LO phase variation at the SIS junction location. The ABCD matrix defining the parallel array circuit is defined by:

$$\begin{pmatrix} v_o \\ i_o \end{pmatrix} = \prod_{n=1}^N \begin{pmatrix} A_n & B_n \\ C_n & D_n \end{pmatrix} \begin{pmatrix} v_n \\ i_n \end{pmatrix} = \begin{pmatrix} \mathbf{A} & \mathbf{B} \\ \mathbf{C} & \mathbf{D} \end{pmatrix} \begin{pmatrix} v_n \\ i_n \end{pmatrix}$$

Since  $i_n=Y_t \cdot v_n$ , we can derive the complete conversion admittance matrix of the array:

$$Y_{array} = \frac{i_o}{v_o} = \frac{(\mathbf{C} + \mathbf{D} \cdot Y_t)}{(\mathbf{A} + \mathbf{B} \cdot Y_t)}$$

If we define the augmented admittance  $Y^{aug}$  as the sum of the source admittance  $Y_s(\omega)$  and  $Y_{array}$ , we can compute the conversion efficiency of any parallel array mixer:

$$G_{SSB} = 4 \cdot \text{Re}(Y_s(\omega_1)) \cdot \text{Re}(Y_s(\omega_0)) \cdot |Z_{01}^{aug}|^2$$

where  $Z^{aug} = (Y^{aug})^{-1}$ .

A similar equivalent circuit as in Fig. 6 was used to calculate the single sideband mixer noise of the junction array. We added to each cell  $m$  a current source (connected in parallel) modelling the shot noise produced by the  $m^{th}$  junction (Again, all small currents and voltages are 3x1 column vectors transformed by the same 3x3 admittance matrices as above). We can legitimately assume that these shot noise sources from different junctions are not correlated, and therefore the total noise produced by the array

at the IF port is merely the sum of the shot noise contributions from all junctions. Since the averaged noise voltage produced at the IF port by any  $m^{\text{th}}$  junction is

$$\langle |V_n^m|^2 \rangle = \sum_{k=-1}^1 \sum_{l=-1}^1 Z_{0k}^m \cdot (Z_{0k}^m)^* \cdot H_{kk}^m,$$

the SSB mixer noise temperature of the whole array can be written:

$$T_{SSB} = \frac{\text{Re}(Y_s(\omega_0))}{k_B \cdot G_{SSB}} \cdot \sum_{m=1}^N \langle |V_n^m|^2 \rangle$$

The algorithm was programmed in C++ and run on a Pentium PC under Linux environment. The software called several input files containing the circuits parameters and geometries, and the complex impedance for all frequencies calculated with CST-Mafia. For each run, the LO pump and the bias voltage could be swept across a chosen range; the output files contained both the noise-optimized data but also the complete set of non-optimized values. The LO voltages across the junctions—calculated using Withington et al's voltage update method [14]—were also stored separately as output data.

## 5. RESULTS

Using the software, we could compute the mixer gain and noise to expect from all the circuits that had been already optimized with HP Libra, and for any frequency, bias voltage and LO incident power. First, we tested our code using for inputs the technological parameters and the geometry of the circuits analyzed by Shi et al [7], for the same numbers of junctions and equivalent inter-junction spacings (i.e., same  $\omega L/R_n$ ), and having set the source impedance to the same value (a typical microstrip source impedance for the center frequency). Figure 2 provides a sample of these simulations. Our results were strikingly similar to those of NRO, in spite of the different algorithm used; we found the same conversion gain and noise, and in particular, large ripples in those curves at the exact same frequencies where they were observed by the NRO group. Yet, we noticed that our ripples would tend to be rounder and smoother than those, peaking rather sharply—especially in the noise curves, found by Shi et al.

We could confirm the major influence of the spacing lengths on the frequency occurrence of the ripples and the band roll-off. We also investigated junction arrays with spacings across the array non-uniform, and arbitrarily varied. They showed a mixing performance degradation at certain frequencies and an improvement at some other, in an unpredictable manner. Optimizing the non-uniform arrays was the next step to set the roll-off at the right frequency and to contain the noise ripple within acceptable limits.

In order to compare them to the  $S_{11}$  calculations, all our mixer noise and gain calculations now assumed the use of one-square-micron junctions with a current density of about 10 kA/cm<sup>2</sup> ( $R=20 \Omega$ ,  $C=80$  fF), regardless of the number of junctions. The

technology parameters (films thicknesses, dielectric constant, fringing field factor) were kept identical.

Fig.7 shows the heterodyne performance to expect from the optimized classical approach: a junction end-loading a three-section Tchebychev transformer, similar to the drawing in Fig.1, superimposed with that of the simplest SIS array of all: a twin-parallel junction circuit designed for the same frequency band. At every frequency, the voltage bias and LO power—the latter being shown on the same figure—were optimized for minimum double-sideband mixer noise. With no surprise, we find that the twin-parallel circuit provides substantially wider bandwidth than the single-junction with its matching transformer, and seems sufficient to achieve a relative 30% bandwidth—at least when one uses a quasioptical antenna or a waveguide mount for which the embedding impedance is almost purely real and constant.

Fig.8 shows the calculated optimum DSB mixer noise temperature, DSB conversion gain, and consumed LO power for the 5-junction array labelled 'A' (see Table 1). The design of this array was particularly aimed at the 480-640 GHz bandwidth. By far, it provides the widest bandwidth of all, clearly extending beyond the 55% relative bandwidth that can be displayed on the graph. The noise bandwidth is therefore larger than what had been projected from Mathcad/HP-Libra  $S_{11}$  calculations. On the other hand, the ripples in the noise and gain curves do not quite reproduce what was seen in Fig.5. This is only half a surprise, and it demonstrates the need for a full Tucker mixer analysis to discriminate efficiently between several parallel array circuits prior to fabrication, and obviously, to finely understand the heterodyne results in the laboratory. In particular, it is clear that the predicted array's behaviour is drastically changed when one replaces the constant source impedance usually assumed for mixer analyses by the complex—and more realistic—mixer mount impedance which changes with frequency. The conversion is much better than  $-8$  dB over the whole band, with conversion *gain* possible at some frequencies.

The LO power required to pump optimally a given type of SIS circuit is a major criterion for practical submillimeter-wave receivers. In a single-junction circuit with a three-section transformer, the LO power reaches a maximum of about 250 nW at the center of the band, where the conversion loss and the mixer noise both undergo a local maximum (see Fig. 7); this is a plain consequence of the 'twin-peak'-shaped response of such Tchebychev transformers when stretched to their maximum available bandwidth, and it could already be seen in the  $S_{11}$  parameter. The twin-parallel junction offers a slightly broader bandwidth, as expected, a similar LO power of 300 nW with, too, local minima coinciding with the local maxima of the mixer noise and conversion loss.

We see in Fig. 8a that for an optimized 5-junction array, the LO power is not five times higher than that needed for a single junction of same current density, as one could have expected; the LO is almost constant across the band, near 300 nW, about equal to the amount of LO needed for a single-junction mixer at the center of the band. This point is to relate to an important issue in arrays: the uniformity with which the LO power is being absorbed by the junctions. The LO pumping level is a critical factor for the SIS mixer performance, thus it is important to know whether some junctions of the

array are insufficiently or over-pumped; playing a fully passive tuning role; simply contributing noise to the mixer. Because of the phase delays between two adjacent junctions, we expect a non-uniform array to exhibit a complex, non-uniform LO power distribution, changing with frequency. This is precisely what the five curves of Fig. 9 show us in the case of 'A'. They represent, plotted versus frequency, the calculated distribution of the LO voltage (normalized to  $hf/e$ ) across each of the 5 junctions of an array. The interweaving of the curves as frequency changes seems to corroborate the importance of the LO phase in the array, causing unequal pumping and possibly unequal mixer noise contribution.

From our results, it appears that the arrays were probably correctly optimized for energy transfer (the mixer bandwidth is correctly centered, and larger than expected from the  $S_{11}$ ), but not necessarily for heterodyne mixing (the conversion loss is a little high; there is more ripple than expected in the conversion gain and in the noise). We conclude, therefore, that a true optimization for sensitivity-bandwidth of the array design requires one to apply a complete mixer analysis to those circuits.

Yet, the non uniform junction distribution resulting from our considering the arrays as bandpass filters and their optimization, looks like a positive step. The ripples are less than in the periodically loaded arrays and the theoretically achievable mixer noise bandwidth is wider. We can safely conclude that with minor improvements the  $N=5$  circuits will provide mixer bandwidths much wider than  $1/RC$  with a DSB mixer noise less than three times the quantum limit.

## 6. PERSPECTIVES

Obviously, more than one parameter can be played with to curtail the broadband response of a parallel array SIS mixer. We have varied the intervals between junctions only, but we could have made the junctions area (hence their capacitance) non uniform as well. We found that the distribution of the LO voltage in the array is non-uniform due to the LO phase, and this needs further investigation. Possibly, certain array configurations, although optimum from the standpoint of the  $S_{11}$  response, provide lousy mixer performances because some of the junctions are under- or over-pumped, and merely add noise to the array. Should this turn out to be a problem, we suggest the arrays be optimized not via their spacings between junctions, but via the junctions areas, therefore allowing a uniform—and appropriately defined—electrical length for all microstrip cells.

The Tucker formalism of quantum mixing is most often used in its simplest three-port approximation, generally justified by the large capacitance of SIS junctions, shorting the LO harmonic frequencies at the expense of quasiparticle tunneling. The strongly non-linear response of the parallel array mixer, however, compels us to look into at least the first LO harmonic in the mixer analysis. In another work [15], we report on the analysis of noise and gain in a parallel 3-junction array using both the three-port and the five-port approximations. Comparing the simulation results, we found a

substantial difference in the gain bandwidth, which one could possibly attribute to the importance of the first LO harmonic. We will soon apply this 5-port mixer analysis to arrays with any number of junctions.

Another area of investigation deals with the incidence on mixing performance of the Josephson effect in these devices. One should expect such parallel arrays—analogs to a parallel-connected SQUIDs—to exhibit dynamical regimes of the Josephson tunneling current, including fluxon motion, as one applies an external magnetic field. From the standpoint of the electrical model, distributed arrays of small junctions are identical to long Josephson junctions. Hence one should expect their  $I$ - $V$  characteristics to display the equivalent of well-known features like Zero-field steps and Fiske steps. It remains to be seen, from simulations and experiments, whether these peculiar AC current regimes will be sources of noise or instabilities for the SIS mixer or not. This problem pertains to how one should quench the LO-driven Shapiro steps with an external magnetic field, as currently done with SIS receivers.

## 7. CONCLUSION

We have used a combination of softwares to optimize the design of parallel-array SIS mixers with  $N=1, 2$  and  $5$  junctions for the same band  $480$ - $640$  GHz. The electrical lengths separating two adjacent junctions were made non uniform in order to curtail the bandpass filter-type response of those circuits over a desired band (more than  $30\%$  relative bandwidth around  $560$  GHz) and in particular to minimize the ripples reported in the case of periodically loaded arrays. We have applied a three-port Tucker mixer analysis to these optimized designs, to investigate their expected mixer noise temperature and conversion gain versus frequency, bias voltage and LO power. We used the embedding impedance of our waveguide mount—computed by a 3D EM software—as the source impedance. We confirm the strong qualitative difference, in terms of mixer noise, conversion gain and LO power needed versus frequency, between the single-junction, twin-parallel junction mixers and the  $5$ -junction array mixers. The level of ripples in the noise is slightly higher than anticipated from the optimization phase. Also, not all three optimized parallel-junction circuits behave identically. Although it seems easier to achieve a flat mixer noise over a  $30\%$  relative bandwidth using the twin-junction mixer, parallel array mixers with  $N=5$  can produce much larger bandwidths at a comparable sensitivity. The required amount of LO power is nearly constant over the whole band and does not exceed that needed by a single-junction mixer at the band center. As anticipated, the distribution of LO voltage within the  $5$ -junction array is not uniform: certain junctions do most of the mixing while others only act as tuning elements; however, in our design, the junctions swap roles as LO frequency changes. This can explain the increase of LO power consumption being non-linear with  $N$  as reported by Shi et al.

It may be too early to conclude that multi-junction array mixers are the most solid answer to the need for tunerless broadband mixers. But it is safe to say that they

represent a satisfying alternative to single-junction and twin-parallel junction mixers. Aiming at the specifications we used for the simulations ( $j_c=10\text{-}15\text{ kA/cm}^2$ ;  $1\text{-}\mu\text{m}^2$  Nb/AlOx/Nb junctions), we have begun the fabrication of batches of circuits at our facility and will report on the heterodyne measurements later. In this study, we have chosen  $N=5$  as a reasonable trade-off between performance and complexity, but more—or less—junctions could have been used. Of course, the unique broadband properties of optimized parallel SIS arrays apply not only to heterodyne mixing but also to direct detection.

#### ACKNOWLEDGEMENTS

This research is partly funded by the Centre National d'Etudes Spatiales, (contract #714/CNES/99/7759/00), and by the Centre National de la Recherche Scientifique (CNRS), Institut National des Sciences de l'Univers. F. Dauplay has been sponsored by CNES. We thank Profs. T. Noguchi and J. Zmuidzinas for helpful discussions, the HIFI consortium for stimulating exchange, and Y. Viala, J-M. Krieg, and G. Beaudin for support.

#### REFERENCES

1. J. R. Tucker and M. J. Feldman, 1985, "Quantum detection at millimeter wavelengths", *Rev. Mod. Phys.*, **57**, 1055
2. J. W. Kooi et al., 1994 "180-425 GHz Low Noise SIS Waveguide Receivers Employing Tuned Nb/AlOx/Nb Tunnel Junctions" *Int. J. of Infrared and Millim. Waves*, **15**, 5, 783
3. C.-Y. E. Tong, R. Blundell et al., 1995, "A fixed tuned low noise SIS receiver for the 600 GHz frequency band", *Proc 6<sup>th</sup> Intl. Symp. Space THz Tech.*, 295
4. J. Zmuidzinas, H. G. LeDuc, J. A. Stern and S. R. Cypher, 1994, "Two-junction tuning circuits for submillimeter SIS mixers", *IEEE Trans. Microwave Theory Tech.*, **MTT-42**, 698
5. R. M. Fano, 1950, "Theoretical limitations on the broadband matching of arbitrary impedances", *J. of the Franklin Institute*, **49**, 57, 139.
6. P. Febvre, W. R. McGrath, P. Batelaan, B. Bumble, H. G. LeDuc, S. George, and P. Feautrier, 1994, "A low-noise SIS receiver measured from 480 GHz to 650 GHz using Nb junctions with integrated RF tuning circuits", *Int. J. of Infrared and Millim. Waves*, **15**, 6, 943.
7. S.-C. Shi, T. Noguchi and J. Inatani, 1997, "Analysis of the bandwidth performance of SIS mixers with distributed junction arrays", *Proc. 8<sup>th</sup> International Symposium on Space Terahertz Tech.* 81.
8. C.-Y. E. Tong, R. Blundell, B. Bumble, J.A. Stern, and H.G. LeDuc, 1995, "Quantum-limited heterodyne detection in superconducting nonlinear transmission lines at sub-millimeter wavelengths", *Appl. Phys. Lett.*, **67**, 9, 1304
9. S.-C. Shi, T. Noguchi, J. Inatani, Y. Irimajiri, and T. Saito, 1998, "Experimental results of SIS mixers with distributed junction arrays", *Proc. 9<sup>th</sup> International Symposium on Space Terahertz Tech.* 223
10. T. Noguchi, S.-C. Shi, H. Iwashita, and M. Takeda, 2000, "Low-noise SIS mixers with a parallel array of junctions at submillimeter wavelengths", *Proc. of the SPIE Conference 'Astronomical Telescopes and Instrumentation'*, March 27-31, Munich, Germany, *in print*
11. C.-Y. E. Tong, L. Chen, and R. Blundell, 1997, "Theory of Distributed Mixing and Amplification in a Superconducting Quasiparticle Nonlinear Transmission Line", *IEEE Trans. Microwave Theory Tech.*, **MTT-45**, 1086
12. P. Dieleman, J. R. Gao, and T. M. Klapwijk, 1998, "Doubled shot noise in niobium SIS mixers", *Proc. 9<sup>th</sup> International Symposium on Space Terahertz Tech.* 235
13. M. Salez, Y. Delorme, F. Dauplay, B. Marchand, and B. Lecomte, 2000, "Design of a fixed-tuned 30% bandwidth SIS receiver for FIRST/HIFI band 1 (480-640 GHz) and other space applications", to

appear in *Proc. 4<sup>th</sup> European Workshop on Low Temperature Electronics*, WOLTE 4, June 21-23, Noordwijk, The Netherlands

14. S. Withington and E. L. Kollberg, 1989, "title" *IEEE Trans. Microwave Theory Tech.*, **MTT-37**, 231
15. M.-H. Chung and M. Salez, 1999, "Numerical simulation based on a five-port model of the parallel SIS junction array mixer", *Proc. 4<sup>th</sup> European Conference on Applied Superconductivity*, EUCAS'99, September 14-17, Sitges, Spain

## FIGURES

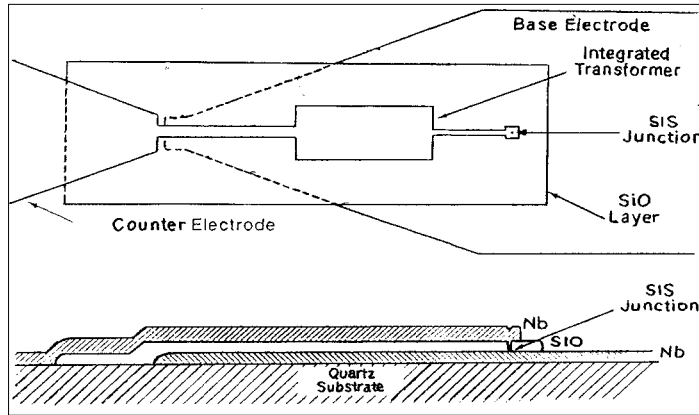


Fig. 1. (a) top and (b) cross-sectional view of a typical single SIS junction microstrip tuning circuit, using a Tchebychev transformer.

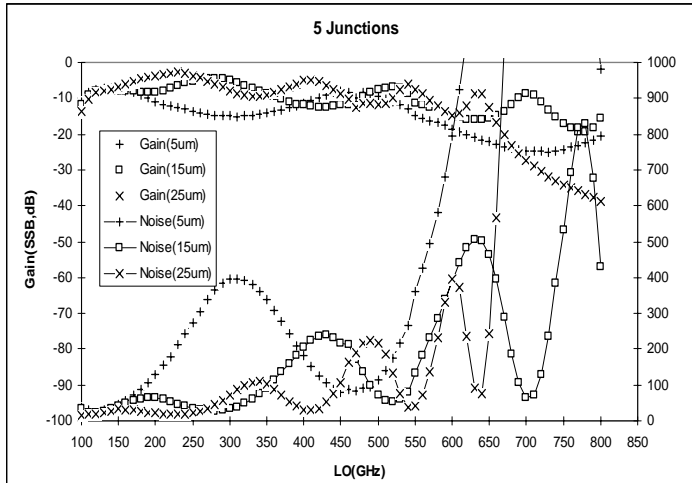


Fig. 2. Simulation of the gain and noise of a periodically loaded 5-junction array mixer, with  $d=15, 20$  and  $25 \mu\text{m}$  spacings. The source admittance was set to  $8 \Omega$  and assumed frequency independent.

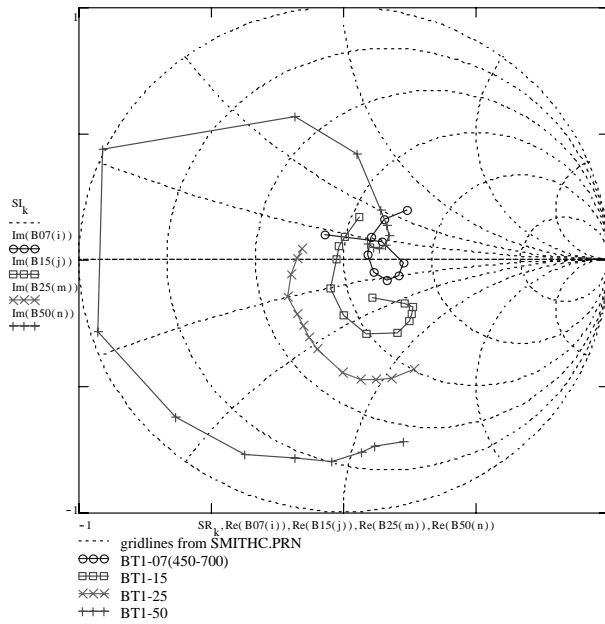


Figure3. Simulated source impedance of the tunerless waveguide mixer mount for different backshort positions. At  $d=0.07\lambda_g$ , this mixer mount provides the input of the integrated circuits with a nearly constant and real impedance of  $\sim 70 \Omega$  over the whole bandwidth.

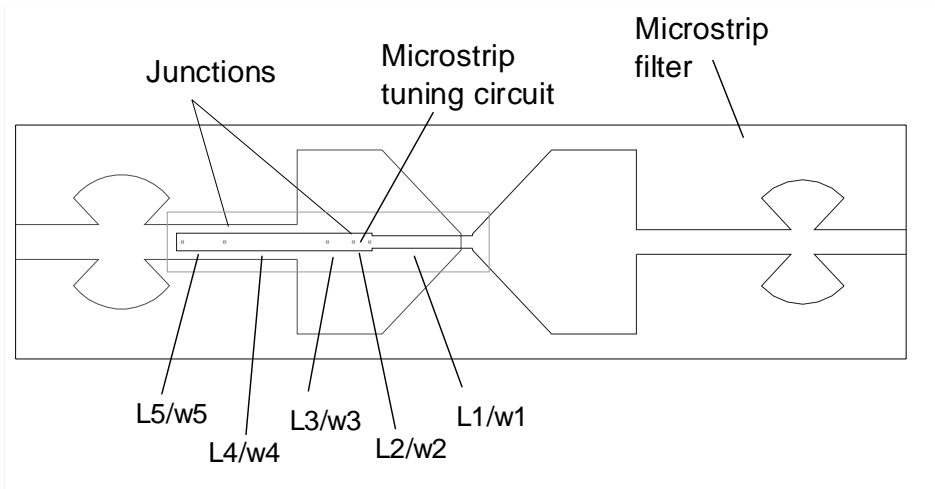


Figure 4. Fabrication mask of a 5-junction array circuit 'A' for 480 - 640 GHz.

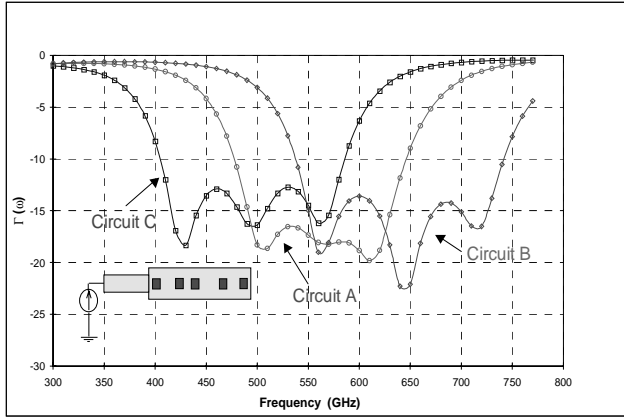


Figure 5. Simulated reflection of three non-uniform 5-junction array circuits designed for a 160 GHz bandwidth at 3 different central frequencies: 520GHz (C), 560GHz (A) and 600GHz (B).

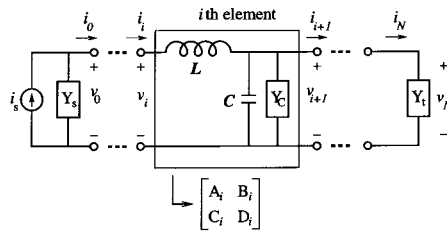


Figure 6. Equivalent circuit of noise analysis in the parallel junction array. The quasiparticle non-linear admittance is represented by its  $3 \times 3$  conversion matrix, and the shot noise produced by the junctions are represented by current sources connected in parallel at the output of each cell.

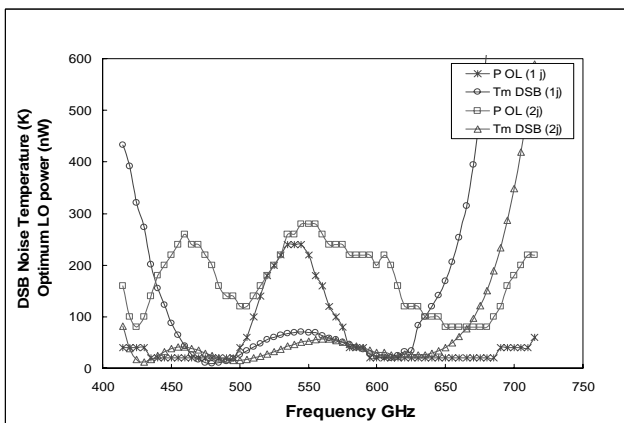


Figure 7. Optimal LO power and double-sideband mixer noise temperature to expect for a single and twin-junction circuits.

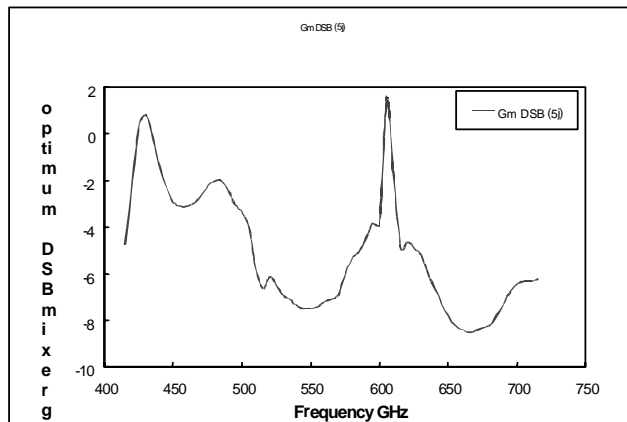
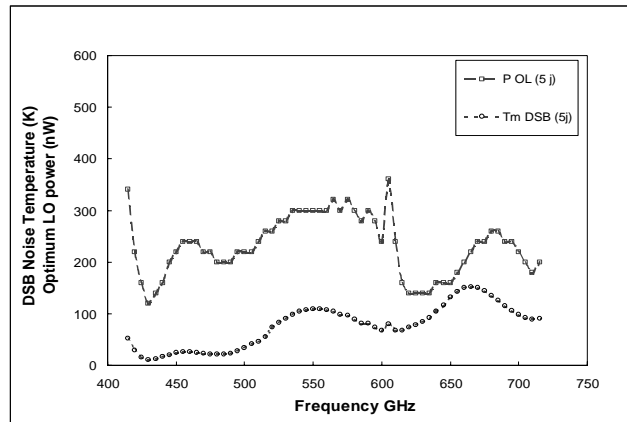


Figure 8. (a) Optimum mixer noise and LO power and (b) optimum conversion gain, calculated for the 5-junction array 'A'.

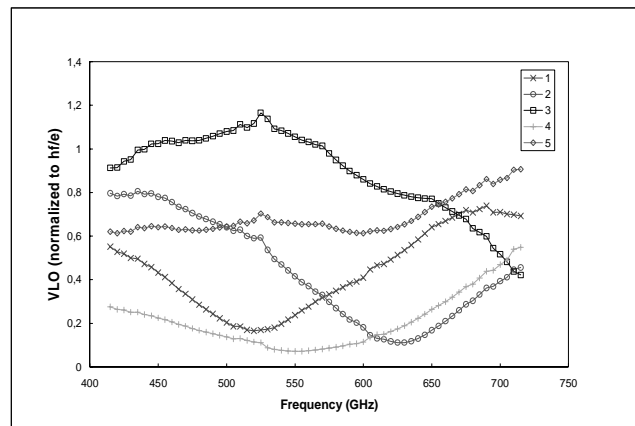


Figure 9. LO voltage distribution within the 5-junction array 'A', versus frequency. The junctions are numbered from 1 (at the entrance) to  $N=5$  (at the open end of the array).

# INTEGRATED SUPERCONDUCTING RECEIVER AS A TESTER FOR SUB-MILLIMETER DEVICES AT 400-600 GHz

S. V. Shitov<sup>1</sup>, A. M. Shtanyuk<sup>2</sup>, V. P. Koshelets<sup>1</sup>, G. V. Prokopenko<sup>1</sup>,  
L. V. Filippenko<sup>1</sup>, An. B. Ermakov<sup>1</sup>, M. Levitchev<sup>3</sup>, A. V. Veretennikov<sup>4</sup>,  
H. Kohlstedt<sup>3</sup> and A. V. Ustinov<sup>5</sup>

<sup>1</sup>Institute of Radio Engineering and Electronics, Russian Academy of Sciences  
(IREE RAS) 103907 Moscow, Russia

<sup>2</sup>Institute of Applied Physics, Russian Academy of Sciences (IAP RAS)  
603600, Nizhny Novgorod, Russia

<sup>3</sup>Institute of Thin Film and Ion Technology (ISI) Research Center Juelich  
D-52425 Juelich, Germany

<sup>4</sup>Institute of Solid State Physics, Russian Academy of Sciences,  
142432, Chernogolovka, Russia

<sup>5</sup>Physics Institute III, University of Erlangen-Nuernberg  
D-91058 Erlangen, Germany

## ABSTRACT

We report on design and first application of a laboratory-purpose tester which can *in situ* detect spectrum of sub-millimeter wave emission within frequency range of 400-600 GHz from virtually any compact low-power source working within temperature range below 100 K. Both the receiver and the sample are placed in vacuum inside a laboratory test stick of diameter 50 mm, which is cooled down in a standard transport vessel for liquid helium. The sensor of the tester is designed on a base of the superconducting integrated receiver (SIR) chip working below 5 K. The chip sensor, beside the quasi-optical SIS mixer, contains an internal electronically tuned superconducting local oscillator, that provide low-noise operation at the level below 300 K DSB at central frequencies of 480-520 GHz as measured with a black body at the position of the test source. The signal detected by the SIS mixer is boosted by a helium-cold low-noise amplifier ( $G=20$  dB,  $T_N=10$  K) within frequency range 1-2 GHz and then by a second room temperature amplifier ( $G=53$  dB,  $T_N=90$  K) both mounted within the same test stick. The output level is sufficient for direct application to most of standard RF recorders, e. g. for a spectrum analyzer. To detect weak signals, a compact chopper-wing has been designed and placed at the input of the receiver module. Details of design and main test data measured at DC and RF are reported.

## INTRODUCTION

The main goal of the project was development of a sensitive laboratory-purpose heterodyne receiver for detection and spectral study of radiation from variety of superconducting oscillators such as a flux-flow oscillators (FFOs), Josephson array oscillators or HTc structures and possibly from coolable semiconductor sources. To enable such a test for oscillators working at different temperatures, the non-contacting (quasi-optical) scheme is the most natural choice. A SIS mixer with integrated planar antenna can be a solution for the front-end of the receiver [1, 2].

It is well-known that SIS mixers are the most sensitive devices for heterodyne reception in the frequency range of 100-1000 GHz with the noise temperature limited only by the quantum value  $hf/k$  [3, 4]. However, the large size, weight and expenses of a regular (room temperature) submm local oscillator along with necessity of use a cryostat with optical window are that serious limitations for extensive use of the SIS receivers in laboratories. To overcome these drawbacks, the concept of a superconducting local oscillator that can be integrated with the SIS mixer has been proposed [5]. Such an oscillator based on FFO has been developed and tested experimentally showing promising performance. Both frequency and phase locking of the FFO to a reference source has been recently demonstrated [6-8]

The operation of the quasioptical superconducting integrated receiver (SIR) [8] at the frequency 500 GHz with the noise temperature of about 100 K, which is just 6 times exceeds the quantum limit, has been demonstrated [10]. This chip-size heterodyne sensor can detect radiation as weak as  $10^{-13}$  W in the frequency range 300-700 GHz (with few exchangeable chips or sensor heads provided). Each set can cover band of about 100 GHz. The estimated cost of the microcircuit can be of the order of \$1,000 which is much lower if compare to that minimum of about \$25,000, - price of a conventional set for the equivalent submm oscillator which may consist of BWO, powerful magnet and high voltage power supply, but the cryostat with SIS mixer is not included! Use of SIR chip, which is that "two-in-one" device with low power consumption, seems very promising for laboratory scale instrumentation. For all these reasons the superconducting integrated receiver was chosen as a heterodyne sensor for laboratory-purpose research on sub-mm emission from a coolable sources which can be mounted at short distance from the sensor in the compact cold environment, e.g. within laboratory test stick.

## EXPERIMENTAL DETAILS

### *A. Design of the stick receiver*

Simplified drawing of the tester receiver cooled down in a transport dewar with liquid helium is presented in Fig. 1. The device is designed as a stick made from stainless steel tube of diameter 50 mm and 1200 mm long, which fits into a standard

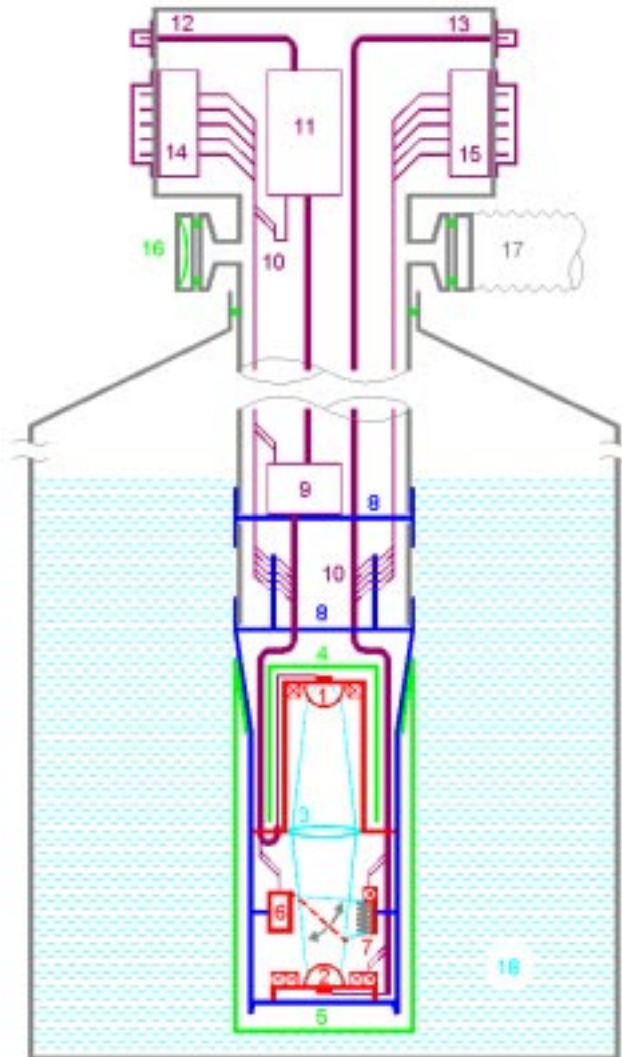


Fig. 1. Simplified drawing of a laboratory-purpose tester which can *in situ* detect spectrum of sub-millimeter wave emission from coolable sources within frequency range of about 400-600 GHz: (1) – receiving chip on silicon lens; (2) – emitting sample on silicon lens; (3) – focusing lens/infrared filter; (4) – magnetic shielding for receiving chip; (5) – vacuumed permalloy shield; (6) – source switch/chopper; (7) – calibration load; (8) – heat sink chains for receiving head and for IF amplifier; (9) – cold IF amplifier; (10) – signal coaxial cables and bias wiring; (11) – buster IF amplifier; (12) and (13) – receiver output and coaxial cable for sample; (14) and (15) – dc connectors for bias of receiving head and sample; (16) and (17) – safety valve and vacuum pump connector; (18) – dewar with liquid helium.

vessel for liquid helium. To protect magnetic-sensitive samples from unwanted interference, the vacuumed permalloy shield is installed at the end of the stick using a precise cone connection. The sample shelf is equipped with a heater, thermometer, magnetic coil, rf coaxial cable and waveguide (2.4 mm x 1.2 mm). To check the noise temperature of the receiver head, which is mounted at higher position, the variable-temperature load (black body) was put at the position of the sample. A compact chopper-wing has been developed on the base of a mechanical relay, which can provide the switching rate of a few hertz. This chopper can switch the input of the receiving head between the sample and the calibration load.

The exchangeable receiving head, which is presented in Fig. 2(a), has its own double-layer magnetic shielding from led (internal layer) and from permalloy (external one). The SIR sensor (1) is installed in the depth of the shield (4), as shown in Fig. 1, and mounted at the flat back of the silicon elliptical lens with antireflection coating [10]. Being combined with the focusing lens, the double dipole antenna SIS mixer [2, 10] provides the beam of about 10 degrees wide pointed to the sample source (2) which can be also equipped with its own lens. An additional focusing lens (3) and/or an infrared filter can be mounted at the adjustable aperture ring of the

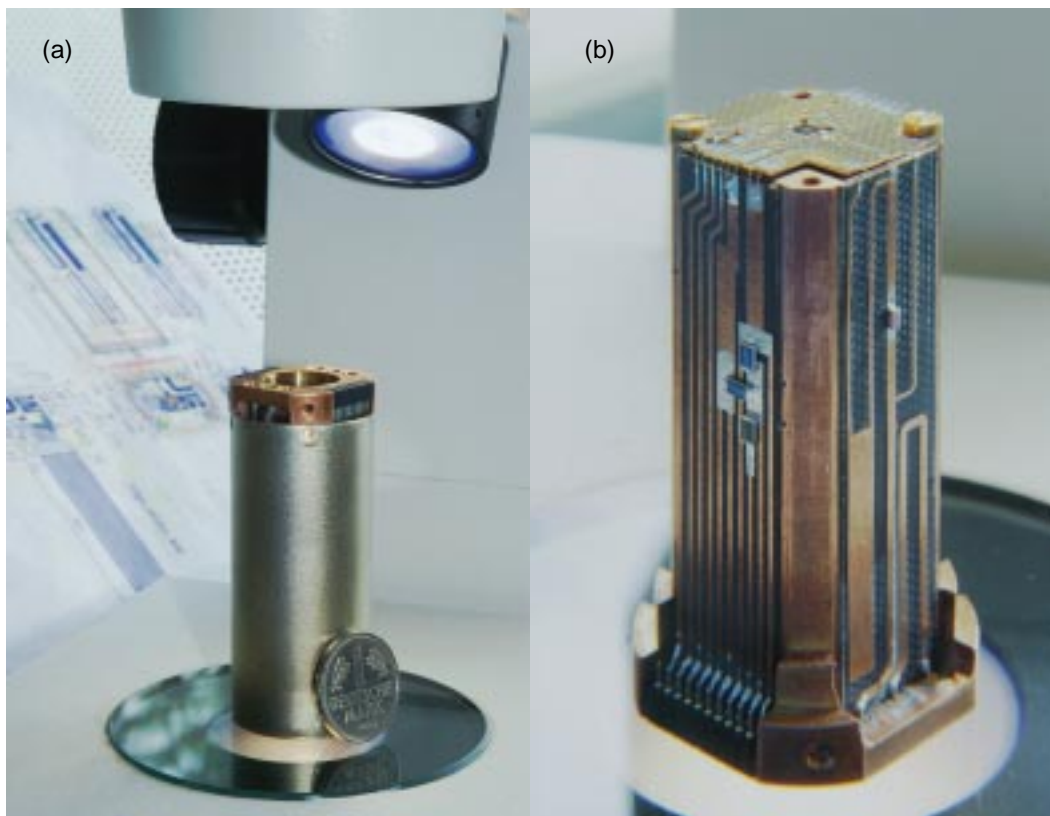


Fig. 2. Photographs of exchangeable receiving head (length 76 mm and diameter 32 mm): (a) magnetic shield is mounted; the input aperture and connectors are seen on the top; (b) magnetic shield is dismantled; the bias circuit and IF filters, including dual directional coupler (-23 dB), are mounted on the walls of the cooper block; the SIR chip of size 4 mm by 4 mm is seen on the top (in the center).

receiving head. The bias circuit contains an IF filter and a printed dual directional coupler (-23 dB) which are mounted inside the shield of the receiving head as shown in Fig. 2(b). Three semirigid coaxial cables are connecting the receiver head: one cable for the cold IF amplifier and two others for the dual directional coupler, which is used for testing both the amplifier performance and the SIS mixer output reflection loss (not shown in Fig. 1). The receiving head is designed as compact as 32 mm in diameter and 76 mm in length; it can be installed not only in a dipstick as shown in Fig. 1, but also in practically any cryostat or close-cycle cooler which provides a cold flange with temperature of about 5 K or lower.

To prevent the receiving head from the excessive heat provided by the first balanced IF amplifier ( $G=20$  dB,  $T_N=10$  K [11]), this amplifier is installed at a separate shelf, which has its own thermal contact to the LHe bath. All dc wires coming to both the receiver and the sample are mounted to a special heat sink PCB. The second IF amplifier ( $G=53$  dB,  $T_N=90$  K [11]) is installed at the top of the stick at 300 K inside the connector box, also in vacuum. To avoid electrical chocks to the receiving chip during the connection procedure, a safety relay is used to short sensitive terminals of the device.

### *B. Test results and discussion*

Performance of the receiver was tested using computer system IRTECON [10], which electronically controls both the SIS mixer and the FFO. IV-curves of the SIS mixer obtained during the self-test procedure are presented in Fig. 3. The IV-curves of the local oscillator (FFO) are presented in Fig. 4 as it is being tuned with magnetic field (each IV-curve is swept at a constant magnetic field). The quasi-color (in gray scale here) is indicating the pump level provided for the SIS mixer. Processed data on the pump level can reveal the frequency response (about equal to instantaneous bandwidth) of the SIS mixer since the coupling circuit of the FFO is much more broadband. Note, that the useful frequency range of the receiver can be essentially wider, than the -3 dB band of the mixer pump (about 420-510 GHz from Fig. 3), because spectral density of a weak narrow-band signal can easily exceed the spectral density of the noise signal of a few thousand Kelvin. Since the noise temperature of the receiver measured with the calibration load is below 300 K (DSB), it is easy to estimate, that a narrow-band signal as weak as 0.1 pW can be detected at IF assuming the signal spectrum to be narrower than 10 MHz.

The spectral resolution of the receiver is about 1-10 MHz, that is defined by the linewidth (LW) and stability of the free-running FFO. The spectra wider than IF band (from 1 GHz to 2 GHz in our case) can be measured by scanning LO frequency, i.e. in the FFO scan mode. Doing this, one can scan FFO in 1 GHz steps integrating signal within complete IF band. To get the coarse spectral information “on-the-fly”, the IRTECON controlling system is being modified. Presence of a signal can be then detected “by eye” using a graph in quasi-color, which shows amplitude of IF power

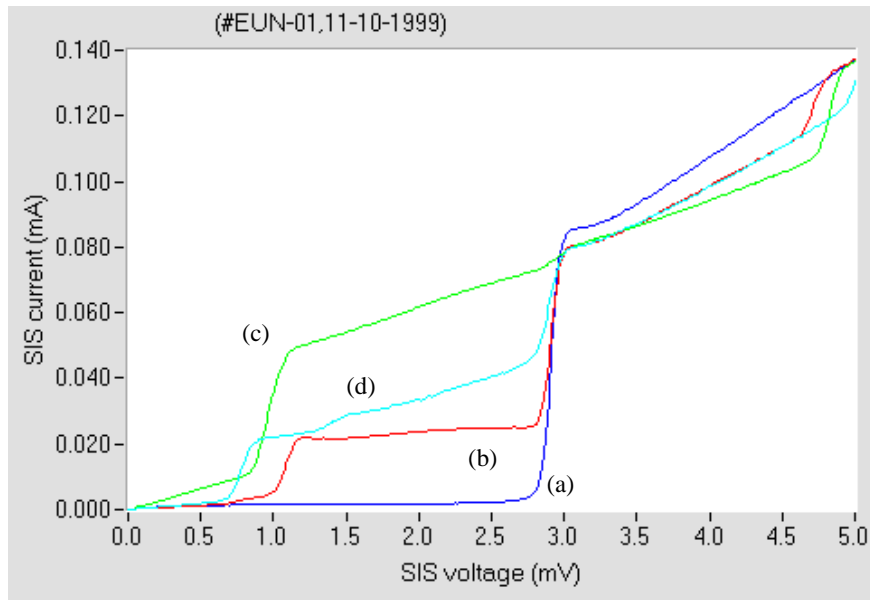


Fig. 3. IV-curves of SIS mixer: unpumped (a) and pumped by FFO at 428 GHz (b), 461 GHz (c), and 500 GHz (d).

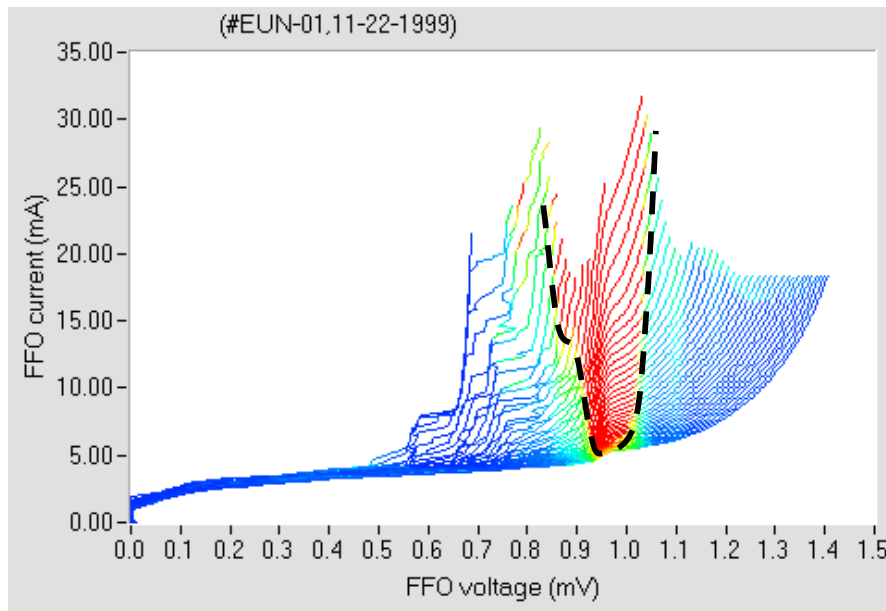


Fig. 4. IV-curves of FFO tuned by magnetic field. The frequency of this Josephson-type local oscillator is proportional to *bias voltage* (about 484 GHz per each mV), while delivered power is proportional to the *bias current*. The dashed curve indicates the region of sufficient pump level.

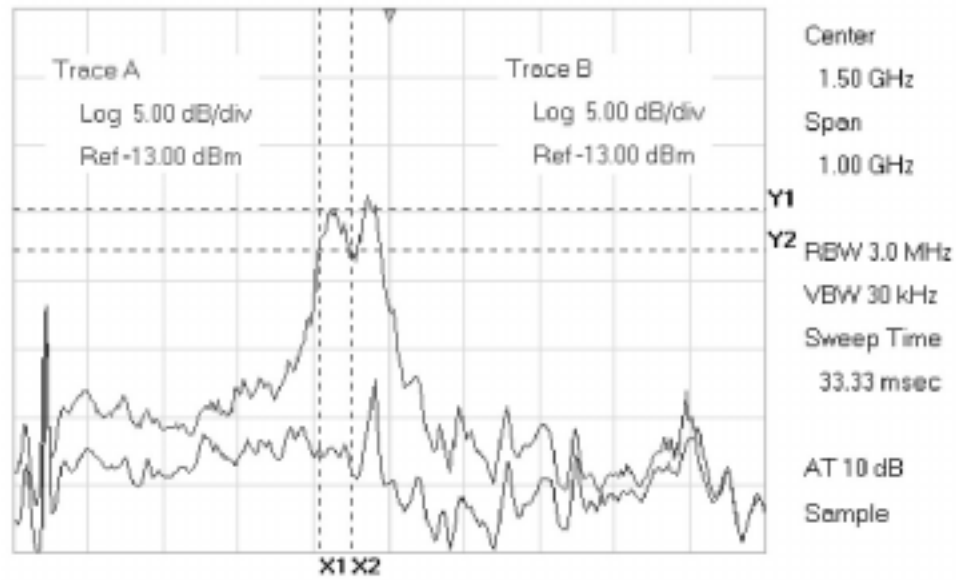


Fig. 5. Response at IF detected for relatively strong emission from a spare receiver chip (i.e. from second FFO) installed at the place of the test device (see Fig. 1).

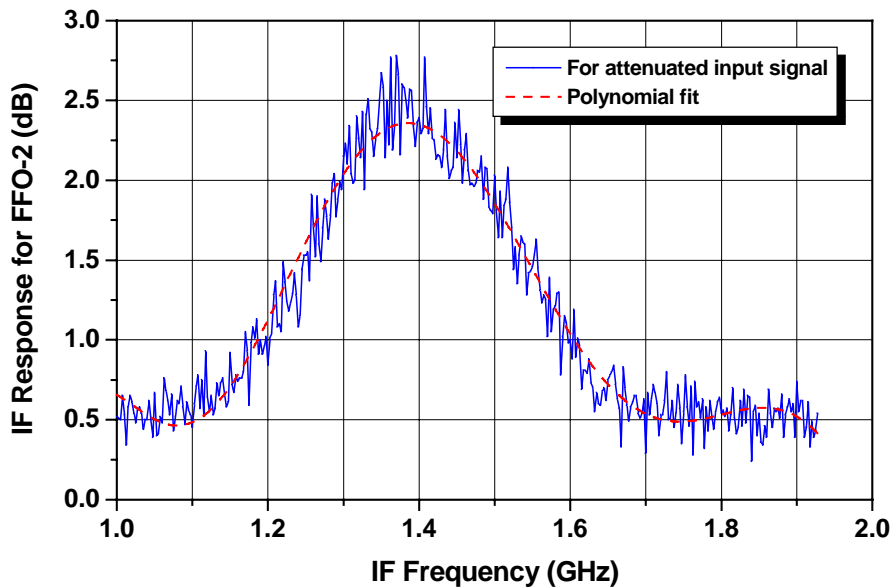


Fig. 6. Relatively wide IF spectrum from weak (attenuated) test source (second FFO) which was tuned for broad-band emission (see text and [12]).

vs. FFO frequency similar to pump level of the SIS mixer as in Fig. 4. Note, that to subtract the noise floor, at least one reference scan is necessary with signal source turned off. The detected spectra can be corrected to the frequency response of the receiver. For this purpose the data on mixer pump can be used.

The spare chip receiver (SIR) on the elliptical lens was used as a specimen of the emitting source, as shown in Fig. 1. The fact, that some LO power is leaking from the SIS mixer towards antennas and eventually emitted [10], was used in this experiment. The measured spectrum of the FFO is presented in Fig. 5 showing mutual instability of two oscillators [6] which is mainly due to unwanted EMI. Since the possibility of frequency/phase locking of the FFO is experimentally proven [6-8], it can be introduced for the stick receiver in the future to resolve finest spectra. The example of a wide and low intensity spectrum is presented in Fig. 6. This spectrum is obtained from the sample SIR with its FFO biased at higher dynamic resistance producing emission of wider linewidth [12]. An absorbing film mounted at the aperture of the receiving head introduced extra attenuation.

## CONCLUSION

A new submillimeter quasioptical laboratory-purpose heterodyne SIS receiver has been developed and tested successfully within frequency range 400-600 GHz. This receiver does not need a separate submillimeter local oscillator since uses ultra-compact Superconducting Integrated Receiver (SIR) chip with its internal electronically controlled local oscillator. The receiving head is developed as a compact general-purpose device, which can be used in variety of setups including a dipstick or an optical cryostat. Authors hope that this development is a beneficial step towards wider use of superconducting receivers in laboratory studies.

## ACKNOWLEDGEMENTS

Authors thank Space Research Organization of the Netherlands and Department of Physics and Material Science Center of University of Groningen for their technical help, and Edward Goldobin for his executive management. This work has been performed under grant BMBF-13N6945/3.

## REFERENCES:

- [1] G. M. Rebeiz, "Millimeter wave and terahertz integrated circuit antennas," *Proc. IEEE*, 80 (11), pp. 1748-1770 (1992)
- [2] A. Skalare, Th. De Graauw and H. van de Stadt, "A planar dipole array antenna with an elliptical lens," *Microwave and Optical Technology Letters*, vol. 4., pp. 9-12 (1991)
- [3] J. R. Tucker, M. J. Feldman, *Rev of Mod Phys* **4**, pp. 1055-113 (1985)

- [4] J. Zmuidzinas and H. G. LeDuc, *IEEE Trans on Microwave Theory and Tech* **40** pp. 1797-804 (1992); J. Zmuidzinas, N. G. Ugras, D. Miller, M. Gaidis, H. G. LeDuc, J. A. Stern, *IEEE Trans on Appl Superconductivity* **5**, pp. 3053-6 (1995)
- [5] V. P. Koshelets, A. V. Shchukin, S. V. Shitov, and L. V. Filippenko, "Superconducting millimeter wave oscillators and SIS mixers integrated on a chip," *IEEE Trans. on Appl. Supercond.*, vol. **3**, No. 1, pp. 2524-2527 (1993)
- [6] J. Mygind, V. P. Koshelets, A. V. Shchukin, S. V. Shitov, and I. L. Lapitskaya, "Properties of the autonomous and injection locked Flux-Flow Oscillators," *IEEE Trans. on Appl. Supercond.*, No 3 (1995)
- [7] V. P. Koshelets, S. V. Shitov, A. V. Shchukin, L. V. Filippenko, P. N. Dmitriev, V. L. Vaks, J. Mygind, A. B. Baryshev, W. Luinge, H. Golstein, "Flux-flow oscillators for sub-mm wave integrated receivers," *IEEE Trans. on Appl. Supercond.* **9** 4133 (1999)
- [8] V. P. Koshelets, A. B. Ermakov, S. V. Shitov, P. N. Dmitriev, L. V. Filippenko, A. M. Baryshev, W. Luinge, J. Mygind, V. L. Vaks, D. G. Pavel'ev, "Eternally Phase Locked SubMM Flux Flow Oscillator for Integrated Receiver," *Proc. 11th Symposium on Space Terahertz Technology*, Ann-Arbor, Univ. Michigan, May 1-3 (2000)
- [9] V. P. Koshelets, S. V. Shitov, L. V. Filippenko, A. M. Baryshev, H. Golstein, T. de Graauw, W. Luinge, H. Schaeffer, H. van de Stadt, "First Implementation of a Superconducting Integrated Receiver at 450 GHz," *Appl. Phys. Lett.*, **68** (9) 1273 (1996)
- [10] S. V. Shitov, V. P. Koshelets, A. B. Ermakov, L. V. Filippenko, A. M. Baryshev, W. Luinge, J.-R. Gao, "Superconducting Chip Receivers for Imaging Application," *IEEE Trans. on Appl. Supercond.* **9** 3773 (1999)
- [11] Oleksandr M. Pylypenko, Open Joint-Stock "Scientific-Production Enterprise "Saturn" (OJS "SPE Saturn"), Kyiv, 03148, Ukraine
- [12] V. P. Koshelets, S. V. Shitov, A. V. Shchukin, L. V. Filippenko, J. Mygind and A. V. Ustinov, "Self-pumping effects and radiation linewidth of FFO," *Phys. Rev. B*, vol. **56**, pp. 5572- 5577 (Sept. 1997)

## MODELLING FEW-MODED HORNS FOR FAR-IR SPACE APPLICATIONS.

Ruth Colgan,<sup>1</sup> J.Anthony Murphy,<sup>1</sup> Bruno Maffei,<sup>2</sup> Creidhe O'Sullivan,<sup>1</sup> Richard Wylde<sup>2</sup> and Peter Ade<sup>2</sup>.

<sup>1</sup> National University of Ireland Maynooth, Co.Kildare. Ireland

<sup>2</sup> Queen Mary and Westfield College, London E1 4NS, UK.

### Abstract:

Few-moded or over-moded horns are now being proposed for far-IR space receiver systems, e.g. the High Frequency Instrument (HFI) on the ESA PLANCK Surveyor. In such systems individual waveguide modes can couple independently to an overmoded detector (such as a bolometer in an integrating cavity). We consider in detail the case of a cylindrically symmetric configuration consisting of a corrugated conical horn connected to waveguide filter also corrugated, such as is proposed for the HFI instrument. Such antenna feeds have the advantage of high coupling efficiency combined with low sidelobe level beam patterns. In the paper we present two alternative techniques for modelling few moded horn antennas. The first is based on a scattering matrix description of propagation in a non-uniform wave-guide structure, while the second approach uses hybrid mode solutions for a waveguide with corrugated walls. We also present computed and experimental data for an example prototype HFI horn.

### 1. Introduction

Few-moded or over-moded horns are finding application in far-IR detector systems where high efficiency is required with the low sidelobe response pattern associated with single mode operation. Using standard techniques borrowed from antenna engineering it is possible to model such partially coherent *multi-moded* horns in a straightforward way [1,2]. We assume that the horn is connected to an integrating cavity containing a black-body source/detector via a wave-guide filter which limits the number of modes that can propagate (see Fig.1). This is best achieved by the use of a flared section at the back of the waveguide, which is then coupled without an impedance mismatch to an integrating cavity. In this configuration the black-body detector/source independently (incoherently) couples to the individual spatially coherent modes of the wave-guide at the cavity end. Only non-evanescent modes propagate through the filter, of course, and there will be scattering of power between modes if the wave-guide is not of uniform cross section (as for example if the guide is corrugated). The calculation of the radiation pattern (including diffraction effects) then amounts to summing the far-field radiation pattern of each non-evanescent mode at the cavity end of the horn/waveguide structure.

The scattering matrix description of non-uniform wave-guides based on mode matching is a powerful computational method and can be used to predict the beam patterns of corrugated horn antenna feeds. The technique is especially useful if the number of corrugations per wavelength is not very large, as then the surface impedance hybrid-mode description referred to below may become unreliable [3]. In the mode matching approach the profile of the waveguide plus horn is replaced by a series of uniform waveguide segments, and the longitudinal cross section can then be viewed as a series of steps. The technique involves matching the total electric and magnetic fields at each junction between the uniform segments so that conservation of complex power is maintained. The technique is discussed in detail by Olver et al [4].

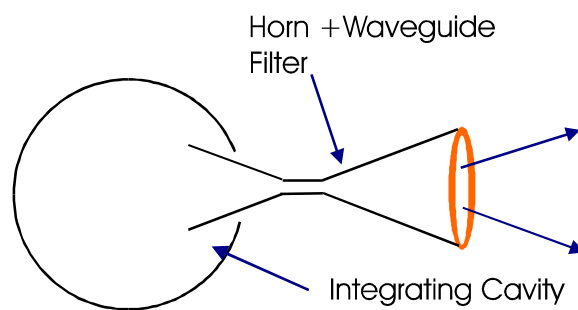


**Figure 1.** Corrugated horn and waveguide filter feeding an integrating cavity

The surface impedance model can also be used in predicting the radiation pattern of a corrugated horn and waveguide in the limit of many corrugations per wavelength. The waveguide is considered as having a surface defined by the edges of the corrugations with different impedances in the axial and transverse directions [3]. The true modes of propagation of such a system cannot be pure TE or TM, but rather a hybrid combination that depends on the depths of the corrugations and the radius (width) of the guide. The application of the boundary conditions leads to the modal propagation coefficients and transverse wavenumbers of a complete set of such hybrid modes. The surface-impedance method is simple and quite accurate and is particularly useful in the design of the wave-guide filter section. However, when the waveguide radius is of order one wavelength, space harmonics must be included if an accurate cross-polar pattern is to be modelled [3].

## 2. Mode Matching Approach to Multi-moded Horns

The mode scattering properties of the system as a whole or any section of it can be represented by a single scattering matrix  $S$ . The reflection and transmission characteristics are determined by the usual equation (see for example Olver 1994 [4]):

$$\begin{bmatrix} B \\ D \end{bmatrix} = [S] \begin{bmatrix} A \\ C \end{bmatrix} = \begin{bmatrix} S_{11} & S_{12} \\ S_{21} & S_{22} \end{bmatrix} \begin{bmatrix} A \\ C \end{bmatrix},$$

where  $A$  and  $B$  are vectors containing the forward and reflected mode coefficients, respectively, looking into the system at the input side, and  $C$  and  $D$  are vectors of the incident and transmitted mode coefficients, respectively, looking into the system at the output plane. We now summarize the derivation of the  $S$  scattering matrix for a cylindrically symmetric waveguide structure (corrugated or smooth walled).

For cylindrical waveguides the transverse electric fields of the corresponding two orthogonal sets of TE modes and two sets of TM modes are:

$$\begin{pmatrix} \mathbf{e}_{nl}^{TE,c} \\ \mathbf{e}_{nl}^{TE,s} \end{pmatrix} = \sqrt{\frac{(2 - \delta_{n0})}{\pi a^2 J_{n+1}^2(p_{nl})}} \left[ J'_n(p_{nl}r/a) \begin{pmatrix} \cos n\phi \\ \sin n\phi \end{pmatrix} \mathbf{r} + \frac{nJ_n(q_{nl}r/a)}{q_{nl}r/a} \begin{pmatrix} -\sin n\phi \\ \cos n\phi \end{pmatrix} \phi \right]$$

$$\begin{pmatrix} \mathbf{e}_{nl}^{TM,c} \\ \mathbf{e}_{nl}^{TM,s} \end{pmatrix} = \sqrt{\frac{(2 - \delta_{n0})}{\pi a^2 (1 - (n/q_{nl})^2) J_n^2(q_{nl})}} \left[ \frac{nJ_n(q_{nl}r/a)}{q_{nl}r/a} \begin{pmatrix} \cos n\phi \\ -\sin n\phi \end{pmatrix} \mathbf{r} - J'_n(q_{nl}r/a) \begin{pmatrix} \sin n\phi \\ \cos n\phi \end{pmatrix} \phi \right],$$

where  $p_{nl}$  represents the  $l$ th zero of  $J_n(z)$ , and  $q_{nl}$  represents the  $l$ th zero of  $dJ_n/dz(z)$  [5]. The constant of proportionality has been chosen to make  $\int_A |\mathbf{e}_l^{te/tm}|^2 r dr d\phi$  equal to unity. The two possible orthogonal modes for each value of  $n$  and  $l$  arise from the choice of the  $z$  component of the appropriate field being either proportional to  $\cos(n\phi)$  or  $\sin(n\phi)$ . On ordering the guide modes by their cutoff wavelength (so that those of odd order are TE while those of even order are TM) any coherent field propagating within the waveguide filter and horn can be represented by:

$$\mathbf{e}_{total} = \sum_{nl} \alpha_{nl}^c \mathbf{e}_{nl}^{TE,c} + \alpha_{nl}^s \mathbf{e}_{nl}^{TE,s} + \beta_{nl}^c \mathbf{e}_{nl}^{TM,c} + \beta_{nl}^s \mathbf{e}_{nl}^{TM,s} = \sum_{ni} A_{ni}^c \mathbf{e}_{ni}^{G,c} + A_{ni}^s \mathbf{e}_{ni}^{G,s},$$

where:  $\mathbf{e}_{n,2l-1}^G = \mathbf{e}_{n,l}^{TE}$ ,  $\mathbf{e}_{n,2l}^G = \mathbf{e}_{n,l}^{TM}$ , and it is understood that the summation is also over both orthogonal mode sets.

Because of the cylindrical symmetry of the junction discontinuity, in propagating through the waveguide and horn only scattering between modes of the same azimuthal index and same  $z$ -component dependence on  $\cos/\sin(n\phi)$  is possible. It is therefore convenient to compute the overall scattering matrix  $S^{(n)}$  for each azimuthal order separately. First it is necessary to divide the overall waveguide/horn structure into a series of segments with a step discontinuity occurring at the beginning and end of each section. At a step discontinuity where the guide radius increases from  $a$  to  $b$  the submatrix elements of the scattering matrix  $S^{(n)}$  can be written as:

$$\begin{aligned}
S_{11} &= (R^* + P^+ Q^{-1} P)^{-1} (R^* - P^+ Q^{-1} P) & S_{12} &= 2(R^* + P^+ Q^{-1} P)^{-1} P^+ \\
S_{21} &= 2(Q + P(R^*)^{-1} P^+)^{-1} P & S_{22} &= -(Q + P(R^*)^{-1} P^+)^{-1} (Q - P(R^*)^{-1} P^+)
\end{aligned}$$

where for both the TE and TM modes defined above  $R_{ij} = (1/Z_{nl}^{TE/TM})^* \delta_{ij}$ , and  $Q_{ij} = (1/Z_{nl}^{TE/TM})^* \delta_{ij}$  and cross coupled powers  $P_{ij} = \int_0^a \mathbf{e}_{nl}^a \times (\mathbf{h}_{nl}^b)^* dA$ , with appropriate values for the guide impedance  $Z$  [5], and  $i$  and  $j$  determined by the ordering of the TE/TM modes. Note the equations here differ slightly from those presented in Olver [4]. The superscripts  $a$  and  $b$  on the  $\mathbf{e}$  and  $\mathbf{h}$  fields indicates the appropriate guide radius for the mode. The  $P_{ij}$  can be evaluated from the following expressions for the cross coupled power between the modes on either side of the discontinuity:

$$P_{TE \rightarrow TE} = -\frac{\pi(1 + \delta_{n0}) D_{nl}(a) D_{nl'}(b) q_{nl} J_n(q_{nl}) J'_n(q_{nl} a/b)}{[(q_{nl'}/b)^2 - (q_{nl}/a)^2] (Z_{TE}^b)^*},$$

$$P_{TM \rightarrow TM} = \frac{\pi(1 + \delta_{n0}) C_{nl}(a) C_{nl'}(b) p_{nl} a/b J'_n(p_{nl}) J_n(p_{nl} a/b)}{[(p_{nl'}/b)^2 - (p_{nl}/a)^2] (Z_{TM}^b)^*},$$

$$P_{TE \rightarrow TM} = \frac{\pi a b n D_{nl}(a) C_{nl'}(b) J_n(p_{nl} a/b) J_n(q_{nl'})}{[p_{nl} q_{nl}] (Z_{TM}^b)^*} \quad \text{and} \quad P_{TM \rightarrow TE} = 0$$

$$\text{where } C_{nl}(a) = \sqrt{\frac{(2 - \delta_{n0})}{\pi a^2 J_{n+1}^2(p_{nl})}} \quad \text{and} \quad D_{nl}(b) = \sqrt{\frac{(2 - \delta_{n0})}{\pi a^2 (1 - (n/q_{nl})^2) J_n^2(q_{nl})}}$$

For a step in which  $a > b$  then  $S_{11}(a > b) = S_{22}(a < b)$ ,  $S_{12}(a > b) = S_{21}(a < b)$ ,  $S_{21}(a > b) = S_{12}(a < b)$ , and  $S_{22}(a > b) = S_{11}(a < b)$ . The propagation of the mode along the waveguide sections can also be described in terms of propagation "scattering" matrices. For a given azimuthal order the overall scattering matrix for the horn and waveguide can be derived by cascading the scattering matrices for the sections in the appropriate way [4]. At the end of the horn the fields are launched into free space. There is a sudden jump in the impedance and there may be significant reflections at that point. We can model this effect to a good approximation by assuming the horn aperture lies in an infinite ground plane. This in turn can be modelled by a very large step into a waveguide of infinite diameter. Finite element analysis can be applied to the real horn aperture configuration, if low level sidelobe effects are important.

The modes at the horn aperture then propagate without scattering to the far-field. In the example multi-moded horns we have chosen to analyse all of the waveguide

modes at the entrance to the waveguide section are assumed to be equally excited. The far field pattern for the horn plus waveguide and flare is then given by:

$$I \propto \sum_{nj} \left( \left| \sum_i [S_{21}^n]_{ij} \mathbf{e}_{ni}^{ff c} \right|^2 + \left| \sum_i [S_{21}^n]_{ij} \mathbf{e}_{ni}^{ff s} \right|^2 \right),$$

where  $c$  and  $s$  refer to the two possible orthogonal modes for a given  $ni$ . The beam patterns on the sky correspond to the field patterns produced after scattering by the individual modes *at the cavity entrance* to the waveguide/horn structure added in quadrature. Note in the above sum the subscript  $n$  refers to the azimuthal order of the mode, and for  $i$  and  $j$  odd or even the modes are TE or TM, respectively. The results of modelling the beam pattern performance of one of the prototype horns for the HFI on the PLANCK Surveyor using the mode-matching approach is discussed in section 4.

### 3. Surface Impedance Model.

A corrugated horn or waveguide is considered as having a surface defined by the edges of the corrugations with different impedances in the axial and transverse directions [3]. The characteristics of the true hybrid TE/TM modes of propagation depend on the depths of the corrugations and the radius (width) of the guide. The fundamental mode in a very wide cylindrical waveguide with corrugation depths of  $\lambda/4$  is the balanced hybrid  $HE_{11}$  mode used in predicting the radiation patterns of single moded corrugated horns. In a multi-moded horn we will still obtain higher order balanced hybrid modes, where such modes all have zero transverse fields at the horn aperture edge. The effective impedance for any currents flowing across the corrugations is infinite, so that  $H_\phi$  is zero and  $E_\phi$  is also zero if there are many corrugations per wavelength. Consequently, such horns will produce beam patterns with low sidelobe levels because of the gradually tapered fields at the horn aperture. Away from the balanced hybrid condition higher sidelobe levels are to be expected as the effective surface impedance across the corrugations is no longer infinite. This may be an issue for the design of broadband horn feed systems.

In the throat of a horn the effective impedance produced by the corrugations becomes mode dependent and is also non-infinite even for slot depths of  $\lambda/4$ . However, it is not necessary to maintain the balanced mode condition in the waveguide at the back of the horn as long as one knows the propagation characteristics. The critical issue for a few-moded horn is the mode filtering properties of this waveguide section. In order to determine which modes can propagate in a corrugated waveguide it is necessary to solve the characteristic equation for the propagation coefficient  $\beta$  (i.e. the guide wavenumber). In this approach the waveguide is regarded as consisting of an inner region of radius  $r_1$  bounded by an impedance surface determined by the corrugation

slot depth. For this to be valid there must be a sufficient number of corrugations per wavelength so that they effectively mimic a continuous surface. It is assumed that the slots are narrow and only a single non-propagating TM mode is capable of existing in the slots.

Matching the admittance of the  $m$ th order TM mode in the slot with that of the mode in the inner region of the guide yields the characteristic equation for  $\beta$  [3]:

$$F_m(Kr_1) - \frac{(m\beta/k)^2}{F_m(Kr_1)} = \left( \frac{Kr_1}{kr_1} \right)^2 S_m(kr_1, kr_0),$$

where  $K^2 + \beta^2 = k^2$ ,  $r_o$  is the radius to the bottom of the corrugation and  $S_m(x, y)$  is given by the equation:

$$S_m(x, y) = x \frac{J'_m(x)Y_m(y) - J_m(y)Y'_m(x)}{J_m(x)Y_m(y) - J_m(y)Y_m(x)}.$$

For the hybrid modes the  $z$  components of the electric and magnetic fields for the two possible orthogonal modes are defined to be:

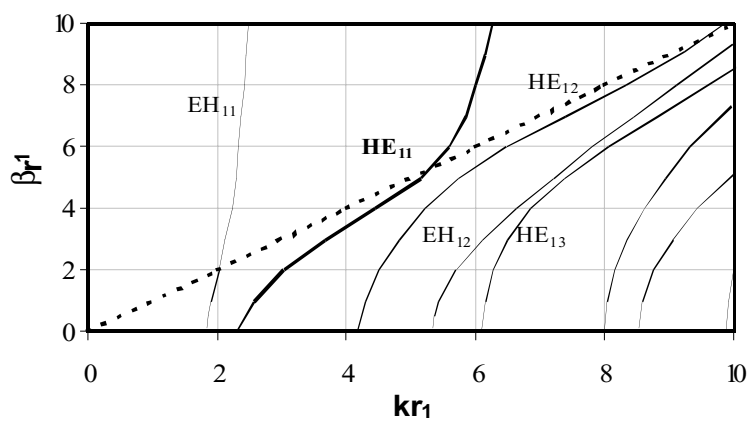
$$E_z(r, \phi) = a_m J_m(Kr) \begin{pmatrix} \cos m\phi \\ \sin m\phi \end{pmatrix} \quad \text{and} \quad H_z(r, \phi) = a_m y_0 \Lambda J_m(Kr) \begin{pmatrix} \sin m\phi \\ \cos m\phi \end{pmatrix},$$

where  $y_0$  is the admittance of free space. The transverse fields can be derived from the  $z$ -component of the fields [5]. The requirement that the  $\phi$  component of the electric field be zero at the corrugations yields the following relationship between  $\Lambda$  and  $\beta$ :

$$\Lambda = - \frac{m\beta/k}{F_m(Kr_1)}.$$

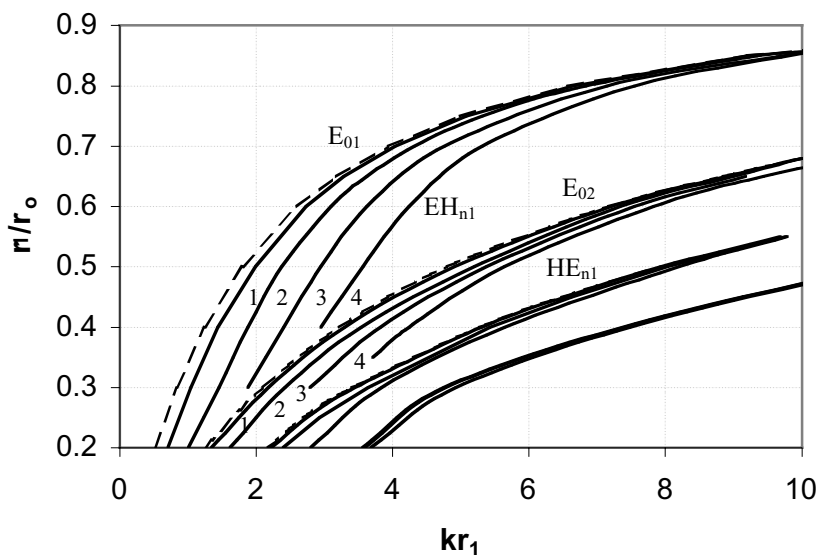
The cut-off condition  $\beta = 0$  yields either  $F_m(Kr_1) = 0$ , where the mode is pure TE-type in the limit, or  $F_m(Kr_1) = S_m(kr_1, kr_0)$ , where the mode exhibits pure TM properties in the limit. In the former case the boundary condition corresponds to that of a TE mode in a guide of radius  $r_1$ , while the latter corresponds to a TM mode in a uniform waveguide of radius  $r_0$ . For fixed values of  $r_1$  and  $r_0$  as the frequency is increased the high frequency cut-off condition is eventually reached where  $\beta/k$  tends to  $\infty$ .

Figure 2 shows dispersion curves for modes of azimuthal order 1. As  $kr_1$  increases from the low-frequency cut-off, a balanced-hybrid condition is reached where  $\Lambda^2 = 1$ . For high frequencies the  $HE_{11}$  mode is balanced hybrid when the corrugation depth approaches  $\lambda/4$ . A fast-wave to slow-wave transition takes place at  $k = \beta$  (dashed line). Beyond this, in the slow-wave domain, a high-frequency cut-off eventually occurs where  $\beta/k$  tends to infinity and the mode terminates. Figure 3 shows a plot of the high-frequency cut-off values for the  $HE_{11}$  and a selection of other modes.



**Figure 2.** Dispersion characteristics for modes of azimuthal order 1 in a corrugated waveguide with  $r_1/r_0 = 0.6$ .

Charts such as Figure 3 can be used to determine the bandwidth of corrugated guide if certain modes are to be propagated. Within the surface impedance model, a mode is sustained with increasing frequency over the range in which the corrugation depth increases by slightly more than  $\lambda/2$ .



**Figure 3.** High-frequency cut-off values as a function of wavenumber for different ratios of  $r_1/r_0$ . (After Olver [4])

In the case of the high-frequency cut-offs, higher-order space harmonics have a non-negligible effect, and an error, depending on the mode and waveguide parameters, is to be expected for the SI model predictions. Olver [4] shows these to be of the order of 10%.

As the wave-guide flares out into the horn, the value of  $\beta$ ,  $K$  and  $\Lambda$  all change as is clear from Fig. 2. The  $x$ - and  $y$ -components of the far field patterns of the  $nl$  hybrid modes in the guide can be shown to depend on:

$$\begin{aligned} e_{x,nl} &= (\beta / k + \Lambda) I_{n,l-1}(\sin \theta) \cos(n-1)\phi + (\beta / k - \Lambda) I_{n,l+1}(\sin \theta) \cos(n+1)\phi, \\ e_{y,nl} &= (\beta / k + \Lambda) I_{n,l-1}(\sin \theta) \sin(n-1)\phi + (\beta / k - \Lambda) I_{n,l+1}(\sin \theta) \sin(n+1)\phi, \end{aligned}$$

for the two orthogonal polarisation directions, where  $I_{n,l}(\sin \theta)$  represents the integral:

$$I_{n,l}(\sin \theta) = \int_0^a J_n(p_{nl}r/a) J_n(kr \sin \theta) \exp(-ikr^2/2L) r dr ,$$

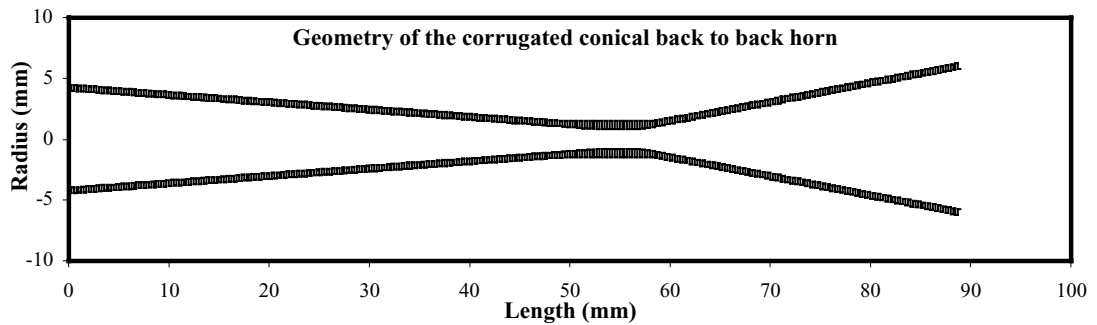
where  $a$  is the radius of the horn aperture, and  $L$  is the axial length of the horn. Thus, the corresponding intensity patterns can be shown to be:

$$P_{nl}(\theta) \propto [(\beta / k + \Lambda) I_{n,l-1}(\sin \theta)]^2 + [(\beta / k - \Lambda) I_{n,l+1}(\sin \theta)]^2$$

If we assume that the hybrid modes independently couple to the cavity then the overall pattern will be given by:  $P(\theta) = \sum_{nl} P_{nl}(\theta)$ .

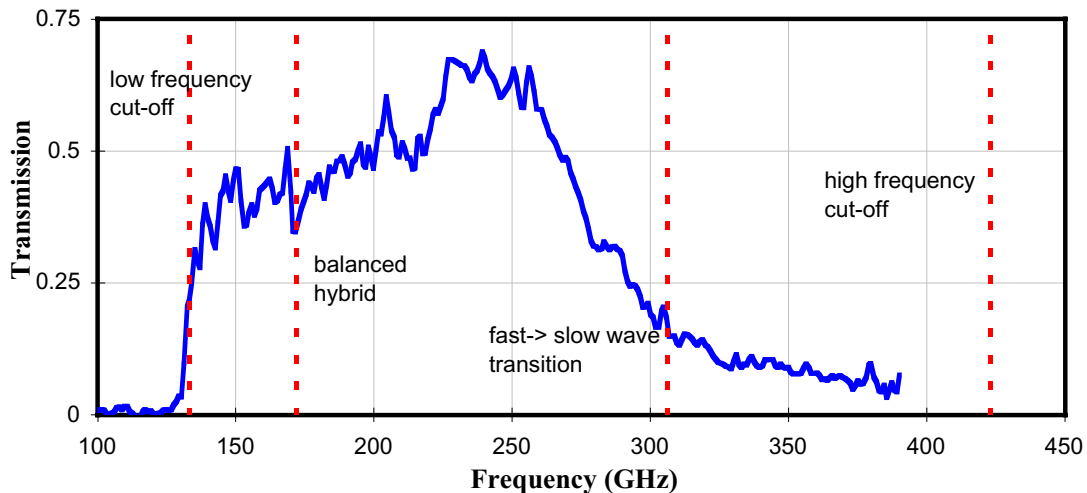
#### 4. Experimental Results

Some preliminary results for multi-moded horn operation, both experimental and theoretical are included here for comparison. The test waveguide corrugated structure is one of the prototype HFI back to back conical horns manufactured for the PLANCK Surveyor [7]. The horn/waveguide structure is 92.75 mm in length and has an aperture diameter of 12.43 mm at the output side. The horn was optimised for single mode operation at 150GHz, but also tested in multi-mode operation at 240GHz. The groove depth is thus 0.5 mm at the horn aperture (i.e. quarter wavelength deep at 150GHz), with both a corrugation and groove width of 0.25 mm, (i.e. 4 corrugations per wavelength at 150GHz). In the filter section the waveguide has  $r_1 - r_0 = 0.5$  mm and  $r_1/r_0 = 0.6$ . A schematic diagram of this type of horn is shown below Fig. 4.



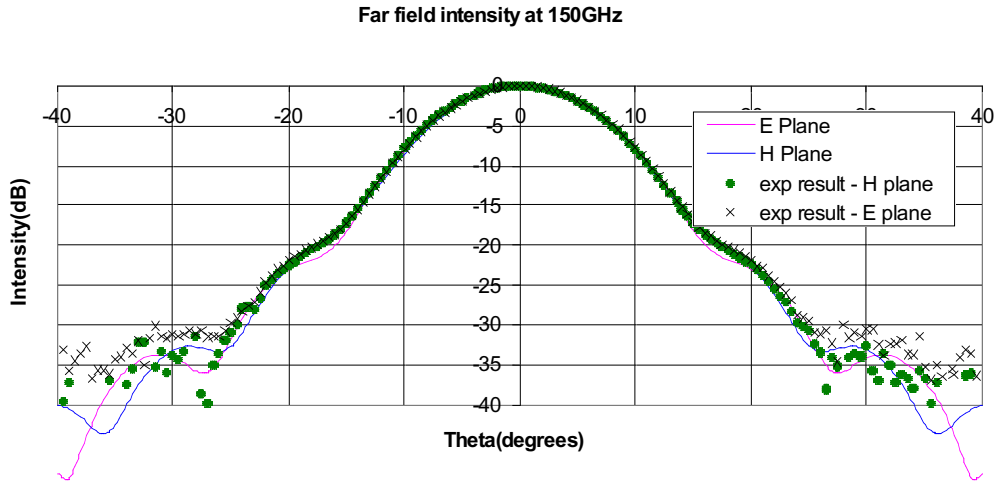
**Figure 4.** Back-to-back horn configuration.

The experimental FTS spectral transmission measurements of the horn/waveguide are plotted in Figure 5. The high- and low-frequency cut-offs, the fast-wave to slow-wave transition point and the balanced hybrid point for the  $HE_{11}$  mode in a waveguide with  $r_1/r_0 = 0.62$  are also marked. The fall-off in efficiency before the high-frequency cut-off may be due to the fast to slow wave transition increasing the losses in the guide and affecting the on-axis gain of the beam pattern of the horn.



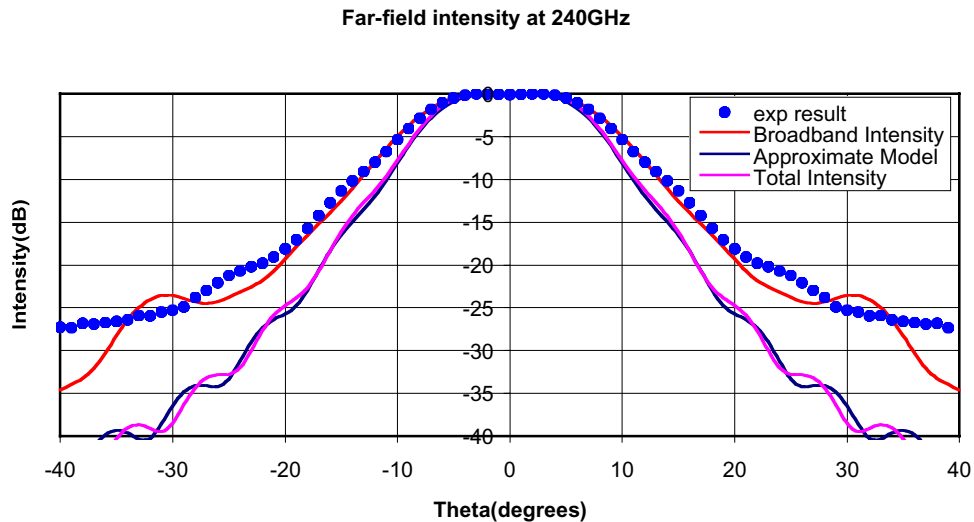
**Figure 5.** The transmission of a pair of back to back conical corrugated horns joined by a waveguide section with  $r_1-r_0 = 0.5\text{mm}$  and  $r_1/r_0 = 0.62$  at its narrowest point

Figure 6 shows the comparison of the theoretical mode-matching model with experimental data taken at 150GHz for single mode operation. The source is plane polarized and spatially coherent (a frequency doubler fed by a Gunn oscillator).



**Figure 6.** Spot frequency beam patterns for HFI prototype back to back horn at 150 GHz.

Figure 7 shows the broadband experimental measurements for the same horn centred at 240GHz with a 25% bandwidth using an incoherent source (mercury arc blackbody source at 2000 K). At 240 GHz we expect to see multi-mode operation. The experimental data compare well with mode-matching model model predictions, where the broadband numerical data was obtained by running the model at the centre and edges of the band and combining the resulting numerical outputs. The experimental data were taken with the test horn in a dewar, with some resultant vignetting at the dewar window suffered by the beam for angles bigger than 20 degrees.



**Figure 7.** Comparison of experimental data with numerical model results at 240 GHz.

The narrower far-field patterns also shown in Fig. 7 are theoretical beam patterns for the same horn at the centre of the frequency band (i.e. at 240GHz) using both the surface impedance and mode-matching approaches. These results show in this case both approaches are in good agreement with each other. It is found from a hybrid mode viewpoint for a horn with an aperture of 6 mm radius, and corrugations of depth  $0.4 \lambda$ , that  $\beta > 0.99 k$ , with  $K = 3.7103, 2.35339$  and  $3.74811$ , and that  $\Lambda = 0, 1.133$  and  $1.170$ , for the  $H_{01}, HE_{11}$  and  $HE_{21}$  modes, respectively. In this case the modes are not pure balanced modes (which require  $\Lambda = +1$  for HE modes), although they are close to meeting the condition. Thus, at least in this example, the depths of the corrugations are not very critical in terms of causing a deterioration in the low sidelobe levels.

## 5. Conclusions

In this paper we have discussed two different approaches to modelling corrugated horn-filter configurations. These types of horns are planned for use as incoherent detector feeds for bolometric detector systems on forthcoming space missions. Good agreement with experimental measurement performed on a prototype horn antenna for the HFI instrument was recorded.

## Acknowledgements

The authors would like to acknowledge the support of Enterprise Ireland in this research programme.

## References

1. J.A. Murphy and R. Padman, "Radiation patterns of few moded horns and condensing lightpipes," *Infrared Physics*, **31**, 291, 1991.
2. R. Padman and J.A. Murphy, "Radiation Patterns of scalar horns," *Infrared Physics*, **31**, 441, 1991.
3. P.J.B. Clarricoats and A.D. Olver, *Corrugated Horns for Microwave Antennas*, Peter Peregrinus (for IEE), 1984.
4. A.D. Olver, P.J.B. Clarricoats, A.A. Kishk and L. Shafai, *Microwave Horns and Feeds*, IEEE Press, 1994.
5. S. Ramo, J.R. Whinnery and T. van Duzer, *Fields and Waves in Communication Electronics*, 2<sup>nd</sup> Edition, Wiley, 1984.
6. S.E. Church et al, "A compact high-efficiency feed structure for cosmic microwave background astronomy at millimetre wavelengths," *30<sup>th</sup> ESLAB Symposium on Submm and Far-IR Space Instrumentation*, ESTEC, Noordwijk, the Netherlands. 1996
7. B. Maffei, et. al. "Corrugated Gaussian Back-to-Back horns for Cosmic Microwave Background continuum receivers," *IEE Antenna Symposium 2000*, QMW, London. April 2000.

# Submillimeter-wave spectral response of twin-slot antennas coupled to hot electron bolometers

R.A. Wyss, A. Neto, W.R. McGrath, B. Bumble, H. LeDuc

*Center for Space Microelectronics Technology, Jet Propulsion Laboratory,  
California Institute of Technology, Pasadena, CA 91109*

## ABSTRACT

The spectral response of quasioptical hot-electron bolometer (HEB) mixers has been measured with a Fourier transform spectrometer. In this study we have measured mixers with a wide range of twin-slot antennas with slot lengths ranging from 26  $\mu\text{m}$  up to 152  $\mu\text{m}$ . For all designs, the measured center of the direct detection response was lower than predictions based on a Method-of-Moment (MoM) calculation of a simplified mixer embedding circuit model. This model took into account the slot antennas and the coplanar waveguide embedding circuit, but not the parasitic effects associated with the couplings of these elements or the HEB device geometry. The frequency shift becomes particularly significant at frequencies beyond 1 THz, and is in excess of 20% for the smallest antennas. Such large shifts reduce the radiation coupling efficiency by more than 3 dB, and hence increase the mixer noise temperature unnecessarily. To resolve the discrepancy between the observations and the model predictions we have introduced two essential refinements into the MoM model which account for (1) the coplanar waveguide (CPW) to slot-antenna transition, and (2) the inductance associated with the effective narrowing of the CPW center lead as represented by the HEB bridge. The results of these model refinements prove to have a small effect on the real-part of the embedding impedance but a dramatic effect on the imaginary-part. In fact, the inductance of the narrow microbridge dominates the estimated frequency shift. Thus we find that properly modeling the entire embedding circuit and the device geometry leads to a better agreement with the measured results.

## Introduction

Previously reported results by Karasik *et al.*<sup>[1]</sup> have shown the center frequency of the peak direct detection response of HEB mixers employing a twin slot-antenna and CPW embedding circuit to be lower than anticipated by up to 20%. The magnitude of the shift is especially dramatic for antenna designs at the very highest frequencies, where HEB mixers have shown their most competitive performance. For example, a twin-slot antenna design, which has been scaled from a 600 GHz design to 2.5 THz, has a peak response at about 2 THz<sup>[2]</sup>. That is a shift of 500 GHz. Several explanations have been

proposed, such as the effects of finite metal thickness<sup>[3]</sup>, limitations of scale-model predictions when extrapolating into the THz frequency region, and parasitics associated with transitions between circuit elements.

In this paper we will report the results of an extensive experimental study of HEB mixers with six different twin-slot antenna designs. The spectral response and hence the center frequency is measured with a Fourier-transform spectrometer. Method-of-Moments (MoM) calculations of both a simplified model<sup>[4]</sup> and a more complete model of the mixer embedding circuit will be compared to the measured results. Understanding the limitations of the circuit models and hence causes of the frequency shift will be critical to designing HEB mixers having a peak response at a desired frequency. Ultimately, this will make possible the design of high-frequency heterodyne mixers that obtain the best possible mixer noise temperatures.

## Experiment

Figure 1(a) shows an SEM photograph of our 2 THz HEB mixer. The submicron-sized HEB device (i.e. “microbridge” in the figure) is connected to the twin slot-antennas by CPW transmission line<sup>[5]</sup>. On the right a flared-shaped center conductor is used as the first element of the intermediate frequency (IF) filter structure (a total of six high and low impedance sections were used).

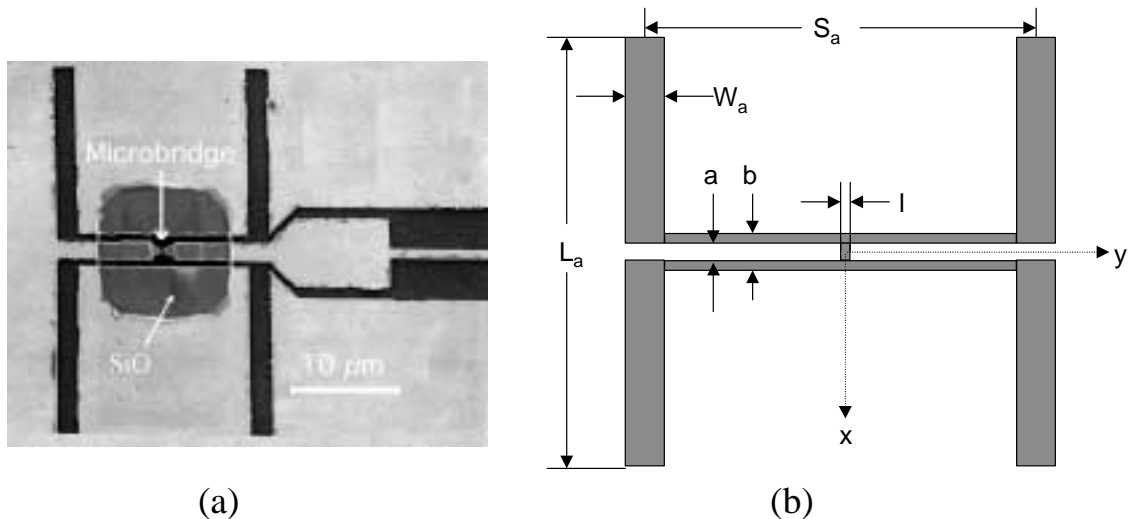


FIG. 1.(a) Photograph of HEB antenna structure. The superconducting bridge is located at the center and coupled to the twin-slot antenna via CPWs. (b) Schematic layout of physical structure used in the simulation with the relevant dimensions defined.

Figure 1(b) defines the relevant parameters for the model we will present in the second half of the paper. The length of the gap between the CPW terminals is  $l$  and the width of the microbridge is  $w$  (not shown in the figure).

The direct detection response of the HEB devices was measured using a Bruker IFS120HR Fourier-transform spectrometer. The spectral resolution during the runs was set to  $1 \text{ cm}^{-1}$  (3 GHz). A mylar beamsplitter thickness of  $50 \text{ }\mu\text{m}$  was used for the  $152 \text{ }\mu\text{m}$ -long slot antenna in order to obtain sufficient signal-to-noise at frequencies below about 1 THz. All the higher frequency twin-slot antennas were measured using a  $23 \text{ }\mu\text{m}$ -thick Mylar beamsplitter which yielded sufficient signal for the range 1 – 3 THz.

For the spectral measurements, the HEB was either constant-current or constant-voltage biased. No difference in the output spectrum was observed for the two different bias schemes. The method used during the measurement was chosen based on better bias stability and lower noise in the output signal. The HEB was operated in a 4 K LHe vacuum-cryostat with an optical access port. The device temperature was set to the transition edge temperature at  $\approx 6 \text{ K}$ . To facilitate stable temperature and minimize the LHe boil-off rate, the mixer block inside the cryostat was mounted on an aluminum post. By applying a dc bias voltage to a heater resistor affixed to the mixer block, the temperature of the block could be controlled and held constant to a precision of  $\pm 10 \text{ mK}$ . The bias point and the mixer block temperature was chosen to maximize the interferogram signal.

## Spectral Response Measurement

Table 1 summarizes the properties of the seven devices measured. We have denoted the antenna design with two numbers: the intended center frequency of the design,  $\nu_c$ , and the length of the slots,  $L_a$ .

Table 1. Mixer characteristics.

Mixer	Antenna Design $\nu_c$ [THz]/ $L_a$ [ $\mu\text{m}$ ]	w [ $\mu\text{m}$ ]	l [ $\mu\text{m}$ ]	$R_{\text{Device}}^{\ddagger}$ T = 295K	$R_{\text{Device}}^{\ddagger}$ T = 4K	$I_c^{\ddagger}$ [ $\mu\text{A}$ ]	$T_{\text{meas}}^{\S}$ [K]
1	2.5/26	0.1	0.2	34	15	240/200	5.03
2	2.5/33	0.1	0.1	-	18	185/171	6.1
3	2.5/36.5	0.1	0.1	-	18	225/107	6.4
4	2.5/36.5	0.15	0.3	-	25	300/120	6.7
5	1.65/44	0.1	0.2	100	46	78/56	5.5
6	1.9/48	0.15	0.3	81	25	172/100	5.68
7	0.6/152	0.15	0.15	75	32	125/50	4.88

$^{\ddagger}R_{\text{Device}}$  is the HEB device DC resistance

$^{\ddagger}I_c$  is the device critical current

$^{\S}T_{\text{meas}}$  is the transition temperature

In Fig. 2 we show the spectral response for mixer 1 and 7, which is representative of the data sets. The spectra have been normalized to the Mylar beamsplitter transmission which was measured using a pyroelectric detector. The response of this reference detector is assumed to be independent of frequency in the range of interest. The measured bandwidths are typically on the order of 50%, increasing slightly for the

highest frequency mixers with the shortest antenna slots. The additional peaks around 1.8 THz for the 152  $\mu\text{m}$  twin-slot antenna are due to a low signal level when using a 50  $\mu\text{m}$  Mylar beamsplitter. The measurements typically required the averaging of 300 spectra having a resolution of 1  $\text{cm}^{-1}$  to achieve the signal-to-noise level displayed in fig. 2. A Gaussian fit was used to find the center and FWHM of the curves.

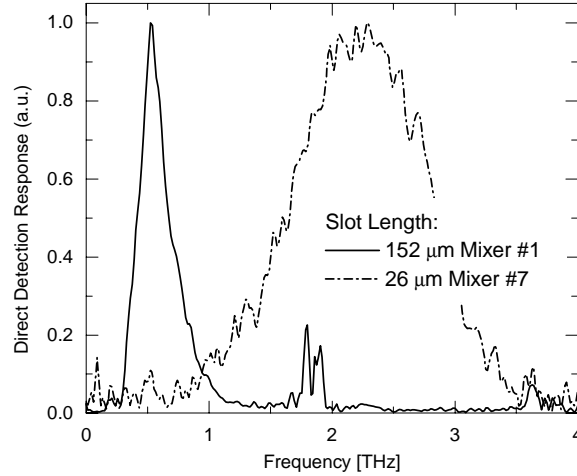


FIG. 2. FTS direct detection response of two mixers (#1 and #7) having slot-antenna lengths equal to 152  $\mu\text{m}$  and 26  $\mu\text{m}$ , respectively.

Table 2 gives a summary of the antenna parameters for each mixer and the measured center frequency. The circuits (CPW lines and slots) are approximately scaled for each frequency, although for the smallest ones, the device fabrication process limited the smallest dimensions of the CPW. Two types of transitions between the slot and the IF-filter were implemented – an abrupt and a tapered transition. The influence on the center frequency and bandwidth is not exactly understood, but based on the current data their influence is found to be secondary. The last column shows the predicted center frequency based on a MoM calculation when treating the twin-slot and CPW as separate elements (that is, no interaction between the two is included). The calculation of the antenna impedance was done using a Fortran code obtained from G. Chattopadyhah<sup>[6]</sup> (similar calculations have been published by several groups). This antenna impedance is then transformed through the length of the CPW line to the device terminals. The coupling efficiency,  $\eta$ , to the HEB device is found using the following well-known impedance-mismatch expression:

$$\eta = 1 - \frac{\left| Z_{\text{HEB}} - 2Z_1 \right|^2}{\left| Z_{\text{HEB}} + 2Z_1 \right|^2},$$

where  $Z_{\text{HEB}}$  is the device impedance (assumed to be real) and  $Z_1$  is the impedance looking into each terminal. Since we assume that the HEB RF impedance is real, the peak response occurs when the imaginary part of the embedded circuit impedance is zero.

Table 2. Antenna parameters, measured and calculated center frequencies.

Mixer	$L_a$ ( $\mu\text{m}$ )	$W_a$ ( $\mu\text{m}$ )	$S_a$ ( $\mu\text{m}$ )	$a$ ( $\mu\text{m}$ )	$b$ ( $\mu\text{m}$ )	$Z_{cpw}$ ( $\Omega$ )	IF-Filter	$\nu_c$ Measured (THz)	$\nu_c$ Calculated (THz)
1	26	3	19	3	4	35.6	abrupt	2.22	2.98
2	33	3	19	3	4	35.6	abrupt	2.19	2.60
3	36.5	2	19	2	3	39.4	tapered	2.02	2.31
4	36.5	2	19	2	3	39.4	tapered	2.01	2.31
5	44	4	25	4.5	6	35.6	abrupt	1.60	2.01
6	48	2.6	25	3	4.4	38.6	tapered	1.71	1.76
7	152	8.3	79.2	8	11	36.4	tapered	0.54	0.57

The three smallest designs are very similar. The intention was to progressively shorten the slot length, and by way of this empirical method to achieve a center frequency of 2.5 THz. This approach worked initially: shortening the slots from 36.5  $\mu\text{m}$  to 33  $\mu\text{m}$  did increase the resonant frequency by the expected 10% or 200 GHz. Further reducing the slot length to 26  $\mu\text{m}$ , however, did not shift the peak response by a proportionate amount. In fact, the shift was as little as 30 GHz. It became clear that some other important physical effect was playing a significant role in determining the frequency response besides just the slot antenna length. The largest discrepancy between the observation and the calculated peak response is for the smallest antenna design (a shift of about 25%).

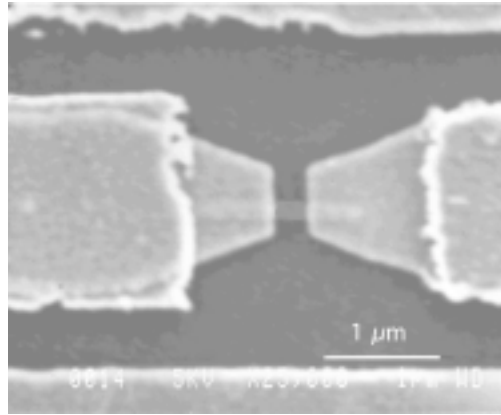


FIG. 3. Photograph of HEB device center region. Terminal connection design is tapered over a distance of about 1  $\mu\text{m}$  with a flare angle of 45°. The bridge is the faint horizontal bar connecting the two terminals. For the CPW shown, the center conductor width is 2  $\mu\text{m}$  and the gaps are 0.5  $\mu\text{m}$ .

## Discussion

The discrepancy between the theoretical predictions and the mixer direct spectral response made clear that our model is incomplete. In this section we present an improved model of the slot antenna/CPW/HEB-microbridge and show that significantly better predictions are possible. The model predicts the general trends that will drive the next

generation mixer designs and helps to better predict the location of the HEB mixer peak response.

The first improvement is to include the transition between the CPW line and the slot antennas. The fringing fields at these junctions add a parasitic reactance to the circuit. The second refinement will be to take account of the reactance (inductance) of the very narrow HEB bridge. Figure 3 shows an SEM photograph of the center region of the embedding circuit. The microbridge is the faint gray horizontal stripe connecting the two terminals. The tapered transition region was introduced to ease alignment during fabrication. The analysis of this geometry has been performed using a previously developed MoM code<sup>[7]</sup>. This code was written to take account of the reactive energy of the bend and the narrowing of the center conductor.

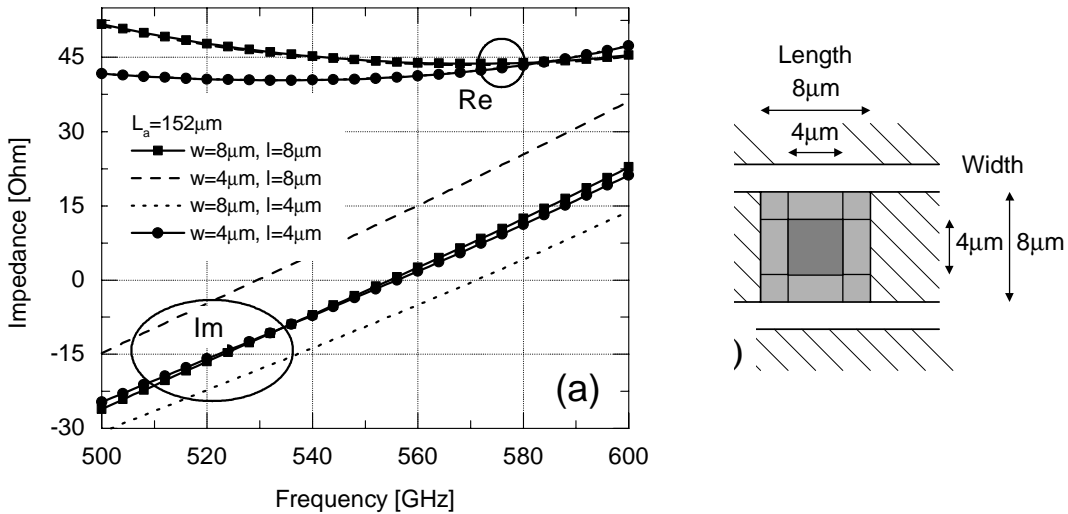


FIG. 4. Dependence of embedding impedance on frequency for several different microbridge sizes. The resonance frequency occurs where the imaginary part passes through zero. (b) The microbridge dimensions used in the simulation.

In Fig. 4 we show the results of the calculation for the mixer with  $152 \mu\text{m}$ -long slot-antennas. To illustrate the general behavior we varied the size of the HEB microbridge while keeping the CPW and slot dimensions fixed. For the largest microbridge ( $8\text{-by-}8 \mu\text{m}^2$ ) the predicted peak response (i.e. where the imaginary part of the impedance crosses zero) is  $555 \text{ GHz}$ , which is very close to the measured  $554 \text{ GHz}$ . When the width of the source region is decreased to  $4 \mu\text{m}$ , the inductance due to the reduced width of the bridge increases and the imaginary impedance increases by about  $15 \Omega$  at  $555 \text{ GHz}$ . Since the frequency dependence of the imaginary impedance is relatively flat, this leads to a large shift in the zero crossing and, hence, the location of the peak coupled power. A shift in the opposite direction can be accomplished by decreasing the length of the bridge and keeping the width constant. This predominantly affects the capacitive reactance of the gap between the center leads of the CPW. Finally, the location of the peak response

is unaffected when keeping the length-to-width ratio constant (4-by-4  $\mu\text{m}^2$ ). The real part of the impedance is barely influenced by the change of the device geometry.

The above example clearly demonstrates the strong influence of the HEB device geometry on the predicted location of the peak. In the next example we have calculated the center frequency of the mixer with a 26  $\mu\text{m}$  twin-slot antenna structure. Since the computational burden on our straightforward MoM implementation is quite large, we employed the following constraints: (1) use a 1  $\mu\text{m}$  resolution ( $\lambda_0/110$ ) which results in  $\sim 200$  piecewise sinusoidal (PWS) functions; (2) set the length of the bridge to 2  $\mu\text{m}$ ; and (3) vary the bridge width from 3  $\mu\text{m}$  to 1  $\mu\text{m}$ . Figure 5 shows a summary of the results.

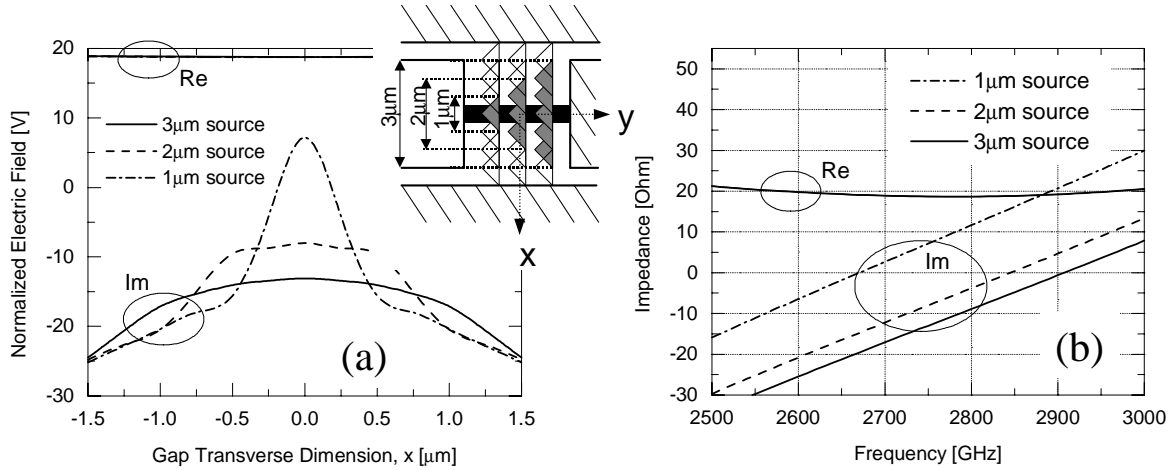


FIG. 5.(a) Real and imaginary amplitude of the normalized electric field along the  $x$ -direction at 2.75 THz. Inset shows the orientation of the seven PWS functions in the device region. (b) Shift in peak response due to reducing the device width. The gap length is kept constant and sufficiently long to minimize the influence of any capacitive induced effects.

Figure 5(a) illustrates that the real part of the electric field (i.e. magnetic current) is completely unaffected by the bridge width. The imaginary part, however, depends dramatically on the transverse dimension. For the 3  $\mu\text{m}$ -wide bridge (solid line) the imaginary part is slowly varying as a function in the gap's transverse direction. For the 2  $\mu\text{m}$  case (dashed line) a more significant growth of about 6  $\Omega$  is observed at the center of the bridge. As the bridge is further reduced to 1  $\mu\text{m}$  (dash-dotted line), the increase amounts to 25  $\Omega$ , which is of the same order of magnitude as the real part of the impedance. The fact that the electric field tends to be peaked in the surrounding of the microbridge can easily be explained. As the bolometer region becomes small in terms of wavelength, the concentrated current flow through the bridge tends to radiate a Hankel function shaped electric field<sup>[7]</sup>. The singularity of this field is logarithmic as the width approaches zero. Thus, we expect a logarithmic growth of the imaginary part of the electric field at the center. This qualitative behavior was observed at all frequencies investigated, and the impact of this behavior is quantified in Fig.5(b).

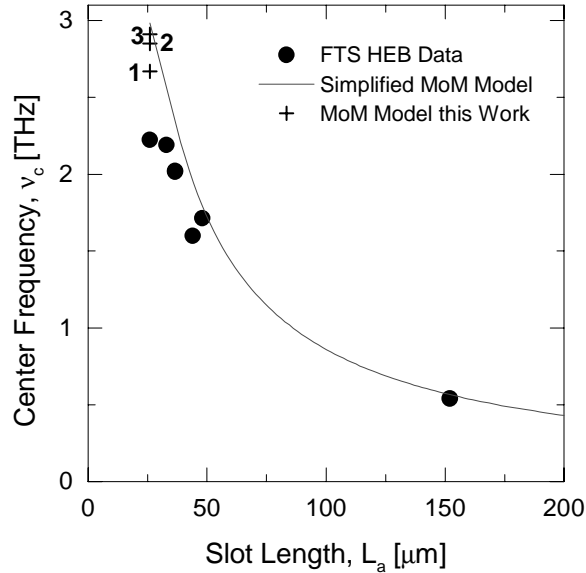


FIG. 6. Summary of experimental data from mixers with six different length twin-slot antenna designs (●). Center frequency of simplified model predicted using G. Chattopadhyah's code<sup>[6]</sup> (solid line). Results of model for the 26  $\mu\text{m}$  twin-slot antenna including parasitics (+). The HEB bridge is either 1, 2 or 3  $\mu\text{m}$  wide.

The zero Ohm level (resonance) is crossed at 2.91 THz as predicted earlier (see Table 2). In this case the HEB device is as wide as the CPW center conductor, and so there is no additional inductance associated with it. However, the resonance frequency is about 3% lower than the 3 THz, which is predicted for the slots and CPW without any interaction. Thus this small shift (3.0 to 2.91 THz) is due to the reactance of the junction of the CPW line with the slot antenna. When a 2  $\mu\text{m}$ -wide device is introduced, a jump of 6  $\Omega$  is observed. Associated with this augmented reactive energy is a shift downward of the resonating frequency to 2.85 THz. A further shift to 2.67 THz follows upon decreasing the device width to 1  $\mu\text{m}$ . It is evident that a further reduction downward in resonating frequency would follow when one further reduces the width of the microbridge. The example has shown that the predominant source of the downward shift is due to the inductive reactance associated with the bolometer itself, while the shift due to the CPW-to-slot junction is small by comparison. We expect to be able to account for the observed 25-30% shift when introducing the actual width of 0.1  $\mu\text{m}$  of the bolometer. Of course, the final calculation will have to take account of the much shorter bridge length, between 0.1 to 0.3  $\mu\text{m}$ . The added capacitance will compensate and shift upwards the resonance frequency somewhat. This "gap capacitance" can potentially be used to provide a low-Q (i.e. broadband) tuning of the device inductance. In Fig. 6 we have summarized the experimental results and the predictions obtained from the two models used to explain the data.

Taking into account the constriction of the RF current caused by the narrow width of the HEB device proved to significantly influence the predicted center frequency. More

importantly, using the refined model made it possible to identify the key source of discrepancy between the observed behavior and predictions. Especially at the highest frequencies, the inductance of the microbridge causes the large frequency shift.

## Conclusion

This paper has presented FTS measurements of THz HEB mixers with a large range of twin slot-antenna designs. A discrepancy had been noted in the actual location of the peak response and predictions based on MoM calculations using a simple circuit model. Refinements of this model, including the CPW-to-slot junction and the narrow width of the HEB device, lead to both an understanding of the causes for the discrepancy and better predictions. The realization that the HEB bridge inductance is responsible for a dominant part of the shift is a breakthrough.

Although further refinements in the model description – possible analytical models – are required to accurately describe the extremely short and narrow bridge correctly, this paper makes a significant contribution in identifying the key elements responsible for the observed downward frequency shifts.

## Acknowledgments

This research was performed in the Center for Space Microelectronics Technology, Jet Propulsion Laboratory, California Institute of Technology, and was sponsored by the National Aeronautics and Space Administration, Office of Space Science.

## References

- [1] B.S. Karasik, M.C. Gaidis, W.R. McGrath, B.Bumble, and H.G. LeDuc, “A low-noise 2.5 THz superconductive Nb hot-electron mixer,” *IEEE Trans. Appl. Supercond.* **7** (2), 3580 (1997).
- [2] R.A. Wyss, ”Noise and bandwidth measurements of diffusion-cooled Nb hot-electron bolometer mixers at frequencies above the superconductive energy gap” *Proc. of the 10<sup>th</sup> Int. Symp. on Space THz Tech.*, University of Virginia, Charlottesville, VA (1999).
- [3] W.F.M. Ganzevles, T.M. Klapwijk, L.R. Swart, J.R. Gao, and P.A.J. de Korte, “Direct response of twin slot antenna coupled hot-electron bolometer mixers designed for 2.5 THz radiation detection”, submitted to *Appl. Phys. Lett.* (12/15/99).
- [4] J. Zmuidzinas and H.G. Leduc, “Quasi-optical slot antenna SIS mixers”, *IEEE Trans. Microwave Theory Tech.*, vol. 40 (9), pp. 1797-1804 (1992).

- [5] B. Bumble and H.G. LeDuc, "Fabrication of a diffusion cooled superconducting hot electron bolometer for THz mixing applications," *IEEE Trans. Appl. Supercond.* **7** (2), 3560 (1997).
- [6] Fortran code calculating the impedance of a coupled twin-slot antenna was obtained from Goutam Chattopadyhah. Computational approach described in Ref. 4.
- [7] A. Neto, P.J.I. de Magt, and S. Maci, "Full wave analysis of slot antennas excited by coplanar waveguides", preprint, (2000).

# Tunable Antenna-Coupled Intersubband Terahertz (TACIT) Detectors for Operation Above 4K

Carey L. Cates, Jon B. Williams, Mark S. Sherwin  
Physics Department and Center for Terahertz Science and Technology,  
UCSB, Santa Barbara, CA 93106

Kevin D. Maranowski, Art C. Gossard  
Materials Department, UCSB, Santa Barbara, CA 93106

## Abstract

The necessity of liquid helium for detectors and sources makes THz space and balloon missions heavy, bulky, and expensive. Tunable Antenna-Coupled Intersubband Terahertz (TACIT) detectors are predicted to operate at temperatures above 4K with good sensitivity. Modeling predicts that TACIT detectors could be operated as direct detectors at 20K with 300K background-limited sensitivity. This flexibility in operating temperature comes from the semiconductor quantum well heterostructures that are used in the detectors. Semiconductor materials and processes also give TACIT detectors flexibility in absorption frequency, time constant and other operating parameters. With this flexibility, it is predicted that TACIT detectors could be made fast enough to operate as sensitive mixers with multi-Gigahertz bandwidths.

A process for making TACIT detectors has been developed. A brief description of TACIT detector fabrication and operation is presented. Flexibility in TACIT detector operating parameters is discussed.

## 1 Introduction

Astronomical observing from space requires sensitive detectors, which with current technology must be cooled with liquid helium. Liquid cryogenics add to the weight and size of satellites, and so add significantly to the overall mission cost. Liquid cryogenics also add to the complexity of operating satellites and can limit mission duration. For all of these reasons, detectors are desirable that are sensitive while operating without liquid cryogenics. These detectors would also be useful in a broader array of applications since they would be more sensitive than current high-temperature detectors such as Schottky diodes.

Low-power mechanical coolers such as hydrogen sorption coolers can offer milliwatt cooling powers at 20K. Current state-of-the-art detectors for space missions are low-temperature composite bolometers and low- $T_c$  superconducting devices. Composite bolometers rely on low temperatures for a large signal to noise ratio. Low  $T_c$  superconductors would be fully in the normal state above 20K, and so would also not be useful. Semiconductor devices, however, including Schottky diodes and FET amplifiers, can operate above 20K. Semiconductor materials also offer great flexibility in designing devices, such that it is possible to design sensitive detectors to operate at these warmer temperatures.

This paper presents how Tunable Antenna-Coupled Intersubband Terahertz (TACIT) Detectors can be operated above 20K with high sensitivity. First the structure and fabrication procedure for a TACIT detector will be discussed. Next the detection mechanism will be described. Then, using a model presented in a previous paper,[1] predictions for operation characteristics will be presented. Lastly, the flexibility of TACIT detectors to be tailored for different applications will be discussed.

## 2 Device

TACIT detectors are made from semiconductor quantum well heterostructures. Current TACIT designs are based on a GaAs/ $Al_{0.3}Ga_{0.7}As$  structure with two quantum wells, shown in Fig. 1. One quantum well is for the active channel region, and the other is designed to connect to the back gate antenna leaf. Electrons are supplied to each quantum well by silicon doping layers outside the wells. The channel quantum well is 400Å wide, which sets the tunable range of the detector. The device consists of a two-level mesa surrounded by GaAs where the quantum wells have been etched away, as shown in Fig. 2. The lower mesa level gives electrical access to the back gate quantum well. The device has four electrical terminals, front and back gates and a source and drain.

Current TACIT detectors are fabricated from the semiconductor heterostructure wafer in five processing steps. The first two steps are chlorine-based reactive ion etches to form the two-tiered mesa structure. Then layers of Ge, Au, and Ni are evaporated onto the sample and annealed to form the ohmic contacts. Next, Ti and Au are evaporated onto the sample to form the antenna. Lastly more Ti and Au are evaporated to create thick metal contacts for wire bonding. The detectors are then cleaved apart, and each one is mounted in a copper sample holder for testing.

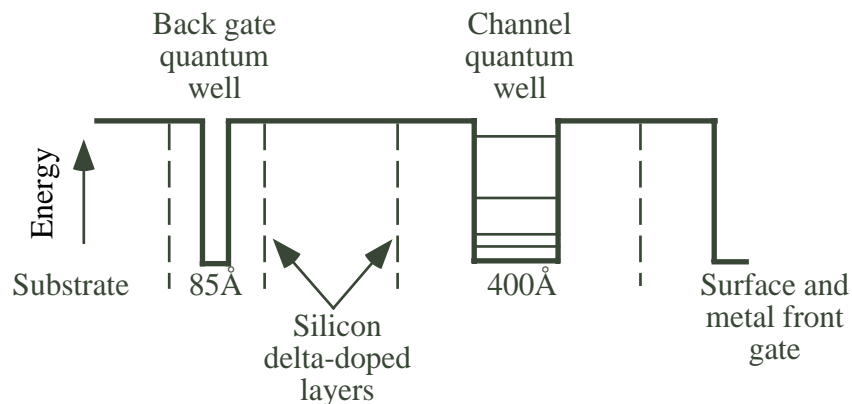


Figure 1: Schematic of one GaAs/ $\text{Al}_{0.3}\text{Ga}_{0.7}\text{As}$  heterostructure being used for a prototype TACIT detector.

### 3 Operation

The basic operation principle of TACIT detectors is that THz light is absorbed in an intersubband transition by electrons in the channel quantum well. with the result that the in-plane resistance of the device changes. There are many mechanisms that can be used to cause the change in resistance. This paper will discuss only one of these mechanisms, but two other mechanisms, one bolometric and the other impurity scattering, have been presented in previous papers.[2, 3]

THz electric fields are concentrated and coupled into the detector with a planar metal antenna. The TACIT detector has four electrical terminals for which signals must be brought to or from the active region. The THz fields are coupled to the front and back gate by a log-periodic toothed antenna. DC voltages are also applied to the antenna leaves via inductive meander lines which block the THz currents. The source and drain are connected to larger contact pads away from the active region by straight wires. This combination is less than ideal, since the straight metal lines can act as a dipole antenna and can also capacitively short the log-periodic antenna. Since there are no published four-terminal antenna designs that are purely planar, for future devices we will use designs that will have a layer of dielectric and a second metal layer to allow the metal leads from the source and drain to cross over the metal of the antenna.

The antenna serves a second important function. The leaves of the antenna are used to change the polarization of the THz electric fields so that they can be absorbed by the electrons in the quantum well in an intersubband transition. Linearly polarized light hitting the antenna at normal incidence induces currents in the antenna leaves. The front gate antenna leaf goes up the side to the top of the mesa.

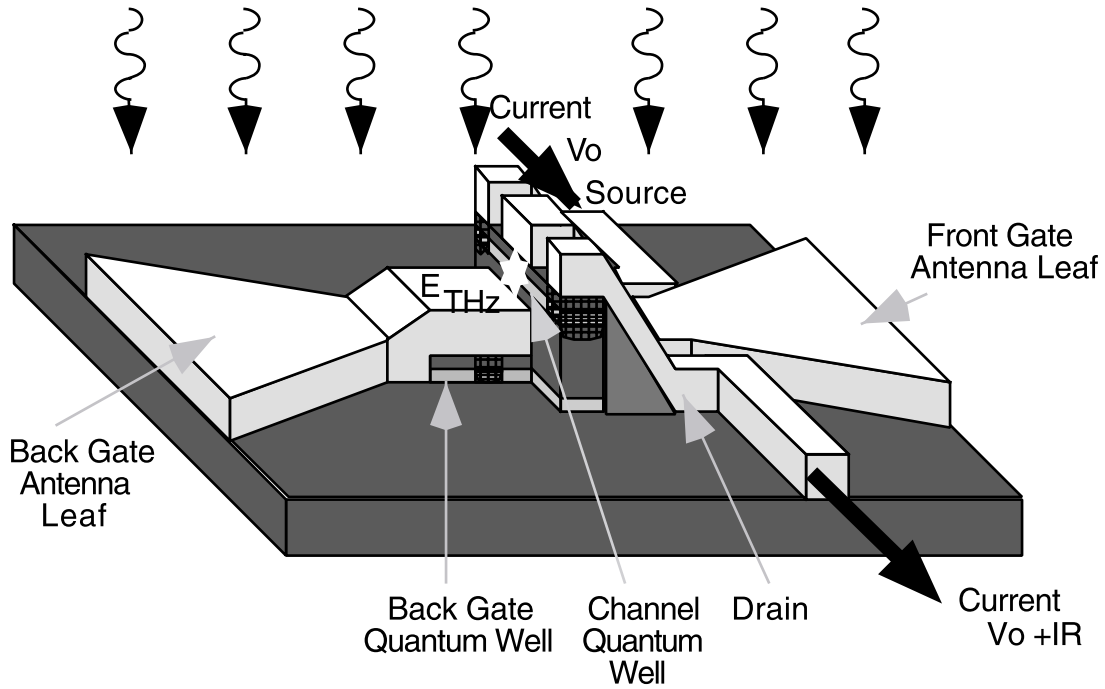


Figure 2: Schematic view of a TACIT detector. Ohmic contacts electrically connect the back gate antenna leaf with the back gate quantum well, and the source and drain contacts to the channel quantum well.

The back gate antenna leaf is electrically connected to the back gate quantum well by an ohmic contact, allowing the oscillating currents to flow from the antenna leaf through the back gate quantum well to the material under the active region. Thus, the THz oscillating electric fields in the active region of the detector are polarized in the direction perpendicular to the quantum well (polarized in the growth direction.) This allows the electrons in the quantum well to absorb the THz radiation in an intersubband transition, which is forbidden for THz fields in the plane of the quantum well. In most previous THz quantum well detectors, the THz oscillating fields were in the plane of the quantum well, and coupled to the electrons via other mechanisms, such as in-plane electron heating. Intersubband transitions are resonant transitions and so yield much stronger coupling between electrons and THz light.

For TACIT detectors, absorbing THz light yields a change in the in-plane electrical resistance of the device. Current TACIT detectors accomplish this by nearly depleting the electrons out of the channel quantum well such that those remaining are trapped in potential fluctuations. The electrons, localized in puddles, can only carry current by hopping conduction, yielding a high effective resistance. Electrons absorbing THz radiation can go to higher energy states that are not localized and thus can carry current with a much lower effective resistance. By analogy with the metal-insulator

Noise equivalent power	$8 \times 10^{-16} \text{ W/Hz}^{1/2}$
Time constant	33ps
Operating (lattice) temperature	20K
THz frequency (tunable)	2.4-4.5 THz
Size of active area	$4 \mu\text{m}^2$
Vertical separation of gates	3430Å
Charge density	$8 \times 10^{10} \text{ cm}^{-1}$
Oscillator strength	0.9
Source-drain voltage	2mV
Source-drain resistance	1kΩ
Mobility ratio	100

Table 1: Model parameters for a TACIT detector operating characteristics.

transition for electrons in a quantum well, we expect to be able to achieve a ratio of effective electron mobilities of around 100.[4] Following modeling presented previously (see Eq. 6 in Ref.[1]), this electron mobility ratio yields a detector that is predicted to have background-limited sensitivity with feasible device parameters, as shown in Table 1.

TACIT detectors have a flexible design allowing them to be optimized toward different operating characteristics. Since the THz (RF) and source/drain (IF) signals travel in different directions, the electrical circuits for each frequency can be designed independently. Additionally, having both a front gate and a back gate allows the charge density and absorption frequency to be independently tuned. By applying a DC voltage on both gates with respect to the channel quantum well, the density of electrons in the channel can be varied. This allows the mobility contrast mechanism mentioned above to be implemented, or could allow the RF impedance of the device to be tuned to precisely match the antenna impedance. By applying differing DC voltages to the gates, an electric field is created across the quantum well, which tunes the intersubband absorption frequency, as shown in Fig. 4.

The time constant of TACIT detectors can also be tailored to fit applications. The time constant can be in the range of a few ps to 1 ns. Longitudinal optical (LO) phonons couple strongly with electrons, making energy relaxation via LO phonons a fast process, taking around 1ps. However, the minimum energy of an LO phonon in GaAs is 36meV (corresponding to a temperature of 420K). Since the energy spacing between the lowest subbands is much smaller, cold electrons in these subbands can only emit acoustical phonons. Purely acoustic phonon cooling at a 10K electron temperature yields a time constant of 1ns.[5] However, if the electron temperature is raised to 50K, the time constant is lowered to below 10ps. The energy of the

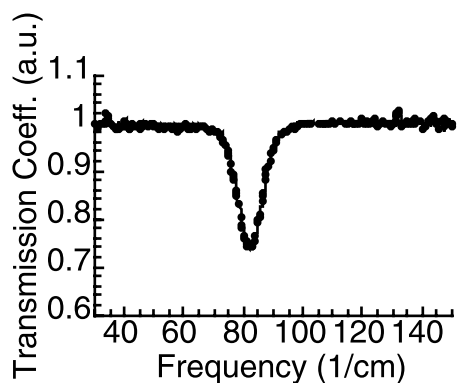


Figure 3: Attenuated transmission measured as a function of frequency for a piece of the heterostructure wafer drawn in Fig. 1.

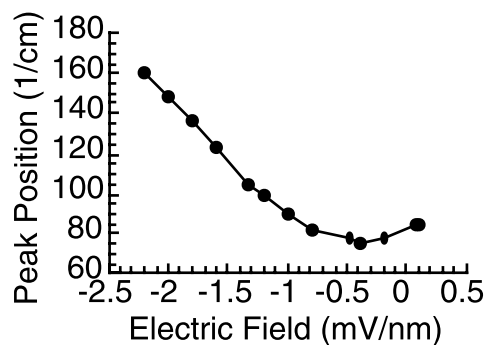


Figure 4: The frequency of peak absorption can be tuned by applying a bias voltage across the detector heterostructure.

majority of electrons is still too low to emit an LO phonon, but a few electrons in the high energy end of the Fermi distribution can, which significantly lowers the time constant of the whole electron gas. Another cooling mechanism that can take part in small semiconductor devices is diffusion of the hot electrons out of the active region. Diffusion cooling has been used in many submicron-sized superconducting hot electron devices. However, the electron mobility of modulation-doped semiconductor quantum wells is orders of magnitude larger than for superconductors, so diffusion cooling in semiconductor devices can dominate for devices that are as long as a few microns. Thus diffusion will add to phonon cooling for many semiconductor devices. The physical dimensions and operating temperatures of TACIT detectors can be chosen to optimize the time constant for a particular application. The time constants can be chosen to be small enough that TACIT detectors could be used as mixers with several GHz predicted intermediate frequency (IF) bandwidth.

The potential barrier walls of quantum wells are sufficiently deep to allow semiconductor-based TACIT detectors to be operated at temperatures of tens of Kelvin. Electrons are still well confined in the quantum well at electron temperatures around 50K. Quantum well heterostructures can be tailored to have strong or weak confinement, as needed, by adjusting the materials used to form the wells. Thus TACIT detectors do not inherently lose all their sensitivity at elevated electron temperatures as low- $T_c$  superconductors do. Material selection and device patterning can also allow control over thermal properties of electrical transport.

## 4 Project Status and Future Work

TACIT detectors have been processed in the UCSB cleanroom facilities. Work is underway to simplify the device design and make a new batch of detectors designed to allow easier study of the detection mechanisms. First, a device structure will be implemented that does not have an antenna, so that operating characteristics will all be due to the detector, and not to a non-optimal four-terminal antenna design. The THz electric fields will be made perpendicular to the plane of the quantum wells by reflecting a free-space propagating, linearly-polarized THz beam off the device through a silicon prism or lens. In the vicinity of the metal front gate, the electric field is constrained to be perpendicular to the gate, and so will be perpendicular to the quantum wells. Direct absorption measurements will be made. Also planned are more and better diagnostic structures, such as contacts for Van der Pauw resistivity measurements, which will be incorporated in or near the detector structure. With these changes the behavior of the TACIT detector can be studied more directly.

Once the TACIT detection mechanisms are verified and more closely studied, then work can proceed on improving and optimizing TACIT detectors for use as direct detectors or for use in THz mixers. Work could also begin on a next-generation TACIT detector that uses two additional voltage-controlled gates to control the in-plane electrical transport. Modeling predicts that mixers incorporating these advanced-design TACIT detectors could achieve quantum-limited sensitivity while operating at a bath temperature of 20K.

## Acknowledgments

This work has been supported by the NSF Science and Technology Center for Quantized Electronic Structures (QUEST) DMR 91-20007, NSF DMR 9623874, AFOSR91-0214, and the NPSC (CC).

## References

- [1] C. Cates, J.B. Williams, M.S. Sherwin, K.D. Maranowski, and A.C. Gossard. Quantum well based tunable antenna-coupled intersubband terahertz (tacit) detectors at 1.8-2.4 thz. *Proceedings of the SPIE - The International Society for Optical Engineering*, 3617:58–66, 1999.

- [2] C.L. Cates, G. Briceno, M.S. Sherwin, K.D. Maranowski, K. Campman, and A.C. Gossard. A concept for a tunable antenna-coupled intersubband terahertz (tacit) detector. *Physica E*, 2(1-4):463-7, July 1998.
- [3] C.L. Cates, G. Briceno, M.S. Sherwin, Maranowski, and A.C. Gossard. A non-bolometric model for a tunable antenna-coupled intersubband terahertz (tacit) detector. *Proceedings of the Ninth International Symposium on Space Terahertz Technology*, 9:597-606, 1998.
- [4] G. Finkelstein, H. Shtrikman, and I. Bar-Joseph. Optical spectroscopy of a two-dimensional electron gas near the metal-insulator transition. *Physical Review Letters*, 74(6):976-9, February 1995.
- [5] J.N. Heyman, K. Unterrainer, K. Craig, B. Galdrikian, M.S. Sherwin, K. Campman, P.F. Hopkins, and A.C. Gossard. Temperature and intensity dependence of intersubband relaxation rates from photovoltage and absorption. *Physical Review Letters*, 74(14):2682-5, April 1995.

# SIS receiver for the 1.2 THz frequency using NbTiN/AlN/Nb junctions

A. Karpov, J. Zmuidzinas, F. Rice, D. Miller, J. A. Stern\*, H. G. LeDuc\*

Downs Laboratory of Physics, California Institute of Technology,  
Pasadena, CA 91125, USA

\* Center for Space Microelectronics Technology, Jet Propulsion Laboratory,  
Pasadena, CA 91109, USA

## Abstract

We present the development of SIS mixer for the band 1.1-1.25 THz of the FIRST heterodyne receiver. The choice of the SIS mixer for the THz frequency receiver is motivated by a relatively low output mixer noise of 20-30 K and by a low intrinsic conversion loss of about 3-5 dB at the frequency of interest. This allows one to consider a possibility to build an SIS receiver with equivalent DSB receiver noise temperature close to 2-3  $h\nu/k$  in the 1-1.3 THz band.

The SIS mixer is using a quasi-optical design with Si hyper hemispherical lens and with a planar twin slot antenna. The two NbN/AlN/Nb  $0.7 \mu\text{m}^2$  area junctions are used in the mixer. The Josephson critical current is close to 45  $\text{kA/cm}^2$  and in the middle of the band  $R\omega C \approx 5$ .

The ground plane of the mixer circuit is made of NbTiN. The critical temperature of the NbTiN film deposited at the Si substrate is close to 16 K. The tuning circuit of the junctions is made of a normal metal.

The expected loss in the junction tuning circuit is about 1 dB and the overall receiver conversion loss is expected to be close to 7 dB. The mixer testing is under way.

# STUDY OF PARYLENE AS ANTI-REFLECTION COATING FOR SILICON OPTICS AT THz FREQUENCIES

M. Ji\*, C. Musante\*, S. Yngvesson\*, A. J. Gatesman\*\* and J. Waldman\*\*

**\*Department of Electrical and Computer Engineering  
University of Massachusetts Amherst  
Amherst, Massachusetts 01003**

**\*\*Submillimeter-Wave Technology Laboratory  
University of Massachusetts Lowell  
Lowell, Massachusetts 01854**

## ABSTRACT

In this paper, we report a study of thin films of Parylene used as an anti-reflection (AR) layer for silicon optics in the THz range. Parylene is a polymer with attractive properties such as thermal stability, good adhesion and conformity, low water absorption and chemical inertness. We had two Si substrate double side coated with Parylene C and D by Specialty Coating Systems, Inc. The film thicknesses were close to 25 $\mu$ m. Transmission spectra were obtained between 450GHz and 2.8THz in a Fourier Transform Spectrometer. By modeling the three-layer structure, a refractive index of 1.62 was obtained for Parylene C and Parylene D, which, in combination with a modest absorption loss, makes them appropriate for AR coating materials at THz frequencies.

## I. INTRODUCTION

Single layer thin films are routinely used as a means of suppressing the reflection of electromagnetic radiation from a surface. The ideal parameters of such a film for zero reflection is:

$$n_{\text{AR}} = \sqrt{n_0} \text{ and,} \quad (1)$$

$$t_{\text{AR}} = \frac{(2m + 1)\lambda}{4n_{\text{AR}}} \quad (m = 0, 1, 2, \dots), \quad (2)$$

where  $n_{\text{AR}}$  and  $n_0$  are the refractive indices of the AR layer and the optical component, respectively, and  $t_{\text{AR}}$  is the thickness of the coating. Assume normal incidence. The thickness of the AR layer can be any odd number of quarter wavelengths and typically is minimized due to film absorption.

AR coatings of this type are routinely achieved in the visible and infrared spectral regions (e.g.  $\text{MgF}_2$  on glass, SiO on silicon, and ZnS on germanium) where such materials can be applied with conventional thin film deposition techniques. At terahertz frequencies, difficulties are encountered when depositing materials at the thickness required for AR behavior ( $t_{\text{AR}} > 10 \mu\text{m}$ ). Alumina-loaded epoxy has been used with good results as an AR coating for silicon lenses [1]. The epoxy material suffers from large absorption loss above 1 THz, however [2]. Common plastics such as Mylar and Kapton are potential candidates because their refractive indices are close to the required value of  $\sqrt{n_{\text{Si}}} \cdot 1.85$ , however, these materials may be difficult to apply to small, curved optics such as a silicon lens. New materials with the necessary refractive index and low-loss behavior must be found which can be deposited in uniform layers at least  $\sim 10 \mu\text{m}$  thick. Vacuum-deposited parylene, a material which is primarily used as a conformal encapsulant in the electronics industry, is one such candidate. Parylene is a thermoplastic polymer which has many attractive properties such as thermal stability, good adhesion properties, chemical inertness, and low water absorption.

Parylene C films have been successfully used between 1 – 8 THz as AR coatings on germanium lenses for the ISO satellite project [3]. The parylene-coated lenses were optimized for maximum broadband sensitivity of a detector field-lens assembly. Transmission of uncoated germanium in that frequency range is  $\sim 47\%$ . Parylene C coatings were used to substantially increase the transmittance of the optics with transmission peaks approaching 90%. Another device which would benefit significantly from low-loss AR coatings at terahertz frequencies is the superconducting hot-electron bolometer (HEB) [4]. These sensitive detectors of terahertz radiation typically use small silicon lenses to focus radiation onto an antenna-coupled detector element. All HEB measurements so far above 1 THz have been done without the use of AR-coated focusing lenses which results in a  $\sim 30\%$  reflection loss at the silicon lens surface. Detector noise temperatures could be improved by 20%-30% by the use of a low-loss AR coating. The ability of parylene to be applied as a uniformly thick, conformal coating would make coating the small, curved surface of a HEB silicon lens possible. Irwin [5] has used parylene as an AR coating on silicon at mid-infrared wavelengths in

construction of dielectric-spaced resonant mesh filters. He reports both refractive index and absorption coefficient data for parylene N. The results indicated that the refractive index was either 1.44 or 1.62 and the absorption coefficient was too large for his application at those frequencies. Chen [6] studied the performance of a parylene-coated metal mesh filter at mid-infrared wavelengths and reported a refractive index of 1.65. In this report, thin coatings of parylene C and parylene D were used as AR coatings for high-resistivity silicon optics. Types C and D were chosen because of their higher dielectric constant compared with parylene N. The refractive index and absorption coefficient were found by studying the transmittance spectra of the parylene-coated silicon.

## II. MEASUREMENTS

Two 25-mm-diameter silicon etalons, polished to a thickness of 1012.0  $\mu\text{m}$ , were coated with parylene C and parylene D by Specialty Coating Systems, Inc., Clear Lake, WI, to a thickness of 24.0  $\mu\text{m}$  and 26.5  $\mu\text{m}$  (both sides), respectively. High-resistivity ( $\rho > 20,000 \text{ } \Omega\text{-cm}$ ), single-crystal silicon was chosen as the substrate material because its properties were well-known at terahertz frequencies [7] and its low-loss behavior would permit the loss of the parylene to be estimated.

Submillimeter-wave spectra were acquired using a Bruker IFS 66v Interferometer configured with a Hg-lamp source, Mylar beamsplitter, and a LHe-cooled Si bolometer detector. Unpolarized, power transmittance measurements were acquired at normal incidence and under vacuum to minimize the influence of atmospheric water vapor at these frequencies. Figure 1 shows an under-resolved transmittance spectrum of one of the high-resistivity silicon etalons prior to coating. The gradual downward trend of the spectrum towards higher frequencies is due to loss in the silicon. From this and prior research on silicon at these frequencies [8], we were able to determine the terahertz behavior of the uncoated silicon substrates. Figures 2 and 3 show the transmittance of the parylene C and parylene D coated silicon, respectively. AR behavior can be observed at approximately 1.9 THz for the parylene C coated silicon and 1.7 THz for the parylene D coated silicon. The two frequencies do not coincide due to slight differences in coating thicknesses. These experimental data, along with the knowledge of the properties of silicon, allowed for the determination of the refractive index  $n$  and absorption coefficient  $\alpha$  of parylene C and parylene D.

## III. ANALYSIS

Theoretical modeling of the spectra in Figures 2 and 3 was performed by using the Fresnel equations and a standard matrix calculation technique [9]. Typically,

the refractive index and absorption coefficient of a single layer of low-loss material can be determined at terahertz frequencies from transmission spectra (such as Fig. 1) provided that the material thickness is known and not too large. However, by theoretical modeling of the 3-layer parylene/silicon/parylene system, we found that it was possible for all three quantities ( $n_{AR}$ ,  $\alpha_{AR}$ , and  $t_{AR}$ ) of the parylene coating to be determined with reasonable accuracy from transmittance data alone, provided that the properties of the silicon substrate were known. We found that the location in frequency of the AR behavior determined the coating's thickness, the width of the transmittance envelope at the AR frequency determined the coating's refractive index, and the amount of transmittance determined the coating's loss. The refractive index  $n_{AR}$  also impacts the location of the AR behavior as may be expected, but not without impacting the width of the envelope of the spectrum. In other words, only one ( $n_{AR}$ ,  $t_{AR}$ ) pair was found to fit the data. It was in this fashion that the optical properties and thickness were obtained for the parylene C and parylene D films from transmittance data alone.

The thicknesses of the films provided by the coater were larger than the thicknesses found by modeling the data. The coater reported thicknesses of 27.2  $\mu\text{m}$  and 32.3  $\mu\text{m}$  for the parylene C and D films, respectively, by using a step profilometer. Optical modeling indicated slightly lower thicknesses of 24.0  $\mu\text{m}$  for parylene C and 26.5  $\mu\text{m}$  for parylene D which agreed well with micrometer measurements of 22.5  $\mu\text{m}$  and 28.0  $\mu\text{m}$  for the two films, respectively.

A refractive index of  $n = 1.62$  was found for both parylene C and D and was observed to be independent of frequency between 450 GHz and 2.8 THz. A value of  $n = 1.62$  is lower than the ideal value of 1.85, however, excellent AR performance was still observed. For the parylene C sample, the average transmittance (averaged over a few fringes) at 1.9 THz reached 89%. Of the 11% difference from unity, loss in the silicon accounted for 1-2%, loss in the parylene accounted for 6%, and the remaining 3-4% was due to parylene C's non-ideal refractive index. For the parylene D sample, the average transmittance at 1.7 THz was 91%. Of the 9% difference from unity, the loss in the silicon accounted for 1-2%, loss in the parylene accounted for 4%, and the remaining 3-4% was due to parylene D's non-ideal refractive index.

In the case where only a single AR layer is required such as a silicon hemispherical lens for a HEB, total absorption losses due to the parylene would be only • 2-3%. Due to the fact that the films were thin and parylene's absorption was relatively small at these frequencies, only upper level estimates were made for the material's loss. The absorption coefficients  $\alpha$  for parylene C and D were modeled with an absorption coefficient linearly increasing with frequency from •

2 cm<sup>-1</sup> to 16 cm<sup>-1</sup> and from • 1 cm<sup>-1</sup> to 10 cm<sup>-1</sup>, respectively, between 450 GHz and 2.8 THz. A summary of the terahertz optical properties of parylene C and parylene D along with the silicon substrate is given in Table I.

#### IV. CONCLUSIONS

We have successfully used thin films of parylene as an AR coating for silicon optics at terahertz frequencies. The measured refractive index of  $n = 1.62$  is not optimal for silicon, which prefers an AR coating to have a refractive index of  $n = 1.85$ , however, excellent AR performance was still observed. Our data indicate that parylene C and parylene D with their reasonably modest absorption coefficients would each make a suitable choice for an AR coating for silicon at terahertz frequencies. Coatings sufficiently thick for AR performance at • 2 THz reduced the average transmittance by < 10% compared to a lossless AR coating of an ideal refractive index. But for frequencies below 1 THz, use of parylene for AR performance may be prohibited due to coating thickness and uniformity issues.

#### V. REFERENCES

1. N. G. Ugras, J. Zmuidzinas, and H. G. LeDuc, "Quasi-optical SIS mixer with a silicon lens for submillimeter astronomy," *Proceedings of the 5<sup>th</sup> Int. Symp. on Space Terahertz Tech.*, p. 125, 1994.
2. J. W. Lamb, "Miscellaneous data on materials for millimeter and submillimeter optics," *Int. J. Infrared and Millimeter Waves*, Vol. 17, No. 12, pg. 1997, Dec. 1996.
3. M. J. M. van der Vorst, "Integrated lens antennas for submillimeter-wave applications," Ph.D. thesis, Techn. University Eindhoven, 1999.
4. E. Gerecht, C. F. Musante, Y. Zhuang, K. S. Yngvesson, T. Goyette, J. Dickinson, J. Waldman, P. A. Yagoubov, G. N. Gol'tsman, B. M. Voronov, and E. M. Gershenson, "NbN hot electron bolometric mixers—a new technology for low-noise THz receivers," *IEEE Trans. on Microwave Theory and Techniques*, Vol. 47, No. 12, pg. 2519, Dec. 1999.
5. P. G. J. Irwin, P. A. R. Ade, S. B. Calcutt, F. W. Taylor, J. S. Seeley, R. Hunneman, and L. Walton, "Investigation of the dielectric spaced resonant

mesh filter designs for PMIRR," *Infrared Physics*, Vol. 34, No. 6, pgs. 549-563, 1993.

6. P. A. Chen, "The performance of dielectric coated mesh filter," *Journal of Infrared and Millimeter Waves*, Vol. 8, No. 1, Jan. 1987.
7. A. J. Gatesman, R. H. Giles, and J. Waldman, "High-precision reflectometer for submillimeter wavelengths," *J. Opt. Soc. Am. B*, Vol. 12, No. 2, February 1995.
8. A. J. Gatesman, "A high precision reflectometer for the study of optical properties of materials in the submillimeter," Ph.D. dissertation, University of Massachusetts Lowell, Lowell, MA, 1993.
9. R. M. A. Azzam and N. M. Bashara, *Ellipsometry and Polarized Light*, North-Holland Publishing Co., 1977.

Table I. Terahertz optical properties of silicon substrate and parylene films

	THz Refractive Index $n$	Absorption Coefficient $\alpha$ (1/cm) from $\nu = 450$ GHz - 2800 GHz
uncoated silicon	3.416*	0.17*
parylene C	1.62	$0.006 \nu - 0.7$
parylene D	1.62	$0.004 \nu - 0.8$

\* at 2 THz

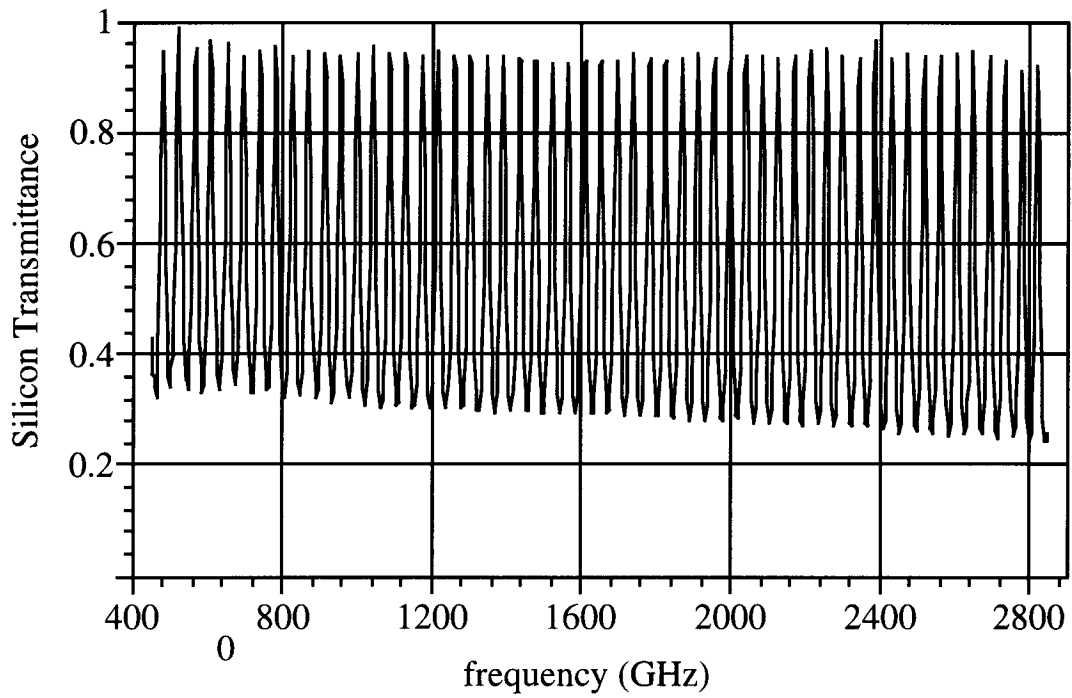


Figure 1. Under-resolved THz transmittance of an uncoated high-resistivity ( $\rho > 20,000 \text{ } \Omega\text{-cm}$ ) 1012- $\mu\text{m}$ -thick silicon substrate.

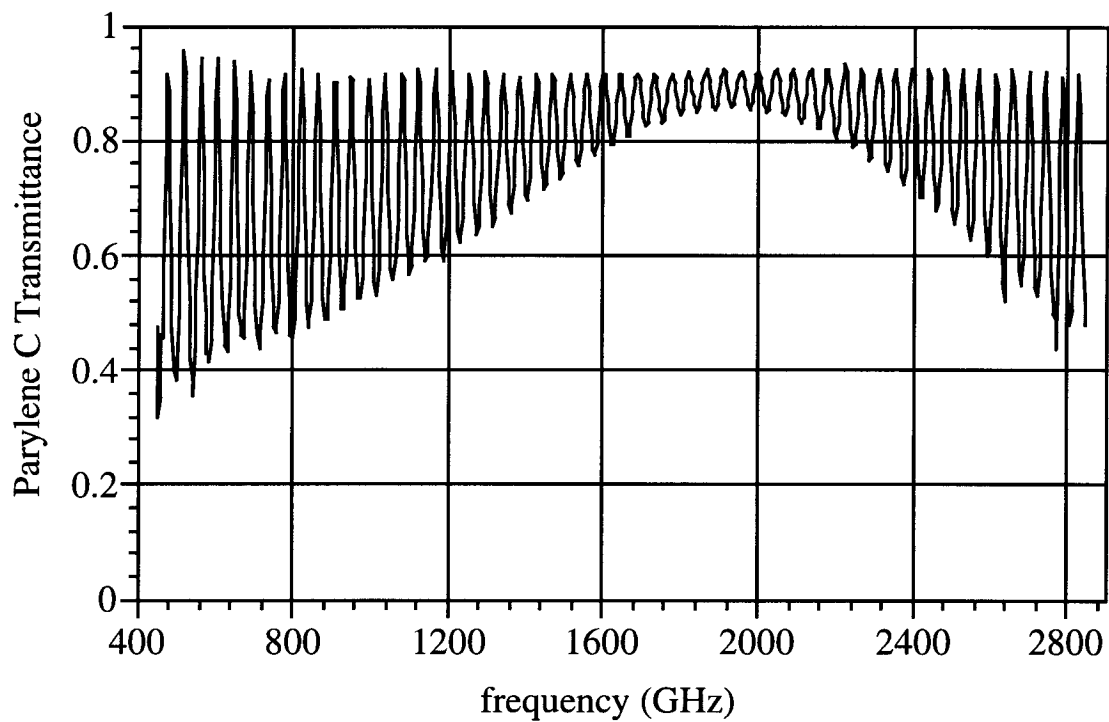


Figure 2. Terahertz transmittance of a high-resistivity ( $\rho > 20,000 \text{ } \Omega\text{-cm}$ ) 1012- $\mu\text{m}$ -thick silicon substrate coated with 24.0  $\mu\text{m}$  of parylene C on both sides.

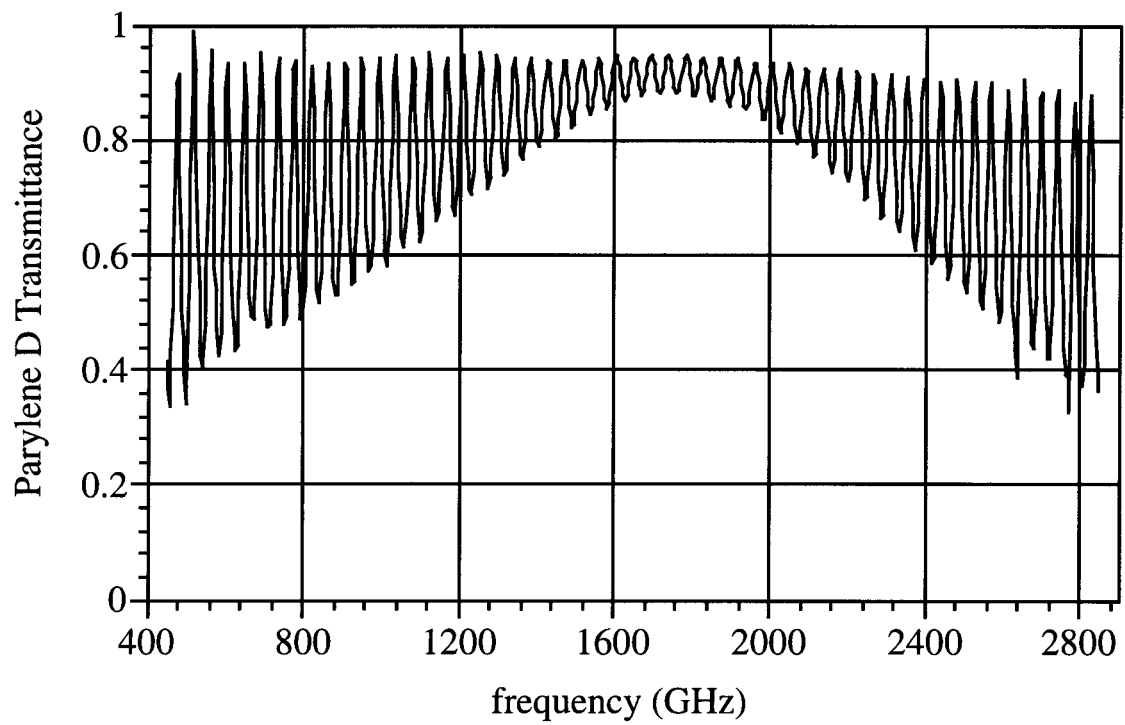


Fig. 3. Terahertz transmittance of a high-resistivity ( $\rho > 20,000 \text{ } \Omega\text{-cm}$ ) 1012- $\mu\text{m}$ -thick silicon substrate coated with 26.5  $\mu\text{m}$  of parylene D on both sides.

# Optimization of Superconducting Hot-Electron Sensors: Controlling of Electron-Phonon Relaxation

A. Sergeev and V. Mitin.

*Department of ECE, Wayne State University, Detroit, MI 48202*

## Abstract

Electron scattering from boundaries and impurities destroys the single-particle picture of the electron-phonon interaction. We show that quantum interference between 'pure' electron-phonon and electron-boundary/impurity scattering may result in the enlargement as well as to the significant reduction of the electron relaxation time. This effect crucially depends on the extent, to which electron scatterers are dragged by phonons. Static and vibrating scatterers may be described by two dimensionless parameters  $q_T l$  and  $q_T L$ , where  $q$  is the wave vector of the thermal phonon,  $l$  is the total electron mean free path,  $L$  is the mean free path due to scattering from static scatterers. According to Pippard, without static scatterers the relaxation rate is  $1/ql$  slower than the rate in pure bulk material. However, in the presence of static potential the relaxation rate turns out to be  $1/qL$  times faster. Thus, at low temperatures, electron energy relaxation may be controlled in a wide range. For instance, we expect that the possible variation of the electron relaxation time at 100 mK spans the interval from  $10^{-6}$  to 0.1 s. Slow relaxation allows us to reach values of NEP of direct resistive detectors as small as  $10^{-21}$  -  $10^{-20}$  W/Hz<sup>1/2</sup> at 100 mK.

## Introduction

The idea of a superconducting hot-electron sensor was proposed more than 15 years ago [1]. In such sensor (for a review see [2]), the radiation overheats only electrons in a superconducting film driven by the current (magnetic field) in a resistive state. The phonons in the film remain in equilibrium with the substrate and play the role of a heat sink for electrons. Thus, the electron-phonon interaction is a bottleneck for the heat transfer from electrons to the heat sink. This regime is achieved by increasing the thermal conductance between the superconducting structure and the environment, opposite to the case of conventional bolometers. The characteristic time of the sensor is determined by the inelastic electron-phonon scattering time. The sensitivity is limited by the fluctuations of electron parameters (electron temperature, quasiparticle chemical potential). High quantum efficiency is reached due to strong electron-electron interaction in disordered conductors. The figure-of-merit of the hot-electron sensor depends only on the heat capacity of electrons (quasiparticles), while in conventional bolometers there is additional large heat capacity of the whole detector. Therefore, the hot-electron sensor offer the best figure-of-merit of any type of bolometers.

Up to now, fast hot-electron detectors with characteristic time 0.1-10 ns operating at helium temperatures have been well developed and are used as broadband mixers. With controllable slow relaxation of hot electrons (quasiparticles) and due to small electron heat capacity, hot-electron superconducting sensors are very promising to use as ultrasensitive resistive detectors and quantum calorimeters. We present new concepts of controlling parameters of hot-electron sensors. The sensitivity of direct detectors

and quantum calorimeters may be significantly improved in comparison with the sensitivity of traditional bolometric devices.

Electron-phonon relaxation rate is controlled by the quantum interference between 'pure' electron-phonon and electron-boundary/impurity scattering [3]. The interference may result in the enlargement as well as to the significant reduction of the electron-phonon relaxation time. This effect crucially depends on the extent, to which electron scatterers, such as boundaries and impurities, are dragged by phonons. Static and vibrating scatterers may be described by two dimensionless parameters  $q_T l$  and  $q_T L$ , where  $q_T$  is the wave vector of the thermal phonon,  $l$  is the total electron mean free path, and  $L$  is the mean free path due to scattering from static scatterers. Without static scatterers the relaxation rate is  $1/ql$  slower than the rate in pure bulk material. However, in the presence of static potential the electron-phonon relaxation rate turns out to be  $1/qL$  times faster. Slow relaxation allows one to reach record values of sensitivity [4]. Due to its unique sensitivity, direct detectors and quantum calorimeters based on electron heating may be successfully employed for many astrophysical measurements of weak electromagnetic radiation and energy of particles.

### Pippard ineffectiveness condition

In recent years, the electron relaxation and dephasing in ultrathin films, nanostructures and mesoscopic devices has been intensively studied. Note, that the temperature-dependent dephasing rate is mainly determined by the electron-electron and electron-phonon interactions. While theoretical results pertaining to electron-electron scattering are confirmed by many experiments, the electron-phonon scattering mechanism is still poorly understood. Unfortunately, most researchers employ the standard clean-limit concept, its uncritical application leads to incorrect and controversial conclusions. A reliable electron-phonon interaction model taking into account electron scattering from boundaries, defects and impurities is of vital importance.

If scattering potential of boundaries and impurities is completely dragged by phonons, the inelastic electron scattering from this potential may be excluded by a transformation to the frame, which moves together with the phonon. In other words, in this case the local lattice velocity plays a role of the hydrodynamical variable. Using transformation to the local frame, Pippard has found that the electron-phonon coupling depends essentially on the parameter  $ql$ , where  $q$  is the wave vector of a phonon, and  $l$  is the electron mean free path. If  $ql < 1$ , the electron-phonon coupling is a factor of  $ql$  weaker than the coupling in the pure limit,  $l \rightarrow \infty$ . This statement is well known as the Pippard ineffectiveness condition [6, 7]. It was confirmed by microscopic calculations in [8].

Obviously the Pippard's assumption about completely dragged scatterers is not valid in micro and nanostructures. The electron scattering from boundaries and defects with a mass different from a mass of host atoms significantly changes effective electron-phonon interaction. To generalize the Pippard's model we take into account additional static potential. We show that even relatively weak static potential drastically changes the effective electron-phonon coupling and corresponding electron dephasing rate.

### Model

We start with the Hamiltonian, which describes the 'pure' electron-phonon interaction and the interaction between electrons and scatterers that are completely dragged by phonons [8, 10],

$$\begin{aligned}
 H_{int} &= \sum_{\mathbf{p}, \mathbf{q}} g(\mathbf{q}) c_{\mathbf{p}+\mathbf{q}}^+ c_{\mathbf{p}} (b_{\mathbf{q}, n} + b_{-\mathbf{q}, n}^+) + \sum_{\mathbf{p}, \mathbf{k}, \mathbf{R}_\alpha} V(\mathbf{k}) c_{\mathbf{p}}^+ c_{\mathbf{p}-\mathbf{k}} \exp(-i\mathbf{k}\mathbf{R}_\alpha) \\
 &+ \sum_{\mathbf{p}, \mathbf{k}, \mathbf{q}, \mathbf{R}_\alpha} \gamma(\mathbf{k}, \mathbf{q}) c_{\mathbf{p}}^+ c_{\mathbf{p}-\mathbf{k}} (b_{\mathbf{q}, n} + b_{-\mathbf{q}, n}^+) \exp[-i(\mathbf{k} - \mathbf{q})\mathbf{R}_\alpha],
 \end{aligned} \tag{1}$$

where  $c_{\mathbf{p}}^+$  is the electron creation operator,  $b_{\mathbf{q}, n}^+$  is the creation operator of a phonon with a wave vector  $\mathbf{q}$  and polarization index  $n$ , and  $\mathbf{R}_\alpha$  are the equilibrium positions of scatterers.

The vertex of pure phonon-electron scattering is given by

$$g = \frac{2\epsilon_F}{3} \frac{\mathbf{q} \cdot \mathbf{e}_n}{(2\rho\omega)^{1/2}}, \tag{2}$$

where  $\epsilon_F$  is the Fermi energy,  $\mathbf{e}_n$  is the phonon polarization vector,  $\rho$  is the density.

The second term describes elastic electron scattering from the scattering potential  $V$ . If this potential is completely dragged by phonons, the vertex of inelastic electron scattering is given by [9]

$$\gamma(\mathbf{k}, \mathbf{q}) = -iV(\mathbf{k}\mathbf{e}_n)/(2\rho\omega_q)^{1/2}, \quad (3)$$

The inelastic electron scattering is characterized by a large value of the electron momentum transferred to impurity ( $k \sim p_F$ ), while the transferred energy is the same as in the pure phonon-electron interaction.

We will assume that the potential  $V$  is  $\delta$ -correlated random potential. Then the electrical resistivity determined by the Hamiltonian in the form of eq. (1) is

$$\rho(T) = \rho_0 + \rho_{BG}(T) + \rho_{int}(T), \quad (4)$$

where  $\rho_0$  is the residual resistivity due to elastic electron scattering,  $\rho_{BG}$  is the Bloch-Grüneisen term due to the pure electron-phonon scattering. The interference term,  $\rho_{int}$ , is determined by the inelastic electron scattering and quantum nonequilibrium corrections to the processes of pure electron-phonon scattering [10]. If  $T > u/l$ , the interference term has a form:  $\rho_{int} = B\rho_0 T^2$ , the longitudinal phonons give a negative correction to the resistivity, while the transverse phonons result in a positive correction [10].

Now take into account the static scatterers (rigid boundaries and heavy defects). Then the total momentum relaxation rate ( $1/\tau$ ) is determined by

$$\tau^{-1} = \tilde{\tau}^{-1} + \tau_{qs}^{-1}, \quad (5)$$

where  $1/\tilde{\tau}$  is the electron momentum relaxation rate due to scatterers that are dragged by phonons, and  $1/\tau_{qs}$  is the relaxation rate due to static scatterers. It is convenient to introduce the electron mean free path,  $l = v_F\tau$ , and the electron free path with respect to scattering from static potential,  $L = V_F\tau$ . As we will see, the modification of the electron dephasing rate crucially depends on the parameter  $l/L$ .

## Electron Relaxation Rate

The electron-phonon collision integral taking into account the interference between different channels of electron scattering may be obtained by means of the Keldysh diagrammatic technique for nonequilibrium processes. Cumbersome calculations will be presented elsewhere. The collision integral, which describes the interaction between longitudinal phonons and electrons in a disordered conductor with static and vibrating scattering potentials is given by

$$I_{e-l.ph}(\epsilon) = -\frac{\beta_l T^3}{(p_F u_l)^2} \int d\omega_q R(\epsilon, \omega_q) \left[ \frac{ql\zeta_0}{1-\zeta_0} - \left(1 - \frac{l}{L}\right) \frac{3}{(ql)^2} \right], \quad (6)$$

where  $\zeta_0 = \arctan(ql)/(ql)$ , the dimensionless constant of the electron-phonon interaction  $\beta_l = (2\epsilon_F/3)^2 \nu / 2\rho u_l^2$  ( $u_l$  is the longitudinal sound velocity), and  $R(\epsilon, \omega_q)$  is the combination of electron ( $n_\epsilon$ ) and phonon ( $N_\omega$ ) distribution functions,

$$R(\epsilon, \omega) = N_\omega n_\epsilon (1 - n_{\epsilon+\omega}) - (1 + N_\omega)(1 - n_\epsilon) n_{\epsilon+\omega}. \quad (7)$$

The electron relaxation rate is determined as

$$\frac{1}{\tau_{e-ph}(\epsilon)} = -\frac{\delta I_{ph-e}}{\delta n_\epsilon} (n_\epsilon = n_\epsilon^{eq}), \quad (8)$$

where  $n_\epsilon^{eq}$  is the equilibrium distribution function.

Finally, the energy relaxation rate of electrons interacting with longitudinal phonons is

$$\frac{1}{\tau_{e-l.ph}(0)} = \frac{7\pi\zeta(3)}{2} \frac{\beta_l T^3}{(p_F u_l)^2} F_l(q_T l), \quad (9)$$

$$F_l(z) = \frac{2}{7\zeta(3)} \int_0^{A_l} dx \Phi_l(xz) (N_x + n_x) x^2, \quad (10)$$

$$\Phi_l(x) = \frac{2}{\pi} \left( \frac{x \arctan(x)}{x - \arctan(x)} - \frac{3}{x} \frac{\tau}{\tilde{\tau}} \right), \quad (11)$$

where  $A_{t(l)} = \theta_D l / u_{t(l)} z$  ( $\theta_D$  is the Debye temperature). In the limiting cases the relaxation rate is given by

$$\frac{1}{\tau_{e-l.ph}(0)} = \frac{7\pi\zeta(3)}{2} \frac{\beta_l T^3}{(p_F u_l)^2} \text{times} \begin{cases} 1, & Tl > u_l, \\ \frac{2\pi^3}{35\zeta(3)} \frac{Tl}{u_l} + \frac{3\pi}{7\zeta(3)} \frac{u_l}{TL}, & Tl < u_l. \end{cases} \quad (12)$$

Now we consider interaction of electrons and transverse phonons. The corresponding collision integral has a form

$$I_{e-t.ph}(\epsilon) = \frac{3\pi^2 \beta_l T^2}{(p_F u_t)(p_F l)} \left(1 - \frac{l}{L}\right) \int d\omega_q R(\epsilon, \omega_q) \left[1 + \left(1 - \frac{l}{L}\right) \frac{3x - 3(x^2 + 1) \arctan(x)}{2x^3}\right], \quad (13)$$

where the dimensionless constant is  $\beta_t = \beta_l (u_l / u_t)^2$ , and  $u_t$  is the transverse sound velocity. Then the electron relaxation rate is

$$\frac{1}{\tau_{e-t.ph}(0)} = \frac{3\pi^2 \beta_l T^2}{p_F^2 u_t} \left(\frac{1}{l} - \frac{1}{L}\right) F_t(q_T l), \quad (14)$$

$$F_t(z) = \frac{4}{\pi^2} \int_0^{A_t} dx \Phi_t(xz) (N_x + n_x^{eq}) x, \quad (15)$$

$$\Phi_t(x) = 1 + \left(1 - \frac{l}{L}\right) \frac{3x - 3(x^2 + 1) \arctan(x)}{2x^3}. \quad (16)$$

In the limiting cases the electron relaxation rate is

$$\frac{1}{\tau_{e-t.ph}(0)} = \frac{3\pi^2 \beta_l T^2}{p_F^2 u_t} \left(\frac{1}{l} - \frac{1}{L}\right) \times \begin{cases} 1, & Tl > u_t, \\ \frac{l}{L} + \left(1 - \frac{l}{L}\right) \frac{\pi^2}{10} \left(\frac{Tl}{u_t}\right)^2, & Tl < u_t. \end{cases} \quad (17)$$

Therefore, in the impure case ( $Tl < u_l, u_t$ ), the electron-phonon scattering rate is given by

$$\frac{1}{\tau_{e-ph}(0)} = \frac{\pi^4 T^4}{5} (p_F l) \left[ \frac{\beta_l}{(p_F u_l)^3} + \frac{3\beta_t}{2(p_F u_t)^3} \left(1 - \frac{l}{L}\right) \right] + \frac{3\pi^2 T^2}{2p_F L} \left[ \frac{\beta_l}{p_F u_l} + \frac{2\beta_t}{p_F u_t} \left(1 - \frac{l}{L}\right) \right].$$

## Discussion

Presence of static and vibrating electron scatterers leads to complex quantum interference between different scattering mechanisms. If boundaries, defects and impurities are completely dragged by phonons ( $L \rightarrow \infty$ ), we reproduce results of Ref. 9 for electron-relaxation rate. In agreement with the Pippard ineffectiveness condition, at low temperatures the electron-phonon relaxation rate is  $u/(Tl)$  times slower than the rate in a pure conductor. Note, that in our model with spherical Fermi surface, in the pure conductor only longitudinal phonons interact with electrons. Transverse phonons may interact with electrons due to vibrating boundaries and impurities, which generate a new channel of the electron-phonon interaction. In the limit  $Tl/u \gg 1$ , this channel is  $Tl/u$  times weaker than the pure electron-phonon interaction. In limit  $Tl/u \ll 1$ , both channels are enhanced due to the diffusion electron motion. However, due to the quantum interference, strong scattering processes cancel each other. Obtained by many authors [11], conclusion about enhancement of the electron-phonon interaction due to disorder in the frame of the Pippard model is wrong.

This picture is changed in the presence of additional static potential (or due to incomplete drag of boundaries and impurities by phonons). In the limit  $Tl/u \ll 1$ , where the interference is important, the electron relaxation rate turns out to be  $u/(TL)$  times faster than the rate in the pure conductor. Note, that the relaxation rate due to transverse phonons consists of the large factor  $(u_l/u_t)^3$  and the factor  $(1 - l/L)$  compared with the relaxation effect of longitudinal phonons. The factor  $(1 - l/L)$  has a simple interpretation: it is proportional to the concentration of vibrating scatterers, which provide the interaction between electrons and transverse phonons. If this factor is not too small, the effect of transverse phonons dominates at low temperatures.

To illustrate our results, we calculate the electron relaxation rate in Al structures. Parameters of Al are  $u_l = 3.2 \cdot 10^5$  cm/s,  $u_t = 1.2 \cdot 10^5$  cm/s,  $v_F = 14 \cdot 10^7$  cm/s,  $\beta_l = 0.2$ , and  $\beta_t = 1.4$ . Temperature dependences of the relaxation rate in the structures with the electron mean free path  $0.05 \mu\text{m}$  and  $0.005 \mu\text{m}$  are presented in figs. 1 and 2. Solid lines show the relaxation rate under the Pippard ineffectiveness condition. At low temperatures the relaxation becomes faster in the presence of the static potential. Comparing figs. 1 and 2, we see that at low temperatures the electron relaxation is determined by transverse phonons.

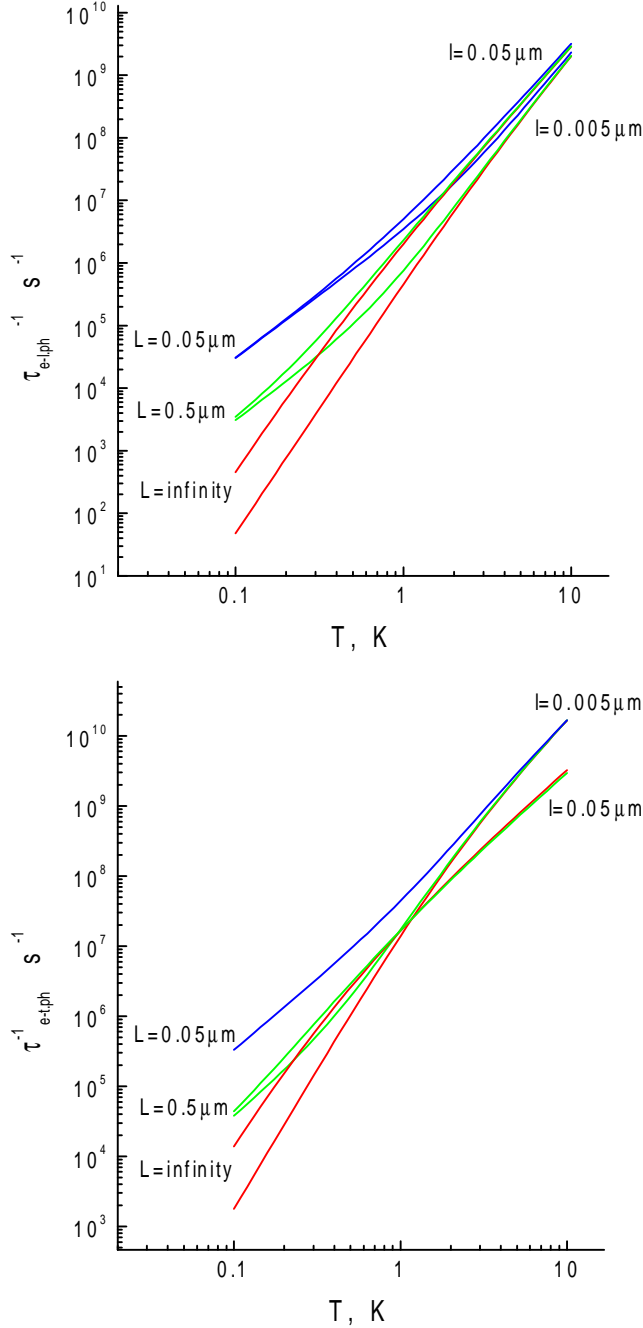


Fig. 1 and 2. Electron relaxation rate due to longitudinal (Fig. 1) and transverse (Fig. 2) phonons in Al structures with electron mean free path  $l=0.005 \mu\text{m}$  and  $0.05 \mu\text{m}$ . Solid lines correspond to complete drag of all scatterers (boundaries and impurities) by phonons. Dashed and dotted lines correspond to the electron mean free path with respect to the static potential  $L=0.05 \mu\text{m}$  and  $0.5 \mu\text{m}$ .

Fig. 3 shows the dependence of the relaxation rate on the electron mean free path. In the case of complete drag of boundaries and defects, the relaxation rate is proportional to  $l$  at low temperatures. In the presence of the static potential, the relaxation rate is determined mainly by the electron mean free path with respect to scattering from this potential.

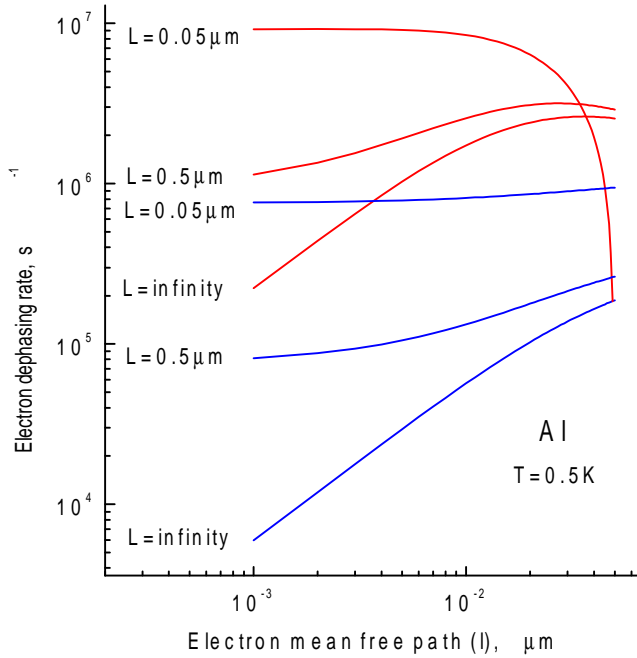


Fig. 3. Dependence of the relaxation rate on the electron mean free path. Solid and dotted lines present contributions of longitudinal and transverse phonons.

It is important for applications, that the electron-phonon scattering rate in micro and nanodevices may be changed in a wide range. It can be increased or decreased compared to the rate in a pure bulk material. For instance, we expect that the possible variation of the electron relaxation time at 100 mK spans the interval from  $10^{-6}$  to 0.1 s. Slow relaxation allows us to reach values of NEP of direct resistive detectors as small as  $10^{-21} - 10^{-20}$  W/Hz $^{1/2}$  at 100 mK [4].

Some experimental data support our conclusions. The enhancement of the electron-phonon interaction due to disorder has been found in thin metallic films [12] and semiconducting heterostructures [13]. The  $T^2$ -dependence of the electron-phonon relaxation rate is widely observed in experiments [14]. The  $T^4$ -dependence has been found in hafnium films on sapphire substrates. We speculate that the last result is due to very good acoustic matching of hafnium and sapphire.

Some important points, such as the modification of the phonon spectrum and vibrations of boundaries and defects, deserve further theoretical investigations. Complex measurements of the relaxation rate and parameters of electron scatterers are also very desirable.

## References

- [1] E.M. Gershenson et. al., JETP Lett. **36**, 297 (1982); JETP1. E.M. Gershenson et. al., JETP Lett. **36**, 297 (1982); JETP **59**, 442 (1984); Solid State Commun. **50**, 207 (1984).
- [2] A.V. Sergeev and M.Yu. Reizer, Int. J. Mod. Phys. B **10**, 635-665 (1996).
- [3] A. Sergeev and V. Mitin, "Electron-phonon interaction in disordered conductors: static and vibrating scattering potentials", Phys. Rev. B **61**, 6041 (2000).

- [4] B. Karasik, W.R. McGrath, M.E. Gershenson and A.V. Sergeev, "Photon-noise limited direct detector based on disorder-controlled electron heating", accepted to *J. Appl. Phys.*
- [5] I.G. Gogidze, P.B. Kuminov, A.V. Sergeev and E.M. Gershenson, "Possibility of fabricating an inductive high-speed detector of electromagnetic radiation using YBaCuO films", *Tech.Phys.Lett.* **25**, 47 (1999).
- [6] A.B. Pippard, *Philos. Mag.* **46**, 1104 (1955).
- [7] J.M. Ziman, *Electrons and Phonons* (Clarendon, Oxford), p. 213, 1960.
- [8] G. Grünvald and K. Scharnberg, *Z. Phys.* **268**, 197 (1974).
- [9] J. Rammer and A. Schmid, *Phys. Rev. B* **34**, 1352 (1986).
- [10] M.Yu. Reizer and A.V. Sergeev, *Zh. Exsp. Teor. Fiz.* **92**, 2291 (1987) [*Sov. Phys. JETP* **65**, 1291 (1987)]; N.G. Ptitsina, G.M. Chulkova, K.S. Il'in et. al, *Phys. Rev. B* **56**, (1997) 10089.
- [11] G. Bergman, *Phys. Rev. B* **3**, 3797 (1971); H. Takayama, *Z. Phys.* **263**, 329 (1973); S.G. Lisitsin, *Sov. J. Low Temp. Phys.* **1**, 728 (1975); S.J. Poon and T.H. Geballe, *Phys. Rev. B* **18**, 233 (1978).
- [12] J.J. Lin and C.Y. Wu, *Europhys. Lett.* **29**, 141 (1995).
- [13] A. Mittal, R.G. Wheeler, M.W. Keller, D.E. Prober, and R.N. Sacks, *Surf. Science* **361-362**, 537 (1996).
- [14] G. Bergmann, *Phys. Rep.* **107**, 1 (1984).
- [15] M.E. Gershenson, D. Gong, T. Sato, B.S. Karasik, W.R. McGrath, and A.V. Sergeev, this issue.

# **A Compact, Fiber-Pigtailed, Terahertz Time Domain Spectroscopy System**

**D. Zimdars, J. V. Rudd, and M. Warmuth**

Picometrix, Inc., P. O. Box 130243, Ann Arbor, MI 48113-0243

## **1. INTRODUCTION**

Terahertz time-domain spectroscopy (TDS) is a field that has been steadily growing in research labs over the last 11 years<sup>1</sup> with demonstrated spectroscopic applications in semiconductors,<sup>2</sup> liquids,<sup>3,4</sup> and gases,<sup>5</sup> as well as more recent applications based on 2D-imaging.<sup>6</sup> However, even with the interest outside of the ultrafast community given to terahertz spectroscopy and imaging (such as the system initially developed by Nuss and co-workers and popularized as “T-Rays” ),<sup>7</sup> the commercialization of a THz TDS system has been hindered by its complexity. In order to build a TDS system, skills in ultrafast lasers and optics, semiconductor physics, and sub-millimeter waves optics are required. Even if all of the individual components, from the photoconductive antennas to the silicon lenses, were available for purchase, the resulting system would not be useful in most manufacturing or even laboratory environments due to the complexity and instability of free-space optical systems. For these technical reasons, it has been simply not feasible, until now, to take advantage of THz spectroscopy techniques outside of specialized laser science laboratories.

In order to make T-Rays available for general use in the labs of all scientists, we have designed and built a fiber-delivered T-Ray system. The central enabling technology of the Picometrix system revolves around two fiber-pigtailed, hermetically sealed modules that work as the T-Ray transmitter and receiver. These devices are installed inside two larger cases that hold not only the electronics necessary for the modules, but also the millimeter wave optics used to collect and collimate the T-Ray beams. Two fiber-optic and electrical umbilical cords attach these cases to a control box, which contains the computer-controlled, fiber-delivered delay system as well as the fiber optic splitter and optical monitors. Finally, an advanced computer program gives the user the ability to control the entire system and take data without having to align any optics beyond the input fiber. This system represents a major leap forward in the accessibility of ultrafast optics to the general research community as well as a first step in getting this extremely useful tool into more general use.

## **2. THE T-RAY SYSTEM**

Figure 1 shows a working fiber-pigtailed terahertz system, while Figure 2 shows a schematic of the system, detailing the components inside each of the boxes. While the group velocity dispersion control (GDC), in the upper right corner of the picture, and the

laser (not shown in Figure 1), must be coupled by free-space optics the remainder of the system is free of the need for an optical table. The control box in particular can sit on a shelf or the floor and not take up valuable space on an optical table. The terahertz cases must be aligned in order to maximize both their signal and their bandwidth, but the required accuracy can be obtained and kept with a simple optical rail and inexpensive alignment components as shown in Figure 1. Furthermore, once the desired alignment for one's particular measurement is determined a mounting bracket can be machined for these two cases, which will then lock them in place for future use.

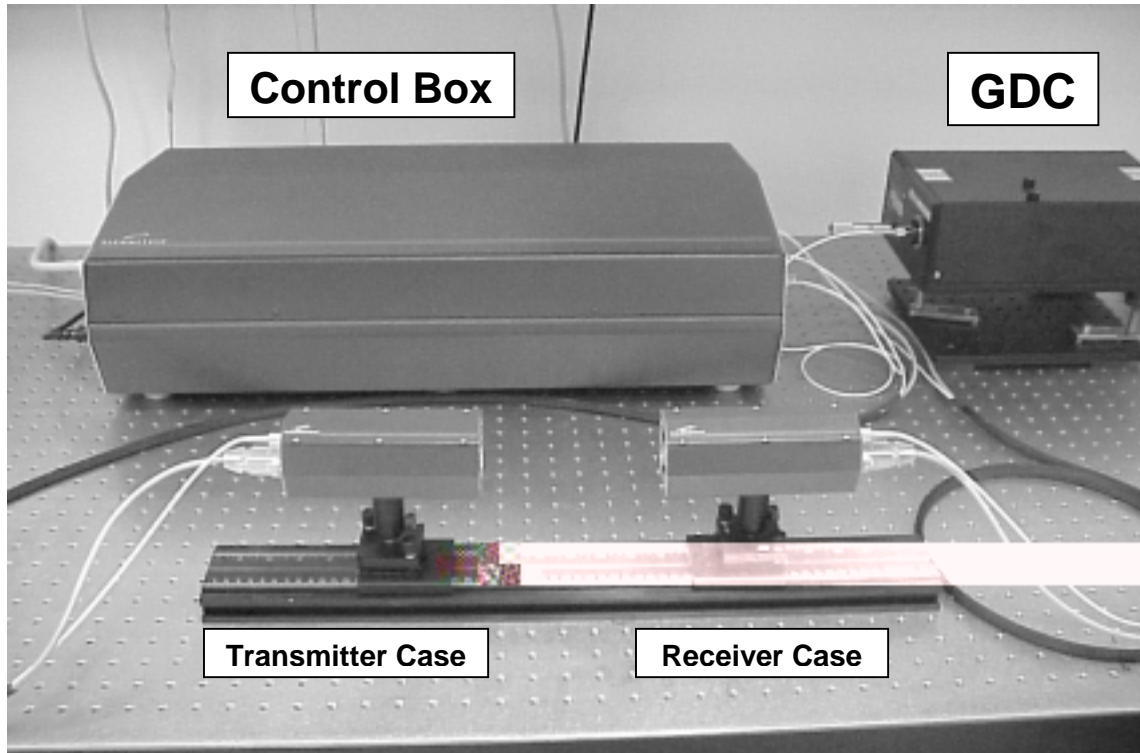


**Figure 1.** The major components of the TDS T-Ray spectroscopy system, less the femtosecond laser and control computer. With the exception of the GDC in the upper right, the other three components do not necessarily have to be on an optical table. The components necessary for imaging are also not shown.

The photoconductive system is powered by a 100-fs laser that works between 750-850 nm and delivers at least 20 mW of optical power. This laser then double-passes a grating-dispersion compensator (the GDC) that imparts negative group-velocity dispersion (GVD) onto the pulse, stretching it to a length of about 5 ps. This stretched pulse is then coupled into a 780-nm singlemode fiber, which delivers the pulse to the control box. The positive GVD of the 5-meters of fiber in our system adds to this negative GVD, compressing the pulse as it travels along the fiber to the terahertz transmitter (Tx) and receiver (Rx). Although the third-order dispersion is additive in these two systems, this only becomes a problem for pulse widths below about 70 fs

and/or fiber lengths greater than about 10 meters. By using a rugged laser that has low variability over time, high-efficiency gratings, as well as by controlling the beam dimensions, GDC systems with 80% of the laser power being coupled into the singlemode fiber have been demonstrated.<sup>8</sup> Since our output electrical signal saturates when optical powers greater than about 10 mW are coupled into the input fiber, this corresponds to only 12.5 mW of total power needed to run the system.

Once the light is in the optical fiber it is taken to the control box, where it is then split into two beams. The first (the pump) is sent directly to the T-Ray transmitter, while the second (the probe) is delivered via fiber to the dual delay system. The delay rail consists of an approximately 20 Hz scanner that has an excursion of 40 ps sitting on top of a stepper-motor rail with a total travel corresponding to 1 ns and speeds ranging from 5-50 ps/sec. This probe pulse is then coupled back into a fiber and delivered to the T-Ray receiver. Both output fibers go through a 99/1 splitter, which picks off 1% so that the user can monitor the power delivered to the transmitter and the receiver by looking at the calibrated readouts in the software.

The two-meter long optical cables deliver the short pulses to the cases while the electrical cables deliver bias voltages to both the receiver amplifier and the transmitter as well as transmit the received signal back to the control box for processing by the computer. Both cases hold their respective fiber-pigtailed module in alignment with the collimating lens such that the terahertz beam exiting the cases has no spatial chirp and is parallel to the case itself. The lenses are 1.5" in diameter with a 3" focal length, and may be made from high-resistivity silicon so that the T-Ray radiation is not absorbed or dispersed by the lens material, or from high density polyethylene for low Fresnel loss. The receiver case also contains a circuit board with the signal amplifier. Finally, the beam path inside the cases is purged with dry nitrogen and sealed in order to eliminate water vapor absorption in this part of the beam.

The T-Ray beam path between the two cases can be used collimated to go through, or reflect off of, large samples, or the user can introduce two more silicon lenses in between them in order to introduce a focus for imaging. Due to the fiber delivery, the two cases can be switched from transmission mode to reflection mode in minutes.

### **Miniature, packaged terahertz transmitter and receiver modules**

The heart of the entire system shown in Figures 1 and 2 is the packaged transmitter and receiver modules shown on the left hand side of Figure 3. These modules, which contain a low-temperature grown GaAs (LT-GaAs) antenna as the photoconductive element, also have a relay lens and fiber anchor inside of them. The fiber is permanently aligned to the THz antenna with sub-micron precision and the module is back-filled with an inert gas and then hermetically sealed using standard telecom packaging methods. The photoconductive device, which has a 2-mm bowtie antenna, is attached to a high-resistivity silicon, aplanatic hyperhemispherical lens which

helps couple the radiation out of the package efficiently without causing beam diffraction. The module is less than 1 inch long by ½ inch square and weighs only a few ounces. This THz module is robust and suitable for use in industrial remote sensing as well as in laboratory spectroscopy.

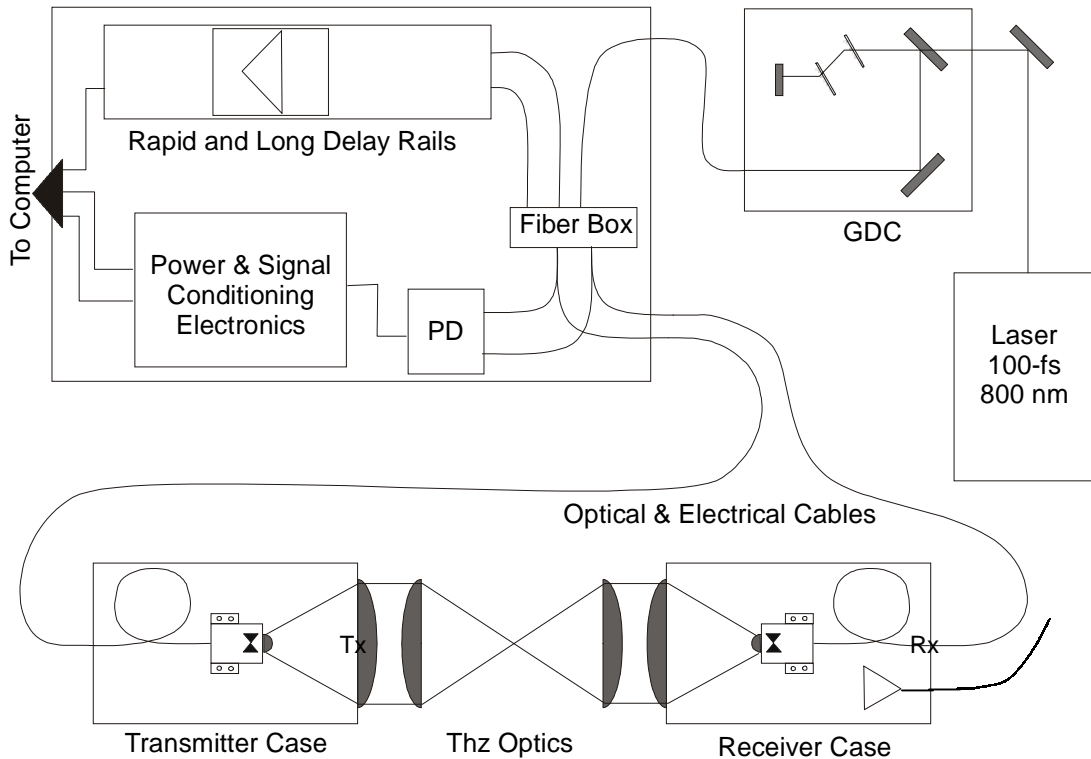


**Figure 2.** A schematic showing the components found in each of the boxes shown in Figure 1. The signals going to computer consist of the amplified terahertz signal, the position signal from both delay rails, and the photodiode signals. PD: two photodiodes. Dashed lines represent the terahertz beam.

The right hand image in Figure 3 shows a fiber coupled THz transmitter aligned with a conventional hi-resolution XYZ stage with differential micrometers. This laboratory unit is approximately 8 x 8 x 8 inches in dimension and weighs more than 5 pounds. It is still superior to previous THz transmitters in that the fiber coupling of the laser source does not rigidly constrain its location. This flexibility has been used to measure the beam patterns from both collimating and aplanatic substrate lenses in both the H and the E-planes from 0 to 50 degrees. Such a measurement would have been impossible using older, free-space systems.<sup>9</sup> However, such a laboratory demonstration unit remains impractical for commercial use since the femtosecond optical pulses must be manually focused with sub-micron precision onto the photoconductive LT-GaAs bow-tie THz antenna using bulky translation stages. Also, despite the precision of these mounts, they are still more susceptible to both vibration and thermal misalignments than the packaged modules.

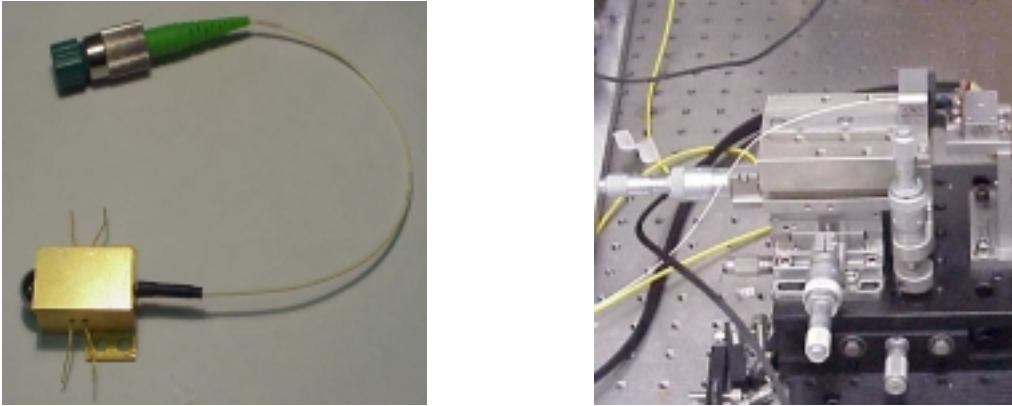


**Figure 3.** **Left:** A fiber-pigtailed T-Ray transmitter module measuring 1" x 0.5" x 0.5" and weighing only a couple of ounces. The silicon hyperhemispherical is visible on the left side of the module. **Right:** A fiber-coupled THz transmitter aligned with a conventional hi-resolution XYZ stage with differential micrometers. This laboratory unit is approximately an 8" cube and weighs more than 5 pounds. It is still superior to previous THz transmitters in that the fiber coupling does not rigidly constrain its location, as does conventional free space optics.

### System performance

The T-Ray system was used with 1 mW of optical power going to both the transmitter and the receiver. The bias on the transmitter was set at 24 volts and the receiver amplifier had a voltage gain of 500. The rapid shaker for this particular system gave a 30-ps excursion at a scan rate of 22 Hz. Figure 4 shows the temporal terahertz waveform, the noise on this waveform, and the signals Fourier transform. The dotted trace in all three graphs corresponds to a one-second-acquisition time, corresponding to 22 averages. The solid trace shows a 5-minute average, corresponding to 6,600 averages. Using the peak-to-peak voltage noise on the inset temporal graph, we obtain a signal to noise of about 600 to 1 for the one-second average and about 10,000 to 1 for the five-minute average. The 10% bandwidth for both traces extends from 0.03 to 1.5 THz with usable bandwidth to 2 THz in the one-second trace and past 3 THz for the 5-minute average. As evidence for this the water absorption lines at 2.64 and 2.77 THz are clearly visible. Looking at our data we find that the position of these lines to be accurate to within the 33 GHz resolution given by our 30-ps window.

While the signal to noise of this system is typical of other photoconductive and electro-optic terahertz systems, the optical power requirements, as well as the voltage requirements, are not. The system used to produce the results given above has used the same photoconductive elements as the transmitter and receiver for over a year without damaging a single one. Typical voltage damage to these devices occurred consistently at a bias of greater than 40 volts and more than 11 mW of optical power. By using them at such a reduced level, the longevity of these sensitive elements is assured.

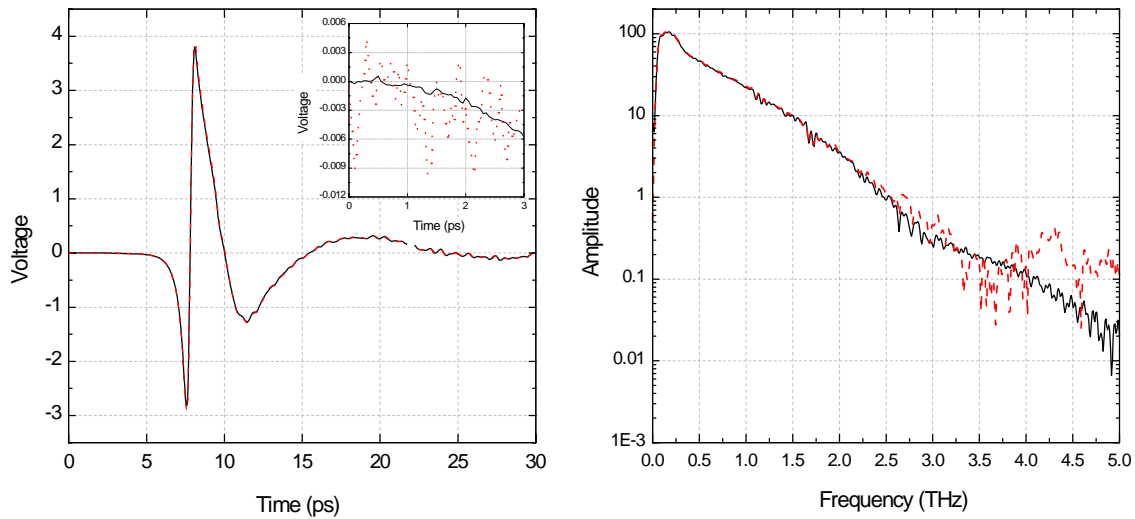


**Figure 4.** Shown are a one-second average (dotted line) and a five-minute average (solid line). The insert in the time graph shows the first 3 ps of the time data to show the noise in the two traces. The Fourier transform on the right shows accurate water absorption lines out to 2.77 THz.

### 3. IMAGING

Imaging is one of the most exciting applications of THz time-domain spectroscopy. T-ray images may be taken using transmission or reflection geometry. By analyzing the THz waveform in either the time domain (material homogeneity or thickness variations) or the frequency domain (frequency-dependent absorption) as well as by other methods, images identifying material properties can be constructed. Due to the huge spectral range of the time-domain system, looking at various places across the terahertz spectrum can form true hyperspectral images. Non-polar solids (such as plastics) are generally at least partially transparent in the 0.2 to 5 THz range. Non-polar liquids are transparent as well, whereas polar liquids, such as water, are highly absorptive. This is because absorption in the THz range of the electromagnetic spectrum is generally due to the rotational motions of dipoles within a material. Crystals formed from polar liquids are substantially more transparent because the dipolar rotations have been frozen out, however these crystals may exhibit phonon resonances in the THz range. Metals completely block THz pulses. Polar species within a gas may have sharp, strong rotational transitions in the THz range.

These T-Ray images can complement or replace existing imaging methods based on mid-IR or ionizing radiation. Furthermore analytical T-Ray images can be made of objects, which would be impossible using these conventional methods. For example polar species could be identified within the image of a flame, even in the presence of strong incoherent background radiation. This is because the photoconductive time gating of the

THz pulse provides extraordinarily good signal to noise by only sampling the ultrafast THz pulse. No thermal shielding or cryogenic cooling is required for a photoconductive THz detector.

Some examples of published T-Ray imaging applications include: identifying raisins in a box of cereal by water content; establishing the rate of water evaporation and uptake in leaves; examining circuit interconnects in packaged IC's; reading text in envelopes or beneath paint; identifying the number of almonds in a candy bar; identifying tooth decay; and locating watermarks in various currencies.<sup>10,11</sup> Not all of these images are what one might expect in a real-world application, and that is because, until now, T-Ray imaging has been restricted to researchers with the ability to hand-construct a complete THz imaging spectrometer. Understandably, most of the researchers taking these images were primarily concerned with the physics of THz generation and propagation. The images were taken more to illustrate THz science rather than to examine the properties of the imaged object. However, with the availability of a commercial turnkey T-Ray imaging spectrometer, T-Ray imaging and spectroscopy is accessible to those who want to examine the benefits of T-Ray imaging but who are not necessarily experts in the field.

The imaging described in the proceeding section was performed with reasonably simple computer control and much post-processing. In order to make this kind of terahertz imaging truly accessible to all users, an intelligent interface has to control the large amounts of data being generated by it. To address this need, we have developed a software system based on LabView that has the look and feel of a standard Windows<sup>®</sup> program and allows a user to not only take real time terahertz waveforms, but also allows one to do 2D imaging quickly and easily.

The software has four modes of operation: Rapid Scan, Long Scan, View Scans, and Image. The screen shot in Figure 5 shows the Rapid-Scan screen. On the left hand side of the screen is a control bar that allows the user to jump between these four modes of operation as well as enter the "Settings" screen, which allows the user to monitor the optical power in the transmitter and receiver fibers, enable or disable the imaging capabilities of the software, and setup the DAQ settings for the data acquisition card used.

In the Rapid Scan screen the user gets updates at a rate of about 5 Hz that allows one to do live tweaks to the system and also allows a user to setup for an image very rapidly. When averaging many traces the acquisition rate equals the scan rate of the shaker (about 20 Hz). The long slider bar across the top of the main graph corresponds to the shakers position on the long rail. This absolute time scale can be displayed on the rapid-scan time axis, which then allows the user to take a background trace at one spot on the rail, and then analyze data taken at a different spot further down the rail. For example, if the long rail was at 60 ps for the background trace, and then a thick sample was placed in the beam, the user could simply move the long rail (by dragging the position box or by typing in a long rail position), and then determine the total delay by tracking the

background with one cursor and the transmitted pulse with the other. This frees the user from having to do long scans, which are plagued by low-frequency noise and long-term drift, but still allows them to take advantage of the full one-nanosecond of delay offered by the long rail. There are times, however, when a long scan is absolutely necessary, for instance, when trying to get fine resolution of sharp resonances, or when looking at complicated pulses that last for more than 40 ps.



**Figure 5.** Rapid-scan acquisition screen for the time-domain terahertz spectrometer software. The main graph shows two time-domain traces. The white trace is the live, rapidly updated THz scan which has passed through a latex balloon. The gray trace is a saved background scan. The secondary graph shows the Fourier transforms of the two traces.

The THz image acquisition and display screen for our imaging spectrometer is shown in Figure 6. As in Figure 5, the control bar to the left allows the user the ability to jump between the various modes of operation. In the image screen the user has the choice of either setting up for and collecting an image or loading a previously taken image and re-analyzing it using new criteria. In order to acquire an image, the user usually first looks at the sample in various locations and sets up the cursors to examine the parameter of interest such as was done in Figure 5. Once this is done, the user then sets up the

parameters of the image consisting of the starting point, size, resolution, and number of averages for the desired image.

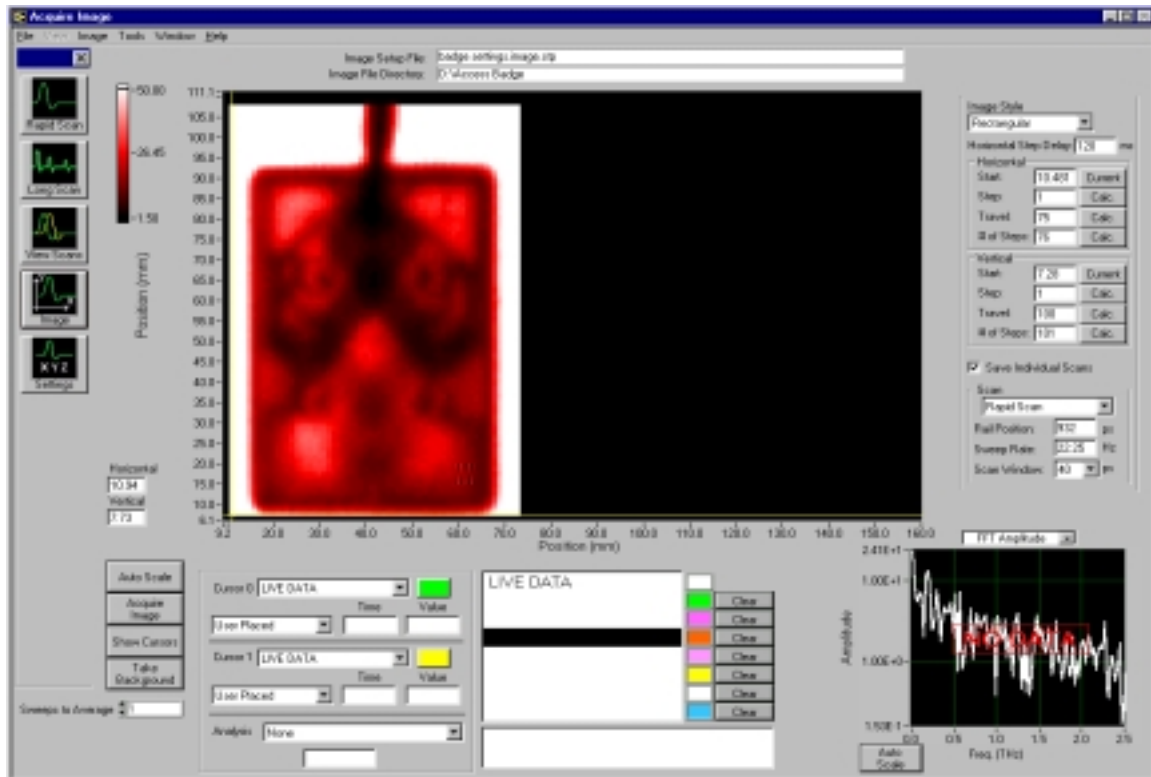


**Figure 6.** Software’s image-acquisition and display screen. The user sets the image size and resolution in the upper right. The full T-Ray waveform is stored for each pixel. The waveform for the pixel under the image cursor is shown in the lower left. In this case the cursor is on a pixel without any data corresponding to it, so the screen is only showing the live data. The image shown is a transmission image of the integrated electric field from 0.4 to 2.0 THz.

The T-Ray image shown in Figure 6 is a transmission image of a commonly used passive RF proximity access card (the vertical rectangle at the top of the card is the support clip). The card is an opaque ABS polycarbonate laminate with a Lexan skin measuring  $85.5 \times 53.9 \times 2.5\text{mm}^3$ . Interior to the card is a metallic inductor and antenna structure, which is unique to each card.

To generate a T-Ray image using the software, the user sets the rectangular scan matrix size and resolution (upper right hand corner Figure 6). The image in Figure 6 was scanned at a resolution of 75 X 100 pixels in 1-mm steps for a total of 7500 pixels. The user chooses an initial analysis; here the integrated electric field from 0.4 to 2.0 THz was chosen. Other frequency or time domain analyses could have been chosen. The software is also capable of generating a 1 dimensional time sequence image or graph. The user presses the “Acquire” button and the object is scanned automatically and the image is

generated. The full THz waveform is stored for each pixel. This allows multiple image analyses to be performed on the same image data set without having to re-scan the object.

#### 4. CONCLUSION

We have developed a time-domain terahertz system based on fiber-pigtailed, hermetically sealed modules that will allow users unskilled in ultrafast photonics to do terahertz spectroscopy and terahertz imaging. This system needs less than 10 mW of optical power and has nearly two decades of spectrum extending from 0.03 to 2 THz. The integrated nature of this system, with its turnkey operation and user-friendly software should help push the use of THz technology and ultrafast optics to new and hitherto unexplored markets.

#### ACKNOWLEDGEMENTS

This work has been partially supported under the Air Force SBIR Initiative, Contract No. F33615-98-C-2820 and contract monitor J. R. Gord.

#### REFERENCES

1. M. C. Nuss and J. Orenstein, *Millimeter and Sub-millimeter Spectroscopy of Solids*, Ch. 2, Springer-Verlag, Berlin, 1998.
2. D. Grischkowsky, S. Keiding, M. van Exter, and Ch. Fattinger, "Far-infrared time-domain spectroscopy with terahertz beams of dielectrics and semiconductors," *J. Opt. Soc. Am. B* **7**, p. 2006, 1990.
3. J. T. Kindt and C. A. Schmuttenmaer, "Far-infrared dielectric properties of polar liquids probed by femtosecond terahertz pulse spectroscopy," *J. Phys. Chem.* **100**, p. 10373, 1996.
4. J. E. Pedersen and S. R. Keiding, "THz time-domain spectroscopy of nonpolar liquids," *IEEE J. Quantum Elect.* **28**, p. 2518, 1992.
5. R. A. Cheville and D. Grischkowsky, "Far-infrared terahertz time-domain spectroscopy of flames," *Opt. Lett.* **20**, p. 1646, 1995.
6. D. M. Mittleman, R. H. Jacobsen, and M. C. Nuss, "T-Ray Imaging," *IEEE J. Quantum Electron.* **20**, p. 679, 1996.
7. P. Coy, "Beyond X-Rays: T-Rays measure content," *Business Week*, p. 11, July 10, 1995. R. Lipkin, "T-Rays for Two," *Science News* **148**, p. 136, 1995.
8. B. Atherton, private communications.
9. D. Mittleman and J. V. Rudd, to be published.
10. Q. Chen, Z. Jiang, and X.-C. Zhang, "All-optical THz imaging," *SPIE Conference on Terahertz Spectroscopy and Applications*, SPIE vol. **3617**, p. 98, 1999.
11. D. M. Mittleman, M. Gupta, R. Neelamani, R. G. Baraniuk, J. V. Rudd, and M. Koch, "Recent advances in terahertz imaging," *Appl. Phys. B* **68**, p. 1085, 1999.

# An Efficient Technique for the Optimization of Submillimeter-wave Schottky-diode Harmonic Multipliers

Chih-Chien Lee<sup>1</sup>, Boris Gelmont<sup>1</sup> and Dwight Woolard<sup>2</sup>

<sup>1</sup>The University of Virginia  
Electrical Engineering Department  
Charlottesville, VA 22903

<sup>2</sup>U.S. Army Research Laboratory  
U.S. Army Research Office  
Research Triangle Park, NC 27709

## Abstract

A simple and efficient modified harmonic-balance technique is presented. This new algorithm is suitable for the large-signal time-dependent analysis of nonlinear millimeter wave circuits. The accurate design and successful implementation of very high frequency nonlinear circuits requires both a detailed understanding of the physical operation of the active devices and of how these nonlinear devices interact with the linear embedding circuit. This work addresses the specific task of establishing a robust simulation tool that combined this novel modified harmonic-balance circuit analysis technique with a physics-based hydrodynamic transport model device simulator. A comparison with the accelerated fixed-point (AFP) harmonic-balance technique has been made through an evaluation of a Schottky-diode multiplier. The result shows that this approach can be used to realize improved multiplier operation with a minimal time of numerical computation.

## I. INTRODUCTION

The development of computer-aid analyses of highly nonlinear circuits requires both a detailed understanding of the physical operation of the active devices and of how these nonlinear devices interact with the linear embedding circuit. Traditionally, the nonlinear active devices are modeled by the lumped quasi-static equivalent circuit analysis. However, this equivalent circuit model has lost validity at higher frequency millimeter wave where the large-signal nonstationary phenomena begin to dominate device operation. It is clearly that a physics-based numerical device model is required for the active device analysis. In an earlier investigation, drift-diffusion and Monte Carlo based harmonic-balance algorithms have been utilized. The drift-diffusion model is a low-order approximation of the Boltzmann transport equation, it implies that mobility of the carrier is only a function of the local electrical field and it does not take account of the non-stationary characteristics such as carrier heating and velocity overshoot. The Monte Carlo simulation has difficulty in treating low-field region. Also, the statistical noise in the solution and the intensive amount of computation time required make this model impractical for device design. An alternative approach is hydrodynamic transport model, which is obtained by taking the first three moments of the Boltzmann Transport Equation [1]. Comparing to quasi-static equivalent circuit and drift-diffusion model, hydrodynamic model is more accurately in treating high-field, nonstationary, and hot-electron effects.

The specific focus of this paper is on energy transport effects and their influence on the harmonic multiplication within reversed-bias Schottky-barrier varactor diodes. Equally important to the characterization of diode multipliers is the optimization of the nonlinear element to the externally coupled embedding impedance. Here, the second-harmonic power (i.e., current and voltage) of the matched diode is optimized before constraints on embedding impedance, local voltage and dc bias are specified. The key of this approach is the reduction of systems variables by an efficient mathematical ordering of the optimization procedure. Specifically, this new method reduces the typical optimization problem (i.e., where device and circuit are considered simultaneously) for a doubler, where 2 harmonics are considered, from  $n+2$  variables to  $n$  variables. As will be shown, this approach leads to a significant computational advantage for Schottky-diode multiplier design.

In this paper, a one-dimensional time-dependent simulation algorithm is presented which employs a fully hydrodynamic transport equation [1,2] with two-valley mobility model to describe the diode physics within the depletion and bulk regions. These studies assume a reversed-biased situation and employ appropriate boundary conditions at the barrier interface. In addition, this work combines the physically accurate diode model with a modified harmonic-balance algorithm to determine diode-circuit designs that maximize power generation and/or power efficiency in the second harmonic [2]. The modified harmonic-balance method utilizes a novel two-step procedure where the available doubler-power and the second-harmonic diode-impedance is first derived as a function of first and second harmonic diode excitation. The harmonic diode-voltages and second-harmonic diode-impedance at the optimum power-point are then used to define the matched embedding impedance and the optimum local-oscillator (LO) voltage. The utility of this simulation tool is illustrated by comparing to prior studies, by others, that employed traditional drift-diffusion transport models, Monte Carlo transport models and a conventional harmonic-balance algorithm. Specifically, this work demonstrates a computationally efficient and accurate physical description as well as a more robust approach for circuit optimization.

## **II. PHYSICS-BASED DIODE MODEL**

These multiplier studies utilize a physics-based Schottky-diode model accurate for both momentum and energy relaxation effects. Here, a one-dimensional time-dependent simulation algorithm is implemented that employs a fully hydrodynamic transport model (i.e. first three moments of the Boltzmann equation) to describe the diode physics within the depletion and neutral regions. The application this type of approach will be necessary for GaAs diodes operating at terahertz frequencies because energy relaxation is important above 300 GHz and momentum relaxation is important above 1 THz. While our method is fully amenable to momentum relaxation these initial studies will consider device operation below 1 THz. These studies consider the large-signal operation of a Schottky-barrier

varactor frequency multiplier and will therefore consider diodes under time-dependent reverse-bias up to the breakdown voltage.

Set of equations of the hydrodynamic model in the single-gas approximation has been written in [1,2] together with appropriate boundary conditions. We have used in [2] one valley approximation. However more adequate description of GaAs Schottky diodes can be obtained utilizing a two-valley model [3]. We'll extract the mobility and the energy relaxation time from this model.

Consider a semiconductor material whose energy band structure can be approximated by a two-valley model with an energy separation  $\Delta_{UL}$  between the upper and lower valleys. The collision terms are modeled by the relaxation-time approximation. The energy collision term is expressed as

$$\left(\frac{\partial w_n}{\partial t}\right)_c = -\frac{w_n - w_0}{t_w}, \quad (1)$$

where  $w_0 = 3k_B T_o / 2$  is the equilibrium energy at the lattice temperature  $T_o$ ,  $t_w$  is the energy relaxation time,  $k_B$  is the Boltzmann constant. The average electron total energy  $w_n$  is defined using the thermal approximation

$$w_n = \frac{3}{2} k_B T_e + \mathbf{h} \Delta_{UL} \quad (2)$$

where  $T_e$  is the electron temperature,  $\mathbf{h}$  is the fraction of the electrons in the upper valley. The energy separation between the upper and lower valleys  $\Delta_{UL}$  is set to 0.29 eV in this work. The total energy relaxation time is given by

$$\frac{1}{t_w} = \frac{1-\mathbf{h}}{t_{wL}} + \frac{\mathbf{h}}{t_{wU}}. \quad (3)$$

The energy relaxation time in the lower-valley and upper-valley are  $\tau_{wL}=1.5$  ps and  $\tau_{wU}=0.8$  ps, respectively. The fraction of the electrons in the upper valley and is given by

$$\mathbf{h} = \frac{n_U}{n_U + n_L} = \frac{r}{r+1} \quad (4)$$

where  $n_L$  and  $n_U$  are the electron densities in the lower valley and upper valley. The ratio of electron densities  $r$  is defined as

$$r = \frac{n_U}{n_L} = \left( \frac{m_U}{m_L} \right)^{3/2} \exp\left( -\frac{\Delta_{UL}}{k_B T_e} \right) \quad (5)$$

where  $m_L$  and  $m_U$  are the density-of-states effective masses of lower valley and upper valley are set equal to  $0.063 m_0$  and  $0.55 m_0$ , respectively. The temperature dependent electron mobility is obtained by

$$\mathbf{m}_n = (1 - \mathbf{h})\mathbf{m}_L + \mathbf{h}\mathbf{m}_U. \quad (6)$$

where  $\mathbf{m}_L$  and  $\mathbf{m}_U$  are the electron mobility in the lower valley and upper valley, respectively. The mobility can be approximated by [4,5]

$$\mathbf{m}_L = \frac{\mathbf{m}_{0L}}{1 + 3k_B \mathbf{g}_L (T_e - T_0)/2}, \quad \mathbf{g}_L = \frac{\mathbf{m}_{0L}}{q \mathbf{t}_{wL} v_{satL}^2} \quad (7)$$

and

$$\mathbf{m}_U = \frac{\mathbf{m}_{0U}}{1 + 3k_B \mathbf{g}_U (T_e - T_0)/2}, \quad \mathbf{g}_U = \frac{\mathbf{m}_{0U}}{q \mathbf{t}_{wU} v_{satU}^2} \quad (8)$$

where the saturation velocities for lower-valley  $v_{satL}$  and upper-valley  $v_{satU}$  are set equal to  $3.2 \times 10^5$  m/s and  $1. \times 10^5$  m/s, respectively. These values were obtained by fitting Monte Carlo simulation results. The low-field, doping-dependent mobility for two valleys are expressed as [1]

$$\mathbf{m}_{0L} = \frac{\mathbf{m}_{00L}}{1 + [\log(N_T) / B_L]^n}, \quad \mathbf{m}_{0U} = \frac{\mathbf{m}_{00U}}{1 + [\log(N_T) / B_U]^n} \quad (9)$$

where  $N_T$  is the total doping density (here total ionization is assumed, so  $N_T = N_D$ ). Here,  $\mathbf{m}_{00L} = 0.85 \text{ m}^2/\text{V}\cdot\text{s}$ ,  $\mathbf{m}_{00U} = 0.26 \text{ m}^2/\text{V}\cdot\text{s}$  [6],  $n = 23$ , and  $B_L = 23$ , and  $B_U = 26$  are used.

As to boundary conditions discussed in [2] we have to change the phenomenological energy-flux boundary condition

$$S_n(0^+) = v_M n_M \mathbf{d} k_B T_0 - v_S n(0^+) (\mathbf{d} k_B T_e(0^+) + \mathbf{h} \Delta_{UL}), \quad (10)$$

where  $\delta = 2.5$  is used.

### III. VARACTOR FREQUENCY-MULTIPLIER NUMERICAL SIMULATION

While an accurate model for the physical diode is very important as one attempts to design varactor multipliers at very high frequencies, the ability to effectively couple the device to

the proper embedding impedance is of paramount importance. In fact, the majority of the analytical and numerical effort involved in realizing efficient multipliers is expended in the matching of the nonlinear device to the embedding circuit [7]. For example, many harmonic-balance methods have been derived (e.g., multiple-reflection algorithm [8] and accelerated fixed point [9]) to improve the matching of the various harmonics between nonlinear device and linear circuit. Here the difficulty lies in the large number of iterations that are required to optimize power-efficiency of a given nonlinear element over both embedding impedance and local oscillator (LO) voltage. This problem becomes compounded for optimization over the physical diode design and in circuits that contain many nonlinear device elements. Of course, in some situations where multiple diodes are involved equivalent-circuits can be developed that reduce groups of diodes to a single nonlinear element [10].

When a conventional harmonic-balance (HB) algorithm is applied to the analysis of a varactor-doubler the problem is to optimize the second-harmonic generation. Here, embedding impedances are selected for the first- and second-harmonic circuits and short-circuit conditions are assumed at the higher harmonics. While there are many HB techniques one of the most popular is the multiple-reflection algorithm [8] that seeks to smooth transients via the introduction of a loss-less transmission-line section. This relaxation method, which in some cases requires long convergence times, has been improved by Tait [9]. Regardless of the exact mathematical algorithm employed, the primary challenge in the design of a doubler is to determine the embedding impedance that will yield the maximum second-harmonic power. In the conventional approach, the physical model of the Schottky diode is used in conjunction with the HB algorithm to optimize the second-harmonic power. Specifically, the HB technique will iterate between the Fourier-domain solutions of the circuit(s) and the current/voltage harmonics derived from steady-state time-domain simulations of the diode. Since this combined Fourier-domain and time-domain analysis inevitably leads to extensive iterations and to a large computational cost, it is natural to seek alternative methods that reduce the numerical burden of the optimization task. In the simulations presented here, a new two-step procedure has been utilized to achieve this goal. This modified HB algorithm introduces a new optimization constraint that enables a natural separation of the device-circuit problem. Specifically, this procedure allows the current/voltage harmonics of the nonlinear device to be optimized independently of the external circuit. Subsequently, the optimum embedding circuit can then be derived from a very simple analysis.

### ***Harmonic-Balance Technique***

The harmonic-balance circuit analysis applied in this paper is the accelerated fixed-point (AFP) method [9]. The iterative process is repeated until the harmonic components of the voltage converge to within a specified tolerance factor of their steady-state value for all harmonics. In this work, the tolerance is set to 0.1%. There is one thing to remind that AFP algorithm has one adjustable convergence parameter  $Z_0$ , the fictitious transmission

line characteristic impedance. The chosen value of  $Z_0$  can affect the convergence property of the iteration.

### ***Modified Harmonic-Balance Technique***

The key to this simplified approach is to formulate the optimization-problem of the varactor-doubler in a completely different way. Specifically, to recognize that the available-power of the diode at the doubler-frequency may be optimized a priori (i.e., independent of the external circuit) and that the Fourier results can be used, subsequently, to determine the embedding impedance and LO voltage. While this technique represents, in a manner of speaking, an inverse transformation of the conventional problem, it is completely valid and offers definite computational advantages. The technique has been outlined in [2].

In present analysis we have included the frequency-dependent parasitic impedances as additional contributions to the linear device embedding circuit. It is important to note that the parasitic impedances of interested here are external to the active region of the nonlinear device. The matching embedding impedances are given by

$$Z_n^{Circuit} = Z_n^{Linear} - Z_n^{Parasitic} . \quad (11)$$

where  $Z_n^{Linear}$  are the matching linear impedances determined using equations from [2].

The power incident from the pump at the input port is

$$P_{in} = V_{C1}I_{C1}/2 + (I_{C1}^2 + I_{S1}^2)Re\{Z_1^{Parasitic}\}/2 . \quad (12)$$

The power delivered to port 2 with impedance  $Z_2^{Circuit}$  is

$$P_{output} = -(V_{C2}I_{C2} + V_{S2}I_{S2})/2 - (I_{C2}^2 + I_{S2}^2)Re\{Z_2^{Parasitic}\}/2 \quad (13)$$

where  $V_{C1}$ ,  $V_{C2}$  and  $V_{S2}$  are the dc, first, and second harmonic voltages, respectively. The current harmonics  $I_{C1}$ ,  $I_{C2}$ ,  $I_{S1}$  and  $I_{S2}$  are supplied by Fourier transforms of time-domain simulations from the physical diode model.

Note that this new approach offers an immediate reduction in problem complexity as compared to the conventional HB approach. Specifically, the traditional HB method will maximize the nonlinear diode-circuit problem over LO voltage (dc and ac) and over the real and imaginary parts of the first- and second-harmonic embedding impedance which is a six-dimensional space. It should be noted that this reduction from N to N-2 in the double problem also occurs in the analysis of a varactor-tripler due to symmetry considerations. As shown, the traditional HB technique requires two iterations. For each mapping over the six-dimensional LO-impedance space, one must perform convergent iteration to

balance the harmonics between the embedding impedance and the nonlinear device. On the other hand, the modified method invokes allowable constraints on the available diode power and the embedding impedance(s) (i.e., are always matched to the diode impedance) to reduce the optimization space by two variables. Furthermore, this method only requires a trivial calculation in the second step to derive the final impedance(s) and the LO voltage. In simplest terms reducing the degrees of freedom allows for a significant reduction in computation.

#### IV. SIMULATION RESULTS

Both harmonic-balance and modified harmonic-balance simulations were utilized with the hydrodynamic diode model to study Schottky diode multiplier operation at a doubler-frequency of 200 GHz. Here, the earlier varactor diode investigations that were presented in [11] were considered for comparison purposes. The GaAs Schottky diode considered was UVA-6P4 with an epitaxial doping density of  $n_D \approx 3.5 \times 10^{16} \text{ cm}^{-3}$ , epitaxial thickness of 1.0  $\mu\text{m}$ , anode diameter 6.3  $\mu\text{m}$ . Experimental results including input power and dc bias were obtained from [12] and were used as the input data for both algorithms. Frequency-dependent parasitic impedances of the UVA 6P4 varactor we used here are similar to those of [8].

##### *Harmonic-Balance Technique*

Since we want to compare our result with Monte Carlo transport model, we have the same constraints as [11]. The following constraints are set on the embedding circuit impedances

$$Z_1^{Circuit} = R_1^{Circuit} + jX_1^{Circuit}, \quad Z_2^{Circuit} = R_1^{Circuit} + j\frac{X_1^{Circuit}}{2}. \quad (14)$$

The embedding impedances of higher harmonics were taken equal to zero. The optimized results obtained from the hydrodynamic model for four simulated input powers are shown in Table I. The simulated result for output power versus incident pump power is shown in Fig. 1. The experimental result and simulated results obtained from the drift-diffusion (DD) and Monte Carlo simulators [11] are also shown in this figure. As seen in this figure, the drift-diffusion model with dc field-dependent mobility is not suitable for high frequency. Since the drift-diffusion model with constant ac mobility did not include the velocity saturation effects, it overpredicted at high input power. The optimal power results of the hydrodynamic model are in good agreement with the result obtained from the simulation of the drift-diffusion model with constant ac mobility at low input power and the result derived from the Monte Carlo simulation at high input power. The output current and voltage waveforms for 18.8 mW pump excitation are shown in Fig 2.

Table I. AFP Harmonic-Balance simulation result by hydrodynamic model

Incident Pump Power (mW)	Output Power (mW)	$P_{out}/P_{in}$ (%)	$Z_1$ ( $\Omega$ )	$Z_2$ ( $\Omega$ )
7.5	3.06	40.85	$31 + j 207$	$31 + j103.5$
18.8	7.69	40.92	$47 + j 234$	$47 + j117$
29.6	9.55	32.27	$61 + j 234$	$61 + j117$
47.0	11.91	25.34	$73 + j 254$	$73 + j127$

### ***Modified Harmonic-Balance Technique***

The optimized results obtained from the modified harmonic-balance technique hydrodynamic model for four simulated input powers are given in Table I. The optimized results are better than the results from the harmonic-balance (AFP) technique as shown in Fig 3. As seen in the figure, the modified harmonic-balance technique got higher optimized results than the harmonic-balance (AFP) technique. Unlike the traditional HB technique where the fictitious transmission line characteristic impedance has to be carefully chosen, there is no fictitious impedance needed in the modified HB technique. The output current and voltage waveforms for Modified Harmonic-balance method is shown in Fig. 4.

Table II. Modified Harmonic-Balance simulation result by hydrodynamic model

Incident Pump Power (mW)	Output Power (mW)	$P_{out}/P_{in}$ (%)	$V_{LO}$ (V)	$Z_1$ ( $\Omega$ )	$Z_2$ ( $\Omega$ )
7.5	3.23	43.10	1.062	$18.7 + j199.4$	$46.2 + j97.2$
18.8	8.06	42.89	1.945	$25.1 + j229.6$	$68.8 + j116.0$
29.6	9.83	33.22	2.759	$32.1 + j227.7$	$81.5 + j120.8$
47.0	12.08	25.71	4.025	$43.0 + j240.5$	$86.3 + j133.6$

The comparison of results by two techniques shows that the efficiency is a rather flat function of the second harmonic embedding resistance if the first harmonic resistance is matched in appropriate way.

## **V. CONCLUSIONS**

In conclusion, a simple and efficient modified harmonic-balance technique is presented. This new algorithm is suitable for the large-signal time-dependent analysis of nonlinear millimeter wave circuits. A robust simulation tool that combined this novel modified harmonic-balance circuit analysis technique with a temperature-dependent hydrodynamic transport model device simulator has been established in this paper. In comparison to the drift-diffusion model, this temperature-dependent hydrodynamic model can more accurately describe the nonstationary high frequency dynamics and velocity saturation of

the electron. In addition, the computational time is much reduced over that of the Monte Carlo method. The results and simulation-time requirements for a Schottky-diode multiplier study have been compared to that utilizing the harmonic-balance algorithms. These results show that this approach can be used to realize improved multiplier operation with a minimal time of numerical computation. This model will be used in the future to optimize multiplier operation at terahertz frequencies.

The authors wish to acknowledge the support of the U.S. Army Research Laboratory, Army Research Office.

## REFERENCES

- [1] H. Hjelmgren, "Numerical Modeling of Hot Electrons in n- GaAs Schottky-Barrier Diodes," *IEEE Transactions on Electron Devices*, **37**, pp. 1228-1234, 1990.
- [2] C. C. Lee, B. L. Gelmont, D. L. Woolard and C. Fazi, "A Modified Harmonic-Balance Analysis of Schottky Diode Multipliers Based upon A Hydrodynamic Transport Model," *Proc. Tenth Int. Symp. on Space Terahertz Technology*, Charlottesville, USA, pp. 313-328, 1999.
- [3] K. Bløtekjær, "Transport Equations for Electrons in Two-Valley semiconductors," *IEEE Transactions on Electron Devices*, ED-17, pp. 38-47, 1970.
- [4] W. Hänsch and M. Miura-Mattausch, "The Hot-Electron Problem in Small Semiconductor Devices," *J. Appl. Phys.*, **60**, pp. 650-656, 1986.
- [5] Y. Zhang and M. E. Nokali, "A Hydrodynamic Transport Model and Its Applications in Semiconductor Device Simulation," *Solid-State Electronics*, **36**, pp. 1689-1696, 1993.
- [6] M. Shur, *GaAs Devices and Circuits*, (Plenum Press, 1987).
- [7] S. A. Maas, *Nonlinear Microwave Circuits*, (Artech House, MA, 1988).
- [8] P. H. Siegel, A. R. Kerr, and W. Hwang, "Topics in the Optimization of Millimeter-Wave Mixers," *NASA Technical Papers*, no. 2287, 1984.
- [9] G. B. Tait, "Efficient Solution Method for Unified Nonlinear Microwave Circuit and Numerical Solid-State Device Simulation," *IEEE Microwave Guided Wave Letters*, **4**, pp. 420-422, 1994.
- [10] M. T. Faber, J. Chramies and M. E. Adamski, *Microwave and Millimeter-Wave Diode Frequency Multipliers*, (Artech House, MA, 1995).
- [11] R. E. Lipsey, S. H. Jones, J. R. Jones, T. W. Crowe, L. F. Horvath, U. V. Bhapkar, and R. J. Mattauch, "Monte Carlo Harmonic-Balance and Drift-Diffusion Harmonic-Balance Analysis of 100-600 GHz Schottky Barrier Varactor Frequency Multipliers," *IEEE Transactions on Electron Devices*, **44**, pp. 1843-1850, 1997.
- [12] T. W. Crowe, W. C. B. Peatman, R. Zimmermann, and R. Zimmermann, "Consideration of velocity saturation in the design of GaAs varactor diodes," *IEEE Microwave Guided Wave Lett.*, Vol. 3, pp. 161-163, 1993.

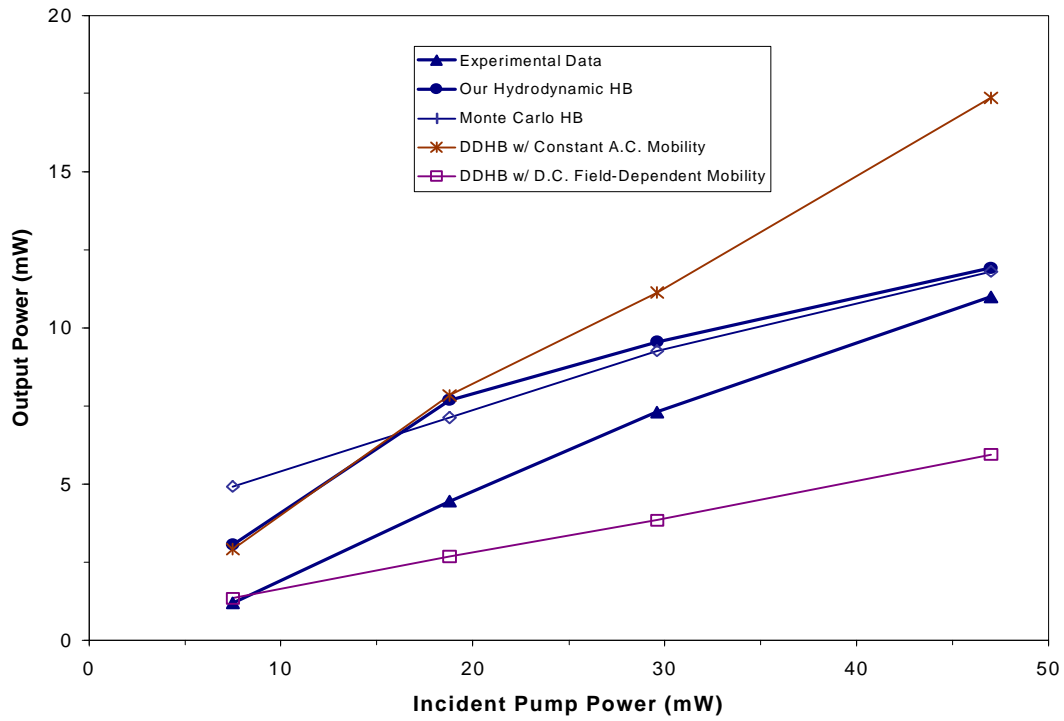


Figure 1. Experimental and AFP theoretical second harmonic output power versus incident pump power for the UVA 6P4 frequency doubler subject to 100 GHz excitation.

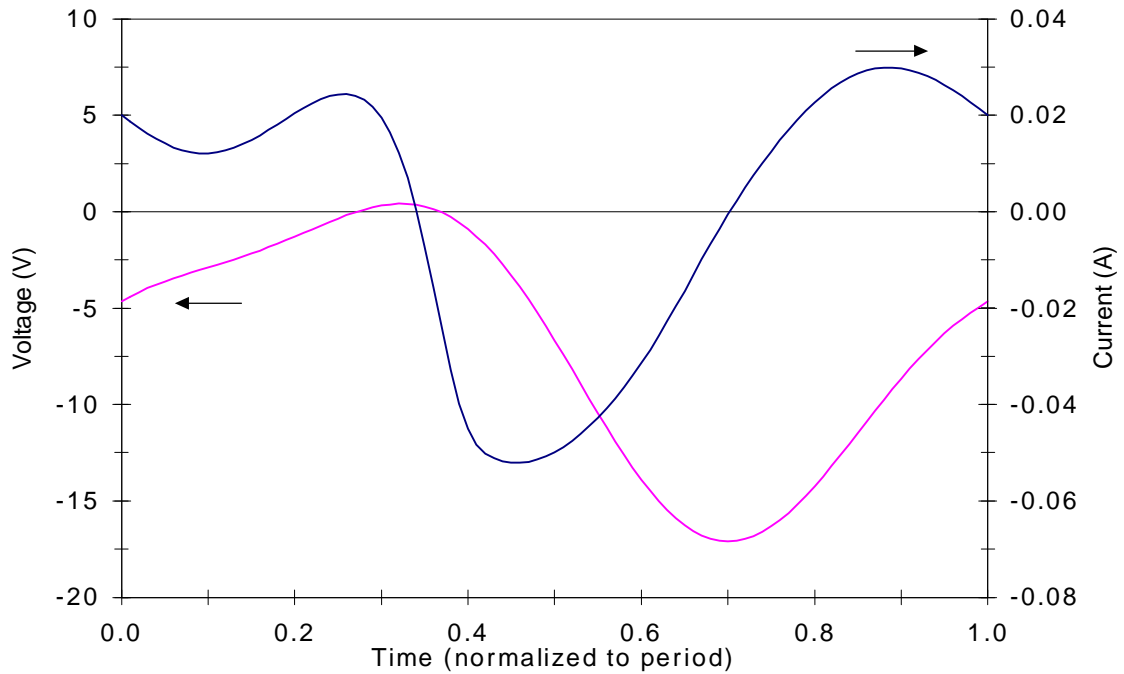


Figure 2. AFP Harmonic-balance current and voltage waveforms for 18.8 mW pump excitation.

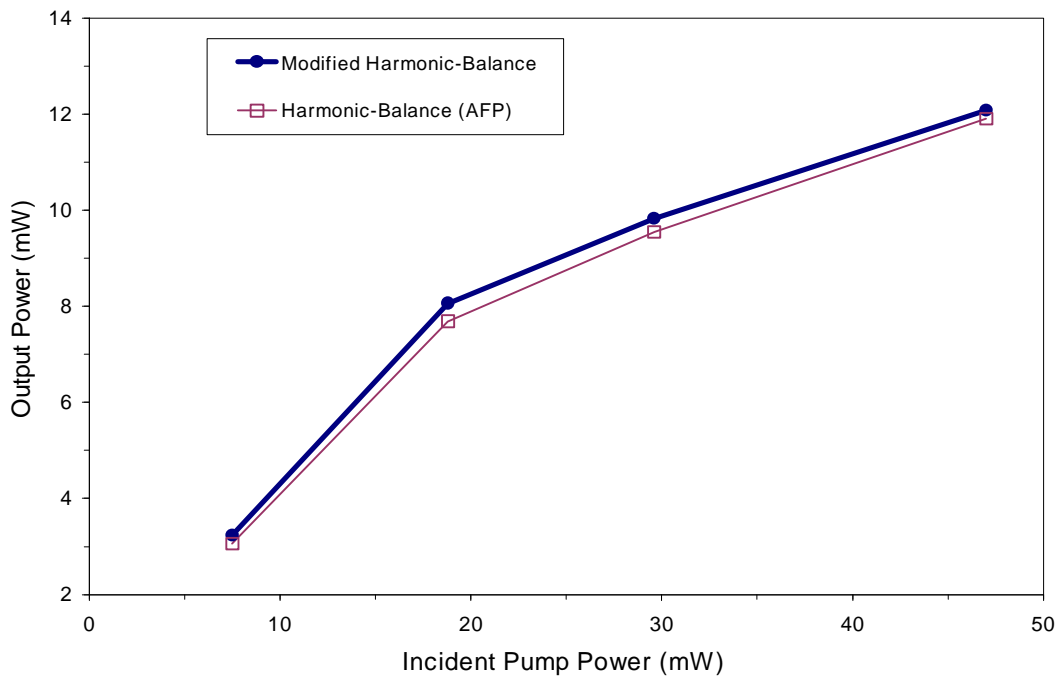


Figure 3. Theoretical second harmonic output power versus incident pump power for the Modified Harmonic-Balance method and Harmonic-Balance (AFP) method.

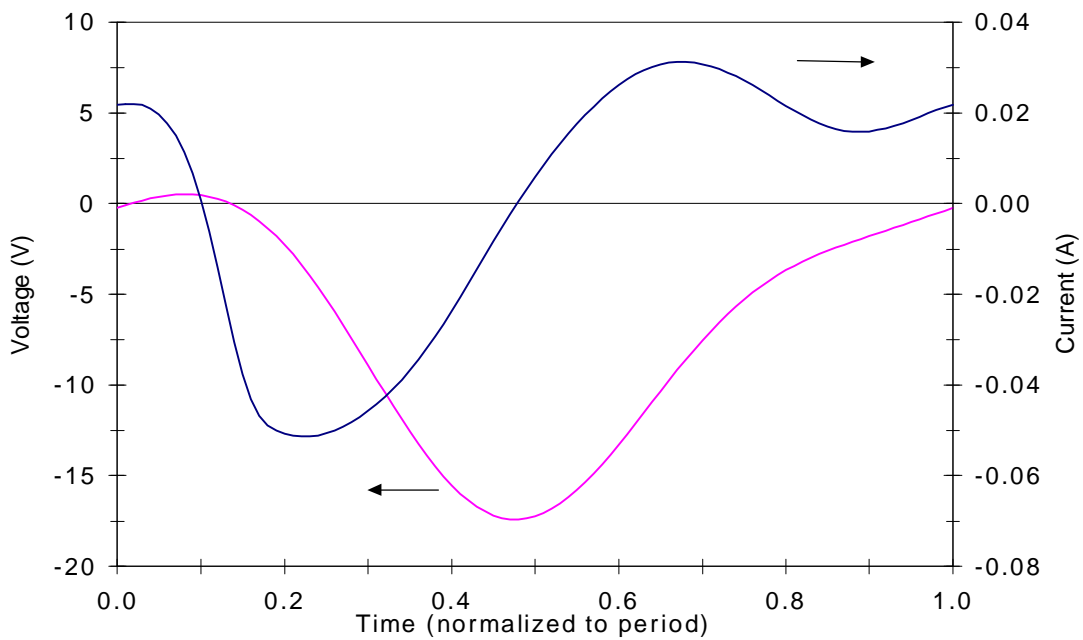


Fig.4. Modified Harmonic-balance current and voltage waveforms for 18.8 mW pump excitation.

# DEVELOPMENTS OF THE 810-GHz SIS RECEIVER WITH Nb-BASED JUNCTIONS

Hiroyuki Maezawa<sup>1</sup>, Takashi Noguchi<sup>2</sup>, Sheng-Cai Shi<sup>3</sup>, Yutaro Sekimoto<sup>2</sup>,  
Satoshi Yamamoto<sup>1</sup>

<sup>1</sup>Department of Physics, The University of Tokyo,  
Hongo 7-3-1, Bunkyo-ku, Tokyo 113-0033, Japan

<sup>2</sup>Nobeyama Radio Observatory, National Astronomical Observatory of Japan  
Nobeyama, Minamisaku, Nagano, 384-1305 Japan

<sup>3</sup>Purple Mountain Observatory, 2 West Beijing Road, Nanjing 210008, China

## 1 Abstract

We present the experimental and astronomical results of the tunerless waveguide 810-GHz SIS receiver. The Nb/AlO<sub>x</sub>/Nb junctions associated with a broadband tuning circuit, namely parallel connected twin junctions, are fabricated at Nobeyama Radio Observatory. The tuning microstrip line is made of a Nb thin film. The lowest receiver noise temperature is 580 K (DSB) measured at 810 GHz, in which the noise contributions of the RF-input section alone and the IF-system account for about 4 % and 20 %, respectively. Note that the applied magnetic field with a permanent magnet to suppress the Josephson effect is 700 - 800 Gauss and the SIS mixer is cooled down to 3.9 K. The  $R_{sub}(2\text{mV})/R_N$  is 16, which suggests relatively good quality of the junctions. This SIS mixer was installed on the receiver of the Mount Fuji submillimeter-wave telescope. We have detected the submillimeter-wave spectral lines of CI (<sup>3</sup>P<sub>2</sub>-<sup>3</sup>P<sub>1</sub> : 809.3432 GHz) and CO (J=7-6 : 806.651 GHz) in the Orion A molecular cloud.

## 2 Introduction

Radio astronomy at millimeter and submillimeter wavelengths has made rapid progress by using the heterodyne mixing with Superconductor-Insulator-Superconductor (SIS) tunnel junctions. The Nb-based SIS mixer associated with various types of integrated tuning structure has achieved the low receiver noise temperature of a few times the quantum limit ( $3 - 5\hbar\omega/k$ ). Recently, the sensitive THz SIS receiver has been required for space-borne astronomical and atmospheric observations. According to the Mattis-Bardeen theory [1], the loss of Nb-stripline increases remarkably due to the photon absorption (breaking Cooper-pairs) above the gap frequency of Nb ( $2\Delta/h \approx 680$  GHz.  $\Delta$  is minimum energy of one quasiparticle excitation). Therefore, Nb-based SIS mixers using low-loss materials such as NbTiN [2, 3, 4], NbN [5, 6] and Al [7, 8, 9, 10] as a microstrip line circuits have been extensively studied theoretically and experimentally. However, Winkler et al. showed analytically that SIS mixer can be used up to twice the gap frequency ( $4\Delta/h$ ) [11]. Lange et al. investigated the noise performance of a Nb-based SIS mixer at 600 - 1500 GHz and compared the results

with the quantum mixing theory [12]. Honingh et al. accomplished the receiver noise temperature of less than 950 K at 780 - 820 GHz using fixed tuned SIS waveguide mixers [13].

We have developed the Nb-based 500-GHz waveguide SIS mixer associated with parallel connected twin junctions (PCTJ) [14, 15], which have been used for the receiver system of the Mount Fuji submillimeter-wave telescope [16, 17]. With this receiver system we have carried out the mapping observations of the CI ( $^3P_1$ - $^3P_0$  : 492 GHz) line toward a number of molecular clouds. Since another transition of CI ( $^3P_2$ - $^3P_1$ ) lies at 810 GHz, immediate extension of the observing frequency up to 810 GHz is strongly required from astronomical reasons. On the basis of this motivation, we have developed the experimental 810-GHz mixer which is a scaled version of the 500-GHz SIS mixer. We have tested the mixer performance under various operating conditions at 810 GHz for future developments of a sensitive Nb-based SIS mixer with the PCTJ and the tuning stripline made of highly conductive normal metal like Al. A special attention has been paid for improvement of the RF-input section.

In this paper we present performance of the Nb-based SIS receiver at 810 GHz. First, the junction properties, the lay-out of the mixer and the experimental setup for performance evaluation are described. Next, we present the DC I-V curve characteristics and frequency response of the mixer measured by a Fourier transform spectrometer (FTS). Finally, the receiver noise temperature, the noise contribution and the astronomical results are presented.

## 3 Lay-out of the 810-GHz Waveguide Mixer

### 3.1 Junction properties

In the 810-GHz SIS mixer presented here Nb/ $AlO_x$ /Nb junctions and Nb-stripline are employed and they are fabricated at Nobeyama Radio Observatory (NRO). The dielectric layer of microstrip line used for impedance transformers is made of  $Nb_2O_5$ (1000 Å) /  $SiO_2$ (2700 Å) /  $Al_2O_3$ (900 Å). The tuning circuit consists of parallel connected twin junctions (PCTJ) associated with a superconducting tuning microstrip line with a width of 6.5  $\mu m$  and a length of 10  $\mu m$ . The PCTJ has advantages of a better RF and IF coupling and a larger tuning inductance than an end-loaded type [18]. In addition, it is also suggested that the structure of the PCTJ might be easier to suppress the Josephson effect. Other circuit elements include a waveguide-to microstrip transition with a DC/IF return path and an offset probe [19], a 75  $\Omega$  and a 45  $\Omega$  microstrip line and the RF choke filter which consists of a series of wide and narrow sections of microstrip line. The crystal substrate is polished down to 50  $\mu m$ . The substrate width is 98  $\mu m$ . These structure are shown in Figure 1. The size and normal-state resistance for a single junction are 1.25  $\mu m \times 1.25 \mu m$  and 22.1  $\Omega$ , respectively. Assuming  $I_C R_N$  of 2.0 mV and the specific capacitance of 90 fF/ $\mu m^2$ , the critical current density and  $\omega R_N C_j$  product are 9 kA/cm<sup>2</sup> and 11, respectively. The tuning bandwidth of the

junctions,  $\Delta f = f/\omega R_N C_j$ , is about 80 GHz, since the Q-factor of the PCTJ is approximately equivalent to junctions'  $\omega R_N C_j$  product [18]. The critical current density of 9 kA/cm<sup>2</sup> seems to be close to the upper limit for the Nb-junction with the high quality because of the fabrication process.

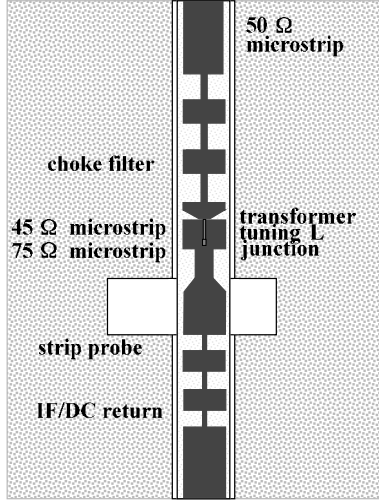


Figure 1: Structures of the 810-GHz SIS chip

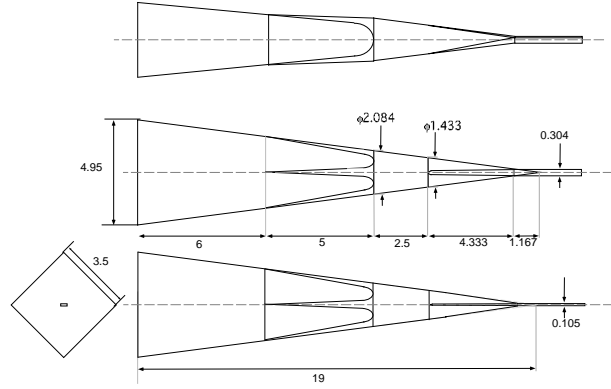


Figure 2: Diagonal horn of the 810-GHz mixer

### 3.2 Waveguide mixer

The 810-GHz SIS mixer is a scaled version of our 500-GHz waveguide SIS mixer. The mixer block is split into two blocks made of copper with electric gilding. The horn antenna and the channel for the SIS chip are included in one block, and the backshort cavity in the other block. This mixer does not employ any mechanical tuners for adjustment of the RF impedance of the mixer [20]. This fixed-tuned design is very important for a remote operation of this receiver on the Mount Fuji submillimeter-wave telescope. Dimensions of the waveguide and the IF-channel of the 810-GHz mixer are  $304 \mu\text{m} \times 105 \mu\text{m}$  and  $105 \mu\text{m} \times 105 \mu\text{m}$ , respectively. The substrate is shifted with  $40 \mu\text{m}$  offset from the center of the waveguide. The IF/DC output port and  $50 \Omega$  microstrip line are connected with  $10 \mu\text{m}$  Al wires. The slot of the ground port is filled with indium metal. A diagonal horn is adopted as the feed horn antenna because of the convenient fabrication. It has a good beam pattern and an efficient coupling to a Gaussian beam. The aperture and the length of the diagonal horn are 3.5 mm and 19.89 mm, respectively. The coupling efficiency of the fundamental mode of a diagonal horn is about 84 % if a field is transmitted smoothly from a horn to a waveguide [21]. The horn and the waveguide taper-transition are shown in Figure 2.

### 3.3 Measurement setup

An overview of the measurement system is shown in Figure 3. The frequency independent quasi-optical system based on the Gaussian beam propagation is installed at 4 K cold stage of a spare dewar for the Mount Fuji submillimeter-wave telescope [17]. The 4 K cold stage is covered by 40 K shield. The material of the dewar window and the IR filter are Kapton with thickness of  $12.5 \mu\text{m}$  and Zitex (G106) with thickness of  $150 \mu\text{m}$ , respectively. These thickness are decided from a standpoint of mechanical strength. The transmission of the IR filter was measured with the FTS at the room temperature, while that of the dewar window was estimated from the calculation. The transmission  $G$  and the equivalent noise temperature  $T_{eff}$  in the dewar are shown in table 1, where the effective temperature is expressed by  $hf/k \times \exp((hf/kT_{amb}) - 1)^{-1}$ .  $T_{amb}$  is the physical temperature. The RF and Local oscillator signal (LO) are combined by a wire grid polarizer as a beam splitter. This polarizer transmits most of the RF signal (95%), while it reflects a small fraction of the LO power. These signals are focused to the horn by an ellipsoidal mirror. The LO signal at 809 GHz is produced by a combination of the W-band (90 GHz) Gunn diode and two triplers, which gives sufficient LO power for the mixing ( $230 \mu\text{W}$ ). The intermediate frequency (IF) is amplified by an S-band low noise HEMT amplifier which is cooled on the 4 K cold stage. The return loss of the Bias T is larger than 25 dB in the frequency range from 1.8 to 2.7 GHz. The equivalent noise temperature and the gain of this amplifier associated with an isolator are about 7 K and 43 dB at 19 K, respectively. The DC SIS bias voltage and the IF line is combined by a Bias T. Finally, the DC I-V curve and the IF output power are measured by using an oscilloscope and a spectrum analyzer, respectively.

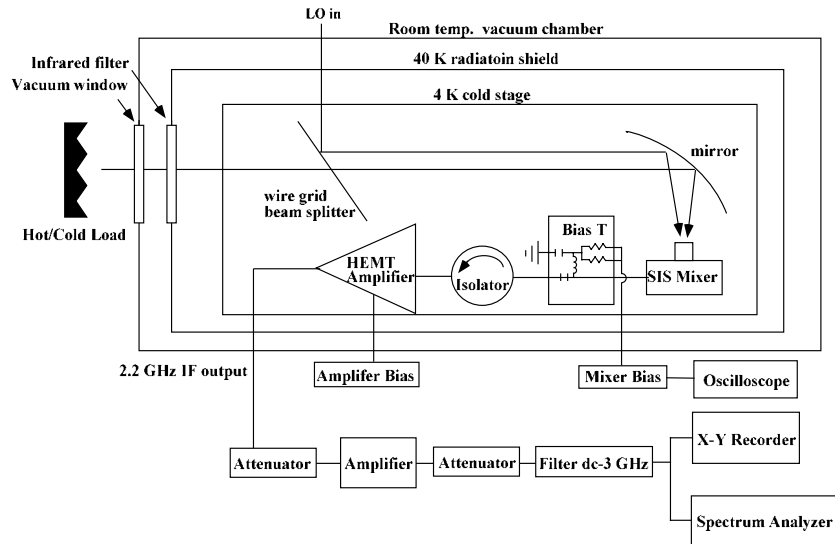


Figure 3: Measurement system.

Table 1. Materials and properties of the RF-input section.

	Dewar window	IR filter	Beam splitter
material	Kapton	Zitex (G106)	Wire Grid
transmission [%]	$93 \pm 1$ ( $12.5 \mu\text{m}$ )	$98 \pm 1$ ( $150 \mu\text{m}$ )	95
$T_{eff}$ [K]	276	43	--

## 4 Results and Discussion

### 4.1 DC I-V performance

The normal resistance  $R_N$  for a single junction is measured to be  $22.6 \Omega$ , which is well consistent with the expected value. The  $R_{sub}(2.0 \text{ mV})/R_N$  is about 16 at 4 K, where  $R_{sub}$  is a resistance at 2.0 mV. The subgap leakage current at 2.0 mV is less than  $10 \mu\text{A}$ . As shown in the sample DC I-V curve (Figure 4), it was difficult to find out the resonance step (even varying the applied magnetic field strength), only seeing the step at the half of the gap voltage ( $\sim 1.5 \text{ mV}$ ). The permanent magnets, giving a magnetic field of 830 Gauss at the position of junctions are attached at the both side of a mixer block to suppress the Josephson current. The magnetic coils are not used, because it can be a source of an unfavorable heat inflow. When we applied the magnetic field of 530 Gauss, the second Shapiro step, the knee structure due to the proximity effect and the increase of gap voltage increased slightly. The field of 830 Gauss is 40 % of the upper critical magnetic field of Nb. Since the properties of magnets and the divergence of the magnetic field at a low temperature are not known accurately, the absolute value of the magnetic field might be overestimated.

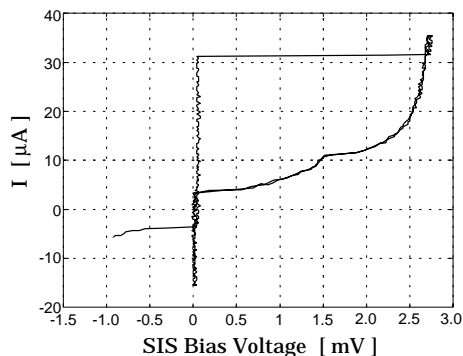


Figure 4: DC I-V curve of the 810-GHz SIS mixer below the gap frequency of Nb.

### 4.2 Frequency Response

The frequency response of the 810-GHz waveguide mixer coupled with the PCTJ was measured with the FTS. The frequency resolution was 3.6 GHz. The result is shown

in Figure 5. The frequency cut-off of the waveguide can be seen around 600 GHz. In addition, the peak around 720 GHz should be neglected due to the direct absorption of a photon at the gap energy. The other subgap structures in the response curve are due in part to the measurement system such as absorptions by H<sub>2</sub>O vapor. Therefore, the basic response curve seems to have a peak around 820 GHz, which is 30 GHz lower than the designed value. This is relatively consistent with the designed value. From this result, the suitable SIS bias voltage is found to be from 2.0 to 2.2 mV.

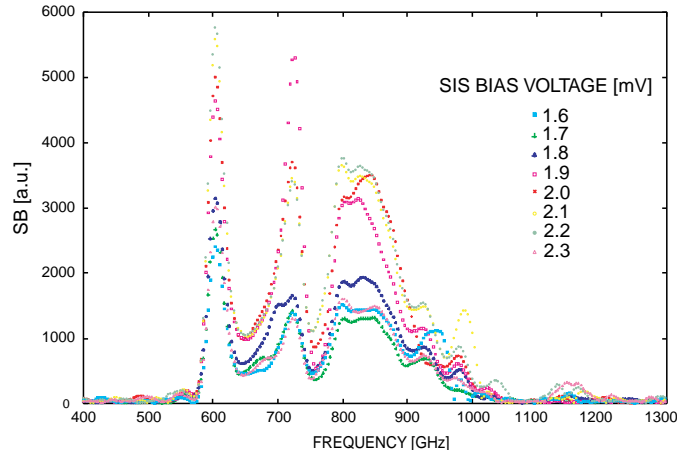


Figure 5: FTS measurement of 810-GHz SIS mixer at various SIS bias voltage.

### 4.3 Receiver noise temperature

Using the Y-Factor method with the hot load (295 K) and the cold load (77 K), the noise temperature of the 810-GHz waveguide SIS mixer has been measured by using a spectrum analyzer. The noise performance in the frequency range of 790 - 830 GHz is shown in Figure 6. The relatively narrow frequency range of measurements is due to limited frequency tunability of the LO source employed here. The frequency is measured by the Shapiro steps so that it has a typical uncertainty of 0.3 GHz. The lowest receiver noise temperature of 580 K (DSB) is obtained around 810 GHz at the SIS bias voltage 2.0 - 2.2 mV. These results are in good agreement with those expected from the FTS measurement. In addition, we measured the receiver noise temperature ( $T_{RX}$ ) at different temperatures. We controlled the temperature by using an electric heater attached on the cold stage. Understanding the temperature dependence is useful, since the actual mixer installed into the telescope is not always cooled at 4 K due to various heat loads. As shown in Figure 7, the noise temperature is found to depend on the temperature substantially even around 4 K. Note that  $T_{RX}$  also depends on the magnetic field applied. The apparent difference in the best receiver noise temperature was not observed between the magnetic field of 530 Gauss and 830

Gauss. However, 0th - 3th Shapiro steps could be seen apparently in the case of 530 Gauss, and the IF output power is slightly unstable around the SIS bias voltage of 2.0 - 2.2 mV. A sample of the measured total IF output power superposed on the DC I-V curve is displayed in Figure 8. The IF output power in Figure 8 is averaged all over the frequency range of DC - 3 GHz, which includes the frequency range with the bad responsivity of the HEMT Amplifier.

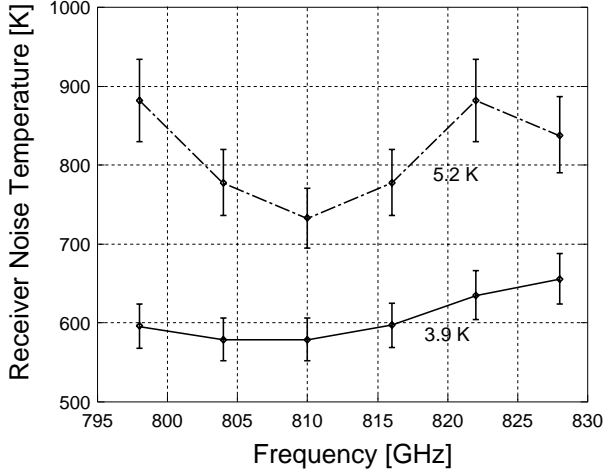


Figure 6: Receiver noise temperature (DSB) of 810-GHz mixer versus frequency

#### 4.4 Noise contribution

The measured receiver noise temperature consists of the noise contributions of the RF-input section, the mixer and the IF-chain, which is simply expressed by

$$T_{RX} = T_{RF} + \frac{T_{MIX}}{G_{RF}^{tot}} + \frac{T_{IF}}{G_{RF}^{tot} G_{MIX}}. \quad (1)$$

where  $T_{RX}$ ,  $T_{RF}$ ,  $T_{MIX}$  and  $T_{IF}$  are the equivalent noise temperature of the receiver, the RF-input section, the mixer, and the IF-chain, respectively. The  $G_{MIX}$  is the gain of the mixer. The  $G_{RF}^{tot}$  is expressed by  $G_{RF}^{opt} \times G_{RF}^{tune}$ , where  $G_{RF}^{opt}$  is a transmission of the RF-input section including the dewar window, the IR filter, the beam splitter and the horn and is evaluated to be about 0.73. The  $G_{RF}^{tune}$  is a gain of a tuning circuit and a microstrip line. In order to study the contribution of the components of each term of Eq.1 above gap frequency, we at first measured  $T_{RF}$  by performing intersecting lines technique [22]. As the result, the equivalent noise temperature of 95 K at the intersection point was obtained from the Figure 9, which is much larger than that of 22 K calculated from the RF-input section alone. According to the Ke's discussion

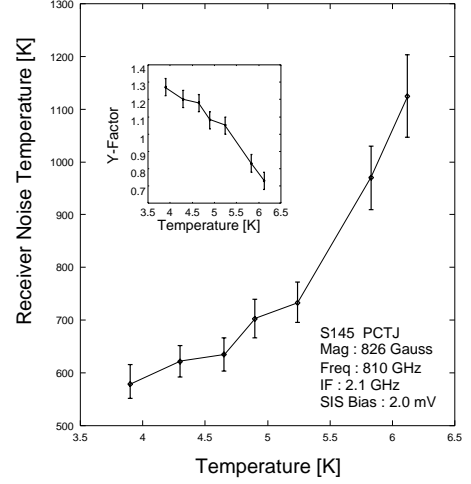


Figure 7: Receiver noise temperature at different temperatures

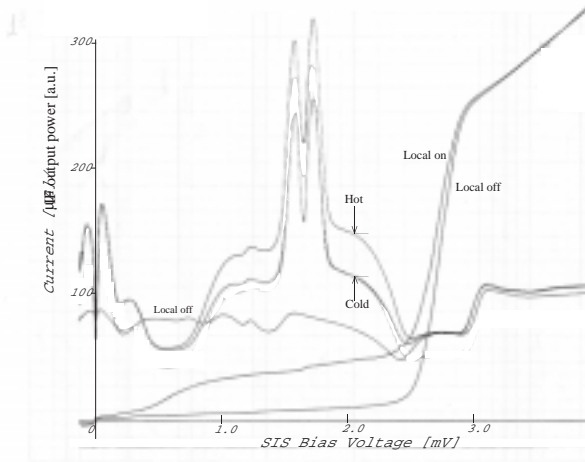


Figure 8: IF output power superimposed on the DC I-V curve versus SIS bias voltage.

[23], this equivalent noise temperature at the intersection point should be expressed by  $T_{RF} + \sum \tau / G_{RF}^{tot}$ .  $\sum \tau$  is the sum of the quantum noise and the correction terms which are independent of  $G_{MIX}$  in case that the SIS mixer is not perfectly matched to the LO source. Therefore, the large residual of 73 K might result from these terms. Since  $\sum \tau / G_{RF}^{tot}$  as well as  $T_{RX}$  is extremely influenced by the  $G_{RF}^{tune}$  above the gap frequency of Nb, it seems likely that the value at the intersection point is reduced by adopting the NbTiN, NbN, or normal metal such as Al as the microstrip line. Next,  $T_{IF}$  of about 6 K is obtained by using the linear relation in the shot noise region of IF output power [24, 25]. In addition,  $T_{IF} / G_{RF}^{tot} G_{MIX}$  is obtained to be 115 K by comparing the total IF output power for the hot load with that of IF-chain alone at the gap voltage [15], where  $G_{RF}^{tot} G_{MIX}$  is estimated to be 0.05.

From above simple estimations, the low noise temperature of our mixer seems likely to be due in part to the low  $T_{RF}$ , the good performance of the tuning circuit of the PCTJ [18], and a comparatively high  $R_{sub} / R_N$ . Therefore, it might be exceedingly important to improve the high quality junction not only with a low loss material but also with a high current density, a low subgap current and a high coupling tuning circuit, as Dieleman et al. suggest [10].

#### 4.5 Observation of $CI(^3P_2-^3P_1)$ and $CO(J=7-6)$ line

We are conducting large mapping observations of  $CI(^3P_1-^3P_0 : 492 \text{ GHz})$  toward various molecular clouds using Mount Fuji submillimeter-wave telescope. Comparison of the  $CI(^3P_1-^3P_0 : 492 \text{ GHz})$  intensity with the  $CI(^3P_2-^3P_1 : 809 \text{ GHz})$  intensity is essential to investigate the physical parameter such as the temperature and  $H_2$  gas density in the region where  $CI$  exists. For this aim, we installed the 810-GHz SIS mixer

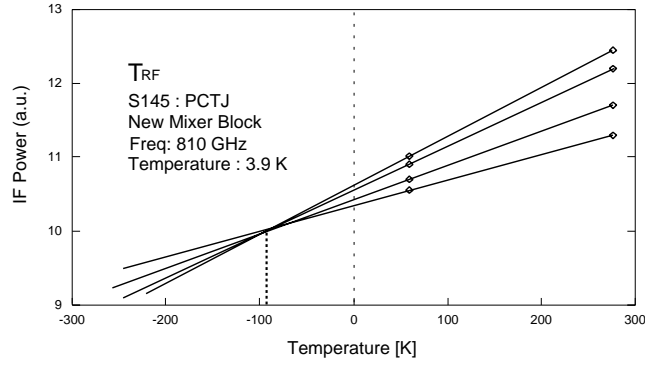


Figure 9: Equivalent noise temperature of the RF-input section measured by performing intersecting lines technique

into the dewar of Mount Fuji submillimeter-wave telescope and carried out the test observations toward the Orion A molecular cloud. As a result, we could detect the CI ( $^3P_2$ - $^3P_1$ ) and the CO (J=7-6) line as demonstrated in Figure 10. The system noise temperature including the loss of the atmosphere and the radome was 6500 K(DSB). This high system noise temperature mainly originates from high physical temperature of the mixer, a loss of bandpass filter, and an insufficient LO-power.

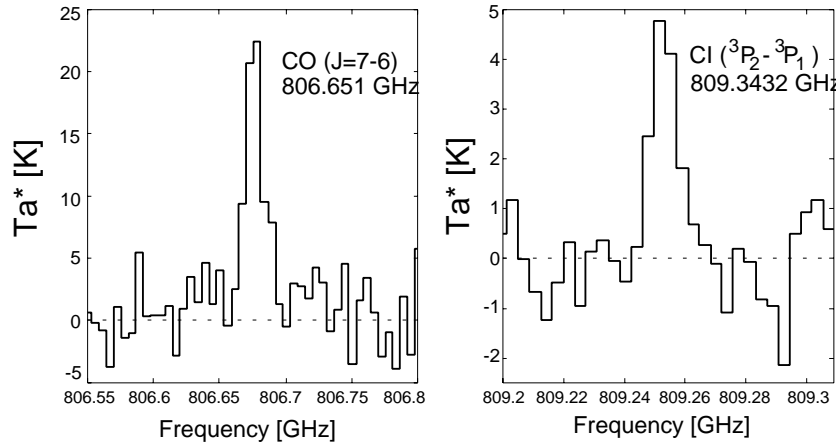


Figure 10: Samples of spectral lines toward Orion A molecular cloud

## 5 Summary

We have produced an experimental Nb-based waveguide 810-GHz SIS mixer. The good receiver noise temperature of about 600 K in the range of 790 - 830 GHz was obtained with the laboratory receiver setup. In the view point of the stability of the

IF output power, the optimized magnetic field and SIS bias voltage were 830 Gauss and 2.0 - 2.2 mV, respectively. These properties agree well with the result of the FTS measurement. It seems likely that this low noise performance of Nb-based mixer above the gap frequency is due to the low  $T_{RF}$ , the efficient couplings of the PCTJ, and relatively high  $R_{sub}/R_N$ . Although the 810-GHz mixer installed in Mount Fuji submillimeter-wave telescope was not used in the ideal condition, we observed the CI ( $^3P_2$ - $^3P_1$ ) and the CO (J=7-6) line toward Orion A molecular cloud.

## Acknowledement

We are grateful especially to S. Saito for lending us a 800 GHz LO source. We are also grateful to the members of the Mount Fuji submillimeter-wave telescope project for the observations of the CI and the CO line. We would like to thank H. Matsuo and T. Matsunaga for the FTS measurement.

## References

- [1] D.C. Mattis and J. Bardeen, Phys. Rev., vol. 111, p. 412, July 1958.
- [2] J.A. Stern, B. Bumble, H.G. LeDuc, W.J. Kooi, and J. Zmuidzinas, Proc. 9th Internat. Symp. on Space Terahertz Technology, CIT, PC, p. 305, Mar. 1997.
- [3] B.D. Jackson, N.N. Iosad, B. Leone, J.R. Gao, T.M. Klapwijk, W.M. Laauwen, G. de Lange, and H. van de Stadt, Proc. 10th Internat. Symp. on Space Terahertz Technology, Charlottesville, p. 144, Mar. 1999.
- [4] J.W. Kooi, J.A. Stern, G. Chattopadhyay, H.G. LeDuc, B. Bumble, and J. Zmuidzinas, Int. J. of IR and MM Waves, vol. 19, 1998.
- [5] Y. Uzawa, Z. Wang, and A. Kawakami, Proc. 9th Internat. Symp. on Space Terahertz Technology, CIT, PC, p. 273, Mar. 1998.
- [6] P. Dieleman, T.M. Klapwijk, H. van de Stadt, M. Schicke, B. Plathner, and K.H. Gundlach, Proc. 8th Internat. Symp. on Space Terahertz Technology, Boston, USA, pp. 291-300, Mar. 1997.
- [7] H. van de Stadt, A. Baryshev, P. Dieleman, Th. de Graauw, T.M. Klapwijk, S. Kovtonyuk, G. de Lange, I. Lapitskaya, J. Mees, R.A. Panhuyzen, G. Prokopenko, and H. Schaeffer, Proc. 6th Internat. Symp. on Space Terahertz Technology, CIT, PC, p. 66, Mar. 1995.
- [8] M. Bin, M.C. Gaidis, J. Zmuidzinas, T.G. Phillips, and H.G. LeDuc, Appl. Phys. Lett., vol. 68(12), p. 1714, Mar. 1996.
- [9] G. de Lange, J.J. Kuipers, T.M. Klapwijk, R.A. Panhuysen, H. van de Stadt, and M.M.W.M. de Graauw, J. Appl. Phys., vol. 77, pp. 1795-1804, 1995.
- [10] P. Dieleman, T.M. Klapwijk, J.R. Gao, and H. van de Stadt, IEEE Trans. Appl. Supercond, vol. 7, no. 2, p. 2566, June 1997.

- [11] D. Winkler and T. Claeson, *J. Appl. Phys.*, vol. 62, pp. 4482-4498, 1987.
- [12] G. de Lange, C.E. Honingh, J.J. Kuipers, H.H.A. Schaeffer, R.A. Panhuysen, T.M. Klapwijk, H. van de Stadt, and M.M.W.M. de Graauw, *Appl. Phys. Lett.*, vol. 64, pp. 3039-3041, 1994.
- [13] C.E. Honingh, S. Haas, D. Hottgenroth, K. Jacobs and J. Stutzki, *IEEE Trans. Appl. Supercond.*, vol. 7, no. 2, June. 1997.
- [14] S.C. Shi, T. Noguchi, J. Inatani, Y. Irimajiri and T. Saito, *Proc. 9th Internat. Symp. on Space Terahertz Technology*, Pasadena, CA, Mar. 1998.
- [15] S.C. Shi and T. Noguchi, *IEEE Trans. Appl. Supercond.*, vol. 7, no. 2, pp. 2587-2590, June. 1997.
- [16] H. Maezawa, M. Ikeda, T. Ito, G. Saito, Y. Sekimoto, S. Yamamoto, K. Tatematsu, Y. Arikawa, Y. Aso, T. Noguchi, S.C. Shi, K. Miyazawa, S. Saito, H. Ozeki, H. Fujiwara, M. Ohishi, and J. Inatani, 1999, *ApJ*, 524, L129.
- [17] Y. Sekimoto, et al., 2000, *Review of Scientific Instruments*, accepted.
- [18] S.C. Shi, and T. Noguchi, *IEICE Trans. Electron.*, vol. E81-C, no. 10, pp. 1584-1594, Oct. 1998.
- [19] S.C. Shi and J. Inatani, *IEEE Trans. Microwave Theory Tech.*, vol. 45, no. 3, pp. 442-445, Mar. 1997.
- [20] S.C. Shi, T. Noguchi, and J. Inatani, *IEEE Trans. Appl. Supercond.*, vol. 7, no. 4, pp. 3850-3857, Dec. 1997.
- [21] P.F. Goldsmith, in *Infrared and Millimeter Waves*, 6, ed. K.J. Button, New York, NY: Academic Press, 1982, 277.
- [22] R. Blundell, R. E. Miller, and K. H. Gundlach, *Int. J. of IR and MM Waves*, vol. 13, no.1, pp. 3-14, Jan. 1992.
- [23] Q. Ke and M. J. Feldman, *IEEE Trans. Microwave Theory Tech.*, vol. MTT-42, no. 4, pp. 752-755, Apr. 1994.
- [24] D.P. Woody, R.E. Miller, and M.J. Wengler, *IEEE Trans. Microwave Theory Tech.*, vol. MTT-33, no. 2, pp. 90-95, Feb. 1985.
- [25] N.B. Dubash, G. Pance, and M.J. Wengler, *IEEE Trans. Microwave Theory Tech.*, vol. MTT-42, no. 4, Apr. 1994.

# Bias Dependence of the Thermal Time Constant in Nb Superconducting Diffusion-Cooled HEB Mixers

D. Wilms Floet<sup>1</sup>, J.R. Gao<sup>1,2</sup>, T.M. Klapwijk<sup>1</sup>, and P.A.J. de Korte<sup>2</sup>

[1] Department of Applied Physics and Delft Institute for Microelectronics and Submicron Technology (DIMES), Delft University of Technology, Lorentzweg 1, 2628 CJ Delft, The Netherlands

[2] Space Research Organization of the Netherlands, Landleven 12, 9700 AV, The Netherlands

In this paper, we present an experimental study of the intermediate frequency bandwidth of a Nb diffusion-cooled hot-electron bolometer mixer for different bias voltages. The measurements show that the bandwidth increases with increasing voltage. Analysis of the data reveals that this effect is mainly caused by a decrease of the intrinsic thermal time of the mixer and that the effect of electro-thermal feedback through the intermediate frequency circuit is small. The results are explained using a qualitative model, in which the time constant is calculated using a weighted average of the diffusion constant as a function of the relative length of the hotspot, and accounting for the lower diffusion constant in the superconducting domain. Thus, we show that for a diffusion-cooled hot-electron bolometer, the intermediate frequency bandwidth is determined not only by the length of the microbridge, as is generally believed, but also by the length of the electronic hotspot.

## I. Introduction

The strong need for sensitive heterodyne mixers at terahertz frequencies is an important stimulus for the ongoing development of hot-electron bolometer (HEB) mixers. Besides the rapid progress on the experimental side, new light has been shed on the physical mechanisms that govern the HEB in heterodyne operation. Classically, the HEB is described as a lumped element, making use of the steep rise of the resistance as a function of temperature  $R(T)$  close to the critical temperature  $T_c$  [1-3]. Under the usual operating conditions of the mixer the presence of a temperature profile in the microbridge has to be taken into account [4], and the experimental dc resistive transition is no longer relevant [5]. A new concept has been introduced in which heterodyne mixing in HEBs is described in terms of an electronic hotspot (EHS) of which the length  $L_h$  oscillates at the intermediate frequency (IF) [6,7]. Recently, a similar physical model was introduced in a somewhat different mathematical approach, although there, the authors continue to relate the mixing properties to the experimentally observed  $R(T)$  [8].

## II. The time constant of a diffusion-cooled HEB

An important figure of merit of a HEB mixer is the IF gain bandwidth, defined as the frequency where the gain has dropped 3 dB below its zero frequency value (roll-off frequency  $f_{-3dB}$ ), and being physically determined by the speed with which the thermal energy can be removed from the microbridge. Based on the ratio between the thermal length  $\lambda_{th} = (D\tau_{e-ph})^{1/2}$  ( $D$  is the electronic diffusion constant and  $\tau_{e-ph}$  is the electron-phonon coupling time) and the length of the microbridge  $L_b$ , HEBs can be divided into two classes.

If  $\lambda_{th}/L_b < 1$ , the hot electrons will primarily lose their energy via inelastic electron-phonon scattering within the microbridge. In this case one speaks of a phonon-cooled HEB [1]. Based on an electron-phonon coupling time of about 12 ps for a thin NbN film, the IF bandwidth can be 10 GHz and thus large enough for practical applications [9]. However, due to relatively long phonon escape time of approximately 40 ps, the IF bandwidth is in practice limited to 3-4 GHz. If, on the other hand,  $\lambda_{th}/L_b > 1$ , the heat transfer in the microbridge will be dominated by outdiffusion of hot electrons to the contacts. The idea of using diffusion-cooling rather than phonon-cooling in order to achieve a large bandwidth was proposed by D. Prober in 1993 [2]. Experimentally, the crossover from phonon-cooling to diffusion-cooling has been demonstrated by varying the length of the microbridge [10,11]. Obviously, if the mixer is made very short, the IF roll-off frequency can be very high. Recently, an IF bandwidth of 9.2 GHz was reported for a 100 nm long Nb HEB, whereas a 80 nm long HEB showed no clear roll-off up to 15 GHz [12].

We now consider the time constant of a diffusion-cooled superconducting HEB mixer in a bit more detail. For a diffusion-cooled *metallic* microbridge, the thermal relaxation time is given by [4,13]:

$$\tau_{th} = \frac{L_b^2}{\pi^2 D} \quad [1]$$

This expression does take into account the presence of a temperature profile, but assumes no spatial variation of the thermal diffusivity, being determined by the (local) ratio of the thermal conductivity  $k$  and the electronic heat capacity  $c_e$ . In case of a diffusion-cooled metallic microbridge, this ratio is the same as the electronic diffusion constant, since heating and heat transport both take place via the electrons. In practice, however, the rf pumped and dc biased HEB is cooled well below  $T_c$ , and operates in an electronic hotspot state. In this case, the center of the bridge is normal (hotspot region), whereas the ends of the microbridge are superconducting. In the normal region, the diffusion constant is independent of the local temperature, because both  $k$  and  $c_e$  have a linear temperature dependence. In the superconducting parts,  $k$  decreases sublinearly with decreasing temperature, whereas the  $c_e$  will be larger than in the normal part of the microbridge [14]. Thus, the thermal diffusivity will be

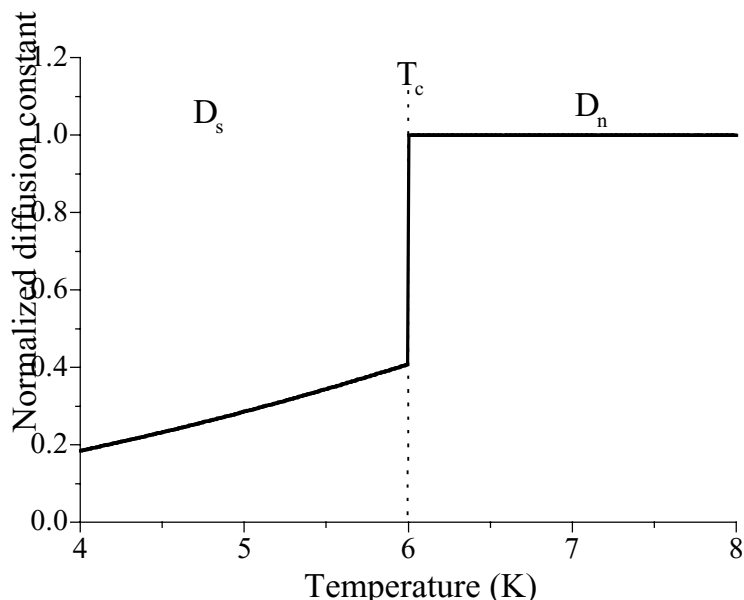


Fig. 1: Thermal diffusivity of Nb as a function of temperature, normalized to the normal state value  $D_n$  ( $1.6 \text{ cm}^2/\text{s}$ ). Calculated is the ratio between the thermal conductance  $k$  and the electronic heat capacity  $c_e$  of a thin Nb film with a critical temperature of 6 K.

considerably lower in the superconducting regions. This can be seen in Fig. 1, where we plot the normalized ratio  $k/c_e$  below and above  $T_c$  for a typical 10 nm thin Nb film on the basis of expressions for  $c_e$  and  $k$  given in Refs. 14 and 15 ( $D_n$  and  $D_s$  refer to the diffusion constant in the normal and superconducting state, respectively). An abrupt decrease in  $k/c_e$  occurs at  $T_c$  because of the discontinuity of  $c_e$ . In our experiments, the device is usually operated at a bath temperature around 4.2 K and it can be seen in the figure that in the temperature range between 4.2 K and 6 K,  $D_n \approx 3\text{-}5 D_s$ . Therefore, we hypothesize that if the length of the hotspot decreases, e.g. due to a decrease of the bias voltage, the effective (or average) diffusion constant along the microbridge will also decrease, resulting in a slower response time of the device.

In this work, we verify this hypothesis. We present the experimental results of the measurement of the IF bandwidth of a Nb diffusion-cooled HEB for different bias voltages i.e. for different lengths of the electronic hotspot. The measured time constants are corrected for electro-thermal feedback through the IF circuit using the EHS model, in order to infer the intrinsic time constant of the mixer. Finally, the time constants are compared with the calculated time constant on the basis of a qualitative model.

### III. Experiment

In this section, we present the measurement of the IF bandwidth of a Nb diffusion-cooled HEB around 700 GHz using two local oscillators. The device used in the

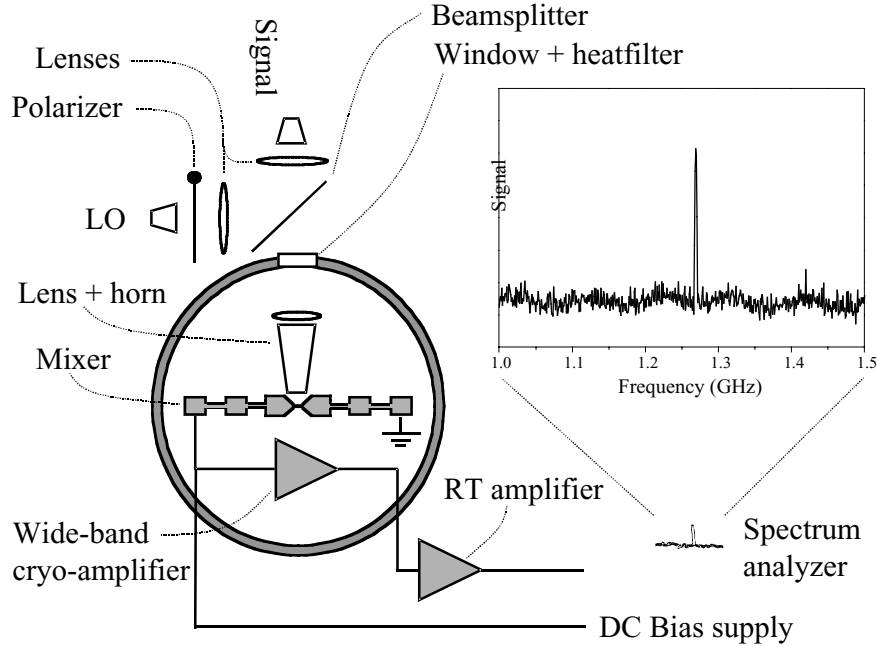


Fig. 2: Schematic representation of the experimental setup used for the gain vs. intermediate frequency measurement. The inset shows an actual measured spectrum.

experiment has a length of 300 nm, a width of 200 nm, and a normal state resistance  $R_n$  of 53  $\Omega$ . The critical temperature  $T_c$  of the microbridge is 5.9 K. The (normal state) diffusion constant was independently determined to be 1.6 cm<sup>2</sup>/s. The fabrication procedure of the device has been given in detail in Ref. 16. The device is mounted in a fixed-tuned waveguide, designed for frequencies around 700 GHz. A schematic representation of the experimental set-up used for the measurements is given in Fig. 2. The rf power to pump the device is provided by a carcinotron with a doubler, whereas a Gunn oscillator with a quadrupler acts as a (weak) signal source. The IF output signal is amplified by a 0.1-8 GHz Miteq cryo-amplifier with an effective input impedance  $R_L$  of 32  $\Omega$  [17] and a 6 dB attenuator at the input to isolate the device from reflections. A 0.1-14 GHz Miteq amplifier is used to amplify the signal at room temperature. The amplified signal is measured with a spectrum analyzer. Special attention is paid to the gain versus frequency calibration of the IF chain and saturation of the second amplifier. During the experiment, the signal frequency is kept constant and the LO frequency is varied. The LO power is kept constant by adjusting the polarizer in the optical path and maintaining a constant current through the device with an accuracy better than 1  $\mu$ A. All measurements reported here are performed in a single run, because of small changes in the electrical behavior of the device upon thermal cycling. The bath temperature  $T_b$  during the experiment is 4.5 K.

The measured relative conversion gain as a function of the intermediate frequency at a bias voltage  $V_b = 0.30$  mV is shown in Fig. 3a. The calculated

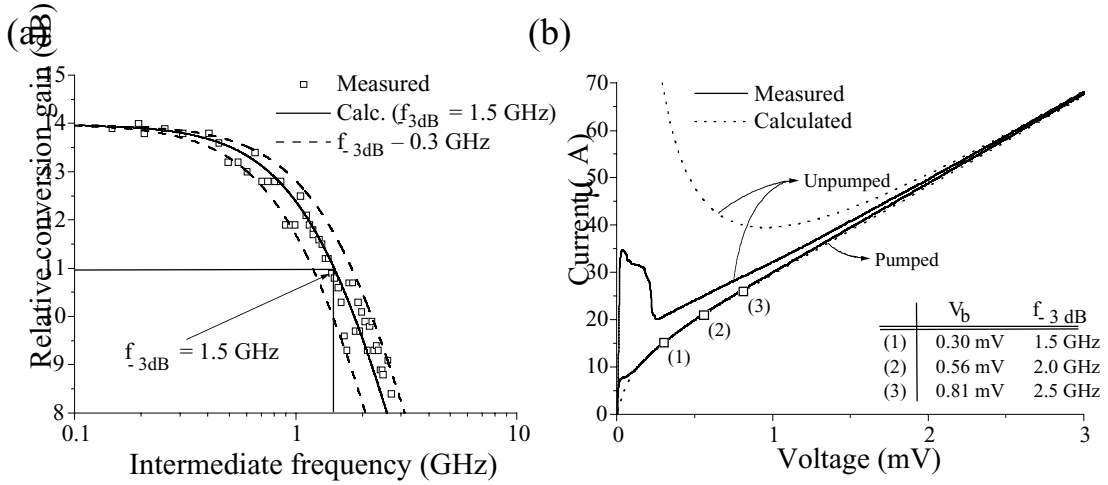


Fig. 3: (a) Relative conversion gain as a function of the intermediate frequency. The solid line is a one-pole calculation with a roll-off frequency  $f_{3dB}$  of 1.5 GHz. The dashed lines represent the error margins ( $1.5 \pm 0.3$  GHz). (b) Unpumped and pumped I(V) curves. The bias points where the IF bandwidth has been measured are indicated by the open squares. Also shown are the calculated I(V) curves based on the EHS model. The coupled LO power in the calculation is 37 nW.

bandwidth from a one-pole fit to the data is 1.5 GHz, corresponding to an effective thermal time of  $\tau_{eff} = (2\pi f_{3dB})^{-1} = 106$  ps. The maximum error in the measurement is 0.3 GHz and the corresponding curves with a roll-off frequency  $f_{3dB}$  of 1.2 GHz and 1.8 GHz are also plotted in Fig. 3a. Fig. 3b shows the unpumped and pumped I(V) curves of the device. The three bias points at which the IF bandwidth has been measured are indicated in the figure, and the corresponding values for the bandwidth are given in the table in the inset. Clearly, the IF bandwidth increases with increasing bias voltage, up to 2.5 GHz at  $V_b = 0.81$  mV. The same effect was observed by Skalare *et.al.* on a comparable device, but the physical origin of the effect was not addressed [17].

#### IV. Data analysis

In this section we calculate the intrinsic time constant from the measured time constant, which is affected by selfheating of the bolometer. We first discuss how to take into account selfheating in the framework of an electronic hotspot. Then the electro-thermal behavior of the mixer is modeled using the appropriate heat balance equations. From the calculated pumped I(V) curve we calculate all relevant parameters to correct the measured time constant for electrothermal feedback.

#### IV.a Selfheating through the IF load in the hotspot framework

In order to understand our experimental results and infer the intrinsic time constant of the mixer, the data have to be corrected for electro-thermal feedback through the IF load [3,19]. The measured effective time constant  $\tau_{eff}$  of a HEB mixer is related to the intrinsic time constant  $\tau_{th}$  via

$$\tau_{eff}(V) = \frac{\tau_{th}}{1 + \alpha(V)\beta(V)} \quad [2]$$

with  $\alpha(V)$  and  $\beta(V)$  given by

$$\alpha(V) = \frac{I_{dc}^2 \left( \frac{dR}{dT} \right)}{G} \quad \text{and} \quad \beta(V) = \frac{R_{dc} - R_L}{R_{dc} - R_L} \quad [3]$$

Here,  $I_{dc}$  is the dc current flowing through the device and  $R_{dc}$  the dc resistance ( $V_{dc}/I_{dc}$ ) in the operating point. The factor  $\alpha(V)$  reflects the selfheating of the device, whereas  $\beta(V)$  accounts for the finite impedance of the IF load, basically suppressing the effect of electro-thermal feedback. In the lumped element approach,  $\alpha(V)$  can be calculated directly from the pumped  $I(V)$  curve [19]. In the hotspot framework, however, a temperature profile is present, and the same change in rf and dc heating has a different effect on the resistance of the HEB [6,7]. Therefore,  $(dR/dT)G^{-1}$  should be rewritten as

$$\left( \frac{dR}{dT} \right) G^{-1} = \frac{C_{rf}G_{rf} + C_{dc}G_{dc}}{G_{rf} + G_{dc}} \quad [4]$$

with

$$C_{rf,dc} = \left( \frac{dR}{dP_{rf,dc}} \right) \quad \text{and} \quad G_{rf,dc} = \left( \frac{dT_{avg}}{dP_{rf,dc}} \right)^{-1} \quad [5]$$

Here,  $C_{rf,dc}$  reflects the change in resistance due to a change in dissipated rf or dc power, respectively,  $G_{rf,dc}$  is the effective thermal conductance for rf or dc heating, and  $T_{avg}$  is defined as the average temperature along the microbridge. Both  $C_{rf,dc}$  and  $G_{rf,dc}$  can be calculated using the appropriate heat balance equations for a HEB. Note that in the case that  $C_{rf} = C_{dc}$  and  $G_{rf} = G_{dc}$ , Eq. 4 reduces to the expression given by Refs. 3 and 19.

#### IV.b Electro-thermal analysis of the mixer

We now proceed by modeling the electro-thermal behavior of the HEB mixer using the physically justified electronic hotspot model [6]. Here, we introduce two

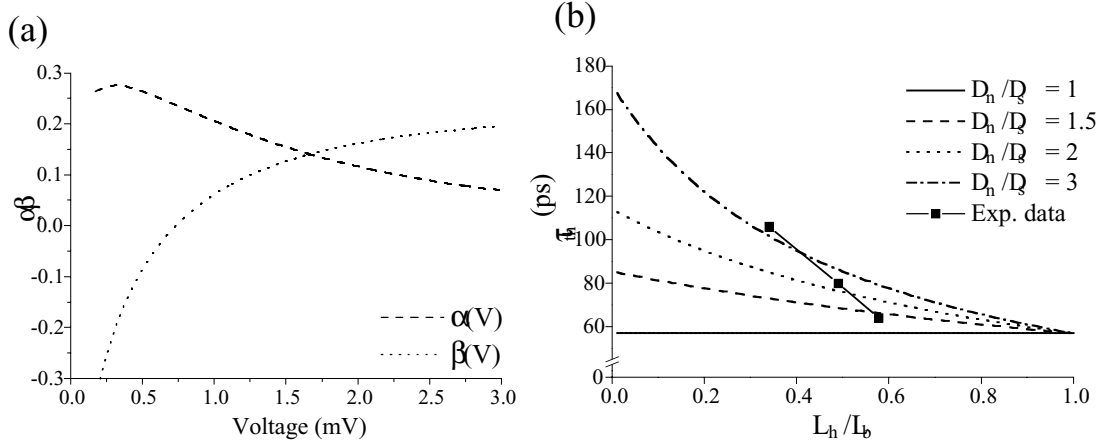


Fig. 4: (a) Calculation of  $\alpha(V)$  and  $\beta(V)$  from the theoretical pumped  $I(V)$  characteristic and Eqs. 3-5. (b) Intrinsic time constant as a function of the relative length of the hotspot. The squares indicate the experimental results. The curves are calculated using different values of the ratio  $D_n/D_s$  ( $D_n = 1.6 \text{ cm}^2/\text{s}$ ,  $L_b = 300 \text{ nm}$ ).

modifications with respect to the model presented in Ref. 6, which physically describe a diffusion-cooled HEB more accurately, although they are found to have little influence on the actual outcome of the calculations. First, we do not take the thermal conductivity  $k$  to be constant but assume that it is linearly increasing with temperature in both normal and superconducting parts according to the Wiedemann-Franz law [20]. Second, we neglect the heat transfer from electrons to phonons, justifiable for a diffusion-cooled HEB, and allowing an analytical solution to the problem. As a result, the heat balance equation for a biased and pumped diffusion-cooled HEB takes the following form: Inside the hotspot, we have

$$-\frac{d}{dx}\left(k(T)\frac{dT}{dx}\right) = j^2\rho + p_{rf} \quad [6]$$

with  $j$  the dc current density in the microbridge and  $p_{rf}$  the rf power density (per unit volume). Outside the hotspot we use the same equation, with the exception that there the dc dissipation is zero ( $j^2\rho \rightarrow 0$ ). In the analysis, it is assumed that rf power is absorbed homogeneously in the microbridge, which is true if the frequency of the radiation is above the gap frequency of the superconductor. In our case, the radiation frequency is 700 GHz, whereas the gap frequency is  $\approx 450$  GHz. The equations are solved by requiring that  $T = T_b$  at the end of the bridge and  $T = T_c$  at the hotspot boundary. The current required to sustain a hotspot of length  $L_h$  when a radiation power density  $p_{rf}$  is absorbed, follows from matching  $dT/dx$  at the hotspot boundary. In Fig. 3b, we plot the calculated pumped and unpumped  $I(V)$  characteristics together with the experimental data. A good agreement is found between measurement and calculation in the case of the pumped  $I(V)$  curve. In the case of the unpumped

characteristic, deviations between model and measurement are observed at low bias voltages, which show that the measured minimum dc current needed to sustain a hotspot is smaller than predicted by the model. This observation has been discussed in more detail in Ref. 21. Using the simulated pumped  $I(V)$  characteristic, we have calculated  $(dR/dT)G^{-1}$  as a function of bias voltage according to Eqs. 4-5. The result is shown in Fig. 4a.

In Table 1, the results of the measurement and calculation for the three different bias points are summarized, from which it becomes clear that the intrinsic time constant of the microbridge increases with increasing length of the hotspot [22]. Note that in our particular case the effect of electro-thermal feedback is largely suppressed by the IF circuit, because the impedances of the IF load and mixer are close to each other. As a result, the effective and intrinsic thermal times do not differ much.

Table 1: Results of experiment and analysis

$V_b$ (mV)	$L_h$ (nm)	$\tau_{\text{eff}}$ (ps)	$\alpha$ (V)	$\beta$ (V)	$\tau_{\text{th}}$ (ps)
0.30	113	106	0.28	-0.21	100
0.56	148	80	0.26	-0.058	79
0.81	173	64	0.23	0.021	64

## V. Discussion

In order to verify whether the outcome of the experiment is physically sensible, we compare the results with a calculation of the time constant on the basis of Eq. 1, taking into account the difference in the diffusion constants of the normal and superconducting parts of the microbridge. We assume that we can use a linearly weighted average value of the diffusion constant according to

$$D_{\text{avg}} = \frac{D_n L_h + D_s (L_b - L_h)}{L_b} \quad [7]$$

with  $D_n$  and  $D_s$  the diffusion constant in the normal and superconducting regions, respectively. In Fig. 4b, we plot the calculated time constant for different values of  $D_n/D_s$  as a function of  $L_h/L_b$ . The ratios  $D_n/D_s$  have been chosen such that they are comparable to the values expected on the basis of Fig. 1. In the case  $D_n/D_s = 1$ , the bandwidth does not depend on the length of the normal domain and thus the time constant is the same as given by Eq. 1, with  $D_n = D_s = 1.6 \text{ cm}^2/\text{s}$ . It is important to note that the experimentally obtained values for the thermal time constant are, as expected, always larger than the value predicted by Eq. 1. Clearly, the predicted trend and the magnitude of the observed effect from Eq. 7 correspond to the experimental observations. However, we do not obtain nor expect a one-to-one correspondence between measurement and calculation, because the model used is oversimplified. A

more realistic calculation would have to include the full time-dependent heat-balance equations, taking into account the bias-dependent modification of the time constant due to electro-thermal feedback.

The results of the measurement and analysis presented here are in contrast to measurements of the IF bandwidth in a Nb *phonon-cooled* HEB mixer, in which case the bias dependence could very well be explained by electro-thermal feedback through the IF load [19]. This observation can be understood by realizing that in a phonon-cooled device the thermal path to the contacts is not relevant since the energy from the hot electrons is removed via inelastic scattering with phonons.

## VI. Conclusions

To conclude, the essential outcome of this experiment is that it demonstrates that the intrinsic time constant of a diffusion-cooled HEB is not only depending on the length of the microbridge, but also on length of the hotspot in the bridge, being determined by the bias conditions of the system. The observations can be understood to a first order by using a qualitative model in which the reduced diffusion constant in the superconducting regions is taken into account.

## Acknowledgements

This work is supported by the European Space Agency (ESA) under Contract No. 11738/95/NL/PB and by the Nederlandse Organisatie voor Wetenschappelijk Onderzoek (NWO) through the Stichting voor Technische Wetenschappen (STW).

## References

- [1] E.M. Gershenzon, G.N. Gol'tsman, I.G. Gogidze, Y.P. Gusev, A.I. Elantiev, B.S. Karasik, and A.D. Semenov, *Sov. Phys. Superconductivity* 3, 1582 (1990).
- [2] D.E. Prober, *Appl. Phys. Lett.* 62, 2119 (1993).
- [3] B.S. Karasik and A.I. Elantiev, *Appl. Phys. Lett.* 68, 853 (1996).
- [4] P. J. Burke, Ph. D. thesis, Yale University (1997).
- [5] D. Wilms Floet, J.J.A. Baselmans, T.M. Klapwijk, and J.R. Gao, *Appl. Phys. Lett.* 73, 2826 (1998).
- [6] D. Wilms Floet, E. Miedema, T.M. Klapwijk, and J.R. Gao, *Appl. Phys. Lett.* 74, 433 (1999).
- [7] H. Merkel, P. Khosropanah, P. Yagoubov, and E. Kollberg, *Proceedings Tenth International Symposium Space Terahertz Technology*, University of Virginia, Charlottesville, March 16-18, 1999, pp. 592-606.
- [8] A. Skalare, W.R. McGrath, B. Bumble, H.G. LeDuc, *Proceedings Tenth International Symposium Space Terahertz Technology*, University of Virginia, Charlottesville, March 16-18, 1999, pp. 215-228.

- [9] Y.P. Gousev, G.N. Gol'tsman, A.D. Semenov, and E.M. Gershenzon, R.S. Nebosis, M.A. Heusinger, and K.F. Renk, *J. Appl. Phys.* 75, 3695 (1994).
- [10] P.J. Burke, R.J. Schoelkopf, D.E. Prober, A. Skalare, W.R. McGrath, B. Bumble, and H.G. LeDuc, *Appl. Phys. Lett.* 68, 3344 (1996).
- [11] K.S. Karasik, K.S. Il'in, E.V. Pechen, and S.I. Krasnosvobodtsev, *Appl. Phys. Lett.* 68, 2285 (1996).
- [12] R.A. Wyss, B.S. Karasik, W.R. McGrath, B. Bumble, and H. LeDuc, *Proceedings of the Tenth International Symposium Space Terahertz Technology*, University of Virginia, Charlottesville, March 16-18, 1999, pp. 215-228.
- [13] H. Carslaw and J. Jeager, *Conduction of Heat in Solids*, Oxford University Press, London (1959).
- [14] M. Tinkham, *Introduction to Superconductivity*, 2<sup>nd</sup> edition, McGraw-Hill, New York (1996).
- [15] F.E. Pobell, *Matter and methods at low temperatures*, Berlin, Springer-Verlag, (1992)
- [16] D. Wilms Floet, J.R. Gao, W. Hulshoff, H. van de Stadt, T.M. Klapwijk, and A.K. Suurling, *IOP Conf. Series* 158, edited by H. Rogalla and D.H.A. Blank, 401 (1997).
- [17] Based on specifications with respect to the voltage standing wave ratio of the amplifier at room temperature by Miteq Inc., 100 Davids Drive, Hauppauge, N.Y. 11788.
- [18] A. Skalare, W.R. McGrath, B. Bumble, H.G. LeDuc, P.J. Burke, A.A. Verheijen, R.J. Schoelkopf, and D.E. Prober, *Appl. Phys. Lett.* 68, 1558 (1996).
- [19] H. Ekström, B.S. Karasik, E. Kollberg, and K.S. Yngvesson, *IEEE Trans.Microwave Theory Tech.* 43, 938 (1995).
- [20] In reality, the thermal conductance in the superconducting regions decreases exponentially with temperature due to the decreased quasi-particle density. Here, we assume that the deviations between the exponential and linear behaviour at the temperatures of interest are not large.
- [21] D. Wilms Floet, J.R. Gao, T.M. Klapwijk, and P.A.J. de Korte, *Proceedings Tenth International Symposium Space Terahertz Technology*, University of Virginia, Charlottesville, March 16-18, 1999, pp. 583-591.
- [22] The length of the hotspot has been calculated on the basis of the dc resistance  $R_{dc}$  of the HEB in the three bias points according to  $L_h = (R_{dc}/R_n)L_b$ .

# A Cryosystem for Optical Evaluation of the Normal Metal Hot-electron Microbolometer

Denis Chouvaev and Leonid Kuzmin

*Chalmers University of Technology, Department of Microelectronics and Nanoscience,  
SE-412 96 Göteborg, Sweden  
e-mail:chouvaev@fy.chalmers.se; tel. +46-31-772 5173*

---

## Abstract

We are presenting our recent results in development of a direct detector of submillimeter waves (bolometer) based on a microscopic power sensor coupled to an integrated antenna. An electrical  $NEP$  of  $5 \times 10^{-18}$  W/Hz<sup>1/2</sup> at 0.1 K has been demonstrated in a dc measurement. A detailed description of design of a cryogenic system for optical evaluation of this detector is presented.

---

## Introduction

In this report we present our recent results in development of an antenna-coupled direct detector of submillimeter wave radiation – the normal metal hot electron bolometer (NHEB). Broadband submillimeter direct detectors (bolometers) are desired in certain fields of radio astronomy where large bandwidth and high sensitivity requirements are more important than a very sharp spectral resolution. An example of such a field is the study of the relict cosmic microwave background (CMB) radiation. Currently there are several projects where new kinds of structures are proposed as alternative to the present blackbody bolometers with thermistors [1-3]. Increase of the power resolution is one objective in the new development, since the new space-borne telescope projects are going to make available cold low-noise reflectors and thus create room for detectors with better sensitivity level than today's  $NEP \approx 10^{-17}$  W/Hz<sup>1/2</sup>. The other objective is to decrease the reaction time by at least one order of magnitude from the present level around  $10^{-2}$  s. The third objective is to develop a detector technology that will make possible to build large (over 100 pixels) imaging camera arrays of detectors, preferably on a single substrate.

## Electrical NEP measurements

The normal metal hot-electron bolometer has been proposed by M. Nahum *et al* in [4] and [5]. It is a microscopic power sensor containing a resistive absorber where a high-

frequency current induced in a planar integrated antenna is converted to heat, which is then detected as change in the electron gas temperature. The operating principle is shortly explained in the Fig. 1.

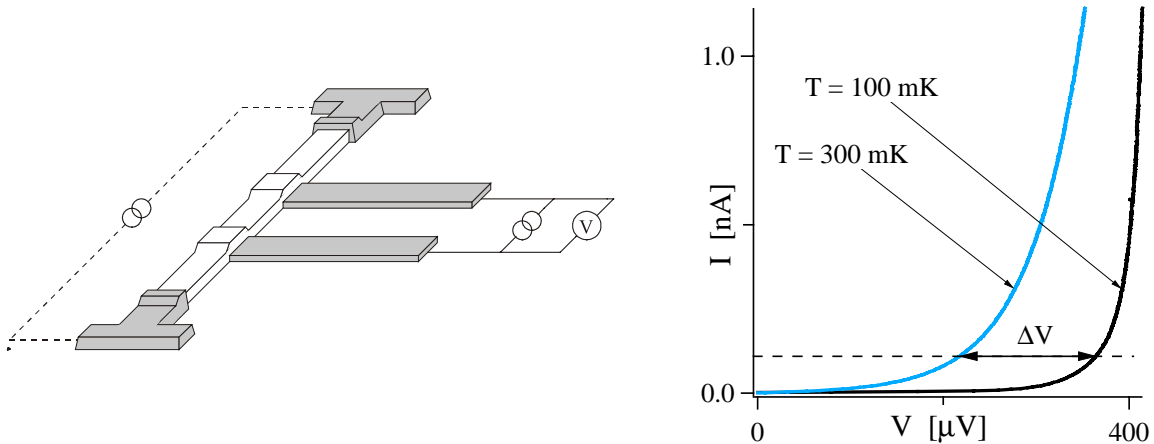


Fig. 1 Left panel – schematic diagram of the power sensor. The structure is fabricated by e-beam lithography and shadow metal evaporation from different angles. The white strip is made of normal metal (copper) and has dimensions  $5 \times 0.25 \times 0.07 \mu\text{m}^3$ . It connects the two superconducting antenna terminals (on the ends) and serves as a resistive load for the antenna. The current induced in the antenna heats electron gas in the strip and these electrons arrive to a thermal equilibrium at a temperature higher than the lattice temperature. This is possible because the electron-phonon thermal exchange is a slower process at the operating temperatures (below 0.5 K). A thermometer consisting of two Normal metal-Insulator-Superconductor (NIS) tunnel junctions (at the middle of the strip) then reads out the electron temperature. The superconducting electrodes are made of aluminum and the tunnel barrier in the junctions is formed by the aluminum oxide.

Right panel – principle of operation of the NIS thermometer. The two junctions in series are biased with a constant current. Voltage over the junctions is then almost linearly dependent on the electron temperature in the normal electrode.

More detailed description of the sensor and its fabrication technology can be found in earlier works [6][3]. We have been working on practical development of this detector since 1997 and reported on our research progress at the previous STT symposiums. Previously our work was mostly focused on improvement of the power sensor parameters, since the ultra sensitive power sensor is the active part of the detector. We measured the so-called electrical power responsivity by heating the sensor with a small dc current. The experiments were conducted in a dilution refrigerator designed for low-frequency measurements at 0.02..2 K. The most difficult problem that we had faced was that the sensor got saturated at operating temperatures (i.e. below 0.3 K) even without any intentional heating. We explained this effect by interference from the noise induced in the wiring of our measured system. Different ways of avoiding this interference have

been attempted [3] and recently we have found that the most reliable method was to install resistors of at least 10 k $\Omega$  cooled to 1.2 K in every measurement lead close to the sample under test. Some of the resistors were chosen to be 10 M $\Omega$  and installed in pairs, so that they provided the two symmetric low-noise current sources for the sensor circuit.

With this improved setup we have managed to measure the electrical noise-equivalent power  $NEP = 5 \times 10^{-18}$  W/Hz $^{1/2}$  with sample cooled to 0.1 K and  $NEP = 3 \times 10^{-16}$  W/Hz $^{1/2}$  with sample at 0.3 K. This corresponds to electrical power responsivities of  $4 \times 10^9$  V/W and  $1 \times 10^8$  V/W, respectively. The output noise in this experiment was dominated by the room-temperature amplifier noise and was in total 22 nV/Hz $^{1/2}$  for  $f_{\text{meas}} = 20$  Hz (slightly decreasing with increase in frequency). The results of the experiment are shown in the Fig. 2.

Our results, as well as previously reported electrical NEP measurements [5], confirm that from the sensitivity point of view the NHEB can be very attractive as a “new generation” bolometer. The measured dependence of the electron temperature in the absorber on the applied heating power (Fig. 3) is very close to the theoretically expected  $P = \Sigma \Omega (T^5 - T_0^5)$  (where  $P$  is the applied heating power,  $T$  is the electron temperature measured by the tunnel junction thermometer,  $T_0$  is the substrate temperature,  $\Omega$  is volume of the absorber film and  $\Sigma$  is a material parameter of the absorber). This theoretical expression is based on the assumption that the electron-phonon inelastic interaction time depends on  $T$  as  $\tau \propto T^{-3}$ , and that would correspond to the reaction time of the bolometer close to  $10^{-6}$  s at 0.3 K.

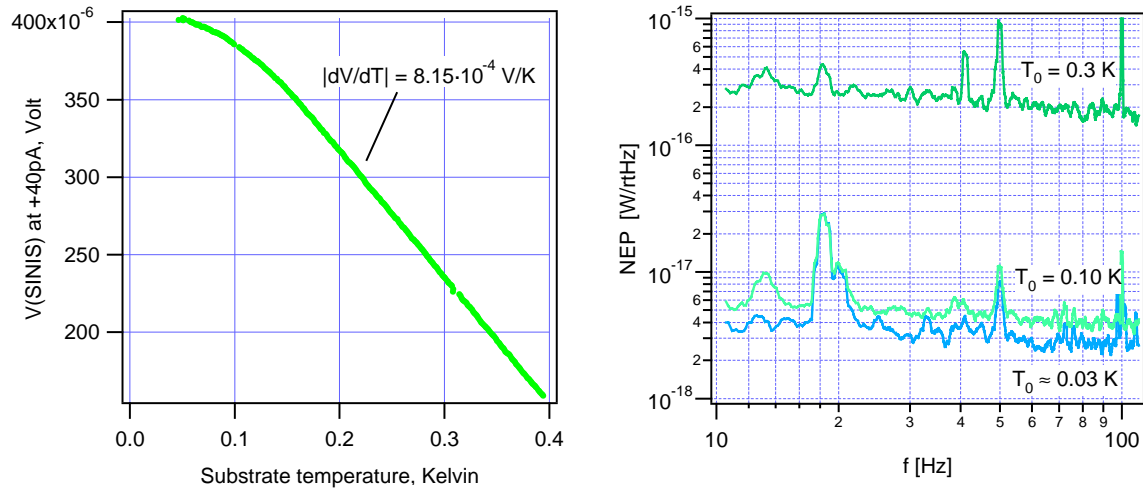


Fig. 2 Experimental results: left panel – calibration curve for the NIS junction thermometer, no heating is applied to the sensor; right panel – electrical Noise Equivalent Power of the sensor measured at three different substrate temperatures.

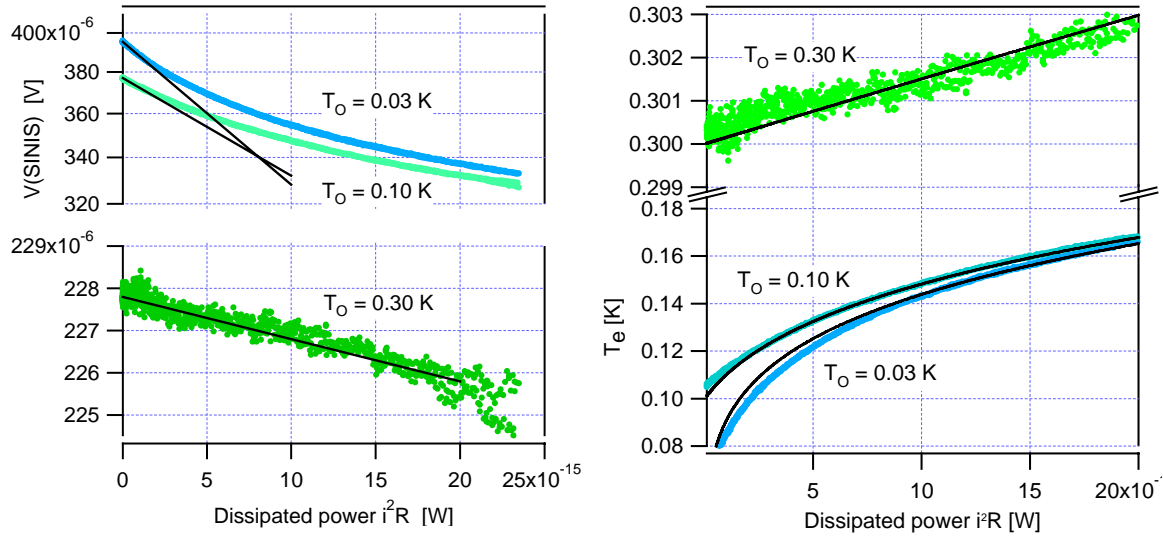


Fig. 3 Experimental results: left panel – electrical responsivity of the power sensor (voltage at the output of the thermometer vs. heating applied to the absorber) for three substrate temperatures  $T_0$ ; black lines show the small-signal responsivity.

Right panel – electron temperature in the absorber computed from the output voltage using the thermometer calibration curve (see fig. 2); black curves are the fits obtained with the expression  $P = \Sigma \Omega (T^5 - T_0^5)$  and a single fitting parameter  $\Sigma = 2.5 \times 10^{-9} \text{ W } \mu\text{m}^{-3} \text{ K}^{-5}$  for all three curves.

### Design of a mm-wave cryosetup

At this stage we are considering an experiment where not only the electrical parameters of the power sensor, but also the optical responsivity of the bolometer as whole could be measured. This requires a measurement setup that would have an optical input with controlled throughput, and at the same time would allow cooling the detector to at least 0.3 K. In the literature one can find successful examples of the similar systems built for testing of heterodyne mixers; however almost none of them involve cooling to below 4.2 K. Some more traditional low-temperature bolometer cryostats have cooling even down to 0.1 K, but their optical setups are adapted for blackbody bolometers and based usually on the Winston concentrator coupling. In the cryogenic system that we are building at the moment we are trying to combine solutions from the both types of detector cryostats and to suit the special experimental requirements for an antenna-coupled bolometer.

#### *Cornerstones of the design*

Since we see the CMB studies as a possible potential application for the detector, we have decided to choose for our setup a frequency band corresponding to 3..5 K blackbody emission (180..300 GHz). The heavy radiation load at higher frequencies that could both

overload the sensor and overheat the substrate will be cut off by a metal-mesh low-pass filter with sharp edge at 450 GHz [7]. Further, a neutral density (ND) filter can be used to attenuate the incoming radiation at all frequencies. To provide a certain frequency resolution and to avoid overriding dynamic range of the bolometer we would like to limit the fractional bandwidth of the detector to about 20%. This band is going to be defined mostly by the frequency response of the double-slot antenna that we are going to use.

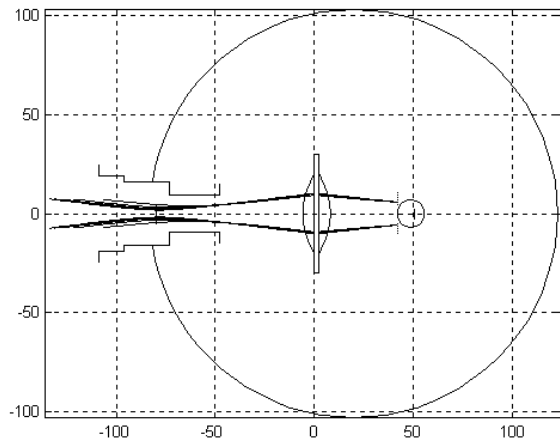
The double-slot antenna is attractive for three reasons:

1. It provides a natural band-pass filter.
2. It has a fairly narrow radiation pattern (compared to *e.g.* the log-periodic antenna), which is important since we need to control the whole throughput of the antenna.
3. It can be matched to a low-resistive load (below  $50 \Omega$ ). This allows to make the absorber strip in the sensor short, which means a smaller film volume and hence a higher responsivity.

Both the sensor structure and the antenna are fabricated on a flat silicon substrate. To provide a proper coupling to the antenna through the backside of the substrate the substrate will be glued on a hyperhemispherical silicon lens [8]. The hemisphere diameter is 13.7 mm and it is extended with a silicon slab so that the antenna is placed 2.20 mm behind the center of the sphere. The combined lens antenna should then have 30 dB-beamwidth of about  $34^\circ$  (10 dB-beamwidth of  $16^\circ$ ). The pattern can be approximated by a gaussian beam diverging from the antenna. This gives a fairly narrow beam, but we preferred to convert it to a converging beam by means of a 50 mm TPX dielectric lens (Fig. 4). This allowed us to choose the optical window and the infrared filters of a small diameter (1 inch), which should help to decrease the overall radiation load on the cryosystem.

Fig. 4

Ray traces in the proposed optical arrangement (at the  $-8.7\text{dB}$  relative power level) for frequencies from 180 GHz to 420 GHz. The components on the drawing are the filter unit aperture, the dielectric lens and the hyperhemispherical lens (shown by a small circle). The traces are calculated in the assumption of the gaussian beam shape.



For cooling of the detector we have chosen a closed-cycle  $^3\text{He}$ -cryocooler that can reach temperatures down to 0.27 K. This unit is manufactured by CEA/DSM/DRFMC/Service des Basse Températures, Grenoble, France. It does not require any external pumps and

could be conveniently mounted in a pit in the cold plate of an 8-inch  $^4\text{He}$ -dewar from Infrared Laboratories (Fig. 5). This is a robust and inexpensive solution compared to an adiabatic demagnetization refrigerator or a dilution refrigerator for cooling to 0.1 K or below. Another consideration was that due to the high total radiation load in the experiment the sensor would have  $T$  [electron gas]  $> 0.3$  K anyway, that is even if the substrate temperature would be below 0.1 K.

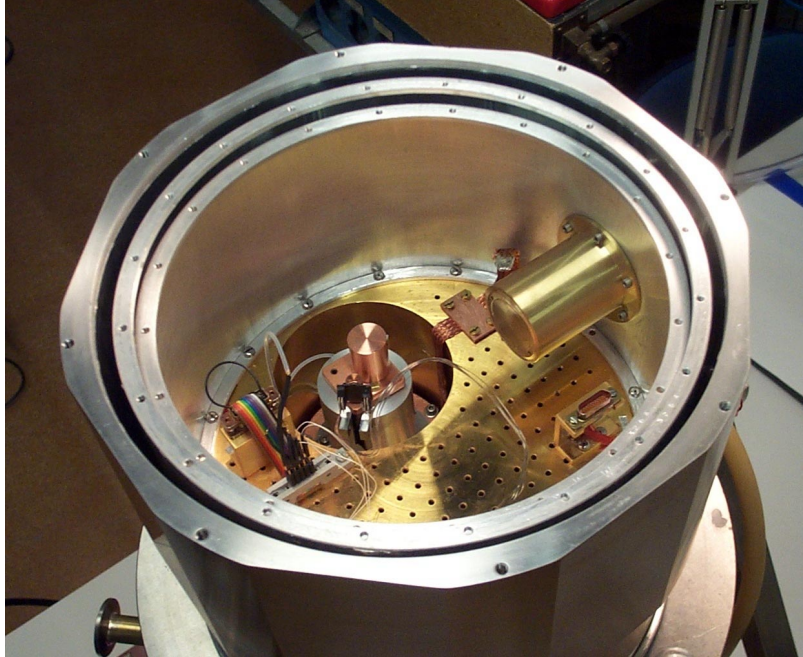


Fig. 5 The current phase in installation of the new system. One can see the  $^3\text{He}$ -cryocooler mounted in a pit in the 2 K-cold plate of an 8-inch HDL dewar from Infrared Labs and a long baffle (here blanked), which will accommodate the stimulator and the filter unit. This longer baffle is exchangeable with a shorter one for the filter unit only.

As for a source of incident radiation we have considered two possibilities. One option is to observe an external blackbody source with a known spectral intensity distribution through an optical window in the dewar. To avoid drifts in the measurements one can modulate the radiation by mechanical chopping between a 295 K source and a 77 K source. A different option is to place a blackbody source inside the dewar. There are certain advantages with the latter solution: peak of the frequency spectrum can be placed at the center frequency of the bolometer band by heating the blackbody to a proper temperature (around 5 K for 300 GHz); low intensity of the source makes possible measurements without an ND filter, which otherwise introduces additional uncertainty in the spectral distribution (because of internal interference fringes); also modulation of the source (possibly up to 100 Hz) can be done simply by modulating the heating current. We are going to employ a commercially available thermal source – “stimulator” – from Haller-Beeman Associates, Inc. It will be placed in the focus of a Winston horn, thus

spreading the emitted radiation to a uniformly illuminated spot about 10 mm in diameter (the larger aperture of the horn).

By arranging a detector mount and the dielectric lens on a compact optical bench inside the dewar it is going to be possible to use the same alignment both for measurements employing the optical window and for the measurements employing the stimulator. In the second case the stimulator is mounted just behind the optical window inside the dewar, a filter set is moved in front of it, and the optical bench with the rest of the setup is shifted back to keep the distance from the antenna to the filter's surface the same (Fig. 6).

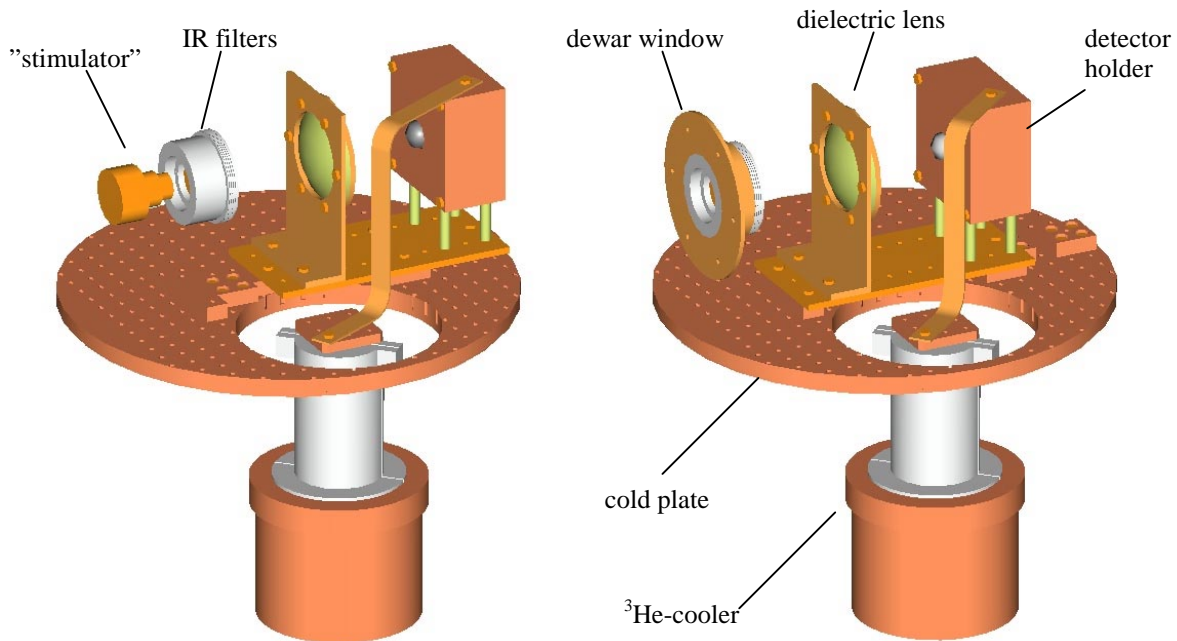


Fig. 6 Computer-generated images of the components inside the  $^4\text{He}$  dewar. Left side – option for measurements with an internal stimulator; right side – option for measurements with irradiation through the dewar window. The two configurations can be exchanged by simple re-mounting of the filter unit and shifting the smaller optical bench along the optical axis.

### *Formulation of the experiment*

From the developer's point of view it is interesting to verify the correctness of the theoretical estimations of the bolometer performance, which are based on what is known about the power sensor's performance. However, we need to consider at least the combination of the power sensor and an antenna as a minimal receiving unit. Since we are planning that our detector is going to be used for a different branch of research we need to specify the bolometer sensitivity independent of an actual observation system. But at the same time it is less straightforward to measure intensity and spectrum of the radiation at the input of the antenna in contrast to measuring it at the input of a

cryosystem as whole. One can formulate this problem in terms of the following algebraic expression:

$$P(f) = C(f) \cdot T_2(f) \cdot T_1(f) \cdot F_2(f) \cdot F_1(f) \cdot K(f).$$

Here  $f$  is frequency of the radiation,  $P$  is the power spectral density incoming the power sensor,  $K$  is the power spectral density of radiation from a source, and the rest of the functions describe the transmitting properties of intermediate components in the radiation coupling system:

$F_1$  is transmission function of the low-pass filter,

$F_2$  is transmission function of the neutral density filter,

$T_1$  is transmission function of the dielectric lens,

$T_2$  is transmission function of the hyperhemispherical antenna lens, and

$C$  is the coupling coefficient for the planar integrated antenna.

The first of our goals in this formulation is to determine the function  $P$  as accurate as possible, because then we can calculate the electrical responsivity of the sensor

$$S_e(f) = (dV/dP)_f$$

(where  $V$  is voltage at the output of the sensor) for heating by a high-frequency excitation and compare it to the theoretical predictions and to the results obtained with a dc heating.

The second goal is to specify the optical responsivity of the detector with a silicon lens antenna, which is

$$S_o(f) = \frac{dV}{d(P(f)/C(f)/T_2(f))} = \frac{dV}{d(K(f) \cdot F_1(f) \cdot F_2(f) \cdot T_1(f))}.$$

The  $K(f)$  can be computed from the Planck's expression for blackbody radiation.  $F_1(f)$  is generally specified by the manufacturer, however some uncertainty can be due to that the filter's performance can be different for rays incident under a finite angle to its surface.  $F_2(f)$  is specified as a constant, but as already mentioned interference due to reflections between the two surfaces of the ND filter substrate can lead to a ripple in the transmission curve.  $T_1(f)$  and  $T_2(f)$  can be computed to a good approximation knowing the properties of the materials (TPX and silicon).

In the initial experiment we plan to compute all these function and substitute them into the formulae in order to evaluate the data. Later on we intend to characterize the components individually by substituting some of them. For example, ND filter can be avoided if we use the internal stimulator as a source; by substituting our test bolometer with a bismuth bolometer with known responsivity we can get information about the  $P(f)$ , etc. Also using a Fourier Transfer Spectrometer as a narrow-band radiation source is an option for a more accurate calibration of the system.

## Conclusions

We have further improved the electrical NEP performance of the normal metal hot-electron bolometer by introducing cold resistors in the sample wiring in our measurement system.  $NEP = 5 \times 10^{-18} \text{ W/Hz}^{1/2}$  at 0.1 K has been achieved. Now we are working on an experiment where we could measure the optical responsivity of the detector in the 1 mm wavelength range. A new cryogenic setup for this purpose has been designed. The cooling facilities of this setup have already been put in operation and the quasioptical components are in the process of installation.

## Acknowledgements

Design of the optical system has been done in close cooperation with the group of Prof. P.L. Richards from University of California at Berkeley. We thank Jonas Zmuidzinis and Michael Tarasov for comments and discussions. This work has been supported by the Swedish Research Council for Engineering Sciences (TFR) and partly by Japanese New Energy and Industrial Technology Development Organization (NEDO).

## References

- [1] J.M. Gildemeister, A.T. Lee, P.L. Richards, *Appl. Phys. Lett.*, **74**(6):868-870, Feb. 1999.
- [2] B.S. Karasik, W.R. McGrath, H.G. LeDuc, M.E. Gershenson, *Supercond. Sci. & Technol.*, **12**(11):745-747, Nov. 1999.
- [3] D. Chouvaev, L. Kuzmin, M. Tarasov, *Supercond. Sci. & Technol.*, **12**(11):985-988, Nov. 1999.
- [4] M. Nahum, P.L. Richards, C.A. Mears, *IEEE Trans. Appl. Supercond.*, **3**(1):2124-2127, Mar. 1993.
- [5] M. Nahum, J. Martinis, *Appl. Phys. Lett.*, **63**(22):3075-3077, Nov. 1993.
- [6] D. Chouvaev, D. Golubev, M. Tarasov, L. Kuzmin, In *Proc. of the 10<sup>th</sup> Int. Symp. on THz Space Technology, Charlottesville, VA, 17-19 March 1999*, pp. 552-565.
- [7] Ken Wood /QMC Instruments Ltd.,  
[http://qmciworks.ph.qmw.ac.uk/Products\\_frame.htm](http://qmciworks.ph.qmw.ac.uk/Products_frame.htm); accessed 2000-04-27.
- [8] D.F. Filipovic, S.S. Gearhart, G.M. Rebeiz, *IEEE Trans. Microwave Theory and Techniques*, **41**(10):1738-1749, Oct. 1993.

# **A distributed device model for phonon-cooled HEB mixers predicting IV characteristics, gain, noise and IF bandwidth**

**P. Khosropanah<sup>\*</sup>, H. Merkel<sup>\*</sup>, S. Yngvesson<sup>#</sup>, A. Adam<sup>§</sup>,**

**S. Cherednichenko<sup>\*</sup>, E. Kollberg<sup>\*</sup>**

<sup>\*</sup>Chalmers University of Technology, Department of Microelectronics, Microwave electronics Laboratory, 412 96 Gothenburg, Sweden

<sup>#</sup>University of Massachusetts, Department of Electrical and Computer Engineering, Amherst, MA 01003

<sup>§</sup>Supélec, Department of Electron Device Physics, 91190 Gif-sur-Yvette, France

## **Abstract**

A distributed model for phonon-cooled superconductor hot electron bolometer (HEB) mixers is given, which is based on solving the one-dimensional heat balance equation for the electron temperature profile along the superconductor strip. In this model it is assumed that the LO power is absorbed uniformly along the bridge but the DC power absorption depends on the local resistivity and is thus not uniform. The electron temperature dependence of the resistivity is assumed to be continuous and has a Fermi form. These assumptions are used in setting up the non-linear heat balance equation, which is solved numerically for the electron temperature profile along the bolometer strip. Based on this profile the resistance of the device and the IV curves are calculated. The IV curves are in excellent agreement with measurement results. Using a small signal model the conversion gain of the mixer is obtained. The expressions for Johnson noise

and thermal fluctuation noise are derived. The calculated results are in close agreement with measurements, provided that one of the parameters used is adjusted.

## I. Introduction

Previously presented HEB models (the "point bolometer" or "standard" model) [1,2] assume a uniform electron and phonon temperature along the superconductor strip. Although these models are quite successful to explain many experimental results, some discrepancies have been reported:

It has been shown that the models are not capable of estimating the absorbed LO power correctly when operating at frequencies above the quasiparticle bandgap [3]. Also accurate measurements and calculations have shown such the "point bolometer" model cannot explain the dependence of the measured conversion loss and the output noise temperature on the bias voltage [4]. Nevertheless in order to optimize the device performance for space applications, an accurate model is needed.

One-dimensional models have been developed assuming that the electron temperature varies along the superconductor strip [5,6]. This assumption leads to different heating efficiencies for the absorbed LO and DC power implying that the resistance change due to a small change in absorbed LO power is not the same as that for absorbed DC power. This is due to the fact that the DC power is only absorbed in the part of the strip where the electron temperature is above the critical temperature whereas LO power absorption is uniform.

In previous one-dimensional hot spot models [5,7] the temperature dependence of resistivity is assumed to be a step function, which goes from zero to normal resistivity at the critical temperature. This and other assumptions were made in order to make it possible to obtain an analytical solution for the temperature profile. The main disadvantage of this model is that while the temperature profile does not exceed the critical temperature no hot spot is formed, and the model predicts zero resistance. Consequently it is not possible to calculate reasonable IV curves at low bias voltages and low LO powers. In practice the resistivity transition is smooth and measurements show that the transition width is about 1.2 K [8]. In order to obtain complete IV curves it is important to model the transition in a more realistic way.

The model presented here assumes that the temperature dependence of the resistivity, although step like, is continuous and has a Fermi form, and the transition width can be chosen as a variable (similar to a model for Nb diffusion cooled bolometers c.f. [9]). This results in a non-linear heat balance equation, which is solved for the electron temperature profile numerically. In section II the one-dimensional heat balance equation and our large signal model are discussed. Section III describes the small signal model. The noise is discussed in section IV. Section V explains a possible method for calculating the IF impedance and the bandwidth of the bolometer. Section VI summarizes the results.

## II. Large signal model

Figure 1 shows the schematic heat flow in a small segment of a bolometer. The electrons are heated by the absorbed LO power ( $P_{LO}$ ) and DC bias power.  $P_{LO}$  is absorbed uniformly along the bolometer with length  $2L$ , but the absorption of DC power is not uniform and depends on the bias current  $I_0$  and the local resistivity  $\rho(T_e)$ . In steady state this heat is partly transferred to the phonons ( $P_{e \rightarrow p}$ ) and partly to the electrons in the neighboring segments due to the electron thermal conductivity. Here it is assumed that power that is carried by the phonons ( $P_{e \rightarrow p}$ ) is directly transferred to the substrate ( $P_{p \rightarrow substrate}$ ). There the thermal conductivity of the phonons in the direction of the bolometer strip is neglected. The electron thermal conductivity,  $\lambda_e$ , is a function of the electron temperature. Below the critical temperature,  $T_c$ , it is proportional to  $T_e^3$  and above  $T_c$  it is proportional to  $T_e^1$  [10].  $A$  denotes the cross section area of the bolometer strip.

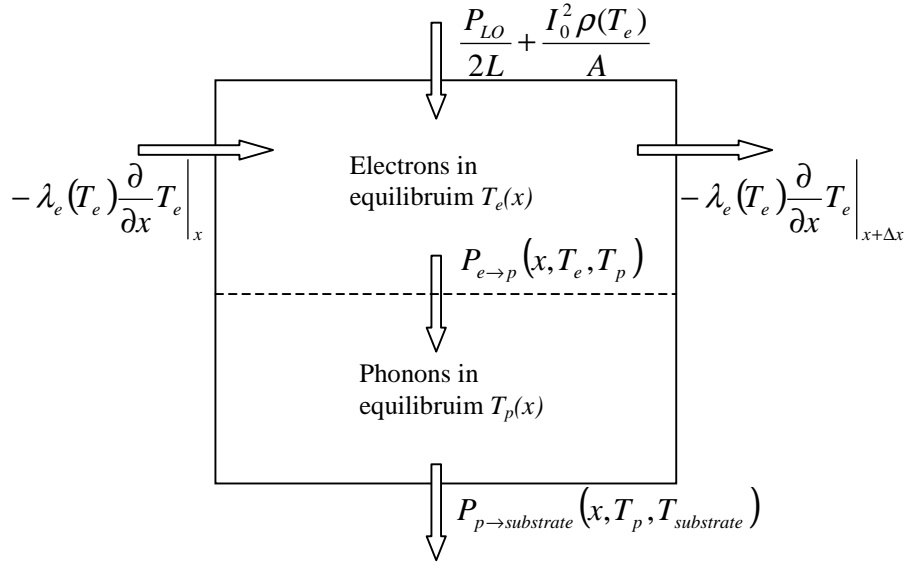


Figure 1. The heat flow in a small segment of the bolometer.

The electron-phonon and phonon-substrate thermal coupling can be written as:

$$P_{e \rightarrow p} = \sigma_e (T_e^n - T_p^n) \quad (1)$$

$$P_{p \rightarrow substrate} = \sigma_p (T_p^4 - T_{substrate}^4) \quad (2)$$

where  $\sigma_e$ ,  $\sigma_p$  are the electron-phonon and phonon-substrate cooling efficiency respectively [8]. For NbN  $n$  is found to be equal to 3.6 in (1) [8].

The heat balance equations for a small segment of the bolometer can be written as:

$$\frac{\partial}{\partial x} \left[ \lambda_e(T_e) \frac{\partial}{\partial x} T_e \right] - \sigma_e (T_e^{3.6} - T_p^{3.6}) + \frac{P_{LO}}{2L} + \frac{I_0^2 \rho(T_e)}{A} = 0 \quad (3.I)$$

$$\sigma_e (T_e^{3.6} - T_p^{3.6}) = \sigma_p (T_p^4 - T_{substrate}^4) \quad (3.II)$$

Solving (3.II) approximately for  $T_p$  and substituting in (3.I) yields:

$$\frac{\partial}{\partial x} \left[ \lambda_e(T_e) \frac{\partial}{\partial x} T_e \right] - \sigma_{eff} (T_e^{3.6} - T_{substrate}^{3.6}) + \frac{P_{LO}}{2L} + \frac{I_0^2 \rho(T_e)}{A} = 0 \quad (4)$$

$$\text{where } \sigma_{eff} = \frac{8\sigma_e \sigma_p \sqrt{T_{substrate}}}{8\sigma_p \sqrt{T_{substrate}} + 7\sigma_e}.$$

Note that the dimension of all the terms in (4) is W/m. and  $\sigma_{eff}$  and  $\lambda_e$  depend on the cross section area of the bolometer [7]. The corresponding dimensions of  $\sigma_{eff}$  and  $\lambda_e$  are given in table 1.

The electron temperature dependence of the resistivity is assumed to be:

$$\rho(T_e) = \frac{\rho_N}{1 + e^{-\frac{T_e - T_c}{\delta T}}} \quad (5)$$

where the  $\rho_N$  is the normal resistivity,  $T_c$  is the critical temperature and  $\delta T$  is a measure for the transition width. Figure 2 shows the resistivity as a function of temperature. If we define  $\Delta T$  as the width of the transition from 10% to 90% of the normal resistivity, it is possible to show from (5) that:

$$\Delta T = 2 \ln 9 \cdot \delta T \approx 4.4 \cdot \delta T.$$

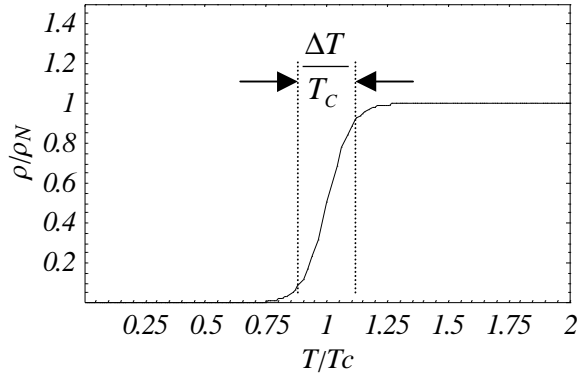


**Figure 2. Resistivity as a function of temperature.**

Equation (4) is solved numerically for  $T_e(x)$  with the boundary conditions:

$$T_e(-L) = T_e(L) = T_{bath}$$

where  $2L$  is the bolometer length. Note that the  $x$ -axis is in the direction of the bolometer strip and the origin is at the center of the bolometer.

Once the temperature profile is calculated the resistance of the bolometer takes the following form:

$$R = \frac{1}{A} \int_{-L}^L \rho(T_e(x)) dx = \frac{1}{A} \int_{-L}^L \frac{\rho_N}{1 + e^{-\frac{T_e(x) - T_c}{\delta T}}} dx \quad (6)$$

### III. Small signal model and conversion gain

The bolometer circuit is shown in figure 3. The mixing term at IF causes resistance fluctuations in the bolometer. The corresponding small signal voltage drives a current through the amplifier at the IF frequency. Note that this current goes through the bolometer as well and causes additional heating and consequently additional change in the resistance, which must be taken in to account. This effect is referred to as *electrothermal feedback*.

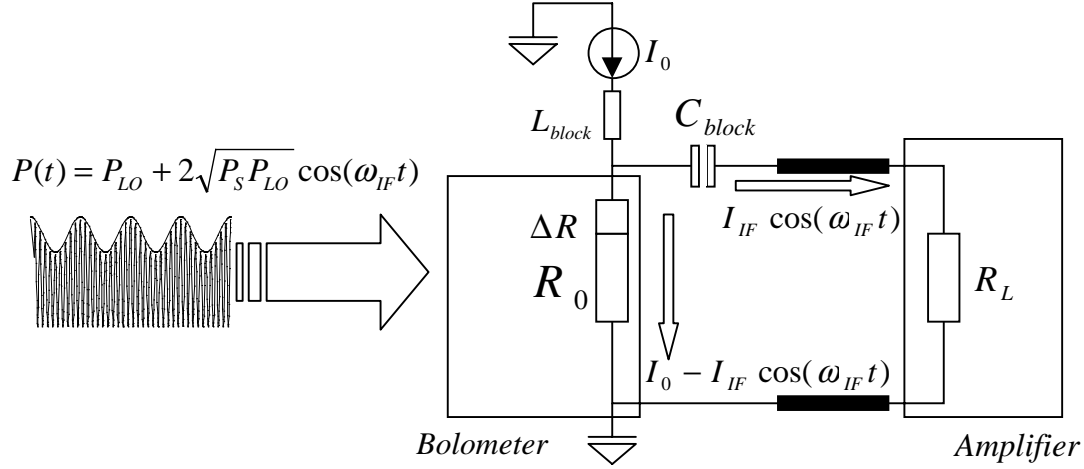


Figure 3. The bolometer circuit

From the above circuit the conversion gain of the mixer is derived as [7]:

$$G = \frac{P_L}{P_S} = \frac{2 \cdot I_0^2 \cdot R_L \cdot C_{RF}^2 \cdot P_{LO}}{(R_0 + R_L)^2 \cdot \left(1 - C_{DC} \cdot I_0^2 \frac{R_L - R_0}{R_L + R_0}\right)^2} \quad (7)$$

where  $P_L$  is the power in the load resistance and  $P_S$  is the absorbed signal power.  $C_{DC}$  and  $C_{RF}$  are the heating efficiencies of the absorbed DC and RF power respectively and defined as:

$$C_{DC} = \left. \frac{\partial R_0}{\partial P_{DC}} \right|_{\Delta P_{LO}=0} \quad \text{and} \quad C_{RF} = \left. \frac{\partial R_0}{\partial P_{LO}} \right|_{\Delta P_{DC}=0} \quad (8)$$

In order to calculate  $C_{DC}$ , the LO power is kept constant and the resistance change due to the small change in the bias current is calculated at each operating point. Special care has to be taken when calculating  $C_{RF}$  because keeping the current constant and applying a small change in LO power will change the absorbed DC power as well, which in turn changes the resistance. This contribution has to be deducted from the total resistance change in order to calculate the resistance change due to the change in the absorbed RF power only.

Assuming equal values for  $C_{DC}$  and  $C_{RF}$ , (7) is reduced to the corresponding relation known from the point bolometer models [1,4].

## IV. Noise

The calculation of the Johnson noise contribution from the HEB noise model in [4] neglected the fact that the dissipated power in the noise source is actually dissipated within the HEB bridge, resulting in additional heating. Ignoring this term leads to a discrepancy between the results when the voltage noise source is replaced by an equivalent current noise source. A complete derivation for Johnson noise is given in the appendix, taking this term in to account.

The contribution of the Johnson noise to the total output noise is:

$$T_{Jn}^{out} = \frac{4R_L R_0 T_0}{(R_0 + R_L)^2 \left(1 - C_{DC} I_0^2 \frac{R_L - R_0}{R_L + R_0}\right)^2} \quad (9)$$

The expression for the DSB Johnson receiver noise temperature is simply obtained by dividing the output noise (9) by two times the gain (7):

$$T_{Jn,DSB}^{in} = \frac{R_0 T_0}{I_0^2 \cdot C_{RF}^2 \cdot P_{LO}} \quad (10)$$

In the one-dimensional hot spot model the electron temperature and the resistivity vary spatially, which requires us to modify (10) as:

$$T_{Jn,DSB}^{in} = \frac{\int_{-L}^L \rho(T_e(x)) T_e(x) dx}{I_0^2 \cdot C_{RF}^2 \cdot P_{LO} \cdot A} \quad (11)$$

From what has been derived originally in the point bolometer model [1,2] the output thermal fluctuation (TF) noise is written as:

$$T_{TFn}^{out} = \frac{I_0^2 \cdot R_L}{(R_{bo} + R_L)^2 \cdot \left(1 - C_{DC} I_0^2 \cdot \frac{R_L - R_0}{RL + R_0}\right)^2} \left(\frac{\partial R}{\partial T_e}\right)^2 \cdot \frac{4T_e^2}{c_e V} \tau_e \quad (12)$$

where  $V$  is the bolometer volume,  $c_e$  is the electron thermal capacity, and  $\tau_e$  is the electron relaxation time.

The double side band receiver noise temperature due to the TF noise is obtained by dividing the TF output noise (12) by two times the gain (7):

$$T_{TFn,DSB}^{in} = \frac{1}{C_{RF}^2 \cdot P_{LO}} \left(\frac{\partial R}{\partial T_e}\right)^2 \cdot \frac{T_e^2}{c_e V} \tau_e \quad (13)$$

This expression also has to be modified for the one-dimensional distributed model. The model presented here assumes that the electron temperature fluctuations in the bolometer segments are uncorrelated. The derivation is given in the appendix B in detail and here we only recall the result:

$$T_{TFn,DSB}^{in} = \frac{1}{C_{RF}^2 \cdot P_{LO}} \int_{-L}^L \frac{\rho_n^2 e^{-2\left(\frac{T_e - T_c}{\delta T}\right)}}{\delta T^2 \cdot \left(1 + e^{-\left(\frac{T_e - T_c}{\delta T}\right)}\right)^4} \cdot \frac{T_e^2 \cdot \tau_e}{c_e \cdot A^3} \cdot dx \quad (14)$$

Note that  $c_e$  and  $\tau_e$  depend on the electron temperature, which in turn depends on  $x$ . The discussion in appendix B indicates that the output fluctuation noise is essentially independent of the correlation length assumed.

The measured noise at the output of the mixer has three contributions and can be written as:

$$T_{noise}^{out} = T_{TFn}^{out} + T_{Jn}^{out} + 2 \times 295 \times G \quad (15)$$

The third term is the ambient temperature (22 °C = 295 K) at the input of the mixer, which contributes to the output noise during this measurement.

The total receiver noise temperature is calculated using the usual expression:

$$T_{RX,DSB} = T_{TFn,DSB}^{in} + T_{Jn,DSB}^{in} + \frac{T_{IF}}{2G} \quad (16)$$

where  $T_{IF}$  is the noise contribution from the low noise IF amplifier ( $\cong 7$  K) and  $G$  is the conversion gain (7).

## V. IF Impedance and Bandwidth

We are currently studying a possible method to calculate the IF impedance and Bandwidth of the bolometer. The method is based on solving the time varying small signal one-dimensional heat balance equation at the operating point. Adding the time varying terms to (4) yields:

$$\begin{aligned} -c_e \cdot (T_e) \cdot \frac{\partial}{\partial t} T_e + \frac{\partial}{\partial x} \left[ \lambda_e(T_e) \frac{\partial}{\partial x} T_e \right] - \sigma_{eff} (T_e^{3.6} - T_{substrate}^{3.6}) \\ + \frac{P_{LO}}{2L} + \frac{I_0^2 \rho(T_e)}{A} + \left( \frac{2\sqrt{P_S P_{LO}}}{2L} + p \right) \cdot e^{j\omega t} = 0 \end{aligned} \quad (17)$$

where  $p$  denotes the small signal power due to the electrothermal feedback per unit length. The electron temperature can be written as:

$$T_e(x) = T_0(x) + \tilde{T}(x) \cdot e^{j\omega t} \quad (18)$$

Inserting (18) in (17) and separating the time varying part, an equation is obtained which can be solved for  $\tilde{T}(x)$ . Preliminary studies show a capacitive behavior of the bolometer, as is well-known from the point bolometer model [1].

A simple way to estimate the IF bandwidth is to assign a time constant for the phonon-cooling process and another time constant for the diffusion-cooling process. The diffusion-cooled power can be calculated by evaluating the gradient of electron temperature at the pads. The power cooled by phonons is then the difference between the total absorbed power and the diffusion-cooled power. The effective mixer time constant can be obtained by weighting the time constants with their contributions to the total cooling power.

## VI. Results

The results of our calculations and measurements presented here apply to a  $0.4 \mu\text{m}$  long,  $4 \mu\text{m}$  wide and  $5 \text{ nm}$  thick NbN HEB device on MgO (Device M2-1). The parameter values used in (4) and (5) are summarized in table 1.

Parameter	$\lambda_e(T_e)$	$\sigma_{eff}$	$\delta T$	$T_c$	$T_{substrate}$	$R_N$
Value	$6 \times 10^{-18} \times T_e^3$	$2 \times 10^{-4}$	0.3	8.5	4.2	75
Dimension	Wm/K	W/(m.K <sup>3.6</sup> )	K	K	K	$\Omega$

**Table 1.** The parameter values used in (4) and (5).

Equation (4) is solved numerically. Figure 4 shows the temperature profile obtained for  $40 \mu\text{A}$  current and different absorbed LO powers.

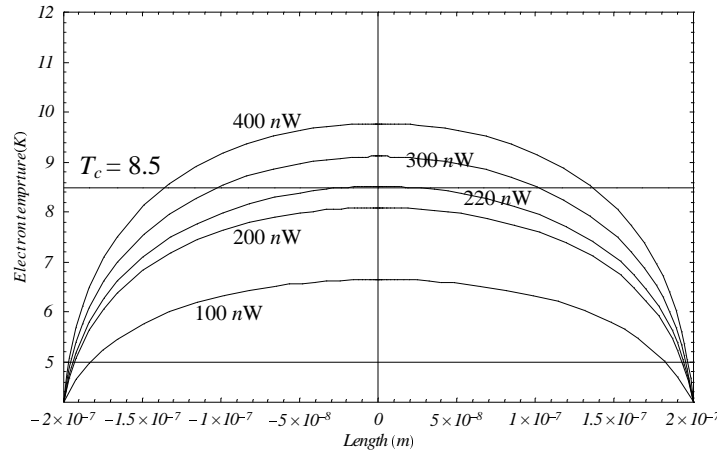


**Figure 4.** The electron temperature profile across the bolometer at  $40 \mu\text{A}$  bias current and mentioned absorbed LO power.

Figure 5 shows the calculated and measured IV curves for device M2-1. Except at bias voltages below .4 mV, the calculated and measured IV curves are in excellent agreement. In general the calculated IV curves tend to bend more at lower voltages than the measured ones. On the other hand below .4 mV the noise is very high and the conversion gain is very low so this region is hardly of any interest.

The optimum operating point was observed around 40  $\mu\text{A}$  and 0.8 mV. Therefore we focus on the middle curve which corresponds to 250 nW absorbed LO power and calculate the conversion gain and the noise.

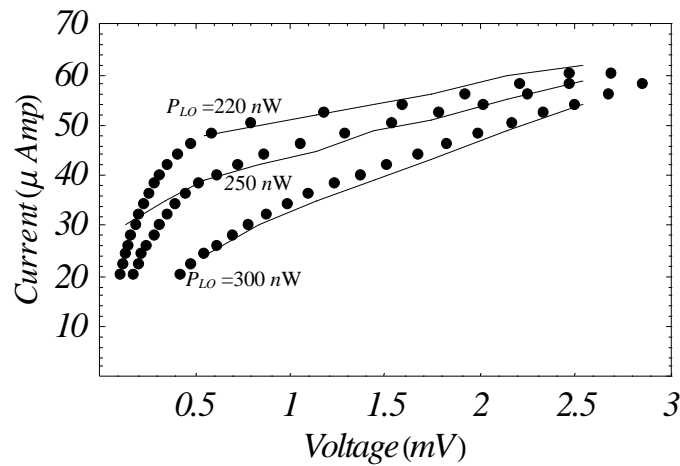


Figure 5. The measured (solid lines) and calculated (dots) IV cures for device M2-1.

The calculated  $C_{DC}$  and  $C_{RF}$  (8) for the 250 nW absorbed LO power curve is shown in figure 6.

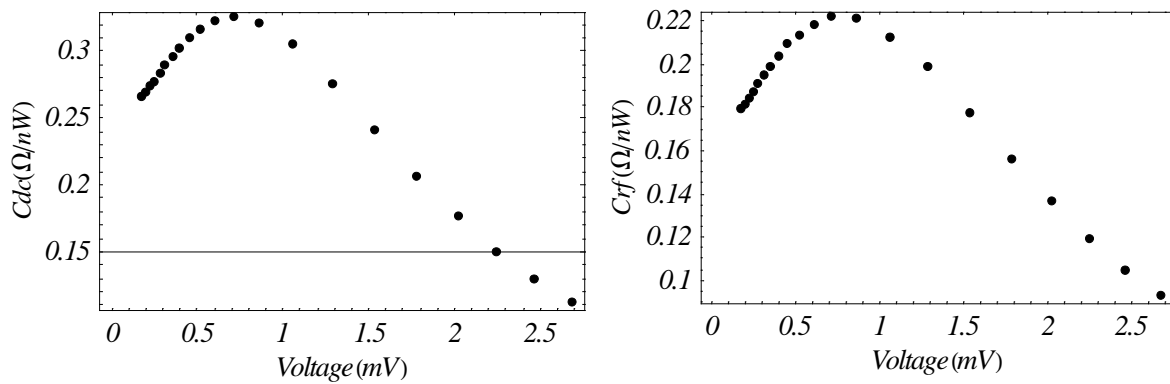


Figure 6. Calculated  $C_{DC}$  (left) and  $C_{RF}$  (right) along the 250nW absorbed LO power curve for different bias voltages.

Inserting these values in (7), the conversion gain is calculated. Figure 7(a) shows the calculated and measured conversion gain. Although the shape of the curves is similar, the calculated values are about 9 dB higher than what we actually measured. The calculated output noise (15) is a factor of 3 higher than what is measured. Figure 8(a) shows the calculated and measured output noise. On the other hand because of the high gain, the model predicts very low receiver noise temperature (16), which is shown in figure 9(a).

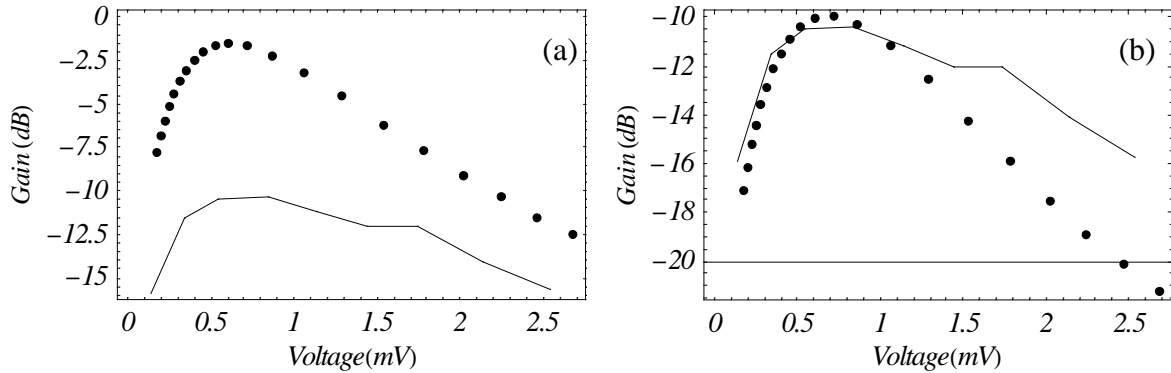


Figure 7. The measured (solid line) and calculated (dots) conversion gain for 250 nW absorbed LO power; (a) for high  $C_{RF}$  values as shown in figure 4; (b) for  $C_{RF}$  values reduced by a factor of three.

This means that the model cannot predict the measured curves. However a close study revealed that this is only due to the high  $C_{RF}$  values. If we reduce the  $C_{RF}$  values by a factor of three, all the measured and calculated curves fit together. The calculated and measured conversion gain, output noise and receiver noise temperature after this reduction is depicted in figures 7, 8, 9 (b) respectively.

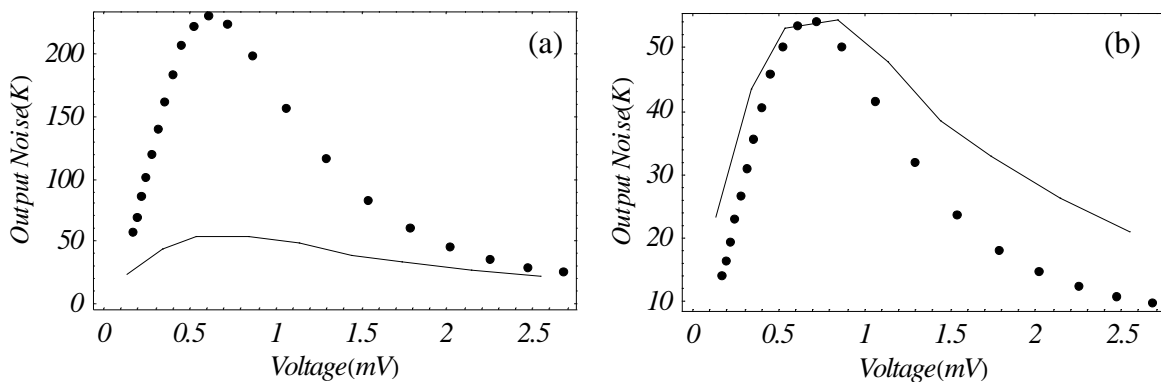
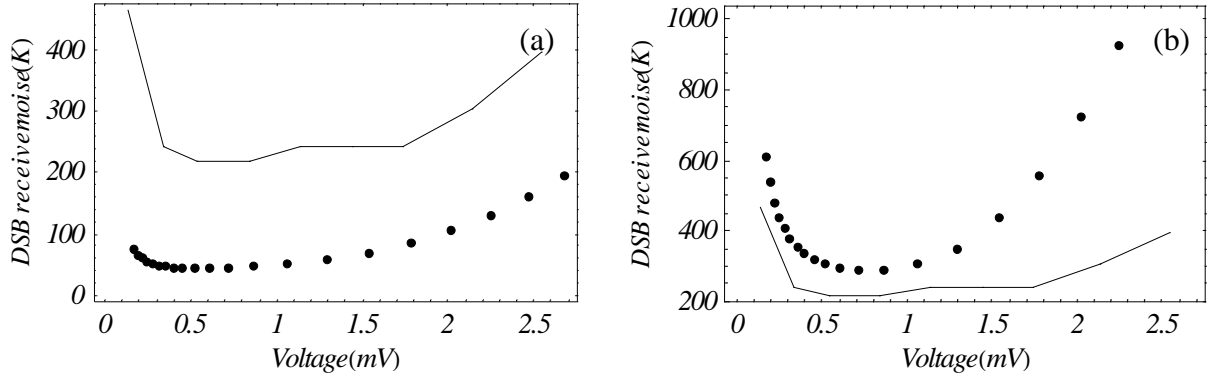


Figure 8 The measured (solid line) and calculated (dots) output noise for 250 nW absorbed LO power; (a) for high  $C_{RF}$  values as shown in figure 4; (b) for  $C_{RF}$  values reduced by a factor of three.



**Figure 9.** The measured (solid line) and calculated (dots) receiver noise temperature for 250 nW absorbed LO power; (a) for high  $C_{RF}$  values as shown in figure 4; (b) for  $C_{RF}$  values reduced by a factor of three.

After reducing  $C_{RF}$ , the value of  $C_{RF} I_0^2$  at a typical optimum operating point is 0.16. Since  $I_0/I_{00}$  ( $I_{00}$  is the current on the unpumped IV curve c.f. [1,4]) is about 0.4 at the optimum point for receiver noise temperature [4],  $C_{RF} I_0^2$  is about 0.7. This quantity was used as an adjustable parameter in [4], and for optimum performance was found to be about 1. This explains why the empirical "standard model" in [4] yields results in agreement with experiment close to the optimum point.

## VII. Conclusion

The one-dimensional distributed model is fully capable of predicting the IV curves, conversion gain, output noise and receiver noise temperature within acceptable accuracy. However this requires applying a tuning factor to the calculated  $C_{RF}$ . This tuning factor was found to be about 0.34 to fit the measured data for device M2-1. It simply means that the resistance oscillation due to the mixing term in the RF is over estimated by calculating a small resistance change due to small change in LO power. The physics behind this factor is currently under investigation. Major progress has been made in comparison with the point-bolometer model in for example [4], in that the variation of all measurable quantities (conversion gain, receiver noise and output noise) with bias voltage and LO power is predicted very well.

## Acknowledgements

This work was partly supported by European Space Agency, ESA (#11738/95/nl/mv).

## References

- [1] H. Ekström, B. Karasik, E. Kollberg, K. S. Yngvesson, IEEE Trans. MTT, Vol. 43 (4), 1995
- [2] B. Karasik, A. I. Elantev, Proc. Sixth International Symposium on Space Terahertz Technology, 1995. Pages: 229-246.
- [3] H. Merkel, P. Yagoubov, P. Khosropanah, E. Kollberg. Proc. Sixth IEEE International Conference on Terahertz Electronics, 1998, Pages: 145-148
- [4] K. S. Yngvesson, E. Kollberg, Proc. Tenth IEEE International Symposium on Space Terahertz Technology, 1999. Pages: 566-582.
- [5] H. Merkel, P. Khosropanah, P. Yagoubov, E. Kollberg, IEEE Transactions on Applied Superconductivity Vol. 9 Issue: 2 Part: 3, June 1999, Page(s): 4201 -4204
- [6] D. W. Floet, E. Miedema, J. R . Gao, T.M. Klapwijk, Proc. Sixth IEEE International Conference on Terahertz Electronics, 1998, Pages: 9-12.
- [7] H. Merkel, P. Khosropanah, P. Yagoubov, E. Kollberg, Proc. Tenth International Symposium on Space Terahertz Technology, 1999. Pages: 592-606.
- [8] S. Cherednichenko, P. Yagoubov, K. Il'in, G. Gol'tsman, E. Gershenson, Proc. 8<sup>th</sup> International Symposium on Space Terahertz Technology, 1997, pages: 245-252.
- [9] D. W. Floet, J. R . Gao, T.M. Klapwijk, P. A. J. de Korte, Proc. Tenth International Symposium on Space Terahertz Technology, 1999. Pages: 583-591.
- [10] Charles P. Poole, Horacio A. Farach, Richards J. Creswick. Superconductivity. Academic press. 1995
- [11] John C. Mather. Applied Optics. Vol. 21, No. 6. March 15, 1982, Pages 1125-1129.

## Appendix A: Johnson noise

The thermal noise from a resistance  $R$  at temperature  $T$  can be written as:

$$\langle v_n^2 \rangle = 4k_B TR, \quad (1.A)$$

where  $k_B$  is the Boltzmann constant. In order to calculate the noise we can insert this noise source in the bolometer circuit. Figure 1.A shows this circuit.  $\Delta R$  and  $\Delta I$  are small variations of resistance and current respectively.

Assuming a point bolometer at temperature  $T_0$  and resistance  $R_0$ , the noise equivalent source is:

$$\langle v_n^2 \rangle = 4k_B T_0 R_0 \quad (2.A)$$

The total dissipated power in the bolometer is:

$$P_0 + \Delta P = (R_0 + \Delta R)(I_0 - \Delta I)^2 + v_n(I_0 - \Delta I) \quad (3.A)$$

Note that the dissipated power in the noise source is actually dissipated in the bolometer as well and it is of great importance to take it into account. Ignoring this term leads to a discrepancy between the results when the voltage noise source is replaced by an equivalent current noise source.

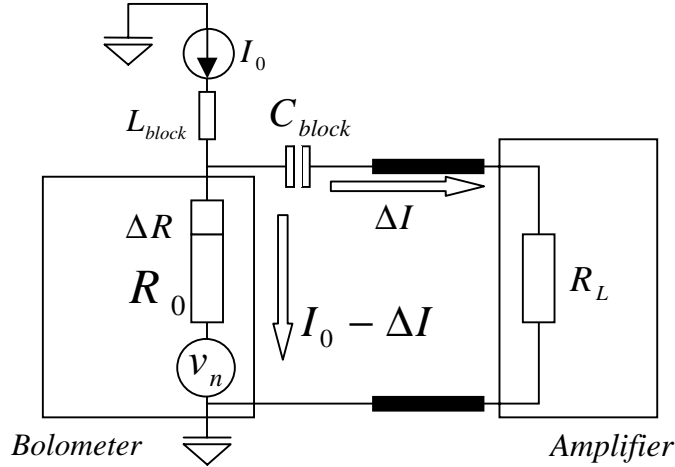


Figure 1.A. Bolometer circuit with equivalent Johnson noise source

Expanding the right side of (3.A) and ignoring the second order small signal terms, (3.A) is simplified to:

$$P_0 + \Delta P = R_0 I_0^2 - 2I_0 R_0 \Delta I + \Delta R I_0^2 + v_n I_0 \quad (4.A)$$

Separating the small signal and large signal parts yields:

$$\Delta P = -2I_0 R_0 \Delta I + \Delta R I_0^2 + v_n I_0 \quad (5.A)$$

since  $\Delta P = C_{DC} \Delta R$ , we can replace  $\Delta P$  and solve (5.A) for  $\Delta R$  which results in:

$$\Delta R = \frac{-2C_{DC} I_0 R_0 \Delta I + C_{DC} v_n I_0}{1 - C_{DC} I_0^2} \quad (6.A)$$

Now it is possible to calculate the voltage across the bolometer:

$$V_0 + \Delta V = (I_0 - \Delta I)(R_0 + \Delta R) + v_n \quad (7.A)$$

Separating the large and small signal here too gives:

$$\Delta V = -\Delta I R_0 + I_0 \Delta R + v_n = \Delta I R_L \quad (8.A)$$

where the small signal voltage  $\Delta V$  is the IF voltage across the load. Solving for  $\Delta I$  and replacing  $\Delta R$  from (6.A) yields:

$$\Delta I = \frac{v_n}{(R_0 + R_L) \left( 1 - C_{DC} I_0^2 \frac{R_L - R_0}{R_L + R_0} \right)} \quad (9.A)$$

The output noise power is simply:

$$P_{Jn}^{out} = R_L \langle \Delta I^2 \rangle = \frac{R_L \langle v_n^2 \rangle}{(R_0 + R_L)^2 \left( 1 - C_{DC} I_0^2 \frac{R_L - R_0}{R_L + R_0} \right)^2} \quad (10.A)$$

Inserting (2.A) in (10.A) results in:

$$P_{Jn}^{out} = \frac{R_L \cdot 4k_B B T_0 R_0}{(R_0 + R_L)^2 \left( 1 - C_{DC} I_0^2 \frac{R_L - R_0}{R_L + R_0} \right)^2} = k_B B T_{Jn}^{out} \quad (11.A)$$

where  $T_{Jn}^{out}$  is the output Johnson noise.

$$T_{Jn}^{out} = \frac{4R_L R_0 T_0}{(R_0 + R_L)^2 \left( 1 - C_{DC} I_0^2 \frac{R_L - R_0}{R_L + R_0} \right)^2} \quad (12.A)$$

The equivalent noise temperature at the input of the mixer is obtained by dividing the output noise by the conversion gain given in (7). The double side band (DSB) equivalent noise temperature is a factor of two smaller than the SSB one. So the expression for the DSB Johnson noise temperature at the input becomes:

$$T_{Jn,DSB}^{in} = \frac{R_0 T_0}{I_0^2 \cdot C_{RF}^2 \cdot P_{LO}} \quad (13.A)$$

This result is in agreement with the expression derived by taking another approach [2], and also with the general results for bolometers derived originally by Mather [11].

## Appendix B: Thermal fluctuation noise

From the point bolometer model [1,2] the output thermal fluctuation (TF) noise is written as:

$$T_{TFn}^{out} = \frac{I_0^2 \cdot R_L}{(R_0 + R_L)^2 \cdot \left( 1 - C_{DC} I_0^2 \cdot \frac{R_L - R_0}{R_L + R_0} \right)^2} \left( \frac{\partial R}{\partial T_e} \right)^2 \cdot \frac{4T_e^2}{c_e V} \tau_e \quad (1.B)$$

where  $V$  is the bolometer volume,  $c_e$  is the electron thermal capacity, and  $\tau_e$  the electron relaxation time.

The double side band receiver noise temperature due to the TF noise is obtained by dividing the TF output noise (1.B) by two times the gain (7):

$$T_{TFn,DSB}^{in} = \frac{1}{C_{RF}^2 \cdot P_{LO}} \left( \frac{\partial R}{\partial T_e} \right)^2 \cdot \frac{T_e^2}{c_e V} \tau_e \quad (2.B)$$

The total resistance fluctuation is the sum of all the resistance fluctuations of each small segment of the bolometer due to temperature fluctuations. Thus  $dr$ , the resistance of such a segment with length  $dx$  is written as:

$$dr = \frac{\rho(T_e(x))dx}{A} \quad (3.B)$$

Note that the resistivity profile  $\rho(T_e(x))$  is obtained from the electron temperature profile  $T_e(x)$  from (5).

the total resistance of the bolometer is obtained by:

$$R = \int_{-L}^L dr = \int_{-L}^L \frac{\rho(T_e(x))}{A} dx \quad (5.B)$$

The resistance fluctuation of a small segment of the bolometer can be written as:

$$\frac{\partial dr(x)}{\partial T_e(x)} = \frac{\partial \rho(T_e(x))}{\partial T_e(x)} \cdot \frac{dx}{A} \quad (6.B)$$

From (6.B) and (2.B) the thermal fluctuation noise temperature from this small part is derived as:

$$\begin{aligned} dT_{TFn,DSB}^{in} &= \frac{1}{C_{RF}^2 \cdot P_{LO}} \left( \frac{\partial dr}{\partial T_e} \right)^2 \cdot \frac{T_e^2(x)}{c_e A \cdot dx} \tau_e \\ &= \frac{1}{C_{RF}^2 \cdot P_{LO}} \left( \frac{\partial \rho(T_e(x))}{\partial T_e(x)} \cdot \frac{dx}{A} \right)^2 \cdot \frac{T_e^2(x)}{c_e A \cdot dx} \tau_e \\ &= \frac{1}{C_{RF}^2 \cdot P_{LO}} \left( \frac{\partial \rho(T_e(x))}{\partial T_e(x)} \right)^2 \cdot \frac{T_e^2(x) \tau_e}{c_e A^3} dx \end{aligned} \quad (7.B)$$

Now if we assume that all these local temperature fluctuations are uncorrelated, the total noise temperature is simply the integral of all the small contributions.

$$\begin{aligned} T_{TFn,DSB}^{in} &= \frac{1}{C_{RF}^2 \cdot P_{LO}} \int_{-L}^L \left( \frac{\partial \rho(T_e(x))}{\partial T_e(x)} \right)^2 \cdot \frac{T_e^2(x) \tau_e}{c_e \cdot A^3} dx \\ &= \frac{1}{C_{RF}^2 \cdot P_{LO}} \int_{-L}^L \frac{\rho_n^2 e^{-2\left(\frac{T_e-T_c}{\delta T}\right)}}{\delta T^2 \cdot \left(1 + e^{-\left(\frac{T_e-T_c}{\delta T}\right)}\right)^4} \cdot \frac{T_e^2 \cdot \tau_e}{c_e \cdot A^3} \cdot dx \end{aligned} \quad (8.B)$$

we have also performed this calculation by assuming different values for the correlation length of the TF noise. The result is essentially unchanged, provided that  $(\partial \rho / \partial T_e)$  varies smoothly. The above assumption of an infinitesimal correlation length thus is justified, unless the correlation length becomes comparable to the length of the bolometer.

# **PROPERTIES OF Nb THIN FILMS AND THEIR APPLICATION FOR DIFFUSION-COOLED HOT-ELECTRON BOLOMETER**

**M. Frommberger, F. Mattiocco, P. Sabon, M. Schicke, K.F. Schuster**

*Institut de Radio Astronomie Millimétrique  
300 rue de la Piscine, Domaine Universitaire Grenoble  
38406 St. Martin d'Hères, France*

**O. Laborde**

*Centre de Recherches sur les Très Basses Températures  
25 Avenue des Martyrs  
38042 Grenoble, France*

## **ABSTRACT**

The performance of hot electron bolometer mixer devices made out of superconducting thin films critically depends on film quality. We discuss various deposition conditions for Nb films and present their properties for a wide thickness range. The obtained film parameters allow to predict the characteristics of our actual devices. We also shortly present a new fabrication process for Nb diffusion cooled hot electron bolometer mixers.

## **I. INTRODUCTION**

Nb diffusion-cooled hot electron bolometer (HEB) mixers offer very competitive performance up to several THz. Although many promising mixer results have been presented little has been published about the necessary thin film qualities and the related processing problems [1, 25].

The difficulty in fabrication of Nb HEBs originates not only from the requirement of very high resolution lithography but also from the need of high quality Nb thin films and their protection throughout the processing steps.

In a first part we report on investigations on Nb thin films in a thickness range from 2 to 80 nm. Different characterisation methods like dc-measurements, x-ray diffraction (XRD) and atomic force microscopy (AFM) were applied. In a second part we

present a new processing sequence for Nb HEBs and high frequency measurements carried out with such devices.

We derived the time constants from thin film characterisations and compared them with values obtained by high frequency measurements.

## II. THIN FILM PREPARATION

For device fabrication it is essential to obtain a high reproducibility in film thickness. As a low deposition rate is one way to improve thickness calibration we started out with a low sputter power ( $\sim 0.5$  nm/s for 200 W). The Nb thin film samples have been produced on 2" fused quartz substrates which underwent a rigorous ultrasonic cleaning in acetone and propanol. Such substrates should also serve as a good reference for silicon substrates with native oxide.

The background pressure in the sputterer chamber is about  $2 \times 10^{-8}$  mbar and the films were deposited by dc-magnetron sputtering at 2 Pa after Ar-plasma RF cleaning of the substrate. No active substrate heating was applied during film deposition.

Figure II.1a shows an AFM image of a 120 nm thick Nb film sputtered with 200 W at 2 Pa. One can observe a polycrystalline film growth with a grain size of about 10 to 30 nm. In comparison, figure II.1b shows a film deposited at 730 W and 2 Pa. The observed grainsize is about 3 times larger than for 200 W.

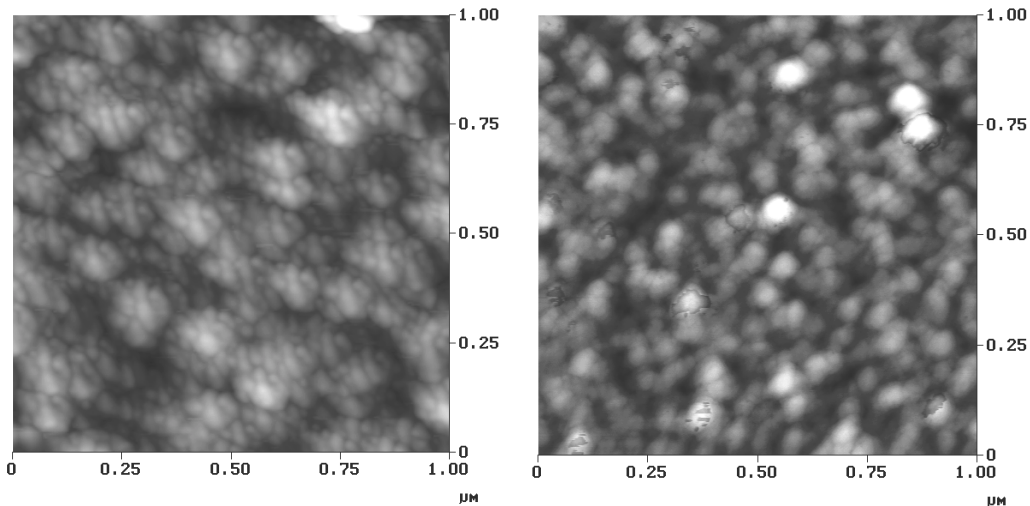


*Fig. II.1a. AFM image of a 120 nm Nb film sputtered at 200 W, 2 Pa.*

*Fig. II.1b. AFM image of a 120 nm Nb film sputtered at 730 W, 2 Pa.*

X-ray diffraction (XRD) measurements which were carried out in the context of stress determination gave comparable results for the crystallinity of our Nb layers [8]. Figure II.2 shows XRD curves for 120 nm Nb films sputtered at different source

powers. Depending on the sputter power we can see a clear transition from polycrystalline to quasi amorphous film growth. Best crystallinity is obtained for 800 W. The grainsizes determined by XRD were:

Power	200 W	400 W	600 W	800 W
$2\theta$	37.682	38.789	38.549	38.468
$W_{fwhm}$	1.051	0.414	0.320	0.288
grainsize	7.6 nm	27 nm	35 nm	39 nm

With decreasing power, intensity of the (110) peak is descending and the peak shifts to higher values of  $2\theta$ , due to increasing tensile stress. Below 400 W film stress becomes highly compressive.

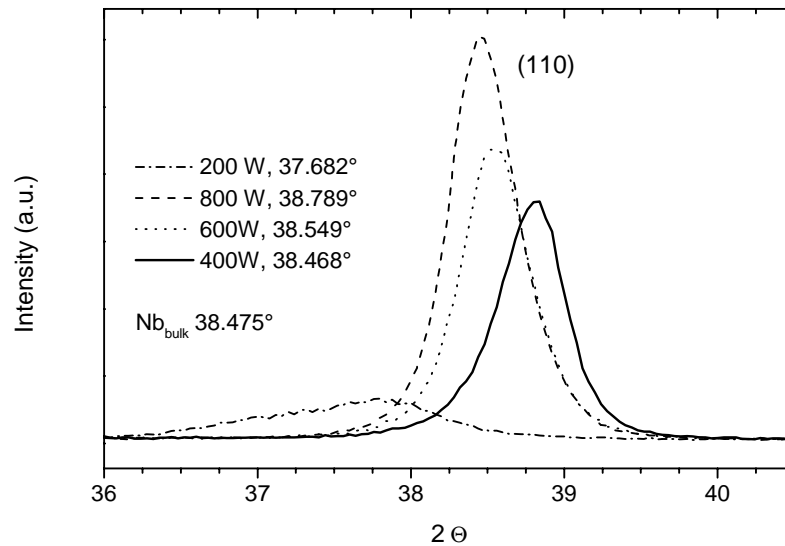


Fig. II.2. X-ray diffraction results of 120 nm Nb films sputtered at 200, 400, 600 and 800 W and 2 Pa.  $2\theta$  for the (110) peak center and for bulk Nb [19] is shown on the plot (Cu  $K\alpha$ ).

### III. ELECTRICAL THIN FILM PROPERTIES

We determined the electrical properties of our films by four point measurements on 1 mm  $\times$  10 mm samples which were carried out in a dip-stick set up. The film thickness has been varied from 2 to 80 nm and verified by anodisation. The residual

resistance ratio RRR and the sheet resistance above the critical temperature  $T_c$  and their dependence on film thickness were investigated.

As can be seen in figure III.1 the sheet resistance at 10 K does not simply follow a curve proportional to the invers of the geometrical cross section for films below 20 nm.

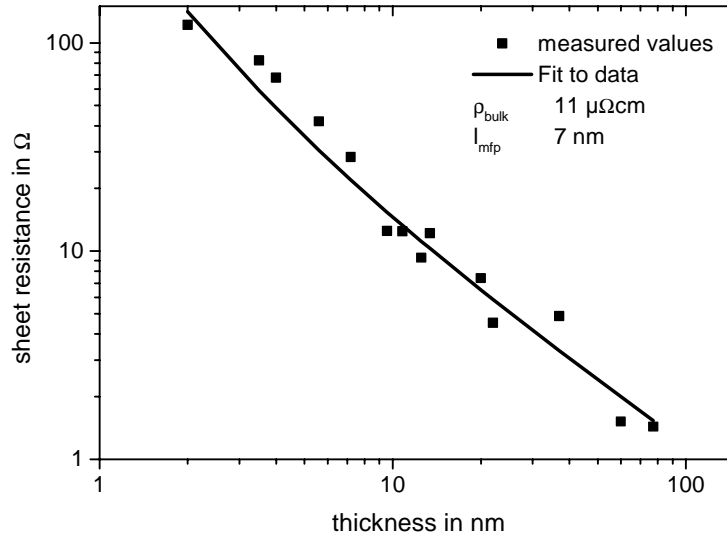


Fig. III.1. Sheet resistance at 10 K versus film thickness. The squares are our measured data, the solid line corresponds to the size effect model. The fit to our data gives a  $\rho_{bulk}$  of  $11 \mu\Omega cm$  and a  $l_{mfp}$  of 7 nm for films sputtered with 200 W.

Different explanations have been given in the past for the observed behavior. A thickness dependent grain size distribution could play a certain role due to interface effects. Jiang showed that weak localisation effects become important for ultra thin epitaxial films [24].

However for our films a simple size effect model taking into account the surface scattering of electrons can explain the measurement to a sufficient accuracy (see fig. III.1). The resistivity in this model is described by

$$\rho \approx \rho_{bulk} \cdot \left( 1 + \frac{3 l_{mfp}}{8 t} \right) \Rightarrow R_s \approx \rho_{bulk} \cdot \left( \frac{1}{t} + \frac{3 l_{mfp}}{8 t^2} \right)$$

which can be derived from kinetic theory arguments ( $R_s$  is the sheet resistance,  $l_{mfp}$  the electron mean free path,  $t$  the film thickness and  $\rho_{bulk}$  the bulk resistivity at 10 K) [2, 23]. This formula should be a reasonable first approximation for a thin film containing a free electron gas in which electrons striking the sample surface are scattered completely diffusely. In our case the surfaces are given by the thin film-

substrate interface and the NbOxide surface layer. Identification of the electron mean free path  $l_{mfp}$  found by the size effect model with a typical grain size gives good agreement with XRD and AFM measurements.

Figure III.2 shows the dependence of the critical temperature on the film thickness. To explain our data, we employ a proximity effect model. For single-crystalline Nb films Yoshii et al. [11] achieved good agreement with such a model considering a system of a superconducting layer (thickness  $d$ ) and a normal-metal layer (thickness  $a$ ) to describe the depression of  $T_c$  with decreasing film thickness.

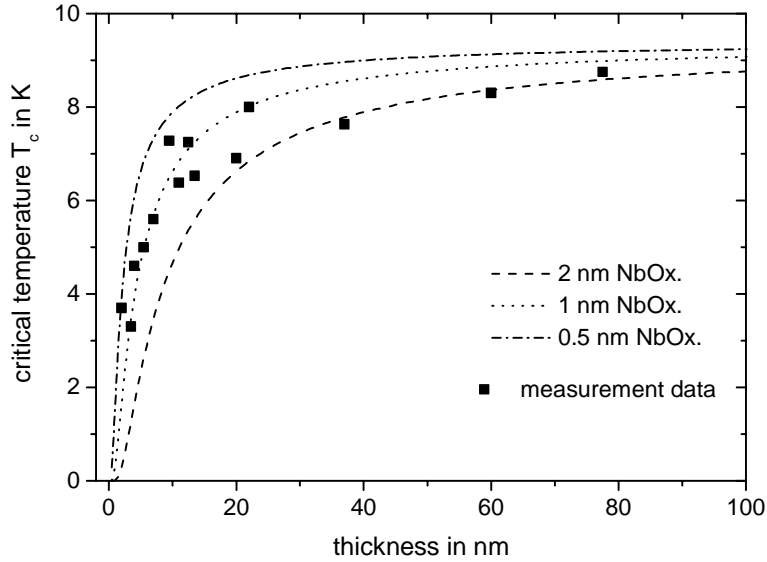


Fig. III.2. Critical temperature  $T_c$  versus film thickness. The curves are calculations assuming a NbOxide layer of 0.5 nm, 1 nm, 2 nm respectively, the squares are the measurement values.

The graphs in fig. II.2 show the calculation of  $T_c$  versus film thickness for different NbOxide layer thicknesses, following their formula

$$T_c = T_{c0} \left( \frac{1.13 \cdot \Theta_D}{T_{c0}} \right)^{-[N_N(0)/N_S(0)](a/d)}$$

which has originally been proposed by McMillan [12, 14]. Here  $T_{c0}$  is the transition temperature of the bulk (9.3 K),  $\Theta_D$  the Debye temperature of the superconducting layer (Nb, 275 K), and  $N_N(0)$  and  $N_S(0)$  are the density of states for normal and superconducting layers respectively [13].

As the McMillan formula is only adequate for the dirty limit case only films below 20 nm will be correctly described. From figure III.2 we can conclude an oxide thickness of 1 nm, a value which is in good agreement with results from ellipsometry for films exposed for some minutes to ambient air [8, 20].

#### IV. DEVICE FABRICATION

Existing diffusion-cooled hot-electron bolometer devices consist out of a sufficiently short and thin superconducting microbridge connected to Au pads which serve as heat sinks [3]. The device impedance must be matched to a given source impedance, typically in the range of 25 to 70  $\Omega$ .

In comparison to the HEB fabrication process used by the JPL group [17], we present a simplified process, avoiding the chlorine containing gas mixture (freon) and the unselective reactive ion etching (RIE) step for the final bridge definition. The actual IRAM diffusion-cooled Nb HEB devices are fabricated in the following steps:

After an overall deposition of a 10-20 nm Nb film and a 10 nm Au oxidation-protection layer on a 2" fused quartz substrate we define the antenna and filter structure by photolithography.

To define the lateral dimensions of the microbridge we use Ebeam lithography. In a first step we fix the microbridge length by defining the Au cooling pads by a double PMMA layer (950K/50K) lift-off process. Here the 10 nm Au layer allows a high pre-bake temperature for the PMMA layers without destroying the Nb film. Such a high bake temperature helps to avoid intermixing of the two layers and stabilizes the resist profile for a better lift-off. Afterwards we remove the Au protection with an argon plasma. In a second Ebeam step we generate a lift-off pattern by which a thin Al strip is defined. This Al strip is used as a selective etch mask. We remove the surrounding Nb by reactive ion etching ( $\text{CF}_4$ ,  $\text{O}_2$ ). The Al etch mask is removed by a strong base. Finally the substrate is diced and the individual devices are characterised by a dc-measurement.

#### V. RF- AND IF- MEASUREMENTS

To measure the RF matching between antenna and detector, we tested our HEB mixer as a direct detector on a Fourier Transform Spectrometer (FTS) using a chopped blackbody source (fig. V.1). As the antenna was designed for high impedance NbN HEBs, the Nb HEBs ( $< 50 \Omega$ ) are strongly mismatched.

Despite this mismatch one can clearly see the water vapour absorption lines between 0.5 and 1 THz.

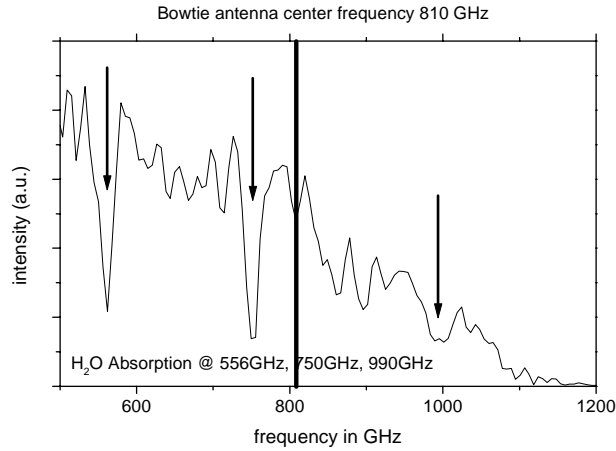


Fig. V.1 Fourier transform spectrometer measurement of a bowtie antenna with central diffusion-cooled HEB. Indicated are the water vapour absorption lines at 556, 750 and 990 GHz and the designed center frequency of the antenna at 810 GHz.

With a comparable device we performed a Y-factor measurements in the range of 800 GHz. Figure V.2. shows the pumped I(V)-curve of the device together with the conversion curves for the hot and cold load. Best mixer noise temperature was 4030 K at 2.2 K bath temperature, 798 GHz local oscillator frequency and an IF of 1.37 GHz. The impedance mismatch mentioned above and the beam splitter loss add about a factor 3 to the noise temperature.

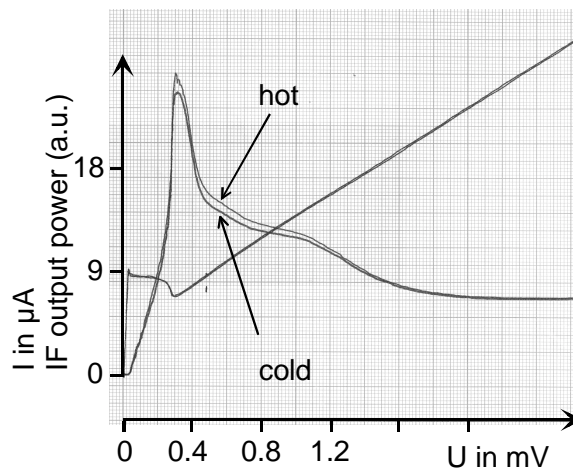


Fig.V.2 Pumped I(V)- and conversion curves for the hot and cold load at 2.2 K. The Y-factor measurement at a local oscillator frequency of 798 GHz and an intermediate frequency of 1.37 GHz gave a non corrected noise temperature of 4030 K.

For application in THz radioastronomy the IF bandwidth of the HEB mixer devices should be as high as possible.

To access the intrinsic time scales of the Nb films which determine the IF bandwidth we executed an impedance measurement similar to the procedure described by Karasik et al. [6,7]. In order to allow a rapid measurement we installed the setup in a dipstick which could be immersed in liquid helium. The measurement was done with a HP8510 network analyzer. The dc bias was directly fed over the internal bias input of the HP8510. The measurements were performed with a sweep between 500 MHz and 10 GHz and a power level of -65 dBm at the device. With a calibration scheme as described by [6] we obtained the complex impedance as plotted in Fig. V.3. The frequency dependence of the device impedance is given by [6]

$$Z(\omega) = R \cdot \frac{1+C}{1-C} \cdot \frac{1+i\omega \frac{\tau_0}{1+C}}{1+i\omega \frac{\tau_0}{1-C}}$$

where  $C$  is the self heating parameter and  $\tau_0$  the electron temperature relaxation time and  $R$  the device resistance at the operating point.

The solid lines in fig. V.1 show  $Z(f)$  calculated with values obtained by a fit to  $ZZ^*$  of the measured data where  $\tau_0$  and  $C$  were the free fitting parameters.

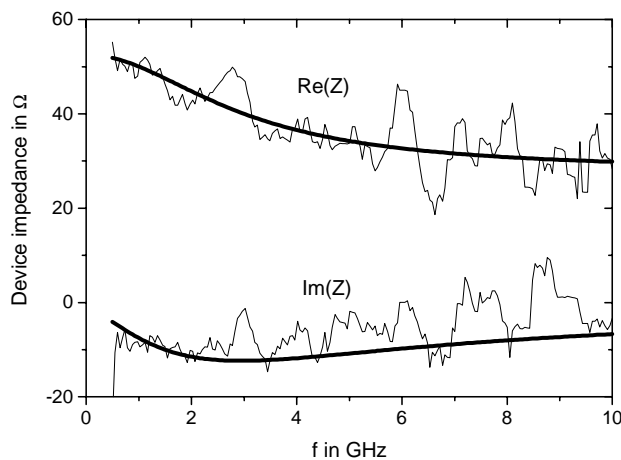


*Fig. V.3. Real and imaginary part of the impedance of a diffusion-cooled Nb hot-electron bolometer over frequency. The solid lines correspond to the best fit parameters obtained by the network analyzer measurement.*

From the impedance measurement one can obtain the electron temperature relaxation time  $\tau_0$  which, for diffusion-cooled Nb HEBs, is in the order of the diffusion time  $\tau_{\text{diff}}$ . The diffusion time can be calculated for a given device geometry by

$$\tau_{diff} = \frac{L^2}{\pi^2 \cdot D},$$

where  $D$  is the diffusion constant [16]. We derived  $D$  from measurements of the slope of the critical magnetic field  $H_{c2}$  [5, 22] near the superconducting transition. For a 14 nm Nb film we obtained a diffusion constant of  $D = 2.2 \text{ cm}^2/\text{s}$ .

The IF bandwidth is directly related with these intrinsic times via

$$\Delta f_{3dB} \approx \frac{1}{2 \cdot \pi \cdot \tau}.$$

As the electrons should thermalize before out-diffusion into the contact pads,  $\tau_0$  should be larger than the electron-electron relaxation time  $\tau_{ee}$  which can be estimated out of the thin film parameters (sheet resistance  $R_s$  and  $T_c$ , see figure III.1 and III.2) by

$$\tau_{ee} \propto (10^8 \cdot R_s \cdot T_c)^{-1} \cdot s,$$

where  $R_s$  is in  $\Omega$  and  $T_c$  is in K [4]. It gives an approximate number for the electron temperature relaxation length  $l_{ee}$  [9]

$$l_{ee} \approx 2 \cdot \sqrt{D \cdot \tau_{ee}}$$

which is in the order of 100 nm. For a short device the hot electrons may diffuse out of the microbridge more quickly than they interact with each other, an effect recently debated for aluminium HEBs [10, 15, 18, 21].

	<b>thin film characterisation</b>	<b>IF bandwidth measurement</b>
<b>intrinsic time constants</b>	electron diffusion time $\tau_{diff} \approx 3 \times 10^{-11} \text{ s}$	electron temperature relaxation time $\tau_0 = 3.35 \times 10^{-11} \text{ s}$
	electron electron relaxation time $\tau_{ee} \approx 1 \times 10^{-11} \text{ s}$	
<b>IF bandwidth</b> $\Delta f_{3dB} = \frac{1}{2\pi \cdot \tau}$	for $\tau_{diff}$ $\Delta f_{3dB} = 5.5 \text{ GHz}$	for $\tau_0$ $\Delta f_{3dB} = 4.3 \text{ GHz}$

*Tab. V.4. Comparison of the intrinsic time scales obtained by calculations on thin film data and the bandwidth measurement of an actual device. In both cases we assume a device length of 250 nm and an effective film thickness of 14 nm.*

In Table V.4. we compare the obtained time constants. For the thin film calculations we assumed a 250 nm long HEB. Starting out with a 20 nm film deposition we assume an effective film thickness of 14 nm due to the NbOxide top layer after processing (4 nm) and the film substrate interface (2 nm) [8]. As expected, the

calculated IF frequency bandwidth is in the same order of magnitude as the experimental value and the electron temperature relaxation time is almost equal to  $\tau_{\text{diff}}$ , confirming the cooling mechanism in the HEB device.

## VI. CONCLUSION

Thin Nb films have been investigated in a wide thickness range. AFM as well as XRD show that using high power sputtering will significantly increase film quality. The electrical properties of the currently used and unoptimised thin films were explained by a size effect and a proximity effect model. The results give us the possibility to predict the final high frequency characteristics of a Nb diffusion-cooled HEB for a given device geometry. We developed a simple Nb HEB process; a mixing experiment at 798 GHz was carried out on a device fabricated with this process. With an maladjusted antenna we obtained an uncorrected receiver noise temperature of 4030 K at an intermediate frequency of 1.37 GHz.. The devices showed a 3dB cut-off frequency of 4 GHz. Future devices will use improved film quality.

## ACKNOWLEDGEMENT

The authors like to thank H. Rothermel (MPE Garching), F. Schäfer (MPI Bonn), J. Halbritter (FZ Karlsruhe) and D. Wilms Floet (RU Groningen) for helpful discussions and J. Schülein (PI3 Erlangen) for the AFM measurements.

## REFERENCES

- [1] B.S. Karasik, A. Skalare, R.A. Wyss, W.R. McGrath, B. Bumble, H.G. LeDuc, J.B. Barner and A.W. Kleinsasser, "*Low noise and Wideband Hot-Electron Superconductive Mixers for THz Frequencies*", 6<sup>th</sup> IEEE Int. Conf. on THz Electronics, Leeds, 1998
- [2] K.L. Chopra, *Thin Film Phenomena*, New York, 1979
- [3] B. Bumble, H.G. LeDuc, "*Fabrication of a Diffusion Cooled Superconducting Hot Electron Bolometer for THz Applications*", IEEE Trans. Appl. Supercond. 7, 3560, 1997
- [4] P. Santhanam, D.E. Prober, "*Inelastic electron scattering mechanisms in clean aluminium films*", Phys. Rev. B 24 (6), 1984
- [5] B.S. Karasik, K.S. Il'in, E.V. Pechen, S.I. Krasnosvobodtsev, "*Diffusion Cooling mechanism in a hot electron NbC microbolometer mixer*", Appl. Phys. Lett. 68 (16), 1996

- [6] B.S. Karasik, M.C. Gaidis, W.R. McGrath, B. Bumble, H.G. LeDuc, "A Low Noise Superconductive Nb Hot-Electron Mixer at 2.5 THz", 8<sup>th</sup> Int. Symp. on Space Terahertz Technology, Harvard University, 1997
- [7] C. Rösch, F. Mattiocco, K.F. Schuster, "Development and Characterisation of NbN Phonon-Cooled Hot-Electron Bolometer Mixers at 810 GHz", 10<sup>th</sup> European Conference on Applied Superconductivity (EUCAS), Sitges, 1999
- [8] P. Sabon, "Optimisation et Caractérisation de films minces de niobium déposés par pulvérisation cathodique", memoire CNAM, 2000
- [9] B.S. Karasik, A.I. Elantev, "Analysis of the Noise Performnace of a Hot-Electron Superconducting Bolometer Mixer", 6<sup>th</sup> Int. Symp. on Space terahertz Technology, 1995
- [10] B.S. Karasik, M.C. Gaidis, W.R. McGrath, B. Bumble, H.G. LeDuc, "Low noise in a diffusion-cooled hot-electron mixer at 2.5 THz", Appl. Phys. Lett. 71 (11), 1997
- [11] K. Yoshii et al., "Superconductivity and electrical properties in single-crystalline ultrathin Nb films grown by molecular-beam epitaxy", Phys. Rev. B, **52** (18), 1995
- [12] L.N. Cooper, "Superconductivity in the neighborhood of metallic comtacts", Phys. Rev. Lett. 6 (12), 689, 1961
- [13] Note that this formula is equivalent to that introduced using the de Gennes's expression of effective  $N(0)V$  [P.G. de Gennes, Rev. Mod. Phys. 36, 225 (1964)] for the interaction constant of normal layer  $V_N = 0$ ; i.e., the normal layer does not show superconductivity at any temperature.
- [14] W.L. McMillan, "Tunneling model of the super-conducting proximity effect", Phys. Rev. **175**, No. 2, 537, 10. Nov. 1968
- [15] A.D. Semenov, G.N. Gol'tsman, "Non-thermal response of a diffusion-cooled hot-electron bolometer", IEEE Trans. Appl. Supercond. 9 (2), 4491, 1999
- [16] B.S. Karasik, W.R. McGrath, R.A. Wyss, "Optimal choice of material for HEB superconducting mixers", IEEE Trans. Appl. Supercond. 9 (2), 4213, 1999
- [17] B. Bumble, H.G. LeDuc, "Fabrication of a diffusion cooled superconducting hot electron bolometer for THz mixing applications", IEEE Trans. Appl. Supercond. 7, 3560, 1997
- [18] A.D. Semenov, G.N. Gol'tsman, "Nonthermal mixing mechanism in a diffusion-cooled hot-electron detector", J. Appl. Phys. 87 (1), 2000
- [19] JCPDS - 35-0789, International Center for Diffraction Data, 1998
- [20] Higher values for the NbOxide layer can be obtained by oxidation in water or by use of an activated oxygen environment, giving a maximum of 7 nm (T. Scherer, IEGI Karlsruhe)
- [21] H. Pothier, S. Guéron, N.O. Birge, D. Esteve, M.H. Devoret, "Energy distribution function of quasiparticles in mesoscopic wires", Phys. Rev. Lett. 79 (18), 1997
- [22] E.M. Gershenzon, M.E. Gershenzon, G.N. Gol'tsman, A.M. Lyul'kin, A.D. Semenov, A.V. Sergeev, "Electron-phonon interaction in ultrathin Nb films", Sov. Phys. JETP 70 (3), 1990

- [23] J. Bass, K.H. Fischer, *"Size Effects"*, Condensed Matter III 15a, Landolt-Börnstein, 1982
- [24] Q.D. Jiang, Y.L. Xie, W.B. Zhang, H. Gut, Z.Y. Ye, K. Wu, J.L. Zhang, C.Y. Li, D.L. Yin, *"Superconductivity and transport properties in ultrathin epitaxial single-crystal niobium films"*, J.Phys.: Condens. Matt. 2, 1990
- [25] W.F.M. Ganzevles, J.R. Gao, D. Wilms Floet, G. de Lange, A.K. van Langen, L.R. Swart, T.M. Klapwijk, P.A.J. de Korte, *"Twin-Slot Antenna coupled Nb hot-electron bolometer mixers at 1 THz and 2.5 THz"*, Proceedings of the 10<sup>th</sup> International Symposium on Space Terahertz Technology, 247-261, 1999

# DIFFUSION-COOLED ALUMINUM HOT-ELECTRON BOLOMETER MIXERS AT SUBMILLIMETER WAVELENGTHS

Anders Skalare, William R. McGrath,  
Pierre M. Echternach, Henry G. LeDuc

*Center for Space Microelectronics Technology, Jet Propulsion Laboratory,  
California Institute of Technology, Pasadena, CA 91109*

Irfan Siddiqi, Aleksandr Verevkin, Daniel E. Prober

*Dept. of Applied Physics, Yale University, New Haven, CT 06520-8482*

## Abstract

We report on the first mixing experiments at submillimeter wavelengths with superconducting diffusion-cooled hot-electron bolometers (HEB's) made from aluminum. The measurements were carried out at frequencies around 618 GHz, and showed conversion bandwidths of up to 3 GHz, and absorbed local oscillator (LO) powers of 0.5 to 6 nW. The highest mixer conversion efficiency was found to be about -21.5 dB single-sideband. A mixer noise temperature of about 1000 K DSB (double sideband) and a receiver noise temperature of about 3100 K DSB can be inferred from measurements of conversion efficiency and intermediate frequency output noise. The ratio of RF power coupled into the electrons to the power at the input of the mixer, that is the RF coupling efficiency, was found to be similar to that of our niobium HEB mixers. This demonstrates that despite the long electron-electron interaction time as measured near the Fermi energy in Al, the "hot" electrons thermalize efficiently in response to the RF power.

## 1. Introduction

During the last five years superconducting hot-electron bolometer (HEB) mixers [1,2] have increasingly come to be regarded as the most promising technology for extremely low-noise molecular spectroscopy observations at frequencies above about 1 THz. This is because unlike competing SIS mixers these devices are not limited to operation around or below the gap frequency of available superconductors. Compared to the more noisy Schottky diode mixers they also require low enough local oscillator (LO) power levels, so that operation with solid-state multiplied sources may be feasible even at terahertz frequencies. This combination of useful properties have made HEB mixers prime candidates for spaceborn, aircraft, or balloon-borne instrument platforms. The spaceborne ESA/NASA FIRST mission, NASA's SOFIA aircraft observatory, and a Long-Duration Balloon instrument all plan to employ HEB receivers. These HEB instruments will focus on low-background astrophysical observations of emission lines in the frequency regime from 1-3 THz.

Aluminum diffusion-cooled HEB devices are expected to have significant advantages over Nb devices, namely lower local oscillator (LO) power requirements and lower mixer noise temperatures with equal or higher intermediate frequency (IF) bandwidths. The lower LO power needs are significant since the solid-state tunable LO sources that are preferred for most applications do not yet exist, and when they do become available in the near future it is not certain that they will produce a sufficient amount of power to operate other HEB mixers. As we will demonstrate for the first time, Al HEB devices require absorbed LO power levels of only a few nW, while Nb diffusion-cooled HEB mixers need about 20-80 nW absorbed in the device [3, 4]. It should be pointed out that Nb devices requiring less LO power can be fabricated, but that they will have reduced IF bandwidths. In this way the aluminum technology gives an increased flexibility to the diffusion-cooled bolometer approach that is not present in the phonon-cooled devices used by other groups. Previously published material shows that the actual amount of LO power required scales as  $T_c^2$ , where  $T_c$  is the critical temperature of the superconductor [5, 6]. In addition, [5, 6] predicts that the mixer input noise temperature should scale in direct proportion to  $T_c$ , which should eventually lead to even lower noise temperatures than those already reported for other HEB mixers. The purpose of this paper is to present the first submillimeter wave measurements with a diffusion-cooled aluminum HEB mixer, and provide experimental data for the conversion efficiency, intermediate frequency bandwidth, and LO power.

## 2. Fabrication and DC properties

The aluminum HEB devices were fabricated using a shadow mask technique, previously described in [7], which allows the device and its contacts to be fabricated using a room temperature process in a single run without breaking the vacuum. This is critical to avoid contamination and/or oxidation of the Al films. The device films were about 13 to 17 nm thick, with contacts of 63 nm Al, 28 nm Ti and 28 nm Au. This is a robust contact design that avoids diffusion of normal metal contact material into the Al microbridge. The devices were 0.1  $\mu\text{m}$  wide with lengths of 0.3, 0.6, and 1.0  $\mu\text{m}$ . The HEB devices are fabricated together with a microstrip or coplanar waveguide circuit that connects to a planar double-slot antenna. The different circuit types require that the aluminum films are fabricated either directly onto the silicon wafer or on the silicon monoxide dielectric used for the microstrip, and it appears that the device process works about as well for both cases. The microstrip circuit requires a few extra process steps, but avoids one of the difficult steps in the CPW process, which is to pattern the narrow gaps required to give the CPW lines the correct characteristic impedance. Fig.1 shows a 0.3 micron long Al HEB device on SiO.

Measurements show that the transition temperatures of the devices are about 1.6 to 1.8 K, while the thicker aluminum of the connecting pads has a reduced transition of about 0.6 to 1.0 K, see Fig.2 . The ends of the devices have an apparent suppressed  $T_c$  as shown schematically in Fig.3 . In fact, for the shortest 0.3 micron most of the device has its transition close to the  $T_c$  of the pads. This critical temperature is too low to operate the device efficiently as a bolometric mixer since it is only barely above the operating temperature of the helium-3 system ( $\sim 400$  mK), which does not allow enough local oscillator power to be applied.

### 3. Mixer Measurement Set-Up

In the experiments the device chips were attached to the plane back side of an elliptical silicon lens of 12 mm diameter using cyanoacrylate glue. The lens was held in a copper fixture, where the devices were connected with an intermediate frequency microstrip circuit on Duroid 6010 with several aluminum bond wires. The intermediate frequency output signal from the mixer was either connected via a low-noise cooled L-band HEMT amplifier at 4 K [8] or, for bandwidth measurements, via a 0.5 to 18 GHz FET at 77 K [9]. Stainless steel coaxial cables were used in several places to reduce heat conduction between different components in the receiver. The mixer was attached to the cold plate of a helium-3 cryostat system that allowed operating temperatures down to about 400 mK [10]. The optical path used to couple in the RF power to the mixer had Zitex and black polyethylene filters on a 77 K heat shield, and a black polyethylene / diamond dust filter on a 4 K heat shield that enclosed the He-3 tank and the mixer. In measurements of mixer conversion and conversion bandwidth, the local oscillator (LO) power was supplied by a broadly tunable backward-wave oscillator (BWO) [11] and the signal was provided by a Gunn oscillator driving 2 cascaded frequency-multipliers [12]. The output power from the multiplier chain was coupled into the optical path using a Mylar beamsplitter. Most of the measurements were done with the multiplier providing a signal frequency of about 618 GHz, which was determined by measuring the Gunn oscillation frequency with a counter. A spectrum analyzer was used to detect the IF output signal.

### 4. RF coupling and LO Power Requirements

The RF coupling to the bolometer can be estimated by switching the receiver input beam between two broadband calibration targets that are maintained at different temperatures, and observing the effect this known difference in broadband thermal emission has on the DC characteristics of the device. In this method, the shift in DC heating that is required to maintain a constant device resistance is considered a measure of the difference in coupled RF power from the two targets. Such a measurement was made with device #6 (see Table 1), and showed a coupling efficiency from the targets of  $-4.7$  dB. This value is similar to those seen earlier for our niobium HEB mixers, that usually fell in the range of  $-5$  dB to  $-8$  dB [4,13] The conclusion that can be made from this is that the 600 GHz RF power appears to couple about as well to this aluminum device as it would to a niobium HEB.

The amount of local oscillator power that is absorbed in the device can also be calculated from the effect on the DC IV curve, which is how the power estimates in Table 1 were deduced. The amount of LO power that is actually incident on a device is harder to estimate, since the mode matching between the source and the device chip is not accurately known. It is possible to calculate an upper limit, however. In one experiment device #6 was pumped strongly enough by a Gunn oscillator/multiplier to cause it to become completely normal conducting. The source gave less than  $100 \mu\text{W}$  of power at 618 GHz, and about  $-7$  dB of this power was coupled into the receiver beam with a beam splitter. A further 20 dB of coupling loss was due to losses in the cryostat window and filters, and to the diverging multiplier output beam. This leads to an upper estimate of the LO power that actually reaches the silicon lens in the mixer of about 200 nW, and most

likely the power that is actually coupling into the chip antenna is substantially less due to the poor focussing. Even this upper limit shows that predictions for devices much shorter than the electron-electron inelastic time, where LO power requirements in the  $\mu\text{W}$  regime have been predicted [14], are not applicable to the devices used here

## 5. Mixer Measurements

The mixer conversion efficiency and its dependence on frequency have been measured for several devices and the data are summarized in Table 1. The conversion efficiency was determined from measurements with a monochromatic signal source, and was calculated as the ratio of the coupled IF output power to the input signal power absorbed in the device. This means that losses in the RF optical path as well as losses in the mixer embedding circuit are not included. The  $-4.7$  dB value for the RF coupling loss that was mentioned earlier refers to device #6 in Table 1, but the losses for the higher resistance devices should be considerably higher due to the larger impedance mismatch.

The highest mixer conversion efficiencies measured were about  $-20$  to  $-21$  dB single sideband (SSB) for several of the devices, with bandwidths up to 3 GHz. It should be pointed out, that in all the measurements shown in the table, except device #5, the LO power was optimized for maximum conversion.

The dependence of IF conversion bandwidth on bias voltage is shown in Figs. 4 & 5 for the  $1\ \mu\text{m}$  long device #1. At the highest bias voltage the bandwidth is at its largest, 2.7 GHz, but at the same time the conversion is quite low,  $-33$  dB (SSB). When the bias voltage is reduced into the regime where self-heating is evident in the IV curve, the conversion increases and the bandwidth is suppressed, which is consistent with the behavior of other superconducting HEB's. At the lowest bias point (V1 in Fig.4) the maximum conversion is at about  $-21$  dBm and the IF bandwidth at 1 GHz. This clearly demonstrates one of the key advantages of Al since even this IF bandwidth is several times larger than the value obtained for Nb devices of this length [3, 15]. Device #3 is  $0.6\ \mu\text{m}$  long and gave the largest bandwidth of 3 GHz, for a similar conversion efficiency of  $-20$  dB. This increase is consistent with the  $L^2$  dependence of the IF bandwidth for diffusion-cooled HEB mixers, and demonstrates that the *entire* length of the Al bridge determines the IF bandwidth despite the presence of the apparently normal conducting ends (discussed below).

While the DC characteristics of the  $1\ \mu\text{m}$  long Al devices tested so far have resistance vs. temperature (RT) and current vs. voltage (IV) curves that are qualitatively similar to the ones seen for diffusion-cooled niobium devices, this is not quite the case for the  $0.6\ \mu\text{m}$  long devices. The end effect in the bridge extends to about  $0.15\ \mu\text{m}$  from the contacts and appears to have a significant impact on the IV curves. This can be seen in Fig.6, which shows such an IV curve with varying amounts of local oscillator power applied. One possible interpretation of Fig.6 is that with increasing amounts of LO power first one, then the other end region become normal conducting at low voltages where the central region of the bridge is still superconducting. Marker "a" in the Fig.6 indicates where one end region is normal conducting, while the other is still superconducting. At marker "b"

both ends are normal. At the higher LO levels required to achieving higher conversion, both ends are normal conducting. This situation is almost the reverse of that which usually gives the best mixer conversion efficiency in niobium devices, where the center of the bridge is normal conducting and the ends are superconducting.

Fig. 7 shows the bias dependence of the mixer output for three different input signal levels. The highest power, which corresponds to a conversion efficiency of  $-21.5$  dB SSB (device #6 in Table 1) occurs when the bridge ends are normal and the central part of the device is at its transition temperature. A separate measurement of output noise and Y-factor was made with the same device under similar conditions. It was found that the output thermal fluctuation noise from the device was about 3 K, the Johnson noise (including noise generated elsewhere and reflected against the device) was about 2 K, and the IF amplifier noise was about 10 K. With the total IF noise thus estimated at 15 K, the conversion efficiency at  $-21.5$  dB, and the RF coupling at about  $-4.7$  dB, the receiver noise temperature can be estimated at about 3100 K double sideband (DSB) of which two thirds is IF amplifier noise and the contribution from the mixer is about 1000 K (the noise temperatures are thus referred to the input window of the cryostat). Although the directly measured Y-factors do indeed show a similar response, they are unfortunately also affected by direct detection of the broadband radiation from the calibration targets, and are not currently used as a verification of these noise estimates.

## 6. Device End Effects

The measurements show that the device is affected by end effects that appear to be extending to about 120 to 150 nm from the contact pads at each end. The precise mechanism behind this is not fully understood at this point, but the cause may be proximity effect from the contact pads, and be further complicated by charge imbalance [16]. The end regions have several non-trivial effects on the HEB mixer, especially for devices that are shorter than  $1\ \mu\text{m}$ . To maximize the mixer conversion efficiency and/or minimize the mixer input noise temperature, a sufficient amount of DC and LO power needs to be dissipated so that the electron temperature in the central part of the device is close to the local critical temperature (about 1.8 K). Under these conditions the end regions will be heated to a temperature higher than their local critical temperature (about 0.6 to 1.0 K), since the temperature provided by the He-3 system is only marginally lower (about 0.4 K), and since the temperature distribution inside the device has a parabolic shape that is determined by the Wiedemann-Franz law and the diffusion-cooling mechanism. One effect of the normal conducting end regions is to change the effective load line of the central part of the device. If the end regions have a combined resistance of  $45\ \Omega$ , for example, the effective load impedance in the IF band will be a total of  $95\ \Omega$  instead of the  $50\ \Omega$  provided by the IF system by itself. This makes it harder to maintain a stable DC bias point close to the  $T_c$  of the central device region, which can cause oscillations and which prevents the mixer from being operated at its optimum bias point. Another effect is dissipation of intermediate frequency output power in the end regions. In the example just given, this would result in almost 3 dB of additional conversion loss. The end effects also define the length of the shortest device that can be efficiently operated as a mixer, since shorter devices appear to have the  $T_c$  lowered significantly by the contact pads, so that only very small amounts of LO power can be applied. Previous

estimates of intermediate frequency bandwidths were based on the assumption that devices could be made very short. An example given in [5] assumes a film diffusivity of  $D=10 \text{ cm}^2/\text{s}$  and a device length of 100 nm, resulting in an IF bandwidth of 157 GHz. With an effective minimum length of 300 nm, the maximum bandwidth is reduced to  $\Delta f = \pi D/(2L^2) = 17 \text{ GHz}$ .

There are a few different ways to reduce the consequences of the end effect, and increase the IF bandwidth of the device: One would be to lower the operating temperature of the mixer so that the device ends do not go completely normal conducting, and maybe also reduce the  $T_c$  of the device film itself. This approach would require a more complex cryocooler than the He-3 system used by us, such as a dilution refrigerator. Another approach would be to modify the geometry of the bolometer, for example by making the device film much wider at the ends, so that the wider (but still affected) regions have lower normal resistance and can act as heat sinks for the central part of the device. Also, the sheet resistance of the device can be lowered, which would reduce the losses associated with having the resistance of the normal conducting end regions in series with the IF system impedance. Such devices have already been fabricated, and will be investigated in the near future.

## 7. Summary

In summary, we have measured the local oscillator power requirements, the conversion efficiency and the IF bandwidth of several diffusion-cooled aluminum HEB mixers at frequencies around 618 GHz. We found that the LO power needed was indeed about 10 to 20 times lower than that required for niobium HEB mixers as would be expected from the ratios of the squares of their critical temperatures. The conversion efficiency was relatively low compared to that achieved for niobium, about  $-21.5 \text{ dB SSB}$ . There are several possible explanations for this, including some relating to the end effects in the device. IF bandwidths of up to 3 GHz were measured, but since the data for different devices were recorded under varying bias and LO pump conditions, the precise dependence on film diffusivity and device length cannot be determined yet. Since these dependencies are primarily low-frequency properties of the device, they can be expected to be similar to the  $D/L^2$  trend found for the 30 GHz measurements in [17]. The conversion efficiency, RF input coupling efficiency and the output noise in the IF band leads to a rough estimate of 3100 K (DSB) receiver temperature, of which about 1000 K (DSB) would be mixer noise. These noise temperatures were not, however, measured directly through a well-calibrated Y-factor measurement. The end effects in the devices were found to be significant, especially in the shorter  $0.3 \mu\text{m}$  and  $0.6 \mu\text{m}$  devices, and future work should clearly be devoted to minimizing the consequences. An estimate of the required input local oscillator power, as well as direct detection measurements using broadband blackbody radiators, show that there are no severe losses in the RF coupling to the device.

## Acknowledgments

This work was performed jointly by the Jet Propulsion Laboratory and Yale University, and was supported by the Space Science Enterprise of the National Aeronautics and

Space Administration (NASA) and by the National Science Foundation. Funding for Irfan Siddiqi was provided by a NASA Graduate Student Fellowship.

## References

- [1] E.M. Gershenzon, G.N. Gol'tsman, I.G. Gogidze, Y.P. Gusev, A.I. Elant'ev, B.S. Karasik, A.D. Semenov, "Millimeter and submillimeter range mixer based on electronic heating of superconducting films in the resistive state," *Sov. Phys. Superconductivity*, Vol.3(10), pp.1582-1597, 1990
- [2] D.E. Prober, "Superconducting Terahertz Mixer using a Transition-Edge Microbolometer," *Appl. Phys. Lett.*, Vol.62(17), pp.2119-2121, 26 April 1993.
- [3] R.A. Wyss, B.S. Karasik, W.R. McGrath, B. Bumble, H. LeDuc, "Noise and bandwidth measurements of diffusion-cooled Nb hot-electron bolometer mixers at frequencies above the superconductive energy gap", *Proc. Tenth Int. Symp. Space Terahertz Tech.*, pp. 215-228, University of Virginia, Charlottesville, Virginia, March 16-18, 1999
- [4] B.S. Karasik, M.C. Gaidis, W.R. McGrath, B. Bumble, H.G. LeDuc, "Low noise in a diffusion-cooled hot-electron mixer at 2.5 THz", *Appl. Phys. Lett.* **71** (11), 15 September 1997, pp.1567-1569.
- [5] B.S. Karasik, W.R. McGrath, R.A. Wyss, "Optimal Choice of Material for HEB Superconducting Mixers", *IEEE Trans. Applied Superconductivity*, Vol.9, No.2, June 1999, pp.4213-4215.
- [6] B.S. Karasik, A.I. Elantev, "Analysis of the noise performance of a hot-electron superconducting bolometer mixer", *Proc. Sixth Int. Symp on Space Terahertz Tech*, California Institute of Technology, Pasadena, California, March 21-23, 1995, pp.229-246
- [7] P.M. Echternach, H.G. LeDuc, A. Skalare, W.R. McGrath, "Fabrication of an aluminum based hot electron mixer for terahertz applications", *Proc. Tenth Int. Symp. Space Terahertz Tech.*, pp. 261-268, University of Virginia, Charlottesville, Virginia, March 16-18, 1999
- [8] The cryogenic HEMT amplifier was supplied by Berkshire Technologies.
- [9] Broadband coolable 05-18 GHz FET by Miteq Inc.
- [10] The 8-inch baseplate He-3 cryostat was supplied by Infrared Laboratories, Inc.
- [11] The BWO tube was manufactured by Istok.
- [12] Both the Gunn oscillator and the x6 multiplier by Radiometer Physics GMBH
- [13] A. Skalare, W.R. McGrath, B. Bumble, H.G. LeDuc, "Measurements with a diffusion-cooled Nb hot-electron bolometer mixer at 1100 GHz," , *Proc. Ninth Int. Symp.*

Space Terahertz Tech., pp.115-120, Jet Propulsion Laboratory, Pasadena, California, March 17-19, 1998.

[14] A.D. Semenov, G.N. Gol'tsman, "Nonthermal mixing mechanism in a diffusion-cooled hot-electron detector", J. Appl. Phys., Vol.87, No.1, Jan.1, 2000, pp.502-510.

[15] P.J. Burke, R.J. Schoelkopf, D.E. Prober, A. Skalare, W.R. McGrath, B. Bumble, H.G. LeDuc, "Length scaling of bandwidth and noise in hot-electron superconducting mixers", Appl. Phys. Lett., Vol. **68** (23), pp.3344-3346, 3 June 1996

[16] D. Wilms-Floet, J.J.A. Baselmans, T.M. Klapwijk, Appl. Phys. Lett. **73**, 2826 (1998)

[17] I.Siddiqi, A. Verevkin, D.E. Prober, A. Skalare, B.S. Karasik, W.R. McGrath, P. Echternach, H.G. LeDuc, "Aluminum sub-micron superconducting hot-electron bolometer mixers", These proceedings

## Tables and Figures

Device	L ( $\mu\text{m}$ )	R ( $\Omega$ )	$\eta$ SSB (dB)	BW (GHz)	LO Power (nW)
#1	1.0	448	-21 to -33	1 to 2.7	0.5
#2	1.0	285	-21	3	1.3
#3	0.6	255	-20	3	3.7
#4	0.6	330	-----	1.7	0.9
#5	0.6	100	-29	3	2.7
#6	0.6	106	-21.5	----	5.7

Table 1; Measured results for Al HEB devices. The conversion efficiency does not include losses in the optical coupling to the mixer embedding circuit. The absorbed LO power was estimated by the effect on the DC IV curves of the HEB's.

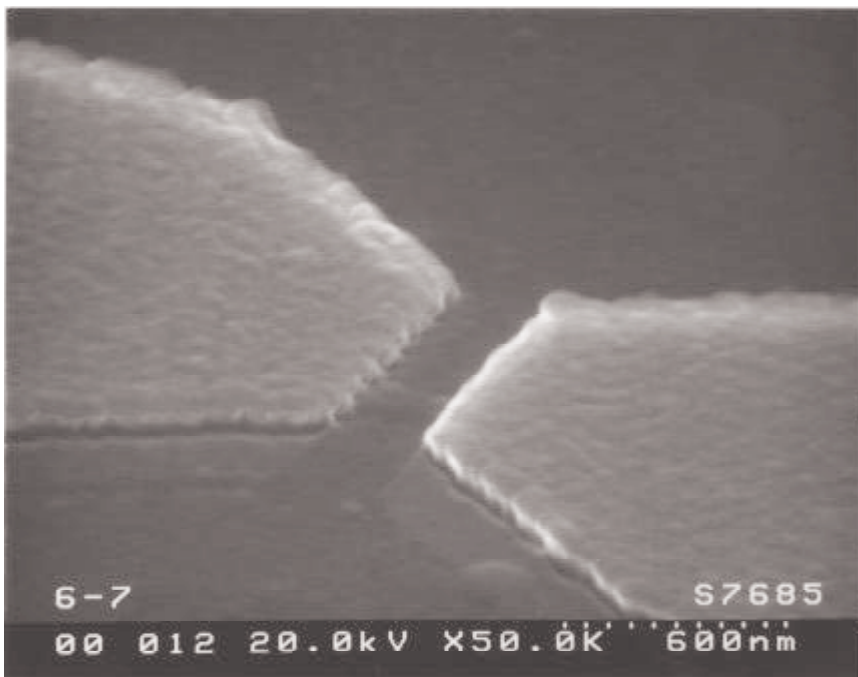


Fig.1; SEM of an Al microbridge. The Al device is faintly visible between the Al-Ti-Au contacts.

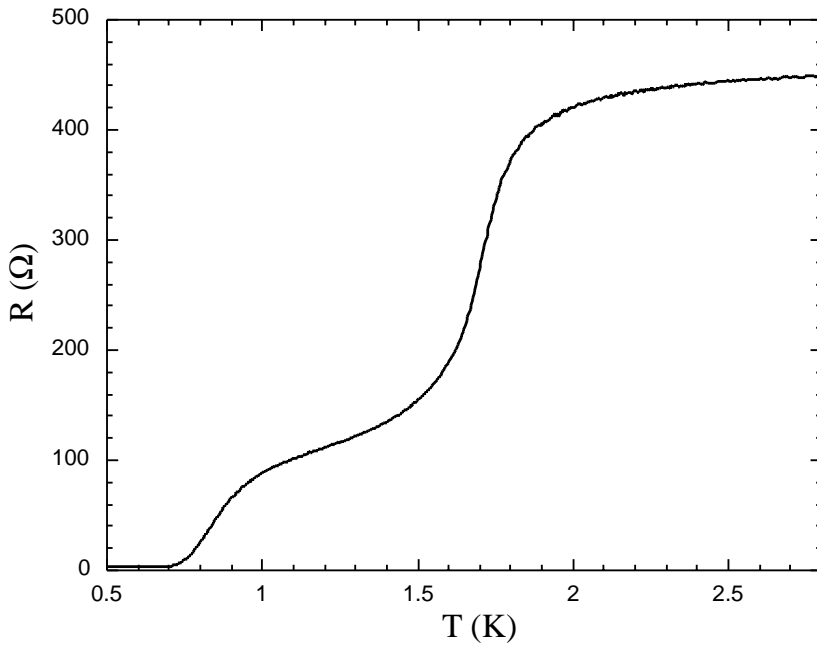


Fig.2; Resistance vs. Temperature characteristic for device #1 in Table 1. The first resistance drop occurs at the transition temperature of the microbridge, the second drop near 0.7 K is due to the transition of the Al contact pads.

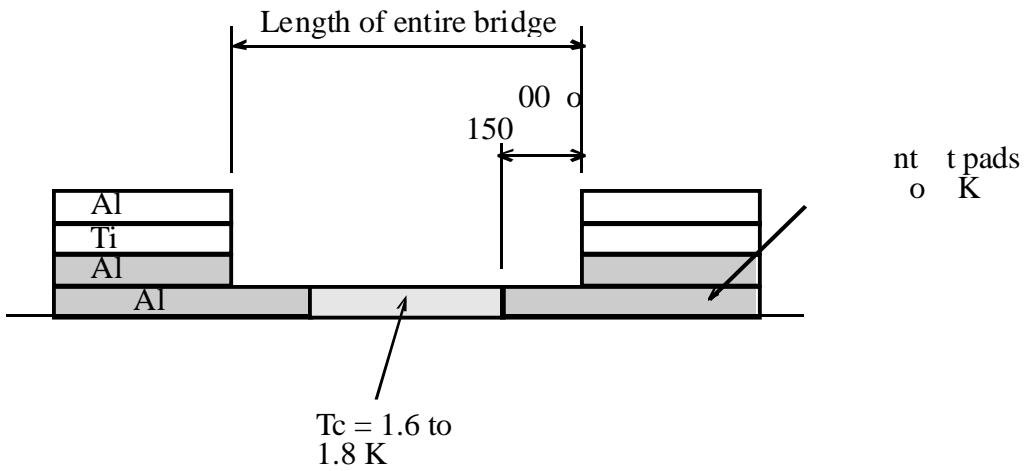


Fig.3; Schematic cross section of the microbridge and contact pads (not to scale).

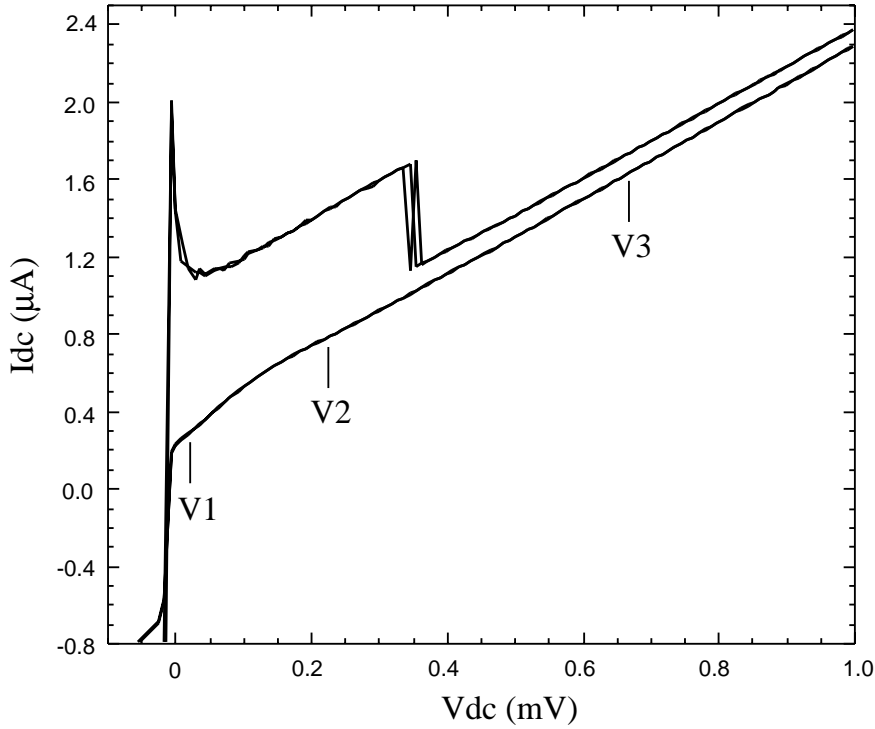


Fig.4; Unpumped and LO-pumped IV curves of device #1 at 0.42 K. The marked points correspond to the bias voltages used for the IF bandwidths shown in Fig. 5.

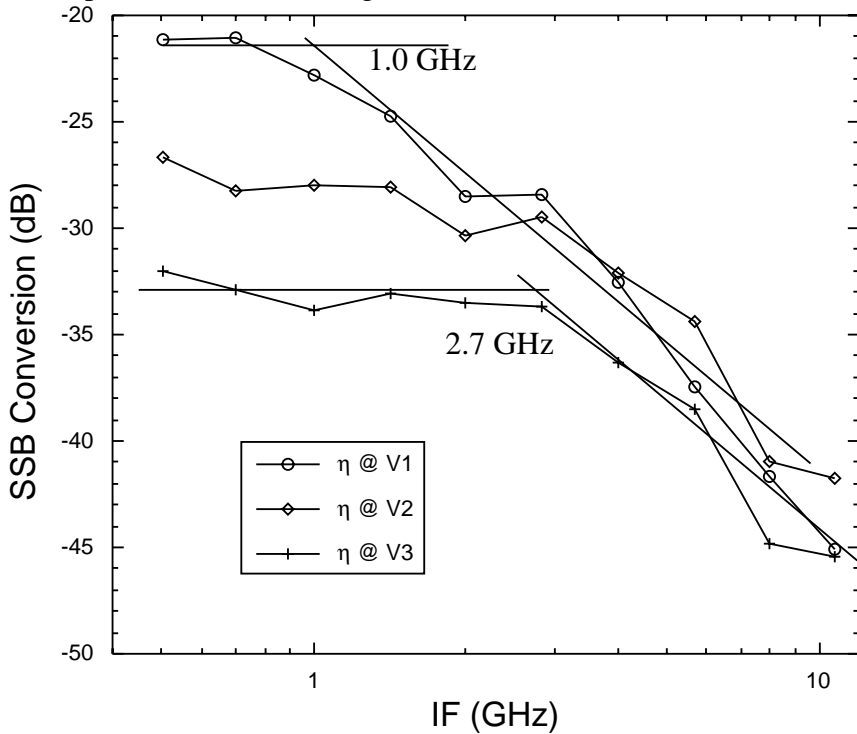


Fig.5; Conversion efficiency vs. intermediate frequency for device #1. The different curves correspond to the marked bias voltages in Fig.4 . The signal was kept at a constant frequency of 618 GHz in the lower sideband, while the local oscillator frequency was varied.

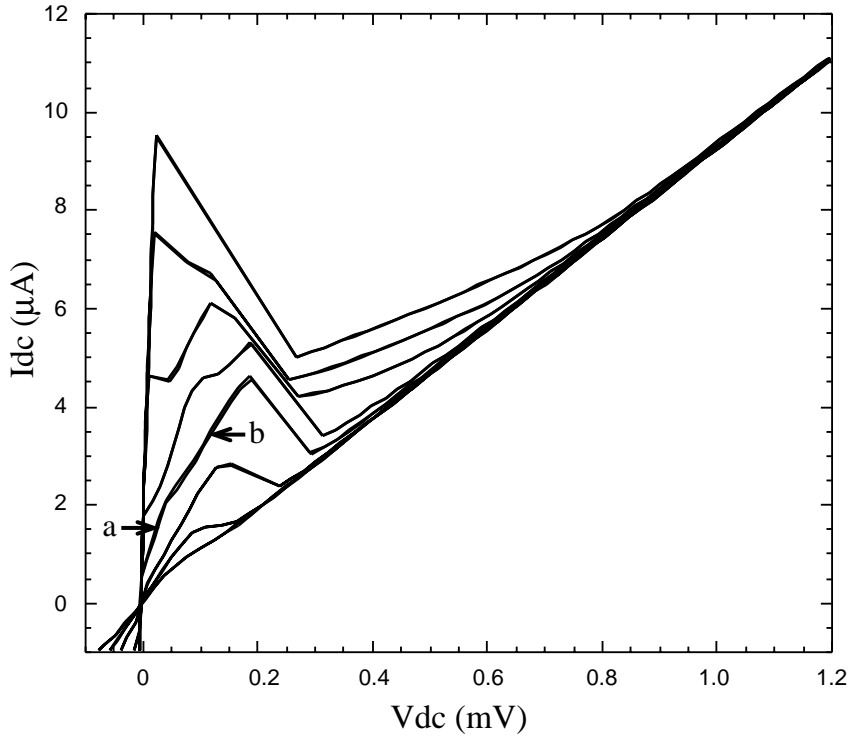


Fig.6; IV curves of the 0.6 micron long device #6 at 0.44 K. One curve is unpumped and the others are local oscillator pumped at varying power levels at 620 GHz. The labels “a” and “b” are explained in the main text.

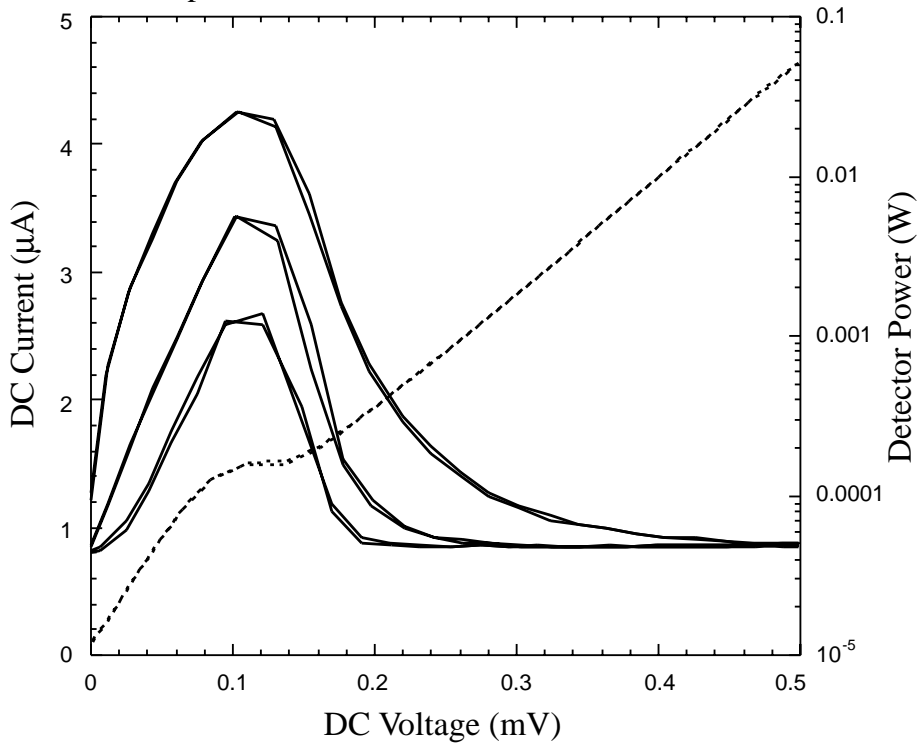


Fig.7; IF output power vs. bias voltage for device #6 for three different RF signal power levels at 618 GHz. Also shown is the pumped DC IV curve. The temperature was 0.44 K.

# Noise and Mixing in Aluminum Based Sub-Micron Hot-Electron Bolometers

**A.Verevkin, I.Siddiqi, and D.E. Prober**

*Department of Applied Physics, Yale University, New Haven, CT 06520-8284*

**A.Skalare, B.S.Karasik, W.R.McGrath, P.M.Echternach, and H.G.LeDuc**

*Center for Space Microelectronics Technology, Jet Propulsion Laboratory, California Institute of Technology, Pasadena, CA 91109-8099*

Previous work with superconducting hot-electron bolometer (HEB) mixers has shown that the primary source of noise in well optimized Nb devices is thermal fluctuation noise [1]. Our results for microwave mixing in sub-micron long diffusion-cooled thin film superconducting aluminum HEB structures ( $T_c \sim 1.7\text{K}-2.4\text{K}$ ) in the bath temperature range of  $T=0.25-1.6\text{K}$  [2] show that it is possible to operate the mixer, with good conversion efficiency and intermediate frequency bandwidth, in a region where the thermal fluctuation noise is very small. In these devices, the resistive transition,  $R$  vs.  $T$ , is very broad. At  $T/T_c \sim 0.3$  we still observe a resistance that is consistent with  $\sim 0.2 \mu\text{m}$  of the total microbridge length being resistive [3]. At  $T=0.25\text{K}$  ( $T/T_c \sim 0.1$ ) in zero magnetic field, the banks of the HEB are superconducting. By applying a magnetic field  $H \pm 0.03\text{T}$ , the banks can be driven normal, in which case we again observe that about  $0.2 \mu\text{m}$  of the  $0.6 \mu\text{m}$  bridge is resistive. Thermal fluctuation noise is largest near the onset of  $T_c \sim 2.5 \text{K}$  for that sample. The best mode of heterodyne mixing in our devices was observed at low bias voltages  $\sim 0.2\text{mV}$ .

If the Al HEB with normal banks is modeled as a N-S-N structure with near ideal transparency, then charge-imbalance arguments [4] can be invoked to explain the behavior of the resistive transition near  $T_c$ . Noticeable fractions of the microbridge edges should be resistive since the characteristic charge-imbalance diffusion length is non-negligible compared with the microbridge length  $L$ . The diffusion length is  $\Lambda_{Q^*}(T) = (D\tau_{Q^*}(T))^{1/2}$  [5]. The charge-imbalance relaxation time  $\tau_{Q^*}$  is estimated from reported values of the inelastic scattering time  $\tau_i$  at the Fermi energy [6], and the diffusion constant  $D$  is measured from  $H_{c2}$ . However, far below  $T_c$  charge-imbalance effects should not be significant, and Andreev transfer of pairs should dominate. The resistance of the N-S boundaries should be negligibly small. At  $T=0.25\text{K}$ , the quasiparticle population which can be injected into the superconductor is exponentially small. Yet we observe a large series resistance at  $0.25 \text{K}$  in a magnetic field  $H \pm 0.03\text{T}$ . Thus, the physical model for the resistance is not complete for the low temperature / low voltage regime, even though excellent heterodyne performance is observed there and diffusion cooling appears to be operative.

We discuss possible mechanisms to account for the measured device resistance as a function of temperature, and how they effect the mixing mechanism and output noise within the context of a diffusion cooling model.

1. Burke et al., Appl. Phys. Lett. **72**, 1516 (1998); B.S. Karasik, and A.I. Elantiev, Appl. Phys. Lett. **68**, 853 (1996).
2. I.Siddiqi et al., Proceedings 11<sup>th</sup> Int'l Symp. Space THz Tech., Ann Arbor, MI, (2000).
3. P.M.Echternach et al., Proceedings 10<sup>th</sup> Int'l Symp. Space THz Tech., Charlottesville, VA, 261(1999).
4. J.R.Waldram, Proc.R.Soc.Lond.A **345**, 231(1975); S.N.Artemenko, and A.F.Volkov, Sov.Phys.JETP **45**, 533(1977); G.E. Blonder et al., Phys. Rev. B **25**, 4515 (1982)
5. D.W. Floet et al., Appl. Phys. Lett. **73**, 2826 (1998); M. Stuiyinga et al., JLTP **53**, 633 (1983)
6. P.Santhanam and D.E.Prober, Phys.Rev.B **29**, 3733(1984); T.M. Klapwijk et al, Phys. Rev. B **33**, 1474 (1986); J.M. Gordon and A.M. Goldman, Phys. Rev. B **34**, 1500 (1986); E.M. Gershenzon et al., Solid State Com. **75**, 639 (1990).

# HOT-ELECTRON DETECTORS: TOWARD RECORD SENSITIVITY VIA DISORDER-SUPPRESSED ELECTRON-PHONON COUPLING

M. E. Gershenson, D. Gong, and T. Sato

Department of Physics and Astronomy, Rutgers University, Piscataway, NJ 08854

B. S. Karasik and W. R. McGrath

Jet Propulsion Laboratory, California Institute of Technology, Pasadena, CA 91109

A. V. Sergeev

Dept. of Electrical and Computer Engineering, Wayne State University, Detroit, MI 48202

Recently we proposed a concept of a submm/FIR direct detector based on electron heating in superconducting microbridges at ultra-low temperatures [1]. The main advantages of the hot-electron direct detectors (HEDDs) are an unparalleled sensitivity, simplicity of fabrication, and large-array scalability. Basic parameters of the HEDDs, the time constant and sensitivity, are determined by the electron-phonon relaxation time,  $\tau_{e-ph}$ . The strong temperature dependence of the electron-phonon coupling and effects of disorder allow to suppress the electron-phonon interaction and to enhance electron heating by electromagnetic radiation. As the first step toward implementation of the HEDDs, we have measured  $\tau_{e-ph}$  at  $T = 0.04 - 1$  K in disordered hafnium films with  $T_c = 0.3-0.5$  K. Below  $T \approx 0.5$  K, we observed the dependence  $\tau_{e-ph}(T) = 6.5 \times 10^{-8} (T/1\text{K})^{-4}$  s, which is in a very good agreement with the theory of electron-phonon interactions in disordered conductors. Slow electron-phonon relaxation with  $\tau_{e-ph}$  as large as 25 ms at  $T = 0.04$  K results in a record sensitivity. Scaling of the in-plane sensor dimensions down to  $\sim 1 \mu\text{m}$  would result in the noise equivalent power  $NEP \approx 10^{-20} \text{ W/Hz}^{1/2}$  at  $T = 0.1$  K, which is two orders of magnitude better than that for the state-of-the-art bolometers.

## ***Introduction***

Future far infrared (FIR) radioastronomy missions (SPIRIT, the 10m FIR telescope, and SPECS) will require significant improvement in the sensitivity of radiation detectors in the 40-500  $\mu\text{m}$  wavelength range, and integration of the detectors in large arrays for sky mapping applications [2]. The photon-limited noise equivalent power ( $NEP$ ) of a detector combined with a cooled space telescope is expected to be better than  $10^{-19} \text{ W}/\sqrt{\text{Hz}}$  [3], or even lower for narrow band applications. The state-of-the-art bolometers currently offer  $NEP \sim 10^{-17} \text{ W}/\sqrt{\text{Hz}}$  at 0.1 K, along with the time constant  $\tau \sim 10^{-3}$  s [4,5]. High sensitivity of these bolometers is achieved by using the so-called spiderweb suspension. For higher sensitivity, thermal conductance between the device and the heat sink should be further reduced. However, this will slow down the bolometer

response and enhance the 1/f-noise. Better detectors will be required to meet the needs of the upcoming space missions.

Recently, we proposed a new approach to the sensitivity improvement, based on implementation of electron heating in superconducting microbridges at sub-Kelvin temperatures [1]. The innovative idea is to use a superconducting hot-electron detector with electron-phonon inelastic scattering time  $\tau_{e-ph}$  controllably adjusted to the required time constant,  $\tau$ . Wide-range variation and precise control of the electron-phonon scattering rate is possible due to a strong temperature dependence of  $\tau_{e-ph}$ ; further increase of  $\tau_{e-ph}$  might be possible by controllably introduced disorder (electron scattering from boundaries, impurities, and defects). The exceptionally high sensitivity of the HEDDs can be achieved due to a very small heat capacity of electrons in a micron-size sensor. We expect that an antenna- or waveguide-coupled micron-size HEDD with a small time constant  $\tau \sim 10^{-3} \div 10^{-5}$  s will exhibit at  $T = 0.1-0.3$  K the photon-noise-limited performance in millimeter, sub-millimeter, and infrared wavelengths [6]. Besides this record sensitivity, the hot-electron detectors will have other attractive features. They can be fabricated on a bulk substrate and integrated into arrays, their impedance can be easily matched with the planar antenna's impedance.

### Concept of the ultra-low-temperature HEDD

Operation of both conventional and hot-electron detectors can be illustrated by Fig. 1. The radiation is absorbed by electrons in a thin-film sensor. The electron-phonon coupling in the sensor is characterized by the electron-phonon thermal conductance  $G_{e-ph} = C_e / \tau_{e-ph}$ , where  $C_e = \gamma T$  is the electron heat capacity and  $\gamma$  is the Sommerfeld constant. Escape of non-equilibrium phonons into the heat bath is described by the escape time  $\tau_{es}$  and the thermal conductance  $G = C_{ph} / \tau_{es}$ , where  $C_{ph}$  is the heat capacity of phonons in the combination thin-film sensor + substrate. High sensitivity of conventional bolometers is due to a significantly reduced coupling to the heat bath ( $G \ll G_{e-ph}$ ). The

noise equivalent power of an optimally designed bolometer is limited by thermodynamic fluctuations of the temperature in the process of the heat transfer to the heat bath:

$$NEP = \sqrt{4k_B T^2 G}. \quad (1)$$

On the other hand, in a hot-electron detector, a weak electron-phonon coupling serves as the bottleneck of the energy transfer between electrons and the environment ( $G_{e-ph} \ll G$ ). This requirement can be easily satisfied at ultra-low temperatures, because  $G$  is typically proportional to  $T^3$  [7], whereas  $G_{e-ph}$  decreases much faster with lowering

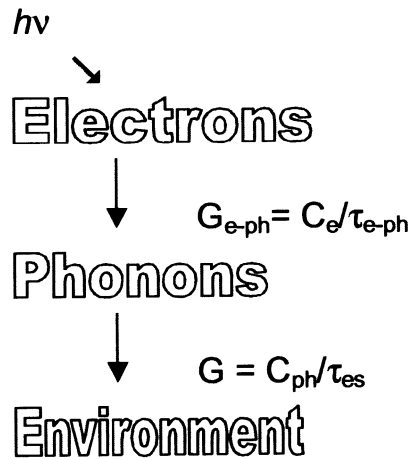


Fig. 1. Scheme of operation for bolometers and hot-electron detectors.

$T$ , usually as  $T^{(4+5)}$ . Reducing the film thickness also helps to satisfy the condition  $G_{e-ph} \ll G$ , because  $G$ , unlike  $G_{e-ph}$ , is inversely proportional to the film thickness [8]. In this hot-electron regime, the radiation overheats the electrons in a superconducting film, while phonons in the film play the role of a heat sink for electrons (for a review, see [9]). The HEDD time constant coincides with the electron-phonon scattering time  $\tau_{e-ph}$ . For a HEDD with the sensitivity limited by fluctuations of the electron temperature,

$$NEP = \sqrt{4k_B T^3 \gamma V / \tau_{e-ph}}, \quad (2)$$

where  $V$  is the sensor volume. Comparison between (1) and (2) shows that for the same time constant  $\tau$  and in-plane dimensions of a sensor, hot-electron detectors offer an ultimate sensitivity [8]. This difference can be further increased, since it is feasible to reduce in-plane dimensions of the hot-electron sensor down to  $\sim 1 \mu\text{m}$ , a very difficult task for a conventional bolometer. Another attractive feature of the HEDDs is that they can be fabricated on a conventional substrate, because the thermal conductivity  $G$  is irrelevant.

The schematic design of a micron-size HEDD is shown in Fig. 2. To maximize the electron heating at sub-Kelvin temperatures, a special design of the current leads is required. The leads should be fabricated from a superconductor with a superconducting energy gap  $\Delta$  much larger than that of the sensor, e.g., Nb. The dc bias and rf currents will flow freely through the structure, whereas outdiffusion of hot electrons with energies

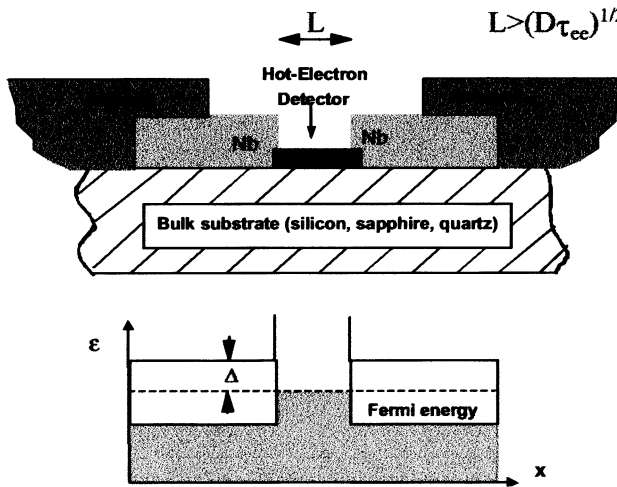


**Fig. 2.** The schematic design of a hot-electron detector. The sensor is flanked by superconducting current leads (“Andreev mirrors”), which prevent outdiffusion of hot electrons. The energy gap in the sensor is suppressed either by the temperature  $T \sim T_c$  or by a weak magnetic field at  $T < T_c$ . This magnetic field does not affect the gap in the leads since  $H_{c2}(\text{leads}) \gg H_{c2}(\text{sensor})$ . The total length of superconducting leads should be small to reduce *rf* losses at high frequencies. The antenna is fabricated from a high-conductivity normal metal (Au).

$\varepsilon < \Delta$  will be blocked by Andreev reflection [10].

The lower limit on the sensor length,  $L$ , is imposed by the proximity effect:  $L$  should be larger than the coherence length in a normal metal,  $L_T = (\hbar D / 2\pi k_B T)^{1/2}$ , to preserve difference between the critical temperatures of the sensor and superconducting leads. Thus, for a disordered film with the diffusion constant  $D \sim 1 \text{ cm}^2/\text{s}$ ,  $L$  should be much larger than  $2L_T \sim 0.1 \mu\text{m}$  at  $T = 0.1 \text{ K}$ . Typically, this requirement is also sufficient to ensure high quantum efficiency of the HEDD at frequencies  $f > \Delta/h$  (e.g., for Nb leads,  $\Delta/h$  corresponds to 360 GHz). Indeed, for high quantum efficiency, the electrons, which are the current carriers in

superconductors at high frequencies  $f > \Delta/h$ , must be thermalized within the HEDD due to electron-electron interactions. The electron-electron inelastic scattering time  $\tau_{e-e}$  is by many orders of magnitude smaller than  $\tau_{e-ph}$  in disordered thin films at low temperatures [8]. For electron thermalization, the length  $L$  should be larger than the diffusion length of electrons with energies  $\epsilon \sim \Delta$ ,  $L_{e-e} = [D\tau_{e-e}(\Delta)]^{1/2}$ . The two scales,  $L_T$  and  $L_{e-e}$ , are of the same order of magnitude in ultra-thin disordered films at  $T < 1$  K. Thus, the sensor length  $\sim 1 \mu\text{m}$  should be sufficient to minimize the proximity effect and to ensure electron thermalization.

***Electron-phonon scattering at sub-Kelvin temperatures.***

As the first step toward development of ultra-sensitive HEDDs, it is necessary to verify if an ultra-long electron cooling time  $\tau_{e-ph} \sim 10^{-3}$  s can be realized within the temperature range  $T = 0.05\text{-}0.3$  K, accessible by modern flight qualified refrigerators. We have measured  $\tau_{e-ph}$  in thin films of hafnium deposited on sapphire substrates. Hafnium is a promising material for ultra-low-temperature HEDDs ( $T_c = 0.13\text{K}$  for bulk Hf). In these preliminary experiments, instead of using superconducting leads to block outdiffusion of hot electrons, we fabricated a very long meander-type structure with the total length  $L \gg \sqrt{D\tau_{e-ph}}$  (Fig. 3). The critical temperature and resistivity of magnetron-sputtered Hf films depend strongly on the argon pressure and deposition rate. By optimizing the deposition parameters, we were able to increase  $T_c$  up to 0.5 K. The superconducting transition and the temperature dependence of the critical magnetic field  $H_{c2}$  for one of the samples is shown in Fig. 4. The thickness of Hf films was varied between 250 Å and 850 Å to keep the sheet resistance  $R$  in the 30-50 Ω range (for better impedance matching of the antenna-coupled HEDDs).

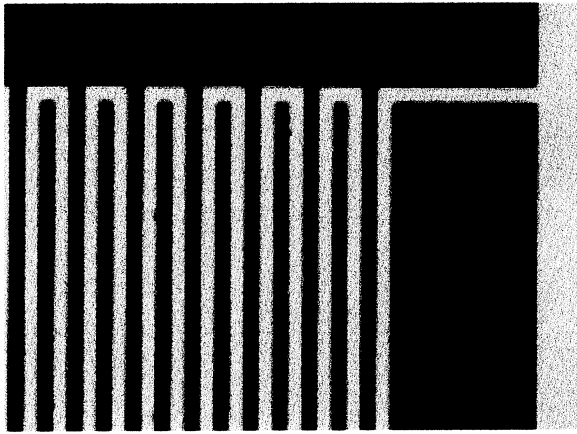


**Fig. 3.** Microphotograph of a portion of the meander-type Hf structure on a sapphire substrate. The width of the strip is 5 μm, the total length is 10 cm, the total area occupied by the meander is 1×1 mm<sup>2</sup>.

In the heating experiments, the resistance of a sample has been measured at a small ac current  $I_{ac}$  by a resistance bridge as a function of the temperature and the heating dc current  $I_{dc}$ . The temperature dependence of quantum corrections to the resistance has been used as an electron “thermometer” in the temperature range  $T > T_c$ . Below  $T_c$ , the sample was driven into the resistive state by applying the magnetic field. The resistive state is very sensitive to electron overheating; this allows measuring  $\tau_{e-ph}$  with an unparalleled accuracy.

The experimental procedure of finding the thermal conductivity between electrons and phonons,  $G_{e-ph}$ , is illustrated in

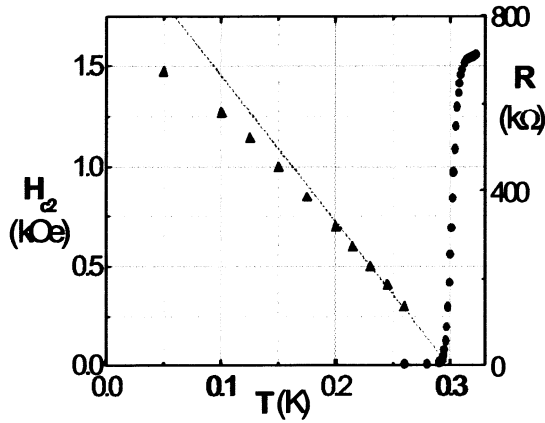


Fig. 4. The superconducting transition  $R(T)$  at  $H=0$  with  $\Delta T_c=7\text{mK}$  (dots) and the temperature dependence of the upper critical field  $H_{c2}$  (triangles) for a Hf meander structure with  $d=250\text{ \AA}$  and  $R=38\ \Omega$ .

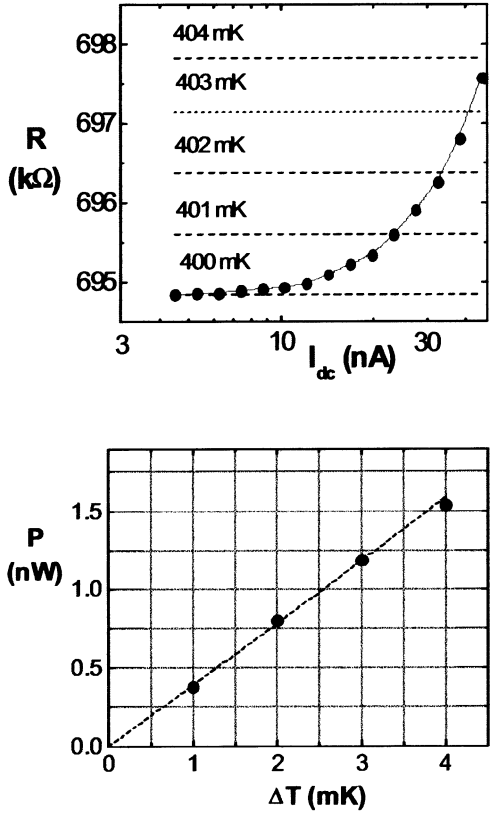


Fig. 5. For small electron overheating, the thermal conductivity between electrons and phonons can be found from the heat balance equation

$$\frac{P}{V} = G_{e-ph} \Delta T = \frac{C_e}{\tau_{e-ph}(T)} \Delta T, \quad (3)$$

where  $P = I_{dc}^2 R$  is the Joule power dissipated in a thin film of volume  $V$ , and  $\Delta T = T_{el} - T_{ph}$ .

The temperature dependences  $G_{e-ph}(T)$  measured for samples with different  $T_c$  are shown in Fig. 6. By assuming that the electron heat capacity in Hf films is the same as in bulk Hf [ $\gamma = 160\text{ W}/(\text{m}^3\text{K}^2)$ ], we can estimate the temperature dependence of the electron cooling time  $\tau_{e-ph}$  in these films (Fig. 7).

We compare the experimental data with the theoretical estimate of the electron cooling time in the “dirty” limit ( $q_T l \ll 1$ , where  $q_T$  is the

Fig. 5. Heating measurements at  $T=0.4\text{ K}$  and  $B=960\text{ G}$  for a sample with  $T_c=0.48\text{ K}$ . Top panel: the difference between the electron and phonon temperatures,  $\Delta T$ , is obtained from comparison of the zero-dc-bias  $R(T)$  (dashed horizontal lines) with the dependence  $R(I_{dc})$  measured at a fixed  $T=0.4\text{ K}$  (solid dots). Bottom panel: the thermal conductivity between electrons and phonons  $G_{e-ph}$  is a coefficient of proportionality between the Joule power  $P$  of the dc current released in the sample and the electron temperature increase  $\Delta T$  (for small electron overheating  $\Delta T \ll T$ ).

wave number of thermal phonons,  $l$  is the electron mean free path):

$$\tau_{e-ph} = 7.6 \cdot 10^{-4} \frac{M}{N_A} \frac{\rho}{R_Q} \frac{p_F^3 u_t^5}{(k_B T)^4 v_F} \quad (4)$$

Here  $N_A$  is the Avogadro constant,  $R_Q = \hbar/e^2 = 4.1 \text{ k}\Omega$  is the quantum resistance,  $u_t$  is the transverse sound velocity,  $M$  is the molar mass, and  $p_F$  and  $v_F$  are the Fermi momentum and velocity, correspondingly. Equation (4) has been derived from the expression  $\tau_{e-ph}(T)$  for electron scattering from transverse phonons [11]. The transverse phonons strongly dominate in electron-phonon interactions in the dirty limit. The condition of the dirty limit,  $q_T l \ll 1$ , is satisfied for our highly disordered Hf films at  $T \leq 50 \text{ K}$ . It has been also assumed in Eq. (4) that the electron scatterers (impurities, defects, etc.) are completely dragged by phonons [12]. Finally, we took into account the energy averaging of  $\tau_{e-ph}$  over the Fermi distribution of electrons (see, e.g., [13]).

Using parameters of bulk Hf ( $M = 178.5 \text{ g/mol}$ ,  $u_t = 1.97 \cdot 10^5 \text{ cm/s}$ ,  $p_F = 1.2 \cdot 10^{-19} \text{ g}\cdot\text{cm/s}$ ,  $v_F = 1.6 \cdot 10^8 \text{ cm/s}$ ), and the resistivity of the films studied ( $\rho = 0.1 \text{ m}\Omega\cdot\text{cm}$ ), we find  $\tau_{e-ph}(T) = 4.8 \cdot 10^{-8} \text{ s} \cdot [1\text{K}/T]^4$  (the solid line in Fig. 7). Below  $T \sim 0.5 \text{ K}$ , the

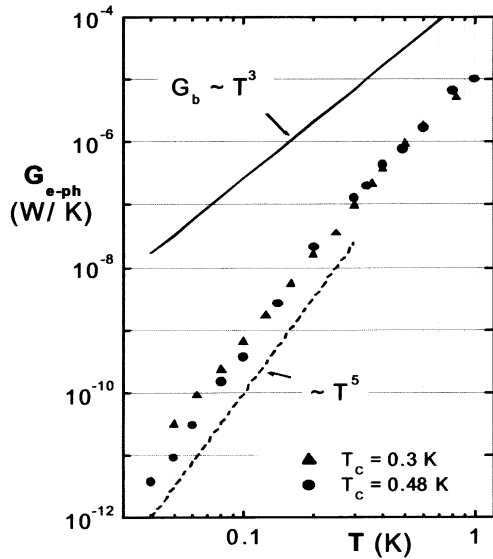


**Fig. 6.** Temperature dependences of the thermal conductivity  $G_{e-ph}$  for 250 Å-thick Hf meanders with the total area  $0.5 \text{ mm}^2$ , deposited on sapphire substrates. The solid line is the theoretical estimate for the thermal conductivity  $G_b$  of the metal-sapphire interface [7].

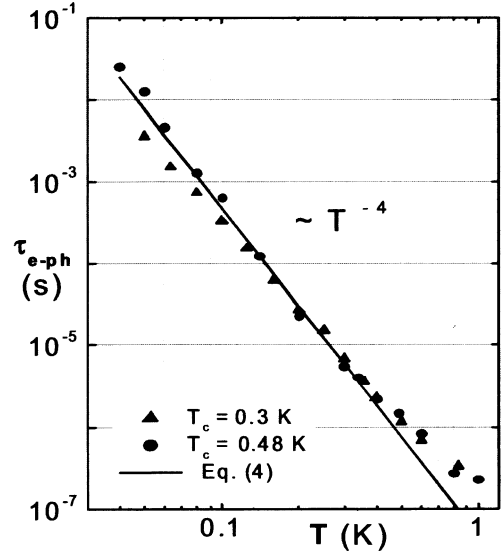


**Fig. 7.** The electron cooling time  $\tau_{e-ph}(T)$  for 250 Å-thick Hf films with the resistivity  $\rho = 0.1 \text{ m}\Omega\cdot\text{cm}$ . For the other three Hf films with similar  $\rho$ ,  $\tau_{e-ph}$  was in the range 4 – 9 ms at  $T = 40 \text{ mK}$ . The solid line is the dependence  $\tau_{e-ph}(T)$  (Eq. 4) calculated for Hf with  $\rho = 0.1 \text{ m}\Omega\cdot\text{cm}$ .

agreement between the experimental data and Eq. 4 is very impressive (note that this comparison does not involve *any* fitting parameters). At higher temperatures, the dependence  $\tau_{e-ph}(T)$  becomes slower than that predicted by Eq. 4.

Two important conclusions can be drawn from these experiments. Firstly, the experimental values of  $\tau_{e-ph}$  are sufficiently large to ensure record sensitivity of HEDDs at temperatures  $T < 0.3$  K. In fact, the value  $\tau_{e-ph} = 25$  ms measured at  $T = 40$  mK is, to our knowledge, the largest value of  $\tau_{e-ph}$  ever observed in metals. Secondly, the theory [11,12] provides a reliable estimate of  $\tau_{e-ph}$  in disordered metal films at millikelvin temperatures.

### ***Performance of a micron-size Hf HEDD***

Let us estimate the performance of HEDDs fabricated from a disordered hafnium film. Our measurements show that  $\tau_{e-ph}$  in these films can be as large as  $\sim 0.7$  ms at  $T = 0.1$  (see Fig. 7). For a HEDD with the sensor dimensions  $1 \times 1 \times 0.02 \mu\text{m}^3$ , we performed a computer modeling of basic characteristics. The modeling procedure, which is similar for all non-equilibrium hot-electron devices, is based on the heat balance equation:

$$\frac{\gamma V}{6\tau_{e-ph}(1K)}(T_e^6 - T^6) = V_b^2 / R(T_e) , \quad (5)$$

where  $V_b$  is the voltage across the device. The temperature-dependent device resistance,  $R(T_e)$ , was modeled as a smooth function with  $dR/dT|_{T=T_c} = R_n/\delta T_c$ , where  $R_n$  is the device normal resistance and  $\delta T_c$  is the width of the superconducting transition. The modeling was performed for  $T_c = 0.3$  K and  $T_c = 0.1$  K, assuming that one can fabricate Hf films with different critical temperatures by varying the film deposition conditions. The bath temperature was assumed to be equal  $T/2$  in both cases.

The fundamental sensitivity limit for the detector is set by fluctuations of the electron temperature (Eq. 2). Besides that, the Johnson-Nyquist noise and amplifier contribution should be considered. The two latter contributions can be minimized, if the responsivity of the detector is sufficiently high. Voltage biasing of superconducting bolometers [14] helps to obtain high current responsivity and, at the same time, to reduce significantly the time constant without affecting the sensitivity. This occurs due to a strong electro-thermal feedback in the bolometer bias circuit. The responsivity  $S_I = -(1/V_b)C/(C+1)$  can be expressed in terms of the self-heating parameter  $C = (V_b/R)^2(dR/dT)/G_{e-ph}$ , also known as the ETF loop gain. The latter parameter is always positive in superconducting bolometers because  $dR/dT > 0$ . In order to take advantage of the ETF effect, the bolometer should be driven by the bias current at  $T < T_c$  to the state with negative differential resistance (this bias current is very close to the critical current). Relationship between  $C$  and the differential resistance  $dV_b/dI$  [15]

$$C = (dV_b/dI - R)/(dV_b/dI + R) \quad (6)$$

shows that the self-heating parameter can be very large if  $-dV_b/dI \sim R$ . Under these conditions, the time constant of the bolometer is reduced by a factor  $(C+1)$ .

Figure 8 shows the results of modeling. The SQUID amplifier contribution was estimated as  $NEP_{SQUID} = i_n/S_I$  (for modern dc SQUID amplifiers, the typical noise  $i_n \sim 1$  pA/ $\sqrt{\text{Hz}}$  [16]). The Johnson-Nyquist noise contribution is given by  $NEP_J = (4k_B T_e V_b^2/R)^{1/2}/C$  [17]. This contribution can be significantly reduced due to a large value of parameter  $C$ . This occurs at low bias voltages, where fluctuations of the electron temperature dominate and the NEP is minimal. The device dc resistance is small

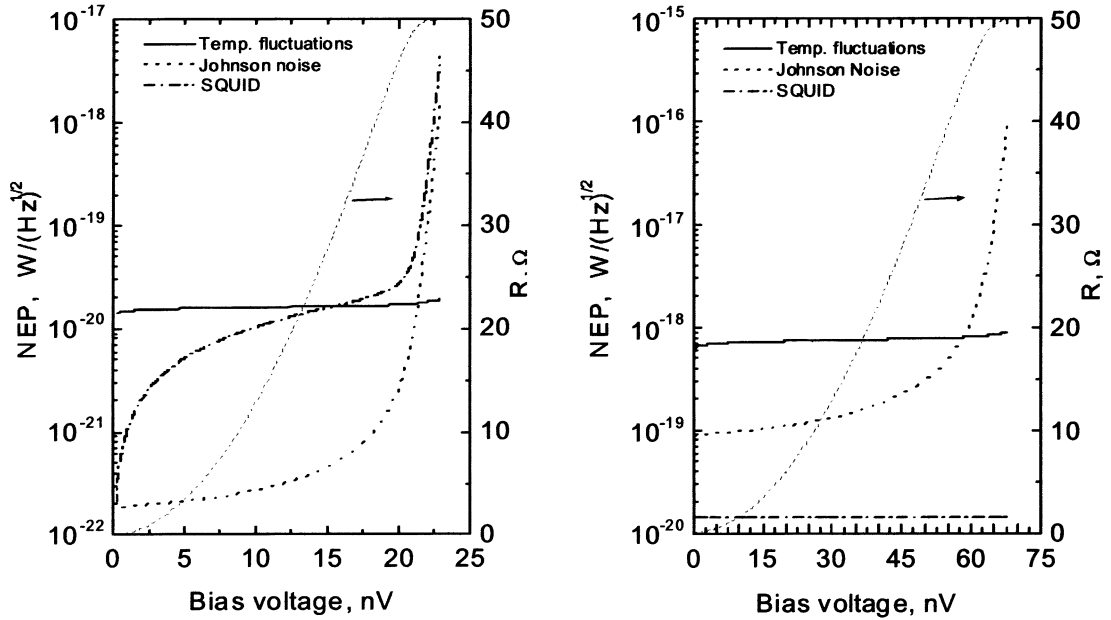


**Fig. 8.** Contributions of different noise sources to the total noise of the HEDD. Left panel:  $T_c = 0.1$  K, right panel:  $T_c = 0.3$  K. The detector should operate at low bias voltages to allow for a larger value of the self-heating parameter and a lower value of the device resistance. In this case, the temperature fluctuation noise dominates and the NEP is minimal.

( $\leq 1 \Omega$ ), which simplifies matching to a SQUID amplifier. At the same time, the device impedance at the signal frequency is high (50-100  $\Omega$ ), since the photon energy is much greater than the suppressed superconducting gap in the microbridge. At 0.1 K, the self-heating parameter can be as large as 30. In this case, the device time constant will be  $\tau = \tau_{e-ph}/(C+1) \sim 20 \mu\text{s}$ , and the energy resolution  $NEP\sqrt{\tau}$  will be  $7 \times 10^{-23}$  J, which corresponds to a  $\sim 100$  GHz photon energy. This sensitivity exceeds by far the performance estimated for the other types of direct detectors [10,18]. Even at  $T = 0.3$  K, the detector noise performance,  $NEP = 7 \times 10^{-19}$  W/ $\sqrt{\text{Hz}}$ , is better than that for the state-

of-the-art bolometers operating at or below 0.1 K. The time constant at this temperature is expected to be  $\sim 7 \mu\text{s}$ .

### **Acknowledgment.**

We thank O. Harnack for fabrication of photomasks. This research was supported by the Caltech President's Fund. The work at the Jet Propulsion Laboratory, California Institute of Technology, was supported by NASA.

### **REFERENCES**

1. B. S. Karasik, W. R. McGrath, H. G. LeDuc, and M. E. Gershenson, "A Hot-Electron Direct Detector for Radioastronomy", *Supercond. Sci. Technol.* **12**, 745 (1999).
2. M. Shao *et al.*, "Space-based interferometric telescopes for the far infrared", presented at the *SPIE Int. Symp. on Astronomical Telescopes and Instrumentation 2000*.
3. J. C. Mather, S. H. Moseley, Jr., D. Leisawitz, E. Dwek, P. Hacking, M. Harwit, L. G. Mundy, R. F. Mushotzky, D. Neufeld, D. Spergel, and E. L. Wright, "The Submillimeter Frontier: a Space Science Imperative", <http://xxx.lanl.gov/astro-ph/9812454>.
4. J. J. Bock, J. Glenn, S. M. Grannan, K. D. Irwin, A. E. Lange, H. G. LeDuc, and A. D. Turner, "Silicon nitride micromash bolometer arrays for SPIRE", *Proc. SPIE* **3357**, 297 (1998).
5. J. M. Gildemeister, A. T. Lee, and P. L. Richards, "A fully lithographed voltage-biased superconducting spiderweb bolometer", *Appl. Phys. Lett.* **74**, 868 (1999).
6. B. S. Karasik, W. R. McGrath, M. E. Gershenson, and A. V. Sergeev, "Photon-noise limited direct detector based on disorder controlled electron heating", *J. Appl. Phys.*, **87**, N10 (2000).
7. E. T. Swartz and R. O. Pöhl, "Thermal boundary resistance", *Rev. Mod. Phys.* **61**, 605 (1989).
8. E. M. Gershenzon, M. E. Gershenzon, G. N. Goltsman, A. D. Semenov, and A. V. Sergeev, "On the limiting characteristics of high-speed superconducting bolometers", *Sov. Phys. - J. Tech. Phys.* **34**, 195 (1989).
9. A. Sergeev and M. Reizer, "Photoresponse mechanisms of thin superconducting films and superconducting detectors", *Int. J. Mod. Phys.* **10**, 635 (1996).
10. M. Nahum and J. M. Martinis, "Ultrasensitive-hot-electron microbolometers", *Appl. Phys. Lett.* **63**, 3075, (1993).
11. M. Yu. Reizer and A. V. Sergeev, *Sov. Phys.-JETP* **63**, 616 (1986); J. Rammer and A. Schmid, *Phys. Rev. B* **34**, 1352 (1987).
12. A. Sergeev and V. Mitin, "Electron -phonon interaction in disordered conductors: Static and vibrating scattering potentials", *Phys. Rev. B.* **61**, 6041 (2000).

13. K. S. Il'in, N. G. Ptitsina, A. V. Sergeev, G. N. Goltsman, E. M. Gershenzon, B. S. Karasik, E. V. Pechen, and S. I. Krasnosvobodtsev, "Interrelation of resistivity and inelastic electron-phonon scattering rate in impure NbC films", *Phys. Rev. B* **57**, 15623 (1998).
14. K. D. Irwin, "An application of electrothermal feedback for high resolution cryogenic particle detection", *Appl. Phys. Lett.* **66**, 1998 (1995); A. T. Lee, P. L. Richards, S. W. Nam, B. Cabrera, and K. D. Irwin, "A superconducting bolometer with strong electrothermal feedback", *Appl. Phys. Lett.* **69**, 1801 (1996).
15. H. Ekström, B.S. Karasik, E.L. Kollberg, and S. Yngvesson, "Conversion gain and noise of niobium superconducting hot-electron-mixers", *IEEE Trans. on Microwave Theory and Technique* **43**, 938 (1995).
16. M. Frericks, H.F.C. Hoevers, P.de Groene, W.A. Mels, and P.A.J. de Korte, "Trade-off study of the SQUID read-out for hot-electron micro calorimetry", *J. Phys. IV France* **8**, Pr3-233 (1998); V. Polushkin, D. Glowacka, R. Hart, and J.M. Lumley, "Broadband SQUID amplifiers for photonic applications", *IEEE Trans. Appl. Supercond.* **9**, 4436 (1999).
17. J.C. Mather, "Bolometer noise: nonequilibrium theory", *Appl. Opt.* **21**, 1125 (1982).
18. A.N. Vystavkin, D.V. Shouvaev, L.S. Kuzmin, M.A. Tarasov, E. Andrestedt, M. Wilander, and T. Claeson, "Normal-metal hot-electron bolometer with Andreev reflection from superconductor boundaries", *Sov. Phys.-JETP* **88**, 598 (1999).

# Quasioptical High- $T_c$ Superconductor Josephson Mixer at Terahertz Frequencies

**Marian Darula**

Institute of Thin Film and Ionotechnology (ISI), Research Center Juelich, 52425  
Juelich, Germany

**Alex D. Semenov**

Physical Department, State Pedagogical University of Moscow, 119891 Moscow,  
Russia

**Heinz-Wilhelm Hbiers, Josef Schubert**

DLR Institute of Space Sensor Technology and Planetary Exploration, D-  
12489 Berlin, Germany

Mixers based on Josephson junctions from conventional superconductor materials have demonstrated excellent performance at subgap frequencies. The advantages of Josephson mixers are low optimal power of the local oscillator and large intermediate frequency bandwidth but their noise temperature increases dramatically at frequencies corresponding to the energy gap of the superconductor, which is typically below 1 THz for widely used materials. The large energy gap of oxide superconductors makes them promising candidates for development of terahertz Josephson mixers. Here we report on experimental study of the quasioptical mixer utilizing bicrystal Josephson junction from high-transition-temperature  $\text{YBa}_2\text{Cu}_3\text{O}_{7-\delta}$  film. Junctions with a width of 2  $\mu\text{m}$  were fabricated from 100 nm thick laser ablated films on bicrystal MgO substrates and had the and the  $J_C R_n$  product of about 2 mV at 4.2 K. The planar complementary logarithmic spiral antenna incorporated into co-planar waveguide was patterned from 200 nm thick gold film thermally evaporated in situ on top of the  $\text{YBa}_2\text{Cu}_3\text{O}_{7-\delta}$  film. The mixer chip was clamped to the extended hemispherical silicon lens. Performance of the mixer was investigated at 4.5 K bath temperature. We used FIR laser as a local oscillator at frequencies 0.698 and 2.52 THz. System noise temperature (DSB) was determined from Y-factor measured with 300 K and 77 K loads. At 0.698 THz the lowest noise temperature 1750 K was observed when the mixer was biased with the fixed current to the region in the vicinity of either the first Shapiro step or the critical current. Between these two bias points the noise temperature increased to  $\approx 20000$  K. As function of the local oscillator power the noise temperature reached the minimum when the critical current was suppressed to the half of its equilibrium value. Power of the local oscillator absorbed by the mixer at optimal operation was of the order 100 nW. The present design of our antenna limits the upper operation frequency to the value of 1.8 THz. Nevertheless, we clearly observed Shapiro steps at the frequency 2.52 THz. Bearing in mind an improved design of the antenna, we estimate the 3000 K DSB noise temperature at this frequency.

# Systematic Study of IF Bandwidth in HTS Hot-Electron Bolometer Mixers

Oliver Harnack, Konstantin Ilin, and Michael Siegel

*Institute of Thin Film and Ion Technology, Research Center Juelich, 52425 Juelich, Germany*

Boris S. Karasik and William R. McGrath

*Center for Space Microelectronics Technology, Jet Propulsion Laboratory*

*California Institute of Technology, Pasadena, CA, USA*

Gert de Lange

*Space Research Organization of the Netherlands, Division Sensor Research and Technology, 9700 AV Groningen, The Netherlands*

The hot-electron bolometer (HEB) mixer made from a high- $T_C$  superconductor (HTS) thin film was introduced recently as an alternative to a Schottky mixer at THz frequencies. The mixer performance depends on the total thermal conductance for heat removal from the phonon subsystem due to either phonon escape to the substrate or phonon diffusion to the normal metal electrodes. We present a systematic study of the length, thickness, temperature, and local oscillator (LO) frequency dependencies of the thermal relaxation times, as inferred from the -3dB intermediate frequency (IF) bandwidth of HTS HEB mixers on MgO and CeO<sub>2</sub>/sapphire substrates.

While a significant length dependence was not found, the bandwidth of a 30 nm thick device at 65 K increased from about 100 MHz to 420 MHz as the device thickness was reduced to 10 nm in accordance with the two-temperature (2T) model.

As reported earlier, at temperatures close to  $T_C$  the IF bandwidths increased to unexpected high values of about 2-3 GHz, and as discovered recently, the IF bandwidth also strongly depends on the bias voltage in this regime. However, these effects gradually vanish as the LO frequency was increased from 1 GHz to 100 GHz, 300 GHz and 480 GHz. At 480 GHz, pure 2T model behavior was observed. We attribute these frequency-dependent effects to the dynamics of vortices in the microbridge. The impact of the device geometry and the use of buffer layers for the optimization of the total thermal conductance will be discussed.

# **YBa<sub>2</sub>Cu<sub>3</sub>O<sub>7-δ</sub> Hot-Electron Bolometer Mixer at 0.6 THz**

**S.Cherednichenko<sup>1</sup>, F.Rönnung<sup>2</sup>, G.Gol'tsman<sup>3</sup>, E.Kollberg<sup>1</sup> and D.Winkler<sup>2</sup>**

<sup>1</sup> Department of Microelectronics, Chalmers University of Technology, Göteborg S-412 96, Sweden

<sup>2</sup> Department of Physics, Chalmers University of Technology and Göteborg University, Göteborg S-412 96, Sweden

<sup>3</sup> Department of Physics, Moscow State Pedagogical University, Moscow 119435, Russia

## ***Abstract***

We present an investigation of hot-electron bolometric mixer based on a YBa<sub>2</sub>Cu<sub>3</sub>O<sub>7-δ</sub> (YBCO) superconducting thin film. Mixer conversion loss of -46 dB, absorbed local oscillator power and intermediate frequency bandwidth were measured at the local oscillator frequency 0.6 THz. The fabrication technique for nanoscale YBCO hot-electron bolometer (HEB) mixer integrated with a planar antenna structure is described.

## ***Introduction***

The hot-electron phenomenon has been proved to be an efficient mixing mechanism for the terahertz range [1]. Heterodyne receivers based on NbN and Nb hot-electron bolometric (HEB) mixers have reached a noise level as low as 20 quantum limits ( $h\nu/2$ ) for frequencies up to 5 THz with instantaneous bandwidth of 4 GHz to 9 GHz [2,3, 4]. At the present time they are the most sensitive broadband receivers for terahertz frequencies. Although HEB mixers based on high- $T_c$  films do not compete with low- $T_c$  mixers with respect to sensitivity, they have much larger instantaneous bandwidth and need much simpler (and, therefore, lighter) refrigeration systems, that makes it possible to use them in airborne and space radiotelescopes. Simple fabrication technology, real impedance, a possibility of low optimum local oscillator power (which is simply proportional to the mixer volume) makes YBCO HEB mixers to be competing with Schottky diode mixers.

The hot-electron phenomenon consists of the heating of electrons in a superconducting film by radiation. Beating of the local oscillator (LO) and the signal

waves causes oscillations of the electron temperature, and, therefore, of the load voltage, at an intermediate frequency ( $\omega_{IF}=\omega_{LO}-\omega_S$ ). Since the impedance of the HEB mixer is the dominantly real, the intermediate frequency (IF) bandwidth of the mixer is limited only by the electron temperature relaxation rate. For such superconductors as YBCO with strong electron-phonon coupling ( $\tau_{e-ph}=1.1$  ps [5]) and large phonon to electron specific heat ratio ( $c_p/c_e\approx 40$ ) electrons are effectively cooled via the electron-phonon interaction. The theoretically predicted IF bandwidth for a YBCO HEB mixer is  $1/(2\pi\tau_{e-ph})=140$  GHz. Due to the film-substrate boundary resistance significant phonon heating occurs in the film. In YBCO films this effect is much stronger than in low- $T_c$  films, since the complicated composition of YBCO does not allow fabrication of ultrathin films with high critical temperature and critical current density. This effect limits the IF spectrum on the lower side to 2 GHz, which can not be treated as a significant disadvantage of YBCO HEB mixers. A much more important effect of the phonon heating is an increase of the mixer conversion loss in the IF bandwidth of interest (i.e. 2-140 GHz). According to theoretical models of the HEB mixer phonon cooling rate could be increased reducing mixer in-plane size and film thickness. Mixer volume reduction also leads to a decrease of LO power request that is quite important in terahertz range where power of solid state radiation sources is quite limited.

### ***Device fabrication and measurement set-up***

In the paper we present a technology for fabrication of sub-micrometer size YBCO mixers integrated into a planar antenna structure. YBCO films on  $\text{LaAlO}_3$  substrates were deposited by a pulsed laser ablation technique in an oxygen atmosphere. The deposition occurred at the substrate temperature  $800^\circ\text{C}$  and the oxygen pressure 0.8 mbar. For the film oxidation the oxygen pressure was increased up to 1 bar and substrate temperature was ramped down with the rate  $15^\circ\text{C}/\text{min}$ . At the room temperature 20 nm gold layer was in-situ deposited. The critical temperature of the films was inductively measured and was around 88-89 K. Using an e-gun evaporation system 200 nm ex-situ gold layer was deposited to form an antenna and IF contacts. As an antenna we used self-complimentary spiral antenna design, which performed well with NbN HEB mixer and has good coupling efficiency with a Gaussian beam [6].

The thick gold layer has also to prevent any deterioration of superconducting properties of the YBCO film during the next fabrication steps. On top of YBCO/gold double-layer two small pads and two arm spiral structure were made using electron-beam lithography, titanium evaporation (40 nm) and standard lift-off procedure. At the next step with an e-beam lithography and a lift-off a carbon pad as thick as 50 nm was made inside the area marked by rectangular in Fig.1. With these Ti and C masks the gold and YBCO films were ion-milled down to the substrate. After that, the

carbon mask was removed in RF oxygen plasma and the substrate was moved into the ion-milling system again. During the second ion-milling process the gold layer between two small pads was removed down to YBCO film. SEM picture of the device is shown in Fig.1.

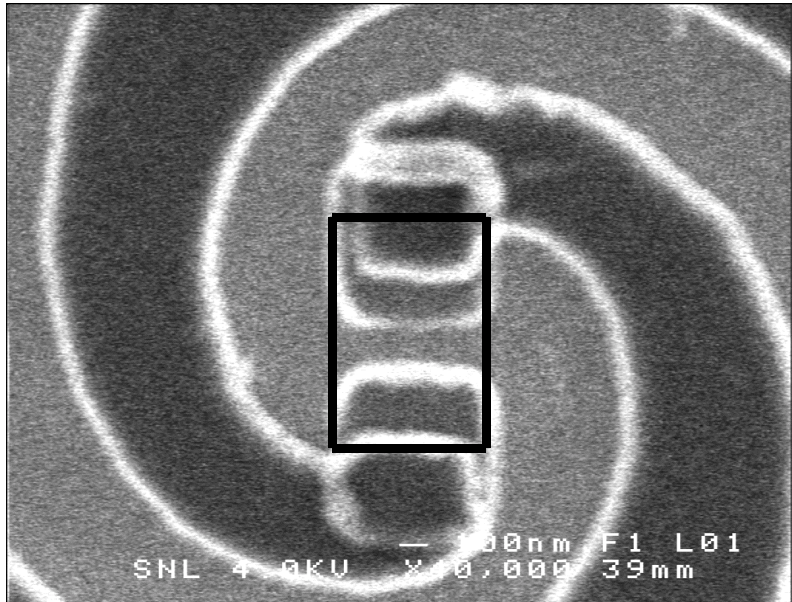


Fig.1 SEM image of a spiral antenna coupled YBCO mixer. The rectangular marks the bolometer area.

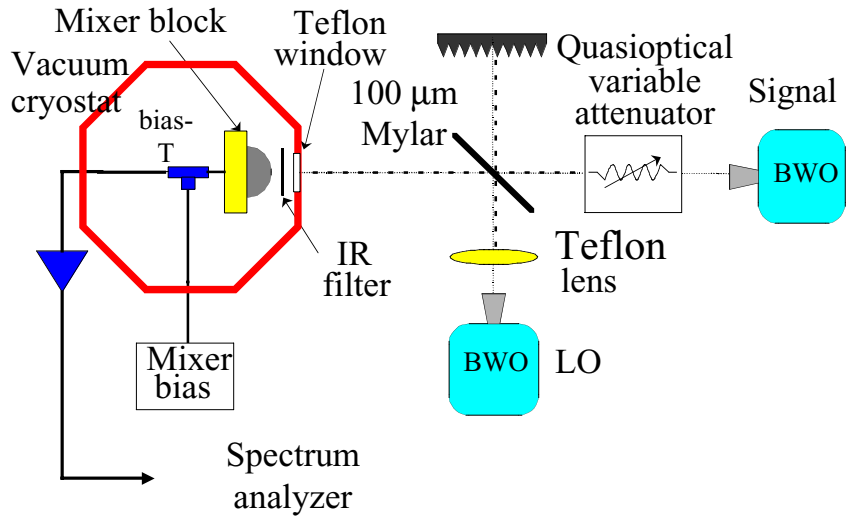


Fig.2. 600 GHz heterodyne measurements set-up.

For the heterodyne measurements we used a set-up, which is shown in Fig.2. The mixer was attached to a Si elliptical lens and mounted in a vacuum cryostat cooled by liquid nitrogen. Two backward wave oscillators (BWO) were used as a local oscillator and a signal source. The frequency of the signal BWO was fixed at 600 GHz and the LO frequency was tuned. At each frequency point the LO power was kept at the same level. For relative measurements of the LO power we used the same mixer as a direct detector. The LO radiation was chopped with low frequency (20 Hz) and a detected signal was measured by a lock-in amplifier connected into the bias circuit. The same technique was also used for the measurements of the signal power relatively to the LO power. The absolute absorbed LO power was measured by isothermal method, which is well described in [3]. The maximum absorbed LO power, which we could obtain was 8  $\mu$ W.

## ***Results***

Mixer IV-curves are shown in Fig.3. At temperature 77 K the mixer conversion efficiency increased considerably as the voltage exceeded 30 mV. But it was accompanied with a very high output noise level, which is attributed to the instability of the resistive state in that region (this region is not shown in the figure). At higher temperatures the output noise becomes smaller, but conversion efficiency decreases. We measured the mixer conversion loss (at the intermediate frequency 450 MHz) at different temperatures, which correspond to a reasonable noise level. The minimum conversion loss was 46 dB, which could be improved by decreasing the ambient temperature, but at the cost of an increase of the output noise. Conversion loss did not depend much on the bias voltage and in a quite large voltage region conversion loss did not drop more than 2 dB. We found that with a decreasing of LO power the IF signal goes down linearly, which shows that the LO power is far from the optimum point. An increasing of the LO power can improve conversion performance of the mixer.

The IF spectrum of the mixer was measured in the range from 200 MHz to 6 GHz and the result is depicted in Fig.4. The hot-electron mode, when only the electron temperature is oscillating, is clearly observed in the range from 3 GHz to 6 GHz. The upper IF range was limited just by bandwidth of the bias-T.

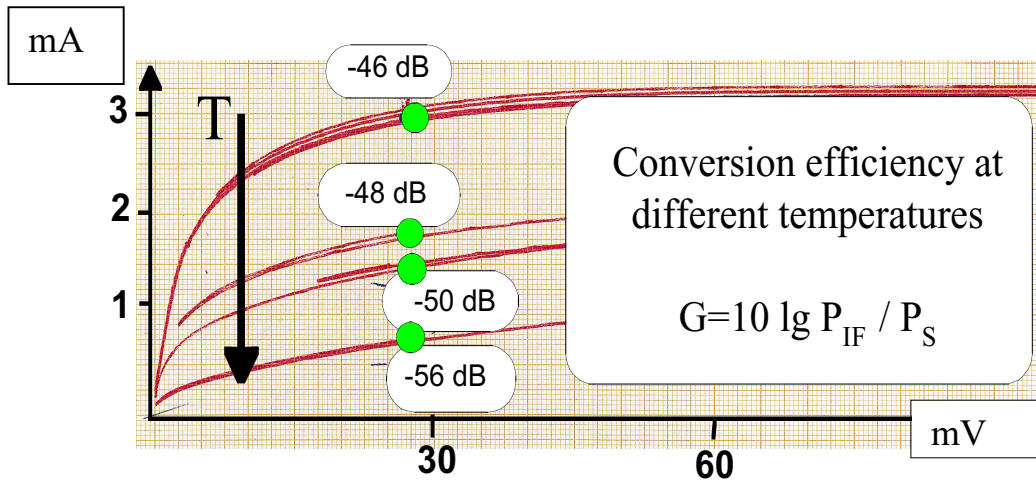


Fig.3 IV-curves of YBCO HEB mixer at different temperatures.

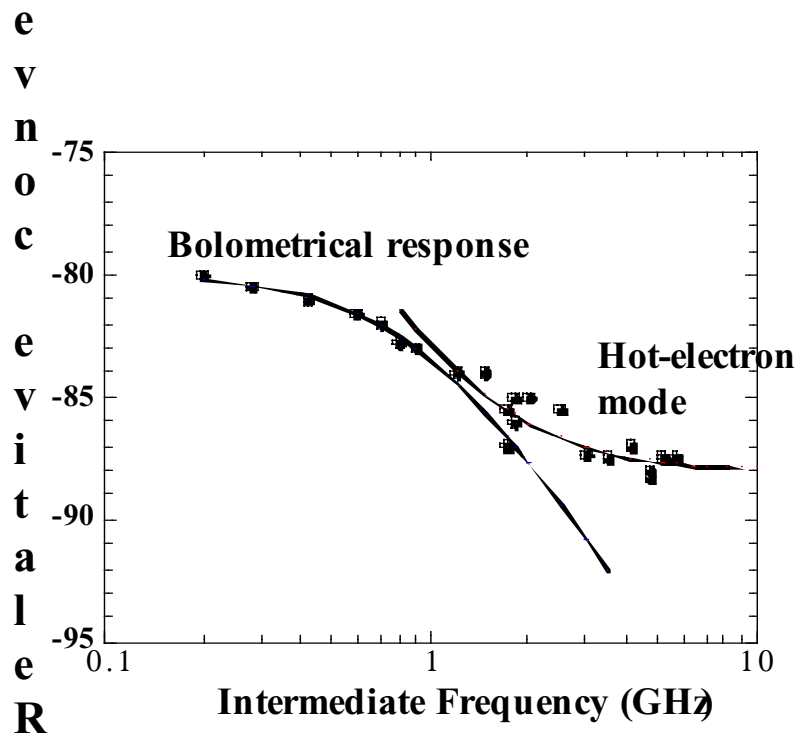


Fig.4. Intermediate frequency spectrum of YBCO HEB mixer measured at LO frequency 600 GHz.

## **Conclusion**

The mixer conversion loss 46 dB was obtained at 8  $\mu$ W LO power. The hot-electron mode in the IF spectrum, previously observed at IR range, is also observed at terahertz frequencies. The obtained results show that the YBCO HEB mixer can be used at the terahertz range.

## **References**

1. E.M.Gershenson, G.N.Gol tsman, I.G.Gogidze, Yu.P.Gousev, A.I.Elant ev, B.S.Karasik, and A.D.Semenov, *Sov. J.Superconductivity* 3, 1582 (1990).
2. P.Yagoubov, M.Kroug, H.Merkel, E.Kollberg, J.Schubert and H.-W. Hueberts, *Supercond.Sci.Technol.* **12** (1999), 989
3. H.Ekstrom, E.Kollberg, P.Yagoubov, G.N.Gol tsman, E.M.Gershenson and S.Yngvesson, *Appl.Phys.Lett.* **70** (24), 1997, 3296.
4. R. Wyss, B. Karasik, W. McGrath, B. Bumble, H. LeDuc, "Noise and Bandwidth Measurements Of Diffusion-Cooled Nb Hot-Electron Bolometer Mixers at Frequencies Above the Superconductive Energy Gap", *Proc. 10th Int. Symp. on Space Terahertz Technology*, Charlottesville, VA, 214, 1999.
5. M.Lindgren, M.Currie, C.Williams, T.Y.Hsiang, P.M.Fauchet, R.Sobolewsky, S.H.Moffat, R.A.Hughes, J.S.Preston, F.A.Hegmann, Intrinsic picosecond response times of Y-Ba-Cu-O superconducting photoresponse , *Appl.Phys.Lett.* v.74, n.6, p.853, 1999.
6. P. Yagoubov, M. Kroug, H. Merkel, E. Kollberg, J. Schubert, H.-W. Huebers, G. Schwaab, G. Gol tsman, and E. Gershenson, NbN Hot Electron Bolometric Mixers at Frequencies Between 0.7 and 3.1 THz , *Proc. 10th Int. Symp. on Space Terahertz Technology*, Charlottesville, VA, 214, 1999.

# Externally Phase Locked Submm-Wave Flux Flow Oscillator for Integrated Receiver

V.P. Koshelets<sup>1</sup>, A.B. Ermakov<sup>1</sup>, S.V. Shitov<sup>1</sup>, P.N. Dmitriev<sup>1</sup>, L.V. Filippenko<sup>1</sup>,  
A.M. Baryshev<sup>2</sup>, W. Luinge<sup>2</sup>, J. Mygind<sup>3</sup>, V.L. Vaks<sup>4</sup>, D.G. Pavel' ev<sup>5</sup>

<sup>1</sup>Institute of Radio Engineering and Electronics (IREE), Russian Academy of Sciences,  
Mokhovaya 11, GSP-3, 103907 Moscow, Russia (e-mail: valery@hitech.cplire.ru)

<sup>2</sup>Space Research Organization of the Netherlands (SRON)  
P.O. Box 800, 9700 AV Groningen, the Netherlands

<sup>3</sup>Department of Physics, Technical University of Denmark,  
B 309, DK-2800 Lyngby, Denmark

<sup>4</sup>Institute for Physics of Microstructure, Russian Academy of Sciences,  
GSP-105, 603600 Nizhny Novgorod, Russia

<sup>5</sup>Nizhny Novgorod State University,  
Gagarin Avenue 23, 603600 Nizhny Novgorod, Russia

## ABSTRACT

The combination of narrow linewidth and wide -band tunability makes the Josephson Flux Flow Oscillator (FFO) a perfect on-chip local oscillator for integrated submm -wave receivers. A noise temperature of about 100 K (DSB) has been achieved for the integrated receiver with the FFO operating near 500 GHz. An instantaneous bandwidth of 15 – 20 % is estimated from Fourier transform spectroscopy (FTS) and heterodyne measurements. The far-field antenna beam is measured as  $\approx f/10$  with sidelobes below -16 dB which is suitable for coupling to a telescope antenna. For application in spectral radio astronomy, besides low noise temperature and good beam pattern, also a local oscillator with narrow-linewidth and long-term stability is required. Recently the feasibility of phase locking of the FFO to an external reference oscillator was demonstrated experimentally. A spectral linewidth as low as 1 Hz (determined by the resolution of the spectrum analyzer) has been measured in the frequency range 270 - 440 GHz relative to a reference oscillator. This linewidth is far below the fundamental level given by shot and thermal noise of the free-running tunnel junction. A new technique for linewidth measurements and FFO phase locking has been devised and put to use. This method employs an off-chip harmonic multiplier that considerably simplifies the design of the chip for a fully superconductive integrated phase-locked receiver. The linewidth of Nb-AlO<sub>x</sub>-Nb FFOs has been carefully studied in the frequency range 250 - 600 GHz. Based on frequency measurements the FFO I-V curve has been reconstructed with an accuracy better than 1 nV. Finally, the results of FFO phase noise measurements are also presented and discussed.

## 1. Introduction

Light-weight and compact ultrasensitive submm-wave Superconducting Integrated Receivers (SIRs) with low power consumption [1,2] are very attractive for both radio-astronomical research and remote monitoring of the Earth atmosphere. The new ambitious radio-astronomy multi-dish projects (e.g. , ALMA) would gain considerably by using single-chip SIRs due to their lower price and better serviceability as compared to conventional approaches. Present single-chip superconducting receivers comprise a SIS-mixer with a quasioptical antenna and a superconducting local oscillator (LO).

Presently, a Flux Flow Oscillator (FFO) based on unidirectional flow of magnetic vortices in a long Josephson tunnel junction [3] looks most promising as LO for on-chip integration with a SIS mixer. Nb-AlO<sub>x</sub>-Nb FFOs which have been successfully tested from about 120 to 700 GHz - gap frequency of Nb - deliver sufficient power ( $\approx 1 \mu\text{W}$  at 450 GHz) to pump a SIS mixer. Both frequency and power of the FFO can be tuned electronically [4,5]. A receiver noise temperature below 100 K (DSB) has been achieved for a SIR with an internal FFO operated in the frequency range 480 - 520 GHz [1,2]. This means that the performance of the SIS mixer is close to the quantum limit. A FFO can be fabricated on the same trilayer - and by the same technological procedure - as a SIS mixer. Further, the complexity of a FFO circuit is much lower than known Josephson junction array oscillators. A free-running FFO linewidth considerably below 1 MHz has been measured near 450 GHz [6-8]. Recently the feasibility of phase locking of the FFO to an external oscillator was demonstrated experimentally [7, 8].

In this report we present an overview of the basic FFO properties as well as the latest FFO linewidth measurements - including FFO phase noise. We also describe a new technique for linewidth measurements and FFO phase locking.

## 2. Flux Flow Oscillators: dc properties and linewidth measurements.

The FFO [3] is a *long* overlap Josephson tunnel junction in which an applied dc magnetic field and a uniformly distributed dc bias current,  $I_b$ , drive a unidirectional flow of fluxons, each containing one magnetic flux quantum,  $\mathbf{F}_0 = h/2e \approx 2 \cdot 10^{-15}$  Wb. Symbol  $h$  is Planck's constant and  $e$  is the electron charge. A dc current,  $I_{CL}$ , in an external coil or an integrated control line generates the magnetic field,  $B_{appl}$ , applied perpendicular to the FFO. According to the Josephson relation a FFO biased at voltage  $V$  oscillates with frequency  $f = (2\mathbf{p}/\mathbf{F}_0) V$  (about 483.6 GHz/mV). Velocity and density of the fluxons, and thus the power and frequency of the emitted mm-wave signal can be adjusted by  $I_b$  and  $I_{CL}$ .

The FFOs considered below are long Nb-AlO<sub>x</sub>-Nb tunnel junctions with overlap geometry (see inset in Fig. 1). The length,  $L$ , and the width,  $W$ , are about 500  $\mu\text{m}$  and 3  $\mu\text{m}$ , respectively. The critical current density,  $j_c$ , is in the range 4 - 8 kA/cm<sup>2</sup>, which corresponds to a specific resistance,  $R_n * L * W \approx 50 - 25 \Omega \mu\text{m}^2$  (the Josephson penetration depth  $\mathbf{I}_J \approx 6 - 4 \mu\text{m}$ ). The tunnel barrier usually is formed in a long window of a relatively thick insulation layer (200 - 350 nm, SiO<sub>2</sub>) between two superconducting Nb films (base and counter electrodes). One of the electrodes also is employed as control line.

A typical set of current-voltage characteristics (IVCs) of the FFO, measured at different magnetic fields ( $I_{CL}$ ), is shown in Fig. 1. Simultaneously with recording the IVCs, the power delivered by the FFO to the integrated SIS detector was measured by a data acquisition system, IRTECON [1, 2]. The criterion for sufficient pumping is a pre-set change of the subgap tunnel current at  $V = 2$  mV,  $\mathbf{D}$ , relative to the gap current  $I_g$  of the SIS detector, due to photon assistant tunneling (PAT). A  $\mathbf{D}/I_g$ -ratio exceeding 0.25 was obtained for FFO voltages from 550 to 1070  $\mu\text{V}$  (see arrow in Fig. 1). This corresponds to a frequency range 270 - 520 GHz. Actually, the operational frequency range is limited by the matching circuit and the SIS tuning structure rather than by the FFO itself.

A detailed study of long Josephson junctions intended for wide-band integrated oscillators was performed [9]. At large fields and voltages (Fig. 1) one can see the smooth so-called Flux Flow Step (FFS), the voltage of which is proportional to  $I_{CL}$ . At moderate fields the FFS splits into a series of resonant Fiske steps (FS) [10]. This resonant mode exists up to a specific "boundary" voltage,  $V_{JSC}$ , at which a "bump" in dc current appears. As also seen from Fig. 1 for  $V > V_{JSC}$  the FFS becomes smooth and with increasing magnetic field it persists up to the gap voltage. It should be noted that this "boundary" is typical for all investigated FFOs with high current density ( $j_c > 1 \text{ kA/cm}^2$ ). This feature neither depends significantly on the junction geometry and its dimensions nor on the coupling to the external microwave circuit.

The boundary voltage is about 930  $\mu\text{V}$  which is 1/3 of the superconductor gap voltage  $V_g$  for Nb-AlO<sub>x</sub>-Nb tunnel junctions. This threshold behavior has been explained

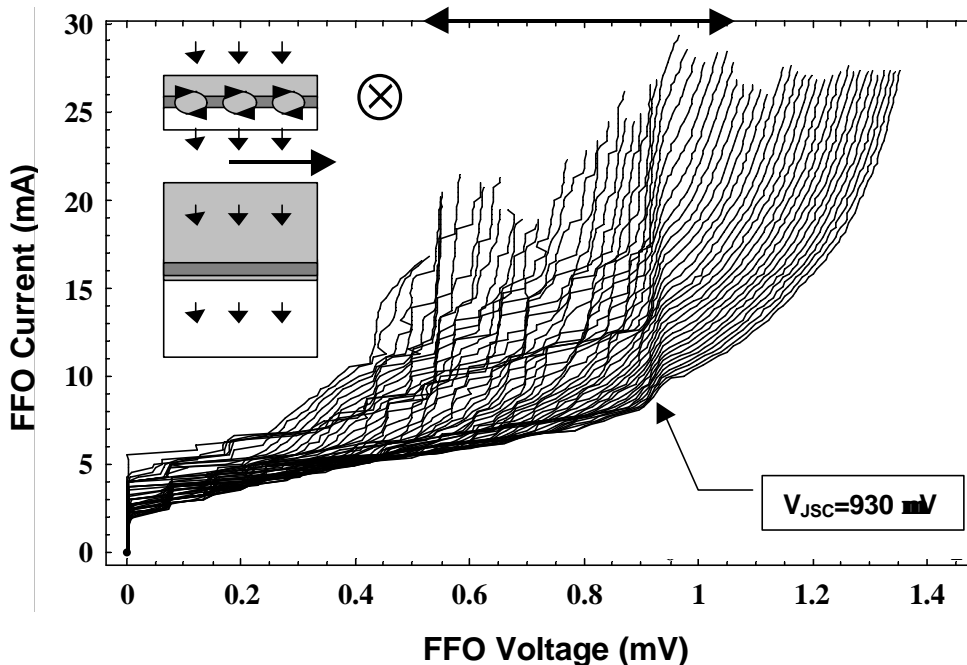


**Fig. 1.** IVCs of a Nb-AlO<sub>x</sub>-Nb FFO recorded at different magnetic fields. Note the abrupt change of the IVC at the boundary voltage  $V_{JSC} \approx 930 \mu\text{V}$ . Insets show the cross section of the long junction with driven vortices (top) and its overlap geometry (bottom).

by Josephson self-coupling (JSC) [9]. The JCS effect is basically absorption of *ac* radiation by the quasi-particles in the cavity of the long junction. The JSC results in current bumps (similar to PAT quasi-particle steps in a SIS mixer) at  $V_{JSC} = V_g/(2n + 1)$ , which gives  $V_{JSC} = V_g/3$  for  $n = 1$ . The effect of self-pumping explains not only the bumps observed in the FFO IVC, but also the abrupt merge of Fiske steps (suppression of the resonant Fiske mode for  $V \approx V_g/3$ ) caused by a strong increase of the internal damping due to quasi-particle tunneling [9].

A specially designed integrated circuit is used for linewidth measurements [7, 8]. It comprises FFO, SIS mixer and elements for rf coupling - see Fig. 2. The signal from the FFO is applied to the harmonic mixer (a SIS junction operated in Josephson or quasiparticle mode) along with the signal from a frequency synthesizer,  $f_{SYN} \approx 10$  GHz. In order to prevent the synthesizer signal (as well as its lower harmonics) from reaching the FFO a high-pass microstrip filter with cut-off frequency about 200 GHz is inserted between the FFO and the harmonic mixer. The intermediate frequency (IF) signal with frequency,  $f_{IF} = \pm (f_{FFO} - n f_{SYN})$  is boosted first by a cooled amplifier and then by a room-temperature amplifier for further use in the PLL system. A part of the signal is applied via a directional coupler to a spectrum analyzer which is also phase locked to the synthesizer using a common reference signal at 10 MHz. Thus, the spectrum observed in the IF channel, as well as the phase noise evaluated from these data, is the difference between the frequency of the FFO signal and the *n*-th harmonic of the synthesizer frequency.

The output signal of the PLL system - proportional to the phase difference - is returned via the Loop Bandwidth Regulator (maximum bandwidth about 10 MHz) to the FFO via a coaxial cable terminated with a cold 50  $\Omega$  resistor mounted on the chip bias plate. It was proven experimentally that the PLL system can considerably narrow the FFO linewidth if  $Df_{AUT}$  (measured at the -3 dB level) is smaller than the PLL regulation bandwidth,  $B_{PLL}$ . Figure 3 [7] shows typical IF power spectra of the phase locked FFO

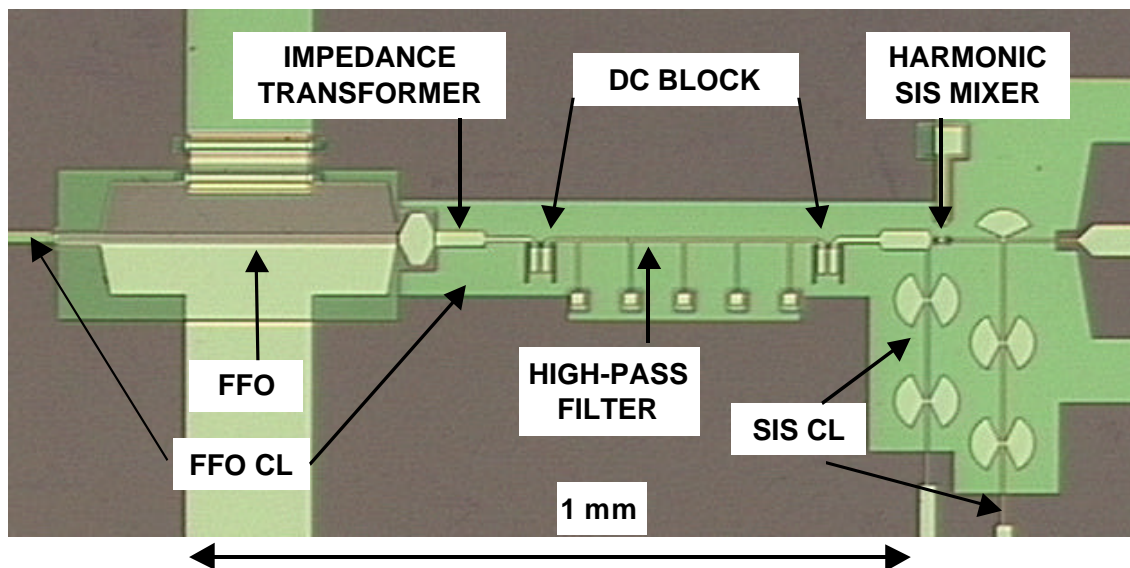


**Fig. 2.** Central part of the microcircuits used for FFO linewidth measurements.

measured at  $f_{FFO} = 439$  GHz for different settings of the spectrum analyzer. A FFO linewidth as low as 1 Hz is presented in Fig. 3b; it is limited by the resolution bandwidth of the spectrum analyzer. This experimental results show that the FFO linewidth can be reduced below the value determined by the fundamental shot and thermal fluctuations of the free-running tunnel junction. To our knowledge it is the first time such a dramatic reduction of the initial linewidth of a Josephson oscillator has been achieved.

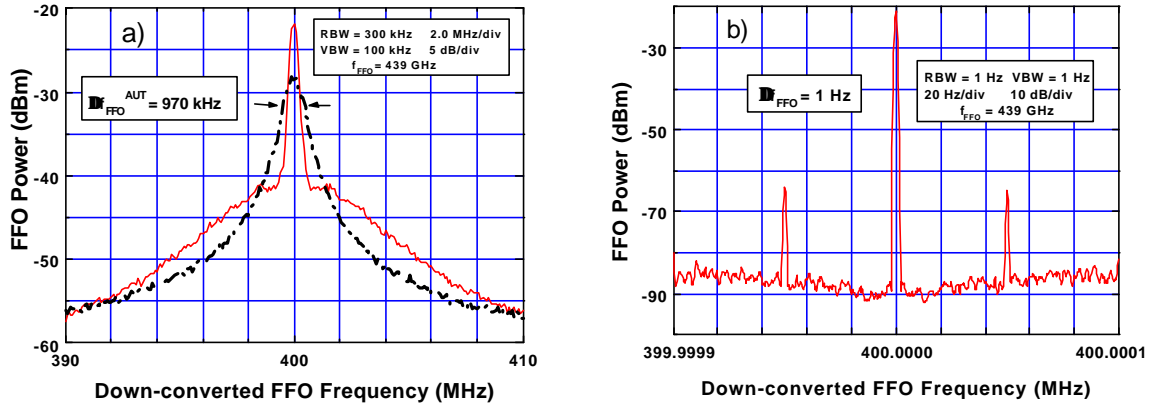


**Fig. 3.** [7] The down-converted IF power spectra of the FFO ( $f = 439$  GHz), recorded with different frequency spans, clearly demonstrate the phase locking.

The residual phase noise of the phase locked FFO - measured relative to the reference synthesizer - is plotted in Fig. 4 for three different FFO frequencies as function of the offset from the 400 MHz carrier. One can see that there is no pronounced dependence of the phase noise on the frequency of the locked FFO. It means that the noise is mainly controlled by the measuring technique and the PLL system. To get the total FFO phase noise, one should add the synthesizer noise multiplied by  $n^2$  to residual phase noise of the FFO. The measured data for the used synthesizer (HP83752B) are also presented in Fig. 4. In this measurement where the FFO, operating at 387 GHz, is locked to the 36-th harmonic of the synthesizer,  $n^2 = 1296$ . The total FFO phase noise (solid line in Fig. 4) is dominated by the synthesizer noise for offsets  $< 100$  kHz. The origin of the noise at larger frequency offset is under investigation.

It should be noted that phase locking of a FFO has been realized only on the step FSs, where the free-running FFO linewidth is about 1 MHz corresponding to small values of  $R_d^B$  and especially  $R_d^{CL}$ , where  $R_d^B = \mathcal{N}_{FFO}/\mathcal{I}_b$  and  $R_d^{CL} = \mathcal{N}_{FFO}/\mathcal{I}_{CL}$  are the differential resistances associated with the bias current,  $I_b$ , and the control-line current,  $I_{CL}$ , respectively. The linewidth increases at voltages above the boundary voltage,  $V_{JSC}$ , [9] where  $R_d^B$  and  $R_d^{CL}$  are considerably larger than on the Fiske steps (as a result of the abrupt increase of internal damping due to Josephson self-coupling [9]). It is still an experimental challenge to obtain phase locked operation in the "true" flux flow regime where the normalized damping is large,  $a/I_J \approx \mu$ , and correspondingly, the initial FFO linewidth exceeds  $\approx 10$  MHz.

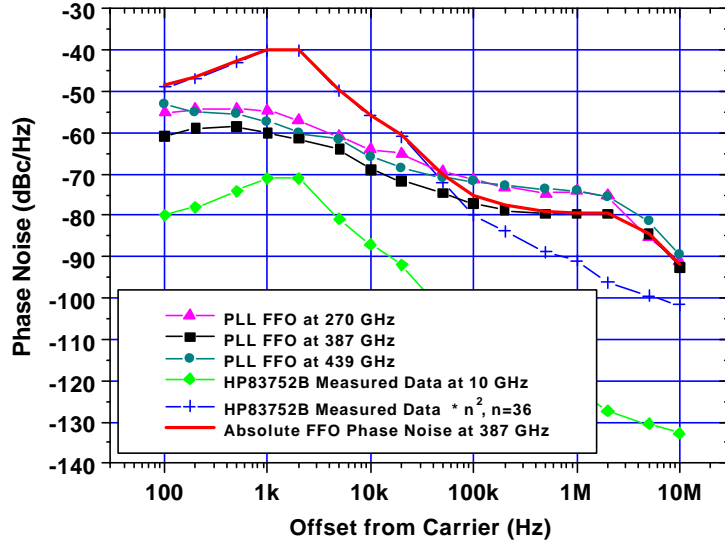


**Fig. 4.** Experimental phase noise of a phase locked FFO at different frequencies. Since the phase noise of the FFO, e.g., at 387 GHz is measured relative to the 36<sup>th</sup> harmonic of the synthesizer, the synthesizer noise, multiplied by a factor  $36^2 = 1296$ , should be added to residual FFO noise to get the total (absolute) FFO phase noise – solid line.

### 3. Super-fine Structure of the FFO IVCs; External Harmonic Multiplier.

Previous FFO linewidth measurements [6,11] have demonstrated the existence of a structure of closely spaced steps in the IVC of long Josephson junctions. The voltage spacing is about 20 nV, corresponding to a frequency separation of 10 MHz, that cannot be recorded by usual dc technique. This structure manifests itself as a nonlinear relation between the measured FFO frequency and the bias or/and control-line currents. Actually, an FFO can irradiate only in a specific range near the corresponding “resonance” frequencies,  $f_r$ , while the oscillator is unstable between these values. This behavior is clearly demonstrated in Fig. 5 ( $f_{\text{synt}} = 17.05$  GHz,  $n = 25$ , Lower Side Band). Traces A and B are recorded at constant bias current:  $I_b = 17\,782$   $\mu\text{A}$  and  $17\,779$   $\mu\text{A}$ , respectively (number of averages,  $N_{\text{av}} = 100$ ). Point A is stable while an attempt to bias at point B fails due to small fluctuations which force the FFO to jump between stable states, spending on the average almost equal time in both states (see curve B).

Figure 6 illustrates this phenomenon in a different way. Trace A is – as above – the down-converted signal of the FFO biased at a stable point, while trace B is recorded when fine-tuning the FFO bias (from  $18\,710$   $\mu\text{A}$  to  $18\,770$   $\mu\text{A}$ ) in the regime “max-hold”. In this regime the spectrum analyzer takes the maximum signal amplitude from many measurements at each frequency point. One can see that FFO frequency can be permanently tuned only in a range of about 5 MHz, while frequencies between these stable regions cannot be obtained. Even a small change of the bias current near the edge of the stable region, the frequency (voltage) of the FFO “jumps” to the next stable region. Note that a 50 MHz frequency shift (which is equivalent to a voltage difference of 100 nV) was obtained for a current change of  $60$   $\mu\text{A}$ , that corresponds to “averaged”  $R_d^B = 0.0017$   $\Omega$ .

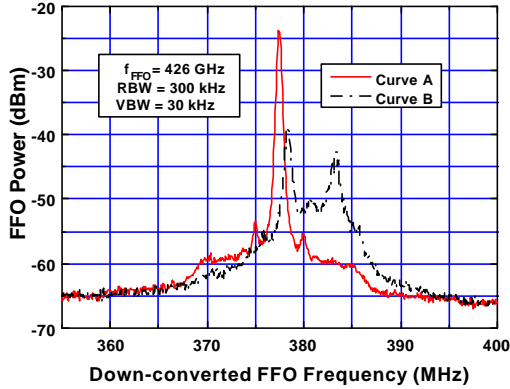


**Fig. 5.** Down-converted FFO signal recorded at constant bias current adjusted inside one of the resonances (curve A) and in between two resonances (curve B).

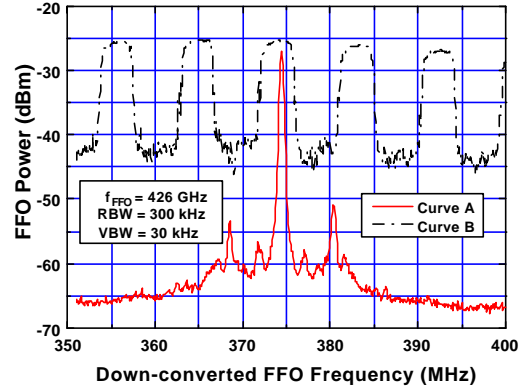


**Fig. 6.** Down-converted FFO signal recorded at fixed bias current inside one of the resonances (curve A) and with the FFO bias tuned in the “max hold” regime (curve B).

Using the Josephson equation the FFO IVC can be reconstructed in detail by measuring the bias current dependence of the FFO output frequency. The accuracy of the frequency (and correspondingly, voltage) measurement can be very high if, e.g., a synthesizer is used as a reference source. Actually, the accuracy is determined by the spectrum analyzer resolution used for the specific span. For the data presented in Fig. 5-8 the resolution bandwidth, RBW, was 300 kHz corresponding to a voltage accuracy of about 0.6 nV. By using a special measuring procedure the frequency reading from the spectrum analyzer was recorded simultaneously with adjusting  $I_b$  and  $I_{CL}$ . The measured dependence of the down-converted FFO frequency on  $I_b$  is shown in Fig. 7. The data sets marked #01, #02 and #03 are recorded at slightly different values of  $I_{CL}$  (what results in jumping to the adjacent resonances and small shift along the  $I_b$ -axis). From these data the exact shape of the FFO can be reconstructed; the “recovered” FFO IVCs demonstrate the existence of well-defined superfine structure (see Fig. 8). Up to now there is no reliable theoretical explanation of this superfine resonant structure. The exact geometry of the FFO influences the resonant structure, in particular, the results presented in Fig. 3 [7, 8] were measured for a tapered FFO where the resonance effect was less pronounced. The results depicted in Figs. 5-8 are from an FFO with a standard rectangular geometry.

From Fig. 8 one can see that the FFO IVC (at low levels of external interference) consists of a set of separate steps rather than being a continuous curve. The differential resistance on these steps is extremely low,  $R_d^B(\text{res}) = 0.00037 \Omega$ . Important to note is, that this value is considerably lower than the average value ( $R_d^B = 0.0016 \Omega$ ) recorded using the traditional technique. An even more dramatic reduction has been measured for the control-line differential resistance,  $R_d^{CL} = \frac{\partial V_{FFO}}{\partial I_{CL}}$ .

Since the frequency separation between adjacent resonances is comparable with the maximum PLL system bandwidth, jumps between adjacent resonances create considerable difficulties for phase locking of the FFO. Nevertheless full phase locking can be realized even in the presence of the resonance structures but only at specific frequencies (see Fig. 9, 10).

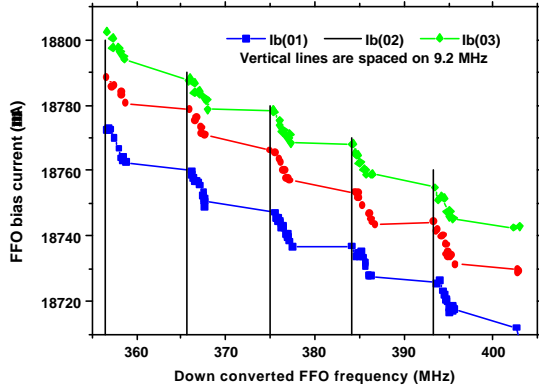


**Fig. 7.** Down-converted FFO frequency versus FFO bias current at slightly different control line currents. Note that the absolute positions of the resonances (and the distance between adjacent resonances) are the same for all curves.

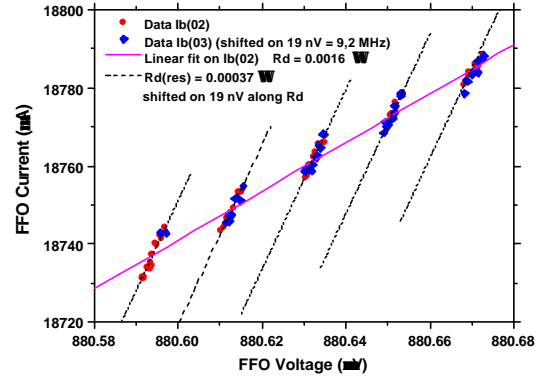


**Fig. 8.** Reconstructed IVC of the FFO. Data #03 are measured at a slightly different  $I_{CL}$  and corresponds to an adjacent resonance. These data are shifted by 19 nV along the Fiske step with slope  $1/R_d^B$ .

In order to exclude that the recorded resonance structure could be due to the integrated harmonic mixer technique, an external harmonic multiplier based on a quasi-planar superlattice electronic device (SLED) [12] has been developed and tested. The SLED was mounted in a circular waveguide (with a cut-off frequency of about 400 GHz) followed by a conical horn with an output diameter of 6 mm. A constant-voltage bias and the pump signal from the synthesizer (frequency 1 - 30 GHz) are applied to the SLED. The signal of multiplier is fed to an integrated receiver of standard design [1,2] via a vacuum window. Heterodyne mixing with the FFO local oscillator signal can be measured up to 500 GHz that corresponds to the 27-th harmonic of the input signal from the synthesizer. The superfine resonance structure is present also in the measurements done by the external multiplier, and thus the resonances can be attributed to properties of the FFO rather than to the measuring method. Actually, Figs. 5-10 are recorded by using the external harmonic multiplier. Figure 9 shows the down-converted FFO signals with the FFO frequency locked - curve A- and phase locked - curve B). Note the extremely narrow linewidth  $\approx 75$  kHz was measured at a FFO frequency of 426 GHz - Fig. 9 (curve A) due to extremely low differential resistance. Actually, this is the linewidth of the free-running FFO since it was recorded with a very narrow ( $< 10$  kHz) PLL regulation bandwidth that only suppresses low-frequency external interference without changing the FFO linewidth (frequency locking).

The external harmonic multiplier enables us to check an alternative concept of the Phase Locked Integrated Receiver. This concept [7] is based on an already proven design of the integrated receiver chip [1,2]. At this approach a submm-wave signal from an external harmonic multiplier driven by a 10 - 20 GHz synthesizer is applied to the integrated receiver via a beam splitter. A small portion of the IF band (about 50 MHz) is used to monitor the mixing product between the  $n$ -th harmonic of the synthesizer signal and the FFO signal. This down-converted signal after narrow-band filtering controls the PLL system while the rest of the IF band is used to analyze the down-converted signal.

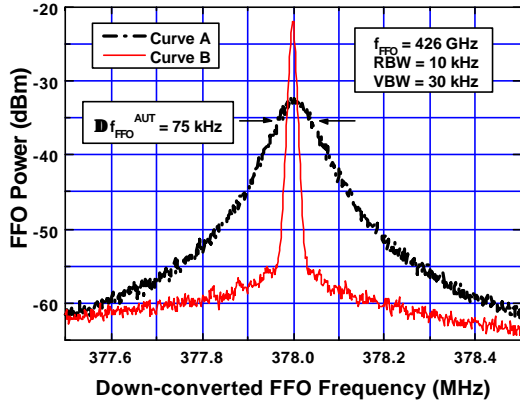


**Fig. 9.** Down-converted spectra of the FFO operated at 426 GHz; frequency locked (curve A) and phase locked (curve B).

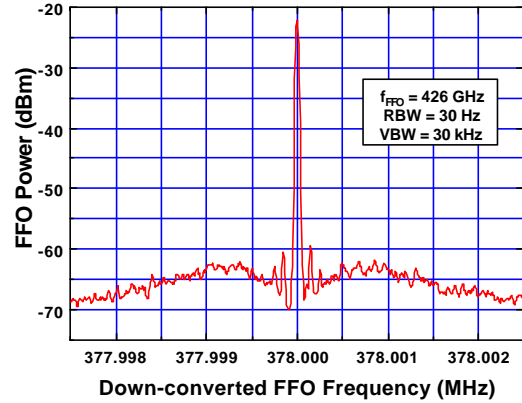


**Fig. 10.** Down-converted spectra of the phase locked FFO operated at 426 GHz, recorded at smaller IF span, see curve B in Fig. 9.

#### 4. Discussion and conclusion

Preliminary tests demonstrate that there is no fundamental difference between results obtained by using either an integrated harmonic mixer or an external multiplier. The proper choice is a matter of convenience relevant for different applications. Phase locking of the FFO to an external reference oscillator is demonstrated experimentally using both measurement schemes. A FFO linewidth as low as 1 Hz (determined by the resolution bandwidth of the spectrum analyzer) has been obtained by both technique in the frequency range 270 - 440 GHz relative to a reference oscillator. To our knowledge it is the first time that the spectral linewidth of any Josephson device has been reduced so much by means of an electronic system. An observed superfine resonance structure in the FFO IVC reduces the FFO linewidth due to smaller differential resistance, but complicates FFO phase locking. In order to use the external multiplier with a thin beam splitter the multiplier output power at high harmonics must be increased at least 100 times. Here the development of a cryogenic multiplier looks very promising. The output power would be increased according to theoretical expectations, and a much thicker beam splitter can be used at cryogenic temperatures.

Implementation of the single-chip Superconducting Integrated Receiver with phase - lock-loop facilities is especially advantageous for new radio-astronomy projects based on an imaging array or multi-receiver approach (e. g., ALMA). The PLL Integrated Receiver is ready to be tested in the nearest future for practical spectral radio-astronomy in the frequency range 350 - 450 GHz. In this frequency range the Fiske steps of Nb-AlO<sub>x</sub>-Nb FFOs are closely spaced and almost overlapping due to dissipation and dispersion in the long Josephson tunnel junction. The frequency gaps between the available LO bands (at subsequent FSs where FFO phase locking is possible), do not exceed 5 GHz. There is a possibility to gap these intervals using a receiver with a wide-band (4 GHz) IF amplifier while the FFO is biased and locked on an adjacent FS. This enables continuous in-phase-lock frequency coverage.

## Acknowledgement.

The work was supported in parts by the RFBR project 00-02-16270, the INTAS project 97-1712, the ISTC project 1199, the Danish Research Academy, the Danish Natural Science Foundation and the Nederlandse Organisatie voor Wetenschappelijk Onderzoek (NWO). Authors thank Thijs de Graauw, Mogens R. Samuelsen, Herman van de Stadt, Paul R. Wesselius, Nick Whyborn and Wolfgang Wild for fruitful and stimulating discussions as well as H. Golstein, S. Kikken, H. Smit, and D. Van Nguyen for help in the experiment.

## References

1. S.V. Shitov, A.B. Ermakov, L.V. Filippenko, V.P. Koshelets, A.B. Baryshev, W. Luinge, Jian-Rong Gao, "Superconducting Chip Receiver for Imaging Applications", presented at ASC-98, Palm Desert, CA, USA, Report EMA-09, *IEEE Trans. on Appl. Supercond.*, **v.9**, No 2, pp. 3773-3776, (1999).
2. V.P. Koshelets, S.V. Shitov, "Integrated Superconducting Receivers", *Superconductor Science and Technology*, **vol 15**, No 5, pp. R1-R 17, (2000).
3. Nagatsuma, T., Enpuku, K., Irie, F., and Yoshida, K. 1983, Flux-Flow type Josephson oscillator for millimeter and submillimeter wave region, *J. Appl. Phys.* **54**, 3302-3309, see also Pt. II: 1984, *J. Appl. Phys.* **56**, p 3284; Pt. III: 1985, *J. Appl. Phys.* **58**, 441; Pt. IV: 1988, *J. Appl. Phys.* **63**, 1130.
4. Mygind, J., Koshelets, V.P., Shchukin, A.V., Shitov, S.V. and Lapytskaya, I.L. 1995, Properties of the autonomous and injection locked Flux-Flow Oscillators, *IEEE Trans. on Appl. Supercond.* **5**, 2951-2954.
5. Koshelets, V.P., Shitov, S.V., Baryshev, A.M., Lapitskaya, I.L., Filippenko, L.V., van de Stadt, H., Mess, J., Schaeffer, H. and de Graauw, T. 1995, Integrated sub-mm wave receivers, *IEEE Trans. on Appl. Supercond.* **5**, 3057-3060.
6. V.P. Koshelets, S.V. Shitov, A.V. Shchukin, L.V. Filippenko, and J. Mygind, "Linewidth of submillimeter wave flux flow oscillators", *Appl. Phys. Lett.*, vol. 69, pp. 699-701, July 1996.
7. V.P. Koshelets, A.M. Baryshev, J. Mygind, V.L. Vaks, S.V. Shitov, L.V. Filippenko, P.N. Dmitriev, W. Luinge, N. Whyborn, "Externally Phase Locked Sub-MM Flux Flow Oscillator for Integrated Receiver ", presented at EUCAS' 99, report 8D-2, Barcelona, September (1999).
8. V.P. Koshelets, S.V. Shitov, L.V. Filippenko, V.L. Vaks, J. Mygind, A.B. Baryshev, W. Luinge, N. Whyborn, " Phase Locking of 270-440 GHz Josephson Flux Flow Oscillator", *Rev. of Sci. Instr.*, **v. 71**, No1, pp. 289-293, (2000).
9. V.P. Koshelets, S.V. Shitov, A.V. Shchukin, L.V. Filippenko, J. Mygind and A.V. Ustinov, "Self-pumping effects and radiation linewidth of FFO," *Phys. Rev. B*, vol. 56, pp. 5572- 5577, Sept. 1997.
10. M. Cirillo, N. Grønbech-Jensen, M. Samuelsen, M. Salerno, and G. Verona Rinati, "Fiske modes and Eck steps in long Josephson junctions: Theory and Experiments", *Phys. Rev. B*, vol. 58, pp. 12 377-12 384, 1998.
11. A.V. Ustinov, private communication.
12. E. Schomburg, R. Scheuerer, S. Brandl, K.F. Renk, D.G. Paveliev, Yu. Koschurinov, V. Ustinov, A. Zhukov, A. Kovsh, P.S. Kop`ev, *Electronics Letters*, Vol.35, No.17 (1999).

# **Evaluation of High-Tc elements in submm-mixers**

**D. Diehl and R. Zimmermann,**  
RPG Radiometer-physics GmbH  
53340 Meckenheim, Germany

**J. Scherbel, M. Darula, O. Harnack and M. Siegel**  
Institut für Schicht- und Ionentechnik  
Forschungszentrum Juelich GmbH  
52425 Juelich, Germany

## **Abstract**

We are performing an extensive study to understand the mixing properties of high-temperature superconductor (HTS) bicrystal Josephson junctions at 345 GHz and high operating temperatures. Results of  $T_{\text{sys}} < 1000\text{K}$  DSB have been achieved at an operating temperature of 17K with a cryocooler. The IF contribution is approx. 300K. L.O. power is coupled by a beam splitter and is around 50 nW.

These results are without any corrections and improvement is possible by applying matching structures. Details will be available at the time of the conference in May. We have mixing elements for 850 GHz in preparation as no degradation is expected in performance due to theory.

# Planar Frequency Doublers and Triplers for FIRST

N.R. Erickson and  
G. Narayanan  
Dept. of Physics and Astronomy  
University of Massachusetts  
Amherst, MA 01003

R.P. Smith, S.C. Martin  
and I. Mehdi  
Jet Propulsion Lab  
4800 Oak Grove Dr.  
Pasadena, CA 91109

T.W. Crowe and W.L. Bishop  
Dept. of Electrical  
Engineering  
University of Virginia  
Charlottesville, VA 22903

## Introduction

Local oscillator sources based on frequency multipliers appear to be the best developed of several types of sources needed for astronomical missions from airborne and space platforms. These applications extend well into the submillimeter range, potentially up to 2.7 THz for FIRST, and similar frequencies for SOFIA receiver systems. A new generation of frequency multipliers is needed for the FIRST mission, in which the old technology of whisker contacted varactor diodes is replaced with new planar devices. This use of planar devices should go well beyond replacement of the diode itself, and should replace much of the circuit used in the earlier devices. The goal is to make these sources far superior to present multipliers in cost, and performance. Desired properties include:

- High reproducibility
- Wide bandwidth with no mechanical tuning
- Easy machining and assembly
- High efficiency, better than the best whiskered designs.

Given that the frequency range for FIRST covers 480-2700 GHz, with nearly full coverage, and the required driver stages cover 140-225 and 280-450 GHz, this multiplier development will essentially fill in the submillimeter range with sources. For purposes of FIRST these sources must cover 10-15% width bands, although wider bandwidths should be possible using the same technology. Progress toward this goal to date is very encouraging although a lot remains to be done:

- Planar diode arrays have produced very large amounts of power, sufficient to strongly pump a following stage.
- A doubler for 185-203 GHz has been completed using a full planar style of construction suitable for fabrication as a MMIC.
- A tripler prototype for 220-275 GHz has been built of nearly full monolithic construction.
- Designs for many other frequencies in the required bands are complete (and some devices fabricated), although the actual complete multipliers have yet to be built.

## Balanced Doublers for 140-210 GHz

The initial development in complex planar diodes was the balanced doubler using series diode arrays. These circuits began as an outgrowth of circuits based on whiskered diodes, and only recently have begun to look like truly planar circuits. So far the highest power and best bandwidth produced has been with a hybrid circuit using a 6 diode array in a circuit using gold ribbon and coaxial components [1]. This circuit was designed to tune 142-158 GHz, which is one of the

required FIRST driver bands. Planar arrays from both JPL and UVa have been used in this circuit with somewhat different results. These arrays are of nearly the same layout and are designed to produce an equal power split among the diodes. The JPL diodes (PBD150) use relatively low doping ( $10^{17}/\text{cm}^3$ ) and have a breakdown voltage of 13V per diode. The UVa diodes (SB7T1) use higher doping ( $2 \times 10^{17}/\text{cm}^3$ ) and have  $V_b$  of 7 V per diode.

With the JPL diodes, the efficiency peaks at 200 mW input (140 GHz output), and is 26% at room temperature. The efficiency was tested at 80 K where it increases to ~39% (a 50% increase). This cold test was done with 280 mW input power producing a maximum output of 116 mW at the point of burnout. No test of safe operating power has been made but it should be ~80 mW output. With the UVa diodes, the room temperature efficiency is 34%, peaking at 150 mW input. The efficiency increases to 41% at 80 K (a 22% increase). While room temperature results differ a lot, the cold efficiencies are very similar because the mobility increase in the lower doped diodes is much larger than that for the higher doping. The frequency response of this doubler with the UVa diode is shown in Figure 1.

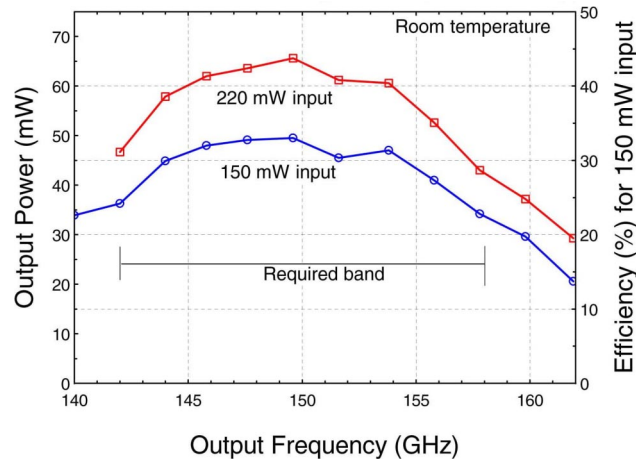


**Figure 1. Frequency response of balanced doubler built to demonstrate one of the driver bands for FIRST. The efficiency corresponds to the lower curve.**

In more recent work, a new doubler has been built for 200 GHz, which is suitable for MMIC fabrication using the “substrateless” fabrication technique [2]. This doubler uses the same 6 anode JPL diode array as the previously described doubler, but scaled down in size by a factor of 0.75. As before, the diode is soldered in place, but the remainder of the assembly is done by gluing and wire bonding. The bias circuit is decoupled with just a planar capacitor, eliminating the distributed filter previously used, and this capacitor is fabricated on GaAs with beam leads for grounding and bias connection. The doubler layout is shown in Figure 2.

The full circuit between the diode and the output waveguide is just a 12  $\mu\text{m}$  diameter bond wire. It is found that more complex impedance matching is not needed in this region, and instead all of the wideband tuning of the circuit is done with waveguide elements. This makes the loss of these elements smaller, and reduces the complexity of assembly.

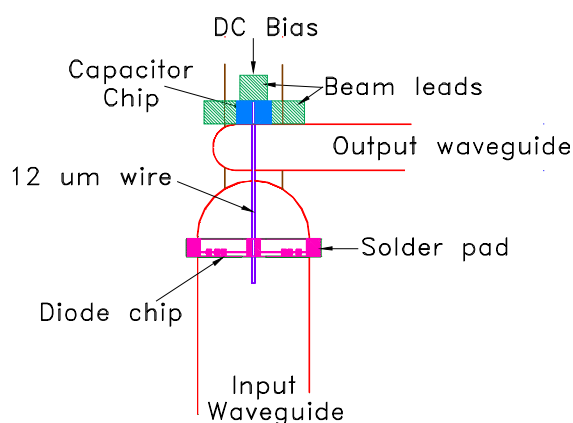


**Figure 2. Drawing of the 200 GHz balanced doubler using a concept suitable for monolithic fabrication.**

The design bandwidth is 188-212 GHz output with a very flat response, but a drafting error led to a loss of bandwidth in the prototype. However, the circuit operates close to the design frequency as shown in Fig 3, and the peak efficiency at room temp is 19% at 195 GHz, roughly consistent with 26% measured for the same diode batch at 140 GHz. The efficiency increases to 31% at 80K, a 60% increase, as shown in Figure 4. The peak efficiency occurs at the highest available input power, which is 220 mW, so it is not possible to be sure of the power handling capabilities.

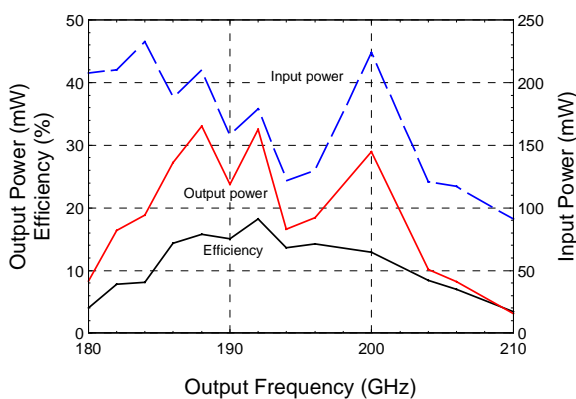


**Figure 3. Frequency response of doubler with input power as noted.**

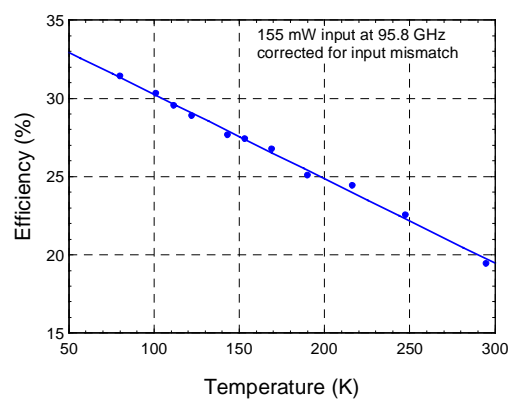


**Figure 4. Efficiency of the doubler vs temperature measured at 95.8 GHz input.**

### MMIC Balanced Tripler

A nearly fully monolithic tripler has been designed which appears suitable for frequencies well into the submillimeter range. The circuit achieves nearly optimal terminations at the three frequencies of importance, in a very simple circuit. The circuit was designed with the aid of HFSS [3], and required many simulations to determine circuit parameters. Because simulations of such a complex structure were slow at the time of the design, the circuit is not well optimized over a wide bandwidth, and this version was viewed mostly as a proof of concept. The layout of the circuit is

shown in Figure 5.

The diodes are connected in antiparallel, with a DC break provided by an overlaid pair of lines with dielectric isolation on the output side of the circuit. Bias is applied to the diodes in series. The input is in a microstrip mode with an impedance near  $50 \Omega$ , and is fed by a waveguide to microstrip transition. At the input frequency the diode pair is in series with a short-circuited stub, which provides the correct input reactance. This stub is grounded using beam leads on the far side of the output waveguide. The output waveguide is cut-off at the input and so no additional filtering is needed at this frequency, but the line crossing the waveguide has very high impedance and so the waveguide must have quite reduced height in order to avoid adding excessive input inductance

At the output frequency, two radial stubs provide short circuits at either diode, and ensure that little power couples back to the input. At this frequency the input stub line becomes the coupling line to the output waveguide, as well as an impedance matching section. The narrow lines connecting to the diodes provide the required output inductance. Additional impedance matching is provided by a step transformer up to full height waveguide, and by a fixed backshort in the waveguide.

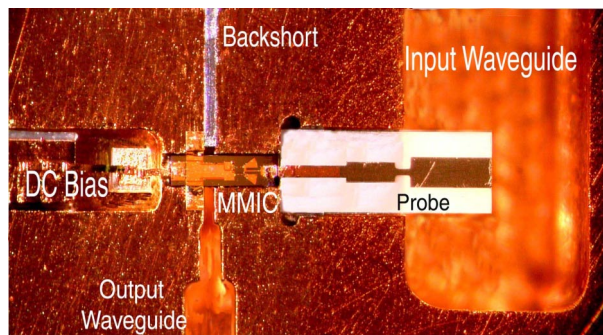
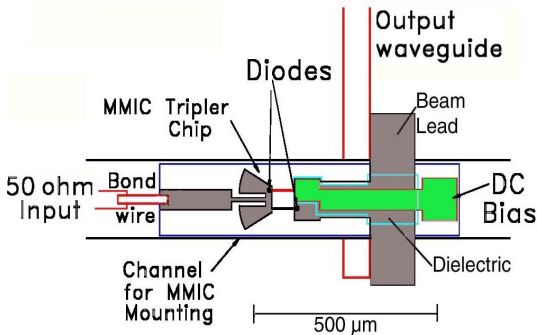


**Figure 5. Drawing of the tripler chip, and its mounting relative to the output waveguide. The output step transformer is not shown.**

**Figure 6. Photograph of the tripler for 280 GHz, showing the input and output waveguides, the alumina input transition and the bias connection.**

At the second harmonic, the diode loop is tuned to provide nearly optimum inductance at midband without producing excess inductance at the output frequency. In part this is because the second harmonic currents flow in a different path, including transverse currents between the stubs, and across the wide output line. In addition, the radial stubs themselves act as quasi-lumped capacitances and load the loop in a way that increases its second harmonic reactance. The overall effect is an idler tuning which is optimized at midband and remains acceptable over quite a wide band, mainly at frequencies below the design band.

The circuit is in microstrip from the input to the radial stubs and switches to suspended stripline for the remainder of the circuit to avoid moding problems for the higher frequency part of the circuit. The channel housing the chip is significantly wider than the chip to further suppress

higher modes. This design is for a substrate thickness of 20  $\mu\text{m}$ , chosen to minimize higher moding problems.

Triplers were designed for center frequencies of 280 and 320 GHz. These chips were fabricated on semi-insulating GaAs with epitaxial doping of  $10^{17} \text{ cm}^{-3}$ . The anodes are made as rectangular strips of  $1.5 \times 9 \mu\text{m}$  with a breakdown voltage of 13 V, and a zero bias capacitance of 19 fF. The DC isolation dielectric is 0.1  $\mu\text{m}$  thick SiN. The substrate has no backside metal, meaning that in the region where the mode is microstrip, the chip must be in good contact with the metal of the block. Chip separation was done by RIE (from the backside) which allows individual devices to be spaced very close to each other and also allows for the use of beam leads and arbitrarily shaped chips. The beam leads are essential to RF and DC ground the end of the chip where little area is available for wire bonding.

A photograph of the assembled tripler is shown in figure 6. Chips were glued down with a low viscosity epoxy, and then the beam leads were bonded to the block. An input transition to the WR10 waveguide was fabricated on 100  $\mu\text{m}$  alumina [4]. Connections were made to the chip by ribbon bonding to the input and bias pads. Assembly was judged to be very easy compared to any other multipliers at a similar frequency.

Tests have been performed using a wide-band Gunn oscillator source, and some wideband power amplifiers. Bias was optimized at each frequency, and varied from 2 V at frequencies very low in the band, to 6-8 V at the higher (design) frequencies. While efficiency peaks at 20-30 mW input, as shown in Figure 7, the efficiency at 260 GHz remains high up to an output power of 7 mW. The input match varies from 6-10 dB return loss, and probably could be improved with some off-chip matching. The best efficiency of the 320 GHz device is 9%, increasing to 11% with the input mismatch corrected with a tuner. The output match has been measured with a sliding tuner only at 320 GHz, where it is very good. It is expected to be good only in the design band. Output power was measured with a wideband calorimeter sensor with an accuracy better than 5% [6]. The 320 GHz tripler survived cooling to 80 K, and its efficiency at 312 GHz increased to 14%, with 7 mW output. This corresponds to a 60% increase in efficiency.

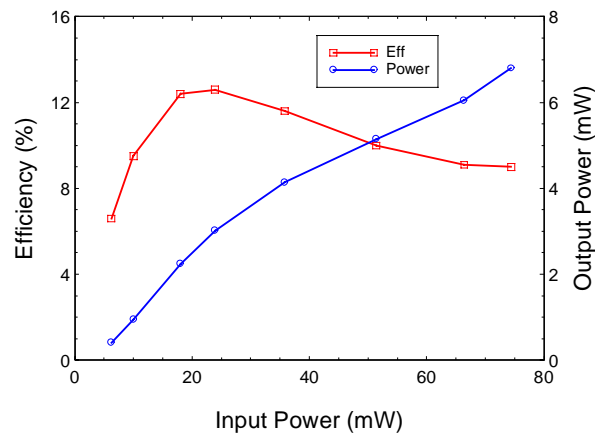


**Figure 7. Efficiency vs input power level for the MMIC tripler at an output frequency of 260 GHz. Tripler is the nominal 280 GHz design on 38  $\mu\text{m}$  substrate.**

The best part of the operating band is very close to the design frequency, and is shifted low in both designs by only 2-5%. The peak efficiency measured at 320 GHz exceeds that obtained with the best whisker contacted triplers at a similar frequency [5], while the bandwidth, even in this non-optimized design, greatly exceeds that of whiskered devices. Fig 8 shows a comparison of a wideband fixed tuned whisker contacted tripler vs. this new design. The bandwidth was verified using a input source consisting of a WR10 tripler followed by a wideband medium power amplifier (25-40 mW output) [8]. The source was swept over an output band of 240-324 GHz with a minimum output of 0.3 mW at fixed bias.

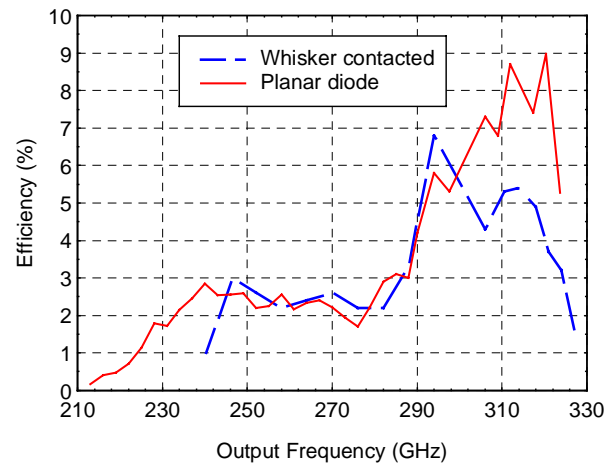


**Figure 8. Efficiency of new MMIC tripler in the nominal 320 GHz design (solid), and older whisker contacted tripler (dashed) over a wide band.**

Substrate thickness was initially thought to be important but later analysis showed that it could be much thicker without difficulties. Chips from the same wafer were also thinned to 38  $\mu\text{m}$  and these devices were found to work as well as the design thickness, but with a frequency offset. Figure 9 shows the performance of chips of the 280 GHz design on the two thicknesses. While the thicker material appears to work better, this is probably due largely to better quality diodes in this chip, since simulations predict that there is no advantage to thicker material.

This design has been scaled to 1.0 and 1.2 THz using the JPL membrane and frame technology [7], and these wafers are in fabrication at this time. The membrane thickness of 3  $\mu\text{m}$  makes the chips quite fragile, but there is no need to handle the thin part of the chip so assembly may prove relatively simple. The presence of the frame makes the block fabrication much more difficult, since waveguides can not cross the frame. However, the chip has been redesigned since this time, as noted below.

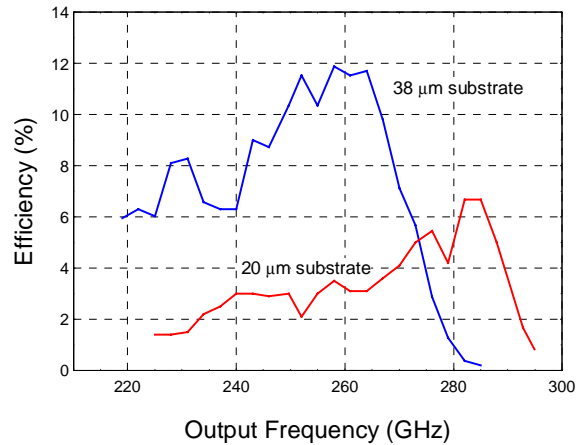


**Figure 9. Triplers of nominal 280 GHz design fabricated on different thicknesses of GaAs. The difference in efficiency is probably due to the quality of the diodes, while the frequency shift is due to substrate thickness.**

### Improved MMIC Tripler

After discovering that the substrate thickness could be much larger, a 220-285 GHz circuit was redesigned for 38  $\mu\text{m}$  GaAs. In this new design the radial stubs were rotated apart to allow the input line to have a lower impedance, which simulations showed was desirable. By increasing the diode capacitance, the idler loop was retuned to set the optimum idler match in midband for this wide bandwidth, rather than near the upper edge of the band. The input and output waveguide circuits were then optimized for flat response, resulting in a circuit that looks nearly the same yet achieves a very flat response at the peak efficiency of the previous design. In this design, the 1 dB bandwidth should be 13%, while the 3 dB bandwidth is 26%.

Thickening the substrate to 50  $\mu\text{m}$ , and increasing the waveguide height by 60% still works with some loss of bandwidth, which makes higher frequency versions much more practical. A 1.1 THz design now uses a 12  $\mu\text{m}$  substrate, practical with mechanical thinning, rather than requiring the membrane process. The output waveguide is 25  $\mu\text{m}$  high, which is quite machinable. On this small chip the input waveguide probe can be integrated with negligible loss of wafer area, leaving only the bias to connect.

### Doublers for 1200-2700 GHz

At much higher frequencies, balanced doublers are still desirable because they do not require filters, which are quite difficult to implement. The primary drawback is that the typical input power becomes so small that there may not be enough power to drive even the smallest practical diodes, and a balanced doubler doubles this power. A great savings in design effort comes about because at these frequencies varactor mode operation is not possible, due to low input power and very strong velocity saturation in GaAs. Designing in varistor mode is much easier

since the diode load is largely resistive, meaning that impedance matching is simplified, and the bandwidth increased.

In these designs, the diodes are placed in series in the output waveguide, rather than in the input as in the previous designs. A coupling probe in the input waveguide connects to the center point between the diodes. The intent is to minimize losses in the output circuit. With this geometry it is not essential to bias the diodes since with a short circuit at the waveguide walls, both diodes are maintained at zero bias. However, at very low power, doublers work much better with forward bias and so a bias circuit is still desired for the highest frequency devices. Two doublers have been designed for these higher bands to test out the concept, both using membrane construction on 3  $\mu\text{m}$  GaAs, with a 50  $\mu\text{m}$  frame surrounding the membrane.

The predicted performance of the two designs is shown in Figure 10, with an efficiency scale that is arbitrary, except as a guide to what might be possible. Too little is known about THz multipliers to make realistic predictions. Both designs work nearly as well as is theoretically possible near their efficiency peak, so they will serve as a good test of device performance. The manufacture of the blocks can be done entirely by milling, boring and broaching, with no difficult assembly. The chip should just drop in with minimal difficulty in positioning it properly. A bias lead is provided on some chips, and zero bias designs are also available. These chips are in fabrication at this time.

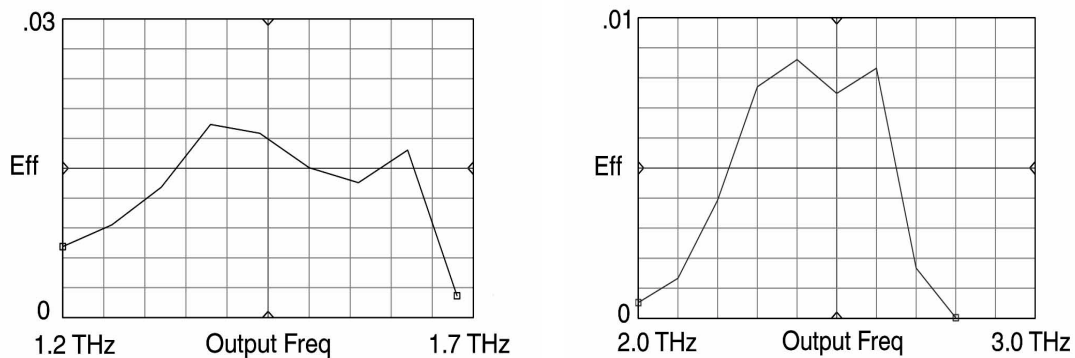


**Figure 10. Predicted bandwidth of balanced doublers in two bands to test the feasibility of THz multipliers. The efficiency scale is largely arbitrary, since almost nothing is known about multiplier performance at these frequencies.**

## Conclusions

Frequency doublers and triplers are being developed for the FIRST mission, using full integration of the circuit onto a GaAs chip. So far progress has been made in developing a doubler of hybrid construction that can readily be converted to a substrate-less MMIC. An output power of 116 mW has been obtained at 140 GHz, and up to 55 mW at 195 GHz. Other doublers of fully monolithic design are in fabrication for much higher frequencies, while designs for 600-900 GHz have been fabricated but not tested.

A fully monolithic tripler has been designed which seems usable for frequencies from 200-1200 GHz. Tests on a prototype near 300 GHz are very encouraging with efficiency and bandwidth superior to the best whiskered designs. Output power is also higher than for any previous designs.

All of these designs indicate that monolithic fabrication is truly the best way to approach the production of submillimeter multipliers and that our goal to reach the THz range is realistic. This will result in much more reproducible, reliable and lower cost LO sources than have been available in the past, and will enable large scale applications.

### **Acknowledgements**

We wish to thank R. Grosslein and J. Wielgus for machining and assembly of the blocks. The work at UMass was supported by NASA under grant NAG5-4272 and by JPL under contract 961614.

### **References**

- [1] Erickson, N.R., "Wideband High Efficiency Planar Diode Multipliers," Ninth Int'l Conference on Space THz Technology, pp. 473-480, Pasadena, CA, 1998.
- [2] J. Bruston, A. Maestrini, E. Schlecht, S. Martin, P. Smith and I. Mehdi, "The Frame-less Membrane: A Novel Technology for THz Circuits," Eleventh Int'l Conference on Space THz Tech., Ann Arbor, MI, May 2000.
- [3] Hewlett Packard (Agilent) High Frequency Structure Simulator.
- [4] Leong, Y.C., "Full Band Waveguide-to-Microstrip Probe Transitions," IEEE Int'l Microwave Symposium, paper Th1B-5. Anaheim, 1999.
- [5] Erickson, N.R., "Wideband Fixed-Tuned Millimeter and Submillimeter Frequency Multipliers," Eighth Int'l Conference on Space THz Tech., pp. 137-148, Cambridge, MA, 1997.
- [6] Erickson, N.R., "A Fast and Sensitive Submillimeter Waveguide Power Sensor," Tenth Int'l Conference on Space THz Tech., pp. 501-507, Charlottesville, VA, 1999.
- [7] P.H. Siegel, R.P. Smith, M. Gaidis, S. Martin, J. Podosek, and U. Zimmerman, "2.5 THz GaAs Monolithic Membrane-Diode Mixer," Ninth Int'l Conference on Space THz Technology, pp. 147-159, Pasadena, CA, 1998.
- [8] Leong, Y.C., and Weinreb, S., "Full W-Band MMIC Medium Power Amplifier," IEEE Int'l Microwave Symposium, Boston, 2000.

# HIGH Q InP-BASED VARACTOR DIODES

T. David\*, S. Arscott, P. Mounaix, X. Miquie, F. Mollot, O. Vanbésien,  
M. Chaubet and D. Lippens

Institut d'Electronique et de Microélectronique du Nord (UMR 8520)  
Université des Sciences et Technologies de Lille  
BP 69, 59652 Villeneuve d'Ascq, France  
M. Chaubet is with the Centre National d'Etudes Spatiales,  
18 Avenue Edouard Belin,  
31401 Toulouse Cedex 4, France

\*Corresponding author: thibaut.david@iemn.univ-lille1.fr

***Abstract*** -We report on high quality-factor Heterostructure Barrier Varactor making benefit of epitaxial stacking and planar integration, with a cut-off frequency in the far infrared region. To this aim, high doping concentrations in the depletion ( $2 \times 10^{17} \text{ cm}^{-3}$ ) and contact ( $1 \times 10^{19} \text{ cm}^{-3}$ ) InGaAs regions lattice matched to an InP substrate and an InAlAs/AlAs blocking barrier scheme were used. Planar integration of the devices with a number of barriers up to eight in coplanar waveguide and series-type configurations shows a zero-bias capacitance of  $3.4 \text{ fF}/\mu\text{m}^2$  per barrier and a conductance of  $3.3 \text{ nS}/\mu\text{m}^2$  along with an intrinsic capacitance ratio of 4.3:1.

***Index terms*** -Varactor diode, harmonic multiplier, heterostructure, substrate-transfer, InP

## I. INTRODUCTION

Recently, we reported record performances in terms of conversion efficiency (12.5%) and delivered power (9mW) for a waveguide Heterostructure Barrier Varactor tripler at 250 GHz [1]. These state-of-the art performances can be explained by the use of InP-based materials, which permit us to dramatically improve the voltage handling of the devices by reducing the leakage current [2] increasing by this fact the intrinsic quality factor of the devices. Also, the use of narrow gap cladding and contacting layers were found to be of great benefit in achieving a high modulation velocity of the depleted region [3] and for reducing the series resistance contribution to the cut-off frequency. In order to further increase these performances in terms of frequency and power capability, some improvements were subsequently brought to the epitaxial layers and to the technology aiming at (i) further increasing the current capability of the devices in the undepleted zone alleviating by this means the saturation effect at higher operation frequencies [3] and (ii) reducing the intrinsic series resistance through the use of highly-degenerated thick access and contact layers. In addition, the functionality of the device for a use as a medium-power high-frequency multiplier was improved with the fabrication of air-bridged devices in double and quadruple mesa configurations, with two barriers being stacked during epitaxy. This means that the overall number of elemental devices can be as high as eight. In this communication, we report on the dc and ac characterization of this new batch of

devices integrated in: planar coaxial schemes, coplanar waveguide (CPW) and planar series-type configurations.

## II. TECHNOLOGICAL GUIDELINES

The epitaxial material used for fabricating the devices starting from a Semi-Insulating InP substrate, consists of: (i) a 1 $\mu$ m-thick  $1 \times 10^{19} \text{ cm}^{-3}$  InGaAs buried layer, (ii) a 200nm-thick  $2 \times 10^{17} \text{ cm}^{-3}$  InGaAs cladding layer, (iii) an undoped InAlAs-5nm/AlAs-3nm/InAlAs-5nm barrier, (iv) a 200nm-thick  $2 \times 10^{17} \text{ cm}^{-3}$  InGaAs cladding layer and (v) a 500nm-thick  $1 \times 10^{19} \text{ cm}^{-3}$  InGaAs capping layer. The Indium content is 53% and 52% for InGaAs and InAlAs respectively, whereas the strained AlAs layer was grown under pseudomorphic conditions. A two barrier-scheme, namely the series integration of two elemental diode structures during epitaxy, was grown without interruption. A higher doping concentration (twice that in previous work [4]) with thicker buried layers was chosen for this batch despite the difficulty to grow under lattice matching thick ternary InGaAs alloys. The epitaxial quality was found to be instrumental in order to achieve the high quality factor device. This fact explains why the AlAs layer thickness was kept at 3nm (3D growth was found for 5nm AlAs layers) hence, two barriers were integrated.

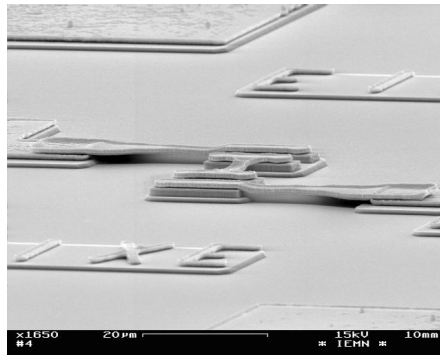


Figure 1: SEM view of an eight-barrier device. The air-bridges, 3 $\mu$ m-width, 40  $\mu$ m-long and 0.8  $\mu$ m-thick, were fabricated by photoresist molding techniques and electron gun evaporation.

## III. INTEGRATION TECHNIQUES

The devices were fabricated for the realization of harmonic triplers at J band (220-325 GHz). Also a more prospective project targeting the integration of the diodes in a non-linear transmission line was investigated. With respect to these goals, it was decided to further integrate the devices by taking advantage of a planar integration in close proximity by low dimensional air-bridge connection. To this aim, advanced fabrication techniques were employed which consist in the writing of the micron-

sized dimension top contacts by electron beam (PMMA resist), the ohmic contact deposition by electron gun evaporation (a sequential Ni/Ge/Au/Ti/Au multilayer ohmic contact annealed by RTA at 400°C during 40 s), the etching of mesas by Reactive Ion Etching (CH<sub>4</sub>/H<sub>2</sub>/Ar gases) and the fabrication of evaporated air-bridges using a double resist layer molding scheme. The underneath resist layer was pyrolyzed in order to achieve a convex mold shape and avoid resist mixing [5]. Figure 1 shows a Scanning Electron Micrograph of a completed device. For the present example, the number of barriers was eight (2 epitaxially × 4 mesas in series).

#### IV. DC AND AC MEASUREMENTS

For the characterization of the devices, we took advantage of various transmission line topologies. The outputs are the values of the small signal equivalent circuit, which permits one to subsequently simulate the large signal behavior of the devices under large signal conditions by a harmonic balance method. Also the electromagnetic (EM) behavior of the devices can be assessed using EM codes combined with network analysis through the use of scattering matrix [6]. The intrinsic elements, namely the level of conductance, which describes the leakage current through (tunneling effects) and over (thermionic emission) the barrier along with the intrinsic capacitance non-linearity, can be obtained using the coaxial type configuration (see Figure 5). Figure 2 shows the locus of the complex reflection coefficient versus frequency between 500 MHz and 40 GHz at zero-bias. A near pure capacitive behavior is apparent in this figure. The real part of the impedance was found to be as low as 0.8 Ω, irrespective of the applied bias.

@ 300K

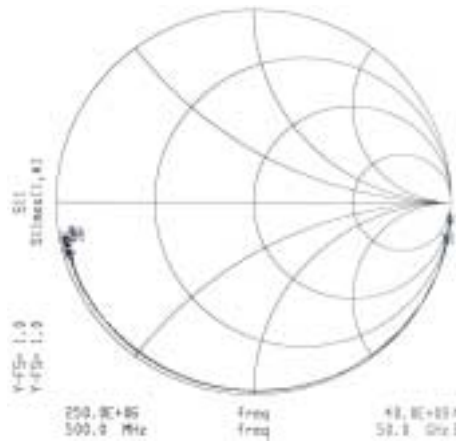


Figure 2: Plot on Smith chart of the frequency dependence of the reflection coefficient at zero-bias for a coaxial-type device configuration ( $\varnothing$  20  $\mu$ m).

These measurements can be used for investigating the intrinsic capacitance-voltage characteristics whose examples are shown in Figure 3. The devices exhibit an excellent symmetry with respect to the Y-axis. For this dual barrier scheme the zero-bias capacitance is  $1.7 \text{ fF}/\mu\text{m}^2$ . At 8V the capacitance reaches practically its saturation value of  $0.39 \text{ fF}/\mu\text{m}^2$ , yielding a capacitance ratio of 4.3:1. Concerning the leakage current, which is characterized by the conductance-voltage plot (also shown in Figure 3), we found a value of  $1.37 \mu\text{S}/\mu\text{m}^2$  at the reference voltage of 6 V, which corresponds to an increase in the conduction mechanisms due to impact ionization in the  $2 \times 10^{17} \text{ cm}^{-3}$  InGaAs ( $E_g = 0.8 \text{ eV}$ ) cladding layer. The quality factors at 5 GHz are 20800 (0V), 2720 (2V), 80 (4V), 11(6V) respectively. By assuming a predominance of displacement current ( $J_D$ ) for  $J_D/J_C = 10:1$  ( $J_C$  being the leakage current) it is believed that the diode could operate correctly under a full 8V peak to peak pump voltage @ 250 GHz.

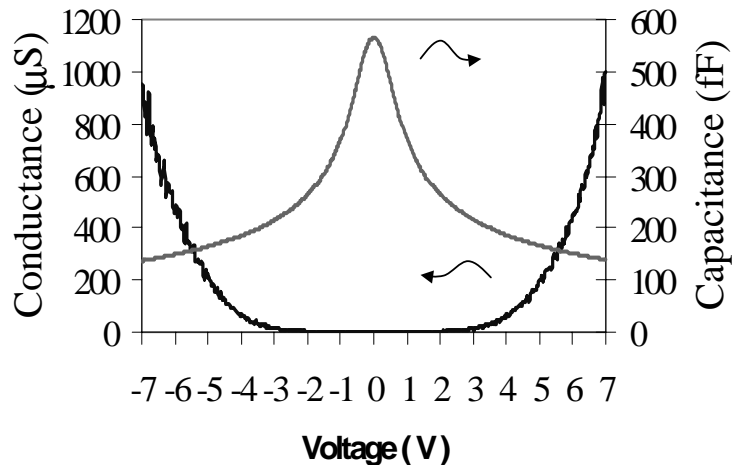


Figure 3: Measured capacitance and conductance-voltage characteristics for a two-barrier coaxial-type device ( $\varnothing 20 \mu\text{m}$ ).

## V. INFLUENCE OF DOPING CONCENTRATION

In order to have further insight into the capacitance-voltage relationship when the doping concentration is varied, we show in Figure 4 the simulated capacitance-voltage curves for a one barrier scheme. In order to obtain these data, we solved the Poisson equation in the Thomas-Fermi approximation. This means that the charges resulting from the leakage current are neglected (zero-current approximation). The electronic charges in the accumulation layer, which are trapped in front of the blocking barrier, can be calculated using a semi-classical distribution function.

Doping ( $\text{cm}^{-3}$ )	$1 \times 10^{17}$	$2 \times 10^{17}$	$4 \times 10^{17}$
$C_0$ (fF/ $\mu\text{m}^2$ )	2.6	3.25 (3.4)	3.6
$C_{\text{sat}}$ (fF/ $\mu\text{m}^2$ )	0.4	0.65 (0.78)	0.9
$C_0 / C_{\text{sat}}$	6.5:1	5:1 (4.3:1)	4:1

Table 1: Summary of C-V characteristics in terms of zero-bias ( $C_0$ ), capacitance saturation ( $C_{\text{sat}}$ ) and capacitance ratio. The measured data are in brackets.

Further details on the assumptions and the numerical procedure can be found in ref [7]. A comparison between calculated and measured data (shown in brackets in table 1), for the  $2 \times 10^{17} \text{ cm}^{-3}$  doping concentration, gives a satisfactory agreement and supports the validity of calculations. With respect to the trends, as a function of the doping concentration, it can be noted, as expected, that any increase in the donor concentration degrades the capacitance contrast with a concomitant increase in the capacitance level. However such a degradation is of minor importance in comparison with the associated benefit in terms of current capability.

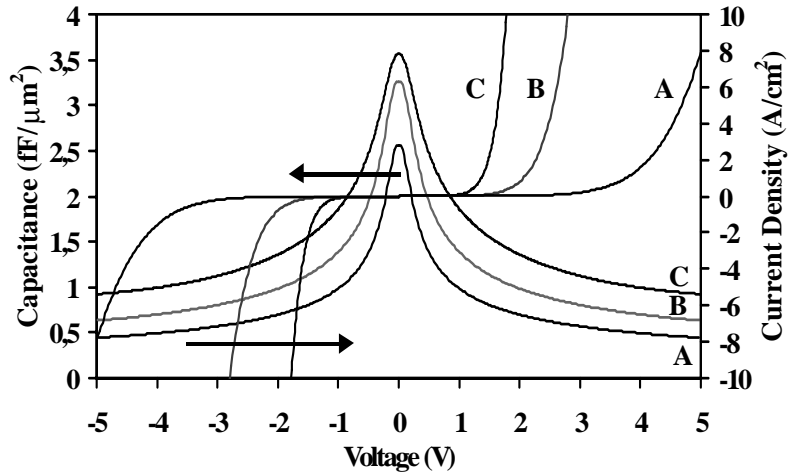


Figure 4: Simulated capacitance and current-density characteristics for different doping concentrations (single barrier), A= $1 \times 10^{17} \text{ cm}^{-3}$ , B= $2 \times 10^{17} \text{ cm}^{-3}$ , C= $4 \times 10^{17} \text{ cm}^{-3}$ .

From the leakage current point of view, a degradation of voltage handling can be observed. Therefore for a  $8 \text{ A/cm}^2$  reference, the breakdown voltages are 5V ( $1 \times 10^{17}$ ), 2.8V ( $2 \times 10^{17}$ ) and 1.9V ( $4 \times 10^{17}$ ), respectively. Tunneling effects through the barrier are responsible for the leakage current at moderate voltages whereas the breakdown effect can be explained by impact ionization in the adjacent low gap layer. Increasing the doping concentration strengthens both leakage mechanisms via an increase in the Fermi level and the internal electric field in the InGaAs layer. On the basis of this study carried out on a single barrier device, which takes the doping concentration as a parameter, the benefit of epitaxial and/or planar stacking is quite

obvious by preserving the voltage handling of the device and a capacitance level which are compatible with high frequency operation. However, in order to alleviate the decrease in the capacitance ratio, it is believed that other routes have to be chosen, notably those involving planar doping or pre- and post-well configurations. In both cases, the basic idea is to shorten the screening length by accumulating electrons closer to the barrier (quantum well scheme or delta doped concentration). Both techniques have respective advantages and some conclusions can be found in ref [8] and [9].

## VI. DE-EMBEDDING AND FURTHER IMPROVEMENTS

The capacitance variations can also be recorded for the CPW and series type configurations. For the latter, which have to be "flip-chip" mounted in the tripler blocks, there are no coplanar footprints for wafer probing of the devices, only pads. In this particular case, two of the three probes were used to contact the two pads facing each other. It can be shown that this kind of arrangement gives experimental data sufficiently accurate for de-embedding an equivalent circuit, which now takes into account, not only the intrinsic elements, but also the parasitics depending on the topology of the diodes.

These parasitics are the self-inductance and the pad-to-pad and bridge-to-pad capacitances, due to interconnections and the series resistance. A knowledge of these parameters is of prime importance for accessing the capability of the device for use in a tripler block, and for operating at very high frequency via the cut-off frequency. Ideally, special patterns have to be planned in the mask set to help in the derivation of parasitics. Notably a TLM pattern is generally set in the test field along with open-circuit ( $C_p$ ) and air-bridged pads ( $L_p$ ). Short-circuited devices yielded a self-inductance value in the 60 pH range for a single device whereas the capacitance parasitic value was found in the 20 fF range, with a large uncertainty due to the calibration and error measurements of reflection coefficients.

It can be shown, provided no extra resistive term was added, that the tripler efficiency is not affected by the reactive elements. This is true only for a perfect matching of the large signal admittance of the diode to the circuit, which is not always satisfied in practice. Improvements in the parasitics were demonstrated over the past through an optimized topology and/or the surface channel technology [10]. Deep etching was not performed here explaining why the parasitic capacitance is relatively high. This can be envisaged on the basis of Schottky technology carried out at the University of Lille [11] for which a post-process deep-etch was conducted, aimed at lowering the value of  $C_p$ .

Another key figure of merit is the series resistance. With respect to this specific issue, encouraging results were shown in Figure 2 with value as low as 0.8  $\Omega$  being observed. However, a major drawback associated with the planar integration of series type devices, instead of full epitaxial stacking, stems from an increase in the series resistance. The overall series resistance increases as the number of interconnected

devices increases, due to the combination of vertical and planar topologies. Reducing the total series resistance can be achieved by reducing the “spreading resistance”, which is believed to be a major contribution towards  $r_s$ . There are currently two methods to achieve this goal : increasing the epitaxial thickness of the buried n+ layer [12] and/or increasing the doping density of this layer. In our current work, we kept the thickness to 1  $\mu\text{m}$  since increasing this thickness to several microns is not technologically realistic using MBE growth, whilst we increased the doping density to  $1 \times 10^{19} \text{ cm}^{-3}$ . We believe that the low value of the series resistance, which was observed in our measurements, is a direct consequence of the elevation of this doping density. Remembering that the n+ layer serves two purposes (i) ohmic contacts and (ii) mesa interconnect, another potential method is to introduce a transfer step [13]. Prior to this transfer, a gold layer can be deposited, this metallic layer can now function as the mesa-contacting layer. By these means we have greater control over the device topology. Therefore a quasi-vertical topology can be achieved. In the past such a scheme had been attempted by taking benefit of substrate-less technology [14]. However such a technology was found to be very difficult to fabricate practically whereas a transfer technique onto a host substrate could avoid most of the difficulties encountered with free standing membrane structures having post-metallization. In order to illustrate the advantages afforded by a substrate-transfer process onto a host quartz substrate, Figure 5 shows an SEM view and corresponding schematics of two transferred devices. In the type I configuration, the “spreading resistance” dominates the value of  $r_s$ , whereas in the type II configuration, a vertical current flow is preserved so that an improvement in the series resistance can be pointed out. Details of the technology of SU-8 grafting techniques and RF assessment can be found in [15].

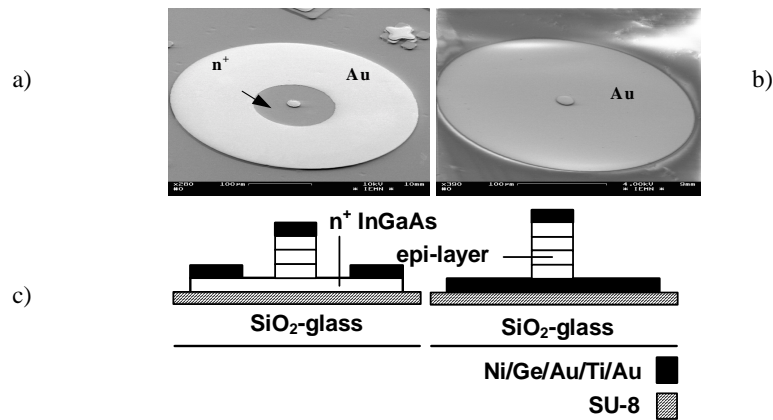


Figure 5: SEM view of various topologies of transferred HBV devices (a) **type I**: n<sup>+</sup> mesa-contact, (b) **type II**: gold mesa-contact and (c) schematics of both topologies.

## V. CONCLUSION

New degrees of freedom in the fabrication of high performance devices were afforded by epitaxial stacking and planar integration, which open the way to a full 3D integrated solid-state multiplier. The advantage of a series type connection was demonstrated with a zero-bias capacitance as low as  $0.425 \text{ fF}/\mu\text{m}^2$  for a eight-barrier scheme, while preserving a capacitance ratio of 4.3:1.

A significant degradation of the series resistance ( $r_s$ ) was noted for air-bridge contacted devices with respect to vertical devices which exhibit a record  $r_s$  as low as  $0.8 \Omega$ . Nevertheless it is believed that intrinsic cut-off frequencies in the far infrared region can be achieved owing to the drastic decrease in the capacitance level. High quality factors have been obtained together with a high power handling capability. A different device topology is also proposed, which could lead to a further reduction in the value of  $r_s$ . This has been made possible by using substrate-transfer techniques.

## VI. ACKNOWLEDGMENTS

The authors would like to thank E. Delos and S. Lepilliet for their help during the characterization.

This work was supported by CNES contract # 714/98/CNES/7280/00 and ESA contract # 13927.99.

## VII. REFERENCES

- [1] X. Mélique, A. Maestrini, P. Mounaix, M. Favreau, O. Vanbésien, J.M. Goutoule, G. Beaudin, T. Nähri and D. Lippens, "Record performance of a 250 GHz InP-based heterostructure barrier varactor tripler", *Electronics Letters*, vol. **35**, n°11, pp. 938-939, May 1999 and to be published in *IEEE Microwave Theory and Techniques*, June 2000.
- [2] J. Stake, L. Dillner, S. Jones, C. Mann, J. Thornton, J. Jones, W. Bishop and E. Kollberg, " Effects of Self-heating on planar heterostructure barrier varactor diodes", *IEEE Transactions on Electron Devices*, vol. **45**, n°45, pp.2298-2303, 1998.
- [3] E. Kollberg, T. Tolmunen, M. Frerking, and J. East, "Current saturation in submillimeter wave varactors", *IEEE Transactions Microwave Theory and Techniques*, vol. **40**, n°5, p.831, May 1992.
- [4] E. Lheurette, P. Mounaix, P. Salzenstein, F. Mollot and D. Lippens, "High performance InP-based heterostructure barrier varactor in single and stack configuration", *Electronics Letters*, vol. **32**, n°15, pp.1417-1418, July 1996.
- [5] G. Porkolab, Y Chen, S. Tabatabaei, S. Agarwala, F. Johnson O. King, R. Frizzel, W. Beard and D. Stone, "Air-bridges, air-ramps, planarization, and encapsulation using pyrolytic photoresist in the fabrication of three dimensionnal microstructures", *J. Vac. Sci. Technol.*, vol. B **15**, n°6, pp.1961-1965, Nov/December 1997.

- [6] J. Carbonell *et al*, Proceedings of the "28<sup>th</sup> European Microwave Conference", Amsterdam, The Netherlands, 1998.
- [7] R. Harvart, E. Lheurette, O. Vanbésien, P. Mounaix, F. Mollet and D.Lippens, "Step-like heterostructure barrier varactor", IEEE Transactions on Electron Devices, vol. **45**, n°11, pp. 2291-2297, November 1998.
- [8] V. Duez, X. Mélique, O. Vanbésien, P. Mounaix, F. Mollet and D.Lippens, "High Capacitance ratio with GaAs/InGaAs/AlAs heterostructure quantum well-barrier varactor", Electronics Letters, vol. **34**, n°19, pp.1860-1861, September 1998.
- [9] E. Lheurette, X. Mélique, P. Mounaix, F. Mollet, O. Vanbésien and D.Lippens, "Capacitance Engineering for InP-based Heterostructure Barrier Varactor", IEEE Electron Device Letters, vol. **19**, n°9, pp.338-340, September 1998.
- [10] S. Marazita, W. Bishop, T. Cunningham, P. Koh, T. Crowe and R. Weikle, "8<sup>th</sup> Symposium on Space Terahertz Technology", Harvard University, March 1997.
- [11] F. Podevin *et al*, "11<sup>th</sup> Symposium on Space Terahertz Technology", Ann Arbor, MI, in this issue.
- [12] J. Jones, W. Bishop, S. Jones, G. Hait, "Planar multibarrier 80/240 GHz heterostructure barrier varactor tripler", IEEE Transactions on Microwave Theory and Techniques, vol. **45**, n°4, p. 512, 1997.
- [13] S. Arscott, P. Mounaix and D. Lippens "Transferred In-P based HBVs on glass substrate", Electronics Letters, vol. **35**, n°17, pp.1493-1494, August 1999 and S. Arscott, P. Mounaix and D. Lippens, "Substrate transfer process for InP-based heterostructure barrier varactor devices", J.Vac. Sci. Technol. , vol. B **18**, n°1, pp.150-155, Jan/February 2000.
- [14] A. Simon, A. Crub, V. Krozer, K. Beilenhoff and H. Hartnagel, "4<sup>th</sup> Symposium on Space Terahertz Technology", Los Angeles, CA, USA, pp. 392-403, Mar.30-Apr.1 1993.
- [15] S. Arscott, T. David, X. Mélique, P. Mounaix, and D. Lippens, "Towards terahertz circuits via InP micromachining techniques", "12<sup>th</sup> International Conference on Indium Phosphide and Related Materials (IPRM00)", Williamsburg, VA, USA, May 2000.

# HETEROSTRUCTURE BARRIER MIXERS FOR TERAHERTZ APPLICATIONS

F. Podevin, P. Mounaix, O. Vanbésien, M. Chaubet\* and D. Lippens

Institut d'Electronique et de Microélectronique du Nord, UMR 8520  
Université des Sciences et Technologies de Lille  
Avenue Poincaré, BP 69, 59652 Villeneuve d'Ascq Cedex, France  
\* Centre National d'Etudes Spatiales  
18 Avenue Edouard Belin, 31401 Toulouse Cedex, France  
Corresponding author: Florence.Podevin@IEMN.univ-Lille1.fr

**Abstract** : This paper deals with Schottky - and Heterostructure - Barrier devices fabricated for planar integration in a 560 GHz Subharmonic Mixer (SHM). Taking advantage of an InP-based technology, two barrier types, metal/InGaAs and metal/InAlAs/InGaAs respectively, have been investigated. The design was carried out by means of self-consistent quantum calculations and the fabrication involved submicron T-shaped contacts and air-bridge technology for back-to-back integrated diode pairs. The trade-offs between the key figures of merit for SHM are discussed and compared to experimental results. In addition, various studies of the potential of a Planar Doped Heterostructure Barrier for single SHM devices are presented.

**Indexing terms** : *Heterostructure devices, Subharmonic Mixer, InP technology, Terahertz, Space applications*

## 1. Introduction

Recently, impressive results have been published about sub-mm subharmonic mixing, notably by the Jet Propulsion Laboratory (JPL) at 560 GHz [1], 640 GHz [2] and 2.5THz [3]. For these demonstrations, a GaAs technology was used with a barrier effect achieved through a metal/GaAs n-doped epilayer junction. The built-in potential (0.7 eV) is adequate for low saturation current, but, as a consequence, the local oscillator power to optimally pump the back-to-back diode pair is relatively high. In addition, the optimization of the series resistance, which is known as one of the key figure of merit for high performance, faces some limits owing to the relatively wide band gap of GaAs (1.4 eV). From this point of view, an InGaAs layer lattice-matched to InP having a narrower gap ( $E_g$

= 0.75 eV) appears to be a better candidate [4]. The ideality factor of InGaAs to metal junctions ranges from ~1.2 to 1.6 (depending on the contact deposition)[5]

However, some drawbacks associated with its low Schottky built-in potential (0.22 eV) could be pointed out, motivating the use of InAlAs/InGaAs epilayers. In this communication, the trade-offs related to the use of a metal/narrow-gap configuration are firstly addressed to the fabrication on the submicron scale of anti-parallel Schottky diodes and secondly followed by theoretical quantum calculations. In a second stage, we investigate a metal/wide gap/narrow-gap configuration, with theoretical and experimental comparisons. Finally, we deal with the potential of a single Heterostructure Barrier set in conduction mode via  $\delta$ -doping.

## 2. Metal/n-type InGaAs contact

From a technological point of view, the active epilayers were grown by a Gas Source MBE on an InP, Fe-doped, substrate. The ohmic contact layer was doped up to  $1 \times 10^{19} \text{ cm}^{-3}$ , whereas the Schottky layer is n-doped with a donor concentration of  $2 \times 10^{17} \text{ cm}^{-3}$ . The anti-parallel diode pair is fully planar. Firstly wet chemical etching was used to perform a recess down to the  $n^+$ -doped layer with a trench formation before evaporating the ohmic contact. Subsequently, a one step molding stage was conducted and followed by the metallization of both the Schottky contacts on the submicron scale (gate length down to  $0.1 \mu\text{m}$ ) and the free standing air-bridges interconnecting the anodes to the pads. Towards this goal, e-beam molds have been fabricated with a bi-layer electron resist (PMMA/copolymer) via an e-beam patterning at various doses. A SEM view of a typical device, interconnected with  $15 \mu\text{m}$  long tapered air bridges, is shown in Figure 1.

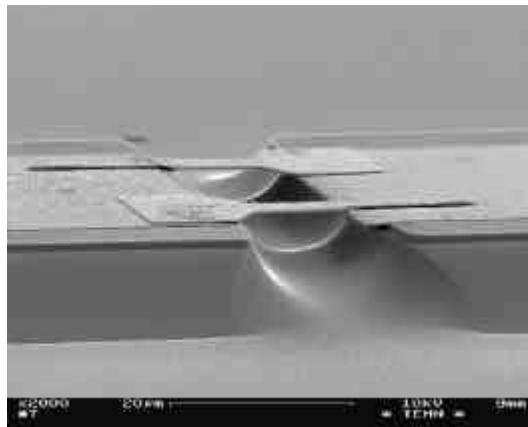
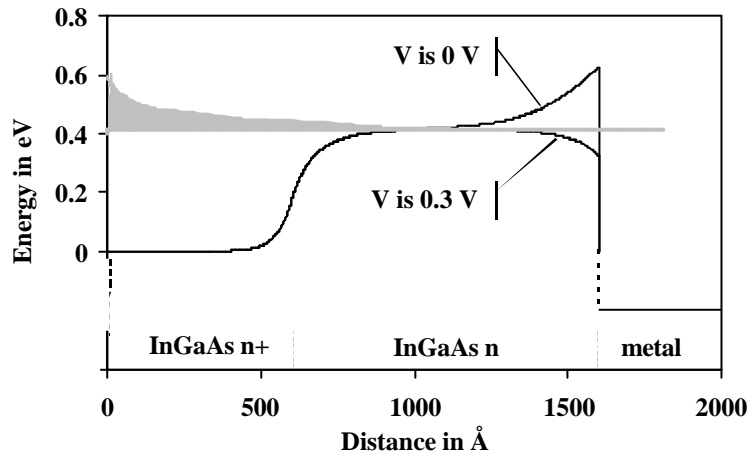


**Figure 1** SEM view of a typical diode pair with T-gate  $0.1 \times 10 \mu\text{m}^2$  finger shaped Schottky anodes.

On the basis of the previous discussion, the metal/InGaAs devices were developed for low driven power devices. The epilayer design was first conducted by extending, to the Schottky diode case, the in-house code developed earlier for quantum-sized devices [6]. This code was performed in order to solve, in a first stage, the one dimensional Poisson equation when voltages are applied to a given structure (Schottky contact, heterostructure Schottky contact, single barrier varactor, resonant tunneling diodes. .). In a second stage, a numerical solution of the Schrödinger equation gives the wave function from which any information concerning the transmission or reflection coefficients is obtained. As shown in the following equation (Eq1), the integral of current density is calculated from the product between the previous transmission and the supply function, on the entire energy continuum :

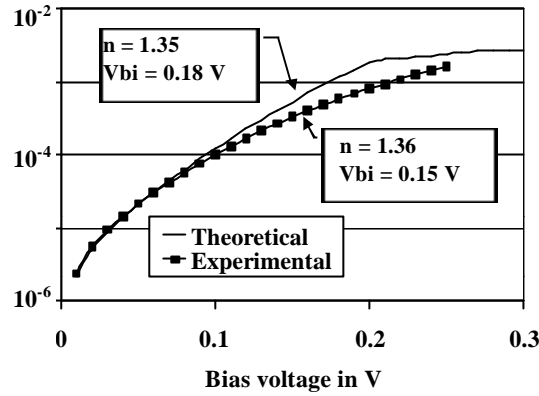
$$J = \int_0^{+\infty} T(E) \times F(E) dE \quad (\text{Eq1})$$

Very shortly, one can see in Figure 2, the conduction band bending at zero bias and at 0.3 V for an InGaAs epilayer. When a voltage is applied, the current flows from the semi-conductor to the metal, which is represented on the schematic by the integral of current "through" the potential curve at 0.3V, in arbitrary units. It is very important to take into account all the conduction current contributions (as tunneling field emission for example) to describe in a realistic way the I-V characteristics of narrow gap materials. As a current manner, we do not observe pure tunneling effect (as it would be the case with high gap materials) and the electronic flow is maximal for quasi thermal energy levels, which explains relatively good values for the ideality factor (n is ~1.3).



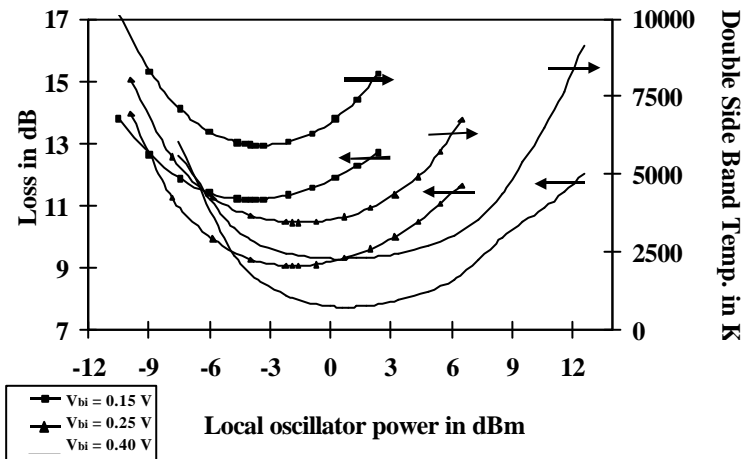
**Figure 2** Conduction Band Bending at zero bias and at 0.3V. The InGaAs lattice-matched to InP structure is affected by the applied voltage (0.3V) and thus the current can flow from the semi-conductor to the metal. The integral of current is also plotted in an arbitrary unit.

Figure 3 shows a comparison between measured and calculated I-V curves, at room temperature. Good agreement is thus obtained between theory and measurement with, as expected, a threshold voltage for conduction onset quite low ( $V_{bi} \sim 0.15V$ ), and correct ideality factors for InP-based devices.



**Figure 3** : Comparison between experimental and calculated I-V characteristics for a metal/InGaAs ( $2 \times 10^{17} \text{ cm}^{-3}$ ) Schottky contact fabricated in our laboratory.

In order to investigate the influence of such low values of  $V_{bi}$  on the mixer performances, some simulations were performed by means of Microwave Design System, by Hewlett Packard. They showed that a strong dependence exists between the mixer performances at 560 GHz and the Schottky diodes electrical characteristics: built-in voltage  $V_{bi}$  and ideality factor  $n$  (see Figure 4).



**Figure 4** Mixer performances vs the local oscillator power across the diodes. Parameter is the built-in voltage  $V_{bi}$ .

As plotted in Figure 4, increasing  $V_{bi}$  could afford less loss ( $L$ ) and smaller double-side-band noise temperature ( $T_{DSB}$ ). Ideally,  $L$  and  $T_{DSB}$  are about 8 dB and 2500 K

respectively for a pump power of 1 dBm. This can be explained from the well-established thermal relationship (Eq2) between  $V_{bi}$  and  $I_s$ , the saturation current :

$$I_s = S_A \cdot T^2 \cdot A^{**} \cdot \exp(-qV_{bi} / k_B T) \quad (\text{Eq2})$$

where  $S_A$  is the area,  $T$  the temperature in K and  $A^{**}$  the Richardson constant for InAlAs. This relation shows that increasing  $V_{bi}$  decreases  $I_s$ , which is known as a source of degradation in terms of mixing performances. Thus, efforts were pointed out towards an heterostructure Schottky diode. By means of an InAlAs layer ( $E_g$  is 1.47 eV) we could raise the knee voltage up to about 0.5 V.

### 3. Metal/InAlAs/InGaAs Schottky contact

As seen previously, the metal/InAlAs/InGaAs junction was fabricated in order to limit the saturation current, which is known as a source of degradation in mixer performances. For all the structures, the InAlAs layer was undoped (doping influence is totally negligible, see Figure 5). Varying its thickness permits us to modulate the conduction properties. Basically the total conduction current is the result of three contributions : (i) pure tunneling from the highly populated states below the Fermi level, (ii) thermally assisted tunneling phenomena and (iii) thermionic emission over the InAlAs barrier. Quantum calculation does not need to make a distinction between these contributions and can be used to investigate the influence of the InAlAs layer. Figure 5 illustrates some of the results showing the thickness dependence of the apparent ideality factor  $*$ . There clearly exists an optimum between an ultra thin barrier where pure tunneling current is dominant and a thick barrier where Fowler-Nordheim field emission becomes the significant component. For comparison, we also reported the ideality factors measured for various devices.

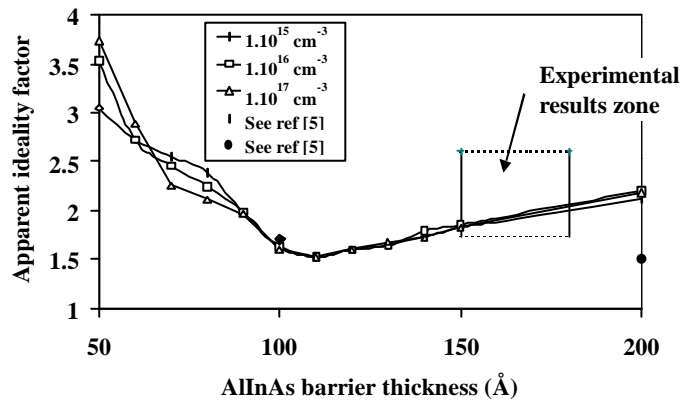


**Figure 5** Thickness dependence of the apparent ideality factor in a metal/InAlAs/InGaAs contact layer. Parameter is the InAlAs doping level. Some experimental results are also presented.

Dots refer to [5] : ideality factor for an InAlAs barrier thickness of 100Å and 200Å.

\* Strictly speaking, the ideality factor is defined for thermionic emission processes. This explains the fact that we used an apparent figure.

As a general rule, the insertion of an InAlAs layer, which was found beneficial for voltage handling, has in counterpart degraded the non-linearity of the diode through an increase of the ideality factor up to 1.5 (in the best case). This result can be explained by observing the energy levels where conduction operates and by studying the different current components. In fact, two effects are in competition. In the thin barriers case, tunneling emission occurs at a relatively low ground energy level  $E_{\text{tun}}$  compared to the barrier height  $\phi_b$ . When the barrier is getting thicker, the deep tunnel contribution is lowered for the benefit of thermally assisted tunneling conduction processes at higher energies, closer to a thermionic emission process (where  $n$  is quasi ideal), which explains the  $n$  improvement. In the same time, thick barriers are strongly affected by the triangular-shaped barrier when a voltage is applied. Then, resonant Fowler-Nordheim current components appear. They consist in preferential conduction paths at well-defined quantum-size energy levels  $E_{\text{FN1}}, \dots, E_{\text{FNn}}$ , revealed by the well-defined peaks in the energy-current distribution. Both cases of the thin and thick barriers for a given electric field in the InAlAs barrier are represented in Figure 6.

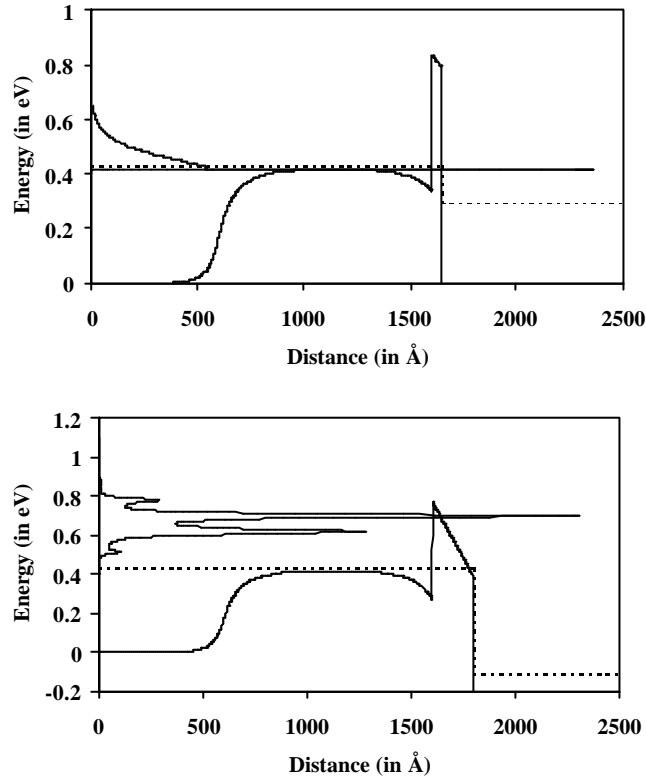


**Figure 6** Both figures represent the conduction band bending of a  $n^+-\text{InGaAs} / n\text{-InGaAs} / \text{InAlAs} / \text{metal}$  Schottky heterojunction. The barrier thickness are  $50\text{\AA}$  and  $200\text{\AA}$  respectively for the above and below figures. Applied voltages are  $0.136\text{V}$  and  $0.545\text{V}$  respectively, in order to keep the same electric field in the triangular shape. In the thin barrier case, conduction is via pure tunneling; in the thick one, four preferential paths are chosen. Dotted lines represent the Fermi level in the semi conductor and the metal.

With an increase of the barrier width, the ground quantum level of the resonant Fowler-Nordheim conduction mode tends to bury in the triangular well formed under bias at the wide-gap semiconductor / metal heterointerface, degrading, as a consequence, the ideality factor. Competition between both opposite behaviors (tunneling and Fowler-Nordheim) implies an optimum, reached for a barrier thickness of about 100Å.

#### 4. $\delta$ -InGaAs / InAlAs / $\delta$ -InGaAs layer

In contrast to the above case, we employed, here, a technology without any Schottky effect. The rectifying barrier is introduced via a Semiconductor Heterostructure Barrier. This gives to the I-V curve, a natural anti-symmetry, in forward and reverse bias conditions. Thus, a Sub Harmonic Mixer could be fabricated by means of a single device, avoiding the parasitic elements inherent to the counter-balanced configuration. Such advantages with a natural anti-symmetry were already exploited for the Heterostructure Barrier Varactors, and hence, for a reactance non-linearity. On this basis, we recently reported the highest performances for a HBV tripler using an InP technology [7].

In the present work, we are taking advantage of the symmetry in a conductive mode. To this end, we designed and fabricated Heterostructure Barrier devices with  $\delta$ -doping grown plane on each side of the barrier ( $\delta$ -HB). The epitaxial sequence is shown in Figure 7 (left side). The  $\delta$ -planes are typically 15Å thick. Practically, their doping concentration can range from  $1 \times 10^{12} \text{ cm}^{-2}$  up to  $1 \times 10^{13} \text{ cm}^{-2}$ . The structure barrier level is 0.54eV with InAlAs (the same barrier as the one used in the heterostructure Schottky contact).

InGaAs	$n+=5 \times 10^{18} \text{ cm}^{-3}$	350Å
InGaAs	$n=1 \times 10^{15} \text{ cm}^{-3}$	40Å
InGaAs	$n_s$	15Å
InGaAs	$n=1 \times 10^{15} \text{ cm}^{-3}$	45Å
InAlAs	$n=1 \times 10^{15} \text{ cm}^{-3}$	h
InGaAs	$n=1 \times 10^{15} \text{ cm}^{-3}$	45Å
InGaAs	$n_s$	15Å
InGaAs	$n=1 \times 10^{15} \text{ cm}^{-3}$	40Å
InGaAs	$n+=5 \times 10^{18} \text{ cm}^{-3}$	350Å
InP	Semi insulating	

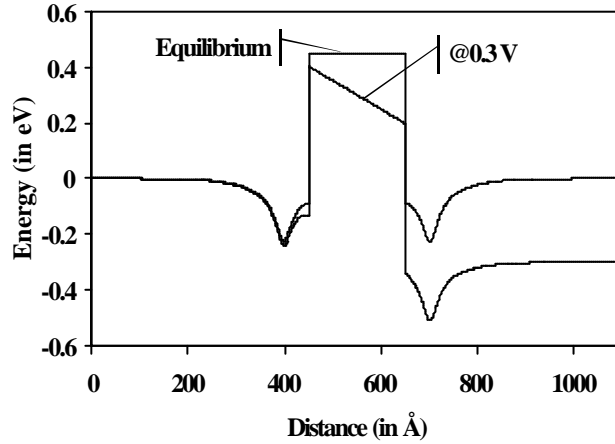


**Figure 7** Epitaxial structure of a  $\delta$ -HB on the left hand side. Potential profile of the same structure at equilibrium and under bias conditions, on the right hand side.

The barrier thickness (h) is 200Å and the sheet doping concentration ( $n_s$ ) is  $1 \times 10^{13} \text{ cm}^{-2}$ .

In Figure 7 (right hand side), one can see the potential profile of such a symmetric heterostructure, at equilibrium and under bias control. The offset between the Fermi levels on each side of the barrier implies a current flow from higher electronic levels down to lower ones. See [8] for more information on the  $\delta$ -HB.

If one reminds the parametric study between the “apparent” ideality factor and the barrier thickness performed in the heterostructure Schottky contact case, one can expect a similar dependence in this case. In fact, same effects are observed with an optimum reached for  $h \sim 100 \text{ \AA}$ . This sounds logical since the triangular barrier well forms identically under bias conditions, and this whatever  $n_s$ . However, the optimum is higher with  $n$  equal to 2.2. This value is bigger than 2; one reason could be the natural symmetry of the structure, as discussed in [9] for a Planar Doped Barrier (PDB).

Concerning the sheet doping concentration, Figure 8 shows the degree of freedom afforded by  $n_s$  variation. It can be shown that the threshold voltage  $V_{th}$  depends on the donor concentration, and can be thus modulated practically at will. The  $\delta$ -doped plane makes the effective barrier height to change. When the planes are highly doped, the wells at each part of the barrier become deeper and the barrier appears to be higher than  $\Phi_b$  (InAlAs barrier height value). For instance,  $V_{th}$  can be as low as 0.2 V for a  $1 \times 10^{13} \text{ cm}^{-2}$  concentration of the  $\delta$ -planes and as high as 0.8 V for  $1 \times 10^{12} \text{ cm}^{-2}$ .

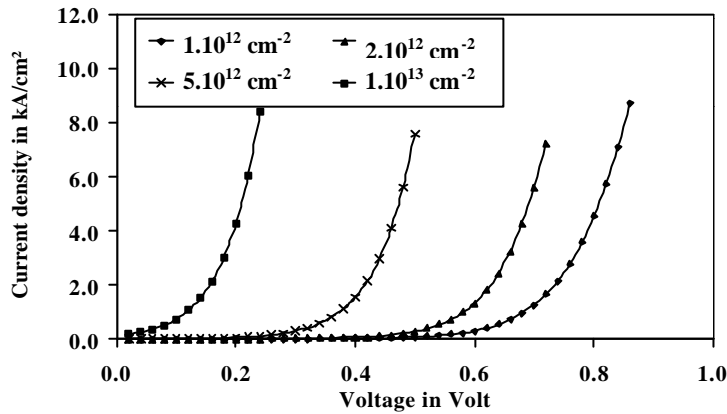


**Figure 8** I-V curves at various sheet carrier concentrations in the planar doping.

Experimental study has been realized yet, on a  $\delta$ -HB with  $n_s = 2 \times 10^{12} \text{ cm}^{-2}$ . The following I-V characteristics (Figure 9) presents a very good asymmetry in the current behavior. The conduction offset is slightly higher than that calculated. This is due to a  $30 \text{ \AA}$  AlAs layer that has been incorporated between two InAlAs layers, in order to obtain a symmetric step-like barrier higher than the single InAlAs barrier. See [8].

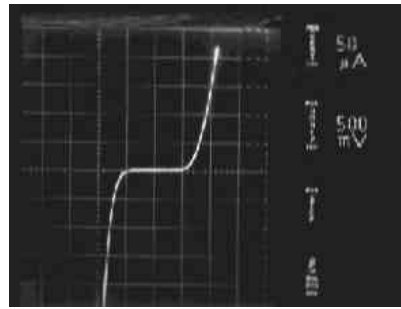


**Figure 9** I-V curve of a  $\delta$ -HB.  $n_s = 1 \times 10^{12} \text{ cm}^{-2}$ . Area =  $1256 \text{ } \mu\text{m}^2$ .

## 5. Conclusion

A compromise can be pointed out between device functionality, technological feasibility, electrical performances and finally compatibility for sub-mm operations. The choice of a specific active layer configuration depends on which features are required for the current framework. Technologically speaking, a knowledge of the pump requirements, loss and noise temperature specifications corresponds to one given component. The large range in the electrical characteristics, which strongly depends on the epitaxial parameters, enables us to choose the most adapted device to the current situation. As an example, the recent advances in solid state sources permits us to relax the pump power in the near future. Concerning the devices design which has been reported here, we aim to use them for applications in the lower part of the Terahertz spectrum. We believe that the advantages of InP could also be exploited at higher frequencies, such as 2.5 THz.

## References

- [1] Oswald *et al*, IEEE Microwave and Guided Wave Let. Vol 8. P 232. 1998.
- [2] Mehdi *et al*, IEEE MTT-S Digest. P 403. 1998.
- [3] Siegel *et al*, IEEE Trans. On MTT. Vol 47. P596. 1999.
- [4] Kordoš *et al*, J. Appl. Phys. Vol 72. P 2347. 1992.
- [5] Marsh *et al*, IEEE Trans. On Electron devices. Vol 45. P 349. 1998.
- [6] Burgnies *et al*, JAP. Vol 75. 1 May 1994.
- [7] Mélique *et al*, Electronics Let. Vol 35. 27 May 1999.
- [8] Lheurette *et al*, IEEE Electron Device Let. Vol 19. No 9. 1998.
- [9] Lee *et al*, Microwave and Optical Tech. Let. Vol 4. No 1. P 53. 1993.

This work was supported by CNES contract # 714/98/CNES/7280/00.

# A 4-8 GHz Quasi-MMIC IF Amplifier for a 690 GHz SIS Receiver

John Ward, David Miller, Jonas Zmuidzinas

California Institute of Technology Pasadena

Peter O'Brien, Henry G. LeDuc, Robert Bicknell-Tassius

Department of Astronomy Pasadena

## Abstract

We are developing a cryogenic low-noise amplifier using quasiparticle transport integrated circuit technology. This amplifier has been demonstrated as a planar quasioptical receiver for the altitude ultraclean laboratory and later will be used on the South Pole Telescope. The circuit consists of a thin pass transistor and a substrate with three  $\mu$  gates. The device is fabricated on a sapphire substrate and is operated at a physical temperature of 4 K. The receiver uses a T-junction plane to achieve a measured uncorrected double-sideband noise temperature of 1.5 K. The receiver was used at the Caltech SOFIA telescope and was used between the receiver and the receiver system. The receiver was developed with a goal of achieving a noise temperature of 1.5 K. The receiver was used at the Caltech SOFIA telescope and was used at the Caltech SOFIA telescope and was used at the Caltech SOFIA telescope.

## I. INTRODUCTION

The IF systems currently in use at ground-based submillimeter observatories typically have bandwidths of 1 GHz. For the higher frequency bands, especially those available to SOFIA and FIRST, a 1 GHz bandwidth will be inadequate for observations of spectral lines from external galaxies. For example, the  $J=6 \rightarrow 5$  emission line of carbon monoxide from the galaxy Arp 220 has a linewidth of over 1.8 GHz. For this reason, the standard IF bandwidth for our Caltech SOFIA instrument and FIRST HIFI will be 4 GHz.

The initial reason for considering a MMIC approach to the amplifier design was to gain better control over parasitics compared to a discrete-component amplifier. However, fabrication of MMIC devices is expensive due to the presence of transistors. Choosing a quasi-MMIC approach not only greatly reduces the fabrication costs, it also permits the selection of transistors from known good wafers. Since many amplifiers will be needed for our SOFIA instrument, the CSO, etc., the relative ease of assembly associated with the MMIC devices was also attractive. Bump-bonding the transistors creates a robust circuit free from wire bond parasitics. Other advantages of the MMIC approach include small size and relatively easy adaptability to different packaging constraints. For example, the MMIC amplifier could more easily be integrated into the mixer block than a discrete-component amplifier.

## II. RECEIVER CONFIGURATION

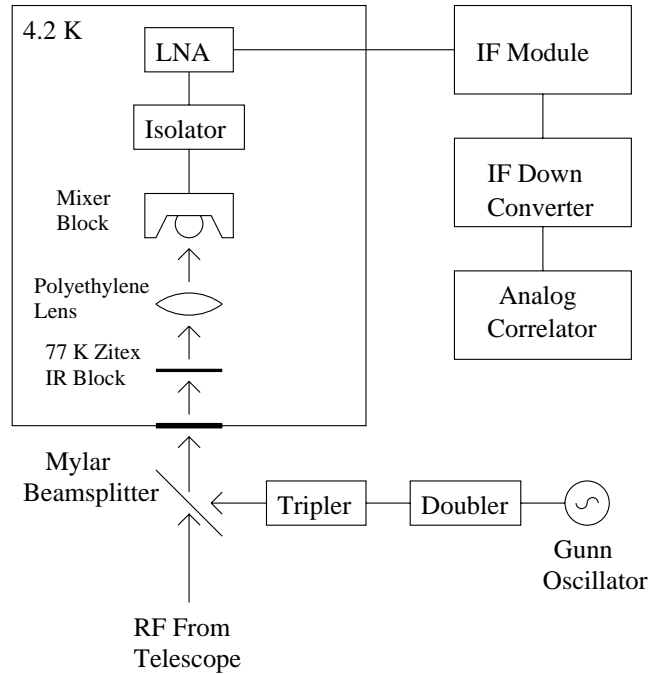


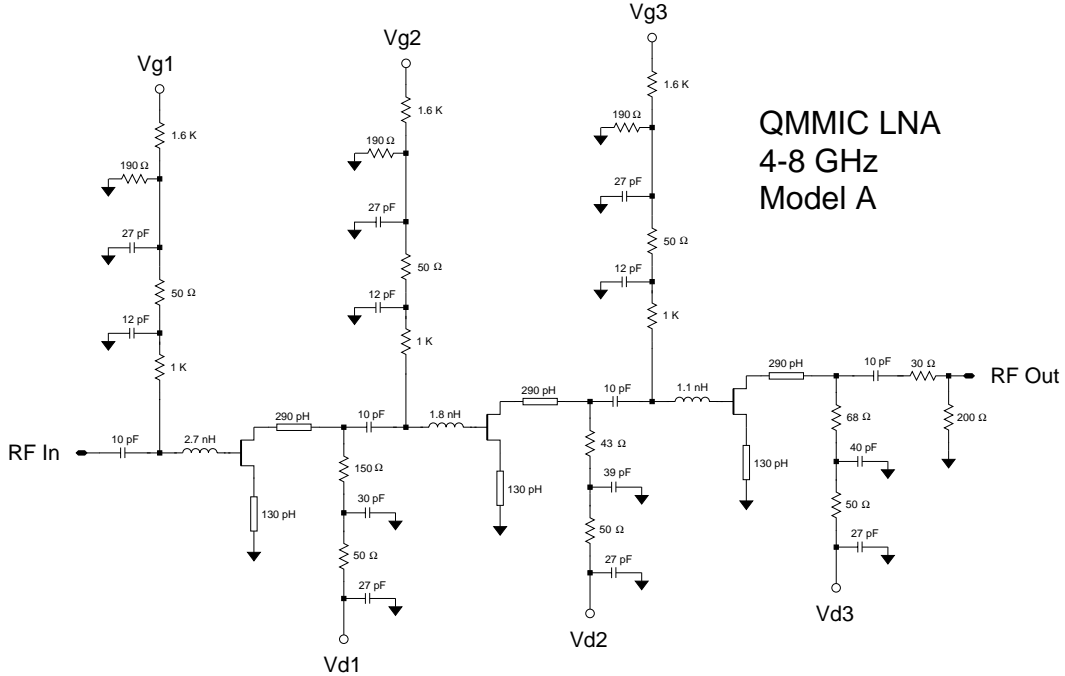
Figure 1: Configuration of the receiver.

A block diagram of the receiver is shown in Figure 1. The local oscillator (LO) is generated by a tunable Gunn oscillator [1] and multiplied by  $\times 2$  and  $\times 3$  varactor multipliers [2]. The LO is combined with the RF signal through a  $13 \mu\text{m}$  mylar beamsplitter, and then enters a liquid helium cryostat through a teflon coated quartz pressure window. A 77 Kelvin Zitex filter blocks infrared radiation. The LO and signal then pass through a polyethylene lens and into a silicon hyperhemisphere antireflection coated with alumina doped epoxy. The hyperhemispherical lens focuses the signal onto a twin slot antenna, which is used for its nearly circular beam profile. Since 690 GHz photons are close to the gap energy of niobium, a NbTiN ground plane ( $T_c=15.75$  Kelvin) is used for the slot antenna to reduce losses associated with the breaking of Cooper pairs. Niobium microstrip lines over the NbTiN ground plane match the signal from the slots into a pair of Nb AlO Nb SIS junctions.

The IF signal is coupled out of the mixer chip through wire bonds to a duroid microstrip circuit that matches the impedance to  $50 \Omega$ . The signal then passes through a 4 to 8 GHz isolator, and into the low noise amplifier. The signal then leaves the 4 Kelvin work surface, exits the cryostat, is amplified by a 4 to 8 GHz room temperature stage, down converted to 0.5 to 4.5 GHz, and analyzed by a 4 GHz analog correlation spectrometer.

### III. QMMIC LNA

The amplifier was designed to operate at 4 Kelvin, with over 30 dB gain in the 4 to 8 GHz band and noise temperatures in that band below about 5 Kelvin. InP HEMTs were obtained from the Microwave and Lidar Technology Section at the Jet Propulsion Laboratory, and their scattering parameters were measured on a microwave probe station. Marian Pospieszalski's FET model [3] was then fit to these data to determine model parameters. The noise prediction from the model, given a best-guess value of the noisy drain-resistor temperature, was used without any direct measurement of the transistor noise correlation matrix. The model was used in the program SuperMix [4] [5] to simulate and evaluate different tuning circuits for the amplifier. The SuperMix software includes an optimizer, which was used to optimize the design for flat gain above 30 dB, low noise, input reflections below about -10 dB, output reflections below -20 dB, and unconditional stability at all frequencies, all while keeping total power consumption low. The DC gate and drain bias for each transistor were kept separate to reduce power consumption on the cryogenic stage and allow performance to be fine-tuned. Two designs were selected for fabrication, one optimized for best performance (Figure 2), and one optimized for greater stability.



g pl er he at

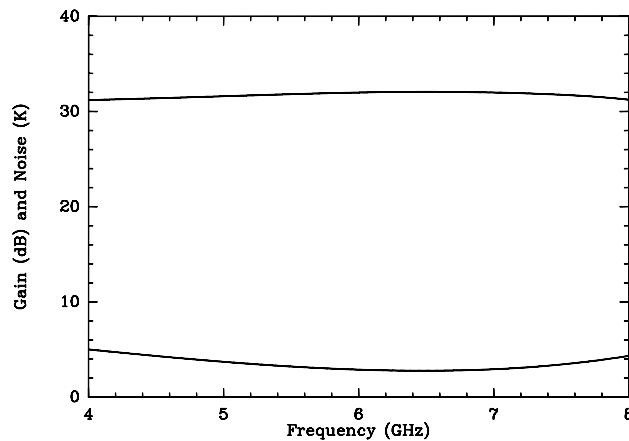
After the ideal circuit designs were completed, physical resistors, capacitors, and inductors were laid out. The substrate includes air bridges and a resistive layer, Table I, but for simplicity does not include via holes. Each component, including five spiral inductors, was simulated with Agilent's EM simulator, *Momentum*. Results of the EM simulations were saved as scattering parameter files which were then imported

<i>Layer</i>	<i>Thickness</i>
Bump Gold	8 $\mu m$
Air Bridge Gold	1 $\mu m$
Air	2 $\mu m$
SiN	296.5 pF/mm <sup>2</sup>
Gold	1 $\mu m$
NiCr Resistor	50 $\Omega$ /square
GaAs	250 $\mu m$

T

LAYERS IN THE QMMIC SUBSTRATE.

back into SuperMix for the final simulation. The results of these simulations are plotted in Figure 3. The final mask layout is show in Figure 4.



g red ted ga a d ose per or a e o the a pl er

The input and output of the MMIC chip are coplanar waveguide (CPW), both to avoid via holes and to allow the devices to be tested on a probe station. A circuit was designed to convert from the MMIC CPW to microstrip, which in turn can be soldered to SMA connector pins. The thickness and dielectric constant of these transition circuit boards were chosen to roughly match those of the MMIC chip. Ground plane spacings for 50  $\Omega$  CPW were calculated for center conductor widths ranging from the MMIC CPW value to that of 50  $\Omega$  microstrip. These values were used to lay out the transition circuit board. Via holes were used to connect the top and bottom ground planes. The EM simulator Momentum predicted reflections below -34 dB in the 4 to 8 GHz band for the transitions.

The amplifier housing was designed to be compact (Figure 5). The microwave and bias circuits were split into two separate cavities on opposite sides of the housing. This way, the microwave side could be kept small to eliminate in-band cavity resonances.

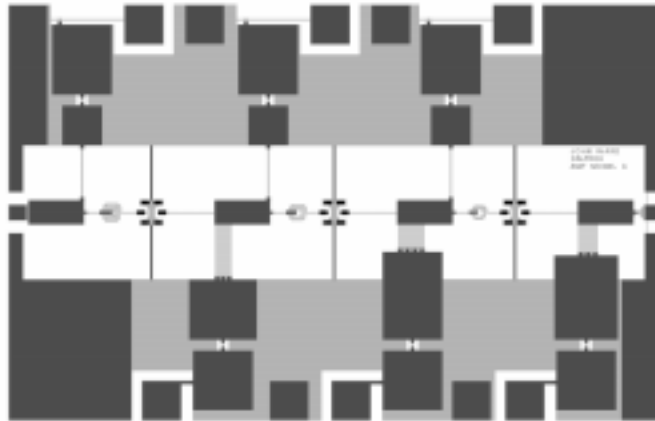


Figure 1 shows the layout of the substrate. The layout is approximately 1.5 mm by 1.5 mm. The layout is divided into three main sections: an input section on the left, a central section, and an output section on the right. There are three input pads at the top, three output pads at the bottom, and three pads in the center. The layout is designed to be compatible with a 50-ohm system.

DC bias for the transistors was brought up to the microwave cavity from the DC cavity using small feed-thru pins. The DC cavity contains filtering capacitors and overvoltage protection diodes.



The assembled amplifier is shown in Figure 2. The length of the device is approximately 1.5 mm. The device is mounted on a substrate and has several pins for DC bias and RF connections.

#### IV. SIS MIXER

The SIS mixer chip was originally designed and fabricated for use with a 1 to 2 GHz IF. The chip was tested with a 1 to 2 GHz IF, and then simulated using the SuperMix library. An IF matching circuit was then designed to allow the chip to be used with a 50-ohm, 4 to 8 GHz low-noise amplifier.

### A. SIS Chip

A photograph of the twin slot antenna is shown in Figure 6. This type of mixer, with twin slot antenna, dual SIS junctions, and anti-reflection coated silicon hyperhemispherical lens, has already been discussed in the literature, and so won't be described in detail here. [6] [7] [8] [9]

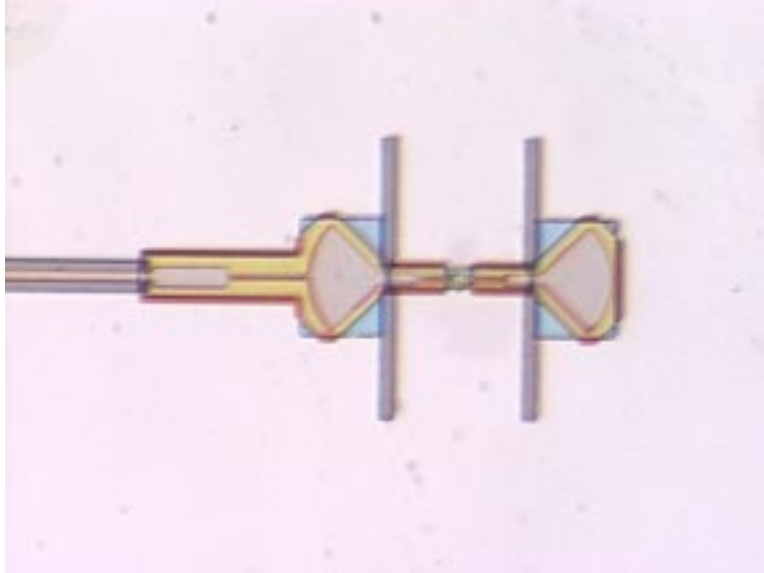


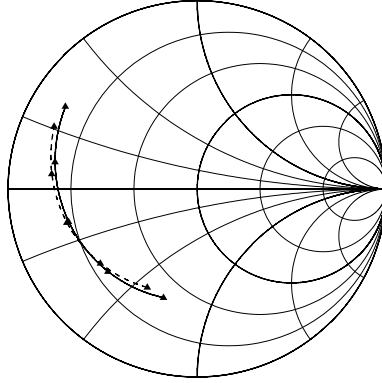
Figure 6: Micrograph of the twin slot antenna structure. The signal enters through the transmission line on the left, passes through the SIS junctions, and is coupled through the slots to the hyperhemispherical lenses. The labels 'hp' and 'ad' refer to the hyperhemispherical lens and antenna design, respectively. The labels 'sg' and 'als' refer to the signal and antenna structure. The labels 'couple' and 'through' refer to the coupling mechanism. The labels 'a sl' and 'o hyperhe' refer to the slot and hyperhemispherical lens. The labels 'sphere u der' refer to the spherical structure under the lens. The labels 'earth the hp' refer to the ground plane. The labels 'The ert al l es are the slots' refer to the slots. The labels 'The u t o s are the la dots ear the' refer to the slots. The labels 'e ter o the' refer to the ground plane. The labels 'The sg al e ts through the tra s s o l e o the le t' refer to the signal and antenna structure.

The mixer was first tested with a 1 to 2 GHz IF system. The unilluminated and pumped current-voltage (IV) curves were measured for a variety of LO frequencies, and the receiver response was measured with a Fourier transform spectrometer (FTS.) The IV and FTS data were used to verify the SuperMix simulations, and to constrain the primary unknown parameter, i.e. the surface impedance of the NbTiN film.

### B. IF Matching Circuit

The IF output impedance of the mixer chip was calculated with the verified SuperMix model. The IF output impedance can be well modeled as a parallel RC circuit, as shown in Figure 7. The capacitance is the combination of the chip capacitance and the quantum susceptance, while the resistance is related to the slope of the pumped IV curve at the bias point. As expected, for a fixed bias voltage and LO power, the IF impedance varies with LO frequency, Figure 8. In particular, the capacitance of the RC model stays constant, while the resistance varies. Similarly, holding the LO frequency constant while varying the LO power also causes the RC model resistance value to vary while the capacitance stays constant. It was found that varying the LO power as a function of LO frequency in a well-defined way will keep the model resistance constant, and thus hold the IF impedance constant with respect to LO fre-

quency. A receiver-tuning lookup table was created to give the target DC pumped SIS current as a function of LO frequency to keep the IF output impedance at a standard value.



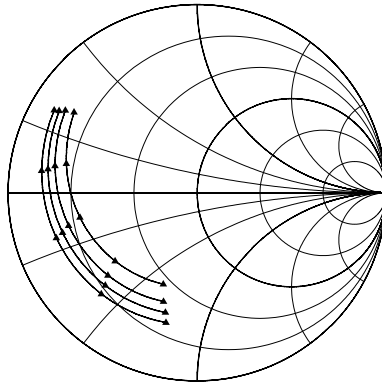
g. The parallel model is compared to the simple parallel model. The parallel model is shown as a dashed line, and the solid line represents the parallel model. The dashed line is a constant impedance, and the solid line is a constant impedance. The dashed line is a constant impedance, and the solid line is a constant impedance. The dashed line is a constant impedance, and the solid line is a constant impedance.

Several considerations had to be kept in mind while designing the IF matching circuit. First of all, the RF return loss is strongly affected by the IF impedance seen by the mixer. For some range of IF impedances, typically for a conjugate-matched IF, there can be reflection gain at the RF port. [10] Secondly, for the parallel RC impedance presented by our mixer chip, the Bode-Fano limit for the return loss matched to 50  $\Omega$  is about -6 dB for a 4 GHz bandwidth. [11] [12] [13] Finally, the primary goal of low system temperature had to be achieved while keeping the passband reasonably flat.

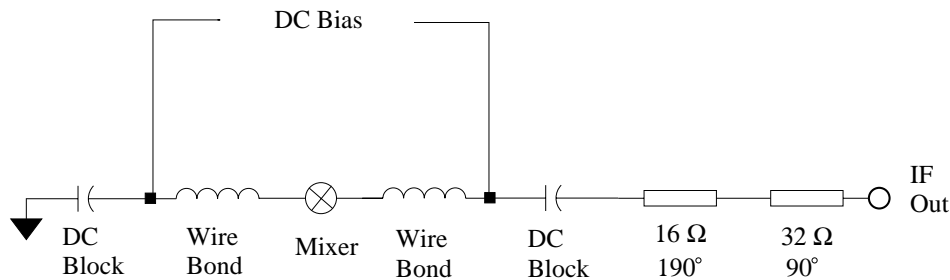
A 2-element microstrip circuit was designed to achieve the Bode-Fano limit for matching the mixer IF impedance to a 50  $\Omega$  line. The receiver was then simulated to see how the entire system would perform using this circuit, computing reflections at the RF ports, total receiver noise temperature including the isolator and IF amplifier, conversion loss, etc. The microstrip matching circuit had to be detuned slightly to improve the RF match and eliminate the possibility of RF reflection gain. Figure 9 shows a schematic of the matching circuit, and Figure 10 shows a photo of the assembled mixer.

## V. MEASUREMENTS AND RESULTS

A prototype LNA was constructed and tested at 4 Kelvin. The gain was found to be above about 32 dB, and the noise ranged from 6 to 12 Kelvin, Figure 11. The power consumption was 8 mW. The LNA was also tested at 4 Kelvin with an isolator at the input. The gain shape within band was essentially unchanged, while the noise



g peda e ro to o the h p or ar ous re ue es The peda e  
 th hart s or al ed to The re ue es are ro let to r ght  
 a d The as oltage a d power are o sta t ote that wre o d du ta e  
 a d lo g apa tors are luded the peda e al ulat o s



g he at dagra o the at h g r ut lud g wre o ds lo g apa tors  
 et

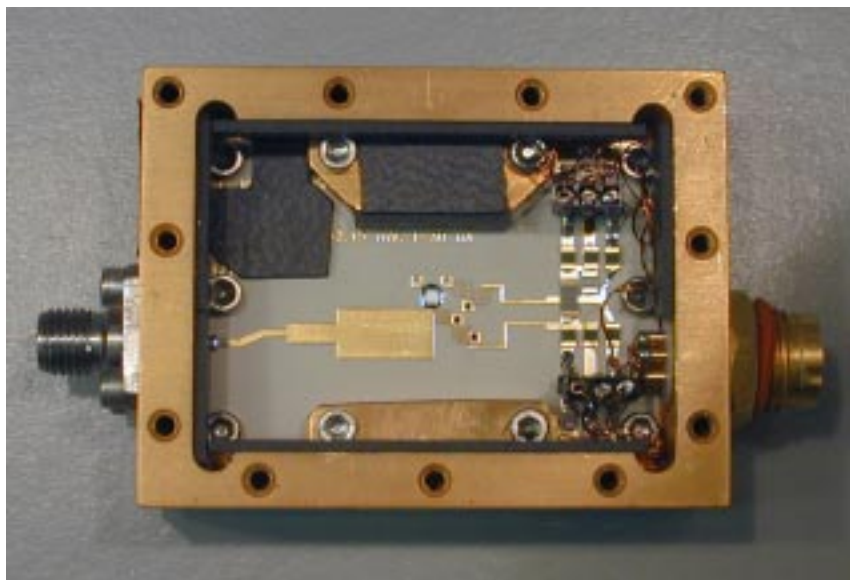
of the amplifier increased by about 35% due to loss from the isolator and cables.

The receiver was assembled and run with the tested amplifier and isolator. Figure 12 shows the cold surface of the cryostat. The double sideband noise temperature was generally below 200 Kelvin, Figure 13. Figure 14 shows the pumped and unpumped IV curves with receiver IF output power for hot and cold RF loads.

The receiver was taken to the Caltech Submillimeter Observatory and used with a 4 GHz analog correlator provided by Andy Harris of the University of Maryland. [14] A photograph of the receiver mounted at the Cassegrain focus of the telescope is shown in Figure 15. The receiver was used to observe the J=6→5 emission line of carbon monoxide from the galaxy M82, Figure 16.

#### ACKNOWLEDGEMENTS

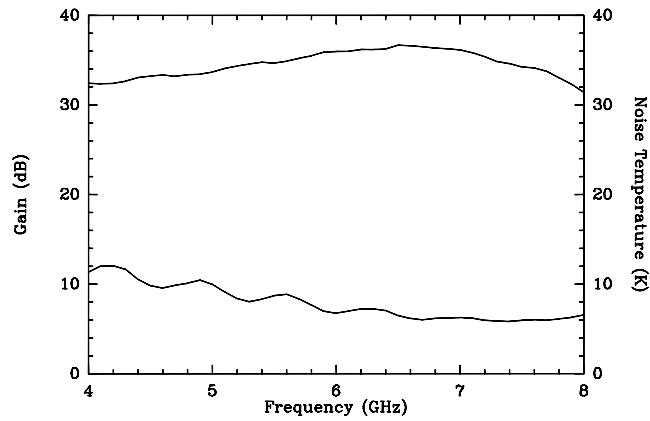
This work was supported in part by NASA/JPL and its Center for Space Microelectronics Technology, by NASA grant NAG5 4890, by the NASA/USRA SOFIA instrument development program, and by the Caltech Submillimeter Observatory (NSF grant AST 9615025).



g The ou ted er h p a d at h g r u t oard The h p s the s all la  
re ta gle the e ter The r u try to the r g t o the h p s or as The at h g  
r u t s to the lower le t o the h p o e ted to the o e tor through a l e  
The la str ps are err te a sor ers

## REFERENCES

- [1] J. E. Carlstrom, R. L. Plembeck, and D. D. Thornton, "A continuously tunable 65–115 GHz Gunn oscillator," *IEEE Trans. Microwave Theory Tech.*, vol. MTT-33, pp. 610–619, July 1985.
- [2] N. R. Erickson, "High efficiency submillimeter frequency multipliers," *1990 IEEE MTT-S Int'l Microwave Symp.*, p. 1301, June 1990.
- [3] M. Pospieszalski, "Modeling of noise parameters of MESFETs and MODFETs and their frequency and temperature dependence," *IEEE Transactions on Microwave Theory and Techniques*, vol. 37, pp. 1340–1350, September 1989.
- [4] J. Ward, F. Rice, G. Chattopadhyay, and J. Zmuidzinas, "SuperMix: A flexible software library for high-frequency circuit simulation, including SIS mixers and superconducting elements," *Proceedings, Tenth International Symposium on Space Terahertz Technology*, pp. 269–281, 1999.
- [5] F. Rice, J. Ward, G. Chattopadhyay, and J. Zmuidzinas, "Fast harmonic balance of SIS mixers with multiple junctions and superconducting circuits," *Proceedings, Tenth International Symposium on Space Terahertz Technology*, pp. 282–297, 1999.
- [6] J. Zmuidzinas and H. G. LeDuc, "Quasi-optical slot antenna SIS mixers," *IEEE Trans. Microwave Theory Tech.*, vol. MTT-40, pp. 1797–1804, 1992.
- [7] J. Zmuidzinas, H. G. LeDuc, J. A. Stern, and S. R. Cypher, "Two-junction tuning circuits for submillimeter SIS mixers," *IEEE Transactions on Microwave Theory Techniques*, vol. 42, pp. 698–706, April 1994.
- [8] J. Zmuidzinas, N. G. Ugras, D. Miller, M. C. Gaidis, and H. G. LeDuc, "Low noise slot antenna SIS mixers," vol. 5, pp. 3053–3056, June 1995.
- [9] M. C. Gaidis, H. G. LeDuc, M. Bin, D. Miller, J. A. Stern, and J. Zmuidzinas, "Characterization of low-noise quasi-optical SIS mixers for the submillimeter band," *IEEE Trans. Microwave Theory Tech.*, vol. MTT-44, pp. 1130–1139, 1996.
- [10] J. W. Kooi, F. Rice, G. Chattopadhyay, S. Sundarum, S. Weinreb, and T. G. Phillips, "Regarding the IF output conductance of SIS tunnel junctions and the integration with cryogenic InP MMIC amplifiers," *Proceedings, Tenth International Symposium on Space Terahertz Technology*, pp. 100–117, 1999.
- [11] H. W. Bode, *Network Analysis and Feedback Amplifier Design*. New York: Van Nostrand, 1945.
- [12] R. M. Fano, "Theoretical limitations on the broad-band matching of arbitrary impedances," *Journal of the Franklin Institute*, vol. 249, pp. 57–83, January 1950.

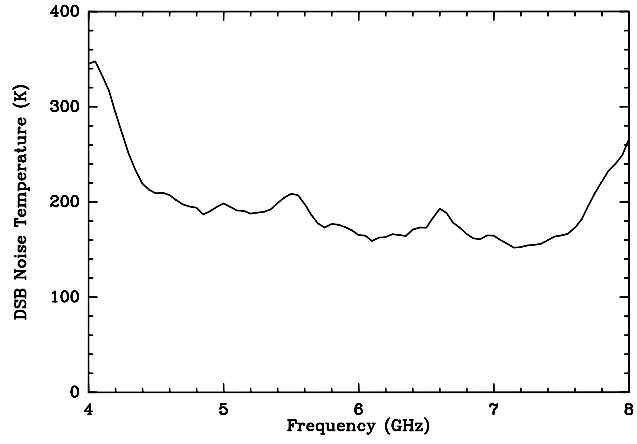


g a a d o se te perature o the easured at el The top ur e  
 s the ga a d the otto the o se te perature

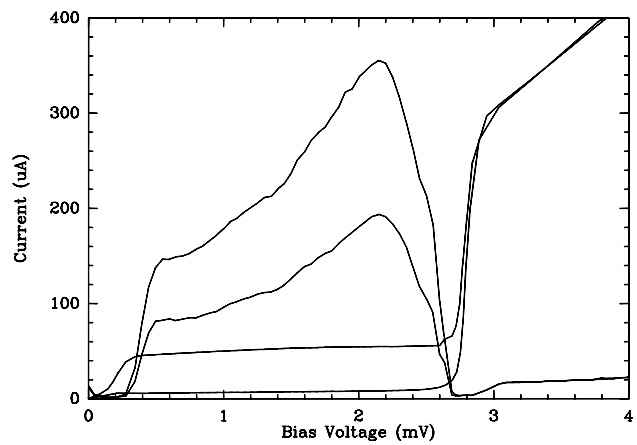


g ryostat old sur a e The a d s g also ter ro a o e go through the polyethyle e  
 le s the e ter a de ter the er lo The s g al goes out the oa a le to the le t  
 through the solator u der opper tape through the a d out the dewar to the upper  
 r ght

- [13] R. M. Fano, "Theoretical limitations on the broad-band matching of arbitrary impedances," *Journal of the Franklin Institute*, vol. 249, pp. 139–154, February 1950.
- [14] A. I. Harris, K. G. Isaak, and J. Zmuidzinas, "WASP: a wideband spectrometer for heterodyne spectroscopy," *Proc. SPIE*, vol. 3357, pp. 384–394, 1998.



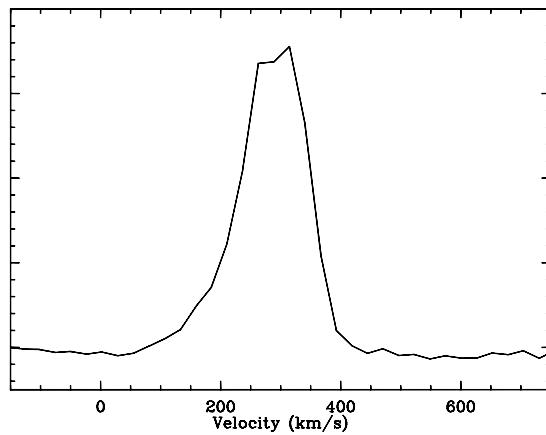
g o se te perature o the re e er as a u t o o re ue y The re ue y s  $V_{SIS}$  . a d  $I_{SIS}$   $\mu$



g llu ated a d pu ped ur es w th hot a d old total power The re ue y s



The receiver is a downward-looking cryostat at the top of the photo. The horn antenna is also mounted to the cryostat. The receiver is housed in a white cylindrical enclosure. The horn antenna is used to suppress radio frequency interference (RFI) as a part of the system.



The spectral line of the  $\text{H}\alpha$  emission line is shown. The width of the line corresponds to the rotation velocity of the galaxy. The

## **NONLINEAR TRANSPORT IN BALLISTIC SEMICONDUCTOR DIODES WITH NEGATIVE EFFECTIVE MASS CARRIERS**

B. R. Perkins, Jun Liu, and A. Zaslavsky,

Div. of Engineering Brown University Providence, RI 02912, U.S.A.,

Z. S. Gribnikov and V. V. Mitin,

Dept. of Electrical and Computer Engineering,

Wayne State Univ. Detroit, MI 48202, U.S.A.

E. P. De Poortere, M. Shayegan,

Dept. of Electrical Engineering,

Princeton University, Princeton, NJ 08544, U. S. A.

We are pursuing a new class of solid-state devices capable of generating high-frequency radiation: short ballistic semiconductor diodes in which the current flow is due to carriers injected into a negative-effective-mass (NEM) region of dispersion [1]. The resulting radiation is tunable by the source-drain voltage applied to the diode and device operation does not require magnetic fields or pumping by other oscillators. The physical mechanism responsible for high-frequency oscillation generation in such diodes lies in the instability of the ballistic NEM carrier quasineutral plasma, which forms in a large fraction of the diode base and stratifies into accumulation and depletion domains. As in the Gunn diode, where the instability arises from intervalley carrier transfer, the domains travel from source to drain and give rise to current oscillations. However, in short ballistic diodes the source-drain distance  $L$  can be much smaller than in a Gunn diode; numerical simulations show that for  $L \leq 0.2 \mu\text{m}$  the ballistic transport of the domains can lead to current oscillations in the THz frequency range [2].

The implementation of such ballistic diodes requires two essential ingredients. First, the current carriers should have an accessible NEM region in their dispersion. Second, the carriers must have a long mean-free-path and the diode a sufficiently short source-drain separation  $L$  for the majority of the carriers to remain ballistic. The most technologically mature semiconductor system with

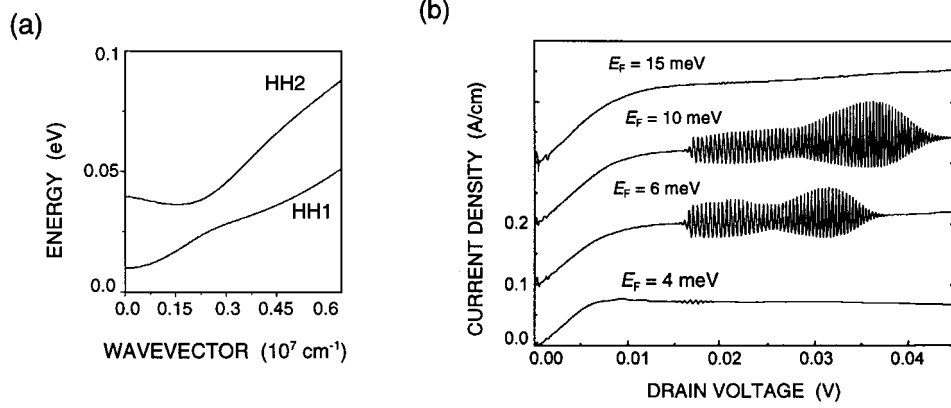


Figure 1: (a) The in-plane dispersion of the two lowest quantized hole subbands in a GaAs/AlAs quantum well of 8 nm width. The lowest subband exhibits NEM. (b) Simulated current-voltage characteristics with oscillations for different Fermi energies of holes entering the base (source-drain distance  $L = 0.1 \mu\text{m}$ ). The voltage sweep rate in the simulation is 0.5 mV/ps.

the required dispersion consists of narrow *p*-GaAs quantum wells (QWs), where the degeneracy of the heavy and light hole branches of the dispersion is lifted by size quantization and the required NEM section appears in the in-plane dispersion due to anti-crossing behavior of the hole subbands. A narrow  $\sim 7\text{-}8$  nm GaAs QW confined by AlAs barriers places the NEM section some 20 meV above the bottom of the lowest subband, as shown in Fig. 1(a). This eliminates optical phonon scattering, the dominant mechanism limiting carrier mean-free-path at low temperatures, because the LO-phonon energy in GaAs is 36 meV. Further, by growing the GaAs/AlGaAs heterostructure on a  $\langle 311 \rangle\text{A}$  GaAs substrate, one can achieve an exceptionally high hole mobility. In modulation-doped  $\langle 311 \rangle\text{A}$  GaAs/AlGaAs heterostructures, mean-free-paths  $\lambda \gg 1 \mu\text{m}$  at low temperature have been reported [3],[4].

Simulated current-voltage characteristics of short *p*-GaAs QW ballistic diodes with in-plane dispersion of Fig. 1(a) and hole densities in the  $10^{11} \text{ cm}^{-2}$  range are shown in Fig. 1(b). These simulations, which assume fully ballistic transport and solve the nonstationary ballistic equations self-consistently with the two-dimensional Poisson equation inside and outside the QW, predict quasiperiodic oscillations for relatively small drain voltages  $V \sim 20\text{--}30$  mV, with maximum oscillation frequency above 1 THz [2].

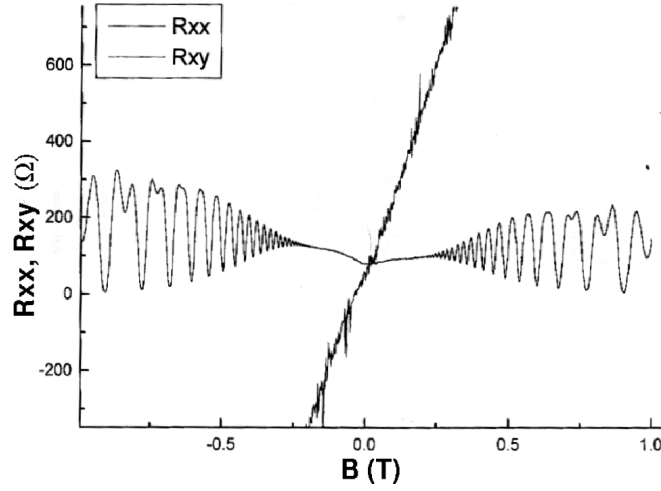


Figure 2: Magnetoresistance data for 2D hole gas in our narrow  $p$ -GaAs QW modulation-doped heterostructure (well width  $\sim 7$  nm) at  $T = 4.2$  K. The Shubnikov-de Haas oscillations are characteristic of hole mobility  $\sim 50,000$   $\text{cm}^2/\text{V}\cdot\text{s}$ .

The initial material for our diodes was narrow  $p$ -GaAs QW modulation-doped heterostructure grown on a  $\langle 311 \rangle \text{A}$  substrate, characterized by magnetoresistance measurements on large Van der Pauw geometry samples at  $T = 4.2$  K shown in Fig. 2. The hole density in the  $\sim 7$  nm QW is  $\sim 2.5 \times 10^{11} \text{ cm}^{-2}$ , while the low-field mobility is  $\sim 50,000 \text{ cm}^2/\text{V}\cdot\text{s}$ . When a two-terminal diode is fabricated from this material, the current-voltage  $I(V)$  characteristics depend on the source-drain separation  $L$ . When  $L$  is large, say  $L = 1 \mu\text{m}$ , the transport is non-ballistic. At very low  $V$  the diode  $I(V)$  should be Ohmic, with the resistance determined by the density and mobility  $\mu$  of the 2D hole gas in the QW. At higher  $V$ , corresponding to a 0.01–0.05 V drop over the base, the  $I(V)$  is non-Ohmic even in the absence of ballistic transport, either due to the heating of holes in high electric fields ( $10^2 - 10^3 \text{ V/cm}$ ) or due to the space-charge-limited injection of holes from the  $p^+$  source contact. However, once  $L$  becomes smaller than the carrier mean-free-path, the  $I(V)$  characteristics can be shown to follow a  $V^{1/2}$  dependence as long as the hole dispersion is parabolic. The existence of a NEM section in the dispersion alters the  $I \sim V^{1/2}$  dependence as shown in Fig. 1(b) because the homogeneous distribution of carriers accelerated to the NEM section is convectively

unstable [1]. The convective instability becomes global, leading to current oscillations (plotted in Fig. 1(b) as a function of the Fermi energy  $E_F$  in the  $p^+$  injecting contact). These oscillations, in turn, transform such diodes into generators of high-frequency radiation. While the high-frequency oscillations are unobservable in dc measurements, simulations [2] predict that the dc  $I(V)$  current will saturate at a source-drain  $V$  sufficient to accelerate a large fraction of the ballistic carriers to the NEM region of the dispersion.

The submicron diodes were fabricated and integrated with an on-chip wideband spiral antenna for coupling out the high-frequency radiation using a two-step lithographic and metal lift-off process illustrated in Fig. 3. First, electron-beam lithography is used to define the initial source and drain contacts. A source drain distance of as low as  $0.2 \mu\text{m}$  is readily achievable. For Ohmic contacts Au/Zn/Au metallization was used, with a thin (5 nm) bottom layer of Au for adhesion, a 10–20 nm layer of Zn for the actual  $p$ -type contact, and a final thick (50–100 nm) layer of Au to encapsulate the volatile Zn [6]. These contacts are subsequently annealed at 500–600 °C for 2–5 minutes. Recently, in order to lower the contact resistance, we began investigating alternative contact metallization schemes, based on the W/Zn/W recipe developed for  $p$ -HEMTs [7]. In either case, once the source and drain contacts are annealed, photolithography is used to define the wideband antenna spiral contacts, shown in Fig. 3, using a lift-off process with Ti/Au metallization. The devices are finally bonded and measured in a variable temperature insert ( $T$  controllable from 1.6 K to room temperature) of an Oxford Instruments magnetocryostat.

Figure 4(a) shows the measured  $I(V)$  characteristics at  $T = 1.7$  K in a diode with metallurgical  $L = 0.5 \mu\text{m}$  with and without a magnetic field  $B$  normal to the plane of the QW (note that the actual source-drain separation  $L_{eff}$  is smaller than  $0.5 \mu\text{m}$  due to sideways diffusion of the contact metal). The  $I(V, B=0)$  lineshape exhibits the saturation predicted by the transport simulations of Fig. 1(b) near to the predicted current density of  $\sim 0.1$  A/cm but in a much higher range of drain voltage. This indicates considerable series resistance in the contacts. In fact, by comparing the measured resistance near  $V = 0$  with what can be expected from the density and mobility of the hole gas in the QW, one arrives at an estimated series resistance in the contacts on the order of  $1\text{k}\Omega$ . Figure 4(b) shows the same data corrected for a contact series resistance of  $800 \Omega$ , which brings the  $B = 0$  resistance at low  $V$  into agreement with the hole gas density and mobility. The voltage needed for current saturation then falls below 50 mV, as predicted by Fig. 1(b).

As can be seen in Figs. 4(a) and (b), the magnetic field  $B$  suppresses the

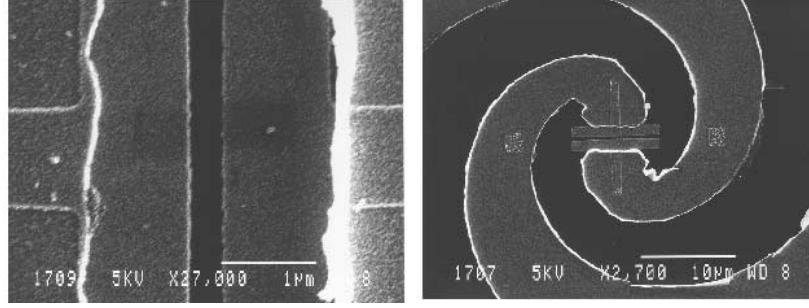


Figure 3: Scanning electron micrograph of the source-drain gap of a ballistic diode fabricated by e-beam lithography, with a metallurgical source-drain distance  $L \sim 0.3 \mu\text{m}$  and Au/Zn/Au contact metallization (left) and the integration of the diode with a wideband spiral antenna defined by optical lithography (right). The width of the source and drain contacts is  $\sim 10 \mu\text{m}$ .

current  $I$ . This suppression is strongest at low  $V$  and then the  $I(V)$  slope begins to increase, as can be seen more clearly in the conductance  $dI/dV$  that is also shown. A rough quantitative picture of the expected  $I(V)$  characteristics in our diodes in a normal  $B$  field can be obtained by assuming the drain current  $I$  can be separated into ballistic and diffusive components that can be treated separately. To first order, a small  $B$  has little effect on the diffusive component, while the ballistic carriers are deflected and follow a cycloid. At a given magnetic field, there is a critical source drain voltage below which ballistic current cannot reach the drain. This critical voltage  $V_c$  has the value:

$$V_c(B) = \frac{eB^2L^2}{2m^*} \quad (1)$$

which increases quadratically with  $B$  and  $L$ . The magnitude of the ballistic current density in the presence of  $B$  can be described for  $V > V_c(B)$  by:

$$J = en_0 \sqrt{\frac{e}{2m^*} \left( V - \frac{eB^2L^2}{2m^*} \right) \left( 1 + \frac{\epsilon B^2}{m^*n_0} \right)} \quad (2)$$

where  $n_0$  is the 2D hole density,  $m^*$  is the effective mass, and  $\epsilon$  is the dielectric constant.

The resulting  $I(V)$  characteristic is schematically shown in Fig. 5 for  $B = 0$ , in which case the total current consists of a linear diffusive component and a saturating ballistic component, and for two magnetic fields  $B_1 < B_2$ , which suppress

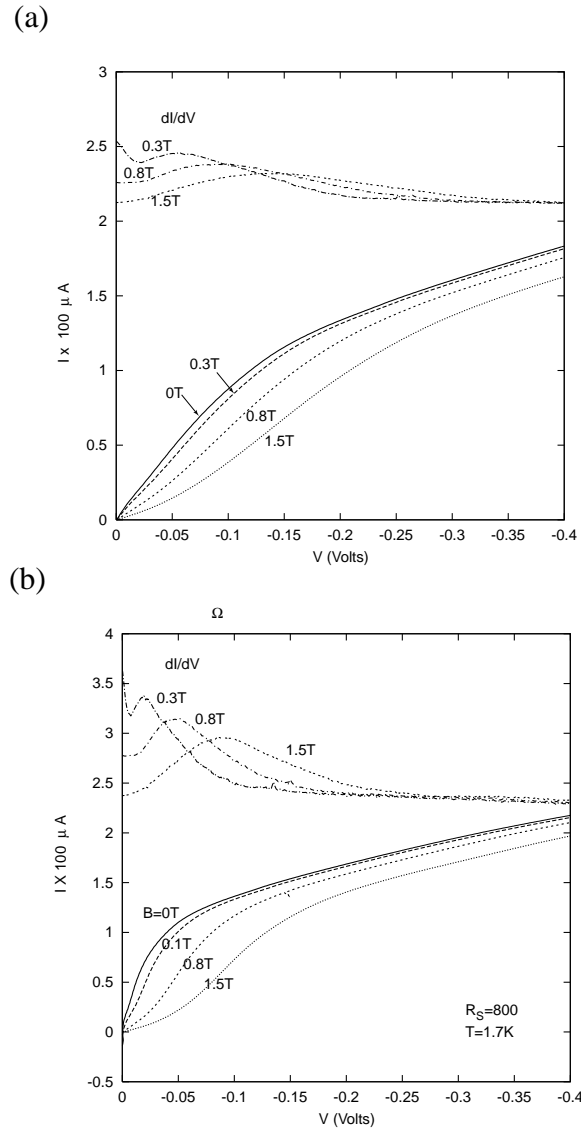


Figure 4: (a) Measured low-temperature  $I(V)$  characteristics for  $B = 0, 0.3, 0.8$  and  $1.5$  T at  $T = 1.7$  K (a) of a planar ballistic diode (metallurgical source-drain separation  $L = 0.5 \mu\text{m}$ , source and drain contact width =  $10 \mu\text{m}$ ). (b) The same data corrected for a series resistance  $R_S = 800 \Omega$  in the contacts. The strong current saturation for  $V < 50$  mV and the quenching of the  $I(V)$  by a small magnetic field are consistent with ballistic transport.

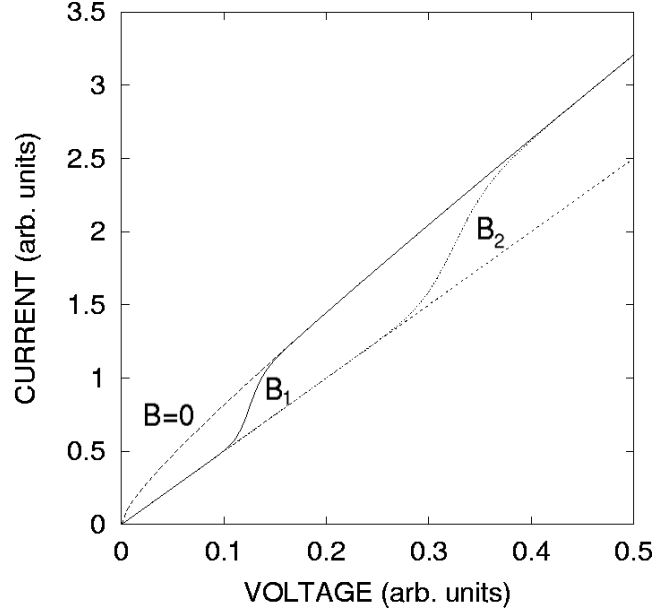


Figure 5: Schematic theoretical  $I(V)$  curve of a short diode in a small magnetic field  $B$ . The current is assumed to consist of two components: diffusive that is largely unaffected by  $B$  (dashed line) and ballistic that is predicted to saturate following a roughly  $V^{1/2}$  dependence, as in Fig. 1(b). In a  $B$  field, the total current is partially suppressed up to the critical field  $V_c$  and then rejoins the  $B = 0$  curve, as shown for two arbitrary  $B$  field values, with  $B_1 < B_2$ .

the current up to the critical drain voltage  $V_c(B)$ . Of course, the approximation in which these two current components are simply summed is quite crude: in reality, the existence of a diffusive component disrupts the electric field distribution in the base used to derive Eq. (2). This, together with the large series resistance in the contacts and the weaker saturation of the source-drain current than predicted by the fully ballistic models [2] makes quantitative comparison with experimental data premature. However, a comparison of the  $I(V, B)$  data corrected for series resistance shown in Fig. 4(b) with Fig. 5 indicates that the measured  $I(V)$  characteristics are consistent with partially ballistic hole transport between source and drain.

We should note that another possible source of the excessively high source-drain resistance in our diodes, in addition to high-resistance contacts, is the escape of hot holes from the QW channel into the acceptor-doped AlGaAs regions that supplied the 2D hole density in the first place. This is the well-known real-space

transfer effect that can occur in heterostructures during in-plane transport [8]. If, after improving the source-drain contacts, we find that real-space transfer affects our  $I(V)$  characteristics by significantly reducing the density of holes in the QW, we may need to redesign the modulation-doping scheme by increasing the Al content in the doped regions.

Encouraged by the measured nonlinearities in the  $I(V)$  curves of our short diodes made from  $p$ -GaAs QW heterostructures with high mobilities and in-plane NEM dispersion, we are continuing to work on improved contacting techniques. When more reliable fabrication technology is available, the devices will be tested for high-frequency radiation. We anticipate that such ballistic diodes, together with related three-terminal devices produced by gating this material in a field-effect transistor geometry [5], will offer an alternative route towards solid-state THz local oscillators for astrophysics applications.

## References

- [1] Z. S. Gribnikov and A. N. Korshak, *Semiconductors* **28**, 812 (1994).
- [2] Z. S. Gribnikov, A. N. Korshak, and V. V. Mitin, *Intern. J. Infrared Millimeter Waves* **73**, 213 (1999) and references therein.
- [3] J. J. Heremans, M. B. Santos, K. Hirakawa, and M. Shayegan, *J. Appl. Phys.* **76**, 1980 (1994).
- [4] M. Henini, R. J. Rodgers, P. A. Crump, B. L. Gallagher, and G. Hill, *Appl. Phys. Lett.* **65**, 2054 (1994).
- [5] A. N. Korshak, Z. S. Gribnikov, N. Z. Vagidov, and V. V. Mitin, *Appl. Phys. Lett.* **75**, 2292 (1999).
- [6] P. J. Rogers, C. J. G. M. Langerak, B. L. Gallagher, R. J. Barraclogh, M. Henini, T. J. Foster, G. Hill, S. A. J. Wieggers and J. A. A. J. Perenboom *Physica B* **184**, 95 (1993).
- [7] S. Tiwari, J. Hintzman, and A. Callegari, *Appl. Phys. Lett.* **51**, 2118 (1987).
- [8] Z. S. Gribnikov, K. Hess, and G. Kosinovsky, *J. Appl. Phys.* **77**, 1337 (1995).

# INSTRUMENTATION AND TESTING OF SUBMILLIMETER WAVE COMPACT ANTENNA TEST RANGES

**Jussi Säily, Juha Ala-Laurinaho, Janne Häkli, Jussi Tuovinen\*,  
Arto Lehto, Antti V. Räsänen**

MilliLab, Radio Laboratory, Helsinki University of Technology

P.O. Box 3000, FIN-02015 HUT, Finland

\*MilliLab, VTT Information Technology

P.O. Box 1202, FIN-02044 VTT, Finland

Email: [Jussi.Saily@hut.fi](mailto:Jussi.Saily@hut.fi)

## Abstract

Testing of antennas in submillimeter wave (>300 GHz) compact antenna test ranges (CATRs) has some specific problems that do not appear with conventional millimeter wave CATRs. The available transmitter power is very low, usually in the range of a few milliwatts. Also, the atmospheric attenuation due to water vapour absorption at certain frequency bands can be very high. For these reasons the CATR should be located inside a controlled, low humidity atmosphere. Furthermore, at submm wavelengths the required quiet-zone quality is more difficult to achieve than at mm wavelengths. A hologram is seen as a feasible alternative to reflectors as the collimating element in a CATR. In this paper, the proposed testing environment using a hologram CATR along with the needed instrumentation for 300–1000 GHz are presented. The results apply also to reflector CATRs.

## 1. Introduction

Planned satellite missions in the next 10–15 years will have spaceborne millimeter and submillimeter wave radiotelescopes and instruments. The European Space Agency (ESA) has several missions for scientific research (FIRST, PLANCK) and atmospheric limb sounding (MASTER, SOPRANO, PIRAMHYD). The diameters of the reflector antennas are from 0.5 to 3.5 meters and they will operate in the frequency range of 200–3000 GHz. However, there are no verified test ranges for antenna diameters over 1 m at frequencies over 300 GHz.

Far-field distances of electrically large antennas at 1 THz can be tens of kilometers, so conventional outdoor and indoor far-field measurements are ruled out by the high atmospheric attenuation and signal distortion. The most feasible alternatives are the near-field scanning method and the compact antenna test ranges. Both of these allow measurements to be done inside a controlled environment with constant temperature and humidity. The near-field method requires a measurement time of several days for electrically large antennas at THz frequencies, and it is not practical due to the inherent instrument unstabilities. The study

presented in [1] indicates that the compact range principle is the most feasible method at submillimeter wavelengths.

The CATR uses a collimating element to transform a spherical wave into a plane wave. The CATR enables direct measurement of the antenna far-field pattern with relatively small distances between the signal source and the receiver, thus with little attenuation. The collimator can be a reflector, a lens, or a hologram. Reflector CATRs have been used up to 200 GHz and their highest operating frequency is limited by the surface inaccuracies of the reflectors [2]. The surfaces of the large antennas to be tested are made already as smooth as possible and to accurately test these, the collimating reflector should be 20–30% larger in size and also have a considerably better surface accuracy. This is clearly very costly even if it can be done. The CATR based on a foam lens is not feasible at submm wavelengths due to manufacturing and material difficulties.

A new type of CATR based on a hologram has been developed at the HUT Radio Laboratory to overcome the very stringent surface accuracy demands of the reflectors at high frequencies [3,4]. Figure 1 shows the hologram CATR operating principle and a typical hologram pattern.

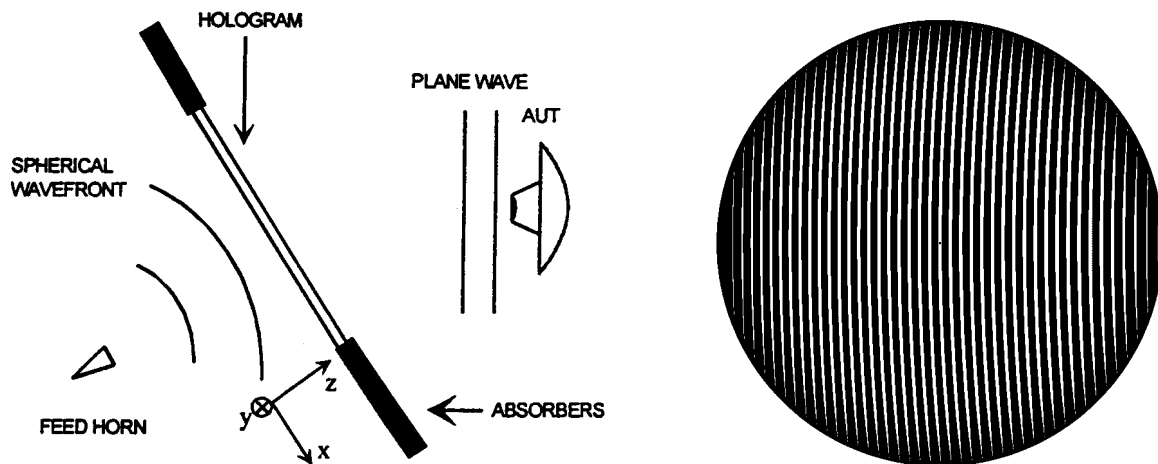


Figure 1. Operating principle of the hologram CATR and a typical hologram pattern.

In a recent project to study the hologram performance at submm wavelengths, a demonstrator CATR based on a 60 cm diameter hologram was constructed and tested at 310 GHz. Test results for this CATR are presented in [5] and [6]. The measured and simulated quiet-zone fields of the CATR were very similar. The quiet-zone area with peak-to-peak amplitude and phase ripples of 1.0 dB and 10 degrees, respectively, was about 25x20 cm<sup>2</sup>. The instrumentation and testing environment presented in this paper apply to all CATRs at short submm wavelengths, but the hologram CATR is used as the primary topology.

## 2. Testing environment for submillimeter wave hologram CATRs

Water vapour is the most significant source of atmospheric attenuation in the antenna test range. It has several strong absorption bands in the millimeter and submillimeter wavelengths, as shown in Figure 2 for two different water vapour concentrations [1]. The strong attenuation at these bands is caused by the excitation of certain molecular rotational modes. The observed bands are centered around the molecular rotational frequencies of water and their widths are determined by the total air pressure (with only a weak temperature dependence). The integrated band-strengths are determined by the water vapour concentration in the air [1].

The other major atmospheric gas molecules include nitrogen, carbon dioxide, and oxygen. Nitrogen and carbon dioxide have zero electrical and magnetic dipole-moments and they do not directly attenuate THz signals. Oxygen has also zero electrical dipole-moment, but a non-zero magnetic dipole-moment, which results in a few oxygen-related absorption bands in the THz range. Oxygen-related absorption is much weaker than the water vapour absorption. However, all gas molecules affect the air pressure and thus contribute to the widening of the absorption bands [1].

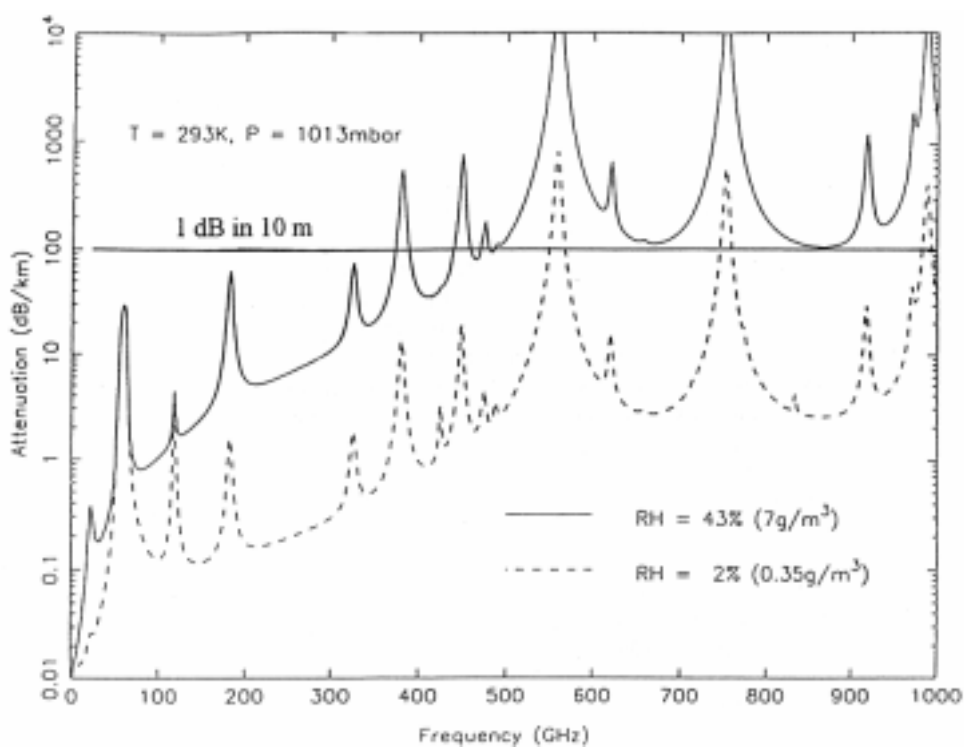


Figure 2. Atmospheric attenuation as a function of frequency for two different water vapour concentrations.

Another problem related to atmospheric water vapour is the variation of the phase-delay of a signal beam in time or in space [1]. In a CATR facility, the variations of phase-delay in time do not have significant effect on the measurement of antenna power pattern. Instead, spatial variations in the refractive index of the air could distort the measurement, because they could spoil the planarity of the plane-wave phase-front in the quiet-zone. This effect is minimised by keeping the water vapour concentration as low as possible.

It is clearly desirable to enclose the THz CATR in a tightly controlled environment in order to reduce the absorption to an acceptable level. The controlled parameters are temperature and water vapour concentration. These parameters must remain stable over the measurement period and the test room volume. The antennas-under-test (AUTs) can normally be tested in normal room temperature of 290 K. This temperature will be used for convenience at submm wavelengths also, since cooling of the atmosphere does not decrease the signal attenuation. Possible cryogenic receivers associated with AUTs will have their own cooling systems.

A perfect vacuum inside the CATR enclosure would be advantageous with respect to atmospheric attenuation, but the required large size of the enclosure makes this impractical. However, the costs of obtaining lower attenuation should be weighted against the cost of increasing the transmitted power. At THz frequencies, the power levels are low and are usually very costly to increase.

The most cost-effective way to reduce the attenuation to an acceptable level is to lower the water vapour concentration of the testing atmosphere. According to [1], the atmospheric attenuation should be below 1 dB/10 m (shown as the horizontal line in Figure 2). The higher curve shown in Figure 2 is calculated for water vapour concentration of 7 g/m<sup>3</sup> (T=293 K and P=1013 mbar). This humidity level can be obtained in a normal laboratory room with air conditioning. The lower curve with water vapour concentration of 0.35 g/m<sup>3</sup> needs a sealed dry-cabinet with a circulating-air drying system. The required hermetic enclosure and the drying system increase the cost of the facility. The cost estimate for a 1000 m<sup>3</sup> sealed cabinet with driers is about 750 000 USD.

Figure 3 shows one possible layout for the hologram CATR enclosure. The CATR is designed for the testing of the ESA ADMIRALS reflector antenna. The diameter of the antenna is about 2 meters. For a quiet-zone diameter of 2.5 meters, a hologram diameter of about 4 meters is required. Separation between the source and receiver in this facility is around 24 meters. The floor size of the planned enclosure excluding the control, air conditioning and air-lock rooms is 170.5 m<sup>3</sup>. The height of the room should be about 6 meters, making the volume of the enclosure 1023 m<sup>3</sup>.

The control room is situated near the source system, because the used vector network analyzer should be placed near the source. Two access doors through air-locks are provided into the enclosure, one for the source and the other for the AUT and receiver. Air conditioning is placed in the middle for maximum drying efficiency. The temperature inside the chamber is kept constant but it is not possible to cool it to cryogenic temperatures.

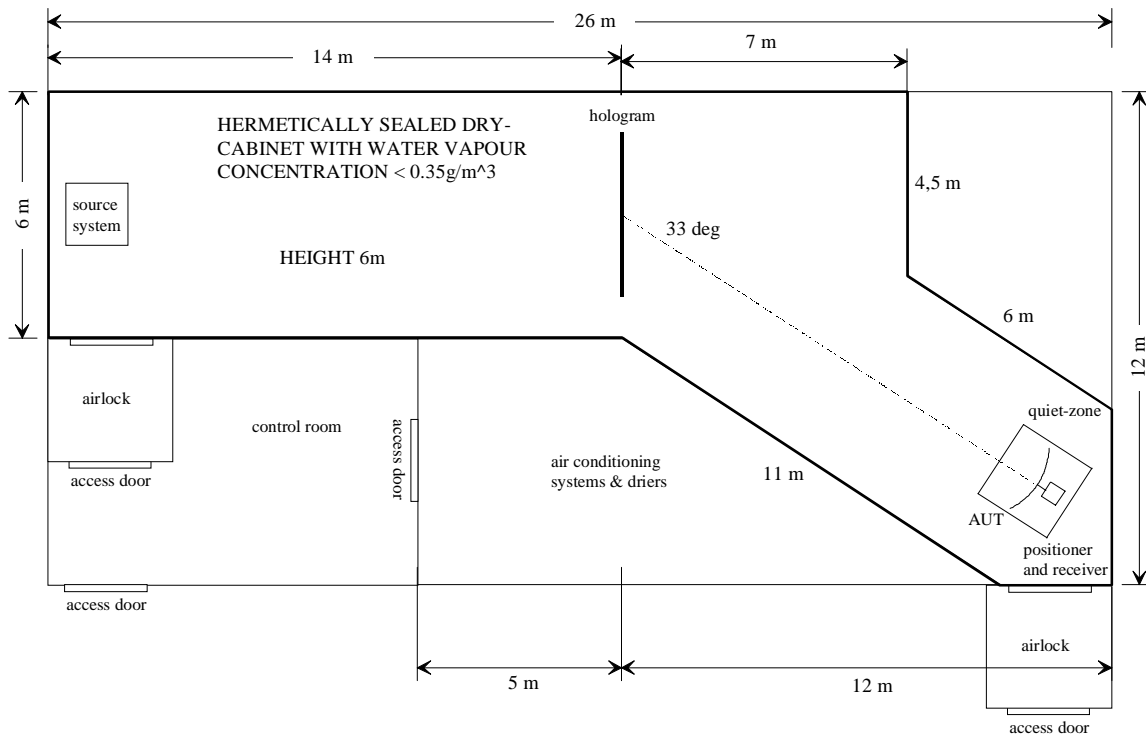


Figure 3. Schematic layout of the 2.5 meter quiet-zone hologram CATR.

The CATR facility needs large quantities of high-quality, broadband radar absorbing material (RAM) to prevent reflections from the walls and the hologram frame. The requirements for a suitable absorbing material include -40 dB reflection coefficient in all angles of incidence, low evolution of dust and water vapour, light weight, and durability. Suitable RAM panels are available from at least two commercial suppliers, but they are very expensive compared to conventional millimeter wave materials. The cost of the absorbers will be so high that preferably a single type of absorber covers the whole frequency band of the CATR. The costs can be reduced by using absorbers of lesser quality in the not-so-critical areas. Only the source system, the hologram frame, the AUT positioner and the wall absorbing the unwanted diffracted fields from the hologram need to be covered with the best possible RAM material.

### 3. Instrumentation for 300–1000 GHz

The required instrumentation for the submillimeter wave CATR include a signal source, a receiver, a measurement controller (vector network analyzer), and the feed and AUT positioners. A planar  $xy$ -scanner is also needed to verify the quiet-zone amplitude and phase quality periodically. Our laboratory uses as the measurement controller a dedicated submillimeter wave vector network analyzer MVNA-8-350 manufactured by AB Millimetre in France. The MVNA is easily adaptable to different frequency bands by changing the source and receiver as required. Our laboratory has used phase-locked Gunn oscillators and

BWOs (backward-wave oscillators) as the source and a Schottky diode mixer pumped by a Gunn-oscillator as the receiver.

The most feasible source oscillators for THz CATR operation are frequency multiplied InP-Gunn oscillators and BWOs. Far-infrared (FIR) lasers have higher powers but they are very large-sized and difficult to tune in frequency. In order to obtain high enough dynamic range in the CATR quiet-zone verification procedure, a relatively high-power transmitter is needed. Frequency multiplied Gunn oscillators have very small output powers at THz frequencies, a few  $\mu\text{W}$  maximum, due to the low efficiency of the multipliers. Also, the electrical tuning range of Gunn oscillators is quite small. Advantages of the Gunn oscillators are the relatively low cost, reliability and small size when compared to the BWOs. Figure 4 shows the phase-locked Gunn oscillator source used at MilliLab for 300–1000 GHz.

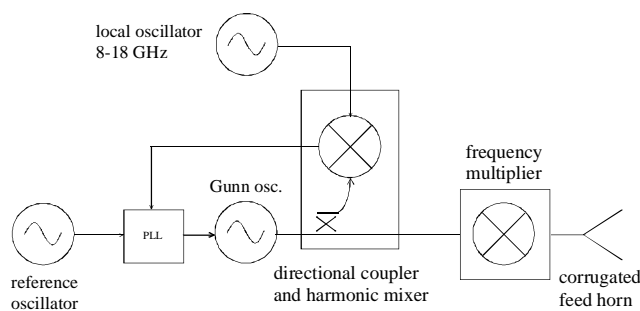


Figure 4. Phase-locked Gunn source for 300-1000 GHz (ABmm ESA-1).

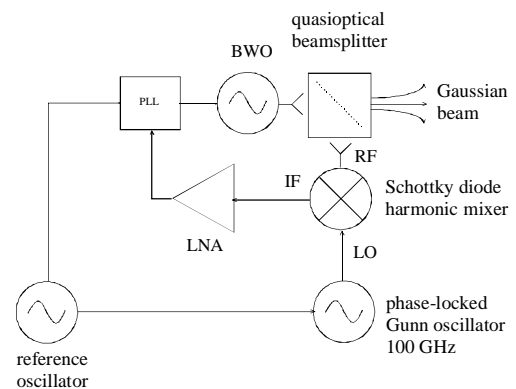


Figure 5. Phase-locked BWO source for 300-1000 GHz (MilliLab).

Wideband BWOs have 1 mW typical output power at 1 THz, and the power can be controlled electrically with the heating current. Narrowband BWOs can have power levels of tens of mWs at the same frequencies, but are not commercially available. Disadvantages of BWOs are the large size and weight of the device, high cost of the tube, the required stable high-voltage supply, and the relatively small lifetime of the tube (typically 1000 hours at high output power levels). However, the BWOs are very suitable for operation in CATRs because the high power level is only needed for relatively short periods during the quiet-zone verification and optimization procedures. When testing a large-sized high-gain telescope antenna, only a small fraction of the available power is needed to saturate the receiver. The lifetime of the tube operated at low power level is expected to increase many times from the 1000 hours.

At MilliLab, phase-locking of a submillimeter wave BWO has been demonstrated at 310 GHz. A similar arrangement shown in Figure 5 will be used for THz operation. A



bands. The most cost-effective and feasible method is to incorporate the CATR in a hermetically sealed cabinet with a circulating-air drying system.

## Acknowledgements

This project is partially supported by ESA ESTEC (ESTEC Contract No. 13096/98/NL/SB), TEKES (Finland) and the Academy of Finland. The authors would also like to thank Mr. Eino Kahra, Mr. Lauri Laakso and Mr. Lorenz Schmuckli from the Radio Laboratory workshop for valuable help with the various mechanical constructions.

## References

- [1] Foster, P.R., Martin, D., Parini, C., Räisänen, A., Ala-Laurinaho, J., Hirvonen, T., Lehto, A., Sehm, T., Tuovinen, J., Jensen, F., Pontoppidan, K., "Mmwave antenna testing techniques - Phase 2", 1996, *MAAS Report 304*, 224 p.
- [2] Habersack, J., Lindemer, W., Steiner, H.-J., "High performance mm-wave measurements up to 200 GHz in the compensated compact range", *Proc. 2<sup>nd</sup> ESA Workshop on Millimetre Wave Technology and Applications: Antennas, Circuits and Systems*, Espoo, Finland, May 1998, pp. 529–535.
- [3] Tuovinen, J., Vasara, A., Räisänen, A., "A new type of compact antenna test range", *Proc. 22<sup>nd</sup> European Microwave Conference*, Espoo, Finland, Aug. 1992, pp. 503–508.
- [4] Hirvonen, T., Ala-Laurinaho, J., Tuovinen, J., Räisänen, A., "A compact antenna test range based on a hologram", *IEEE Trans. on Antennas and Propagation*, Vol. 45, No. 8, Aug. 1997, pp. 1270–1276.
- [5] Säily, J., Ala-Laurinaho, J., Häkli, J., Tuovinen, J., Lehto, A., Räisänen, A.V., "Development of a 310 GHz hologram compact antenna test range", *Proc. 21<sup>st</sup> Annual Meeting & Symposium of the AMTA*, Monterey, CA, USA, Oct. 1999, pp. 464–469.
- [6] Säily, J., Ala-Laurinaho, J., Häkli, J., Tuovinen, J., Lehto, A., Räisänen, A.V., "Test results of 310 GHz hologram compact antenna test range", *Electronics Letters*, Vol. 36, No. 2, Jan. 20<sup>th</sup>, 2000, pp. 111–112.

# **A Pickett Potter Horn-Reflector Antenna for Submillimetre-Wave Applications**

**Phichet Kittara, Ghassan Yassin, Stafford Withington  
and Harry Smith**

**Department of Physics, University of Cambridge,  
Madingley Road, Cambridge CB3 0HE, UK**

email: [pk201@mrao.cam.ac.uk](mailto:pk201@mrao.cam.ac.uk), [ghassan@mrao.cam.ac.uk](mailto:ghassan@mrao.cam.ac.uk)

## *ABSTRACT*

In this paper, we present a new type of horn-reflector antenna. The design employs an offset parabolic reflector fed by a Pickett-Potter horn. The horn is essentially a smooth-wall conical horn with a single step at its throat. This arrangement is a simplified version of the conventional Potter horn and is much easier to manufacture than the corrugated horn. We designed a Pickett-Potter horn-reflector antenna for a 700 GHz SIS mixer. We also developed and tested a 15 GHz scale model. We found that the Pickett-Potter horn and horn-reflector antenna has good beam circularity and a return loss value better than  $-25$  dB over a bandwidth of about 15%.

## **INTRODUCTION**

Astronomical interest in submillimetre wavelengths has increased considerably in recent years. High quality SIS heterodyne detectors led to new discoveries in the area of spectroscopic submillimetre astronomy. Conventionally, a high-quality mixer feed consisted of a corrugated horn corrected by a dielectric lens. This is because a collimated circular beam (near equal E-plane and H-plane radiation patterns) with low sidelobes is required for many astronomical applications.

At short wavelengths, however, machining of scalar horns is difficult, expensive, and time consuming, in particular for large format imaging arrays where many detectors are needed. In addition, dielectric lenses introduce considerable problems such as multiple reflections and diffraction which, if not carefully considered, could result in high sidelobe levels.

In this paper, we present an alternative design which retains the beam circularity of the corrugated horn and yet is much easier to fabricate. The proposed design is horn-reflector antenna [1], which comprises a  $90^\circ$  offset parabolic reflector fed by a Potter horn [2]. The feed is a dual-mode horn of the type developed by Potter which is essentially a smooth-wall conical horn with a single step at its throat. It is a simplified version of the classical Potter horn and is clearly much easier to manufacture than the corrugated horn.

As we shall see later, this horn has many of the desirable properties of the scalar horn, namely, low sidelobes and cross polarisation. The parabolic reflector is located very close to the horn aperture (the case in the conventional horn-reflector design) and corrects the phase error at the horn aperture, resulting in a high efficiency antenna with a collimated beam without the use of dielectric lenses.

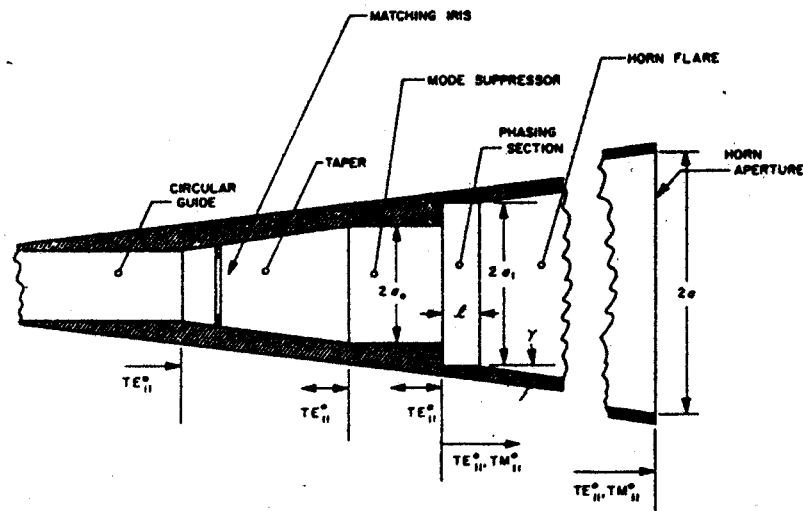
We have conducted extensive theoretical investigation of the Potter horn-reflector antenna at 700 GHz in view of its application in submillimetre receivers. In particular, we developed software packages to calculate the parameters which determine the bandwidth of the antenna such as the return loss, the cross polarisation and the sidelobe levels. The Software calculates the scattering matrix of the horn using a modal matching method and then conformally maps the horn aperture field onto the projected aperture plane.

Based on our theoretical model we designed and fabricated a 700 GHz Potter horn reflector antenna machined into an aluminum split-block. The block has already been loaded with a 700 GHz finline chip and beam pattern tests of the antenna is in progress. In addition we constructed a 15 GHz scale model antenna and carried out extensive out-door radiation pattern tests of this antenna. We obtained excellent agreement between the computed and measured results. In particular, we demonstrated that the bandwidth of the antenna can approach 15% which exceeds 100 GHz at a central frequency of 700 GHz. Our work also suggests that Potter horn reflector antennae could be fabricated at frequencies well above 1 THz.

## 1. The Pickett-Potter Horn

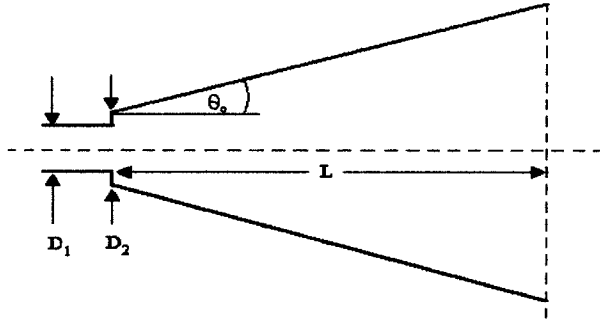
A dual mode of the type developed by Potter [2] is shown in Fig 1. It has a tapered section connecting two circular wave guides, a step transition to a larger circular waveguide, a phasing section and a conical horn section.

Figure 1. Potter Horn



The step transition generates a small fraction of  $TM_{11}$  mode as well as the propagating  $TE_{11}$  mode. The phasing section and the conical horn combine to create a phase difference between the two modes at the aperture relative to the phase generated at the step. The dimension of the phasing section and the horn length are chosen so that the  $TM_{11}$  and  $TE_{11}$  reach the horn aperture in phase. Consequently, the effect of the  $TM_{11}$  mode is to make the E plane aperture distribution more tapered than it would be for a standard single-mode conical horn. The E-plane and the H-plane aperture distributions therefore become similar to those in a corrugated horn.

A simplified version of the conventional Potter horn was first introduced by Pickett [3] in 1984. Here, the phasing section is removed, leaving a single step discontinuity at the throat of the horn, as shown Fig. 2.



**Figure 2: Pickett Potter Horn Design for semi-flare angle  $15^\circ$ .  
 $D_1 = 1.036\lambda_0$ ,  $D_2 = 1.295\lambda_0$ ,  $L=13.53\lambda_0$  and  $\theta_0 = 15^\circ$**

The modification simplifies greatly the horn fabrication; however, the relative phases between modes can now only change as the modes propagate along the horn itself. Consequently, the horn dimensions, normally chosen to obtain a predetermined beam shape, are now constrained by the requirements of minimum phase difference between the two modes. In all other respects, the electrical properties of this simplified horn are identical to the original Potter horn.

### 1.1 Calculations of the electrical properties of the Pickett-Potter horn

We have developed software that allows us to predict the performance of the Pickett-Potter horn-reflector antenna. This is done by calculating the scattering matrix and the aperture field distribution of the horn using a modal matching technique. In this method, the horn is divided into discrete sections with a minimum of 20 sections per wavelength. At each junction, a scattering matrix is calculated by matching the coefficients of the modal fields. The overall scattering matrix of the horn is calculated by cascading the matrices of the individual sections. The transmitted and reflected coefficients are extracted from the resulting scattering matrix.

Calculations of radiation patterns are done using Kirchhoff's aperture diffraction theory. The co-polar and cross-polar patterns are defined using Ludwig's third definition of cross polarization as:

$$\begin{pmatrix} E_{cp} \\ E_{xp} \end{pmatrix} = \begin{pmatrix} \sin \theta & \cos \phi \\ \cos \theta & -\sin \phi \end{pmatrix} \begin{pmatrix} E_\theta \\ E_\phi \end{pmatrix}$$

where  $\theta$  and  $\phi$  are respectively the polar and azimuthal angles on the observational plane. The following parameters were used to design the horn: a centre frequency of 700 GHz, a semi-flare angle at  $15^\circ$ , an aperture diameter of 3.8 millimetres and the two radii of the step discontinuity at the throat are 0.222 and 0.775 mm.

## **1.2 Measurements of Pickett-Potter horn**

To verify the integrity of our theoretical method under ideal conditions, we designed a scale model at 15 GHz. The horn was fabricated in two sections and has the dimensions as in Fig 2. The horn was placed on a turntable at 10 m from a transmitter. We measured the E and H planes and the cross-polar pattern at  $45^\circ$ . The measured patterns agree very well with the calculated values, as can be seen in Fig 3. The dynamic range of our receiver was about 27 dB.

In Fig 3, we also compare the measured patterns of the scale modal with those predicted at the high frequency range. It can be seen that the pattern quality at the design frequency (700 GHz) is comparable to that of a corrugated horn. The sidelobe levels are low and the maximum cross-polarization is  $-27$  dB. At 770 GHz, however, the cross polarization level has increased to  $-18$  dB. The return loss of the antenna was better than  $-25$  dB across the bandwidth, as shown in Fig. 4. The best indicator of the bandwidth of the Pickett horn is the cross-polarization level, as given in Fig 5, and is used to define the useful bandwidth of the antenna. For example, a  $-20$  dB cross-polarization level can be maintained over a fractional bandwidth of 15%.

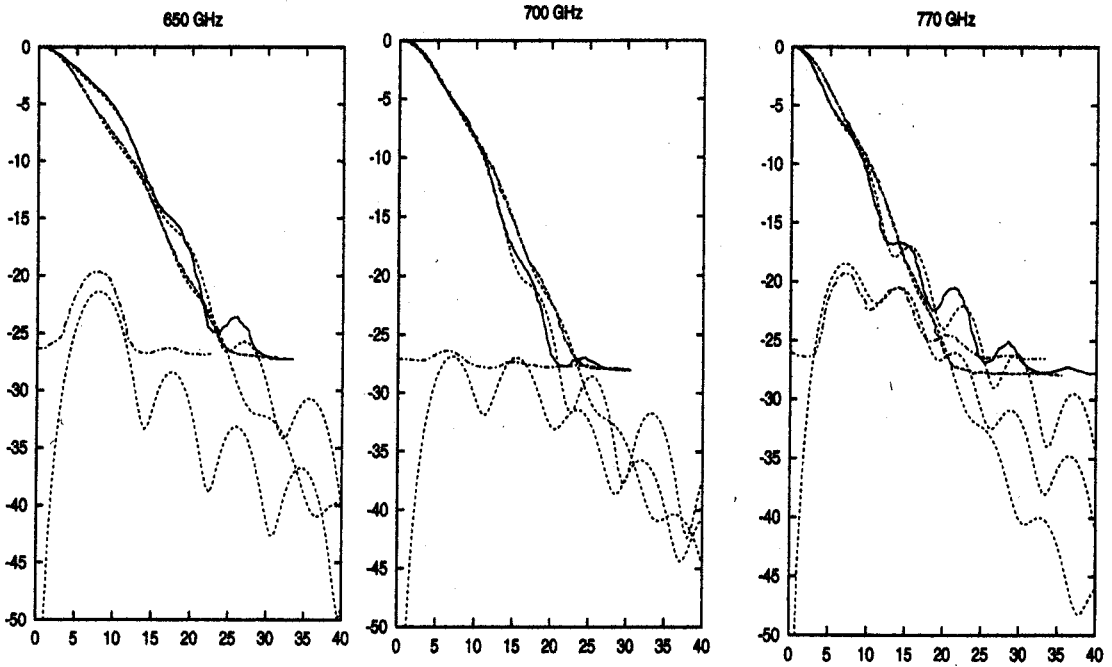


**Figure 3a.** 14.0 GHz

**Figure 3b.** 15.0 GHz

**Figure 3c.** 16.5 GHz

Radiation patterns of Pickett horn. Solid lines are measured E planes.  
 Dashed lines are measure H planes. Dash-dotted lines are measured cross-polar.  
 Dotted lines are calculated values.

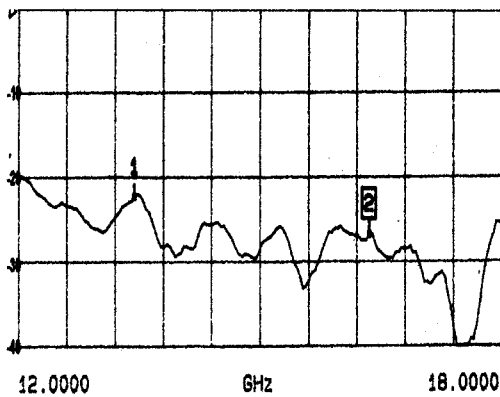


**Figure 4.** measured return loss

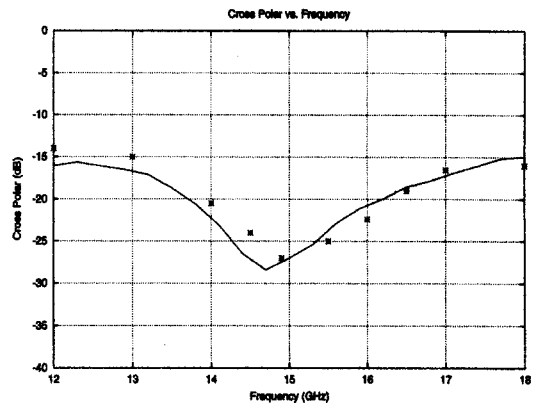


**Figure 5.** Cross polarization  
 Points are measured values

## 2. THE PICKETT-POTTER HORN-REFLECTOR ANTENNA

We calculated the horn-reflector antenna radiation patterns by assuming that the field at the horn aperture is given by that of a cylindrical waveguide at the step junction, multiplied by the spherical phase error factor,  $\exp(-jkr^2/2L)$ , where  $r$  is the radial distance in the horn aperture,  $k$  is the free space wavenumber and  $L$  is the distance from the aperture to the apex. We compared this method with a full modal-matching technique and found that the two methods agree very well for semi flare angle under  $15^\circ$ . The field distribution of the horn aperture was then mapped onto the project aperture using conformal mapping [5].

We would like to emphasize at this stage that designing Potter horn-reflector antenna is not a straight forward extension of the design of the corrugated horn-reflector antennas. This is because in the latter case, the mode propagating in the horn is a single  $HE_{11}$  hybrid mode. For a given horn aperture, and assuming that the apex of the horn is located at the focal point of the reflector, the radiation pattern of the antennas is almost independent on the length of the horn. This fact is no longer valid in case of the Pickett-Potter horn feed since the length of the horn determines the relative phase between the  $TE_{11}$  and  $TM_{11}$  modes. Our analysis nevertheless shows that it is indeed feasible to realize a horn-reflector fed by a Pickett-Potter horn with performance comparable to that of a corrugated horn-reflector.

We measured the radiation patterns of the antenna for two orthogonal polarisation, one in the plane of symmetry (longitudinal plane, L), and the other in the plane of asymmetry (Transverse plane, T). For each polarisation, the far field patterns was also observed in both the longitudinal (L) and transverse (T) planes. From Fig. 6 we notice that that the main beam shapes resemble that of a corrugated horn. Fig.7 shows measured values of half beam-width and Fig 8 shows the measured and calculated maximum cross polarization level of the Pickett horn-reflector antenna. The discrepancy between the measured and computed values of the cross polarisation levels in Fig. 8 is caused by the fact that the side plates which supported the reflector have very slightly clipped the beam.

It can be seen that the agreement between the measured and computed results at the design frequency is excellent down to  $-25$  dB level. We would like to

emphasis that the beam circularity of the Pickett horn-reflector antenna is significantly better than that of the horn alone.

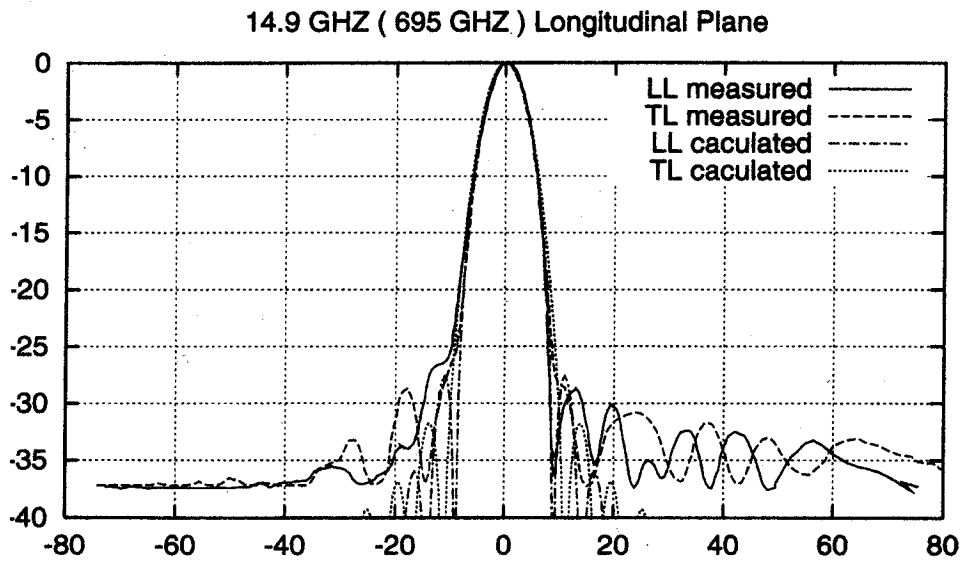


**Figure 6a.** Measured beam patterns at 14.9 GHz  
(Longitudinal Plane of Observation)

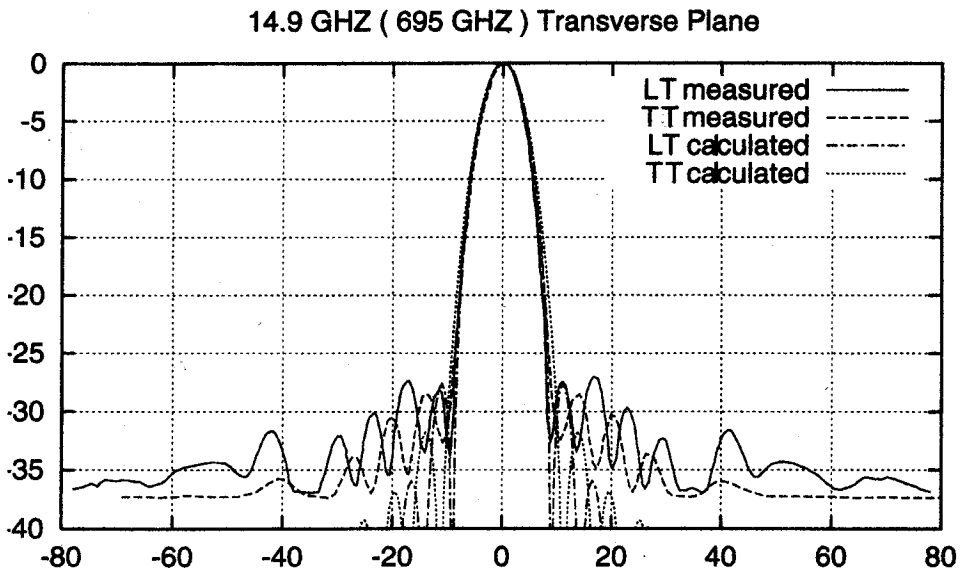


**Figure 6a.** Measured beam patterns at 14.9 GHz  
(Transverse Plane of Observation)

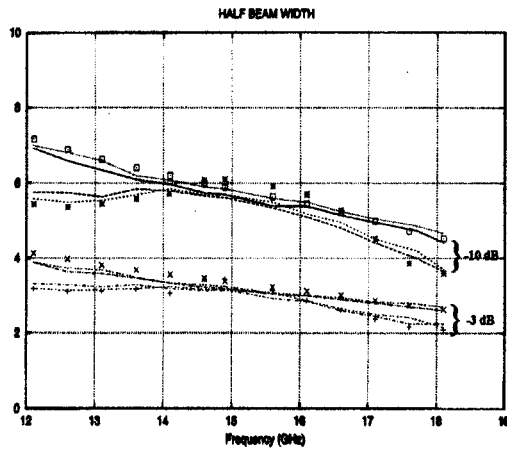


**Figure 7.** Calculated and measured half width at -beam width 3dB and -10 dB

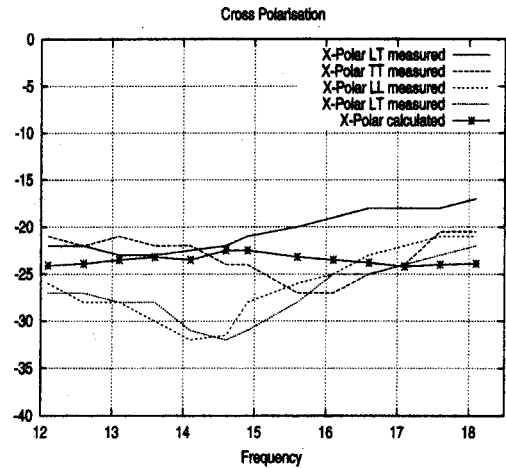


**Figure 8.** Measured maximum cross polarization level of Pickett-Potter Horn-Reflector Antenna.

## CONCLUSION

We have shown that the Pickett-Potter horn can be employed in conjunction with horn-reflector antennas, provided that TE<sub>11</sub> and TM<sub>11</sub> modes reach the projected aperture in phase. Although the absence of a phasing section in the Pickett-Potter horn restricts the horn design flexibility, our study showed that practical horn-reflector antenna dimensions suitable for submillimetre wave array receivers can still be found. We designed and tested a Pickett-Potter horn-reflector antenna. We found that a -20 dB cross-polarization level can be maintained over a fractional bandwidth of 15%. Testing of a 700 GHz Pickett-Potter horn-reflector antenna is in progress.

## ACKNOWLEDGEMENTS

We would like to thank Peter Doherty for machining the 15 GHz horn and assisting in the radiation pattern measurements.

## Reference:

- [1] S. Withington, G. Yassin, M. Buffey, C. Nordan, "A Horn-Reflector antenna for high performance submillimetre imaging arrays," *Int'l J. IR and MM Waves.*, vol. 18, no.2, pp. 341-358, 1997.
- [2] P. D. Potter, "A new horn antenna with suppressed sidelobes and equal beamwidths," *Microwave J.*, vol 6 pp.71-78, 1963.
- [3] H. M. Pickett, J. C. Hardy, and J. Farhoomand, "Characterisation of a dual mode horn for submillimetre wavelengths," *IEEE Trans. Microwave Theory Tech.*, MTT-32, no.8, pp. 936-937, 1984.
- [4] S. Silver, *Microwave antenna theory and design*, McGraw-Hill Book Co., Inc., New York, 1949.
- [5] G. Yassin, M Robson, and P. J. Duffett-Smith, "the electrical characteristics of a conical horn-reflector antenna employing a corrugated horn," *IEEE Antennas and propagation*, vol. AP41, pp.357-361, April 1993.
- [6] A. D. Olver, P. J. B. Clarricoats, A. A. Kishk and L. Shafai, *Microwave horns and feeds*, Bookcraft, Bath, 1994.
- [7] S. Dicke, G. Yassin and S. Withington, "A two-element horn-reflector antenna for cosmic microwave background astronomy" submitted to *IEEE Trans. Antenna and propagation 1999*.

# A Novel Type of Phase Grating for THz Beam Multiplexing

Urs U. Graf and Stefan Heyminck

KOSMA, I. Physikalisches Institut, Universität zu Köln  
Zülpicher Straße 77, 50937 Köln, Germany; E-mail: *lastname@ph1.uni-koeln.de*

## Introduction

Phase gratings have become popular as local oscillator beam multiplexers for array receivers in the submillimeter wavelength domain. In general, binary or multilevel gratings, also known as Dammann gratings, are used [1][2][3][4]. Dammann gratings can be designed and manufactured easily and perform satisfactorily for most one-dimensional applications. Two-dimensional dispersion, however, is much more difficult to achieve. This is mainly due to the fact that a two-dimensional multilevel structure can not be machined easily.

We introduce a new type of phase grating, the Fourier grating, which replaces the sharp edges of the multilevel gratings by a smooth grating structure. These gratings can be machined easily with standard machine shop equipment. The grating design is relatively simple and the diffraction efficiency is usually significantly higher than the efficiency of Dammann gratings. Typical efficiencies for two-dimensional gratings are above 80%. For one-dimensional dispersion, efficiencies beyond 90% are typical.

In this paper we describe the design and the manufacturing of one- and two-dimensional Fourier gratings, and present beam measurements performed with reflection gratings at a frequency of 0.5 THz.

## The Grating Concept

The Fourier grating concept is an extension of the well known sinusoidal phase grating. In the following we describe the design of symmetric one-dimensional gratings. The general case is an obvious extension of this.

The spatial phase modulation within the grating unit cell is modeled by a finite Fourier series:

$$\Delta\phi(x) = \sum_{n=1}^N a_n \cos\left(n \cdot \frac{2\pi x}{D}\right), \quad (1)$$

where the unit cell extends from  $-D/2$  to  $D/2$ . Every member in this sum corresponds to a sinusoidal phase grating whose far field diffraction pattern is given by the Fourier

transform of  $\exp[a_n \cos(n \cdot 2\pi x/D)]$ , the electric field in the grating plane [5]:

$$U_n(\theta) = U_0 \times \sum_{q=-\infty}^{\infty} J_q(a_n) \delta(\theta - nq \frac{\lambda}{D}). \quad (2)$$

$J_q$  denotes the Bessel function of the first kind of order  $q$ .

Taking the complete Fourier series of eq. (1) corresponds to multiplying the fields of many sinusoidal gratings. This results in a diffraction pattern consisting of a multiple convolution of the diffraction fields of the individual Fourier components:

$$U(\theta) = U_0 \times \bigotimes_{n=1}^N \left[ \sum_{q=-\infty}^{\infty} J_q(a_n) \delta(\theta - nq \frac{\lambda}{D}) \right]. \quad (3)$$

This expression is mathematically fairly elegant, but for computational purposes it is usually much more efficient, to calculate the Fourier transform of the aperture field using a numerical FFT algorithm.

Thus, the set of Fourier components  $a_n$  of the phase modulation defines a set of complex coefficients  $b_i$ , each of which describes the field in one diffraction order of the grating. Since we are only interested in the intensity distribution within the diffraction pattern, our task consists of finding a set of  $a_n$ , which produces the desired set of  $b_i b_i^*$ . For our standard example — a one-dimensional grating producing a symmetric pattern of four beams — this set is  $b_i b_i^* = \{\dots, 0, 0, \frac{1}{4}, 0, \frac{1}{4}, 0, \frac{1}{4}, 0, \frac{1}{4}, 0, 0, \dots\}$ .

We cannot calculate the set of  $a_n$  directly, and therefore have to resort to a numerical optimization to find the best values. This optimization is made difficult by the fact that the parameter space contains an extremely large number of local optima, and only for a very small fraction of all possible starting values the optimization converges to the global optimum.

We have developed two strategies to obtain good starting values. The first method is to randomly choose a large number of starting values. Although this is very crude, it proved to be rather efficient for gratings using a relatively small number of Fourier components (i.e.  $N \lesssim 10$ ). This range of  $N$  includes most common one-dimensional gratings and a large number of simple two-dimensional gratings.

For larger numbers of Fourier components, we perform an inverse Fourier transform on the desired diffraction field. By varying the relative phases between the diffraction orders, we try to obtain a flat amplitude distribution in the grating plane. The resulting phase distribution is expanded into a Fourier series, which then serves as starting values for the optimization. This technique is faster but less complete than the first one. Although it may miss the global optimum, it usually still gives very good results.

For a large enough number of randomly chosen starting values the first method necessarily finds the global optimum for a given number of Fourier components. As long as the diffraction pattern is not too complex, we find that the optimum grating structure only requires a few non-zero Fourier components. Due to the completeness of the Fourier series expansion, this means that our approach converges rapidly to *the best possible phase grating* for the desired diffraction pattern.

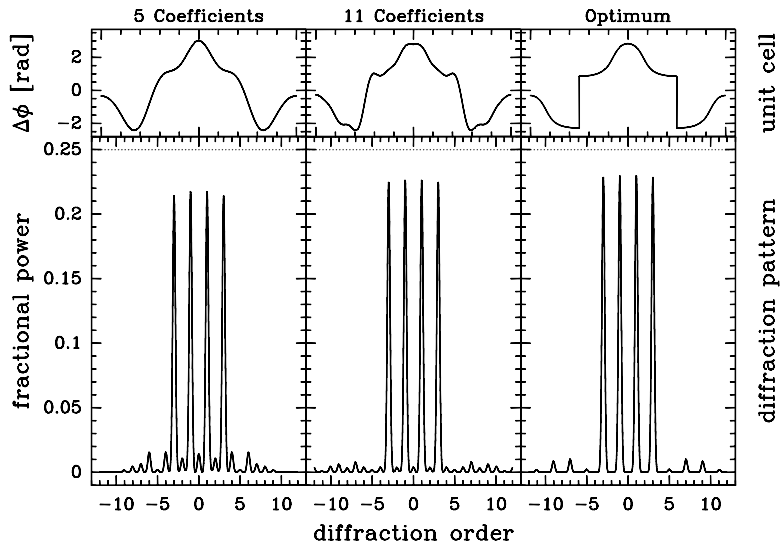


Figure 1: Comparison of Fourier gratings using different numbers of Fourier coefficients. The lower panels show the diffraction patterns produced by the grating profiles in the upper panels.

### Grating Performance

To illustrate the potential of the Fourier grating concept, we now take a closer look at one example, a grating that splits an incoming beam into four equally spaced beams of equal intensity. In the symmetric case the power is then distributed between the diffraction orders  $-3$ ,  $-1$ ,  $+1$ , and  $+3$ . Fig. 1 shows the diffraction patterns obtained for different numbers of Fourier components together with the corresponding grating unit cell structure. It is obvious that already with a very smooth structure composed of 5 components we get a very good grating with  $\approx 87\%$  efficiency. The power lost into parasitic diffraction orders decreases rapidly, as we increase the number of coefficients. Correspondingly, the grating efficiency rapidly approaches the limiting efficiency of 92% (Fig. 2).

In Fig. 3 we compare grating efficiencies for different one-dimensional gratings producing a certain number of identical beams. Typical efficiencies that can be reached are higher than 90%. Gratings for an even number of beams require a larger number of Fourier components and usually have a somewhat lower limiting efficiency than

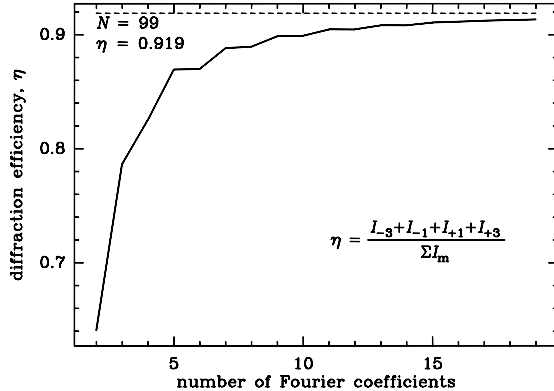


Figure 2: Diffraction efficiency of a Fourier grating plotted against the number of coefficients used in the optimization. The grating was optimized to produce four identical beams in a symmetric pattern.

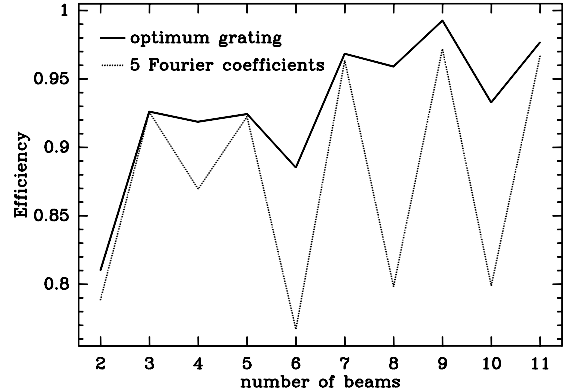


Figure 3: Diffraction efficiency of Fourier gratings producing a given number of identical beams, using  $N = 5$  Fourier coefficients (dotted line) or  $N \rightarrow \infty$  (solid line).

gratings for odd numbers. The reason for this is that, in order to produce a symmetric pattern of an even number of beams, we need to suppress all the even diffraction orders. This is achieved by the sharp steps in the grating unit cell (right hand panel in Fig. 1) which splits the unit cell into two identical sub-cells with a relative phase shift of  $\pi$ . To closely approximate this phase step, a relatively large number of Fourier components would be required. However, as we have seen, excellent grating efficiencies can be achieved with surprisingly crude approximations of the phase step.

The question arises, whether an asymmetric diffraction pattern could yield higher grating efficiencies in this case. For instance, we could produce an asymmetric four beam pattern consisting of the diffraction orders  $-2$ ,  $-1$ ,  $0$ , and  $+1$ . The optimum grating we obtained for this beam arrangement has the same efficiency as the symmetric grating, and its unit cell is basically identical (Fig. 4). The only difference in the grating structure is that the above mentioned phase step is replaced by a sawtooth pattern with a grating blaze angle corresponding to the  $-0.5^{\text{th}}$  diffraction order.

## Two-dimensional Gratings

For the common case of a rectangular beam pattern, the corresponding grating is just an orthogonal overlay of two one-dimensional gratings. Accordingly, the grating efficiency is typically about 80 to 90%, the product of the efficiencies of the one dimensional gratings. Since the two orthogonal patterns can be optimized independently, this case is not fundamentally different from the one-dimensional problem.

In the general two-dimensional case similarly high efficiencies are obtained as long as the grating structure is sufficiently simple that our method of choosing the starting values for the optimization works well enough. Very complex beam patterns requiring

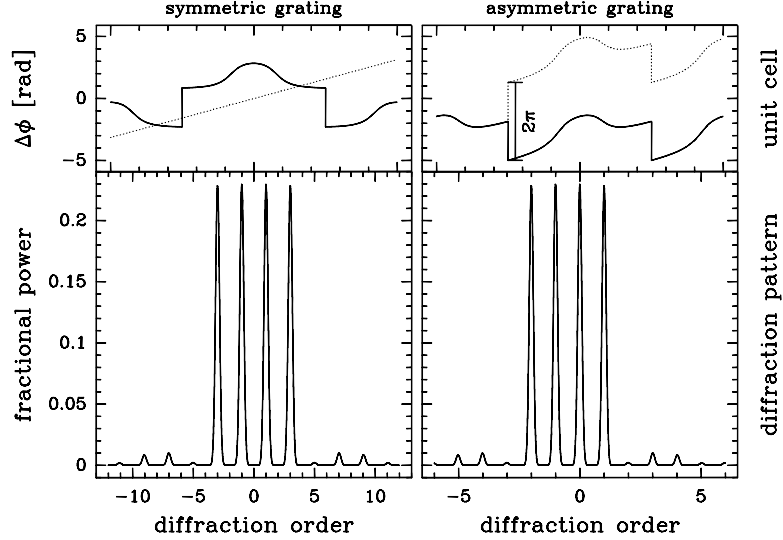


Figure 4: Transition from a symmetric grating to an equivalent asymmetric grating. Adding a phase gradient to the symmetric structure and flipping the sign of every other phase step yields the optimum asymmetric structure. Effectively, the step function in the symmetric grating thus changes into a blaze function to the  $-0.5^{\text{th}}$  diffraction order.

a highly structured grating unit cell may end up with somewhat lower efficiencies. Since the number of Fourier components to be optimized is now  $N^2$ , it is much more difficult to find the global optimum. However, for the application we have in mind, namely the distribution of LO power to an array of heterodyne mixers, the beam patterns are usually sufficiently simple that this is not a real concern.

### Bandwidth

The bandwidth of phase gratings is limited by two effects. First, the intensity balance between the diffraction orders is wavelength dependent and, second, due to the frequency dispersion of the grating, the spacing between beams also varies with wavelength. Usually the latter effect is dominating. However, it can be compensated for by some sort of zoom optics. The frequency dependent intensity balance is intrinsic to the phase grating concept and can not be influenced by external optics.

Since the gratings are so easily manufactured, we deal with this problem by making several gratings that cover different parts of the required total receiver band. In our application, we can cover a relative bandwidth of approximately 10 to 20% with each grating. Thus, the need to change the grating only arises when the receiver frequency is changed by a considerable amount.

Having exchangeable gratings requires a means of relocating the gratings with high accuracy in order to maintain the optical alignment when gratings are swapped. To achieve this, we machine the mounting surfaces of the gratings together with the

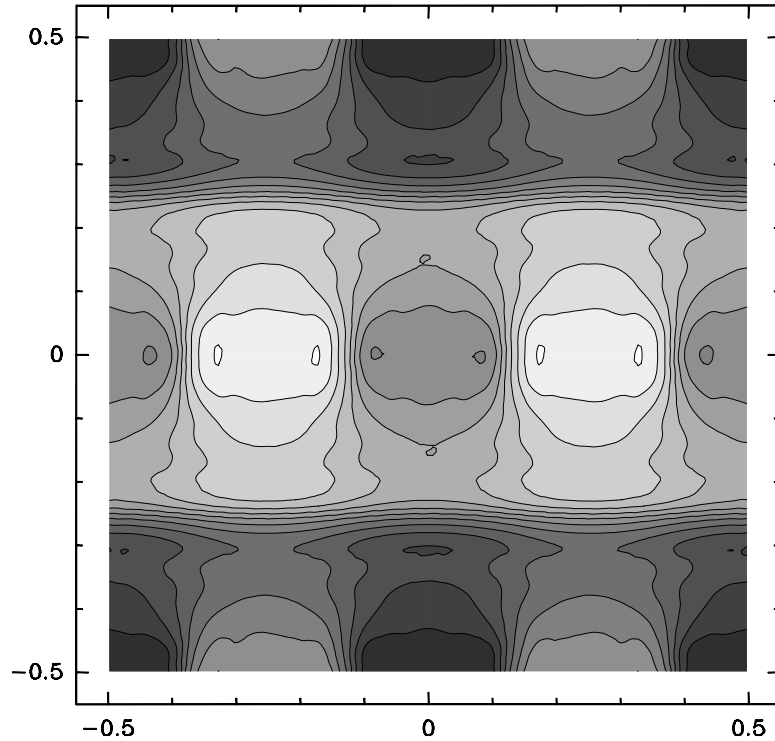


Figure 5: Surface topology of the grating used in the beam measurements shown in Fig. 6.  $13 \times 13$  coefficients have been used in the optimization. The theoretical efficiency is 84%

grating structure. In our measurements we could not detect any alignment changes, when these gratings were exchanged.

### Manufacturing

The main advantage of the Fourier grating is that high diffraction efficiencies are reached with very smooth grating surfaces. This allows us to manufacture reflection gratings by directly machining them with a relatively large diameter cutting tool. We produced a number of gratings with a unit cell size of  $30 \times 30 \text{ mm}^2$  for a frequency of 492 GHz. The grating structures used 13 Fourier components per dimension, resulting in a minimum radius of curvature of approximately 7 mm, which is comfortably larger than the 3 mm tool radius we used for machining.

Our Fourier gratings are manufactured by directly milling the structure into a block of brass, using a spherical end mill on a numerically controlled milling machine. Measurements with a dial indicator show that the resulting surface accuracy is approximately  $2 \mu\text{m}$  RMS. This accuracy corresponds to  $\lambda/300$  at the design frequency and should be good enough for gratings operating well into the THz region.

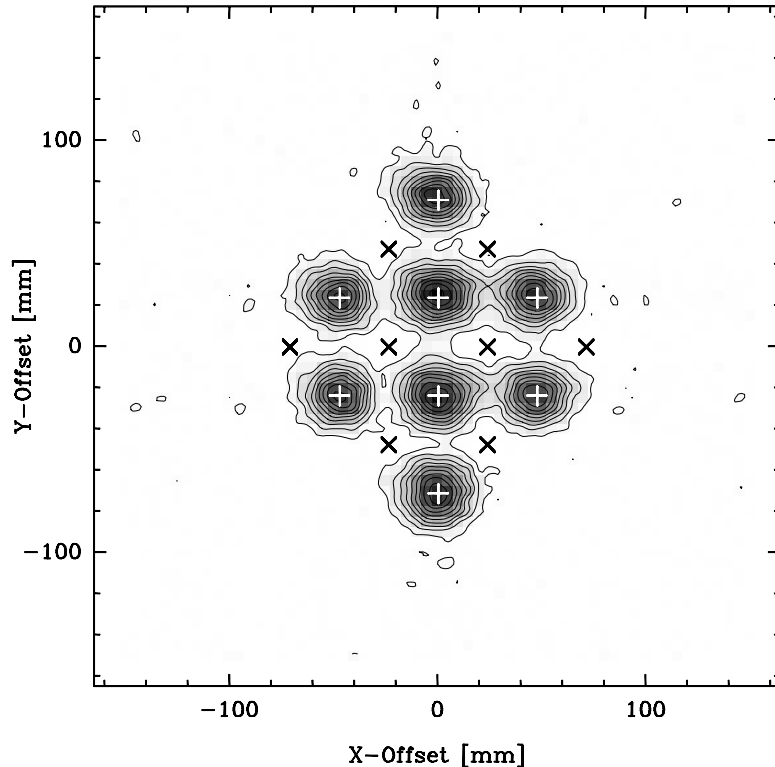


Figure 6: Measured 490 GHz diffraction pattern of the grating structure shown in Fig. 5. From the extremely low side lobe level it is obvious that the grating efficiency is very high.

### Measurements

As an example for the practical results obtained with the Fourier gratings, we present the measurements made with a grating producing a two-dimensional pattern of 2, 4 and 2 beam in 3 parallel rows (Figs. 5 and 6). This pattern is important for the use in square  $4 \times 4$  arrays that are split into two interleaved sub-arrays. Two identical versions of this beam pattern, rotated by 90 degrees with respect to each other combine to a 16 pixel square array.

For the measurements, the beam of a 492 GHz SIS receiver [6] was re-imaged to form a waist at the plane of the grating. The diffracted beam pattern was then scanned with a chopped liquid nitrogen load mounted on an  $xy$ -translation stage. The clean beam pattern and the low side lobe level (Fig. 6) show immediately that the concept works well and that the grating efficiency is very high. In fact, within the measurement accuracy there is no deviation from the predicted beam pattern and the measured diffraction efficiency is within 1% of the theoretical value.

## Conclusion

We have shown that the novel concept of designing submillimeter phase gratings as Fourier gratings works very well. The gratings are relatively easy to design and have very high diffraction efficiency. Due to their smooth surface structure, they can be machined directly, even as reflection gratings with two-dimensional dispersion.

We have manufactured a series of gratings and tested them at 490 GHz showing that they can be produced sufficiently accurate with standard machine shop equipment, and that they perform as predicted.

## Acknowledgments

This work was supported by the *Verbundforschung Astronomie* through grant 05 AH9PK1, by the *Deutsche Forschungsgemeinschaft* through grant SFB 301, and by the *Ministerium für Wissenschaft und Forschung des Landes Nordrhein-Westfalen*.

## References

- [1] S. Jacobsson, A. Lundgren, and J. Johansson, "Computer generated phase holograms (kinoforms) for millimeter and submillimeter wavelengths," *Intl. J. IR mm Waves*, vol. 11, no. 11, 1990.
- [2] J.A. Murphy, S. Withington, and H. Van de Stadt, "Dammann gratings for local oscillator beam multiplexing," in *Multi-Feed Systems for Radio Telescopes*, D.T. Emerson and J.M. Payne, Eds. 1994, ASP Conference Series, Vol. 75.
- [3] R. Güsten et al., "CHAMP — the carbon heterodyne array of the MPIfR," in *Advanced Technology MMW, Radio, and Terahertz Telescopes*, Thomas G. Phillips, Ed. 1998, Proceedings of SPIE Vol. 3357.
- [4] H. Dammann and E. Klotz, "Coherent optical generation and inspection of two-dimensional periodic structures," *Optica Acta*, vol. 24, 1977.
- [5] Joseph W. Goodman, *Introduction to Fourier Optics*, McGraw-Hill Book Company Inc., second edition, 1996.
- [6] S. Haas, C.E. Honingh, D. Hottgenroth, K. Jacobs, and J. Stutzki, "Low noise broadband tunerless waveguide SIS receivers for 440–500 GHz and 630–690 GHz," *Intl. J. IR mm Waves*, vol. 17, no. 3, 1996.

# QUASI-OPTICAL MULTIPLEXING USING REFLECTION PHASE GRATINGS.

W. Lanigan<sup>1</sup>, N. Trappe<sup>1</sup>, J.A. Murphy<sup>1</sup>, R. Colgan<sup>1</sup>, C. O'Sullivan<sup>1</sup> & S. Withington<sup>2</sup>.

<sup>1</sup>Experimental Physics Department, National University of Ireland, Maynooth, Ireland.

<sup>2</sup>Cavendish Laboratory, Cambridge University, CB3 0HE, England

## Abstract

Heterodyne array receiver systems for both ground based and satellite telescope facilities are now becoming feasible for imaging in the submillimetre/terahertz regions of the EM spectrum. Phase gratings can be usefully employed as high efficiency passive multiplexing devices in the local oscillator (LO) injection chain of such receivers, ensuring that each element of the array is adequately biased and that the reflected LO power level at the array is minimised. For the wavelengths of interest both transmission and reflection gratings can be manufactured by milling an appropriate pattern of slots into the surface(s) of a suitable material. Thus, the required phase modulation is produced by the resulting pattern of varying optical path lengths suffered by the incident wave-front. We report on work we are undertaking to develop all reflection quasi-optical multiplexing systems so as to reduce reflection losses at the grating and minimise the number of surfaces that can contribute to standing wave effects in the optical system. As part of this endeavour we have also developed a quasi-optical technique for analysing the inevitable degradation due to multiple reflections on transmission grating design. This analysis is based on the Gaussian beam mode technique, and a further application of this technique allows one to assess tolerance limitations on the grating.

## 1. INTRODUCTION

In previous papers we reported on our work on transmission Dammann gratings [1,2], one of the simplest types of grating to model and manufacture. The Dammann grating is a binary optical component consisting of a regular arrangement of slots or recesses of equal depth in a suitable transparent dielectric material such as quartz [3]. The phase grating as a whole consists of a repeated two-dimensional array pattern of basic cells. At the location of the Fourier plane in the subsequent optical system a regular two-dimensional pattern of non-overlapping beams is formed for a grating illuminated by a collimated beam. The number of basic cells illuminated by the incident beam controls the ratio of the beam width to the inter-beam spacing of the Fourier pattern, while the phase modulation function produced by a basic cell governs the peak-

intensity of individual beams. For a typical imaging array the ideal is a pattern of equal intense closely spaced images of the LO feed.

In section 2 we describe an experimental procedure for prototyping and testing the equivalent reflection gratings to those transmission gratings already developed. This allows the use of metal rather than quartz as the basic grating material into which slots are to be milled. One benefit of using metal is that it greatly reduces the model-manufacture-test cycle time. The technique, if used in conjunction with ferrite polarising materials, can be used to develop a complete reflection based quasi-optical multiplexing system. We can thus considerably improve standing wave performance for use in high sensitivity detector arrays.

In section 3 a Gaussian Beam Mode Analysis is applied to the problem of multiple reflections and standing waves associated with transmission phase gratings. At each interface of the grating some energy is transmitted and some is reflected. To take this effect into account an analogous modal scattering matrix approach to that applied in horn antenna modeling is used [4]. For quasi-optical systems the forward scattering matrices of a number of optical components have already been considered in the literature (e.g. [5,6]). In the full scattering matrix approach necessary to analyze standing waves, track has to be kept of both the backward and forward going components of the propagating fields. By combining a scattering matrix description of the partial reflection at each grooved face with a propagation matrix to describe the beam travelling through the grating standing wave effects are investigated. In the examples considered a Gaussian beam illuminates transmission gratings of refractive index of 1.66 and 2. In section 4 a Gaussian beam mode analysis of the effects of tolerance errors associated with the gratings is also presented.

## **2. MANUFACTURE AND TESTING OF DAMMANN GRATINGS.**

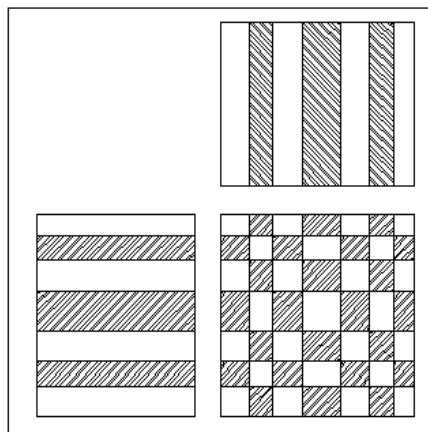
The Dammann grating, whether produced as a transmission or reflection grating, is a binary phase modulating structure which acts on the incoming wavefront to produce phase steps of 0 or  $\pi$  in the propagating beam. When imaged in the far field the desired result of this phase modulation is to produce an array of equi-intense images of the input field. This array of images can then be used, for example, to efficiently couple local oscillator energy into a multi-pixel heterodyne receiver. Algorithms have been developed to find the optimum phase transition points within a basic unit grating cell for a design to produce arrays of 2,3,4 and 5 output beams of equal intensity [1].

In the case of a transmission grating the modulation is achieved by arranging grooves in the surface of some transparent dielectric material such that the wave-front passing through the ungrooved portions suffer a phase delay of  $\pi$ , with respect to the rest of the wave-front phase. This is achieved by setting the groove depth to  $\lambda/2n$ , where  $n$  is the refractive index of the grating material. Multiple reflections within the grating

can cause losses and upset the distribution of power between the beams. These problems can be minimized if the grating thickness is chosen to be resonant at the wavelength of interest, i.e.  $N\lambda/2n$  where  $N$  is odd. Of course the grating needs to be resonant both at the top and bottom of the grooves and this can only be achieved by choosing materials of the correct refractive index. Quartz is a good candidate for transmission gratings because it is low loss and has a refractive index of approximately 2. The effect when  $n$  is not optimum is discussed in section 3, in which multiple reflections in transmission gratings is analysed.

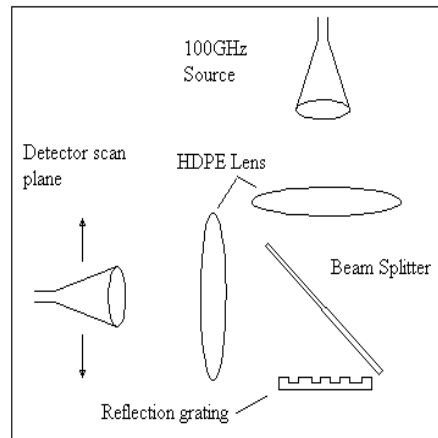
Conceptually a 2 D array can be obtained by passing the beam through two successive 1 D gratings rotated about the beam axis by 90 degrees with respect to each other. In reality this is achieved by forming each 1 D grating on opposite sides of a slab of quartz. This method is suited to quartz because the grooves are machined using a diamond grinding wheel, which can create long grooves easily but is not suitable for producing square sided pockets in a surface, as is required to produce a 2 D grating on one surface.

A reflection grating works on the same principles as the transmission grating. The phase transition points are the same as for the transmission grating but the groove depths need to be  $\lambda/4$  to produce the required  $\lambda/2$  phase delay in the reflected beam. Of course the grating needs to create the 2-D modulation on one surface and the drawing in *FIG. 1* shows how this is achieved.



Combining two 1-D Patterns.

*FIG. 1.*



Reflection Grating Test Set-Up.

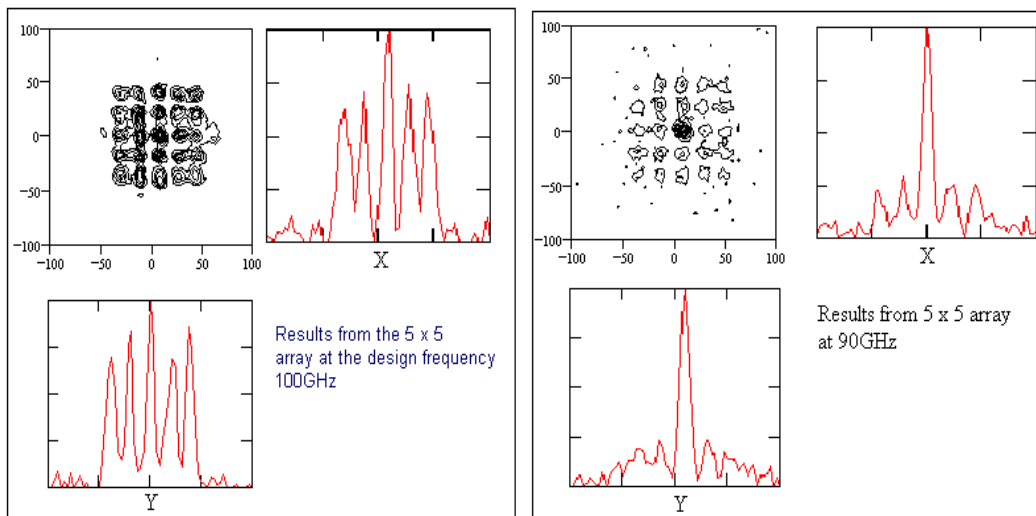
*FIG. 2.*

The shaded squares show where  $\lambda/4$  pockets need to be formed in the surface. Notice the white squares where two grooves overlap. No metal need be removed here, because two overlapping grooves cause a phase shift of  $2\pi$  which is equivalent to zero.

The resulting cutting pattern is more complex than that of the two sided transmission grating but it can be easily cut in aluminium sheet using a CNC milling machine. The milling machine can cut the pattern for a 5 x 5 reflection grating in about 2 hours. When compared with the 2 or 3 months required to have a quartz grating manufactured by a specialist optics company, it can be seen that using reflection gratings can greatly accelerate the design, build, test-cycle.

Simple reflection gratings need to be illuminated with a beam at normal incidence to prevent shadowing of the grooves, and this means that the test set-up is a little more complex than the standard inline 4-f configuration required by the transmission grating. The test set-up is shown in *FIG. 2*. The test facility consists of a Fourier 4-f optics set-up with a conical horn antenna feed driven by a variable frequency Gunn oscillator operating over the 90 to 105GHz range. In testing the system HDPE lenses are also used as the focussing elements because they produce less aberration in the beam pattern compared to the 90 degree throw off-axis ellipsoidal mirrors used previously [2]. The reflection grating is placed in the Fourier plane of the first lens and illuminated by a normally incident beam. The phase modulated reflection is coupled out to a computer controlled raster scanned detector through a large aperture beam splitter. The use of the beam splitter is not ideal because even with a perfect 50/50 split, only 25% of the initial beam power is directed towards the scanning detector. A better option would be to use a ferrite polarisation rotator to maximise the efficiency of the system, but for the purpose of grating testing at 100GHz where there is plenty of power available this is not a problem.

Several one and two dimensional gratings have been manufactured and tested using this system. A 5 x 5 reflection grating was cut and tested and the resulting patterns are shown in *FIG. 3*. The results are in good agreement with the software model.



Results for the  $5 \times 5$  array at the centre frequency and beyond the band limit.

*FIG. 3.*

The results at 90GHz show that the grating still produces the 5 x 5 array but that the pattern is dominated by the central peak. We believe that this is caused by a combination of standing waves in the test setup and the degradation in grating performance at or near the band edges.

The bandwidth and manufacturing tolerances are closely related. A 10% change in operating frequency at 100GHz is equivalent to a change in the optimum groove depth of 0.08mm. In [1] we showed that the useful bandwidth of a transmission grating is approximately  $\pm 10\%$  so a dimensional error of this size would render the grating useless. In terms of manufacturing tolerances, this level of accuracy is easily achieved in aluminum, and not so easily in quartz, but care must be taken to achieve good surface flatness over the entire grating area. It is interesting to note that the effect of groove depth tolerance errors is doubled in a reflection grating, where the phase shift is achieved by the two way trip in and out of the groove.

### 3. MULTIPLE REFLECTIONS IN TRANSMISSION GRATINGS

Analysing reflections in a quasi-optical system requires that the appropriate scattering matrices associated with a grating and all the other components involved be calculated. The quasi-optical system as a whole or any component is represented by a single scattering matrix  $[S]$  with the reflection and transmission characteristics determined by the equation:

$$\begin{bmatrix} [B] \\ [D] \end{bmatrix} = \begin{bmatrix} [S_{11}] & [S_{12}] \\ [S_{21}] & [S_{22}] \end{bmatrix} \begin{bmatrix} [A] \\ [C] \end{bmatrix}.$$

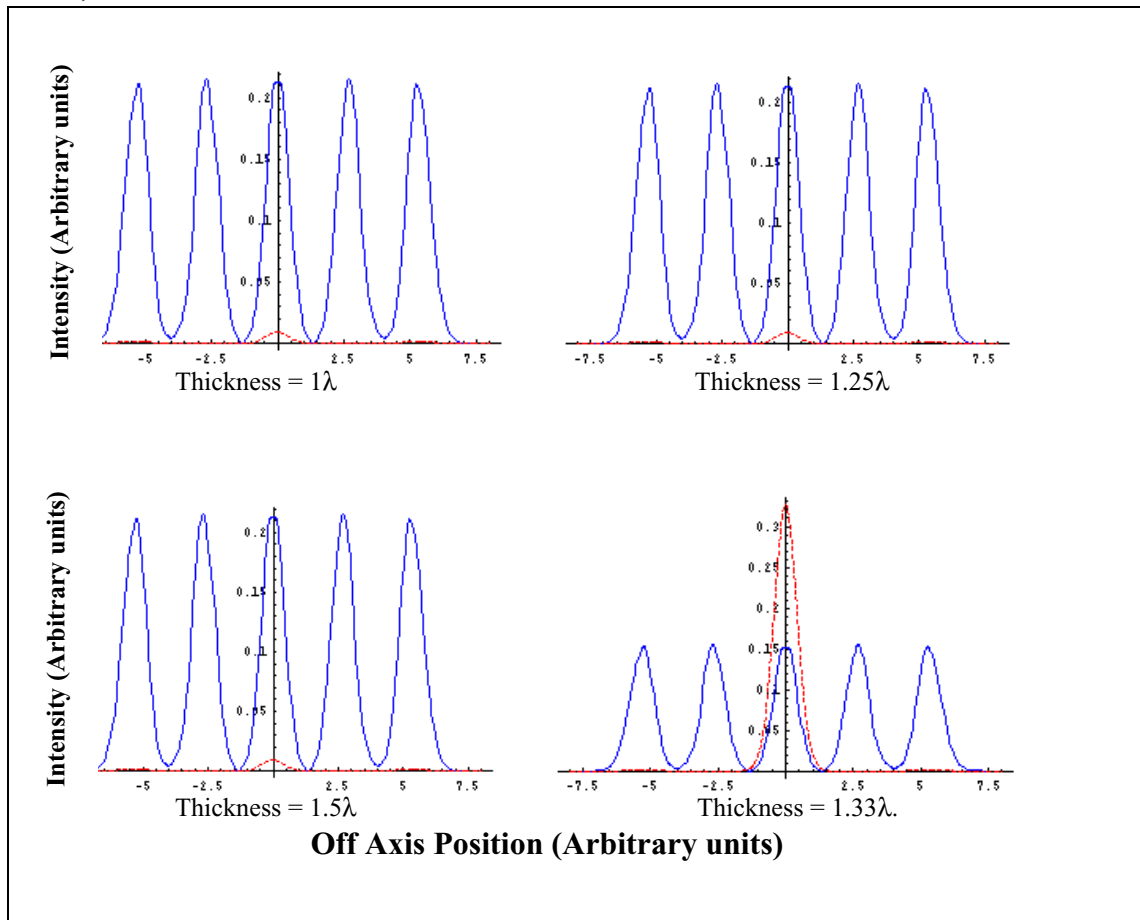
$[A]$  and  $[B]$  are vectors containing the forward and reflected mode coefficients,  $A_n$  and  $B_n$ , respectively, looking into the system at the input side.  $[C]$  and  $[D]$  are vectors of the mode coefficients,  $C_n$  and  $D_n$ , of all the modes looking into the system at the output plane.

In the case of a grating there is a partially reflected wave at each of the free space/dielectric interfaces. The reflected and transmitted electric fields are given by the Fresnel equation for normal incidence:  $E_{refl} = \rho E_{inc}$ , where  $\rho = (n_1 - n_2)/(n_1 + n_2)$ , and  $E_{trans} = \tau E_{inc}$ , where  $\tau = 2 n_1 / (n_1 + n_2)$ . In these equations  $n_1$  and  $n_2$  are the refractive indices of the media for the incident and transmitted radiation, respectively. The reflected field  $E_{refl}$  can be written in terms of the modes travelling in the negative  $z$  direction  $E_{refl} = \sum_n B_n \psi_n^-$ . Since  $E_{inc}$  itself is written as a sum of modes travelling in the positive  $z$  direction  $E_{inc} = \sum_n A_n \psi_n^+$ , then the  $B_n$  can be derived from the scattering relationship:  $B_n = \sum_m S_{mn} A_m$ , where  $S_{mn} = \rho \int_A (\psi_n^-)^* \psi_m^+ dx$ . Since it is assumed that the modes travelling in the negative  $z$  direction have the same waist position and waist radius as those travelling in the positive  $z$  direction:  $S_{mn} = \rho \int_A (\psi_n^+)^* \exp(-ikr^2/R) \psi_m^+ dx$ , integrated over the grating surface. The quadratic complex exponential term represents the fact that the reflected wave suffers a sign change of its phase front

radius of curvature on reflection, or in other words that the reflected field continues to diverge after reflection.

In the following example the above theory is applied to the case where the incident Gaussian beam is transformed into  $5 \times 5$  beams at the output Fourier plane of the grating. The gratings considered have refractive indices of 1.66 and 2.00 and the cell parameters were set to those appropriate values (see [1]). In general to accurately describe the phase variation introduced on the incident beam by the grating a large number of higher order modes are needed in any Gaussian beam mode analysis. However, one can increase the accuracy with a limited mode set by careful choice of the beam width parameter  $W$  (and not setting it equal to the beam width of the incident Gaussian). In fact, the best choice is determined by the scale of the structure on the grating rather than the width of the incident Gaussian so that fewer modes are needed to describe the grating more accurately. The incident Gaussian field must then of course be expanded in terms of a best choice mode set.

The transmitted and reflected far-field patterns of a grating with refractive index 2 and 1.66 are shown in figures 4 and 5, respectively, for a thickness value of  $1\lambda$ ,  $1.25\lambda$ ,  $1.5\lambda$ , and  $1.33\lambda$ .



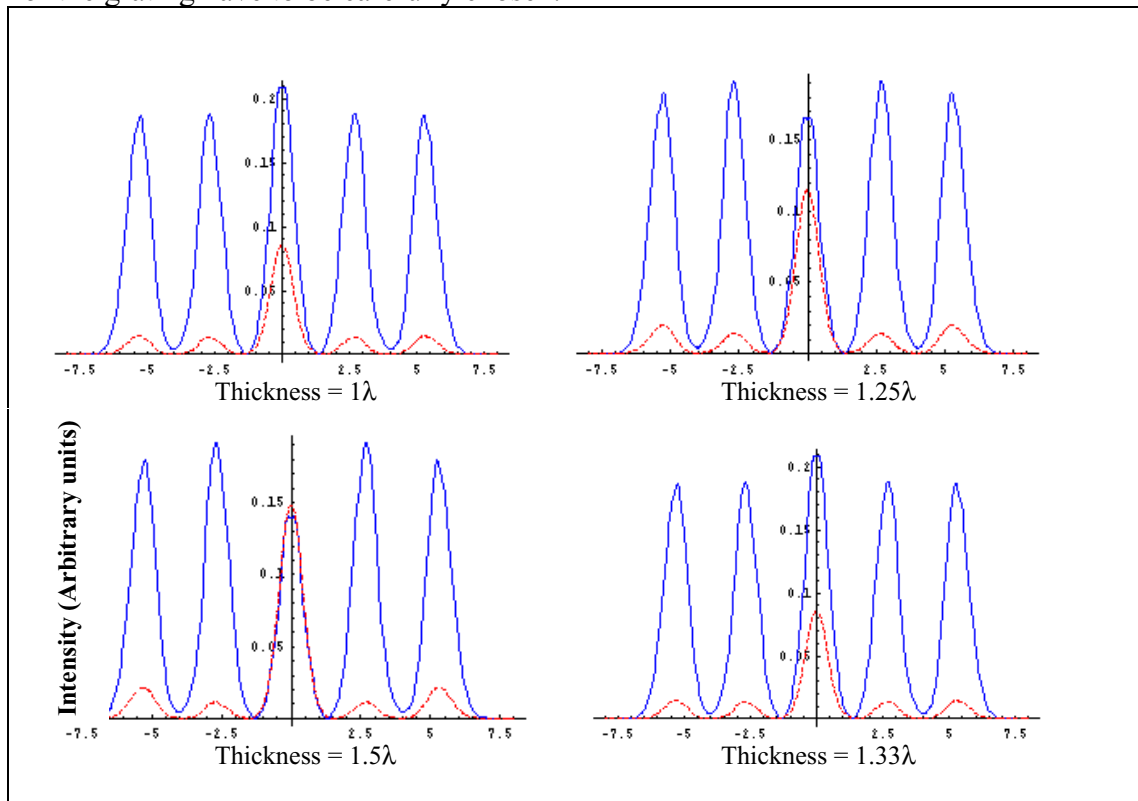
Cross section of beam patterns of  $5 \times 5$  grating ( $n = 2$ ) of thickness  $1\lambda$ ,  $1.25\lambda$ ,  $1.5\lambda$ , and  $1.33\lambda$ .

FIG. 4.

The overall reflection and transmission coefficients for a slab of dielectric of thickness  $t$  are given by  $r = \frac{\rho + (-\rho)e^{2i\beta}}{1 + \rho(-\rho)e^{2i\beta}}$  and  $t = \frac{\tau\tau e^{i\beta}}{1 + \rho(-\rho)e^{2i\beta}}$ , where  $\beta = 2\pi nt / \lambda_0$

For maximum and minimum transmission in the grating  $e^{2i\beta}$  will either be zero or one. This means that both the refractive index  $n$  and the thickness of the grating must be chosen correctly to insure maximum transmission.

It can be seen that the transmission peaks for the grating of refractive index 2 are all equal intensity while for the grating of refractive index of 1.66 the transmission peaks are of unequal intensity. This is due to the contribution to the overall field from the wave that has been multiply reflected within the grating and does not add with the same phase lag as the straight through beam. What this clearly indicates is that for idealised grating operation both the refractive index of the material and the thickness of the grating have to be carefully chosen.



Cross section of beam patterns of 5x5 grating ( $n = 1.66$ ) of thickness  $1\lambda$ ,  $1.25\lambda$ ,  $1.5\lambda$ , and  $1.33\lambda$ .

FIG. 5.

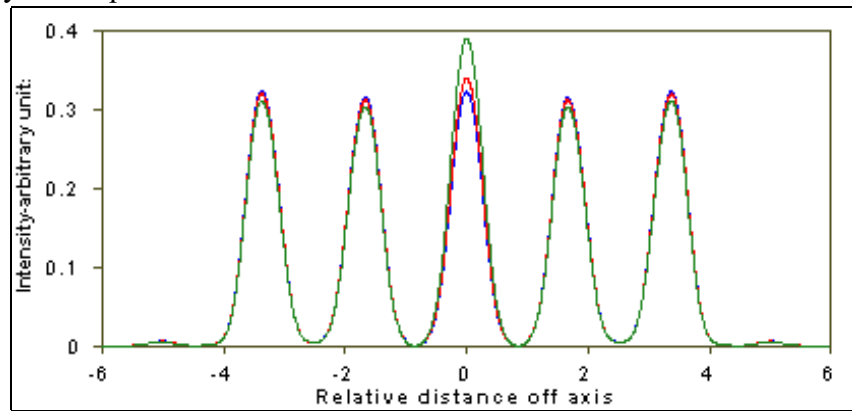
#### 4. MODE ANALYSIS OF GRATING TOLERANCES.

An investigation of the effect of errors in the width and depth of the slots making up one of the faces of the grating was undertaken using Gaussian Beam Mode Analysis. The phase shift difference for the distinct binary paths through the grating, depends on the groove depth,  $h$  and the refractive index of the grating material,  $n$ . The phase shift and groove depth are related by:

$$\Delta\phi = \frac{2\pi h(n-1)}{\lambda_0} = \pi,$$

where  $\lambda_0$  is the wavelength of the incoming radiation in a vacuum and  $\Delta n$  is the difference between the refractive index of the grating material and the surrounding medium.

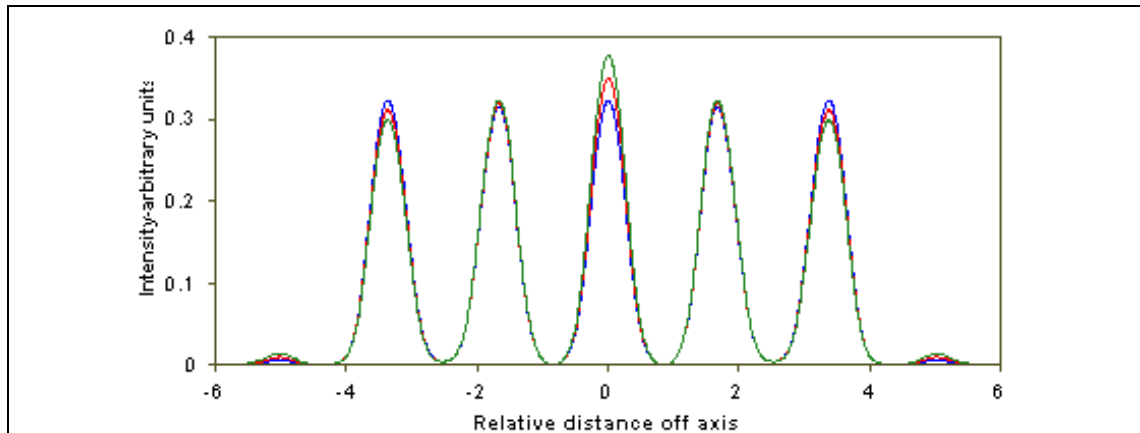
The cell depth or equivalently phase, was changed with addition of a small deviation,  $\delta$  to the phase shift term. Thus, setting  $\delta=0$  the phase change remains  $\pi$  corresponding to a groove depth of  $\lambda/4$  for a reflection grating and the expected symmetric array of equi-intense images are obtained. The resulting field patterns for  $\delta = \pi/16, \pi/8$  are superimposed on the ideal case for comparison in Figure 6. A phase change of  $\pi/8$  illustrates the change in relative peak intensity and the deterioration of the uniformity of the peaks indicates that the tolerance threshold is exceeded with  $\delta > \pi/8$ .



The output field patterns for grating with phase errors of  $\delta = \pi/16, \pi/8$  are superimposed on the ideal case for comparison.

*FIG. 6.*

Similarly by modifying the groove widths from the ideal values by approximately 0.2% of the cell width quite a substantial reduction in the efficiency of the operation of the grating as a multiplexor is observed. The results are shown in Figure 7.



Reduction in ideal grating operation for case where cell widths are varied.

FIG. 7.

## 5. CONCLUSION.

In this paper we have described some recent work on the manufacture and testing of reflection phase gratings. The analysis of reflection gratings using Gaussian Beam Mode Analysis was described and standing wave effects were shown to have a deleterious effect on ideal grating function unless the refractive index and thickness of the grating are carefully chosen. It may be possible to combine the ease of manufacture of metal gratings with a moldable powder[7] of the correct refractive index to produce transmission gratings with optimised characteristics. We have also summarised some modal modelling work we have carried out into assessing grating tolerances.

## ACKNOWLEDGEMENTS

The authors would like to acknowledge the support of Enterprise Ireland in this research programme. Special thanks to Mr. David Watson for his precision engineering skills and expertise in CNC milling of the gratings.

## References

- [1] J. Anthony Murphy, C. O Sullivan, N. Trappe, W. Lanigan, R. Colgan and S. Wittington, *Modal Analysis of the Quasi-Optical performance of Phase Gratings*. International Journal of Infrared and Millimetre Waves, **20**, No. 8, 1999
- [2] W. Lanigan, R. Colgan, J. Anthony Murphy and S. Wittington, *Theoretical and experimental investigation of phase gratings*, 23<sup>rd</sup> International conference on Infrared and Millimetre Waves, Colchester, UK. Sept. 1998.
- [3] H. Dammann and E. Klotz, *Coherent optical generation and inspection of two-dimensional periodic structure*, Optica Acta, 24, 505, 1977

- [4] R. Padman and J.A. Murphy, "A scattering matrix formulation for Gaussian beam-mode analysis," Proc. ICAP, York, April 1991.
- [5] J.A. Murphy, S. Withington and A. Egan: "Mode conversion at diffracting apertures in millimetre and submillimetre-wave optical systems," *IEEE Trans. Microwave Theory Techniques*, 41, pp. 1700-1702, October 1993.
- [6] S. Withington, J.A. Murphy, and K.G. Isaak, "Representation of mirrors in beam waveguides as inclined phase-transforming surfaces", *Infrared Phys. Technol.*, 36, pp 723-734, March 1995.
- [7] L. Noel, J-M. Munier, F. Garet, L. Duvillaret, P. Febvre, G. Beaudin, " A New Material with adjustable refractive index for applications in the millimetre and sub-millimetre frequency range." *Proceedings of the 2<sup>nd</sup> ESA Workshop on Millimetre Wave Technology and Applications*, pp 400-405.

# DESIGN AND ANALYSIS OF A HYBRID FEED ANTENNA FOR A FLUX-FLOW OSCILLATOR INTEGRATED 460 GHz SIS RECEIVER

**M.-H. Chung and M. Salez**

DEMIRM, Observatoire de Paris, 61, avenue de l'Observatoire, 75014 Paris, France

E-mail : moon-hee.chung@obspm.fr

## *Abstract*

We have designed a 460 GHz FFO-driven integrated SIS receiver in which the signal is fed via a quasi-optical hybrid antenna feeding system. Since in such quasi-optical SIS receivers the contribution of the quasi-optics to the overall receiver noise is considerable, it is important to be able to analyze the antenna efficiency in order to optimize its coupling and improve the noise temperature of the receiver. The goal of this paper is an attempt to analyze the gaussian coupling efficiency, far-field pattern and loss of the system, applying the geometrical optics-physical optics combined method to our hybrid integrated feed antenna. The computation of the loss contributed by different quasi-optical solutions can be a decision factor for selecting one particular design (optics materials, geometries, and configuration). Quite commonly adopted solutions employ a substrate hemispherical lens in conjunction with (or without) an objective lens of HDPE or Teflon located in the Fresnel region of the hemispherical lens. Such solutions have advantages and drawbacks, and other solutions, better for the receiver noise, may exist. In addition, computing the radiation characteristics of the quasi-optical system will be useful to interpret the integrated receiver measured performances and evaluate the diverse noise sources in this complicated system. A numerical tool based on the ray-tracing and diffraction mixed approach was implemented to examine the radiation characteristics of the feed structure of FFO integrated SIS receiver.

## **1 Introduction**

Flux-Flow Oscillators (FFO) integrated with SIS receivers have been proposed as an attractive alternative to commonly used submillimeter wavelength local oscillators; they are compact, low-mass and low-power consumption devices, and they can provide individually optimized LO power to the SIS mixers of a focal plane heterodyne receiver array. The most recent and extensive experimental work aiming at producing a fully operational-and phase-locked-integrated SIS receiver, for array applications, has been done by Shitov *et al* [1].

There is a growing need for heterodyne focal plane imaging arrays, either to speed up commonly time-consuming mapping observations, or to do interferometry with a single-dish telescope. In this context we have designed an integrated FFO SIS receiver chip for 460 GHz, and the receiver is now under construction. Our goal is to test the mixing performance of this new kind of superconducting submillimeter receivers, using slightly different technological choices than those of [1], for a frequency range of typical interest for radioastronomical studies.

Since the relatively complicated superconducting circuits (FFO, integrated diplexer) require more contact pads which hardly fit within the regular dielectric chips for waveguide mounts, the quasi-optical solution is generally the adopted one to feed the FFO integrated SIS mixers. It usually consists of a combination of planar antenna and dielectric lens, and for array applications, either the 'fly's eye' configuration-where each planar antenna and integrated receiver pixel has its own dielectric lens-and the 'single-lens' configuration-where only one lens illuminates the whole array can be considered. Several other options can be considered for the design, depending on the type of planar antenna (bow-tie, double-dipole, double-slot, log-periodic, etc), the type of lens (elliptic, hyperhemispherical, extended hemispherical), the lens material and the nature of the substrate on which the superconducting receiver is fabricated.

Choosing among these design options not only drives the receiver optical coupling scheme and geometry, but it may also have consequences on the RF losses which often considerably contribute to the total noise of receiver-although the sensitivity of the SIS mixer itself is quantum noise limited [2]. Therefore, it is necessary to analyze in detail the RF characteristics of the quasi-optical solutions considered to estimate their impact on the receiver system.

Most of all, the radiation properties of the FFO integrated SIS mixer is critical in the case of a focal plane imaging array receiver in which the beam pattern of the feed antenna must be well matched to the radiotelescope optics. In particular, it is important to pay attention to the feed antenna's directivity and sidelobes. For an array, high directivity with low sidelobes is required, to optimize the pixels aperture efficiency and to have each pixel sample the sky in a clean way.

The hybrid feed antenna for our quasi-optical receiver consists of an extended hemispherical lens with a double dipole as the elementary radiator and, potentially, one additional-'objective'-dielectric lens. This type of integrated lens antenna has been widely used in the millimeter and submillimeter wavelength domain [4]. Yet our goal was to determine, before finalizing the receiver's design, whether this configuration was the best suited for our purpose, given our experimental constraints.

A numerical tool was implemented to estimate the radiation properties (gaussian coupling, directivity, sidelobes) of our quasi-optical feed system and to investigate the influence on those of the lenses geometry, such as the hemispherical lens extension. Since a direct application of the diffraction theory for our hybrid feed antenna would be very time consuming, we used a mixed approach[7], combining a ray-tracing technique within the substrate lens and the diffraction theory to calculate the far fields.

## 2 Design aspects

Hybrid antennas-substrate lenses combined with elementary planar antennas-are widely used in open structure integrated receivers. One reason is that they solve the problem of substrate modes at submillimeter wavelengths-the dielectric lens can be considered as half space. Most of the radiation occurs within the substrate, yet some amount still radiates in the air, resulting in extra RF losses. If a high dielectric constant material cannot be used for the lens-or is not wished-then a back plane reflector must be placed about  $1/4$  wavelength away from the planar antenna to fold the back-radiated beam onto the main beam in the lens, without modifying its radiation pattern. Most people use silicon lenses for this reason; the power loss in the air side of double-slot antennas on silicon ( $\epsilon = 11.7$ ) is only 8% [5]. However, silicon lenses induce important reflection losses at their front surface, which must be minimized by hard-to-manufacture antireflection coating.

Our choice of dielectric material for the lens was mostly driven by SIS technology-our superconducting FFO-SIS receiver is made on fused quartz substrates ( $\epsilon = 3.8$ ). Having a different dielectric for the lens would cause spurious and inevitable reflections at the interface, and restore potential substrate modes in the receiver chip. Fused quartz is not a bad choice, compared to silicon, for spillover and polarization efficiencies. And the lower dielectric constant of fused quartz compared to silicon gives an advantage of lower reflection loss without anti-reflection layer. However, due to its low dielectric constant, the power loss radiated into the air side in our case is about  $20 \sim 30\%$ , and therefore a metallic back reflector must be used. This can be done because we use microstrip structures and double-dipole antennas, hence leaving most of the chip's surface unoccupied. The beam pattern of the double-dipole antenna does not change with the reflector. The double-dipole size and spacing were determined so as to produce a symmetric radiation pattern in the E- and H-plane [3].

If we place the elementary radiator at the aplanatic point of the hemispherical lens (i.e.  $R/n$ , where  $R$  is the lens radius and  $n = \sqrt{\epsilon_r}$ , as one often conveniently does, it is then necessary to add an objective lens to enhance the directivity of the overall feed system. But there is a possibility of using a simpler configuration, with no objective lens. This depends on the elementary radiator's position relative to the center of the hemispherical lens-the hemispherical lens extension. Büttgenbach [10] defined the hybrid antenna as a special case of extended hemispherical lens with the extension length beyond the aplanatic point, combined with a planar feed antenna. Then the lens, which approximates an elliptical lens, is diffraction-limited. He proposed to use this hybrid antenna as an alternative to the hyperhemispherical lens antennas used in conjunction with an objective lens, and discussed related problems of gaussian coupling efficiency. These feed structures seem very attractive because they allow simpler designs and low cost fabrication. As a consequence, we have considered with no a priori the addition of an objective lens and the extension length of the hemispherical lens as a free parameter for our feed design.

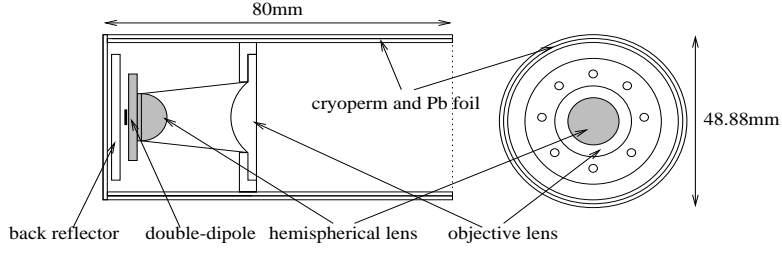


Figure 1: Feed structure of a FFO integrated SIS receiver

When the extended hemispherical lens is diffraction-limited and use without objective lens, its radius determines the f-number of the quasi-optical system. Therefore several geometrical factors had to be taken into account as boundary conditions.

The FFO being a very sensitive device to magnetic field, one must enclose FFO-integrated SIS receivers in magnetic shielding assemblies. In our case, the shield consists of a cylinder with one closed end, made of two concentric 1.47-mm thick Cryoperm layers and one inner 0.25-mm thick lead foil layer, in order to provide approximately 70 dB of magnetic shielding at 4.2K[6]. To maximize the shielding and reduce the open end effect, the length-to-diameter ratio should be as large as possible. The length of our cylinder assembly is 80mm and its inner diameter is 42.5mm. So, we have to make a very compact quasi-optical mixer design, with a f-number larger than 8.

Figure 1 shows the overall feed structure of our FFO integrated SIS mixer.

### 3 Theoretical analysis

#### 3.1 Hemispherical lens fed by double-dipole antenna

Figure 2 shows the structure to be analyzed. To calculate the radiation properties of the hemispherical lens antenna, the ray tracing and diffraction theory similar to the approach of [7] is used in this report. We consider here only on-axis feed position case but this method can be easily generalized to off-axis feed positions. Ray-tracing can be used to treat the radiation in the lens only because its dimensions are much larger than the wavelength.

The double-dipole antenna is located on the planar surface of the hemispherical lens with distance,  $e$  from the center of hemispherical lens. The electromagnetic fields on the internal curved surface of the lens,  $(\theta_s, \phi_s)$  coordinate system, can be determined from the far-fields of the double-dipole antenna,  $\vec{F}(\theta_d, \phi_d)$ , assuming that the size of lens is enough large compared to the wavelength to satisfy the conditions of the geometrical optics,

$$\vec{E}_s(\theta_s, \phi_s) = \frac{jk_d e^{-jk_d r_d}}{4\pi r_d} \left[ F_{\theta_d}(\theta_d, \phi_d) \hat{\theta}_d + F_{\phi_d}(\theta_d, \phi_d) \hat{\phi}_d \right] \quad (1)$$



where the radiation vectors  $\vec{N}$  and  $\vec{L}$  are defined as the followings,

$$\vec{N}(\theta, \phi) = \int \int_S \vec{J}_s(\vec{r}') e^{jkR \cos \Psi} dS \quad (11)$$

$$\vec{L}(\theta, \phi) = \int \int_S \vec{M}_s(\vec{r}') e^{jkR \cos \Psi} dS \quad (12)$$

$k$  is the propagation constant in the free space,  $R$  is the radius of the hemispherical lens,  $\Psi$  is the angle between the integration point and the observation point, and the integration is done on the surface  $S$  of the hemispherical lens.

### 3.2 Hyperhemispherical lens combined with an objective lens

By definition, a hyperhemispherical lens is an extended hemispherical lens with the elementary radiator located at the aplanatic point. Such a feed system is characterized by a high gaussian coupling efficiency. However, the directivity is not sufficient to match most f-numbers of practical use in receiver applications, and it must therefore be used together with an objective lens to increase the global directivity.

Even though one needs a full-wave numerical modeling to analyze the radiation properties in the Fresnel zone which is located between the hemispherical lens and the objective lens, we believe that the ray-tracing method can provide a first approximation of the radiation pattern of the extended hemispherical lens combined with an objective lens[8]. In the calculations, we assume that the objective lens has hyperbolic surface on the back side and a plane surface on the front side as shown in Fig.3. To simplify the ray-tracing method, the curved surface of the hemispherical lens is assumed to have an anti-reflection layer - to neglect the reflected rays.

Since we assume the hyperhemispherical lens to be ideal, we can virtually move the focal point,  $-R/n$ , of the hyperhemispherical lens into the one,  $-nR$ , of the objective lens. In the Fig.3,  $n$ ,  $R$ ,  $D$ ,  $F$  are respectively the refractive index and radius of the hyperhemispherical lens, and the diameter and focal length of the objective lens. In the diffraction limit, the diameter  $D$  will define the feed system's FWHP (Full Width Half-Power) .

## 4 Results of computation and design considerations

To confirm the validity of our computer program, we compared the calculated results with the published ones of [7] for the same data and found good agreements.

The radiation properties of the feed structure of FFO integrated SIS receiver were then calculated, first with an extended hemispherical lens, the extension length of which could be varied, and no objective lens.

Figure 4 shows the beam pattern of our double-dipole antenna, used as an elementary radiator on the planar surface of the fused quartz hemispherical lens. The length

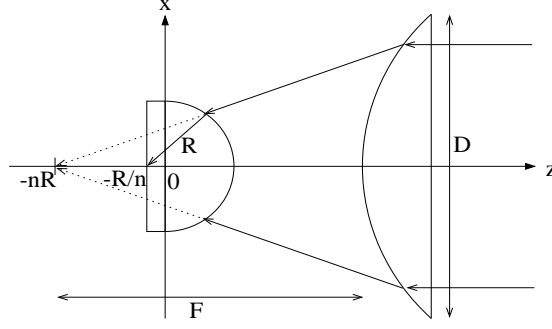


Figure 3: Hyperhemispherical lens combined with an objective lens

of the double-dipole antenna is  $0.5\lambda_d$ , its distance,  $0.4\lambda_d$  and the distance of the back reflector,  $0.25\lambda_d$  where  $\lambda_d$  is the wavelength of 460 GHz in the fused quartz ( $\epsilon = 3.8$ ).

Figure 5,6,7,8, and 9 show the far-field pattern at 460 GHz of the hemispherical lens, the diameter of which is 12 mm, for different extension lengths varied from 2.5 to 6.5mm by steps of 1.0mm. The extension length of 3mm approximately corresponds to our  $R/n$ . We note a good E and H plane symmetry in Fig.10. As with the elliptic lens, the phase, shown in Fig.10, is flat (top-hat) across the main lobe. The extension length referred here is in fact the distance from the center of hemispherical lens to the back reflector. As expected, the radiation lobe of the hemispherical lens becomes sharper when the extension length increases; the sidelobes level decreases; it seems to converge toward a diffraction limit.

Figure 11 shows the directivity and gaussian coupling efficiency of the hemispherical lens with the variation of the extension length. The gaussian coupling efficiency is defined in (13)[9],

$$\eta = \frac{\left| \int \int_S \vec{E}_g \cdot \vec{E}_a ds \right|^2}{\int \int_S |\vec{E}_g|^2 ds \int \int_S |\vec{E}_a|^2 ds} \quad (13)$$

where  $\vec{E}_g$  is the electric field represented by the incident gaussian beam,  $\vec{E}_a$  is the field of the hemispherical lens antenna and  $S$  is the spherical surface of integration centered on the position of the hemispherical lens antenna. The amplitude and phase of electric field of the incident gaussian beam,  $\vec{E}_g$ , must be varied to find the maximum gaussian coupling efficiency. As already mentioned in [7], Figure 11 shows that when the extension length increases, the gaussian coupling efficiency decreases while the directivity of the hemispherical lens increases to reach a maximum value around the extension length of 5.5 mm. Past the extension length of 5.5 mm, the side lobe levels increase again, hence degrading the directivity of the extended hemispherical lens.

Now, we made similar calculations in the case of a hyperhemispherical lens combined with an objective lens. For practical reasons (the magnetic shield) our objective lens has a diameter of 18 mm, a focal length of 41.78 mm. It is made of Teflon

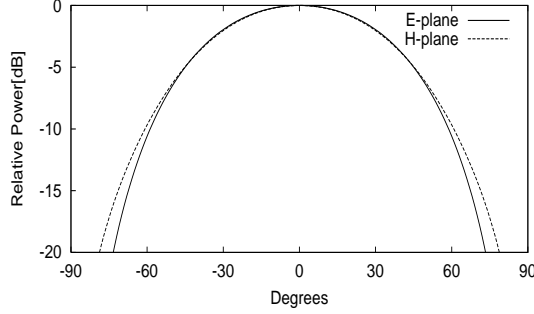


Figure 4: Beam pattern of double-dipole antenna with back reflector

( $\epsilon_r = 2.3$ )-a common choice at these frequencies-and is 4.0 mm thick at the widest. Again to simplify the ray-tracing technique, we assumed that its front side is coated with an anti-reflection layer.

Figure 12 shows the calculated beam pattern of hyperhemispherical lens combined with an objective lens at 460 GHz. The calculated directivity is 34.9 dB and the estimated FWHP is  $2.7^\circ$ . This is close to the FWHP of about  $2.49^\circ$  at 460 GHz expected from diffraction theory for our objective lens, according to (14):

$$\theta_{FWHP} \simeq 1.2 \frac{\lambda}{D} \quad (14)$$

It means that the hyperhemispherical lens combined with the objective lens reaches the diffraction limit.

From the calculated results, it would seem a priori a reasonable choice to select the maximum gaussian coupling efficiency solution, that is, a hyperhemispherical lens with an objective lens which increases the directivity of the system, and makes it diffraction-limited. But the calculated result of the gaussian coupling efficiency is always an optimized value: it needs the appropriate gaussian beam to obtain this maximum coupling efficiency. Experimentally, it is very difficult to obtain, so as to measure the gaussian coupling efficiency[7],[10]. Also, the coupling efficiency depends on other factors, such as antireflection coating, alignment, etc. Figure 13 shows the calculated gaussian coupling efficiency with variations of the amplitude and phase of the incident gaussian beam. We see that the coupling efficiency is very easily affected by the amplitude and phase of the incident beam. This means that only a small misalignment or error in focusing will get us off the maximum gaussian coupling efficiency.

On the other hand, we have calculated the gaussian coupling efficiency and directivity of a hemispheric lens without objective lens, and have shown that for an extension length past beyond the aplanatic point, the directivity reaches a maximum, and the beam is diffraction-limited. We believe this criterion is more important than optimum coupling efficiency in practice, especially from the point of view of making reliable and optimized feed arrays for spectro-imaging systems. By choosing the lens diam-

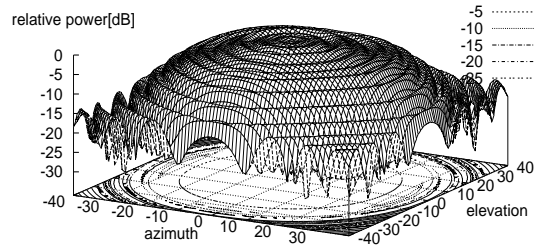


Figure 5: Beam pattern of hemispherical lens for the extension length of 2.5 mm

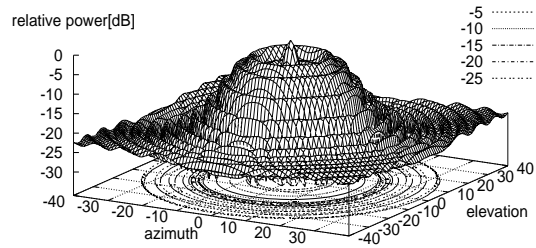


Figure 6: Beam pattern of hemispherical lens for the extension length of 3.5 mm

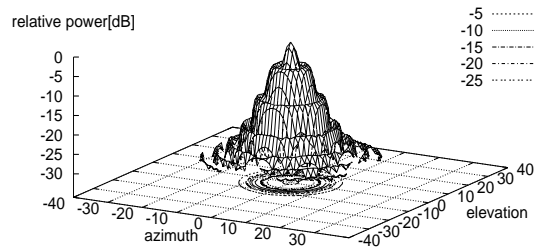


Figure 7: Beam pattern of hemispherical lens for the extension length of 4.5 mm

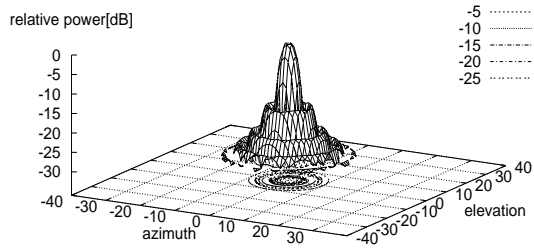


Figure 8: Beam pattern of hemispherical lens for the extension length of 5.5 mm

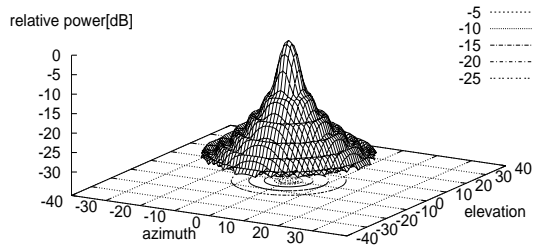


Figure 9: Beam pattern of hemispherical lens for the extension length of 6.5 mm

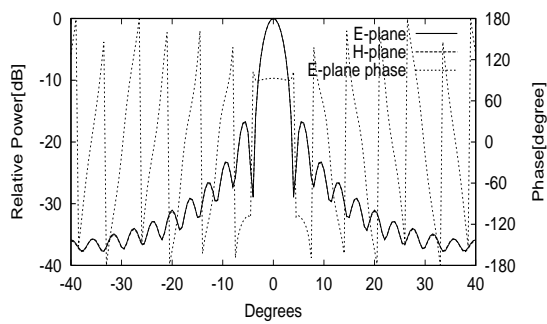


Figure 10: E and H-plane power pattern and phase for the extension length of 5.5mm

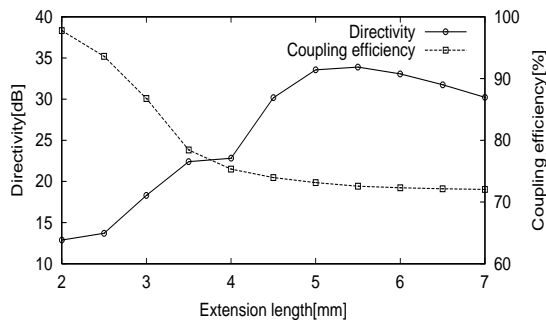


Figure 11: Directivity and gaussian coupling efficiency of the hemispherical lens at 460 GHz

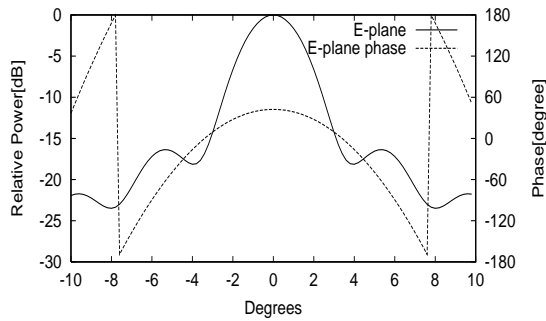


Figure 12: Far-field pattern of hyperhemispherical lens combined with an objective lens at 460 GHz

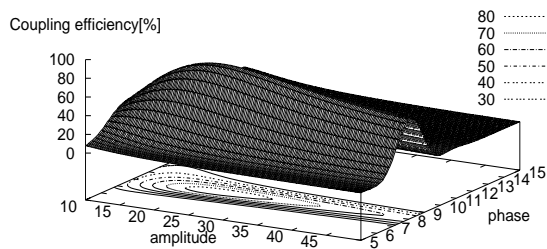


Figure 13: Calculated gaussian coupling efficiency of the hemispherical lens fed by double-dipole antenna at 460 GHz for the extension length of 3mm and the amplitude and the phase are for the electric field representation of the incident gaussian beam.

eter (hence the beam f-number) and dielectric material (hence minimizing the risk of reflection loss and back-radiated power loss), we can not only design an efficient lens for a pixel, but make it easy to fabricate and low-cost. It remains to decide whether the best configuration for an array receiver using these extended hemispherical lenses is the fly's eye or one single lens illuminating many pixels. Probably the former is the best, when we want performance uniformity among the pixels-our drive to make FFOs initially. Our future work will include calculations of antenna gain and directivity for different off-axis positions of the double-dipole antennas within the lens plane.

Another advantage of this solution without objective lens concerns the associated RF loss and its influence on the SIS receiver noise. Aside from reflection losses, the objective lens has dielectric losses which will contribute to the RF noise, especially since large Teflon lenses may not cool down uniformly, while fused quartz lenses on the mixer block are certain to be at 4.2 K (be it the SIS device temperature) .

## 5 Conclusion

We implemented a numerical tool based on the the ray-tracing and diffraction mixed approach which is similar to [7] to examine the radiation characteristics of the feed structure of our FFO integrated SIS receiver, which consists of an extended hemispherical lens fed by a double-dipole antenna, backed by a plane reflector, and with or without an objective lens. In the latter case (no objective lens), we found results very similar to those of [7], and confirming the experimental results of [10], showing a maximum of the directivity obtained for a lens extension larger than  $R/n$  -the hyperhemispherical lens plane of truncation. Then, the beam's FWHP almost reaches the diffraction limit. In our case, this extension length is about  $0.9R$ , and the beam divergence is small enough to be compatible with our FFO receiver design, where the mixer must be housed in the rear end of a rather long cylindrical magnetic shield. We believe it is not necessary to use an objective lens, even though the calculated gaussian coupling efficiency of this hybrid lens antenna is smaller than in the case of a hyperhemispherical lens: what seems most important to us when selecting the configuration of the feed system-especially in view of an array application-is the beam quality and directivity. Furthermore, the gaussian coupling efficiency is very hard to measure at submillimeter wavelengths since it requires the measurement of absolute powers[10]. There is no clear experimental indication, therefore, that this parameter is so drastically reduced with our design that it should forbid it. In addition, there is one secondary-but not negligible for an array-advantage in using extended hemispherical lenses without objective lens: the low fabrication cost compared to expensive elliptic lenses.

## References

- [1] S.V.Shitov, V.P. Koshelets, A.M.Baryshev, L.V. Filippenko, Th.de Graauw, J.R. Gao, W.Luinge, H. van de Stadt, N.D.Whyborn, P.Lehikoinen, "Development of superconducting integrated receiver for application in imaging arrays," *Proc. 7th Intl. Conf. Space Terahertz Technology*, 1996.
- [2] Tucker J.R. and Feldman M.J., "Quantum detection at millimeter wavelengths," *Rev. Mod. Phys.*, vol. 57, pp. 1055-1113, 1985.
- [3] A.Skalare, "SIS Heterodyne receivers using broadside and endfire double dipole antennas," Internal Report, S.R.O.N., Postbox 800, 9700 AV Groningen, the Netherlands, February, 1993.
- [4] M.C.Gaidis, H.G.LeDuc, M.Bin, D.Miller, J.A.Stern, and J.Zmuidzinas, "Characterization of low-noise quasi-optical SIS mixers for the submillimeter band," *IEEE Microwave Theory Tech.*, vol.44,no.7, pp. 1130-1138, 1996.
- [5] M.Kominami, D.M. Pozar, and D.H. Schaubert, "Dipole and slot elements and arrays on semi-infinite substrates," *IEEE Trans. Antennas Propagat.* vol.33, pp.600-607, June 1985
- [6] Private communication with Larry Maltin of Amuneal Manufacturing Corp.4737 Darrah Street Philadelphia, PA 19124-2705
- [7] D.F.Filipovic, and G.M.Rebeiz, "Double-slot antennas on extended hemispherical and elliptical quartz dielectric lenses," *Intl. J. Infrared Millimeter-Waves*, vol.14, No.10, pp 1905-1924, 1993.
- [8] M.J.M.Van der Vorst, P.J.I. de Maagt, and M.H.A.J. Herben, "Electromagnetic modeling of objective lenses in combination with integrated lens antennas," *Proc. 9th Intl. Conf. Space Terahertz Technology*, pp.389-395, 1998.
- [9] S.E.Schwarz, "Efficiency of quasi-optical couplers," *Intl. J. Infrared Millimeter-Waves*, vol.5, No.12, pp 1518-1525, 1984.
- [10] T.Büttgenbach, "An improved solution for integrated array optics in quasi-optics mm and submm receivers: the hybrid antenna," *IEEE Microwave Theory Tech.*, vol.41,no.10, pp. 1750-1761, 1993.

**11TH INTERNATIONAL SYMPOSIUM ON SPACE TERAHERTZ TECHNOLOGY**  
**Registrants and Authors**

A. Adam  
Supélec  
Department of Electron Device Physics  
91190 Gif-sur-Yvette, France

Peter Ade  
Queen Mary and Westfield College  
London E1 4NS, UK

Juha Ala-Laurinaho  
MilliLab, Radio Laboratory  
Helsinki University of Technology  
P.O. Box 3000  
FIN-02015 HUT  
Finland

Dr. Egor Alekseev  
University of Michigan  
Solid-State Electronics Laboratory  
1301 Beal Ave.  
Ann Arbor, MI 48109-2122  
Email: yegor@umich.edu

Christine A. Allen  
NASA / GSFC  
Code 685  
Greenbelt, MD 20771

S. Arscott  
I.E.M.N.  
Université des Sciences et Technologies de Lille  
Avenue Poincaré B.P. 69  
59652 Villeneuve D'Ascq Cedex  
France

Andrey Baryshev  
SRON-Groningen  
Landleven 12, P.O.Box 800  
9700 AV Groningen  
The Netherlands  
Email: andrey@sron.rug.nl

Dominic Benford  
NASA / GSFC  
Code 685  
Greenbelt, MD 20771  
Email: dominic.benford@gsfc.nasa.gov

Robert Bicknell-Tassius  
JPL  
4800 Oak Grove Drive  
Pasadena, CA 91109

W. L. Bishop  
University of Virginia  
Department of Electrical Engineering  
351 McCormick Road  
PO Box 400743  
Charlottesville, VA 22904-4743

Raymond Blundell  
Harvard-Smithsonian Center for Astrophysics  
60 Garden St.  
Cambridge, MA 02138  
Email: rblundell@cfa.harvard.edu

Faouzi Boussaha  
DEMIRM, Observatoire de Paris  
61, avenue de l'Observatoire  
75014 Paris France  
Email: faouzi.boussaha@obspm.fr

Jean Bruston  
JPL  
4800 Oak Grove Dr.  
Pasadena, CA 91109

B. Bumble  
JPL  
4800 Oak Grove Dr.  
Pasadena, CA 91109

Malcom Caplan  
Calabazas Creek Research, Inc.  
20937 Comer Dr.  
Saratoga, CA 95070

G. Chin  
NASA / GSFC  
Code 685  
Greenbelt, MD 20771

Carey Cates  
University of California Santa Barbara  
Quantum Institute  
Santa Barbara, CA 93106  
Email: isabel@physics.ucsb.edu

Denis Chouvaev  
MINA - Fysik 4  
Chalmers University of Technology  
SE-412 96 Göteborg  
Sweden  
Email: chouvaev@fy.chalmers.se

Prem Chahal  
12516 Audelia Rd., #1606  
Dallas, TX 75243  
Email: pchahal@raytheon.com

David H. Chow  
HRL Laboratories - RL63  
3011 Malibu Canyon Rd.  
Malibu, CA 90265  
Email: chow@hrl.com

Goutam Chattopadhyay  
Caltech  
320-47 Caltech.  
Pasadena, CA 91125  
Email: goutam@caltech.edu

Moon-Hee Chung  
DEMIRM, Observatoire de Paris  
61, avenue de l'Observatoire  
75014 Paris, France  
Email: moon-hee.chung@obspm.fr

M. Chaubet  
Centre National d'Etudes Spatiales  
18 Avenue Edouard Belin  
31401 Toulouse Cedex 4, France

Ruth Colgan  
Experimental Physics Dept.  
National University of Ireland  
Maynooth, Co. Kildare, Ireland  
Email: ruth.m.colgan@may.ie

J. Chen  
Research Institute of Electrical Communication  
Tohoku University  
Sendai 980-8577, Japan

James A. Cook  
Air Force Research Laboratory  
AFRL/SNDM BLDG 620  
2241 AVIONICS CIRCLE RM C2G69  
WRIGHT-PATTERSON AFB OH 45433-7322  
Email: James.Cook@wpafb.af.mil

Serguei Cherednichenko  
Chalmers University of Technology  
Department of Microelectronics  
Rannvagen 6  
Göteborg S-412 96, Sweden  
Email: serguei@ep.chalmers.se

K. Crady  
National Radio Astronomy Observatory  
2015 Ivy Road, Ste. 219  
Charlottesville, VA 22903

James A. Chervenak  
NIST - Boulder  
MS 814.09  
Boulder, CO 80303

Thomas W. Crowe  
University of Virginia  
Department of Electrical Engineering  
351 McCormick Road  
PO Box 400743  
Charlottesville, VA 22904-4743  
Email: twc8u@virginia.edu

H. L. Cui  
Dept. of Physics and Engineering Physics  
Stevens Institute of Technology  
Hoboken, NJ 07030  
Email: hcui@stevens-tech.edu

Marian Darula  
Institut für Schicht-und Iontentechnik  
Forschungszentrum Juelich GmbH  
52425 Juelich, Germany

C. Drouet D'Aubigny  
University of Arizona  
Steward Observatory  
933 N. Cherry Ave.  
Tucson, AZ 85721

Aaron Datesman  
Univ. of Virginia  
351 McCormick Road  
POB 400473  
Charlottesville, VA 22904  
Email: ad3d@virginia.edu

F. Dauplay  
DEMIRM  
Observatoire de Paris  
77 avenue Denfert-Rochereau  
75014 Paris, France

Thibaut David  
I.E.M.N.  
Université des Sciences et Technologies de Lille  
Avenue Poincaré B.P. 69  
59652 Villeneuve D'Ascq Cedex  
France  
Email: thibaut.david@iemn.univ-lille1.fr

Yan Delorme  
Observatoire de Paris  
61, Av de l'Observatoire  
75014 Paris, France  
Email: yan.delorme@obspm.fr

Dirk Diehl  
Radiometer Physics GmbH  
Birkenmaarstr. 10  
D-53340 Meckenheim  
Germany  
radiometer.physics@t-online.de

P. N. Dmitriev  
Institute of Radio Engineering and Electronics  
Mokhovaya 11, GSP-3  
103 907 Moscow, Russia

Yiwei Duan  
University of Virginia  
Department of Electrical Engineering  
351 McCormick Road  
PO Box 400743  
Charlottesville, VA 22904-4743

H. L. Dunlap  
HRL Laboratories, LLC  
3011 Malibu Canyon Road  
Malibu, CA 90265

Jack East  
University of Michigan  
1301 Beal Ave.  
Ann Arbor, MI 48109-2122  
Email: jeast@engin.umich.edu

Pierre M. Echternach  
JPL  
4800 Oak Grove Dr.  
Pasadena, CA 91109

Geoffrey Ediss  
National Radio Astronomy Observatory  
2015 Ivy Road, Ste. 219  
Charlottesville, VA 22903  
Email: gediss@nrao.edu

G. A. Ediss  
MPIfR-Bonn  
Auf dem Hügel 69  
53121 Bonn  
Germany

L. V. Filippenko  
Institute of Radio Engineering and Electronics  
Russian Academy of Sciences  
Mokhovaya 11  
103907 Moscow, Russia

J. E. Effland  
National Radio Astronomy Observatory  
2015 Ivy Road, Ste. 219  
Charlottesville, VA 22903

Joel Fontanella  
DeMaria ElectroOptics Systems, Inc.  
1280 Blue Hills Ave.  
Bloomfield, CT 06002

Heribert Eisele  
University of Michigan  
1301 Beal Ave.  
Ann Arbor, MI 48109-2122  
Email: heribert@engin.umich.edu

Gary Frazier  
Raytheon Electronic Systems - MS 35  
13532 North Central Expressway  
Dallas, Texas 75243  
Email: gary-frazier@raytheon.com

Andreas Eisenbach  
University of Michigan  
Solid-State Electronics Laboratory  
1301 Beal Ave.  
Ann Arbor, MI 48109-2122

Michael Frommberger  
IRAM  
Domaine Universitaire  
300, rue de la Piscine  
38406 St. Martin d'Hères, France  
Email: frommber@iram.fr

A. I. Elantiev  
Moscow State Pedagogical University  
29 M. Pirogovskaya str.  
Physical Department  
119891 Moscow, Russia

A. Fung  
JPL  
4800 Oak Grove Dr.  
Pasadena, CA 91109

Neal Erickson  
University of Massachusetts  
Radio Astronomy  
Lederle 619  
Univ. Mass.  
Amherst, MA 01003  
Email: neal@ieee.org

A. Galvanauskas  
IMRA America  
1044 Woodridge Ave.  
Ann Arbor, MI 48105

A. B. Ermakov  
Institute of Radio Engineering and Electronics  
Russian Academy of Sciences  
Mokhovaya 11  
103907 Moscow, Russia

Walter Ganzevles  
Delft University of Technology  
Dept. of Applied Physics and Delft Institute for  
Microelectronics and Submicron Technology  
(DIMES)  
Landleven 12  
9747 Av Groningen, The Netherlands  
Email: walter@sron.rug.nl

Jian-rong Gao  
DIMES  
Delft University of Technology  
Lorentzweg 1  
2628 CJ Delft  
The Netherlands  
Email: jrgao@dimes.tudelft.nl

A. J. Gatesman  
Submillimeter-Wave Technology Lab.  
University of Massachusetts  
Lowell, MA 01854

Dr. Boris Gelmont  
Thornton Hall  
Department of Electrical Engineering  
University of Virginia  
351 McCormick Road  
P. O. Box 400743  
Charlottesville, VA 22904-4743  
e-mail: gb7k@Virginia.edu

Dr. Eyal Gerecht  
Department of Physics and Astronomy  
817 LGRC  
University of Massachusetts  
Amherst, MA 01003  
gerecht@astro.umass.edu

Michael E. Gershenson  
Rutgers University  
Dept. of Physics and Astronomy  
136 Frelinghuysen Rd.  
Piscataway NJ 08854-8019  
Email: gersh@physics.rutgers.edu

E. M. Gershenzon  
Moscow State Pedagogical University  
29 M. Pirogovskaya str.  
Physical Department  
119891 Moscow, Russia

Gregory N. Gol'tsman  
Moscow State Pedagogical University  
29 M. Pirogovskaya str.  
Physical Department  
119891 Moscow, Russia  
Email: goltsman00@mail.ru

D. Gong  
Rutgers University  
Dept. of Physics and Astronomy  
136 Frelinghuysen Rd.  
Piscataway NJ 08854-8019

Art C. Gossard  
UCSB  
Materials Department  
Santa Barbara, CA 93106

Dr. Philippe Goy  
AB Millimetre  
52 Rue Lhomond  
75005 Paris, France  
Email: abmm001@attglobal.net

T. Goyette  
Submillimeter Technology Lab.  
University of Massachusetts  
Lowell, MA 01854

Dr. Urs Graf  
KOSMA  
I. Physikalisches Institut  
Universität zu Köln  
Zùlpicher Str. 77  
50937 Köln, Germany  
Email: graf@ph1.uni-koeln.de

Thijs de Graauw  
SRON  
PO Box 800  
9700 AV Groningen, NL  
thijsdg@srong.rug.nl

Zinovi S. Gribnikov  
Wayne State University  
Dept. of ECE  
Detroit, MI 48202  
Email: zinovi@ciao.eng.wayne.edu

C. Groppi  
University of Arizona  
Steward Observatory  
933 N. Cherry Ave.  
Tucson, AZ 85721

Erich N. Grossman  
NIST - Boulder  
MS 814.09  
Boulder, CO 80303

Robert Henschke  
DeMaria ElectroOptics Systems, Inc.  
1280 Blue Hills Ave.  
Bloomfield, CT 06002

Dr. Rolf Güsten  
MPIfR-Bonn  
Auf dem Hügel 69  
53121 Bonn  
Germany  
Email: rguesten@mpifr-bonn.mpg.de

Stefan Heyminck  
KOSMA  
I. Physikalisches Institut  
Universität zu Köln  
Zülpicher Str. 77  
50937 Köln, Germany

Sybille Haas  
KOSMA  
I. Physikalisches Institut  
Universität zu Köln  
Zülpicher Str. 77, D 50937 Köln, Germany

Netty Honingh  
KOSMA  
I. Physikalisches Institut  
Universität zu Köln  
Zülpicher Str. 77, D 50937 Köln, Germany

George I. Haddad  
University of Michigan  
Solid-State Electronics Laboratory  
1301 Beal Ave.  
Ann Arbor, MI 48109-2122  
Email: gih@eecs.umich.edu

N. Horner  
National Radio Astronomy Observatory  
2015 Ivy Road, Ste. 219  
Charlottesville, VA 22903

Janne Häkli  
MilliLab, Radio Laboratory  
Helsinki University of Technology  
P.O. Box 3000  
FIN-02015 HUT  
Finland

Dirk Hottgenroth  
KOSMA  
I. Physikalisches Institut  
Universität zu Köln  
Zülpicher Str. 77, D 50937 Köln, Germany

C. D. Haeussler  
HRL Laboratories, LLC  
3011 Malibu Canyon Road  
Malibu, CA 90265

Seth M. Hubbard  
University of Michigan  
Solid-State Electronics Laboratory  
1301 Beal Ave.  
Ann Arbor, MI 48109-2122  
Email: hubbard@umich.edu

Oliver Harnack  
Institut für Schicht-und Iontentechnik  
Forschungszentrum Juelich GmbH  
52425 Juelich, Germany

Dr. Heinz-Wilhelm Hübers  
German Aerospace Center (DLR)  
Institute of Space Sensor Technology and Planetary Exploration  
Rutherfordstr. 2  
12489 Berlin, Germany  
Email: heinz-wilhelm.huebers@dlr.de

Dr. Jeffrey L. Hesler  
E310 Thornton Hall  
University of Virginia  
Charlottesville, VA 22903  
Email: hesler@virginia.edu

K. Hui  
University of Virginia  
Department of Electrical Engineering  
351 McCormick Road  
PO Box 400743  
Charlottesville, VA 22904-4743

Todd R. Hunter  
Harvard-Smithsonian Center for Astrophysics  
60 Garden St.  
Cambridge, MA 02138

Konstantin Ilin  
Institut für Schicht-und Iontentechnik  
Forschungszentrum Juelich GmbH  
52425 Juelich, Germany

N. Iosad  
Dept. of Applied Physics and Delft Institute for  
Microelectronics and Submicron Technology  
(DIMES)  
Delft University of Technology  
Lorentzweg 1, 2628 CJ Delft, The Netherlands

Kent D. Irwin  
NIST - Boulder  
MS 814.09  
Boulder, CO 80303

Lawrence Ives  
Calabazas Creek Research, Inc.  
20937 Comer Dr.  
Saratoga, CA 95070

Brian D. Jackson  
SRON  
Postbus 800  
9700 AV Groningen  
The Netherlands  
Email: brian@sron.rug.nl

Dr. Karl Jacobs  
KOSMA  
I. Physikalisches Institut  
Universität zu Köln  
Zùlpicher Str. 77, D 50937 Köln, Germany  
Email: jacobs@ph1.uni-koeln.de

Ming Ji  
Dept. of Electr. and Comp. Eng.  
350 Montague Rd.  
University of Massachusetts  
Amherst, MA 01003  
mji@ecs.umass.edu

Ridha Kamoua  
SUNY at Stony Brook  
Dept. of ECE  
SUNY at Stony Brook  
Stony Brook, NY 11794-2350  
Email: ridha@ece.sunysb.edu

Boris S. Karasik  
Jet Propulsion Laboratory  
4800 Oak Grove Drive  
M/S 168-314  
Pasadena, CA 91109  
Email: Boris.S.Karasik@jpl.nasa.gov

Alexandre Karpov  
Caltech  
Downs Lab 320-47  
Pasadena, CA 91125  
Email: karpov@submm.caltech.edu

C. Kasemann  
MPIfR-Bonn  
auf dem Hügel 69  
53121 Bonn  
Germany

Linda Katehi  
University of Michigan  
2464 LEC  
Ann Arbor, MI 48109-2102  
Email: katehi@eecs.umich.edu

Jonathan Kawamura  
Caltech  
Downs Labs 320-47  
Pasadena, CA 91125  
Email: kawamura@submm.caltech.edu

Anthony R. Kerr  
National Radio Astronomy Observatory  
2015 Ivy Road, Ste. 219  
Charlottesville, VA 22903  
Email: akerr@nrao.edu

Pourya Khosropanah  
Chalmers University of Technology  
Microelectronics Department ED  
Microwave Electronics Laboratory  
412 96 Göteborg, Sweden  
E-mail: pourya@ep.chalmers.se

Ken'ichi Kikuchi  
Space Utilization Research Program,  
National Space Development Agency of Japan,  
2-1-1 Sengen Tsukuba-shi Ibaraki 305-8505,  
Japan  
Email: Kikuchi.Kenichi@nasa.go.jp

Phichet Kittara  
Dept. of Physics  
University of Cambridge  
Madingley Road  
Cambridge CB3 0HE, UK  
Email: pk201@mrao.cam.ac.uk

T. M. Klapwijk  
Dept. of Applied Physics and Delft Institute for  
Microelectronics and Submicron Technology  
(DIMES)  
Delft University of Technology  
Lorentzweg 1, 2628 CJ Delft, The Netherlands

Thomas Klein  
MPIfR-Bonn  
Auf dem Hügel 69  
53121 Bonn  
Germany  
tklein@mpifr-bonn.mpg.de

H. Kohlstedt  
Institute of Thin Film and Ion Technology (ISI)  
Research Center Juelich  
D-52425 Juelich, Germany

Erik Kollberg  
Chalmers University of Technology  
Dept. of Microelectronics  
SE-412 96 Göteborg, Sweden  
Email: kollberg@ep.chalmers.se

James Kolodzey  
University of Delaware  
Dept. of Electrical and Computer Engineering  
University of Delaware  
216 Evans Hall  
Newark, DE 19716  
Email: kolodzey@ee.udel.edu

Jacob W. Kooi  
Caltech  
MS 320-47  
Caltech  
Pasadena Ca 91125  
Email: kooi@submm.caltech.edu

Dr. P.A.J. de Korte  
Space Research Organization Netherlands  
Sorbonnelaan 2  
3584 CA UTRECHT  
the Netherlands  
Email: p.a.j.de.korte@sron.nl

Dr. Valery Koshelets  
Institute of Radio Engineering and Electronics  
Mokhovaya 11, GSP-3  
103 907 Moscow, Russia  
Email: valery@hitech.cplire.ru

Mrs. Alla G. Kovalenko  
Institute of Radio Engineering and Electronics  
Russian Academy of Sciences  
11 Mokhovaya Str.  
103907 Moscow, Russian Federation  
alla@hitech.cplire.ru

Matthias Kroug  
Chalmers University of Technology  
S-41296 Gothenburg  
Sweden  
Email: kroug@fy.chalmers.se

D. S. Kurtz  
University of Virginia  
Department of Electrical Engineering  
351 McCormick Road  
PO Box 400743  
Charlottesville, VA 22904-4743

Alexander S. Kuttyrev  
NASA / GSFC  
Code 685  
Greenbelt, MD 20771

Leonid Kuzmin  
Chalmers University of Technology  
SE-412 96 Göteborg  
Sweden

W. M. Laauwen  
Space Research Organization of the Netherlands  
Postbus 800, 9700 AV Groningen  
The Netherlands

O. Laborde  
Centre de Recherches sur les Très Basses  
Températures  
25 Avenue des Martyres  
38042 Grenoble, France

Roger Lake  
Raytheon  
PO Box 660246 MS35  
Dallas, TX 75266  
Email: r-lake@raytheon.com

Gerhard de Lange  
Space Research Organization of the Netherlands  
Landleven 12  
9747 AD Groningen  
the Netherlands  
Email: gert@sron.rug.nl

Bill Lanigan  
NUI Maynooth  
Dept. of Physics  
NUI Maynooth  
Co. Kildare, Ireland  
Email: bill.lanigan@may.ie

Bernard Lazareff  
IRAM  
300, rue de la Piscine  
38406 ST MARTIN D'HERES Cedex  
FRANCE  
Email: lazareff@iram.fr

Henry G. LeDuc  
MS 302-231  
JPL  
4800 Oak Grove Drive  
Pasadena, CA 91109  
Email: rleduc@jpl.nasa.gov

Chih-Chien Lee  
The University of Virginia  
Electrical Engineering Department  
Charlottesville, VA 22903

Mark Lee  
Bell Labs - Lucent Technologies  
Rm. 1C-360  
600 Mountain Ave.  
Murray Hill, NJ 07974  
Email: markl@lucent.com

Trong-Huang "Tracy" Lee  
JPL  
4800 Oak Grove Dr.  
Pasadena, CA 91109  
thlee@merlin.jpl.nasa.gov

Y.-S. Lee  
University of Michigan  
Center for Ultrafast Optical Science  
2200 Bonisteel Blvd  
Ann Arbor, MI 48109-2099

Jamie Leech  
Cavendish Laboratory  
University of Cambridge  
Madingley Road  
Cambridge  
CB3 0HE UK  
Email: jl200@mrao.cam.ac.uk

Bruno Leone  
University of Groningen  
Dept. of Applied Physics and Mat. Science Center  
Nijenborgh 4.13,  
9747 AG Groningen,  
The Netherlands  
Email: B.Leone@phys.rug.nl

Arto Lehto  
MilliLab, Radio Laboratory  
Helsinki University of Technology  
P.O. Box 3000  
FIN-02015 HUT  
Finland

Burt Levin  
SPC  
1000 Wilson Blvd.  
Arlington, VA 22209-2211  
Email: blevin@sysplan.com

M. Levitchev  
Institute of Thin Film and Ion Technology (ISI)  
Research Center Juelich  
D-52425 Juelich, Germany

A. W. Lichtenberger  
University of Virginia  
Charlottesville, VA 22904

D. Lippens  
I.E.M.N.  
Université des Sciences et Technologies de Lille  
Avenue Poincaré B.P. 69  
59652 Villeneuve D'Ascq Cedex  
France

Jun Liu  
Div of Engineering  
Brown University  
Providence, RI 02912

W. Luinge  
SRON-Groningen  
Landleven 12, P.O.Box 800  
9700 AV Groningen  
The Netherlands

Alain Maestrini  
JPL  
4800 Oak Grove Dr.  
Pasadena, CA 91109

Hiroyuki Maezawa  
Yamamo Group, Department of Physics  
The University of Tokyo  
7-3-1 Hongo, Bunkyo-ku, Tokyo 113-0033, Japan  
Email: maezawa@taurus.phys.s.u-tokyo.ac.jp

Bruno Maffei  
Queen Mary and Westfield College  
London E1 4NS, UK

Frank Maiwald  
JPL  
4800 Oak Grove Drive, 168-214  
Pasadena, CA 91109  
fmaiwald@mail1.jpl.nasa.gov

Kevin D. Maranowski  
UCSB  
Materials Department  
Santa Barbara, CA 93106

Steve Marazita  
Virginia Millimeter Wave, Inc.  
706 Forest St. Suite D  
Charlottesville, VA 22903  
Email: marazita@cstone.net

Suzanne Martin  
JPL  
4800 Oak Grove Dr.  
Pasadena, CA 91109

Dr. Edgar J. Martinez  
Microsystems Technology Office  
DARPA  
3701 N. Fairfax Drive  
Arlington, Va 22203  
emartinez@darpa.mil

John M. Martinis  
NIST - Boulder  
MS 814.09  
Boulder, CO 80303

F. Mattiocco  
IRAM  
Domaine Universitaire  
300, rue de la Piscine  
38406 St. Martin d'Hères, France

William R. McGrath  
JPL  
4800 Oak Grove Dr.  
Pasadena, CA 91109

Timothy F. Meade  
Center for Ultrafast Optical Science  
University of Michigan  
2200 Bonisteel Blvd., 1006 IST  
Ann Arbor, MI 48109-2099  
Email: tmeade@umich.edu

Imran Mehdi  
JPL  
4800 Oak Grove Dr.  
Pasadena, CA 91109

Harald F Merkel  
Chalmers University of Technology  
Rännvägen 6  
SE-412 96 Gothenburg  
Sweden  
Email: harald@ep.chalmers.se

X. Mélique  
I.E.M.N.  
Université des Sciences et Technologies de Lille  
Avenue Poincaré B.P. 69  
59652 Villeneuve D'Ascq Cedex  
France

David Miller  
Caltech  
Downs Laboratory of Physics  
Pasadena, CA 91125

Vladimir Mitin  
Wayne State University  
Dept. of ECE  
Detroit, MI 48202  
Email: mitin@ece6.eng.wayne.edu

F. Mollot  
I.E.M.N.  
Université des Sciences et Technologies de Lille  
Avenue Poincaré B.P. 69  
59652 Villeneuve D'Ascq Cedex  
France

S. Harvey Moseley  
NASA / GSFC  
Code 685  
Greenbelt, MD 20771

P. Mounaix  
I.E.M.N.  
Université des Sciences et Technologies de Lille  
Avenue Poincaré B.P. 69  
59652 Villeneuve D'Ascq Cedex  
France

Eric R. Mueller  
DeMaria ElectroOptics Systems, Inc.  
1280 Blue Hills Ave.  
Bloomfield, CT 06002  
Email: e.r.mueller@deoslaser.com

Jeremy Muldavin  
University of Michigan  
EECS Department  
1301 Beal Avenue  
Ann Arbor, MI 48109-2122

J. Anthony Murphy  
National University of Ireland  
Maynooth, Co. Kildare, Ireland

C. F. Musante  
Department of Electrical and Computer Eng.  
University of Massachusetts  
Amherst, MA 01003

J. Mygind  
Department of Physics  
Technical University of Denmark  
B 309, DK-2800 Lyngby, Denmark

Dr. Gopal Narayanan  
Lederle GRC  
FCRAO  
University of Massachusetts  
Amherst MA 01003  
Email: gopal@ieee.org

Alessandro Navarrini  
IRAM  
300, rue de la Piscine  
F-38406 St. Martin d' Heres  
France  
Email: navarrin@iram.fr

Jeff Neilson  
CCR, Inc.  
10 Black Fox Way  
Redwood City, CA 94062  
Email: jeff@calcreek.com

A. Neto  
JPL  
4800 Oak Grove Dr.  
Pasadena, CA 91109

Takashi Noguchi  
Nobeyama Radio Observatory  
National Astronomical Observatory of Japan  
Nobeyama, Minamisaku, Nagano  
384-1305 Japan  
Email: noguchi@nro.nao.ac.jp

Ted Norris  
University of Michigan  
Center for Ultrafast Optical Science  
2200 Bonisteel Blvd  
Ann Arbor, MI 48109-2099  
Email: tnorris@eecs.umich.edu

Peter O'Brien  
JPL  
4800 Oak Grove Drive  
Pasadena, CA 91109

Creidhe O'Sullivan  
National University of Ireland  
Maynooth, Co. Kildare, Ireland

S.-K. Pan  
National Radio Astronomy Observatory  
2015 Ivy Road, Ste. 219  
Charlottesville, VA 22903

D. Cosmo Papa  
Harvard-Smithsonian Center for Astrophysics  
60 Garden St.  
Cambridge, MA 02138

John Papapolymerou, Ph.D.  
Department of Electrical and Computer Eng.  
The University of Arizona  
1230 E. Speedway Blvd.  
Tucson, AZ 85721-0104  
Email: papapol@ece.arizona.edu<

J. R. Pardo  
Caltech  
MS 320-47  
Caltech  
Pasadena Ca 91125

Ferdinand Patt  
Submillimeter Telescope Observatory  
933 N. Cherry Ave.  
Tucson, AZ 85721

Vijay Patel  
Department of Physics  
SUNY at Stony Brook  
Stony Brook  
NY 11794-3800  
Email: Vijay.Patel@sunysb.edu

D. G. Pavel'ev  
Institute for Physics of Microstructure  
Russian Academy of Sciences  
GSP-105, 603600 Nizhny Novgorod, Russia

Dimitris Pavlidis  
University of Michigan  
Solid-State Electronics Laboratory  
1301 Beal Ave.  
Ann Arbor, MI 48109-2122

John Pearson  
Jet Propulsion Laboratory  
4800 Oak Grove Drive  
Pasadena, California 91109-8099  
M/S 183-301  
Email: jcp@spec.jpl.nasa.gov

Brian Perkins  
Div of Engineering  
Brown University  
Providence, RI 02912  
Email: Brian\_Perkins@brown.edu

V. Perlin  
University of Michigan  
Center for Ultrafast Optical Science  
2200 Bonisteel Blvd  
Ann Arbor, MI 48109-2099

Dr. Sabine D. Philipp  
Max-Planck-Institute for Radioastronomie  
Auf dem Huegel 69  
D - 53121 Bonn, Germany  
Email: sphilipp@mpifr-bonn.mpg.de

T. G. Phillips  
Caltech  
MS 320-47  
Caltech  
Pasadena Ca 91125

C. W. Pobanz  
HRL Laboratories, LLC  
3011 Malibu Canyon Road  
Malibu, CA 90265

Florence Podevin  
IEMN  
Université des Sciences et Technologies de Lille  
BP 69  
59652 VILLENEUVE D'ASCQ  
FRANCE

Email: florence.podevin@iemn.univ-lille1.fr

E. P. De Poortere  
Dept. of Electrical Engineering  
Princeton University  
Princeton, NJ 08544

Daniel E. Prober  
Yale University  
PO Box 208284  
Becton Ctr Rm 405  
15 Prospect St,  
New Haven, CT 06520-8284  
Email: daniel.prober@yale.edu

G. V. Prokopenko  
Institute of Radio Engineering and Electronics  
Russian Academy of Sciences  
Mokhovaya 11  
103907 Moscow, Russia

D. Pukala  
JPL  
4800 Oak Grove Dr.  
Pasadena, CA 91109

Antti V. Räsänen  
MilliLab, Radio Laboratory  
Helsinki University of Technology  
P.O. Box 3000  
FIN-02015 HUT  
Finland

Gabriel Rebeiz  
University of Michigan  
EECS Department  
1301 Beal Avenue  
Ann Arbor, MI 48109-2122  
Email: rebeiz@umich.edu

Carl D. Reintsema  
NIST - Boulder  
MS 814.09  
Boulder, CO 80303

Frank R. Rice  
Caltech  
Mail Code 320-47  
Pasadena, CA 91125-4700  
Email: rice@submm.caltech.edu

Jad Rizk  
University of Michigan  
EECS Dept, Rad Lab Room 3322  
1301 Beal Avenue  
Ann Arbor, MI 48109  
Email: jrizek@umich.edu

Ronald Roelfsema  
Space Research Organization Netherlands  
Landleven 12  
P.O. Box 800  
9700 AV Groningen  
The Netherlands  
R.F.B.Roelfsema@sron.rug.nl

F. Rönnung  
Chalmers University of Technology  
Department of Physics  
Göteborg S-412 96, Sweden

J. V. Rudd  
Picometrix, Inc.  
PO Box 130243  
Ann Arbor, MI 48113-0243

P. Sabon  
IRAM  
Domaine Universitaire  
300, rue de la Piscine  
38406 St. Martin d'Hères, France

Jussi Säily  
MilliLab, Radio Laboratory  
Helsinki University of Technology  
P.O. Box 3000  
FIN-02015 HUT  
Finland  
Email: jussi.saily@hut.fi

Morvan Salez  
DEMIRM  
Observatoire de Paris  
61 avenue de l'Observatoire  
75014 Paris, France  
Email: morvan.salez@obspm.fr

T. Sato  
Rutgers University  
Dept. of Physics and Astronomy  
136 Frelinghuysen Rd.  
Piscataway NJ 08854-8019

J. Scherbel  
Institut für Schicht-und Iontentechnik  
Forschungszentrum Juelich GmbH  
52425 Juelich, Germany

Erich Schlecht  
JPL  
4800 Oak Grove Dr.  
Pasadena, CA 91109  
Email: erichs@merlin.jpl.nasa.gov

M. Schicke  
IRAM  
Domaine Universitaire  
300, rue de la Piscine  
38406 St. Martin d'Hères, France

Gerhard Schoenthal  
The University of Virginia  
Semiconductor Device Lab.  
351 McCormick Road, Room C-112  
P.O. Box 400743  
Charlottesville, VA 22904-4743  
Email: gerhard@virginia.edu

Josef Schubert  
German Aerospace Center (DLR)  
Institute of Space Sensor Technology and Plane-  
tary Exploration  
Rutherfordstr. 2  
12489 Berlin, Germany

Fritz Schuermeyer  
AFRL/SNDD  
2241 Avionics Circle  
Wright Patterson AFB, OH 45433-7322  
Email: fritz.schuermeyer@wpafb.af.mil

J. N. Schulman  
MS RL 62  
HRL Laboratories, LLC  
3011 Malibu Canyon Road  
Malibu, CA 90265  
schulman@hrl.com

K. F. Schuster  
IRAM  
Domaine Universitaire  
300, rue de la Piscine  
38406 St. Martin d'Hères, France

Alex D. Semenov  
Moscow State Pedagogical University  
29 M. Pirogovskaya str.  
Physical Department  
119891 Moscow, Russia

Yutaro Sekimoto  
Nobeyama Radio Observatory  
National Astronomical Observatory of Japan  
Nobeyama, Minamisaku, Nagano  
384-1305 Japan

Andrei Sergeev  
Wayne State University  
Dept. of ECE  
Detroit, MI 48202  
sergeev@ciao.eng.wayne.edu

Richard A. Shafer  
NASA / GSFC  
Code 685  
Greenbelt, MD 20771

Wen-Lei Shan  
Purple Mountain Observatory  
2 West Beijing Road  
Nanjing 210008  
P. R. China  
Email: shawn@mwlab.pmo.ac.cn

M. Shayegan  
Dept. of Electrical Engineering  
Princeton University  
Princeton, NJ 08544

Mark Sherwin  
UCSB  
Physics Department  
Santa Barbara, CA 93106  
Email: sherwin@physics.ucsb.edu

Sheng-Cai Shi  
Purple Mountain Observatory  
2 West Beijing Road  
Nanjing 210008  
P. R. China

Dr. Sergey V. Shitov  
Institute of Radio Engineering and Electronics  
Russian Academy of Sciences  
Mokhovaya 11  
103907 Moscow, Russia  
e-mail: sergey@hitech.cplire.ru

A. M. Shtanyuk  
Institute of Applied Physics  
Russian Academy of Sciences (IAP RAS)  
603600, Nizhny Novgorod, Russia

Irfan Siddiqi  
Yale University  
Rm. 405 Becton Center  
15 Prospect Street  
New Haven, CT 06520-8284  
Email: irfan.siddiqi@yale.edu

Michael Siegel  
Institut für Schicht-und Ionentechnik  
Forschungszentrum Juelich GmbH  
52425 Juelich, Germany

Andrez Skalare  
JPL  
4800 Oak Grove Dr.  
Pasadena, CA 91109

Harry Smith  
Cavendish Laboratory  
University of Cambridge  
Madingley Road  
Cambridge  
CB3 0HE UK

Michael Smith  
Harvard-Smithsonian Center for Astrophysics  
60 Garden St.  
Cambridge, MA 02138

Peter Smith  
JPL  
4800 Oak Grove Dr.  
Pasadena, CA 91109

R. P. Smith  
JPL  
4800 Oak Grove Dr.  
Pasadena, CA 91109

J. A. Stern  
JPL  
4800 Oak Grove Dr.  
Pasadena, CA 91109

William Sutton  
University of Michigan  
Solid-State Electronics Laboratory  
1301 Beal Ave.  
Ann Arbor, MI 48109-2122  
Email: changmir@engin.umich.edu

Guang-Leng Tan  
University of Michigan  
EECS Department  
1301 Beal Avenue  
Ann Arbor, MI 48109-2122

Serey Thai  
AFRL / SNDP  
25 Electronic Pkwy  
Rome, NY 13441  
Email: thais@rl.af.mil

Sergey K. Tolpygo  
Dept. of Physics and Astronomy  
SUNY at Stony Brook  
Stony Brook, NY 11794-3800  
Email: sergey.tolpygo@sunysb.edu

C.-Y. Edward Tong  
Harvard-Smithsonian Center for Astrophysics  
60 Garden St., MS 42  
Cambridge, MA 02138  
etong@cfa.harvard.edu

N. Trappe  
Experimental Physics Dept.  
National University of Ireland  
Maynooth, Co. Kildare, Ireland

R. Tsang  
JPL  
4800 Oak Grove Dr.  
Pasadena, CA 91109

Jussi Tuovinen  
MilliLab  
VTT Information Technology  
PO Box 1202  
FIN-02044 VTT, Finland

Fawwaz Ulaby  
University of Michigan  
4080 Fleming  
Ann Arbor, MI 48109-1340  
Email: ulaby@umich.edu

A. V. Ustinov  
Physics Institute III  
University of Erlangen-Neurnberg  
D-91058 Erlangen, Germany

Nizami Vagidov  
Wayne State University  
Dept. of ECE  
Detroit, MI 48202  
nizami@besmb.eng.wayne.edu

V. L. Vaks  
Institute for Physics of Microstructure  
Russian Academy of Sciences  
GSP-105, 603600 Nizhny Novgorod, Russia

O. Vanbésien  
I.E.M.N.  
Université des Sciences et Technologies de Lille  
Avenue Poincaré B.P. 69  
59652 Villeneuve D'Ascq Cedex  
France

A. V. Veretennikov  
Institute of Solid State Physics  
Russian Academy of Sciences  
142432, Chernogolovka, Russia

Aleksandr Verevkin  
Yale University  
Dept. of Applied Physics  
15 Prospect St.  
New Haven, CT 06520  
Email: aleksandr.verevkin@yale.edu

B. M. Voronov  
German Aerospace Center (DLR)  
Institute of Space Sensor Technology and Planetary Exploration  
Rutherfordstr. 2  
12489 Berlin, Germany

Prof. A.N. Vystavkin  
Institute of Radio Engineering and Electronics  
Russian Academy of Sciences  
11 Mokhovaya Str.  
103907 Moscow, Russian Federation  
vyst@hitech.cplire.ru

J. Waldman  
Submillimeter-Wave Technology Lab.  
University of Massachusetts  
Lowell, MA 01854

Christopher K. Walker  
University of Arizona  
Steward Observatory  
933 N. Cherry Ave.  
Tucson, AZ 85721  
Email: cwalker@as.arizona.edu

John Ward  
Caltech  
Mail Code 320-47  
Pasadena, CA 91125  
Email: ward@submm.caltech.edu

M. Warmuth  
Picometrix, Inc.  
PO Box 130243  
Ann Arbor, MI 48113-0243

Wolfgang Wild  
NOVA/SRON  
P.O. Box 800  
9728 WJ Groningen  
The Netherlands  
Email: wild@astro.rug.nl

Jon B. Williams  
UCSB  
Physics Department  
Santa Barbara, CA 93106

Danny Wilms-Floet  
Delft University of Technology  
Nijenborgh 4  
9747 AG  
Groningen, The Netherlands  
Email: wilms@phys.rug.nl

Herb Winful  
University of Michigan  
Center for Ultrafast Optical Science  
2200 Bonisteel Blvd  
Ann Arbor, MI 48109-2099

D. Winkler  
Chalmers University of Technology  
Department of Physics  
Göteborg S-412 96, Sweden

Stafford Withington  
Cavendish Laboratory  
University of Cambridge  
Madingley Road  
Cambridge  
CB3 0HE UK

Dr. Dwight Woolard  
U.S. ARL/ARO  
P.O. Box 12211  
RTP, NC 27709  
Email: woolardd@aro-emh1.army.mil

Stephan Wulff  
KOSMA  
I. Physikalisches Institut  
Universität zu Köln  
Zùlpicher Str. 77, D 50937 Köln, Germany

Richard Wylde  
Queen Mary and Westfield College  
London E1 4NS, UK

Rolf Wyss  
JPL  
4800 Oak Grove Dr.  
Pasadena, CA 91109

K.-C. Xiao  
Nagoya University  
Japan

Dr. Pavel Yagoubov  
SR&T Division  
Space Research Organization of the Netherlands  
Landleven 12  
9747 AD Groningen  
the Netherlands  
e-mail: P.A.Yagoubov@sron.rug.nl

Satoshi Yamamoto  
Department of Physics  
The University of Tokyo  
7-3-1 Hongo, Bunkyo-ku, Tokyo 113-0033, Japan

Ghassan Yassin  
Cavendish Laboratory  
University of Cambridge  
Madingley Road  
Cambridge  
CB3 0HE UK  
Email: ghassan@mrao.cam.ac.uk

K. Sigfrid Yngvesson  
Department of Electrical and Computer Eng.  
University of Massachusetts  
Amherst, MA 01003  
Email: yngvesson@ep.chalmers.se

A. Zaslavsky  
Div of Engineering  
Brown University  
Providence, RI 02912

Peiji Zhao  
Dept. of Physics and Engineering Physics  
Stevens Institute of Technology  
Hoboken, NJ 07030

Yan Zhuang  
990 N. Pleasant St.  
Apt. C12  
Amherst, MA 01002  
yzhuang@ecs.umass.edu

David Zimdars  
Picometrix, Inc.  
2901 Hubbard Rd.  
Ann Arbor, MI 48105  
Email: dzimdars@picometrix.com

R. Zimmerman  
Radiometer Physics GmbH  
Birkenmaarstr. 10  
D-53340 Meckenheim  
Germany

Jonas Zmuidzinis  
Caltech  
MS 320-47  
Pasadena, CA 91125